Transactions of the ASME

Transactions of the ASME, Journal of Heat Transfer (ISSN 0022-1481) is published quarterly (Feb., May, Aug., Nov.) for $150 per year by The American Society of Mechanical Engineers, 345 East 47th Street, New York, NY 10017. Second class postage paid at New York, NY and additional mailing offices. POSTMASTER: Send address changes to The Journal of Heat Transfer, c/o THE AMERICAN SOCIETY OF MECHANICAL ENGINEERS, 22 Law Drive, Box 2300, Fairfield, NJ 07007-2300.
CHANGES OF ADDRESS must be received at Society headquarters seven weeks before they are to be effective. Please send old label and new address.
PRICES: To members, $24.00, annually; to nonmembers, $150.00.
Add $6.00 for postage to countries outside the United States and Canada.
STATEMENT from By-Laws. The Society shall not be responsible for statements or opinions advanced in papers or . . . printed in its publications (B7.1, para. 3).

INDEXED by Engineering Information

Journal of Heat Transfer

Published Quarterly by The American Society of Mechanical Engineers

VOLUME 108 • NUMBER 4 • NOVEMBER 1986

ANNOUNCEMENTS

TECHNICAL PAPERS

(Contents continued)

TECHNICAL NOTES

Analytical Solution of the Transient Response of Gas-to-Gas Crossflow Heat Exchanger With Both Fluids Unmixed

D. D. Gvozdenac
Institute of Fluid, Thermal, and Chemical Engineering, University of Novi Sad, Novi Sad, Yugoslavia

The dynamic response of a single-pass crossflow heat exchanger with both fluids unmixed to arbitrary time varying inlet temperatures of fluids is investigated analytically. The initial spatial temperature distribution of the heat exchanger core is arbitrary as well. Analytical solutions for temperature distributions of both fluids and the wall as well as the mean mixed fluid temperatures at the exit are presented. The solutions are found by using Laplace transform method and special functions in the form of series of modified Bessel functions.

Introduction

Problems related to the transient response of a single-pass crossflow heat exchanger with neither fluid mixed are of increasing interest. In the case where engineering devices such as compact-type heat exchangers form a part of the engineering plant like aircraft gas turbines, process plants, and air-conditioning systems, it is important to study dynamic behavior of a heat exchanger in order to choose the most suitable design, control, and operation.

Several investigations of heat exchanger transients have been carried out. However, the transient response of crossflow heat exchangers has received very little attention owing to its complexity. The transient behavior of a crossflow heat exchanger with neither fluid mixed was determined numerically by Dusinberre [1]. Only one specific case for a gas-to-gas heat exchanger was considered and no parametric study was attempted. Myers et al. [2] carried out a study concerning a crossflow heat exchanger, but they analyzed only the case of one mixed fluid. They used an approximate integral technique to compute outlet fluid temperatures for a unit step increase of the mixed fluid inlet temperature. Their solution is generally satisfactory if both fluids are gases. Yamashita et al. [3] applied finite difference methods to calculate the outlet temperature responses for crossflow heat exchangers with both fluids unmixed. Effects of an initial condition and various parameters concerning heat transfer performance on the transient responses in the temperature efficiency were shown. Makarov [4] presented analytical solutions to the transient response of gas-to-gas crossflow heat exchangers with neither gas mixed by using Rieman's method. These solutions apply to the case of a heat exchanger with uniform initial temperature as well as to arbitrary varying inlet gas temperatures. However, analysis and applicability of the solutions were not even attempted. Romie [5] gives the transient mixed temperatures of the gases leaving a crossflow heat exchanger for a unit step increase in the entrance temperature of either gas. Solutions are found by using the Laplace transform method and they apply to single-pass crossflow heat exchangers with neither gas mixed.

This paper presents solutions to the energy equations governing convective heat transfer between a heat exchanger core, which is initially at an arbitrary spatial temperature distribution, and a steady flow of fluids entering the exchanger at constant mass velocities with arbitrary time varying temperatures. Solutions are restricted to the case when thermal capacities of the masses of two fluids contained in the exchanger are negligibly small relative to the thermal capacity of the heat exchanger core. They are found by using the Laplace transform method, which leads to an extensive use of special functions in the form of series of modified Bessel functions.

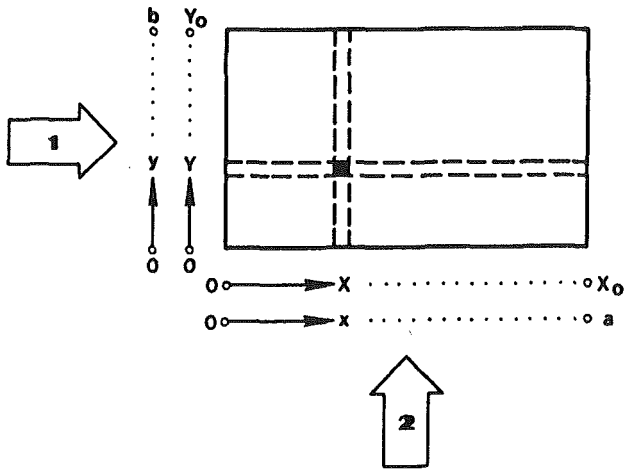

Fig. 1 Schematic description of single-pass crossflow heat exchanger

Availability of such solutions gives the engineer and the designer much more insight into the nature of transient heat transfer in single-pass crossflow heat exchangers with neither fluid mixed.

Basic Differential Equations. Inlet and Initial Conditions

The simplifying assumptions in the derivation of differential equations are as follows:

(*a*) Heat transfer characteristics and physical properties are independent of temperature, position and time;
(*b*) the fluid velocity is constant in each flow passage;
(*c*) the thickness of a solid wall is sufficiently small in comparison with the dimensions of the heat exchanger surface, so it is assumed that heat flows only in the direction perpendicular to the heat exchanger surface;
(*d*) conduction through the fluid is negligible;
(*e*) overall heat losses are negligible;
(*f*) the heat generation and viscous dissipation within the fluids are negligible.

Under what conditions and to what extent these assumptions are justified can be determined either by experiment or by some other theoretical analysis. An inquiry into the practical applications of the theory will not be made in this paper,

Contributed by the Heat Transfer Division for publication in the JOURNAL OF HEAT TRANSFER. Manuscript received by the Heat Transfer Division March 26, 1985.

the main purpose being to present the mathematical treatment of the problem.

On the basis of these assumptions and applying the energy equation to both fluids and the wall, we obtain three simultaneous partial differential equations in the coordinate system as shown in Fig. 1

$$-c_{p1}\dot{m}_1 X_0\left(\frac{\partial T_1}{\partial X}+\frac{1}{U_1}\frac{\partial T_1}{\partial t}\right)=\eta_1 h_1 A_{1T}(T_1-T_w) \tag{1}$$

$$c_{p2}\dot{m}_2 Y_0\left(\frac{\partial T_2}{\partial Y}+\frac{1}{U_2}\frac{\partial T_2}{\partial t}\right)=\eta_2 h_2 A_{2T}(T_w-T_2) \tag{2}$$

$$c_w M_w\frac{\partial T_w}{\partial t}=\eta_1 h_1 A_{1T}(T_1-T_w)-\eta_2 h_2 A_{2T}(T_W-T_2) \tag{3}$$

The space and time-independent variables, X, Y, and t, range from 0 to the heat exchanger lengths X_0 and Y_0, and from 0 to ∞, respectively. Other symbols are listed in the Nomenclature.

Introducing thus the dimensionless space and time-independent variables

$$x=\frac{X}{X_0}\text{NTU}\frac{W_{\min}}{W_1};\qquad y=\frac{Y}{Y_0}\text{NTU}\frac{W_{\min}}{W_2};\qquad z=\frac{t}{t^*} \tag{4}$$

and parameters

$$\text{NTU}=\frac{(\eta_1 h_1 A_{1T})(\eta_2 h_2 A_{2T})}{\eta_1 h_1 A_{1T}+\eta_2 h_2 A_{2T}}\frac{1}{W_{\min}} \tag{5}$$

$$t^*=\frac{c_w M_w}{\eta_1 h_1 A_{1T}+\eta_2 h_2 A_{2T}} \tag{6}$$

$$K_1=\frac{\eta_1 h_1 A_{1T}}{\eta_1 h_1 A_{1T}+\eta_2 h_2 A_{2T}};\qquad K_2=1-K_1 \tag{7}$$

$$C_1=X_0\frac{W_1}{c_w M_w}\frac{1}{U_1}\frac{1}{K_1};\qquad C_2=Y_0\frac{W_2}{c_w M_w}\frac{1}{U_2}\frac{1}{K_2} \tag{8}$$

the governing equations read as follows

$$-K_2\frac{\partial T_1}{\partial x}-C_1\frac{\partial T_1}{\partial z}=T_1-T_w \tag{9}$$

$$K_1\frac{\partial T_2}{\partial y}+C_2\frac{\partial T_2}{\partial z}=T_w-T_2 \tag{10}$$

$$\frac{\partial T_w}{\partial z}=K_1(T_1-T_w)-K_2(T_w-T_2) \tag{11}$$

The inlet and initial conditions for equations (9), (10), and (11) are

$$\left.\begin{aligned} T_1'(y,z)&=T_1\ (0,y,z)\\ T_2'(x,z)&=T_2\ (x,0,z)\\ T_{1,0}(x,y)&=T_1\ (x,y,0)\\ T_{2,0}(x,y)&=T_2\ (x,y,0)\\ T_{w,0}(x,y)&=T_w\ (x,y,0)\end{aligned}\right\} \tag{12}$$

The above model equations describe adequately the dynamic behavior of single-pass crossflow heat exchanger with both fluids unmixed at an arbitrary time varying inlet fluid temperatures. This model is not limited to the large wall capacitance condition.

Characteristics of the system (9), (10), and (11) are the lines $x=\text{const}$ and $y=\text{const}$ as well as the space $z-C_1 x/K_2-C_2 y/K_1=\text{const}$, so that the occurrence of traveling waves can be expected at speeds K_2/C_1 and K_1/C_2, in the planes z, x and z, y, respectively, corresponding to speeds U_1 and U_2 in the physical planes t, X and t, Y. No waves are allowed for C_1 and $C_2=0$.

If the thermal capacities of the masses of the two fluids contained in the exchanger core are negligibly small relative to the thermal capacity of the core itself, then the capacity ratios C_1 and C_2 will be equated to zero. These ratios are very small if the fluids are gases. The smallness of the capacity ratios means that the fluid transit or dwell times are small compared to the

Nomenclature

A_{1T}, A_{2T} = total heat transfer area on side 1 and side 2, respectively, m^2
a, b = arguments, defined in equation (33)
c_p = specific heat at constant pressure, J/kgK
c_w = specific heat of core material, J/kgK
F, G, H = functions defined in equations (20), (21), and (22), respectively
h = heat transfer coefficient between the fluid and the wall, W/Km^2
$I_n(\cdot)$ = modified Bessel function of nth (integer) order
$\dot{m}$ = mass flow rate, kg/s
M_w = mass of exchanger core, kg
NTU = number of transfer units, defined in (5)
p, r = Laplace transform variables
T = temperature, K
t = time, s
t^* = parameter, defined in equation (6), s
K_1, K_2 = parameters, defined in equation (7)
C_1, C_2 = parameters, defined in equation (8)
U = fluid velocity, m/s
W = thermal capacity rate $=\dot{m}\ c_p$, W/K
$W_{\min}$ = lesser of W_1 and W_2, W/K
u, v, w = dummy variables
V_n = function defined in equation (31)
$V_{k,0}$ = function defined in equation (30)
X, Y = distance from fluids 1 and 2 entrances, respectively, m
X_0, Y_0 = heat exchanger lengths, m
x, y, z = dimensionless independent variables, defined in equation (4)
η = overall finned surface efficiency
ρ = density, kg/m^3
δ = Dirac delta function
ϕ = inlet temperature distribution, defined in equation (14)
ψ = initial temperature distribution, defined in equation (14)
θ = dimensionless temperature, defined in equation (15)
$\bar{\theta}$ = dimensionless mean mixed fluid temperature at the exit
β, γ = parameters
ξ, η = dummy variables

Subscripts

1 = fluid 1
2 = fluid 2
w = wall
i, j, k, n = integers

Superscripts

$'$ = at the inlet
$''$ = at the outlet
$\tilde{}$ = Laplace transform with respect to the variable x
$\hat{}$ = Laplace transform with respect to the variable y

duration of the transient. It can be easily seen from equations (9) and (10) that, in such a case, the initial temperatures $T_{1,0}$ and $T_{2,0}$ do not affect T_i ($i=1, 2, w$) since the time derivatives of the fluid temperatures are canceled.

Taking these simplifications ($C_1=C_2=0$) into account and introducing the dimensionless temperatures θ_i ($i=1, 2, w$), we obtain the mathematical model of the considered single-pass crossflow heat exchanger in the form of the following set of differential equations

$$\left.\begin{aligned} -K_2\frac{\partial\theta_1}{\partial x}&=\theta_1-\theta_w \\ K_1\frac{\partial\theta_2}{\partial y}&=\theta_w-\theta_2 \\ \frac{\partial\theta_w}{\partial z}&=K_1(\theta_1-\theta_w)-K_2(\theta_w-\theta_2) \end{aligned}\right\} \tag{13}$$

The inlet and initial conditions associated with this set of equations are as follows

$$\left.\begin{aligned} \theta_1'&=\theta_1(0, y, z)=\phi_1(y, z) \\ \theta_2'&=\theta_2(x, 0, z)=\phi_2(x, z) \\ \theta_{w,0}&=\theta_w(x, y, 0)=\psi_w(x, y) \end{aligned}\right\} \tag{14}$$

In order to define dimensionless temperatures, it is appropriate to choose a reference temperature T_r and a characteristic temperature difference ΔT_r, so that

$$\theta_i(x, y, z)=\frac{T_i(x, y, z)-T_r}{\Delta T_r} \qquad (i=1, 2, w) \tag{15}$$

The three equations (13) containing θ_1, θ_2, and θ_w can be transformed into three equations containing only θ_1 or θ_2 or θ_w. The following results are obtained

$$\frac{\partial^3\theta_i}{\partial x\partial y\partial z}+\frac{\partial^2\theta_i}{\partial x\partial y}+\frac{1}{K_1}\frac{\partial^2\theta_i}{\partial x\partial z}+\frac{1}{K_2}\frac{\partial^2\theta_i}{\partial y\partial z}+\frac{\partial\theta_i}{\partial x}+\frac{\partial\theta_i}{\partial y}+\frac{1}{K_1K_2}\frac{\partial\theta_i}{\partial z}=0 \qquad (i=1, 2, w) \tag{16}$$

This equation can be rewritten in the following forms

$$\frac{\partial}{\partial x}\left(\frac{\partial^2\theta_i}{\partial y\partial z}+\frac{\partial\theta_i}{\partial y}+\frac{1}{K_1}\frac{\partial\theta_i}{\partial z}+\theta_i\right)+\frac{1}{K_2}\frac{\partial^2\theta_i}{\partial y\partial z}+\frac{\partial\theta_i}{\partial y}+\frac{1}{K_1K_2}\frac{\partial\theta_i}{\partial z}=0 \tag{17}$$

or

$$\frac{\partial}{\partial y}\left(\frac{\partial^2\theta_i}{\partial x\partial z}+\frac{\partial\theta_i}{\partial x}+\frac{1}{K_2}\frac{\partial\theta_i}{\partial z}+\theta_i\right)+\frac{1}{K_1}\frac{\partial^2\theta_i}{\partial x\partial z}+\frac{\partial\theta_i}{\partial x}+\frac{1}{K_1K_2}\frac{\partial\theta_i}{\partial z}=0 \tag{18}$$

or

$$\frac{\partial^2}{\partial x\partial y}\left(\frac{\partial\theta_i}{\partial z}+\theta_i\right)+\frac{1}{K_1}\frac{\partial^2\theta_i}{\partial x\partial z}+\frac{1}{K_2}\frac{\partial^2\theta_i}{\partial y\partial z}+\frac{\partial\theta_i}{\partial x}+\frac{\partial\theta_i}{\partial y}+\frac{1}{K_1K_2}\frac{\partial\theta_i}{\partial z}=0 \tag{19}$$

Equation (16) will be solved using the double Laplace transform (with respect to the variable x and y) but to achieve this, the following functions will be defined

$$F_i(y, z)=\theta_i(0, y, z)+\frac{1}{K_1}\frac{\partial\theta_i(0, y, z)}{\partial z}+\frac{\partial\theta_i(0, y, z)}{\partial y}+\frac{\partial^2\theta_i(0, y, z)}{\partial y\,\partial z} \tag{20}$$

$$G_i(x, z)=\theta_i(x, 0, z)+\frac{1}{K_2}\frac{\partial\theta_i(x, 0, z)}{\partial z}+\frac{\partial\theta_i(x, 0, z)}{\partial x}+\frac{\partial^2\theta_i(x, 0, z)}{\partial x\partial z} \tag{21}$$

$$H_i(z)=\theta_i(0, 0, z)+\frac{\partial\theta_i(0, 0, z)}{\partial z} \tag{22}$$

These are now boundary conditions for equation (16). Connection with the original boundary (inlet) conditions can be found easily.

The initial condition applicable to equation (16) is as follows

$$\psi_i(x, y)=\theta_i(x, y, 0) \tag{23}$$

Using equation (14) as well as equation (13) the inlet and initial conditions for each fluid and the wall become

Fluid 1

$$\left.\begin{aligned} F_1(y, z)&=\phi_1(y, z)+\frac{1}{K_1}\frac{\partial\phi_1(y, z)}{\partial z}+\frac{\partial\phi_1(y, z)}{\partial y}+\frac{\partial^2\phi_1(y, z)}{\partial y\partial z} \\ G_1(x, z)&=\phi_2(x, z) \\ H_1(z)&=\phi_1(0, z)+\frac{\partial\phi_1(0, z)}{\partial z} \\ \psi_1(x, y)&=\phi_1(y, 0)\exp\left(-\frac{x}{K_2}\right)+\frac{1}{K_2}\int_0^x\psi_w(u, y)\exp\left(-\frac{x-u}{K_2}\right)du \end{aligned}\right\} \tag{24}$$

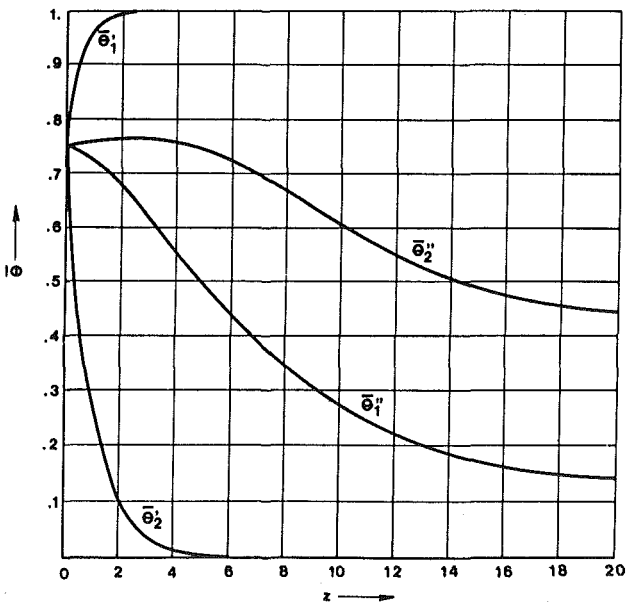

Fig. 2 Inlet and outlet mean mixed temperatures versus dimensionless time z for NTU = 4, $W_1/W_2=0.5$, $K_1=0.25$, $\beta=0.75$, $\gamma_1=2$, and $\gamma_2=1$

Wall

$$\left.\begin{aligned} F_w(y, z) &= \phi_1(y, z) + K_1 \frac{\partial \phi_1(y, z)}{\partial y} \\ G_w(x, z) &= \phi_2(x, z) + K_2 \frac{\partial \phi_2(x, z)}{\partial x} \\ H_w(z) &= K_1 \phi_1(0, z) + K_2 \phi_2(0, z) \\ \psi_w(x, y) &= \psi_w(x, y) \end{aligned}\right\} \quad (25)$$

Fluid 2

$$\left.\begin{aligned} F_2(y, z) &= \phi_1(y, z) \\ G_2(x, z) &= \phi_2(x, z) + \frac{1}{K_2}\frac{\partial \phi_2(x, z)}{\partial z} \\ &\quad + \frac{\partial \phi_2(x, z)}{\partial x} + \frac{\partial^2 \phi_2(x, z)}{\partial x\, \partial z} \\ H_2(z) &= \phi_2(0, z) + \frac{\partial \phi_2(0, z)}{\partial z} \\ \psi_2(x, y) &= \phi_2(x, 0)\exp\left(-\frac{y}{K_1}\right) \\ &\quad + \frac{1}{K_1}\int_0^y \psi_w(x, v)\exp\left(-\frac{y-v}{K_1}\right) dv \end{aligned}\right\} \quad (26)$$

Analytical Solutions

Equation (16) will be solved using the double Laplace transform. Laplace transforms of the function $\theta_i(x, y, z)$ $(i=1, 2, w)$ with respect to the variable x using p as the Laplace transform parameter can be represented by $\tilde{\theta}_i(p, y, z)$ and with respect to the variable y using r as the parameter, they can be represented by $\hat{\theta}_i(x, r, z)$. Taking the Laplace transform $\hat{\tilde{\theta}}_i(p, r, z)$ of equation (16), one obtains

$$\frac{d\hat{\tilde{\theta}}_i}{dz} + \frac{p+pr+r}{(p+1/K_2)(r+1/K_1)}\hat{\tilde{\theta}}_i = \frac{\hat{F}_i + \tilde{G}_i + H_i}{(p+1/K_2)(r+1/K_1)} \quad (27)$$

Equation (27) is a linear differential equation with respect to the variable z. This equation integrates to

$$\begin{aligned} \hat{\tilde{\theta}}_i(p, r, z) &= \hat{\tilde{\theta}}_i(p, r, 0)\exp\left(-\frac{pK_2}{pK_2+1}K_1 z\right) \\ &\quad \cdot \exp\left(-\frac{rK_1}{rK_1+1}K_2 z\right) \\ &\quad + K_1K_2\int_0^z \frac{\hat{F}_i(r, w) + \tilde{G}_i(p, w) + H_i(w)}{(pK_2+1)(rK_1+1)} \\ &\quad \cdot \exp\left[-\frac{pK_2}{pK_2+1}K_1(z-w)\right]\cdot\exp\left[-\frac{rK_1}{rK_1+1}K_2(z-w)\right] dw \end{aligned} \quad (28)$$

from which, by convolution theorem

$$\begin{aligned} \theta_i(x, y, z) &= \frac{1}{K_1K_2}\int_0^x\int_0^y \psi_i(u, v)\left[\delta\left(\frac{x-u}{K_2}\right)\exp(-K_1 z)\right. \\ &\quad \left. + V_{2,0}\left(\frac{x-u}{K_2}, K_1 z\right)\right]\cdot\left[\delta\left(\frac{y-v}{K_1}\right)\exp(-K_2 z)\right. \\ &\quad \left. + V_{2,0}\left(\frac{y-v}{K_1}, K_2 z\right)\right] du\, dv + \int_0^z\int_0^y F_i(v, w) \\ &\quad \cdot V_{1,0}\left[\frac{x}{K_2}, K_1(z-w)\right] V_{1,0}\left[\frac{y-v}{K_1}, K_2(z-w)\right] dv\, dw \\ &\quad + \int_0^z\int_0^x G_i(u, w) V_{1,0}\left[\frac{x-u}{K_2}, K_1(z-w)\right] \\ &\quad \cdot V_{1,0}\left[\frac{y}{K_1}, K_2(z-w)\right] du\, dw + \int_0^z H_i(w) \\ &\quad \cdot V_{1,0}\left[\frac{x}{K_2}, K_1(z-w)\right] V_{1,0}\left[\frac{y}{K_1}, K_2(z-w)\right] dw \end{aligned} \quad (29)$$

where u, v, and w are dummy variables of the independent variables x, y, and z, respectively.

$V_{k,0}(\xi, \eta)$ and $V_n(\xi, \eta)$ $(k, n=1, 2, 3, \ldots)$, functions appearing in equation (29) and later, can be expressed in the form of series of modified Bessel functions as described below [7]

$$V_{k,0}(\xi, \eta) = \exp(-\xi-\eta)\left(\frac{\eta}{\xi}\right)^{\frac{k-1}{2}} I_{k-1}(2\sqrt{\xi\eta}) \quad (30)$$

$$V_n(\xi, \eta) = \sum_{k=n-1}^{\infty}\binom{k}{n-1} V_{k+1,0}(\xi, \eta) \quad (31)$$

Some other relations for the functions $V_{k,0}$ and V_n are given in [6, 8].

The temperatures $\theta_i(x, y, z)$ $(i=1, 2, w)$ are contributed by the time decay of the initial condition plus a weighted average of the inlet conditions history.

Solutions are, therefore, completely determined in a closed analytical form. It can be noted here that the solutions technique given in this paper allows for simultaneous arbitrary forcing at both inlets of the single pass crossflow heat exchanger.

Knowing the temperature fields, equation (29), the mean mixed outlet temperatures are calculated according to

$$\left.\begin{aligned} \bar{\theta}_1''(z) &= \frac{1}{b}\int_0^b \theta_1(a, y, z) dy \\ \bar{\theta}_2''(z) &= \frac{1}{a}\int_0^a \theta_2(x, b, z) dx \end{aligned}\right\} \quad (32)$$

where

$$a = \mathrm{NTU}\frac{W_{\min}}{W_1}; \qquad b = \mathrm{NTU}\frac{W_{\min}}{W_2} \quad (33)$$

Calculation Results

The purpose of this work was to provide an exact analytical solution by which performances of the single-pass crossflow heat exchanger can be evaluated and compared. Because many parameters are involved in the temperature distributions of fluids and the wall as well as the mean outlet temperatures of each fluid, it is virtually impossible to present quantitative influence of all of these parameters in this paper. However, there is enough space here to give only one particular result showing the main characteristics of solution.

For the case of constant initial temperature of the wall and for inlet conditions given by exponential functions, i.e.

$$\theta_1(0, y, z)=\phi_1(y, z)=\begin{cases}1-(1-\beta)\exp(-\gamma_1 z) & \text{for } z\geq 0\\ \beta & \text{for } z<0\end{cases}$$

$$\theta_w(x, y, 0)=\psi_w(x, y)=\beta$$

$$\theta_2(x, 0, z)=\phi_2(x, z)=\begin{cases}\beta\exp(-\gamma_2 z) & \text{for } z\geq 0\\ \beta & \text{for } z<0\end{cases} \qquad (34)$$

equations (24)-(26) are reduced to

$$F_1(y, z)=1-\left(1-\frac{\gamma_1}{K_1}\right)(1-\beta)\exp(-\gamma_1 z)$$

$$F_2(y, z)=F_w(y, z)=1-(1-\beta)\exp(-\gamma_1 z)$$

$$G_1(x, z)=G_w(x, z)=\beta\exp(-\gamma_2 z)$$

$$G_2(x, z)=\left(1-\frac{\gamma_2}{K_2}\right)\beta\exp(-\gamma_2 z) \qquad (35)$$

$$H_1(z)=1-(1-\gamma_1)(1-\beta)\exp(-\gamma_1 z)$$

$$H_w(z)=K_1[1-(1-\beta)\exp(-\gamma_1 z)]+K_2\beta\exp(-\gamma_2 z)$$

$$H_2(z)=(1-\gamma_2)\beta\exp(-\gamma_2 z)$$

$$\psi_1(x, y)=\psi_w(x, y)=\psi_2(x, y)=\beta$$

Temperature fields are given by the equation

$$\theta_i=\sum_{j=1}^{4} f_{ji} \qquad (i=1, 2, w) \qquad (36)$$

where

$$f_{11}=f_{1w}=f_{12}=\beta V_1\left(K_1 z, \frac{x}{K_2}\right)V_1\left(K_2 z, \frac{y}{K_1}\right)$$

$$f_{2i}=K_1\int_0^z F_i(w)\,V_{1,0}\left[\frac{x}{K_2}, K_1(z-w)\right]\cdot\left\{1-V_1\left[\frac{y}{K_1}, K_2(z-w)\right]\right\}dw$$

$$f_{3i}=K_2\int_0^z G_i(w)\left\{1-V_{1,0}\left[\frac{x}{K_2}, K_1(z-w)\right]\right\}\cdot V_{1,0}\left[\frac{y}{K_1}, K_2(z-w)\right]dw$$

$$f_{4i}=\int_0^z H_i(w)\,V_{1,0}\left[\frac{x}{K_2}, K_1(z-w)\right]\cdot V_{1,0}\left[\frac{y}{K_1}, K_2(z-w)\right]dw \qquad (37)$$

The mean mixed outlet temperatures are calculated according to equation (32). This procedure yields

$$\bar{\theta}_i''=\sum_{j=1}^{4}\bar{f}_{ji} \qquad (i=1, 2) \qquad (38)$$

where

$$\bar{f}_{11}=\frac{\beta K_1}{b}V_1(K_1 z, \frac{a}{K_2})V_2\left(K_2 z, \frac{b}{K_1}\right)$$

$$\bar{f}_{21}=\frac{K_1^2}{b}\int_0^z F_1(w)\cdot V_{1,0}\left[\frac{a}{K_2}, K_1(z-w)\right]\left\{\frac{b}{K_1}-1-K_2(z-w)+V_1\left[\frac{b}{K_1}, K_2(z-w)\right]+V_2\left[\frac{b}{K_1}, K_2(z-w)\right]\right\}dw$$

$$\bar{f}_{31}=\frac{K_1 K_2}{b}\int_0^z G_1(w)\left\{1-V_1\left[\frac{a}{K_2}, K_1(z-w)\right]\right\}\cdot\left\{1-V_1\left[\frac{b}{K_1}, K_2(z-w)\right]\right\}$$

$$\bar{f}_{41}=\frac{K_1}{b}\int_0^z H_1(w)V_{1,0}\left[\frac{a}{K_2}, K_1(z-w)\right]\cdot\left\{1-V_1\left[\frac{b}{K_1}, K_2(z-w)\right]\right\}dw$$

$$\bar{f}_{12}=\frac{\beta K_2}{a}V_2(K_1 z, \frac{a}{K_2})V_1\left(K_2 z, \frac{b}{K_1}\right)$$

$$\bar{f}_{22}=\frac{K_1 K_2}{a}\int_0^z F_2(w)\left\{1-V_1\left[\frac{a}{K_2}, K_1(z-w)\right]\right\}\cdot\left\{1-V_1\left[\frac{b}{K_1}, K_2(z-w)\right]\right\}dw$$

$$\bar{f}_{32}=\frac{K_2^2}{a}\int_0^z G_2(w)\left\{\frac{a}{K_2}-K_1(z-w)-1+V_1\left[\frac{a}{K_2}, K_1(z-w)\right]+V_2\left[\frac{a}{K_2}, K_1(z-w)\right]\right\}\cdot V_{1,0}\left[\frac{b}{K_1}, K_2(z-w)\right]dw$$

$$\bar{f}_{42}=\frac{K_2}{a}\int_0^z H_2(w)\left\{1-V_1\left[\frac{a}{K_2}, K_1(z-w)\right]\right\}\cdot V_{1,0}\left[\frac{b}{K_1}, K_2(z-w)\right]dw \qquad (39)$$

Figure 2 shows inlet and outlet mixed fluid temperatures versus dimensionless time z. In this case, steady-state values are $\bar{\theta}_1''(z\to\infty)=0.130313$ and $\bar{\theta}_1''(z\to\infty)=0.434844$.

Concluding Remarks

The exact and explicit formulas of the temperature fields and outlet temperatures for the single-pass crossflow heat exchanger with both fluids unmixed are presented in this paper. Examination of these solutions reveals that they may be used

effectively in practice for computer-aided design, control, and operation procedures.

Acknowledgements

This work was performed as a part of the research supported under SIZ NR SAP Vojvodine Contract No. 01-804/4 for 1983.

References

1 Dusinberre, G. M., "Calculation of Transients in a Cross-Flow Heat Exchanger," ASME JOURNAL OF HEAT TRANSFER, Vol. 81, 1959, pp. 61–67.

2 Myers, G. E., Mitchell, J. W., and Norman, R. F., "The Transient Response of Crossflow Heat Exchangers, Evaporators, and Condensers," ASME JOURNAL OF HEAT TRANSFER, Vol. 89, 1967, pp. 75–80.

3 Yamashita, H., Izumi, R., and Yamaguchi, S., "Analysis of the Dynamic Characteristics of Cross-flow Heat Exchangers With Both Fluids Unmixed," *JSME Bulletin*, Vol. 21, 1978, pp. 479–485.

4 Makarov, B. A., "Integrirovanie uravnenij dinamiki perekrestnotochnogo teploobmennika s gazovymi teplonositelyami" (Solution of Dynamic Equations of Gas-to-Gas Crossflow Heat Exchanger), *Tr. MVTU*, No. 296, 1979, pp. 32–39.

5 Romie, F. E., "Transient Response of Gas-to-Gas Crossflow Heat Exchangers With Neither Gas Mixed," ASME JOURNAL OF HEAT TRANSFER, Vol. 105, 1983, pp. 563–570.

6 Serov, E. P., and Korol'kov, B. P., *Dinamika parogeneratorov* (Dynamics of Steam Generators), Energoizdat, Moscow, 1981.

7 Baclić, B. S., Sekulić, D. P., and Gvozdenac, D. D., "Performances of Three-Fluid Single Pass Crossflow Heat Exchanger," in: *Heat Transfer 1982*, Vol. 6, U. Grigull, E. Hahne, K. Stephan, and J. Straub, eds., Hemisphere, Washington, D. C., 1982, pp. 167–172.

8 Baclic, B. S., and Heggs, P. J., "On the Search for New Solutions of the Single-Pass Crossflow Heat Exchanger Problem," *Int. J. Heat Mass Transfer*, Vol. 28, No. 10, 1985, pp. 1965–1978.

Thermal Transport From a Heated Moving Surface

M. V. Karwe

Y. Jaluria
Mem. ASME

Department of Mechanical and Aerospace Engineering, Rutgers University, New Brunswick, NJ 08903

A numerical and analytical study of the transport process arising due to the movement of a continuous heated body has been carried out. The relevant heat transfer mechanisms are of interest in a wide variety of practical applications, such as continuous casting, extrusion, hot rolling, and crystal growing. The conjugate problem, which involves a coupling between the heat transfer in the moving material and the transport in the fluid, is considered. The thermal fields in the material and in the fluid are computed. The temperature level is found to decay gradually with distance along the moving material, as expected. Results are obtained for a wide range of governing parameters, particularly the Peclet number Pe and the parameter R, *which depends on the properties of the fluid and the material. The results obtained are compared with those for the idealized cases of an assumed surface heat transfer coefficient and of a moving isothermal surface. Of particular interest were the nature of the flow generated by the moving surface and the resulting thermal transport. The results obtained are also considered in terms of the underlying physical processes in the problem.*

Introduction

In many manufacturing processes, such as hot rolling, drawing, extrusion, and continuous casting, heat transfer occurs in a continuously moving material. The speed at which the material moves can be as low as a few centimeters per hour, as in the case of the Czochralski crystal growth process [1], or as high as a few meters per second, as in the case of hot rolling or drawing. For short periods of time, after the onset of the process, the thermal field has not been established and the transient process is of interest. However, at longer times, the process reaches steady state. For instance, in an extrusion process, as the free end of the extruded material moves farther away from the die, a steady flow situation is eventually attained, for constant boundary conditions (see Fig. 1*c*, *d*).

The essential features of the flow induced by a two-dimensional continuously moving surface are shown in Fig. 1(*c*). The material issues from a slot and moves at uniform speed, as a two-dimensional sheet, through an otherwise quiescent fluid environment. Due to viscous effects, the fluid near the moving surface is set into motion. With increasing downstream distance x, as measured from the slot, the effect of this motion penetrates deeper into the environment and the thickness of the flow region increases. A steady-state situation eventually arises for a long, moving surface. Assuming the flow to be of boundary layer form, Sakiadis [2, 3] studied the growth of the two-dimensional velocity boundary layer over a continuously moving flat plate, emerging from a wide slot, at uniform velocity. The problem was solved using a similarity transformation, which is applicable for a semi-infinite surface.

The velocity boundary layer is seen to grow in the direction of motion of the surface. This characteristic is somewhat similar to that observed near the leading edge of a semi-infinite flat plate immersed in a moving fluid stream, wherein the boundary layer develops along the direction of the fluid motion [4]. Figure 1(*a*) shows this circumstance resulting from an externally induced flow over a flat plate. Tsou et al. [5] have shown experimentally that the present flow is of the general form sketched in Fig. 1(*c*). To demonstrate the flow, they selected a rotating drum system with a skimmer plate, in order to model the boundary layer on a continuously moving surface. Keeping the radius of the cylinder sufficiently large, they were able to ignore the effects of curvature. Thus, the flow was very similar to that over a plane moving surface. They found excellent agreement between the measured velocity profile, for a laminar flow, with the theoretical results. A fair agreement was also obtained for turbulent flow. Griffin and Thorne [6] observed the growth of the thermal boundary layer on a continuous, flat, moving belt, using the shadowgraph technique. Their results were in fair agreement with the theoretical results of Erikson et al. [7]. Griffin and Thorne have also discussed the effect of the wall, above and below the slot through which the belt emerges, on the heat transfer coefficient near the slot.

In the cases considered by Sakiadis [2, 3] and Tsou et al. [5], the thickness of the plate, or of the material, was considered to be negligibly small as compared to the distance along the surface. However, in most practical problems, such as continuous casting, interest lies mainly in the temperature distribution in the moving material, which is of finite thickness and which is subjected to energy transfer at the surface. This case was solved by Jaluria and Singh [1], assuming a constant heat transfer coefficient at the surface. They also considered transient effects at small finite distances from the die to the end of the moving material.

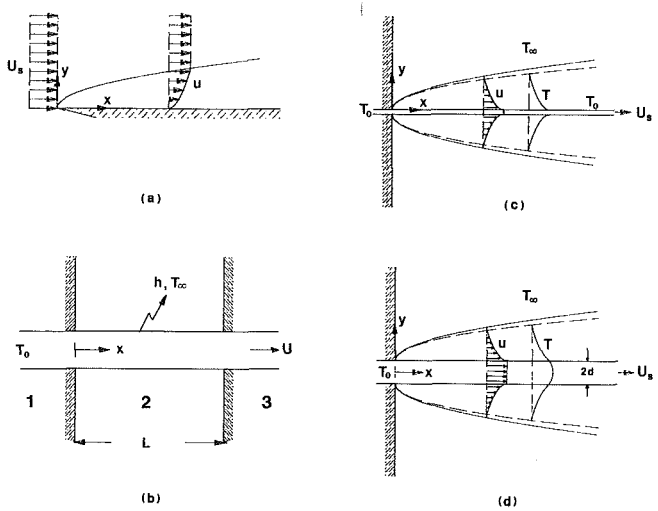

Fig. 1 *(a)* **Schematic of flow over a semi-infinite stationary flat plate; *(b)* one-dimensional conduction in a moving material with an assumed value of surface heat transfer coefficient *h* (Case I); (c) flow induced by a moving isothermal plate (Case II); *(d)* the conjugate problem (Case III)**

Contributed by the Heat Transfer Division and presented at the 23rd National Heat Transfer Conference, Denver, Colorado, August 4–7, 1985. Manuscript received by the Heat Transfer Division April 23, 1985.

Chida and Katto [8] considered the flow induced by a continuously moving plate of finite thickness. They included the effect of conduction within the plate in their calculations. However, they only considered large Peclet numbers Pe. There are a few other studies in the literature. Glicksman [9] studied cooling of fast-moving glass fibers. Khader [10] developed a model for transient laminar mixed convection from a vertically moving, isothermal plate.

The present work considers the heat transfer occurring in a process where a long strip of material, of finite thickness and large width, moves continuously after emerging from a furnace or an oven. It is assumed that the temperature at the slot is held constant. As the hot material moves away from the slot, the movement of the surface induces motion in the fluid due to viscous effects. The plate also loses thermal energy to the ambient fluid by convection and radiation. In some cases, for instance, in spray drying, the surface heat transfer coefficient has been assumed to be constant in the literature. However, in general, the conjugate problem involving conduction in the material and transport in the fluid must be considered.

Analysis

The analyses of the flow situations shown in Figs. 1(*b*) and 1(*c*) are well documented in literature and will, therefore, be discussed very briefly here. They are important in providing idealized situations for which exact solutions may be obtained. Also, the analysis will be used to obtain some results that have not been presented in the literature.

Consider a rod or a plate, of perimeter P and cross-sectional area A, moving at a constant speed U. For the one-dimensional model shown in Fig. 1(*b*), the temperature is taken as uniform over any cross section. This is referred to as Case I in this paper. The temperature T in the plate is then governed by the following equations:

In region 1, $-\infty \le x < 0$

$$\frac{d^2T_1}{dx^2} - \frac{\rho_s CU}{K_s}\frac{dT_1}{dx} = 0 \tag{1}$$

In region 2, $0 \le x \le L$

$$\frac{d^2T_2}{dx^2} - \frac{\rho_s CU}{K_s}\frac{dT_2}{dx} - \frac{hP}{K_s A}(T_2 - T_\infty) = 0 \tag{2}$$

In region 3, $L < x \le \infty$

$$\frac{d^2T_3}{dx_2} - \frac{\rho_s CU}{K_s}\frac{dT_3}{dx} = 0 \tag{3}$$

where the subscripts 1, 2, and 3 refer to the three regions, and the various symbols used are defined in the Nomenclature. Appropriate boundary conditions at $x = 0$ and $x = L$ are obtained by assuming continuous temperature and heat flux across the cross sections. Temperature T is assumed to approach T_0 as $x \to -\infty$ and to remain finite as $x \to \infty$. The solution is obtained analytically and the results are presented in the next section.

For the flow situation shown in Fig. 1(*c*), where a continuous plate emerges from a slot at a constant velocity U_s, the temperature of the plate is assumed to be at a constant uniform value T_0. Also, T_0 is assumed to be greater than the ambient temperature T_∞. The flow is assumed to be steady and two-dimensional. The usual boundary layer approximations are employed. This is referred to as Case II here.

An exact solution of the boundary layer equations may be obtained by employing the similarity transformation given by

$$\psi = \sqrt{2\nu U_s x}F(\eta), \qquad \eta = y\sqrt{U_s/2\nu x}, \qquad \theta = \frac{T - T_\infty}{T_0 - T_\infty}$$
$$u = \frac{\partial\psi}{\partial y} = U_s F'(\eta), \quad v = -\frac{\partial\psi}{\partial x} = \sqrt{\frac{\nu U_s}{2x}}\{\eta F' - F\} \tag{4}$$

The resulting governing equations are

$$F''' + FF'' = 0 \tag{5}$$

$$\theta'' + \mathrm{Pr}F\theta' = 0 \tag{6}$$

where the primes indicate differentiation with respect to η.

These equations are the same as those for forced convection heat transfer from a stationary semi-infinite flat plate with externally induced flow over it, as shown in Fig. 1(*a*). However, the boundary conditions are different, since $u \to 0$ as $\eta \to \infty$ in this case, whereas for the stationary plate $u \to U_\infty$, the free-stream velocity. The physical boundary conditions $u = U_s$, $v = 0$, and $T = T_0$ at the plate surface, and $u \to 0$ and $T \to T_\infty$ far away from the plate surface, give

$$F(0) = 0, F'(0) = 1, \theta(0) = 1, F'(\infty) = 0, \theta(\infty) = 0 \tag{7}$$

Let us now consider the flow situation shown in Fig. 1(*d*). The plate has a finite thickness $2d$ and conduction within the

Nomenclature

A = area of cross section
Bi = Biot number = $4h\beta/K_s$
C = specific heat of the plate
C_f = specific heat of the fluid
d = half-thickness of the plate
F = dimensionless stream function
$h(x)$ = heat transfer coefficient = $q/(T_s - T_\infty)$
K_f = thermal conductivity of the fluid
K_s = thermal conductivity of the plate material
L = length
Nu(x) = Nusselt number = $h(x) \cdot x/K_f$
P = perimeter
Pe = Peclet number = $U_s d^2/\alpha L$
Pr = Prandtl number = ν/α_f
q = surface heat flux per unit width
R = property parameter = $\left(\frac{K_f\rho_f C_f}{K_s\rho_s C}\right)^{1/2}$
Re = Reynolds number = $U_s L/\nu$
T = temperature
T_0 = specified temperature of the plate
$T_s(x)$ = temperature at the surface of the moving plate
T_∞ = ambient temperature
U, U_s = velocity of the plate
u = velocity of the fluid in x direction
u^* = dimensionless velocity in x direction
v = velocity of the fluid in y direction
v^* = dimensionless velocity in y direction
x = coordinate distance along the plate length
X, X^* = dimensionless coordinate distance along the moving plate
y = coordinate distance perpendicular to the plate surface
Y^* = dimensionless distance perpendicular to the surface
y_s = y coordinate distance within the plate
Y_s^* = dimensionless coordinate distance in y direction within the solid material
α = thermal diffusivity of the plate material = $K_s/\rho_s C$
α_f = thermal diffusivity of the fluid
β = parameter = A/p
δ = parameter = β/L
η = similarity variable
θ, θ^* = dimensionless temperature
θ_c^* = dimensionless temperature at the center line of the plate
ν = kinematic viscosity of the fluid
ρ_f = density of the fluid
ρ_s = density of the plate material
ψ = stream function

plate is taken into account. However, only conduction in the y direction is considered, at present, neglecting conduction in the x direction. If axial conduction is included, the boundary layer assumption for the flow can no longer be employed and the elliptic effects must be considered, since thermal effects can travel upstream due to axial diffusion. For thin plates, since the cross section is small, the axial conduction can generally be ignored in practical problems. However, conduction along the y direction may be considered, although under the present assumptions, the effect of transverse conduction in the material is also found to be small. This means that the decrease in temperature in the x direction is only due to the heat lost at the surface and not due to axial conduction, which is neglected. It will be shown later that the assumption of negligible x-direction conduction is valid for relatively higher values of the Peclet number Pe. Also, for this analysis, the induced flow velocities are assumed to be high enough and the temperature difference between the plate and the ambient to be small enough to neglect the buoyancy effects [11].

Assuming a boundary layer flow, the governing equations for the fluid in this case are [11]

$$u\frac{\partial u}{\partial x}+v\frac{\partial u}{\partial y}=\nu\frac{\partial^2 u}{\partial y^2} \tag{8}$$

$$\frac{\partial u}{\partial x}+\frac{\partial v}{\partial y}=0 \tag{9}$$

$$u\frac{\partial T}{\partial x}+v\frac{\partial T}{\partial y}=\alpha_f\frac{\partial^2 T}{\partial y^2} \tag{10}$$

In addition, for the plate

$$\rho_s C U_s\frac{\partial T}{\partial x}=K_s\frac{\partial^2 T}{\partial y_s^2} \tag{11}$$

These equations may be generalized by using the following nondimensionalization

$$X^*=x/L,\ Y^*=y\sqrt{\mathrm{Re}}/L,\ \mathrm{Re}=U_sL/\nu,\ u^*=U/U_s$$

$$v^*=v\sqrt{\mathrm{Re}}/U_s,\ \theta^*=(T-T_\infty)/(T_0-T_\infty),\ Y_s^*=y_s/d$$

where we have chosen two different scales in the y direction, one within the plate (Y_s^*) and another outside the plate (Y^*). The nondimensionalized equations are:

For the fluid

$$u^*\frac{\partial u^*}{\partial x^*}+v^*\frac{\partial u^*}{\partial y^*}=\frac{\partial^2 u^*}{\partial Y^{*2}} \tag{12}$$

$$\frac{\partial u^*}{\partial X^*}+\frac{\partial v^*}{\partial Y^*}=0 \tag{13}$$

$$u^*\frac{\partial\theta^*}{\partial X^*}+v^*\frac{\partial\theta^*}{\partial Y^*}=\frac{1}{\mathrm{Pr}}\frac{\partial^2\theta^*}{\partial Y^{*2}} \tag{14}$$

Within the plate

$$\frac{\partial\theta^*}{\partial X^*}=\frac{1}{\mathrm{Pe}}\frac{\partial^2\theta^*}{\partial Y_s^{*2}} \tag{15}$$

where $\mathrm{Pr}=\nu/\alpha_f$ and $\mathrm{Pe}=U_sd^2/\alpha L$.

The no-slip conditions at the surface of the plate and at the wall above the slot give

$$X^*>0,\ Y^*=0 \text{ or } Y_s^*=1:\quad u^*=1,\ v^*=0 \tag{16}$$

$$X^*=0,\ Y^*>0:\quad u^*=0,\ v^*=0 \tag{17}$$

Far away from the plate, the velocity goes to zero, since a quiescent ambient medium is assumed. Therefore

$$\text{as } Y^*\to\infty,\ u^*\to 0 \tag{18}$$

The boundary conditions on the temperature are:

Within the plate

$$X^*=0,\ 0\le Y_s^*\le 1:\quad \theta^*=1 \tag{19}$$

and within the fluid

$$X^*=0,\ Y^*>0:\quad \theta^*=0 \tag{20}$$

Since we have neglected natural convection, we can assume symmetry about the x axis, which gives rise to the condition

$$X^*>0,\ Y_s^*=0:\quad \frac{\partial\theta^*}{\partial Y_s^*}=0 \tag{21}$$

At the surface of the plate, the continuity of heat flux implies

$$X^*>0,\ Y_s^*=1 \text{ or } Y^*=0:\quad \frac{\partial\theta^*}{\partial Y_s^*}=\frac{\partial\theta^*}{\partial Y^*}R\sqrt{\frac{\mathrm{Pe}}{\mathrm{Pr}}} \tag{22}$$

Again, far from the plate, the assumption of a quiescent medium yields

$$X^*>0, \text{ as } Y^*\to\infty,\ \theta^*\to 0 \tag{23}$$

Since the governing equations are parabolic in x, boundary conditions are not needed downstream.

Solution Procedure

Equations (1)–(3) were solved analytically, following the procedure discussed by Arpaci [12]. The solutions obtained are important for comparison with the results obtained in other cases, for validation of the numerical scheme, and for indicating the basic nature of the transport process. Equations (5) and (6) were integrated with respect to the similarity variable η, using the fourth-order Runge-Kutta scheme [13]. A correction scheme, based on the Newton-Raphson method [14], was employed to vary the guessed values of $F''(0)$ and $\theta'(0)$, so that the boundary conditions given by equation (7) were satisfied to within a convergence criterion, on $F'(\infty)$, of 10^{-6}. A step size of 0.005 was employed and the condition $F'(\infty)=(0)$ was applied at $\eta=10$. All these numerical parameters were varied to ensure a negligible dependence of the results on the values chosen.

Equations (12)–(15), with boundary conditions given by equations (16)–(23), were solved using the Crank-Nicolson finite difference method [14]. The computational region, $X^*>0$ and $Y_s^*>0$, was subdivided by means of a uniform grid. The extent of the grid in the y direction was chosen so that the ambient conditions could be specified at a distance which was at least twice the estimated thickness of the boundary layer at the maximum value of x. The grid size was varied to ensure that the results were not significantly affected by further grid refinement. The values of ΔX^* and ΔY^* chosen in this study were 0.05 and 0.2, respectively. The truncation error in the Crank-Nicolson method is of the order of $(\Delta X^*)^2$ and $(\Delta Y^*)^2$. The numerical scheme was tested by applying it to Case II which involves an isothermal moving plate (Fig. 1*c*) and comparing the results obtained with the similarity solution. The agreement was excellent away from the slot.

Results and Discussion

The solution to equations (1)–(3), with the appropriate boundary conditions, after nondimensionalization is obtained as:

For region 1, $-\infty\le X<0$

$$\frac{T_1-T_0}{T_\infty-T_0}=\left\{1+\frac{2\mathrm{Pe}[\sigma e^{(\sigma/2\delta)}-\rho e^{(\rho/2\delta)}]}{[\rho^2e^{(\rho/2\delta)}-\sigma^2e^{(\sigma/2\delta)}]}\right\}e^{(\mathrm{Pe}X)} \tag{24}$$

For region 2, $0\le X\le 1/\delta$

$$\frac{T_2-T_0}{T_\infty-T_0}=1+\frac{2\mathrm{Pe}[\sigma e^{(\sigma/2\delta)}e^{(\rho X/2)}-\rho e^{(\rho/2\delta)}e^{(\sigma X/2)}]}{[\rho^2e^{(\rho/2\delta)}-\sigma^2e^{(\sigma/2\delta)}]} \tag{25}$$

For region 3, $1/\delta<X\le\infty$

$$\frac{T_3-T_0}{T_\infty-T_0}=1+\frac{2\mathrm{Pe}[\sigma-\rho]e^{(\mathrm{Pe}/\delta)}}{[\rho^2e^{(\rho/2\delta)}-\sigma^2e^{(\sigma/2\delta)}]} \tag{26}$$

where $X=x/\beta$, $\delta=\beta/L$, $\alpha=K_s/\rho_sC$, $\beta=A/p$, $\mathrm{Pe}=U\beta/\alpha$,

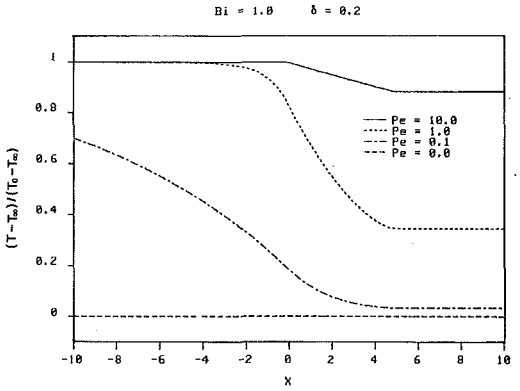

Fig. 2 Effect of varying the Peclet number Pe on the temperature distribution for Case I, at Bi = 1.0 and δ = 0.2

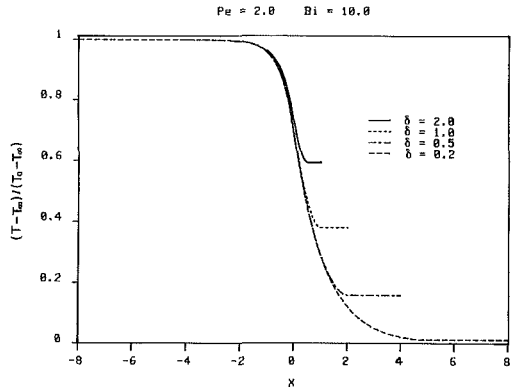

Fig. 3 Effect of varying δ (= β/L) on the temperature distribution for Case I, at Pe = 2.0 and Bi = 10

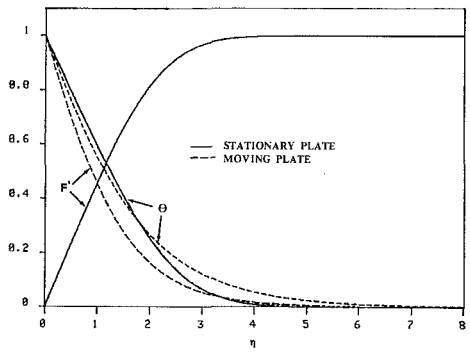

Fig. 4 Variation of F' and θ with the similarity variable η for the moving plate in a quiescent medium, as well as for a stationary plate with externally induced flow over it

$\mathrm{Bi} = 4h\beta/K_s$, $\rho = \mathrm{Pe} + (\mathrm{Pe}^2 + \mathrm{Bi})^{1/2}$, $\sigma = \mathrm{Pe} - (\mathrm{Pe}^2 + \mathrm{Bi})^{1/2}$. Here, β is taken as the characteristic length.

The temperature variation along the x direction, corresponding to equations (24)–(26), is shown in Fig. 2. The effect of varying Pe on the thermal field is shown. At higher values of Pe, with Bi held constant, the penetration of the diffusion effects into the negative x direction is found to be smaller. For constant Pe, an increase in Bi resulted in an increase in the upstream penetration of the thermal effects. However, the effect of Pe was found to be more dominant than that of Bi. Figure 3 shows the temperature profiles with the values of Pe and Bi fixed at 2.0 and 10.0, respectively, for decreasing values of δ. Since $\delta = \beta/L$, a decrease in δ implies an increase in L, for a given β. As L is increased, region 3 moves away from region 1, increasing the extent of region 2. Therefore, any point on the plate is exposed to the ambient fluid for a longer time. Therefore, as the value of δ is decreased, the temperature near the end of region 2 approaches the ambient temperature, which indicates that the effect of region 3 on the temperature distribution in region 1 and 2 is reduced.

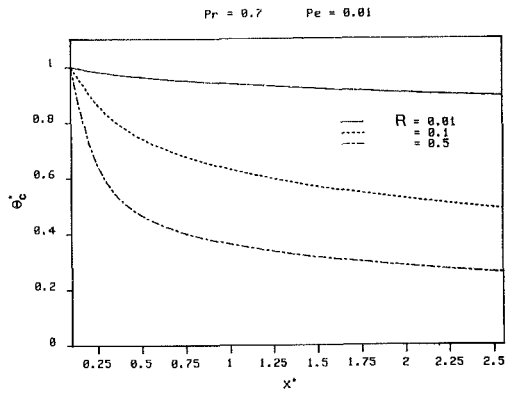

Fig. 5 Downstream variation of the centerline temperature for the conjugate case at Pr = 0.7 and Pe = 0.01

The solutions for Case II were obtained by the numerical integration of equations (5) and (6). The results obtained were also compared with the corresponding results for an externally induced flow over a semi-infinite flat plate. Figure 4 shows the basic trends observed. It was found that the magnitude of $[F''(0)]$ was higher for the moving plate $[F''(0) = 0.6280]$ than for the stationary plate $[F''(0) = 0.4692]$. This means that the shear stress, at the plate surface, being proportional to the magnitude of $[F''(0)]$, is higher for the moving plate. The x-component velocity profile for the moving plate is similar to that for a nonbuoyant jet, except for the fact that the shear stress is not zero at $y = 0$. The y-component velocity v is negative for the moving plate, as compared to positive values of v for flow over a stationary plate [3]. Also, the magnitude of $[-\theta'(0)]$ is higher $[\theta'(0) = 0.4939]$ for the flow over a moving plate as compared to flow over a stationary plate $[\theta'(0) = 0.4122]$ (see Fig. 4). Therefore, the local heat transfer coefficient $h(x)$ is higher for the moving surface. This means that, for a given fluid and velocity U_s, the moving plate loses more energy to the flow than the semi-infinite stationary plate, with flow over it.

The above result may be explained in terms of the transverse velocity v. Since this velocity v is negative (i.e., toward the plate), the fluid at ambient temperature is brought toward the plate in the case of a continuously moving plate. This increases the temperature gradient at the surface and, hence, the heat transfer [11]. This is not the case for a semi-infinite isothermal plate, where v is positive. Thus, the results for Cases I and II, Figs. 1(b) and 1(c), indicate the basic nature of the transport process, lend support to the numerical scheme, and present some numerical results which have not been presented in the literature.

The results for the conjugate problem, Fig. 1(d), are obtained at various values of Pe, Pr, and R. As mentioned earlier, in all the cases considered, conduction in the x direction was neglected. The value of temperature was specified as T_0 at $X^* = 0$. Figure 5 shows the computed centerline temperature variation with X, for Pr = 0.7 and Pe = 0.01, at different values of R. For very small values of R, say for a highly conducting plate, the temperature of the plate drops very gradually. Thus, the downstream penetration of thermal effects is large, as expected. For large values of R, say for a poorly conducting plate, the plate cools rapidly between with increasing X^*. However, it must be noted that for a given fluid, i.e., Pr and K_f unchanged, a decrease in K_s must be accompanied by a decrease in the thermal capacity $\rho_s C$ of the material as well, if Pe (Pe = $U_s d^2/\alpha L$, $\alpha = K_s/\rho_s C$) is to remain unchanged. A decrease in thermal capacity of the material implies more loss of energy to the fluid. Similarly, for a given plate material, as the conductivity of the fluid in-

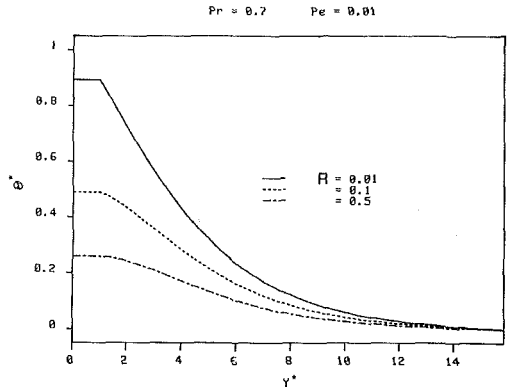

Fig. 6 Temperature along the y direction within the plate and the fluid at Pr = 0.7, Pe = 0.01, and X^* = 2.4 in the conjugate case

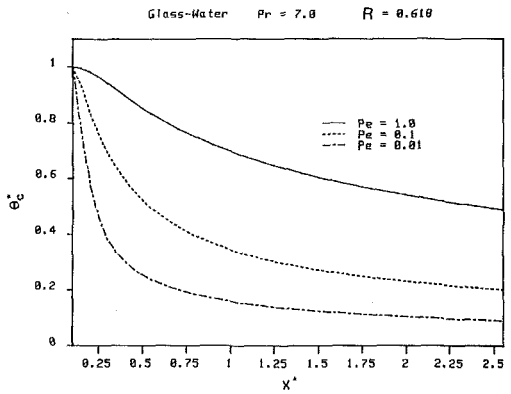

Fig. 7 Downstream variation of centerline temperature for a glass plate with water as the fluid, in the conjugate case

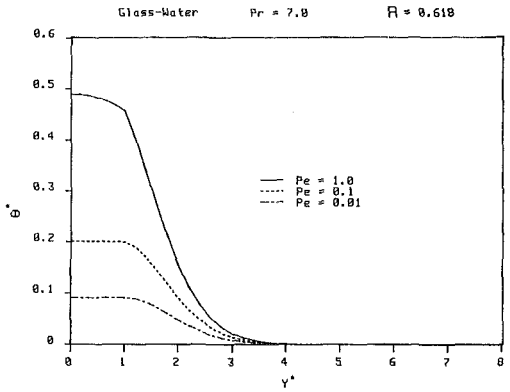

Fig. 8 Temperature along the y direction within the glass and the water, at X^* = 2.4

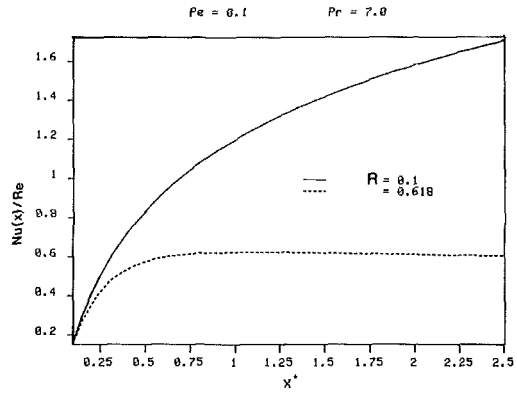

Fig. 9 Downstream variation of the Nusselt number Nu(x) at Pe = 0.1 in the conjugate case

creases, the plate loses energy faster. From Fig. 5, it is clear that the temperature profiles in the x direction, within the plate, are fairly steep near the slot, at small values of Pe. Therefore, the assumption of negligible conduction in the x direction may not be valid in this region, particularly at small Pe.

Figure 6 shows the temperature profiles in the y direction at $X^* = 2.4$, within the plate and the fluid, for the same parameters as in Fig. 5. One can see that the temperature profile within the plate is fairly uniform. However, the temperature gradients at the surface of the plate ($Y_s^* = 1$) are steeper for small values of R. This indicates higher heat transfer coefficients, for a given fluid, if the ratio of thermal conductivities is reduced, i.e., K_s is increased.

A typical case of a moving glass plate, with water as the fluid, is illustrated in Figs. 7 and 8. The temperature within the plate along the x direction decreases more gradually at Pe = 1.0, as compared to that at Pe = 0.01. However, at Pe = 1.0, the temperature gradients in the y direction at the plate surface ($Y^* = 0$) are higher. At smaller values of Pe, the temperatures are more or less uniform within the plate but the centerline temperatures are lower. This is because, at larger values of Pe, for a given location along x, the plate is exposed for a shorter duration to the cooler environment. Therefore, less energy is lost from the surface. Note that the temperature within the plate ($0 \le Y_s^* \le 1$) is not uniform at Pe = 1.0 and Pr = 7.0. At Pe = 0.01, the temperature within the plate becomes fairly uniform, indicating a longer exposure of the plate to the ambient.

Figure 9 shows the variation of the heat transfer parameter Nu(x)/Re with the distance along the plate. Here

$$\mathrm{Nu}(x) = \{h(x)\}\{x\}/K_f, \text{ with } h(x) = q/(T_s - T_\infty)$$

Also, q is the surface heat transfer rate per unit area. From Fig. 9 one can see that Nu(x) becomes nearly constant at $X^* >$ 0.6 for the case when Pe = 0.1, Pr = 7.0, and R = 0.618. Keeping Pr and Pe unchanged and lowering K_f/K_s to 0.1 increases Nu(x), but it takes a longer distance for Nu(x) to approach a constant value. Now, consider the case when Pe, Pr, and K_s are kept unchanged. An increase in K_f increases $h(x)$. However, the increase in $h(x)$ is less than the proportionate increase in K_f. Therefore, by definition, Nu(x) decreases.

The applicability of each of the three cases discussed here depends upon the physical process of interest. If one is interested mainly in the cooling of the material, for instance in quenching, the first case is generally appropriate. One can also compute the length of region 2, for the design of the system to achieve the given process. The situation considered in the first case is, in fact, encountered frequently in practice. If the thickness of the plate is small and the material of the plate has a high thermal capacity, for example, copper, then the assumption of an isothermal plate, as in Case II, is valid. Case III, which is considered in detail, is of importance when one is interested in the transport mechanisms as well as the temperature gradients within the plate. For instance, in the continuous casting process, the control of the transverse temperature gradients within the material can significantly change the physical properties of the material. In such cases, the conjugate transport is of interest.

Conclusions

An analytical and numerical study of the steady-state, self-induced forced convection heat transfer from a moving plate has been carried out. The one-dimensional conduction problem, with an assumed surface heat transfer coefficient, is solved analytically. The effect of the Peclet number Pe and the Biot number Bi on the penetration of conduction effects upstream is discussed. The flow over a moving plate, with and without conduction effects within the plate, is solved

numerically. Solutions are first obtained for a moving isothermal flat plate. It is found that, for an isothermal moving surface, the velocity boundary layer is thicker and the surface heat transfer coefficient is higher than the corresponding externally driven flow over a semi-infinite, stationary flat plate.

The governing parameters for the conjugate problem are found to be the Peclet number Pe, Prandtl number Pr, and the parameter R. In the conjugate problem, for a given fluid and for a fixed value of R, the transverse temperature within the plate at a downstream location was found to be fairly uniform at small Pe. For a given fluid at a constant Pe, a decrease in the thermal conductivity of the plate was found to result in a rapid decrease in the temperature in the axial direction, indicating greater energy loss at the surface. The Nusselt number $\mathrm{Nu}(x)$ was observed to approach a constant value as the distance from the slot increased. For given Pe and Pr, $\mathrm{Nu}(x)$ was lower at higher values of R. The results obtained are found to agree with earlier studies of similar problems and with the physical trends expected on the basis of the governing transport mechanisms.

Acknowledgments

The authors acknowledge the support provided by the Department of Mechanical and Aerospace Engineering, Rutgers University, and by the National Science Foundation, under Grant No. MEA-82-14325, for this work.

References

1 Jaluria, Y., and Singh, A. P., "Temperature Distribution in a Moving Material Subjected to Surface Energy Transfer," *Comp. Meth. Appl. Mech. Eng.*, Vol. 41, 1983, pp. 145–157.

2 Sakiadis, B. C., "Boundary Layer Behavior on Continuous Solid Surfaces: I. Boundary Layer Equations for Two-Dimensional and Axisymmetric Flow," *AIChE Journal*, Vol. 7, No. 1, 1961, pp. 26–28.

3 Sakiadis, B. C., "Boundary Layer Behavior on Continuous Solid Surfaces: II. The Boundary Layer on Continuous Flat Surface," *AIChE Journal*, Vol. 7, No. 2, 1961, pp. 221–225.

4 Schlichting, H., *Boundary Layer Theory*, McGraw-Hill, New York, 1963.

5 Tsou, F. K., Sparrow, E. M., and Goldstein, R. J., "Flow and Heat Transfer in the Boundary Layer on a Continuous Moving Surface," *Int. J. Heat Mass Transfer*, Vol. 10, 1967, pp. 219–235.

6 Griffin, J. F., and Thorne, J. L., "On Thermal Boundary Layer Growth on Continuous Moving Belts," *AIChE Journal*, Vol. 13, No. 6, 1967, pp. 1210–1211.

7 Erikson, L. E., Fan, L. T., and Fox, V. G., *Ind. Eng. Chem. Fundamentals*, Vol. 5, No. 19, 1966.

8 Chida, K., and Katto, Y., "Conjugate Heat Transfer of Continuously Moving Surfaces," *Int. J. Heat Mass Transfer*, Vol. 19, 1976, pp. 461–470.

9 Glicksman, L. R., "The Cooling of Glass Fibres," *Glass Technology*, Vol. 9, No. 5, 1968, pp. 131–138.

10 Khader, M. S., "Transient Laminar Mixed Convection From a Moving Vertical Surface," ASME Paper No. 81-HT-40.

11 Jaluria, Y., *Natural Convection Heat and Mass Transfer*, Pergamon Press, Oxford, 1980.

12 Arpaci, V. S., *Conduction Heat Transfer*, Addison-Wesley, Reading, MA, 1966, pp. 115–120.

13 James, M. L., Smith, G. M., and Wolford, J. C., *Applied Numerical Methods for Digital Computations with Fortran and CSMP*, Harper & Row, New York, 1977.

14 Carnahan, B., Luther, H. A., and Wilkes, J. O., *Applied Numerical Methods*, Wiley, New York, 1969.

Y. F. Hsu

B. Rubinsky

University of California—Berkeley,
Department of Mechanical Engineering,
Berkeley, CA 94720

K. Mahin

Lawrence Livermore National Laboratory,
Livermore, CA 94550

An Inverse Finite Element Method for the Analysis of Stationary Arc Welding Processes

An inverse finite element computer code was developed to facilitate the experimental analysis of two-dimensional stationary arc welding processes. The method uses transient temperature data from thermocouples imbedded in the solid region of the work piece to determine through a Newton–Raphson interpolation procedure the transient position of the solid–liquid interface and the transient temperature distribution in the solid region of the work piece. The accuracy of the method was demonstrated through comparison with results obtained with a direct finite element code and through comparison with experiments.

Introduction

Fusion welding is a process by which the edges of two pieces of metal are melted and fused together. This is done using an intense local energy source. The thermal energy transferred causes the metal to melt and form a molten pool usually referred to as a weld pool. It is important to be able to control the size and shape of the weld pool. It must be small enough to be manageable and to minimize energy consumption but large enough to bond the two pieces properly. The temperature distribution in the solid pieces as well as the rate of melting and the rate of solidification of the weld pool affect the stress distribution [1, 2] and the recrystallization process [3] in the metal, which in turn affects the strength of the metal pieces. Therefore, it is important to be able to determine, along with the weld pool shape and size, the temperature distribution in the solid region as a function of time. The small size of the weld pool and the high temperatures that occur during the welding process so far have precluded experimental determination of the transient variations of the weld pool and the temperature distributions in the solid. During typical welding experiments the shape of the weld pool is determined either by using an impact decanting technique or by rapidly quenching the sample and investigating the grain size and distribution. These methods cannot provide the transient temperature distributions in the solid. Furthermore, because of the short duration of welding processes (several seconds), it is impossible to obtain detailed information on the transient growth of the weld pool.

Recently, analytical studies [5–7] have been reported on attempts to predict the transient shape of the weld pool and the associated temperature distribution during welding as functions of various welding parameters. To provide a fundamental understanding on the heat transfer and fluid flow phenomena which occur during welding many researchers [8–12] concentrate on the stationary TIG (tungsten-inert-gas) arc welding process. During this process an arc (plasma) is being generated between an inert electrode and the object to be welded (workpiece). The stationary arc welding process is an experimental procedure, in which the arc does not move relative to the workpiece. After the arc is generated, melting starts in the workpiece. Since the arc is stationary the molten pool grows as a function of time and is axisymmetric. The stationary arc and the consequent axisymmetry simplify the study of the melting process and, as indicated previously, this mode of welding is commonly used for fundamental research. Analytical models simulating the stationary arc welding process usually assume a certain heat flux distribution from the arc, then solve for the fluid motion in the weld pool, for the energy convection process in the pool, and the energy conduction in the solid region. The analysis is complex in that the solid–liquid interface is moving in time while the fluid flow in the molten region is driven by Lorentz forces, surface tension, and local liquid density gradients. Although novel methods are being developed to model the welding problem, it is very difficult to validate and compare these analytical results with experimental results, since, as indicated previously, such experimental data are still not available.

As a part of an experimental methodology that can generate data on the shape of the solid–liquid interface as a function of time and the transient temperature distribution in the solid region during welding, a new two-dimensional inverse finite element method was developed and is presented in this work. This method uses several discrete temperature measurements in the solid region of the welded object, outside the melt region, to extrapolate the shape of the solid–liquid interface as a function of time as well as the temperature distribution in the solid during a stationary arc welding process. The accuracy of the inverse finite element method was demonstrated through comparison with results derived from direct analytical models of the welding process and through comparison with experiments.

A heat transfer problem with phase change is considered direct when the boundary conditions are described at the outer surface of the domain. Then the thermal conditions at the interior points and the phase change location inside the domain are found. In contrast an inverse heat transfer problem requires temperatures or heat fluxes at interior points in the domain to find the temperature profile of the region of analysis, the boundary condition, and the phase change location. This type of problem is referred to, mathematically, as a mathematically ill-posed problem, since we are solving a boundary-value problem where the conditions on one of the boundaries are not specified.

Many solutions are available for the direct problem of heat transfer in the presence of phase transformation. Some of them are summarized in [13–15]. However, very few studies have been published on the inverse heat transfer problem. Most of the reported studies have dealt with problems without phase change [16–25].

One of the first studies of inverse heat transfer problems using numerical methods was presented by Stolz [16]. Stolz formulates the inverse problem as though it were a direct problem. He obtains an integral equation for the unknown surface condition and finds a solution by numerically inverting the integral equations. His procedure becomes unstable if the time

Contributed by the Heat Transfer Division for publication in the JOURNAL OF HEAT TRANSFER. Manuscript received by the Heat Transfer Division October 18, 1985.

steps chosen are too small. However, a more accurate solution would be obtained if smaller time steps were used. Beck [17] makes this possible by using a procedure that involves minimization of the sum squared difference between the actual and calculated temperatures at the known temperature location. Burggraf [18] finds an exact series solution to a one-dimensional inverse problem with the lump capacitance approximation as the leading term. The temperature and heat flux histories are given at a single internal point. Approximate results are found if discrete or experimental data are used. Another work on inverse heat transfer problems was presented by Beck [19]. In that work the thermal properties of the material are considered to be a function of temperature; thus the problem becomes nonlinear.

A two-dimensional inverse finite element program has been reported in [26]. The authors describe an inverse finite element technique to determine heat fluxes on the outer surface of nuclear fuel rods from the internal thermocouple measurements.

Studies involving inverse heat conduction problems with phase change are much more limited. The current literature on inverse phase change problems includes a paper by Macqueene et al. [27], who investigated the efficiency of an arc welding process by an inverse finite-element method. In their model, the latent heat of fusion is accounted for by the variation of the elemental specific heat when the average elemental temperature is in the melt range. Conduction heat transfer is assumed in both the solid and liquid regions and continuous solution is found for both domains.

Rubinsky and Shitzer [28] derived analytic infinite-series solutions to the one-dimensional inverse Stefan problem in Cartesian and spherical conditions. Conduction heat transfer was assumed in the liquid region.

Landram [29] also used the inverse technique to identify from experimental results the fusion boundary (liquid–solid interface) and energy transport mechanisms during welding. Vaporization energy losses were found to be important during the growth of the fusion boundary. This boundary is nearly hemispheric, indicating approximately one-dimensional radial symmetry of the heat transfer in the hemispheric samples used. Also, Landram found convective heat transfer to be significant in the weld pool.

Recently Katz and Rubinsky have developed a "front tracking" finite element method for the study of the inverse one-dimensional conduction heat transfer problem with phase change [30]. Since that study serves as the foundation of this work it will be described here briefly. A finite element method was used to obtain the transient position of the solid–liquid interface and the transient temperature distribution in the solid region of the work piece during stationary arc welding. In that work it was assumed that the heat source is located at the origin, that the weld pool is axisymmetric and has a hemispherical shape. Under these conditions the problem becomes one dimensional. The method uses the temperature data from two thermocouples imbedded in the solid region at different distances from the origin. The thermocouple closer to the origin is referred to as the "internal" thermocouple while the thermocouple farther away from the origin is referred to as the "external" thermocouple. During each time step the position of the solid–liquid interface was guessed, the temperature profile between the solid-liquid interface and the external thermocouple was calculated using the finite element method and the calculated temperature at a location corresponding to that of the internal thermocouple was compared to the real value. An iterative process was used to readjust the location of the solid–liquid interface until the difference between the measured temperature and the calculated temperature at the internal thermocouple location was minimized. The predictions of the inverse method were compared to closed-form solutions for one-dimensional phase transformation processes. The major purpose of that work was to determine the accuracy of the inverse method and the sensitivity of the results to: (*a*) the location of the "internal" thermocouple; (*b*) the location of the "external" thermocouple; and (*c*) experimental errors in data. It was found that the results are very sensitive to the location of the internal thermocouple. Extensive numerical experiments have shown that for optimal results the distance of the "internal" thermocouple from the origin x_1 must be correlated to the time step Δt through a Fourier number of the form $\mathrm{Fo} = \alpha_s \cdot \Delta t / x_1^2$ such that for an optimal result $\mathrm{Fo} \cong 0.07$. The results have also shown that the inverse method was insensitive to the location of the "external" thermocouple and could tolerate an accuracy of 1 percent in the experimental data. The criteria established in [30] concerning the location of the thermocouples and their accuracy were implemented in this work.

Inverse methods for the study of multidimensional problems with phase change have not been reported in the open literature. The purpose of this work is to describe an inverse finite element method for the analysis of two-dimensional stationary arc welding processes. This method can be used to predict the position of the solid–liquid interface as a function of time, the heat flux on the interface, and the transient temperature profile in the solid region during the stationary arc welding process from discrete temperature measurements in the solid region of the welded workpiece. The significance of this numerical technique is that it can be coupled with experimentation to allow for greater control and understanding of the heat transfer in phase change problems of relevance to weld analysis and that it does not require a solution in the liquid region to predict the position of the change of phase interface.

Nomenclature

c = heat capacity
$\mathbf{C}$ = heat capacity matrix
$\mathbf{D}$ = vector of interior thermocouple data
f = distance between origin of coordinates to the node on the solid–liquid interface
$\mathbf{f}$ = vector of distance from origin to the node at the interface
$\mathbf{F}$ = vector of nodal temperatures calculated at interior thermocouple locations
h = interpolation function used in the finite element formulation
$\mathbf{H}$ = interpolation matrix
$\mathbf{J}$ = Jacobian matrix
k = thermal conductivity
$\mathbf{K}$ = heat conduction matrix
$\mathbf{Q}$ = vector of heat input per unit area
r = radial coordinate
$\mathbf{r}$ = vector of radial coordinates
T_0 = initial temperature
T_i = interior thermocouple data
T_e = exterior thermocouple data
$\mathbf{T}$ = vector of nodal temperature
y = axial coordinate
$\mathbf{y}$ = vector of axial coordinate
ϵ = convergence tolerance
θ = angle
ρ = density

Subscripts

i, k = index of nodes

Superscripts

$\dot{}$ = time derivative
t = time t
Δt = time step
T = transpose of matrix
-1 = inverse of matrix
i = iteration step index
k = time-step index

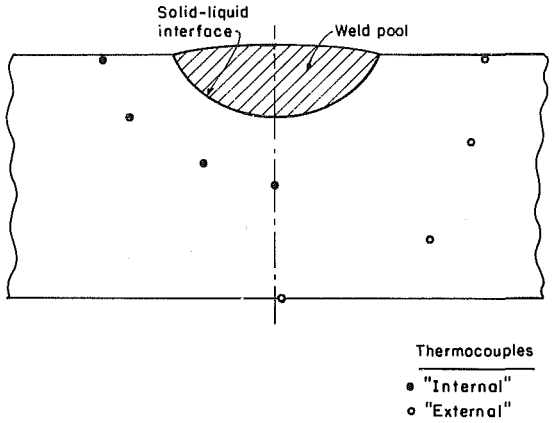

Fig. 1 Schematic of the weld pool and thermocouple location

Analysis

An inverse finite element technique will be described for the analysis of stationary arc welding processes. Figure 1 illustrates a typical two-dimensional axisymmetric weld pool. Embedded thermocouples used in the inverse analysis are also shown in the figure. The thermocouples are classified as either "exterior" or "interior," according to their role in the analysis. A homogeneous isotropic medium with temperature-dependent thermal properties is considered.

Because of the physical process occurring during stationary arc welding the problem will be separated into two time periods of analysis, nonmelting and melting.

In the first time domain the workpiece is heated, no melting occurs, and the inverse finite element technique is used to determine the temperature distribution in the solid region and the heat flux on the outer surface under the arc. The second time period starts when the outer surface temperature under the arc reaches the phase change temperature. During the second time period the domain consists of a solid region and a liquid region separated by a solid–liquid interface whose location changes in time. In the second time period the inverse method is used to determine the transient temperature distribution in the solid region, the transient position of the solid–liquid interface and the heat flux across the solid–liquid interface. The inverse analysis in both time domains requires the solution of the energy equation only in the solid region. This is an advantage of the inverse method for this allows the determination of the transient solid–liquid interface location without the need to assume heat transfer modes in the molten liquid region.

The energy equation to be solved in the solid region is given below

$$\rho c \frac{\partial T}{\partial t} = \frac{1}{r} \frac{\partial}{\partial r}\left(kr \frac{\partial T}{\partial r}\right) + \frac{\partial}{\partial y}\left(k \frac{\partial T}{\partial y}\right) \tag{1}$$

The solution must satisfy known initial conditions

$$T(r, y, 0) = T_0(r, y) \tag{2}$$

The solution of equation (1) must also agree with the temperature measured by the thermocouples embedded in the solid region

$$\begin{aligned} T(r_i, y_i, t) &= T_i(t), \; i = 1, n \\ T(r_e, y_e, t) &= T_e(t), \; e = 1, m \end{aligned} \tag{3}$$

where the subscript i represents internal thermocouple data and e represents external thermocouple data.

Equation (1) can be solved using a standard finite element procedure [31], where the geometric domain and the attendant temperature are divided into isoparametric elements with a variable number of nodes such that

$$y = \mathbf{H} \cdot \mathbf{y} \qquad r = \mathbf{H} \cdot \mathbf{r} \qquad T = \mathbf{H} \cdot \mathbf{T} \tag{4}$$

$\mathbf{H}$ is the interpolation matrix and $\mathbf{y}$, $\mathbf{r}$, and $\mathbf{T}$ are vectors of nodal point coordinates and nodal point temperatures. The finite-element formulation is then given by [31]

$$\mathbf{C} \cdot \dot{\mathbf{T}} + \mathbf{K} \cdot \mathbf{T} = \mathbf{Q} \tag{5}$$

where $\dot{\mathbf{T}}$ is the time derivative of the nodal temperature vector and $\mathbf{Q}$ is the heat flux vector on the nodes.

Typical expressions for the matrices in equation (5) are

$$\mathbf{C} = \sum_m \int_{A^{(m)}} \mathbf{H}^{(m)T} \rho c \mathbf{H}^{(m)} r dA \tag{6}$$

$$\mathbf{K} = \sum_m \int_{A^{(m)}} \mathbf{B}^{(m)T} k \mathbf{B}^{(m)} r dA \tag{7}$$

where the summation is over all the elements, $\mathbf{H}^{(m)}$ is the local interpolation matrix for each element, and $\mathbf{B}^{(m)}$ defines the temperature gradient within each element as a function of nodal values. Using an Euler backward integration scheme for the time derivative in equation (5) yields

$$\mathbf{G}^t \cdot \mathbf{T}^t = \mathbf{Q}^t + \mathbf{C}^t \cdot \mathbf{T}^{t-\Delta t} \tag{8}$$

where $\mathbf{G}^t = \mathbf{K}^t \cdot \Delta t + \mathbf{C}^t$ and $\mathbf{Q}^t = \mathbf{Q}^t \cdot \Delta t$.

Equation (8), which is a standard finite element formulation for the heat conduction transfer equation, will be used in this analysis. In addition to initial conditions, boundary conditions are required for the solution of equation (8).

The temperature data measured by the exterior thermocouples shown in Fig. 1 can provide appropriate boundary conditions on a surface passing through the thermocouples. In the finite element formulation temperatures are expressed in terms of nodal temperature values connected by predetermined interpolation functions, i.e., equation (4). In this work the exterior thermocouple temperature data are used for the nodal value of temperatures and the temperature between the exterior thermocouples is determined using interpolation functions compatible with the finite element formulation equation (4)

$$\text{on the boundary: } T = \mathbf{H}_e \cdot \mathbf{T}_e \tag{9}$$

where $\mathbf{T}_e$ are nodal temperatures on the boundary corresponding to the exterior thermocouple location and $\mathbf{H}_e$ is the interpolation function vector on that boundary. Equation (9) was used as a boundary condition to equation (8) during both the nonmelting and the melting time periods.

During the nonmelting time period, boundary conditions on the top surface facing the arc are also required to solve equation (8). Since these conditions describing the arc heat flux distribution are usually not available, a special procedure, based on the Newton–Raphson method, and the interior thermocouple data are used in this work to simultaneously determine the temperature distributions in the solid domain and the heat flux distribution on the top surface. In this procedure the top surface heat flux is expressed in terms of nodal heat flux values and interpolation functions as

$$Q = \sum_{i=1}^{m} h_m \cdot Q_m = \mathbf{H} \cdot \mathbf{Q}^k \tag{10}$$

where Q_m is the nodal value of the heat flux, h_m is the finite element interpolation function on the outer surface of the domain, and m indicates the number of interpolation segments and nodal heat fluxes.

During each time step k, an initial guess is made for the nodal heat flux vector $\mathbf{Q}^k$ in equation (10). The temperature distribution is evaluated in the solid domain using this boundary condition for the solution of equation (8). Then the temperature calculated at nodal points corresponding to the location of the internal thermocouples (denoted by the vector

$\mathbf{F}$) are compared to the temperatures measured experimentally by these thermocouples (denoted by the vector $\mathbf{D}$). Finally, a Newton-Raphson procedure is used to modify the nodal values of the heat flux vector $\mathbf{Q}^k$ to minimize the difference between vector $\mathbf{F}$ and $\mathbf{D}$ using the updating formula

$$(\mathbf{Q}^k)^{i+1} = (\mathbf{Q}^k)^i - ((\mathbf{J}^{-1})^k)^i(((\mathbf{F})^k)^i - \mathbf{D}) \tag{11}$$

where the superscript k stands for time step and i for iteration. The Jacobian $\mathbf{J}$ at timestep k and iteration i is given by

$$((J_{ij})^k)^i = \left(\left(\frac{\partial F_i}{\partial Q_j}\right)^k\right)^i \tag{12}$$

or in a numerical form

$$(J_{ij}^k k)^i = \frac{((F_i)^k)^i - ((F_i)^k)^{i-1}}{((Q_j)^k)^i - ((Q_j)^k)^{i-1}} \tag{13}$$

The new heat flux vector $(\mathbf{Q}^k)^{i+1}$ is used to determine the temperature distribution in the solid domain and the iterative procedure is continued until the least square mean error, i.e., the square root of the sum of all the differences between the calculated and measured temperature data at the interior thermocouple location, converges to a predetermined tolerance

$$\left[\sum_{i=1}^{n}(F_i - D_i)^2\right]^{1/2} \leq \epsilon \tag{14}$$

This procedure is continued in time until the outer surface temperature under the arc reaches the phase transition value. This starts the analysis of the second time period, the melting process.

The purpose of the analysis in the second time period is to determine the temperature distribution in the solid region and the transient position of the solid-liquid interface. During the second time period the boundary conditions on the surfaces surrounding the solid domain are known. They include temperature boundary conditions at the exterior thermocouple location, and the temperature on the solid-liquid interface which is the phase transition temperature. It should be emphasized that this study was undertaken in conjuncture with an experimental system that uses feedback control to stabilize the arc heat flux to a constant value. Consequently the heat flux conditions on the surface facing the arc are assumed to be constant in time, the same as those determined during the first time period. However, the extent of the solid domain is unknown. Therefore a procedure similar to that used in determining the top surface heat flux during the first time period is developed to determine the transient position of the solid-liquid interface as a function of time. Because of the nature of the stationary arc welding process and the anticipated hemispherical axisymmetric shape of the solid-liquid interface, the position of the interface is defined in this work in terms of the radial distance r_k between the origin under the arc and the interface at a predetermined angle θ_k measured in a plane that passes through the central axis of the axisymmetric weld pool. The radial distance of the interface as a function of angle can be expressed by

$$r(\theta) = \sum_{i=1}^{l} h_i(\theta_k) f_i = \mathbf{H}(\theta_k) \cdot \mathbf{f} \tag{15}$$

where f_i is the distance from the origin to specific nodes on the solid-liquid interface while $h_i(\theta_k)$ are typical finite element interpolation functions dependent on the angle θ_k between nodes, and l is the number of nodes on the interface. Following is a description of the procedure used to determine the position of the solid-liquid interface and the temperature distribution in the solid region. First a finite element mesh is generated based on the nodal points on the solid-liquid interface given by equation (15). The nodal distance vector $\mathbf{f}$ in equation (15) is determined using a Newton-Raphson interpolation technique. During each time step k, an initial guess is made for the interface nodal distance vector $\mathbf{f}^k$. A mesh is generated, and the temperature distribution in the solid region is determined using equation (8) and the known boundary conditions. The temperature calculated at nodal points corresponding to the location of internal thermocouples (denoted by the vector $\mathbf{F}$) is then compared to the temperatures measured experimentally ($\mathbf{D}$). The Newton-Raphson method is used to update the nodal vector $\mathbf{f}$ to minimize the difference between vectors $\mathbf{F}$ and $\mathbf{D}$ using the updating formula.

$$(\mathbf{f}^k)^{i+1} = ((\mathbf{f})^k)^i - ((J^{-1})^k)^i(((\mathbf{F})^k)^i - \mathbf{D}) \tag{16}$$

where the superscript k stands for the time step and i for the iteration number. The Jacobian is given by

$$((J_{i,j})^k)^i = \left(\left(\frac{\partial F_i}{\partial f_j}\right)^k\right)^i \tag{17}$$

or in a numerical form

$$((J_{i,j})^k)^i = \frac{((F_i)^k)^i - ((F_i)^k)^{i-1}}{((f_j)^k)^i - ((f_j)^k)^{i-1}} \tag{18}$$

A new mesh is generated for the updated location of the solid-liquid interface and the iterative process continued during each time step until the difference between the measured and calculated temperature at the internal thermocouple location is minimized in a least square mean sense as given by equation (14). The solution provides the temperature distribution in the solid region and the solid-liquid interface location during each time step, while following the solid-liquid interface location in time from the onset of the melting process.

Results and Discussion—Numerical Experiments

The inverse finite element procedure described above was implemented on a VAX 780. The program has the ability to handle arbitrary numbers of internal and external thermocouples. In this section, however, we will discuss only numerical and experimental results in which three internal and three external thermocouples were used. This choice is motivated by the practical physical limitations on the number of thermocouples that can be embedded in a workpiece and the desire to present and discuss a computer code that can be used in experiments. The location of the internal thermocouples in this work was determined using the criteria established in [30] in terms of a typical Fourier number. Those criteria were given in the introduction. Satisfying the criteria results in optimal results for the position of the solid-liquid interface as a function of time and for the temperature distribution in the solid region. The meshing procedure during the first and second time period are automated. In the first time period the meshing procedure is based on the location of the exterior and interior thermocouples. During the second time period, the melting period, the mesh is automatically updated during each time step and is based on the location of the interface nodes and that of the interior and exterior thermocouples. The automatic mesh subroutine has the ability to change the number of elements during melting to minimize distortion of elements. Four-node and seven-node elements were used in the analysis.

The inverse finite element computer code was verified through comparison with results obtained from a direct code for the simulation of stationary arc welding processes and by comparison with experimental results.

Stationary arc welding on 1/4 in. thick stainless steel 304 plate was simulated using TOPAZ [32], a computer code developed at Lawrence Livermore Laboratory for the general solution of conduction heat transfer problems (Table 1). The direct code provides the transient temperature distributions in the workpiece and the transient position of the solid-liquid interface assuming a conduction heat transfer mechanism in the liquid region.

Table 1 Thermal properties of AISI 304 stainless steel as a function of temperature

Temperature T, K	Thermal conductivity k, W/m K	Heat capacity c, J/kgK
273.151	14.3	460.
400.	16.6	515.
600.	19.8	556.
1100.	26.7	623.
1500.	31.7	682.
1670.	33.3	707.
1727.	28.8	812.
2000.	31.5	812.

Density = 7900 kg/m^3; assumed isotherm for the phase transition temperature: 1400°C.

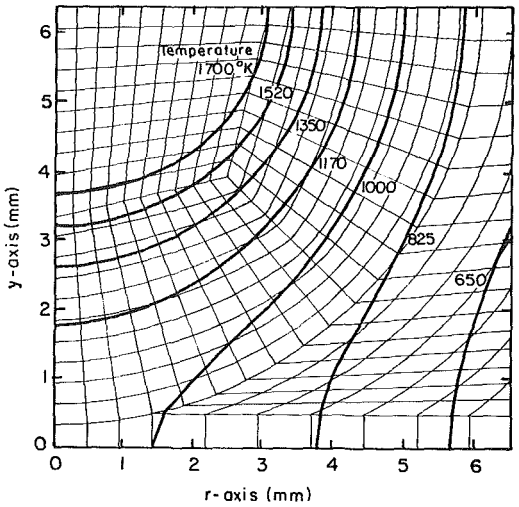

Fig. 2 Temperature distribution and finite element mesh used in the direct simulation of a stationary arc welding process

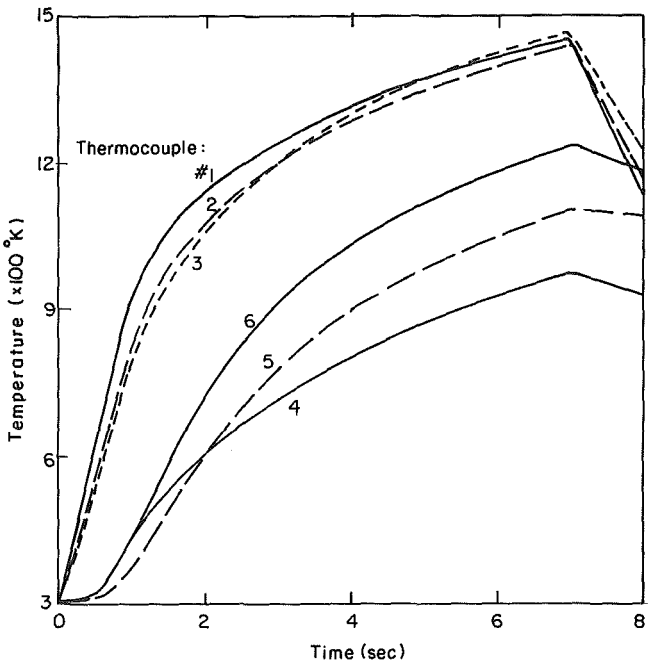

Fig. 3 Discrete temperature data from the direct code used to simulate internal and external thermocouple measurements

Typical results of the direct code at two seconds after the onset of the welding process are shown in Fig. 2. Isotherms are shown in the figure superimposed over a typical finite element mesh. To verify the inverse finite element code, numerical experiments were performed in which the temperature history

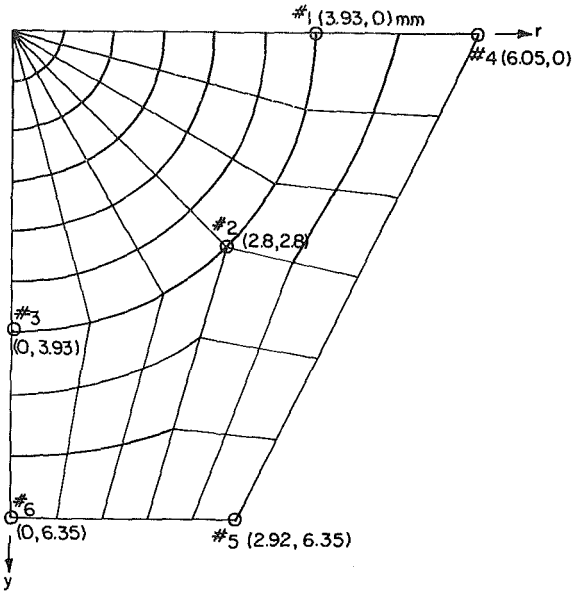

Fig. 4 Finite element mesh during the nonmelting time period of analysis and the position of the internal and external thermocouples

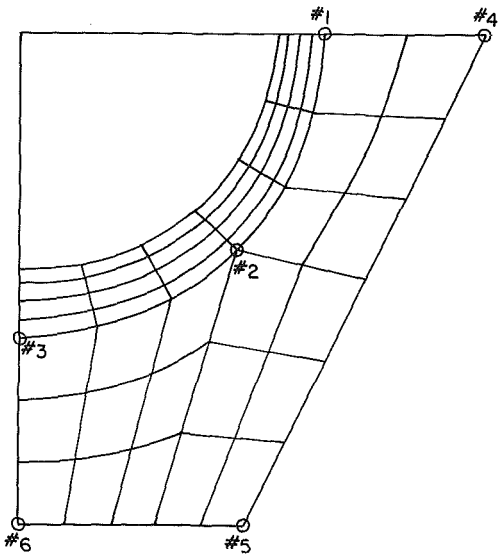

Fig. 5 Finite element mesh and position of the solid-liquid interface, 7 s after the onset of the welding process

obtained from the direct code at discrete points in the solid region was used as input to simulate internal and external thermocouple data in the inverse code. The position of the solid-liquid interface was calculated as a function of time from the transient temperature data using the inverse code and compared to that obtained from the direct code. Excellent agreement was found. Figures 3 to 6 illustrate the numerical experiment results. Figure 3 shows the inverse code input excerpted from the direct simulation results mentioned above. The temperature curves 1 to 3 were used as the internal thermocouple reading while the temperature curves 4 to 6 were used as the external thermocouple data. The location of the internal thermocouples was chosen according to the criteria given in [30]. We also found through numerical experiments that the results were insensitive to the location of the exterior thermocouples. This is also consistent with the observations made in [30]. The finite element mesh used during the first time period and the nodes simulating the thermocouple position and used for the automatic mesh generation are shown in Fig. 4. Figure 4 indicates that although there are only three ex-

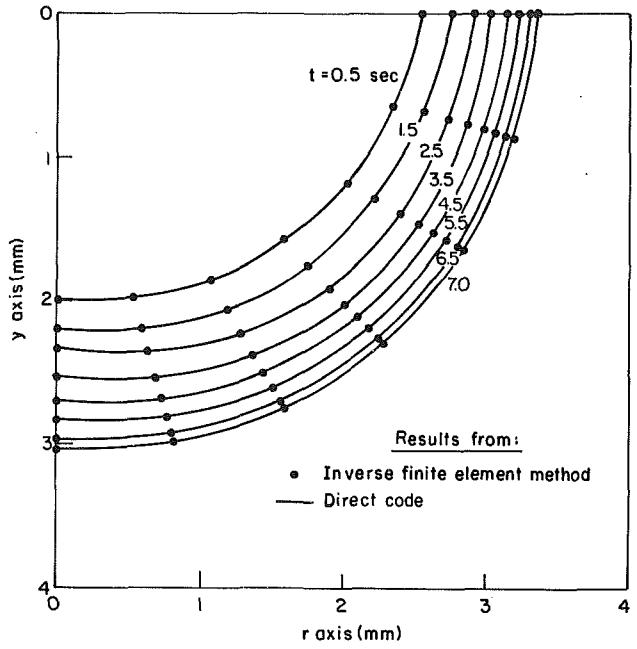

Fig. 6 Position of nodes on the solid-liquid interface as a function of time calculated using the inverse finite element method in comparison to results obtained by the direct method

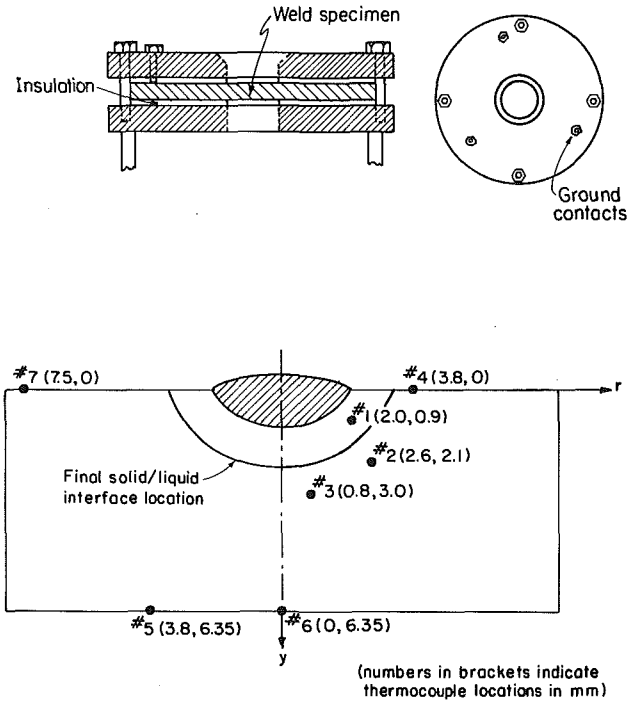

Fig. 7 Schematic diagram of the experimental setup

terior thermocouples there are many more nodes on the exterior boundaries. To implement equation (9) a linear temperature distribution was assumed between thermocouples 4 and 5 and between thermocouples 5 and 6. The temperature at each of the exterior nodes was calculated during the automated mesh generation procedure based on the location of the exterior nodes and the assumed temperature profile. The positions of the solid-liquid interface as well as the mesh at 7 s following the onset of the welding process are shown in Fig. 5. Note that the mesh bounded by the external and internal node thermocouples is not changed when compared to the first time period (Fig. 4). The number of elements in the region bounded by the solid-liquid interface and the interior thermocouples has changed, however, to automatically minimize the distortion of the elements. In this example seven nodal points were set on the solid-liquid interface and their distance from the origin r_k was determined using equations (15) to (18). The transient position of the solid-liquid interface (the 1400°C isotherm) obtained using the inverse code is compared in Fig. 6 with the position given with the direct code. The good agreement is evident.

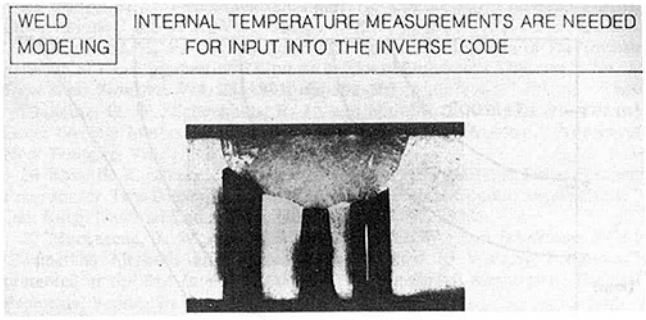

Fig. 8 Cross section of a 5 s GTA weld showing the location of the embedded thermocouples

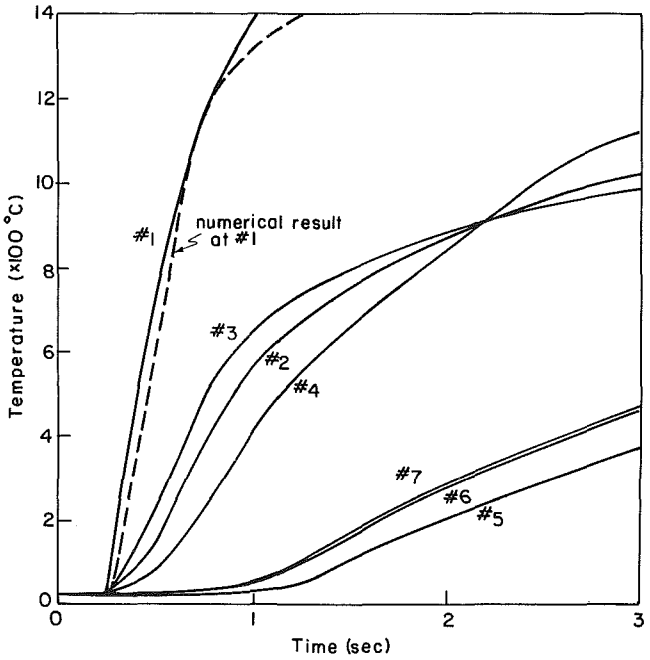

Fig. 9 Temperature history at different thermocouple locations

Welding experiments were performed with a stationary Gas Tungsten Arc welding system. The experimental results were compared with predictions made using the inverse finite element method. A HOBART CYBERTIG welding system was used with a 1/8 in. diameter thoriated tungsten electrode. The welding system is operated by a feedback stabilized power supply (135A, 15V) and typical welding processes of 3 s to 7 s arc-on time were performed. The workpiece was 3 in. diameter, 0.25 in. thick, 304 stainless steel plate. The experimental setup is shown schematically in Fig. 7. Type R thermocouples were embedded and percussion welded in the workpiece as shown in the figure. The exact location of the thermocouple in terms of x, y coordinates, in millimeters, is given in the brackets next to the thermocouple number. The location of the interior thermocouples was chosen to correspond to the criteria established in [30]. A cross section of a 5 s GTA weld showing the location of some embedded thermocouples and the final shape of the

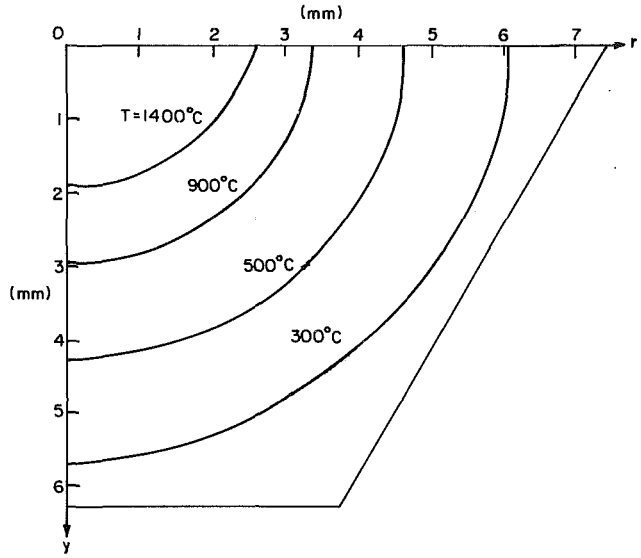

Fig. 10 Temperature isotherm in the workpiece and position of the solid-liquid interface 2 s after the onset of the welding process

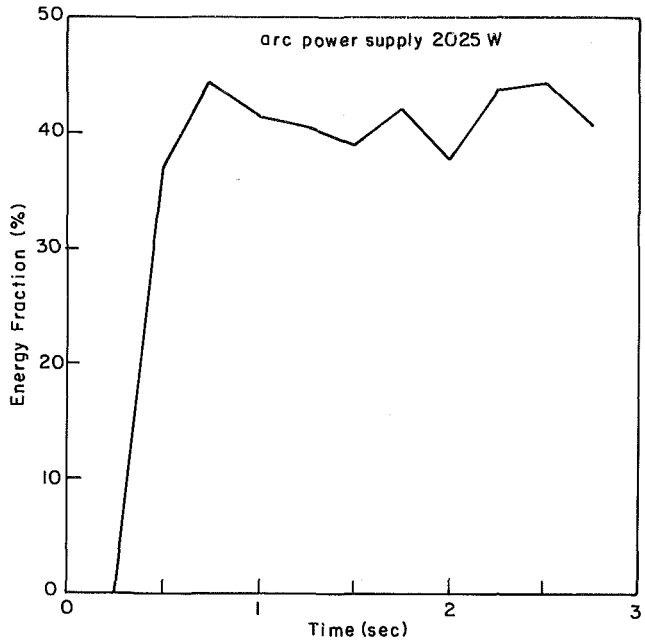

Fig. 11 Fraction of arc energy which goes into melting and transferred conduction as a function of time

molten region is presented in Fig. 8. Temperature data at six locations were used wtih the inverse finite element code to determine the temperature distributions in the solid region as well as the transient position of the solid-liquid interface. To verify the accuracy of the inverse finite element code, the temperature measured by a different thermocouple (#1 in Fig. 7), not used with the inverse code, was compared to the temperature history calculated using the inverse code at that thermocouple location. The thermocouple data measured during an experiment in which the arc power was set to be 2025W are given in Fig. 9. Based on this temperature information, a time step of 0.25 s, and a finite element mesh similar to that in Fig. 5, an inverse code calculation was performed. As can be seen from Fig. 8, the calculated temperature matches the measurements at the number 1 thermocouple location. This agreement between the experimental data and the analytical results indicates the possibility of employing the inverse code to analyze welding processes. Typical temperature isotherms in the workpiece and the position of the solid-liquid interface at 2 s after the onset of welding are shown in Fig. 10. It is evident that during this welding process the weld pool shape is not radially symmetric. The width of the weld pool is larger than its depth. This kind of weld pool shape is commonly observed during welding and is usually attributed to capillary-driven fluid motion and the arc energy distribution.

Figure 11 is presented to illustrate the potential use of the inverse code. Shown in Fig. 11 is the percentage of the total energy generated by the welding device which goes into melting of the material and that is transferred by conduction into the workpiece. As can be seen, this percentage was rather constant at about 45 percent. In addition, the analysis showed that less than 5 percent of the total energy was used for melting of the material. Thus, it can be concluded that about 40 percent of the welding energy is lost by conduction in the workpiece. This result implies the importance of the conduction heat transfer mechanism in the workpiece during the welding process.

Conclusions

An inverse finite element method was developed for the analysis of two-dimensional stationary arc welding process. The method uses discrete temperature data from thermocouples embedded in the solid region of the workpiece to determine the transient position of the solid-liquid interface and the temperature distribution in the solid region of the workpiece. The applicability of the inverse finite element numerical code was demonstrated through comparison with results obtained through direct numerical simulation of the welding process and comparison with experimental data.

The significance of this numerical technique is that it can be coupled with experimentation to allow greater understanding of the thermophysical phenomena involved in the welding process. Another potential use of the inverse code is as a part of the experimental methodology to benchmark the direct simulation models of the welding process.

Acknowledgments

This research was supported by Lawrence Livermore National Laboratory grant No. 5250405. The authors gratefully acknowledge the help by Dr. A. B. Shapiro from the Lawrence Livermore National Laboratory who provided for us his direct finite element analysis results on welding processes derived using the TOPAZ code.

References

1 Andersson, B., and Karisson, L., "Thermal Stresses in Large Butted-Welded Plates," *J. of Thermal Stresses*, Vol. 4, 1981, pp. 491-500.

2 Friedman, E., "Thermomechanical Analysis of the Welding Process Using the Finite Element Method," ASME *J. Press. Vessel Tech.*, Vol. 97, 1975, pp. 206-213.

3 Ashby, M. F., and Easterling, K. E., "A First Report on Diagrams for Grain Growth in Welds," *Act. J. Metallurgy*, Vol. 130, 1982, pp. 1969-1978.

4 Zanner, F. J., Nippes, E. F., and Savage, W. F., "Determination of GTA Weld-Puddle Configurations by Impulse Decanting," *Welding J.*, Vol. 57, 1978, pp. 2015-2021.

5 Glickstein, S. S., Friedman, E., and Yeniscavich, W., "Investigation of Alloy Gas Welding Parameters," *Welding J.*, Vol. 54, 1975, pp. 113s-122s.

6 Giedt, W. H., Wei, X. C., and Wei, S. R., "Effect of Surface Convection on Stationary GTA Weld Zone Temperatures," *Welding J.*, Vol. 63, 1984, pp. 376s-383s.

7 Friedman, E., and Glickstein, S. S., "An Investigation of the Thermal Response of Stationary Gas Tungsten Arc Welds," *Welding J.*, Vol. 55, 1976, pp. 408s-420s.

8 Shercliff, J. A., "Fluid Motions Due to an Electric Current Source," *J. Fluid Mechanics*, Vol. 40, 1970, pp. 241-250.

9 Andrews, J. G., and Craine, R. E., "Fluid Flow in a Hemisphere Induced by a Distributed Source of Current," *J. Fluid Mechanics*, Vol. 84, 1978, pp. 284-290.

10 Orepar, G. M., and Szekely, J., "Heat and Flow Phenomena in Weld Pools," *J. Fluid Mechanics*, Vol. 147, 1984, pp. 53–79.

11 Yokoya, S., Asako, Y., and Matsunawa, A., "Surface Tension Driven Flow in Semicylindrical Basin," *Trans. of Japan Welding Society*, Vol. 14, No. 2, 1983, pp. 135–142.

12 Kou, S., and Sun, D. K., "Fluid Flow and Weld Penetration in Stationary Arc Welds," *Metallurgical Trans.*, Vol. 16A, 1985, pp. 203–213.

13 Okendon, J. R., and Hodgkins, W. R., *Moving Boundary Problems in Heat Flow and Diffusion*, Clarendon, Oxford, 1977.

14 Wilson, D. G., Solomon, A. D., and Boggs, P. T., *Moving Boundary Problems*, Academic Press, New York, 1978.

15 Lunardini, V. J., *Heat Transfer in Cold Climates*, Van Nostrand Reinhold, New York, 1981.

16 Stolz, G., Jr., "Numerical Solutions to an Inverse Problem of Heat Conduction for Simple Shapes," ASME JOURNAL OF HEAT TRANSFER, Vol. 82, 1960, p. 20.

17 Beck, J. V., "Surface Heat Flux Determination Using an Integral Method," *Nucl. Eng. Des.*, Vol. 1, 1968, pp. 170–178.

18 Burggraf, D. R., "An Exact Solution of the Inverse Problem in Heat Conduction Theory and Applications," ASME JOURNAL OF HEAT TRANSFER, Vol. 86, 1964, pp. 373–382.

19 Beck, J. V., "Nonlinear Estimation Applied to the Nonlinear Inverse Heat Conduction Problem," *Int. J. Heat Mass Transfer*, Vol. 13, 1970, pp. 703–716.

20 Mehta, R. C., "Extension of the Solution of Inverse Combustion Problem," *Int. J. Heat Mass Transfer*, Vol. 22, 1979, pp. 1149–1150.

21 Weber, C. F., "Analysis and Solution of the Ill-Posed Inverse Heat Conduction Problem," *Int. J. Heat Mass Transfer*, Vol. 24, 1981, pp. 1783–1792.

22 Imber, M., "Temperature Extrapolation Mechanism for Two-Dimensional Heat Flow," *AIAA J.*, Vol. 12, No. 8, 1974, pp. 1089–1093.

23 Imber, M., "Two-Dimensional Inverse Conduction Problem—Further Observations," *AIAA J.*, Vol. 13, No. 1, 1975, pp. 114–115.

24 Blackwell, B. F., "Some Comments on Beck's Solution of the Inverse Problem of Heat Conduction Through the Use of Duhamel's Theorem," *Int. J. Heat Mass Transfer*, Vol. 26, 1983, pp. 302–305.

25 Krutz, G. W., Schoenhals, R. J., and Hore, P. S., "Application of the Finite Element Method to the Inverse Heat Conduction Problem," *Numerical Heat Transfer*, Vol. 1, 1978, pp. 489–498.

26 Bass, B. R., Drake, J. B., and Ott, L. J., "ORMDIN: A Finite Element Program for Two-Dimensional Nonlinear Inverse Heat Conduction Analysis," Oak Ridge National Laboratory, NUREG/CR-1709, 1980.

27 Macqueene, J. W., Akau, R. L., Kratz, G. W., and Schoenals, R. J., "Numerical Methods and Measurements Related to Welding Processes," presented at the 2nd International Conf. on Numerical Methods in Thermal Problems, Venice, Italy, 1981.

28 Rubinsky, R., and Shitzer, A., "Analytic Solutions to the Heat Equation Involving a Moving Boundary With Applications to the Change of Phase Problem (the Inverse Stefan Problem)," ASME JOURNAL OF HEAT TRANSFER, Vol. 101, 1978, pp. 300–304.

29 Landram, C. S., "Measurement of Fusion Boundary Energy Transport During Arc Welding," ASME JOURNAL OF HEAT TRANSFER, Vol. 105, 1983, pp. 550–554.

30 Katz, M. A., and Rubinsky, B., "An Inverse Finite Element Technique to Determine the Change of Phase Interface Location in One-Dimensional Melting Problems," *Numerical Heat Transfer*, Vol. 7, 1984, pp. 269–283.

31 Baker, E. B., Carey, G. F., and Oden, J. T., *Finite Elements*, Vol. I, Prentice Hall Inc., Englewood Cliffs, NJ, 1981.

32 Shapiro, A. B., "TOPAZ—A Finite Element Heat Conduction Code for Analyzing 2-D Solids," Method Development Group, Mechanical Engineering Department, Lawrence Livermore National Laboratory, 1986.

M. A. Paolino[1]
Professor.
Mem. ASME

R. B. Kinney[2]
Visiting Professor.
Mem. ASME

E. A. Cerutti
Assistant Professor
Mem. ASME

Department of Mechanics,
U.S. Military Academy,
West Point, NY 10996

Numerical Analysis of the Unsteady Flow and Heat Transfer to a Cylinder in Crossflow

The unsteady, two-dimensional viscous flow of an incompressible, constant-property fluid flowing over a cylinder is numerically analyzed by integrating the vorticity transport equation and the energy equation. Departing from the usual stream function approach, the velocity distribution is obtained from the vorticity distribution by integrating the velocity induction law. Calculations start with the impulsive motion of the free stream and a step change in the surface temperature of the cylinder. The solution is advanced in time until steady-state conditions are achieved. Results are obtained for a Prandtl number of 0.7 and Reynolds numbers of 3000 and 70,800. Local and average Nusselt numbers and force coefficients are presented and compared to available experimental data.

Introduction

A knowledge of the heat transfer between the surface of a circular cylinder and a fluid flowing perpendicular to its axis is fundamental to many heat transfer applications. Early empirical studies have shown the effect of Reynolds number on the overall or average Nusselt number. These results are presented in many of the fundamental textbooks dealing with heat transfer (see, e.g., McAdams [1]).

Subsequent experimental studies have been concerned with obtaining information on the local heat transfer coefficient over the surface of the cylinder. Schmidt and Wenner [2] reported the first such measurements for air flowing over a cylinder with constant wall temperature. The Reynolds number covered the range 5000 to 426,000. Giedt [3] later reported results for a cylinder in air for Reynolds numbers in the range 70,800 to 219,000. A surface heating condition approaching constant wall heat flux was used. In comparing his results with those of [2], Giedt [3] found appreciable differences in the behavior of the local Nusselt number over the back side of the cylinder, where separated flow is encountered. It was conjectured that these could be due to several causes, including: (1) end effects, which destroyed the two dimensionality of the flow, (2) the presence of free-stream turbulence, and (3) the failure of the stream to behave as though it were infinite in extent. Giedt [4] repeated his tests in the same wind tunnel with an improved model designed to eliminate the end effects. Also, the intensity of the free-stream turbulence could be varied. The local pressure coefficients did change, indicating that the earlier data should be interpreted with caution. Shortly thereafter, Seban [5] used an entirely different apparatus to extend the work of Giedt [4] in an attempt to clarify the role that free-stream turbulence plays in determining the local heat transfer coefficient. The working fluid was air, and the surface heating condition approximated that of constant wall heat flux.

All of these experimental studies reveal that the local heat transfer coefficients are very sensitive to the physical nature of the viscous flow field. Therefore, it is very desirable to obtain fundamental results for the local heat transfer coefficient under conditions for which extraneous flow effects can be eliminated. This is possible in principle through the use of numerical predictions. Indeed, the results of studies are now appearing in the literature which address this issue. Jain and Goel [6] give numerical results for Reynolds numbers equal to 100 and 200. The agreement with available data is good. Chang et al. [7] used numerical predictions to assess the effects of variable viscosity on the steady-state distribution of the local Nusselt number. Results are presented for air and variable viscosity liquids for Reynolds numbers in the range 1 to 50.

It appears that numerical predictions for the heat transfer characteristics of cylinders in cross flow can be of significant practical importance, and there is a need to obtain results at substantially higher Reynolds numbers. It is known that at even moderate Reynolds numbers, useful predictions can only be obtained with careful numerical modeling. To this end, Kinney and co-workers (see, e.g. [8–10]) have developed a general approach for calculating the unsteady two-dimensional and incompressible flow past cylindrical bodies. The advantage of this approach is that it is well suited to modeling an unconfined flow since it is not based on the stream function, and therefore values for this quantity need not be specified on the boundaries of the computational domain surrounding the body. As pointed out by Fornberg [11], the enforcement of proper far-field boundary conditions for the stream function is needed if accurate flow predictions are to be obtained even near the body.

In the present work, results are obtained for the local and average Nusselt number for heat transfer to a circular cylinder in unconfined crossflow. The working fluid has a Prandtl number equal to 0.7. The method for predicting the flow field is taken from [10]. The velocity and temperature fields develop simultaneously with time from an initial state, which corresponds to a cylinder at rest in a motionless fluid. At time $t=0$, the fluid is moved impulsively, and the surface of the cylinder is subjected to a step change in temperature. The wall temperature is held fixed thereafter, as is the velocity of the fluid. The objective of this study is to obtain numerical results for the heat transfer at Reynolds numbers which are one to two orders of magnitude greater than those used in previous studies, and for which some experimental measurements exist. Particular attention is given to the variation of the local Nusselt number over the surface of the cylinder in light of the behavior of the predicted pressure and wall shear-stress distributions.

Analysis

A polar coordinate system is adopted with its origin at the

[1]Currently Director of Engineering and Professor of Mechanical Engineering, Lafayette College, Easton, PA 18042.

[2]Currently Professor, Aerospace Mechanical Engineering Department, The University of Arizona, Tucson, AZ 85721.

Contributed by the Heat Transfer Division for publication in the JOURNAL OF HEAT TRANSFER. Manuscript received by the Heat Transfer Division June 3, 1985.

center of the cylinder. All the flow variables are rendered dimensionless with the undisturbed free-stream velocity of the fluid U_∞, the cylinder diameter D, and the fluid kinematic viscosity ν. The temperature is measured relative to the free-stream value and it is normalized by the difference between the surface and free-stream temperatures.

The energy equation is given by

$$\frac{\partial T}{\partial t}+\frac{1}{r}\frac{\partial}{\partial r}(rv_rT)+\frac{1}{r}\frac{\partial}{\partial\theta}(v_\theta T)$$
$$=\frac{1}{\mathrm{Re}_D\mathrm{Pr}}\left[\frac{1}{r}\frac{\partial}{\partial r}\left(r\frac{\partial T}{\partial r}\right)+\frac{1}{r^2}\frac{\partial^2 T}{\partial\theta^2}\right] \quad (1)$$

where effects of viscous dissipation and variable fluid properties have been neglected. The temperature is unity on the surface of the cylinder and zero far from it.

The velocity field is governed by the integral relationship involving the free vorticity of the fluid and the bound vorticity of the cylinder surface. This is in accordance with the method outlined in [10], which will be described here only briefly.

Consider a free vortex element of strength $\omega_0 dA_0$ to be located at point 0 in the fluid, and a bound vortex element of strength $\gamma_s dl_s$ to be located at point s on the surface of the cylinder. The elemental velocity induced at any point p in the fluid is given by

$$d\mathbf{V}_P=-\mathbf{i}+\frac{1}{2\pi}\left(\frac{\omega_0\mathbf{k}\times\mathbf{r}_{0p}}{r_{0p}^2}dA_0+\frac{\gamma_s\mathbf{k}\times\mathbf{r}_{sp}}{r_{sp}^2}dl_s\right) \quad (2)$$

where the onset flow velocity has been taken to be $-\mathbf{i}$. The terms in parentheses in equation (2) represent the velocity induction law. The variables have been made dimensionless using the free-stream velocity and the cylinder diameter. Also, $\mathbf{k}$ is the unit vector perpendicular to the plane of flow, and $\mathbf{r}_{0p}$ and $\mathbf{r}_{sp}$ are vectors directed from points 0 and s to p, respectively.

In practice, the velocity in the direction of the polar angle θ is obtained from equation (2). This can be expressed by

$$v_\theta(p)=\sin\theta_p+\frac{1}{2\pi}\left[\int\int K(r_p, r_0, \theta_p, \theta_0)\omega_0 dA_0 + \int K(r_p, r_s, \theta_p, \theta_s)\gamma_s dl_s\right] \quad (3)$$

where

$$K(r_p, r_0, \theta_p, \theta_0)=\frac{r_p-r_0\cos(\theta_0-\theta_p)}{r_p^2+r_0^2-2r_0r_p\cos(\theta_0-\theta_p)} \quad (4)$$

The velocity in the radial direction is obtained from the continuity equation, given as follows

$$\frac{1}{r}\frac{\partial}{\partial r}(rv_r)+\frac{1}{r}\frac{\partial}{\partial\theta}(v_\theta)=0 \quad (5)$$

once the distribution of v_θ has been determined.

The free vorticity of the fluid is governed by the usual transport equation, which is

$$\frac{\partial\omega}{\partial t}+\frac{1}{r}\frac{\partial}{\partial r}(rv_r\omega)+\frac{1}{r}\frac{\partial}{\partial\theta}(v_\theta\omega)$$
$$=\frac{1}{\mathrm{Re}_D}\left[\frac{1}{r}\frac{\partial}{\partial r}\left(r\frac{\partial\omega}{\partial r}\right)+\frac{1}{r^2}\frac{\partial^2\omega}{\partial\theta^2}\right] \quad (6)$$

The bound vorticity of the cylinder is governed by an integral equation which ensures that the zero penetration condition imposed on the fluid is satisfied at every point on the cylinder surface. That equation is

$$\gamma_q-\frac{1}{2\pi}\int_0^{2\pi}\gamma_s d\theta_s=2[u_\omega(q)+\sin\theta_q] \quad (7)$$

where q is any given point on the cylinder surface, and s is any other point.

The nonhomogeneous term of the right-hand side is due to the velocity of the onset flow and the tangential velocity induced by the free vorticity at the cylinder surface. This latter quantity has been represented by the symbol u_ω. It is given by

$$u_\omega(q)=\frac{1}{2\pi}\int\int K(r_q, r_0, \theta_q, \theta_0)\omega_0 dA_0 \quad (8)$$

The solution to equation (7) is made unique by enforcing the condition that the total free vorticity of the outer fluid is zero at all times. This also insures that the pressure distribution on the cylinder is single valued.

The presence of bound vorticity on the cylinder surface signifies that there is an apparent tangential slip velocity there. This must be canceled by the production of free vorticity. Therefore, the local value for the bound vorticity γ determines the local boundary condition to be imposed on the vorticity transport equation, equation (6). This boundary condition for any point on the surface of the cylinder can be stated as

$$-\frac{1}{\mathrm{Re}_D}\int_t^{t+\Delta t}\left(\frac{\partial\omega}{\partial r}\right)_{r=0.5}dt=\gamma(t) \quad (9)$$

while far from the cylinder, the free vorticity is zero.

Initially the fluid is at rest. At time $t=0$, the fluid moves impulsively, and the surfaced temperature of the cylinder is given

Nomenclature

A_0 = dimensionless area (relative to D^2)
AF = amplification factor to expand the node spacing in the computational grid
C_d = drag/$0.5\rho U_\infty{}^2 D$ = drag coefficient per length of cylinder
C_f = shear/$0.5\rho U_\infty{}^2$ = skin friction coefficient
C_l = lift/$0.5\rho U_\infty{}^2 D$ = lift coefficient per length of cylinder
C_p = $(P-P_o)/0.5\rho U_\infty{}^2$ = pressure coefficient
D = dimensional cylinder diameter
h = convective heat transfer coefficient
$\mathbf{i}$ = unit vector
k = thermal conductivity
$\mathbf{k}$ = unit vector
l_s = dimensionless arc length on surface of cylinder (relative to D)
Nu_D = hD/k = Nusselt number
n = dimensional frequency
P = dimensional pressure
P_0 = dimensional pressure at the front stagnation point, $\theta=0$
Pr = ν/α = Prandtl number
r = dimensionless radial coordinate (relative to D)
Re_D = $U_\infty D/\nu$ = Reynolds number
S_D = nD/U_∞ = Strouhal number
T = dimensionless temperature ($T=1$ on the cylinder surface, $T=0$ in the free stream)
t = dimensionless time (relative to D/U_∞)
U_∞ = dimensional free-stream velocity
u_ω = dimensionless velocity given by equation (8)
v_r, v_θ = dimensionless fluid velocity components in r and θ directions (relative to U_∞)
α = thermal diffusivity
γ = dimensionless bound vorticity on the cylinder surface (relative to U_∞)
θ = angle in cylindrical coordinates measured positive in a counterclockwise direction
ν = kinematic viscosity
ρ = fluid density
ω = dimensionless free vorticity in the boundary layer and wake (relative to U_∞/D)

Table 1 Summary of radial and time increments

Re_D	Number of node points	Minimum Δr	AF	Δt	Maximum radius
3000	80 × 40	$\Delta r(1) = 0.0060$	$\Delta r(1) = \Delta r(2) = 0.0060$ Nodes 3 through 9 $\Delta r(i+1) = \Delta r(i) + 0.002$ $\Delta r(10) = 0.0025$ $\Delta r(11) = 0.0030$ Nodes 12 through 18 $\Delta r(i+1) = \Delta r(i) + 0.01$ Nodes 19 through 40 $\Delta r(i) = 0.1$	0.014	3.30
70,800	80 × 40	$\Delta r(1) = 0.0013$	Nodes 2 through 40 $\Delta r(i+1) = 1.2\Delta r(i)$	0.012	9.25
70,800 (predictor corrector)	80 × 40	$\Delta r(1) = 0.0013$	Nodes 2 through 40 $\Delta r(i+1) = 1.2\Delta r(i)$	0.010	9.25
70,800	80 × 80	$\Delta r(1) = 0.0013$	$\Delta r(2) = \Delta r(1) = 0.0013$ Nodes 3 through 80 $\Delta r(i+1) = 1.08\Delta r(i)$	0.010	7.32

a step change. The free vorticity of the fluid is initially zero, and thus $u_\omega(q)$ in equation (7) is also zero immediately following the impulsive start. The solution for γ_q from (7) corresponds to pure potential flow past a cylinder, and obviously $\gamma_q = 2 \sin \theta_q$. This distribution, according to equation (9), determines the vorticity production at the cylinder surface at time $t = 0$. That is all that is needed to solve for the free vorticity of the fluid at the end of time step by integrating equation (6) over the time increment Δt. Similarly, the energy equation (1) is integrated forward over the same time increment. The boundary conditions is imposed that $T = 1$ on the surface.

At any later instance in time, the solution for ω is advanced forward in time by integrating equation (6), subject to the boundary condition (9). Simultaneously, the solution for the temperature field is obtained by integrating equation (1). The velocity component in the θ direction is obtained from equation (3), having obtained γ from equation (7), and v_r is evaluated from the continuity equation (5).

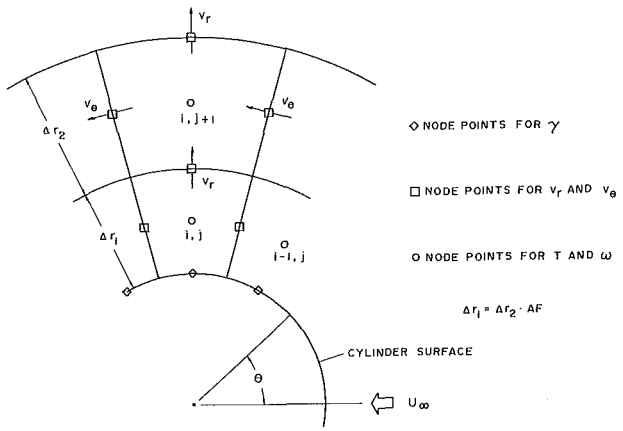

Fig. 1 Schematic of a typical node arrangement for numerical computations

Numerical Calculations

The numerical integration of equations (1), (5), and (6) is accomplished by discretizing the flow field surrounding the cylinder into a finite number of control volumes. Each control volume has a node point located at its centroid. A typical node arrangement is depicted in Fig. 1. The grid spacing varies from a fine mesh near the surface of the cylinder, to a coarse mesh far from the cylinder.

This work follows the same control volume approach used in earlier studies (see, e.g., [10]) and explained by Anderson et al. [12]. The preference for this approach stems from the fact that the governing partial differential equations are themselves obtained by applying basic conservation principles to infinitesimal control volumes. The procedure is briefly described below.

The solution is advanced in time by using an explicit technique. All variables are represented at the current time level except in the unsteady term, $\partial(\ )/\partial t$, where the solution is advanced forward in time. In contrast to [10], two different procedures were used in this study to advance the solution to the next time level. They are a first-order Taylor series representation and a second-order predictor-corrector scheme.

The terms on the right-hand side of equations (6) and (1) represent the diffusion of vorticity or energy as a result of gradients. With respect to the grid arrangement shown in Fig. 1, the diffusion terms are represented using the difference between the dependent variables, vorticity or temperature, at adjacent nodes. Thus, for example, the temperature gradient in the radial direction (from node i, j to node i, $j+1$) is represented as $(T_{i,j} - T_{i,j+1})/(0.5\Delta r_1 + 0.5\Delta r_2)$. The identical procedure is used for representing the gradient in the circumferential direction (between node $i-1$, j and node i, j) which is $(T_{i-1,j} - T_{i,j})/(r_{ij}\Delta\theta)$. This procedure is equivalent to central differencing and is second-order accurate.

The convective transport terms on the left-hand side of equations (6) and (1) are numerically more difficult to represent. As shown in Fig. 1, the convective velocities are obtained directly at the midpoint of the sides of the control volume surrounding each node. This is done by numerically integrating equations (3) and (5). Unlike the usual numerical finite-difference methods, there is no need to peform numerical averaging of velocities at adjacent points to obtain convective velocities on the boundary of a control volume. This is a distinct advantage of the present method. The convective flux is computed using the upwind procedure.

Attempts by the authors to use the higher order Time-Split MacCormack Method [12] encountered numerical difficulties, and it appears to be unstable for reasonable time steps. These will be discussed more fully in the next section.

The selection of the grid spacing and the time step is a trial and error procedure that must be guided by the physics of the problem. To obtain information such as force coefficients and heat transfer coefficients, it is necessary to place several nodes in the region occupied by the boundary layer. For a given Reynolds number, an estimate of the steady-state boundary-layer thickness can be made by examining known boundary-layer solutions. For example, a solution for flow over a cylinder is available in Schlichting [13]. Once the spacing between the cylinder surface and the first circle of nodes around the cylinder has been selected, subsequent node spacings are obtained by multiplying the Δr grid spacing by an appropriate amplification factor (AF). This permits the expansion of the grid from a fine mesh at the surface of the cylinder to a coarse mesh at the end of the computational grid. The selection of the time step Δt is controlled by the diffusion distance of the vor-

ticity generated at the surface of the cylinder. That is, if the first node is a distance $\Delta r/2$ from the surface of the cylinder, then Δt is governed by the equation $\Delta t \approx \mathrm{Re}_D \Delta r^2/10$. This result is obtained from a one-dimensional diffusion model. Experience has shown that a time step selected in this manner is close to the limit imposed by stability considerations.

In the present study, the basic computational region contains 80 nodes around the cylinder (i.e., $\Delta\theta = 2\pi/80$), and either 40 or 80 nodes in the r direction. To detect any occurrence of periodic vortex shedding, flow symmetry was not enforced. The Δr spacing is selected such that no fewer than four node points are in the boundary layer in the vicinity of the flow separation point. The spatial and time increments are summarized in Table 1 and discussed in the next section.

Throughout the entire flow field, the θ component of velocity v_θ is obtained by integrating equation (3). The velocity has one contribution from the free vorticity and a second contribution from the bound vorticity on the surface of the cylinder. The numerical integration is performed by treating the vorticity as a constant within a grid control volume and along a Δl spacing on the surface of the cylinder. At any time level, the integral expressions given by equation (3) and evaluated over a control volume or surface segment can be considered to be a constant vorticity value times an integrand which is a function of geometry. The integrated results yield geometric coefficients which are fixed for a given grid. They were calculated using Gauss quadrature with 40 Gauss points, after which they were stored in a data file. For an 80 by 40 grid, with an additional 80 grid points along the surface of the cylinder, there are in excess of ten million geometric coefficients. That is, for each grind point (3280 of them), there are 3280 geometric coefficients. However, many coefficients are the same because of symmetry. Therefore, the number of different geometric coefficients sotred in a data file can be reduced to 1.34×10^5. The evaluation of a single velocity component in the θ direction at the surface of a control volume is performed by multiplying the appropriate instantaneous bound and free vorticity values by the appropriate geometric coefficient, and then summing the result of these 3280 multiplications. This product and summing procedure is repeated for each velocity in the flow field. Once the value of v_θ is calculated throughout the flow field, the value of v_r is obtained from the continuity equation (5). Calculations for v_r begin at the surface of the cylinder, where $v_r = 0$, and march outward.

To obtain the local values of Nu_D and C_f, the slope of the temperature profile and the slope of the velocity profile must be calculated at the surface of the cylinder. The slope is obtained by fitting the temperature and velocity distributions to a second-order polynomial of the form $a + br + cr^2$. The boundary conditions at the surface of the cylinder, $T = 1$ and $v_\theta = 0$, and the instantaneous distribution in the flow field permit the determination of the constants a, b, and c. The instantaneous average Nusselt number Nu_D is obtained by integrating the local Nu_D around the surface of the cylinder using the trapezoidal rule.

As in [10], the distribution for the bound vorticity, γ satisfies a Fredholm integral equation (7). For a grid with 80 points on the surface of the cylinder, enforcement of equation (7) results in 80 simultaneous equations for the 80 unknown values of γ. For the case of a circular cylinder it is found that a particular solution to equation (7) is given by the nonhomogeneous term. Therefore, γ does not have to be found by solving simultaneous equations. After a particular solution for γ is evaluated at the 80 specified node points on the surface of the cylinder, the general solution is then generated and made unique using the procedure as described in [10].

The dimensionless pressure distribution along the surface of the cylinder is obtained by numerically integrating the equation

$$\frac{\partial P}{\partial \theta} = \frac{1}{\mathrm{Re}_D}\left(\frac{\partial \omega}{\partial r}\right)_{r=0.5} \tag{10}$$

around the surface of the cylinder using the trapezoidal rule. As in previous studies (e.g., [10]) the slope of the vorticity distribution at the surface of the cylinder is numerically represented by the equation

$$\frac{1}{\mathrm{Re}_D}\left(\frac{\partial \omega}{\partial r}\right)_{r=0.5} = -\frac{\gamma}{\Delta t} \tag{11}$$

Since the distribution of the bound vorticity γ is known, the pressure distribution can be calculated. Once the pressure distribution and shear stress are known along the surface of the cylinder, the lift and drag coefficients are obtained by resolving the forces into components parallel and normal to the free stream.

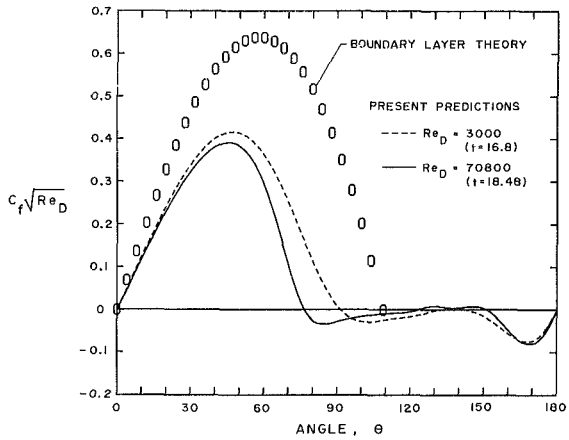

Fig. 2 Local skin friction coefficient at steady state

Results and Discussion

The choice of $\mathrm{Re}_D = 70{,}800$ permits a comparison of the numerical results with those obtained by Giedt [3]. When comparing results, it is necessary to consider the experimental methods used to obtain the data. Experimental results are sensitive to such factors as free-stream turbulence, wind-tunnel blockage, and end effects. The latter are especially important when the intention is to represent two-dimensional flow over a cylinder. Giedt [4] noted that the addition of end plates on a cylinder made a noticeable change in the measured pressure distribution. These altered results were obtained in the same wind tunnel and with the same cylinder model. Seban [5], using a different test facility and a different size cylinder, reported a difference in the measured pressure distribution as compared to the findings of Giedt [4].

Although experimental procedures are constantly improving, it is difficult for measurements to reveal the fine details of flow behavior in region where the flow field separates from a body, such as on the back side of a cylinder. While it is possible to represent two-dimensional flow over a cylinder in a numerical computational procedure, the results obtained are subject to uncertainties resulting from the discretization of the flow field and the subsequent numerical representation of the governing equations. It is therefore reasonable to expect that the experimental and numerical results will agree only qualitatively. At the same time, however, the numerical results may reveal details of the flow field which cannot be measured by experimental techniques.

The present study is concerned with transient as well as steady-state results. It can be appreciated that judgment is required in determining when steady state is achieved. This is because the approach to steady state is always asymptotic. For

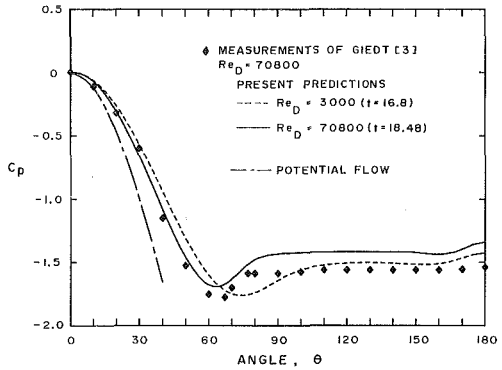

Fig. 3 Comparison of predicted and experimental pressure coefficient at steady state

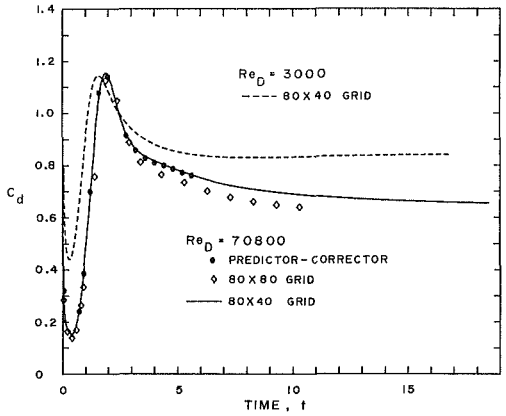

Fig. 4 Time variation of the drag coefficient

purposes of the present study, steady state was assumed to exist when the drag coefficient and average Nusselt were essentially unchanging with time. For Re = 3000 and 70,8000, this occurred at $t = 16.8$ and 18.48, respectively. These time values are restated on the figures for completeness.

An understanding of the details of the flow field around a cylinder is obtained from an examination of Fig. 2, which shows the computed skin friction coefficient at steady-state conditions. For $\mathrm{Re}_D = 70{,}800$, the skin friction coefficient has a zero value at θ equal to 78 deg, 124 deg, 151 deg, and 180 deg. The first zero value at 78 deg represents the point where flow separation occurs. This result is in excellent agreement with Giedt's [3] findings, which also show separation occurring at 78 deg. It is also in good agreement with the generally accepted value of 82 deg for laminar boundary layers and moderate Reynolds numbers. The zero skin friction coefficient at 124 deg represents a stagnation point in the flow. Between the separation point and this stagnation point, there is reverse flow over the cylinder. The zero skin friction at 151 deg represents a second flow separation point. Between 124 deg and 151 deg, the flow is in a counterclockwise direction toward the rear of the cylinder. From the point of separation, 151 deg, to the rear stagnation point, 180 deg, the flow is again in the reversed (clockwise) direction.

A careful examination of Fig. 2 reveals the same phenomena at the lower Reynolds number of 3000. The flow separation at 92 deg is apparent. An examination of the numerical results shows a stagnation point at 133 deg and a second separation point at 142 deg. Although this behavior has not been previously reported at Re_D as low as 3000, the formation of a stagnation point and a second separation point is in qualitative agreement with the results of Thoman and Szewczyk [14], who reported similar observations at Re_D greater than 4×10^4. The diminishing of the intensity of the stagnation point flow at $\mathrm{Re}_D = 3000$ and the movement of the first separation point rearward along the surface of the cylinder indicate that at lower Re_D, the flow separates on the backside of the cylinder, and the flow from the rear stagnation point, 180 deg, to the point of separation is a reversed flow. This behavior is in agreement with the results of Thoman and Szewczyk [14].

For the purpose of comparison, the results for the skin friction coefficient obtained from boundary-layer theory [13] are presented in Fig. 2. The boundary-layer result is dependent on the pressure distribution, which is based on potential flow theory. This pressure distribution is shown in Fig. 3 and is known to be incorrect away from the forward stagnation point. Thus the flow separation angle of 108 deg is in obvious disagreement with the present results obtained for moderate Re_D.

Figure 3 shows the pressure coefficient around the cylinder at steady-state conditions. For $\mathrm{Re}_D = 70{,}800$, the numerical results can be compared to the experimental results of Giedt [3]. The agreement along the front of the cylinder is good. The numerical results obtained in the present work indicate more of a pressure recovery on the back of the cylinder than is indicated in the experimental results. Giedt [4] reported that the pressure distribution shown in Fig. 3 was altered with the addition of end plates to the flow apparatus, but the direction of the change was not reported. The pressure coefficient depicted in Fig. 3 is consistent with the skin friction results depicted in Fig. 2. This can be seen by comparing the first point of separation in Fig. 2, 78 deg, to the point where the pressure coefficient levels off to a constant value in Fig. 3.

The behavior of the drag coefficient C_d as the flow field develops is shown in Fig. 4. The qualitative behavior of C_d is the same as observed by Thoman and Szewczyk [14] and others. At early times, C_d reaches a minimum value, followed by a maximum value, and then it approaches a steady-state value. No oscillation in C_d, as a result of vortex shedding, was noted. In the present work, oscillation had to be artificially started by perturbing the flow field. The magnitude of the perturbation was not sufficient to cause a fluctuation in the drag coefficient. This point will be discussed subsequently.

For $\mathrm{Re}_D = 3000$, at $t = 16.8$, the value of C_d is 0.84. This result is in excellent agreement with accepted experimental values. The contribution of the friction drag to the total drag is approximately 5 percent. For $\mathrm{Re}_D = 70{,}800$, at $t = 18.48$, the value of C_d is 0.66. This result is lower than the value of 1.2 given in Schlichting [13]. At this higher Re_D, the contribution of the skin friction to the total drag is approximately one percent. An examination of the available literature indicates a tendency for numerical results to predict lower values of C_d than those found experimentally. Deffenbaugh and Marshall [15] examined flow over an impulsively started cylinder in the high Reynolds number laminar regime ($10^4 < \mathrm{Re}_D < 10^5$) and obtained a value of $C_d \approx 0.9$. Chorin [16] utilized numerical methods for solving the flow over a cylinder by numerically simulating the process of vorticity generation and dispersal. At $\mathrm{Re}_D = 10{,}000$, the value of the C_d was 0.87. At $\mathrm{Re}_D = 100{,}000$, $C_d = 0.29$. Chorin conjectured that the rough representation of the boundary layer triggers a premature onset of the drag crisis. Loc [17] used higher order finite-difference numerical methods to investigate flow over an impulsively started cylinder. Although his numerical calculations were not carried to the point where the drag coefficient approaches a steady-state value, the results indicate that at $\mathrm{Re}_D = 1000$, C_d will be much less than the experimental value. Fornberg [11] used a numerical finite-difference approach to solve for low Reynolds number flow ($\mathrm{Re}_D < 300$) over a cylinder. His value of $C_d = 0.722$ at $\mathrm{Re}_D = 300$ is considerably below the experimental value of $C_d \approx 1.5$.

To assess the effect of discretization error on the results obtained for $\mathrm{Re}_D = 70{,}800$, the calculations were repeated using a second-order predictor-corrector scheme with the original 80

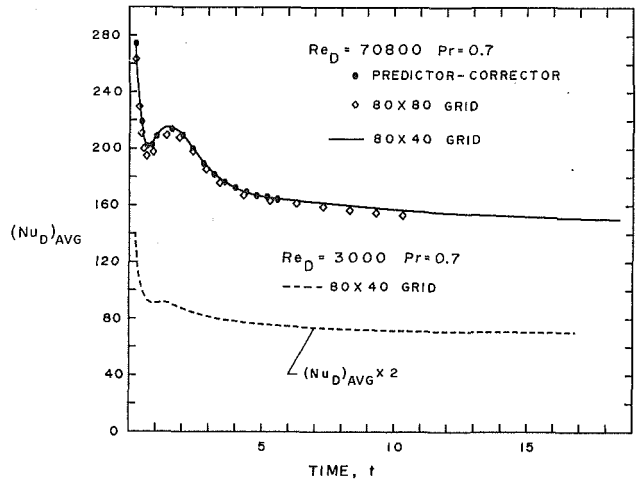

Fig. 5 Time variation of the average Nusselt number

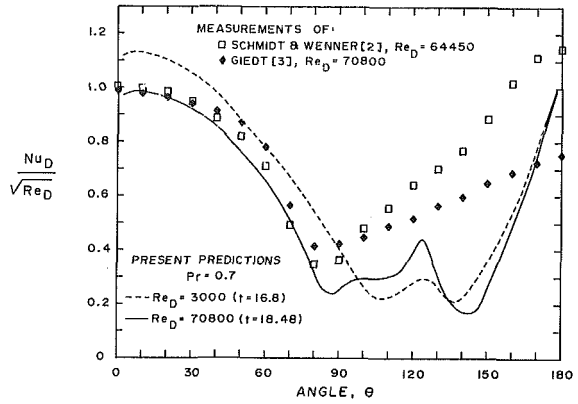

Fig. 6 Comparison of predicted and experimental local Nusselt number at steady state

by 40 grid, and repeated a second time with the original explicit formulation with an 80 by 80 grid. A summary of the radial increments and the corresponding time steps is tabulated in Table 1.

Since the present explicit scheme is only first-order accurate in the time integration Δt, a predictor-corrector scheme, which is second-order accurate, Δt^2, was used to integrate the governing equations forward in time. The results obtained are shown in Figs. 4 and 5. The agreement between the first-order and second-order accurate integration is excellent. This is due to the small size of the time step. The second numerical experiment was performed by altering the grid to an 80 × 80 node arrangement and using the explicit first-order time-integration scheme. This node arrangement permitted a finer grid spacing to nearly the same maximum radius as achieved for the 80 × 80 grid. For each case, the size of the first grid spacing at the surface of the cylinder, $\Delta r = 0.0013$, was not changed. The behavior of the drag coefficient, as shown in Fig. 4, was changed only slightly. As can be seen, the steady-state drag coefficient appears to be lower. The behavior of Nu_D, shown in Fig. 5, was essentially unchanged from that obtained with the 80 × 40 grid. A second-order accurate scheme (in both time and distance) known as the Time-Split MacCormack Method [12], was used to integrate the energy equation, and the results will be discussed subsequently.

The heat transfer results were obtained for a $Pr = 0.7$. Figure 5 shows the transient behavior of the average Nusselt number. After the impulsive start of the flow, $(Nu_D)_{avg}$ decreases to a minimum value, then increases to a relative maximum, and finally decreases asymptotically, approaching the steady-state value. For $Re_D = 3000$, the value of $(Nu_D)_{avg} = 35$ was obtained for $t = 16.8$. For $Re_D = 70{,}800$, the value of the $(Nu_D)_{avg} = 150$ was obtained for $t = 18.48$. For $Re_D = 3000$, empirical correlations predict $(Nu_D)_{avg} = 28$. McAdams [1] shows experimental results for air flowing normal to a cylinder, and the numerical result obtained in this study for $Re_D = 3000$ is well within the scatter of available experimental data. At $Re_D = 70{,}800$, empirical correlations predict that $131 < (Nu_D)_{avg} < 190$. The authors numerically integrated Giedt's local results [3] for $Re_D = 70{,}800$ around the surface of the cylinder and obtained $(Nu_D)_{avg} = 181$. Again, the numerical result obtained in this study for $Re_D = 70{,}800$ is within the scatter of available experimental data.

To investigate the use of higher order numerical procedures, the energy equation was integrated forward in time using the Time-Split MacCormack Method [12], which is second-order accurate in time and distance. Since the vorticity transport equation and the energy equation are uncoupled, the procedure used was to integrate the vorticity transport equation using the explicit time method with the upwind differencing method. The energy equation was then integrated using the time-split method and the same time step Δt. The results obtained indicated that the integration of the energy equation was unstable. That is, in the transient behavior of the average Nusselt number, as shown in Fig. 5, $(Nu_D)_{avg}$ reached a minimum, but then continued to increase indefinitely. The behavior of the local Nu_D around the cylinder was also a source of concern. Because the velocity field is essentially symmetric on the top and bottom of the cylinder, it is expected that the temperature field should behave in the same manner. However, it was observed that the temperature distribution in the flow field lost symmetry starting at the rear stagnation point. Several attempts were made to obtain results at reduced time steps. The value of Δt was reduced from 0.012 to 0.004, but this did not eliminate the difficulty. There is concern that the representation of the convective transport terms by this higher-order numerical scheme is not consistent with the physical situation in regions of reversed flow. Further attempts to reduce the time step were not made since a reduced time step requires excessive computer time to reach conditions approximating steady state.

The behavior of the local Nu_D at steady-state conditions is shown in Fig. 6. The data of Giedt [3] and the present numerical calculations are in good agreement along the front of the cylinder up to the point of separation. The behavior of the local Nu_D along the back of the cylinder, as obtained in the present work, is entirely consistent with the behavior of the skin friction coefficient shown in Fig. 2. The local Nu_D will have relative maxima at stagnation points. The behavior at $\theta = 0$ deg and $\theta = 180$ deg is thus as expected. For $Re_D = 3000$, a stagnation point is present at $\theta = 133$, and from Fig. 6, a relative maximum can be seen near this location. The same observation can be made for $Re_D = 70{,}800$ at $\theta = 124$ deg. The minimum values in the local Nu_D occur near the separation points. These are at $\theta = 92$ deg and 142 deg for $Re_D = 3000$, and $\theta = 78$ deg and 151 deg for $Re_D = 70{,}800$. This behavior in the local Nu_D was observed by Giedt [3] at higher Re_D ($> 140{,}000$), but it was not observed at the lower Re_D.

In [3], Giedt reported that the first minimum in Nu_D occurred at the point where the boundary layer undergoes transition from laminar to turbulent flow, and the second minimum occurred at the point of flow separation. Subsequently [4], Giedt noted that throughout the entire range of Reynolds numbers (70,800 to 219,000) covered in his earlier experiments, laminar separation occurred prior to the 90 deg point, and in no case was there a turbulent boundary layer present. It is the authors' opinion that the behavior of the local Nusselt number, as reported in [3], should be explained based on the occurrence of flow separation/stagnation/separation, rather than transition/separation. The fact that local maxima did not appear in Giedt's data at low Reynolds numbers does not imply that a stagnation point does not exist between the point of separation and 180 deg. Rather, it is the opinion of

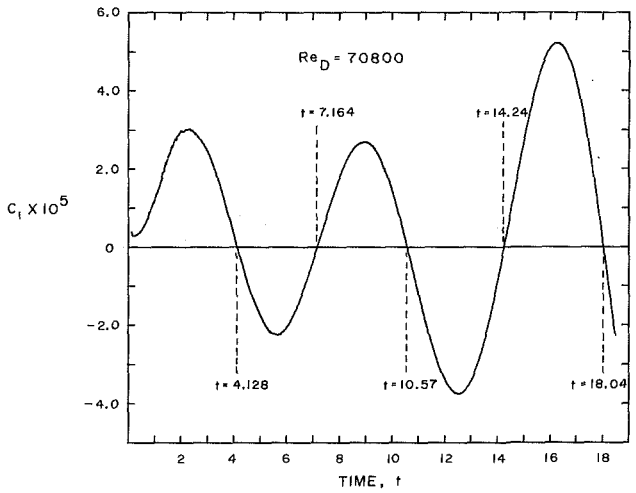

Fig. 7 Time variation of the lift coefficient

the authors that the instrumentation was not sufficiently sensitive to reveal the details of the flow field at lower Reynolds numbers.

The data of Schmidt and Wenner [2] at $Re_D = 64{,}450$ are shown in Fig. 6 to illustrate the sensitivity of the experimental results to changes in the surface boundary conditions and the physical arrangement of the cylinder. In Schmidt's tests, the cylinder was mounted in an airstream issuing from a rectangular nozzle. The data of Giedt were obtained in an open-throat-type wind tunnel for conditions which approximate constant wall heat flux, while the data of Schmidt and the present results are for an isothermal surface. All results are in good agreement, up to the point of separation. Beyond this point, the numerical results reveal details in the region of flow separation which are not apparent in the experimental results.

The variation of computed values of C_l with time for $Re_D = 70{,}800$ is shown in Fig. 7. The first results obtained in the present study were for $Re_D = 3000$, and these produced a zero lift coefficient. That is, there was no periodic shedding of vorticity from the rear of the cylinder as is known to occur in actual flow situations. The absence of shedding in the numerical calculations results from the fact that in the numerical formulation, the cylinder surface is perfectly smooth, and no disturbances are present in the flow field.

When the results for $Re_D = 70{,}800$ were obtained, to induce periodic shedding, the flow field was perturbed by changing the velocity induced by the free vorticity in the flow field at the surface of the cylinder. The magnitude of the perturbation was to decrement the induced velocity by 2 percent on one side of the cylinder near the expected point of flow separation. The velocity was perturbed at $t = 0.024$, on the second time step, and only for this one time step. Yet as can be seen from Fig. 7, the perturbation to the flow field persisted for all times thereafter. In retrospect, the magnitude and duration of the perturbation were too small. The fluctuating lift coefficient yields a Strouhal number of $S_D = 0.14$, which is below the generally accepted value of 0.21. However, this is in general agreement with the value of 0.17 obtained by Thoman and Szewczyk [14]. From Fig. 7 it can be seen that the amplitude of C_l is still increasing after $t = 14.24$. The authors expect that eventually a periodic behavior with a constant amplitude will be achieved.

By way of closing, it is noted that all the numerical calculations were performed in double precision on a PRIME 850 superminicomputer at the United States Military Academy, West Point. No attempt was made to record the CPU time needed to complete the present calculations. The PRIME 850 is not structured for the fast execution of repetitive calculations such as those needed in these numerical studies. Therefore, comparisons of execution times for different algorithms run on different machines are of little value.

Conclusions

The present work has shown that it is possible to use the computational procedure previously developed and presented by Kinney and Cielak [8] and Taslim et al. [10] to compute the flow field around a circular cylinder at Re_D approaching 100,000. The numerical solution of the energy equation is conjunction with the vorticity transport equation yields average heat transfer results which are in good with experimental values. The results obtained for local values of the skin friction coefficient and the Nusselt number reveal the details of the flow field, especially in the region of flow separation which had not been previously reported. The use of different numerical schemes does not seem to change the results significantly. Furthermore, it is shown that certain higher-order schemes may be inappropriate to obtain numerical solutions in flow situations involving regions of reversed flow.

Acknowledgments

The authors express their appreciation to the Computer Center at the U.S. Military Academy for providing access to the PRIME 850 computer on which this work was performed.

References

1 Mc Adams, W. H., *Heat Transmission*, 3rd ed., McGraw-Hill, New York, 1954.

2 Schmidt, E., and Wenner, K., "Heat Transfer Over the Circumference of a Heated Cylinder in Transverse Flow," NACA TM 1050, Oct. 1943; see also "Wärmeabgabe über den Umfang eines angeblasenen geheizten zylinders," *Forschung auf dem Gebiete des Ingenieurwesens*, Vol. 12, Mar.-Apr. 1941, pp. 65-73.

3 Giedt, W. H., "Investigation of Variation of Point Unit Heat-Transfer Coefficient Around a Cylinder Normal to an Air Stream," *Transactions of the ASME*, Vol. 71, May 1949, pp. 725-730.

4 Giedt, W. H., "Effect of Turbulence Level of Incident Air Stream on Local Heat Transfer and Skin Friction on a Cylinder," *Journal of Aerospace Science*, Vol. 18, Nov. 1951, pp. 725-730.

5 Seban, R. A., "The Influence of Free Stream Turbulence on the Local Heat Transfer From Cylinders," ASME JOURNAL OF HEAT TRANSFER, Vol. 82, May 1960, pp. 101-107.

6 Jain, P. C., and Goel, B. S., "A Numerical Study of Unsteady Laminar Forced Convection From a Circular Cylinder," ASME JOURNAL OF HEAT TRANSFER, Vol. 98, May 1976, pp. 303-307.

7 Chang, M. W., Finlayson, B. A., and Sleicher, C. A., "Heat Transfer in Flow Past Cylinders With Variable Viscosity," in: *Numerical Properties and Methodologies in Heat Transfer*, Hemisphere Publication Corporation, Washington, 1983, pp. 349-360.

8 Kinney, R. B., and Cielak, Z. M., "Analysis of Unsteady Viscous Flow Past an Airfoil: Part I - Theoretical Development," *AIAA Journal*, Vol. 15, Dec. 1977, pp. 1712-1717.

9 Cielak, Z. M., and Kinney, R. B., "Analysis of Unsteady Viscous Flow Past an Airfoil: Part II - Numerical Formulation and Results," *AIAA Journal*, Vol. 16, Feb. 1978, pp. 105-110.

10 Taslim, M. E., Kinney, R. B., and Paolino, M. A., "Analysis of Two-Dimensional Viscous Flow over Cylinders in Unsteady Motion," *AIAA Journal*, Vol. 22, No. 5, May 1984, pp. 586-594.

11 Fornberg, B., "A Numerical Study of Steady Viscous Flow Past a Circular Cylinder," *Journal of Fluid Mechanics*, Vol. 98, Part 4, June 1980, pp. 819-855.

12 Anderson, D. A., Tannehill, J. C., and Pletcher, R. H., *Computational Fluid Mechanics and Heat Transfer*, 1st ed., McGraw-Hill, New York, 1984.

13 Schlichting, H., *Boundary-Layer Theory*, 7th ed., McGraw-Hill, New York, 1979.

14 Thoman, D. C., and Szewczyk, A. A., "Time-Dependent Viscous Flow Over a Circular Cylinder," *Physics of Fluids*, Vol. 12, Supplement II, Dec. 1969, pp. II-76-II-86.

15 Deffenbaugh, F. D., and Marshall, F. J., "Time Development of the Flow About an Impuslively Started Cylinder," *AIAA Journal*, Vol. 14, No. 7, July 1976, pp. 908-913.

16 Chorin, A. J., "Numerical Study of Slightly Viscous Flow," *Journal of Fluid Mechanics*, Vol. 57, Part 4, Mar. 1973, pp. 785-796.

17 Loc, T. P., "Numerical Analysis of Unsteady Secondary Vorticies Generated by an Impulsively Started Circular Cylinder," *Journal of Fluid Mechanics*, Vol. 100, Part 1, Sept. 1980, pp. 111-128.

Electric Field Effects on Natural Convection in Enclosures

D. A. Nelson
Assistant Professor,
Department of Mechanical Engineering—
Engineering Mechanics,
Michigan Technological University,
Houghton, MI 49931
Assoc. Mem. ASME

E. J. Shaughnessy
Professor,
Department of Mechanical Engineering
and Materials Science,
Duke University,
Durham, NC 27706
Mem. ASME

The enhancement of convective heat transfer by an electric field is but one aspect of the complex thermoelectric phenomena which arise from the interaction of fluid dynamic and electric fields. Our current knowledge of this area is limited to a very few experimental studies. There has been no formal analysis of the basic coupling modes of the Navier–Stokes and Maxwell equations which are developed in the absence of any appreciable magnetic fields. Convective flows in enclosures are particularly sensitive because the limited fluid volumes, recirculation, and generally low velocities allow the relatively weak electric body force to exert a significant influence. In this work, the modes by which the Navier–Stokes equations are coupled to Maxwell's equations of electrodynamics are reviewed. The conditions governing the most significant coupling modes (Coulombic forces, Joule heating, permittivity gradients) are then derived within the context of a first-order theory of electrohydrodynamics. Situations in which these couplings may have a profound effect on the convective heat transfer rate are postulated. The result is an organized framework for controlling the heat transfer rate in enclosures.

Introduction

There are several mechanisms through which an electric field may affect a velocity field in a fluid. One interaction, the so-called "corona wind," was described in the literature over two hundred years ago [10]. The corona wind is attributed to the Coulombic force, which is the force exerted on a free charge by an electric field. Movement of the gaseous medium results from momentum transfer from the ions to the neutral molecules via collisions [24]. The Coulombic force and the associated corona wind have been the subjects of several investigations of electrofluid interactions during corona discharge [3, 22, 28]. This interaction is of particular interest in electrostatic precipitator theory. A significant body of recent work has developed due to this application [16, 29].

The Coulombic force in the corona wind is but one of several electrohydrodynamic interactions whch may be present in a real fluid subject to property variations under the influence of thermal and pressure gradients. Electrohydrodynamics is defined as the coupling of an electric field and a velocity field in a fluid continuum [6]. This encompasses both situations in which the momentum equations are coupled to the governing electrical equations, and situations in which the equations describing the electric field depend upon solutions to the momentum equations. Additionally, there are instances in which the coupling extends both ways, though this case obviously presents a high degree of mathematical difficulty.

The literature suggests that for selected goemetries, thermal convection may be enhanced substantially in the presence of an appropriate electric field. The precise mechanism is not clear for every case, however. An electric field potentially can affect convection via at least four distinct electrohydrodynamic coupling modes. The four modes will be referred to here as Coulombic forces, electrostriction, dielectric gradients, and Joule heating.

Franke [7] was able to double the free-convection rate from a vertical flat plate by means of corona discharge from properly spaced vertical wire electrodes. Later work by Franke and Hutson [8] demonstrated a comparable effect in a heated vertical cylinder with vertical wire electrodes placed about the inner circumference of the cylinder. In both cases the increase in the heat transfer rate was accompanied by the production of columnar vortices in the boundary layer. Although this might indicate induced secondary flow in the boundary layer as the primary mechanism for electrical enhancement of thermal convection, an earlier study by Marco and Velkhoff [19] demonstrated augmented heat transfer from flat plates which they attributed to "the corona wind stream impinging on the heated plate . . . ." Corona-driven stagnation flow was the mechanism cited by Chuang and Velkoff [4] for the observed threefold increase in the mass transfer rate during frost formation on a flat plate in the presence of a needle electrode. Reynolds and Holmes [21] attempted to augment forced convection by placing wire electrodes parallel to the axis of a finned-tube heat exchanger, but were unable to demonstrate an effect. This is consistent with the findings of Kulacki [14], which indicate forced convection enhancement is significant only at low Reynolds numbers.

The role of electrostriction in electrical enhancement of convective heat transfer was considered by Lykoudis and Yu [18]. Electrostrictive forces, which are due to the variation in electrical permittivity with mass density, are commonly neglected in comparison to the Coulomb force. Electrostriction is of special concern at voltages below the corona point where there are, presumably, no free charges and hence no Coulombic force.

A comparison of electrostrictive and Coulombic forces in free convection from a horizontal plate performed by Windischmann [26] concludes that neither force alone is sufficient to explain the magnitude of cooling enhancement detected in the presence of corona discharge.

An analysis of electrically enhanced thermal convection by Lazarenko [15] presumes an incompressible, low-conductivity fluid medium. Thus buoyancy forces and electrostriction, as well as thermal gradients due to Joule heating, are not included in that discussion. Velkoff [25] similarly considers the role of Coulombic forces in convection enhancement.

Prior investigations into electrical enhancement of convective heat transfer have been specific and restricted to a very few geometries and field configurations. The discussion presented here will consist of a development of the reduced governing equations and an analysis of the relevant electrohydrodynamic coupling mechanisms. This will yield some guidelines for the designer utilizing electric means to enhance natural convection in enclosures.

First-Order Theory

Unless otherwise noted, the analyses presented in this work will be for the specific case of air at 288 K and 1 atm, although the theory applies to many gases and liquids.

Contributed by the Heat Transfer Division and presented at the ASME Winter Annual Meeting, New Orleans, Louisiana, December 9–13, 1984. Manuscript received by the Heat Transfer Division January 14, 1985.

The governing equations of electrohydrodynamics are the conservation equations of fluid dynamics (mass, momentum, and energy) and of electrodynamics (Maxwell's equations, Ohm's law). For an isotropic, linear fluid with zero second viscosity, the governing equations are [2, 6]

$$\frac{D\rho_m}{Dt}+\rho_m\frac{\partial u_j}{\partial x_j}=0 \tag{1}$$

$$\rho_m\frac{Du_i}{Dt}=\frac{\partial \sigma_{ij}}{\partial x_j}+F_i \tag{2}$$

$$\rho_m C_p\frac{DT}{Dt}=\frac{\partial}{\partial x_j}\left(k\frac{\partial T}{\partial x_j}\right)+\gamma T\frac{Dp}{Dt}+\mu\Phi_v$$
$$+\beta|\rho_c|E_i(E_i+\epsilon_{ijk}u_jB_k)-\rho_m T\frac{DS_e}{Dt} \tag{3}$$

$$\frac{\partial D_j}{\partial x_j}=\rho_c \tag{4}$$

$$\frac{\partial B_j}{\partial x_j}=0 \tag{5}$$

$$\epsilon_{ijk}\frac{\partial H_k}{\partial x_j}=J_i+\frac{\partial D_i}{\partial t} \tag{6}$$

$$\epsilon_{ijk}\frac{\partial E_k}{\partial x_j}=-\frac{\partial B_i}{\partial t} \tag{7}$$

$$J_i=\beta|\rho_c|(E_i+\epsilon_{ijk}u_jB_k)+\rho_c U_i \tag{8}$$

The relevant constitutive relations are

$$D_i=\epsilon E_i \tag{9}$$

$$B_i=\mu_m H_i \tag{10}$$

$$\sigma_{ij}=-\left(p+\mu\frac{2}{3}\frac{\partial u_k}{\partial x_k}\right)\delta_{ij}+\mu\left(\frac{\partial u_i}{\partial x_j}+\frac{\partial u_j}{\partial x_i}\right) \tag{11}$$

$$\Phi_v=\frac{\partial u_i}{\partial x_j}\left[\frac{\partial u_i}{\partial x_j}+\frac{\partial u_j}{\partial x_i}\right]-\frac{2}{3}\left(\frac{\partial u_k}{\partial x_k}\right)^2 \tag{12}$$

$$s_e=\frac{E_jE_j}{2\rho_m}\left(\frac{\partial\epsilon}{\partial T}\right)+\frac{H_jH_j}{2\rho_m}\left(\frac{\partial\mu_m}{\partial T}\right) \tag{13}$$

$$F_i=\rho_m g_i+f_i \tag{14}$$

Attention is restricted here to cases of weakly ionized fluids. Formally, the magnitudes of the current density and length scales are limited to no more than 10 nA-cm^{-2} and 10 m, respectively. Under quasi-steady conditions, this yields an upper bound of 10^{-9} Tesla on any induced magnetic fields. If it is stipulated that there are no applied magnetic fields, terms involving B_i and H_i may be neglected in equations (6)–(8) and in equation (13).

The electric body force per unit volume on a fluid element is given by [20]

$$f_i=\rho_c E_i-\frac{E_jE_j}{2}\frac{\partial\epsilon}{\partial x_i}+\frac{1}{2}\frac{\partial}{\partial x_i}\left(\rho_m E_jE_j\frac{\partial\epsilon}{\partial\rho_m}\right) \tag{15}$$

The first term is the Coulombic, or electrophoretic, force. The presence of this force requires that there be some mechanism for space charge generation. The mechanism may be corona discharge if a mobility model is assumed for the medium, or thermally induced conductivity gradients in the case of a conductivity model [27].

The second term of the electric force expression is present whenever there is a significant permittivity gradient in the fluid. It will be referred to here as simply the permittivity gradient term. The third term, the electrostriction, results from the relationship between permittivity and mass density. The total body force on a fluid element is thus

$$F_i=\rho_m g_i+\rho_c E_i-\frac{E_jE_j}{2}\frac{\partial\epsilon}{\partial x_i}+\frac{1}{2}\frac{\partial}{\partial x_i}\left(\rho_m E_jE_j\frac{\partial\epsilon}{\partial\rho_m}\right) \tag{16}$$

Equation (16) couples the Navier–Stokes equations directly to Maxwell's equations via the final three terms of the right-hand side. What is not so apparent is that the gravitational term is also coupled to the electric field via the energy equation. The existence of space charge in the medium contributes a Joule heating term, $\beta|\rho_c|E_jE_j$, to the energy equation, and may therefore produce or enhance thermal buoyant forces.

The couplings between the electric, fluid velocity, and thermal fields are highly dependent upon the nature of property variations within the fluid medium. A description of the significant terms requires development of a theory of electrohydrodynamics which is in many respects analogous to the classic Boussinesq approximation. A first-order theory of electrohydrodynamics will be described here in which the fluid properties are expressed as Taylor series expansions in terms of thermodynamic state variables about some arbitrary datum point. As the fields considered in this work are either stationary or low-frequency, dispersive effects are absent. Thus it is reasonable to treat all properties solely as functions of temperature and pressure. Furthermore, if the pressure and temperature excursions are modest the medium is accurately described by a truncated series in which second and higher order terms are neglected. The various fluid properties are then written as follows

$$\rho_m=\rho_{m_d}[1-\gamma_d(T-T_d)+B_{1_d}(p-p_d)]$$
$$\gamma=\gamma_d[1+A_{2_d}(T-T_d)+B_{2_d}(p-p_d)]$$
$$\epsilon=\epsilon_d[1+A_{3_d}(T-T_d)+B_{3_d}(p-p_d)]$$
$$k=k_d[1+A_{4_d}(T-T_d)+B_{4_d}(p-p_d)]$$
$$\mu=\mu_d[1+A_{5_d}(T-T_d)+B_{5_d}(p-p_d)]$$
$$C_p=C_{pd}[1+A_{6_d}(T-T_d)+B_{6_d}(p-p_d)]$$
$$\beta=\beta_d[1+A_{7_d}(T-T_d)+B_{7_d}(p-p_d)]$$

Nomenclature

A_n = nth thermal coefficient
B_i = magnetic induction vector
B_n = nth pressure coefficient
C_p = specific heat at constant pressure
D_i = electric displacement vector
E_i = electric field vector
f_i = electric body force vector
F_i = total body force vector
g_i = gravitational acceleration vector
G = gravitational acceleration constant
H_i = magnetic field vector
J_i = current density vector
k = thermal conductivity
p = fluid pressure
p^* = modified pressure
s_e = electric entropy
t = time
T = fluid temperature
u_i = velocity vector
x_i = position vector
β = ion mobility
γ = coefficient of thermal expansion
δ_{ij} = Kronecker delta function
ϵ = electric permittivity
ϵ_{ijk} = permutation tensor
θ = characteristic temperature difference
μ = viscosity
μ_m = magnetic permeability
π = characteristic pressure difference
ρ_c = space charge density
ρ_m = mass density
σ_{ij} = fluid stress tensor
Φ_v = viscous dissipation term

In the expressions above, the subscript d indicates the value taken at the datum point. The variable γ is the coefficient of thermal expansion, $\gamma = -(1/\rho_m)(\partial\rho_m/\partial T)$.

The other coefficients are similarly defined as

$$B_{1_d} = \frac{1}{\rho_m}\frac{\partial \rho_m}{\partial p}; \qquad A_{2_d} = \frac{1}{\gamma}\frac{\partial \gamma}{\partial T}; \qquad \text{etc.}$$

The gravitational body force g_i may be expressed in terms of the expanded mass density as the sum of a conservative force per unit volume, $\rho_{m_d} g_i$, and a nonconservative component

$$\rho_m g_i = \rho_{m_d} g_i + \rho_{m_d}[-\gamma_d(T-T_d) + B_{1_d}(p-p_d)]g_i \tag{17}$$

It is now possible to define a modified pressure which will remove the conservative body forces from the momentum equation. The modified pressure, denoted by p^*, is defined by the following expression

$$\frac{\partial p^*}{\partial x_i} = \frac{\partial p}{\partial x_i} - \rho_{m_d} g_i - \frac{\partial}{\partial x_i}\left(\frac{E_j E_j \rho_m}{2}\frac{\partial \epsilon}{\partial \rho_m}\right) \tag{18}$$

Both the electrostriction and that portion of the gravitational body force associated with a constant mass density have been removed from the equations of motion. This demonstrates that, in the absence of a free surface, electrostriction can have no effect on the flow. Any enhancement of the heat transfer therefore must be due to a combination of Coulombic, Joule heating, and permittivity gradient effects only.

Expressed in terms of the modified pressure and the first-order expanded properties, the equations of conservation of mass, momentum, and energy are

$$-\gamma_d \frac{DT}{Dt} + B_{1_d}\frac{Dp}{Dt} + [1-\gamma_d(T-T_d) + B_{1_d}(p-p_d)]\frac{\partial u_j}{\partial x_j} = 0 \tag{19}$$

$$\begin{aligned}
&\rho_{m_d}[1-\gamma_d(T-T_d)+B_{1_d}(p-p_d)]\frac{Du_i}{Dt} = \frac{-\partial p^*}{\partial x_i} \\
&+\rho_{m_d}[-\gamma_d(T-T_d)+B_{1_d}(p-p_d)]g_i \\
&+\mu_d[1+A_{5_d}(T-T_d) \\
&+B_{5_d}(p-p_d)]\frac{\partial}{\partial x_j}\left[\frac{\partial u_i}{\partial x_j}+\frac{\partial u_j}{\partial x_i}-\frac{2}{3}\frac{\partial u_k}{\partial x_k}\delta_{ij}\right] \\
&+\mu_d\left[A_{5_d}\frac{\partial T}{\partial x_j}+B_{5_d}\frac{\partial p}{\partial x_j}\right]\left[\frac{\partial u_i}{\partial x_j}+\frac{\partial u_j}{\partial x_i}-\frac{2}{3}\frac{\partial u_k}{\partial x_k}\delta_{ij}\right] \\
&+\rho_c E_i - \frac{\epsilon_d E_j E_j}{2}\left[A_{3_d}\frac{\partial T}{\partial x_i}+B_{3_d}\frac{\partial p}{\partial x_i}\right]
\end{aligned} \tag{20}$$

$$\begin{aligned}
&\rho_{m_d} C_{p_d}[1-\gamma_d(T-T_d)+B_{1_d}(p-p_d)] \\
&\times[1+A_{6_d}(T-T_d)+B_{6_d}(p-p_d)]\frac{DT}{Dt} \\
&= k_d[1+A_{4_d}(T-T_d)+B_{4_d}(p-p_d)]\frac{\partial^2 T}{\partial x_j \partial x_j} \\
&+k_d\left[A_{4_d}\frac{\partial T}{\partial x_j}+B_{4_d}\frac{\partial p}{\partial x_j}\right]\frac{\partial T}{\partial x_j} \\
&+\gamma_d[1+A_{2_d}(T-T_d)+B_{2_d}(p-p_d)]T\frac{Dp}{Dt} \\
&+\mu_d[1+A_{5_d}(T-T_d)+B_{5_d}(p-p_d)]\Phi_v \\
&+\beta_d[1+A_{7_d}(T-T_d)+B_{7_d}(p-p_d)]|\rho_c|E_j E_j \\
&+\frac{\epsilon_d A_{3_d} E_j E_j}{2[1-\gamma_d(T-T_d)+B_{1_d}(p-p_d)]} \\
&\times T\left[-\gamma_d\frac{DT}{Dt}+B_{1_d}\frac{Dp}{Dt}\right]
\end{aligned} \tag{21}$$

The equations as written are intractable. However, it is possible to neglect the majority of the property variations in cases where the pressure and temperature gradients are modest. The precise restrictions will be developed here in terms of the temperature and length scales of the problem. This development is similar to that proposed by Gray and Giorgini [9] for free convective flows. In that construction of the classical Boussinesq approximation, most of the property variations in the conservation equations are neglected for situations which meet the stated restrictions on the temperature and length scales. The sole exception is the thermal buoyancy term in the momentum equation.

In the first-order theory of electrohydrodynamics, additional terms introduced via couplings between the electric field and fluid velocity field are retained in addition to the thermal buoyancy term. The restrictions on the theory require that the products of the various coefficients γ_d, B_{1_d}, A_{2_d}, B_{2_d}, etc., and the appropriate pressure or temperature scale be small in comparison to one; i.e., $\gamma_d\theta << 1$; $B_{1_d}\pi << 1$; $A_{2_d}\theta << 1$, etc., where θ is the characteristic temperature difference of the system and π is the pressure difference characterizing the system. Additionally, requiring that the property variations be negligible to first order uncouples the electrical equations from the energy equation by eliminating fluctuations in the electrical transport coefficients ϵ and β in equations (8) and (9).

The dynamic pressure is characterized by

$$\pi_d \approx \rho_{m_d} U^2$$

where U is an appropriate velocity scale. The static pressure is scaled by

$$\pi_s \approx \rho_m GL$$

where $G = |g_i|$.

The specific restrictions which must be satisfied to obtain the reduced equations are:

$$\begin{aligned}
&|\gamma_d\theta| << 1 \qquad |B_{1_d}\rho_{m_d} GL| << 1 \\
&|A_{2_d}\theta| << 1 \qquad |B_{2_d}\rho_{m_d} GL| << 1 \\
&|A_{3_d}\theta| << 1 \qquad |B_{3_d}\rho_{m_d} GL| << 1 \\
&|A_{4_d}\theta| << 1 \qquad |B_{4_d}\rho_{m_d} GL| << 1 \\
&|A_{5_d}\theta| << 1 \qquad |B_{5_d}\rho_{m_d} GL| << 1 \\
&|A_{6_d}\theta| << 1 \qquad |B_{6_d}\rho_{m_d} GL| << 1 \\
&|A_{7_d}\theta| << 1 \qquad |B_{7_d}\rho_{m_d} GL| << 1 \\
&\left|\frac{B_{3_d}\rho_{m_d} GL}{A_{3_d}\theta}\right| << 1 \\
&\left|\frac{B_{1_d}\rho_{m_d} U^2}{\gamma_d\theta}\right| << 1
\end{aligned}$$

The last two restrictions eliminate pressure effects in the dielectric gradient and buoyant terms of the momentum equation.

An additional restriction is imposed in the form of $|(U/\beta E)| \leq 0.1$, which is necessary in order that the charge carrier convection term may be dropped from Ohm's law. This uncouples the electrical equations from the momentum equation.

The reduced equations demonstrate three distinct force terms available to drive the fluid: thermal buoyancy force, Coulombic, and dielectric gradient. Their associated velocity scales are:

Table 1 Properties of dry air at 288 K, 1 atm

Property	Value	Ref.
ρ_m	1.2 kg-m^{-3}	1
γ	3.5×10^{-3} K^{-1}	1
B_i	9.9×10^{-6} m^{2}N^{-1}	1
A_2	-3.5×10^{-3} K^{-1} (ideal gas)	
B_2	0 (ideal gas)	
ϵ	8.9×10^{-12} f-m^{-1}	13
A_3	-1.9×10^{-6} K^{-1}	13
B_3	5.5×10^{-9} m^2-N^{-1}	13
k	2.5×10^{-2} W-m^{-1}K^{-1}	12
A_4	2.4×10^{-3} k^1	12
B_4	0	17
μ	1.8×10^{-5} kg-m^{-1}s^{-1}	1
A_5	2.8×10^{-3} K^{-1}	1
B_5	0	17
C_p	1.0×10^3 J-kg^{-1}K^{-1}	11
A_6	2.6×10^{-5} K^{-1}	11
B_6	1.6×10^{-8} m^2-N^{-1}	11
β	1.8×10^{-4} m^2-V^{-1}s^{-1}	13
A_7	4.4×10^{-3} K^{-1}	13
B_7	9.9×10^{-6} m^2-N^{-1}	13

1 buoyant $U = (\gamma\theta GL)^{1/2}$
2 Coulombic $U = (JL/\beta\rho_m)^{1/2}$
3 dielectric gradient $U = (\epsilon E^2 |A_3| \theta/\rho_m)^{1/2}$

where E and J are scales of the magnitude of the electric field and current density, respectively. The subscripted d's have been dropped for convenience.

For a given situation, the largest of the three velocity scales is employed in developing the numerical restrictions on θ, L, E, and J which are consistent with the reduced equations. Thus, three sets of conditions are developed, each associated with a different dominant forcing term in the momentum equation. The case of air at 288 K and 1 atm will be considered here for each of the three cases. Property data are listed in Table 1.

The first set of conditions corresponds to the case of free convection. The buoyant velocity scale is employed for U, and the conditions to be satisfied for the case of air nominally at 288 K and 1 atm are:

1 $\theta \leq 22°C$
2 $L \leq 8.6 \times 10^2$ m
3 $L/\theta \leq 2.9$ m/°C
4 $\theta L/E^2 \leq 9.4 \times 10^{-9}$ m^3°C/V^2

where the fourth condition is consistent with neglecting charge carrier convection in Ohm's law. Note that the upper bound on the length scale far exceeds the maximum of 10 m assumed in neglecting induced magnetic fields. It is retained here for the sake of completeness.

An example of a free convective flow which meets the above conditions is one in which the current density and electric field magnitudes are 0.1 nA-cm^{-2} and 10 kV-cm^{-1}, respectively, with a temperature difference of 10°C and a governing length scale of 10 cm. The resulting buoyant velocity scale is this case would be 180 cm-s^{-1}.

Secondly, a flow regime dominated by Coulombic forces requires

1 $\theta \leq 22°C$
2 $L \leq 8.6 \times 10^2$ m
3 $L/\theta \leq 2.9$ m/°C
4 $JL/E^2 \leq 7.0 \times 10^{-14}$ A-m/V^2

Flows driven by Coulombic forces are maintained under the general conditions of small temperature variations, moderate-to-large length scales, and relatively large current densities; e.g., a temperature difference of 1.0°C, a length scale of 10 cm, a current density scale of 5.0 nA-cm^{-2}, and an electric field of 10 kV-cm^{-1}. These conditions yield a Coulombic velocity scale of 15 cm-s^{-1}.

Finally, if the dielectric gradient is the dominant force term, the corresponding conditions are:

1 $\theta \leq 22°C$
2 $L \leq 8.6 \times 10^2$ m
3 $L/\theta \leq 2.9$ m/°C
4 $E \leq 4.6 \times 10^{12}$ V/m

The fourth condition far exceeds the spark-over field for air at standard conditions, and is unnecessary for this case.

A distinguishing feature of flows driven by dielectric gradient forces is a small length scale. An example of conditions in which the dielectric gradient is the controlling force term and which satisfy the above restrictions consists of a current density of 1.0 nA-cm^2, an electric field magnitude of 100 kV-cm^{-1}, a temperature variation of 1.0°C, and a governing length scale of 1.0 mm. These conditions yield a governing velocity scale of 3.7 cm-s^{-1}.

Satisfying the appropriate conditions produces the reduced first-order equations of electrohydrodynamics

$$\frac{\partial u_j}{\partial x_j} = 0 \tag{22}$$

$$\rho_m \frac{Du_i}{Dt} = -\frac{\partial p^*}{\partial x_i} - \rho_m \gamma (T - T_d) g_i + \rho_c E_i - \frac{\epsilon A_3}{2} E_j E_j \frac{\partial T}{\partial x_i} + \mu \frac{\partial^2 u_i}{\partial x_j \partial x_j} = 0 \tag{23}$$

$$\rho_m C_p \frac{DT}{Dt} = k \frac{\partial^2 T}{\partial x_j \partial x_j} + E_j J_j + \mu \frac{\partial u_i}{\partial x_j}\left(\frac{\partial u_i}{\partial x_j} + \frac{\partial u_j}{\partial x_i}\right) + \gamma T \frac{Dp}{Dt} - \frac{\gamma \epsilon A_3 E_j E_j}{2} T \frac{DT}{Dt} \tag{24}$$

$$\frac{\partial E_j}{\partial x_j} = \frac{\rho_c}{\epsilon} \tag{25}$$

$$J_i = \beta |\rho_c| E_i \tag{26}$$

The subscripted d's have been suppressed in the equations above. The viscous dissipation term in equation (24) is often omitted under the Boussinesq approximation. Neglect of this term is not demanded under the first-order theory, however.

Enhancement Mechanisms

Because the velocities in natural convection are small, the generally weak electric forces may have a significant role in determining convection rates. Furthermore, in an enclosure it is relatively easy to achieve the high electric fields necessary for significant enhancement of the convective heat transfer rate.

As demonstrated by equation (23), there are three coupling modes which hold some prospect for convection enhancement. The Coulombic and permittivity gradient terms couple the momentum equation directly to Maxwell's equations, while the buoyancy term couples the equations via the Joule heating term of the energy equation.

Coulombic and Joule heating effects in a dielectric require some method of space charge generation. This is commonly accomplished via corona discharge, which imposes some constraints on the electrode geometry. Corona discharge generally occurs from surfaces with a high degree of curvature, such as a wire or a sharp edge. This requires, for example, that if parallel flat plate electrodes are to be utilized the surfaces must be sufficiently irregular that there is effectively an array of point sources. Additionally, corona discharge occurs only in regions of substantial field intensities. For air at standard conditions, the corona is confined to regions where the field exceeds an approximate value of 30 kV-cm^{-1}.

Because the Coulombic force is not directly affected by property variations in the medium, it is the only electrical force which can be externally controlled. It is the Coulombic force which is commonly cited as the principal mechanism for electrical enhancement of convective heat transfer [21, 23]. Coulombic or corona wind enhancement of natural convection requires electrode configurations for which the charge density gradient and the electric field are not parallel. This requires that the Coulombic force be nonconservative. In the first-order approximation, the nonconservative Coulombic force condition is equivalent to requiring a rotational current density. Flippen [6] has shown that the current density is irrotational for concentric cylinder electrodes, concentric spheres, and parallel flat planes with a uniform discharge on one electrode. Thus, the Coulombic force acts simply as another modified pressure term in the common examples of long co-axial cylindrical electrodes with electrically insulated ends, or a rectangular box with opposed electrodes and insulated sidewalls. Corona wind enhancement of convection is only possible for a nonuniform discharge with these enclosure geometries. The goal of the designer attempting to utilize corona wind to enhance free convection in an enclosure should be to maximize the extent to which the current density is rotational. This is particularly important near the surfaces where convective heat transfer is to be enhanced. This may be accomplished by using sharply irregular or asymmetric electrodes oriented such that surfaces of constant electric potential ϕ and charge density ρ_c are orthogonal or nearly orthogonal. This would appear difficult in cases where the electrode surfaces are also heat transfer surfaces, as the gradients of change density and electric potential will be approximately parallel in regions near the electrodes. It is recommended, therefore, that an enclosure designed to take advantage of corona-wind enhancement of natural convection incorporate asymmetric electrodes which are not the primary surfaces of convective heat transfer.

In the absence of space charge (e.g., below the corona starting voltage) there is obviously neither Coulombic force nor Joule heating. Hence, the permittivity gradient term is the only mechanism for electrically altering convection in a dielectric fluid. As with the Coulombic force, convection enhancement via the permittivity gradient requires a rotational force; i.e.,

$$\epsilon_{ijk} \frac{\partial E_n E_n}{\partial x_j} \frac{\partial T}{\partial x_k} \neq 0$$

This requires that the gradient of the electric field magnitude and the temperature gradient not be parallel. This restriction excludes, for example, parallel flat plates and concentric cylinders and spheres in which the two electrode surfaces are maintained at uniform but different temperatures. These arrangements are static in the absence of a perturbing force on the fluid. The presence of a rotational permittivity gradient term is a sufficient condition for demonstrating an electrical effect on the convection in an enclosure. In general, enclosures will have regions in which the permittivity gradient term is locally rotational. Consider, for example, the interior of a rectangular box with a temperature difference maintained between the top and bottom surfaces. By maintaining a potential between two or more of the vertical surfaces, a rotational permittivity gradient term develops. Solutions of the governing equations are extremely difficult to obtain for cases of convection driven by permittivity gradients, as the momentum equation is directly coupled to the energy equation and to Maxwell's equations via the permittivity gradient term.

In the three enclosures which are known to produce irrotational permittivity gradient and Coulombic terms (concentric cylinders, concentric spheres, and parallel plates in a box), convection enhancement may still result from buoyancy forces due to Joule heating. The Joule heating term in the energy equation, which is associated with electrical current in the fluid, has the effect of a known distributed heat source. This enhancement mode is perhaps the most promising in terms of obtaining solutions to the governing equations. Current efforts are directed toward solving the concentric cylinder enclosure problem using the perturbation technique employed by Custer and Shaughnessy [5] for free convection in a horizontal cylindrical annulus.

Summary

The first-order approximation of electrohydrodynamic coupling in dielectric fluids demonstrates that, for moderate temperature and length scales, free convective heat transfer in enclosures may be affected electrically via one or more of three coupling terms: Coulombic forces on free charges and the associated corona wind, buoyancy forces attributed to Joule heating of the fluid, and a gradient term associated with a varying permittivity of the fluid. The extent to which a given coupling term affects natural convection depends on the constitutive nature of the fluid, the electrode geometry, the applied potential, and the thermal boundary conditions. Attention must be given to each of these variables when attempting to control free convection in an enclosure.

Convection enhancement via corona wind requires a rotational current density and electrode surfaces which possess sharply different radii of curvature. Corona wind as a means of convection enhancement is thus most effective in asymmetric or irregular enclosures. Enhancement of free convection through the permittivity gradient term in the momentum equation requires that surfaces of constant electric field magnitude and constant temperature not be parallel everywhere in the enclosure. Unlike Joule heating and corona wind effects, convection enhancement from the permittivity gradient does not require corona discharge nor any other method of space charge generation. Joule heating, which is due to an electric current in the fluid, effectively produces a distributed heat source, creating buoyancy forces. The Joule heating term is the only one of the three coupling terms discussed which can drive a fluid in an enclosure between coaxial cylinders, concentric spheres, or flat plates.

References

1 Batchelor, G. K., *An Introduction to Fluid Dynamics*, Cambridge University Press, Cambridge, 1967.

2 Bird, R. B., Stewart, W. E., and Lightfoot, E. N., *Transport Phenomena*, Wiley, New York, 1960.

3 Chattock, A. P., "On the Velocity and Mass of Ions in the Electric Wind in Air." *Phil. Mag.*, Vol. 48, 1899, pp. 401–420.

4 Chaung, T. H., and Velkoff, H. R., "Frost Formation in a Non-uniform Electric Field," *AIChE Symposium Series 113*, Vol. 67, 1971, pp. 10–18.

5 Custer, J. R., and Shaughnessy, E. J., "Thermoconvective Motion of Low Prandtl Number Fluids Within a Horizontal Cylindrical Annulus," ASME JOURNAL OF HEAT TRANSFER, Vol. 99, 1977, pp. 596–602.

6 Flippen, L. D., "Electrohydrodynamics," Ph.D. Dissertation, Duke University, 1982.

7 Franke, M. E., "Effect of Vortices Induced by Corona Discharge on Free-Convection Heat Transfer From a Vertical Plate," ASME JOURNAL OF HEAT TRANSFER, Vol. 91, 1969, pp. 427–433.

8 Franke, M. E., and Hutson, K. E., "Effects of Corona Discharge on the Free-Convection Heat Transfer Inside a Vertical Hollow Cylinder," ASME Paper No. 82-WA/HT-20.

9 Gray, D. G., and Giorgini, A., "The Boussinesq Approximation for Liquids and Gases," *Int. J. Heat Mass Transfer*, Vol. 19, 1976, pp. 545–550.

10 Hauksbee, F., *Physico-Mechanical Experiments on Various Subjects*, 2nd ed., London, 1719.

11 Hilsenrath, J., Beckett, C. W., Benedict, W. S., Fano, L., Hoge, H. J., Masi, J. F., Nuttall, R. L., Touloukian, Y. S., and Woollery, H. W., *Tables of Thermal Properties of Gases*, Circular 564, National Bureau of Standards, Washington, 1955.

12 Holman, J. P., *Heat Transfer*, 4th ed., McGraw-Hill, New York, 1976.

13 Washburn, E. W., ed., *International Critical Tables of Numerical Data, Physics, Chemistry, and Technology*, Vol. 6, McGraw-Hill, New York, 1929.

14 Kulacki, F. A., "Electrohydrodynamic Enhancement of Convective Heat and Mass Transfer," in: *Advances in Transport Processes*, Vol. II, A. S. Mujumdar and R. A. Mashelkar, eds., Halstead Press, New York, 1982.

15 Lazarenko, B. R., Grosu, F. P., and Bologa, M. K., "Convective Heat-Transfer Enhancement by Electric Fields," *Int. J. Heat Mass Transfer*, Vol. 18, 1975, p. 1433–1441.

16 Leonard, G. L., Mitchner, M., and Self, S. A., "Precipitation From Turbulent Flows," Int'l Conf. on Electrostatic Precipitation, Monterey, CA, 1981.

17 Liepmann, H. W., and Roshko, A., *Elements of Gas Dynamics*, Wiley, New York, 1957.

18 Lykoudis, P. S., and Yu, C. P., "The Influence of Electrostrictive Forces in Natural Thermal Convection," *Int. J. Heat Mass Transfer*, Vol. 6, 1963, pp. 853–862.

19 Marco, S. M., and Velkoff, H. R., "Effect of Electrostatic Fields on Free-Convection Heat Transfer Inside a Vertical Hollow Cylinder," ASME Paper No. 63-HT-9.

20 Panofsky, W. K. H., and Phillips, M., *Classical Electricity and Magnetism*, 2nd ed., Addison-Wesley, Reading, MA, 1962.

21 Reynolds, B. L., and Holmes, R. E., "Heat Transfer in a Corona Discharge," *Mechanical Engineering*, Vol. 98, 1976, pp. 44–49.

22 Robinson, M., "Movement of Air in the Electric Wind of the Corona Discharge," *Trans. Am. Inst. Elec. Engrs.*, Vol. 80, Part 1, 1961, pp. 143–149.

23 Sadek, S. E., Fax, R. G., and Hurwitz, M., "The Influence of Electric Fields on Convective Heat and Mass Transfer From a Horizontal Surface Under Forced Convection," ASME JOURNAL OF HEAT TRANSFER, Vol. 94, 1972, pp. 144–148.

24 Steutzer, O. M., "Ion Drag Pressure Generation," *J. Appl. Phys.*, Vol. 30, 1959, p. 984–994.

25 Velkoff, H. R., "Electrofluidmechanics: Investigation of the Effects of Electrostatic Fields on Free-Convection Heat Transfer From Flat Plates," TDR-62-650, Aero Propulsion Laboratory, Wright Patterson Air Force Base, OH, 1962.

26 Windischmann, H., "Investigation of Corona-Discharge Cooling (CDC) of a Horizontal Plate Under Free Convection," *AIChE Symposium Series 138*, Vol. 70, 1974, pp. 23–30.

27 Worraker, W. J., and Richardson, A. T., "The Effect of Temperature-Induced Variations in Charge Carrier Mobility on Stationary Electrohydrodynamic Instability," *J. Fluid Mech.*, Vol. 93, Part 1, 1978, pp. 29–45.

28 Yabe, A., Mori, Y., and Hijikata, K., "EHD Study of the Corona Wind Between Wire and Plate Electrodes," *AIAA Journal*, Vol. 16, 1978, pp. 340–345.

29 Yamamoto, T., and Velkoff, H. R., "Electrohydrodynamics in an Electrostatic Precipitator," *J. Fluid Mech.*, Vol. 108, 1981, p. 1–18.

K. E. Lankford

A. Bejan
Assoc. Mem. ASME

Department of Mechanical Engineering
and Materials Science,
Duke University,
Durham, NC 27706

Natural Convection in a Vertical Enclosure Filled With Water Near 4°C

The natural circulation of near-4°C water in a vertical cavity heated from the side was studied experimentally in a 0.74-m-tall enclosure. The results of a scale analysis were used in order to correlate the overall wall-to-wall heat transfer rate measured experimentally in the Rayleigh number range 10^8–10^{11}. An analytical similarity solution was obtained for the slender enclosure limit. In that limit the flow pattern is one of incomplete vertical penetration, with stagnant maximum-density water filling the lower end of the vertical enclosure.

Introduction

The subject of natural convection heat transfer has received an increasing amount of attention since the pioneering work of Schmidt and Beckmann [1]. The interest in this class of heat transfer phenomena is due to a large number of engineering and geophysical applications that during the past two decades have been inspired by problems popularly associated with the issues of "energy" and "ecology." Comprehensive reviews of what has been accomplished to date in this field are available in textbooks and monographs [1–5]; the vigor of the field of natural convection research is best illustrated by the volume and diversity of points of view attracted by two recent meetings [6, 7].

The vast majority of the natural convection studies published so far pertain to fluids whose density decreases (or increases) monotonically with temperature at constant pressure. However, in a number of liquids such as water, bismuth, antimony, and gallium, the density-temperature curve exhibits a maximum. Since the coefficient of thermal expansion changes sign through this maximum, the use of the linear approximation $\rho \cong \rho_0[1-\beta(T-T_0)]$ to model such liquids is inappropriate in the range of temperatures that correspond to the density maximum.

Among the anomalous liquids mentioned above, water is by far the most important because its density maximum occurs near 4°C (more precisely 3.98°C) at atmospheric pressure, and because near-4°C water temperatures are the rule rather than the exception in lakes, rivers, and a series of industrial processes. In his recent review of research advances in natural convection in water near the density maximum, Gebhart [8] points out that this branch of natural convection research is still in its early stage of development. Among the few studies that have focused on the effect of the density maximum on heat transfer, the larger share deals with the external boundary layer regime near a single vertical wall. The circulation of near-4°C water in an enclosed space heated from the side has received very little attention.

The object of the research work summarized in this report is to shed new light on the phenomenon of natural convection in near-4°C water confined in a vertical space heated and cooled from the side (Fig. 1). What is known so far in connection with this phenomenon has been reported by Watson [9], Vasseur and Robillard [10, 11], and Inaba and Fukuda [12]. Watson [9] presented a numerical study of the circulation in a rectangular cavity where one vertical wall was kept at 0°C, while the opposing wall was heated to temperatures above 0°C. Vasseur and Robillard [10, 11] conducted numerical studies of the transient problem of cooling a rectangular mass of water through 4°C by maintaining the boundaries at 0°C or by subjecting the boundaries to a uniform cooling rate. Most recently, Inaba and Fukuda [12] documented the effect of inclination angle on the natural convection of cold water in an inclined rectangular enclosure.

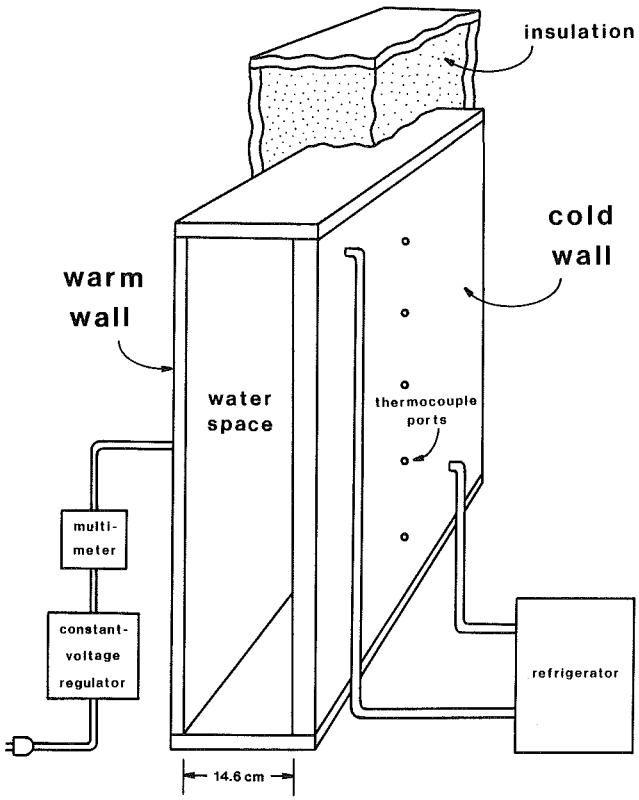

Fig. 1 Schematic of experimental apparatus

Relative to the preceding studies, the focus of the present work is on: (1) experimental documentation of the main features of the flow at relatively high Rayleigh numbers; (2) proper scales of the heat and fluid flow phenomena; (3) use of the heat and fluid flow scales to correlate the heat transfer rates obtained experimentally; and (4) an analytical solution for the slender enclosure limit.

Part I High Rayleigh Number Convection

Experimental Apparatus. The apparatus constructed for this experiment is shown in Fig. 1. The water-filled core of the enclosure is contained between two parallel vertical plates spaced 14.6 cm apart. The top, bottom, and side walls are constructed of 2.5-cm-thick acrylic plexiglass which permitted

Contributed by the Heat Transfer Division for publication in the JOURNAL OF HEAT TRANSFER. Manuscript received by the Heat Transfer Division April 18, 1985.

viewing the flow and at the same time provided the apparatus with good thermal insulating characteristics and good structural strength over a wide range of temperatures. The height of the cavity was 73.7 cm. The length, 55.9 cm, was large enough to minimize three-dimensional effects.

The aluminum hot plate (1.8 cm thick) was heated by eight uniformly spaced strip heaters attached horizontally to the outer side of the plate and connected in parallel. This arrangement simulated a wall heating effect that is close to the uniform heat flux model. The total power input was monitored by measuring the voltage and current through the strip heaters.

The aluminum cold plate was cooled by circulating chilled alcohol through a hollow chamber in the cold wall. The chilled alcohol stream was supplied by a constant-temperature bath refrigerator which was capable of controlling the coolant temperature to within $\pm 0.1°C$.

The enclosure was supported by a wooden frame and surrounded by a 15-cm-thick layer of fiberglass insulation housed in an outer plywood container. Apertures were built into the ends of the outer container (and insulated with removable blocks of rigid styrofoam) to allow visual observation of the flow.

The experimental procedure consisted of first selecting a heat input and then fine-tuning the minimum cold-wall temperature by adjusting the refrigerator setting. The apparatus required up to 24 hr to reach steady state whenever the heat input or refrigerator setting was changed. Arrival at steady state was determined by monitoring the hot and cold-plate temperatures until fluctuations had stabilized.

Two sets of heat transfer data were collected, one set for temperatures high enough that the water consistently expands upon heating (i.e., where the linear approximation $\rho \cong \rho_0[1 - \beta(T - T_0)]$ may be applied), and another set at average temperatures around 4°C. For obtaining each set, the total power dissipated in the strip heaters varied from 0 to 1100 W, or in terms of average heat flux, from 0 to 2700 W/m^2.

Flow Visualization. The flow was made visible using the thymol blue pH indicator technique originally described by Baker [13] and used extensively in water natural convection experiments. The technique consists of adding a small amount of thymol blue to the water and inserting two wire electrodes into the lightly tea-colored flow; imposing 1.25–3 V between the electrodes creates a higher pH in the fluid next to the cathode, causing a local color change toward deep blue. The dark blue fluid is then swept away from the cathode, marking the flow for a significant length of time, until diffusion effects return the fluid to its original tea color. Further improvements to this technique (including the addition of a small amount of NaCl to the indicator solution and carefully adjusting the voltage to eliminate any bubbles formed by electrolysis) were utilized as suggested by Quraishi and Fahidy [14]. In addition to providing an overall view of the entire flow, the technique allowed the calculation of velocities from timed sequences of photographs of certain regions of the flow.

When the entire enclosure was at temperatures well above the temperature of the density maximum, the flow was very similar to the well-documented single cell circulation between two vertical walls at different temperatures (see, for example, Elder [15]). The flow in this regime consisted of a wall jet that rises along the warm wall and sinks along the cold wall. Visible signs of transition to turbulence were observed only at the highest Rayleigh numbers investigated ($Ra_H \sim 10^{11}$).

When the maximum and minimum temperatures in the enclosure were maintained on either side of 4°C, the circulation pattern was characterized by two counterrotating cells driven by boundary layers (wall jets) rising along both vertical walls. A very distinct sinking jet emerged at the point where the two wall jets met. For each different heat input the sinking jet emerged at a different location along either the warm wall, the cold wall, or the top of the enclosure. For example, when only the bottom half of the warm wall was above 4°C, the jet emerged from halfway up along that wall. As the heat input was increased while holding the minimum cold-wall temperature constant, the jet emerged from higher and higher levels along the warm wall. Further increases in heat input continued this trend across the top and on down the cold wall.

The local velocity profiles of the two wall jets lining the differentially heated vertical walls were measured using the thymol blue technique [13, 14] and the calibration reported in [16]. The measurement consisted of inserting a 1-mm-thick wire electrode normal to the vertical wall and taking a timed sequence of close-up photographs of the marked fluid as it was swept away from the electrode. Figure 2 shows an example of such a sequence of photographs. Velocities measured at several conveniently selected distances from the wall form the velocity profile which corresponds to that particular region of the flow.

Three velocity profiles measured for a typical run are

Nomenclature

c_1, c_2 = constants of order one
f = similarity variable for the x profile of the stream function
g = gravitational acceleration
H = vertical dimension of water space
k = thermal conductivity
L = horizontal dimension of water space
L_y = height of the flow regime in the slender enclosure limit
Nu = Nusselt number
Q = overall heat transfer rate, W
R = relative wall temperature = $(T_m - T_C)/(T_H - T_C)$
R_C = thermal resistance of cold-side boundary layer
R_H = thermal resistance of hot-side boundary layer
Ra_H = Rayleigh number based on H and the Boussinesq approximation
Ra_L = Rayleigh number based on L for fluid with density extremum
$Ra_{\gamma C}$ = cold-side Rayleigh number for fluid with density extremum
$Ra_{\gamma H}$ = hot-side Rayleigh number for fluid with density extremum
T = temperature
T_{avg} = average temperature of enclosure
T_C = cold-wall temperature
T_H = hot-wall temperature
T_m = core temperature, also the temperature of the density maximum = 3.98°C
u = horizontal velocity
v = vertical velocity
W = width of water space
x = horizontal coordinate
y = vertical coordinate
α = thermal diffusivity
β = coefficient of thermal expansion
γ = coefficient in a parabolic model for cold water density; $\rho \cong \rho_{3.98°C}[1 - \gamma(T - 3.98°C)^2]$; the numerical value of γ is 8×10^{-6} $(°C)^{-2}$
δ_C = scale of cold-side boundary layer thickness
δ_H = scale of hot-side boundary layer thickness
ν = kinematic viscosity
θ = dimensionless temperature
τ = similarity variable for the x profile of θ
ψ = dimensionless stream function
(*) = subscript denoting dimensionless quantities
$\bar{(\ )}$ = averaged over the entire height of the enclosure

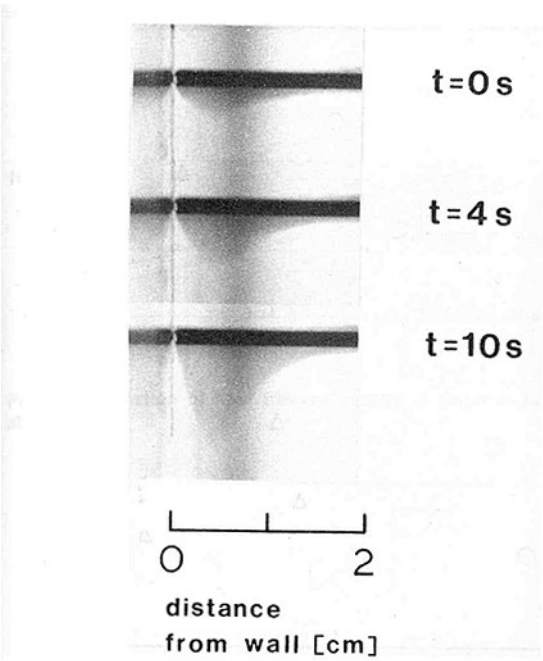

Fig. 2 Measurement of the vertical wall jet velocity profile using the thymol blue method (heat input: 60 W; minimum temperature: 0.2°C; vertical location: 31.8 cm from the bottom along the warm wall)

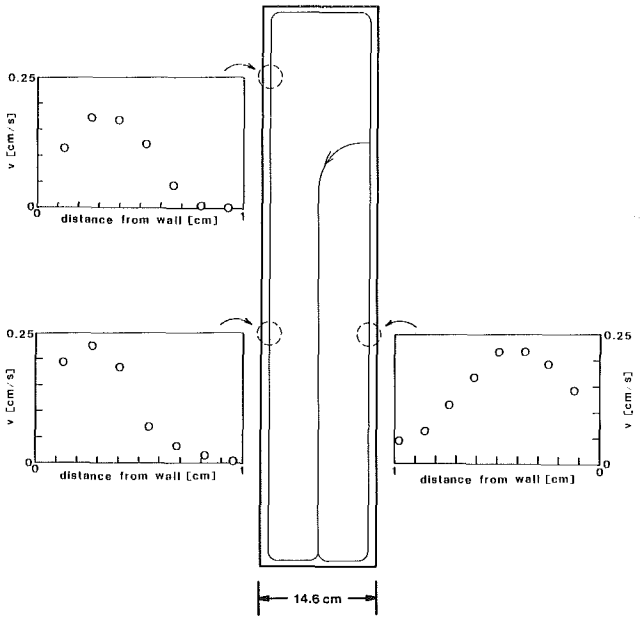

Fig. 3 Wall jet velocity profile measurements (heat input 148 W; minimum temperature 0°C)

displayed in Fig. 3 around a schematic diagram of the flow pattern. It is worth noting that along each wall jet the velocity profiles are similar and the peak velocity scale is practically the same. This observation is explained by the fact that the temperature difference between the core and each vertical wall is the same (about 4°C). Additional velocity measurements [17], omitted here due to space limitations, show that the wall jets slow down considerably as both wall temperatures approach 4°C.

Figure 4 shows a timed sequence of photographs taken in a case where the sinking jet was coming off the upper end of the cold wall. The voltage was applied across the electrodes suddenly, at a time before $t = 0$ s; the (0 s, 13 s, 24 s) sequence allows us to see how the jet fluid advances into the core of the enclosure (Fig. 3), and permits an approximate measurement of the longitudinal velocity scale of the jet. Laminar and well defined at first, the sinking jet becomes wavy as it turns and sinks to the bottom of the enclosure. Later, the same fluid is entrained and recirculated as laminar boundary layer flow along the differentially heated sides of the enclosure. In the case illustrated in Figs. 3 and 4 the velocity of the jet as it comes off the upper end of the cold wall is approximately 0.25 cm/s. In cases where the circulation is slowed down by side wall temperatures that approach 4°C from above and from below, the starting velocity of the sinking jet drops to values as low as 0.04 cm/s.

Temperature Measurements. Temperatures of the hot and cold walls were measured at four different heights along the centerline of the apparatus. Type K (chromel-alumel) thermocouples imbedded to within 1.6 mm of the inside surface of each plate allowed temperature measurements accurate to within ±0.2°C. The results are reported numerically for two distinct series of heat transfer measurements: first, experiments using water at temperatures well above 4°C (Table 1) and, second, experiments using water near 4°C (Table 2).

When the temperature everywhere in the enclosure is well above 4°C, the wall temperature increases almost linearly with height and, at each level, the wall-to-wall temperature difference is practically constant (Fig. 5). These features are consistent with the wall temperature distribution expected in enclosures heated with uniform heat flux from the side and

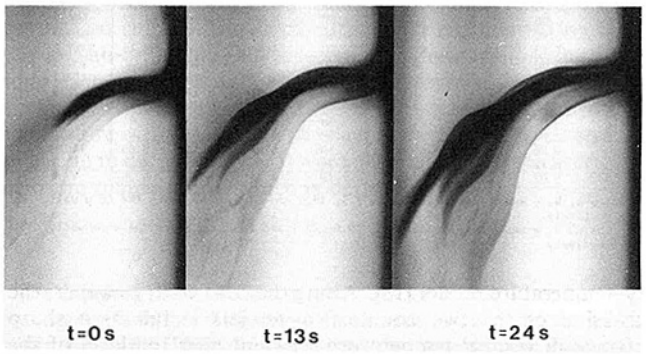

Fig. 4 The evolution of the sinking jet emerging from the upper end of the cold wall (heat input: 148 W; minimum temperature: 0°C)

filled with a fluid whose density varies linearly with temperature [18].

In a number of experimental runs the entire enclosure was at temperatures below 4°C; hence, the water density consistently increased upon heating. The wall temperature distribution in such cases is similar to the pattern described in the preceding paragraph, i.e., the wall-to-wall temperature difference is practically independent of vertical position. However, unlike in the preceding paragraph, the temperature of both walls decreases with height.

The sinking core jet emerges from near the top of the warm wall when the enclosure temperature range includes 4°C and when the average enclosure temperature is slightly less than 4°C. Along the cold wall the water jet rises all the way to the top as it is cooled to a temperature close to 0°C. The same jet turns around the top of the enclosure and descends along the warm wall, because its density increases as its temperature increases from 0°C to 4°C.

When the average enclosure temperature is slightly above 4°C, the sinking core jet emerges from a point near the top of the cold wall. Along the warm wall, which is swept by a jet whose density decreases monotonically with temperature, the temperature distribution has the same features as in an enclosure heated with uniform heat flux from the side and filled with a fluid whose density conforms to the linear densi-

Table 1 Temperature and heat transfer data obtained using water well above 4°C

Cold Wall Temperature (°C)			Hot Wall Temperature (°C)			Q (watts)
Bottom	Midheight	Top	Bottom	Midheight	Top	
20.8	22.0	25.1	24.4	25.4	28.3	197.7
21.3	21.7	23.3	23.3	23.6	25.6	96.9
19.6	20.6	23.3	22.8	23.5	25.9	154.6
18.7	21.0	26.0	23.7	25.8	30.2	289.5
17.5	20.5	26.3	23.7	26.4	31.6	391.9
14.1	18.5	26.9	23.1	26.9	33.9	577.5
12.7	18.4	28.5	24.1	29.0	37.4	791.9
13.0	20.0	31.1	25.7	32.5	41.4	1001.0
12.5	20.6	33.9	20.8	34.1	44.8	1136.0
10.8	16.5	28.0	23.8	28.5	38.2	898.2
13.4	17.3	26.6	23.9	27.0	36.2	698.5
12.0	18.5	30.7	25.6	31.0	40.6	1021.7
12.5	19.3	31.7	22.0	32.2	42.2	1065.9
13.2	15.5	22.2	20.5	22.7	28.6	449.9
16.4	19.0	24.7	23.7	25.8	31.1	445.3
17.9	19.6	23.9	23.7	25.2	29.6	345.7
19.1	20.2	23.7	23.4	24.3	27.9	244.5
19.2	19.8	21.9	21.9	22.3	24.5	125.3
18.2	18.9	20.9	20.8	21.3	23.5	124.9
16.6	17.2	18.0	18.5	18.8	19.9	74.9
14.3	20.4	32.1	28.5	33.2	44.0	1146.0
17.2	23.5	34.6	32.0	36.2	46.8	1143.1
15.4	20.7	30.7	27.7	32.0	40.6	941.3
16.8	17.2	18.6	18.5	18.8	20.4	70.1

Table 2 Temperature and heat transfer measurements obtained using water near 4°C

TEMPERATURE (°C)								Heat Input
Cold Wall				Warm Wall				
a	b	c	d	e	f	g	h	Q (watts)
0.58	0.10	0.22	0.30	3.18	2.45	2.12	2.08	49.4
0.55	0.18	0.45	0.42	6.90	6.48	4.55	4.00	99.7
0.15	0.00	0.35	1.48	7.88	7.62	8.50	9.00	144.4
0.05	0.00	0.78	3.30	8.95	8.70	9.98	10.80	204.9
0.28	0.98	5.40	7.75	12.25	12.45	15.70	17.18	403.3
2.23	4.20	9.05	12.05	16.20	16.88	21.20	23.32	603.5
2.25	4.80	10.75	14.50	18.98	19.92	25.22	27.95	811.6
0.28	0.08	0.12	0.15	6.56	5.90	4.78	3.48	96.7
0.18	0.00	0.18	0.08	6.58	6.00	3.82	3.50	96.9
0.01	0.00	1.95	4.08	8.62	8.50	10.30	11.32	205.2
3.25	6.40	13.18	17.68	20.92	22.52	28.78	31.80	1010.0
3.60	7.18	14.65	19.65	23.00	24.80	31.72	35.15	1163.2
0.02	0.00	0.00	0.04	2.38	1.72	1.38	1.32	150.5
0.10	0.00	0.23	0.32	7.32	7.08	6.98	5.95	123.7
0.03	0.01	0.38	2.45	8.13	7.95	9.10	9.78	172.9
0.22	0.01	0.00	0.01	4.03	3.18	2.48	2.38	75.3
0.12	0.02	3.25	5.22	9.35	9.33	11.45	12.45	251.5
0.28	0.03	0.30	0.30	6.58	6.30	5.98	5.00	109.8
0.20	0.00	0.78	2.88	7.10	6.88	8.13	8.85	148.0
0.45	0.25	0.20	0.22	4.98	3.95	2.85	2.70	64.4
2.10	2.02	2.23	2.40	4.78	4.55	5.15	5.35	17.4

Points a, b, c and d are located 4.5, 9.5, 19.5 and 24.5 cm up along the cold wall, respectively.
Points e, f, g and h are located 6.9, 10.6, 22.1 and 26 cm up along the warm wall, respectively.

ty-temperature model [18]. Along the cold wall, however, the collision of the two counterflowing jets is felt as a sharp change in vertical temperature gradient near the level of the collision. This feature is illustrated in Fig. 6.

A general characteristic revealed by the temperature measurements discussed above is that the wall temperature is not totally insensitive to the flow pattern that exists inside the enclosure. This characteristic is a direct consequence of the large size of the apparatus: Since the goal of these experiments was the study of convection at high Rayleigh numbers, we designed the largest size enclosure that could be machined accurately in our shop. In view of the height of the enclosure, the wall thickness is not thermally massive enough, even though from a manufacturing standpoint the aluminum plate material is massive. Despite the tradeoff between the accessibility to high Rayleigh numbers and the sensitivity of the wall temperature distribution, the experiments approach the uniform heat flux wall-heating model, and the overall heat transfer results that are discussed next submit themselves to correlations that are correct from the point of view of scale analysis. The existence of scaling-correct heat transfer correlations is the ultimate test of the suitability of the heat transfer apparatus.

Heat Transfer Measurements. Table 1 shows the heat transfer measurements obtained at relatively high temperatures, that is, at temperatures high enough so that the water density throughout the entire cavity consistently increases upon heating. The total heat input Q (W) and the thermocouple readings of the temperature along each wall were recorded for each steady state achieved.

The negligible heat leak from enclosure to ambient, determined from experiments performed previously on a similar apparatus, was roughly 1.5 percent of the total heat input to the warm wall [19]. These previous experiments consisted of shutting off the flow of coolant to the cold wall and supplying a low heat input to the warm wall, so that an apparatus-ambient temperature difference comparable to those recorded for the actual experimental runs was produced. The present apparatus was first built for an experiment on natural convection in a triangular enclosure [19]. The only design modification that produced the present apparatus was the use

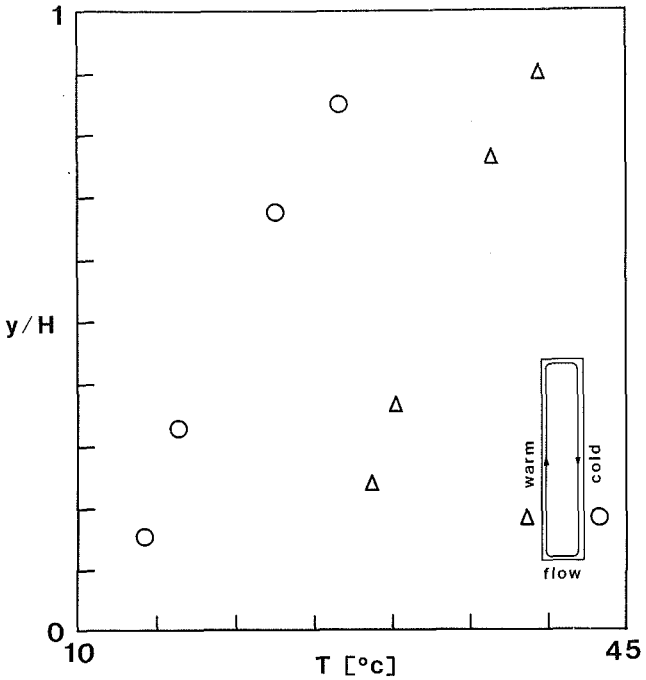

Fig. 5 Example of wall temperature distribution when T_H and T_C are consistently greater than T_m

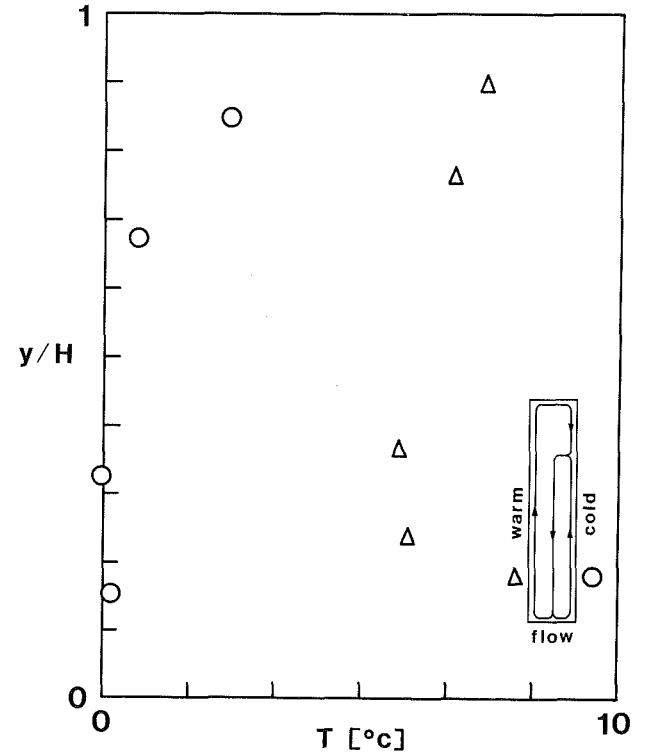

Fig. 6 Example of wall temperature distribution when T_H and T_C embrace T_m

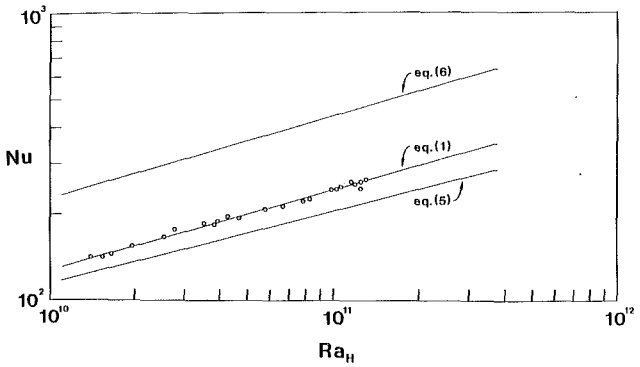

Fig. 7 Correlation of heat transfer results in water at temperatures above 4°C

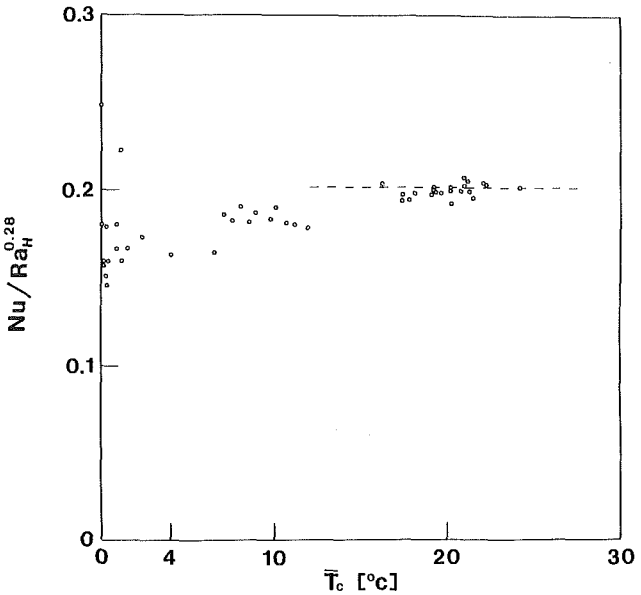

Fig. 8 The breakdown of the Nu (Ra_H) correlation, equation (1), as the temperature of maximum density is approached

of equal-size top and bottom walls (spacers) in order to insure the parallelism of the long differentially heated walls.

The temperature distribution along each wall was almost linear. Each distribution was curve fitted with a parabola and the resulting calculations for the temperatures at three levels (bottom, midheight, top) are listed in Table 1. Therefore, one purpose of the table is to show that in the present apparatus the wall temperature distribution approaches the distribution expected along constant-heat-flux walls in Boussinesq fluids.

Heat transfer measurements were also made when the enclosure average temperature was comparable with or less than 4°C. These measurements are summarized in Table 2; however, since the task of correlating them requires a theoretical understanding of the scales of natural convection in a fluid with density maximum, their discussion is postponed until the end of this section.

Returning to the data of Table 1, it is shown in Fig. 7 that at average temperatures sufficiently above 4°C the heat transfer measurements can be correlated in the usual manner [20]

$$\mathrm{Nu} \cong 0.203\ \mathrm{Ra}_H^{0.28} \tag{1}$$

where the Nusselt and Rayleigh numbers are defined as

$$\mathrm{Nu} = \frac{Q}{Wk(\bar{T}_H - \bar{T}_C)} \tag{2}$$

$$\mathrm{Ra}_H = \frac{g\beta H^3(\bar{T}_H - \bar{T}_C)}{\alpha\nu} \tag{3}$$

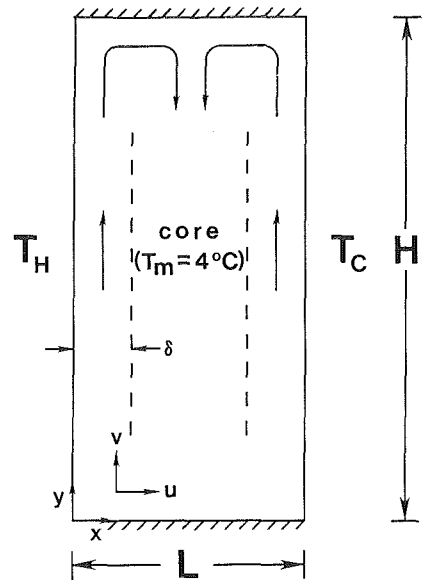

Fig. 9 Schematic of the boundary layer regime in a vertical space filled with cold water at a mean temperature of 4°C

In the above definitions, the height-averaged wall temperatures $\bar{T}_H$ and $\bar{T}_C$ were calculated using an appropriate averaging scheme based on the extrapolated temperature distribution curves mentioned earlier and represented by the data in Table 1. Note that since the temperature distribution along each wall is nearly linear, the difference $\bar{T}_H - \bar{T}_C$ is practically the same as the nearly constant wall-to-wall temperature difference. The physical properties k, α, β, and ν appearing in definitions (2, 3) were all evaluated at the average enclosure temperature, which is defined as

$$T_{\mathrm{avg}} = \frac{1}{2}(\bar{T}_H + \bar{T}_C) \tag{4}$$

The Nu(Ra_H) correlation of the data of Table 1, equation (1), agrees within 5 percent with empirical correlations published earlier [20]. Of interest is that the data in Table 1 and equation (1) fall between the two theoretical curves recommended by Oseen-linearized analysis of laminar flow, under the assumption of isothermal walls or constant-heat-flux walls, respectively

$$\mathrm{Nu} = 0.364\ \mathrm{Ra}_H^{1/4}, \text{ isothermal walls [21]} \tag{5}$$

$$\mathrm{Nu} = 0.25\left(\frac{H}{L}\right)^{1/7} \mathrm{Ra}_H^{2/7}, \text{ constant-heat-flux wall [18]} \tag{6}$$

The experimental measurements agree better with the isothermal wall formula (5); however, the slope of the empirical correlation (1) on the log Nu–log Ra_H field is nearly identical to that of equation (6) [note that 2/7 = 0.286; note also that equation (6) is the same as equation (33) of [18] translated here in the language of definitions (2, 3)].

The task of correlating the near-4°C heat transfer data summarized in Table 2 requires special attention, because the correlation method on which equation (1) and Fig. 7 are based is the result of linearizing the density-temperature function. Figure 8 shows clearly how this correlation method deteriorates as temperatures approach 4°C. The maximum density flow pattern inhibits the transfer of heat causing a decrease in the Nusselt number which has not been accounted for in the development of the high-temperature correlation [equation (1)]. Note also that even in the range of temperatures immediately above 4°C, where the density maximum has not necessarily been crossed, the data still tend to deviate from the constant value assumed by equation (1) (shown as a dashed line in Fig. 8). This is because the coeffi-

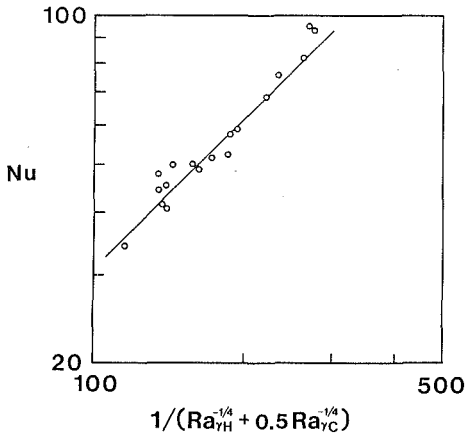

Fig. 10 Correlation of heat transfer results in water at temperatures near 4°C

cient of thermal expansion β, used in connection with the linear density–temperature approximation, changes so rapidly in the range of temperatures near the density maximum that averaging it in the normal fashion leads to significant errors.

The approach to correlating the near-4°C heat transfer data is conceptually the same as the one that leads to the high-temperature correlation: It consists of first identifying the proper scales of natural convection in fluid with density maximum, much in the way that equation (1) follows from having first identified the proper scales of natural convection in a Boussinesq-incompressible fluid (the scale analysis recommends a proportionality of type $Nu \sim Ra_H^{1/4}$ as in equation (5); however, empirical data and more refined analyses [21, 22] recommend a relationship in which the exponent of Ra_H is slightly greater than 1/4).

Scale Analysis. Consider the boundary layer regime for natural convection in near-4°C water: In cases where the sidewall temperatures occur symmetrically above and below 4°C, the maximum density sinking jet originates from near the top of the enclosure as shown in Fig. 9. The convection pattern consists of two boundary jets rising along the differentially heated side walls, and a maximum density sinking core whose temperature is $T_m \cong 4°C$. The scales of the two thermal boundary layer thicknesses δ_H and δ_C can be deduced from the classical conclusion that in $Pr > 1$ fluids the thermal boundary layer thickness scales as [5]

$$\delta_H \sim H\left(\frac{gH^3\Delta\rho/\rho}{\alpha\nu}\right)^{-1/4} \tag{7}$$

Modeling the relationship between density and temperature near 4°C as parabolic

$$\rho = \rho_{3.98°C}[1-\gamma(T-3.98°C)^2] \tag{8}$$

the term $\Delta\rho/\rho$ appearing in equation (7) is replaced by $\gamma(T_H - T_m)^2$, hence

$$\delta_H \sim H\left[\frac{g\gamma H^3(T_H-T_m)^2}{\alpha\nu}\right]^{-1/4} \tag{9}$$

Similarly, for the cold-side boundary layer we obtain

$$\delta_C \sim H\left[\frac{g\gamma H^3(T_m-T_C)^2}{\alpha\nu}\right]^{-1/4} \tag{10}$$

The quantity in the square brackets in equations (9) and (10) is the Rayleigh number for fluids with parabolic density variation near the density maximum. It is worth keeping in mind that although more general water density models exist (e.g., [23]), the parabolic model (8) is sufficiently accurate in the temperature range 0°C–10°C [24].

The scale of the overall heat transfer rate from T_H to T_C can

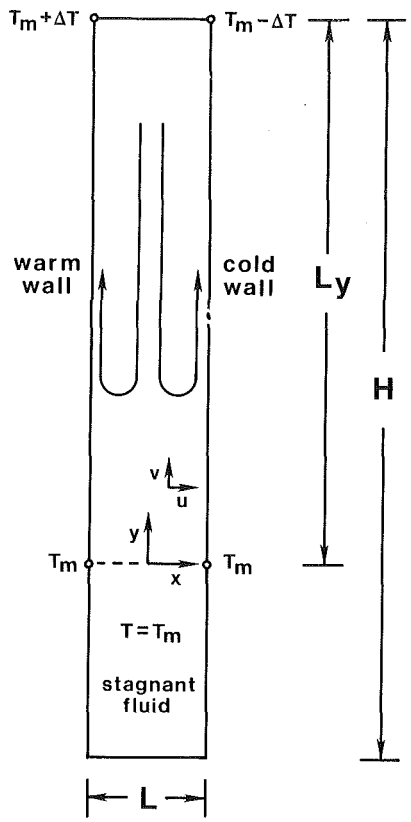

Fig. 11 Schematic of slender vertical slot filled with cold water at a mean temperature of 4°C

be estimated as the heat current through two boundary layer resistances R_H, R_C in series

$$Q \sim \frac{T_H - T_C}{R_H + R_C} \tag{11}$$

where $R_H \sim \delta_H/(kHW)$ and $R_C \sim \delta_C/(kHW)$. In dimensionless Nusselt number notation, equation (11) assumes the form

$$Nu = \frac{c_1}{Ra_{\gamma H}^{-1/4} + c_2\, Ra_{\gamma C}^{-1/4}} \tag{12}$$

where

$$Ra_{\gamma H} = \frac{g\gamma H^3(T_H-T_m)^2}{\alpha\nu}, \qquad Ra_{\gamma C} = \frac{g\gamma H^3(T_m-T_C)^2}{\alpha\nu} \tag{13}$$

By definition, the numerical coefficients c_1 and c_2 must be constants whose value is near unity [for example, c_1 represents the ratio between the actual thermal resistance R_H and its scale $\delta_H/(kHW)$, in other words $R_H = c_1\delta_H/(kHW)$].

Figure 10 shows that equation (12) correlates successfully the low-temperature heat transfer measurements of Table 2. The solid line drawn through the swarm of experimental points is the same as equation (12) in which the numerical constants have assumed the values $c_1 = 0.31$, $c_2 = 0.5$. These constants were chosen such that the standard deviation between equation (12) and measurements was minimized when summed over all the experimental points.

In the present scale analysis the positioning of T_H and T_C relative to T_m is accounted for by means of the two Rayleigh numbers $Ra_{\gamma H}$ and $Ra_{\gamma C}$. Alternatives to this description are the use of Gebhart's parameter $R = (T_m - T_C)/(T_H - T_C)$, or the inversion parameter of Nguyen et al. [25], namely $-2(T_m - T_c)/(T_H - T_C)$.

Part II The Slender Enclosure Limit

The experiments and scale analysis presented so far refer to

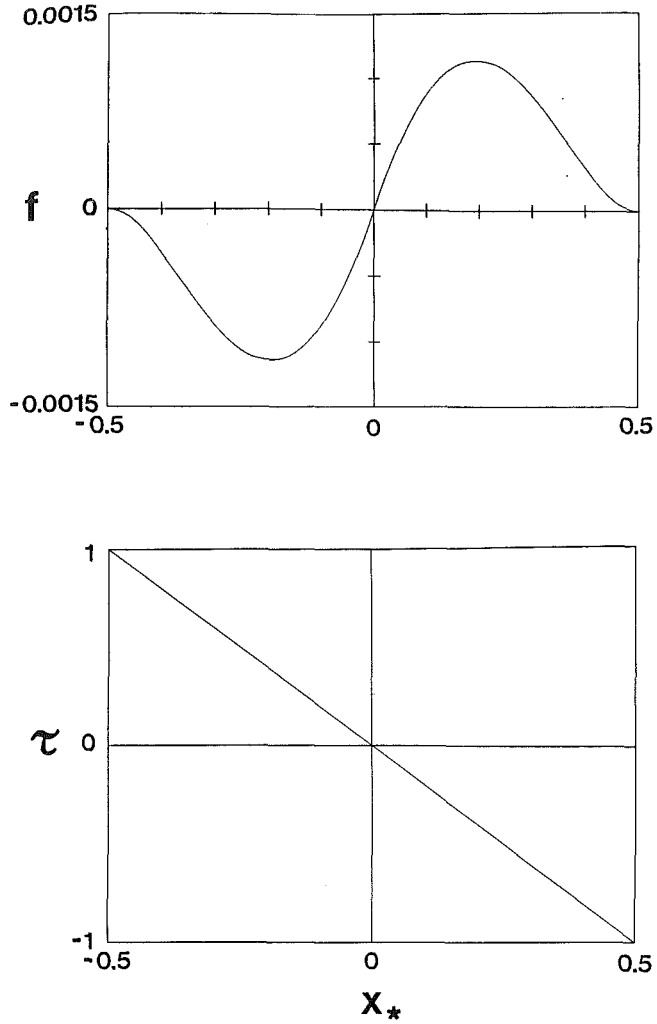

Fig. 12 Results of the analytical solution for the slender enclosure limit

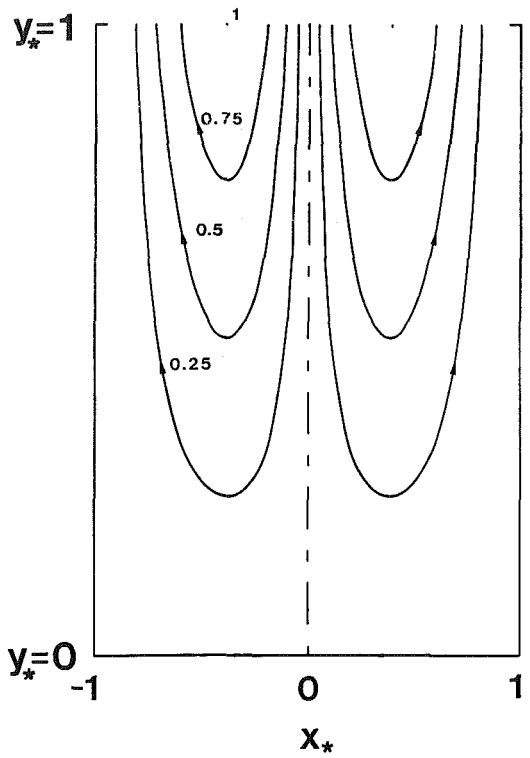

Fig. 13 Streamline pattern obtained from the analytical solution for the slender enclosure limit

the "high Rayleigh number regime" in which the vertical side walls are lined by distinct boundary layers. In this second part of the study we focus on the laminar flow in the limit of extremely narrow vertical slots, $L/H \to 0$.

Scale Analysis. In order to construct an analytical solution for the flow in the closed cavity of Fig. 11, we begin with the conservation equations for mass, momentum, and energy

$$\frac{\partial u}{\partial x}+\frac{\partial v}{\partial y}=0 \tag{14}$$

$$\rho\left(u\frac{\partial u}{\partial x}+v\frac{\partial u}{\partial y}\right)=-\frac{\partial P}{\partial x}+\mu\nabla^2 u \tag{15}$$

$$\rho\left(u\frac{\partial v}{\partial x}+v\frac{\partial v}{\partial y}\right)=-\frac{\partial P}{\partial y}+\mu\nabla^2 v-\rho g \tag{16}$$

$$\left(u\frac{\partial T}{\partial x}+v\frac{\partial T}{\partial y}\right)=\alpha\nabla^2 T \tag{17}$$

Assuming that the region occupied by the flow is slender, $L/L_y \ll 1$, the Laplacian operators appearing in equations (15)–(17) can be replaced with $\partial^2/\partial x^2$. Furthermore, since water near 4°C is a high Prandtl number fluid, Pr ≅ 12, the inertial terms appearing in the momentum equations can be neglected relative to the terms accounting for friction and buoyancy ([5], Ch. 4). Finally, substituting the parabolic density-temperature model into the buoyancy term of equation (16), the momentum and energy equations assume the considerable simpler form

$$0=\nu\frac{\partial^3 v}{\partial x^3}+2g\gamma(T-T_m)\frac{\partial T}{\partial x} \tag{18}$$

$$u\frac{\partial T}{\partial x}+v\frac{\partial T}{\partial y}=\alpha\frac{\partial^2 T}{\partial x^2} \tag{19}$$

If the temperature difference maintained across the flow region is of order ΔT (Fig. 11) then the scaling implications of the mass, momentum, and energy equations (14), (18), and (19) in the flow region of thickness L and height L_y are

$$\frac{u}{L}\sim\frac{v}{L_y} \tag{20}$$

$$\nu\frac{v}{L^3}\sim g\gamma\frac{(\Delta T)^2}{L} \tag{21}$$

$$u\frac{\Delta T}{L},\ \text{or}\ v\frac{\Delta T}{L_y}\sim\alpha\frac{\Delta T}{L^2} \tag{22}$$

Solving equations (20)–(22) for the unknown scales of the flow we find

$$L_y\sim L\ \mathrm{Ra}_L,\qquad u\sim\frac{\alpha}{L},\qquad v\sim\frac{\alpha}{L}\mathrm{Ra}_L \tag{23}$$

where Ra_L is the Rayleigh number based on slot width, $\mathrm{Ra}_L = gL^3\gamma(\Delta T)^2/(\alpha\nu)$.

Similarity Solution. The chief conclusion of the scale analysis is that L_y is of order $L\ \mathrm{Ra}_L$; in other words the vertical extent of the flow region is directly proportional to $(\Delta T)^2$. A more refined version of this conclusion is available in the form of an interesting similarity solution for the penetrative flow sketched in Fig. 11 (note that since the side wall temperatures embrace the temperature of the density maximum, the flow is upward along both walls). Introducing the set of dimensionless variables recommended by the results of scale analysis

$$u_* = \frac{u}{\alpha/L},\ v_* = \frac{v}{\frac{\alpha}{L}\mathrm{Ra}_L},\ x_* = \frac{x}{L},\ y_* = \frac{y}{L\mathrm{Ra}_L},\ \theta = \frac{T - T_m}{\Delta T} \tag{24}$$

and making use of the dimensionless stream function $\psi(x_*, y_*)$ defined as $u_* = \partial\psi/\partial y_*$ and $v_* = -\partial\psi/\partial x_*$, the governing equations (14), (18), and (19) reduce to

$$\frac{\partial^4\psi}{\partial x_*^4} = 2\theta\frac{\partial\theta}{\partial x_*} \tag{25}$$

$$\frac{\partial\psi}{\partial y_*}\frac{\partial\theta}{\partial x_*} - \frac{\partial\psi}{\partial x_*}\frac{\partial\theta}{\partial y_*} = \frac{\partial^2\theta}{\partial x_*^2} \tag{26}$$

The unknowns of the problem are the flow and temperature fields ψ and θ. The y_* dependence of both fields is already known from the scale analysis; for example, from equation (23) we deduce that u is independent of y, hence ψ must be directly proportional to y_*. In conclusion, the x_* and y_* dependence of both ψ and θ can be made visible through the transformation

$$\psi = y_* f(x_*),\ \theta = y_*^{1/2}\tau(x_*) \tag{27}$$

where the unknown functions f and τ are the similarity stream function and temperature profiles across the cavity. Substituting equations (27) into the governing equations (25, 26), we obtain the two similarity equations for f and τ

$$f''' = \tau^2 \tag{28}$$

$$f\tau' - \frac{1}{2}f'\tau = \tau'' \tag{29}$$

The boundary conditions for f and τ, which must also be y_* independent, are

$$f = f' = 0,\ \tau = 1 \text{ at } x_* = -\frac{1}{2} \tag{30}$$

$$f = 0,\ \tau = 0 \text{ at } x_* = 0$$

Note the physical implication of the $\tau(-1/2) = 1$ condition relative to the system shown in Fig. 11. Along the warm wall θ is equal to $y_*^{1/2}$, which means that the wall temperature decreases from $T_m + \Delta T$ at $y = L_y$ to T_m at $y = 0$. This type of wall temperature variation must be assumed if the solution (27) is to exist. This assumption, however, is realistic if we keep in mind: (1) the tendency of sinking core fluid to accumulate at the bottom of the cavity, and (2) the presence of longitudinal conduction through the material of the vertical wall (the conduction effect will bridge the gap between the T_m-cold fluid accumulated near the bottom of the wall and the heated upper portion of the wall; in this way the warm wall assumes a temperature distribution that resembles the form demanded by the present similarity solution). In conclusion, the similarity solution for the slender enclosure limit is valid for values of R close to 1/2, which correspond to cases where the flow density along the warm wall is about the same as that along the cold wall. The same restriction on the size of R is implicit in the scale analysis presented at the end of Part I.

The problem stated as equations (28)–(30) was solved numerically via finite differences and relying on a trial-and-error "shooting" method in order to satisfy the boundary conditions at the end of the integration interval (i.e., at $x_* = 0$). The resulting f and τ profiles are reported graphically in Fig. 12. The temperature profile is almost linear, indicating that the side-to-side heat transfer mechanism is by diffusion, albeit in a flow region whose height varies as $(\Delta T)^2$. The stream-function profile f, shown in the upper half of Fig. 12, was used in conjunction with equation (27) in order to plot the ψ = constant lines reported in Fig. 13. The flow is symmetric with respect to the centerline of the vertical slot, as the side wall temperature distributions have been assumed symmetric relative to the temperature of maximum density (Fig. 11). The vertical penetrative flow of Fig. 13 is similar to the one encountered in open thermosyphons in the same limit of sufficiently slender vertical spaces [26, 27]. The vertical velocity profile fills the entire width of the cavity: This feature distinguishes the slender enclosure limit from the distinct boundary layer regime of Part I.

Heat Transfer. The overall heat transfer rate effected by the similarity flow documented above can be expressed in the Nusselt number notation employed earlier [equation (2)], as

$$\mathrm{Nu} = 0.667\mathrm{Ra}_L \tag{31}$$

The overall heat transfer rate increases as Ra_L because the L_y/L ratio increases and, at the same time, the height of the pool filled with inert (isothermal) T_m fluid decreases. This last comment is in fact the basis for determining the parametric domain in which the "slender-cavity" results discussed above are valid. These results are valid as long as the cavity is tall enough so that the overall height H exceeds the height of the flow $H \gg L_y$, in other words when

$$\mathrm{Ra}_L \ll \frac{H}{L} \tag{32}$$

In a slender cavity with fixed geometry ($H/L \gg 1$), as the temperature difference ΔT of Fig. 11 increases, the flow extends downward and reaches the bottom of the cavity when Ra_L is of order H/L. As ΔT increases beyond this critical value, the flow enters the boundary layer or high Rayleigh number regime discussed in the first part of this study.

The criterion that defines the slender enclosure limit, equation (32), bridges the gap between Part I and Part II of the present study. The experiments outlined in Part I fall in the high Rayleigh number domain of distinct vertical boundary layers, whereas Part II covers only the slender enclosure limit: This is why the slender enclosure heat transfer scaling $\mathrm{Nu} \sim \mathrm{Ra}_L$ of equation (31) was not compared with the experimental data. Regarding experimental results for the slender enclosure limit, the evidence that such flows exist and that they follow the similarity theory is quite plentiful in the field of open thermosyphon convection [the equivalence between the slender enclosure limit of the present flow and the slender enclosure limit of the open thermosyphon is noted in the paragraph below equation (30)]. Together, Part I and Part II cover the cold water convection phenomenon over a complete Ra range in the laminar flow regime.

Concluding Remarks

The primary objective of this study has been to document the flow features and the proper scales of the phenomenon of natural convection in a vertical space filled with near-4°C water. Experiments conducted in an enclosure 0.74 m in height have shown that when the warm and cold vertical side walls are maintained at temperatures above and below 4°C, respectively, the natural circulation pattern consists of boundary layers that rise along these two side walls. The rising boundary layers meet at the top of the enclosure and form a maximum density jet with a temperature very close to 4°C that sinks through the core of the enclosure. The sinking jet is wavy in its early stages; eventually it stagnates near the bottom of the enclosure before being entrained into the two jets that rise along the side walls. The two wall jets are laminar over their entire height.

Because of the large height of the experimental apparatus, the flow regime documented in the experimental part of this report may be termed the "high Rayleigh number regime" or the "boundary layer regime." The overall heat transfer rate measured between the differentially heated side walls was successfully correlated as a Nusselt number–Rayleigh number function, by making use of the results of scale analysis.

It was shown analytically that, in the limit of extremely narrow vertical slots ($L/H \ll 1$, Fig. 11), the Nusselt number and the vertical penetration depth of the flow are proportional to the Rayleigh number based on slot width and on the parabolic density temperature relationship of water near 4°C. The lower portion of the vertical enclosure fills with maximum density fluid up to a certain level governed by the Rayleigh number.

Finally, this study draws attention to the boundary of the domain in which water natural convection heat transfer measurements can be correlated using the assumption that density varies linearly with temperature.

Acknowledgments

This research was supported by the National Science Foundation through Grants No. MEA-82-07779 and MEA-84-21250.

References

1 Jaluria, Y., *Natural Convection Heat and Mass Transfer*, Pergamon Press, Oxford, England, 1980.

2 Ostrach, S., "Natural Convection in Enclosures," *Adv. Heat Transfer*, Vol. 8, 1972, pp. 161–227.

3 Gebhart, B., *Heat Transfer*, McGraw-Hill, New York, 1971.

4 Catton, I., "Natural Convection Heat Transfer in Enclosures," *Proc. 6th Int. Heat Transfer Conf.*, Toronto, 1979, Vol. 6.

5 Bejan, A., *Convection Heat Transfer*, Wiley, New York, 1984.

6 Yang, K. T., and Lloyd, J. R., *Proceedings of a Workshop on Natural Convection*, Breckenridge, CO, July 18–21, 1982; sponsored by the National Science Foundation and the University of Notre Dame.

7 Kakac, S., Aung, W., and Viskanta, R., eds., *Natural Convection: Fundamentals and Applications*, Hemisphere, Washington, D.C., 1985.

8 Gebhart, B., "Boundary Region Transport in Cold Pure and Saline Water," in: *Natural Convection: Fundamentals and Applications*, S. Kakac, W. Aung, and R. Viskanta, eds., Hemisphere, Washington, D.C., 1985.

9 Watson, A., "The Effect of the Inversion Temperature on Natural Convection of Water in an Enclosed Rectangular Cavity," *Q. J. Mech. Applied Math.*, Vol. 25, Part 4, 1972, pp. 423–446.

10 Vasseur, P., and Robillard, L., "Transient Natural Convection Heat Transfer in a Mass of Water Cooled Through 4°C," *Int. J. Heat Mass Trans.*, Vol. 23, 1980, pp. 1195–1205.

11 Robillard, L., and Vasseur, P., "Convective Response of a Mass of Water Near 4°C to a Constant Cooling Rate Applied on Its Boundaries," *J. Fluid Mech.*, Vol. 118, 1982, pp. 123–141.

12 Inaba, H., and Fukuda, T., "An Experimental Study of Natural Convection in an Inclined Rectangular Cavity Filled With Water at its Density Maximum," ASME JOURNAL OF HEAT TRANSFER, Vol. 106, 1984, pp. 109–115.

13 Baker, J. D., "A Technique for the Precise Measurement of Small Fluid Velocities," *J. Fluid Mech.*, Vol. 26, Part 3, 1966, pp. 573–575.

14 Quraishi, M. S., and Fahidy, T. Z., "A Flow Visualization Technique Using Analytical Indicators: Theory and Some Applications," *Chem. Engg. Sci.*, Vol. 37, No. 5, 1982, pp. 775–780.

15 Elder, J. W., "Laminar Free Convection in a Vertical Slot," *J. Fluid Mech.*, Vol. 23, 1965, pp. 77–98.

16 Kimura, S., and Bejan, A., "Experimental Study of Natural Convection in a Horizontal Cylinder With Different End Temperatures," *Int. J. Heat Mass Transfer*, Vol. 23, 1980, pp. 1117–1126.

17 Lankford, K. E., "Natural Convection in a Vertical Slot Filled With Water Near 4°C," M. S. Thesis, Department of Mechanical Engineering, University of Colorado, Boulder, Dec. 1984.

18 Kimura, S., and Bejan, A., "The Boundary Layer Natural Convection Regime in a Rectangular Cavity With Uniform Heat Flux From the Side," ASME JOURNAL OF HEAT TRANSFER, Vol. 106, 1984, pp. 98–104.

19 Poulikakos, D., and Bejan, A., "Natural Convection Experiments in a Triangular Enclosure," ASME JOURNAL OF HEAT TRANSFER, Vol. 105, 1983, pp. 652–655.

20 MacGregor, R. K., and Emery, E. F., "Free Convection Through Vertical Plane Layers—Moderate and High Prandtl Number Fluids," ASME JOURNAL OF HEAT TRANSFER, Vol. 91, 1969, pp. 391–401.

21 Bejan, A., "A Note on Gill's Solution for Free Convection in a Vertical Enclosure," *Journal of Fluid Mech.*, Vol. 90, 1979, pp. 561–568.

22 Blythe, P. A., and Simpkins, P. G., "Thermal Convection in a Rectangular Cavity," *Physiochemical Hydrodynamics*, Vol. 2, 1977, pp. 511–524.

23 Gebhart, B., and Mollendorf, J. C., "A New Density Relation for Pure and Saline Water," *Deep Sea Res.*, Vol. 24, 1977, pp. 831–841.

24 Goren, L., "On Free Convection in Water at 4°C," *Chem. Engg. Sci.*, Vol. 21, 1966, pp. 515–518.

25 Nguyen, T. H., Vasseur, P., and Robillard, L., "Natural Convection Between Horizontal Concentric Cylinders With Density Inversion of Water for Low Rayleigh Numbers," *Int. J. Heat Mass Transfer*, Vol. 25, 1982, pp. 1559–1568.

26 Lighthill, M. J., "Theoretical Considerations on Free Convection in Tubes," *Q. J. Appl. Math.*, Vol. 6, 1953, pp. 398–439.

27 Bejan, A., "Natural Convection in a Vertical Cylindrical Well Filled With Porous Medium," *Int. J. Heat Mass Transfer*, Vol. 23, 1980, pp. 726–729.

Natural Convection in an Inclined Rectangular Channel Heated From the Bottom Surface

H. Inaba
Associate Professor,
Department of Mechanical Engineering,
Kitami Institute of Technology,
Koen-Cho 165, Kitami,
Hokkaido 090, Japan

The phenomenon of natural convection in an inclined rectangular channel heated from the bottom surface has been experimentally investigated. The experiments covered a range of modified Rayleigh numbers Ra_d^*, by using the shortest distance d *between two opposing side walls as a representative length, between 1.8×10^2 and 6×10^5, and a range of inclination angles of the side wall with respect to the horizontal θ between 30 deg and 90 deg. Air was used as the working fluid. An experimental correlation equation is given for the Nusselt number Nu_d as a function of sin θ and Ra_d^* for* W/l (*width to length of the channel*) = 0.1–0.5.

Introduction

Natural convection in an inclined rectangular channel heated from below is caused by density differences in a body force which result from heat transfer. In general, this circulating fluid system is called an open thermosyphon. The information relating to open thermosyphons can be used to predict the natural convection heat transfer rate in heat exchangers with fins and to estimate the convective heat loss from an air gap in the insulation materials of heat storage vessels. Other industrial thermosyphon applications include gas turbine cooling, natural ventilation in underground passageways, and the use of thermosyphons for the preservation of permafrost under buildings in arctic regions. Analytical and experimental studies for open thermosyphons with either a circular or rectangular-shaped cross section have been conducted extensively in the vertical arrangement, giving rise to a gravitational acceleration component parallel to the axis of the thermosyphon. For example, Lighthill [1] and Martin [2] studied a circulating flow driven by buoyancy forces in a vertically open thermosyphon with a circular cross section. Hasegawa et al. [3] conducted the initial study of a vertical parallel plate thermosyphon. Using an equivalent hydraulic radius, they compared their results with Lighthill's laminar analysis and obtained generally good agreement in the boundary layer flow region. Japikse [4] has provided a review of previous results of various thermosyphons up to 1972.

For a vertical open rectangular thermosyphon heated from below, the interference or mixing between incoming cold fluid and the issuing of hot fluid from the thermosyphon has a strong influence on the heat transfer in the thermosyphon. For an inclined open thermosyphon heated from below, it could be presumed that the mingling of hot and cold fluids would be reduced in the entrance region of the thermosyphon since the incoming cold fluid (heavier) descends along the lower side wall and the issuing hot fluid (lighter) ascends along the upper side wall.

The primary objective of the present study is to clarify experimentally the effects of inclination angle, dimensions of the rectangular channel, and temperature difference between the incoming cold fluid and the heated bottom surface on the heat transfer rates in an inclined rectangular channel heated from the bottom surface. The temperature profiles, flow visualization in the inclined rectangular channel, and measurements of heat transfer rate from the bottom heated surface are presented. A useful nondimensional correlation of heat transfer is derived from the experimental data involving the abovementioned factors.

Contributed by the Heat Transfer Division for publication in the JOURNAL OF HEAT TRANSFER. Manuscript received by the Heat Transfer Division January 2, 1985.

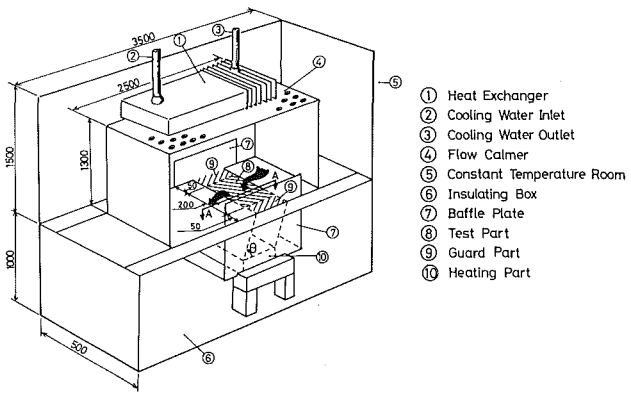

Fig. 1(*a*) Schematic diagram of experimental apparatus

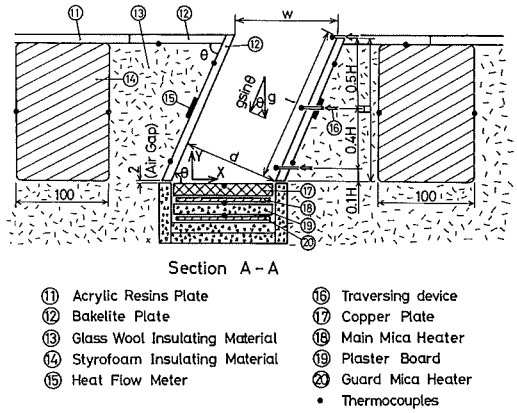

Fig. 1(*b*) Detail of test section

Experimental Apparatus and Procedure

A schematic diagram of the experimental apparatus is shown in Fig. 1(*a*). The major components of the experimental apparatus are the heating part as a heat source, the inclined open rectangular channel as a test section, and the cooling part as a heat reservoir. The cooling part consists of a large acrylic resin box (3.5 m × 1.5 m × 0.5 m), a fin-type heat exchanger cooled by circulating tap water to control the temperature in the box, and a baffle plate with many circular holes to calm the air flow. A detailed diagram of the heating and the inclined open rectangular test section is presented in Fig. 1(*b*). The test section was an inclined rectangular channel constructed of two parallel inclined side walls (2-mm-thick bakelite plate) with a length of l = 100 mm, a bottom heating surface (5-mm-thick copper plate), and baffle plates (2-mm-thick glass plate) at the front and the rear in the depth direc-

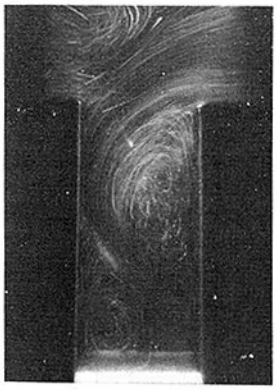

Fig. 2(a) θ = 90 deg

Fig. 2(b) θ = 75 deg

Fig. 2(c) θ = 60 deg

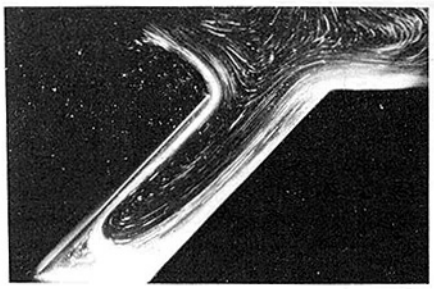

Fig. 2(d) θ = 45 deg

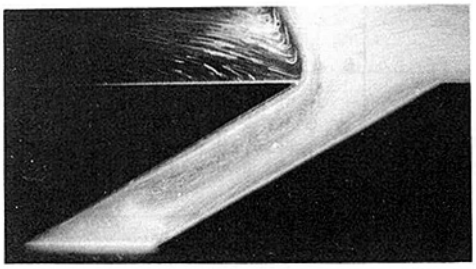

Fig. 2(e) θ = 30 deg

Fig. 2 Visual observation of flow patterns for W = 50 mm

tion (Z direction). A center part of 200 mm in the depth direction was used as the test section and both sides (50 mm length) of the test section in the depth direction were used as a guard part of heat losses. Five different test sections were constructed by changing the width W of the channel (W = 5 mm, 10 mm, 20 mm, 30 mm, and 50 mm) under a constant length of sloping side walls l = 100 mm. The inclination angle θ with respect to the horizontal was increased from 30 deg to 90 deg (vertical) by increments of 15 deg. The heating part positioned at the bottom of the test section consisted of a well-polished copper plate (emissivity ϵ = 0.065, 5 mm thick) as a heating surface, a main mica electric heater (maximum output of 1 kW), and a guard mica electric heater of the same capacity as the main heater. It was, therefore, possible to maintain the surface temperature of the heating wall at an almost uniform temperature condition since the temperature gradient was within $\pm$ 2 $\times$ 10^{-3} °C/cm in both the X and Z directions.

In order to minimize the heat loss from the two sloping side walls to the environment, an air gap (2 mm) was provided between the heating surface and the bottom end of the sloping wall, and insulating materials were packed behind the sloping side walls. The heat loss from the experimental apparatus to the environment was ascertained to be less than $\pm$ 6 percent from the use of heat flux meters which were attached to the rear side of the sloping side walls. Three traversing probes (0.8 mm o.d.), each mounted with a 0.1 mm copper-constantan

Nomenclature

A = heating surface area
d = the shortest distance between two opposing inclined side walls
g = gravitational acceleration
H = height of rectangular channel
h = heat transfer coefficient = $q/\Delta T$
l = length of side wall
Nu_d^*, Nu_W^* = Nusselt numbers = hd/λ, hW/λ, respectively
Q_T = total heat input to heating surface
Q_l = heat loss
q = net heat flux = $(Q_T - Q_l)/A$
Ra_r = Rayleigh number = $g\beta\Delta Tr^3/(\nu\alpha)$
Ra_d^*, Ra_W^* = modified Rayleigh numbers = $(\sin\theta)\beta\Delta Td^3/(\nu\alpha)$, $(\sin\theta)\beta\Delta TW^3/(\nu\alpha)$, respectively
r = hydraulic radius, $WZ/2(W+Z)$
T = temperature
ΔT = temperature difference between heating surface and average fluid temperature in the entrance region of the channel
W = width of rectangular channel
X, Y = coordinates
Z = depth of rectangular channel
α = thermal diffusivity
β = thermal expansion coefficient
ϵ = emissivity of radiation
θ = inclination angle from the horizontal
λ = thermal conductivity
ν = dynamic viscosity

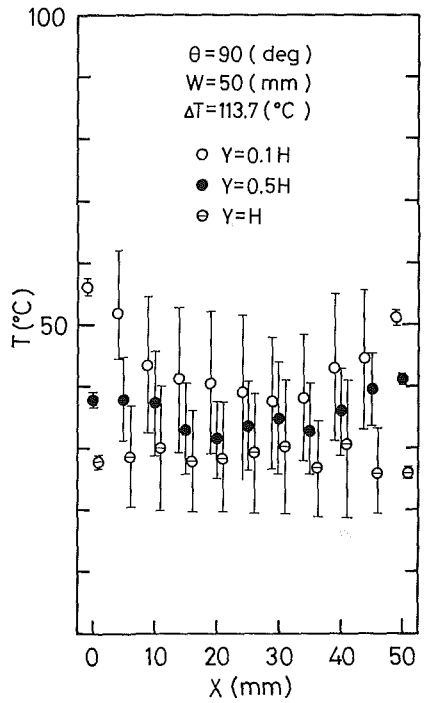

Fig. 3(a) θ = 90 deg

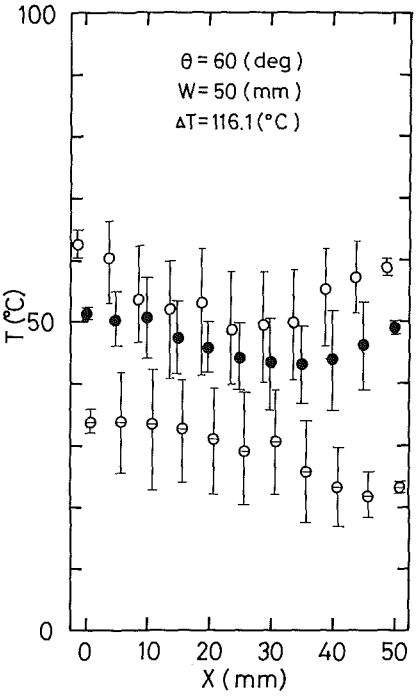

Fig. 3(b) θ = 60 deg

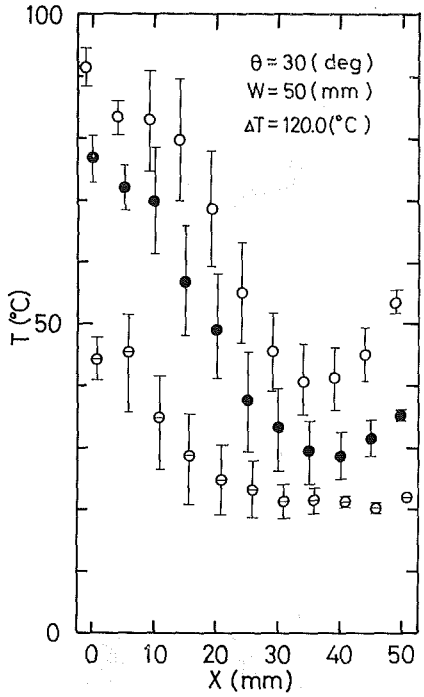

Fig. 3(c) θ = 30 deg

Fig. 3 Temperature distributions in the X direction for W = 50 mm

thermocouple, were set at the position of $Y = 0.1H$, $0.5H$, and H (height of the rectangular channel) to obtain the temperature distribution of the air layer. Experimental data were taken after the thermal and fluid-dynamic conditions had reached steady state. Steady state was achieved by obtaining a constant temperature over time at each measuring point and also by observing the flow behavior by means of smoke wire visualization. It took 5–12 hr to reach the steady-state condition after starting an experimental run, mainly because it was necessary to adjust the temperature at each measuring point and heat balance of main and guard heaters. The physical properties which were used to determine the nondimensional variables were evaluated at the average of the heated surface temperature and mean fluid temperature in the entrance region of the rectangular channel. Error estimation of the heat loss was performed by evaluating the heat loss from the side walls by heat flux meters mounted on them. The conduction loss from the electric wire and thermocouple wire were found to be negligible. In the preliminary experiments, the heat loss from the apparatus was confirmed to be within a few percent by calculating the heat flow when soft rubber of known thermal conductivity (= 0.16 W/mK) was packed into the cavity without an air gap for various surface temperatures of the bottom heating wall.

Another apparatus basically similar to that mentioned above was constructed to study the flow patterns visually. Water was the working fluid. To visualize the flow pattern, a 200-W projection lamp was arranged over the test section. The tracer particle was a mixture of aluminum powder and white liquid detergent. The aluminum particles (diameter 5–10 μm) were mixed with distilled water containing alcohol and the detergent in order to obtain a good affinity between the tracer particles and test fluid (water). After the tracer was left in a beaker for one day, the tracer particles floating in the middle depth of the beaker were withdrawn by a syringe and then injected slowly into the test section. Photographs of the flow patterns were taken using ASA 400 film. Typical exposure times varied between 8 and 50 s.

Results and Discussion

Flow Patterns. Typical flow patterns for various inclination angles θ are shown in Fig. 2 for W = 50 mm ($Ra_d^* = 9.4 \times 10^4 - 9 \times 10^5$). For θ = 90 deg (vertical) and $Ra_d^* = 9 \times 10^5$ in Fig. 2(*a*), the incoming cold water from the right side impinges on the left side wall and descends along the left side wall while spreading in the depth direction (Z direction). One large eddy appears near the upper part of the right side wall due to a generation of flow separation of incoming cold fluid at the upper right corner, while another small eddy emerges near the lower left corner. This small eddy may be induced

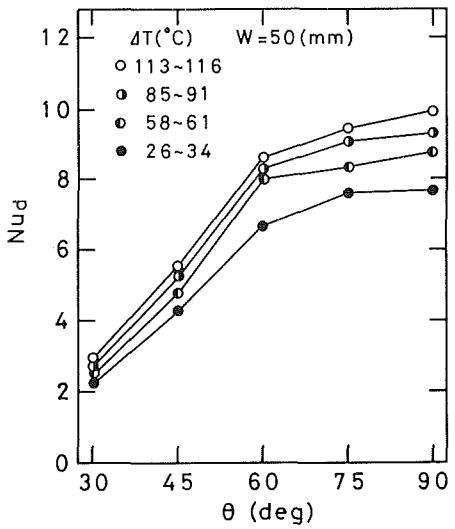

Fig. 4 The relationship between Nusselt number Nu_d and inclination angle for $W = 50$ mm

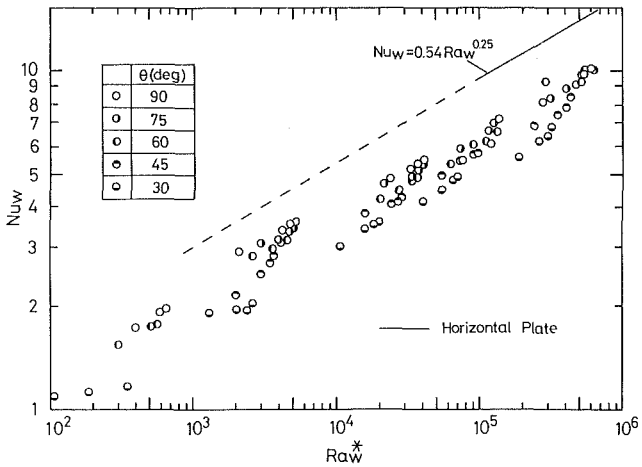

Fig. 5 A comparison between the present data and the empirical correlation of a horizontal flat plate with heated surface facing upward

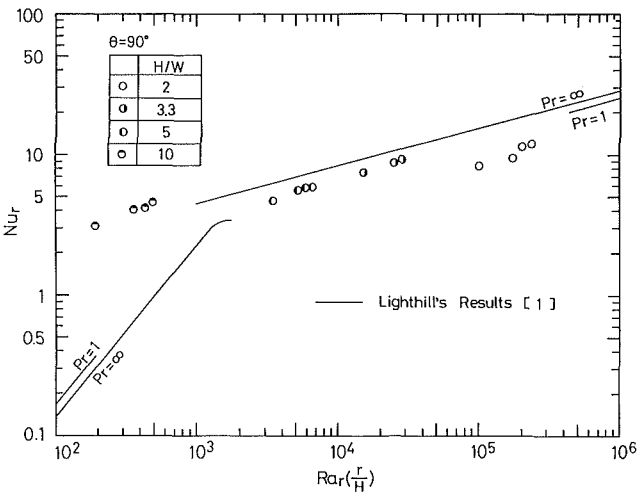

Fig. 6 A comparison between the present data and Lighthill's results for an open thermosyphon with circular cross section

mainly by a buoyancy force generated with the heat from the upward-facing bottom surface. From this flow behavior for $\theta = 90$ deg, it is said that the flow pattern for $\theta = 90$ deg becomes three dimensional and unstable because of interference between incoming cold fluid and issuing hot fluid. For $\theta = 75$ deg and $Ra_d^* = 7.8 \times 10^5$ in Fig. 2(*b*), one can note that the issuing hot fluid ascends along the upper part of the sloping wall and it collides with the incoming cold fluid from the right side. Consequently, the interference between both fluids appears to generate some complicated eddies in the center core region in the rectangular channel. For $\theta = 60$ deg and $Ra_d^* = 6.1 \times 10^5$ in Fig. 2(*c*), the vigor of the ascending hot fluid is increased and the incoming cold fluid descends along the sloping wall at the right side. Note that the difference in Ra_d^* between $\theta = 75$ and 60 deg or other θ is caused not only by the inclination angle θ but also by the temperature difference ΔT in the experiments. One large eddy emerges between both fluid flows and the flow pattern tends to become two dimensional and stable. As the inclination angle θ is decreased from 45 deg in Fig. 2(*d*) for $Ra_d^* = 4.5 \times 10^5$ to 30 deg in Fig. 2(*e*) for $Ra_d^* = 9.4 \times 10^4$, the interference between the incoming cold fluid and the issuing hot fluid is reduced, and the flow circulating speed of both fluids is decreased. As the value of θ is decreased, it is noticed that the stability and two dimensionality of the flow are promoted, and the region of stagnation is enlarged to the left of the bottom surface.

Temperature Distributions. Typical temperature distributions T in the X direction at positions of $Y = 0.1H$, $0.5H$, and H are presented in Fig. 3 for $W = 50$ mm. In this figure, the vertical bars indicate the temperature fluctuations which are caused by flow instability or flow interaction between incoming cold fluid and issuing hot fluid. As a result of comparing these temperature profiles for air and flow patterns for water, the temperature profiles seem to be consistent with the flow patterns. In the case of a vertical arrangement ($\theta = 90$ deg) as shown in Fig. 3(*a*) for $Ra_d^* = 7.2 \times 10^5$, one can note that the fluid temperature at the entrance region of $Y = H$ is lower than that of $Y = 0.1H$ and $0.5H$ and its variation in the X direction becomes small. This behavior of the fluid temperature profile can be explained by the fact that the incoming cold fluid spreads widely in the entrance region of the channel. For $Y = 0.1H$ in the vicinity of the bottom heating surface, the fluid temperatures near both sides of $X = 0$ mm and 50 mm become higher than the fluid temperature at the center region of $X = 23$–30 mm. These higher temperatures near both side walls result from the ascending hot fluid heated by the heating surface. For $\theta = 60$ deg and $Ra_d^* = 4.9 \times 10^5$ in Fig. 3(*b*), the fluid temperature at $Y = H$ is reduced gradually with increasing X. This temperature behavior corresponds to the flow behavior of the incoming cold fluid at the right side of $Y = H$ and the issuing hot fluid at the left side of $Y = H$. The tendency of fluid temperature distribution for $Y = 0.1H$ and $0.5H$ for $\theta = 60$ deg is similar to that for $\theta = 90$ deg; however, the temperatures for the former become higher than those for the latter. For the small inclination angle $\theta = 30$ deg and $Ra_d^* = 9.1 \times 10^4$, as can be seen in Fig. 3(*c*), it is understood that the difference of fluid temperatures in the vicinity of $W = 0$ mm and 50 mm becomes larger than that for $\theta = 90$ or 60 deg. These behaviors of the temperature profiles are caused by the interference of the incoming cold fluid and the issuing hot fluid in the entire cavity.

Effect of Inclination Angle θ on Nusselt Number Nu_d

The effects of θ on the average Nusselt number Nu_d are presented in Fig. 4 under various temperature conditions for $W = 50$ mm. From Fig. 4, it is seen that the variation of Nu_d is very small in the range of 60 deg $\leqq \theta \leqq 90$ deg and for $\theta <$ 60 deg the value of Nu_d is decreased abruptly with a decrease of θ. This abrupt decrease of Nu_d in the range of small inclination angle is induced by the enlargement of the stagnation region at the left side of the heated bottom surface.

Nondimensional Presentation of Heat Transfer Data

The present data are compared with the empirical correla-

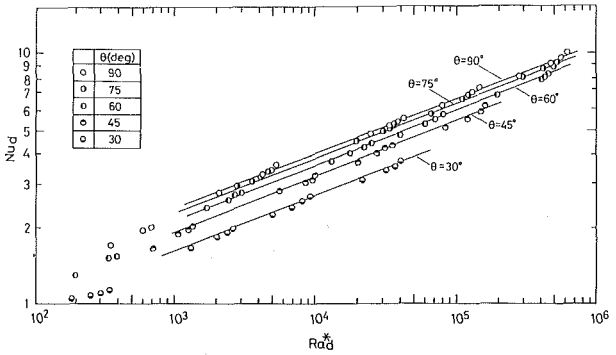

Fig. 7 The relationship between Nusselt number Nu_d and modified Rayleigh number Ra_d^*

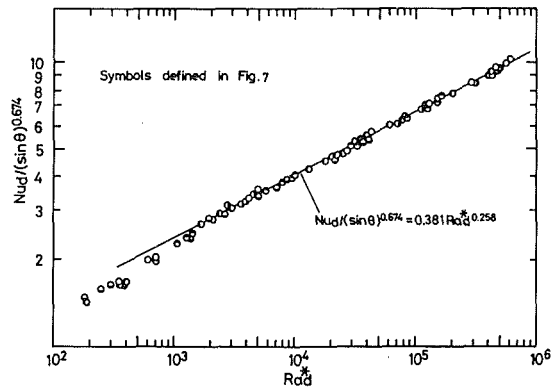

Fig. 8 The relationship between $Nu_d/(\sin\theta)^{0.674}$ and Ra_d^*

tion [5] of convection heat transfer for a horizontal plate with heated surface facing upward in the relation of Nu_W versus Ra_W^* using a width of the rectangular channel as a representative length. The results obtained are presented in Fig. 5. In Fig. 5, the dashed line is the extension of the experimental correlation of a horizontal plate shown by the solid line reported by some researchers [5–9]. From this figure, it can be seen that the present data lie below the empirical correlation of the horizontal plate with the heated surface facing upward.

Using an equivalent hydraulic radius, the present data for the inclined channel heated from the bottom surface with a rectangular cross section for $\theta = 90$ deg are compared with Lighthill's analysis [1] of the circular thermosyphon heated from the vertical side and bottom surfaces. The results obtained are presented in Fig. 6. In Fig. 6, it is noticed that the present data are somewhat lower in magnitude than those from the analysis for boundary layer flow analysis, but higher than those from the analysis for the impeded laminar regime provided by Lighthill [1]. These differences of Nu_r may be explained by the fact that there are differences in the cross-sectional shape and the heating surface between these studies.

As noted above, it is difficult to correlate the heat transfer data of the inclined thermosyphon of rectangular cross section with the method of [1]. The function cos θ or sin θ has been used in the past as a correlating parameter for natural convection in inclined slots [10]. In this study the heat transfer data are replotted in Fig. 7 as the Nusselt number Nu_d versus modified Rayleigh number Ra_d^*, using the shortest distance d between the two opposing side walls as a representative length and the gravitational component to the sloping direction sin θ (see Fig. 1*b*). In Fig. 7, one can note that the value of Nu_d increases at a constant rate with increasing Ra_d^* and inclination angle θ, and it decreases with decreasing θ at a given Ra_d^* number. This inclination angle θ influences not only the gravitational component to the main flow direction, but also represents the effects of the dimension of inclined rectangular channel on the convection heat transfer. That is, the value of sin θ implies the nondimensional dimensions of H/l and d/W. For the nondimensional variables of H/l, the value of sin θ decreases with increasing length of sloping wall l under the condition of constant height of the channel H. Consequently, the value of Nu_d is decreased with a decrease of sin θ ($= H/l$) owing to the fact that the flow velocity decreases because of the increase of the resultant viscous force of fluid from the sloping walls with increasing H, as can be observed by photographs of flow patterns in Fig. 2.

With regard to the nondimensional variable d/W, the value of sin θ decreases with d for constant W. Consequently, the value of Nu_d is decreased with a decrease in sin θ ($= d/W$), since the influence of the resultant viscous force from both sloping walls is enhanced with a decrease in d. While the value of W increases for constant d, the value of Nu_d is decreased, because the stagnant region of flow in the vicinity of the bottom heating surface is enlarged with a decrease in sin θ ($= d/W$). From these results, it may be said that the value of sin θ is suitable to express the variable of the dimension effect of the inclined channel with a rectangular cross section. Therefore the heat transfer data can be nondimensionalized with the function of $Nu_d = c(\sin\theta)^m Ra_d^{*n}$. The experimental correlation equation for Nu_d was obtained with a standard deviation of ± 8 percent by using the least square method as follows

$$Nu_d = 0.381\,(\sin\theta)^{0.674} Ra_d^{*0.258}$$

$$30\ \text{deg} \leqq \theta \leqq 90\ \text{deg}, \qquad 2\times 10^3 \leqq Ra_d^* \leqq 6\times 10^5$$

Figure 8 presents plots of $Nu_d/(\sin\theta)^{0.674}$ versus Ra_d^* for all data. This method of plotting data tends to bring the data together for different angles of inclination. From this figure, it is understood that the correlation equation proposed in the present study is a good representation of these experimental data in the range $Ra_d^* = 2 \times 10^3$–6×10^5. On the other hand, for $Ra_d^* < 2 \times 10^3$ data lie below the experimental correlation curve. This disagreement can be explained by the fact that the heat transfer rate for $Ra_d^* < 2 \times 10^3$ becomes smaller than that of the boundary layer flow for $Ra_d^* > 2 \times 10^3$ since for weaker heat flux in the range of $Ra_d^* < 2 \times 10^3$ the buoyancy force is less and the effect of shear is relatively enhanced, causing the boundary layer to try to fill the entire cavity. Thus, the flow is impeded, compared with the boundary layer flow for $Ra_d^* > 2 \times 10^3$. For still weaker heat flux (small Rayleigh number), the volume of stagnant flow is increased with decreasing Rayleigh number in the cavity, which results in a small Nusselt number. Moreover, it can be noted that the slope of Nu_d to Ra_d^* in the present inclined channel is almost similar to that for a heated plate as shown in Fig. 5, but the present data are below those in the case of an upward-facing heated plate. This difference is due to the fact that the channel flow in the present study is more restricting than the free flow of the bottom heating wall, which causes the flow interaction in the inlet and outlet and the friction loss in the side walls.

Conclusions

The present study appears to be the first systematic experimental investigation of natural convection in an inclined rectangular channel heated from the bottom surface. From the results obtained, it was demonstrated that the inclination angle had an important role in the determination of flow pattern and the convective heat transfer coefficient in a rectangular channel. It was also found that the value of sin θ is an important parameter in predicting the effect of the inclined angle on the heat transfer coefficient. Finally the nondimensional heat transfer coefficient in terms of Nusselt number was found to be $Nu_d = 0.381\,(\sin\theta)^{0.674}\,Ra_d^{*0.258}$ in the range of inclination angle $\theta = 30 - 90$ deg and modified Rayleigh number $Ra_d^* = 2 \times 10^3 - 6 \times 10^5$.

Acknowledgments

The author wishes to express his sincere thanks to Mr. T. Fukuda and Mr. Miyamoto for their assistance in performing the present experiments.

References

1 Lighthill, M. J., "Theoretical Consideration on Free Convection in Tubes," *Q. J. Mech. Appl. Math.*, Vol. 6, 1953, pp. 398–439.

2 Martin, B. W., "Free Convection in an Open Thermosyphon With Special Reference to Turbulent Flow," *Proc. R. Soc.*, Vol. 230A, 1955, pp. 502–530.

3 Hasegawa, S., Yamagata, K., and Nishikawa, K., "Heat Transfer in an Open Thermosyphon," *Bull. of Japan Society of Mechanical Engineers*, Vol. 6, 1963, pp. 230–250.

4 Japikse, D., "Advances in Thermosyphon Technology," *Advances in Heat Transfer*, Vol. 9, Academic Press, New York, 1973.

5 Fishenden, M., and Saunders, O. A., *Introduction to Heat Transfer*, Clarendon Press, New York, 1950.

6 Chu, T., and Goldstein, R., "Turbulent Convection in a Horizontal Layer of Water," *J. Fluid Mech.*, Vol. 60, 1973, pp. 141–159.

7 Hollands, K. G. T., Raithby, G. D., and Konicek, L., "Correlation Equations for Free Convection Heat Transfer in Horizontal Layers of Air and Water," *Int. J. Heat Mass Transfer*, Vol. 18, 1975, pp. 879–884.

8 Fujii, T., and Imura, H., "Natural Convection Heat Transfer From a Plate With Arbitrary Inclination," *Int. J. Heat Mass Transfer*, Vol. 15, 1972, pp. 755–767.

9 Dropkin, D., and Somerscales, E., "Heat Transfer by Natural Convection in Liquids Confined by Two Parallel Plates Which are Inclined at Various Angles With Respect to the Horizontal," ASME JOURNAL OF HEAT TRANSFER, Vol. 87, 1965, pp. 77–84.

10 Buchberg, H., Catton, I., and Edwards, D. K., "Natural Convection in Enclosed Space—a Review of Application to Solar Energy," ASME JOURNAL OF HEAT TRANSFER, Vol. 98, 1976, pp. 182–188.

P. Singh

J. A. Liburdy
Assoc. Mem. ASME

Thermal Fluids Laboratory,
Mechanical Engineering Department,
Clemson University,
Clemson, SC 29631

Effect of Plate Inclination on Natural Convection From a Plate to Its Cylindrical Enclosure

Presented in this paper are the local and mean heat transfer coefficients for an inclined, thin, heated flat surface enclosed in a long isothermal cylinder. Holographic interferometry was used to identify variations of the convective coefficient on both sides of the plate. There are significant local variations when the surface is oriented at different angles to the gravitation vector. An overall heat transfer coefficient is identified which is influenced by opposing inclination effects on either side of the surface. Results are significantly different from those of a surface in an infinite environment due to the recirculation required by the enclosure geometry. The effects of inclination become minor at angles greater than 60 deg from the horizontal.

Introduction

Natural convective heat transfer is of significant importance in the design of many energy converting devices and energy distributing systems. In particular, natural convection within enclosures is receiving intense study in the areas of environmental control, thermosyphons, waste heat control, and the applications of solar energy. By comparison, nonenclosed natural convection is much better understood than enclosed natural convection. In an enclosure the boundaries impose constraints on the flow and temperature distribution and thereby influence the local and overall heat transfer rates. Recirculating systems impose additional complexities associated with restrictive length scales and influences of nearby boundaries.

In recirculating natural convection the geometry and its orientation to the driving potential (the buoyancy force) influences the process. From experimental observation it is known that parameters such as aspect ratio (normally some measure of the relative dimensions parallel and normal to the buoyancy force) and details of the surface thermal boundary conditions play an important role. The specific geometry to be addressed in this paper consists of an air-filled cylindrical enclosure with its longitudinal axis horizontal. Within the enclosure is a flat rectangular plate whose span is slightly less than the cylinder diameter. The plate can be rotated within the cylinder a full 360 deg. The geometry is shown in Fig. 1 as viewed along the cylinder axis. The main objectives of the study are to determine the effects of the enclosure on the plate heat transfer rate and the effects of plate orientation on the local and overall heat transfer.

Many studies can be found in the open literature of natural convective heat transfer from horizontal and vertical flat surfaces. In addition, inclined surfaces have been studied by Fujii and Imura [1], Miller and Gebhart [2], Unny [3], Hassan and Mohamed [4], and others. Most enclosure studies have addressed inclined rectangular enclosures [5, 6, and others]. A few studies have been carried out in geometries similar to the plate-in-tube of concern here, such as by Ortabasi [7] and Roberts [8]. However, they have not detailed the phenomenological effects of orientation on the local heat transfer rates.

The results presented are confined to the specific geometry indicated. Effects such as the ratio of plate span to cylinder diameter, Prandtl number, and other fluid properties are not considered. The boundary conditions are an isothermal, cooled, cylinder wall and an isothermal, heated plate (the plate temperature being equal on both sides). The functional form for the nondimensional heat transfer correlation is assumed to be

$$\mathrm{Nu} = f(\mathrm{Ra}, \theta) \tag{1}$$

where Nu is the Nusselt number, Ra is the Rayleigh number, and θ the angle of inclination. A length scale is implied in the definition of Nu and Ra. This scaling is not immediately obvious from the geometry. We have attempted several different measures of the length scale, such as the average separation between plate and tube, a hydraulic diameter, and the plate span. We have found that the plate span L (in this case nearly the cylinder diameter) tends to correlate the data best. For further details of the results of other correlations see Singh [9].

The experimental techniques used in this study provide a means of measuring the local values of Nu and two independent means of measuring the overall or mean Nusselt number on both sides of the plate. The experimental range of Ra_L extends from 2.8×10^1 to approximately 2.1×10^6 and the plate orientation extends from $\theta = 0$ to 90 deg at 30 deg intervals where θ is measured from the horizontal.

Experimental Apparatus and Procedure

A drawing of the experimental apparatus is shown in Fig. 2. The cylinder was fabricated from aluminum with end flanges used to mount 1.27-cm-thick optical glass end plates. A larger, second cylinder was secured about the inner cylinder with the annular space containing a reverse flow helical coolant jacket. Water was circulated from a constant temperature reservoir capable of being cooled or heated, as needed, to maintain the reservoir at a preset temperature within ± 0.1°C. A flow rate of 1.3×10^{-4} m^3/s assured a uniform inner cylinder temperature within 5 percent of the plate–cylinder temperature difference for all test conditions. The uniformity was monitored using six thermocouples, four mounted at 90 deg intervals at the midplane and one at either end of the

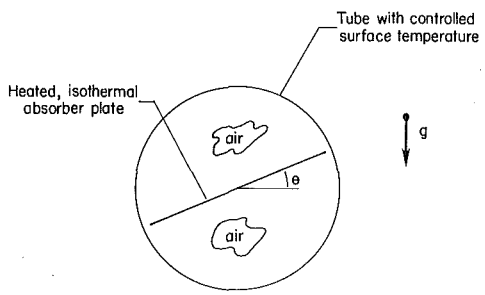

Fig. 1 Geometry and orientation of the plate-in-tube arrangement

Contributed by the Heat Transfer Division and presented at the ASME/JSME Thermal Engineering Conference, Honolulu, Hawaii, March 1983. Manuscript received by the Heat Transfer Division February 15, 1984.

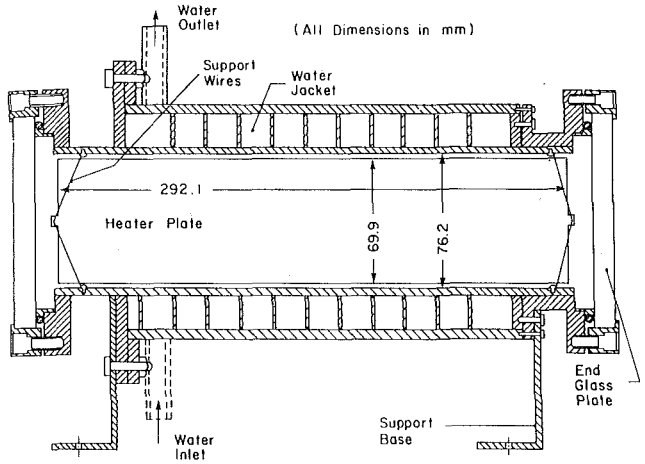

Fig. 2 Schematic of experimental apparatus

cylinder. The entire apparatus was mounted, using vertically adjustable supports, on a vibration isolation table.

The heated plate assembly was constructed from a uniform resistance foil heater sandwiched between two 0.76-mm-thick aluminum plates. A high thermal conductivity paste was used to assure uniform thermal contact between the heater and each plate. The total thickness was 1.8 mm. The temperature of the plate was measured with five thermocouples embedded between the heater and each aluminum plate. During all runs the spatial temperature variation was never more than six percent of the plate-cylinder temperature difference.

A given experiment was initiated once the plate was oriented at the desired angle. This was accomplished by adjusting the plate held by three fine wires connected to the center of each end of the plate as shown in Fig. 2. The orientation was determined by illuminating the cylinder with an expanded plane wave from a helium-neon laser. First the cylinder axis was configured parallel with the wave direction, then, with the plate in position, its shadow was projected onto a fixed, rigid screen. The plate was then adjusted to the desired position. Once set, coolant water was circulated through the annular space forming the heat sink. The plate assembly was supplied with d-c power and the interior of the cylinder was brought to the desired operating pressure. The inner cylinder was evacuated with a mechanical two-stage pump connected to a 0.5-cm-dia pipe. This opening was also used to extract all of the thermocouple and heater wires. A two-way solenoid valve was used to maintain the desired pressure inside the enclosure. The pressure was measured with a mercury manometer referenced to a barometer housed in the laboratory.

Once a desired pressure was attained, the pump was shut off, and the power to the plate heater was adjusted to set the final plate temperature. Steady state was determined once time-independent readings of the plate and cylinder temperatures were achieved. For a given plate orientation a range of Rayleigh numbers was achieved by varying both the plate temperature and cylinder pressure. A summary of the test conditions is given in Table 1. Note that the temperature given is for the plate surface, the average temperature is the arithmetic average between plate and cylinder and was used to evaluate thermodynamic properties.

Table 1 Listing of test conditions

θ	T(°C)	P(mm of Hg)	T_{ave}(°C)	Ra_L	θ	T(°C)	P(mm of Hg)	T_{ave}(°C)	Ra_L
0°	31.0	4.0	40.6	28.5	60°	30.2	4.0	40.8	28.1
	73.6	4.0	62.8	45.1		72.3	4.0	62.1	48.7
	153.6	4.0	102.8	61.9		153.9	4.0	103.3	61.4
	30.9	30.0	40.6	1609		30.7	30.0	41.0	1587
	73.7	30.0	62.9	2770		72.9	30.0	62.6	2752
	154.1	30.0	103.2	3475		156.4	30.0	104.9	3458
	31.1	100.0	40.7	17957		30.7	100.0	40.9	17658
	73.5	100.0	62.8	30747		73.0	100.0	62.6	30635
	153.3	100.0	103.3	38577		156.0	100.0	104.8	38373
	31.2	200.0	40.7	72004		30.4	200.0	40.8	70070
	73.6	200.0	62.9	123046		72.6	200.0	62.4	122214
	153.9	200.0	103.4	153730		155.1	200.0	104.5	153108
	31.0	743.8	40.6	990454		30.1	744.2	40.8	960037
	73.4	748.5	62.8	1725409		71.6	744.1	62.1	1673513
	152.1	748.5	103.8	2131438		152.7	746.0	103.8	2114072
30°	30.7	4.0	41.0	28.1	90°	30.7	4.0	40.9	28.5
	72.7	4.0	62.2	49.1		73.8	4.0	62.8	49.5
	154.5	4.0	103.3	61.8		154.5	4.0	103.4	61.8
	30.7	30.0	41.0	1589		30.6	30.0	40.8	1587
	73.4	30.0	62.6	2771		73.9	30.0	62.8	2780
	156.4	30.0	104.6	3466		153.5	30.0	102.9	3471
	30.8	100.0	41.0	17674		30.5	100.0	40.8	17597
	73.5	100.0	62.6	30816		73.9	100.0	62.8	30899
	156.2	100.0	104.7	38466		154.1	100.0	103.3	38558
	30.6	200.0	41.0	70456		30.7	200.0	40.9	70609
	73.0	200.0	62.5	122731		73.9	200.0	62.8	123555
	155.6	200.0	104.6	153920		154.8	200.0	103.1	154086
	30.3	745.0	40.7	972025		30.5	742.4	40.8	970021
	72.0	742.0	62.0	1674074		73.4	737.8	62.6	1676819
	153.4	741.5	103.9	2094817		153.7	734.9	104.0	2060757

An overall energy balance was used to determine the functional form implied in equation (1). This required a knowledge of the individual components of heat transfer due to convection, radiation, and all losses. The radiative heat transfer was modeled analytically for the situation of an isothermal surface forming a diameter of a semicylindrical enclosure where the curved surface is at a different temperature than the flat surface. The shape factor was calculated based on the analysis presented by Leuenberger [10]. The conductive heat transfer was calculated from a two-dimensional fine grid finite difference approximation. In order to check these calculations the apparatus was evacuated to 0.1 mm Hg so as to suppress convection. The resultant combined radiation and conduction heat transfer was measured and agreed to within 10 percent of the calculated values for all temperature differences used. At this low pressure the plate orientation did not alter the experimentally determined heat transfer rate which indicated that convective heat transfer was suppressed. As a comparison, Ortabasi [7], in a smaller apparatus, found no orientation effect on heat transfer below 1 mm Hg. Thus the convective heat transfer was determined by subtracting the radiative heat transfer and all losses from the total power input to the heater.

Energy losses consisted of conduction along the thin support wires holding the plate, the heater lead wires, and conduction from the glass end plates. Losses along the support and electrical wires were calculated to be ±0.5 to 1.0 percent of the heat input depending on the heating rate. The loss from the glass end plates was determined experimentally and checked analytically. During trial runs the end plates were instrumented with thermocouples on their inner and outer surfaces. Based on the measured temperature drop across the glass and an assumed linear radial temperature distribution, the loss was calculated for steady-state conditions. This

Nomenclature

A = surface area of the heated plate
Gr = Grashof number = $g\beta L^3\Delta T/\nu^2$
h = natural convection coefficient
k = thermal conductivity
L = length scale equal to the plate width
Nu = Nusselt number = hL/k
$\overline{\text{Nu}}$ = mean Nusselt number
Pr = Prandtl number = ν/α
q'' = local plate heat flux
Q_{conv} = convective plate heat transfer
Ra = Rayleigh number = Gr•Pr
ΔT = plate-cylinder temperature difference
x = distance measured along the plate from the leading edge
α = thermal diffusivity
β = thermal expansion coefficient
θ = plate tilt angle measured from the horizontal
ν = kinematic viscosity

Subscripts

t = top side of plate
b = bottom side of plate

calculation was then experimentally verified by insulating the glass ends and performing on overall energy balance at low pressure for various plate temperatures. The end losses were then determined from a comparison of the known power input and total radiation and conduction between the plate and cylinder with and without the ends insulated. This result agreed to within ±5 percent of the calculated loss determined from the measured temperature drop across the glass. Based on the overall energy balance, the convective heat transfer, expressed as the mean Nusselt number based on the plate span L, was calculated from its definition

$$\overline{\mathrm{Nu}} = \frac{Q_{\mathrm{conv}} L}{kA\ \Delta T} \tag{2}$$

where the symbols are defined in the Nomenclature.

In addition to the mean Nusselt number, representing convective heat transfer from both sides of the plate, the local Nusselt number was determined from interferograms. The test apparatus was mounted in a holographic interferometer on a vibration isolation table. The dual exposure, infinite fringe method was used to determine the local variation of index of refraction. Refraction errors were calculated to be insignificant. The fringes were photographically recorded and their pattern expanded onto a large screen so as to resolve fringe data to within ±0.3 mm. The local variation of the index of refraction was found and the temperature inferred using the Gladstone–Dale equation. The local heat transfer coefficient was determined at discrete points along the plate from the surface temperature gradient using both two and three-point approximations. The local temperature gradient times the thermal conductivity divided by the plate–cylinder temperature difference defines the local heat transfer coefficient h.

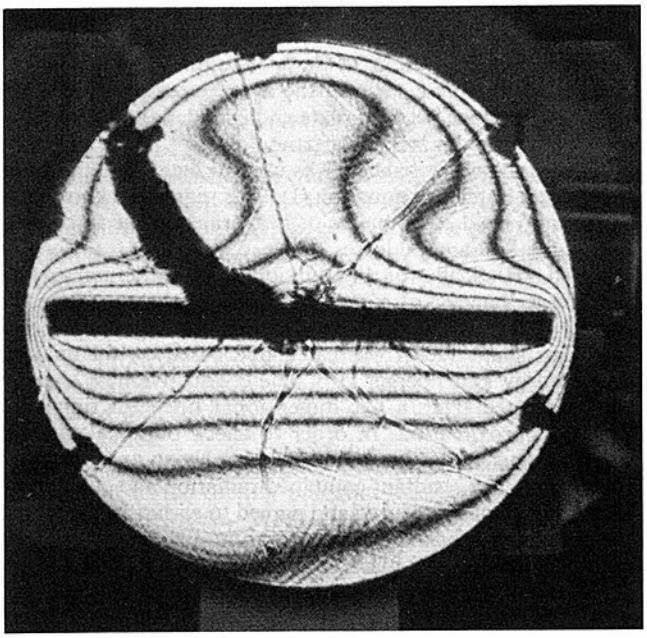

Fig. 3(a)

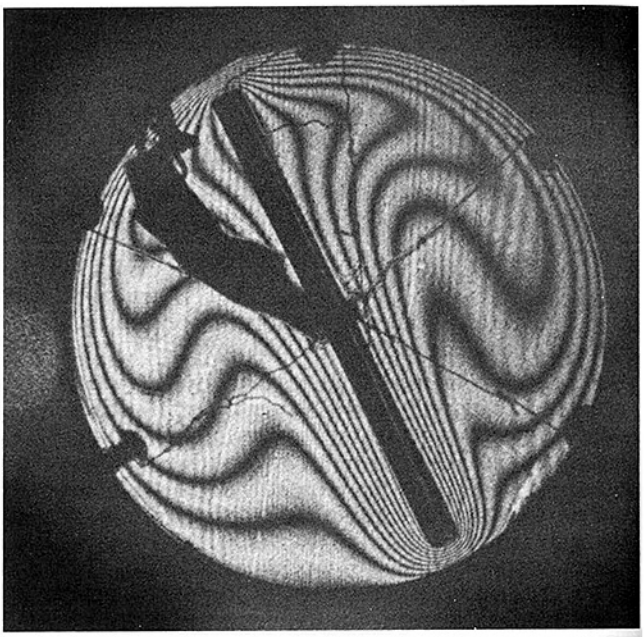

Fig. 3(c)

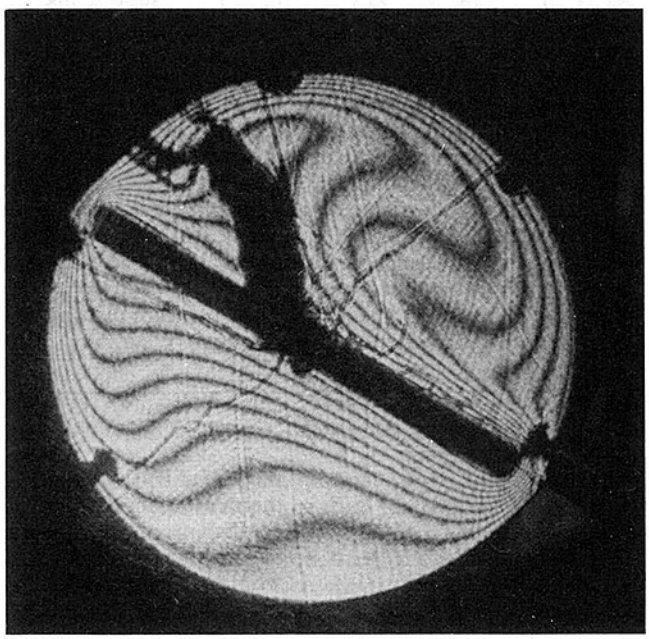

Fig. 3(b)

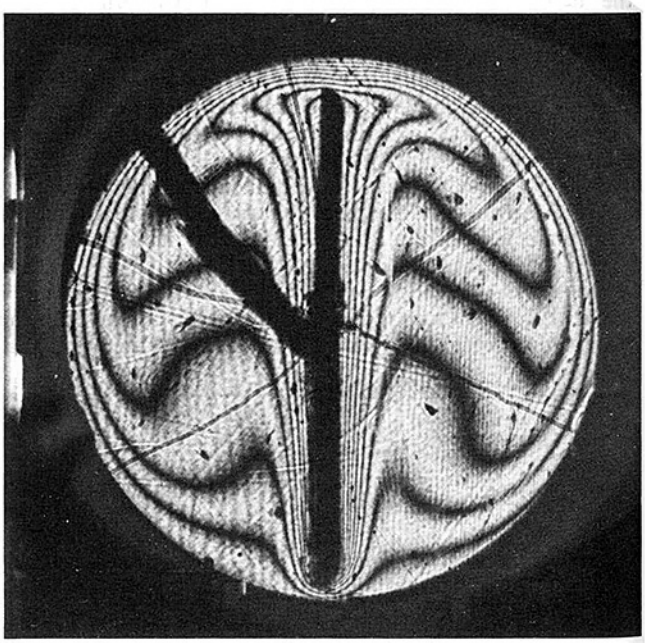

Fig. 3(d)

Fig. 3 Photographs of interferograms for four plate orientations: (a) θ = 0 deg, (b) θ = 30 deg, (c) θ = 60 deg, (d) θ = 90 deg

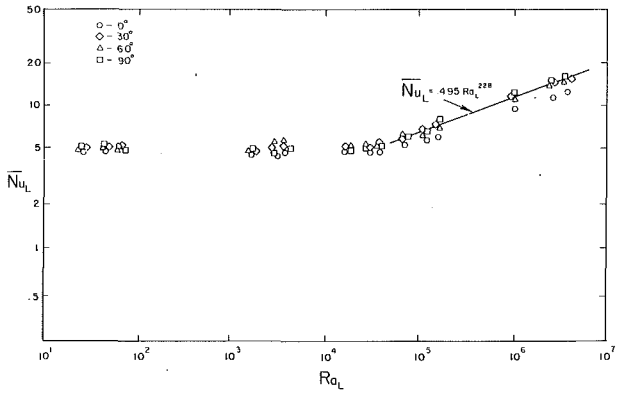

Fig. 4 Combined upper and lower plate mean heat transfer: Nu_L versus Ra_L

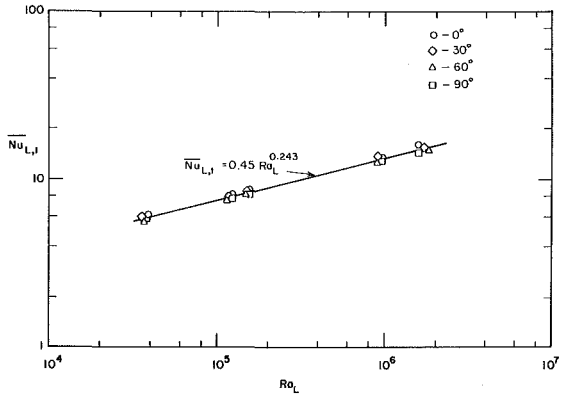

Fig. 5 Upper plate mean Nusselt number versus Rayleigh number

As a consistency check the interferometric data were compared to the overall Nusselt number calculated from the energy balance. The local heat transfer rate was evaluated at twenty positions along both the upper and lower sides of the plate. A numerical integration along each side of the plate was then used to evaluate the Nusselt number. The mean values calculated from the energy balance and the interferometric data agreed to within ±10 percent for the worse case. An error analysis was performed for each data value; the worse case for the mean Nusselt number resulted in an uncertainty of ±12 percent.

Results and Discussion

The results presented consist of the mean Nusselt number, based on heat transfer from both sides of the plate, the mean Nusselt number on each side of the plate, and the local variation of the heat transfer coefficient on each side of the plate. Each of these results is related to the Rayleigh number and plate inclination angle. Before presenting the quantitative results insight into the convective process can be obtained by examining the interferograms shown in Fig. 3. Representative interferograms are provided for inclinations of 0, 30, 60, and 90 deg from the horizontal. Fringes represent isotherms but also allow interference of the flow pattern. For $\theta = 0$ deg the pattern is symmetric about a central plume which rises from the center of the plate and impinges on the cylinder wall. This indicates a dual cell configuration with recirculation along the cool cylinder wall back toward the outer edges of the plate. This and all other patterns shown were stable for the range of Rayleigh numbers studied.

As the plate is tilted to 30 deg the buoyancy produces a force along the plate directed from the leading edge. (The leading edge is designated as the lower edge when tilted.) This causes the flow separation to occur higher up along the plate. The interferogram in Fig. 3(*b*) indicates separation prior to the end of the plate. Thus, for 30 deg tilt a dual cell structure exists. However, it is no longer symmetric; there is a large central cell and a smaller cell near the upper edge of the plate. When tilted to 60 deg the separation, which occurs in the upper region of the cylinder, is nearly at the upper edge. This implies that the dual cell formation is eliminated in favor of one large recirculation pattern. There is, most likely, a very small secondary cell near the top, but this is not discernible and not significant in the overall heat transfer rate.

In each of the above mentioned cases, $\theta = 0$, 30, and 60 deg, there is asymmetry between the upper and lower sides of the plate. For $\theta = 0$ deg nearly horizontal isotherms exist along the lower side indicating a nearly uniform heat loss from the lower side of the plate. At $\theta = 30$ deg a mild convection pattern exists in the lower region with separation far up along the plate, this is most likely a single cell pattern. At $\theta = 60$ deg the convection pattern in the lower region appears weaker than in the upper region as evidenced by the weaker down turn of the isotherms. However, separation occurs at approximately the same location on both the upper and lower sides of the plate.

At $\theta = 90$ deg a symmetric flow on either side of the plate exists. The isotherm pattern is evidence of a boundary layer near the plate until very near the upper edge where the flow must separate. Away from the plate the fluid is stratified but the downflow near the cylinder wall influences the stratification pattern such that the isotherms are not horizontal. The location of separation is nearly identical to the 60 deg tilt condition.

The correlation of the combined heat transfer based on the plate span L from both sides of the plate for all angles of inclination is shown in Fig. 4. Note that the Rayleigh number is not modified to include only the component of the gravitational vector which is parallel with the plate. Data below $Ra_L = 10^3$ essentially are independent of Ra_L which indicates that convection has not been firmly established. This is in agreement with Ortabasi [7] who found no effect of inclination below $Ra_L \sim 10^3$. Between Ra_L of approximately 10^3 and 3×10^4 there is a fair degree of scatter as the onset of convection occurs.

In the region of established convection, $Ra_L > 6 \times 10^4$, the mean Nusselt number is shown to correlate with Ra_L in Fig. 4. There is good agreement, regardless of the tilt angle, except for $\theta = 0$ deg. For $\theta \geq 30$ deg the following is a best fit for all the data

$$\overline{Nu}_L = 0.495\ Ra_L^{0.228}; \qquad 30\ \text{deg} \leq \theta \leq 90\ \text{deg} \tag{3}$$

The data for $\theta = 0$ deg are consistently below the above correlation, in fact the data for $\theta = 30$ deg are also somewhat below equation (3).

The heat transfer averaged over each of the upper and lower surfaces of the plate indicates reasons for the decreasing effect of inclination on the overall heat transfer as the angle of inclination increases. First, the upper surface mean correlation is shown in Fig. 5. The data for all angles of inclination agree well with the following correlation

$$\overline{Nu}_{L,t} = 0.45\ Ra_L^{0.243}; \qquad 0\ \text{deg} \leq \theta \leq 90\ \text{deg} \tag{4}$$

where $\overline{Nu}_{L,t}$ is the averaged Nusselt number on the top of the plate. Apparently the inclination effect is of minor importance in the correlation on the upper surface, even though the interferograms indicate significant variations in the temperature distribution within the enclosure. As a comparison, the heat transfer from upward facing, horizontal, heated, surfaces has been correlated by Goldstein et al. [11] as $\overline{Nu}_L = 0.54\ Ra_L^{1/4}$, where L is the surface area per perimeter. The present results show a slight reduction in both the coefficient and exponent of Ra_L, a possible result of the enclosure.

In contrast to the upper surface the lower surface is significantly affected by the inclination of the plate. Figure 6 shows the mean lower Nusselt number versus Ra_L. As θ increases the buoyancy has an increasing influence on the rate of

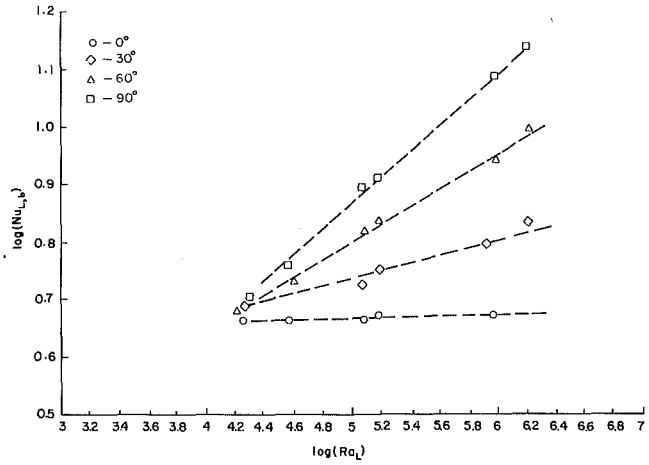

Fig. 6 Lower plate mean Nusselt number versus Rayleigh number

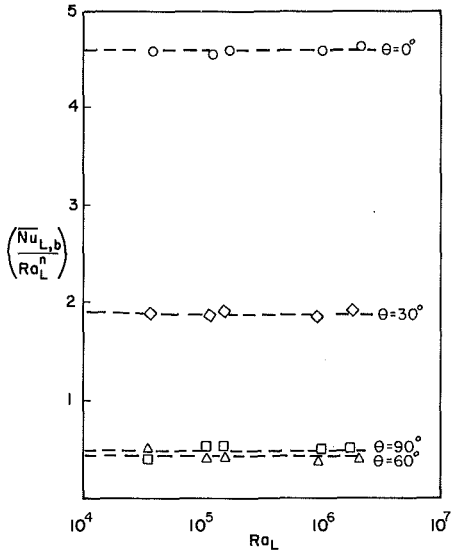

Fig. 7 Lower plate mean heat transfer correlation

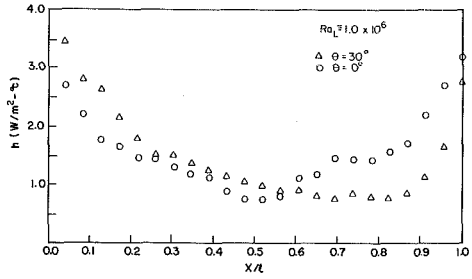

Fig. 8(a)

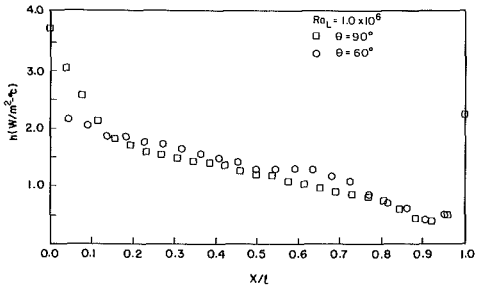

Fig. 8(b)

Fig. 8 Upper plate local heat transfer coefficient for $Ra_L = 1.0 \times 10^6$: (a) $\theta = 0$ and 30 deg, (b) $\theta = 60$ and 90 deg

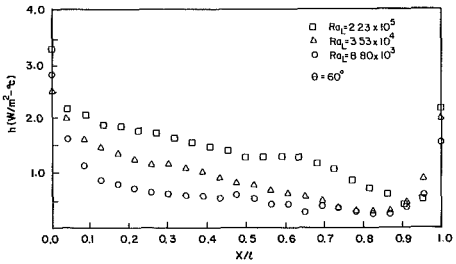

Fig. 9 Upper plate local heat transfer coefficient for $\theta = 60$ deg and various values of Ra_L

heat transfer (increasing slope). When $\theta = 0$ deg, Ra_L does not influence the overall heat transfer, for the range of Ra_L investigated. The value of $\overline{Nu}_{L,b}$ at $\theta = 0$ deg is not unity because of the chosen length scale. We have examined each angle separately to determine the best fit slope of the correlation n. An inclination angle dependence on n was found to be

$$n = n_v + 0.159(\sin\theta)^4 + 0.175\sin\theta - 0.247 \quad (5)$$

or very nearly

$$n \cong 1/6[(\sin\theta)^4 + (\sin\theta)] \quad (6)$$

where n_v, the slope of the correlation when the plate is vertical, equals 0.237. Using equation (5) the lower surface heat transfer results are presented in Fig. 7. The value of $\overline{Nu}_{L,b}/Ra_L^n$ does not collapse to a single value for all θ because of the effect of inclination on the onset of convection. Only a very small difference occurs between $\theta = 60$ deg and $\theta = 90$ deg. This result is consistent with the interferograms which indicate nearly identical isotherm patterns and locations of separation for these two cases. This evidence suggests that once the dual cellular structure is eliminated, by reaching a sufficiently large tilt angle, the effect of inclination very nearly vanishes. We conclude that for $\theta \geq 60$ deg inclination effects for the total (both sides) heat transfer are negligible. This is substantiated by the results presented in Fig. 4. For $\theta < 60$ deg there is an increasing effect of inclination, which is dominant on the lower surface heat transfer because of its inherently more stable configuration at lower angles of tilt, as shown later.

Figure 8 shows the local variation of the heat transfer coefficient h on the upper side of the plate for a single Rayleigh number and four angles of inclination. All other Rayleigh numbers studied have the same general trend. In Fig. 8(*a*) the upper side heat transfer coefficient is shown to be nearly symmetric about the central axis when $\theta = 0$ deg. The central minimum is a result of the separation caused by the plume. In the outer 40 percent of the plate (20 percent of the span near the edge) h increases rapidly toward the outer edge. As the plate is tilted the symmetry is lost and the minimum value of h is shifted toward the raised end of the plate. This minimum value location corresponds to the separation inferred from the interferograms. As shown in Fig. 8(*b*), the minimum values for $\theta = 60$ deg and $\theta = 90$ deg coincide. Comparing Figs. 8(*a*) and 8(*b*) shows a decrease in the minimum value of h at larger tilt angles. Comparing the interference pattern between 30 and 60 deg it can be seen that there is a change from a dual to a single cell recirculation pattern and it is postulated that the relative strength of separation is increased for the single cell pattern.

The rate of decrease of h toward the raised edge of the plate is affected by the value of Ra_L. Figure 9 shows, for $\theta = 60$ deg, the local variation of h on the upper side of the plate for three different Rayleigh numbers. The tendency of separation to cause a minimum of the local h is increased as Ra_L increases. That is, the minimum value of h per average h decreases as Ra_L increases. The location of separation moves

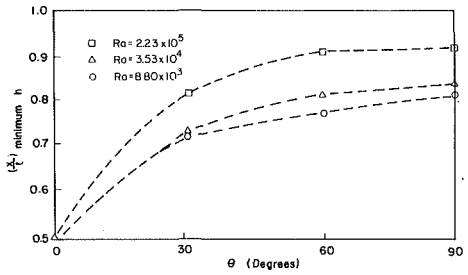

Fig. 10 Local minimum heat transfer coefficient location versus inclination angle

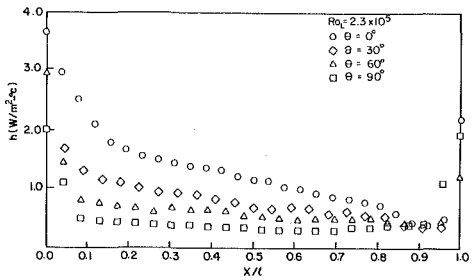

Fig. 11 Lower plate local heat transfer coefficient

up the plate as Ra_L increases. Figure 10 illustrates the location of the minimum value of h versus inclination angle for three different Rayleigh numbers. For small changes of inclination from the horizontal the position of the minimum value of h changes rapidly as it moves toward the raised end of the plate. Beyond 60 deg little change is observed for the range of Rayleigh numbers studied.

The local, lower side convective coefficient is shown in Fig. 11. For $\theta = 0$ deg a nearly uniform distribution exists with rapidly increasing values very near the edges of the plate. For the tilted plate, the increased heat transfer rate is evidence of the increased flow along the lower edge, up to the surface. As shown in the interferograms, the eventual separation causes the isotherms to diverge away from the surface in that region of the lower side of the plate. This causes a reduced local heat transfer rate. Only for $\theta = 60$ and 90 deg is there strong evidence of a local minimum for the convective coefficient; however, this minimum value is weaker than the upper surface minimum.

Conclusions

Based on the experimental results presented several conclusions can be made. First, the onset of convection for this plate-in-tube geometry occurs near $Ra_L = 10^3$ and fully developed laminar conditions begin near 6×10^4. A correlating equation is given for the combined heat transfer from both sides of the plate which is a result of opposing effects of inclination on the upper and lower sides of the plate. Second, the heat transfer from the upper surface can be fairly well correlated regardless of the inclination angle for the range of Rayleigh numbers studied. Third, the mean lower side heat transfer rate is strongly affected by the angle of inclination and the exponent of Rayleigh number changes significantly for θ less than 60 deg. Fourth, the local heat transfer coefficient is reduced by flow separation which is significantly affected by the angle of inclination. More definitive data need to be acquired to accurately determine the onset of convection. Also, more data should be provided for inclinations near the horizontal since it has been found that small variations from the horizontal cause large changes in the temperature and heat transfer distributions.

Acknowledgments

Partial support for this work was provided by the NSF under grant number ISP-8011451 and the Mechanical Engineering Department at Clemson University and is gratefully acknowledged. We also thank several reviewers for their thoughtful comments.

References

1 Fujii, T., and Imura, H., "Natural-Convection Heat Transfer From a Plate With Arbitrary Inclination," *Int. J. Heat Mass Transfer*, Vol. 15, 1972, pp. 755–767.

2 Miller, R. M., and Gebhart, B., "An Experimental Study of the Natural Convection Flow Over a Heated Ridge in Air," *Int. J. Heat Mass Transfer*, Vol. 21, 1978, pp. 1229–1239.

3 Unny, T. E., "Thermal Instabilities in Differentially Heated Inclined Fluid Layers," *J. Applied Mech.*, 1972, pp. 41–47.

4 Hassan, K., and Mohamed, S. A., "Natural Convection From Isothermal Flat Surfaces," *Int. J. Heat Mass Transfer*, Vol. 13, 1970, pp. 1873–1886.

5 Elsherbiny, S. M., Raithby, G. D., and Hollands, K. G. T., "Heat Transfer by Natural Convection Across Vertical and Inclined Air Layers," ASME JOURNAL OF HEAT TRANSFER, Vol. 104, 1982, pp. 96–102.

6 Ozoe, H., Sayama, H., and Churchill, S. W., "Natural Convection in an Inclined Rectangular Channel at Various Aspect Ratios and Angles – Experimental Measurement," *Int. J. Heat Mass Transfer*, Vol. 18, 1975, pp. 1425–1431.

7 Ortabatsi, U., "Indoor Test Methods to Determine the Effect of Vacuum on the Performance of a Tubular Flat Plate Collector," ASME Paper No. 76-WA/SOL-24.

8 Roberts, G. T., "Heat Loss Characteristics of an Evacuated Plate-in-Tube Collector," *Solar Energy*, Vol. 22, 1979, pp. 137–140.

9 Singh, P., "An Investigation of Thermal Characteristics of Plate-in-Tube Solar Receivers," Ph.D. Dissertation, Clemson University, 1982.

10 Leuenberger, H., "Compilation of Radiation Shape Factors for Cylindrical Assemblies," ASME Paper No. 56-A-144.

11 Goldstein, R. J., Sparrow, E. M., and Jones, D. C., "Natural Convection Mass Transfer Adjacent to Horizontal Plates," *Int. J. Heat Mass Transfer*, Vol. 16, 1973, pp. 1025–1034.

Effect of Solute Concentration Gradients on the Onset of Convection: Uniform and Nonuniform Initial Gradients

M. Kaviany
Department of Mechanical Engineering and Applied Mechanics, University of Michigan, Ann Arbor, MI 48109
Mem. ASME

M. Vogel
General Dynamics, Thermodynamics Division, Fort Worth, TX 76101

The time of the onset of convection in a fluid layer, which is initially stably stratified and then heated from below in a transient manner, is determined experimentally and analytically. The initial stratification is due to the presence of a solute concentration gradient. In addition to initial linear solute concentration distributions two other specific initial solute concentration distributions are considered. In Case 1, a zero gradient layer is located underneath a nonzero and uniform gradient layer. In Case 2, the zero gradient layer is on the top. The linear amplification theory is applied to the prediction of the onset time. Interferometry is used as a means of determining the onset time experimentally. It is shown that since the adverse temperature gradient is concentrated near the bottom, any nonuniformity in the solute concentration gradient in this region reduces the effectiveness of the gradient in delaying the onset. Experimental and predicted results are in good agreement.

1 Introduction

In horizontal fluid layers, a potentially unstable temperature profile can be neutralized by a stable solute concentration distribution [1-12]. The required gradient for steady-state profiles has been determined through application of the linear stability theory [7, 13] and also verified experimentally [6, 8]. Recently, the effects of nonuniformity in the solute concentration gradient and their practical implications have been studied [14]. It was found that convection begins in the region of the weakest concentration gradient, which was also observed experimentally.

A situation in which an initially stably stratified fluid layer is heated in a time-dependent manner has been studied and the onset time has been determined analytically [15] for shear-free surfaces (on the top and bottom) where one of the surface temperatures was allowed to change linearly with time while the other one was kept constant. An allowance was made for temporal variations in the solute concentration distribution. Since the buoyancy force is concentrated near the heated (or cooled) surface, any nonuniformity in the concentration gradient in this region can alter the onset time significantly.

In this study the analysis of [15] has been extended to include a rigid boundary at the bottom and an adiabatic surface on top. These are conditions which are mostly encountered in experiments. Also considered are the effects of a zero solute concentration gradient layer located beneath or above the nonzero gradient layer. The onset times for these cases are determined analytically and verified experimentally for a sodium chloride-heat-water system.

2 Analysis

Consider a fluid layer of depth L (with the z axis in the direction of gravity) confined by a rigid boundary at the bottom and a shear-free surface at the top. The fluid layer is initially at a uniform temperature and stably stratified by a solute concentration distribution. Then the temperature of the lower surface is increased linearly with time, at a rate ϕ (°C/s), while the upper surface is maintained adiabatic. A destabilizing buoyancy force evolves due to the presence of the adverse temperature gradient, and eventually leads to the onset of convection.

Contributed by the Heat Transfer Division for publication in the JOURNAL OF HEAT TRANSFER. Manuscript received by the Heat Transfer Division July 3, 1984.

The variables have been nondimensionalized using

$$z=\frac{z^*}{L},\ \delta=\frac{\delta^*}{L},\ t=\frac{t^*\alpha}{L^2},\ w=\frac{w^*L}{\alpha},\ T=\frac{(T^*-T_i^*)\alpha}{\phi L^2},$$

$$\theta=\frac{\theta^* g\beta L^3}{\nu\alpha},\ S=\frac{S^*-S_U^*}{S_L^*-S_U^*},\ \text{and}\ \psi=\frac{\psi^* g\gamma L^3}{\nu\alpha_s}$$

The variables with asterisks indicate dimensional quantities. The significant nondimensional parameters are

$$\mathrm{Ra}_T=\frac{g\beta\phi L^5}{\nu\alpha^2},\ \mathrm{Ra}_s=\frac{g\beta(S_L^*-S_U^*)L^3}{\nu\alpha_s},\ \mathrm{Pr}=\frac{\nu}{\alpha},$$

$$\text{and}\ \mathrm{Le}=\frac{\alpha}{\alpha_s}=\Gamma^{-1}$$

For a Boussinesq fluid and a linear equation of state, the linearized dimensionless conservation equations are

$$(\mathrm{Pr}^{-1}\partial_t-\nabla^2)\nabla^2 w=-\nabla_1^2\theta+\Gamma\nabla_1^2\psi \tag{1}$$

$$(\partial_t-\nabla^2)\theta=-\mathrm{Ra}_T w\ T_z \tag{2}$$

$$(\partial_t-\Gamma\nabla^2)\psi=-\mathrm{Ra}_s w\ S_z \tag{3}$$

$$(\partial_t-\nabla^2)T=0 \tag{4}$$

$$(\partial_t-\Gamma\nabla^2)S=0 \tag{5}$$

Γ is the inverse of the Lewis number Le and, along with the other symbols, is defined in the nomenclature. Subscripts indicate differentiations and $\nabla_1^2=\partial_{xx}+\partial_{yy}$.

The boundary and initial conditions are

$$t=0:\ T(z)=0,\ S(z)=f(z),\ w(z)=w_i,\ \theta(z)=\theta_i,\ \psi(z)=\psi_i$$

$$t>0:\ T_z(0)=0,\ T(1)=t,\ S_z(0)=S_z(1)=0,$$

$$w(0)=w_{zz}(1)=0,$$

$$\theta_z(0)=\theta(1)=0,\ \psi_z(0)=\psi(1)=0 \tag{6}$$

The solutions to equations (4) and (5) subject to the above conditions are

$$T=t+2^{-1}(z^2-1)+2\sum_{l=1}^{\infty}(l-2^{-1})^{-3}\pi^{-3}(-1)^{l-1}$$

$$\cdot\exp[-(l-2^{-1})^2\pi^2 t]\cos(l-2^{-1})\pi z \tag{7}$$

and, when the initial solute concentration gradient is uniform, we have

$$S = 2^{-1} - 4 \sum_{n=1,3,\ldots}^{\infty} (n\pi)^{-2} \exp(-n^2\pi^2\Gamma t) \cos n\pi z \qquad (8)$$

An rms for the vertical perturbation velocity is defined as

$$w_{\text{rms}} = \left[w^2(z,\ t) / \int_0^1 w_i^2(z)dz \right]^{1/2} \qquad (9)$$

A normalized density is defined as

$$\tilde{\rho} \equiv \alpha(\rho_0 - \rho)(\phi L^2 \rho_0 \beta)^{-1} = -T + \Gamma\ \text{Ra}_s \text{Ra}_T^{-1} S \qquad (10)$$

In practice, due to the severe initial mixing during construction of the solute gradient, the gradient adjacent to the lower surface is usually smaller than elsewhere. Also, adjacent to the impermeable boundaries the gradient gradually deteriorates due to molecular diffusion [6]. It is interesting to know the effect of this initial gradient nonuniformity on the onset time. A similar question arises with respect to the presence of a nonideal solute gradient at the top of the layer.

In solving the emerging characteristic equations, when $S_z(t, z)$ is a continuous and smooth function, in its Fourier series presentation only about 15 terms are needed. Any initial discontinuity in S_z requires that a large number of terms be used which is not computationally economical. For this reason, when S_z is not continuous we neglect the molecular diffusion of the mean solute concentration. This limits the analysis to cases in which the onset is not significantly delayed so that the mean solute concentration gradient is not severely deteriorated. Note that for heat and salt in water, Γ is about 10^{-2}, i.e., the molecular diffusion of salt is much slower than that of heat.

If the gradient in a portion of the fluid layer δ is zero, the above two nonideal cases become

$$\textit{Case 1} \quad S_z = \begin{cases} 1, & 0 \le z < 1-\delta \\ 0, & 1-\delta \le z \le 1 \end{cases} \qquad (11)$$

i.e., a zero gradient layer located adjacent to the lower rigid boundary, and

$$\textit{Case 2} \quad S_z = \begin{cases} 0, & 0 \le z \le \delta \\ 1, & \delta < z \le 1 \end{cases} \qquad (12)$$

i.e., a zero gradient layer located adjacent to the upper shear-free boundary.

Note that as δ increases from its ideal value of zero, the solute gradient outside δ remains the same. Therefore, as δ is varied the solute Rayleigh number which is based on the solute concentration difference for $\delta = 0$ remains the same.

The solution method is an extension of the linear amplification theory [16]. Other methods have been used for single-component problems [17, 18]. A discussion of the advantages and disadvantages of linear amplification theory, for a single component Bénard problem, is offered in [19]. In general, good agreement has been found between its prediction and experimental results [20]. The steps leading to the determination of the onset time are as follows:

(*i*) The white noise initial conditions [16] along with the horizontal periodicity are assumed for w, θ, and ψ.

(*ii*) Trial functions satisfying the boundary conditions are selected for w, θ, and ψ.

(*iii*) Using orthogonality properties of those functions, equations (1)–(3) are integrated over $0 \le z \le 1$. These equations and the eigenvalues are given in the appendix.

(*iv*) The emerging set of coupled initial value ordinary differential equations is solved numerically.

(*v*) Since the layer is initially stably stratified, the introduced disturbances may completely vanish. If this happens, they are reintroduced and the process is repeated until the proper buoyancy force has evolved and the disturbances grow and lead to instability.

(*vi*) The onset time is marked as the time when the average vertical velocity disturbance reaches a magnitude one thousand times its initial value.

(*vii*) The wave number corresponding to the shortest onset time is determined (the critical wave number).

The analysis results in $t_c = t_c$ (Γ, Pr, Ra_s, Ra_T, δ). The results that follow are for sodium chloride–heat–water (thermophysical properties from [21]). The results for a uniform initial solute concentration gradient (i.e., equation (8) for mean solute concentration distribution) will be given first.

3 Experiment

The experimental apparatus was that used in [20]. The solute used was sodium chloride and the solvent was water. The solute concentration gradient was constructed as recommended in [22]. Two tanks (the KONTES (trademark) Gradient Elution apparatus) were used, with one containing

Nomenclature

A = cross-sectional area of the test cell, cm^2
f = a function describing the initial distribution of solute concentration, equation (6)
g = gravitational constant, ms^{-2}
L = layer depth, m
Le = Lewis number = $\alpha\,\alpha_s^{-1}$
m = mass of salt in the test cell, g
N = total number of fringes over L
Pr = Prandtl number = $\nu\alpha^{-1}$
Ra_s = solute Rayleigh number = $g\gamma(S_L - S_U)L^3\nu^{-1}\alpha_s^{-1}$
Ra_T = thermal Rayleigh number = $g\beta\phi L^5\nu^{-1}\alpha^{-2}$
S = mean solute concentration, weight percent
t = time, s
T = mean temperature, °C
T_s = initial surface temperature, °C
V = volume of the test cell filled with the solution, cm^3
w = perturbation vertical velocity, ms^{-1}
x, y, z = dimensionless Cartesian coordinate axes
α = thermal diffusivity, m^2s^{-1}
α_s = solute diffusivity, m^2s^{-1}
β = volumetric thermal expansion coefficient, $°\text{C}^{-1}$
δ = dimensionless thickness of the layer with zero solute concentration gradient
γ = volumetric solute expansion coefficient, (weight percent)$^{-1}$
Γ = $\alpha_s\alpha^{-1} = \text{Le}^{-1}$
θ = perturbation temperature, °C
ν = kinematic viscosity, m^2s^{-1}
ρ = density, kg m^{-3}
ϕ = temporal rate of increase of the temperature of the lower surface, $°\text{Cs}^{-1}$
ψ = perturbation solute concentration, weight percent

Superscripts

$*$ = dimensional

Subscripts

c = critical
c, m = measured
c, p = predicted
i = initial
L = lower surface
rms = root mean square
s = solute
T = thermal
U = upper surface
t, x, y, z = derivatives
0 = reference

Table 1 Experimental results for sodium chloride-heat in water for a layer depth of 8.6 cm; the predicted values of the onset time are also given

Run #	$S_z^* \times 10^3$ % cm^{-1}	$\phi \times 10^4$ Cs^{-1}	L cm	T_s^* C	$\beta \times 10^6$ C^{-1}	$\nu \times 10^7$ $cm^2 s^{-1}$	Pr	Γ	$t^*_{c,m}$ Graphical s	$t^*_{c,m}$ Interferometry s	Δt^*_o s	$\alpha L^{-2} \times 10^5$ s^{-1}	$t_{c,m} \times 10^3$	$Ra_s \times 10^9$	$Ra_T \times 10^8$	$t_{c,p} \times 10^3$	$\frac{t_{c,m}-t_{c,p}}{t_{c,p}} \times 100$
25	7.41-9.44	4.65	8.6	24.8	256.3	9.00	6.15	0.0102	1590	1610	45	1.98	32.0-32.9	2.14	2.85	35.7	7.84-10.4
29	9.23-9.90	96.67		26.3	270.8	8.69	5.92		129	103	46		2.57-3.48	2.76	64.45	2.98	13.7-(-16.8)
4	11.3	5.33		24.8					1560	1650	0		31.0-32.8	3.26	3.27	42.5	22.8-27.1
5	12.5-13.4	9.96		24.8					693	761	0		13.8-15.1	3.61	6.11	23.3	35.2-40.8
8	13.7-17.8	4.88		25.4	262.1	8.87	6.06		2360	2553	67		48.3-52.1	4.02	3.19	54.9	5.10-12.0
6	15.0-20.0	9.58		25.4					1187	1027	73		23.6-25.1	4.40	6.09	27.5	8.73-14.2
28	18.1-19.8	35.50		22.5	233.9	9.47	6.52		460	335	60		9.15-10.3	4.97	19.16	9.79	-4.95-6.54
7	18.2-20.0	19.08		25.3	261.2	8.89	6.07		635	595	55		12.6-13.6	5.33	12.05	16.0	15.0-21.2
2	18.3	4.43		26.5	272.8	8.62	5.88		2920	NA	100		58.1-60.1	5.53	3.01	78.2	23.1-25.7
9	36.5-42.1	19.92		24.8	256.3	9.00	6.15		967	930	40		19.2-20.0	10.56	12.21	30.2	33.8-36.4
3	36.5-42.1	10.21		26.5	272.8	8.62	5.88		1960	1910	120		39.0-41.4	11.02	6.86	60.7	31.8-35.7
10	41.1-44.5	10.08		25.7	265.0	8.81	6.01		2380	2273	60		47.4-48.6	12.14	6.50	75.6	35.7-37.3
15	60.0-68.3	10.10		26.0	267.9	8.72	5.96		3000	2840	40		59.7-60.5	17.91	6.68	110.6	45.3-46.0
16	64.2-66.1	10.50		26.4	271.8	8.66	5.90		3580	3550	140		71.2-74.0	19.29	7.05	112.6	34.3-36.8
12	64.6-69.9	18.75		27.2	279.3	8.51	5.78		1630	1650	90		32.8-34.6	19.76	13.09	54.1	36.0-39.4
11	64.1-71.9	19.58		27.5	282.0	8.46	5.75		1650	1685	190		33.5-37.3	19.72	13.90	50.2	25.7-33.3
13	69.2-71.6	37.71		24.5	253.4	9.04	6.20		798	755	25		15.9-16.4	19.92	22.92	27.4	40.1-42.0
14	79.0-83.7	75.00		25.5	263.1	8.85	6.04		420	435	55		8.66-9.76	23.23	47.88	14.4	32.2-39.9
19	110-130	79.17		25.9	267.0	8.77	5.98		577	547	77		11.5-13.0	32.64	51.66	18.0	27.8-36.1
17	111-128	40.42		26.6	273.8	8.60	5.87		850	990	20		17.3-22.9	33.59	27.64	37.3	38.6-53.6
22	111-126	79.17		27.8	284.6	8.42	5.71		540	465	45		10.7-11.6	34.31	56.73	18.5	37.3-42.2
21	124-138	10.29		28.2	288.2	8.32	5.66		NA	5620	NA		111.8	38.79	7.60	228.3	51.0
18	129-141	19.79		27.5	282.0	8.46	5.75		2600	2730	120		54.1-56.9	39.69	14.05	111.0	48.7-51.3
20	131-146	153.8		27.3	280.2	8.50	5.77		355	310	50		7.06-8.06	40.11	107.71	10.9	26.0-35.2
24	138-145	20.92		28.7	292.7	8.26	5.60		3060	3060	40		60.9-61.7	43.48	15.71	101.4	39.2-39.9

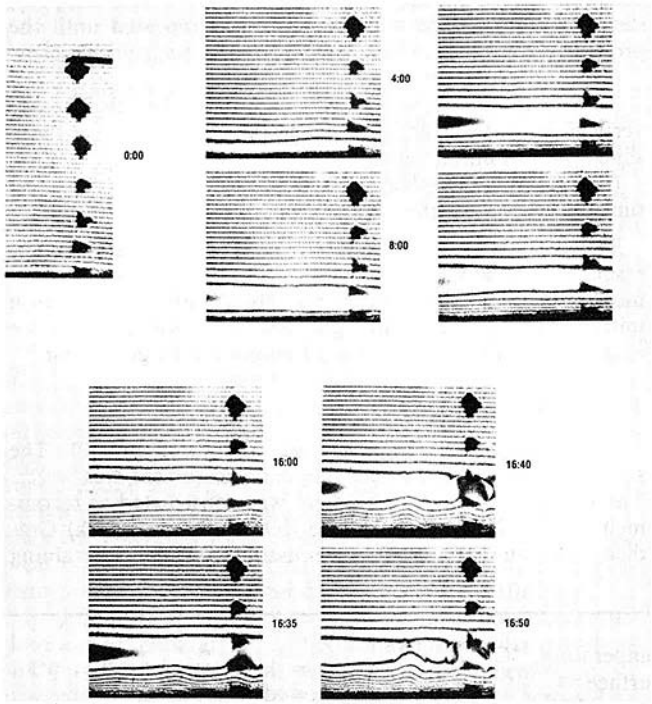

Fig. 1 Fringe patterns created by interferometry. The elapsed times, after the heating began, are marked for each frame. The spots are markers used for measuring the distance from the lower surface. The average distance between the markers is 9 mm, except for that between the first two bottom markers, which is 5.3 mm. At the lower surface the thermal fringes first nullify the solute fringes and then appear as separate fringes. The onset time is marked to be at 16:35.

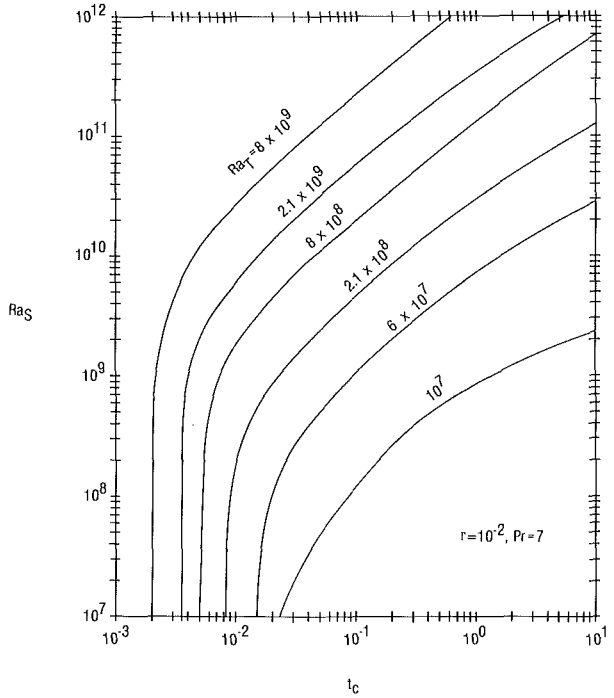

Fig. 2 Predicted variation in the onset time with respect to Ra_S for various values of Ra_T. The results are for Pr = 7 and $\Gamma = 10^{-2}$.

distilled water and the other containing the solution which was being stirred. These were connected at the base, and the solution flowed from the base of the second tank into the test cell. For calibration the solute concentration construction tanks were filled to the level where they would empty completely once the test cell was filled. Then a measured amount of salt was added. By neglecting the salt that is lost to the contact surfaces,[1] the number of fringes observed must be such that this measured salt appears in the test cell. The amount of salt dissolved in water was determined by noting that the solute fringes are caused by a nonzero gradient of the solute concentration, which means that the total amount of salt is

$$m = \int_V dm = A\,L \int_0^L \rho_z dz^* = A\,L \int_0^L d\rho = 3.51 \times 10^{-3} ALN \tag{13}$$

where N is the total number of fringes observed over the layer depth L, A is the cross-sectional area of the cell, and the constant relates a solute fringe to the corresponding change in density. This led to agreement to within 3 percent between the preweighed amount of salt and that determined using equation (13), which was considered satisfactory.

The onset time was determined by observing sudden changes in the fringe patterns and also through examining the heat transfer rate at the lower surface as given in [20]. Figure 1

[1] While the solution tank was being emptied, its inner walls were rinsed in order to remove any salt that might have been absorbed by it. Also, after the solution tank was completely emptied, the bottom of it was rinsed. Therefore, the amount of salt lost to the surfaces was minimized.

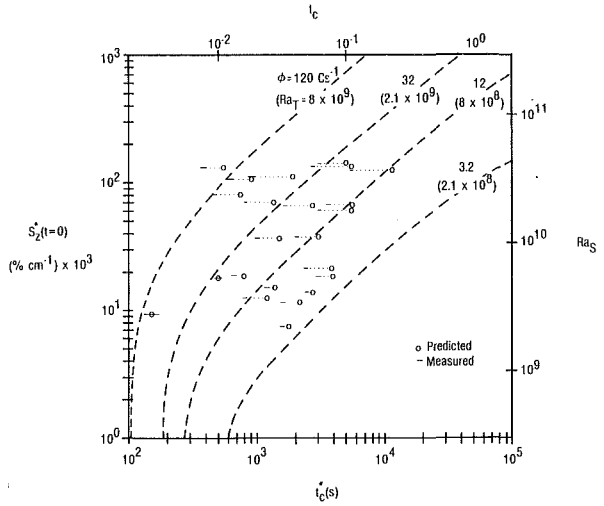

Fig. 3 Comparison of the experimental and predicted results for the onset time. The results are for sodium chloride and heat in water ($\Gamma \simeq 10^{-2}$ and Pr $\simeq$ 7).

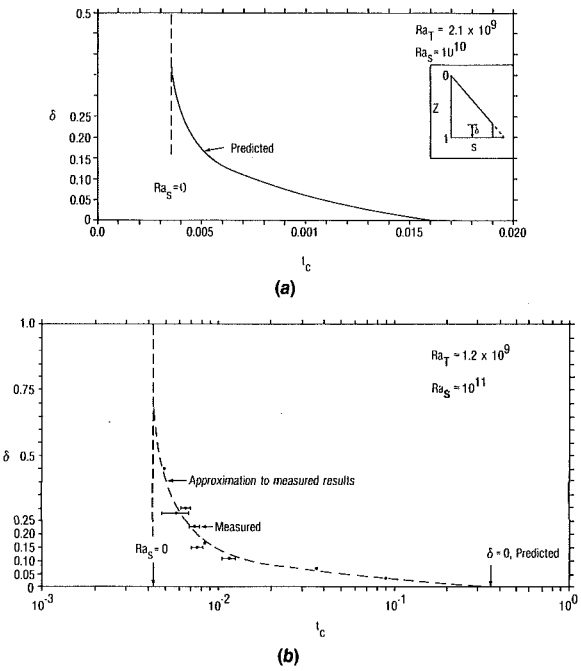

Fig. 4 Effect of the presence of a zero solute gradient layer located beneath the nonzero solute gradient layer on the onset time. The predicted results are based on the assumption of no diffusion of mean solute concentration: (*a*) predicted, (*b*) measured.

gives an example of the fringe evolutions. A 4.89×10^{-3} percent weight change of solute concentration produces one fringe. The counterpart for heat is 0.085°C. The density change corresponding to a solute fringe is 3.51×10^{-5} g cm^{-3}. The counterpart for heat is 2.27×10^{-5} g cm^{-3}. Most of the experimental results are for $L = 8.6$ cm, initial linear solute gradients in the range of 7.5×10^{-3} to 138×10^{-3} percent weight solute concentration per cm, and heating rates in the range of 4.5×10^{-4} to 154×10^{-4}°Cs^{-1}. In terms of nondimensional parameters these are $2 \times 10^9 < \text{Ra}_s < 4 \times 10^{10}$, and $3 \times 10^8 < \text{Ra}_T < 10^{10}$. Due to the relatively strong dependence of β and ν on temperature, these properties were evaluated at the surface temperature at the onset. This accounts for the concentration of the buoyancy force near the lower surfaces but is inadequate in allowing for the actual spatial variation. When S_z was not uniform, the smallest value in the first 5 cm (measured from the lower surface) of the layer was used. In general the variation of S_z in the layer was less than 10 percent except for the small zone adjacent to the lower surface.

4 Results and Discussion

4.1 Uniform Solute Gradient. For a given Ra_T the magnitude of Ra_s must be raised to a critical value before it can cause any noticeable delay in onset. Figure 2 gives the predicted results for several values of Ra_T (chosen to include the range covered in the laboratory experiment that will be discussed shortly). The effect of the stabilizing solute gradient begins to be noticeable at approximately (of the order of) $\text{Ra}_s = 0.1\ \text{Ra}_T$.

The experimental results for $L = 8.6$ cm are given in Table 1. Figure 3 shows the experimental and predicted results for the onset time. The results are presented in a form similar to Fig. 2; however, for the experimental results Ra_T was not kept constant while Ra_s changed. The dashed lines showing constant Ra_T (or constant ϕ) lines are given for the sake of reference. The experimental results are given with horizontal lines. The extent of these lines shows the error ranges associated with determining the onset times. The smaller value is that associated with the smaller of the graphic (this is when the time rate of change of the surface temperature suddenly changes as described in [20]) or holographic results and the large value is associated with the larger of these plus Δt_0^*.[2] The corresponding predicted values are given with open circles. For constant ϕ lines the properties are evaluated at 26°C. In general the measured onset times are smaller than those predicted. The differences, given with respect to the predicted values, ranged from −16.8 to 53.8 percent with an average of 30.1 percent. The results show that as S_z increases and ϕ decreases this difference becomes larger. However, the linear amplification theory predicts the trend of the increase in t_c^* rather satisfactorily.

The largest delay obtained experimentally is 43-fold (over that for no solute gradient present). No experiment with a t_c^* of larger than one and a half hours was attempted because the change in the ambient temperature could affect the results.

4.2 Zero Solute Gradient at the Bottom. For Case 1, the predicted variation of the onset time with δ for a situation where the onset is delayed by up to fivefold (over that for no solute concentration gradient) is given in Fig. 4(*a*). Since here in presenting S_z the molecular diffusion of the solute is neglected, a more pronounced delay of the onset was not chosen. The results which are for $\Gamma = 10^{-2}$, Pr = 7, $\text{Ra}_T = 2.1 \times 10^9$, and $\text{Ra}_s = 10^{10}$ show that as δ increases from its ideal value of zero, the onset time decreases sharply. Examination of the distribution of w_{rms} reveals (not shown) that the location of its maximum remains at $z = 0.91$ while δ increases. The upper nonzero gradient layer delays the onset even up to $\delta = 0.25$. However, for $\delta > 0.25$ the growth of the disturbances is not affected by its presence.

The effect of the upper nonzero gradient on the lower region may be considered analogous to the suppression of disturbances in a convective zone by a stably stratified stagnant upper zone ([13], p. 155 and p. 235). In practice, it is difficult to construct a solute concentration distribution with discontinuity in its gradient. Moreover, such discontinuities are smoothened very rapidly by molecular diffusion. Figure 5 is for $S_z^* = 34.9\text{–}40.3 \times 10^{-3}$ percent cm^{-1} and $\phi = 9.5 \times 10^{-4}$°Cs^{-1}. The desired δ^* was about 7 mm. However, as seen in the figure, at $t = 0$ due to diffusion two undesired fringes are present in the region of "zero gradient."

The experimental results for a situation corresponding to

[2] Δt_0^* was the elapsed time between the start of heating and the time at which the desired linear increase in the surface temperature was observed [20].

Case 1 are given in Table 2 and also are shown in Fig. 4(*b*). The dashed line labeled approximation is curve fit to experimental results. Since the contribution of Δt_0^* is not significant, it is not given. The predicted delay for $\delta = 0$ is about 80-fold. This rather noticeable delay was chosen so that variations in δ could result in significant and measurable variations in the onset time. For $\delta = 0$ no experimental data are available because it was not possible to determine the gradient for the first 1–2 mm from the lower surface. As can be seen from the results, the predicted onset time for $\delta = 0$ is in general agreement with that found by extrapolation of the experimental results for $\delta \neq 0$. The results show that for these sets of parameters a δ^* as small as a few mm (total depth is 11 cm) can appreciably reduce the onset time.

As was mentioned earlier, since in the predicted results the molecular diffusion of the solute was neglected, the values of Ra_s and Ra_T (predicted results) are taken such that this assumption holds, i.e., the onset time is not delayed by many folds over that for $S_z = 0$. Comparison of Figs. 4(*a*) and 4(*b*) shows that the trend found experimentally is similar to that predicted, i.e., for $\delta > 0.25$ the upper nonzero gradient layer has no significant effect on the onset of convection in the lower layer. This limit on δ varies with Ra_T and Ra_s; however, it is clear that nonideal solute gradients near the lower surface greatly hinder its effectiveness.

Table 2 A zero solute gradient layer located beneath the nonzero solute gradient layer, L = 11 cm

RUN #	δ	$\phi \times 10^4$ Cs^{-1}	$S_z^* \times 10^3$ % cm^{-1}	$t^*_{c,m}$ Graphical s	$t^*_{c,m}$ Interferometry s	$t_{c,m} \times 10^3$	$Ra_T \times 10^{-9}$	$Ra_s \times 10^{-11}$
U4	0.41	4.2	132	NA	403	4.88	1.05	1.12
U3	0.28	4.3	127	560	560–530	6.05–6.78	1.08	1.07
U2	0.25	4.5	109	395	445–545	4.78–6.60	1.13	0.922
U1	0.23	5.0	124	640	567–597	6.86–7.75	1.25	1.05
U5	0.16	4.6	139	NA	687	8.31	1.15	1.16
U6	0.15	5.7	138	580	670	7.02–8.11	1.43	1.17
U7	0.11	5.6	129	853	1033	10.3–12.5	1.40	1.09
U8	0.064	4.8	108	NA	2970	35.9	1.20	0.913
U9	0.027	4.9	117	NA	7500	90.8	1.23	0.989

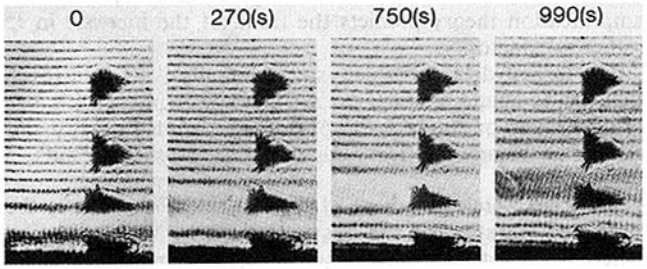

Fig. 5 Interferometry observation of the evolution of the density distribution. At t = 0, the fringes are due to the initial solute concentration distribution which consists of a zero gradient layer located beneath the nonzero (and nearly constant) solute gradient layer. The markers are in the same locations as those given in Fig. 2.

4.3 Zero Solute Gradient at the Top. For Case 2, the predicted variation in the onset time with respect to δ is shown in Fig. 6(*a*) for the same set of parameters used in Fig. 4. As the elapsed time increases, the effect of lower surface heating penetrates farther into the layer and gradually reaches the top surface. Then the temperature of the top surface, which is maintained as adiabatic, begins to increase. Therefore, as δ increases, it becomes possible for the temperature distribution in the region $0 < z < \delta$ to lead to instability. It is seen, too, that for $\delta < 0.8$ convection initiates inside the nonzero gradient layer while for $\delta > 0.8$ convection initiates in the zero gradient upper layer near the interface between the two layers. Here it is evidence that as long as the onset takes place inside the nonzero gradient layer the onset time is nearly the same as that for $\delta = 0$.

Figure 6(*a*) also shows that for $\delta < 0.5$ the onset time does not reach an asymptotic value but rather increases slightly at first and then in a more pronounced manner as $\delta \to 0$. This may be explained as follows. After the effect of lower surface heating reaches the top surface, a nonzero and potentially

Table 3(*a*) A zero solute gradient layer located on top of the nonzero solute gradient layer, L = 11 cm

RUN #	δ	$\phi \times 10^4$ Cs^{-1}	$S_z^* \times 10^3$ % cm^{-1}	$t^*_{c,m}$ Graphical s	$t^*_{c,m}$ Interferometry s	$t_{c,m} \times 10^3$	$Ra_T \times 10^{-9}$	$Ra_s \times 10^{-10}$
U10	0.0	23.0	41.1–48.1	870	745	9.0–10.5	5.48	3.49–4.08
U11	0.5	23.0	40.0–44.0	950	810	9.8–11.5	5.48	3.40–3.73
U12	0.6	23.3	39.1–43.3	860	760	9.2–10.4	5.55	3.32–3.67
U13	0.77	21.6	32.3	NA	795	9.6	5.15	2.74
U14	0.86	22.9	35.9–39.1	848	658	7.97–10.3	5.46	3.05–3.32
U16	0.90	24.2	26.7–36.9	453	430	5.15–5.43	5.76	2.27–3.13
U15	0.94	21.1	36.9	280	270	3.27–3.39	5.03	3.13

Table 3(*b*) A zero solute gradient layer located on top of the nonzero gradient layer, L = 11 cm

RUN #	δ	$\phi \times 10^{-4}$ Cs^{-1}	$S_z^* \times 10^3$ % Cm^{-1}	$t^*_{c,m}$ Graphical s	$t^*_{c,m}$ Interferometry s	$t_{c,m} \times 10^3$	$Ra_T \times 10^{-9}$	$Ra_s \times 10^{-10}$
U17	0.0	23.6	105.6–119.6	NA	1668	20.2	5.62	8.97–10.2
U18	0.59	22.8	93.5–99.8	NA	1350	16.3	5.38	7.94–8.47
U19	0.69–0.77	23.3	78.2–97.8	1637	1120	13.5–19.8	5.55	6.64–8.30
U20	0.72–0.78	23.4	77.3–90.0	1203	1340	14.6–16.2	5.58	6.56–7.64
U21	0.82–0.89	23.8	51.3–92.3	1063	730	8.82–12.9	5.67	4.36–7.84
U22	0.91	22.4	83.0	597	390	4.71–7.23	5.34	7.05

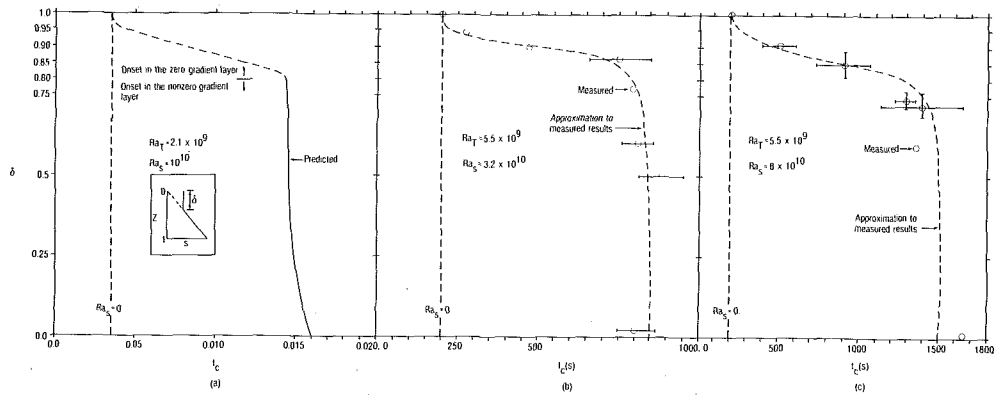

Fig. 6 Same as Fig. 4 except that the zero solute gradient layer is on the top: (*a*) predicted; (*b*) and (*c*) measured

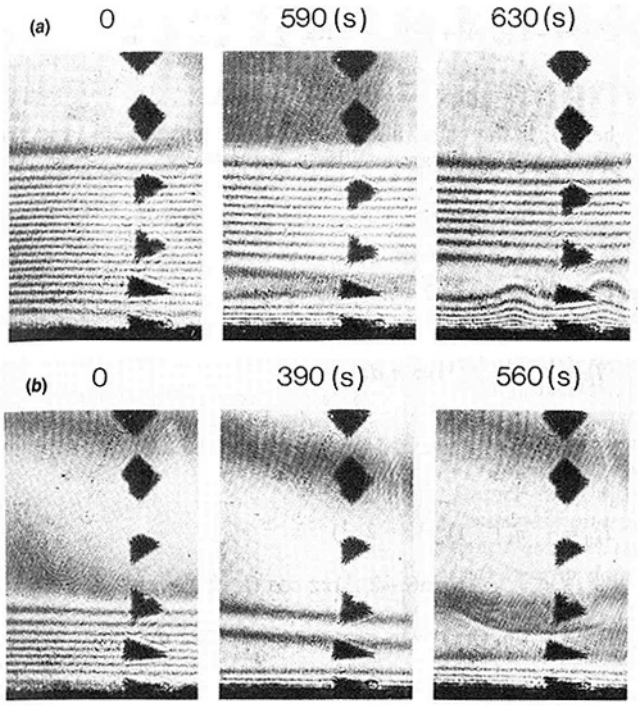

Fig. 7 Same as Fig. 5, except that the zero solute gradient layer is on the top, $Ra_T = 5.5 \times 10^9$, $Ra_S = 3.5 \times 10^{10}$. (*a*) The onset takes place inside the nonzero solute gradient layer, $\delta = 0.73$. (*b*) The onset takes place inside the zero solute gradient layer, $\delta = 0.87$.

unstable temperature gradient will be established a short distance from the upper surface. Also, due to the shear free boundary condition imposed on this surface (i.e., $w = w_{zz} = 0$), a significant, positive constant gradient for w can develop. This happens when there is no salt gradient in this area to suppress the growth of the disturbances. The growth of the disturbances in this region contributes slightly to the overall growth and accelerates the onset, but the presence of a solute gradient adjacent to the upper surface eliminates this contribution.

The experimental results are given in Tables 3(*a*) and 3(*b*) and are also shown in Figs. 6(*b*) and 6(*c*). The salt concentration gradient in Fig. 6(*c*) is more than twice that for Fig. 6(*b*). Figure 7 shows the evolution of the density profiles and the onset times as observed by interferometry. Figure 7(*a*) is a typical experiment for the cases where δ is not sufficiently large to affect the onset time, and Fig. 7(*b*) is for a case where the onset time is lower than what it would have been for no zero gradient zone. The trends found in Figs. 6(*b*) and 6(*c*) are similar to those predicted, i.e., for $\delta > 0.8$, the onset is accelerated and takes place inside the zero gradient layers. No appreciable change in t_c is found for the cases where convection initiates in the lower layers.

5 Conclusion

The delay in the onset of convection caused by a stabilizing solute concentration gradient has been investigated analytically using the linear amplification theory and experimentally using heat-sodium chloride in water. In general good agreements have been found.

It is found that the nonuniformity (due to nonideal conditions) in the gradient can signficantly alter its effectiveness if the nonuniformity is in the area where the temperature gradient is the largest.

When the lower portion of the layer has a zero solute concentration gradient, if this portion constitutes more than 20 percent of the layer depth, the gradient is not effective. Even when this layer constitutes only a few percent of the total layer depth, the onset time is significantly less than that for the ideal case (i.e., no zero gradient layer).

When the zero gradient layer is on the top, the lower nonzero gradient remains effective (i.e., not significantly different from the ideal case) as long as the temperature gradient in the upper layer is not large enough to cause onset in that layer.

Acknowledgments

Ths support of the National Science Foundation through Grant MEA 82-04837 is greatly appreciated. The constructive comments made by the reviewers are also appreciated.

References

1 Stern, M. E., "The 'Salt Fountain' and Thermohaline Convection," *Tellus*, Vol. XII, 1960, pp. 172–175.

2 Nield, D. A., "The Thermohaline Rayleigh–Jeffreys Problem," *J. Fluid Mech.*, Vol. 29, 1967, pp. 545–558.

3 Turner, J. S., "The Behavior of a Stable Salinity Gradient Heated From Below," *J. Fluid Mech.*, Vol. 33, 1968, pp. 183–200.

4 Veronis, G., "Effect of a Stabilizing Gradient of Solute on Thermal Convection," *J. Fluid Mech.*, Vol. 34, 1968, pp. 315–336.

5 Baines, P. A., and Gill, A. E., "On Thermohaline Convection With Linear Gradients," *J. Fluid Mech.*, Vol. 37, 1969, pp. 289–306.

6 Shirtcliffe, T. G. L., "An Experimental Investigation of Thermosolute Convection at Marginal Stability," *J. Fluid Mech.*, Vol. 25, 1969, pp. 677–688.

7 Schechter, R. S., Verlarde, M. G., and Platten, J. K., "The Two-Component Bénard Problem," *Adv. Chem. Phys.*, Vol. 26, 1974, pp. 265–301.

8 Wright, J. H., and Loehrke, R. I., "The Onset of Thermohaline Convection in a Linearly-Stratified Horizontal Layer," ASME JOURNAL OF HEAT TRANSFER, Vol. 98, 1976, pp. 550–563.

9 Huppert, H. E., and Linden, P. E., "On Heating a Stable Salinity Gradient From Below," *J. Fluid Mech.*, Vol. 95, 1979, pp. 431–464.

10 Proctor, M. R. E., "Steady Subcritical Thermohaline Convection," *J. Fluid Mech.*, Vol. 105, 1981, pp. 507–521.

11 Huppert, H. E., and Turner, J. S., "Double Diffusion Convection," *J. Fluid Mech.*, Vol. 106, 1981, pp. 299–329.

12 Gutkowicz-Krusin, D., Collins, M. A., and Ross, J., "Rayleigh-Bénard Instability in Nonreactive Binary Fluids, I. Theory and II. Results," *Phys. Fluids*, Vol. 22, 1979, pp. 1443–1460.

13 Turner, J. S., *Buoyancy Effects in Fluids*, Cambridge University Press, 1973.

14 Walton, I. C., "Double-Diffusive Convection With Large Variable Gradients," *J. Fluid Mech.*, Vol. 125, 1982, pp. 123–135.

15 Kaviany, M., "Effect of a Stabilizing Solute Gradient on the Onset of Thermal Convection," *Phys. Fluids*, Vol. 27, 1984, pp. 1108–1113.

16 Foster, T. D., "Stability of Homogeneous Fluid Cooled Uniformly From Above," *Phys. Fluids*, Vol. 8, 1965, pp. 1249–1257.

17 Wankat, P. C., and Homsy, G. M., "Lower Bound for the Onset of Instability in Heated Layers," *Phys. Fluids*, Vol. 20, 1977, pp. 1200–1201.

18 Ahlers, G., Cross, M. C., Hohenberg, P. C., and Safran, S., "The Amplitude Equation Near the Convective Threshold: Application to Time-Dependent Heating Experiments," *J. Fluid Mech.*, Vol. 110, 1981, pp. 297–334.

19 Mahler, E. G., Schechter, R. S., and Wissler, E. H., "Stability of a Fluid Layer With Time-Dependent Density Gradients," *Phys. Fluids*, Vol. 11, 1968, pp. 1901–1912.

20 Kaviany, M., "Onset of Thermal Convection in a Fluid Layer Subjected to Transient Heating From Below," ASME JOURNAL OF HEAT TRANSFER, Vol. 106, 1984, pp. 817–823.

21 *Saline Water Conversion Engineering Data Book*, Office of Saline Water, Department of Interior, published by Kellogg Company, Piscataway, NJ, 1975.

22 Oster, G. D., "Density Gradients," *Scientific American*, Vol. 213, 1965, pp. 70–76.

APPENDIX

The trial functions which satisfy the boundary conditions are

$$w = \sum_{k=1}^{\infty} A_k(t)\eta_k(z) = \sum_{k=1}^{\infty} A_k(t)[(\sinh \lambda_k)^{-1}\sinh(\lambda_k z) - (\sin \tau_k)^{-1}\sin(\tau_k z)],$$

$$\theta = \sum_{m=1}^{\infty} B_m(t)\cos(m - 2^{-1})\pi z, \text{ and}$$

$$\psi = \sum_{i=1}^{\infty} C_i(t)\cos(i - 2^{-1})\pi z$$

where λ_k and τ_k are the eigenvalues that are found by applying the boundary conditions to w. The orthogonality property of η is

$$\int_0^1 [(\eta_k)_z(\eta_l)_z + a^2\eta_k\eta_l]dz = \int_0^1 [-\eta_l(\eta_k)_{zz} + a^2\eta_k\eta_l]dz = \begin{cases} 0 & \text{for } k \neq l \\ N_k & \text{for } k = l \end{cases}$$

With the above trial functions and norm, the characteristic equations become

$$(A_j)_t = -\mathrm{Pr}(\delta_j + a^2)A_j + N_j^{-1}\mathrm{Pr}\ a^2 \sum_{k=1}^{\infty} A_k I_{kj} - N_j^{-1}\mathrm{Pr}\ a^2 \sum_{m=1}^{\infty} B_m I_{mj} + N_j^{-1}\Gamma\ \mathrm{Pr}\ a^2 \sum_{i=1}^{\infty} C_i I_{ij}$$

$$j = 1, 2, 3, \ldots$$

$$(B_j)_t = -[(j-2^{-1})^2\pi^2 + a^2]B_j - 2\ \mathrm{Ra}_T \sum_{k=1}^{\infty}\sum_{l=1}^{\infty} A_k\{I_{k0j} + I_{klj}\exp[-(l-2^{-1})^2\pi^2 t]\}$$

$$j = 1, 2, 3, \ldots$$

$$(C_j)_t = -\Gamma[(j\pi)^2 + a^2]C_j - 2\ \mathrm{Ra}_s \sum_{k=1}^{\infty}\sum_{n=1,3,.}^{\infty} A_k I_{knj} \cdot \exp(-n^2\pi^2\Gamma t) \qquad j = 1,2,3, \ldots$$

where δ_j is the eigenvalue related to λ_j and τ_j [20], and the following integrals are evaluated analytically

$$I_{kj} = \int_0^1 (\eta_k)_{zz}\eta_j dz$$

$$I_{mj} = \int_0^1 \cos\,(m-2^{-1})\pi z\eta_j dz$$

$$I_{ij} = \int_0^1 (i-2^{-1})\pi z\ n_j dz$$

$$I_{k0j} = \int_0^1 z\eta_k \cos\,(j-2^{-1})\pi z\ dz$$

$$I_{klj} = \int_0^1 \eta_k(-1)^{l-1}(l-2^{-1})^{-2}\pi^{-2} \cdot \sin(l-2^{-1})\pi z \cos\,(j-2^{-1})\pi z\ dz$$

$$I_{knj} = \int_0^1 4\eta_k(n\pi)^{-1}\sin\,n\pi z \cos\,(j-2^{-1})\pi z\ dz$$

Numerical Investigation of Variable Property Effects on Laminar Natural Convection of Gases Between Two Horizontal Isothermal Concentric Cylinders

D. N. Mahony[1]

R. Kumar

E. H. Bishop
Mem. ASME

Department of Mechanical Engineering,
Clemson University,
Clemson, SC 29631

A numerical finite difference investigation has been conducted to determine the effects of variable properties on the laminar natural convection of gases between horizontal isothermal concentric cylinders. Velocity profiles, temperature profiles, and heat transfer rates have been computed for diameter ratios of 1.5, 2.28, 2.6, and 5.0 and Rayleigh numbers based on gap width up to 1.8×10^5. The temperature difference ratio θ_o was varied from 0.2 to 3.0, and the range of validity of the Boussinesq approximation was determined to be $\theta_o = 0.2$. A volume-weighted mean temperature was shown to be the most effective reference temperature to reduce the heat transfer data for each diameter ratio to a single curve of the form $k_{eq} = C\, Ra_L^n$, for $0.2 \leq \theta_o \leq 3.0$ and $Ra_L = 2.0 \times 10^5$.

Introduction

The natural convection flow of gases between horizontal isothermal concentric cylinders has been studied by many researchers. This enclosure geometry has application in solar collector receiver design, thermal storage systems, and pressurized-gas high-voltage electric transmission cables. A large number of reports of experimental investigations and of numerical analysis of the constant property-Boussinesq approximation problem are available in the literature. However, the question of the effect of variable transport properties on the heat transfer has not been totally answered, especially for cases of large values of the temperature difference ratio $(T'_H - T'_C)/T'_C$. Also, the range of validity of the Boussinesq approximation has not been conclusively established. It is the purpose of this paper to answer these two questions by presenting the results of a numerical analysis of the variable properties (density and transport properties) problem and comparing these results with data currently available in the literature.

Crawford and Lemlich [1] were the first to numerically solve the governing equations of motion and energy in the cylindrical annulus by invoking the Boussinesq approximation and using a finite difference Gauss-Seidel procedure. They showed the effect of diameter ratio on the heat transfer results. Powe et al. [2] used a stepwise Gauss-Siedel numerical technique and investigated the transition to unsteady flow for a small diameter ratio. They predicted the transition Rayleigh number for a wide range of diameter ratios and a Prandtl number of 0.71 by checking for counterrotating eddies. Mack and Bishop [3] analytically solved the equations for low Rayleigh numbers by using the first three terms in a power series of Rayleigh number based on inner radius.

The successive overrelaxation method was used by Kuehn and Goldstein [4, 5] who obtained heat transfer results up to a Rayleigh number of 10^5. Upwind differencing was used in their numerical scheme at high Rayleigh numbers. Prandtl number and diameter ratio effects were investigated at specified Rayleigh numbers. Kuehn and Goldstein [6] also presented a correlating equation for the equivalent conductivity which improved upon previous published correlations that were based upon a double boundary layer concept.

The following methods have been used by previous investigators to solve the constant properties problem numerically: an alternating direction-implicit (ADI) scheme by Charrier-Mojtabi et al. [7], a modified Stone's strongly implicit method by Projahn et al. [8], an SOR method by Cho et al. [9], and an SOR method using Gosman's model for both laminar and turbulent flow by Farouk and Guceri [10]. All of these researchers used the Boussinesq approximation-constant properties assumption to obtain results which compared well with the experiments reported in [4]. The temperature difference ratio $\theta_o = (T'_H - T'_C)/T'_C$ used in all of the abovementioned papers was smaller than 0.1, so that heat transfer results were not affected by the constant property assumption.

The importance of the variable property effect on the heat transfer for high temperature difference ratios was first shown by Zhong et al. [11] for the square enclosure. They used a semi-implicit scheme based on primitive variables and staggered cells for the velocity components to solve the flow problem. They established the range of validity of the Boussinesq approximation and also analyzed the reference temperature issue. Gray and Giorgini [12] presented an analysis technique for establishing in a systematic manner the conditions for which the governing equations of continuity, momentum, and energy reduce to the Boussinesq equations and applied the technique to the Rayleigh-Benard problem for water and air at room temperature and atmospheric pressure.

The only studies of the variable property problem in the horizontal cylindrical annulus were by Hessami et al. [13] and Hessami et al. [14]. They used a hybrid differencing technique which is a baseline SOR method that introduces upwind differencing when the coefficients in the SOR scheme become negative at regions of high velocity. Their solution procedure included both air and glycerine, but the results were presented for a large diameter ratio of 11.4 in [13]; in [14] results were presented at only a single value of Rayleigh number and diameter ratio for air for comparison to Kuehn and Goldstein [4].

This paper presents numerical results for the steady natural convection flow of gases between horizontal isothermal concentric cylinders where the gas properties are allowed to vary.

[1] Presently at CARRE, Inc, Seneca, SC.

Contributed by the Heat Transfer Division and presented in the Technical Session on Natural Convection at the 23rd National Heat Transfer Conference, Denver, CO, August 1985. Manuscript received by the Heat Transfer Division February 7, 1985.

The cylinders are assumed to be long; hence the flow is two dimensional, with the inner cylinder hotter than the outer cylinder. The variable property results are compared with the Boussinesq approximation–constant property results and differences discussed. The question of reference temperature is addressed, and the equivalent thermal conductivities are plotted versus Rayleigh number up to $Ra_L = 1.8 \times 10^5$ and compared with results in the literature.

Problem Formulation

The governing equations for steady laminar flow with no heat generation, negligible viscous dissipation, and negligible variations in the specific heat capacity may be written as follows.

Continuity

$$\nabla' \cdot (\rho' \mathbf{V}') = 0 \tag{1}$$

Momentum

$$\rho'(\mathbf{V}' \cdot \nabla')\mathbf{V}' = -\nabla P' + \mathbf{F}' - \nabla' \times (\mu'(\nabla' \times \mathbf{V}') + \nabla'\left[\frac{4}{3}\mu' \nabla' \cdot \mathbf{V}'\right] - 2(\nabla'\mu')(\nabla' \cdot \mathbf{V}') + 2\nabla'\mu' \times (\nabla' \times \mathbf{V}') + 2(\nabla'\mu' \cdot \nabla')\mathbf{V}' \tag{2}$$

Energy

$$\nabla' \cdot (k' \nabla' T') = -(\mathbf{V}' \cdot \nabla')P' + \rho' C_p'(\mathbf{V}' \cdot \nabla')T' \tag{3}$$

$\mathbf{F}'$ is the body force given by

$$\mathbf{F}' = (-\rho' g' \cos\theta \mathbf{e}_R + \rho' g' \sin\theta \mathbf{e}_\theta) \tag{4}$$

A vector potential can be introduced to satisfy the continuity equation by setting

$$\rho' \mathbf{V}' = \nabla' \times \xi' \tag{5}$$

The flow variables are nondimensionalized using

$$u = \frac{V_R' r_o'}{\alpha_R'}, \quad v = \frac{V_\theta' r_o'}{\alpha_R'}, \quad \eta_R = \beta_R' T_R'$$

$$R = \frac{r'}{r_o'}, \quad \epsilon = \frac{T_H' - T_C'}{T_R'}, \quad \tau = \frac{T' - T_C'}{T_H' - T_C'} \tag{6}$$

where $\alpha_R' = k_R'/\rho_R' C_{p_R}'$ is the thermal diffusivity, r_o' is the outer radius, T_H' is the inner-cylinder temperature, T_C' is the outer-cylinder temperature, and T_R' is the reference temperature. The dimensional properties ρ', k', μ, and C_p' are nondimensionalized by the corresponding properties evaluated at the reference temperature (ρ_R', k_R', μ_R', and C_{p_R}'). Finally, the nondimensional quantities appear as ρ, k, μ, and C_p. To retain the Rayleigh number in the equation, the coefficient of the body force term $g' r_o'^3/\alpha_R'^2$ is written as $\mathrm{Ra\ Pr}/\epsilon\ \eta_R$, following Leonardi and Reizes [16]. The reference temperature is an artificial concept, but the Rayleigh number defined using reference properties evolves naturally from the nondimensionalization.

After introducing vorticity and nondimensionalizing the equations, the final set of equations to be solved is

$$\frac{1}{R^2}\frac{\partial^2 \xi}{\partial \theta^2} + \frac{\partial^2 \xi}{\partial R^2} + \frac{1}{R}\frac{\partial \xi}{\partial R} = -\rho\zeta + \frac{1}{\rho}\left\{\frac{1}{R^2}\frac{\partial \xi}{\partial \theta}\frac{\partial \rho}{\partial \theta} + \frac{\partial \xi}{\partial R}\frac{\partial \rho}{\partial R}\right\} \tag{7}$$

$$\rho u \frac{\partial \zeta}{\partial R} + \frac{\rho v}{R}\frac{\partial \zeta}{\partial \theta} = \mathrm{Pr}\left\{\frac{1}{R^2}\frac{\partial^2(\mu\zeta)}{\partial \theta^2} + \frac{\partial^2(\mu\zeta)}{\partial R^2} + \frac{1}{R}\frac{\partial}{\partial R}(\mu\zeta)\right\} + \left(\frac{\mathrm{Ra \cdot Pr}}{\epsilon \eta_R}\right)\left(\frac{\partial \rho}{\partial R}\sin\theta + \frac{1}{R}\frac{\partial \rho}{\partial \theta}\cos\theta\right) - \frac{1}{R}\left[\frac{\partial \rho}{\partial R}\left(u\frac{\partial u}{\partial \theta} + v\frac{\partial v}{\partial \theta}\right) - \frac{\partial \rho}{\partial \theta}\left(u\frac{\partial u}{\partial R} + v\frac{\partial v}{\partial R}\right)\right]$$

Nomenclature

C_p = specific heat = C_p'/C_{p_R}'
D_i' = inner cylinder diameter
D_o' = outer cylinder diameter
$\mathbf{e}_R$ = unit vector in the radial direction
$\mathbf{e}_\theta$ = unit vector in the tangential direction
$\mathbf{F}'$ = body force
g' = acceleration due to gravity
$\bar{h}'$ = average convection coefficient
k = thermal conductivity of the fluid = k'/k_R'
k_{eff}' = effective thermal conductivity = $q' \ln(r_o'/r_i')/2\pi l'(T_H' - T_C')$
k_{eq} = equivalent thermal conductivity = k_{eff}'/k_R'
l' = annulus length
L' = gap width = $r_o' - r_i'$
Nu_{D_i} = Nusselt number based on inner cylinder diameter = $\bar{h}' D_i'/k' = 2\,[\ln r_o'/r_i']^{-1} k_{eq}$
P = pressure = P'/P_R'
Pr = Prandtl number = $\mu_R' C_{p_R}'/k_R'$
q' = convection heat transfer rate
r' = radial coordinate
r_{avg}' = average radius = $(r_i' + r_o')/2$
R = nondimensional radial coordinate = r'/r_o'
Ra_L = Rayleigh number = $\beta_R' g' \rho_R'(T_H' - T_C')L'^3/\alpha_R'\mu_R'$
Ra = Rayleigh number = $\beta_R' g' \rho_R'(T_H' - T_C')r_o'^3/\alpha_R'\mu_R'$
s = Sutherland constant = $1 + 1.47\ T_{bp}'/T_R'$
s_1 = Sutherland constant = $T_c'/T_R' + 1.47\ T_{bp}'/T_R'$
T' = temperature
u = nondimensional radial velocity component = $V_R' r_o'/\alpha_R'$
v = nondimensional tangential velocity component = $V_\theta' r_o'/\alpha_R'$
$\mathbf{V}'$ = velocity vector = $V_r'\mathbf{e}_r + V_\theta'\mathbf{e}_\theta$
V_R' = radial velocity component
V_θ' = tangential velocity component
α = thermal diffusivity = α'/α_R' where $\alpha' = k'/\rho' C_p'$
β = coefficient of volumetric expansion β'/β_R'
γ = r_i'/r_o'
ϵ = nondimensional temperature difference = $(T_H' - T_C')/T_R'$
ζ = vorticity
η_R = nondimensional parameter = $\beta_R' T_R'$
θ = angular coordinate, measured positive clockwise from upper vertical
θ_o = temperature difference ratio = $(T_H' - T_C')/T_C'$
μ = dynamic viscosity = μ'/μ_R'
ξ = compressible vector potential
ρ = density = ρ'/ρ_R'
τ = nondimensional temperature = $T' - T_C'/T_H' - T_C'$
$'$ = dimensional quantity

Subscripts

bp = boiling point
C = outer cylinder (cold) condition
H = inner cylinder (hot) condition
i = inner cylinder surface
o = outer cylinder surface
R = reference quantity evaluated at the reference temperature

$$+2\mathrm{Pr}\left[\frac{\partial^2\mu}{\partial R^2}\left(\frac{1}{R}\frac{\partial u}{\partial\theta}-\frac{v}{R}\right)+\frac{\partial^2\mu}{\partial\theta\partial R}\left(\frac{1}{R^2}\frac{\partial v}{\partial\theta}+\frac{u}{R^2}\right.\right.$$
$$-\frac{1}{R}\frac{\partial u}{\partial R}\Big)-\frac{\partial^2\mu}{\partial\theta^2}\left(\frac{1}{R^2}\frac{\partial v}{\partial R}\right)+\frac{\partial\mu}{\partial R}\left(\frac{1}{R^2}\frac{\partial u}{\partial\theta}\right.$$
$$+\frac{1}{R}\frac{\partial^2 u}{\partial\theta\partial R}+\frac{1}{R^2}\frac{\partial^2 v}{\partial\theta^2}-\frac{1}{R}\frac{\partial v}{\partial R}\Big)-\frac{\partial\mu}{\partial\theta}\left(\frac{1}{R}\frac{\partial^2 u}{\partial R^2}\right.$$
$$\left.\left.+\frac{1}{R^2}\frac{\partial^2 v}{\partial\theta\partial R}\right)\right] \tag{8}$$

$$C_P\left\{\rho u\frac{\partial\tau}{\partial R}+\frac{\rho v}{R}\frac{\partial\tau}{\partial\theta}\right\}=k\left(\frac{1}{R}\frac{\partial\tau}{\partial R}+\frac{\partial^2\tau}{\partial R^2}\right.$$
$$\left.+\frac{1}{R^2}\frac{\partial^2\tau}{\partial\theta^2}\right)+\left(\frac{\partial k}{\partial R}\frac{\partial\tau}{\partial R}\right)+\left(\frac{1}{R^2}\frac{\partial\tau}{\partial\theta}\frac{\partial k}{\partial\theta}\right) \tag{9}$$

For the Boussinesq approximation and constant property assumption, ρ, μ, k, and C_p are constant in all the terms in equations (7)–(9), except in the second term on the right-hand side of equation (8), where density is written as

$$\rho=\rho'/\rho'_R=\{1-\beta'_R(T'-T'_R)\} \tag{10}$$

The density is obtained from the ideal gas law as follows

$$\rho=\frac{P}{\epsilon\tau+\left(\frac{T'_C}{T'_R}\right)} \tag{11}$$

The transport properties can be evaluated using the Sutherland formula [15] which relates both the dynamic viscosity and the thermal conductivity as functions of temperature in the range of temperatures considered as follows

$$k=\mu=\left(\frac{s}{\epsilon\tau+s_1}\right)\left(\epsilon\tau+\frac{T'_C}{T'_R}\right)^{3/2} \tag{12}$$

where

$$s=1+1.47\frac{T'_{bp}}{T'_R} \tag{13}$$

and

$$s_1=\frac{T'_C}{T'_R}+1.47\frac{T'_{bp}}{T'_R} \tag{14}$$

and T'_{bp} is the boiling point temperature of the gas. The range of temperature used for helium in obtaining the results was between 150 K and 600 K for which the Sutherland's formulas are valid. Based on the results presented in [16], the pressure variation in the annulus is assumed to be negligibly small. The boundary conditions can be stated as

$$\begin{aligned}
&R=\gamma \quad \tau=1 \quad \xi=0 \quad \zeta=-\frac{1}{\rho}\frac{\partial^2\xi}{\partial R^2}\\
&R=1 \quad \tau=0 \quad \xi=0 \quad \zeta=-\frac{1}{\rho}\frac{\partial^2\xi}{\partial R^2}\\
&\theta=0,\ \pi \quad \frac{\partial\tau}{\partial\theta}=0 \quad \xi=0 \quad \zeta=0
\end{aligned} \tag{15}$$

The overall equivalent thermal conductivity k_{eq} can be evaluated at the inner and outer cylinder surfaces from the relations

$$\begin{aligned}
k_{eq_i}&=\frac{\gamma}{\pi}\ln\gamma\int_0^\pi k_i\frac{\partial\tau}{\partial R}\bigg|_i d\theta\\
k_{eq_o}&=\frac{1}{\pi}\ln\gamma\int_0^\pi k_o\frac{\partial\tau}{\partial R}\bigg|_o d\theta
\end{aligned} \tag{16}$$

where the subscripts i and o denote the inner and the outer cylinder surfaces, respectively. The resulting k_{eq} is found to be a function of Rayleigh number Ra_L, a temperature difference ratio θ_o, and the radius ratio r'_o/r'_i.

Numerical Procedure

The vorticity transport equation and the energy equation were solved by the false transient/ADI method, and the vector potential equation was solved by the successive overrelaxation scheme. The advantage of the false transient formulation is that the stability can be controlled by the proper choice of false transient parameters that appear in the pseudo-time-dependent terms in the equation. A relaxation parameter of 1.55 was chosen in the SOR method by running computational experiments. The details of the numerical procedures are not presented here and they are available in [17]. The choice of the fluid, the inner- and outer-cylinder temperatures, their diameters, and the pressure in the annulus uniquely determine the relevant parameters such as Prandtl number, Rayleigh number, the temperature difference ratio, and the diameter ratio. The following criteria were used to check convergence at each nodal point

$$|\phi_{\mathrm{new}}-\phi_{\mathrm{old}}|/|\phi_{\mathrm{new}}|_{\max}\le\Gamma \tag{17}$$

where ϕ was the primary variable being tested, the subscripts old and new were the previous and present iterative values, respectively, and Γ was a prespecified constant. This constant was usually set to 10^{-3} for the semi-uniform mesh and 10^{-4} for the uniform mesh. A uniform $r\times\theta$ grid of 18×31 was chosen for low Rayleigh number conditions, and a semi-uniform grid of 18×31, closely spaced near the walls and the vertical boundaries, was chosen for more severe flow conditions that occurred at high Rayleigh numbers. Central difference approximations were applied to derivatives. The spatial variations for R in the semi-uniform grid range from $L/48$ at the walls to $L/12$ in the core region. For θ, the variations ranged from 1 deg at the symmetry boundaries to 9 deg in the core. For $\mathrm{Ra}_L\lesssim 3\times 10^4$ a uniform grid was used and for $\mathrm{Ra}_L\gtrsim 3\times 10^4$ a semi-uniform grid was used. The number of iterations needed for convergence was dependent upon the choice of starting condition; however, on the average, the number ranged from 100 steps for $\mathrm{Ra}_L<2\times 10^4$ to 400 steps for $\mathrm{Ra}_L>5\times 10^4$.

In order to satisfy conservation of thermal energy, the average equivalent thermal conductivities on the inner- and outer-cylinder surfaces must be equal. This requirement was also used as a monitor of the validity of the numerical scheme. For all the results presented in this paper, k_{eq} on the two cylinder surfaces differed by less than 2 percent, with a majority of the results having discrepancies of less than 1 percent. For a few results, produced at high Rayleigh numbers (mainly for comparison purposes), a discrepancy of up to 3 percent was encountered.

Validation studies of the numerical solution technique were performed by generating solutions that could be directly compared with previously published results. At very low Rayleigh numbers, the heat transfer solution was that for conduction. A constant property solution by both Crawford and Lemlich [1] and Kuehn and Goldstein [4] at $\mathrm{Ra}_L=8.925\times 10^3$, $\mathrm{Pr}=0.714$, and $L'/D'_i=0.5$ was obtained using an 18×31 semi-uniform grid. The agreement in equivalent thermal conductivity was good, with a value of 1.82 compared with 1.765 for Crawford and Lemlich [1] and 1.792 for Kuehn and Goldstein [4]. Additional comparisons to check the validity of the numerical scheme are presented in the Results section. The effect of decreasing grid size also was investigated and grids smaller than those used were found to give the same results.

Discussion of Results

There were three primary objectives of this study. The first

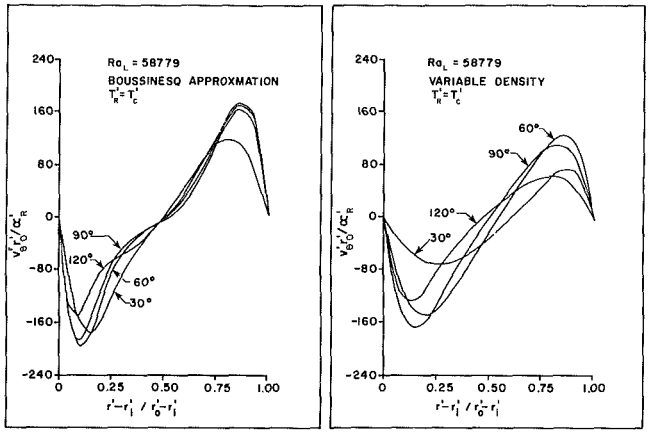

Fig. 1 Nondimensional tangential velocity profiles for Pr = 0.7, $D'_o/D'_i = 2.28$, and $\theta_o = 2.0$ for the case of (a) Boussinesq approximation and constant properties, (b) variable density. The angular positions are marked on the profiles.

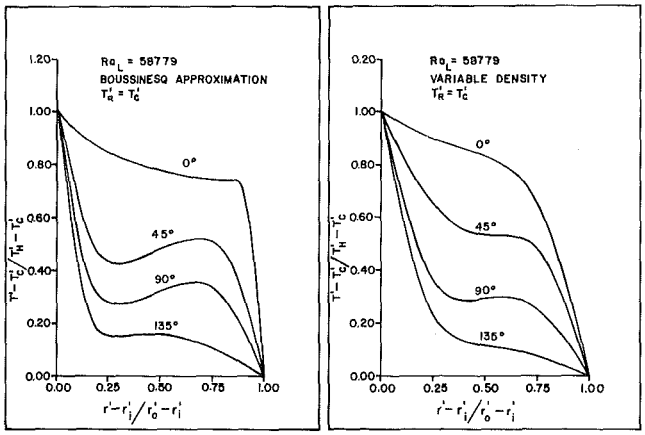

Fig. 2 Nondimensional temperature profiles for Pr = 0.7, $D'_o/D'_i = 2.28$, and $\theta_o = 2.0$ for the case of (a) Boussinesq approximation and constant properties, (b) variable density. The angular positions are marked on the profile.

objective was to determine the range of validity of the Boussinesq approximation for natural convection in horizontal annular enclosures. This objective was accomplished by computing heat transfer rates, temperature profiles, and velocity profiles for both the Boussinesq approximation case with constant transport properties and the variable density case with constant transport properties and then comparing the results. The second objective was to determine the combined effects of variable density, variable viscosity, and variable thermal conductivity. This objective was accomplished by computing heat transfer rates, temperature profiles, and velocity profiles under the variable property condition and then comparing these results with the Boussinesq approximation-constant transport property results. The third objective was to compare the results for the total variable property problem with experimental results available in the literature. The discussion to follow will address these three objectives in the order given.

Range of Validity of the Boussinesq Approximation

Zhong et al. [11], in their paper on variable property effects in laminar natural convection in a square enclosure, examined the driving force under perfect gas and Boussinesq conditions and concluded that the Boussinesq approximation should be adequate for $\theta_o < 0.10$. They approximated the driving force as $(\rho'_C - \rho'_H)/\rho'_C$ and confirmed by numerical finite difference calculations that the Boussinesq approximation is indeed valid for $\theta_o < 0.10$ and can be used up to $\theta_o = 0.20$ to predict heat transfer rates with reasonable accuracy. Since the driving force in the annulus problem can be approximated by $(\rho'_C - \rho'_H)/\rho'_C$, the same conclusion can be made with regard to the maximum θ_o for which the Boussinesq approximation is expected to be valid, i.e., $\theta_o < 0.10$.

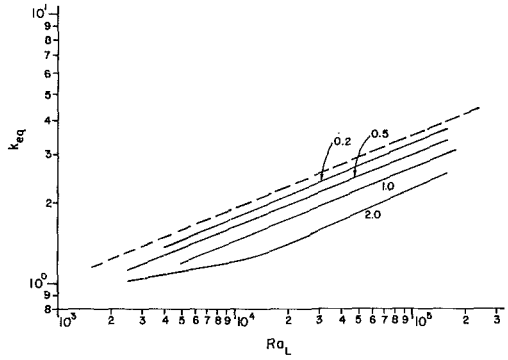

Fig. 3 Mean equivalent thermal conductivity as a function of Ra_L for Pr = 0.7 and $D'_o/D'_i = 2.28$. - - - - -, Boussinesq approximation and constant properties; ——, variable density case for different temperature difference ratios θ_o. θ_o's are marked on the profiles.

Figures 1(*a*) and 1(*b*) show the computed tangential velocities at four angular positions for the Boussinesq approximation and variable density cases, respectively. In each case $\theta_o = 2.0$, $Ra_L \cong 5.9 \times 10^4$ and $D'_o/D'_i = 2.28$. As can be easily seen, the tangential velocities in the regions immediately adjacent to the inner and outer surfaces are overpredicted by the Boussinesq approximation. Higher velocities in these regions should give rise to steeper temperature gradients, and thus higher heat transfer rates are obtained for the Boussinesq approximation than for the variable density case. Figures 2(*a*) and 2(*b*) show the corresponding temperature profiles and confirm that the gradients are in fact steeper for the Boussinesq approximation.

Figure 3 shows a plot of equivalent thermal conductivity, $k_{eq} = (k_{eq_i} + k_{eq_o})/2$, versus Ra_L for θ_o values of 0.2, 0.5, 1.0, and 2.0. (The reference temperature used was the outer-cylinder temperature T'_C.) The Boussinesq approximation clearly gives heat transfer results which are higher than the variable density results with the difference becoming significant as θ_o exceeds 0.20. For $\theta_o \leq 0.20$ and $Ra_L \leq 2 \times 10^5$, the Boussinesq approximation yields reasonably accurate results, with a maximum error of approximately 5 percent at $\theta_o = 0.2$.

Combined Effects of Variable Density, Variable Viscosity, and Variable Thermal Conductivity

Before proceeding to the presentation of the results for the total variable property problem, it is necessary to first discuss the question of reference temperature. For the cylindrical annulus, the hot temperature, the cold temperature, or the average of these two temperatures are the obvious choices. However, it is clear that none of these three could be expected to satisfactorily collapse all of the heat transfer results to a single curve for a given diameter ratio. Previous experimental investigators have used the average of the hot and cold temperatures to correlate their experimental data. This has yielded reasonable results in that single equations for a given diameter ratio have been obtained which give results valid within the accuracy of the experiments. Since the average of these two temperatures gives equal weight to the hot and to the cold temperature, it would be reasonable to use an arithmetic mean reference temperature only for small diameter ratios. This is due to the fact that as the diameter ratio increases, a greater volume of the fluid in the annulus is closer to the cold temperature than to the hot temperature. It seems then that it would be more appropriate to use a "volume-weighted" mean temperature defined as

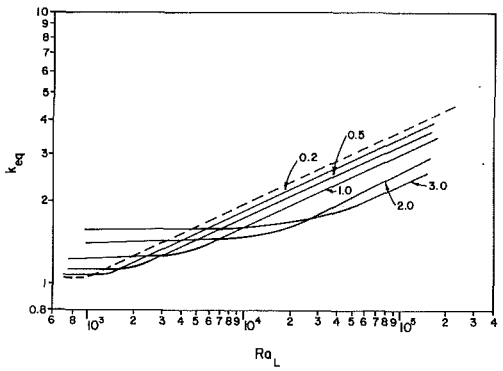

Fig. 4(a) Heat transfer results for the full variable property case for Pr = 0.7 and $D_o'/D_i' = 2.28$. T_C' is the reference temperature. - - - - -, Boussinesq approximation and constant properties; ———, full variable property case for different θ_o. θ_o's are marked on the profiles.

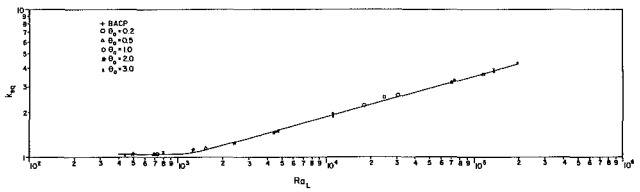

Fig. 4(b) Heat transfer results for the full variable property case for Pr = 0.7 and $D_o'/D_i' = 2.28$. T_R' given by equation (16) is the reference temperature; +, Boussinesq approximation and constant properties; □, $\theta_o = 0.2$; Δ, $\theta_o = 0.5$; , $\theta_o = 1.0$; *, $\theta_o = 2.0$; ×, $\theta_o = 3.0$.

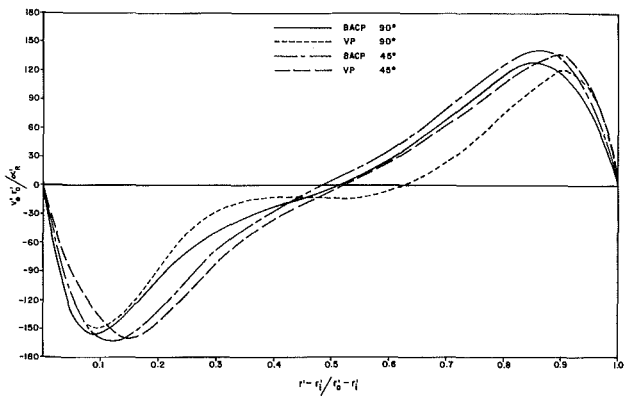

Fig. 5 Nondimensional tangential velocity profiles for $Ra_L = 50{,}000$, Pr = 0.7, $D_o'/D_i' = 2.6$, comparing Boussinesq approximation ($\theta_o = 0.09$) and variable property ($\theta_o = 2.0$) cases. Volume-weighted reference temperature was used.

$$T_R' = \left(\frac{r_{avg}'^2 - r_i'^2}{r_o'^2 - r_i'^2}\right) T_H' + \left(\frac{r_o'^2 - r_{avg}'^2}{r_o'^2 - r_i'^2}\right) T_C' \qquad (18)$$

This reference temperature is a function of the diameter ratio and increases the weight given to the cold temperature as the diameter ratio increases. In the limit as the diameter ratio goes to infinity, the reference temperature will become $T_R' = 0.25T_H' + 0.75T_C'$. It is interesting to note that this is the reference temperature proposed by Zhong et al. [11] for the square cavity problem.

Figure 4(*a*) shows the equivalent thermal conductivity versus Rayleigh number for a diameter ratio of 2.28 and values of the temperature ratio from 0.2 to 3 for the case where the reference temperature is fixed at the cold temperature. If the volume-weighted mean temperature is used as the reference temperature, the single curve shown in Fig. 4(*b*) results. It is apparent that the volume-weighted mean temperature is the appropriate reference temperature to use to account for property variations over a wide range of temperature ratios, 0.2 to 3.0. Results were also obtained for both the hot temperature and the arithmetic mean temperature as reference temperatures. The reference temperature of T_H' was not effective in reducing the data to a single curve. Although the arithmetic mean reference temperature collapsed the data reasonably well for diameter ratios of less than 2.6, the scatter became prominent for higher diameter ratios. These results are not presented in this paper.

Before determining the combined effects of the variable properties, each of the transport properties was varied separately while invoking the Boussinesq approximation, and the equivalent thermal conductivity calculated for θ_o values of 0.20, 0.50, 1.0, and 2.0. Having previously determined the variable density effect on the equivalent thermal conductivity, each of the individual property variation effects could be evaluated and compared to determine what the relative contributions of each should be when all were allowed to vary simultaneously. For gases, as the temperature is increased, the thermal conductivity and viscosity both increase in magnitude. Therefore, as θ_o is increased, variable viscosity should reduce k_{eq} and variable thermal conductivity should increase k_{eq} over the values obtained when these properties are considered constant. The computational results are not presented in this paper; however, they showed that variable viscosity reduces k_{eq} for all values of θ_o, by a maximum of approximately 8 percent at $\theta_o = 2.0$; variable thermal conductivity increases k_{eq} for all values of θ_o, by a maximum of approximately 20 percent at $\theta_o = 2.0$; and variable density reduces k_{eq} for all values of θ_o, by a maximum of approximately 45 percent at $\theta_o = 2.0$. The net result when all three properties are allowed to vary simultaneously should be a decrease in k_{eq} for all values of θ_o and Ra_L. The density plays by far the most important role; however, this is not surprising in that it appears in all of the governing equations, while the thermal conductivity appears only in the energy equation. Variable viscosity was not expected to be of great influence on k_{eq} because of the low velocities encountered in laminar natural convection; however, at high Rayleigh numbers, velocity profiles were affected by variable viscosity.

Figure 5 shows the tangential velocity profiles at two angular positions (45 and 90 deg) for the Boussinesq approximation-constant property (BACP) case and for the variable property (VP) case at $r_o'/r_i' = 2.6$, $\theta_o = 2.0$, and $Ra_L = 50{,}000$. For clarity, only two angular positions are shown. In the upflow region immediately adjacent to the hot inner-cylinder surface, the BACP assumption overpredicts the tangential velocity for these two angular positions. In the remainder of the upflow region, $0.1 < (r' - r_i')/(r_o' - r_i') < 0.5$, the trend seems to be opposite in character, with the BACP assumption overpredicting the tangential velocities at 90 deg and underpredicting for the 45 deg case. It is also seen that at 90 deg the zero-crossing of the tangential velocity profile is extended to $(r' - r_i')/(r_i') = 0.625$, showing a remarkably flat velocity profile for the variable property case. This means that at 90 deg the effect of variable properties is to create a relatively large low-velocity upflow region; however, there is no such dramatic difference in the 45 deg case. In the downflow region, at both angles, the BACP overpredicts tangential velocities by a significant amount, particularly in the case of 90 deg in the region $0.6 < (r' - r_i')/(r_o' - r_i') < 0.85$. Tangential velocities are slightly lower for the BACP at both angles close to the outer cylinder. Tangential velocities were also computed for other angular positions and similar trends were observed. Figure 6 shows temperature profiles under the same annulus operating conditions for the angular positions 0, 45, 90, and 135 deg. As expected, the BACP assumption underpredicts the temperature in the region adjacent to the inner cylinder, overpredicts the temperature in the core region $0.25 < (r' - r_i')/(r_o' - r_i') < 0.75$, and underpredicts the temperature in the region adjacent to the outer cylinder. The overall effect of the BACP assumption is that the tangential

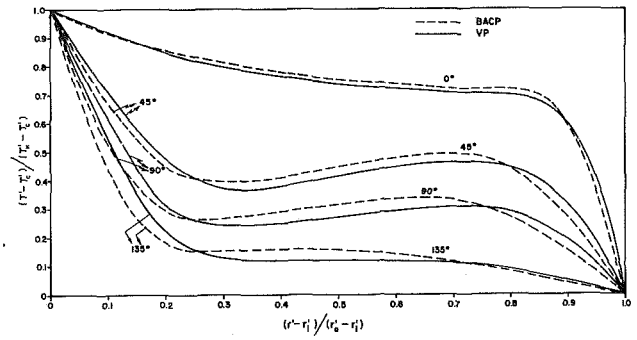

Fig. 6 Nondimensional temperature profiles for $Ra_L = 50{,}000$, $Pr = 0.7$, $D_o'/D_i' = 2.6$, - - - - -, Boussinesq approximation and constant properties ($\theta_o = 0.09$); —, full variable property case ($\theta_o = 2.0$). Angular positions are given on the profiles. Volume-weighted reference temperature was used.

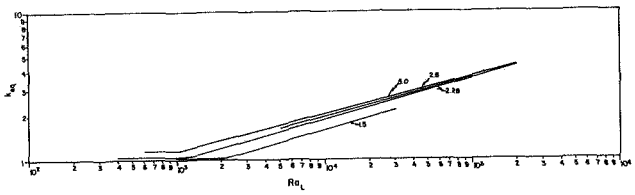

Fig. 7 Mean equivalent thermal conductivity as a function of Ra_L for $Pr = 0.7$ for different diameter ratios. Diameter ratios are indicated on the profiles. Volume-weighted reference temperature was used.

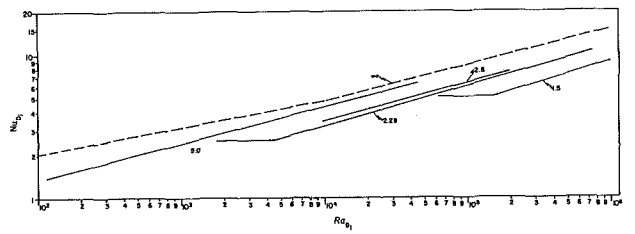

Fig. 8 Mean Nusselt number as a function of Ra_{D_i} for various diameter ratios compared with a single horizonal cylinder. Diameter ratios are indicated on the profiles. Volume-weighted reference temperature was used. Single cylinder heat transfer correlation is given by Morgan [18] and is indicated by $D_o'/D_i' = \infty$.

velocities are higher close to the inner cylinder surface which increases the temperature gradient and lower near the outer cylinder surface which decreases the temperature gradient. Numerous tangential velocity and temperature profiles were computed for diameter ratios of 1.5, 2.28, 2.6, and 5.0, temperature ratios of 0.2, 0.5, 1.0, 2.0, and 3.0, and Rayleigh numbers based on gap width up to 1.8×10^5. In each case, the trends discussed above were observed.

An example of the heat transfer results for a diameter ratio of 2.28 is shown in Figs. 4(*a*) and 4(*b*), which were presented earlier in the paper when the question of reference temperature was discussed. The results shown in these figures are consistent with what is expected based on the temperature profiles; the Boussinesq approximation–constant property assumption overpredicts the heat transfer rate for all values of θ_o. Figure 7 shows curves of k_{eq} for diameter ratios of 1.5, 2.28, 2.6, and 5.0, where for each diameter ratio the temperature ratio was varied from 0.2 to 3.0. These curves were obtained by using the volume-weighted mean temperature as the reference temperature in all calculations. Since the curves beyond the pseudo-conduction region are straight lines when plotted on log–log coordinates, k_{eq} for each diameter ratio may be represented by an equation of the form $k_{eq} = C\mathrm{Ra}_L^n$. The values of C and n are dependent on the diameter ratio; however, it is clear that when the diameter ratio exceeds approximately 2.0 and $\mathrm{Ra}_L > 10^4$, the dependence is small.

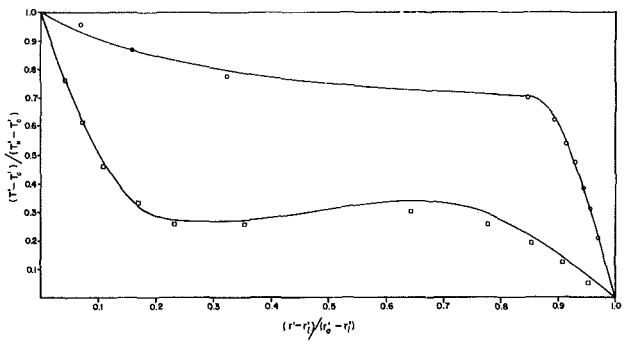

Fig. 9(a) Comparison of nondimensional temperature profile with the experimental values of Kuehn and Goldstein [4] for $Ra_L = 50{,}000$, $D_o'/D_i' = 2.6$, $T_H' \approx 322$ K, and $T_C' \approx 295$ K, —— present numerical calculations; ⊙, □, experimental values [4]

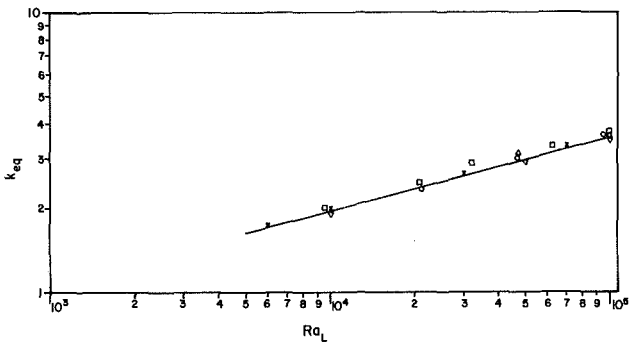

Fig. 9(*b*) Equivalent thermal conductivity k_{eq} versus Rayleigh number Ra_L for $D_o'/D_i' = 2.6$ and $Pr = 0.7$: solid line represents present numerical results; ×, Kuehn and Goldstein's [4] numerical points; ○, Kuehn and Goldstein's [5] experimental points; △, Hessami et al. [14] numerical point; and ▽, Bishop's [19] corresponding equation

As the diameter ratio is increased, the heat transfer approaches that for a horizontal cylinder in an infinite atmosphere. Figure 8 shows Nu_{D_i} plotted versus Ra_{D_i} for various values of D_o'/D_i'. For comparison, the horizontal cylinder equation recommended by Morgan [18] is plotted and is indicated by $D_o'/D_i' = \infty$. In the convection region for the diameter ratios shown the heat transfer is less than for the horizontal cylinder. For $\mathrm{Ra}_{D_i} = 10^4$, when a diameter ratio of 5 is reached, the heat transfer is within 9 percent of that for a horizontal cylinder; and, at a diameter ratio of 10, there is no appreciable difference in the heat transfer at $\mathrm{Ra}_{D_i} > 10^3$. It appears from these results that for gases in the annulus (unlike high Prandtl number fluids) the influence of the outer-cylinder boundary on the heat transfer coefficient in the convection region is negligibly small at a diameter ratio of 10. Kuehn and Goldstein [6] reported that for $Pr = 100$ and $\mathrm{Ra}_{D_i} = 10^7$ the diameter ratio had to exceed 360 to obtain heat transfer coefficients within 5 percent of those for a free cylinder. As found by Kuehn and Goldstein [6] for a Prandtl number of 100, the annulus results for gases show that the free cylinder heat transfer coefficients are approached monotonically as the diameter ratio is increased.

Comparisons With Published Results

The numerical results obtained for the variable property problem have been compared with both experimental and numerical results currently in the literature. The experimental temperature profile data available in the literature are from interferometer studies and are restricted to one diameter ratio and values of the temperature ratio $\theta_o = (T_H' - T_C')/T_C'$ where variable property effects are shown to be negligibly small. The available heat transfer data includes both numerical and experimental results.

Figure 9(*a*) shows computed temperature profiles and the

temperature data of Kuehn and Goldstein [4] for $\theta = 0$ and 90 deg, $Ra_L = 4.7 \times 10^4$, and a diameter ratio of 2.6. In calculating the Rayleigh number for use in the numerical solution, the values of gap thickness, temperature difference, pressure, and temperature ratio were made identical to those used by [4]. The agreement between the computed profiles and the experimentally obtained profiles is good. The Boussinesq approximation–constant property solution would also show the same good agreement for this case since the temperature difference ratio is equal to 0.09, a value for which this assumption is valid.

The solid line in Fig. 9(*b*) represents the variable property solution for k_{eq} for $5 \times 10^3 \leq Ra_L \leq 10^5$ and a diameter ratio of 2.6. The various points shown represent numerical and experimental results of previous investigators. The Boussinesq approximation–constant property solution of Kuehn and Goldstein [4] and the variable property solution of this study give nearly identical results, although their solution gives consistently slightly higher values of k_{eq} for all Rayleigh numbers. These results also agree well with Kuehn and Goldstein's [4, 5] experimental results; however, the agreement is better for their data obtained by interferometry. The only datum currently available in the literature for this geometry with variable gas properties is one point given by Hessami et al. [14]. This point gives a k_{eq} value of 3.11 for $Ra_L = 4.7 \times 10^4$ as compared to 2.95 for the present variable property solution and 3.00 for Kuehn and Goldstein's [4] experimental result and constant properties numerical solution. Kuehn and Goldstein's experimental results given [5] are consistently higher (2–5 percent) than the variable property solution; however, this could be the result of underestimating the heat losses from their apparatus. The equation given by Bishop [19], which correlates the experimental data (obtained by interferometry) of Grigull and Hauf [20], gives results which are only slightly lower than this solution. The numerical results of Cho et al. [9] and Farouk and Guceri [10] showed good agreement with Kuehn and Goldstein's solution and hence they are not reproduced in this paper.

Conclusion

The problem of variable property natural convection of gases between horizontal, isothermal concentric cylinders was examined by numerical analysis for a range of diameter ratios, Rayleigh numbers, and temperature ratios. The following major conclusions can be made:

1 As was found for the square enclosure in [11], the Boussinesq approximation is valid for $\theta_o < 0.1$ and can be used up to $\theta_o = 0.2$ to predict the heat transfer rates with reasonable accuracy.

2 The Boussinesq approximation–constant property assumption overpredicts the tangential velocity and the temperature gradient near the hot inner cylinder while underpredicting both close to the cold outer cylinder.

3 The full variable property heat transfer results can be correlated over the entire range of Rayleigh numbers and temperature ratios studied by the use of a "volume-weighted" mean reference temperature.

4 As was found for the square enclosure in [11], for all values of θ_o the transition region between conduction-dominated and convection-dominated heat transfer is very limited in extent.

5 In the convection-dominated region k_{eq} can be represented by an equation of the form $k_{eq} = CRa_L^n$. The values of C and n are dependent on the diameter ratio; however, this dependence is small when the diameter ratio exceeds 2.0 and $Ra_L > 10^4$.

6 The heat transfer results show that for gases in the annulus the influence of the outer-cylinder boundary on the heat transfer coefficient in the convection region is negligibly small at a diameter ratio of 10. Free cylinder heat transfer coefficients are approached monotonically as the diameter ratio is increased.

Acknowledgments

The authors wish to acknowledge the National Science Foundation for support under Grant No. MEA-8403467 and Clemson University for computer time.

References

1 Crawford, L., and Lemlich, R., "Natural Convection in Horizontal Concentric Cylindrical Annuli," *I.E.C. Fund.*, Vol. 1, 1962, pp. 260–264.

2 Powe, R. E., Carley, C. T., and Carruth, S. L., "A Numerical Solution of Natural Convection in Cylindrical Annuli," ASME JOURNAL OF HEAT TRANSFER, Vol. 92, 1971, pp. 210–220.

3 Mack, L. R., and Bishop, E. H., "Natural Convection Between Horizontal Concentric Cylinders," *Quart. J. of Mech. Appl. Math.*, Vol. 21, Part 2, 1968, pp. 223–241.

4 Kuehn, T. H., and Goldstein, R. J., "An Experimental and Theoretical Study of Natural Convection in the Annulus Between Horizontal Concentric Cylinders," *J. Fluid Mech.*, Vol. 74, 1976, pp. 695–719.

5 Kuehn, T. H., and Goldstein, R. J., "A Parametric Study of Prandtl Number and Diameter Ratio Effects on Natural Convection Heat Transfer in Horizontal Cylindrical Annuli," ASME JOURNAL OF HEAT TRANSFER, Vol. 102, 1980, pp. 768–770.

6 Kuehn, T. H., and Goldstein, R. J., "Correlating Equations for Natural Convection Heat Transfer Between Horizontal Circular Cylinders," *Int. J. Heat Mass Transfer*, Vol. 19, 1976, pp. 1127–1134.

7 Charrier-Mojtabi, M. C., Mojtabi, A., and Caltagirone, J. P., "Numerical Solution of a Flow Due to Natural Convection in Horizontal Cylindrical Annulus," *Numerical Heat Transfer*, Vol. 4, 1979, pp. 171–173.

8 Projahn, V., Reiger, H., and Beer, H., "Numerical Analysis of Laminar Convection Between Concentric and Eccentric Cylinders," Vol. 4, 1981, pp. 131–146.

9 Cho, C. H., Chang, K. S., and Park, K. H., "Numerical Simulation of Natural Convection in Concentric and Eccentric Horizontal Cylindrical Annuli," ASME JOURNAL OF HEAT TRANSFER, Vol. 104, 1982, pp. 624–630.

10 Farouk, B., and Guceri, S. I., "Laminar and Turbulent Natural Convection in the Annulus Between Horizontal Concentric Cylinders," ASME JOURNAL OF HEAT TRANSFER, Vol. 104, 1982, pp. 631–636.

11 Zhong, Z. Y., Yang, K. T., and Lloyd, J. R., "Variable Property Effects in Laminar Natural Convection in A Square Enclosure," ASME JOURNAL OF HEAT TRANSFER, Vol. 107, 1985, pp. 133–138.

12 Gray, D. D., and Giorgini, A., "The Validity of the Boussinesq Approximation for Liquids and Gases," *International Journal of Heat and Mass Transfer*, Vol. 19, 1976, pp. 545–551.

13 Hessami, M. A., Pollard, A., Rowe, R. D., and Ruth, D. W., "A Study of Free Convection Heat Transfer in a Horizontal Annulus with a Large Radii Ratio," *21st National Heat Transfer Conference*, HTD, Vol. 26, *Natural Convection in Enclosures*, 1983, pp. 95–102.

14 Hessami, M. A., Pollard, A., and Rowe, R. D., "Numerical Calculation of Natural Convection Heat Transfer Between Horizontal Concentric Isothermal Cylinders – Effects of the Variation of Fluid Properties," ASME JOURNAL OF HEAT TRANSFER, Vol. 106, 1984, pp. 668–671.

15 Bretsznajder, S., *Prediction of Transport and Other Physical Properties of Fluids*, Pergamon Press, Oxford, 1971.

16 Leonardi, E., and Reizes, J. A., "Convection Flows in Closed Cavities With Variable Fluid Properties," *Numerical Methods in Heat Transfer*, Wiley, Chichester, 1981, pp. 387–412.

17 Mahony, D. N., "A Numerical Investigation of Variable Property Effects on Natural Convection Between Two Horizontal Isothermal Concentric Cylinders," M.S. Thesis, Clemson University, 1984.

18 Morgan, V. T., "The Overall Convective Heat Transfer From Smooth Circular Cylinders," in: *Advances in Heat Transfer*, T. F. Irvine and J. P. Hartnett, eds., Vol. 11, Academic Press, New York, 1975, pp. 199–265.

19 Bishop, E. H., "Discussion 3rd Int. Heat. Transfer Conf.," Chicago, Vol. 6, 1966, pp. 155–156.

20 Grigull, U., and Hauf, W., "Natural Convection in Horizontal Cylindrical Annuli," *Proceedings of the Third International Heat Transfer Conference*, Vol. 2, 1966, pp. 182–195.

M. L. Ng

J. P. Hartnett
Fellow ASME

E. Y. Kwack

University of Illinois at Chicago
Energy Resources Center
Chicago, IL

Natural Convection From Horizontal Wires to Viscoelastic Fluids

Natural convection heat transfer from horizontal wires of three different diameters (0.0254, 0.0508, and 0.0826 cm) to a pool of viscoelastic liquid was studied. Aqueous solutions of Natrosol and Polyox constituted the viscoelastic test fluids. The experimental Nusselt numbers were found to agree with the correlations recommended by Fand and Brucker for Newtonian fluids if the zero shear rate viscosity is used in the Rayleigh and Prandtl numbers.

1 Introduction

The study of free convection from horizontal wires and cylinders to the surrounding fluid has generated considerable interest during the past years. This is understandable, given the wide range of application of such studies, including hot-wire anemometry and rating of electrical conductors. Furthermore, such free convection studies provide essential background information to the study of nucleate boiling from cylindrical geometries.

A number of review articles surveying the research on free convection from horizontal cylinders have appeared in recent years, including the works of Morgan [1], Raithby and Holland [2], and Fand and Brucker [3]. These studies have dealt with Newtonian fluids with major emphasis on air and water as the surrounding fluid, although some experimental results are available for high Prandtl number fluids such as oils [3].

A recent review article by Shenoy and Mashelkar [4] has treated the problem of free convection to non-Newtonian fluids, including both purely viscous and viscoelastic fluids. They predict that the average Nusselt number for free convection from a horizontal cylinder to a viscoelastic fluid increases slightly from the Newtonian value at low values of the Weissenberg number (i.e., at low polymer concentration), reaches a peak, and then decreases dramatically with increasing Weissenberg number. They argue that this conclusion is confirmed by the experimental results of Lyon et al. [5] which revealed a decrease in measured heat transfer with an increase in the polymer concentration.

In contrast, the experimental results of Liang and Acrivos [6] for free convection from an upward-facing flat plate indicate that the Nusselt number increases with increasing elasticity (i.e., Weissenberg number) at a fixed Rayleigh number. This observation is confirmed by a Soviet investigation [7].

Against this background, it was decided to undertake a more detailed study of free convection from a horizontal wire to a well-defined viscoelastic fluid.

2 Experimental Apparatus

The experimental apparatus consists of the heat transfer test set up, the power supply, and measuring system as shown in Fig. 1. In addition, there is an auxiliary system for preparing the aqueous polymer solutions and for carrying out detailed rheological measurements.

(a) Heat Transfer Equipment. The heat transfer studies were carried out with three different diameter platinum wires of 0.0254, 0.0508, and 0.0826 cm, all 15.24 cm in length. Each wire was placed, in turn, horizontally inside a rectangular stainless steel tank equipped with pyrex glass windows on opposing sides (Fig. 1). The tank, which is 10.2 cm wide, 30.5 cm long, and 35.6 cm deep is in turn placed in another tank 30.5 cm × 45.7 cm × 40.6 cm also equipped with glass windows on the same opposite sides. The four glass windows are aligned and a fluorescent lamp is located at the back of the outside tank so that the experiments can be viewed clearly through the windows. The outside tank is filled with a clear transparent oil of high boiling point (Arcopak 70 from the Atlantic Richfield Oil Company, boiling point 274°C) and serves as a constant temperature bath. Four 1000 watt heating rods placed horizontally under the inner tank serve as the heat source for the constant temperature bath. The temperature of the bath is regulated by two 30.5 cm × 30.5 cm heating pads attached to the two windowless sides of the tank which are connected to a manually controlled variac. The temperature of the oil is measured by a mercury thermometer positioned inside the outside tank.

The ends of the platinum wire are soldered to two brass terminals, one of which is screwed onto the support while the other is tightened to the support by a carefully selected stainless steel spring such that the wire is under a constant minimal tension to ensure a straight horizontal heating geometry as its temperature increases. The power lines, which

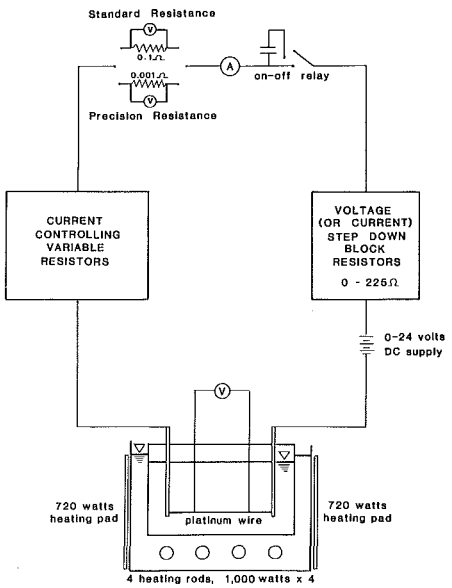

Fig. 1 Experimental setup

Contributed by the Heat Transfer Division for publication in the JOURNAL OF HEAT TRANSFER. Manuscript received by the Heat Transfer Division May 15, 1985. Paper No. 85-HT-43.

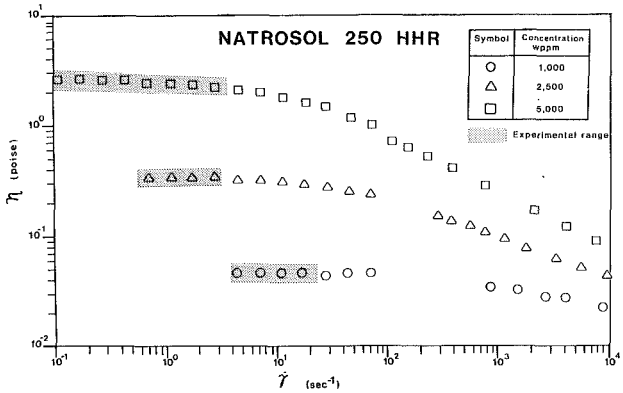

Fig. 2 Steady shear viscosity of Natrosol solutions at room temperature

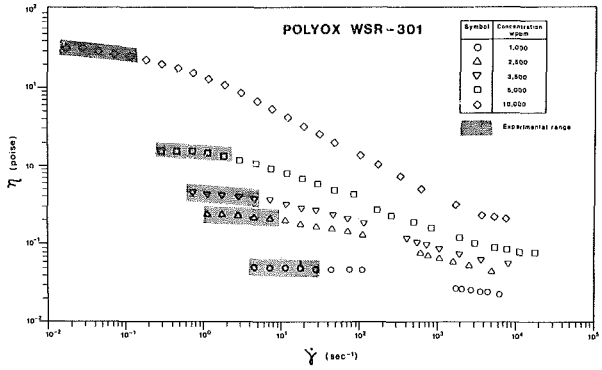

Fig. 3 Steady shear viscosity of Polyox solutions at room temperature

are No. 12 gauge copper wires fitted with teflon tubing, are connected to the end of the brass terminals. To minimize the end effects, the test section is chosen to be the center of the wire. A copper wire, also fitted with teflon tubing, is silver-soldered to each end of the test section and connected to the measuring taps on the top cover of the tank. Because of its function as the support of the electrical terminals, the cover is made of thick delrin plastic which is a good electrical insulator. The cover is lined with an O-ring and is tightened to the tank with 18 screws.

The temperature of the fluid is measured by four copper-constantan thermocouples fitted in 0.3 cm thermowells, which can be raised or lowered to cover a large area in the fluid. The tips of the thermowells are bent 90 deg to minimize conduction errors.

(b) **Power Supply and Measurement System.** The heat source of the test wire is a series of direct current (d-c) rechargeable batteries which are capable of delivering a range of fixed voltages such that heat transfer under different values of heat flux can be studied. Direct current is used here for the purpose of obtaining a steady supply of heat. The heat supplied is further regulated by variable resistors which are compatible with large currents. Block resistors are installed so that the resistance of the platinum wire can be measured accurately by passing very small currents through the wire. A circuit diagram is shown in Fig. 1.

The current is accurately determined from the voltage drop measurement through a standard resistance of 0.1 ohm (Leeds and Northrop Company). This and the voltage drop across the platinum wire are measured simultaneously by two digital multimeters (Hewlett-Packard Company).

(c) **Preparation of Polymer Solutions.** Two kinds of polymer, namely hydroxyethyl cellulose (Natrosol 250 HHR, Hercules Company) and polyethylene oxide (Polyox WSR-301, Union Carbide Company) were selected for the experimental study. Both are high-molecular-weight polymers and it is well established that aqueous solutions of these polymers are viscoelastic. In order to cover a range of elastic behavior several concentrations of each polymer were used.

Since direct current is used in these heat transfer experiments deionized water is used as the solvent to minimize complications which might be created by free ions present in tap water. The deionized cartridges are arranged as recommended by their manufacturer Cole-Parmer Company.

The polymer solutions are prepared in 40 liter drums. In preparing the viscoelastic fluids air bubbles are trapped in the polymer solution, especially the more concentrated ones. This creates complications as the bubbles adhere to the heating wire especially when heat is passing through the wire. A vacuum pump manufactured by the Welch Scientific Company was found to be very efficient in removing the air bubbles in a relatively short time.

(d) **Steady Shear Viscosity Measurements.** The steady shear viscosities of the polymer solutions as a function of shear rate are measured by a Weissenberg rheogoniometer (model R-18 from Sangamon Company), a Brookfield viscometer (model LVT from Brookfield Company), and a capillary viscometer. These instruments were described in detail in [8, 9]. The Weissenberg rheogoniometer and Brookfield viscometer are used to measure the low shear rate viscosity of the polymer solutions. The main advantage of the Brookfield viscometer is that it is capable of measuring the low shear rate viscosity at different temperature levels. The capillary viscometer was used to measure the high shear rate viscosity at different temperature levels.

Nomenclature

A = surface area of the wire, cm^2
C_p = specific heat at constant pressure evaluated at T_f, J/g•K
d = diameter of heated wire, cm
g = acceleration of gravity, cm/s^2
Ge = Gebhart number = $g\beta d/C_p$
h = heat transfer coefficient = $q/A\ (T_W - T_b)$, W/cm^2•K
K = power-law consistency, $dyne\text{-}s^n/cm^2$
k = thermal conductivity of fluid evaluated at T_f, W/cm•K
k_{Pt} = thermal conductivity of platinum wire, W/cm•K
n = power-law index
Nu = Nusselt number = hd/k
Pr = Prandtl number = $\eta_0 C_p/k$
Pr_N = Prandtl number for power-law fluids = $(k/\rho\alpha)(\alpha/d^2)^{n-1}$
q = heat transfer from wire to fluid, W
Ra = Rayleigh number = $\rho g\beta\Delta T d^3/\eta_0\alpha$
Ra_N = Rayleigh number for power-law fluid = $\rho g\beta\Delta T d^{1+2n}/K\alpha^n$
T = absolute temperature, K
T_b = mean fluid temperature, K
T_f = film temperature = $(T_w + T_b)/2$, K
T_m = mean temperature of the wire, K
T_w = surface temperature of wire, K
v = characteristic velocity = $[g\beta\Delta T/d]^{1/2}$, cm/s
Ws = Weissenberg number = $\lambda v/d$
α = thermal diffusivity = $k/\rho C_p$
β = coefficient of thermal expansion, K^{-1}
$\dot{\gamma}$ = shear rate, s^{-1}
λ = Powell-Eyring characteristic time, s
η = steady shear viscosity, poise
η_0 = zero shear rate viscosity, poise
η_∞ = steady shear viscosity at $\dot{\gamma} \to \infty$, poise

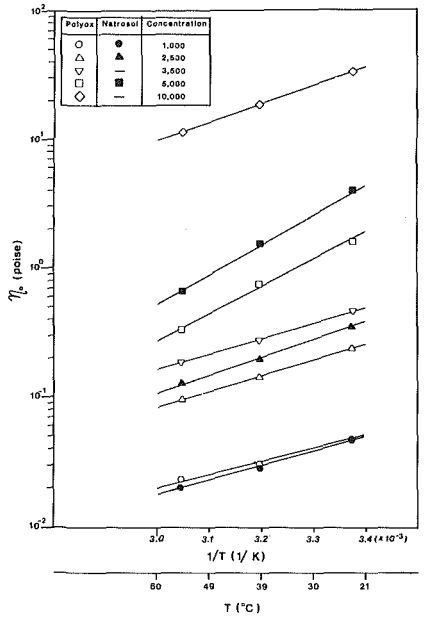

Fig. 4 Temperature dependence of the zero-shear-rate viscosity of the polymer solutions

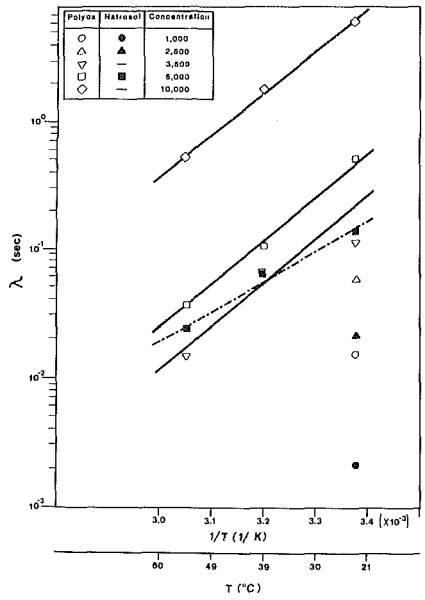

Fig. 5 Temperature dependence of the characteristic time of the polymer solutions

3 Experimental Results

(a) Property Measurements of the Polymer Solutions. The physical properties of the dilute polymer solutions have been shown to be in good agreement with those of pure water [9, 10] except for their rheological properties. The steady shear viscosity as a function of shear rate at room temperature is shown for three different concentrations of Natrosol in Fig. 2 and for five concentrations of Polyox in Fig. 3. For each polymer the viscosity of the solution increases over the whole range of shear rate including the zero shear rate as the concentration of polymer increases.

The steady shear viscosity of each polymer solution was measured at three different temperature levels covering the range of experiments. The temperature dependency was correlated in the way suggested by Christiansen et al. [11]. The results are presented in Fig. 4, which shows the zero shear rate viscosity as a function of $1/T$.

(b) Elasticity of the Polymer Solutions. A measure of the elasticity of the polymer solutions is given by the characteristic time λ. One way of obtaining the characteristic time of the polymer solutions is through the generalized Newtonian models. This is done by curve-fitting the steady shear viscosity data to the model selected. It has been shown that characteristic time derived from the Powell–Eyring model [12] successfully represents the elasticity of the polymer solutions [13]. The Powell–Eyring characteristic time is given by the following equation

$$\eta = \eta_\infty + (\eta_0 - \eta_\infty)\left(\frac{\sinh^{-1}\lambda\dot{\gamma}}{\lambda\dot{\gamma}}\right) \tag{1}$$

The temperature dependency of the characteristic time is assumed to vary with $1/T$. Since the steady shear viscosity is known as a function of temperature for the different polymer concentrations, it is possible to determine the behavior of the characteristic time as a function of $1/T$ as shown in Fig. 5.

(c) Heat Transfer Results. The temperature of the platinum wire is measured by the resistance of the wire. The platinum wire is calibrated by placing the wire inside the rectangular tank where the temperature of the test fluid is controlled by varying the heat input to the surrounding constant temperature bath. The resistance of the platinum wire at specified temperature levels (measured by the calibrated thermocouples) is determined by passing a small current through the wire and the respective voltage drop is recorded. This process is repeated several times. The average value of the resistance of the wire thus calculated is taken as the resistance of the wire at the specified temperature. Five temperature levels are covered in this way and a linear correlation is used to interpolate the temperature of the wire at intermediate temperatures. It is recognized that a platinum wire may be easily contaminated by moisture or by a reducing atmosphere [14]. Such contamination may vary the temperature-dependent resistance of the platinum wire. Therefore recalibration of the platinum wire is performed after each run with water and with the polymer solutions.

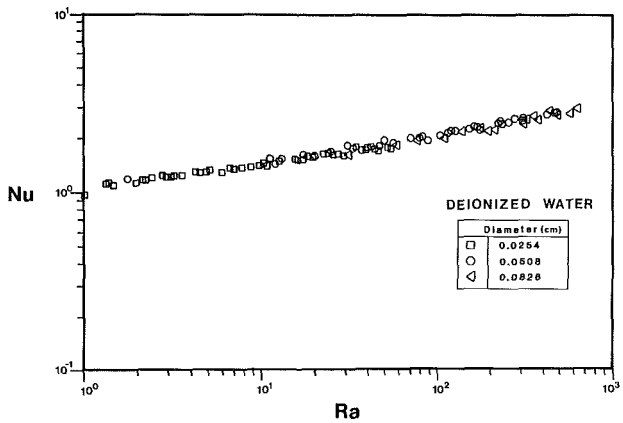

Fig. 6 Free convection data for water

To obtain the surface temperature of the wire the radial gradient in temperature is subtracted from the mean wire temperature according to the relationship

$$T_w = T_m - \frac{(q/A)d}{k_{\mathrm{Pt}}} \tag{2}$$

which may be derived by assuming uniform generation of electric heat in the wire and constant thermal conductivity of the platinum.

In a typical heat transfer experiment the fluid temperature is monitored by four type T calibrated thermocouples placed at locations 2 to 5 cm away from the test wire. The electrical measurements determine the heat transfer from platinum wire to the fluid, as well as the mean platinum wire temperature.

Table 1 Experimental ranges of wall shear rates, Rayleigh, Prandtl, and Weissenberg numbers for Natrosol solutions

	Concentration (wppm)	$\left(\frac{\partial u}{\partial y}\right)_{y=0}$ (1/sec)	Ra (-)	Pr (-)	Ws (-)
	Diameter = 0.0254 cm (0.010")				
(1)	1,000	$4.00\times10^{+0}$ - $1.60\times10^{+1}$	1.90×10^{-1} - $1.26\times10^{+1}$	$1.35\times10^{+1}$ - $2.62\times10^{+1}$	9.23×10^{-3} - 2.61×10^{-2}
(2)	2,500	6.00×10^{-1} - $3.90\times10^{+0}$	3.35×10^{-2} - $1.42\times10^{+0}$	$9.33\times10^{+1}$ - $2.23\times10^{+2}$	3.86×10^{-2} - 1.28×10^{-1}
(3)	5,000	1.00×10^{-1} - $3.72\times10^{+0}$	1.44×10^{-3} - $1.13\times10^{+0}$	$2.53\times10^{+2}$ - $3.00\times10^{+3}$	6.73×10^{-1} - $1.67\times10^{+0}$
	Diameter = 0.0508 cm (0.020")				
(4)	1,000	$4.00\times10^{+0}$ - $2.71\times10^{+1}$	$3.70\times10^{+0}$ - $1.54\times10^{+2}$	$1.24\times10^{+1}$ - $2.86\times10^{+1}$	1.15×10^{-2} - 2.07×10^{-2}
(5)	2,500	6.00×10^{-1} - $7.10\times10^{+0}$	3.83×10^{-1} - $2.60\times10^{+1}$	$7.27\times10^{+1}$ - $2.08\times10^{+2}$	1.65×10^{-2} - 8.79×10^{-2}
(6)	5,000	1.00×10^{-1} - $2.98\times10^{+0}$	4.68×10^{-2} - $8.26\times10^{+0}$	$2.37\times10^{+2}$ - $1.96\times10^{+3}$	6.47×10^{-1} - $1.06\times10^{+0}$
	Diameter = 0.0826 cm (0.033")				
(7)	1,000	$4.00\times10^{+0}$ - $9.82\times10^{+0}$	$1.86\times10^{+1}$ - $1.55\times10^{+2}$	$2.00\times10^{+1}$ - $2.87\times10^{+1}$	9.86×10^{-3} - 1.60×10^{-2}
(8)	2,500	6.00×10^{-1} - $3.22\times10^{+0}$	$3.01\times10^{+0}$ - $3.47\times10^{+1}$	$1.13\times10^{+2}$ - $1.89\times10^{+2}$	3.35×10^{-2} - 6.12×10^{-2}
(9)	5,000	1.15×10^{-1} - $1.80\times10^{+0}$	4.07×10^{-1} - $1.57\times10^{+1}$	$3.71\times10^{+2}$ - $1.54\times10^{+3}$	5.55×10^{-1} - 7.91×10^{-1}

Table 2 Experimental ranges of wall shear rates, Rayleigh, Prandtl, and Weissenberg numbers for Polyox solutions

	Concentration (wppm)	$\left(\frac{\partial u}{\partial y}\right)_{y=0}$ (1/sec)	Ra (-)	Pr (-)	Ws (-)
	Diameter = 0.0254 cm (0.010")				
(1)	1,000	$4.00\times10^{+0}$ - $1.26\times10^{+1}$	1.56×10^{-1} - $9.09\times10^{+0}$	$1.64\times10^{+1}$ - $3.21\times10^{+1}$	7.34×10^{-2} - 1.97×10^{-1}
(2)	2,500	$1.00\times10^{+0}$ - $4.83\times10^{+0}$	4.15×10^{-2} - $2.47\times10^{+0}$	$6.46\times10^{+1}$ - $1.33\times10^{+2}$	2.41×10^{-1} - 5.36×10^{-1}
(3)	3,500	7.00×10^{-1} - $3.41\times10^{+0}$	1.52×10^{-2} - $1.48\times10^{+0}$	$1.28\times10^{+2}$ - $3.09\times10^{+2}$	5.24×10^{-1} - 9.39×10^{-1}
(4)	5,000	3.00×10^{-1} - $2.04\times10^{+0}$	3.54×10^{-3} - 7.73×10^{-1}	$2.71\times10^{+2}$ - $1.07\times10^{+3}$	$1.19\times10^{+0}$ - $4.10\times10^{+0}$
(5)	10,000	1.50×10^{-2} - 2.01×10^{-1}	1.94×10^{-4} - 3.08×10^{-2}	$6.88\times10^{+3}$ - $2.21\times10^{+4}$	$1.64\times10^{+1}$ - $4.20\times10^{+1}$
	Diameter = 0.0508 cm (0.020")				
(6)	1,000	$4.00\times10^{+0}$ - $2.97\times10^{+1}$	$3.37\times10^{+0}$ - $1.72\times10^{+2}$	$1.09\times10^{+0}$ - $2.71\times10^{+1}$	7.43×10^{-2} - 1.40×10^{-1}
(7)	2,500	$1.00\times10^{+0}$ - $1.04\times10^{+1}$	7.33×10^{-1} - $4.18\times10^{+1}$	$4.68\times10^{+1}$ - $1.29\times10^{+2}$	2.97×10^{-1} - 4.56×10^{-1}
(8)	3,500	7.00×10^{-1} - $5.17\times10^{+0}$	2.48×10^{-1} - $1.57\times10^{+1}$	$1.20\times10^{+2}$ - $3.20\times10^{+2}$	3.03×10^{-1} - 6.09×10^{-1}
(9)	5,000	3.00×10^{-1} - $2.44\times10^{+0}$	9.42×10^{-2} - $5.62\times10^{+0}$	$2.80\times10^{+2}$ - $9.77\times10^{+2}$	7.55×10^{-1} - $2.57\times10^{+0}$
	Diameter = 0.0826 cm (0.033")				
(10)	1,000	$4.00\times10^{+0}$ - $1.11\times10^{+1}$	$2.37\times10^{+1}$ - $1.77\times10^{+2}$	$1.73\times10^{+1}$ - $2.55\times10^{+1}$	7.06×10^{-2} - 1.07×10^{-1}
(11)	2,500	$1.00\times10^{+0}$ - $3.85\times10^{+0}$	$4.05\times10^{+0}$ - $4.51\times10^{+1}$	$7.96\times10^{+1}$ - $1.29\times10^{+2}$	2.64×10^{-1} - 3.69×10^{-1}
(12)	3,500	7.00×10^{-1} - $2.31\times10^{+0}$	$1.74\times10^{+0}$ - $2.14\times10^{+1}$	$1.85\times10^{+2}$ - $3.16\times10^{+2}$	4.02×10^{-1} - 4.99×10^{-1}
(13)	5,000	3.00×10^{-1} - $1.57\times10^{+0}$	5.27×10^{-1} - $1.18\times10^{+1}$	$4.00\times10^{+2}$ - $9.75\times10^{+2}$	$1.02\times10^{+0}$ - $2.15\times10^{+0}$

Table 3 Proposed correlation

(1) $10^{-4} < \mathrm{Ra} < 10^{-2}$	$\mathrm{Nu} = 0.893\mathrm{Ra}^{0.079}$
(2) $10^{-2} < \mathrm{Ra} < 10^{0}$	$\mathrm{Nu} = 1.080\mathrm{Ra}^{0.121}\mathrm{Pr}^{0.006}$
(3) $10^{0} < \mathrm{Ra} < 10^{3}$	$\mathrm{Nu} = 1.010\mathrm{Ra}^{0.152}\mathrm{Pr}^{0.027}$

Table 4 Error estimation for the proposed correlation for water and viscoelastic fluids

	Test Fluids	Total No of Data	Average Error %	Root Mean Square Error %	Maximum Absolute Error %	No. of Data within 10% of Correlation
(A)	$10^{-4} < \mathrm{Ra} < 10^{-2}$					
(a)	Total Data Set	22	0.1	5.1	11.8	20
(b)	Water	0	-	-	-	0
(c)	Natrosol and Polyox Solutions	22	0.1	5.1	11.8	20
(d)	Natrosol Solutions	6	-1.1	4.4	6.9	6
(e)	Polyox Solutions	16	0.6	5.4	11.8	14
(B)	$10^{-2} < \mathrm{Ra} < 10^{0}$					
(a)	Total Data Set	140	-0.2	4.8	12.8	136
(b)	Water	10	6.7	7.7	12.8	8
(c)	Natrosol and Polyox Solutions	130	-0.7	4.5	12.1	128
(d)	Natrosol Solutions	53	-1.9	4.0	12.1	52
(e)	Polyox Solutions	77	-2.5	4.9	10.6	76
(C)	$10^{0} < \mathrm{Ra} < 10^{3}$					
(a)	Total Data Set	797	0.1	4.8	19.9	771
(b)	Water	569	0.7	3.8	9.2	569
(c)	Natrosol and Polyox Solutions	228	-1.3	6.6	19.9	202
(d)	Natrosol Solutions	96	0.6	5.6	19.9	91
(e)	Polyox Solutions	132	-2.8	7.3	17.9	111

The surface temperature of the wire is determined from equation (2). The heat transfer coefficient is then determined by the expression

$$h = \frac{q/A}{T_w - T_f} \tag{3}$$

Calibration free convection runs with water as the test fluid were carried out for the three different diameter wires. A total of 579 runs were made covering a range of Rayleigh number from 1 to 750, while the Prandtl number varied from 3 to 7. The results, shown in Fig. 6 in the form of Nusselt number versus Rayleigh number, are within 7 percent of the correlation proposed by Morgan [1].

Having established the reliability of the experimental procedure, heat transfer data were obtained for the Natrosol solutions over the test range outlined on Table 1. Noting that an

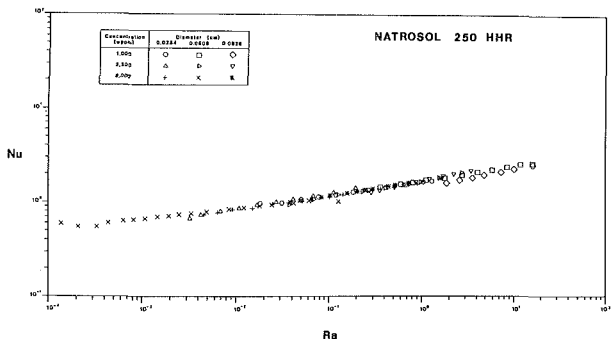

Fig. 7 Free convection data for Natrosol solutions

upper limit on the velocity v is given by $\sqrt{g\beta\Delta Td}$, a corresponding upper limit on the wall shear rate v/d may be obtained from $\sqrt{g\beta\Delta T/d}$. As pointed out by Ostrach [15], this is applicable in the region where the inertia force dominates. A more realistic estimate of the characteristic shear rate may be obtained by using the prediction of Acrivos which is valid for power-law fluids [16]. The power law may be expressed as

$$\tau = K\left(\frac{\partial u}{\partial y}\right)^n \tag{4}$$

where τ = shear stress; K = power-law consistency; n = power-law index.

The shear rate near the wall given by Acrivos can be shown [17] to be given by

$$\left(\frac{\partial u}{\partial y}\right)_{y=0} \sim \sqrt{\frac{g\beta\Delta T}{d}} \cdot \frac{\mathrm{Ra}_N^{(5-3n)/2(3n+1)}}{\mathrm{Pr}_N^{1/2}} \tag{5}$$

where $\mathrm{Ra}_N = (\rho g\beta\Delta T d^{1+2n})/(K\alpha^n)$; $\mathrm{Pr}_N = (K/\rho\alpha)(\alpha/d^2)^{n-1}$.

It should be pointed out that the calculation of the wall shear rate requires the numerical values of the power-law parameters K and n. For each experiment the values of K and n depend on the wall shear rate, which is initially unknown. Therefore, the calculation procedure involves an initial estimate of the value of the power-law parameters by assuming the shear rate to be equal to $\sqrt{g\beta\Delta T/d}$. The resultant shear rate calculated by equation (5) can then be evaluated using the initial values of K and n. The result is then compared with the initial estimation of the shear rate. This iterative procedure is repeated until the wall shear rate and the values of the power-law parameters are consistent. The experimental range of the resulting wall shear rate for the Natrosol solutions is presented in Table 1 and is also highlighted in Fig. 2. It appears that the zero shear rate viscosity η_0 is the appropriate viscosity to use in the dimensionless variables such as Prandtl and Rayleigh numbers. In addition, the Weissenberg number $\lambda v/d$, which provides a quantitative measure of the elasticity of the fluid, may be of importance and is given in Table 1.

The Nusselt number is given as a function of the Rayleigh number for the Natrosol runs in Fig. 7 where it may be seen that the Rayleigh number is the major controlling variable and that the effect of Prandtl and Weissenberg numbers on the Nusselt number is of secondary importance over the wide range of test variables covered in the experiments.

A similar procedure was followed in the case of Polyox. The experimental Nusselt numbers are shown in Fig. 8 as a function of Rayleigh number for the aqueous Polyox solutions. It may be seen that there is more scatter than in the case of Natrosol particularly at the high Rayleigh numbers. In this region there is some evidence of a slight increase in the Nusselt number with Weissenberg number. At the lower Rayleigh number range there appears to be little or no effect of Weissenberg number. This suggets that the Weissenberg number may become more important as the Rayleigh number increases [6, 7].

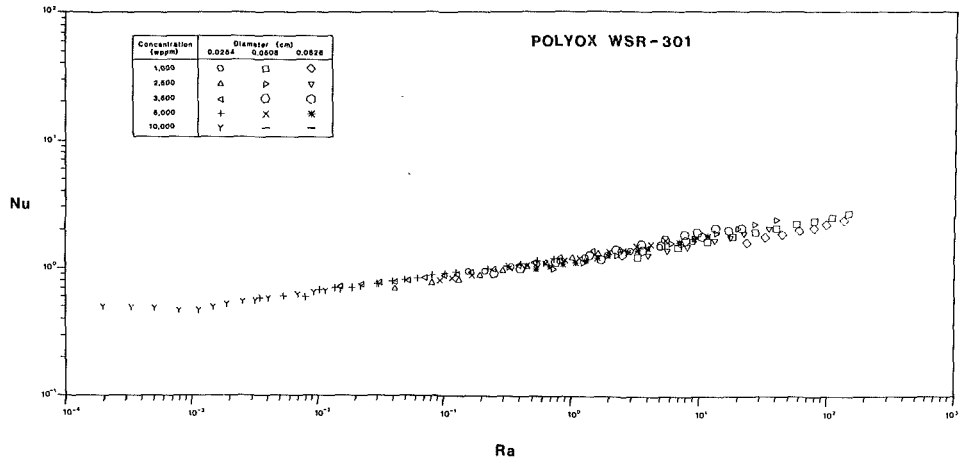

Fig. 8 Free convection data for Polyox solutions

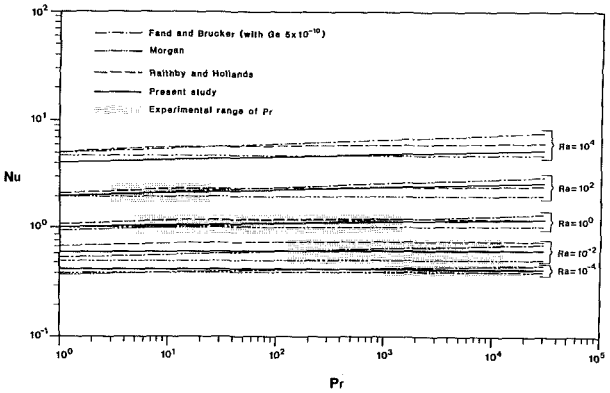

Fig. 9 Comparison of available empirical correlations

(*d*) **Statistical Treatment of Experimental Results.** A statistical evaluation of the experimental heat transfer results of water and the Natrosol and Polyox solutions revealed that the Nusselt number is a strong function of the Rayleigh number and a weak function of the Prandtl number. Empirical correlations in the form of $Nu = a\,Ra^b Pr^c$ were obtained, with the terms *a*, *b*, and *c* being functions of the Rayleigh number range as shown in Table 3.

The experimental data are compared with the proposed correlation in Table 4, where it can be seen that the agreement is very good, especially in the range of Rayleigh number from 10^{-4} to 10^0.

In the range of $10^0 < Ra < 10^3$ the prediction may be off by 20 percent in the case of the polymer solutions, although the root mean square error is only 6 to 7 percent. Generally speaking, the prediction is in better agreement with the Natrosol measurements than with the Polyox. Comparing Tables 1 and 2, it can be seen that the Weissenberg numbers of the Natrosol solutions are lower and cover a narrower range than the corresponding values for the Polyox solutions. This further supports the earlier observation that the Weissenberg number may play a role in free convective heat transfer to viscoelastic fluids at larger Rayleigh numbers.

(*e*) **Comparison With Other Correlations.** The proposed new correlation is compared in Fig. 9 with several well-established empirical and analytical correlations, namely Morgan [1], Raithby and Hollands [2], and Fand and Brucker [3]. Kuehn and Goldstein [15], although not shown, are in general agreement with Raithby and Hollands. Except for Morgan's result, which assumes the Nusselt number to be a function only of the Rayleigh number, these correlations indicate that the Nusselt number is a function of Rayleigh and Prandtl numbers. Furthermore, Fand and Brucker include a viscous dissipation term (the Gebhart number = $g\beta d/C_p$). In the present experimental study the Gebhart number ranges from 10^{-10} to 10^{-9} and its contribution is minor.

The experimental range of Prandtl number covered in the current program is shown as shaded in Fig. 9, along with the various predictions. It may be concluded that of the available correlations the prediction of Fand and Brucker yields the best agreement with the current measurements over the range of the test variables. In fact, in the range of Rayleigh number from 10^0 to 10^3 the prediction of Fand and Brucker lies within 10 percent of the experimental data for 770 points out of a total data set of 797. Thus the proposed new correlation is found to be within a few percent of the Fand and Brucker correlation over the entire experimental range.

4 Conclusions

The following conclusions can be drawn from this study:

(*a*) The zero shear rate viscosity of polymer solutions which exhibit viscoelastic behavior may be the appropriate choice for correlating free convection heat transfer results.

(*b*) Based on the zero shear rate viscosity the free convection heat transfer performance of a horizontal wire in a viscoelastic fluid found to be the sasme as in the case of Newtonian fluids. The correlations proposed by Fand and Brucker is found to yeild good agreement over the range of variables studies ($3 < Pr < 22{,}000$ and $10^{-4} < Ra < 10^3$).

(*c*) New correlations including water, Natrosol, and Polyox solutions are proposed in the form of $Nu = a\,Ra^b Pr^c$. They offer no major improvement over the correlation of Fand and Brucker.

(*d*) Elasticity plays a negligible secondary role in the case of free convection from a horizontal wire to a surrounding viscoelastic fluid over the range of variables studied. There is some evidence that the effect of elasticity may become important at Rayleigh numbers above 10^3.

Acknowledgments

The authors acknowledge the financial support of the Division of Engineering of the Office of Basic Energy Sciences of the U.S. Department of Energy under its Grant No. 85 ER 13311. The authors also wish to express their appreciation to Professor R. M. Turian for the use of his Brookfield viscometer.

References

1 Morgan, V. T., "The Overall Convective Heat Transfer From Smooth Circular Cylinders," in: *Advances in Heat Transfer*, Vol. 11, Academic Press, New York, 1975, pp. 199-264.

2 Raithby, G. D., and Hollands, K. G. T., "A General Method of Obtaining Approximate Solutions to Laminar and Turbulent Free Convection Problems," in *Advances in Heat Transfer*, Vol. 11, Academic Press, New York, 1975, pp. 265–317.

3 Fand, R. M., and Brucker, J., "A Correlation for Heat Transfer by Natural Convection From Horizontal Cylinders That Accounts for Viscous Dissipation," *Int. J. Heat Mass Transfer*, Vol. 25, No. 5, 1983, pp. 709–726.

4 Shenoy, A. V., and Mashelkar, R. A., "Thermal Convection in Non-Newtonian Fluids," in: *Advances in Heat Transfer*, Vol. 15, Academic Press, New York, 1982, pp. 143–225.

5 Lyons, D. W., White, J. W., and Hatcher, J. D., "Laminar Natural Convection Heat Transfer in Dilute Aqueous Polymer Solutions," *Ind. Eng. Chem. Fund.*, Vol. 11, No. 4, 1972, pp. 586–588.

6 Liang, S. F., and Acrivos, A., "Experiments on Buoyancy-Driven Convection in Non-Newtonian Fluid," *Rheol. Acta*, Vol. 9, No. 3, 1970, pp. 447–455.

7 Garifulin, F. A., Zapparou, F. I., Mingaleyer, N. Z., Norden, P. A., and Tazukov, F. K. H., "Convection in a Horizontal Layer of a Viscoelastic Fluid," *Heat Transfer—Soviet Research*, Vol. 14, No. 1, 1982, pp. 121–126.

8 *The Weissenberg Rheogoniometer Instruction Manual*, Sangamon Controls, Ltd., England.

9 Yoo, S. S., "Heat Transfer and Friction Factors for Non-Newtonian Fluids in Turbulent Pipe Flow," Ph.D. Thesis, University of Illinois, Chicago, 1974.

10 Lee, W. Y., Cho, Y. I., and Hartnett, J. P., "Thermal Conductivity Measurements of Non-Newtonian Fluids," *Lett. Heat Mass Transfer*, Vol. 8, 1981, pp. 255–259.

11 Chistiansen, G. B., Craig, S. E., Jr., and Carter, T. R., "The Effect of Temperature on the Consistency of Fluids," *J. Rheology*, Vol. 10, 1966, pp. 419–430.

12 Powell, R. L., and Eyring, H., "Mechanisms for the Relaxation Theory of Viscosity, *Nature*, Vol. 154, 1944, pp, 427–428.

13 Kwack, E. Y., "Effect of Weissenberg Number on Turbulent Heat Transfer and Friction Factor of Viscoelastic Fluids," Ph.D. Thesis, University of Illinois, Chicago, 1983.

14 Preobrazhensky, V., *Measurements and Instrumentation in Heat Engineering*, Vol. 1, Mir Publishers, Moscow, 1980.

15 Ostrach, S., private communication.

16 Acrivos, A., "A Theoretical Analysis of Laminar Natural Convection Heat Transfer to Non-Newtonian Fluids," *AIChE J.*, Vol. 6, No. 4, 1960, pp. 584–590.

17 Ng, M. L., "An Experimental Study on Natural Convection Heat Transfer of Non-Newtonian Fluids From Horizontal Wires," Ph.D. Thesis, University of Illinois, Chicago, 1985.

18 Kuehn, T. H., and Golstein, R. J., "Numerical Solution to the Navier–Stokes Equations for Laminar Natural Convection About a Horizontal Isothermal Circular Cylinder," *Int. J. Heat Mass Transfer*, Vol. 23, 1980, pp. 971–979.

A. S. Lavine
Mechanical, Aerospace, and Nuclear Engineering Department, University of California, Los Angeles, Los Angeles, CA
Assoc. Mem. ASME

R. Greif
Mem. ASME

J. A. C. Humphrey
Mem. ASME

Department of Mechanical Engineering, University of California, Berkeley, Berkeley, CA

Three-Dimensional Analysis of Natural Convection in a Toroidal Loop: Effect of Tilt Angle

A three-dimensional numerical analysis of natural convection in a toroidal thermosyphon has been performed. The results confirm the experimental observations of three dimensionality, streamwise flow reversal, and secondary motion. The flow reversals reduce the wall friction and buoyancy forces, and consequently have a strong effect on the average axial velocity.

Introduction

This study concerns the steady-state natural convection flow through a toroidal loop oriented in a vertical plane (see Fig. 1). One half of the loop is heated, and the other half is cooled. When the loop is tilted as shown in the figure, flow occurs in the counterclockwise direction.

This system is a simple example of a class of devices known as thermosyphons or natural circulation loops, which have many applications [1–7]. For instance, in solar thermosyphon hot water heaters, the heat transfer fluid is heated at the solar collector and rises through a pipe to a raised storage tank. Here it transfers heat to the water in the tank, and consequently falls back down to the collector. Natural circulation may also arise in the emergency cooling of nuclear reactor cores, e.g., when a pump failure occurs. Other applications include cooling of internal combustion engines and turbine blades, geothermal power production, thermosyphon reboilers, heat exchanger fins, permafrost protection, ice production, and computer cooling.

Two early analyses of simplified natural circulation loops were performed by Welander [8] and by Keller [9]. These yielded steady-state and oscillatory solutions.

Creveling et al. [10] carried out an experimental and analytical investigation of the toroidal thermosyphon configuration with zero tilt angle (i.e., $\alpha = 0$ in Fig. 1). They observed a region of flow reversal near the entrance to the cooling section.

Damerell and Schoenhals [11] extended this work by investigating, both experimentally and analytically, the effect of tilting the thermosyphon about its horizontal axis ($\alpha \neq 0$ in Fig. 1). A one-dimensional, steady-state analysis predicted that the mass flow rate would decrease monotonically with increasing tilt angle. Experimentally, however, it was found that for small tilt angles, the flow rate did not vary strongly with tilt angle, and fell below the predictions. The discrepancy was attributed to the regions of streamwise flow reversal which were once again observed near the entrance to the cooling section.

Many one-dimensional thermosyphon analyses have been performed to investigate various aspects of the problem. For instance, Ramos et al. [12] addressed the effect of a variable cross-sectional area. Greif et al. [13] and Mertol et al. [14] extended the one-dimensional analysis to the transient case. Mertol et al. [15, 16] performed a two-dimensional (r and θ) numerical analysis of the toroidal thermosyphon. The predicted mass flow rate was compared to the experimental data reported by Creveling et al. [10] and good agreement was obtained.

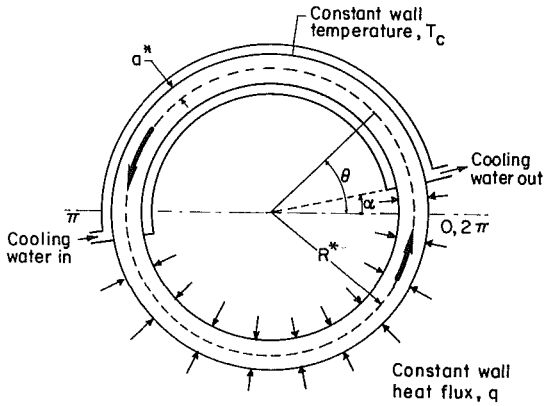

Fig. 1 The toroidal thermosyphon

Stern and Greif [17] undertook further experimental investigation of the same thermosyphon configuration. Three-dimensional effects were observed, such as flow reversal, nonzero cross-stream velocities, and nonaxisymmetric temperature profiles. Gorman et al. [18] applied the concepts of nonlinear dynamics to their experimental observations of flow in the toroidal thermosyphon.

To summarize, experiments on the toroidal thermosyphon have shown that under stable flow conditions, the axial velocity and the temperature are nonaxisymmetric (depend on ϕ), the cross-stream velocities are nonzero, and regions of streamwise flow reversal exist. The one- and two-dimensional analyses performed to date, because of their simplifications, have not predicted any of these flow phenomena.

Accurate prediction of the details of the flow and heat transfer requires the use of a three-dimensional analysis, with all three velocity components included. This paper describes some of the results of such an analysis, especially as they pertain to the effect of the tilt angle on the flow. A future paper will discuss the effect of the Grashof number.

Analysis

For the numerical analysis of the thermosyphon, the flow was taken to be three dimensional, and all three velocity components and pipe curvature were included. The only simplifying assumptions were that the flow: (1) was steady state, (2) was symmetric about the vertical plane containing the circle of radius R^* formed by the pipe centerline, (3) was laminar, (4)

Contributed by the Heat Transfer Division for publication in the JOURNAL OF HEAT TRANSFER. Manuscript received by the Heat Transfer Division April 17, 1985. Paper No. 85-WA/HT-7.

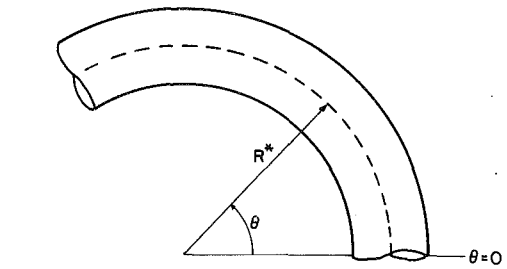

curved pipe

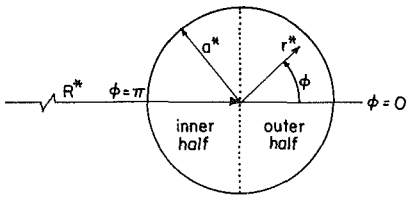

pipe cross-section

Fig. 2 Coordinate system, (r^*, ϕ, θ)

was incompressible, (5) had constant properties (except for the use of the Boussinesq approximation for the density), (6) had negligible viscous dissipation, and (7) had negligible Coriolis acceleration due to the earth's rotation. These assumptions are believed to introduce little error into the solution [19].

Given these assumptions, the nondimensional differential equations, expressed in the coordinate system shown in Fig. 2, are as follows (see Nomenclature)

Continuity

$$\frac{1\partial}{r\partial r}(r(R+r\cos\phi)u)+\frac{1\partial}{r\partial\phi}((R+r\cos\phi)v)+\frac{\partial w}{\partial\theta}=0$$

r-Momentum

$$(\mathbf{u}\cdot\nabla)u-\frac{v^2}{r}-\frac{\cos\phi}{R+r\cos\phi}w^2=-\frac{\partial p}{\partial r}+\frac{16\pi^4}{\mathrm{Gr}}\Phi\sin\theta\cos\phi+\frac{4\pi^2}{\mathrm{Gr}}\left[\nabla^2u-\frac{2}{r^2}\frac{\partial v}{\partial\phi}-\frac{u}{r^2}+\frac{\sin\phi}{r(R+r\cos\phi)}v+\frac{\cos\phi}{(R+r\cos\phi)^2}\left(v\sin\phi-u\cos\phi-2\frac{\partial w}{\partial\theta}\right)\right]$$

φ-Momentum

$$(\mathbf{u}\cdot\nabla)v+\frac{uv}{r}+\frac{\sin\phi}{R+r\cos\phi}w^2=-\frac{1\partial p}{r\partial\phi}-\frac{16\pi^4}{\mathrm{Gr}}\Phi\sin\theta\sin\phi+\frac{4\pi^2}{\mathrm{Gr}}\left[\nabla^2v+\frac{2}{r^2}\frac{\partial u}{\partial\phi}-\frac{v}{r^2}-\frac{\sin\phi}{r(R+r\cos\phi)}u-\frac{\sin\phi}{(R+r\cos\phi)^2}\left(v\sin\phi-u\cos\phi-2\frac{\partial w}{\partial\theta}\right)\right]$$

θ-Momentum

$$(\mathbf{u}\cdot\nabla)w+\frac{w}{R+r\cos\phi}(u\cos\phi-v\sin\phi)=-\frac{1}{R+r\cos\phi}\frac{\partial p}{\partial\theta}+\frac{16\pi^4}{\mathrm{Gr}}\Phi\cos\theta+\frac{4\pi^2}{\mathrm{Gr}}\left[\nabla^2w+\frac{2}{(R+r\cos\phi)^2}\left(\frac{\partial u}{\partial\theta}\cos\phi-\frac{\partial v}{\partial\theta}\sin\phi-\frac{w}{2}\right)\right]$$

Nomenclature

a^* = pipe radius
c = specific heat
$f\mathrm{Re}$ = peripherally averaged friction factor times Reynolds number $= \frac{1}{2\pi}\int_0^{2\pi}-\frac{4}{\bar{w}}\frac{\partial w}{\partial r}\Big|_1 d\phi$
g = gravitational constant
Gr = Grashof number = $g\beta\Delta Ta^{*3}/\nu^2$
h = height above a datum
$\dot{m}$ = characteristic mass flow rate = $\rho_c\pi a^{*2}W$
$\overline{\mathrm{Nu}}$ = peripherally averaged Nusselt number = $\dfrac{\int_0^{2\pi}\frac{\partial\Phi}{\partial r}\Big|_1 d\phi}{2\int_0^{2\pi}(\Phi_b-\Phi_w)d\phi}$
p^* = $\hat{p}+\rho_c gh$
$\hat{p}$ = thermodynamic pressure
p = $p^*/\rho_c W^2$ = nondimensional pressure
Pr = Prandtl number
q = constant wall heat flux in heating section
Q = total heat input in heating section = $q2\pi a^*\pi R^*$
r^* = radial coordinate
r = r^*/a^* = nondimensional radial coordinate
R^* = pipe radius of curvature
R = R^*/a^* = nondimensional pipe radius of curvature
T = temperature
T_b = bulk (or mixed mean) temperature = $\dfrac{1}{\bar{w}^*\pi a^{*2}}\int_0^{2\pi}\int_0^{a^*}w^*Tr^*dr^*d\phi$
T_c = constant wall temperature in the cooling section
T_w = $T(a^*,\phi,\theta)$
$\mathbf{u}$ = nondimensional vector velocity
u^* = radial velocity
u = u^*/W = nondimensional radial velocity
v^* = circumferential velocity
v = v^*/W = nondimensional circumferential velocity
w^* = axial velocity
w = w^*/W = nondimensional axial velocity
$\bar{w}^*$ = cross-sectionally averaged axial velocity
$\bar{w}$ = $\bar{w}^*/W$
W = characteristic axial velocity = $(g\beta Q/4\pi^3\mu c)^{1/2}$
α = tilt angle
β = coefficient of thermal expansion
ΔT = $Q/\dot{m}c$ = characteristic bulk temperature difference
θ = axial coordinate
μ = dynamic viscosity
ν = kinematic viscosity
ρ_c = density evaluated at T_c
ϕ = circumferential coordinate
Φ = $(T-T_c)/\Delta T$ = dimensionless temperature
Φ_b = $(T_b-T_c)/\Delta T$ = bulk (or mixed mean) dimensionless temperature
Φ_w = $(T_w-T_c)/\Delta T$ = dimensionless temperature at wall (zero in cooling section, but not in heating section)
$\bar{\Phi}$ = cross-sectionally averaged dimensionless temperature

Energy

$$(\mathbf{u}\cdot\nabla)\Phi=\frac{4\pi^2}{\mathrm{PrGr}}\nabla^2\Phi$$

where

$$(\mathbf{u}\cdot\nabla)=u\frac{\partial}{\partial r}+\frac{v\partial}{r\partial\phi}+\frac{w}{R+r\cos\phi}\frac{\partial}{\partial\theta}$$

$$\nabla^2=\frac{1}{r(R+r\cos\phi)}\left[\frac{\partial}{\partial r}\left(r(R+r\cos\phi)\frac{\partial}{\partial r}\right)+\frac{1\partial}{r\partial\phi}\left((R+r\cos\phi)\frac{\partial}{\partial\phi}\right)+\frac{1}{R+r\cos\phi}\frac{\partial}{\partial\theta}\left(r\frac{\partial}{\partial\theta}\right)\right]$$

The nondimensional boundary conditions are:

(*i*) zero velocity at wall: $u(1,\ \phi,\ \theta)=v(1,\ \phi,\ \theta)=w(1,\ \phi,\ \theta)=0$

(*ii*) specified wall temperature in cooling section: $\Phi(1,\ \phi,\ \theta)=0,\ \alpha\le\theta\le\pi+\alpha$

(*iii*) specified wall heat flux in heating section:

$$\frac{\partial\Phi}{\partial r}(1,\ \phi,\ \theta)=\frac{1}{2\pi R}\frac{\mathrm{PrGr}}{4\pi^2},\ \pi+\alpha\le\theta\le2\pi+\alpha$$

(*iv*) finiteness at pipe centerline:

$u(0,\ \phi,\ \theta),\ v(0,\ \phi,\ \theta),\ w(0,\ \phi,\ \theta),\ \Phi(0,\ \phi,\ \theta)$ all finite

(*v*) symmetry about the plane $\phi=0,\ \pi$:

$$\frac{\partial u}{\partial\phi}(r,\ 0,\ \theta)=\frac{\partial u}{\partial\phi}(r,\ \pi,\ \theta)=\frac{\partial v}{\partial\phi}(r,\ 0,\ \theta)$$

$$=\frac{\partial v}{\partial\phi}(r,\ \pi,\ \theta)=\frac{\partial w}{\partial\phi}(r,\ 0,\ \theta)=\frac{\partial w}{\partial\phi}(r,\ \pi,\ \theta)$$

$$=\frac{\partial\Phi}{\partial\phi}(r,\ 0,\ \theta)=\frac{\partial\Phi}{\partial\phi}(r,\ \pi,\ \theta)=0$$

(*vi*) periodicity:

$$u(r,\ \phi,\ 0)=u(r,\ \phi,\ 2\pi),\ v(r,\ \phi,\ 0)=v(r,\ \phi,\ 2\pi),$$

$$w(r,\ \phi,\ 0)=w(r,\ \phi,\ 2\pi),\ \Phi(r,\ \phi,\ 0)=\Phi(r,\ \phi,\ 2\pi)$$

The solution to these equations depends on the four parameters Gr, Pr, R, and α. Both the buoyancy and viscous terms are multiplied by 1/Gr. This does *not* mean that buoyancy becomes less important as the Grashof number increases. Rather, since the characteristic velocity was derived based on a balance between buoyancy and friction, the nondimensional equations reflect this balance.

The differential equations were solved using a finite difference computer program. The computer program is a version of the TEACH code [20], a finite difference program for solving the continuity, momentum, and energy equations in their complete elliptic form. The concepts underlying this computer program are discussed by Patankar [21], and a version for curved pipes is described by Humphrey [22]. The computer program solves for the primitive variables (u, v, w, p, and Φ). The hybrid differencing technique [21] (a combination of upwind and central differencing) is used for the convection and diffusion terms in the momentum and energy equations. The pressure is determined by using the SIMPLER algorithm [21], which converts the continuity equation into an equation for the pressure. The solution procedure is iterative, and must be underrelaxed at each step to ensure stability of the sequence of iterations. The solution converges extremely slowly; each case required thousands of iterations, which took 1 to 2 *days* of cpu time on an IBM 4341.

The computer program was validated on several flows which are simpler than the thermosyphon flow, and for which

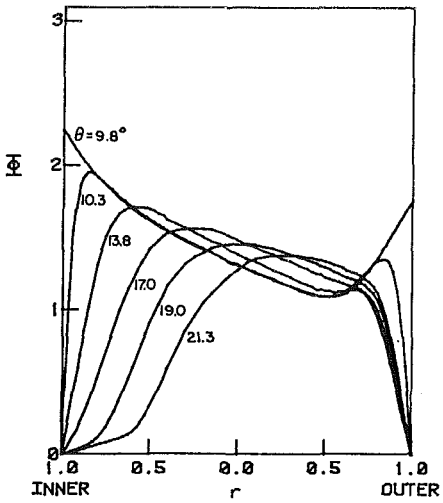

Fig. 3 Temperature profiles in symmetry plane, near cooling section entrance, 10 deg tilt

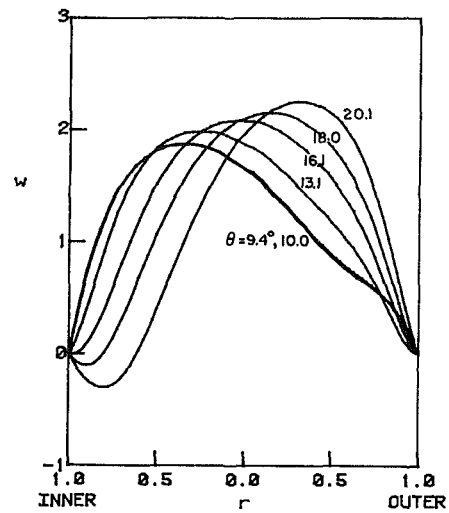

Fig. 4 Axial velocity profiles in symmetry plane, near cooling section entrance, 10 deg tilt

experimental data or analytical solutions were available. These cases were chosen so as to verify that distinct aspects of the computer program were properly implemented. The cases were: (1) flow in a curved pipe with no heat transfer, (2) thermally developing flow in a straight pipe with no buoyancy, for constant wall temperature and for constant wall heat flux boundary conditions, (3) hydrodynamically and thermally developing flow in a vertical pipe with buoyancy, and (4) hydrodynamically and thermally developing flow in a horizontal pipe with buoyancy. Satisfactory agreement was obtained in every case [19].

For the solution procedure used in this research, "convergence" can have two meanings. The solution procedure is iterative; for a particular finite difference grid, the sequence of iterations must converge to a reasonably accurate solution of the finite difference equations. Secondly, as the finite difference grid is refined, the sequence of solutions must converge to a reasonably grid-independent result. When both of these criteria are met, the numerical solution will be a good approximation to a solution of the differential equations. The first of these two criteria will be referred to as convergence, and the second will be termed grid independence. Both of these criteria were met for the thermosyphon cases reported here.

Convergence of the iterations is judged by the magnitude of the residuals. For each of the five governing equations, i.e., r,

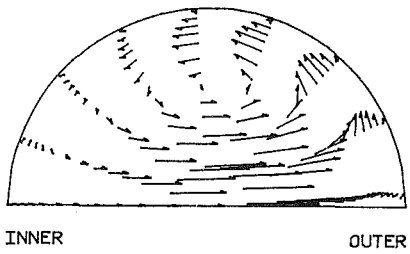

Fig. 5 Secondary velocity vectors at $\theta = 21.3$ deg, 10 deg tilt

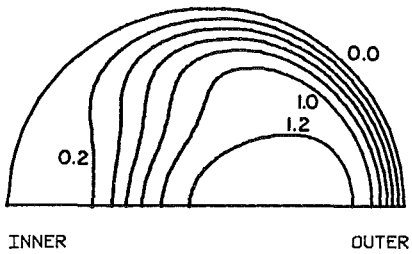

Fig. 6 Temperature contours (isotherms) at $\theta = 21.3$ deg, 10 deg tilt

ϕ, and θ momentum, continuity (pressure), and energy, the residual is the sum over all the nodes of the amount by which the finite difference equation is not satisfied. The residuals are normalized appropriately, e.g., the axial momentum residual is normalized by the quantity $\rho_c W^2 \pi a^{*2}$. For one case, the computer program was run using two different convergence criteria; the residuals for all five equations were required to be less than 0.04 and less than 10^{-3}, respectively. The calculated results corresponding to these two convergence criteria were compared graphically, and were generally indistinguishable. Based on this information, all residuals for other cases were required to be less than 0.04 for convergence to be considered satisfactory. Note that the number of nodes was around 10^5, so that the error per node is extremely small.

Two different cases were investigated with various finite difference grids, to determine the number of grids needed in each of the three coordinate directions to obtain reasonably grid-independent results. For the Grashof number value considered here, a $39 \times 26 \times 100$ grid (in the r, ϕ, and θ directions, respectively) was found to be satisfactory. The r grid was nonuniform, with finer spacing near the wall, the ϕ grid was uniform, and the θ grid spacing was finer near the heating and cooling section entrances. For one of the cases reported, it was also verified that global force and energy balances (over the entire thermosyphon volume) were satisfied to within 1 percent.

Results

Recall that the solution for the flow in the thermosyphon depends on the four parameters Gr, Pr, R, and α. The cases which are investigated in this study correspond to the geometry of the toroidal thermosyphons at Purdue University and the University of California, Berkeley, i.e., $R = 24.6$. The Prandtl number is a typical value for water, i.e., $\mathrm{Pr} = 6.5$. Unfortunately, as explained by Lavine [19] it was not possible to obtain converged results for values of the Grashof number corresponding to the experimental data of Creveling et al. [10] and Stern and Greif [17], which were on the order of 10^4. Failure to obtain converged results may be related to the observed unsteady nature of the flow at these values of the Grashof number. The cases presented here are for $\mathrm{Gr} = 1900$ and tilt angles of 10, 45, and 90 deg. A future paper will consider $\mathrm{Gr} = 3600$.

Since α is between 0 and 90 deg for the cases investigated here, the main flow is in the counterclockwise direction. However, regions of flow reversal do exist for some of the

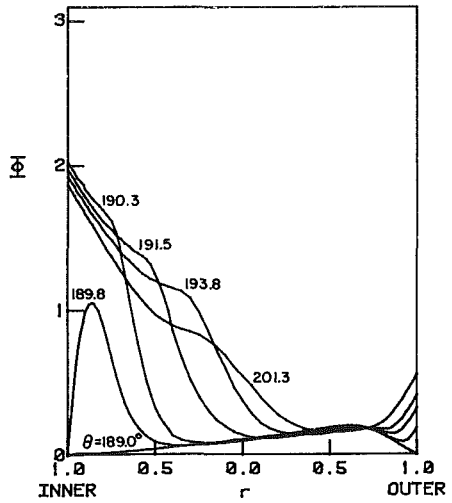

Fig. 7 Temperature profiles in symmetry plane, near heating section entrance, 10 deg tilt

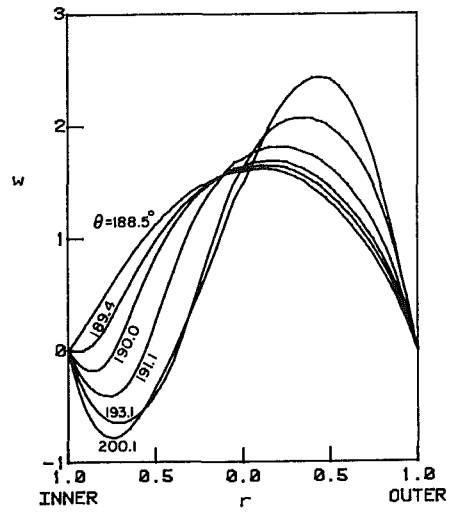

Fig. 8 Axial velocity profiles in symmetry plane, near heating section entrance, 10 deg tilt

cases. Secondary or cross-stream motion (i.e., motion perpendicular to the axial or θ direction) was also predicted by the numerical analysis.

Figures 3 and 4 show the dimensionless temperatures and axial velocity profiles in the symmetry plane, near the entrance to the cooling section ($\theta = \alpha$) for $\alpha = 10$ deg. The left and right-hand sides of the graph correspond to the inner and outer pipe halves, respectively. In Fig. 3, before the flow enters the cooling section ($\theta = 9.8$ deg), the temperature peak is at the inner wall. This is because buoyancy causes the hotter, lighter fluid to rise, and in the bottom half this brings the hotter fluid toward the inner wall. The fluid enters the cooling section at $\theta = 10$ deg (see $\theta = 10.3$ deg in Fig. 3) and the temperature at the wall drops to the specified wall temperature. As the flow proceeds downstream the pipe becomes more inclined; thus the hot fluid near the inner wall tends to rise toward the outer wall, and so the temperature peak shifts toward the outer wall. This contributes to the secondary motion which is illustrated in Fig. 5 at the location $\theta = 21.3$ deg.

Next, consider the axial velocity profiles (Fig. 4). Before the flow enters the cooling section ($\theta = 9.4$ deg), the velocity peak is near the inner wall. This is because the hotter fluid there rises more quickly than the cooler fluid at the outer wall. Due to the rapid cooling at the walls, the flow begins to decelerate there. At the same time, the velocity peak is moving toward the outer wall due to the secondary motion. This shift in the

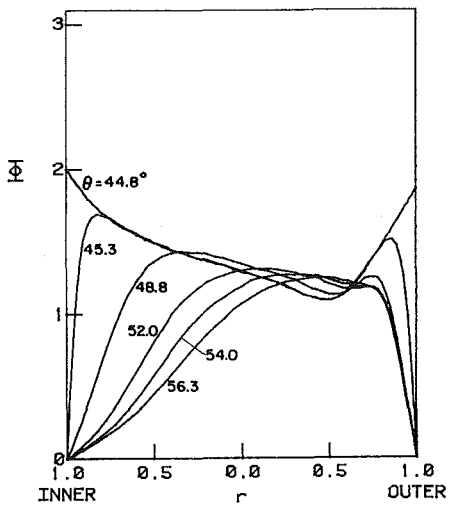

Fig. 9 Temperature profiles in symmetry plane, near cooling section entrance, 45 deg tilt

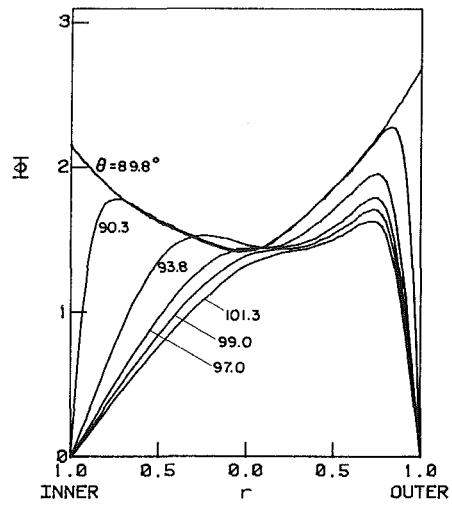

Fig. 11 Temperature profiles in symmetry plane, near cooling section entrance, 90 deg tilt

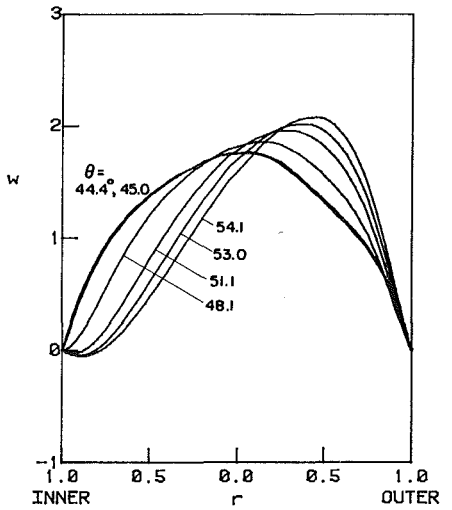

Fig. 10 Axial velocity profiles in symmetry plane, near cooling section entrance, 45 deg tilt

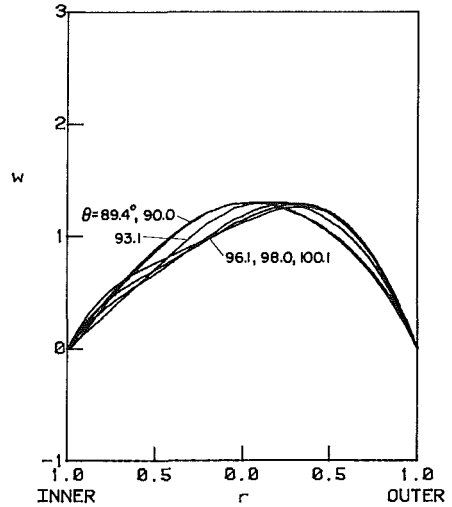

Fig. 12 Axial velocity profiles in symmetry plane, near cooling section entrance, 90 deg tilt

velocity peak is consistent with the temperature peak near the outer wall. The secondary motion brings the cold, slowly moving fluid in the neighborhood of the wall toward the inner wall. This fluid begins to fall, creating a region of flow reversal near the inner wall. The temperature is considerably lower in the region of flow reversal than in the remainder of the cross section. This is especially apparent in the temperature contour plot (Fig. 6) for $\theta = 21.3$ deg.

The temperature decreases throughout the remainder of the cooling section. As the flow proceeds toward the top of the loop, the component of the gravitational force in the axial direction decreases. Therefore, the region of flow reversal gradually diminishes, and vanishes by $\theta = 60$ deg.

Figures 7 and 8 are temperature and axial velocity profiles in the symmetry plane, near the beginning of the heating section, again for the $\alpha = 10$ deg case. Note that the right sides of these (and all other) plots still correspond to the outer wall, even though if the thermosyphon is viewed as in Fig. 1, the outer wall is now to the left. At $\theta = 189.8$ deg in Fig. 7, the temperature has risen significantly near the inner wall, even though the flow is still in the cooling section. This temperature increase is due to a region of flow reversal which causes fluid from the heating section to flow back into the cooling section.

Upon entering the heating section ($\theta = 190.3$ deg) the wall temperature increases. It increases much more at the inner wall than at the outer wall, and remains higher near the inner wall throughout the entire heating section. This is because the heated fluid near the walls tends to rise, bringing it toward the inner wall. This creates a secondary motion in the same direction as in the cooling section. The secondary motion brings the hot, slowly moving fluid in the neighborhood of the wall toward the inner wall, where it rises, forming a flow reversal, as seen in Fig. 8. The speed of the reversed flow is greater in the heating section than in the cooling section. This is because a constant wall heat flux boundary condition allows greater temperature variation over a cross section than does a constant wall temperature boundary condition. This in turn causes a larger variation in axial momentum due to buoyancy. Thus the velocity minimum and maximum are more extreme in the heating section than in the cooling section. The flow reversal is stronger in the heating section, and is therefore able to penetrate back into the cooling section.

The $\alpha = 45$ and 90 deg cases are discussed next. Note that $\alpha = 90$ deg corresponds to cooling the left-hand side of the loop and heating the right-hand side.

The temperature and axial velocity profiles in the symmetry plane near the cooling section entrance are shown in Figs. 9–12 for the $\alpha = 45$ and 90 deg cases. The θ values of these curves are the same as for the $\alpha = 10$ deg case, *relative to the tilt angle*. For example, the curve for $\theta = 30$ deg for the 10 deg tilt

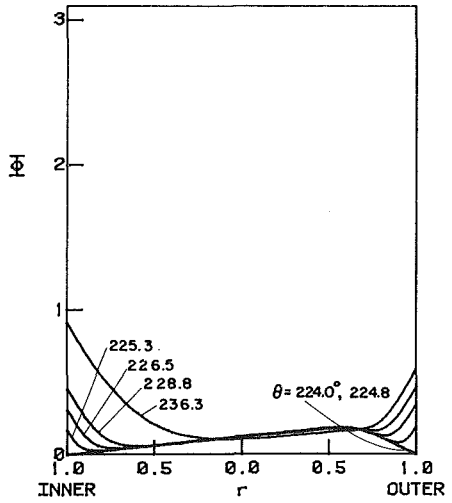

Fig. 13 Temperature profiles in symmetry plane, near heating section entrance, 45 deg tilt

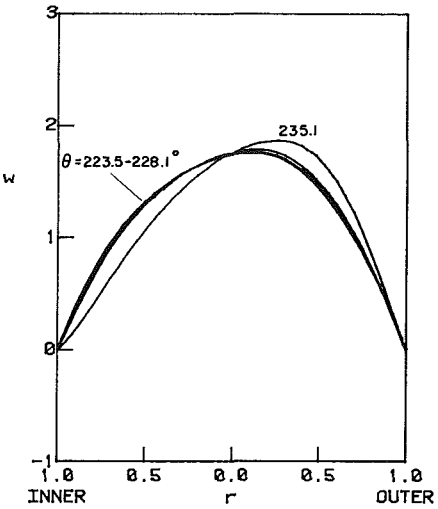

Fig. 14 Axial velocity profiles in symmetry plane, near heating section entrance, 45 deg tilt

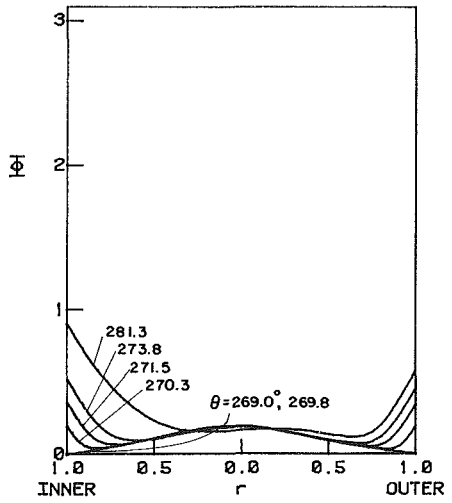

Fig. 15 Temperature profiles in symmetry plane, near heating section entrance, 90 deg tilt

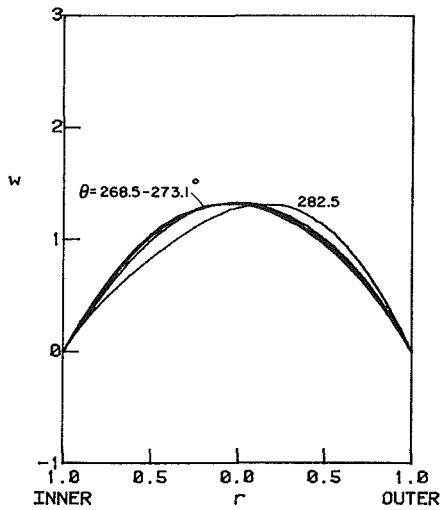

Fig. 16 Axial velocity profiles in symmetry plane, near heating section entrance, 90 deg tilt

case corresponds to $\theta = 65$ and 110 deg for the 45 and 90 deg tilt cases, respectively. The results have been presented in this way because many of the phenomena observed in the thermosyphon are related to the distance from the heating or cooling section entrances.

The temperature profiles near the entrance to the cooling section can be compared in Figs. 3, 9, and 11 for the $\alpha = 10$, 45, and 90 deg cases, respectively. Recall that for the $\alpha = 10$ deg case, the temperature peak was at the inner wall at a location shortly upstream of the cooling section entrance (see Fig. 3 for $\theta = 9.8$ deg). This was caused by the hotter fluid rising toward the inner wall in the bottom half of the thermosyphon. In the upper half, however, the hotter fluid tends to rise toward the outer wall. Thus, for $\alpha = 45$ deg, by the time the fluid reaches the cooling section entrance, the temperature difference between the inner and outer walls has decreased substantially. For $\alpha = 90$ deg, the cooling section entrance is at the top of the loop, and by the time the fluid reaches *this* location the temperature peak has moved to the outer wall. Once inside the cooling section, the temperature decreases in all three cases.

The axial velocity profiles can be compared in Figs. 4, 10, and 12. The profiles for $\alpha = 10$ and 45 deg both exhibit a flow reversal at the inner wall. However, for $\alpha = 45$ deg, the flow reversal is considerably weaker than for $\alpha = 10$ deg. This is because the component of gravity in the axial direction is less at $\theta = 45$ deg than at $\theta = 10$ deg (i.e., cos 45 deg/cos 10 deg = 0.72). Note that for $\alpha = 90$ deg, there is no flow reversal, because the cooling section begins at the top of the loop, and the cooled fluid near the walls falls in the main flow direction.

The results near the entrance to the heating section are shown in Figs. 7, 13, and 15 for the temperature profiles, and Figs. 8, 14, and 16 for the axial velocity profiles. The results for $\alpha = 45$ and 90 deg are quite similar. The temperature increases gradually near the wall and is only slightly higher at the inner wall. There is no flow reversal in either case. The behavior is substantially different from the $\alpha = 10$ deg case, for which there is a strong flow reversal and corresponding large temperature peak, near the inner wall. The lack of flow reversal for the $\alpha = 90$ deg case is to be expected, since heating starts at the bottom of the loop, and the heated fluid near the walls rises in the main flow direction. For $\alpha = 45$ deg, however, the lack of flow reversal may seem surprising, especially when it is recalled that for $\alpha = 10$ deg, the flow reversal was actually *stronger* in the heating section than in the cooling section. This apparent contradiction can be explained as follows. In the heating section, the wall heat flux is fixed, and the wall temperature will vary with location. In the absence of a flow reversal, the wall temperature tends to increase gradually through the heating section, and to become gradually larger at the inner wall. If attention were restricted to the region very

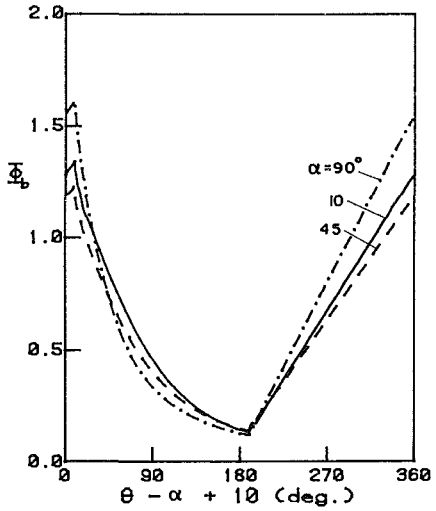

Fig. 17 Bult temperature, all three tilt angles

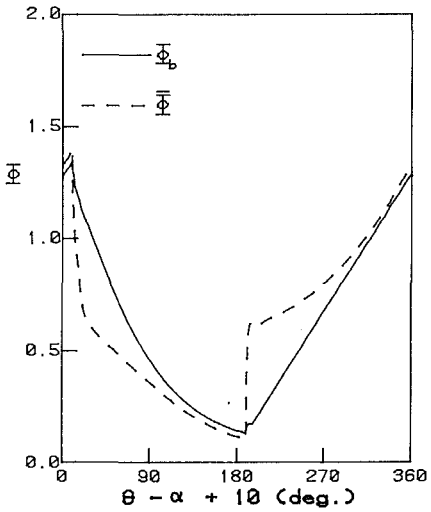

Fig. 18 Bulk and average temperatures, 10 deg tilt

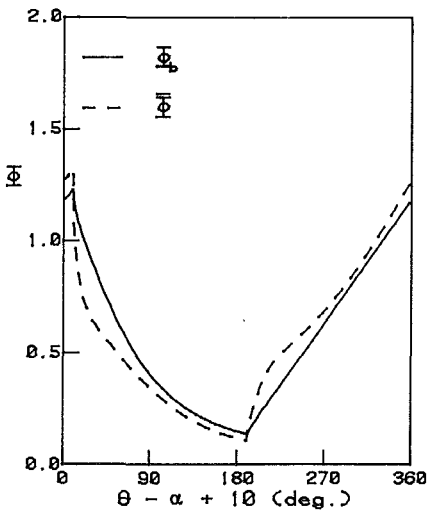

Fig. 19 Bulk and average temperatures, 45 deg tilt

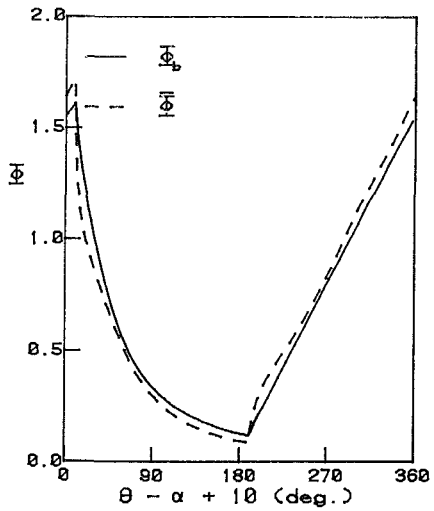

Fig. 20 Bulk and average temperatures, 90 deg tilt

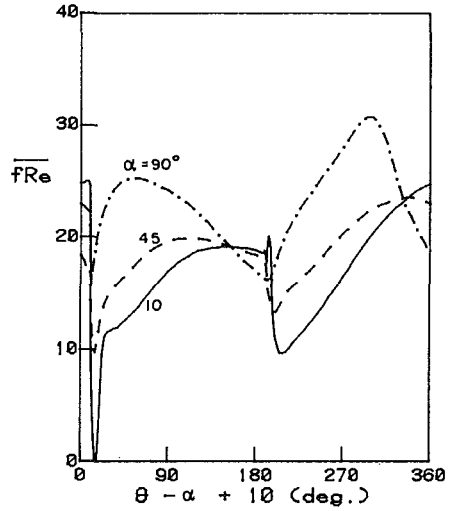

Fig. 21 Wall friction, peripherally averaged

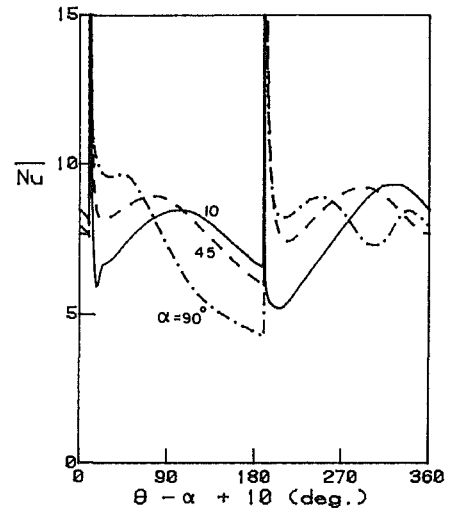

Fig. 22 Nusselt number, peripherally averaged

near the entrance to the heating section, a flow reversal would not be expected to form, no matter what the tilt angle, because the temperature will have changed very little from its distribution in the cooling section. For $\alpha = 10$ deg, however, the flow reversal can be thought of as being "initiated" further downstream, at a location where the temperature profile has had an opportunity to develop, and the fluid has become hotter near the inner wall. Of course, as the bottom of the loop is approached, the axial component of gravity goes to zero. Therefore, if heating begins sufficiently close to the bottom of the loop, the temperature profile will not have developed enough to cause a flow reversal to occur before the axial com-

ponent of gravity becomes small. Apparently this is the case for a tilt angle of 45 deg, since there is no flow reversal.

The values of the dimensionless average velocity for these three cases are 0.824, 0.915, and 0.669 for $\alpha = 10$, 45, and 90 deg, respectively. Note that the velocity does not vary monotonically with tilt angle. This will be discussed later.

The dimensionless bulk (or mixed mean) temperature Φ_b as a function of θ is shown in Fig. 17 for all three tilt angles. The abscissa is $\theta - \alpha + 10$ deg, so that the locations of the heating and cooling section entrances coincide for all three cases. The shapes of the curves are quite similar. From an energy balance on the heating section, the difference between the maximum and minimum temperatures (at $\theta = \alpha$ and $\theta = \alpha + 180$ deg) must be inversely proportional to the average axial velocity. It can be confirmed that the temperature differences shown on the graph are indeed inversely proportional to the average axial velocities given in the preceding paragraph.

If the momentum equation is averaged over a cross section, the buoyancy force is found to be proportional to the average temperature $\bar{\Phi}$. The quantity $\bar{\Phi}$ is not the same as the bulk temperature Φ_b because the bulk temperature is a *velocity*-weighted average. For the $\alpha = 10$ deg case (Fig. 18), near the entrance to the cooling section, the region of higher temperature is associated with higher velocity. Thus, the bulk temperature Φ_b will tend to be larger than the average temperature $\bar{\Phi}$ (which is not velocity weighted). Similarly, near the heating section entrance, the region of higher temperature is associated with low or even negative velocity. Thus the bulk temperature will tend to be lower in this region than the average temperature. As the tilt angle increases, and the flow reversals diminish, the average temperature $\bar{\Phi}$ deviates less from the bulk temperature Φ_b (Figs. 19 and 20). Note that the flow reversals are associated with a "cold spot" near the cooling section entrance, and a "hot spot" near the heating section entrance. This is important in understanding how the average axial velocity varies with tilt angle.

Figure 21 shows the peripherally averaged quantity $\overline{f\mathrm{Re}}$ as a function of θ, for all three tilt angles. Note that once again the abscissa is $\theta - \alpha + 10$ deg. The cooling and heating section entrances are at $\theta - \alpha + 10$ deg = 10 deg and 190 deg, respectively, for all three cases.

By definition, the wall shear stress is positive when it opposes the main flow, i.e., when it acts in the negative θ direction. In the flow reversal regions, the wall shear stress is locally negative, since it acts in the same direction as the main flow (i.e., it opposes the reversed flow). For $\alpha = 10$ deg, the average friction drops rapidly near the cooling and heating section entrances, because the negative friction near the inner wall more than compensates for any increased positive friction near the outer wall. For $\alpha = 45$ deg, the flow reversals are not as strong as for $\alpha = 10$ deg, and therefore $\overline{f\mathrm{Re}}$ does not decrease as much near the cooling and heating section entrances. For the $\alpha = 90$ deg case there is no flow reversal. Cooling begins at the top of the loop, and the colder fluid near the wall accelerates, causing $\overline{f\mathrm{Re}}$ to increase as soon as the fluid enters the cooling section ($\theta - \alpha + 10$ deg = 10 deg). Similarly, heating begins at the bottom of the loop, and the hotter fluid near the wall accelerates, causing $\overline{f\mathrm{Re}}$ to increase when the fluid enters the heating section ($\theta - \alpha + 10$ deg = 190 deg). The fact that the flow reversal regions tend to *decrease* the peripherally averaged wall friction is important in understanding how the average axial velocity varies with tilt angle.

The peripherally averaged Nusselt number $\overline{\mathrm{Nu}}$ is shown in Fig. 22 as a function of θ for all three tilt angles. The Nusselt number decreases rapidly near the cooling and heating section entrances, as a thermal boundary layer develops. Throughout the remainder of the thermosyphon, however, $\overline{\mathrm{Nu}}$ varies nonmonotonically with θ, in a complicated manner which has not been predicted by any of the earlier analyses. Furthermore, $\overline{\mathrm{Nu}}$ is substantially larger than for laminar flow in a straight pipe. This fact has been experimentally observed by Creveling et al. [10].

Discussion of the Average Axial Velocity

The axial momentum equation, when averaged over the entire volume of the thermosyphon, reduces (to a very close approximation [19]) to a balance between the total buoyancy and total wall frictional forces:

"total buoyancy" = "total friction"

$$\int_0^{2\pi} \bar{\Phi} \cos\theta d\theta = \frac{2\bar{w}}{\pi^2} \int_0^{2\pi} \frac{\overline{f\mathrm{Re}}}{16} d\theta$$

Thus

$$\bar{w} = \frac{\frac{\pi}{4} \int_0^{2\pi} \bar{\Phi} \cos\theta d\theta}{\frac{1}{2\pi} \int_0^{2\pi} \frac{\overline{f\mathrm{Re}}}{16} d\theta}$$

Table 1 lists the quantities $(\pi/4) \int_0^{2\pi} \bar{\Phi} \cos\theta d\theta$, $(1/2\pi) \int_0^{2\pi} \overline{f\mathrm{Re}}/16\, d\theta$, and $\bar{w}$ for the one-, two-, and three-dimensional analyses, for the three cases considered in the current study. The two-dimensional results are from Mertol et al. [15], for the case of zero tilt angle. The one-dimensional results are derived using the analysis of Greif et al. [13], with the inclusion of a variable tilt angle. For the one-dimensional analysis, the values $\overline{f\mathrm{Re}} = 16$ and $\overline{\mathrm{Nu}} = 3.658$ (in the cooling section) are used, based on the result for fully developed laminar flow and heat transfer in a straight pipe with a constant wall temperature.

First consider the three-dimensional results. As described earlier, the friction generally increases with increasing tilt angle, due in part to the weaker flow reversals for the higher tilt angles. This result was not expected. Indeed, Damerell and Schoenhals [11] suggested that the flow reversal regions cause *increased* friction, and they used this to explain why their one-dimensional analysis overpredicted the average velocity for tilt angles between 0 and 60 deg. While this explanation seemed plausible at the time, the results of the current study indicate a different interpretation. In agreement with experimental observation [10], the friction in the thermosyphon is indeed found to be greater than for fully developed laminar flow in a straight pipe (i.e., $\overline{f\mathrm{Re}} = 16$). However, the flow reversals which occur for low tilt angles actually *reduce* the friction relative to the higher tilt angle cases. The current analysis demonstrates that the flow reversals also substantially decrease the total buoyancy (as shall soon be reiterated) and this is the cause of the reduced velocity for the lower tilt angles.

The total buoyancy varies nonmonotonically with tilt angle, due to two competing effects. The first is that as the tilt angle increases, the colder fluid moves toward the bottom half of the loop, while the hotter fluid moves toward the top half of the loop. This causes the total buoyancy to decrease. Thus, in the absence of any other effect, tilting the loop would cause the total buoyancy to *decrease* with increasing tilt angle. The second effect is related to the flow reversals. Flow reversals cause a "cold spot" in the cooling section at a location where the main flow is rising, and a "hot spot" in the heating section at a location where the main flow is falling. Thus, the flow reversals decrease the total buoyancy. It has been shown previously that flow reversals are strongest for low tilt angles, and diminish as the tilt angle increases. Thus, in the absence of any other effect, the diminishing of the flow reversals would cause the total buoyancy to *increase* with increasing tilt angle. This latter effect dominates for low tilt angles, so that the total buoyancy *increases* for tilt angles between $\alpha = 10$ and 45 deg. The former effect dominates for higher tilt angles, so that the total buoyancy *decreases* between $\alpha = 45$ and 90 deg. The net result is that the average axial velocity, like the total buoyan-

Table 1 Comparison of wall friction, buoyancy, and average axial velocity for one-, two-, and three-dimensional analyses

	Three-dimensional			One-dimensional			Two-dimensional
α	10 deg	45 deg	90 deg	10 deg	45 deg	90 deg	0 deg
$\frac{1}{2\pi}\int_0^{2\pi} \frac{\overline{fRe}}{16} d\theta$	1.05	1.19	1.44	1.00	1.00	1.00	1.05
$\frac{\pi}{4}\int_0^{2\pi} \bar{\Phi} \cos\theta d\theta$	0.87	1.09	0.96	1.00	0.90	0.52	0.97
$\bar{w}$	0.82	0.92	0.67	1.00	0.90	0.52	0.92
Percent difference in w relative to three-dimensional case				21 percent	−2 percent	−22 percent	12 percent

cy, varies nonmonotonically with tilt angle, increasing between $\alpha = 10$ and 45 deg, and decreasing between $\alpha = 45$ and 90 deg.

The one-dimensional analysis assumed a value of 16 for $\overline{fRe}$, which in general is seen to be inaccurate. The one-dimensional analysis also yields an inaccurate prediction of the total buoyancy. For the $\alpha = 10$ deg case, the bulk and average temperatures differ substantially (see Fig. 18). The three-dimensional analysis shows that, as compared to the bulk temperature, the average temperature drops more rapidly near the cooling section entrance and rises more quickly near the heating section entrance. As mentioned earlier, this tends to reduce the total buoyancy. Thus, the one-dimensional analysis, which neglects this effect, overpredicts the total buoyancy for the $\alpha = 10$ deg case. For the $\alpha = 45$ and 90 deg cases, however, the average temperature does not differ greatly from the bulk temperature (see Figs. 19 and 20). The error in the one-dimensional analysis for these two cases is probably due mainly to the $\overline{Nu} = 3.658$ assumption. The true Nusselt number in the cooling section is considerably higher than 3.658 (see Fig. 22), causing a greater decrease in the bulk temperature in the cooling section. For the $\alpha = 45$ and 90 deg cases, most (or all) of the cooling section is in the left-hand side of the loop, where the flow is falling. Thus the lower bulk temperature in the cooling section tends to drive the flow, and the total buoyancy is increased. Therefore, since the one-dimensional analysis uses a Nusselt number which is too low, it underpredicts the total buoyancy for the $\alpha = 45$ and 90 deg cases. Due to the inaccuracy in predictions of the total friction and the total buoyancy, the one-dimensional analysis predicts values of the average axial velocity which are in error by between −22 and +21 percent, and perhaps more importantly, it does not predict the nonmonotonic variation of the velocity with tilt angle.

The two-dimensional analysis yields an excellent estimate of the total frictional force for the single case presented (assuming that the results for $\alpha = 0$ deg would be approximately the same as for $\alpha = 10$ deg). The predicted total buoyancy, however, is substantially in error. This is due to the neglect of three-dimensional effects and the consequent inability to predict the flow reversals. In the absence of flow reversal, the bulk and average temperatures differ much less. Thus, while the two-dimensional analysis does *not* make the assumption that the bulk and average temperatures are equal, the result is much the same as if it did. Therefore, like the one-dimensional analysis of the 10 deg case, the two-dimensional analysis overpredicts the total buoyancy. Consequently, the average axial velocity is also overpredicted by 12 percent. It would be very interesting to see how accurate the two-dimensional analysis would be for the higher tilt angle cases, for which the bulk and average temperatures do not differ as greatly.

Conclusions

The results of this analysis have revealed some interesting and important characteristics of the flow and heat transfer in a toroidal thermosyphon. The most significant of these are:

1 The flow is strongly three dimensional.

2 The friction factor and Nusselt number vary around the loop in a complicated manner not predicted by earlier analyses, and they are both higher than for fully developed laminar flow in a straight pipe.

3 Regions of streamwise flow reversal are predicted for the low tilt angle cases.

4 The flow reversals cause the friction to *decrease*, contrary to what may have been expected.

5 The flow reversals cause the total buoyancy to decrease. This effect has apparently not been recognized previously in the literature.

6 The flow reversals have a strong effect on the average axial velocity (due to points 4 and 5).

It is recognized that the applicability of these results to real systems is limited by the low value of the Grashof number and by the simplicity of the geometry. However, the phenomena which are predicted in these numerical calculations have also been experimentally observed for higher Grashof numbers, and so it is believed that these numerical results are valuable in understanding the physics of the flow and heat transfer in a toroidal thermosyphon. Furthermore, flow reversals may be found in other natural or mixed convection flows in which there is a change in the thermal boundary conditions, and so these results have qualitative application to a broader class of problems.

Acknowledgments

The authors gratefully acknowledge the support received from the National Science Foundation and from IBM.

References

1 Japikse, D., "Advances in Thermosyphon Technology," in: *Advances in Heat Transfer*, T. F. Irvine, Jr. and J. P. Hartnett, eds., Vol. 9, Academic Press, New York, 1973, pp. 1–111.

2 Ostrach, S., "Natural Convection in Enclosures," in: *Advances in Heat Transfer*, T. F. Irvine, Jr. and J. P. Hartnett, eds., Vol. 8, Academic Press, New York, 1972, pp. 161–227.

3 McKee, H. R., "Thermosiphon Reboilers—A Review," *Ind. Engng. Chem.*, Vol. 62, 1970, pp. 76–82.

4 Zvirin, Y., "A Review of Natural Circulation Loops in Pressurized Water Reactors and Other Systems," *Nuclear Engng. and Design*, Vol. 67, 1981, pp. 203–225.

5 Mertol, A., Place, W., Webster, T., and Greif, R., "Detailed Loop Model

(DLM) Analysis of Liquid Solar Thermosyphons With Heat Exchangers," *Solar Energy*, Vol. 27, 1981, pp. 367–386.

6 Norton, B., and Probert, S. D., "Natural-Circulation Solar-Energy Stimulated Systems for Heating Water," *Applied Energy*, Vol. 11, 1982, pp. 167–196.

7 Mertol, A., and Greif, R., "A Review of Natural Circulation Loops," in: *Natural Convection: Fundamentals and Applications*, S. Kakac, W. Aung, and R. Viskanta, eds., Hemisphere, Washington, D.C., 1985, pp. 1033–1071.

8 Welander, P., "On the Oscillatory Instability of a Differentially Heated Fluid Loop," *J. Fluid Mech.*, Vol. 29, 1967, pp. 17–30.

9 Keller, J. B., "Periodic Oscillations in a Model of Thermal Convection," *J. Fluid Mech.*, Vol. 26, 1966, pp. 599–606.

10 Creveling, H. F., De Paz, J. F., Baladi, J. Y., and Schoenhals, R. J., "Stability Characteristics of a Single-Phase Free Convection Loop," *J. Fluid Mech.*, Vol. 67, 1975, pp. 65–84.

11 Damerell, P. S., and Schoenhals, R. J., "Flow in a Toroidal Thermosyphon With Angular Displacement of Heated and Cooled Sections," ASME JOURNAL OF HEAT TRANSFER, Vol. 101, 1979, pp. 672–676.

12 Ramos, E., Sen, M., and Treviño, C., "A Steady-State Analysis for Variable Area One- and Two-Phase Thermosyphon Loops," *Int. J. Heat Mass Transfer*, Vol. 28, No. 9, 1985, pp. 1711–1719.

13 Greif, R., Zvirin, Y., and Mertol, A., "The Transient and Stability Behavior of a Natural Convection Loop," ASME JOURNAL OF HEAT TRANSFER, Vol. 101, 1979, pp. 684–688.

14 Mertol, A., Lavine, A., and Greif, R., "A Study of the Variation of the Pressure in a Natural Circulation Loop," *Int. J. Heat Mass Transfer*, Vol. 27, 1984, pp. 626–630.

15 Mertol, A., Greif, R., and Zvirin, Y., "Two-Dimensional Study of Heat Transfer and Fluid Flow in a Natural Convection Loop," ASME JOURNAL OF HEAT TRANSFER, Vol. 104, 1982, pp. 508–514.

16 Mertol, A., Greif, R., and Zvirin, Y., "Two Dimensional Analysis of Transient Flow and Heat Transfer in a Natural Circulation Loop," *Wärme- und Stoffübertragung*, Vol. 18, 1984, pp. 89–98.

17 Stern, C., and Greif, R., "Measurements in a Natural Convection Loop," in preparation.

18 Gorman, M., Widmann, P. J., and Robbins, K. A., "Chaotic Flow Regimes in a Convection Loop," *Physical Review Letters*, Vol. 52, No. 25, 1984, pp. 2241–2244.

19 Lavine, A. G., "A Three-Dimensional Analysis of Natural Convection in a Toroidal Loop," Ph.D. Dissertation, University of California, Berkeley, 1984.

20 Gosman, A. D., and Ideriah, F. J. K., "TEACH-2E: A General Computer Program for Two-Dimensional, Turbulent, Recirculating Flows," Imperial College, London; available as Department of Mechanical Engineering Report No. FM-83-2, University of California, Berkeley, 1983.

21 Patankar, S. V., *Numerical Heat Transfer and Fluid Flow*, McGraw-Hill, New York, 1980.

22 Humphrey, J. A. C., "Numerical Calculation of Developing Laminar Flow in Pipes of Arbitrary Curvature Radius," *Canadian J. Chem. Engng.*, Vol. 56, 1978, pp. 151–164.

Numerical Calculation of Three-Dimensional Turbulent Natural Convection in a Cubical Enclosure Using a Two-Equation Model for Turbulence

H. Ozoe

A. Mouri

M. Hiramitsu

Department of Industrial and Mechanical Engineering,
School of Engineering,
Okayama University,
Okayama 700 Japan

S. W. Churchill

Department of Chemical Engineering,
University of Pennsylvania,
Philadelphia, PA 19104 U.S.A.

N. Lior

Department of Mechanical Engineering and Applied Mechanics,
University of Pennsylvania,
Philadelphia, PA 19104 U.S.A.

This paper presents a model and numerical results for turbulent natural convection in a cubical enclosure heated from below, cooled on a portion of one vertical side wall and insulated on all other surfaces. Three-dimensional balances were derived for material, energy, and the three components of momentum, as well as for the turbulent kinetic energy k *and the rate of dissipation of turbulent kinetic energy* ϵ. *The constants used in the model were the same as those used by Fraikin et al. for two-dimensional convection in a channel. Illustrative transient calculations were carried out for* $Ra = 10^6$ *and* 10^7 *and* $Pr = 0.7$. *Both the dominant component of the vector potential and the Nusselt number were found to converge to a steady state. Isothermal lines and velocity vectors for vertical cross sections normal to the cooled wall indicated three-dimensional effects near the side walls. A top view of the velocity vectors revealed a downward spiral flow near the side walls along the cooled vertical wall. A weak spiral flow was also found along the side walls near the wall opposing the partially cooled one. The highest values of the eddy diffusivity were 2.6 and 5.8 times the molecular kinematic viscosity for* $Ra = 10^6$ *and* 10^7, *respectively. A coaxial double spiral movement, similar to that previously reported for laminar natural convection, was found for the time-averaged flow field. This computing scheme is expected to be applicable to other thermal boundary conditions.*

1 Introduction

Turbulent natural convection is observed in many circumstances. The primary aim of this work was to study natural convection in large enclosures such as passive solar rooms with a heated floor and a cooled window. The method is also expected to be useful for turbulent natural convection in other applications such as for the equalization of temperature in a large nuclear reactor containment filled with fluid, and for removal of the heat generated within the casing of electronic equipment by integrated circuits. Natural convection in such applications necessarily becomes turbulent and three-dimensional due to the large scale of a solar room and/or the large temperature difference. Prior numerical calculations of turbulent natural convection have been limited primarily to boundary-layer flow and to two-dimensional flows in enclosures.

Turbulent free convection in the boundary layer along a vertical heated plate in an unconfined fluid has been computed by Plumb and Kennedy [1] and Lin and Churchill [2] using a two-equation model, and by Fujii and Fujii [3] using a Glushko model. Farouk and Güceri [4] computed turbulent free convection about a horizontal cylinder in an unconfined fluid using a k–ϵ model developed for forced convection.

Turbulent natural convection in a square channel with isothermally heated and cooled vertical walls and linear temperature profiles along the lower and upper horizontal boundaries was computed by Fraikin et al. [5], also using a two-equation model. Their calculations were for air at Grashof numbers of 10^7, 5×10^7, and 10^8, which they postulated to be in the turbulent regime. Their maximum computed turbulent viscosity ranged from 4 times the molecular viscosity at Gr = 10^7 to 9.6 times at 10^8. They carried out a sensitivity analysis of several of the constants in the k–ϵ model. Perturbation of $\pm$10–20 percent for the constants in the model caused $\pm$40–50 percent changes in the turbulent properties but only 10 percent or less in the Nusselt number. However, this result may be limited to their specific boundary conditions.

Farouk and Güceri [6] calculated turbulent natural convection for Ra up to 10^7 using a k–ϵ model in cylindrical coordinates for a horizontal concentric annulus whose inner cylinder was heated and outer cylinder cooled. They pointed out that at higher Rayleigh numbers a finer grid size would be necessary to compute the thin boundary layer next to the walls.

Ozoe et al. [7] developed a computing scheme using a k–ϵ model for two-dimensional turbulent natural convection in a long square channel heated on one vertical wall, cooled on the opposite one, and thermally insulated along the upper and lower horizontal walls. They carried out computations for water for Rayleigh numbers up to 10^{11} and obtained good agreement with experimental values for the overall Nusselt number and fair agreement for the time-averaged vertical velocity. The latter agreement was improved by using modified values for the empirical constants in the k–ϵ model as identified through a sensitivity analysis.

A primary objective of the present study was to develop a program for characterizing the heat transfer in a passive solar room which invokes three-dimensional turbulent natural convection. A cubical enclosure was chosen for modeling with the floor heated and part of one of the vertical walls cooled to simulate a window. This model also simulates natural convective cooling of the casing of electronic equipment. The two-dimensional computing scheme developed and verified experimentally by Ozoe et al. [7] was utilized for this three-dimensional problem.

Contributed by the Heat Transfer Division and presented at the 23rd National Heat Transfer Conference, Niagara Falls, NY, August 1984. Manuscript received by the Heat Transfer Division February 7, 1985.

2 Turbulent Mathematical Model

A direct extension of the two-dimensional mathematical model for turbulent natural convection used by Fraiklin et al. [5], Farouk and Güceri [6], and Ozoe et al. [7] was used in this three-dimensional investigation. As reported by Ozoe et al. [7], the k–ϵ model proposed for low-Reynolds-number flow by Jones and Launder [8] was found to produce a numerically unstable solution for natural convection in a two-dimensional channel and was therefore not employed herein.

The following seven equations represent in order and in dimensionless form the conservation of time-averaged momentum in the X, Y, and Z directions, of material, of energy, of turbulent kinetic energy, and of the rate of dissipation of turbulent kinetic energy.

The angle of inclination ϕ of the X axis from a horizontal plane about the horizontal Y axis was included in the equations. However, this angle of inclination was set to zero in the sample calculations in this work.

$$\frac{\partial U}{\partial \tau}+U\frac{\partial U}{\partial X}+V\frac{\partial U}{\partial Y}+W\frac{\partial U}{\partial Z}=\frac{\partial}{\partial X}\left[(\sigma+\nu_t^*)\left(\frac{\partial U}{\partial X}+\frac{\partial U}{\partial X}\right)\right]+\frac{\partial}{\partial Y}\left[(\sigma+\nu_t^*)\left(\frac{\partial U}{\partial Y}+\frac{\partial V}{\partial X}\right)\right]+\frac{\partial}{\partial Z}\left[(\sigma+\nu_t^*)\left(\frac{\partial U}{\partial Z}+\frac{\partial W}{\partial X}\right)\right]+\sigma\, T\sin\phi-\frac{\partial}{\partial X}\left(P+\frac{2}{3}K\right) \quad (1)$$

$$\frac{\partial V}{\partial \tau}+U\frac{\partial V}{\partial X}+V\frac{\partial V}{\partial Y}+W\frac{\partial V}{\partial Z}=\frac{\partial}{\partial X}\left[(\sigma+\nu_t^*)\left(\frac{\partial V}{\partial X}+\frac{\partial U}{\partial Y}\right)\right]+\frac{\partial}{\partial Y}\left[(\sigma+\nu_t^*)\left(\frac{\partial V}{\partial Y}+\frac{\partial V}{\partial Y}\right)\right]+\frac{\partial}{\partial Z}\left[(\sigma+\nu_t^*)\left(\frac{\partial V}{\partial Z}+\frac{\partial W}{\partial Y}\right)\right]-\frac{\partial}{\partial Y}\left(P+\frac{2}{3}K\right) \quad (2)$$

$$\frac{\partial W}{\partial \tau}+U\frac{\partial W}{\partial X}+V\frac{\partial W}{\partial Y}+W\frac{\partial W}{\partial Z}=\frac{\partial}{\partial X}\left[(\sigma+\nu_t^*)\left(\frac{\partial W}{\partial X}+\frac{\partial U}{\partial Z}\right)\right]+\frac{\partial}{\partial Y}\left[(\sigma+\nu_t^*)\left(\frac{\partial W}{\partial Y}+\frac{\partial V}{\partial Z}\right)\right]+\frac{\partial}{\partial Z}\left[(\sigma+\nu_t^*)\left(\frac{\partial W}{\partial Z}+\frac{\partial W}{\partial Z}\right)\right]-\sigma\, T\cos\phi-\frac{\partial}{\partial Z}\left(P+\frac{2}{3}K\right) \quad (3)$$

$$\frac{\partial U}{\partial X}+\frac{\partial V}{\partial Y}+\frac{\partial W}{\partial Z}=0 \quad (4)$$

$$\frac{\partial T}{\partial \tau}+U\frac{\partial T}{\partial X}+V\frac{\partial T}{\partial Y}+W\frac{\partial T}{\partial Z}=\frac{\partial}{\partial X}\left[\left(1+\frac{\nu_t^*}{\sigma_t}\right)\frac{\partial T}{\partial X}\right]+\frac{\partial}{\partial Y}\left[\left(1+\frac{\nu_t^*}{\sigma_t}\right)\frac{\partial T}{\partial Y}\right]+\frac{\partial}{\partial Z}\left[\left(1+\frac{\nu_t^*}{\sigma_t}\right)\frac{\partial T}{\partial Z}\right] \quad (5)$$

$$\frac{\partial K}{\partial \tau}+U\frac{\partial K}{\partial X}+V\frac{\partial K}{\partial Y}+W\frac{\partial K}{\partial Z}=\left(\sigma+\frac{\nu_t^*}{\sigma_k}\right)\left(\frac{\partial^2 K}{\partial X^2}+\frac{\partial^2 K}{\partial Y^2}+\frac{\partial^2 K}{\partial Z^2}\right)+\frac{1}{\sigma_k}\left(\frac{\partial \nu_t^*}{\partial X}\frac{\partial K}{\partial X}+\frac{\partial \nu_t^*}{\partial Y}\frac{\partial K}{\partial Y}+\frac{\partial \nu_t^*}{\partial Z}\frac{\partial K}{\partial Z}\right)+\nu_t\left[\left(\frac{\partial U}{\partial Y}+\frac{\partial V}{\partial X}\right)^2+\left(\frac{\partial V}{\partial Z}+\frac{\partial W}{\partial Y}\right)^2+\left(\frac{\partial W}{\partial X}+\frac{\partial U}{\partial Z}\right)^2+2\left(\frac{\partial U}{\partial X}\right)^2+2\left(\frac{\partial V}{\partial Y}\right)^2+2\left(\frac{\partial W}{\partial Z}\right)^2\right]-E-\sigma\frac{\nu_t^*}{\sigma_t}\left(\frac{\partial T}{\partial X}\sin\phi-\frac{\partial T}{\partial Z}\cos\phi\right) \quad (6)$$

$$\frac{\partial E}{\partial \tau}+U\frac{\partial E}{\partial X}+V\frac{\partial E}{\partial Y}+W\frac{\partial E}{\partial Z}=\left(\sigma+\frac{\nu_t^*}{\sigma_\epsilon}\right)\left(\frac{\partial^2 E}{\partial X^2}+\frac{\partial^2 E}{\partial Y^2}+\frac{\partial^2 E}{\partial Z^2}\right)+\frac{1}{\sigma_\epsilon}\left(\frac{\partial \nu_t^*}{\partial X}\frac{\partial E}{\partial X}+\frac{\partial \nu_t^*}{\partial Y}\frac{\partial E}{\partial Y}+\frac{\partial \nu_t^*}{\partial Z}\frac{\partial E}{\partial Z}\right)+C_1\frac{E}{K}\nu_t^*\left[\left(\frac{\partial U}{\partial Y}+\frac{\partial V}{\partial X}\right)^2+\left(\frac{\partial V}{\partial Z}+\frac{\partial W}{\partial Y}\right)^2+\left(\frac{\partial W}{\partial X}+\frac{\partial U}{\partial Z}\right)^2+2\left(\frac{\partial U}{\partial X}\right)^2+2\left(\frac{\partial V}{\partial Y}\right)^2+2\left(\frac{\partial W}{\partial Z}\right)^2\right]-C_2\frac{E^2}{K}-C_\epsilon\sigma\frac{E}{K}\left(\frac{\partial T}{\partial X}\sin\phi-\frac{\partial T}{\partial Z}\cos\phi\right)\frac{\nu_t^*}{\sigma_t} \quad (7)$$

The dimensionless eddy diffusivity is related as follows, per Jones and Launder [8], to the dimensionless time-averaged turbulent kinetic energy and the dimensionless time-averaged rate of dissipation of turbulent kinetic energy

Nomenclature

c_1 = parameter in k–ϵ model
c_2 = parameter in k–ϵ model
c_D = constant $= C_\mu^{3/4}$
c_μ = parameter in k–ϵ model
c_ϵ = parameter in k–ϵ model
D = y length of the enclosure, m
E = dimensionless time-averaged rate of dissipation of turbulent kinetic energy $= \epsilon/(\alpha^3 \mathrm{Ra}_L^{4/3}/L^4)$
g = acceleration due to gravity, m/s^2
H = height of the enclosure, m
$\bar{H}$ = dimensionless height of the enclosure $= \mathrm{Ra}_H^{1/3}$
K = dimensionless time-averaged turbulent kinetic energy $= k/[(\alpha/L)\mathrm{Ra}_L^{1/3}]^2$
k = turbulent kinetic energy $= (\overline{u'^2}+\overline{v'^2}+\overline{w'^2})/2$, m^2/s^2
L = x length of the enclosure, m
l = length scale, m
l_m = Prandtl mixing length, m
n = normal direction, m
Nu = overall Nusselt number
p = time-averaged pressure, Pa
Pr = Prandtl number $= \nu/\alpha$
Ra_L = Rayleigh number $= g\beta(\theta_h-\theta_l)L^3/(\alpha\nu)$
T = dimensionless time-averaged temperature
t = time, s
U = dimensionless time-averaged velocity in x direction $= u/[(\alpha/L)\mathrm{Ra}_L^{1/3}]$
u = component of time-averaged velocity in x direction, m/s
V = dimensionless time-averaged velocity in y direction $= v/[(\alpha/L)\ \mathrm{Ra}_L^{1/3}]$
v = component of time-averaged velocity in y direction, m/s
W = dimensionless time-averaged velocity in z direction $= w/[(\alpha/L)\ \mathrm{Ra}_L^{1/3}]$
w = component of time-averaged velocity in z direction, m/s
X = dimensionless x coordinate $= x/(L/\mathrm{Ra}_L^{1/3})$
x = horizontal coordinate, m

$$\nu_t^* = C_\mu \frac{K^2}{E} \tag{8}$$

The dimensionless time-averaged variables in the above equations are defined as

$$X=\frac{x}{x_0},\ Y=\frac{y}{y_0},\ Z=\frac{z}{z_0},\ U=\frac{u}{u_0},\ V=\frac{v}{v_0},\ W=\frac{w}{w_0},$$

$$\tau=\frac{t}{t_0},\ P=\frac{p}{p_0},\ K=\frac{k}{k_0},\ E=\frac{\epsilon}{\epsilon_0},\ T=\frac{\theta-\theta_0}{\theta_h-\theta_l},$$

$$\nu_t^*=\frac{\nu_t}{\nu_{t_0}},\ x_0=y_0=z_0=\left[\frac{g\beta(\theta_h-\theta_l)}{\alpha\nu}\right]^{-\frac{1}{3}}=\frac{L}{\mathrm{Ra}_L^{1/3}},$$

$$u_0=v_0=w_0=\frac{\alpha}{x_0}=\frac{\alpha}{L}\,\mathrm{Ra}_L^{1/3},\ p_0=\rho\alpha^2/x_0^2$$

$$=(\rho\alpha^2/L^2)\mathrm{Ra}_L^{2/3},$$

$$k_0=\left(\frac{\alpha}{x_0}\right)^2=\left(\frac{\alpha}{L}\,\mathrm{Ra}_L^{1/3}\right)^2,$$

$$\epsilon_0=\alpha^3/x_0^4=\alpha^3\mathrm{Ra}_L^{4/3}/L^4,\ \nu_{t_0}=\alpha,$$

and

$$t_0=\frac{x_0}{u_0}=L^2/(\mathrm{Ra}_L^{2/3}\alpha).$$

The equations for the conservation of momentum were cross-differentiated and subtracted to eliminate the pressure terms, resulting in the following three equations for the components of the vorticity

$$\frac{\partial\Omega_1}{\partial\tau}+U\frac{\partial\Omega_1}{\partial X}+V\frac{\partial\Omega_1}{\partial Y}+W\frac{\partial\Omega_1}{\partial Z}-\Omega_1\frac{\partial U}{\partial X}-\Omega_2\frac{\partial U}{\partial Y}$$
$$-\Omega_3\frac{\partial U}{\partial Z}=(\sigma+\nu_t^*)\left(\frac{\partial^2\Omega_1}{\partial X^2}+\frac{\partial^2\Omega_1}{\partial Y^2}+\frac{\partial^2\Omega_1}{\partial Z^2}\right)+\frac{\partial\nu_t^*}{\partial X}\frac{\partial\Omega_1}{\partial X}$$
$$+2\frac{\partial\nu_t^*}{\partial Y}\frac{\partial\Omega_1}{\partial Y}+2\frac{\partial\nu_t^*}{\partial Z}\frac{\partial\Omega_1}{\partial Z}-\frac{\partial\nu_t^*}{\partial Y}\frac{\partial\Omega_2}{\partial X}-\frac{\partial\nu_t^*}{\partial Z}\frac{\partial\Omega_3}{\partial X}$$
$$-\left(\frac{\partial^2\nu_t^*}{\partial Y^2}+\frac{\partial^2\nu_t^*}{\partial Z^2}\right)\Omega_1+\frac{\partial^2\nu_t^*}{\partial X\partial Y}\Omega_2+\frac{\partial^2\nu_t^*}{\partial X\partial Z}\Omega_3$$
$$+2\left[\frac{\partial^2\nu_t^*}{\partial X\partial Y}\frac{\partial W}{\partial X}+\frac{\partial^2\nu_t^*}{\partial Y^2}\frac{\partial W}{\partial Y}+\frac{\partial^2\nu_t^*}{\partial Y\partial Z}\frac{\partial W}{\partial Z}\right.$$
$$\left.-\left(\frac{\partial^2\nu_t^*}{\partial X\partial Z}\frac{\partial V}{\partial X}+\frac{\partial^2\nu_t^*}{\partial Y\partial Z}\frac{\partial V}{\partial Y}+\frac{\partial^2\nu_t^*}{\partial Z^2}\frac{\partial V}{\partial Z}\right)\right]$$
$$-\sigma\frac{\partial T}{\partial Y}\cos\phi \tag{9}$$

$$\frac{\partial\Omega_2}{\partial\tau}+U\frac{\partial\Omega_2}{\partial X}+V\frac{\partial\Omega_2}{\partial Y}+W\frac{\partial\Omega_2}{\partial Z}-\Omega_1\frac{\partial V}{\partial X}-\Omega_2\frac{\partial V}{\partial Y}$$
$$-\Omega_3\frac{\partial V}{\partial Z}=(\sigma+\nu_t^*)\left(\frac{\partial^2\Omega_2}{\partial X^2}+\frac{\partial^2\Omega_2}{\partial Y^2}+\frac{\partial^2\Omega_2}{\partial Z^2}\right)+2\frac{\partial\nu_t^*}{\partial X}\frac{\partial\Omega_2}{\partial X}$$
$$+\frac{\partial\nu_t^*}{\partial Y}\frac{\partial\Omega_2}{\partial Y}+2\frac{\partial\nu_t^*}{\partial Z}\frac{\partial\Omega_2}{\partial Z}-\frac{\partial\nu_t^*}{\partial X}\frac{\partial\Omega_1}{\partial Y}-\frac{\partial\nu_t^*}{\partial Z}\frac{\partial\Omega_3}{\partial Y}$$
$$+\frac{\partial^2\nu_t^*}{\partial X\partial Y}\Omega_1-\left(\frac{\partial^2\nu_t^*}{\partial X^2}+\frac{\partial^2\nu_t^*}{\partial Z^2}\right)\Omega_2+\frac{\partial^2\nu_t^*}{\partial Y\partial Z}\Omega_3$$
$$+2\left[\frac{\partial^2\nu_t^*}{\partial X\partial Z}\frac{\partial U}{\partial X}+\frac{\partial^2\nu_t^*}{\partial Y\partial Z}\frac{\partial U}{\partial Y}+\frac{\partial^2\nu_t^*}{\partial Z^2}\frac{\partial U}{\partial Z}\right.$$
$$\left.-\left(\frac{\partial^2\nu_t^*}{\partial X^2}\frac{\partial W}{\partial X}+\frac{\partial^2\nu_t^*}{\partial X\partial Y}\frac{\partial W}{\partial Y}+\frac{\partial^2\nu_t^*}{\partial X\partial Z}\frac{\partial W}{\partial Z}\right)\right]$$
$$+\sigma\left(\frac{\partial T}{\partial Z}\sin\phi+\frac{\partial T}{\partial X}\cos\phi\right) \tag{10}$$

$$\frac{\partial\Omega_3}{\partial\tau}+U\frac{\partial\Omega_3}{\partial X}+V\frac{\partial\Omega_3}{\partial Y}+W\frac{\partial\Omega_3}{\partial Z}-\Omega_1\frac{\partial W}{\partial X}-\Omega_2\frac{\partial W}{\partial Y}$$
$$-\Omega_3\frac{\partial W}{\partial Z}=(\sigma+\nu_t^*)\left(\frac{\partial^2\Omega_3}{\partial X^2}+\frac{\partial^2\Omega_3}{\partial Y^2}+\frac{\partial^2\Omega_3}{\partial Z^2}\right)+2\frac{\partial\nu_t^*}{\partial X}\frac{\partial\Omega_3}{\partial X}$$
$$+2\frac{\partial\nu_t^*}{\partial Y}\frac{\partial\Omega_3}{\partial Y}+\frac{\partial\nu_t^*}{\partial Z}\frac{\partial\Omega_3}{\partial Z}-\frac{\partial\nu_t^*}{\partial X}\frac{\partial\Omega_1}{\partial Z}-\frac{\partial\nu_t^*}{\partial Y}\frac{\partial\Omega_2}{\partial Z}$$
$$+\frac{\partial^2\nu_t^*}{\partial X\partial Z}\Omega_1+\frac{\partial^2\nu_t^*}{\partial Y\partial Z}\Omega_2-\left(\frac{\partial^2\nu_t^*}{\partial X^2}+\frac{\partial^2\nu_t^*}{\partial Y^2}\right)\Omega_3$$
$$+2\left[\frac{\partial^2\nu_t^*}{\partial X^2}\frac{\partial V}{\partial X}+\frac{\partial^2\nu_t^*}{\partial X\partial Y}\frac{\partial V}{\partial Y}+\frac{\partial^2\nu_t^*}{\partial X\partial Z}\frac{\partial V}{\partial Z}\right.$$

Nomenclature (cont.)

Y = dimensionless y coordinate = $y/(L/\mathrm{Ra}_L^{1/3})$
y = horizontal coordinate, m
Z = dimensionless vertical coordinate = $z/(L/\mathrm{Ra}_L^{1/3})$
z = vertical coordinate, m
α = thermal diffusivity, m^2/s
α_t = eddy diffusivity for heat transfer, m^2/s
β = volumetric coefficient of expansion with temperature, K^{-1}
ϵ = time-averaged rate of dissipation of turbulent kinetic energy, m^2/s^3
θ = temperature, K
θ_0 = $= (\theta_h + \theta_l)/2$, K
κ = von Karman's constant = 0.42
μ = viscosity, Pa•s
ν = kinematic viscosity = μ/ρ, m^2/s
ν_t = eddy diffusivity, m^2/s
ν_t^* = dimensionless eddy diffusivity = $\nu_t/\alpha = c_\mu K^2/E$
ρ = density, kg/m^3
σ = Prandtl number = ν/α
σ_K = Prandtl number for the turbulent kinetic energy
σ_t = turbulent Prandtl number = ν_t/α_t
σ_ϵ = Prandtl number for the rate of dissipation of turbulent kinetic energy
τ = dimensionless time = $t/[L^2/(\mathrm{Ra}_L^{2/3}\alpha)]$
τ_w = wall shear stress, N/m^2
ϕ = angle of inclination of the X axis of the cube from a horizontal plane about the horizontal Y axis
ψ_i = dimensionless time-averaged vector potential
Ω_i = dimensionless time-averaged vorticity

Subscripts

0 = dimensional reference value
1, 2, 3 = empirical constants of turbulent model, or x, y, and z directions
c = center or central-plane value
H = height as a reference value
h = heated wall
L = width as a reference value
l = cooled wall

$$-\left(\frac{\partial^2 \nu_t^*}{\partial X \partial Y}\frac{\partial U}{\partial X}+\frac{\partial^2 \nu_t^*}{\partial Y^2}\frac{\partial U}{\partial Y}+\frac{\partial^2 \nu_t^*}{\partial Y \partial Z}\frac{\partial U}{\partial Z}\right)\Bigg]$$

$$-\sigma \frac{\partial T}{\partial Y}\sin\phi \tag{11}$$

The dimensionless vorticity is here defined as follows:

$$\Omega=\begin{pmatrix}\Omega_1\\ \Omega_2\\ \Omega_3\end{pmatrix}=\begin{pmatrix}\dfrac{\partial W}{\partial Y}-\dfrac{\partial V}{\partial Z}\\ \dfrac{\partial U}{\partial Z}-\dfrac{\partial W}{\partial X}\\ \dfrac{\partial V}{\partial X}-\dfrac{\partial U}{\partial Y}\end{pmatrix} \tag{12}$$

The three-dimensional vector potential is related to the velocity vector as follows, thereby automatically satisfying the continuity equation:

$$\mathbf{V}=\begin{pmatrix}U\\ V\\ W\end{pmatrix}=\begin{pmatrix}\dfrac{\partial \psi_3}{\partial Y}-\dfrac{\partial \psi_2}{\partial Z}\\ \dfrac{\partial \psi_1}{\partial Z}-\dfrac{\partial \psi_3}{\partial X}\\ \dfrac{\partial \psi_2}{\partial X}-\dfrac{\partial \psi_1}{\partial Y}\end{pmatrix} \tag{13}$$

The vector potential is presumed to be solenoidal ($\nabla \cdot \psi = 0$), and the vector potential is therefore related to vorticity as follows:

$$\Omega=\nabla\times\mathbf{V}=-\nabla^2\psi \tag{14}$$

Ozoe et al. [7] performed a sensitivity analysis for the constants of k–ϵ turbulent model and determined different values for C_1 and σ_t rather than those listed below. However, since the applicability of these values for different geometric and thermal boundary conditions is not known, they were not employed herein. The following empirical constants recommended by Launder and Spalding [9] were used, except for C_ϵ in the buoyant term of the E equation, which was adopted from Fraikin et al. [5]: $C_\mu = 0.09$, $C_1 = 1.44$, $C_2 = 1.92$, $C_\epsilon = 0.7$, $\sigma_K = 1$, $\sigma_\epsilon = 1.3$, and $\sigma_t = 1$.

The boundary conditions for the cubic room shown in Fig. 1 are summarized as follows:

1 Temperature

$T=0.5$ at $Z = \mathrm{Ra}_H^{1/3} = \overline{H}$

$T=-0.5$ for $Z = 0.106\overline{H}$ to $0.679\overline{H}$ at $X = 0$.

$\partial T/\partial n = 0$ on all other walls.

2 Velocity

All components of the velocity are zero on the wall, i.e.,

$$\begin{aligned} U=V=W=0 \text{ at } X=0 \text{ and } \mathrm{Ra}_H^{1/3}(L/H)\\ Y=0 \text{ and } \mathrm{Ra}_H^{1/3}(D/H)\\ Z=0 \text{ and } \mathrm{Ra}_H^{1/3}\end{aligned} \tag{15}$$

3 Vorticity

The components of vorticity are extrapolated from the fluid velocity at one time step earlier. (This approximation holds rigorously at the final steady state.) Thus

$$\begin{aligned} &\Omega_1=0,\ \Omega_2=-\frac{\partial W}{\partial X},\ \Omega_3=\frac{\partial V}{\partial X} \text{ at } X=0 \text{ and } \mathrm{Ra}_H^{1/3}(L/H)\\ &\Omega_1=\frac{\partial W}{\partial Y},\ \Omega_2=0,\ \Omega_3=-\frac{\partial U}{\partial Y} \text{ at } Y=0 \text{ and } \mathrm{Ra}_H^{1/3}(D/H)\\ &\Omega_1=-\frac{\partial V}{\partial Z},\ \Omega_2=\frac{\partial U}{\partial Z},\ \Omega_3=0 \text{ at } Z=0 \text{ and } \mathrm{Ra}_H^{1/3}\end{aligned} \tag{16}$$

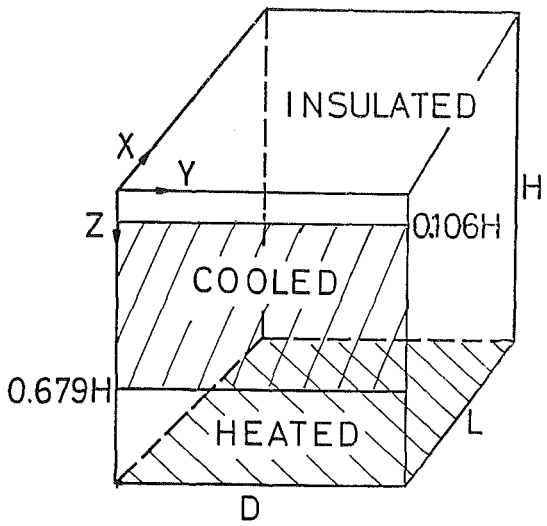

Fig. 1 Thermal boundary conditions for illustrative calculations for a cubical box

4 Vector potential

The following boundary conditions by Hirasaki and Hellums [10] for a rigid wall were adopted

$$\begin{aligned} &\frac{\partial \psi_1}{\partial X}=\psi_2=\psi_3=0 \text{ at } X=0 \text{ and } \mathrm{Ra}_H^{1/3}(L/H)\\ &\psi_1=\frac{\partial \psi_2}{\partial Y}=\psi_3=0 \text{ at } Y=0 \text{ and } \mathrm{Ra}_H^{1/3}(D/H)\\ &\psi_1=\psi_2=\frac{\partial \psi_3}{\partial Z}=0 \text{ at } Z=0 \text{ and } \mathrm{Ra}_H^{1/3}\end{aligned} \tag{17}$$

5 Dimensionless turbulent kinetic energy K

The turbulent kinetic energy K was set to zero on all of the walls.

6 Rate of dissipation of dimensionless turbulent kinetic energy E

The rate of dissipation of turbulent kinetic energy is proportional to $k^{3/2}/l$, where l is a characteristic length expressing the scale of the turbulence. Since both k and l are zero on the wall, the value of ϵ is indeterminant. However, the rate of dissipation ϵ at a short distance from the wall can be derived as follows according to Kawamura [11]. First, let

$$\epsilon = C_D \frac{k^{3/2}}{l} \tag{18}$$

where C_D is an unknown constant to be decided. Near the wall the characteristic length can be taken as equal to the Prandtl mixing length $l_m = l = \kappa y$ where y is the distance from the wall. Since $\tau_w = \rho \nu_t\, du/dy$ and $\nu_t = l_m^2\, du/dy$, $du/dy = u^*/l_m$ where u^* is the friction velocity $\sqrt{\tau_w/\rho}$. Then $\nu_t = l_m u^*$ and $\nu_t = C_\mu k^2/\epsilon = C_\mu k^{1/2} l_m / C_D$. Hence $k = (C_D u^*/C_\mu)^2$. Presuming local equilibrium, i.e., a rate of production equal to the rate of dissipation, then gives $|\overline{u'v'}|\, du/dy = \nu_t (du/dy)^2 = \epsilon$. Finally considering $\nu_t = C_\mu k^2/\epsilon$ and $du/dy = u^*/l$, we get $k = C_\mu (u^*)^2/C_D^2$. Hence $C_D = C_\mu^{3/4}$ and $\epsilon_{\Delta y} = C_\mu^{3/4} k^{3/2}/(\kappa \Delta y)$ at $y = \Delta y$. Fraikin et al. [5] used this approximation, although they did not describe the derivation in detail.

The E equation was solved only in a reduced region excluding the walls. A finite-difference approximation was developed for equations (5) to (7) and (9) to (12), using a first-order forward approximation for the time step and a second-order central difference for the length derivatives.

According to Ozoe et al. [7] too coarse a grid size in comparison to the velocity resulted in too large a cell Reynolds

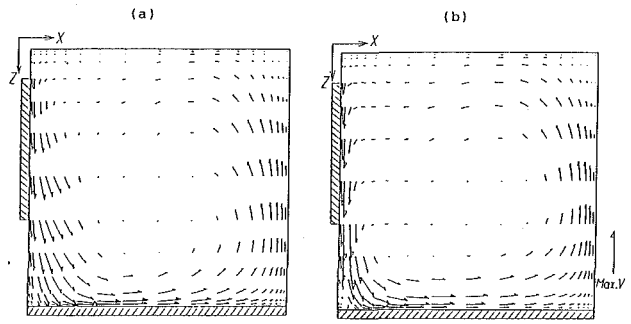

Fig. 2 Computed velocity vectors in vertical planes normal to the heated and cooled walls at Ra = 10^7 and Pr = 0.7: (a) Y = 0.05$\bar{H}$; (b) Y = 0.5$\bar{H}$

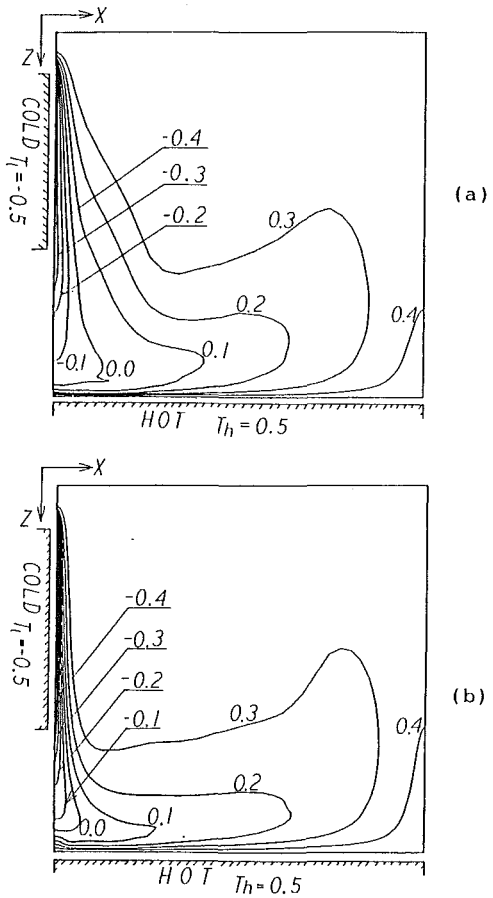

Fig. 3 Computed isothermal lines in vertical planes normal to the heated and cooled walls at Ra = 10^7 and Pr = 0.7: (a) Y = 0.05$\bar{H}$; (b) Y = 0.5$\bar{H}$

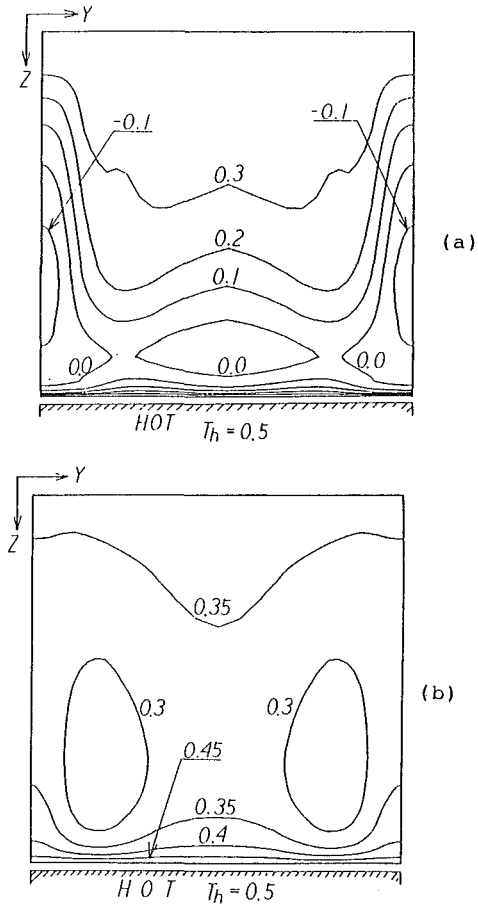

Fig. 4 Computed isothermal lines in vertical planes parallel to the cooled wall at Ra = 10^7 and Pr = 0.7: (a) X = 0.041$\bar{H}$; (b) X = 0.904$\bar{H}$

number and a strange mode of flow for two-dimensional turbulent natural convection. They therefore adopted a hybrid scheme suggested by Patankar [12] in which the upwind scheme was employed only when the matrix coefficient became negative. This scheme yielded the stable, experimentally observed mode of flow. A similar scheme was employed in this work. The numerical scheme of integration, which utilized the A.D.I. method, is the same as that of [7].

3 Computed Results

The turbulent regime begins at Gr = 10^9 for convection along a heated vertical wall in an unconfined fluid and at Ra = 2×10^4 for convection in an enclosure heated from below and cooled from above. The boundary conditions of this investigation encompass these two limiting cases. Hence the primary calculations were carried out for Ra = 10^6 and 10^7 and Pr = 0.7. The number of divisions are 20 by 10 by 10 for Ra = 10^6 and 24 by 10 by 14 for Ra = 10^7 in the X, Y, and Z directions, respectively. Closer spacings were employed near the surfaces except for the one in the Y direction at Ra = 10^6. The grid sizes were determined on a trial basis. At least two grid points were taken beteween the surface and the point of local peak velocity for the boundary-layer-type flow over the vertical cooled wall and over the hot horizontal floor. This scheme was based on the experience obtained from the computations for the two-dimensional turbulent natural convection by Ozoe et al. [7].

The overall Nusselt number on the heated floor and the Y component of the vector potential at the center of the region were used as a measure of convergence. The criterion of convergence was a relative change of the average Nusselt number on the heated floor of less than 10^{-4}. The Y component of the vector potential was also used as an indication of the trend of convergence. The number of iterations required for Ra = 10^6 was 1600 and for Ra = 10^7 was 1400. The initial condition for Ra = 10^6 was the numerical solution for the laminar model.

The converged overall Nusselt number on the heated floor was 6.04 at Ra = 10^6 and 13.27 at Ra = 10^7. The ratio of these two Nusselt numbers is 2.2, suggesting the proportionality of the overall Nusselt number to the 1/3 power of the Rayleigh number, as is known to hold for the turbulent regime.

Representative results, mostly for Ra = 10^7 and Pr = 0.7, are shown in graphic form as follows. The computed velocity vectors at a steady state of Ra = 10^7 and Pr = 0.7 are described in Fig. 2 for two vertical planes of constant Y. The length of the arrow represents the magnitude of the velocity projected on the indicated vertical X–Z plane. The velocity vectors at $Y = 0.21\bar{H}$ (not shown) and $0.5\ \bar{H}$ are similar to each other but that at $Y = 0.05\ \bar{H}$ differs greatly due to the

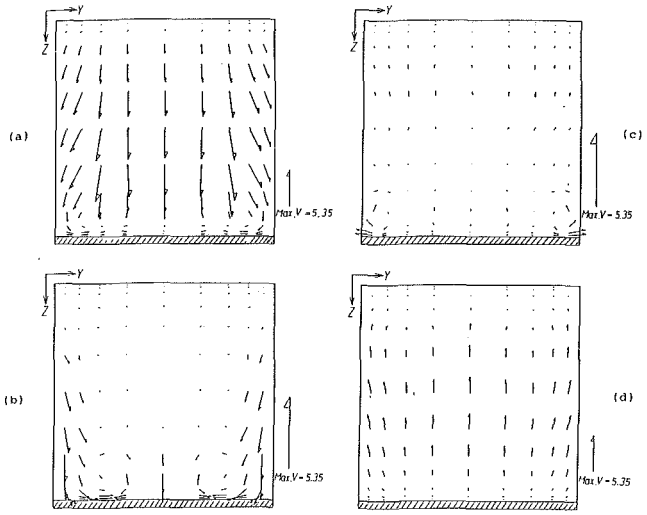

Fig. 5 Computed velocity vectors in vertical planes parallel to the cooled wall at Ra = 10^7 and Pr = 0.7: (*a*) $X = 0.016\bar{H}$; (*b*) $X = 0.14H$; (*c*) $X = 0.5\bar{H}$; (*d*) $X = 0.935\ \bar{H}$

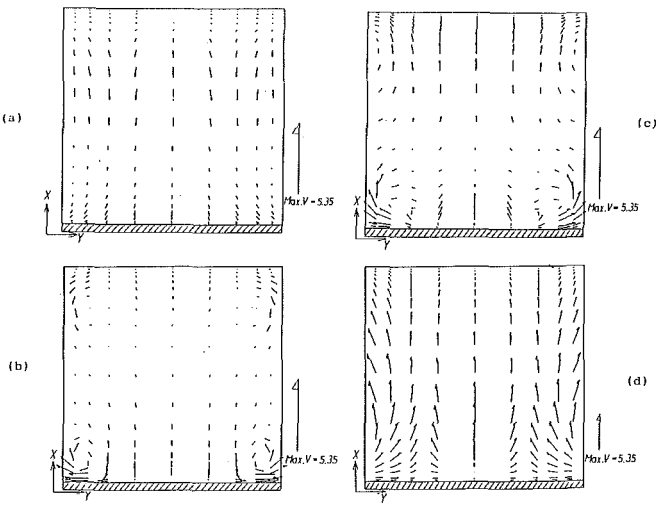

Fig. 6 Computed velocity vectors in horizontal planes at Ra = 10^7 and Pr = 0.7: (*a*) $Z = 0.05\bar{H}$; (*b*) $Z = 0.5\bar{H}$; (*c*) $Z = 0.79\bar{H}$; (*d*) $Z = 0.98\bar{H}$

presence of the wall and the resulting three-dimensional effect. Boundary-layer-type flow can be seen along the vertical cold window and the heated floor in Fig. 2(*b*).

The computed isothermal lines at Ra = 10^7 and Pr = 0.7 are shown in Fig. 3 for two vertical planes of constant Y and in Fig. 4 for two vertical planes of constant X. The isothermal lines are dense over the left window due to the cooling and also over the heated floor, especially under the window. The isothermal lines at $Y = 0.05\bar{H}$ differ from those at $Y = 0.5\bar{H}$ due to the presence of the side wall. The computed isothermal lines for two vertical planes of constant X can be seen in Fig. 4. The isothermal lines are symmetric with respect to $Y = 0.5\bar{H}$ due to the symmetric boundary condition. The symmetry of the computed values about $Y = 0.5\bar{H}$ assures to some extent the reliability of the computations. A cold area prevails along the side walls at $Y = 0$ and $\bar{H}$ as seen in Fig. 4(*a*) at $X = 0.041\bar{H}$, but in Fig. 4(*b*) at $X = 0.904\bar{H}$ two cold areas like cat eyes appear near the rear wall. These characteristics are apparently due to the three-dimensional effects.

The three dimensionality of the flow can also be seen in the vertical view of the velocity vectors as shown in Fig. 5 for various planes of X. These vectors are those seen from the window side. The symmetry with respect to $Y = 0.5\bar{H}$ is clear. The downward velocity near the $X = 0$ plane is described for $X = 0.016\bar{H}$ in Fig. 5(*a*). Near the rear wall at $X = 0.935\bar{H}$, the flow is upward as seen in Fig. 5(*d*). An interesting but weak pattern of flow can be seen at $X = 0.14\bar{H}$ and $0.5\bar{H}$ in Fig. 5(*b*) and Fig. 5(*c*), respectively. Near the side walls at $Y = 0$ and $\bar{H}$ in Fig. 5(*c*), a weak spiral motion appears to exist with its axis in the direction of the main flow.

The three dimensionality of the flow is best indicated by velocity vectors in the horizontal plane, as shown in Fig. 6 for various heights at Ra = 10^7. On the right-hand side of each graph, the arrow of the maximum velocity is drawn to indicate the relative magnitude of the velocity components. The flow pattern is symmetric with respect to the $Y = 0.5\bar{H}$ plane. The main flow near the top plane is toward the cooled window at $X = 0$, as seen in Fig. 6(*a*). Figure 6(*d*) shows flow in the reverse direction just above the floor, as expected from Fig. 2. However, as seen in Figs. 6(*b*) and 6(*c*) a secondary flow in the form of a spiral apparently occurs along the vertical corner over the cooled window adjacent to the two side walls. The velocity component in the Y direction is one order less than that in the X direction, and these spiral velocity components may not be strong enough to make a complete spiral at the indicated locations, even though they reveal some deflection from the main circulating flow.

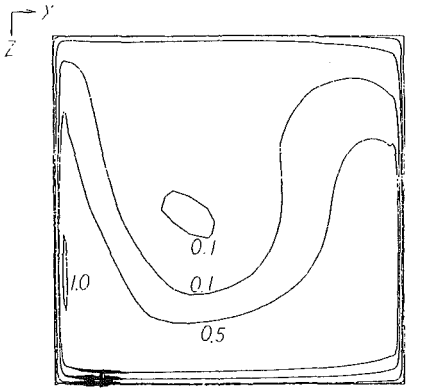

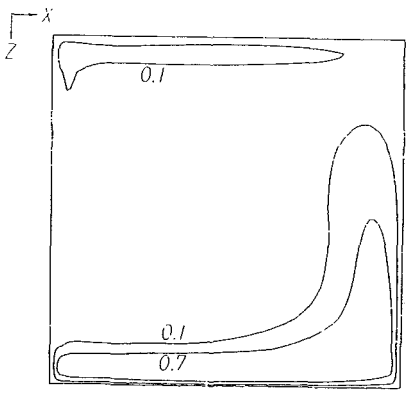

Fig. 7 Computed contours of the dimensionless eddy diffusivity in vertical planes perpendicular to the heated and cooled walls at Ra = 10^6 and Pr = 0.7: (*a*) $Y = 0.1\bar{H}$; (*b*) $Y = 0.5\bar{H}$

The turbulent intensity is not strong, and the maximum values of the dimensionless eddy diffusivity are 1.84 and 4.03 for Ra = 10^6 and 10^7, respectively. As shown in Table 1, these are 2.6 and 5.8 times the molecular kinematic viscosity. Contour maps of the eddy diffusivity at Ra = 10^6 are shown in Fig. 7, and those at Ra = 10^7 in Fig. 8. The peak value of ν_t^* occurs in the vertical plane $Y = 0.1\bar{H}$ at Ra = 10^6, and in the plane $Y = 0.05\bar{H}$ at Ra = 10^7 as shown in Figs. 7(*a*) and 8(*a*). The eddy diffusivity is also relatively large along the heated floor. Contour maps for a symmetric plane are shown in Figs. 7(*b*) and 8(*b*) for Ra = 10^6 and 10^7, respectively. The maximum eddy diffusivity probably occurs near the side

Table 1 Summary of the computed results

	Ra = 10^6	10^7
Nu on the floor	6.04	13.27
Dimensionless maximum velocity, W	3.025	5.350
Maximum of ν_t^*	1.84	4.03
Maximum of ν_t^*/ν	2.6	5.8

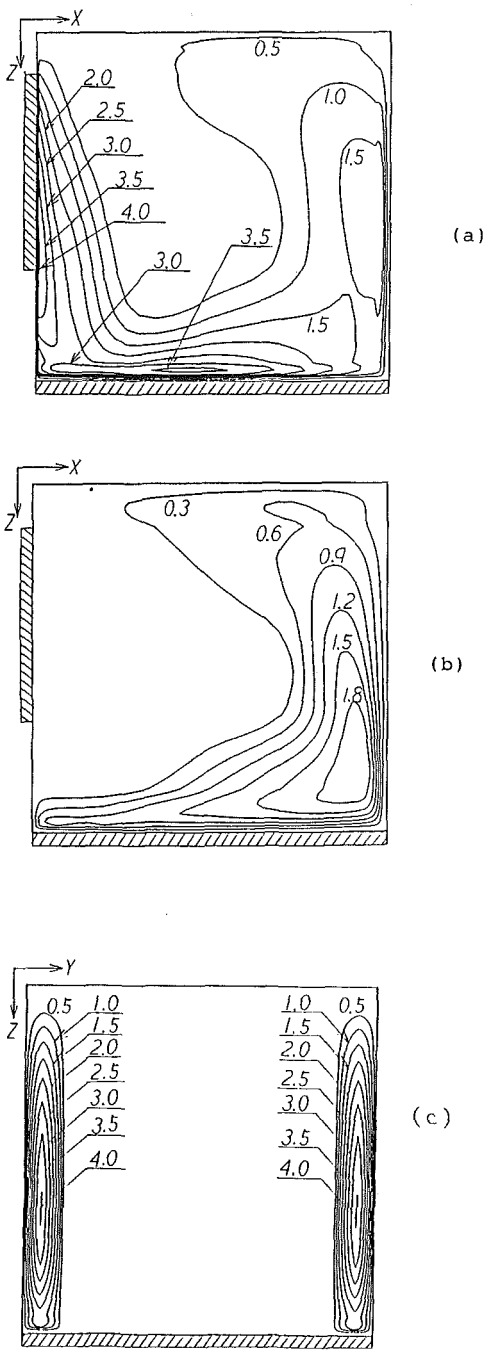

Fig. 8 Computed contours of the dimensionless eddy diffusivity in vertical planes at Ra = 10^7 and Pr = 0.7: (a) $Y = 0.05\bar{H}$; (b) $Y = 0.5\bar{H}$; (c) $X = 0.0046\bar{H}$

wall because of the downward spiral movement seen in Figs. 6(*b*) and 6(*c*). This is more evident in the contour maps of the eddy diffusivity in a vertical plane $X = 0.0046\bar{H}$ as seen from the cold window per Fig. 8(*c*). The eddy diffusivity has a peak value near the side walls adjacent to the corner over the vertical cooled window. These characteristics, which were observed for both Ra = 10^6 and 10^7, confirm the importance

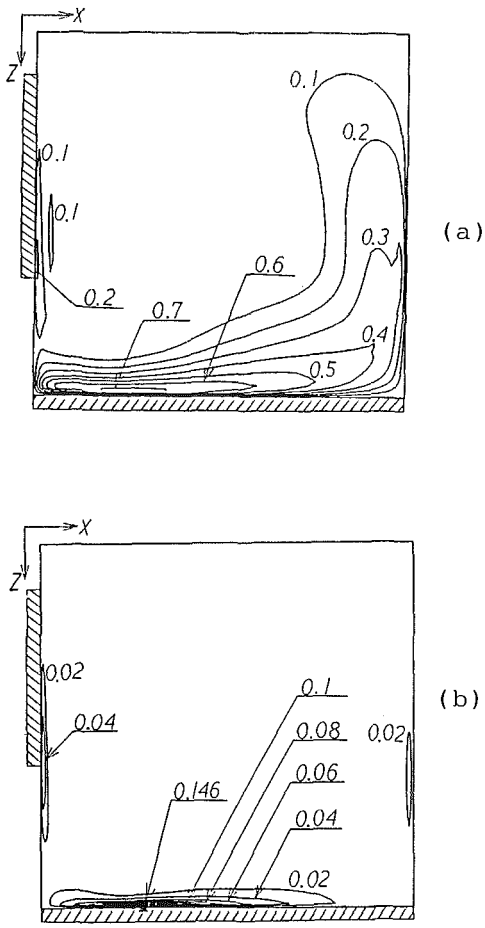

Fig. 9 Computed contours in a vertical plane at $Y = 0.5\bar{H}$ perpendicular to the heated and cooled walls at Ra = 10^7 and Pr = 0.7: (a) dimensionless time-averaged turbulent kinetic energy; (b) dimensionless time-averaged rate of dissipation of turbulent kinetic energy

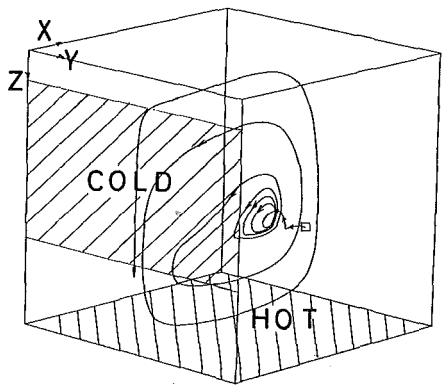

Fig. 10 Perspective view of a computed streakline for the time-averaged velocity: Ra = 10^6, Pr = 0.7; starting point (X_0, Y_0, Z_0) = ($0.66\bar{H}$, $0.7\bar{H}$, $0.63\bar{H}$); duration τ = 1500; eye point (X, Y, Z) = ($-12\bar{H}$, $12\bar{H}$, $-5\bar{H}$)

of three-dimensional computations for the turbulent convection.

The contour maps of the turbulent kinetic energy and the rate of dissipation of turbulent kinetic energy are shown in Fig. 9 at Ra = 10^7 and Pr = 0.7, both in the vertical plane of symmetry at $Y = 0.5\bar{H}$. The peak values of these turbulent properties occur both along the cold window and over the heated floor due to the strong shear in a fluid stream between a rigid wall and a stagnant core.

The flow characteristics can be identified more clearly from plots of streaklines than from the velocity vectors. Figure 10 is

a perspective view for Ra = 10^6 and Pr = 0.7 of the streakline for the time-averaged velocity of a particle starting from (X_0, Y_0, Z_0) = (0.66$\bar{H}$, 0.7$\bar{H}$, 0.63$\bar{H}$) as shown by the rectangular symbol. This streakline reveals the characteristic coaxial double spiral movement computed and observed experimentally by Ozoe et al. [13] for laminar natural convection in various enclosures. The particle should return to the starting point following a reduction in its radius of circulation near $Y = \bar{H}$. The axis of the strong circulating flow is not at the center of the X–Z cross section but lower and away from the cooled area due to the nonsymmetric thermal boundary conditions. The velocity is very slow at the initial, small radius of circulation due to the rather stagnant core. However, once the particle joins the main flow along the walls, its circulating velocity increases greatly. In this example, 80 percent of the time of the particle generating this streakline was spent in the central spiral of small radius. This result suggests that such a spiral movement exists for the time-averaged velocity field even in the turbulent regime in spite of significant differences in the geometric and thermal boundary conditions, and also that this spiral movement is a general characteristic of natural convection in a confined regime.

Although the computation was limited up to Ra = 10^7 due to the computational time of more than an hour, the scheme itself would be expected to be applicable at least up to Ra = 10^{11}, if a finer grid size were used, based on our experience with two-dimensional natural convection in [7].

Summary

A three-dimensional k–ϵ model for turbulent natural convection in a cubical room heated on the floor and cooled on a part of one of the vertical walls was solved numerically for Ra = 10^6 and 10^7 and Pr = 0.7. The maximum eddy diffusivity was 2.6 and 5.8 times the molecular kinematic viscosity at Ra = 10^6 and 10^7, respectively. The overall Nusselt numbers on the heated floor were 6.04 and 13.27 for Ra = 10^6 and 10^7, respectively, suggesting proportionality of the Nusselt number to the 1/3 power of the Rayleigh number.

Complicated spiral vectors were found to exist in the downward and horizontal time-averaged flows both for Ra = 10^6 and 10^7.

The computed values of all variables were found to be symmetric in terms of the central vertical plane normal to the cooled area, thus confirming to some extent the reliability of the computations. A coaxial double spiral movement, similar to that previously reported for laminar natural convection, was found for the time-averaged flow field.

The computational scheme developed herein is expected to be applicable for other thermal boundary conditions which generate turbulent three-dimensional natural convection in a confined regime.

Although the computed results in this paper are for a cubical enclosure oriented horizontally, and for a particular set of boundary conditions, the finite-difference model is applicable for other aspect ratios, arbitrary boundary conditions, and arbitrary inclinations.

Experimental measurements apparently do not exist to test these particular computations critically. However, the model itself has been tested and found to be reliable for closely related two-dimensional convection [7].

The computations were necessarily limited by computer demands to 24 grids or fewer in each direction. However, based on tests of similar two-dimensional calculations, this grid is presumed to be sufficient to reveal the correct pattern of flow.

Acknowledgments

A part of this work was supported by a Grant in Aid for Scientific Research on Energy Problems sponsored by the Ministry of Education, Science and Culture, Japan. The computations were carried out on Acos 1000, at the Okayama University Computer Center.

References

1 Plumb, O. A., and Kennedy, L. A., "Application of a k–ϵ Turbulence Model to Natural Convection From a Vertical Isothermal Surface," ASME JOURNAL OF HEAT TRANSFER, Vol. 99C, 1977, pp. 79–85.

2 Lin, S. J., and Churchill, S. W., "Turbulent Free Convection From a Vertical Isothermal Plate," *Num. Heat Transfer*, Vol. 1, 1978, pp. 129–145.

3 Fujii, M., and Fujii, T., "Numerical Calculation of Turbulent Free Convection Along a Vertical Plate," *Trans. JSME*, Vol. 43, No. 374, 1977, pp. 3825–3834; Vol. 44, No. 384, 1978, pp. 2797–2807.

4 Farouk, B., and Güceri, S. I., "Natural Convection From a Horizontal Cylinder—Turbulent Regime," ASME JOURNAL OF HEAT TRANSFER, Vol. 104C, 1982, pp. 228–235.

5 Fraikin, M. P., Portier, J. J., and Fraikin, C. J., "Application of a k–ϵ Turbulence Model to an Enclosed Buoyancy-Driven Recirculating Flow," *19th ASME-AIChE Nat. Heat Transfer Conf.*, Orlando, Florida, 1980, Paper No. 80-HT-68.

6 Farouk, B., and Güceri, S. J., "Laminar and Turbulent Natural Convection in the Annulus Between Horizontal Concentric Cylinders," ASME JOURNAL OF HEAT TRANSFER, Vol. 104, 1982, pp. 631–636.

7 Ozoe, H., Mouri, A., Ohmuro, M., Churchill, S. W., and Lior, N., "Numerical Calculations of Laminar and Turbulent Natural Convection in Water in Rectangular Channels Heated and Cooled Isothermally on the Opposing Vertical Walls," *Int. J. Heat Mass Transfer*, Vol. 28, No. 1, 1985, pp. 125–138.

8 Jones, W. P., and Launder, B. E., "The Prediction of Laminarization With a Two-Equation Model of Turbulence," *Int. J. Heat Mass Transfer*, Vol. 15, 1972, pp. 301–314.

9 Launder, B. E., and Spalding, D. B., "The Numerical Computation of Turbulent Flows," *Comp. Meth. Appl. Mech. and Eng.*, Vol. 3, 1974, pp. 269–289.

10 Hirasaki, G. J., and Hellums, J. D., "A General Formulation of the Boundary Conditions on the Vector Potential in Three-Dimensional Hydrodynamics," *Quart. Appl. Math.*, Vol. 26, 1968, pp. 331–342.

11 Kawamura, H., private communication.

12 Patankar, S. V., *Studies in Convection*, Vol. 1, B. E. Launder, ed., Academic Press, New York, 1975.

13 Ozoe, H., Sato, N., and Churchill, S. W., "Experimental Confirmation of the Three-Dimensional Helical Streaklines Previously Computed for Natural Convection in Inclined Rectangular Enclosures," *Kagaku Kogaku Ronbunshu*, Vol. 5, 1979, pp. 19–25 (in Japanese); English translation, *International Chem. Eng.*, Vol. 19, 1979, pp. 454–462.

D. Littlefield
Weyerhauser Fellow.

P. Desai
Assoc. Professor.

School of Mechanical Engineering,
Georgia Institute of Technology,
Atlanta, GA 30332

Buoyant Laminar Convection in a Vertical Cylindrical Annulus

Solution to natural convective motion in a vertical cylindrical annulus of large aspect ratio is examined, with the inner wall subject to a constant heat flux. Similar transformations of the appropriately simplified Navier-Stokes model of the annular flow are sought. The issue of boundary condition limitations for the considered flow is resolved in terms of acceptable error bounds for valid solutions. Results are generated for a variety of outer wall boundary conditions over various ranges of the Rayleigh number, highlighting the effects on the patterns of streamlines and "heatlines." Correlations presented for the Nusselt number are shown to be dependent on both the boundary conditions and the geometry.

Introduction

This work examines temperature-induced buoyant convection in a uniform section annulus of large aspect ratio, subject to a constant heat flux at the inner wall. Isothermal and constant heat flux conditions at the outer wall are considered. Previous research for this geometry includes several analytical studies for isothermal boundary conditions, as well as a few experimental investigations for the present boundary conditions. The heat flux condition at the outer wall has not been studied previously, and serves as a supplement to the study of this configuration.

Numerical studies are available for natural convection in a vertical annulus for respective ranges of Prandtl number, radius ratio, aspect ratio, and Rayleigh number given at $0.5 \le \mathrm{Pr} \le 5$, $1 \le R \le 4$, $1 \le A \le 20$, and $\mathrm{Ra}_c \le 2 \times 10^5$ [1]. For $\mathrm{Pr} = 1$ and $\mathrm{Ra}_c \le 10^5$, a unicellular flow was discovered, while at larger Ra_c, multicellular flow was observed. For both walls isothermal, a correlation of the form

$$\mathrm{Nu} = \Phi(\mathrm{Pr}, R)\,\mathrm{Ra}_c^{0.3}\,A^{-1/3} \tag{1}$$

was proposed for overall heat transfer coefficients [2]. The function $\Phi(\mathrm{Pr}, R)$ was found to be related to the flow field and the type of fluid.

An experimental study considered natural convection in a vertical annulus with the inner wall at constant heat flux and the outer wall at constant temperature. A correlation for the average Nusselt number was presented as

$$\mathrm{Nu} = 0.25\,\mathrm{Ra}_c^{0.30}\,A^{-0.25} \tag{2}$$

where $10^5 \le \mathrm{Ra}_c \le 10^8$ [3]. The data included annuli of three radius ratios, $R = 1.23$, 1.10, and 1.03, with aspect ratios of $A = 38$, 76, and 228, respectively.

A recent experimental investigation examined an annulus with a radius ratio of 4.33 and an aspect ratio of 27.6, with the inner wall assumed to be at constant heat flux and the outer wall isothermal [4]. It was discovered that thermal radiation can become a significant heat transfer mechanism, depending on the Rayleigh number and the working fluid. A correlation for the average Nusselt number was given by

$$\mathrm{Nu} = 0.291\,\mathrm{Ra}^{0.244}\,A^{-0.238}\,R^{0.442} \tag{3}$$

where $1.8 \times 10^4 \le \mathrm{Ra} \le 4.21 \times 10^7$, and the geometric dependence was adapted from previous analysis [2]. It was assumed that the effect of geometric parameters was independent of the boundary conditions.

The current study examines vertical annuli for $\mathrm{Pr} = 10$, $1.5 \le R \le 5$, $10 \le A \le 50$, $|\lambda| \le 0.5$, and $\mathrm{Ra} \le 10^8$, where λ is the heat flux ratio. Not all combinations of the parameters were considered. The majority of analysis considers a radius ratio of 1.5 and an aspect ratio of 10. It is discovered that the streamlines and "heatlines" [5] are highly dependent on the boundary conditions and Rayleigh number. Overall heat transfer coefficients exhibit a geometric dependence which varies as the boundary conditions are changed.

Analysis

The continuity, momentum, and energy equations for steady, axisymmetric incompressible laminar buoyant flow in a vertical annulus may be, respectively, written as

$$\frac{\partial}{\partial z}(ru) + \frac{\partial}{\partial r}(rv) = 0 \tag{4}$$

$$u\frac{\partial u}{\partial z} + v\frac{\partial u}{\partial r} = \nu\left[\frac{\partial^2 u}{\partial r^2} + \frac{1}{r}\frac{\partial u}{\partial r} + \frac{\partial^2 u}{\partial z^2}\right] - \frac{1}{\rho}\frac{\partial p}{\partial z} + G\left(\frac{\rho_\infty - \rho}{\rho}\right) \tag{5}$$

$$u\frac{\partial v}{\partial z} + v\frac{\partial v}{\partial r} = \nu\left[\frac{\partial^2 v}{\partial r^2} + \frac{1}{r}\frac{\partial v}{\partial r} - \frac{v}{r^2} + \frac{\partial^2 v}{\partial z^2}\right] - \frac{1}{\rho}\frac{\partial p}{\partial r} \tag{6}$$

and

$$u\frac{\partial T}{\partial z} + v\frac{\partial T}{\partial r} = \alpha\left[\frac{\partial^2 T}{\partial r^2} + \frac{1}{r}\frac{\partial T}{\partial r} + \frac{\partial^2 T}{\partial z^2}\right]. \tag{7}$$

Substitution of the dimensionless variables $r^* = r/l$, $z^* = z/l$, $u^* = ul/\nu$, $v^* = vl/\nu$, $p^* = pl^2/\rho\nu^2$, and $T^* = (T - T_r)k/q_0''l$ into a composite of equations (4), (5), and (6) yields the normalized vorticity transport equation

$$\frac{1}{r^{*2}}\frac{\partial\psi^*}{\partial r^*}\frac{\partial^3\psi^*}{\partial r^{*2}\partial z^*} - \frac{1}{r^{*3}}\frac{\partial\psi^*}{\partial r^*}\frac{\partial^2\psi^*}{\partial r^*\partial z^*} - \frac{1}{r^{*2}}\frac{\partial\psi^*}{\partial z^*}\frac{\partial^3\psi^*}{\partial r^{*3}} + \frac{3}{r^{*3}}\frac{\partial\psi^*}{\partial z^*}\frac{\partial^2\psi^*}{\partial r^{*2}} - \frac{3}{r^{*4}}\frac{\partial\psi^*}{\partial z^*}\frac{\partial\psi^*}{\partial r^*} - \frac{1}{r^*}\frac{\partial^4\psi^*}{\partial r^{*4}} + \frac{2}{r^{*2}}\frac{\partial^3\psi^*}{\partial r^{*3}} - \frac{3}{r^{*3}}\frac{\partial^2\psi^*}{\partial r^{*2}} + \frac{3}{r^{*4}}\frac{\partial\psi^*}{\partial r^*} - \frac{\partial T^*}{\partial r^*} = 0 \tag{8}$$

where the stream function is defiend as

$$r^*u^* = \frac{\partial\psi^*}{\partial r^*} \quad \text{and} \quad r^*v^* = -\frac{\partial\psi^*}{\partial z^*} \tag{9}$$

and the natural length scale is defined as

$$l = \left[\frac{k\nu^2}{G\beta q_0''}\right]^{1/4}. \tag{10}$$

Contributed by the Heat Transfer Division for publication in the JOURNAL OF HEAT TRANSFER. Manuscript received by the Heat Transfer Division Oct 10, 1985.

In addition to the use of the Boussinesq approximation in equation (8), a few of the terms have been eliminated by restricting the analysis to an annulus of large aspect ratio. The corresponding normalized energy equation becomes

$$\frac{1}{r^*}\frac{\partial\psi^*}{\partial r^*}\frac{\partial T^*}{\partial z^*}-\frac{1}{r^*}\frac{\partial\psi^*}{\partial z^*}\frac{\partial T^*}{\partial r^*}-\frac{1}{\mathrm{Pr}}\frac{\partial^2 T^*}{\partial r^{*2}}$$

$$-\frac{1}{\mathrm{Pr}}\frac{1}{r^*}\frac{\partial T^*}{\partial r^*}=0. \tag{11}$$

Group transformation of equations (8) and (11) may be performed under the Dilatation Group [6], for which the variants are expressed as

$$\eta=\frac{r^*}{z^{*m}},\quad f=\frac{\psi^*}{z^*},\quad \text{and}\quad g=\frac{T^*}{z^{*(1-4m)}}. \tag{12}$$

Reformulation of the problem in terms of the new variables η, f, and g yields the ordinary differential equations

$$\eta^3 f''''+(\eta^2 f-2\eta^2)f'''+[(4m-1)\eta^2 f'-3\eta f+3\eta]f''$$
$$+[(1-4m)\eta f'+3f-3]f'+\eta^4 g'=0 \tag{13}$$

and

$$\eta g''+(\mathrm{Pr}f+1)g'+\mathrm{Pr}f'(4m-1)g=0. \tag{14}$$

Satisfaction of the no-slip condition at both walls requires that

$$f=f'=0 \tag{15}$$

thus prescribing a no-net-flow condition within the annulus, consistent with the analysis of enclosures. For external flow over vertical wires, the conditions on the temperature function g become $g'=1$ at $\eta=0$ and $g\to 0$ as $\eta\to\infty$, with $m=1/5$. Unfortunately, for an annulus the boundary conditions on g as well as the values for η which define the profile of the enclosure cannot be explictily expressed in terms of the similarity variables. This has prevented the use of similarity analysis by researchers in the past. However, these conditions can be met approximately by minimizing the respective errors between the desired constant heat flux profile and constant cross section profile with their corresponding axially dependent similarity functions

$$g'=\frac{\partial T^*}{\partial r^*}/z^{*(1-5m)}\quad\text{and}\quad \eta=\frac{r^*}{z^{*m}} \tag{16}$$

(see appendix). The requirement that the integrated squares of the errors in the boundary and heat flux profiles be a minimum results in a complete set of boundary conditions

$$\left.\begin{array}{l} f=f'=0 \\ g'=-\dfrac{(3-10m)}{(2-5m)}\dfrac{\mathrm{Gr}^{\left(\frac{5m-1}{4}\right)}}{A^{(1-5m)}} \end{array}\right\}\eta=\frac{(2m+1)}{(m+1)}\frac{\mathrm{Gr}^{\left(\frac{1-m}{4}\right)}}{A^m(R-1)}$$

and (17)

$$\left.\begin{array}{l} f=f'=0 \\ g'=\dfrac{(3-10m)}{(2-5m)}\lambda\dfrac{\mathrm{Gr}^{\left(\frac{5m-1}{4}\right)}}{A^{(1-5m)}} \\ \text{or} \\ g=0 \end{array}\right\}\eta=\frac{(2m+1)}{(m+1)}\frac{R\mathrm{Gr}^{\left(\frac{1-m}{4}\right)}}{A^m(R-1)}$$

where λ is the outer to inner wall heat flux ratio, q_1''/q_0'' [7]. The constant m is chosen such that the sum of the integrated square errors is minimized, and thus satisfies the polynomial

$$W(m+1)^4(250m^2-150m+20)-2m(m+1)(2-5m)^4=0 \tag{18}$$

where W is a weight function which depends on the boundary condition selected for the outer wall. For the constant heat flux condition $W=1$ and

$$m=0.1951. \tag{19}$$

For the isothermal condition $W=1/2$ and

$$m=0.1895. \tag{20}$$

The transport of mass and energy within the annulus can be easily visualized through examination of the streamlines and heatlines, respectively. The heatlines are determined from a heat function which identically satisfies the energy equation. Group transformation of the defining equations for the heat function

$$\frac{\partial H^*}{\partial z^*}=\frac{r^*}{\mathrm{Pr}}\frac{\partial T^*}{\partial r^*}+\frac{\partial\psi^*}{\partial z^*}T^*\quad\text{and}\quad \frac{\partial H^*}{\partial r^*}=\frac{\partial\psi^*}{\partial r^*}T^* \tag{21}$$

yield the variants

$$\eta=\frac{r^*}{z^{*m}}\quad\text{and}\quad h=\frac{H^*}{z^{*(2-4m)}}. \tag{22}$$

The solution for the similarity function h is determined explicitly in terms of the similarity variables f and g upon integration of the defining equations. This formulation yields

Nomenclature

A = aspect ratio = L/r_1-r_0
E = error expression (equation (A10))
f = similarity stream function
g = similarity temperature function
G = gravitational acceleration
Gr = modified Grashof number = $G\beta q_0''(r_1-r_0)^4/k\nu^2$
h = similarity heat function
H = heat function
k = thermal conductivity
l = natural length scale = $(k\nu^2/G\beta q_0'')^{1/4}$
L = height of annulus
m = similarity parameter
Nu = Nusselt number based on gap = r_1-r_0
p = absolute pressure
Pr = Prandtl number
q'' = heat flux
r = radial coordinate
$\bar{r}$ = normalized radial coordinate = r/r_0
R = radius ratio = r_1/r_0
Ra = modifed Rayleigh number = $G\beta q_0''(r_1-r_0)^4/k\nu\alpha$
Ra_c = conventional Rayleigh number = $G\beta(T_1-T_0)(r_1-r_0)^3/\nu\alpha$
T = temperature
u = axial velocity
v = radial velocity
W = weight function
z = axial coordinate
$\bar{z}$ = normalized axial coordinate = z/L

Greek Symbols

α = thermal diffusivity
β = coefficient of thermal expansion
u = similarity independent variable
λ = heat flux ratio = q_1''/q_0''
ν = kinematic viscosity
ρ = density
ψ = stream function

Subscripts

0 = pertain to inner wall
1 = pertaining to outer wall
∞ = bulk property

Superscripts

* = dimensionless quantity

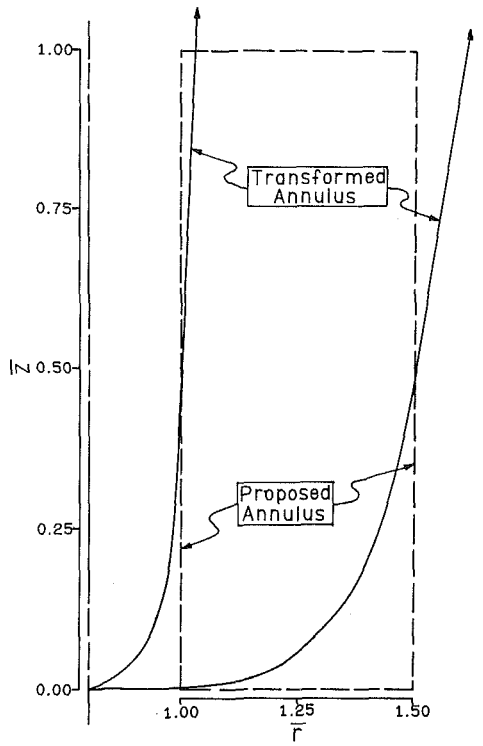

Fig. 1 Comparison of transformed geometry with a uniform section vertical annulus

$$h(\eta)=\left(\frac{\eta-\eta_0}{\eta_1-\eta_0}\right)h(\eta_1)+\left(\frac{\eta_1-\eta}{\eta_1-\eta_0}\right)h(\eta_0)$$
$$+\int_{\eta_0}^{\eta_1}K(\zeta,\eta)[f''(\zeta)g(\zeta)+f'(\zeta)g'(\zeta)]d\zeta \tag{23}$$

where

$$K(\zeta,\eta)=\begin{cases}\left(\frac{\zeta-\eta_0}{\eta_1-\eta_0}\right)\eta-\left(\frac{\zeta-\eta_0}{\eta_1-\eta_0}\right)\eta_1 & \zeta\le\eta\\ \left(\frac{\eta-\eta_0}{\eta_1-\eta_0}\right)\zeta-\left(\frac{\eta-\eta_0}{\eta_1-\eta_0}\right)\eta_1 & \eta>\zeta\end{cases} \tag{24}$$

$$h(\eta_0)=\frac{\eta_0 g'(\eta_0)}{\mathrm{Pr}(2-4m)},\quad h(\eta_1)=\frac{\eta_1 g'(\eta_1)}{\mathrm{Pr}(2-4m)}$$

$$\eta_0=\left(\frac{2m+1}{m+1}\right)\frac{\mathrm{Gr}^{\left(\frac{1-m}{4}\right)}}{A^m(R-1)}$$

and

$$\eta_1=\left(\frac{2m+1}{m+1}\right)\frac{R\mathrm{Gr}^{\left(\frac{1-m}{4}\right)}}{A^m(R-1)}$$

Integration of equations (13) and (14) may be accomplished through application of a fourth-order Runge–Kutta method with modified Gill coefficients. A Newton–Raphson scheme can be implemented to iterate the unknown three initial conditions until an acceptable convergence criterion is reached. This method proves to be quite successful, exhibiting rapid convergence which is insensitive to the initial guesses at low Rayleigh numbers (Ra $\le 10^4$).

Results and Discussion

Solutions generated in this research examined vertical annuli for Pr = 10, $1.5 \le R \le 5$, $10 \le A \le 50$, $|\lambda| \le 0.5$, and Ra $\le 10^8$. The focus of the analysis was for a radius ratio of 1.5 and an aspect ratio of 10 exclusively, because variations in geometric parameters have only minor effects on the transfer of mass and heat in the annulus. Changes in the Rayleigh number and heat flux ratio, however, profoundly affect heat and mass transfer and are therefore presented in detail. Prandtl number effects become independently significant only in the low Prandtl number limit and consequently analysis is restricted to Pr = 10.

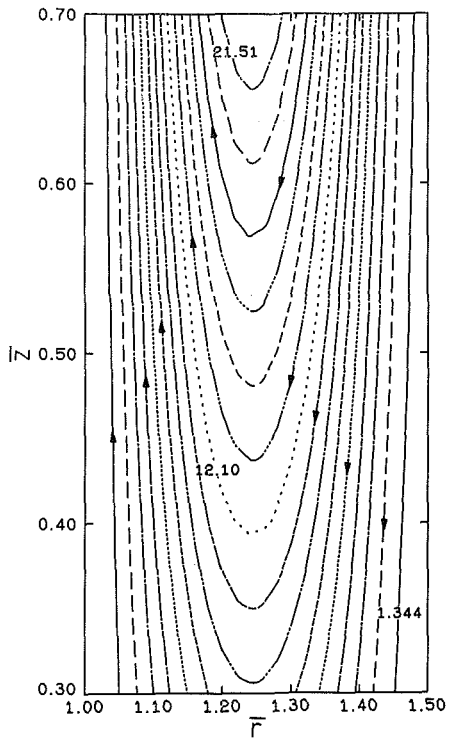

Fig. 2 Streamlines for a low Rayleigh number case (Ra = 10^4) with isothermal outer boundary and Pr = 10, A = 10, R = 1.5

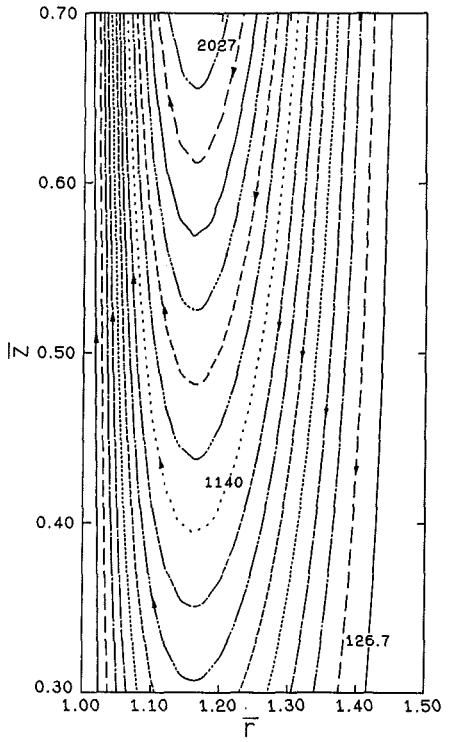

Fig. 3 Streamlines for a high Rayleigh number case (Ra = 10^7) with insulated outer boundary and Pr = 10, A = 10, R = 1.5

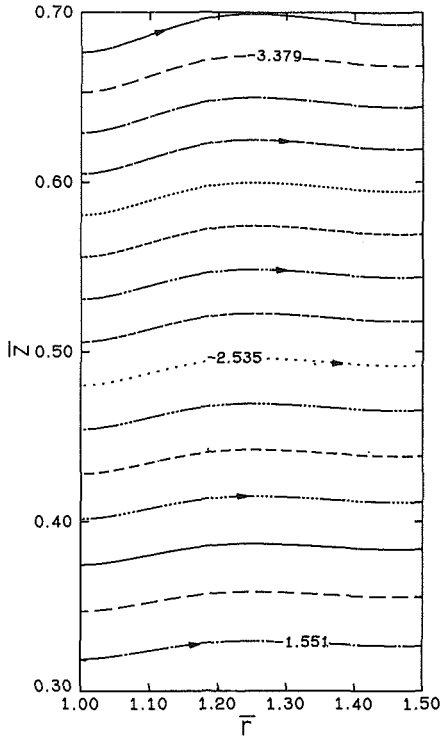

Fig. 4 Heatlines for a low Rayleigh number case (Ra = 100) with isothermal outer boundary and Pr = 10, A = 10, R = 1.5

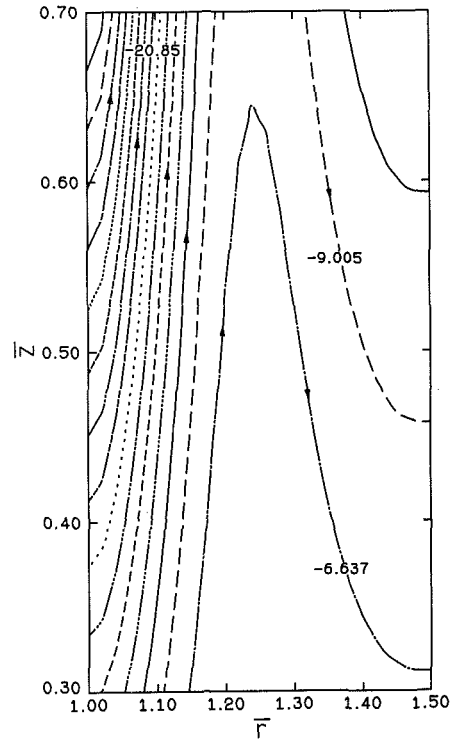

Fig. 5 Heatlines for a high Rayleigh number case (Ra = 10^4) with isothermal outer boundary and Pr = 10, A = 10, R = 1.5

The present study is an approximation to a uniform section vertical annulus whose inner wall is at constant heat flux. Figure 1 compares the geometry of the proposed annulus with the transformed geometry analyzed by the similarity solution. The walls of the transformed annulus are slightly sloped, forming a blunt cone at the base, extending toward infinity at the top. The aspect ratio becomes a scaling parameter for the slope of the walls, rather than their height, after transformation. Similarity analysis preserves the no-slip condition as an implied axial boundary condition, and requires that the radial temperature gradient be specified along the inner periphery as an implied thermal boundary condition. Although the differences are significant close to the base and at large heights, Fig. 1 illustrates that the similarity solution closely approximates the proposed annulus in the midregion. The graphic and numerical results that follow concentrate on this region.

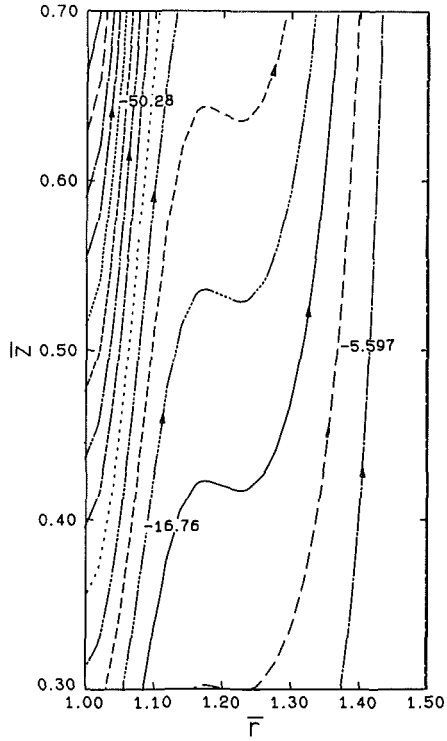

Fig. 6 Heatlines for an intermediate Rayleigh number case (Ra = 5 × 10^4) with insulated outer boundary and Pr = 10, A = 10, R = 1.5

Figure 2 illustrates a typical streamline pattern encountered at low Rayleigh numbers. Although this example considers the outer wall at constant temperature, it is also characteristic of the outer wall at constant heat flux. The symmetry of the streamlines, as well as their relative low numerical value, is indicative of a conduction dominant mode. Small gradients in the central region of the annulus indicate an almost quiescent core region. Figure 3, on the other hand, exemplifies a typical streamline pattern at large Rayleigh numbers for the insulated wall condition ($\lambda = 0$). Results for the isothermal wall case tended to be very similar, mainly because insulated walls tend to be approximately isothermal. Asymmetric profiles exhibiting large velocities close to the inner wall are characteristic of this convection-dominated mode. Quantitative comparisons in the stream function give a volumetric circulation rate 17 times larger under the conditions in Fig. 3 than in Fig. 2 (since the natural length scale was Rayleigh number dependent, a geometric length scale was used for this comparison).

Figure 4 shows a heatline profile at very low Rayleigh numbers. The conduction solution for the heatline pattern, given that the outer wall as isothermal, is a set of uniformly spaced horizontal lines, which clearly indicates that conduction is the primary heat transfer mode. Thermal boundary conditions in the axial direction require that heat leaving the inner wall be released at the outer wall, which is illustrated in Fig. 4. At higher Rayleigh numbers and for different boundary conditions, the heatline patterns are very different. Figure 5, for instance, is the heatline pattern under the same conditions as Fig. 4, but at a higher Rayleigh number. The influence of bouyancy on the transfer of heat becomes more

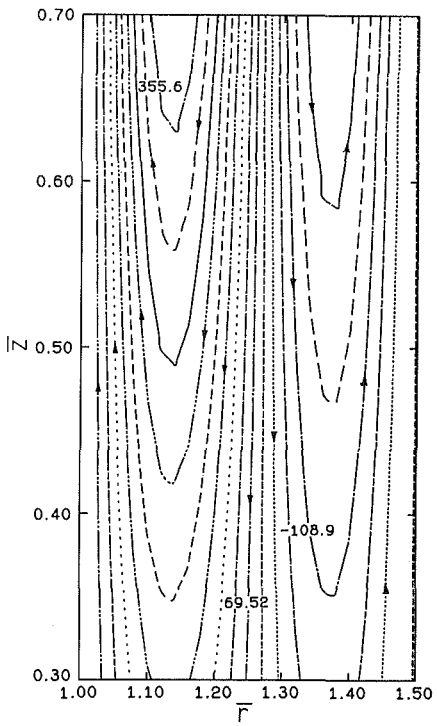

Fig. 7 Streamlines for a high Rayleigh number case (Ra = 10^6) with uniform heat input at outer boundary (λ = 2/9) and Pr = 10, A = 10, R = 1.5

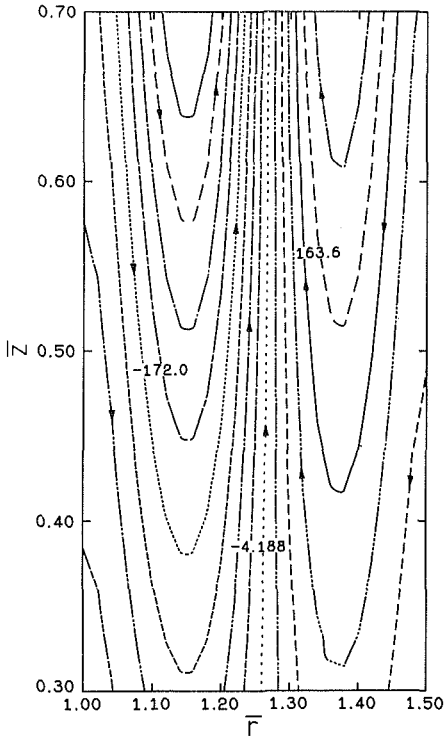

Fig. 8 Heatlines for a low Rayleigh number case (Ra = 10^5) with uniform heat input at outer boundary (λ = 4/9) and Pr = 10, A = 10, R = 1.5

significant, but it is still channeled from the inner wall to the outer wall. When the outer wall is insulated, however, the axial boundary conditions require that the thermal energy be transported upward. Since this boundary is at infinity it can act as a heat sink, absorbing all energy released from the inner wall. Although this case has little physical significance, it is thermodynamically sound just the same. Figure 6 illustrates heat transport for the insulated wall case. This particular figure shows the heatlines undergoing a transition from a conduction to convection dominated heat transfer. Buoyancy-generated mass flow tends to carry enthalpy vertically, whereas conduction effects tend to channel heat horizontally shown in Fig. 4.

Heat inputs at the outer wall ($\lambda > 0$) initiate bicelluar streamline patterns within the annulus. Figure 7 is an example of this configuration. Bouyancy-driven flow at each wall induces the development of two horizontally aligned counter rotating cells. Due to the low heat flux ratio (λ = 2/9), fluid velocities adjacent to the inner wall are much larger than at the outer wall. In addition, the volumetric circulation rate is about three times larger for the inner cell. The variation in the mass circulation rate is, however, much smaller due to the density gradient. Multicellular growth is also exhibited by the heatlines for positive heat flux ratios, as illustrated in Figs. 8 and 9. Figure 8 is a low Rayleigh number example of this behavior. Thermal diffusion is responsible for the majority of the heat transport, as enthalpy flow opposes mass flow at almost every location in the annulus. Due to the imposed thermal boundary conditions, the far boundary must act as a heat sink; thus the heatlines tend to converge at that location. Figure 9, on the other hand, is a high Rayleigh number example in which the influence of convection is clearly evident and exhibits transitional behavior observed previously in Fig. 6. The large gradient in the heatlines adjacent to the inner wall is due primarily to the rapid fluid motion. The increased thermal load initiates the transport of enthalpy along a more direct path.

Heat rejection at the outer wall ($\lambda < 0$)generates streamline and heatline patterns which tend towards vertically aligned

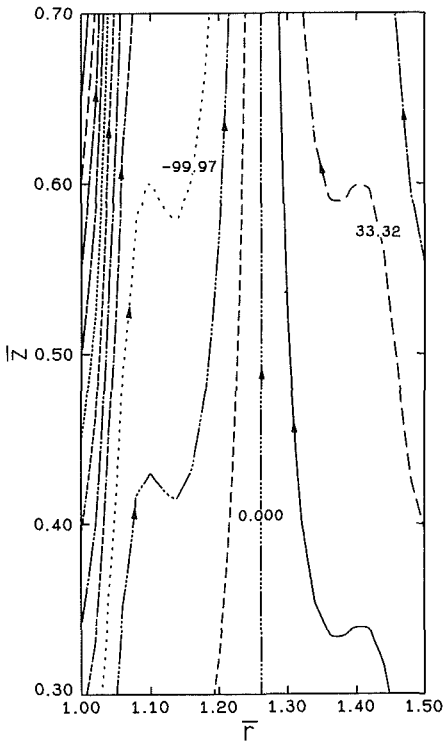

Fig. 9 Heatlines for a high Rayleigh number case (Ra = 10^6) with uniform heat input at outer boundary (λ = 2/9) and Pr = 10, A = 10, R = 1.5

cells. Figure 10 illustrates a typical streamline profile for large Rayleigh numbers. Close to the walls the streamlines are similar in shape to those encountered for the insulated wall case. However, in the central region multiple inflection points characterize the transition to a multicellular flow. The large opposing buoyancy-generated velocities at the inner and outer walls induce a mass flux away from the core region of the annulus. Satisfaction of continuity requires that this mass flow

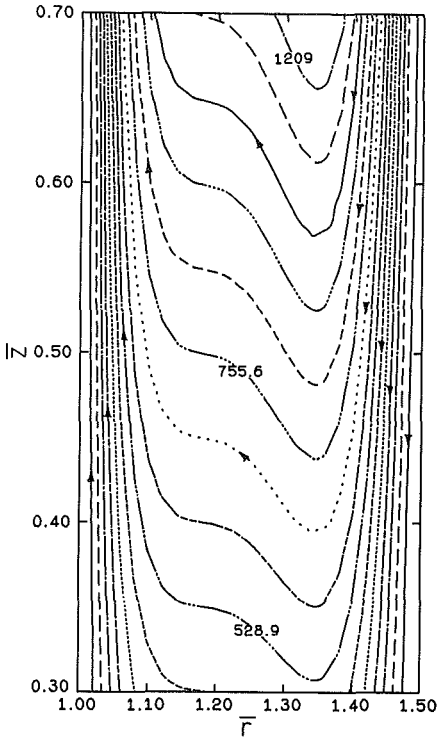

Fig. 10 Strealines for a high Rayleigh number case (Ra = 10^7) with uniform heat rejection at outer boundary ($\lambda = -2/9$) and Pr = 10, A = 10, R = 1.5

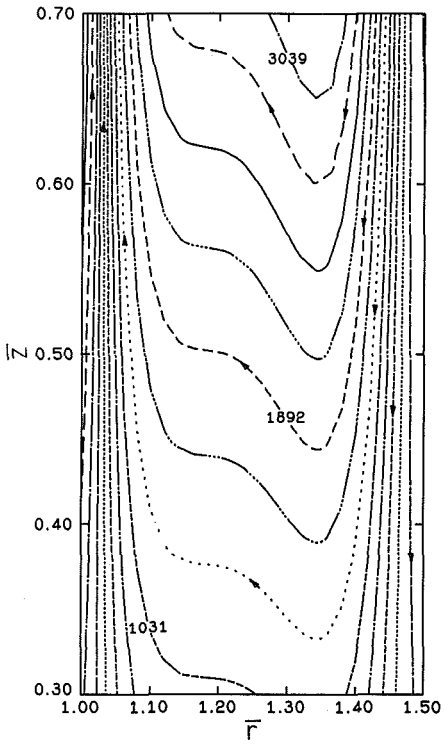

Fig. 11 Heatlines for a high Rayleigh number case (Ra = 10^7) with uniform heat rejection at outer boundary ($\lambda = -2/9$) and Pr = 10, A = 10, R = 1.5

be in two directions simultaneously. At low Rayleigh numbers there is enough mass in the core region to satisfy this flow requirement, but as the Rayleigh number increases it becomes increasingly difficult until a breakdown begins to occur, as show in in Fig. 10. Further increases in the Rayleigh number induce multicellular behavior characterized by vertically aligned rotating cells. This flow regime, however, is apparently out of the domain of similarity solutions.

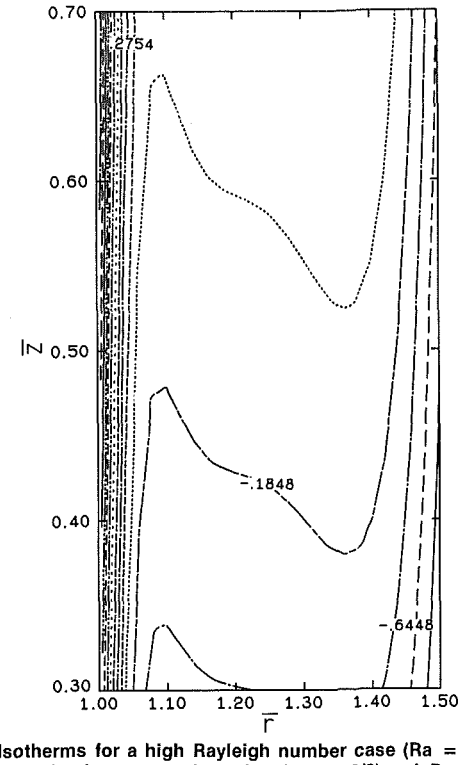

Fig. 12 Isotherms for a high Rayleigh number case (Ra = 10^7) with uniform heat rejection at outer boundary ($\lambda = -2/9$) and Pr = 10, A = 10, R = 1.5

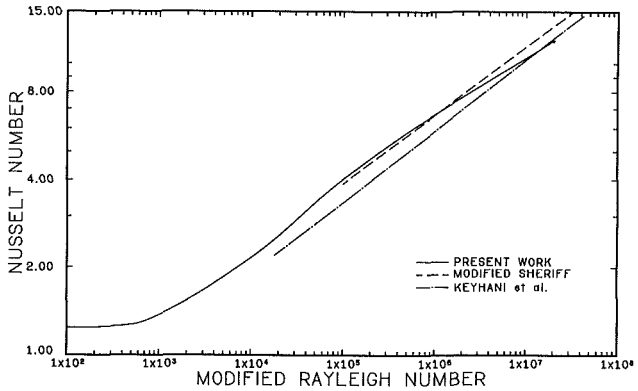

Fig. 13 Present results with equation (2, modified) and (3) subject to isothermal outer boundary conditions and Pr = 10, A = 10, R = 1.5

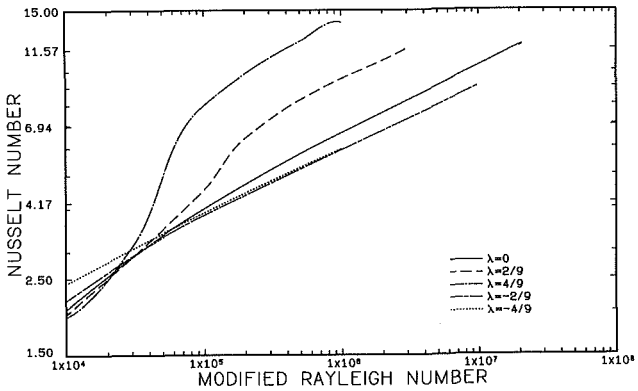

Fig. 14 Average Nusselt number as a function of modified Rayleigh number with uniform heat flux at outer boundary and Pr = 10, A = 10, R = 1.5

Figure 11 illustrates a heatline pattern for boundary conditions identical to those for the streamlines of Fig. 10. This pattern exhibits peculiar characteristics, also indicative of a multicellular transition. The boundary conditions for this configuration require that heat leaving the inner wall be rejected at the outer wall of the annulus, in the same manner as that for the isothermal outer wall condition. The heatlines are therefore very similar for these conditions at low Rayleigh numbers. At high Rayleigh numbers, however, heat is channeled from the inner wall to the outer wall without passing through the center, generating a core region that cannot release its enthalpy to the outer wall. This situation leads to the transitional heatline profile as shown in Fig. 11. The isotherms, in addition, exhibit characteristics of a multicellular transition. Figure 12 shows the isotherm pattern for this case with multiple inflection points. The core region exhibits a slight inversion in its temperature structure caused by the unusual manner in which heat is transported under these conditions. Localized cooling of the core region close to the inner wall and heating close to the other wall establish a relative maximum and minimum of the temperature profile.

Several previous analytical models for buoyant convection in internal geometries have relied upon the boundary layer model to approximate flow close to the wall, accompanied by an idealized core region. A common condition that is often used is to assume the core to be isothermal and of constant vorticity. For the boundary conditions studied in this work the constant vorticity assumption is fairly substantiated, but for almost every case examined the temperature strucutre of the core exhibits stratification. The isothermal core assumption becomes particularly bad at low Rayleigh numbers. In fact, only one set of conditions examined exhibits a core region which could truly be considered isothermal ($Ra = 1 \times 10^6$ and $\lambda = 2/9$). In general, the presence of an isothermal core is not evident and hence a very questionable assumption.

Figure 13 shows the average Nusselt number versus Rayleigh number for the isothermal outer wall condition. Equations (2) and (3) are included for a radius ratio of 1.5 and an aspect ratio of 10 (equation (2) was augmented with a radius ratio and modified Rayleigh number dependence). The current study clearly shows the transition from the convection mode to the Rayleigh independent conduction mode at $Ra = 800$, as the limiting Nusselt number asymptotically approaches a value of 1.23. Deviations between correlation equations (2) and (3) and the current study are 12 percent at their maximum. The differences can be attributed to several factors. First, the geometry for the similarity solution differed from the geometry for the experimental studies. An error analysis revealed that these differences result in a 10 percent variation in the local Nusselt number. The average Nusselt number, however, varied by much less ($\sim$ 1 percent) because the similarity solution tends to overestimate the heat transfer in the upper region of the annulus, and underestimate in the lower region. Second, the axial boundary conditions were different (the experimental studies assumed axial boundaries to be insulated). Third, differences can be attributed to experimental scatter, which could account for at least a 10 percent variation in the Nusselt number. Given the limitations for comparison with the current analysis the agreement is claimed to be quite good. Figure 14 exhibits Rayleigh number dependence of the average Nusselt number for the uniform heat flux condition at the outer boundary. Heat outputs at the outer wall ($\lambda < 0$) do not have appreciable effects on the Nusselt number. However, heat inputs significantly change both its magnitude and Rayleigh number dependence. These effects are caused primarily by the increased enthalpy in the system as well as the efficient mixing exhibited by the multicellular streamline profile. The inversion of Nusselt numbers at $Ra = 3 \times 10^4$ indicates the initiation of a conduction-dominated regime. No conduction solution exists for the outer wall heat flux boundary conditions, so Rayleigh numbers less than 10^4 were not investigated for this configuration.

Correlations for the average Nusselt number in the current study include $Pr = 10$, $1.5 \le R \le 5$, and $10 \le A \le 50$. For the isothermal outer wall condition the numerical results suggest a correlation of the form

$$Nu = 0.443 A^{-0.245} R^{0.440} Ra^{(0.233 - 0.009R)} \tag{25}$$

where $Ra \le 10^8$. For positive heat flux ratios the correlation becomes

$$Nu = 0.488 A^{-0.255} R^{0.038} e^{-1.25\lambda R} Ra^{(0.266 + 0.118\lambda R - 0.0005R)} \tag{26}$$

whereas negative heat flux ratios suggest the correlation

$$Nu = 0.488 A^{-0.255} R^{0.038} e^{-0.330\lambda R} Ra^{(0.266 + 0.057\lambda/R - 0.0005R)} \tag{27}$$

where $10^4 \le Ra \le 10^8$ and $|\lambda| \le 0.5$. The average of the wall temperatures should be used to evaluate the properties needed for the Nusselt number and Rayleigh number.

These equations indicate that geometric parameters as well as boundary conditions affect the overall heat transfer. Although the curve-fitting parameters in equations (25) through (27) were chosen for their physical significance to this configuration, their placement in the correlation equations was based solely on statistical methods. The product λR, for instance, is the ratio of enthalpy input/rejection at the outer wall to total heat input at the inner wall. The inverse radius ratio is a dimensionless measure of the curvature of the annulus. The current analysis also predicts a radius ratio dependence of the power in the Rayleigh number not present in equations (2) and (3). This effect becomes quite significant for $R \ge 2.0$ and $Ra \ge 10^5$. Since a limiting case of internal flow is external flow ($R \to \infty$), this power law dependence is not unexpected. However, the dependence is much more complex than presented in equations (25) through (27). First-order effects of geometric parameters on the Nusselt number are included in this discussion to simplify the results.

Acknowledgments

This work was supported by the department of Mechanical Engineering, Georgia Institute of Technology, Atlanta, Georgia 30332. Fellowship support by the Weyerhauser Corporation during the research is gratefully acknowledged. The authors also thank Miss Melinda Wilson for preparing the typed manuscript.

References

1 de Vahl Davis, G., and Thomas, R. W., "Natural Convection Between Concentric Vertical Cylinders," *High Speed Computing in Fluid Dynamics, Physics of Fluids*, Supplement II, 1969, p. 198–207.

2 Thomas, R. W., and de Vahl Davis, G., "Natural Convection in Annular and Rectangular Cavities," *Proceedings Fourth International Heat Transfer Conference*, Paris, Elseveir, Amsterdam, 1970, Vol. 4, Paper NC 2.4.

3 Sheriff, N., "Experimental Investigation of Natural Convection in Single and Multiple Vertical Annuli With High Pressure Carbon Dioxide," *Proceedings Third International Heat Transfer Conference*, Chicago, Vol. 2, 1966, pp. 132–138.

4 Keyhani, M., Kulacki, F. A., and Christensen, R. N., "Free Convection in a Vertical Annulus With Constant Heat Flux on the Inner Wall," ASME Journal of Heat Transfer, Vol. 105, 1983, pp. 454–459.

5 Kimura, S., and Bejan, A., "The 'Heatline' Visualization of Convective Heat Transfer," ASME Journal of Heat Tranfer, Vol. 105, 1983, pp. 916–919.

6 Ames, K. A., and Ames, W. F., "On Group Analysis of the Von-Karman Equations," *Nonlinear Analysis, Theory, Methods and Application*, Vol. 6, 1982, pp. 845–853.

7 Littlefield, D. L., "Similarity Solutions for Buoyant Laminar Convection in Vertical Cylindrical Annuli," M.S. Thesis, School of Mechanical Engineering, Georgia Institute of Technology, 1984.

APPENDIX

Derivation of Equations (17) and (18)

In order for the group transformation to be successful, η and either g or g' must be constant at the inner and outer walls of the annulus. Thus the boundary profile must obey the functional relationship

$$r^* = \eta z^{*m} \tag{A1}$$

where η is a constant. Similarly, the boundary and heat flux/temperature profiles must obey the corresponding relationships

$$q''/q_0'' = -g' z^{*(1-5m)} \tag{A2}$$

and

$$T^* = g z^{*(1-4m)} \tag{A3}$$

where g and g' are constants. Either (A2) or (A3) must be satisfed at each boundary, depending on the boundary condition chosen.

For the inner boundary profile, an η_0 must be determined which makes r^* as close to a constant as possible. It is therefore appropriate to minimize the expression

$$E_0 = (L/l)\int_0^{(L/l)} [(r_0/l) - \eta_0 z^{*m}]^2 dz^* \tag{A4}$$

This results in an optimum value for η_0 given by

$$\eta_0 = \frac{(2m+1)}{(m+1)} \frac{\mathrm{Gr}^{\left(\frac{1-m}{4}\right)}}{A^m (R-1)}. \tag{A5}$$

A similar analysis for the outer boundary profile gives

$$\eta_1 = \frac{(2m+1)}{(m+1)} \frac{R\mathrm{Gr}^{\left(\frac{1-m}{4}\right)}}{A^m (R-1)}. \tag{A6}$$

For the inner boundary heat flux profile, a g_0' must be determined such that q''/q_0'' is as close to 1 as possible. This results in an optimum value for g_o' given by

$$g_0' = -\frac{(3-10m)}{(2-5m)} \frac{\mathrm{Gr}^{\left(\frac{5m-1}{4}\right)}}{A^{(1-5m)}}. \tag{A7}$$

A similar analysis at the outer boundary gives

$$g_1' = \frac{(3-10m)}{(2-5m)} \lambda \frac{\mathrm{Gr}^{\left(\frac{5m-1}{4}\right)}}{A^{(1-5m)}}, \tag{A8}$$

or

$$g_1 = 0, \tag{A9}$$

depending on the boundary condition selected for the outer wall.

The free parameter m is chosen such that the sum of the errors incurred in the boundary and heat flux profiles is minimized. This sum is given by

$$E = \left[1 + W - \frac{2m+1}{(m+1)^2} - W\frac{(3-10m)}{(m+1)^2}\right](L/l) \tag{A10}$$

where W is a weight function depending on the thermal boundary condition selected for the outer wall. Minimization of equation (A10) gives equation (18) in the main text.

The Buoyant Plume-Driven Adiabatic Ceiling Temperature Revisited

L. Y. Cooper
National Bureau of Standards,
Gaithersburg, MD 20899

A. Woodhouse
University of Maryland,
College Park, MD 20742

In previous works, convective heat transfer from buoyant plume-driven ceiling jets to unconfined ceilings has been estimated using a formula for the temperature distribution below an adiabatic ceiling T_{ad} *obtained from experimental data in the range* $0 \leq r/H < 0.7$ (r *is the radial distance from the plume and* H *is the plume source-to-ceiling distance*). *The present study re-evaluates these data, and develops an independent estimate for* T_{ad}. *The analysis takes account of the effect of ceiling surface reradiation, and use is made of the previously established similarity between plume/ceiling- and jet/wall-driven heat transfer phenomena. The latter similarity is the basis of a correlation of recently reported free jet-wall jet "recovery temperature" data into a normalized* T_{ad} *distribution. All of the analysis leads to new formulae for estimating the convective heat transfer to ceilings during enclosure fires. These new results confirm previous formulae, and extend them into the larger range* $0 \leq r/H \leq 2.2$.

Introduction

The convective heat transfer to ceilings during enclosure fires can be related to the heat transfer to unconfined ceiling surfaces from buoyant plume-driven ceiling jets [1]. Results of unconfined ceiling experiments [2] suggest a relatively simple means of estimating this heat transfer rate

$$q = h(T_{ad} - T_s) \tag{1}$$

Figure 1 depicts the phenomena in question near the fire plume. In equation (1), T_{ad} is defined as the temperature distribution (a function of radial distance r from the plume–ceiling impingement point) established at the surface of an adiabatic ceiling (i.e., perfectly insulated and with zero absorptivity and emissivity) by the gas flow from the plume of a fire of strength Q and effective fire-to-ceiling distance H; T_s is the instantaneous lower surface ceiling temperature distribution; and h is the heat transfer coefficient based on the temperature difference $T_{ad} - T_s$. In the experiments [2] the transient thermal response of unconfined 0.00159-m-thick, cold-rolled steel plate ceilings, insulated on the top side and initially at ambient temperature, were measured when heated by weakly radiating premixed propane fires of constant strength between 1.17–1.53 kW (H between 0.58 and 0.81 m). Analysis of the data which led to the equation (1) formulation used long-time, "near-ceiling" gas temperatures to estimate T_s ($t \to \infty$), which was then used as a surrogate for the T_{ad} distribution.

The original h results [2] did not distinguish between variations in the characteristic Reynolds number Re_H of the plume (which only varied in the narrow range $1.5 \times 10^4 < \mathrm{Re}_H < 2.0 \times 10^4$ in the laboratory experiments). In a subsequent study [3], it was noted that inertial forces compared to buoyancy forces are generally large (i.e., characteristic Richardson numbers are small) in plume-driven ceiling jets for the most interesting range of small to moderate values of r/H. For this range it was conjectured that the near-ceiling flow and heat transfer characteristics of interest could be directly related to the analogous characteristics of wall or ceiling jets driven by heated or unheated free turbulent jets (e.g., the same configuration of Fig. 1, but with a turbulent jet replacing the fire and its buoyant plume). This led to a proposed correlation for h which *does* depend on the impingement point Reynolds number Re_H, namely

$$h/\tilde{h} = \begin{cases} A\,\mathrm{Re}_H^{1/2}\,\mathrm{Pr}^{-2/3}(1 + B\,r/H), & 0 \leq r/H \leq 0.2 \\ C\,\mathrm{Re}_H^{0.3}\,\mathrm{Pr}^{-2/3} w(r/H), & 0.2 \leq r/H \end{cases}$$

where A and C are numerical constants, $B = B(\mathrm{Re}_H)$, $h/\tilde{h}$ is a continuous function of r/H, and

$$\lim_{r/H \to \infty} w \sim (r/H)^{-1.2} \tag{3}$$

In the above

$$\tilde{h} = \rho_{amb} C_p g^{1/2} H^{1/2} Q^{*1/3}$$
$$\mathrm{Re}_H = g^{1/2} H^{3/2} Q^{*1/3} / \nu \tag{4}$$
$$Q^* = (1 - \lambda_r) Q / (\rho_{amb} C_p T_{amb} g^{1/2} H^{5/2})$$

where λ_r is the fraction of Q which is lost by radiation from the fire's combustion zone and from the plume itself, i.e., $(1 - \lambda_r)\,Q$ is the effective portion of Q which actually drives the plume's upward convection. Also, ρ_{amb}, C_p, T_{amb}, ν, and Pr are the density, specific heat at constant pressure, temperature, kinematic viscosity, and Prandtl number of the ambient environment, respectively.

The above correlation was based on measured heat transfer (to an elevated-temperature wall) [5] and flow properties [10] of unheated free jet-driven wall jets (where $T_{ad} = T_{amb}$), and on the application of a criterion of equivalence for free jets

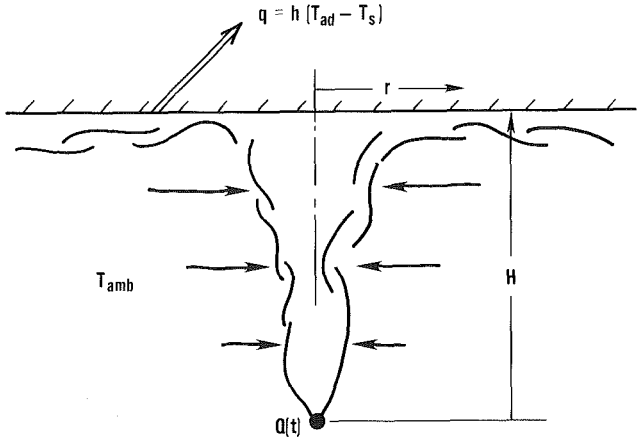

Fig. 1 Heat transfer to an unconfined ceiling

Contributed by the Heat Transfer Division and presented at the 23rd National Heat Transfer Conference, Denver, Colorado, 1985. Manuscript received by the Heat Transfer Division September 10, 1985.

and buoyant plumes at their respective sections of wall/ceiling impingement (Appendix of [3]).

With the data of [2], data from the similar "reduced-scale" fire-plume-driven heat transfer experiments of [4], and unheated, free jet-driven wall jet heat transfer measurements of [5], it was shown in [3] that with the proposed h correlation of equation (2), the equation (1) formulation would provide reasonable q estimates for Re_H at least in the range 0.73×10^4–27×10^4. (Full-scale hazardous fires with fire-to-ceiling distances of 2–3 m and convected energy fluxes of 200–2000 kW would have Re_H in the range $20 \times 10^4 < \mathrm{Re}_H < 50 \times 10^4$ [1].)

In [3] the h values from the experiments in [2, 4] were derived from equation (1) with the use of measured values of q, T_s, and the long-time, near-ceiling gas temperature measurements of [2] which were assumed to be representative of T_{ad}. The h values from the free-jet experiments of [5] were derived in a similar way, but, as mentioned earlier, the values of T_{ad} in this case required no special measurements as they are identically equal to T_{amb}.

A Re-evaluation of Existing Data

The present investigation involves a re-evaluation of the data of [2] within the context of the equation (1) formulation. The goal is to obtain new estimates for T_{ad} and h which would (1) be consistent with an equation (2) type of Re_H-dependent h; (2) would only use the initial transient data (t = 1, 2, 3, 5, and 7 min) of [2], and not the 25–30 min, long-time, near-surface gas temperatures which were previously used to represent the "true" T_{ad} [2]; (3) would include the previously neglected effect of exposed ceiling surface re-radiation to far-field surfaces; and (4) use recently reported data of free jet-driven wall jet heat transfer experiments to extend the r/H range of validity.

With regard to item (2) above, there are two reasons for avoiding the use of the long-time measurements in a new analysis of the data of [2]. First, there is indication from the transient data that in-plate radial conduction is important even at steady state for r/H at least up to 0.25. Also, a nonzero plate emissivity could lead to nonnegligible plate radiation to the far field. Under either of these circumstances the steady-state plate response would differ from that of an adiabatic ceiling. Second, all the reported transient data are from thermocouples mounted directly on the plate itself, whereas the long-time temperature data in [2] were measured in the gas at a distance below the plate surface of 0.0016 m.

Consistent with the above remarks, another analysis of the tabulated data of [2] was carried out. The analysis involved application of energy conservation of elemental volumes of the plate, at the seven locations of plate-mounted thermocouples (placed at 0.07 m radial intervals from the point of plume–ceiling impingement), and at different times during the plate heating. New, dimensionless T_{ad} data were generated from the expression

$$\Delta T^*_{ad} \equiv \frac{(T_{ad} - T_{amb})}{T_{amb} Q^{*2/3}} = \frac{(T_s - T_{amb})}{T_{amb} Q^{*2/3}} + \frac{1}{h T_{amb} Q^{*2/3}} [q_1 + q_c + \Delta E + \epsilon\sigma(T_s^4 - T_{amb}^4)] \tag{5}$$

where σ is the Stefan–Bolzmann constant and where q_1, q_c, and ΔE are the respective instantaneous rates of heat transfer per unit area of plate conducted and lost to the rear insulation, conducted radially outward, and absorbed and retained in the plate itself. The right-hand term of equation (5) represents the lower plate radiation to far-field surfaces which are taken to be at the ambient temperature, and ϵ is the effective plate emissivity.

A review of the data of [2] indicates that by seven minutes into the experiments a value of ϵ greater than a few tenths would have led to a significant contribution (on the order of 35 percent for $\epsilon = 1$) to the net value of the bracketed term of equation (5). It would therefore appear that an equation (5) type of analysis of the data requires an estimate for the plate's ϵ. Unfortunately, the literature has little to offer for ϵ values of cold-rolled steel plate. Indeed, while tables of the ϵ of solid surfaces typically provide values of 0.6–0.8 for rolled steel plate of various descriptions, the authors found only one primary reference [6] for the ϵ of *cold*-rolled steel. Such an ϵ is reported to have been measured at the remarkably low values of 0.075 (93°C) and 0.085 (260°C). (Reference [7] reports these results of [6] incorrectly as 0.75–0.85.) To confirm this the authors had the ϵ of available samples of "old and uncleaned" cold-rolled steel measured at the National Bureau of Standards. A room-temperature value of 0.12 was obtained [8]. As will be seen below, the new analysis of the data of [2] suggests that the "true" ϵ of the plate of [2] was indeed in the range of these low values.

Nomenclature

A, B = constants, equation (2)
b = nozzle-to-wall separation distance
C_p = specific heat at constant pressure
f, f_1 = functions, equations (7) and (A2), respectively
g = acceleration of gravity
H = plume source-to-ceiling distance
h = heat transfer coefficient, equation (1)
$\tilde{h}$ = characteristic heat transfer coefficient, equation (4)
K = kinematic momentum flux of jet
Pr = Prandtl number
Q = energy release rate of fire
Q_j = enthalpy flux of jet
Q^* = dimensionless Q, equation (4)
q = rate of heat transfer, equation (1)
q_c = rate of in-plate radial heat transfer
q_1 = rate of heat transfer to insulation
Re_H = Reynolds number, equation (4)
Re_5 = Reynolds number defined in [3, 5]
r = radial distance from impingement point
$r_{1/2}$ = r of jet where velocity is half of axial value
T_{ad} = surface temperature for adiabatic ceiling
T_{amb} = ambient temperature
T_s = ceiling surface temperature
t = time
V = velocity profile of wall/ceiling jet
$V_{\max}$ = maximum of V
w = function, equation (2)
$\tilde{Z}$ = b divided by diameter of jet orifice
z = distance from wall
α = constant, equation (A4)
δ = (largest) z where $V/V_{\max} = 1/2$
ϵ = plate emissivity
ΔE = rate of heat transfer retained in plate
ΔT^*_{ad} = dimensionless T_{ad}, equation (5)
λ_r = fraction of Q lost by radiation
ν = kinematic viscosity
σ = Stefan–Bolzmann constant

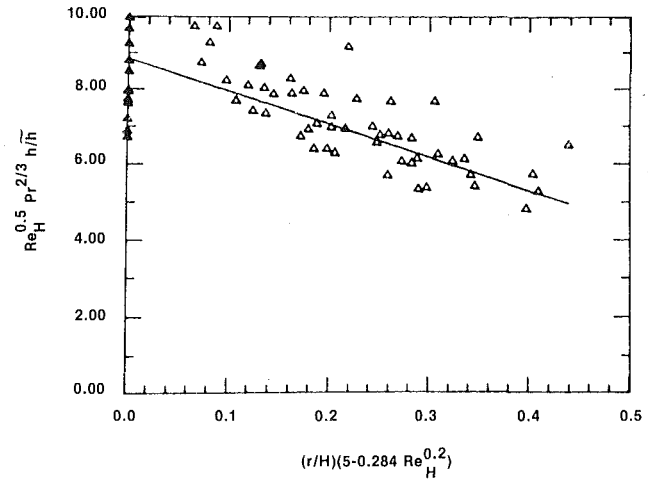

Fig. 2 Plot of the h data of [5], $7.3 \times 10^4 < Re_H < 27 \times 10^4$, and the estimate of equation (6); in the stagnation zone, $0 \le r/H < 0.2$

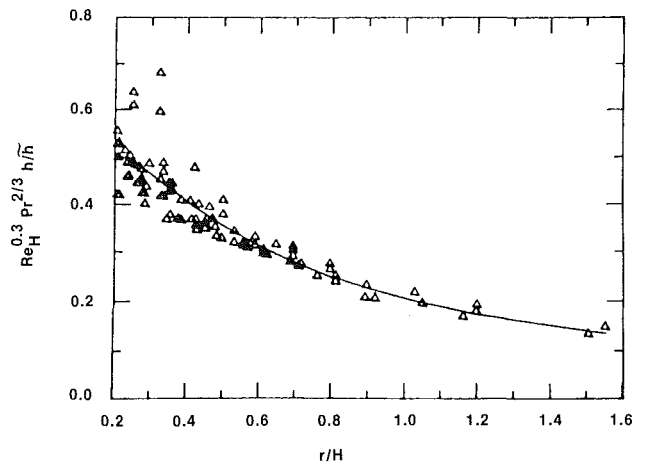

Fig. 3 Plot of the h data of [5], $7.3 \times 10^4 < Re_H < 27 \times 10^4$, and the estimate of equation (6); outside the stagnation zone, $0.2 \le r/H$

Except for ϵ (assumed for now to be unknown) and h, all terms on the right-hand side of equation (5) are available from tabular data presented in [2]. To carry out the equation (5) analysis the following h distribution was used

$$h/\tilde{h} = \begin{cases} 8.82\ \mathrm{Re}_{\bar{H}}^{-1/2}\ \mathrm{Pr}^{-2/3}[1-(5.0-0.284\ \mathrm{Re}_{\bar{H}}^{0.2})(r/H)], \\ \qquad 0 \le r/H < 0.2 \\ 0.283\ \mathrm{Re}_{\bar{H}}^{0.3}\ \mathrm{Pr}^{-2/3}\,(r/H)^{-1.2}\,\dfrac{(r/H-0.0771)}{(r/H+0.279)}, \\ \qquad 0.2 \le r/H \end{cases} \tag{6}$$

This expression, which is in the form of the correlation of equations (2)–(3), was developed by using the free jet/buoyant plume equivalency relations proposed in equations (A9) and (A10) of [3] and by a curve fitting of the free-jet-driven wall jet h data of [5] ($7.3 \times 10^4 < Re_H < 27 \times 10^4$). Plots of the h data of [5] and the equation (6) correlation are presented in Figs. 2 and 3 (residual standard deviations, rsd, of 0.87 and 0.04, respectively) for r/H values within ($0 \le r/H < 0.2$) and outside the stagnation zone, respectively.[1]

[1] Note that the data of [5] were incorrectly plotted in Figs. 6–8 of [3]. Instead of $Re_H^{0.3}\ Pr^{2/3}\ h/\tilde{h}$ and $Re_H^{0.5}\ Pr^{2/3}\ h/\tilde{h}$ as indicated on the ordinates of Figs. 6–7 and Fig. 8, respectively, the actual plots are of $Re_5^{0.3}\ Pr^{2/3}\ h/\tilde{h}$ and $Re_5^{0.5} \cdot Pr^{2/3}\ h/\tilde{h}$, where Re_5 is defined in [3, 5] and is approximately $Re_5 = 0.422 \cdot Re_H$. All of the data are correctly plotted here in Figs. 2 and 3.

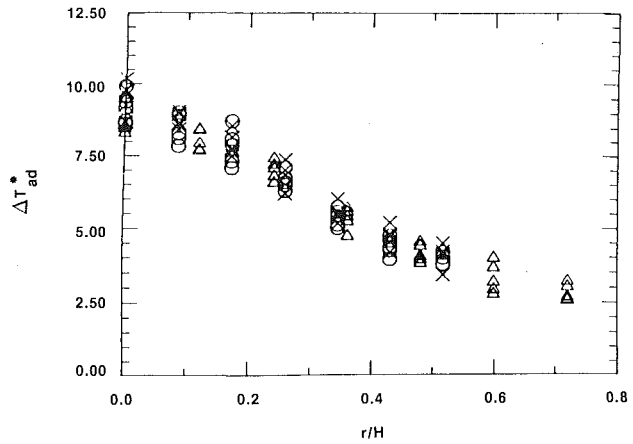

Fig. 4 Plots of the new ΔT^*_{ad} data for $\epsilon = 0$ (test 1: ○, test 2: △, test 3: X [2])

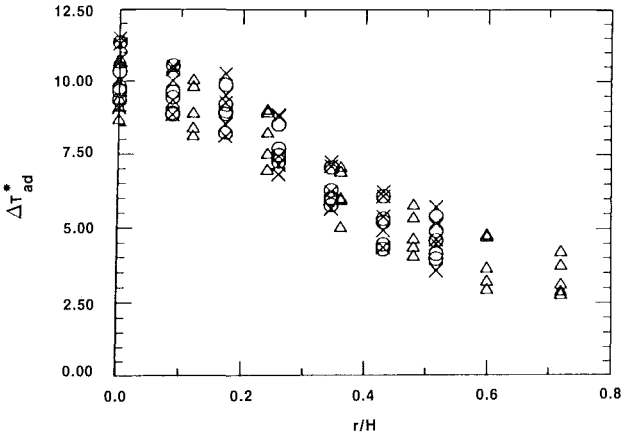

Fig. 5 Plots of the new ΔT^*_{ad} data for $\epsilon = 1$ (test 1: ○, test 2: △, test 3: X [2])

The new ΔT^*_{ad} values were computed from equations (5) and (6) and the data of Tables IV–IX of [2] for different assumed values of ϵ ranging from 0 to 1. Figures 4 and 5 are plots of these data for the $\epsilon = 0$ and $\epsilon = 1$ cases, respectively.

A Formula for $\Delta T^*_{ad}(r/H)$ and an Independent Indication of the True Value of ϵ

The correspondence between the flow and heat transfer characteristics of plume-driven ceiling jets and heated or unheated free turbulent jet-driven wall jets was mentioned earlier. Relative to this correspondence which was conjectured and supported in [3], and which was introduced into the present analysis via the equation (6) description for h, important new experimental results have been reported recently in [9]. Using data from that work, which studied heated jet-driven wall flows, the development of the following expression for the normalized ΔT^*_{ad} distribution was presented in the Appendix

$$\frac{\Delta T^*_{ad}(r/H)}{\Delta T^*_{ad}(r/H=0)} = f(r/H)$$

$$= \frac{1-1.10(r/H)^{0.8}+0.808(r/H)^{1.6}}{1-1.10(r/H)^{0.8}+2.20(r/H)^{1.6}+0.690(r/H)^{2.4}} \tag{7}$$

This result is plotted in Fig. 6 together with the (equivalent) data from which it was derived.

To use an equation (7) correlation for the new ΔT^*_{ad} values it is necessary to determine the best value for the ϵ, ΔT^*_{ad} pair.

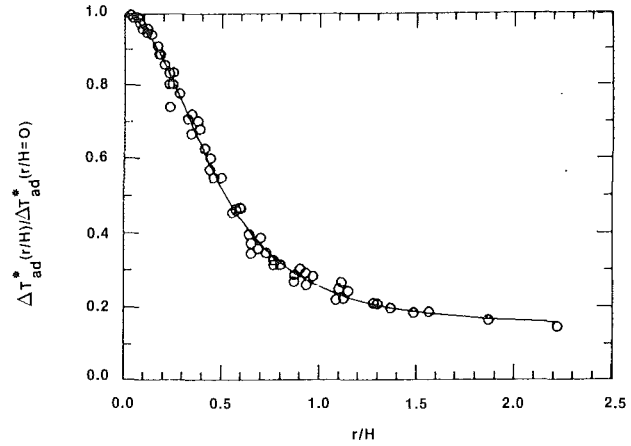

Fig. 6 Plots of the normalized ΔT^*_{ad} data of [9] and the estimate of equation (7)

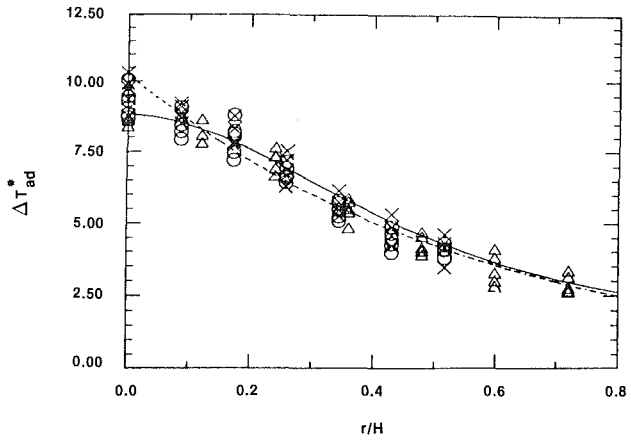

Fig. 7 Plot of the new ΔT^*_{ad} data for $\epsilon = 0.1$ (test 1: ○, test 2: △, test 3: X [2]), the ΔT^*_a estimate of equations (7) and (8) (_____), and the correlation (equations (11) and (12) of [3]) for the measured, long-time, near-ceiling gas temperatures of [2] (---)

Toward this end the following procedure was carried out: (1) compute new $\Delta T^*_{ad}(r/H=0)$ values for a given ϵ as discussed above; (2) obtain the corresponding $\Delta T^*_{ad}(r/H=0)$ which provides a least-squares, equation (7) fit to the new values.

Carrying out the procedure led to the following results: For ϵ in the range $0 \le \epsilon \le 1$, the values of $\Delta T^*_{ad}(r/H=0)$ and the rsd increase monotonically with ϵ over the relatively narrow ranges from 8.59 and 0.56 to 9.75 and 0.78, respectively.

The above procedure favors $\epsilon = 0$ as the best or true value. However, in view of the abovementioned results of [6] and [8]

$$\Delta T^*_{ad}(r/H=0) = 8.70 \tag{8}$$

which corresponds to $\epsilon = 0.1$ and a rsd of 0.57 would appear to be a preferred value for the normalizing factor of equation (7). Using equations (7) and (8) leads to a new estimate for ΔT^*_{ad} which is plotted in Fig. 7 along with the new, $\epsilon = 0.1$, ΔT^*_{ad} data.

Also plotted in Fig.7 is a correlation from [3] of the measured, late-time, near-ceiling gas temperatures of [2]. As can be seen, except for small r/H values the new estimate for ΔT^*_{ad} is close to, and slightly above, the measurements. Near the stagnation point, however, the measured temperatures generally suggest a plate temperature distribution with relatively large radial gradients and with an $r/H = 0$ value which actually exceeds the new ΔT^*_{ad}. The large gradients can be explained by the nonadiabatic, in-plate, radial conduction effect discussed earlier. However, near-ceiling gas temperatures could never have exceeded T_{ad}, and the fact that they do so is a strong basis for disqualifying the equation (7) estimate of ΔT^*_{ad} near the stagnation point.

In [2] it was noted that "appreciable error" in the estimates of in-plate radial conduction (q_1 of equation (5)) "has to be expected" near $r/H = 0$. This fact together with the above discussion and previous remarks suggest (1) that the long-time near-surface temperature measurements of [2] continue to be the basis of the ΔT^*_{ad} estimate within the stagnation zone, albeit with some uneasiness; (2) the latter estimate be continued at $r/H = 0.2$ by a new equation (7) type ΔT^*_{ad} estimate which would be used outside the stagnation zone; and (3) that the selection of an optimum normalizing factor to use in equation (7) be made without consideration of those new ΔT^*_{ad} values which correspond to the two smallest radial positions, $r = 0$ and $r = 0.07$ m, of the experiments.

The above ideas were implemented, and they resulted in the following newly recommended estimate for ΔT^*_{ad}

$$\Delta T^*_{ad} = \begin{cases} 10.22 - 14.9\, r/H, & 0 \le r/H \le 0.2 \\ 8.39\, f(r/H), & 0.2 < r/H \end{cases} \tag{9}$$

where $f(r/H)$ is defined in equation (7).

Conclusions

The new ΔT^*_{ad} estimate of equation (9) provides an experimentally based extension of earlier results from a maximum r/H value of 0.7 to an r/H value of 2.2. The results of the present analysis provide independent confirmation that, except for some uncertainty in the stagnation zone, the measured, long-time, near-ceiling gas temperatures of [2] accurately represent values of T_{ad}, and that ceiling reradiation in those experiments was negligible because of very low effective values of surface emissivity. Also, the results of this paper are consistent with and provide additional support for the notion, introduced in [3], that up to moderate values of r/H there is an equivalence between the flow dynamics and heat transfer characteristics of free jet-driven wall flows and buoyant plume-driven ceiling jets.

A recommended procedure for estimating the convective heat transfer from a fire plume to an unconfined ceiling, from the point of plume impingement to moderate r/H, was developed in [3]. This procedure is still recommended. However, the new results for T_{ad} and h, developed here and presented in equations (6), (7), and (9), should replace the corresponding equations (11), (12), (17), (18), and (20) estimates of [3]. The new results should also be used to modify equations (5), (6), (16), and (17) of [1] where the unconfined ceiling equations are used to estimate heat transfer to the confined ceilings of real compartment fire scenarios.

Acknowledgments

The authors acknowledge C. Marks of the University of Maryland for his valuable advice, and D. W. Stroup, S. Thorne, and D. Walton who designed and carried out preliminary experiments and data analysis which led to the ideas presented here. The work was supported by the U.S. Department of Health and Human Services, the Bureau of Mines and the National Park Service of the U.S. Department of Interior, and the Federal Aviation Administration of the U.S. Department of Transportation.

References

1 Cooper, L. Y., "Convective Heat Transfer to Ceilings Above Enclosure Fires," *19th Symp. (Inter.) on Combustion*, 1982, pp. 933-939.

2 Veldman, C. C., Kubota, T., and Zukoski, E. E., "An Experimental Investigation of the Heat Transfer From a Buoyant Gas Plume to a Horizontal Ceiling—Part 1. Unobstructed Ceiling," Cal. Inst. Tech., Nat. Bur. Stand. (U.S.) NBS-GCR-77-97, 1975.

3 Cooper, L. Y., "Heat Transfer From a Buoyant Plume to an Unconfined Ceiling," ASME JOURNAL OF HEAT TRANSFER, Vol. 104, 1982, pp. 446-451.

4 You, H.-Z., and Faeth, G. M., "Ceiling Heat Transfer During Fire Plume and Fire Impingement," *Fire and Materials*, Vol. 103, 1979, pp. 140-147.

5 Donaldson, C. DuP., Snedeker, R. S., and Margolis, D. P., "A Study of

Free Jet Impingement. Part 2. Free Jet Turbulent Structure and Impingement Heat Transfer," *J. Fluid Mech.*, Vol. 45, Part 3, 1971, pp. 447-512.

6 McDermott, P. F., "An Apparatus for Measurement for the Total Normal Thermal Emissivity of Sheet Materials in the Temperature-Range 140-500°F," *Rev. of Scientific Instruments*, Vol. 8, 1937, pp. 185-192.

7 Gubareff, G. G., Janssen, J. E., and Torborg, R. H., *Thermal Radiation Properties Survey*, Honeywell Research Center, Minneapolis, 1960, p. 98.

8 Roberts, W., National Bureau of Standards, private communication.

9 Hollworth, B. R., and Wilson, S. I., "Entrainment Effects on Impingement Heat Transfer. Part I: Measurements of Heated Jet Velocity and Temperature Distributions and Recovery Temperatures on a Target Surface," ASME JOURNAL OF HEAT TRANSFER, Vol. 106, 1984, pp. 797-803.

10 Poreh, M., Tsuei, Y. G., and Cermak, J. E., "Investigation of a Turbulent Radial Wall Jet," ASME *Journal of Applied Mechanics*, June 1967, pp. 477-512.

APPENDIX

T_{ad} for the Wall Jet Away From the Stagnation Zone

Consider a wall jet driven by a heated turbulent jet impinging on an adiabatic plane surface. Let Q_j be the constant enthalpy flux of the jet relative to T_{amb}. Assume that jet temperatures near the impingement point are close enough to T_{amb} so that, for the purpose of applying conservation of energy to the wall jet, the density field and C_p can be approximated by their ambient values. Then

$$Q_j = 2\pi r \rho_{amb} C_p V_{\max} (T_{ad} - T_{amb}) \int_0^\infty \left(\frac{T - T_{amb}}{T_{ad} - T_{amb}}\right) \frac{V}{V_{\max}}\, dz \tag{A1}$$

where the integration is over the thickness of the wall jet at the radial position of interest. In the above, V is the distribution of the radial component of velocity and $V_{\max}$ is its maximum value. T_{ad} is the temperature distribution at the wall surface.

Let δ be the distance from the wall, at the outer portion of the wall jet, where $V/V_{\max} = 1/2$. Then the experimental study of [10] for unheated jets indicates that $V/V_{\max}$ profiles at different r stations are similar in the sense that they can be closely approximated by

$$V/V_{\max} = f_1(z/\delta) \text{ for } r/b > 0.75 \tag{A2}$$

where b is the effective jet nozzle-to-wall separation distance. We assume that this latter result is applicable even for heated jets since momentum forces will typically dominate buoyancy forces in the zero to moderate r/b values of interest. Furthermore, it is reasonable to assume that $(T - T_{amb})/(T_{ad} - T_{amb})$ can also be approximated as a function of z/δ in the $r/b > 0.75$ range. Using the latter assumptions in equation (1) leads to

$$T_{ad} - T_{amb} = \alpha\, Q_j/(\rho_{amb} C_p V_{\max} r\delta),\ r/b > 0.75 \tag{A3}$$

$$1/\alpha = 2\pi \int_0^\infty \left(\frac{T - T_{amb}}{T_{ad} - T_{amb}}\right) \frac{V}{V_{\max}}\, d\left(\frac{z}{\delta}\right) \tag{A4}$$

Besides equation (A2), other results in [10] of interest here are

$$V_{\max}/(\sqrt{K}/b) = 1.32(r/b)^{-1.1};\ \delta/b = 0.098(r/b)^{0.9} \tag{A5}$$

where $\rho_{amb} K$ is the (constant) momentum flux along axial sections of the unheated jet prior to impingement.

For the case of the heated jet it is reasonable to expect that the unheated jet results of equations (A5) would still be valid provided K and b are redefined. This could be done, for example, by drawing an equivalence at the jet/wall impingement point between a heated jet of interest and the unheated jets for which equations (A5) are valid. This notion of equivalence was used, e.g., in [3]. There, a buoyant plume (i.e., the far field of a limiting, small-K or low-momentum jet) was taken to be equivalent to an unheated jet at respective points of wall/ceiling impingement if the total mass and momentum flux of the plume and jet were identical. Applying these criteria for equivalence led to the results in [3] that the flow of a buoyant plume-driven ceiling jet, at least up to moderate values of r/H, would simulate the flow of an unheated, free jet-driven wall jet if b and K in the results of [10] were replaced by point-heat-source-driven plume parameters as follows

$$K^{1/2} = 0.636\, g^{1/2} H^{3/2} Q^{*1/3};\ b = 1.17\, H \tag{A6}$$

Following the above, it is assumed that the idea of equivalence at impingement between the K, b pair of an unheated jet and related parameters of a heated jet has some generality. Accordingly, equations (A5) are used in equation (A3) with the result

$$\frac{T_{ad} - T_{amb}}{Q_j/(\rho_{amb} C_p b \sqrt{K})} = 7.73\, \alpha (r/b)^{-0.8};\ r/b > 0.75 \tag{A7}$$

For the case of a buoyant plume, the equivalence relationships of equation (A6) together with the substitution of $(1 - \lambda_r)Q$ for Q_j are used in equation (A7) to yield

$$\Delta T^*_{ad} = 11.8\, \alpha (r/H)^{-0.8};\ r/H > 0.88 \tag{A8}$$

A Normalized ΔT^*_{ad} Distribution

T_{ad} data for heated jet-driven wall jets have been recently acquired and plotted in Fig. 9 of [9]. This plot is in the form

$$\frac{T_{ad}(r) - T_{amb}}{T_{ad}(0) - T_{amb}} = f_2(r/r_{1/2}) \tag{A9}$$

where $r_{1/2}$ is defined as the radial position of the impinging jet, at the plane of impingement, where the jet velocity, in the absence of the wall, would have dropped to 1/2 of its value on the jet axis. Plotted in this way, the data ($r/r_{1/2} < 20.6$) correlate well for all test cases where the ratio of jet orifice-to-wall-distance to jet orifice diameter $\bar{Z}$ exceeds 1 (i.e., for jets of different Q_j and with $\bar{Z}$ of 5, 10, and 15). Interpreting equation (A7) as an asymptotic result for large $r/r_{1/2}$, the following curve fit to the $\bar{Z} > 1$ data of [9] has been obtained with a residual standard deviation of 0.02

$$\frac{T_{ad}(r/r_{1/2}) - T_{amb}}{T_{ad}(0) - T_{amb}} = \frac{1 - 0.199(r/r_{1/2})^{0.8} + 0.0258(r/r_{1/2})^{1.6}}{1 - 0.199(r/r_{1/2})^{0.8} + 0.0640(r/r_{1/2})^{1.6} + 0.00443(r/r_{1/2})^{2.4}} \tag{A10}$$

In the experiments of [9], buoyancy forces compared to inertial forces in the impinging downward-directed jet were reported to be small enough so that within jet axis distances studied, centerline velocities varied on the order of a few percent at most when the jet was turned upward. Accordingly it is reasonable to assume that the velocity distributions (e.g., the values of $r_{1/2}$) of the jets at impingement would be closely approximated by the corresponding velocity distributions of similarly configured but unheated free jets. Equation (A9) of [3] suggests the following equivalence between the $r_{1/2}$ of an unheated jet and the H (distance from the source) of a buoyant plume

$$r_{1/2} = 0.109\, H \tag{A11}$$

Using this in equation (A10) suggests the normalized ΔT^*_{ad} distribution for plume-driven ceiling jets which is presented in equation (7). This together with the data of [6] (made equivalent with the use of equation (A11)) is plotted in Fig. 6.

Structure of Turbulent Adiabatic Wall Plumes

M.-C. Lai

S.-M. Jeng[1]

G. M. Faeth
Fellow ASME

Department of Aerospace Engineering,
The University of Michigan,
Ann Arbor, MI 48109-2140

Weakly buoyant turbulent wall plumes were studied for surfaces inclined 0–62 deg from the vertical (stable orientation). The source of buoyancy was carbon dioxide/air mixtures in still air, assuring conserved buoyancy flux. Profiles of mean and fluctuating concentrations and streamwise velocities were measured at several stations along the wall. Flow structure was also observed by Mie scattering from a laser light sheet. Tests with inclined walls showed that low levels of ambient stratification caused the wall plumes to entrain fluid in the horizontal direction, rather than normal to the wall. Structure predictions were made for vertical wall plumes, considering Favre-averaged mixing-length and k–ϵ–g models of turbulence. Both methods yielded encouraging predictions of flow structure, in spite of the presence of large-scale coherent turbulent structures observed in the flow visualization.

Introduction

Wall plumes are encountered above fires along surfaces, near baseboard heaters and electronic circuit boards, and in other confined natural convection processes. The main objective of this study was to complete new nonintrusive measurements of the mean and turbulent structure of wall plumes, useful for evaluating models of the process. Attention was confined to weakly buoyant (maximum density variations of 4 percent) wall plumes, having conserved buoyancy flux, along surfaces inclined 0–62 deg from the vertical (stable orientation). Model evaluation was also initiated, for flows along vertical surfaces, considering methods typical of current practice.

Although wall plumes are an interesting buoyant turbulent flow, they have not received much attention. Turner [1] describes some of the earliest work, where wall plumes having conserved buoyancy flux were studied using saline solutions. Observations showed that entrainment decreased as effects of stratification were increased by increasing wall inclination from the vertical. Furthermore, the entrainment of vertical wall plumes was lower than free line plumes, measured by Rouse et al. [2], due to stabilization of flow meandering by the wall.

Grella and Faeth [3] made probe measurements of mean and fluctuating streamwise velocities and mean temperatures, in adiabatic, weakly buoyant, thermal plumes, along vertical surfaces. Similarity of mean properties, aside from a near-wall region, was observed with respect to height above the source.

Liburdy and co-workers [4, 5] studied weakly buoyant thermal plumes along vertical isothermal surfaces. Hot-wire anemometry was used to measure mean and turbulent structure. Local similarity, in terms of local buoyancy flux and height above the source, was observed, aside from the near-wall region. The structure of adiabatic and isothermal wall plumes on vertical surfaces was also analyzed, using several eddy-viscosity and mixing-length models of turbulence. The approach of Cebeci and Khattab [6], developed for non-buoyant flow, yielded encouraging predictions of mean properties measured in [3–5]. This agreement was only obtained, however, by reducing turbulent Prandtl numbers from values near unity, prescribed by Cebeci and Khattab [6], to a value of one half (which agreed with direct measurements by Liburdy et al. [5] and values observed in two-dimensional free shear layers [7]).

Ljuboja and Rodi [8] recently tested a buoyancy-extended k–ϵ turbulence model using the adiabatic wall plume data of Grella and Faeth [3]. Fair agreement was obtained between predictions and measurements. However, effects of local Reynolds numbers in the near-wall region, observed in both the measurements and the mixing-length analyses [3, 5], were not reproduced and were attributed to data scatter.

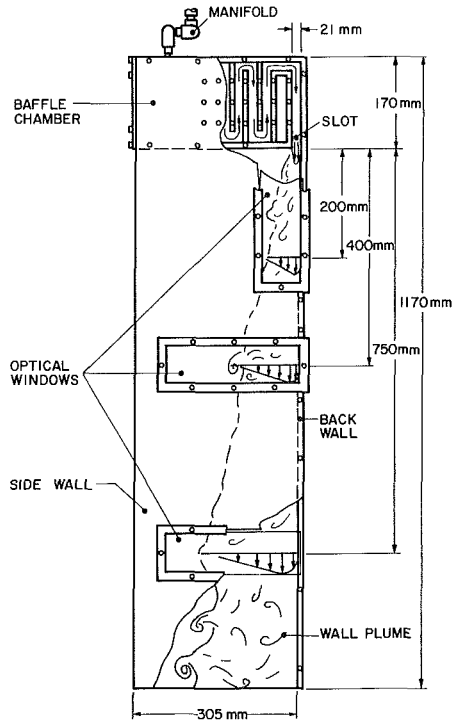

Fig. 1 Sketch of the test wall

In spite of past progress, current understanding of weakly buoyant wall plumes is uncertain and incomplete. Probes yield large experimental uncertainties over much of the flow, due to effects of flow reversals and high turbulence intensities. Turbulence structure data are very limited: No measurements have been repeated, only streamwise turbulence intensities are available for adiabatic wall plumes, and no information has been reported on effects of stratification along inclined surfaces. Past structure measurements have been for thermal plumes, yielding uncertainties due to parasitic heat losses. Finally, existing measurements have poorly defined initial conditions and uncertain levels of ambient stratification, which limits their value for developing predictive methods.

The present study seeks to remove some of these limitations. New structure measurements were completed for weakly buoyant plumes along a plane surface at various inclinations

[1] Present address: The University of Tennessee Space Institute, Tallahoma, TN 37388.

Contributed by the Heat Transfer Division and presented at the 23rd National Heat Transfer Conference, Denver, Colorado, August 1985. Manuscript received by the Heat Transfer Division March 15, 1985.

Table 1 Test conditions for vertical wall flows[a]

Case	1	2	3
Flow type	Wall jet	Wall plume	Wall plume
Density ratio $= \rho_0/\rho_\infty$	1.00	1.02	1.04
Initial mean velocity, m/s	0.43	0.31	0.43
Initial Reynolds number[b]	474	390	474
Initial Froude number[c]	∞	5.0	5.0

[a]Carbon dioxide/air mixtures, 21 mm source height, 800 mm wall width, 1000 mm wall length. Ambient pressure and temperature 97 kPa, 300 ± 3 K. Temperature stratification 0.26 ± 0.06 K/m over the period of testing. Ambient carbon dioxide concentrations were uniform with levels less than 5 percent of the slot flow concentration.
[b]$\mathrm{Re} = u_0 b/\nu_0$.
[c]$\mathrm{Fr} = (\rho_0 {u_0}^2/(ab(\rho_0 - \rho_\infty)))^{1/2}$.

Table 2 Summary of turbulence model parameters

ϕ	$\mu_{\mathrm{eff},\phi}$	S_ϕ
1	–	0
$\tilde{u}$	$\mu + \mu_t$	$a(\tilde{\rho} - \rho_\infty)$
$\tilde{f}$	$(\mu/\mathrm{Sc}) + (\mu_t/\sigma_f)$	0
k	$\mu + (\mu_t/\sigma_k)$	$\mu_t\left(\frac{\partial \tilde{u}}{\partial y}\right)^2 - \tilde{\rho}\epsilon$
ϵ	$\mu + (\mu_t/\sigma_\epsilon)$	$\left(C_{\epsilon 1}\mu_t\left(\frac{\partial \tilde{u}}{\partial y}\right)^2 - C_{\epsilon 2}\tilde{\rho}\epsilon\right)(\epsilon/k)$
g	$(\mu/\mathrm{Sc}) + (\mu_t/\sigma_g)$	$C_{g1}\mu_t\left(\frac{\partial \tilde{f}}{\partial y}\right)^2 - C_{g2}\tilde{\rho}g\epsilon/k$

Mixing length model

$$\mu_t = \tilde{\rho} \min\{[0.4y(1-\exp(-y/A))]^2; (0.075\delta)^2\}\left|\frac{\partial \tilde{u}}{\partial y}\right|$$

$\delta = y@\tilde{u} = 0.1\,\tilde{u}_m$ (outer position)
$A = 26\,\nu(\rho/\tau_\omega)^{1/2}$
$\sigma_f = 0.5$, $\mathrm{Sc} = 1.0$

k–ϵ–g model

$\mu_t = \tilde{\rho} C_\mu k^2/\epsilon$

C_μ	$C_{\epsilon 1}$	C_{g1}	$C_{\epsilon 2} = C_{g2}$	σ_k	σ_ϵ	$\sigma_f = \sigma_g$	Sc
0.09	1.44	4.0	1.87	1.0	1.3	0.5	1.0

(stable orientation). The source of buoyancy was carbon dioxide/air mixtures, assuring conserved buoyancy flux. Nonintrusive optical diagnostics were used to measure mean and fluctuating concentrations and streamwise velocities, including definition of initial and boundary conditions. Flow visualization provided information on the general features of the turbulent structure.

Analysis was undertaken to assist interpretation of measurements and to develop predictive methods. Vertical wall plumes were considered using Favre-averaged mixing-length and k–ϵ–g turbulence models, similar to past work in this laboratory [5, 9].

In the following, experimental and theoretical methods are described first. This is followed by discussion of experimental findings and comparison between predictions and measurements. The present discussion is brief; full details and a complete tabulation of data are provided by Lai [10].

Experimental Methods

Apparatus. A sketch of the test wall appears in Fig. 1. The flow was generated by carbon dioxide/air mixtures flowing downward along a plane wall in still air. The carbon dioxide/air mixture entered a plenum at the top of the wall and then passed through a series of baffles to achieve a uniform, two-dimensional flow at the 21-mm-high exit slot. The test wall was 1000 mm long, 800 mm wide, and had 305-mm-high side walls to help preserve two dimensionality. Windows in the side walls provided optical access for structure measurements at $x/b = 0.1$ (for initial conditions), 10, 20, and 37.5.

The tests were conducted in an interior room with the apparatus mounted on a concrete bed roughly 1 m above the floor. The remainder of the floor area was covered by a grating at the same level. The flow passed through the grating and was removed by a blower. The apparatus was separated from electronics (except optical detectors) and personnel by a 4 m × 3 m × 5 m high enclosure, to minimize ambient disturbances.

Optical instruments were mounted rigidly; therefore, profiles of flow properties were measured by traversing the entire wall on a bearing track. Positioning accuracy, normal to the wall, was 250 μm. The wall could be mounted at various vertical positions (accurate to 1 mm) and inclined 0, 31, and 62 deg (accurate to 1 deg) from the vertical (looking upward, e.g., in the stable configuration) while still accommodating traverses normal to the wall.

Gas flows to the top of the wall were provided by an oil-free air compressor and commercial-grade carbon dioxide stored in cylinders. Flows were controlled with pressure regulators and metered with critical-flow orifices, which were calibrated with a positive-displacement meter and a wet-test meter. After mixing, the flows passed through a 25 mm i.d. × 37 m long tube, to ensure complete mixing and equilibration to local room temperature, before entering the plenum at the top of the wall. Uncertainties in flow measurements and initial gas composition were less than 3 percent.

Instrumentation. Velocities were measured using laser-

Nomenclature

a = acceleration of gravity
A = constant in mixing-length model, Table 2
b = slot height at exit
C_i = constants in turbulence model
f = mixture fraction
Fr = Froude number, Table 1
g = square of mixture fraction fluctuations
k = turbulent kinetic energy
Re = Reynolds number, Table 1
Sc = laminar Schmidt number
S_ϕ = source term
u = streamwise velocity
v = velocity normal to wall
x = streamwise distance
y = distance normal to wall
δ = boundary layer thickness, Table 2
ϵ = rate of dissipation of turbulence kinetic energy
θ = wall inclination from the vertical
μ, μ_{eff}, μ_t = laminar, effective, and turbulent viscosity
ν = kinematic viscosity
ρ = density
σ_i = turbulent Prandtl/Schmidt number
τ_W = wall shear stress
ϕ = generic property

Subscripts

m = maximum quantity
0 = slot exit condition
∞ = ambient condition

Superscripts

$(\bar{\ })$ = time-averaged mean quantity
$(\tilde{\ })$ = Favre-averaged mean quantity
$(\bar{\ })'$ = time-averaged fluctuating quantity

Doppler anemometry (LDA). Concentrations were measured using laser-induced fluorescence (LIF) as well as isokinetic sampling and analysis by nondispersive infrared spectroscopy (NDIR). The flow was visualized by Mie scattering from a light sheet.

An argon-ion laser, yielding 800 mW at a wavelength of 514.5 mm, was used for the LDA. A dual-beam forward-scatter configuration was used, having a horizontal optical axis which was parallel to the wall. The measuring volume was 300 μm in diameter and 410 μm long (along the wall). Fringe spacing was 6.14 μm, calibrated with a rotating disk. A Bragg cell frequency shifter was used to eliminate effects of directional bias and flow reversals. Natural seeding was supplemented using 500-nm aluminum oxide particles in both the slot flow and the surroundings, yielding a seeding density of 0.36/measuring volume. Turbulence microscales were in the range 2–20 mm; therefore, burst densities were low but data densities were high. The data were processed with a burst counter (TSI, model 1980-A). Since data densities were high, the analog output of the processor was recorded using an integrating digital voltmeter (Hewlett-Packard 240IC), in conjunction with a true rms meter (TSI 1076) for velocity fluctuations, to yield unbiased time averages. Uncertainties in mean and fluctuating velocities were less than 5 percent and were repeatable within this range.

Laser-induced fluorescence of iodine vapor seeded into the slot flow, by passing it through a bed of iodine crystals, was used to measure the instantaneous concentration of slot fluid. The LIF signal was produced by an argon-ion laser, yielding 800 mW at 514.5 nm. The laser beam was horizontal and parallel to the wall. The scattering signal was observed normal to the wall yielding a cylindrical measuring volume having a diameter of 1 mm and a length (normal to the wall) of 1.3 mm. The fluorescence signals were observed using a monochrometer as a wide-band filter, observing the 533–540-nm wavelength range, where several strong fluorescence lines are present, while eliminating scattered and reflected light from the laser line. This allowed measurements close to the wall, in spite of strong reflections of the laser beam itself. Laser beam intensity was measured before and after passing through the flow. This allowed corrections for variations in initial beam power and for absorption of laser light before reaching the measuring volume, as well as an independent mean concentration measurement using the absorption signal. Iodine seeding levels in the slot flow were monitored by passing the flow through an absorption cell placed near the end of the mixing tube. Fluctuations of seeding levels were small, about 1 percent. The absorption and LIF signals were calibrated by measurements across the slot exit and through the cell – varying the fraction of the slot flow which was seeded with iodine. The LIF signal was linear in the mass fraction of slot fluid (the mixture fraction) while reabsorption of scattered light was small (less than 10 percent at the worst condition). The four detector signals were sampled at 40 Hz (each) using a 40 Hz cutoff with a sixth-order Chebychev anti-aliasing filter. Frequency spectra showed that there was negligible signal energy above 20 Hz. Signals were processed using a DEC MINC 11-23 computer to yield time-averaged mean concentrations by both absorption and LIF and fluctuating concentrations by LIF. Uncertainties in mean concentrations were less than 5 percent and were less than 10 percent for concentration fluctuations – both being repeatable well within this range.

Mean concentrations were also measured by isokinetic sampling at the mean velocity, and analysis using NDIR. The sampling probe was a cylindrical tube having inside and outside diameters of 1.6 and 3.2 mm, tapered from the tip at an angle of 20 deg, to provide a sharp leading edge. The sampling tube was parallel to the streamwise direction and could be positioned normal to the wall with an accurcy of 250 μm. The concentration of carbon dioxide was measured continuously using a Beckman model 864 infrared analyzer. Meter output was slightly nonlinear over the total range used, but was essentially linear over the concentration fluctuation range at any measuring position. Effects of reversed flow near the edge of the plumes, $y/x > 0.1$, are difficult to evaluate quantitatively. At other locations, uncertainties in mean concentrations were less than 10 percent, and were repeatable well within this range.

An argon-ion laser, yielding 2W (multiline mode), was used for flow visualization. The original beam (1.3 mm diameter to the e^{-2} intensity points) was spread into a light sheet and directed along the wall from top to bottom. The seeding particles used for LDA measurements, but placed only in the slot flow, yielded Mie-scattered light from the sheet to provide a visualization of the mixing process. The illuminated particles were photographed from the side (1 m from the sheet, at $x/b = 20$) using a Canon AE-1 Program Camera (35 mm focal length lens at f2.8 and 1/60s with Kodak ASA 1000 print film).

Test Conditions. Test conditions for vertical walls are summarized in Table 1 (only the Froude number changed for inclined walls, due to the reduced gravitational acceleration along the wall). Three flows were considered: a constant density wall jet, as a baseline, and two wall plumes having initial density ratios of 1.02 and 1.04. Initial velocities of the wall plumes were chosen to yield initial Froude numbers (for vertical walls) similar to the asymptotic Froude numbers measured by Grella and Faeth [3] for adiabatic wall plumes; therefore, the flow was neither under- nor overaccelerated at the slot exit which reduces the streamwise distance needed for flow development (cf. George et al. [11]).

Two dimensionality was checked by computing momentum and buoyancy fluxes along the wall [10], similar to Launder and Rodi [12], using measured mean properties. Mean momentum was conserved within 10 percent (including some uncertainty in wall friction estimates) and buoyancy flux was conserved within 5 percent. These levels are well within expectations, in view of effects of turbulent fluctuations on conserved properties of the flows (List [13]), suggesting reasonably good levels of two dimensionality. Aspect ratios, based on displacement, momentum, scalar mixing, and analogous flow half widths, were all greater than 10, also suggesting conditions conducive to two-dimensional flow.

Initial profiles of streamwise mean and fluctuating velocities were measured [10]. Profiles of $\bar{u}/\bar{u}_m$ and $\bar{u}'/\bar{u}_m$ were similar for all the flows. In spite of the low slot Reynolds numbers, $\bar{u}'/\bar{u}_m$ was in the range 0.10-0.15 for the central 80 percent of the slot. Ambient stratification could not be reduced below the levels indicated in Table 1 without unduly disturbing the desired stagnant ambient environment of the wall.

Theoretical Methods

Description of Analysis. The analysis treats a steady (in the mean), two-dimensional wall jet or vertical wall plume in a stagnant environment having constant properties. Boundary layer approximations are applied, and viscous dissipation and kinetic energy are ignored in the governing equations for mean quantities, with little error. Carbon dioxide and buoyancy fluxes are conserved. Typical of most analyses of turbulent mixing, the exchange coefficients of all species are assumed to be the same; therefore, scalar properties are only a function of mixture fraction (the fraction of mass which originated from the slot), termed the state relationships [9]. Mixture fraction is also a conserved scalar of the flow.

Turbulence properties were treated using either the mixing-length model of Cebeci and Khattab [6] or the k–ϵ–g model used by Jeng and Faeth [9]. The mixing-length model was developed for forced-convection flows, but was modified,

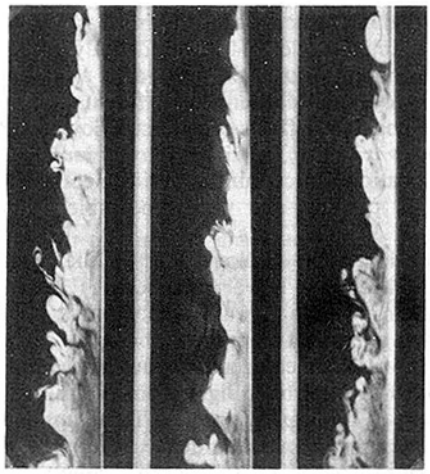

Fig. 2 Flow visualization of the wall plume, $\rho_0/\rho_\infty = 1.04$

following Liburdy et al. [5], to use a fixed turbulent Prandtl/Schmidt number of 0.5, rather than the original prescription which yields values of this parameter near unity. The k–ϵ–g model also ignores effects of buoyancy on turbulence properties, but has been reasonably successful for vertical buoyant flows [9]; its formulation has been changed very little from an early version used by Lockwood and co-workers [14, 15]. The analysis is formulated using mass-weighted or Favre averages, as recommended by Bilger [16], rather than conventional time or Reynolds averages. This avoids ad hoc neglect of many terms involving density fluctuations. As a practical matter, however, density variations were small for present flows and the differences between these averages are small in comparison to experimental uncertainties.

Formulation. Since scalar properties are only a function of mixture fraction, mean quantities are found by solving equations for conservation of mass, momentum, and mixture fraction. The solution is closed at this level for the mixing-length model, but closure of the k–ϵ–g analysis requires solution of modeled governing equations for turbulence kinetic energy k and its rate of dissipation ϵ. A modeled governing equation for the square of mixture fraction fluctuations g is also solved for comparison with measurements. This quantity is also needed to formally close analysis for scalar properties when density variations are significant, although this is not the case for current conditions.

The governing equations for both models can be written in the following generalized form

$$\frac{\partial}{\partial x}(\bar{\rho}\tilde{u}\phi)+\frac{\partial}{\partial y}(\bar{\rho}\tilde{v}\phi)=\frac{\partial}{\partial y}\left(\mu_{\text{eff},\phi}\frac{\partial\phi}{\partial y}\right)+S_\phi \qquad (1)$$

where $\phi = 1$ (for conservation of mass), $\tilde{u}$, $\tilde{f}$, k, ϵ, and g. Expressions for $\mu_{\text{eff},\phi}$ and S_ϕ for both models appear in Table 2. Changes in the mixing-length model of Cebeci and Khattab [6] involve $\sigma_f = 0.5$, as noted earlier, and Sc = 1, which is more appropriate for carbon dioxide diffusion in air than the earlier value of 0.7 used for heat transfer [5]. The same values of ϕ_f and Sc have been adopted for the k–ϵ–g model, as opposed to the value 0.7 used earlier for both [9]. Furthermore, since $C_{g1} = 2/\sigma_f$; $C_{g1} = 4$ rather than 2.8, used earlier [9]. Wall damping functions, used in most higher-order turbulence closures for wall flows [7, 8], were not used since wall jets and plumes are thick and approximate free shear layers over most of their width. An advantage of this is that empiricism is reduced.

The formal boundary conditions for equations (1) are

$$y=0,\ \tilde{u}=\tilde{v}=\frac{\partial\tilde{f}}{\partial y}=k=\epsilon=g=0 \qquad (2)$$

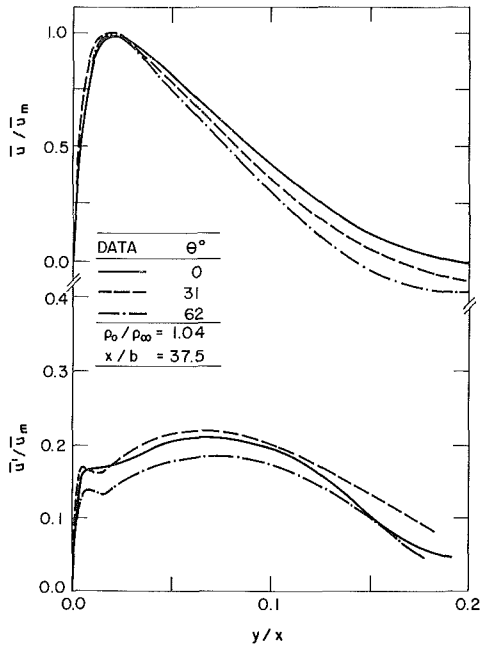

Fig. 3 Influence of wall inclination on mean and turbulent structure, $\rho_0/\rho_\infty = 1.04$, $x/b = 37.5$

$$y\to\infty,\ \tilde{u}=\tilde{f}=k=\epsilon=g=0 \qquad (3)$$

Initial conditions were specified from measurements of $\tilde{u}_0$, $\tilde{u}_0'$, $\tilde{v}_0'$, and $\widetilde{u'v'_0}$ at the slot exit. The measured values of $\tilde{u}_0'$ and $\tilde{v}_0'$ were used to compute k_0, assuming $\tilde{w}_0' = \tilde{v}_0'$; $\tilde{f}_0$ and g_0 are unity and zero, by definition; and ϵ_0 was estimated from the governing equations for Reynolds stress in the turbulence model [10]. Based on these considerations, initial conditions were prescribed as follows

$$\begin{aligned}
&x=0,\ 0\le y\le b:\\
&\tilde{u}_0(y)=\text{meas.},\ k_0(y)=\tilde{u}_0'^2(y)/2+v_0'^2(y)=\text{meas.}\\
&\tilde{f}_0(y)=1,\ g_0(y)=0\\
&\epsilon_0(y)=c_\mu k_0^2(y)\left(\frac{\partial\bar{u}(y)}{\partial y}\right)_0\Big/\overline{u'v'(y)_0}=\text{meas.}
\end{aligned} \qquad (4)$$

where the distinction between Favre and Reynolds averages has been ignored, since the density is constant at the slot exit.

Scalar Properties. Methods for computing Reynolds- and Favre-averaged scalar properties from the k–ϵ–g analysis are described elsewhere [9, 10, 16]. Since $\rho^{-1}\sim f$ for present conditions [10], $\bar{\rho} = \rho(\tilde{f})$, which closes the scalar property formulation needed to solve equations (1)–(4). Other scalar properties, e.g., the mass fraction of carbon dioxide or tracer gas, can be found by assuming a two-parameter functional form for the PDF of mixture fraction – a clipped Gaussian function was used similar to past work in this laboratory [9, 17]. As noted earlier, however, effects of density fluctuations were small in present flows; therefore, Favre and Reynolds averages of scalar properties are essentially the same and are little different from values at $\tilde{f}$.

Computations. Equations (1)–(4) were solved using a modified version of GENMIX, developed by Spalding [18], with a computational grid and convergence requirements similar to past practice [9, 17]. As usual, the number of grid points was minimized by not integrating the equations clear to the wall, but by using modified boundary conditions in the region where the Law of the Wall applies, following the approach of Ljuboja and Rodi [8].

Table 3 Summary of predicted and measured properties of vertical wall flows

x/b	10		20		37.5	
Condition	$\bar{u}_m/\bar{u}_0$	$\bar{f}_m/\bar{f}_0$	$\bar{u}_m/\bar{u}_0$	$\bar{f}_m/\bar{f}_0$	$\bar{u}_m/\bar{u}_0$	$\bar{f}_m/\bar{f}_0$
Wall jet, $\rho_0/\rho_\infty = 1$:						
Measurements	0.760	–	0.571	–	0.458	–
k–ϵ–g analysis	0.690	0.941	0.532	0.796	0.395	0.621
Mixing-length analysis	0.700	0.946	0.501	0.802	0.348	0.582
Wall plume, $\rho_0/\rho_\infty = 1.02$:						
Measurements	0.905	0.940	0.819	0.750	0.760	0.541
k–ϵ–g analysis	0.875	0.931	0.813	0.731	0.760	0.491
Mixing-length analysis	0.856	0.923	0.827	0.761	0.817	0.562
Wall plume, $\rho_0/\rho_\infty = 1.04$:						
Measurements	0.932	0.931	0.851	0.723	0.811	0.525
k–ϵ–g analysis	0.899	0.925	0.839	0.723	0.791	0.481
Mixing-length analysis	0.885	0.931	0.867	0.760	0.862	0.564

Preliminary Observations

Flow Visualization. Three typical flow visualization photographs appear in Fig. 2. The photographs show the full length of a vertical wall. The flow is random; therefore, while large turbulent structures are visible, patterns are not repetitive, unlike many shear layers in the transition region [19]. Flow properties are also characterized by rather well-defined vortex structures ("jelly rolls") near the edge of the flow, and by penetration of unmixed ambient fluid to points very near the surface.

Inclined Walls. Measurements of streamwise mean and fluctuating velocities for vertical and inclined walls are illustrated in Fig. 3. The width of free line plumes [2] and wall plumes [3–5] is proportional to height above the source; therefore, y/x is roughly a similarity variable for wall plumes, aside from the near-wall region where boundary-layer growth rates differ [3–5]. As a result, $\bar{u}/\bar{u}_m$ is plotted as a function of y/x in Fig. 3, to illustrate this scaling. A startling feature of these results is that the mean velocity becomes *negative* near the edge of the flow for inclined walls, rather than approaching the expected value of zero seen for the vertical wall plume. The magnitude of the negative edge velocity progressively increases with increasing wall inclination from the vertical, reaching 10–15 percent of the maximum streamwise velocity for a wall inclination of 62 deg. The outer boundary of the mean velocity profiles is roughly the same for the three flows, after allowing for the region of negative velocities. Streamwise fluctuations are comparable for the three cases, but there is a tendency for reduced fluctuations at larger angles from the vertical. This could be due either to lower Reynolds numbers, to lower mean velocities at larger inclinations, or to effects of stratification on turbulence properties.

After thoroughly checking the apparatus, it was concluded that the negative velocities near the flow edge were caused by the entrained flow moving nearly *horizontally* from the surroundings to the plume, rather than normal to the wall. Therefore, as the inclination of the wall is increased, this horizontal flow has a negative velocity component parallel to the wall, for the stable wall inclinations considered during the tests, e.g., $\bar{u}_\infty = \bar{v}_\infty \tan\theta$, where $\bar{v}_\infty$ is the entrainment velocity (which is negative and has a magnitude of about 0.1 $\bar{u}_m$ [3]), while θ is the inclination of the wall from the vertical. Effects of ambient stratification cause the entrained flow to enter the plume horizontally, particularly for present test conditions. This follows since entrainment velocities are small, yielding small static pressure differences to initiate the motion of the entrained gas, in comparison to pressure differences due to stratification which stabilize vertical motion.

The problem of low-level ambient stratification on entrainment has not been given much attention (and probably would not be detected when using probes), but has been observed before, e.g., Fujii and Imura [20] observed horizontal entrainment during laminar natural convection along inclined surfaces. The implications of this phenomenon concerning past measurements of wall plume entrainment on inclined surfaces should be considered. Rather than attempt to deal with this ambient flow, which would require an elliptic formulation with subsequent loss of the computational efficiency of boundary-layer flows, subsequent work was limited to vertical wall plumes where effects of stratification on the direction of entrainment are small.

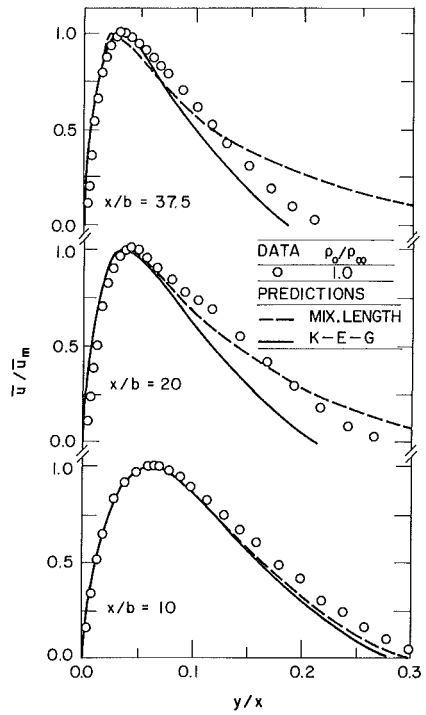

Fig. 4 Mean velocities in a wall jet

Results and Discussion

Mean Quantities. $\bar{u}_m$ and $\bar{f}_m$ are used to normalize velocities and concentrations in the following; therefore, predicted and measured values of these quantities are summarized in Table 3. For fully developed, two-dimensional turbulent free jets, $\bar{u}_m$ and $\bar{f}_m \sim x^{-1/2}$, while for free line plumes $\bar{u}_m \sim x^0$ and $\bar{f}_m \sim x^{-1}$ [2, 3, 21]. Wall jets and plumes only approximate these scaling rules, due to low Reynolds number effects near surfaces. Furthermore, the present flows are developing from the slot exit condition, which also tends to obscure these trends somewhat. However, similarity to the previous scaling rules is evident, e.g., $\bar{u}_m$ and $\bar{f}_m$ both decrease for the wall jet, while $\bar{u}_m$ is relatively constant and $\bar{f}_m$ decreases more rapidly

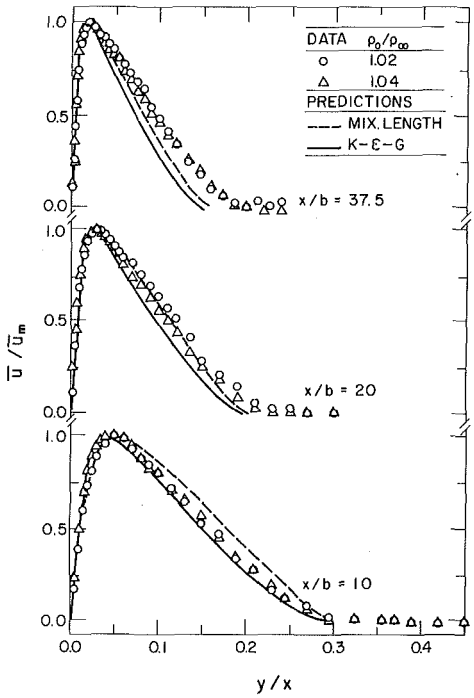

Fig. 5 Mean velocities in wall plumes

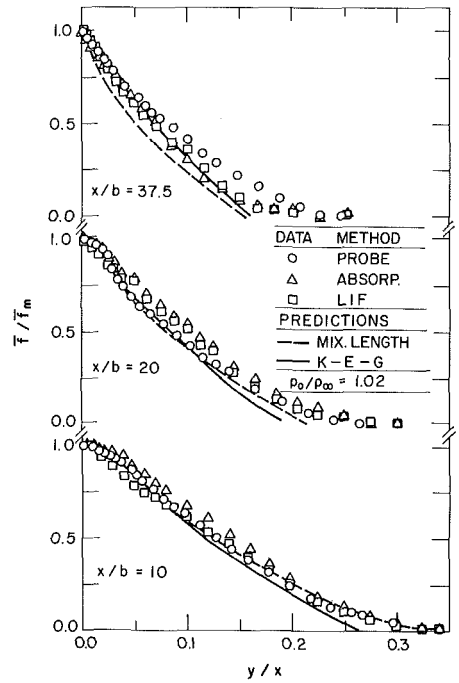

Fig. 6 Mean mixture fraction in a wall plume, $\rho_0/\rho_\infty = 1.02$

for the wall plumes. Mixing-length and k-ϵ-g predictions are generally within 10 percent of the measurements; however, the latter model generally yields the best overall results.

Predicted and measured values of $\bar{u}/\bar{u}_m$ for the wall jet are plotted as a function of y/x in Fig. 4. The present flow is developing as Reynolds numbers increase in the streamwise direction; therefore, it becomes progressively narrower in terms of normalized distance from the wall. The mixing-length model overestimates flow width, particularly far from the source, probably since the Reynolds numbers of present flows are well below the range where this model was developed. The k-ϵ-g model tends to underestimate flow widths but is in fair agreement with the measurements.

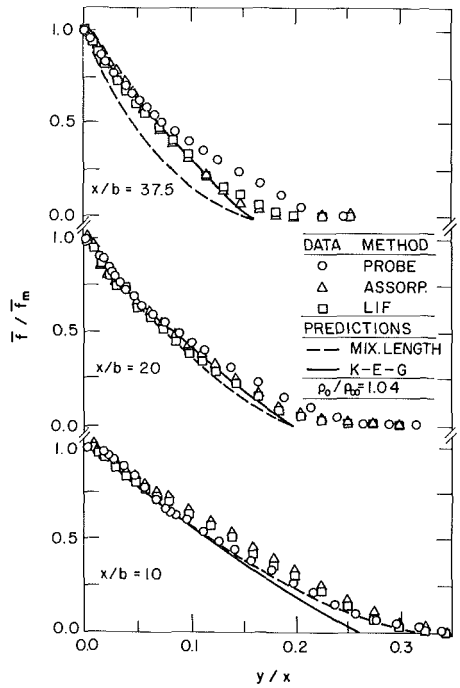

Fig. 7 Mean mixture fraction in a wall plume, $\rho_0/\rho_\infty = 1.04$

Similar results for the wall plumes appear in Fig. 5. When plotted in this manner, results for both wall plumes are nearly the same. Predictions support this observation; therefore, a single line for each prediction represents both flows. Predictions of both models are similar – yielding the location of the maximum velocity reasonably well but underestimating the flow width, particularly far from the source. The fact that turbulence models which ignore effects of buoyancy on turbulence properties yield reasonably good predictions of mean properties in vertical buoyant flows agrees with past experience [5, 9, 17, 22].

Predicted and measured values of $\bar{f}/\bar{f}_m$ are plotted as a function of y/x in Figs. 6 and 7, for the two wall plumes. Three sets of measurements are shown: probe sampling, laser absorption, and LIF. The latter two agree quite well with each other, supporting the accuracy of the optical diagnostics, but probe sampling yields higher values near the flow edge. This is probably due to sampling problems in this region, where turbulence intensities are high and flow reversals are frequent. Clearly, neither of these problems can be cured by sampling isokinetically at the local mean velocity. Results for the two density ratios are plotted separately, to reduce cluttering; however, both predictions and measurements are nearly identical for the two flows. While the concentration gradient at the surface is formally zero, this is not very evident in Figs. 6 and 7, similar to past observations for adiabatic wall plumes [3]. Damping of turbulence reduces mass diffusivities close to the wall; therefore, the zero-gradient region is too small to observe on the scale of these figures.

Mixing-length predictions in Figs. 6 and 7 are reasonably good near the source, but underestimate flow widths at downstream positions. The cause for this erratic behavior, underestimating widths of wall plumes and overestimating widths of wall jets, is not well understood. One possibility is that the turbulent mass diffusivity is proportional to the velocity gradient for this model and becomes zero at the maximum velocity position; therefore, reduced rates of mass diffusion in this region inhibit lateral transport of mass, and its attendent buoyancy forces, causing the flow width to be underestimated for plumes. Naturally this effect is absent for the wall jet. The k-ϵ-g model always yields nonzero turbulent mass exchange coefficients and provides improved results for

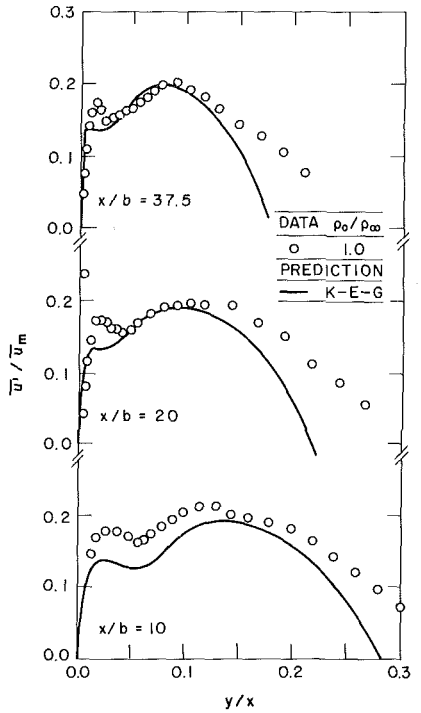

Fig. 8 Streamwise velocity fluctuations in a wall jet

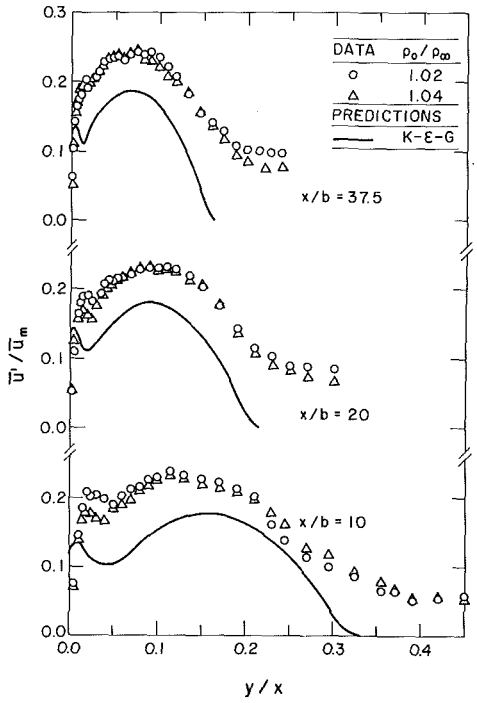

Fig. 9 Streamwise velocity fluctuations in wall plumes

plumes; however it still underestimates flow width to some extent. Measurements of turbulent fluctuations, to be discussed next, show relatively high levels of ambient disturbances, which could be responsible for this behavior. Similar to Liburdy et al. [5], however, use of $\sigma_f = 0.7$, with analogous changes in other parameters, causes further underestimation of flow widths.

Turbulence Quantities. More insight concerning the measurements of mean quantities, and model predictions of them, is provided by measurements of turbulence quantities. The mixing-length model provides no predictions of turbulence quantities; therefore, only the k–ϵ–g model will be

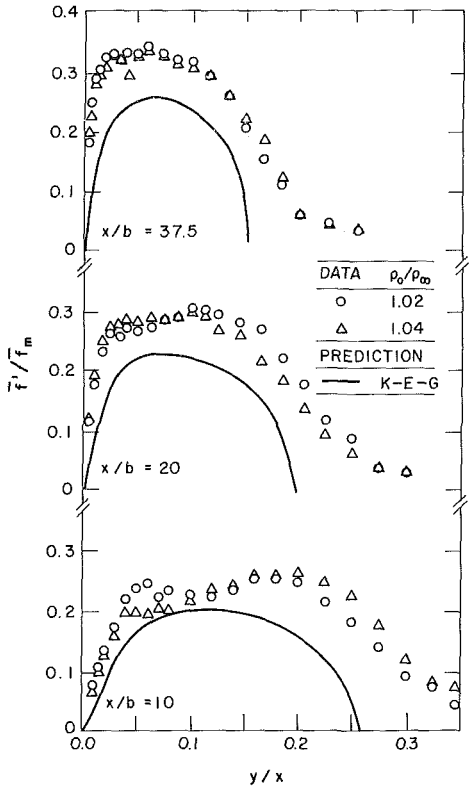

Fig. 10 Mixture fraction fluctuations in wall plumes

considered. Model predictions of k are related to $\tilde{u}'$ by assuming the usual levels of anisotropy of turbulent fluctuations observed in shear flows [21], namely $\tilde{u}'^2 = k$, while $g^{1/2} = \bar{f}'$, by definition.

Predicted and measured $\tilde{u}'/\tilde{u}_m$ are plotted as a function of y/x for the wall jet in Fig. 8. $\tilde{u}'/\tilde{u}_m$ increases from low values near the wall, dips near the maximum velocity location, and then decreases near the flow edge. Relatively high values near the edge are probably due to ambient disturbances, which are difficult to control for low velocity flows. The dip in turbulence intensity near the maximum velocity location is due to low rates of turbulence production where the mean velocity gradient is zero (Table 2).

Predictions of the k–ϵ–g model are only in fair agreement with measurements in Fig. 8. $\tilde{u}'/\tilde{u}_m$ is underestimated everywhere at $x/b = 10$. Farther from the source, peak values of $\tilde{u}'/\tilde{u}_m$ are predicted reasonably well, but the near-wall peak and values near the flow edge are underestimated. Liburdy et al. [5] show that turbulence properties near the maximum velocity position are complex for wall plumes, e.g., the peak mean velocity position is not coincident with the zero-stress point. The present k–ϵ–g model cannot represent such effects. High ambient disturbance levels may account for problems near the flow edge.

Similar results for wall plumes are illustrated in Fig. 9. Both wall plumes yield identical results when plotted in this manner. Measured levels of streamwise fluctuations are higher in wall plumes than the wall jet, but predictions are comparable for both flows (compare Figs. 8 and 9). Buoyancy/turbulence interactions, which were ignored for present predictions, are probably responsible for this deficiency. Maximum values of $\tilde{u}'/\tilde{u}_m$ are in the range 0.20-0.23, which are comparable to levels observed in wall plumes using probes [3, 5].

Predicted and measured $\bar{f}'/\bar{f}_m$ are plotted as a function of y/x in Fig. 10. Predictions for the two flows were nearly identical when plotted in this manner; measurements are nearly identical as well. Measurements indicate a slight dip in $\bar{f}'/\bar{f}_m$ near the maximum velocity point, possibly due to reduced pro-

duction of turbulence in this region; however, the model gives no evidence of a dip. Predictions generally underestimate measurements, particularly near the flow edge. Low levels of iodine tracer accumulating in the surroundings could account for this behavior. Measured values of $\bar{f}'/\bar{f}_m$ in Fig. 10 are somewhat greater than temperature fluctuations, normalized in the same manner, measured by Liburdy et al. [5] for isothermal wall plumes, e.g., the latter correspond roughly to present predictions. Higher ambient fluctuations and effects of intermittency for the lower Reynolds number range of present measurements are offered as possible explanations of the differences, but the matter deserves further study.

Conclusions

Structure measurements in inclined wall plumes showed that even low levels of flow stratification caused these flows to entrain ambient material in the horizontal direction, rather than normal to the wall, yielding negative streamwise ambient velocities for the present stable orientation. Past measurements of properties for inclined walls should be reconsidered in view of these findings. Probe measurements of mean concentrations were above actual values near the edge of the wall plumes, due to high turbulence intensities and flow reversals; therefore, nonintrusive measurements of scalar properties are recommended for these flows. The present LIF system is attractive for wall flows, since effects of reflections of the laser beam from surfaces can be eliminated.

The k–ϵ–g model yielded reasonably good predictions of the mean structure of the present wall jets and plumes, but only after using a turbulent Prandtl/Schmidt number of one half (which is a value consistent with past measurements in wall plumes [5]). This was achieved without direct consideration of effects of buoyancy on turbulence properties, at relatively low Reynolds numbers, and in the presence of large-scale turbulent structures and deeply penetrating intermittency – seen by flow visualization. Wall plumes are thick; therefore, this performance could be obtained without the added empiricism of wall damping functions. The mixing-length model of Cebeci and Khattab [6] yielded only slightly poorer predictions, even though it was used in a Reynolds number range generally well below the region where it was developed.

Acknowledgments

This research was supported by the United States Department of Commerce, National Bureau of Standards, Grant No. NB81NADA2044, with J. G. Quintiere and B. J. McCaffrey, of the Center for Fire Research, serving as Scientific Officers. This research was completed when the authors were affiliated with The Pennsylvania State University.

References

1 Turner, J. S., *Buoyancy Effects in Fluids,* Cambridge University Press, Cambridge, 1973, p. 165ff.

2 Rouse, H., Yih, C. S., and Humphreys, H. W., "Gravitational Convection From a Boundary Source," *Tellus*, Vol. 4, 1952, pp. 201–210.

3 Grella, J. J., and Faeth, G. M., "Measurements in a Two-Dimensional Thermal Plume Along a Vertical Wall," *J. Fluid Mech.*, Vol. 71, 1975, pp. 701–710.

4 Liburdy, J. A., and Faeth, G. M., "Heat Transfer and Mean Structure of a Turbulent Thermal Plume Along a Vertical Isothermal Wall," ASME JOURNAL OF HEAT TRANSFER, Vol. 100, 1978, pp. 177–183.

5 Liburdy, J. A., Groff, E. G., and Faeth, G. M., "Structure of a Turbulent Thermal Plume Rising Along an Isothermal Wall," ASME JOURNAL OF HEAT TRANSFER, Vol. 101, 1979, pp. 249–255.

6 Cebeci, T., and Khattab, A., "Predictions of Turbulent Free Convection From Vertical Surfaces," ASME JOURNAL OF HEAT TRANSFER, Vol. 97, pp. 469–471.

7 Launder, B. E., and Spalding, D. B., *Mathematical Models of Turbulence*, Academic Press, London, 1972, pp. 23–49.

8 Ljuboja, M., and Rodi, W., "Prediction of Horizontal and Vertical Turbulent Buoyant Wall Jets," ASME JOURNAL OF HEAT TRANSFER, Vol. 103, 1981, pp. 343–349.

9 Jeng, S.-M., and Faeth, G. M., "Species Concentration and Turbulence Properties in Buoyant Methane Diffusion Flames," ASME JOURNAL OF HEAT TRANSFER, Vol. 106, 1984, pp. 721–727.

10 Lai, M.-C., "Structure of Turbulent Adiabatic Wall Plumes," Ph.D. Thesis, The Pennsylvania State University, University Park, PA, 1985.

11 George, W. K., Jr., Alpert, R. L., and Tamanini, F., "Turbulence Measurements in an Axisymmetric Buoyant Plume," *Int. J. Heat Mass Transfer*, Vol. 20, 1977, pp. 1145–1154.

12 Launder, B. E., and Rodi, W., "The Turbulent Wall Jet," *Prog. Aerospace Sci.*, Vol. 19, 1981, pp. 81–128.

13 List, E. J., "Turbulent Jets and Plumes," *Ann. Rev. Fluid Mech.*, Vol. 14, 1982, pp. 189–212.

14 Lockwood, F. C., and Naguib, A. S., "The Prediction of the Fluctuations in the Properties of Free, Round-Jet, Turbulent Diffusion Flames," *Comb. Flame*, Vol. 24, 1975, pp. 109–124.

15 Gosman, A. D., Lockwood, F. C., and Syed, S. A., "Prediction of a Horizontal Free Turbulent Diffusion Flame," *Sixteenth Symposium (International) on Combustion*, The Combustion Institute, Pittsburgh, PA, 1977, pp. 1543–1555.

16 Bilger, R. W., "Turbulent Jet Diffusion Flames," *Prog. Energy Combust. Sci.*, Vol. 1, 1976, pp. 87–109.

17 Jeng, S.-M., Chen, L.-D., and Faeth, G. M., "The Structure of Buoyant Methane and Propane Diffusion Flames," *Nineteenth Symposium (International) on Combustion*, The Combustion Institute, Pittsburgh, PA, 1982, pp. 349–358.

18 Spalding, D. B., *GENMIX: A General Computer Program for Two-Dimensional Parabolic Phenomena*, Pergamon Press, Oxford, 1978.

19 Brown, G. L., and Roshko, A., "On Density Effects and Large Structure in Turbulent Mixing Layers," *J. Fluid Mech.*, Vol. 64, 1974, pp. 775–816.

20 Fujii, T., and Imura, I., "Natural-Convection Heat Transfer From a Plate With Arbitrary Inclination," *Int. J. Heat Mass Trans.*, Vol. 15, 1972, pp. 755–767.

21 Hinze, J. O., *Turbulence*, 2nd ed., McGraw-Hill, New York, 1975.

22 Lin, G.-J., and Churchill, S. W., "Turbulent Free Convention From a Vertical Isothermal Plate," *Num. Heat Transfer*, Vol. 1, 1978, pp. 129–145.

Correlations for Laminar Mixed Convection Flows on Vertical, Inclined, and Horizontal Flat Plates

T. S. Chen
Fellow ASME

B. F. Armaly
Mem. ASME

N. Ramachandran
Assoc. Mem. ASME

Department of Mechanical and Aerospace Engineering, University of Missouri—Rolla, Rolla, MO 65401

Local Nusselt numbers for laminar mixed convection flows along isothermal vertical, inclined, and horizontal flat plates are presented for the entire mixed convection regime for a wide range of Prandtl numbers, $0.1 \leq Pr \leq 100$. Simple correlation equations for the local and average mixed convection Nusselt numbers are developed, which are found to agree well with the numerically predicted values and available experimental data for both buoyancy assisting and opposing flow conditions. The threshold values of significant buoyancy effects on forced convection and forced flow effects on free convection, as well as the maximum increase in the local mixed convection Nusselt number from the respective pure convection limits, are also presented for all flow configurations. It is found that the buoyancy or forced flow effect can increase the surface heat transfer rate from pure forced or pure free convection by about 20 percent.

Introduction

Mixed convection arises in many transport processes in engineering devices (such as heat exchangers, solar collectors, nuclear reactors, hot-wire anemometers, heat storage and rejection systems, and electronic equipment) and in nature (such as atmospheric boundary layer flows) in which the effect of buoyancy force on a forced flow or the effect of forced flow on a buoyant flow becomes significant. Mixed convection in laminar boundary layer flow along vertical, inclined, and horizontal flat plates has been extensively analyzed and some experimental studies on these flow geometries have been reported. A relatively comprehensive summary of mixed convection laminar boundary layer flows has been given recently in [1].

In past studies, heat transfer results have been presented either for the forced flow situations with relatively weak to moderately strong buoyancy forces or for the buoyant flow situations with a weak forced flow (see, for example, [2–15]). Recently, Raju et al. [16] presented an analysis for the entire mixed convection regime for isothermal vertical and horizontal flat plates, but their results were limited to Prandtl numbers between 0.1 and 10. To summarize the analytical studies in connection with a flat plate, it is noted that relatively comprehensive local Nusselt number results have been presented for certain ranges of buoyancy parameters and Prandtl numbers. They include vertical flat plates covering $0 \leq Gr_x/Re_x^2 \leq 4$ for $0.003 \leq Pr \leq 100$ [4], $-0.2 \leq Gr_x/Re_x^2 \leq 16$ for $Pr = 0.7$ [17], and $0 \leq Re_x^4/(Gr_x^2 + Re_x^4) \leq 1$ for $0.1 \leq Pr \leq 10$ [16], inclined flat plates covering $-0.25 \leq Gr_x \cos\gamma/Re_x^2 \leq 5$ for $Pr = 0.7$ and 7 [7] and $-1.0 < Gr_x/Re_x^2 \leq 2$ for $Pr = 0.7$ and 7 [8], and horizontal flat plates covering $0 \leq Gr_x/Re_x^{5/2} \leq 10$ for $0.01 \leq Pr \leq 100$ [15] and $0 \leq Re_x^5/(Gr_x^2 + Re_x^5) \leq 1$ for $0.1 \leq Pr \leq 10$ [16]. Experimental results for the local Nusselt number have also been reported for air flow along an isothermal vertical plate [17], inclined plate [18], and horizontal plate [19], as well as for water flow over an isothermal horizontal plate [20].

In the present paper, comprehensive results are presented for the entire mixed convection regime, ranging from pure forced convection to pure free convection, for a wide range of Prandtl numbers. They cover isothermal vertical, inclined, and horizontal flat plates. The major aims of the paper are to present new local Nusselt number results to cover the entire mixed convection regime for $0.1 \leq Pr \leq 100$, to establish the upper and lower bounds of the mixed convection regime, and to present simple comprehensive correlation equations for determining the local and average Nusselt numbers in mixed convection for these flow configurations.

Analysis and Correlations

The formulation and treatment of laminar mixed convection flow adjacent to isothermal, semi-infinite flat plates have been presented for vertical, inclined, and horizontal geometries [1]. It will suffice to summarize in the Appendix the final expressions for the local and average Nusselt numbers. New numerical results have been generated for these geometries to cover the entire mixed convection regime for the buoyancy assisting flow case and the forced convection dominated regime for the buoyancy opposing flow case. In addition, these results are used to validate the accuracy of proposed simple correlations for the local and average mixed convection Nusselt numbers.

It has been proposed by Churchill [21] that the local Nusselt number in mixed convection laminar boundary layer flows for a given geometry Nu_x can be correlated well by combining the local Nusselt number for pure forced convection Nu_F and the local Nusselt number for pure free convection Nu_N for the same geometry in an equation of the form

$$Nu_x^n = Nu_F^n \pm Nu_N^n \tag{1}$$

In the above equation, n is a constant exponent and the plus and minus signs pertain respectively to buoyancy assisting and buoyancy opposing flow cases. Equation (1) can be written as

$$Y^n = 1 \pm X^n \tag{2}$$

where

$$Y = Nu_x/Nu_F, \qquad X = Nu_N/Nu_F \tag{3}$$

It is noted here that equations (2) and (3) apply also to the average mixed convection Nusselt number correlation if the local Nusselt numbers Nu_x, Nu_F, and Nu_N are replaced, respectively, with the corresponding average Nusselt numbers $\overline{Nu}$, $\overline{Nu}_F$, and $\overline{Nu}_N$. Correlations equivalent to equation (2) for vertical, horizontal, and inclined plates are presented below.

Contributed by the Heat Transfer Division for publication in the JOURNAL OF HEAT TRANSFER. Manuscript received by the Heat Transfer Division August 1, 1985.

Vertical Flat Plates. The local Nusselt number for pure forced convection in laminar boundary layer flow adjacent to an isothermal flat plate has been correlated by the expression [22]

$$\mathrm{Nu}_F = F_1(\mathrm{Pr})\mathrm{Re}_x^{1/2},$$

$$F_1(\mathrm{Pr}) = 0.399\mathrm{Pr}^{1/3}[1+(0.0468/\mathrm{Pr})^{2/3}]^{-1/4} \quad (4)$$

The corresponding correlation equation for pure free convection along an isothermal vertical plate is given by [23]

$$\mathrm{Nu}_N = F_2(\mathrm{Pr})\mathrm{Gr}_x^{1/4},$$

$$F_2(\mathrm{Pr}) = \frac{3}{4}\,\mathrm{Pr}^{1/2}[2.5(1+2\mathrm{Pr}^{1/2}+2\mathrm{Pr})]^{-1/4} \quad (5)$$

The local Nusselt number for mixed convection flow, according to equation (2), is then expressible as

$$\mathrm{Nu}_x\mathrm{Re}_x^{-1/2}/F_1(\mathrm{Pr}) = \{1 \pm [F_2(\mathrm{Pr})(\mathrm{Gr}_x/\mathrm{Re}_x^2)^{1/4}/F_1(\mathrm{Pr})]^n\}^{1/n} \quad (6)$$

Similarly, the average mixed convection Nusselt number for this flow geometry can be correlated as

$$\overline{\mathrm{Nu}}\mathrm{Re}_L^{-1/2}/2F_1(\mathrm{Pr}) = \{1 \pm [2F_2(\mathrm{Pr})(\mathrm{Gr}_L/\mathrm{Re}_L^2)^{1/4}/3F_1(\mathrm{Pr})]^n\}^{1/n} \quad (7)$$

It is noted here that equations (6) and (7) have the form $Y = (1 \pm X^n)^{1/n}$.

Horizontal Flat Plates. The local Nusselt number expression for pure forced convection flow adjacent to isothermal horizontal plates is given by equation (4). A correlation for the local Nusselt number for free convection over an upward-facing, heated, isothermal flat plate has been developed from the results of the present calculations for $0.1 \le \mathrm{Pr} \le 100$ and is given by the equation

$$\mathrm{Nu}_N = F_3(\mathrm{Pr})\mathrm{Gr}_x^{1/5},$$

$$F_3(\mathrm{Pr}) = (\mathrm{Pr}/5)^{1/5}\mathrm{Pr}^{1/2}[0.25+1.6\,\mathrm{Pr}^{1/2}]^{-1} \quad (8)$$

where the function $F_3(\mathrm{Pr})$ has a maximum error of 5 percent for Pr = 0.1. Thus, the local mixed convection Nusselt number correlation for this flow geometry can be written in accordance with equation (2) as

$$\mathrm{Nu}_x\mathrm{Re}_x^{-1/2}/F_1(\mathrm{Pr}) = \{1 \pm [F_3(\mathrm{Pr})(\mathrm{Gr}_x/\mathrm{Re}_x^{5/2})^{1/5}/F_1(\mathrm{Pr})]^n\}^{1/n} \quad (9)$$

The corresponding expression for the average Nusselt number is

$$\overline{\mathrm{Nu}}\mathrm{Re}_L^{-1/2}/2F_1(\mathrm{Pr}) = \{1 \pm [5F_3(\mathrm{Pr})(\mathrm{Gr}_L/\mathrm{Re}_L^{5/2})^{1/5}/6F_1(\mathrm{Pr})]^n\}^{1/n} \quad (10)$$

Again, equations (9) and (10) have the form $Y = (1 \pm X^n)^{1/n}$.

Inclined Flat Plates. In the work of Mucoglu and Chen [7], it has been established that the local Nusselt number for inclined plates may be obtained directly from that of the vertical plates by simply replacing Gr_x with $\mathrm{Gr}_x \cos\gamma$ in the equations provided that $\tan\gamma \ll \delta/x$, where δ is the boundary layer thickness, γ is the angle measured from the vertical, and x is the streamwise coordinate. Such a simple approximation has been shown to hold for inclination angles γ as large as 45 to 80 deg from the vertical in the Reynolds number range of $10^3 \le \mathrm{Re}_x \le 10^5$. Thus, equations (6) and (7) for the vertical plates may be employed for the inclined plates in the range of 0 deg $< \gamma <$ 75 deg if the Gr_x and Gr_L appearing in these equations are replaced, respectively, with $\mathrm{Gr}_x \cos\gamma$ and $\mathrm{Gr}_L \cos\gamma$.

For larger inclination angles 75 deg $\le \gamma \le$ 90 deg, different correlation equations are recommended. The local Nusselt number for pure free convection along an isothermal, inclined flat plate with inclination angle of 75 deg $\le \gamma \le$ 90 deg, has been correlated by Chen et al. [24] as

$$\mathrm{Nu}_N = F_4(\mathrm{Pr})\mathrm{Gr}_x^{1/5+C(\gamma)}, \qquad 10^3 \le \mathrm{Gr}_x\mathrm{Pr} \le 10^9 \quad (11)$$

where

$$F_4(\mathrm{Pr}) = \mathrm{Pr}^{1/2}[0.25+1.6\,\mathrm{Pr}^{1/2}]^{-1}(\mathrm{Pr}/5)^{1/5+C(\gamma)} \quad (12)$$

and

$$C(\gamma) = 0.070(\cos\gamma)^{1/2} \quad (13)$$

The use of equations (4) and (11) in equation (2) provides the correlation equation for the local mixed convection Nusselt number in the inclination angle range of 75 deg $\le \gamma \le$ 90 deg as

$$\mathrm{Nu}_x\mathrm{Re}_x^{-1/2}/F_1(\mathrm{Pr}) = \{1 \pm [F_4(\mathrm{Pr})(\mathrm{Gr}_x/\mathrm{Re}_x^{5/2})^{1/5}\mathrm{Gr}_x^{C(\gamma)}/F_1(\mathrm{Pr})]^n\}^{1/n} \quad (14)$$

Nomenclature

$C(\gamma)$ = function of γ, equation (13)

$F_1(\mathrm{Pr})$, $F_2(\mathrm{Pr})$, $F_3(\mathrm{Pr})$, $F_4(\mathrm{Pr})$ = functions of Prandtl number defined, respectively, by equations (4), (5), (8), and (12)

g = gravitational acceleration, m/s^2

Gr_x = local Grashof number = $g\beta(T_w - T_\infty)x^3/\nu^2$

Gr_L = Grashof number based on L = $g\beta(T_w - T_\infty)L^3/\nu^2$

h, $\bar{h}$ = local and average heat transfer coefficients, W/m^2-K

k = thermal conductivity, W/m-K

L = length of plate, m

n = constant exponent, equations (1) and (2)

Nu_F, Nu_N, Nu_x = local Nusselt numbers for pure forced, pure free, and mixed convection = hx/k

$\overline{\mathrm{Nu}}_F$, $\overline{\mathrm{Nu}}_N$, $\overline{\mathrm{Nu}}$ = average Nusselt numbers for pure forced, pure free, and mixed convection = $\bar{h}L/k$

Pr = Prandtl number = ν/α

Re_x = local Reynolds number = $u_\infty x/\nu$

Re_L = Reynolds number based on L = $u_\infty L/\nu$

T = fluid temperature, K

u, v = streamwise and normal velocity components, m/s

x, y = streamwise and normal coordinates, m

X = ratio of Nusselt numbers = $\mathrm{Nu}_N/\mathrm{Nu}_F$

Y = ratio of Nusselt numbers = $\mathrm{Nu}_x/\mathrm{Nu}_F$

α = thermal diffusivity, m^2/s

β = volumetric coefficient of thermal expansion, K^{-1}

γ = angle of inclination from the vertical, deg

δ = boundary layer thickness

η = dimensionless pseudo-similarity variable, equation (A2)

θ = dimensionless temperature = $(T - T_\infty)/(T_w - T_\infty)$

ν = kinematic viscosity, m^2/s

ξ = dimensionless streamwise coordinate and buoyancy parameter, equation (A2)

Ω = buoyancy parameter = $\mathrm{Gr}_x/\mathrm{Re}_x^{5/2}$

Subscripts

w = condition at wall

∞ = condition at free stream

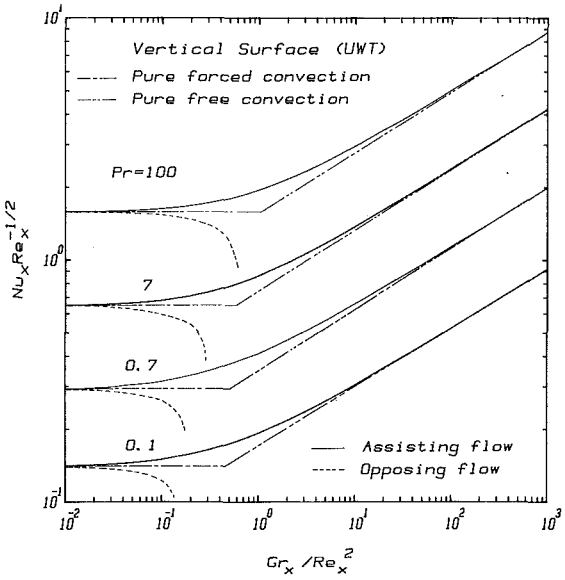

Fig. 1 Local Nusselt number results for flow along an isothermal vertical flat plate

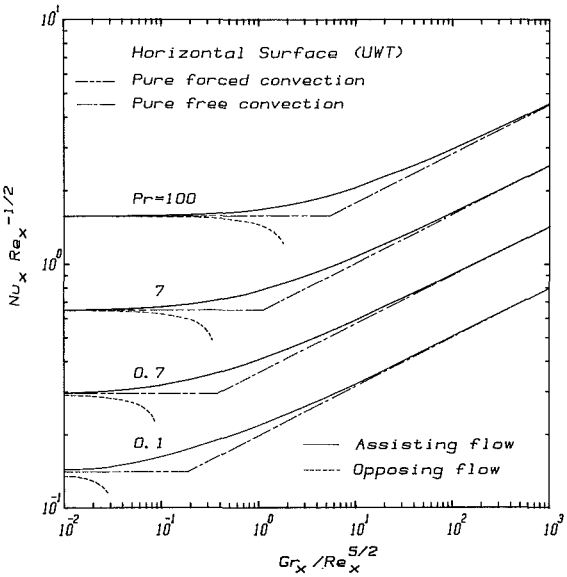

Fig. 2 Local Nusselt number results for flow over an isothermal horizontal flat plate

The corresponding correlation equation for the average Nusselt number is given by

$$\overline{\mathrm{Nu}}\mathrm{Re}_L^{-1/2}/2F_1(\mathrm{Pr}) = \left\{1 \pm \left[\frac{F_4(\mathrm{Pr})(\mathrm{Gr}_L/\mathrm{Re}_L^{5/2})^{1/5}\mathrm{Gr}_L^{C(\gamma)}}{6[1/5+C(\gamma)]F_1(\mathrm{Pr})}\right]^n\right\}^{1/n} \quad (15)$$

As before, equations (14) and (15) are expressed in the form $Y = (1 \pm X^n)^{1/n}$.

Results and Discussion

The numerical results to be presented are for Pr = 0.1, 0.7, 7, and 100. They cover the entire mixed convection regime for the buoyancy assisting situation and forced convection dominated regime for the buoyancy opposing situation.

Figure 1 illustrates the local mixed convection Nusselt number $\mathrm{Nu}_x\mathrm{Re}_x^{-1/2}$ as a function of the buoyancy parameter $\mathrm{Gr}_x/\mathrm{Re}_x^2$ for the vertical flat plate for Pr = 0.1, 0.7, 7, and 100. A similar plot for the horizontal flat plate is shown in Fig. 2 in terms of the buoyancy parameter $\mathrm{Gr}_x/\mathrm{Re}_x^{5/2}$. In both figures, results are shown for buoyancy assisting and opposing flow conditions. It is seen from the figures that when the buoyancy force assists the forced flow (the curves with solid lines), the local Nusselt number for mixed convection is always larger than those for pure forced convection and pure free convection, with the latter two curves forming asymptotes to the local mixed convection Nusselt number curve. On the other hand, when the buoyancy force opposes the forced flow (curves with dotted lines), the local Nusselt number for mixed convection is always smaller than that for pure forced convection. The curves for the latter case drop rather quickly and terminate at relatively small values of the buoyancy parameters when the opposing buoyancy forces become strong enough to cause flow separation inside the boundary layer. Flow separation occurs when the velocity gradient at the wall becomes zero. It should be noted that Fig. 1 can also be applied to inclined plates in the angle range 0 deg $\leq \gamma \leq$ 75 deg with good accuracy if the abscissa in the figure is replaced with $\mathrm{Gr}_x \cos\gamma/\mathrm{Re}_x^2$.

Table 1 Lower/upper bounds of significant buoyancy/forced-flow effects and maximum percentage increase in the local Nusselt number for assisting flow

Prandtl number	Vertical/Inclined Plates $a \leq \mathrm{Gr}_x\cos\gamma/\mathrm{Re}_x^2 \leq b$			Horizontal Plates $a \leq \mathrm{Gr}_x/\mathrm{Re}_x^{5/2} \leq b$		
Pr	a	b	max. increase in Nu_x, %	a	b	max. increase in Nu_x, %
0.1	0.06	7.0	21	0.04	2.8	20
0.7	0.07	7.5	22	0.05	9.5	23
7	0.10	8.5	23	0.16	20	23
100	0.20	12.0	24	0.75	80	23

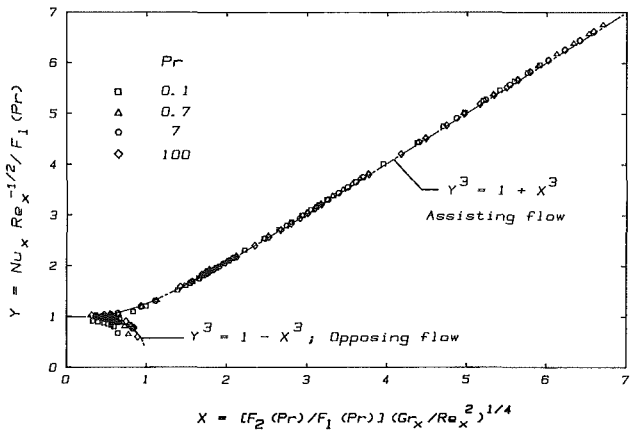

Fig. 3 A comparison between predicted and correlated local Nusselt numbers for isothermal vertical plates

It is of practical interest to know the threshold values of significant buoyancy effects on forced convection and forced flow effects on free convection, as well as the maximum increase in the local Nusselt number in mixed convection from those of pure convection limits. The threshold values of the lower and upper bounds, $a \leq \mathrm{Gr}_x/\mathrm{Re}_x^m \leq b$, based on a 5 percent departure from the pure forced convection and pure free convection local Nusselt numbers, respectively, for all cases are listed in Table 1. Included also in the table are the maximum percentage departure of the local mixed convection Nusselt number from those of pure forced and pure free convection. It can be seen from the table and also from Figs. 1 and 2 that as the Prandtl number increases the value of $\mathrm{Gr}_x/\mathrm{Re}_x^m$ for the significant buoyancy effect or forced-flow effect increases accordingly.

The correlation equation for the local mixed convection

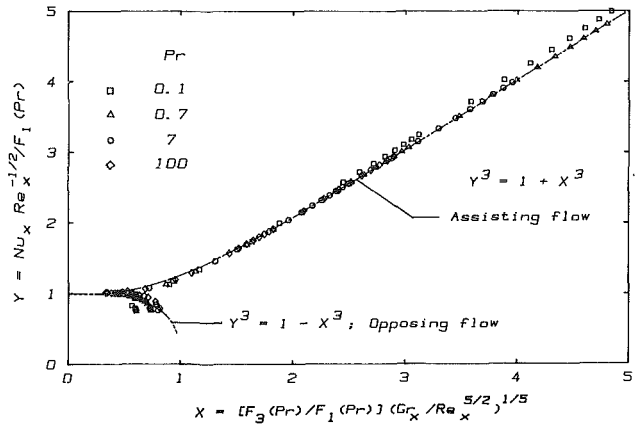

Fig. 4 A comparison between predicted and correlated local Nusselt numbers for isothermal horizontal plates

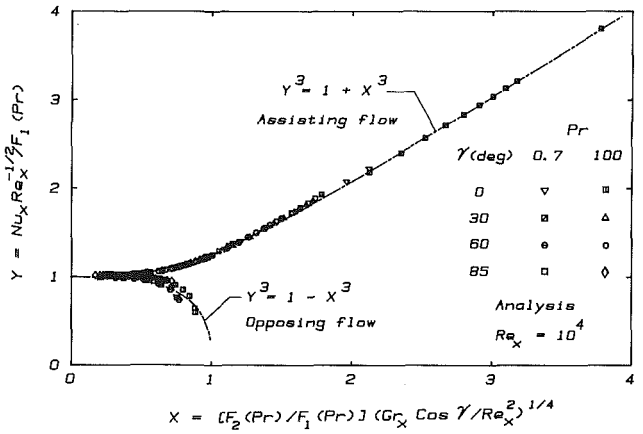

Fig. 5 A comparison between predicted and correlated local Nusselt numbers for isothermal inclined plates

Nusselt number for isothermal vertical flat plates ($\gamma = 0$ deg), equation (6), is shown as $Y^3 = 1 \pm X^3$ in a Y versus X plot and compared with the calculated results for Pr = 0.1, 0.7, 7, and 100 in Fig. 3. It is clear that an exponent value of $n = 3$ correlates very well with the analytically predicted results from equations (A1) and (A9) with $\gamma = 0$ deg. A similar good agreement between the proposed correlation equation (9) and the numerically calculated results from equations (A6) and (A13) for the horizontal plate ($\gamma = 90$ deg) is illustrated in Fig. 4, again with an exponent value of $n = 3$. The maximum deviation between the correlated and predicted local mixed convection Nusselt numbers shown in Figs. 3 and 4 is less than 5 percent for assisting flow and about 10 percent for the opposing flow. A larger deviation associated with a wider scattering of points for the opposing flow in these figures shows some limitations to the correlation equation $Y^3 = 1 - X^3$. It is noted here that Fig. 3 can also be used for inclined plates (0 deg $\leq \gamma < 90$ deg) in mixed convection boundary layer flow by simply replacing Gr_x in the X variable in the abscissa with $Gr_x \cos\gamma$. This is verified by examples with Pr = 0.7 and 100 in Fig. 5.

Finally, a comparison between the proposed correlation equations and available experimental data [17, 18] for the local mixed convection Nusselt number in air flow (Pr = 0.7) is made in Fig. 6 for angles of inclination γ of 0 and 45 deg for both buoyancy assisting and opposing cases. It is seen that the agreement between the correlation and the experimental results is very good (within 10 percent). It should be noted here that A(Pr), B(Pr), and ξ^m in the (X, Y) coordinates in Fig. 6 stand, respectively, for F_1(Pr), F_2(Pr), and $(Gr_x/Re_x^2)^{1/4}$ for a vertical plate ($\gamma = 0$ deg) and for F_1(Pr), F_2(Pr), and $(Gr_x \cos\gamma/Re_x^2)^{1/4}$ for an inclined plate. They could also stand for

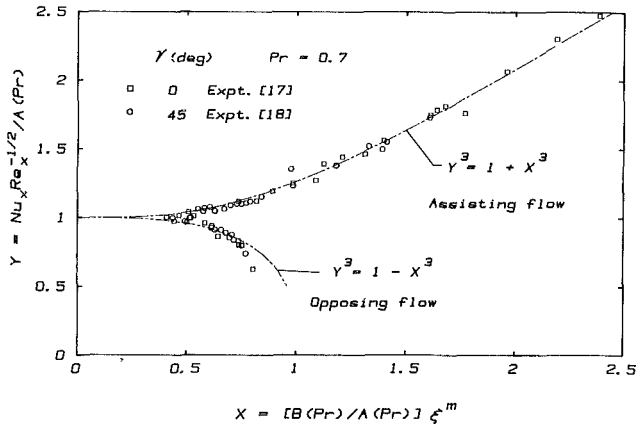

Fig. 6 A comparison between experimental and correlated local Nusselt numbers for isothermal vertical and inclined plates

F_1(Pr), F_4(Pr), and $(Gr_x/Re_x^{5/2})^{1/5}$ $Gr_x^{C(\gamma)}$ for an inclined plate and for F_1(Pr), F_3(Pr), and $(Gr_x/Re_x^{5/2})^{1/5}$ for a horizontal plate ($\gamma = 90$ deg). Thus, results for all angles of inclination (0 deg $\leq \gamma \leq 90$ deg) can be correlated in a single plot in terms of A(Pr), B(Pr), and ξ^m as in Fig. 6.

The average Nusselt numbers for vertical, inclined, and horizontal plates were also calculated from equations (A4), (A7), (A12), and (A16). They were then correlated with equations (7), (10), and (15), and a good agreement between the correlated and the calculated results was found to exist, as was in the case of local Nusselt number. Thus, separate figures for the average Nusselt number correlations need not be presented. Instead, Figs. 3–6 may be used for the appropriate geometries provided the Y and X coordinates in these figures are represented by those given in equations (7), (10), and (15) for the corresponding geometries.

It should be pointed out that in the domain of $X > 1$ for the opposing flow, natural convection would be the dominant mode of transport when $X \gg 1$. However, owing to the interaction between a strong buoyant flow and an opposing free stream, such flow along a (semi-infinite) flat plate can no longer be of the boundary layer type. Thus, for the opposing flow, calculations were terminated at $X < 1$, just before the flow separation, and no calculations for $X > 1$ were performed. Furthermore, no experimental work in the domain of $X > 1$ has been reported for the opposing flow. Finally, it must be pointed out that the correlation equations for the mixed convection Nusselt number, equations (6), (7), (9), (10), (14), and (15), are for laminar boundary layer flow. In developing these correlation equations, instability, transition, or turbulence of the flow that could occur at high Reynolds or Grashof numbers or at high inclination angles was not taken into account. Thus, care must be exercised when employing these equations in the heat transfer calculation outside the laminar mixed-convection boundary layer flow regime. Such a regime must be established by experiments which are currently lacking. From Fig. 6, it may be suggested that the correlation equations perhaps should be restricted in their applications to $X < 3$ for $\gamma = 0$ deg (vertical plates), to $X < 2$ for $\gamma = 45$ deg, and to $X < 1$ for $\gamma = 90$ deg (horizontal plates), pending further experimental verification.

Conclusion

In this paper, the local Nusselt numbers for mixed convection flows on vertical, inclined, and horizontal flat plates are presented for the entire mixed convection regime over a wide range of Prandtl numbers. Simple correlation equations provide local and average mixed convection Nusselt numbers that agree very well with the analytically predicted values for both buoyancy assisting and opposing flow conditions. Good

agreement was found to exist between the correlation and available experimental data for isothermal vertical and inclined plates. The surface heat transfer rate should be calculated from mixed convection correlations when the buoyancy or forced flow effect exceeds a certain threshold value from pure forced or pure free convection.

Acknowledgments

The work reported in this paper was supported in part by a grant (NSF MEA 83-00785) from the National Science Foundation.

References

1 Chen, T. S., Armaly, B. F., and Aung, W., "Mixed Convection in Laminar Boundary-Layer Flow," in: *Natural Convection: Fundamentals and Applications*, S. Kakac et al., eds., Hemisphere, Washington, D.C., 1985, pp. 699-725.

2 Szewczyk, A. A., "Combined Forced and Free-Convection Laminar Flow," ASME JOURNAL OF HEAT TRANSFER, Vol. 86, 1964, pp. 501-507.

3 Merkin, J. H., "The Effect of Buoyancy Forces on the Boundary-Layer Flow Over a Semi-Infinite Vertical Flat Plate in a Uniform Free Stream," *Journal of Fluid Mechanics*, Vol. 35, 1969, pp. 439-450.

4 Lloyd, J. R., and Sparrow, E. M., "Combined Forced and Free Convection Flow on Vertical Surfaces," *International Journal of Heat and Mass Transfer*, Vol. 13, 1970, pp. 434-438.

5 Oosthuizen, P. H., and Hart, R., "A Numerical Study of Laminar Combined Convective Flow Over Flat Plates," ASME JOURNAL OF HEAT TRANSFER, Vol. 95, 1973, pp. 60-63.

6 Wilks, G., "Combined Forced and Free Convection Flow on Vertical Surfaces," *International Journal of Heat and Mass Transfer*, Vol. 16, 1973, pp. 1958-1964.

7 Mucoglu, A., and Chen, T. S., "Mixed Convection on Inclined Surfaces," ASME JOURNAL OF HEAT TRANSFER, Vol. 101, 1979, pp. 422-426.

8 Moutsoglou, A., Tzuoo, K. L., and Chen, T. S., "Mixed Convection in Boundary Layer Flows Over Inclined Surfaces," *AIAA 15th Thermophysics Conference*, Snowmass, CO, July 14-16, 1980, Paper No. AIAA-80-1525.

9 Sparrow, E. M., and Minkowycz, W. J., "Buoyancy Effects on Horizontal Boundary Layer Flow and Heat Transfer," *International Journal of Heat and Mass Transfer*, Vol. 5, 1962, pp. 505-511.

10 Hauptmann, E. G., "Laminar Boundary-Layer Flows With Small Buoyancy Effects," *International Journal of Heat and Mass Transfer*, Vol. 8, 1965, pp. 289-295.

11 Leal, L. G., "Combined Forced and Free Convection Heat Transfer From a Horizontal Flat Plate," *Journal of Applied Mathematics and Physics (ZAMP)*, Vol. 24, 1973, pp. 20-42.

12 Hieber, C. A., "Mixed Convection Above a Heated Horizontal Surface," *International Journal of Heat and Mass Transfer*, Vol. 16, 1973, pp. 769-785.

13 Chen, T. S., Sparrow, E. M., and Mucoglu, A., "Mixed Convection in Boundary Layer Flow on a Horizontal Plate," ASME JOURNAL OF HEAT TRANSFER, Vol. 99, 1977, pp. 66-71.

14 Mucoglu, A., and Chen, T. S., "Mixed Convection on a Horizontal Plate With Uniform Surface Heat Flux," *Proceedings of the 6th International Heat Transfer Conference*, Vol. 1, 1978, pp. 85-90.

15 Ramachandran, N., Armaly, B. F., and Chen, T. S., "Mixed Convection Over a Horizontal Plate," ASME JOURNAL OF HEAT TRANSFER, Vol. 105, 1983, pp. 420-423.

16 Raju, M. S., Liu, X. Q., and Law, C. K., "A Formulation of Combined Forced and Free Convection Past Horizontal and Vertical Surfaces," *International Journal of Heat and Mass Transfer*, Vol. 27, 1984, pp. 2215-2224.

17 Ramachandran, N., Armaly, B. F., and Chen, T. S., "Measurements and Predictions of Laminar Mixed Convection Flow Adjacent to a Vertical Surface," ASME JOURNAL OF HEAT TRANSFER, Vol. 107, 1985, pp. 636-641.

18 Ramachandran, N., Armaly, B. F., and Chen, T. S., "Measurements of Laminar Mixed Convection Flows Adjacent to an Inclined Surface," ASME JOURNAL OF HEAT TRANSFER (in press).

19 Wang, X. A., "An Experimental Study of Mixed, Forced, and Free Convection Heat Transfer From a Horizontal Flat Plate to Air," ASME JOURNAL OF HEAT TRANSFER, Vol. 104, 1982, pp. 139-144.

20 Imura, H., Gilpin, R. R., and Cheng, K. C., "An Experimental Investigation of Heat Transfer and Buoyancy Induced Transition From Laminar Forced Convection to Turbulent Free Convective Over a Horizontal Isothermally Heated Plate," ASME JOURNAL OF HEAT TRANSFER, Vol. 100, 1978, pp. 429-434.

21 Churchill, S. W., "A Comprehensive Correlating Equation for Laminar Assisting, Forced and Free Convection," *AIChE Journal*, Vol. 23, 1977, pp. 10-16.

22 Churchill, S. W., and Ozoe, H., "Correlations for Laminar Forced Convection in Flow Over an Isothermal Flat Plate and in Developing and Fully Developed Flow in an Isothermal Tube," ASME JOURNAL OF HEAT TRANSFER, Vol. 95, 1973, pp. 416-419.

23 Ede, A. J., "Advances in Free Convection," in: *Advances in Heat Transfer*, Vol. 4, 1967, pp. 1-64.

24 Chen, T. S., Tien, H. C., and Armaly, B. F., "Natural Convection on Horizontal, Inclined, and Vertical Plates With Variable Surface Temperature or Heat Flux," *International Journal of Heat and Mass Transfer* (in press).

APPENDIX

Expressions for predicting the local and average mixed convection Nusselt numbers for vertical, inclined, and horizontal plates in laminar boundary layer flow are presented in this Appendix. In this presentation the systems of equations (conservations of mass, momentum, and energy) which have been numerically solved for finding the quantities $\theta'(\xi, 0)$, $\theta'(\Omega, 0)$, $\theta_1'(\xi_1, 0)$, and $\theta_2'(\xi_2, 0)$ are described in [1].

Forced Convection Dominated Case. The local mixed convection Nusselt number for this condition is given by [1, 7]

$$\mathrm{Nu}_x \mathrm{Re}_x^{-1/2} = -\theta'(\xi, 0) \tag{A1}$$

where $\mathrm{Re}_x = u_\infty x/\nu$ is the local Reynolds number, $\theta'(\xi, \eta) = \partial\theta/\partial\eta$, and $\mathrm{Nu}_x = hx/k$, with $h = -k(\partial T/\partial y)_{y=0}/(T_w - T_\infty)$. The dimensionless coordinates (ξ, η) and the dimensionless temperature $\theta(\xi, \eta)$ are defined, respectively, by

$$\xi = \mathrm{Gr}_x \cos\gamma/\mathrm{Re}_x^2, \quad \eta = (y/x)\mathrm{Re}_x^{1/2} \tag{A2}$$

$$\theta(\xi, \eta) = [T(x, y) - T_\infty]/(T_w - T_\infty) \tag{A3}$$

in which $\mathrm{Gr}_x = g\beta(T_w - T_\infty)x^3/\nu^2$ is the local Grashof number and γ is the angle of inclination from the vertical. It should be noted here that $\theta'(\xi, 0)$ depends on the Prandtl number $\mathrm{Pr} = \nu/\alpha$ and ξ is the buoyancy parameter. The expression for the average mixed convection Nusselt number, $\overline{\mathrm{Nu}} = \bar{h}L/k$, can be derived to yield

$$\overline{\mathrm{Nu}}\mathrm{Re}_L^{-1/2} = \xi_L^{-1/2}\int_0^{\xi_L} \xi^{-1/2}[-\theta'(\xi, 0)]d\xi \tag{A4}$$

in which Re_L and ξ_L are, respectively, Re_x and ξ based on the length of the plate L in the flow direction. The average heat transfer coefficient $\bar{h}$ is evaluated from

$$\bar{h} = \frac{1}{L}\int_0^L h\, dx \tag{A5}$$

The above expressions are valid for vertical ($\gamma = 0$ deg) and inclined plates.

For horizontal flat plates ($\gamma = 90$ deg), the buoyancy parameter has a different form and the expressions for the local and average mixed convection Nusselt numbers assume the respective expressions

$$\mathrm{Nu}_x \mathrm{Re}_x^{-1/2} = -\theta'(\Omega, 0) \tag{A6}$$

$$\overline{\mathrm{Nu}}\mathrm{Re}_L^{-1/2} = 2\Omega_L^{-1}\int_0^{\Omega_L} [-\theta'(\Omega, 0)]d\Omega \tag{A7}$$

where $\theta'(\Omega, \eta) = \partial\theta/\partial\eta$, the buoyancy parameter Ω is defined as

$$\Omega = \mathrm{Gr}_x/\mathrm{Re}_x^{5/2} \tag{A8}$$

and Ω_L is Ω based on L.

Free Convection Dominated Case. For this condition, the expression for the local mixed convection Nusselt number is given by [1]

$$\mathrm{Nu}_x(\mathrm{Gr}_x \cos\gamma/4)^{-1/4} = -\theta_1'(\xi_1, 0) \tag{A9}$$

in which $\theta_1'(\xi_1, \eta_1) = \partial\theta_1/\partial\eta_1$, and

$$\xi_1 = \frac{1}{2}\mathrm{Re}_x/(\mathrm{Gr}_x \cos\gamma)^{1/2}, \qquad \eta_1 = (y/x)(\mathrm{Gr}_x \cos\gamma/4)^{1/4} \tag{A10}$$

$$\theta_1(\xi_1, \eta_1) = [T(x, y) - T_\infty]/(T_w - T_\infty) \tag{A11}$$

The average mixed convection Nusselt number $\overline{\mathrm{Nu}}$ then has the expression

$$\overline{\mathrm{Nu}}(\mathrm{Gr}_L \cos\gamma/4)^{-1/4} = -2\xi_{1L}^{3/2}\int_0^{\xi_{1L}} \xi_1^{-5/2}[-\theta_1'(\xi_1, 0)]d\xi_1 \tag{A12}$$

where Gr_L and ξ_{1L} are, respectively, Gr_x and ξ_1 based on the length L.

Equations (A9)–(A12) are good for vertical ($\gamma = 0$ deg) and inclined plates. They are not valid for horizontal plates ($\gamma = 90$ deg), however, because ξ_1 and ξ_{1L} become singular when $\gamma = 90$ deg. Thus, for a horizontal plate one employs a different expression for the local mixed convection Nusselt number given by [1]

$$\mathrm{Nu}_x(\mathrm{Gr}_x/5)^{-1/5} = -\theta_2'(\xi_2, 0) \tag{A13}$$

with $\theta_2'(\xi_2, \eta_2) = \partial\theta_2/\partial\eta_2$,

$$\theta_2(\xi_2, \eta_2) = [T(x, y) - T_\infty]/(T_w - T_\infty) \tag{A14}$$

and

$$\xi_2 = \frac{1}{5}\,\mathrm{Re}_x/(\mathrm{Gr}_x/5)^{2/5}, \qquad \eta_2 = (y/x)(\mathrm{Gr}_x/5)^{1/5} \tag{A15}$$

The corresponding average mixed convection Nusselt number expression can be derived as

$$\overline{\mathrm{Nu}}(\mathrm{Gr}_L/5)^{-1/5} = -2\xi_{2L}^{3}\int_0^{\xi_{2L}} \xi_2^{-4}[-\theta_2'(\xi_2, 0)]d\xi_2 \tag{A16}$$

where ξ_{2L} is ξ_2 based on L.

It is noted that in obtaining the local Nusselt number results for the entire mixed convection regime as shown in Figs. 1 and 2, all calculations were performed from the forced convection dominated end for values of the buoyancy parameter $\mathrm{Gr}_x/\mathrm{Re}_x^2$ or $\mathrm{Gr}_x/\mathrm{Re}_x^{5/2}$ from 0 to 10 or larger for the buoyancy assisting flow case. For values larger than 10, calculations were done from the free convection dominated end. A good agreement was found to exist between results from the two sets of calculations for a common value of the buoyancy parameter.

Numerical Prediction of Turbulent Flow and Heat Transfer Within Ducts of Cross-Shaped Cross Section

A. Nakayama
Associate Professor.

H. Koyama
Professor.

Department of Energy and Mechanical Engineering, Shizuoka University, Hamamatsu, 432 Japan

Calculations were carried out for fully developed turbulent flows within ducts of cross-shaped cross section using the numerical method based on the pressure correction method developed by Patankar and Spalding. The Reynolds stress driven secondary flows were simulated successfully by Launder and Ying's algebraic stress model coupled to the k–ϵ turbulence model. A parametric study was made on the friction and heat transfer characteristics in terms of the parameter α associated with the decrease in the cross-sectional area, namely, α = 0 for a square duct, and α → 1 for infinite parallel plates. Through performance evaluations, it has been found that both the Reynolds analogy factor and the heat transfer coefficient under equal pumping power decrease slightly, while the heat transfer coefficient obtained with equal mass flow rate increases appreciably with α, suggesting effective turbulent heat transfer within ducts of cross-shaped cross section.

Introduction

Since secondary flow of the second kind (i.e., Reynolds stress driven secondary flow [1]) arises in a turbulent flow in a straight noncircular duct, this flow is of a three-dimensional nature, even when it is fully developed. Nikuradse [2] reported mean velocity fields obtained in various noncircular ducts such as square, triangular, and trapezoidal ducts. Although the magnitude of the secondary flow scarcely amounts to a few percent of the bulk velocity, its presence displaces the lines of constant axial velocity (i.e., isovels) considerably toward the corner regions, yielding a high velocity gradient field there. Thus, the effect of the secondary flow on momentum and heat transfer must be taken into consideration for the study of heat and fluid flows in noncircular ducts.

Since the gradients in the cross-planar Reynolds stresses are fully responsible for the secondary motions of this kind [3], the so-called "isotropic viscosity formulation" (which is a direct extension of the laminar deformation law) cannot predict the turbulent cross flows in noncircular ducts. Launder and Ying [4] reduced algebraic stress equations from the Reynolds stress transport equation, and subsequently employed them with the turbulent kinetic energy transport equation for the prediction of a fully developed turbulent flow in a square duct. This innovative work on the secondary flow prediction was followed by many workers (e.g., [5–7]), and even extended to a three-dimensional developing turbulent flow in a square duct [8, 9]. Comprehensive reviews on theoretical and experimental works on straight noncircular ducts may be found elsewhere [6, 10].

The present study is concerned with the numerical prediction of fully developed turbulent flows in ducts of cross-shaped cross section as depicted in Fig. 1. The perimeters of these ducts (i.e., heat transfer areas) are the same as that of the corresponding square duct, namely $4D_{h0}$, while the flow cross sections are less than that of the square duct. These ducts are considered here as possible candidates for compact heat exchanger configurations. A series of turbulent flow calculations has been carried out using the aforementioned Launder and Ying's algebraic stress model along with the k–ϵ turbulence model to investigate the secondary flow motions, as well as their effects on the friction and heat transfer characteristics. A parametric study was carried out to assess the performance of heat exchange surfaces, upon changing the geometric parameter α associated with the decrease in the flow cross section (namely, $\alpha = 0$ for a square duct, and $\alpha \to 1$ for infinite parallel plates; see Fig. 1). Detailed performance evaluations are presented in terms of the mass flow rate under equal pumping power, the Reynolds analogy factor, the heat transfer coefficient under equal pumping power, and that under equal mass flow rate.

Governing Equations

Upon choosing the x coordinate in the axial direction for fully developed flows, the general conservation equation may be given in Cartesian coordinates (x, y, z) as

$$\frac{\partial}{\partial y}\left(v\phi - \Gamma \frac{\partial \phi}{\partial y}\right) + \frac{\partial}{\partial z}\left(w\phi - \Gamma \frac{\partial \phi}{\partial z}\right) = \mathrm{So} \qquad (1)$$

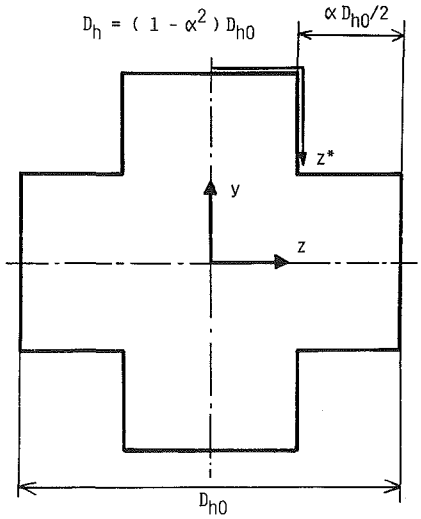

Fig. 1 Physical model and coordinates

Contributed by the Heat Transfer Division for publication in the JOURNAL OF HEAT TRANSFER. Manuscript received by the Heat Transfer Division July 1, 1985.

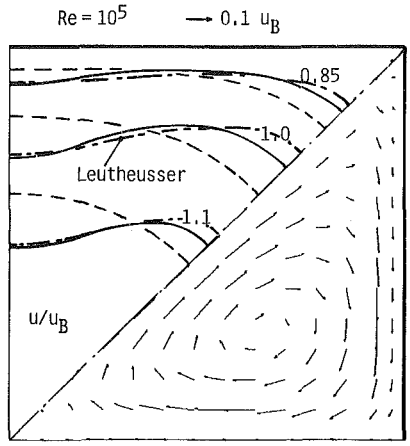

Fig. 2(a)

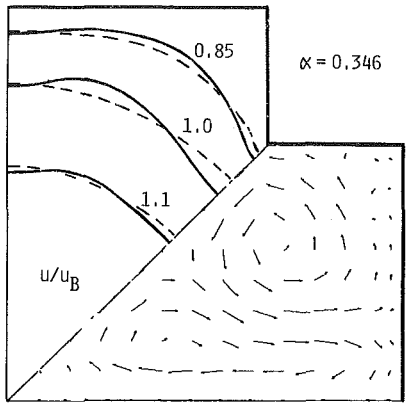

Fig. 2(c)

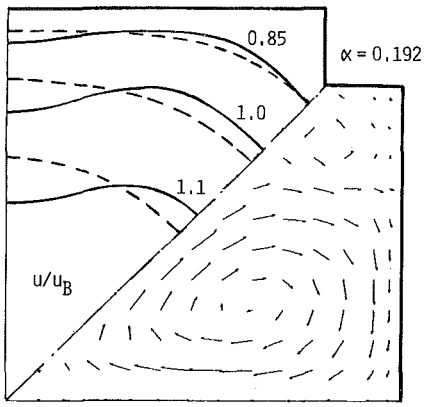

Fig. 2(b)

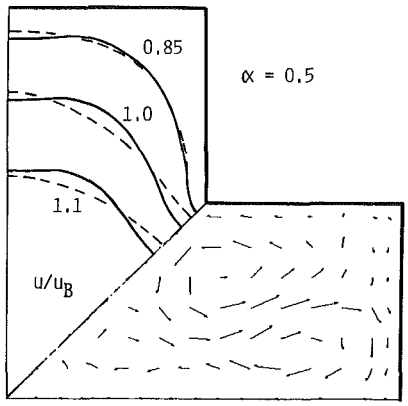

Fig. 2(d)

Fig. 2 Mean velocity field: (a) $\alpha = 0$, (b) $\alpha = 0.192$, (c) $\alpha = 0.346$, (d) $\alpha = 0.5$

where u, v, and w are the mean velocity components in the x, y, and z directions, respectively. The general dependent variable ϕ stands for any one of the dependent variables in consideration, while Γ and So represent the corresponding diffusion coefficient and source term. Each governing equation may be presented by setting ϕ, Γ, and so in equation (1) as follows:

For the continuity equation:

$$\phi = 1,\ \Gamma = 0,\ \mathrm{So} = 0 \tag{2}$$

For the v cross-flow momentum equation:

$$\phi = v,\ \Gamma = \nu,\ \mathrm{So} = -\frac{1}{\rho}\left(\frac{\partial p}{\partial y} - \frac{\partial \tau_{yy}}{\partial y} - \frac{\partial \tau_{yz}}{\partial z}\right) \tag{3}$$

For the w cross-flow momentum equation:

$$\phi = w,\ \Gamma = \nu,\ \mathrm{So} = -\frac{1}{\rho}\left(\frac{\partial p}{\partial z} - \frac{\partial \tau_{zz}}{\partial z} - \frac{\partial \tau_{yz}}{\partial y}\right) \tag{4}$$

For the u axial-flow momentum equation:

$$\phi = u,\ \Gamma = \nu + \nu_t,\ \mathrm{So} = -\frac{1}{\rho}\frac{\partial p}{\partial x} \tag{5}$$

For the energy equation:

$$\phi = T,\ \Gamma = \nu/\mathrm{Pr} + \nu_t/\sigma_T,\ \mathrm{So} = -u\frac{\partial T}{\partial x} \tag{6}$$

For the turbulent kinetic energy equation:

$$\phi = k,\ \Gamma = \nu + \nu_t/\sigma_k,\ \mathrm{So} = P - \epsilon \tag{7}$$

For the turbulent kinetic energy dissipation rate equation:

$$\phi = \epsilon,\ \Gamma = \nu + \nu_t/\sigma_\epsilon,\ \mathrm{So} = (c_1 P - c_2\epsilon)\epsilon/k \tag{8}$$

where p, T, ρ, ν, and Pr denote the mean pressure, temperature, density, kinematic viscosity, and Prandtl number, respectively, while the turbulent kinetic energy, its production rate, and its dissipation rate are given by k, P, and

Nomenclature

C_f = friction coefficient
C_p = specific heat
D_h = hydraulic diameter
h = heat transfer coefficient
$\dot{m}$ = mass flow rate
Nu = Nusselt number
p = pressure
PP = pumping power
Pr = Prandtl number
q = heat flux
Re = Reynolds number
St = Stanton number
T = temperature
u, v, w = velocity components
x, y, z = Cartesian coordinates
α = geometric parameter
ν = kinematic viscosity
τ = shear stress

Subscripts

av = value averaged over duct periphery
B = bulk
0 = square duct

ϵ. The turbulent Prandtl numbers σ_ϕ and the coefficients c_1 and c_2 are all constants to be determined empirically. The turbulent kinematic viscosity ν_t is related to k and ϵ through the near-wall constant c_D as

$$\nu_t = c_D k^2/\epsilon \tag{9}$$

It should be noted that the terms associated with the cross-planar stresses τ_{yy}, τ_{zz}, and τ_{yz} (which do not follow the isotropic viscosity formulation described by the foregoing equation) are absorbed into the source terms in the cross-flow momentum equations (3) and (4). Furthermore, usual boundary layer consideration suggests that the production rate of kinetic energy may be approximated by

$$P = \frac{1}{\rho}\left(\tau_{xy}\frac{\partial u}{\partial y} + \tau_{zx}\frac{\partial u}{\partial z}\right) \tag{10}$$

Algebraic Stress Model

The effective viscosity formulation cannot predict the secondary flow induced by the turbulent stress field since the stress and strain fields under such a formulation are coaligned. The algebraic stress model originally developed by Launder and Ying [4] was later evolved into explicit expressions for all six Reynolds stress components by Gessner and Emery [11]. This explicit set is given as follows:

$$\tau_{xx}/\rho = -c'_{k0}k \tag{11a}$$

$$\tau_{xy}/\rho = \nu_t\frac{\partial u}{\partial y} \tag{11b}$$

$$\tau_{zx}/\rho = \nu_t\frac{\partial u}{\partial z} \tag{11c}$$

$$\tau_{yy}/\rho = c' c_D\frac{k^3}{\epsilon^2}\left(\frac{\partial u}{\partial y}\right)^2 - c'_k k \tag{11d}$$

$$\tau_{zz}/\rho = c' c_D\frac{k^3}{\epsilon^2}\left(\frac{\partial u}{\partial z}\right)^2 - c'_k k \tag{11e}$$

$$\tau_{yz}/\rho = c' c_D\frac{k^3}{\epsilon^2}\left(\frac{\partial u}{\partial y}\right)\left(\frac{\partial u}{\partial z}\right) \tag{11f}$$

where c'_k, c'_{k0}, and c' are empirical constants. It is most interesting to observe that the cross-planar stress components τ_{yy}, τ_{zz}, and τ_{yz} responsible for the secondary flow generation are not related to the mean strain rates in the cross-sectional plane, but to the mean strain rates normal to it, namely, $\partial u/\partial y$ and $\partial u/\partial z$. Recently, Demuren and Rodi [12] proposed a more refined algebraic stress model which retains the secondary flow velocity gradient terms. The influence of these terms on the cross-planar stresses were reported rather significant. The friction and heat transfer characteristics of our primary interest, however, would not be affected by including these terms. Throughout the present study, a single set of empirical constants was used. These values are

$c_D = 0.09$, $c'_{k0} = 0.915$, $c'_k = 0.552$, $c' = 0.0185$, $c_1 = 1.44$, $c_2 = 1.92$, $\sigma_k = 0.9$, $\sigma_\epsilon = 1.3$, $\sigma_T = 0.9$

The Prandtl number Pr was set to Pr = 0.7, where air was assumed to be the working fluid.

Method of Calculation

Although the velocity field considered here is three dimensional, an economical two-dimensional numerical scheme may still be used for the fully developed flows of present concern. It is well known that the cross-sectional pressure gradients in a straight noncircular duct are extremely small, so that the pressure is virtually constant over the cross section at a given axial station [13]. The fact has been substantiated through a fully elliptic three-dimensional calculation [9]. Thus, upon integrating the axial momentum equation (5) over the cross section, one obtains

$$-\frac{1}{\rho}\frac{\partial p}{\partial x} = 4\frac{\tau_{av}}{D_h\rho} = 4\frac{c_D^{1/2}k_{av}}{D_h} \tag{12}$$

where τ_{av} is the mean wall shear which is related to the kinetic energy averaged over the duct periphery k_{av} through the local equilibrium relationship. D_h is the hydraulic diameter of the duct which may be evaluated using the geometric parameter α as

$$D_h = (1-\alpha^2)D_{h0} \tag{13}$$

Similarly, the energy equation (6) is integrated over the cross section to yield the following equation

$$-u\frac{\partial T}{\partial x} = -u\frac{dT_B}{dx} = \frac{4uq_{av}}{\rho C_p u_B D_h} \tag{14}$$

where u_B is the bulk velocity; T_B, the bulk temperature; C_p, the specific heat; and q_{av}, the wall heat flux averaged over the duct periphery. If a constant axial heat transfer rate with constant peripheral temperature is assumed, q_{av} is constant, and the wall temperature T_w is a function of x alone. The source terms in equations (5) and (6) may now be evaluated from equations (12) and (14). Thus, one needs only two-dimensional storage in computations since the x coordinate is completely eliminated from the governing equations. These seven partial differential equations (2) through (8) must be solved simultaneously for the specified boundary conditions.

Discretization is carried out by integrating the general conservation equation (1) over a grid volume. Following the procedure similar to Patankar and Spalding [14], the continuity equation is reformulated as the so-called" pressure correction equation," which is equivalent to the Poisson equation for the pressure field.

Calculation starts with solving the cross-flow momentum equations (3) and (4), and subsequently this estimated cross-flow velocity field is corrected by solving the aforementioned pressure correction equation so that the velocity field fulfills the continuity principle. With the axial pressure and temperature gradients estimated from equations (12) and (14), the axial momentum equation (5) and the energy equation (6) are solved next. Finally, the turbulence quantities k and ϵ are solved. This iteration sequence is repeated until convergence is achieved. Convergence is measured in terms of the maximum change in each variable during an iteration. The maximum change allowed for the convergence check is set to 10^{-6}, when the reference length, velocity, and temperature were taken as D_h, u_B, and $q_{av}/\rho\ C_p\ u_B$, respectively. For actual calculations, usual wall functions based on the constant stress layer assumption were applied to the grid nodes next to the wall in order to match the interior flow with the required wall conditions. The procedure for calculating k and ϵ must be consistent with the constant stress layer assumption. Thus, the turbulent kinetic energy diffusion through the wall surface is set to zero when evaluating k near the wall, while its rate of dissipation is specified using the local equilibrium relation. In this near wall treatment, the first grid nodes must be located in a fully turbulent region. (In the present study, the y^+ values at these nodes are around 100.)

Preliminary calculations on both laminar and turbulent flows were carried out using the grid systems (11 × 11) and (15 × 15) for a quadrant of a duct cross section. No significant grid number effects were observed on either calculation result, except that the secondary flow velocity magnitude for the case of turbulent flow was slightly amplified for the finer grid system. Thus, all turbulent calculations were carried out using the finer grid system (15 × 15) to ensure sufficient accuracy of calculated results.

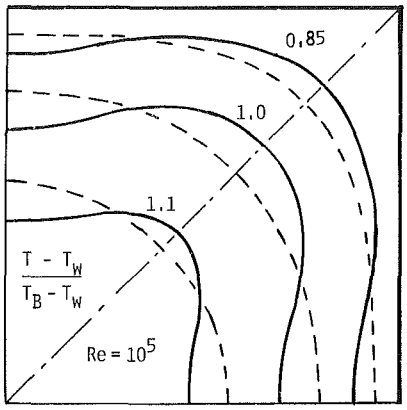

Fig. 3(*a*)

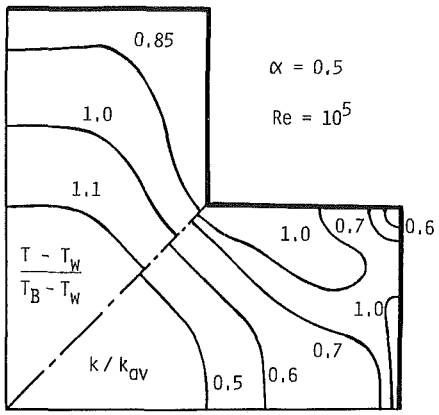

Fig. 3(*b*)

Fig. 3 Mean temperature and turbulent kinetic energy fields: (*a*) $\alpha = 0$; (*b*) $\alpha = 0.5$; secondary flow present; ···· secondary flow suppressed

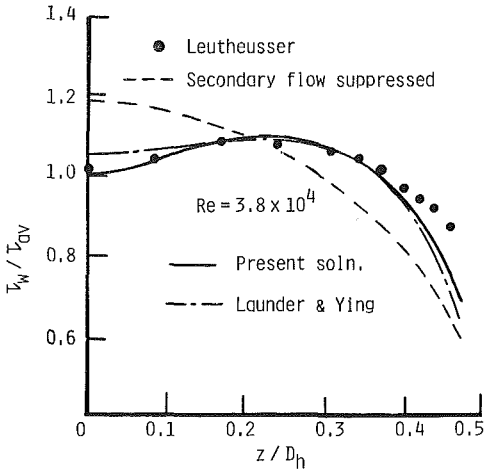

Fig. 4(*a*)

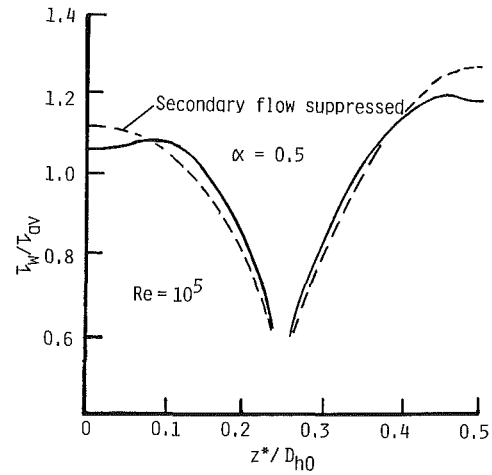

Fig. 4(*b*)

Fig. 4 Wall shear stress distribution: (*a*) $\alpha = 0$, (*b*) $\alpha = 0.5$

Mean Velocity Field

A series of calculations was performed with the geometric parameter α and the Reynolds number $\mathrm{Re} = u_B D_h/\nu$ as the parameters. Predicted mean velocity fields are presented in Figs. 2(*a–d*). In the figures, the isovels are shown above the diagonal of a duct while the secondary flow velocity vectors are plotted below it. Calculations were repeated also by suppressing the secondary flow motions (i.e., setting $c' = 0$). The isovels thus obtained are also presented by dashed lines to contrast the effects of the secondary motions. The square duct results (i.e., $\alpha = 0$) are shown in Fig. 2(*a*) along with the experimental data by Leutheusser [13]. The isovels in the figure indicate good agreement between the experiment and the present prediction based on the Launder and Ying algebraic stress model. The secondary flow motions are induced such that the current along the diagonal carries the core fluid of high axial momentum to the corner along the diagonal, while the current along the wall bisector brings the near-wall fluid of low axial momentum towards the core. Consequently, the isovels become significantly distorted, as may be appreciated through a comparison of the predictions with and without secondary flow motions.

Figure 2(*b*) shows the velocity field in the duct of cross-shaped cross section for the case of $\alpha = 0.192$. It is clearly seen that another secondary vortex forms around the "convex" corner (on the diagonal). Differences in the solid and dashed isovels again suggests significant effects of secondary flow motions. As the duct cross section decreases further (such that $\alpha = 0.346$; see Fig. 2*c*), this secondary vortex penetrates deep to the core, and its effect on the isovels becomes appreciable. Since the secondary flow current also carries low-momentum fluid toward the core along the diagonal, the bulges on the isovels along the diagonal are directed toward the core in contrast with the square duct case. As seen in Fig. 2(*d*), plotted for the case of $\alpha = 0.5$, this secondary vortex generated around the convex corner grows further and eventually dominates the entire secondary flow motions. Obviously, the presence of the convex corner creates a region of high strain rate there. However, the aforementioned secondary current somewhat relaxes the field of high strain rate by carrying the fluid of low momentum near the wall toward the core. On the other hand, the low axial momentum region (say the region where $u/u_B < 0.85$) spreads deep into a pair of "concave" corners located away from the convex corner. Consequently, the friction drag in total decreases for the ducts of cross-shaped cross section. This point will be discussed later.

Mean Temperature and Turbulent Kinetic Energy Fields

Isotherms obtained for $\alpha = 0$ and 0.5 are plotted in Figs. 3(*a*) and 3(*b*) in terms of the dimensionless temperature $(T-T_w)/(T_B-T_w)$. As the figures are compared against Fig. 2, the similarity between the temperature and velocity fields becomes appreciable. The isotherms without secondary flow motions are also shown by dashed lines in Fig. 3(*a*), which indicates considerable influence of the secondary motions on the temperature field. The contour map of the turbulent kinetic energy is presented below the diagonal in Fig. 3(*b*) to show a typical kinetic energy distribution in a duct of cross-shaped

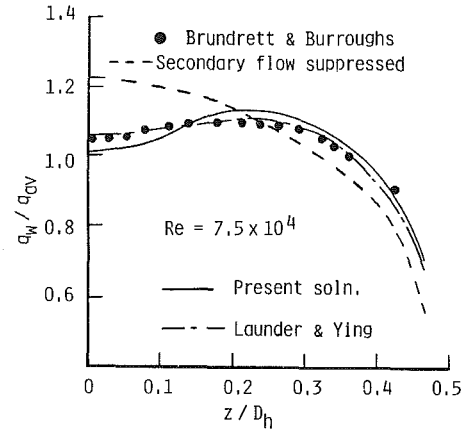

Fig. 5(a)

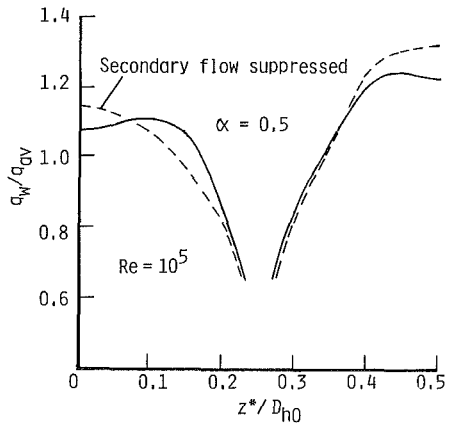

Fig. 5(b)

Fig. 5 Wall heat flux distribution: (a) $\alpha = 0$, (b) $\alpha = 0.5$

cross section. The map pattern is very much similar to that of the temperature shown above the diagonal. Relatively high turbulent kinetic energy level is maintained around the convex corner due to the formation of high mean strain field.

Wall Shear and Heat Flux Distributions

In order to illustrate the effects of the secondary flows on friction and heat transfer behavior, the distributions of the wall shear and wall heat flux are shown in Figs. 4 and 5 with available experimental data for a square duct [12, 14]. The peripheral wall shear distribution in a square duct is presented in Fig. 4(*a*), where the experiment by Leutheusser [13] and the prediction by Launder and Ying [4] using the one-equation model are also indicated, along with the present predictions with (solid line) and without (dashed line) secondary motions (note, $z/D_h = 0$ for the wall bisector and 0.5 for the corner). Agreement of the experiment and the present prediction with the secondary flow is fairly good. Comparison of the solid and dashed lines suggests the tendency of the secondary flow motion to smooth out variations in the wall shear stress around the perimeter of the duct. Figure 4(*b*) shows the wall shear stress distribution over an octant of the cross-shaped cross-section duct for the case of $\alpha = 0.5$. Here, the abscissa variable is chosen such that the upper wall bisector, concave corner, and convex corner correspond to $z^*/D_h = 0$, 0.25, and 0.5, respectively (see Fig. 1). The wall shear stress decreases drastically around $z^*/D_h = 0.25$ due to the damping effect of the concave corner on the turbulent fluctuations.

The similarity confirmed between the velocity (Fig. 2) and temperature (Fig. 3) fields reflects on the wall shear and wall

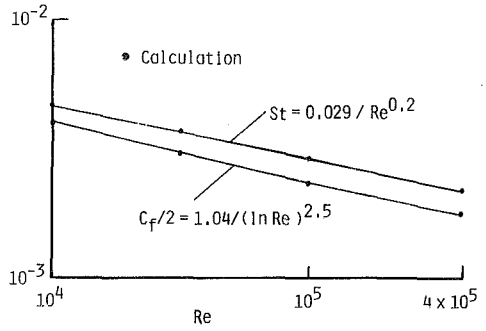

Fig. 6 Friction coefficient and Stanton number in a square duct

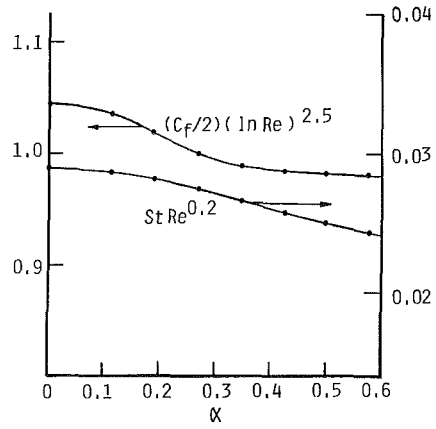

Fig. 7 Effects of α on friction and heat transfer

heat flux distributions over the duct periphery. The wall heat flux distributions for the cases of $\alpha = 0$ and 0.5 are presented in Figs. 5(*a*) and 5(*b*) in a manner similar to the wall shear distribution. The experimental data obtained by Brundrett and Borroughs [14] are also shown for the case of a square duct. As the figures show, the secondary flow, even though its level is small in magnitude, can significantly influence the friction and heat transfer characteristics within noncircular ducts.

Friction Coefficient and Stanton Number

The friction coefficient and Stanton number have been deduced from the calculated results. An attempt was made to correlate the friction coefficients obtained for different Re in the form of a power function of Re as in the Blasius friction law. However, it was found difficult to cover a wide range of Re with a constant exponent. After some trials, the following functional form suggested by White [16] was selected for the correlation of the calculated friction coefficients (see Fig. 6)

$$(C_f/2)(\ln \mathrm{Re})^{2.5} = \text{const}\ (\alpha) \tag{15}$$

For the Stanton number, namely, $\mathrm{St} = q_{av}/\rho\, u_B\, C_p(T_w - T_B)$, on the other hand, the power function suggested by Dittus and Boelter [17] as given below was found to be quite effective for the correlation of the calculated results

$$\mathrm{St}\ \mathrm{Re}^{0.2} = \text{const}\ (\alpha) \tag{16}$$

Upon assuming the functional forms given by equations (15) and (16), the proportional constants (i.e., the right-hand side terms of equations (15) and (16)) have been determined from the numerical results obtained at $10^4 \le \mathrm{Re} \le 4 \times 10^5$, using a least-squares technique. In the case of a square duct, for example, this procedure yields $\mathrm{St}\ \mathrm{Re}^{0.2} = 0.029$ (indicated by a solid line in Fig. 6) which turns out to be very close to the Dittus-Boelter formula, namely, $\mathrm{St}\ \mathrm{Re}^{0.2} = 0.0285$ (for Pr = 0.7). The multiplicative constants thus obtained for different α are plotted all together in Fig. 7. The figure shows that both

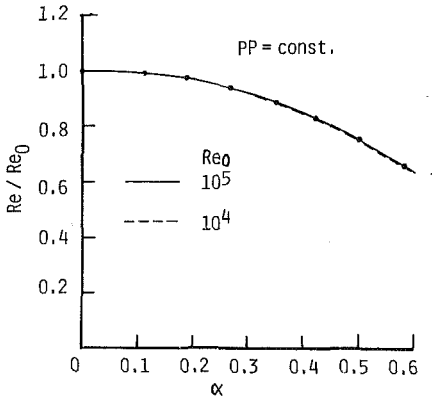

Fig. 8 Mass flow rate under equal pumping power

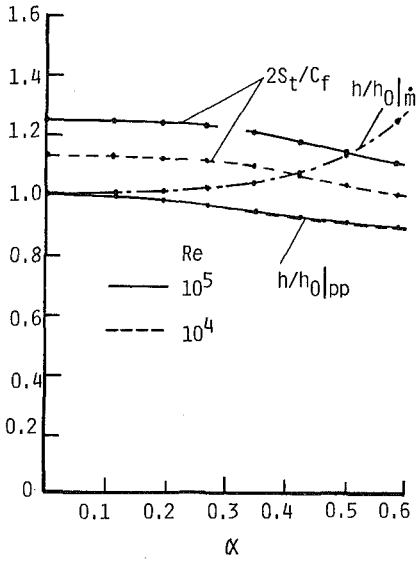

Fig. 9 Performance evaluations

$(C_f/2)(\ln \mathrm{Re})^{2.5}$ and $\mathrm{St}\,\mathrm{Re}^{0.2}$ decrease with increasing α (i.e., decreasing the flow cross-sectional area). As discussed in connection with the isovels, the tendency observed here is associated with the fact that the low axial momentum regions appear around a pair of the concave corners for large α.

Performance Evaluations

Performance evaluations are most practical and meaningful when the comparison is made under equal pumping power. For the duct of axial length X, the pumping power PP may be given by

$$PP \equiv \frac{\dot{m}}{\rho}\frac{dp}{dx}X = \rho\nu^3(4\,D_{h0}X)\left(\frac{\mathrm{Re}}{D_h}\right)^3\frac{C_f}{2} \tag{17}$$

Since the total heat transfer surface $(4D_{h0}X)$ is constant for the duct of cross-shaped cross section of the present concern, the mass flow rate $\dot{m}$ under equal pumping power may be evaluated according to

$$(\mathrm{Re}/\mathrm{Re}_0)^3/\left(1+\frac{\ln(\mathrm{Re}/\mathrm{Re}_0)}{\ln \mathrm{Re}_0}\right)^{2.5}$$

$$=\frac{[(C_f/2)(\ln \mathrm{Re})^{2.5}]_0}{(C_f/2)(\ln \mathrm{Re})^{2.5}}(1-\alpha^2)^3 \tag{18}$$

where the subscript 0 indicates quantities associated with a square duct, namely, $\alpha = 0$. Since the perimeter is kept constant, the ratio of the Reynolds numbers $\mathrm{Re}/\mathrm{Re}_0$ is identical to that of the mass flow rates $\dot{m}/\dot{m}_0$. It is noted that the right-hand side term of equation (18) is a function of α alone, which may readily be evaluated by substituting the results $(C_f/2)(\ln \mathrm{Re})^{2.5}$ plotted in Fig. 7. Hence, for given Re_0, the foregoing equation may be solved for the ratio $\mathrm{Re}/\mathrm{Re}_0$. The results obtained for $\mathrm{Re}_0 = 10^4$ and 10^5 are presented in Fig. 8 which shows that the mass flow rate under equal pumping power decreases with the cross-sectional area. The difference in the two curves is hardly discernible so that the mass flow rate ratio $\mathrm{Re}/\mathrm{Re}_0$ may virtually be considered a function of α alone for the Reynolds number range of present interest.

The performance of heat exchange surfaces made up of different passage geometries may be contrasted in terms of the Reynolds analogy factor $2\mathrm{St}/C_f$ (equivalent to the area goodness factor), the heat transfer coefficient under equal pumping power $h|_{pp}$ (equivalent to the volume goodness factor [18]), or the heat transfer coefficient under equal mass flow rate $h|_{\dot{m}}$ [19]. The Reynolds analogy factor $2\mathrm{St}/C_f$ evaluated from equations (15) and (16) is presented in Fig. 9 for $\mathrm{Re} = 10^4$ and 10^5. Unlike in laminar flows, the factor increases with Re, suggesting effective turbulent heat transfer. Since the factor is fairly insensitive to the geometry parameter α, no drastic increase due to the change of the duct geometry is expected. Upon noting the definition $\mathrm{St} = h/\rho\, C_p\, u_B \propto h\, D_h/\mathrm{Re}$, the ratio of heat transfer coefficients may be expressed as

$$h/h_0 = \frac{(\mathrm{St}\,\mathrm{Re}^{0.2})}{(\mathrm{St}\,\mathrm{Re}^{0.2})_0}\frac{(\mathrm{Re}/\mathrm{Re}_0)^{0.8}}{(1-\alpha^2)} \tag{19}$$

where h_0 is the heat transfer coefficient for the corresponding square duct. The ratio $h/h_0|_{PP}$ may be evaluated by substituting the multiplicative constants $(\mathrm{St}\,\mathrm{Re}^{0.2})$ (plotted in Fig.7), and the mass flow rate ratio $\mathrm{Re}/\mathrm{Re}_0$ (plotted in Fig. 8) into the right-hand side term of equation (19). The curves obtained for $\mathrm{Re}_0 = 10^4$ and 10^5 almost overlap onto each other, indicating the insensitivity of $h/h_0|_{PP}$ to the Reynolds number. The ratio $h/h_0|_{PP}$ decreases only slightly with increasing α. Thus no appreciable geometric effect is observed on $h/h_0|_{pp}$ either. This is related to the fact that the enhanced turbulent mixing and the secondary motions work to smooth out the wall shear and heat flux distributions over the duct periphery. The phenomenon seems peculiar to turbulent flows in noncircular ducts, since the velocity and temperature fields in laminar flows are quite sensitive to a particular duct geometry. (The laminar flow solution [18] shows that $C_f\mathrm{Re}/2$, for example, varies from 7.1 for a square duct to 12 for infinite parallel plates.)

For some specific applications, performance evaluations could be more meaningful when the comparison is made under the constraint of equal mass flow rate. The ratio $h/h_0|_{\dot{m}}$ calculated by setting $\mathrm{Re}/\mathrm{Re}_0 = 1$ in the right-hand side of equation (19) is presented in the same figure. The heat transfer coefficient increases significantly with increasing α (i.e., decreasing the duct cross section), suggesting that effective heat transfer is possible within a duct of cross-shaped cross section. Thus, this type of duct could be considered a promising candidate for compact heat transfer configurations under the constraint of equal mass flow rate.

Conclusions

Numerical calculations were carried out for fully developed turbulent flows ranging from square to cross-shaped cross section. The secondary motions induced by the Reynolds stresses were simulated using Launder and Ying's algebraic stress model with the k–ϵ turbulence model. The predicted velocity and temperature fields reveal significant effects of the secondary flow and show good agreement with some available square duct flow data.

Performance evaluations were made under the constraints

of equal pumping power and equal mass flow rate. It has been found that both the Reynolds analogy factor and the heat transfer coefficient under equal pumping power are fairly insensitive to the geometric parameter α, as a result of the turbulent mixing and secondary motions, while the heat transfer coefficient obtained under equal mass flow rate increases appreciably with α, indicating effective heat transfer within ducts of cross-shaped cross section.

References

1 Prandtl, L., *Essentials of Fluid Mechanics*, Hafner, New York, 1953, p. 148.

2 Nikuradse, J., "Untersuchungen über die Geschwindingkeitsverteilung in Turbulenten Strömungen," *Diss. Göttingen*, VID-Forschungsheft 281, 1926.

3 Brundrett, E., and Baines, W. D., "Production and Diffusion of Vorticity in Duct Flow," *J. Fluid Mechanics*, Vol. 19, 1964, pp. 375–394.

4 Launder, B. E., and Ying, W. M., "Prediction of Flow and Heat Transfer in Ducts of Square Cross Section," *Heat and Fluid Flow*, Vol. 3–2, 1973, pp. 115–121.

5 Aly, A. M. M., Trupp, A. C., and Gerrard, A. D., "Measurements and Prediction of Fully Developed Turbulent Flow in an Equilateral Triangular Duct," *J. Fluid Mechanics*, Vol. 85, 1978, pp. 57–83.

6 Gosman, A. D., and Rapley, C. W., "Fully Developed Flow in Passages of Arbitrary Cross Section," *Recent Advances in Numerical Methods in Fluids*, Vol. 1, C. Taylor and K. Morgan, eds., Pineridge, 1980, pp. 335–399.

7 Nakayama, A., Chow, W. L., and Sharma, D., "Calculation of Fully Developed Turbulent Flows in Ducts of Arbitrary Cross Section," *J. Fluid Mechanics*, Vol. 128, 1983, pp. 199–217.

8 Gessner, F. B., and Emery, A. F., "The Numerical Prediction of Developing Turublent Flow in Rectangular Ducts," *2nd Symp. Turbulent Shear Flows*, Imperial College, London, 1979, pp. 17.1–17.6.

9 Nakayama, A., Chow, W. L., and Sharma, D., "Three-Dimensional Developing Turbulent Flow in a Square Duct," *Bulletin of Japan Society of Mechanical Engineering*, Vol. 27–229, 1984, pp. 1438–1445.

10 Nakayama, A., and Chow, W. L., "Turbulent Flows Within Straight Ducts," *Encyclopedia of Fluid Mechanics*, Vol. I, Chap. 21, N. Cheriminisinoff, ed., Gulf Book, 1985, pp. 638–674.

11 Gessner, F. B., and Emery, A. F., "A Reynolds Stress Model for Turbulent Corner Flows; Part I: Development of the Model," ASME *J. Fluids Engineering*, Vol. 98, 1976, pp. 261–268.

12 Demuren, A. O., and Rodi, W., "Calculation of Turbulence-Driven Secondary Motion in Non-circular Ducts," *J. Fluid Mechanics*, Vol. 140, 1984, pp. 189–222.

13 Leutheusser, H. J., "Turbulent Flow in Rectangular Ducts," ASCE *J. Hydraulic Division*, Vol. 89, (HY3), 1963, pp. 1–19.

14 Patankar, S. V., and Spalding, D. B., "A Calculation Procedure for Heat Mass and Momentum Transfer in Three-Dimensional Parabolic Flows," *Int. J. Heat Mass Transfer*, Vol. 15, 1972, pp. 551–559.

15 Brundrett, E., and Burroughs, P. R., "The Temperature Inner Law and Heat Transfer for Turbulent Air Flow in a Vertical Square Duct," *Int. J. Heat Mass Transfer*, Vol. 10, 1967, pp. 1133–1142.

16 White, F. M., *Viscous Fluid Flow*, McGraw-Hill, New York, 1974, p. 485.

17 Dittus, F. W., and Boelter, L. M. K., *Univ. of California Pubs. Eng.*, Vol. 2, 1930, p. 443.

18 Shah, R. K., and London, A. L., "Laminar Flow Forced Convection in Ducts," *Advances in Heat Transfer*, Supplement 1, Academic Press, New York, 1978, p. 393.

19 O'Brien, J. E., and Sparrow, E. M., "Corrugated-Duct Heat Transfer, Pressure Drop, and Flow Visualization," ASME JOURNAL OF HEAT TRANSFER, Vol. 104, 1982, pp. 411–416.

Two-Fluid and Single-Fluid Natural Convection Heat Transfer in an Enclosure

E. M. Sparrow

L. F. A. Azevedo

A. T. Prata

Department of Mechanical Engineering,
University of Minnesota,
Minneapolis, MN 55455

Natural convection experiments were performed for an enclosure of square cross section containing either a single fluid or two immiscible fluids in a layered configuration. The two vertical walls of the cross section were respectively heated and cooled, while the two horizontal walls were adiabatic. The single-fluid experiments, performed with distilled water and with n*-hexadecane paraffin (Pr = 5 and 39.2, respectively), yielded Nusselt numbers whose Rayleigh and Prandtl number dependences were perfectly correlated by a single dimensionless group. These single-fluid results were used as baseline information for the development of methods to predict the heat transfer in two-fluid layered systems. To test the utility of the predictive methods, experiments were carried out for water–hexadecane systems in which the position of the interface separating the liquids was varied parametrically. It was found that the experimentally determined, two-layer Nusselt numbers were in excellent agreement with the predicted values. The prediction methods are not limited to the particular fluids employed here, nor do they require additional experimental data for their application.*

Introduction

Natural convection in rectangular enclosures has been the subject of extensive numerical and experimental investigation. With few exceptions, that work has dealt with enclosures containing a single fluid, either a liquid or a gas. In the experiments to be described here, a two-fluid situation is considered wherein the enclosure is filled with two immiscible liquids arranged in layers one atop the other. During the course of the research, the height of the interface between the layers was varied parametrically in four steps and, in addition, baseline experiments were performed with the enclosure filled with each of the individual liquids.

The liquids used in the experiments were distilled water and research-grade (99 percent pure) *n*-hexadecane paraffin, with respective Prandtl numbers of 5 and 39.2. The experiments were performed with the two vertical bounding surfaces of the enclosure maintained isothermal, with one of the surfaces being heated and the other being cooled. Adiabatic conditions were imposed at the two horizontal bounding surfaces. The cross-sectional aspect ratio (height/width) of the enclosure was unity, while the aspect ratios of the individual layers in the investigated two-fluid systems were less than unity.

Aside from the collection of heat transfer data for the two-fluid systems and the baseline single-fluid systems, the main focus of the work was to develop methods for predicting the two-fluid heat transfer results from the single-fluid results. Two methods were developed, one for predicting the heat transfer rate and the other for predicting the Nusselt number. These predictive schemes were tested by comparing the results obtained therefrom with the experimental data collected for the two-fluid systems.

The strengths of the aforementioned predictive schemes lie in their simplicity and in the universal nature of the single-fluid Nusselt number correlation on which they are based. This correlation was developed here from the single-fluid data collected for distilled water and *n*-hexadecane.

To the best knowledge of the authors, the only prior experimental work on two-fluid natural convection in a rectangular enclosure with thermally active vertical walls is that of [1], but no Nusselt number data are presented. Numerical work on the problem was undertaken in [2], but the governing equations were in error [3]. A vertical flat plate partially immersed in water and with its upper end in air was investigated in [3]. Layered systems heated from below were studied in [4–6], and the layered problem with internal heat generation in one of the layers and heat loss at the horizontal bounding surfaces was considered in [7].

Experiments

Apparatus. The experimental apparatus was designed to provide well-defined and precisely controlled thermal boundary conditions and to virtually eliminate extraneous heat losses. The description of the apparatus is facilitated by reference to Fig. 1, which is a schematic diagram of a typical cross section. As seen there, the internal cross section of the enclosure is a square of side L, where $L = 5.04$ cm. In the direction perpendicular to the plane of the cross section, the length of the enclosure (denoted by W) is 26.065 cm, which is 5.17 times the side of the square. This relatively large length-to-side ratio was chosen to minimize end effects.

The two vertical walls of the enclosure, both thermally active, were made from 0.950-cm-thick copper plate. As illustrated in the diagram, the edges of the plates were beveled at 45 deg in order to virtually eliminate thermal contact with the other bounding walls, thereby minimizing extraneous heat transfer. After the machining operations were completed, the surfaces of the plates which bounded the enclosure were hand polished using a succession of increasingly fine lapping compounds.

Heating of one of the plates was accomplished by means of electrical resistance wire (0.013-cm-dia, Teflon-coated chromel) embedded in 28 equally spaced, longitudinal grooves milled in its rear face. To enable the attainment of temperature uniformity on the heated plate, the wiring was arranged so that there were four independently controlled heating circuits. During the experiments, it was found that the desired temperature uniformity could be attained by operating the lowermost and next-to-lowermost heaters at the same setting, with a similar pairing for the uppermost and next-to-uppermost heaters. Power was provided by a regulated a-c supply and controlled by autotransformers.

The temperature of the heated plate was measured with ten precalibrated, 0.013-cm-dia, chromel-constantan thermocouples installed in holes drilled into the rear face of the plate. The junctions were situated 0.05 cm from the active surface, and copper oxide cement was used to fix the ther-

Contributed by the Heat Transfer Division for publication in the JOURNAL OF HEAT TRANSFER. Manuscript received by the Heat Transfer Division December 16, 1985.

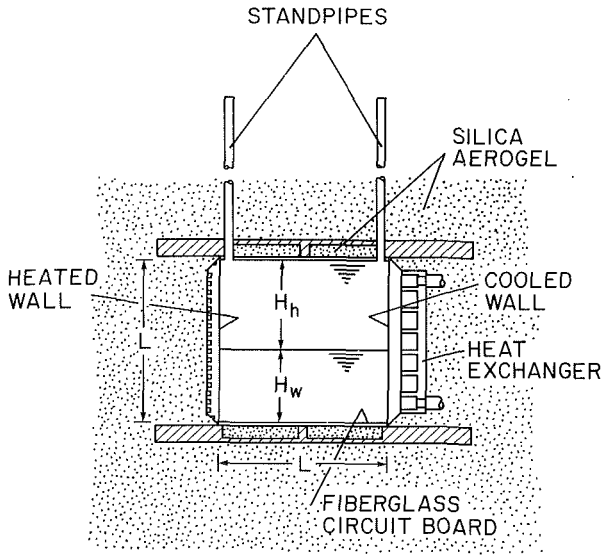

Fig. 1 Cross-sectional view of the experimental apparatus

mocouples in position. Eight of the thermocouples were deployed in a vertical line at the longitudinal midplane of the enclosure, and two thermocouples were installed adjacent to the outboard edges of the plate. The thermocouple outputs, read to 1 μV, were used to guide the settings of the heating circuits.

The other copper plate was cooled by means of a multichannel heat exchanger mounted on its rear face as shown in Fig. 1. The heat exchanger was made of brass because of its high thermal conductivity and its compatibility with water. Cooling water was recirculated through the heat exchanger, entering at one end of the enclosure and exiting at the other. The cooling water was supplied by a thermostatic bath having exceptional temperature stability, resulting in wall temperature constancy within 0.03°C during a data run. Eight thermocouples were installed in the cooled plate, six along a vertical line at the longitudinal midplane and two others adjacent to the outboard edges.

With the aforementioned design features, temperature uniformity at both thermally active plates was achieved to within one percent of the temperature difference between the plates.

In the experiments, it was desired that the heat flowing between the heated and cooled walls pass through the fluid which fills the enclosure and not through the thermally passive horizontal walls. To this end, a special design which created a thermal barrier was employed for the horizontal walls. The fabrication of each horizontal wall was initiated with a 0.950-cm-thick plexiglass plate. Two parallel longitudinal grooves, each 0.700 cm deep and 2.286 cm wide, separated by a thin rib, were milled into one surface of the plate. Each groove was filled with silica aerogel powder insulation whose thermal conductivity is 15 percent less than that of air. The thus-filled insulation pockets were sealed by a 0.05-cm-thick sheet of fiberglass circuitboard. As shown in Fig. 1, the horizontal walls were positioned so that the insulation pockets were directly beneath and directly above the enclosure proper.

The enclosure was completed by end walls made of 0.950-cm-thick plexiglass. Plexiglass was chosen to provide visual access to the enclosure to enable the detection and elimination of undesired air bubbles. Sealing of contacting surfaces was accomplished with silicone rubber applied in minimal amounts to avoid enlarging the conduction path between the surfaces.

Two standpipes were installed in the upper wall of the enclosure, one at either end. The standpipes were used to fill the enclosure, with the participating liquid(s), to change the height of the interface between the two liquids, and to accommodate their thermal expansion. The standpipes were fully insulated.

During the experiments, the entire apparatus was situated in a cardboard-walled housing filled with silica aerogel insulation. The size of the housing was such that the apparatus was surrounded by about 30 cm of insulation.

Experimental Procedure. In terms of the notation of Fig. 1, the interface position will be characterized by the H_w/L ratio, where H_w is the height of the water in the enclosure (H_h is the height of the hexadecane, and $H_w + H_h = L$). At the operating conditions of the experiments, the density of water is about 30 percent greater than that of the *n*-hexadecane. Experiments were performed for two-fluid systems for which $H_w/L = 0.25$, 0.40, 0.50, and 0.75. The single-fluid cases, hexadecane alone and water alone, may be characterized by $H_w/L = 0$ and 1, respectively.

The experiments for the various two-fluid systems were carried out in a regular sequence, starting with the uppermost position of the interface ($H_w/L = 0.75$) and proceeding toward lower and lower interface positions. The sequence was initiated by introducing into the enclosure a carefully weighed mass of water which, at the operating temperature of the experiments, would correspond to the $H_w/L = 0.75$ position of the interface. Prior to the filling operation, the amount of mass required had been calculated from the accurately known dimensions (to within 0.001 in. or better) of the enclosure and the density of water at the operating temperature.

The water was introduced into the enclosure through one of the standpipes, while the air displaced from the enclosure escaped from the other standpipe. Then, the hexadecane was introduced in sufficient amount to completely fill the enclosure and the lower portion of the standpipes. Any bubbles present in the enclosure were eliminated by tilting the apparatus so that they exited via a standpipe. The enclosure was then leveled with the aid of adjustable legs in conjunction with a precision bubble level. Any insulation that had been remov-

Nomenclature

F = function of Prandtl number, equation (3)
F^* = form of F for two-fluid case, equation (6)
g = acceleration of gravity
H_h = thickness of hexadecane layer
H_w = thickness of water layer
h = single-fluid heat transfer coefficient, equation (1)
k = thermal conductivity
L = side of square enclosure
Nu = single-fluid Nusselt number $= hL/k$
Nu* = two-fluid Nusselt number, equation (4)
Pr = Prandtl number
Q = heat transfer rate
Ra = single-fluid Rayleigh number, equation (2)
Ra_h = equation (2) evaluated with hexadecane properties
Ra_w = equation (2) evaluated with water properties
Ra* = two-fluid Rayleigh number, equation (5)
T_C = temperature of cooled wall
T_H = temperature of heated wall
$\bar{T}$ = mean temperature $= (T_H + T_C)/2$
W = dimension of enclosure perpendicular to cross section
β = coefficient of thermal expansion
ν = kinematic viscosity

Subscripts

h = pertaining to hexadecane
w = pertaining to water

ed to facilitate the foregoing setup operations was replaced, after which the data run proper was initiated.

Once the data runs for the $H_w/L = 0.75$ interface position had been completed, the interface was lowered to $H_w/L = 0.50$. This was accomplished by extracting an accurately weighed (to within 0.05 g) mass of water with a long-nose syringe and introducing an appropriate amount of hexadecane to fill the enclosure and the lower portion of the standpipes. This same procedure was used to achieve the $H_w/L = 0.40$ and 0.25 interface positions.

The experiments for the single-fluid cases were carried out separately from those for the two-fluid cases. Prior to charging the enclosure with either of the individual liquids, the apparatus was disassembled and all walls of the enclosure were thoroughly cleaned. Then, after assembly, the enclosure was fully filled with either water or hexadecane.

The procedure followed in the execution of the data runs was the same for the single-fluid and two-fluid cases. For all runs, the temperatures T_H and T_C of the respective heated and cooled walls were adjusted so that their mean value $\bar{T} = (T_H + T_C)/2$ was the same, namely, $\bar{T} = 33.5°C$. The use of a fixed value of $\bar{T}$ ensured that the Prandtl numbers of the respective liquids, based on $\bar{T}$ as a reference temperature, would be constant throughout the experiments, namely, Pr = 5 for water and 39.2 for *n*-hexadecane.

Each data run was characterized by a prescribed value of $(T_H - T_C)$. The respective magnitudes of T_H and T_C were independently controllable to high precision, so that the aforementioned $\bar{T}$ = constant condition was readily achieved. For each interface position H_w/L (including 0 and 1), as many as five values of $(T_H - T_C)$ were employed spanning the overall range from 3 to 20°C. In view of the considerable amount of thermal insulation surrounding the test section, an equilibration period of about 24 hours was required for the attainment of steady state.

Data Reduction

The experimental data will be presented both in dimensional and dimensionless forms. In the dimensional presentation, the rate of heat transfer Q will be plotted as a function of the temperature difference $(T_H - T_C)$ between the heated and cooled walls. Supplementary calculations had demonstrated that the heat loss through the insulation was negligible, so that Q was taken directly from the electric power input to the heated wall. The temperatures T_H and T_C were determined by respectively averaging the ten thermocouples in the heated wall and the eight thermocouples in the cooled wall. As noted earlier, the deviations from the respective averages were within one percent of $(T_H - T_C)$.

The groups used in the dimensionless presentation were evaluated differently for the single-fluid and two-fluid cases. The single-fluid Nusselt and Rayleigh numbers were based on the conventional definitions. For the Nusselt number,

$$h = Q/(LW)(T_H - T_C), \qquad \mathrm{Nu} = hL/k \tag{1}$$

in which W is the dimension of the enclosure perpendicular to the cross section (i.e., perpendicular to the plane of Fig. 1). For the Rayleigh number,

$$\mathrm{Ra} = [g\beta(T_H - T_C)L^3/\nu^2]\mathrm{Pr} \tag{2}$$

In the correlation of the single-fluid results, the separate dependence of the Nusselt number on the Rayleigh and Prandtl numbers will be taken into account by utilizing the group Ra/F, where F is a function of Prandtl number given by

$$F = F(\mathrm{Pr}) = [1 + (0.492/\mathrm{Pr})^{9/16}]^{16/9} \tag{3}$$

This expression was developed in [8] for correlation of the Nusselt number for natural convection boundary layer flow on a vertical flat plate. All of the fluid properties appearing in equations (1)–(3) were evaluated at $\bar{T} = (T_H + T_C)/2$.

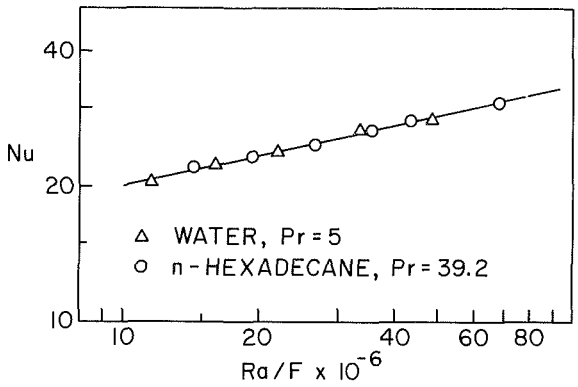

Fig. 2 Nusselt numbers for the single-fluid case

For the correlation of the two-fluid heat transfer results, the Nusselt number, to be designated as Nu*, will be defined as

$$\mathrm{Nu}^* = \frac{QL}{W[(kH)_w + (kH)_h](T_H - T_C)} \tag{4}$$

where the subscripts w and h respectively refer to water and hexadecane. Note that since $H_w + H_h = L$, equation (4), when applied to the single-fluid case, reduces identically to equation (1). Indeed, equation (4) was developed by replacing the kA product (A = surface area = WL) by $W[(kH)_w + (kH)_h]$. Furthermore, for the Rayleigh number and the Prandtl number factor, now to be denoted by Ra* and F^*,

$$\mathrm{Ra}^* = (H_w/L)\mathrm{Ra}_w + (H_h/L)\mathrm{Ra}_h \tag{5}$$

$$F^* = (H_w/L)F_w + (H_h/L)F_h \tag{6}$$

In equation (5), Ra_w and Ra_h were obtained by respectively evaluating equation (2) using water properties and hexadecane properties. Similarly, the F_w and F_h were calculated by introducing Pr_w and Pr_h into equation (3). All properties were evaluated at $(T_H + T_C)/2$. The definitions conveyed by equations (4)–(6) were selected because they are the simplest two-fluid correlating parameters which reduce identically to those for a single fluid when $H_w = 0$ or L.

Results and Discussion

The presentation of results will begin with the single-fluid case. The Nusselt numbers for water and hexadecane have been brought together in Fig. 2 and plotted as a function of Ra/F, where F is the Prandtl-number-dependent parameter defined by equation (3). From the figure, it is seen that the data for the two fluids are virtually perfectly correlated by the Ra/F group. Furthermore, the correlated data are logarithmically linear and are very well represented by the following least-squares fit

$$\mathrm{Nu} = 0.546(\mathrm{Ra}/F)^{0.2236} \tag{7}$$

A straight line depicting equation (7) has been drawn in Fig. 2. Among the 11 data points plotted in the figure, the majority fall within one percent of the line, and the most deviant point is only 1.77 percent from the line. Thus, the factor F provides a virtually perfect correlation of Prandtl number effects in the investigated range, which extends from Pr = 5 to 39.2.

There has been a considerable amount of published work on natural convection in enclosures containing a single fluid. Although experiments have been performed for a wide range of Prandtl numbers (e.g., [9]), it appears that there were no prior attempts to correlate the Ra and Pr dependences of the Nusselt number with a single group such as the Ra/F group used here. The present correlation, equation (7), covers the Prandtl number range between 5 and 39 and, until there is other definitive information, it is available for use for other Prandtl numbers outside of this range.

The present Nusselt numbers for water were compared with

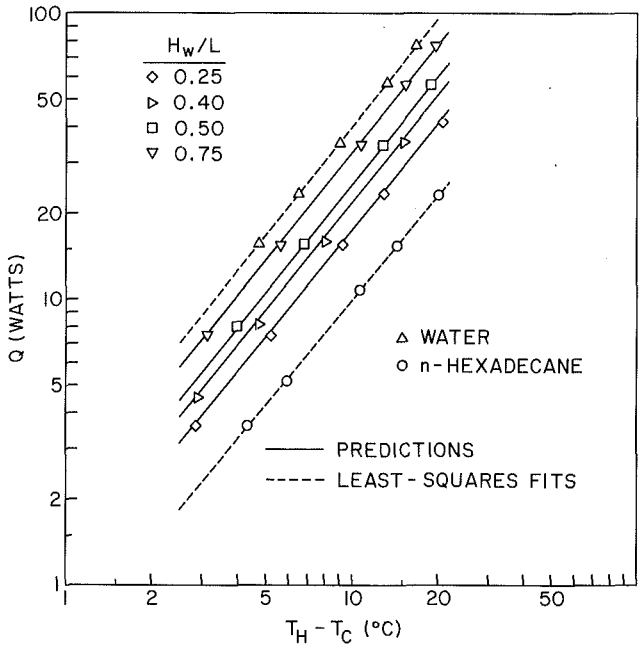

Fig. 3 Heat transfer rates for the single-fluid and two-fluid cases

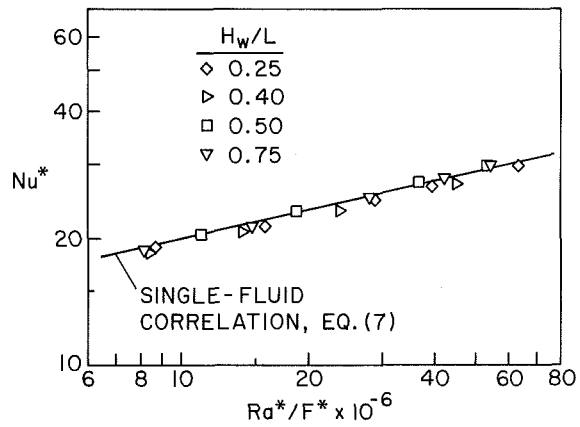

Fig. 4 Nusselt numbers for the two-fluid cases

those of [9] and very good agreement was found to prevail. No prior Nusselt number data for hexadecane could be found in the literature.

Attention will now be turned to the two-fluid case, for which results will be presented in both dimensionless and dimensional forms. In both formats, particular consideration will be given to the prediction of the two-fluid results from those for the single fluids.

Figure 3 conveys the dimensional presentation, where the rate of heat transfer Q is plotted against the temperature difference $(T_H - T_C)$ between the heated and cooled walls. In addition to the results for the various two-fluid systems, the figure also contains results for the single-fluid case (water and hexadecane). All of the results of Fig. 3 are for $(T_H + T_C)/2 = 33.5°C$.

As expected, the highest rate of heat transfer was achieved when the enclosure was filled with water and the lowest when it was filled with hexadecane. The rates of heat transfer to the water are about four times those to the hexadecane. The various two-fluid systems are contained between the respective single-fluid limits and are ordered in a regular manner according to the height of the interface.

Least-squares straight lines (the dashed lines in the figure) have been respectively passed through the water data and the hexadecane data. These lines represent the power-law relation $Q \sim \Delta T^m$. The data point deviations from the fitted lines were less than one percent.

The solid lines appearing in Fig. 3 represent predictions of two-fluid heat transfer from the single-fluid heat transfer for water and hexadecane. They were derived from

$$Q = (H_w/L)Q_w + (H_h/L)Q_h \tag{8}$$

where Q_w and Q_h were obtained from the aforementioned least-squares fits. Equation (8) is a simple prorating of the single-fluid heat transfer results. The data symbols enumerated in the legend for $H_w/L = 0.25$, 0.40, 0.50, and 0.75 represent the actual experimental data. These data are seen to be in excellent accord with the predicted lines. The agreement is nearly perfect for $H_w/L = 0.50$ and 0.75, within 2–3 percent for $H_w/L = 0.25$, and within 5 percent for $H_w/L = 0.40$.

The aforementioned excellent agreement lends strong support to the use of equation (8) as a means for predicting two-fluid heat transfer from single-fluid heat transfer information. Thus, if the two fluids are designated as i and j, it is recommended that the two-fluid Q be obtained from

$$Q = (H_i/L)Q_i + (H_j/L)Q_j \tag{9}$$

Furthermore, in view of the general correlation conveyed by equation (7), it is not necessary to perform experiments to determine Q_i and Q_j. Instead, Q_i and Q_j can be computed from equation (7) for given values of $(T_H - T_C)$ and of $\bar{T} = (T_h + T_C)/2$, the latter for the evaluation of the thermophysical properties. Thus, by making use of equations (7) and (9), the two-fluid heat transfer can be found without having to perform any experiments.

The dimensionless presentation of the two-fluid heat transfer results is conveyed in Fig. 4, where Nu* is plotted versus Ra*/F* (Nu*, Ra*, and F^* are defined by equations (4)–(6)). Also appearing in the figure is a solid line which represents the single-fluid Nusselt number correlation of equation (7). The agreement of the two-fluid data with the single-fluid correlation is seen to be generally very good. The maximum deviation of the data from the line is about 5 percent, corresponding to $H_w/L = 0.40$. For the other H_w/L values, the deviations are even smaller, with virtually perfect agreement in evidence for $H_w/L = 0.50$.

Thus, within a tolerance no greater than 5 percent, equation (7), with a * now affixed to Nu, Ra, and F, also applies to the two-fluid systems. If equation (7) is so accepted, it can be used to predict the two-fluid heat transfer by making use of the definitions of Nu*, Ra*, and F^* in equations (4)–(6).

Concluding Remarks

The experiments performed here have provided readily applicable information for natural convection in enclosures containing either a single fluid or two immiscible fluids in a layered configuration. The single-fluid experiments, performed with distilled water and with n-hexadecane paraffin, were carried out to provide baseline data for the development of methods to predict the heat transfer in two-fluid, layered systems. To test the utility of the predictive methods, water–hexadecane experiments were performed at four different heights of the interface between the liquids. At the operating conditions of the experiments, the respective Prandtl numbers of the water and the hexadecane are 5 and 39.2.

The single-fluid Nusselt number results for the water and the hexadecane were perfectly correlated by the single dimensionless group Ra/F, where F is a Prandtl-number-dependent function given by equation (3). Although natural convection in enclosures has been previously studied for a wide range of Prandtl numbers, it appears that the Ra and Pr dependences of the Nusselt number have not heretofore been correlated by

a single group. The present correlation, equation (7), covers the Prandtl number range between 5 and 39 and, until there is other definitive information, it is available for use for other Prandtl numbers outside of this range.

For two-fluid systems, it was proposed that the heat transfer rate be predicted, as set forth in equation (9), as a weighted sum of the single-fluid heat transfer rates. The predictions based on this rule were in excellent agreement with the data for the various investigated water–hexadecane systems. In practice, to use this method, it is not necessary to perform experiments to determine the single-fluid heat transfer rates since they can be calculated with high accuracy from the aforementioned correlation, equation (7). Indeed, by using equations (7) and (9), the two-fluid heat transfer can be found without having to carry out any experiments.

To facilitate a dimensionless presentation of the measured two-fluid heat transfer results, new definitions (equations (4)–(6)) of Nu, Ra, and F were employed. It was found that within a tolerance no greater than 5 percent, the dimensionless two-fluid heat transfer data agreed with the single-fluid heat transfer correlation, equation (7). This finding provides an alternate method for predicting two-fluid heat transfer.

Of the two methods set forth here for predicting the two-fluid heat transfer rates, that which is a weighted sum of the single-fluid heat transfer rates is preferred by the authors because it has a better-defined physical basis.

The results obtained here are based on experiments in an enclosure of square cross section (aspect ratio of unity), although the cross-sectional aspect ratios of the individual fluid layers differed from unity. The possible influence of the enclosure cross-sectional aspect ratio on the two-fluid correlation schemes remains to be determined.

References

1 Szekeley, J., and Todd, M. R., "Natural Convection in a Rectangular Cavity: Transient Behavior and Two Phase Systems in Laminar Flow," *International Journal of Heat and Mass Transfer*, Vol. 14, 1971, pp. 467–482.

2 Knight, R. W., and Palmer, M. E., III, "Simulation of Free Convection in Multiple Fluid Layers in an Enclosure by Finite Differences," *Numerical Properties and Methodologies in Heat Transfer*, T. M. Shih, ed., Hemisphere, Washington, D.C., 1983, pp. 305–319.

3 Projahn, U., and Beer, H., "Theoretical and Experimental Study of Transient and Steady-State Natural Convection Heat Transfer From a Vertical Flat Plate Partially Immersed in Water," *International Journal of Heat and Mass Transfer*, Vol. 28, 1985, pp. 1487–1498.

4 Stork, K. W., "Zellularkonvektion in Behältern und in geschichteten Flüssigkeiten," Doctoral Thesis, Universität Karlsruhe, 1974.

5 Bourde, G. I., and Simanovskii, I. B., "Determination of Equilibrium Boundaries of a Two-Layer System Convection Instability," *Journal of Applied Mathematics and Mechanics*, Vol. 43, 1979, pp. 1091–1097.

6 Simanovskii, I. B., "Numerical Investigation of Convection in a System of Two Immiscible Fluids Heated From Below," *Convection Flows and Hydrodynamic Stability*, Izd. Ural. Nauch. Tsentr, Akad. Nauk SSSR, Sverdlovsk, 1979, pp. 126–131.

7 Schramm, R., and Reineke, H. H., "Natural Convection in a Horizontal Layer of Two Different Fluids With Internal Heat Sources," *Proceedings of the Sixth International Heat Transfer Conference*, Vol. 2, 1978, pp. 299–304.

8 Churchill, S. W., and Chu, H. H. S., "Correlating Equations for Laminar and Turbulent Free Convection From a Vertical Plate," *International Journal of Heat and Mass Transfer*, Vol. 18, 1975, pp. 1323–1329.

9 Kamotani, Y., Wang, L. W., and Ostrach, S., "Experiments on Natural Convection Heat Transfer in Low Aspect Ratio Enclosures," *AIAA Journal*, Vol. 21, 1983, pp. 290–294.

Mass Transfer at the Base of a Cylindrical Cavity Recessed in the Floor of a Flat Duct

E. M. Sparrow

D. L. Misterek

Department of Mechanical Engineering,
University of Minnesota,
Minneapolis, MN 55455

Experiments involving either sublimation or evaporation at the base surface of a cylindrical cavity were performed respectively using naphthalene and water as the transferred vapor. The cavity was mounted in the lower wall of a flat rectangular duct through which turbulent air was passed. Supplementary experiments were also carried out using a cavity with a constricted opening (i.e., a Helmholtz resonator). The base surface mass transfer did not decrease monotonically with increasing cavity depth. Rather, there were two local maxima, respectively at about 0.06D and 0.5D (D = cavity diameter). Of these, the first is due to the reattachment of the shear layer on the cavity base. For the second, both fluid-elastic and fluid-resonant oscillations were ruled out as causes on the basis of definitive experimental data, leaving fluid-dynamic oscillations as a possible cause. The base surface Sherwood number was well correlated by power-law dependences on the Reynolds and Schmidt numbers. Fluid flow experiments encompassing oil-lampblack flow visualization, helium bubble flow visualization, and spectral analysis of the pressure field at the cavity base were also carried out.

Introduction

The research described here was undertaken to investigate fundamental aspects of heat transfer and fluid flow in a cavity and to provide information applicable to heat transfer enhancement and contaminant removal from cavities. Specific consideration is given to mass transfer from the base surface of a cylindrical cavity to an airflow which passes over the cavity opening. The cavity is mounted in the lower wall of a flat rectangular duct such that its opening is flush with the surface of the wall which bounds the airflow. The work is primarily experimental, with supporting computations where appropriate. To supplement the mass transfer experiments, fluid-flow-related measurements were also performed. In view of the analogy between heat and mass transfer, the mass transfer results obtained here should also be applicable to heat transfer.

A literature survey revealed the virtual absence of prior work on heat or mass transfer at the base of a duct-mounted cylindrical cavity. The only encountered investigation [1] was performed using a cylindrical container that was partially filled with a liquid, so that the liquid constituted the bottom surface of the cavity. The results of [1] were contrary to expectation in that the rate of evaporative mass transfer did not decrease montonically as a function of increasing cavity depth. Rather, the mass transfer rate displayed a maximum value at a cavity depth-to-diameter ratio of approximately 0.5. This finding was presented without accompanying rationalization.

The fluid flow characteristics of cavities have been studied extensively, as reflected in the survey paper of [2]. There, three different types of fluid oscillations were identified: fluid dynamic, fluid resonant, and fluid elastic. Among these, fluid-dynamic oscillations arise from the amplification of instabilities in the shear layer which originates at the upstream edge of the cavity opening. Fluid-resonant oscillations are associated with resonant waves within the cavity, the nature of which depends on the geometric details of the cavity. The Helmholtz resonator, a cavity with a partially constricted opening, is an especially convenient configuration for studying possible fluid-resonance effects. Fluid-elastic oscillations are a consequence of the motion of the cavity walls (if the walls are nonrigid).

The relationships between the aforementioned oscillations and mass transfer at the cavity base have not heretofore been explored. Nevertheless, it may be conjectured that one or more of these oscillations is responsible for the reported mass transfer maximum of [1]. The possible effects of fluid-elastic oscillations will be investigated here by means of mass transfer experiments in which the cavity base is a rigid solid (naphthalene), instead of a liquid as in [1]. Fluid resonance will be explored in mass transfer experiments performed with a Helmholtz resonator cavity. In the latter experiments, which were initiated as a follow-on of [1], the cavity base surface was a liquid.

The instrumentation needed for the direct investigation of fluid dynamic oscillations was not available. However, several supplementary experiments were performed to provide information about the flow field. The oil-lampblack technique was used to visualize the pattern of fluid flow adjacent to the base surface of the cavity, while the entire flow field was observed via the helium bubble technique. Pressure measurements were made at the cavity base, and the resulting signals were resolved into a frequency spectrum. Such data were obtained for cavities of different depths in order to determine whether a marked change in the spectral distribution occurred at the depth at which the mass transfer maximum was achieved.

The foregoing discussion has dealt with the fundamentals-oriented aspects of the present investigation. Practice-oriented results were also obtained from the mass transfer experiments performed with the naphthalene-bottomed cavity. These experiments extended over a range of cavity depth-to-diameter ratios from 0 to 2, a tenfold variation of the Reynolds number, and rectangular ducts of two different cross-sectional aspect ratios. A correlation effort was undertaken to provide a generalized functional relationship between the base-surface Sherwood number and the parameters on which it depends.

Mass Transfer Experiments

The description of the experimental apparatus is facilitated

Contributed by the Heat Transfer Division for publication in the JOURNAL OF HEAT TRANSFER. Manuscript received by the Heat Transfer Division January 23, 1986.

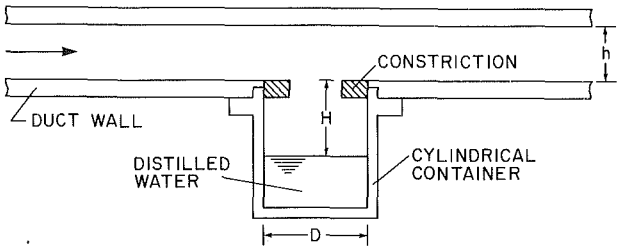

Fig. 1 Longitudinal sectional view of the Helmholtz resonator cavity and the adjacent duct

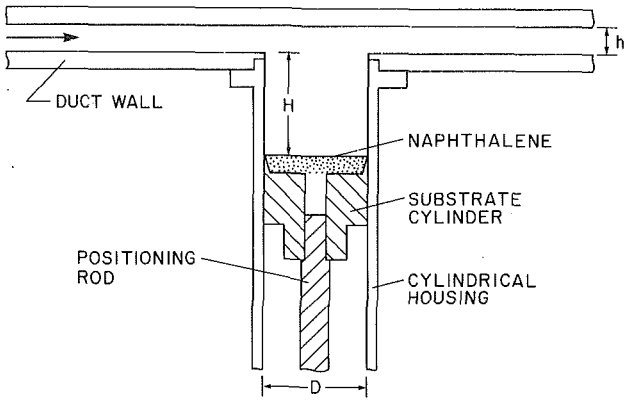

Fig. 2 Longitudinal sectional view of the unconstricted cylindrical cavity and the adjacent duct

by reference to Figs. 1 and 2. The first of these figures is a longitudinal sectional view of the Helmholtz resonator cavity and the adjacent portion of the host rectangular duct, while the second is a similar view of the naphthalene-bottomed cavity and its host duct. The two cavities will be described in the order shown.

As seen in Fig. 1, the Helmholtz cavity consisted of three parts: (*a*) a cylindrical container, (*b*) a constriction at the cavity opening, and (*c*) distilled water which partially filled the container and whose surface formed the base of the cavity. The container was machined to close tolerances with an integral flange which facilitated its mating with the lower wall of the host rectangular duct. The installation of the container in the duct wall could be accomplished in a matter of seconds and the same for the removal of the container. All interior surfaces of the container were coated with a thin, polished film of paint to prevent electrochemical reactions between the water and the aluminum, yielding a finished inside diameter D of 3.800 cm.

Constriction of the cavity opening was accomplished by an annular disk made of Delrin, a free-machining plastic. The disk had an inner diameter of 1.905 cm and a thickness of 0.615 cm. With water in place in the container, the cavity depth (i.e., the distance between the surface of the water and the top of the cavity) is denoted by H. In the absence of the water, $H = 4.684$ cm.

Two thermocouples were installed in the cylindrical container in order to measure the surface temperature of the evaporating water during the experiments. The thermocouples were made from Teflon-coated, 0.0254-cm diameter chromel and constantan wire chosen for compatibility with water and for high emf per °C. The junctions of the thermocouples were positioned as close to the surface as was compatible with the evaporation-related recession of the surface.

The naphthalene-bottomed cylindrical cavity was also a multipart component, as shown in Fig. 2. As seen there, a layer of solid naphthalene, implanted in a recess in the upper surface of a substrate, served as the base of the cavity. The substrate was an aluminum cylinder with a finished diameter after polishing and lapping of 3.805 cm and a length of 3.810 cm. The recess, which was 0.76 cm deep, was machined into the upper face of the cylinder, with the outer wall of the recess being tapered to virtually zero thickness (0.004 cm) at its upper edge. To aid in the adhesion of the naphthalene, which was implanted by a casting process, the bottom of the recess was roughened.

The cylinder was drilled along its axis to provide an access hole through which molten naphthalene was poured during the casting process. The hole, which was threaded at its lower end, also received the threaded upper end of an aluminum rod which served to set the vertical position of the cylinder and, thereby, that of the naphthalene surface. In addition to the main axial hole, two smaller axial holes (not shown) were drilled through the centerbody to serve as passageways for the escape of air displaced from the recess during the casting process. One of these holes also served as a conduit through which lead wires were drawn in order to enable a thermocouple junction to be embedded in the exposed surface of the cast naphthalene.

The cylinder was housed in a brass sleeve (the cylindrical housing) whose bore diameter after polishing and lapping was 0.00254 cm greater than the diameter of the cylinder. With the aid of the positioning rod, the cylinder could be moved freely to any height within the housing. The portion of the inner surface of the housing which extended upward from the naphthalene surface served as the sidewall of the cavity.

The use of dissimilar metals for the cylinder and the housing (aluminum and brass) effectively avoided galling. The housing was machined with integral flanges at its upper end to facilitate its mating with the lower wall of the duct, with installation and removal being accomplished in seconds.

The lower end of the housing was closed by an annular disk (not shown). The positioning rod passed snugly through the center hole of the disk and was locked in place with a set screw, thereby fixing the cavity depth H. The length of the housing was chosen to give a range of H extending from 0 to $2.1D$.

Two rectangular ducts were used during the course of the experiments. One had a flow cross section of 1.928 × 8.270 cm (height h × width W), while the cross section of the other was 0.960 × 8.270 cm. All the experiments for the Helmholtz cavity and the initial experiments for the naphthalene-bottomed cavity were performed with the former duct, while

Nomenclature

A = cross-sectional area of cavity
D = cavity diameter
D_h = hydraulic diameter of duct
$\mathfrak{D}$ = mass diffusion coefficient
H = cavity depth, Figs. 1 and 2
h = duct height
K = base surface mass transfer coefficient
$\dot{M}$ = mass transfer rate
p = pressure
Re = Reynolds number = $\bar{u}D/\nu$
$\mathrm{Re}_{\mathrm{duct}}$ = duct Reynolds number $\bar{u}D_h/\nu$
Sc = Schmidt number
Sh = base surface Sherwood number
T = temperature
$\bar{u}$ = mean velocity in duct
W = duct width
W = specific humidity
ν = kinematic viscosity
$\rho_{v,\mathrm{base}}$ = vapor density at cavity base
$\rho_{v,\mathrm{duct}}$ = vapor density in duct

the latter duct was used for the main body of experiments for the naphthalene-bottomed cavity. For both ducts, the cavity was centered in the width of the lower bounding wall of the cross section, leaving a lateral clearance of about 2.23 cm between the edge of the cavity opening and the adjacent side wall of the duct. This clearance ensured that the air flow passing over the opening would be unaffected by spanwise variations in the velocity profile which occur adjacent to the side walls.

The cavity was situated about 65 duct heights downstream of the inlet of the first duct and about 130 duct heights downstream of the inlet of the second duct. The distance between the duct inlet and the cavity served as a hydrodynamic development length. Downstream of the cavity, the duct continued for a length of 25 and 50 heights, respectively, for the first and second ducts.

The ducts were fabricated primarily from aluminum plate stock. The interior surfaces of the duct walls (those which bounded the air flow) were polished to a high degree of smoothness. To enable visual observations, the portion of the upper wall situated above the cavity was made of plexiglass.

The system was operated in the open-circuit mode and in suction. Air was drawn from the temperature-controlled laboratory into the duct through a sharp-edged inlet. After traversing the length of the duct, the air passed to a flowmeter (a calibrated rotameter), a control valve, and a blower situated in a service corridor adjacent to the laboratory. The compression-heated, vapor-enriched discharge of the blower was vented outside the building.

The rate of mass transfer was determined from the change of mass which occurred during a measured period of time in which the cavity was exposed to the air flow. For the Helmholtz cavity, the cylindrical container and its inventory of distilled water were weighed immediately before and after the air flow period. Similarly, for the naphthalene-bottomed cavity, before and after mass measurements were made of the substrate cylinder and its embedded layer of naphthalene. The mass measurements were accomplished with a solid-state analytical balance having a resolution of 0.00001 g. Calibration runs were made to assess the extent of any extraneous mass transfer which might have occurred between the before and after weighings. Special precautions were taken to attain isothermal conditions at the mass transfer surface during the data run. The mass transfer rates are believed accurate to one percent.

Thermocouples were installed in the duct, both upstream and downstream of the cavity, to measure the temperature of the air flow. The humidity of the air was measured by a specially designed psychrometric unit whose intake was positioned very close to the inlet of the duct. In the psychrometer, the wet- and dry-bulb temperatures were measured to 0.1°F or better by ASTM-certified thermometers.

Fluid Flow Experiments

As noted in the Introduction, the fluid flow experiments involved flow visualization by the oil-lampblack and helium bubble techniques and pressure measurements at the cavity base. These experiments will now be described.

The oil-lampblack technique [3] was used to visualize the pattern of fluid flow adjacent to the bottom of the fully open cylindrical cavity (i.e., without the Helmholtz-type constriction) and, in particular, to identify changes in the flow pattern as a function of the cavity depth. To implement the experiments, the naphthalene base surface was first covered by a sheet of white, plasticized, self-adhering contact paper. Then, a suitably fluid mixture of lampblack powder and oil was prepared, and small, uniformly sized droplets were placed at specific locations on the contact paper. The air flow was then initiated and maintained for a fixed time interval. During this period, the droplets moved under the stresses exerted by the flow, forming vectorlike traces on the surface. The lengths and directions of these vectors were compared for different cavity depths.

The helium bubble technique was used to visualize the general flow field in the cavity. To facilitate the use of the technique, the brass cylindrical housing of the unconstricted cavity (Fig. 2) was replaced by a plexiglass housing, and the substrate cylinder and its embedded layer of napthalene was replaced by a Delrin plastic cylinder. Variation of the cavity depth was accomplished by moving the Delrin cylinder vertically within the housing. The helium-filled soap bubbles were introduced either at the duct inlet or at the base of the cavity. To facilitate the observation of the bubbles, the cavity was illuminated from directly above, and all surrounding surfaces were blackened. The bubble motions were recorded on video tape for subsequent examination.

The pressure measurements at the base of the cavity were made with a Bruel and Kjaer condenser-type microphone (No. 4148) with a manufacturer-specified operating range from 10 to 5000 Hz. For these experiments, the substrate cylinder and its embedded naphthalene layer were replaced by either of two Delrin plastic disks, each fabricated with a hole which enabled the face of the microphone to be flush with the surface of the disk which formed the base of the cavity. In one of the disks, the microphone was centered at the axis of the cavity, while in the other, it was positioned adjacent to the side wall of the cavity. The cavity depth was varied by changing the vertical positioning of the disk.

The output of the microphone was connected to a spectrum analyzer (Hewlett-Packard No. 3582A), which performed an 8-bit fast Fourier transform on the data. The spectrum analyzer yielded the voltage versus frequency distribution for the pressure signals, where the voltage is a measure of the strength of the pressure disturbance.

Data Reduction

For both the water vapor evaporation and naphthalene sublimation experiments, the mass transfer characteristics at the cavity base will be expressed via the mass transfer coefficient K and its dimensionless counterpart, the Sherwood number Sh, respectively defined as

$$K = (\dot{M}/A)/(\rho_{v,\text{base}} - \rho_{v,\text{duct}}), \qquad \text{Sh} = KD/\mathfrak{D} \tag{1}$$

In the equation for K, the quantity $\dot{M}$ is the rate of mass transfer at the cavity base, determined from the measured change of mass and the duration of the data run. The area A is that of the cavity cross section, equal to $\pi D^2/4$. In the denominator, $\rho_{v,\text{base}}$ is the value of the density at the cavity base for the transferred vapor (either water or naphthalene), while $\rho_{v,\text{duct}}$ is the vapor density in the duct at a position above the cavity opening.

The value of $\rho_{v,\text{base}}$ for water vapor was determined under the assumption that liquid–vapor equilibrium existed at the liquid surface. On this basis, $\rho_{v,\text{base}}$ was read from steam tables using the measured liquid surface temperature as input. For naphthalene, it was assumed that solid–vapor equilibrium prevailed at the solid surface, and the vapor pressure was evaluated from the vapor pressure–temperature relation [4] at the measured surface temperature. Then, $\rho_{v,\text{base}}$ was obtained from the perfect gas law using the vapor pressure and temperature as inputs.

For the naphthalene sublimation experiments, the air drawn into the duct was free of naphthalene vapor, so that $\rho_{v,\text{duct}} = 0$. On the other hand, $\rho_{v,\text{duct}} > 0$ for the water evaporation experiments, and its determination will now be described. From the data collected at the psychrometer in conjunction with the barometric pressure, the specific humidity of the air entering the duct was calculated by standard thermodynamic methods (e.g., [5], pp. 396–397). Then, in the duct at a position above

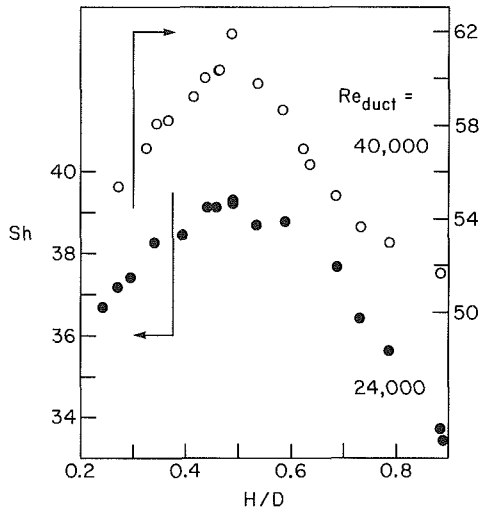

Fig. 3 Sherwood numbers for evaporation of water at the base surface of a Helmholtz cavity

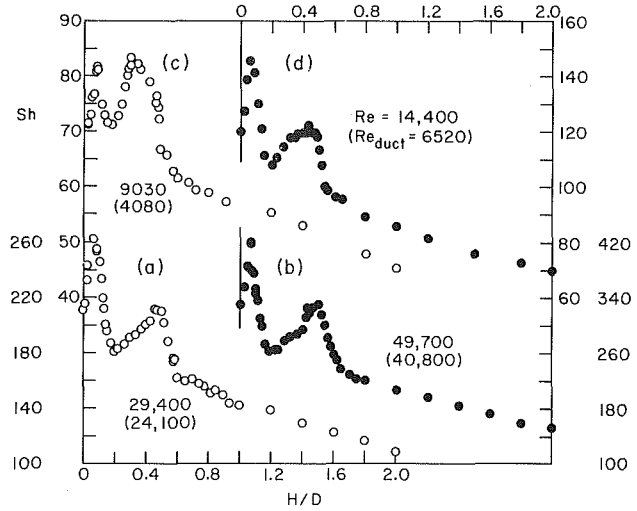

Fig. 4 Sherwood numbers for naphthalene sublimation at the base of an unconstricted cylindrical cavity. Parts (*a*) and (*b*) are for experiments performed in the larger height duct, and parts (c) and (*d*) are for the smaller height duct.

the cavity opening (measured pressure = p), the partial pressure $p_{v,\text{duct}}$ of the water vapor is

$$p_{v,\text{duct}} = pW/[(M_w/M_a) + W] \tag{2}$$

where M_w and M_a are the respective molecular weights of water and air. The density $\rho_{v,\text{duct}}$ was then obtained from the perfect gas law using $p_{v,\text{duct}}$ and the temperature as inputs.

To complete the evaluation of the Sherwood number, it remains to specify the mass diffusion coefficient $\mathfrak{D}$. For the water vapor–air system, $\mathfrak{D}$ was taken from [6, p. 10], while for the naphthalene–air system, $\mathfrak{D}$ was evaluated by using the well-established form

$$\mathfrak{D} = \psi T^{1.75}/p \tag{3}$$

where ψ is a constant whose value was fixed by using data listed in [4]. Testimony as to the accuracy of the $\mathfrak{D}$ values is provided by the fact that when they were used to compute the Schmidt number Sc, the resulting values were 0.60 and 2.52, respectively for water vapor–air and naphthalene–air. These Schmidt numbers are in excellent agreement with those of the literature.

The Sherwood number results will be parameterized by the Reynolds number Re based on the cavity diameter D and on the mean velocity $\bar{u}$ in the duct

$$\text{Re} = \bar{u}D/\nu \tag{4}$$

The duct Reynolds number Re_{duct}

$$\text{Re}_{\text{duct}} = \bar{u}D_h/\nu \tag{5}$$

will also be used as a parameter, where D_h is the hydraulic diameter of the duct.

For the water vapor experiments, the cavity depth H (Fig. 1) was determined indirectly from a knowledge of the mass of the water in the container and the dimensions of the container. In the case of the naphthalene experiments, H (Fig. 2) was determined directly by measuring the length of the positioning rod which extended beyond the closure disk at the lower end of the cylindrical housing. In the presentation of the results, the cavity depth will appear in the dimensionless ratio H/D.

Mass Transfer Results

The presentation of the mass transfer results will successively focus on the Helmholtz cavity and on the cylindrical cavity. The Helmholtz cavity experiments were primarily concerned with examining the possible role of fluid-resonant oscillations. On the other hand, those for the cylindrical cavity not only explored the possible role of fluid-elastic oscillations but were also intended to provide sufficient data on which to base a reliable Sherwood number correlation. In view of this, the Helmholtz cavity experiments were less extensive than those for the cylindrical cavity.

Helmholtz Cavity. The depth dependence of the Sherwood number for evaporative mass transfer (Sc = 0.6) at the base surface of a Helmholtz cavity is presented in Fig. 3 for duct Reynolds numbers of 24,000 and 40,000. As mentioned earlier, the Helmholtz cavity experiments were performed using the duct with the greater of the two interwall heights h.

From the figure, it is seen that for both of the investigated cases, the Sherwood number at first increases with H/D, attains a maximum at approximately $H/D = 0.5$, and decreases thereafter. As already noted in the Introduction, the Sh versus H/D distribution for evaporation of water at the base surface of a cylindrical cavity with an unconstricted opening also displayed a maximum at $H/D \cong 0.5$ [1]. Therefore, the altered fluid flow pattern associated with the presence of the constricted opening of the Helmholtz cavity did not affect the position of the maximum.

To examine the issue of fluid resonance, the natural frequency of the Helmholtz cavity corresponding to $H/D = 0.5$ was calculated in accordance with [7], yielding 1780 Hz. Then, the frequency of the imposed external disturbance (i.e, oscillations of the shear layer) was calculated for each of the investigated Reynolds numbers. The frequency of the external disturbance is embedded in the Strouhal number which, from [8], is a function of the Mach number. The Mach numbers corresponding to $\text{Re}_{\text{duct}} = 24{,}000$ and 40,000 were calculated and the corresponding Strouhal numbers obtained from [8], yielding disturbance frequencies of 225 and 840 Hz. Both of these frequencies differ appreciably from the natural frequency of 1780 Hz. Therefore, resonance did not occur when $H/D = 0.5$, from which it follows that resonance was not responsible for the Sh peak at $H/D = 0.5$.

Cylindrical Cavity. The first set of experiments for the naphthalene-bottomed cylindrical cavity (without constriction of the opening) was performed using the duct having the greater of the two interwall heights h. The variation of the Sherwood number with the cavity depth resulting from these experiments is plotted in Figs. 4(*a*) and (*b*), where H/D ranges from 0 to 2. These results are parameterized by values of the Reynolds number Re (equation (4)) of 29,400 and 49,700, which correspond to duct Reynolds numbers Re_{duct} (equation (5)) of 24,100 and 40,800.

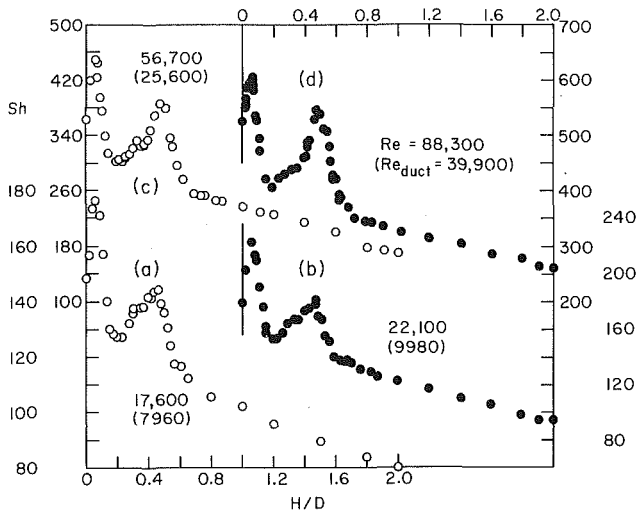

Fig. 5 Sherwood numbers for naphthalene sublimation at the base of an unconstricted cylindrical cavity for experiments performed in the smaller height duct

From an examination of Figs. 4(*a*) and (*b*), it is seen that there is a maximum in the Sh versus H/D distributions at $H/D=0.5$, which is the same cavity depth at which a maximum was encountered in [1]. However, in [1], the cavity bottom was a nonrigid surface (liquid water), whereas here the cavity bottom is rigid (naphthalene). This finding indicates that fluid-elastic oscillations are not the cause of the Sherwood number maximum at $H/D=0.5$.

The other noteworthy feature of Figs. 4(*a*) and (*b*) is the presence of a second maximum in the Sh versus H/D distributions. This other maximum occurs at $H/D=0.06$ for both of the investigated Reynolds numbers and has a larger value than that at the $H/D=0.5$ maximum. It may be noted that the second maximum was not encountered in [1] because a liquid-bottom cavity could not be operated at small H/D without loss of liquid due to the scrubbing action of the air. However, no such problem existed with the naphthalene-bottomed cavity, so that experiments could be performed for arbitrarily small H/D, even $H/D=0$.

As will be confirmed later via flow visualization, the $H/D=0.06$ maximum corresponds to the reattachment of the shear layer spawned by the cavity opening onto the cavity base. The presence of the two maxima gives rise to a complex, undulating Sh distribution for H/D between 0 and 0.6–0.7. Thereafter, Sh decreases monotonically and virtually linearly with H/D.

The next set of experiments was performed using the duct having the smaller of the two interwall heights h. The results of these experiments are presented in Figs. 4(*c*) and (*d*) and in Figs. 5(*a–d*). These results encompass the Re range from 9030 to 88,300, which corresponds to the Re_{duct} range from 4080 to 39,900. The dimensionless cavity depth was varied from 0 to 2.

All of the six Sh versus H/D distributions for this set of experiments displayed double maxima and were generally of the same form as those of Figs. 4(*a*) and (*b*), which have already been discussed. However, there are interesting differences in detail depending on the Reynolds number.

At the higher Reynolds numbers, 88,300 and 56,700, the Sh maxima respectively occur at $H/D=0.06$ and 0.5. As the Reynolds number decreases to 22,100, the outer maximum moves to a slightly smaller H/D ($=0.47$), then to $H/D=0.46$ at $Re=17{,}600$, and to $H/D=0.43$ at $Re=14{,}400$. The results for the lowest Reynolds number, $Re=9030$, tend to be deviant from the others, probably because the duct flow is not fully turbulent ($Re_{duct}=4080$). For this case, the outer maximum has moved inward to $H/D=0.3$, while the inner maximum has moved outward to $H/D=0.09$. Furthermore, the magnitude of the outer maximum now exceeds that of the inner maximum.

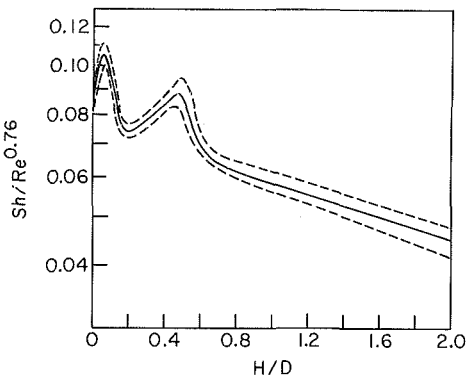

Fig. 6 Reynolds number correlation of the Sherwood number at the base of an unconstricted cylindrical cavity

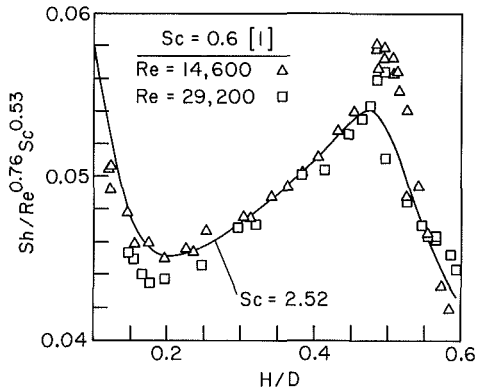

Fig. 7 Reynolds and Schmidt number correlations of the Sherwood number at the base of an unconstricted cylindrical cavity

The presence of the maxima can be regarded as giving rise to localized mass transfer enhancement. If the linear Sh versus H/D dependence which prevails for cavity depths beyond the maxima were to be extrapolated back to $H/D=0$, an assessment of the extent of the enhancement can be obtained. For Re between 14,400 and 88,300, the enhancements at the inner and outer maxima respectively range from 35 to 65 percent and 25 to 50 percent. At $Re=9030$, the corresponding enhancements are 18 and 28 percent.

Correlation of the Cylindrical Cavity Results. Aside from the lowest Reynolds number, the similarity in the shapes of the Sh versus H/D distributions of Figs. 4 and 5 suggests that it may be possible to bring them together by using a suitable scaling. The most compact correlation of the results of Figs. 4 and 5 (excluding Fig. 4*c*) was accomplished by using the group $Sh/Re^{0.76}$.

The end result of the correlation effort is presented in Fig. 6, where $Sh/Re^{0.76}$ is plotted versus H/D. In the figure, the solid line represents the average of the data, while the dashed lines represent the maximum deviations from the data. Since the extreme deviation of any data point from the average is only 8 percent, the correlation may be regarded as highly effective.

As a further generalization of the results, a Schmidt number correlation was sought using the data of [1] for Sc = 0.6 (evaporation of water) and the present data for Sc = 2.52 (sublimation of naphthalene). In [1], the Sherwood number results were correlated by the group $Sh/Re^{0.75}$ over the range from $H/D=0.12$ to 0.6. That correlation was rephrased as $Sh/Re^{0.76}$ to coincide with the present scaling (Fig. 6). Then, a correlation group $Sh/Re^{0.76}\,Sc^{m}$ was used to bring together the data of [1] with those obtained here.

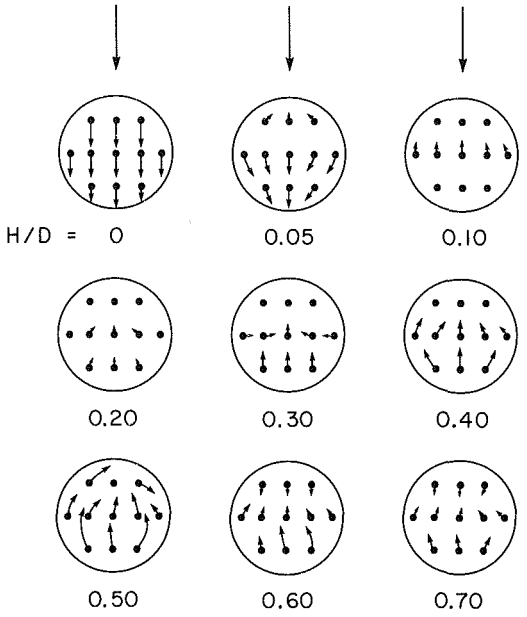

Fig. 8 Oil-lampblack flow visualization patterns at the base of an unconstricted cylindrical cavity

The best fit was achieved with $m=0.53$, and Fig. 7 was prepared to show the end result of the correlation effort. In the figure, the solid line represents the average of the present results (taken from Fig. 6), while the data are those of [1]. In general, the Sc = 0.6 and 2.52 results are correlated within a few percent but with an isolated deviation as large as 7 percent.

Fluid Flow Results

All of the fluid flow experiments were performed for the cylindrical cavity (without constriction of the opening) situated in the duct with the smaller of the two interwall heights h. Results will be successively presented for the oil-lampblack and helium bubble flow visualizations and for the base surface pressure measurements.

Oil-lampblack flow visualizations at the base surface of the cavity are presented in Fig. 8 for nine different cavity depths characterized by H/D values ranging from 0 to 0.7. The 11 black dots in each visualization pattern represent the positions of the oil-lampblack droplets prior to the initiation of the air flow, whereas the vectorlike traces emanating from the dots represent the disposition of the droplets at the end of the air flow period. The air flow period was identical for all cases depicted in Fig. 8 (15 s), as was the Reynolds number (~ 27,000). In view of this, the lengths of the various vectors provide an indication of the relative magnitudes of the base-adjacent velocities.

For the $H/D=0$ case, there is no cavity, and the base surface is flush with the lower wall of the duct. For this case, the vectors are all approximately the same length and are parallel to the direction of the mainflow. At $H/D=0.05$, the base-adjacent flow in the downstream portion of the cavity is in the mainflow direction, while the backflow at the upstream end of the cavity is indicative of a recirculation zone. This visualization pattern corresponds to the reattachment of the shear layer spawned by the cavity opening onto the cavity base. It is the reattachment onto the base that is responsible for the inner maximum in the Sh versus H/D distribution.

At $H/D=0.10$ and 0.20, the flow pattern is characterized by relatively low velocities. Furthermore, the presence of backflow in the downstream portion of the cavity indicates that the reattachment occurs on the downstream portion of the cylindrical wall. As the cavity depth increases from 0.3 to 0.4 to 0.5, the velocities grow progressively larger. The largest velocities occur for $H/D=0.5$, which accounts for the existence of a Sherwood number maximum at that cavity depth. With further increases in H/D, the velocities diminish, giving rise to a decrease in the Sherwood number.

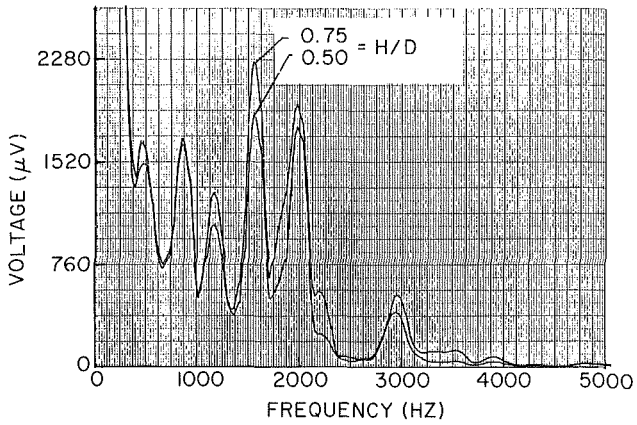

Fig. 9 Frequency spectra of the pressure measured at the center of the base of an unconstricted cylindrical cavity

Attention is next turned to the helium-bubble flow visualization. Bubbles introduced at the duct inlet were carried along with the mainflow and regularly entered the cavity. By careful observation of the motion of the bubbles, it was deduced that the flow entered the cavity at its downstream end and rolled up upon itself due to the blocking action of the downstream portion of the cylindrical wall. The rolling-up process continued until a spiraling vortex escaped from the cavity at its lateral edges. However, these events were no more intensive at $H/D=0.5$ than at any other cavity depth, so that no information was obtained about the $H/D=0.5$ Sherwood number maximum.

The pressure measurements at the cavity base were made to examine whether a marked change in the frequency spectrum occurred at $H/D=0.5$, i.e., at the cavity depth corresponding to the outer maximum in Sh. The measurements were carried out for H/D from 0 to 2 at a fixed Reynolds number and for a sevenfold range of the Reynolds number at $H/D=0.5$. Pressures were measured at the center of the base and also adjacent to the cylindrical wall.

The frequency spectra of the pressure did not reveal any unusual characteristics at $H/D=0.5$, as is illustrated in Fig. 9. This figure shows spectra at $H/D=0.5$ and 0.75 at Re = 53,000. These spectra are virtually congruent. On the other hand, as can be seen in Figs. 4 and 5, the Sh value at $H/D=0.75$ is significantly lower than the $H/D=0.5$ maximum. Therefore, the frequency spectra do not provide information about the cause of the maximum.

Concluding Remarks

The experiments performed here have demonstrated a complex behavior for the rate of mass transfer at the base of a cylindrical cavity situated in the lower wall of a flat rectangular duct. Starting with a cavity of zero depth ($H/D=0$) and then systematically increasing the depth, the mass transfer increased sharply to a maximum at $H/D\cong 0.06$. This maximum can be attributed to the reattachment of the shear layer spawned by the cavity opening onto the cavity base. With further increases in depth, the mass transfer dropped off, attained a minimum at $H/D\cong 0.2$, and then increased to a second maximum at $H/D\cong 0.5$. Thereafter, the mass transfer decreased monotonically, and for $H/D>0.6$–0.7, the decrease was more or less linear with H/D.

For all duct flows which were fully turbulent, it was found

that the Sherwood number could be correlated with a 0.76-power Reynolds number dependence. Sherwood number data for Schmidt numbers of 0.6 and 2.52 were correlated with $Sc^{0.53}$.

Investigation of the causes of the second maximum indicated that fluid-elastic and fluid-resonant oscillations could definitely be ruled out, suggesting that fluid-dynamic oscillations may have played a key role. Flow visualization studies performed with the oil-lampblack technique showed that the highest base-surface-adjacent velocities occurred at $H/D \cong 0.5$. The helium bubble technique was used to obtain an overview of the flow pattern in the cavity, and the frequency spectrum of the pressure at the cavity base was also measured.

References

1 Prata, A. T., and Sparrow, E. M., "Evaporation of Water From a Partially Filled Cylindrical Container to a Forced Convection Air Flow," *Int. J. Heat Mass Transfer*, Vol. 29, 1986, pp. 539–547.

2 Rockwell, D., and Naudascher, E., "Review – Self-Sustaining Oscillations of Flow Past Cavities," ASME *J. Fluids Engng.*, Vol. 100, 1978, pp. 152–165.

3 Merzkirch, W., *Flow Visualization*, Academic Press, New York, 1974.

4 Sogin, H. H., "Sublimation From Disks to Air Streams Flowing Normal to Their Surfaces," *Trans. Am. Soc. Mech. Engrs.*, Vol. 78, 1958, pp. 61–71.

5 Reynolds, W. C., and Perkins, H. C., *Engineering Thermodynamics*, 2nd edn., McGraw-Hill, New York, 1977.

6 Sherwood, T. K., and Pigford, R. L., *Absorption and Extraction*, 2nd edn., McGraw-Hill, New York, 1952.

7 Panton, R. L., and Miller, J. M., "Resonant Frequencies of Cylindrical Helmholtz Resonators," *J. Acoust. Soc. Am.*, Vol. 57, 1975, pp. 1533–1535.

8 Harrington, M. C., and Dunham, W. H., "Studies of the Mechanism for Flow-Induced Cavity Resonance," *J. Acoust. Soc. Am.*, Vol. 32, 1960, p. 921.

King-Leung Wong
Graduate Student.

Shun-Ching Lee
Graduate Student.

Chao-Kuang Chen
Professor.

Department of Mechanical Engineering,
National Cheng-Kung University,
Tainan, Taiwan,
Republic of China

Finite Element Solution of Laminar Combined Convection From a Sphere

The purpose of this investigation is to study the flow and heat transfer characteristics of laminar combined convection from an isothermal sphere. The full Navier–Stokes and energy equations are solved by a finite element method. The variations of surface shear stress, pressure, and Nusselt number are obtained over the entire surface of the sphere including the zone beyond the separation point. The predicted values of average Nusselt number, location of separation point, total drag shear force, and some plots of the flow and temperature fields are also presented. The results are compared with those of previous numerical and experimental investigations and the agreement is satisfactory.

Introduction

In recent times there has been much interest in heat transfer, mass transfer, and motion of small spheres in studies of combustion, condensation, absorption, and other processes where there are liquid drops or small particles. Many related engineering applications from the standpoint of either pure free convection or pure forced convection [1–10] have been presented. Neglecting the effect of buoyancy force on forced convective heat transfer may not be justified when the velocity is small and the temperature difference between the surface and the ambient fluid is large. Thus, predictions of the local heat transfer rate in combined convection are practical interest, as are the conditions under which the buoyancy-force effects first become significant.

The first theoretical study on combined convection from bodies in the existence of boundary-layer flows was carried out by Acrivos [11] who obtained the Nusselt number for stagnation flow for the limiting Prandtl number cases of $Pr \to 0$ or $Pr \to \infty$. The problem of combined convection from a sphere has received relatively little attention. The experimental works of Yuge [12] and Klyachko [13] and the analytical work of Hieber and Gebhart [14] were conducted under conditions of very small Reynolds and Grashof numbers. Dennis and Walker [15] obtained accurate solution for Reynolds numbers in the range of 0.1 to 40. Chen and Mucoglu [16] solved the problem by a finite difference method for large Reynolds and Grashof numbers. Tal et al. [17] used cylindrical cell models to investigate the problem of hydrodynamics and heat transfer in sphere assemblages. In boundary layer analyses the results are limited to the region from the forward stagnation point up to the point of separation. Accordingly, the average Nusselt number over the surface of the sphere could not be obtained.

In the present work, the problem of laminar combined convection from a hot isothermal sphere is solved by a finite element method. The method is based on the solution of the full Navier–Stokes and energy equations. The numerical results are obtained over the entire surface of the sphere including the zone beyond the separation point.

Problem Statement

Consider an isothermal sphere, of diameter $2R_0$ and temperature T_w, which is placed in a uniform free stream of temperature T_∞. The free stream is directed opposite to the direction of gravitational acceleration. Owing to the axisymmetry of the sphere, the flow and thermal fields are two dimensional. With the principle of axisymmetric ring element introduced by Chung [18], the cylindrical coordinate system similar to that of Tal et al. [17] has been used in the present work. R and X denote the radial and streamwise coordinates, respectively. The angle θ is measured from the rear stagnation point. The calculated flow domain, boundary conditions, and coordinates of the flow field are shown in Fig. 1.

The fluid is considered to be incompressible except for the calculation of the buoyancy force, which is computed using the Boussinesq type equation of state. All other fluid properties are assumed constant. The dimensionless governing equations can be written as follows:

Continuity equation

$$\frac{\partial u}{\partial x}+\frac{v}{r}+\frac{\partial v}{\partial r}=0 \tag{1}$$

Momentum equations

$$u\frac{\partial u}{\partial x}+v\frac{\partial u}{\partial r}=$$

$$-\frac{\partial p}{\partial x}+\frac{1}{\mathrm{Re}}\left(\frac{\partial^2 u}{\partial x^2}+\frac{1}{r}\frac{\partial u}{\partial r}+\frac{\partial^2 u}{\partial r^2}\right)+\frac{\mathrm{Gr}}{\mathrm{Re}^2}\phi \tag{2}$$

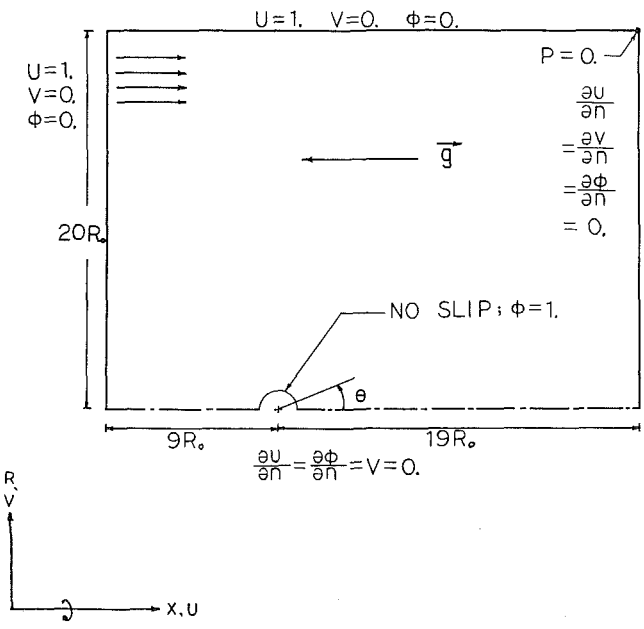

Fig. 1 The calculated flow domain, boundary conditions, and coordinates of the flow field

Contributed by the Heat Transfer Division for publication in the JOURNAL OF HEAT TRANSFER. Manuscript received by the Heat Transfer Division June 22, 1984.

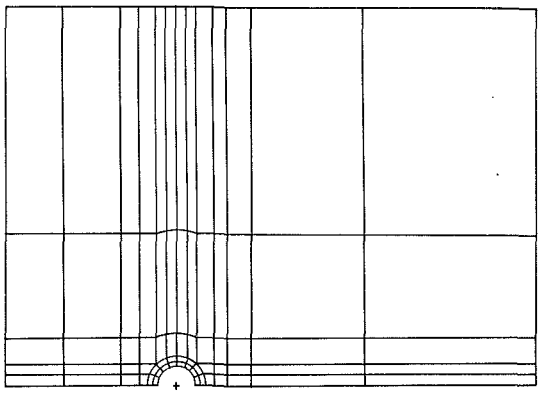

Fig. 2 Element discretization of the calculated flow domain

$$u\frac{\partial v}{\partial x}+v\frac{\partial v}{\partial r}=$$

$$-\frac{\partial p}{\partial r}+\frac{1}{\mathrm{Re}}\left(\frac{\partial^2 v}{\partial x^2}+\frac{1}{r}\frac{\partial v}{\partial r}-\frac{v}{r^2}+\frac{\partial^2 v}{\partial r^2}\right) \tag{3}$$

Energy equation

$$u\frac{\partial \phi}{\partial x}+v\frac{\partial \phi}{\partial r}=\frac{1}{\mathrm{Pe}}\left(\frac{\partial^2 \phi}{\partial x^2}+\frac{1}{r}\frac{\partial \phi}{\partial r}+\frac{\partial^2 \phi}{\partial r^2}\right) \tag{4}$$

where

$$u=\frac{u^*}{u_\infty},\quad v=\frac{v^*}{u_\infty},\quad p=\frac{P^*-P_\infty}{\rho u_\infty^2},\quad \mathrm{Re}=\frac{2u_\infty R_0}{\nu}$$

$$x=\frac{x^*}{2R_0},\quad r=\frac{r^*}{2R_0},\quad \mathrm{Pr}=\frac{\mu c}{k},\quad \mathrm{Pe}=\mathrm{PrRe}$$

$$\phi=\frac{T-T_\infty}{T_w-T_\infty},\quad \mathrm{Gr}=\frac{8g\beta(T_w-T_\infty)R_0^3}{\nu^2}$$

Finite Element Method

Owing to symmetry of the flow field, only one half of the total domain is discretized into 73 elements as shown in Fig. 2. All the elements are isoparametric quadrilateral containing eight nodes, one at each corner and one at the midpoint of each side. All eight nodes are associated with velocities as well as the temperature; only the corner nodes are associated with pressures. Following an accepted [19, 20] practice of depicting the variation in pressure by shape functions M_l, of one order lower than those defining the velocity and temperature N_i, they can be written as follows

$$u=\sum_{j=1}^{8}N_j u_j,\qquad V=\sum_{j=1}^{8}N_j v_j$$
$$\phi=\sum_{j=1}^{8}N_j \phi_j,\qquad p=\sum_{l=1}^{4}M_l P_l \tag{5}$$

By employing the Galerkin weighted residual approach equations (1)–(4) can be discretized as:

Continuity equation

$$\sum_{1}^{n^e}\int_{A^e}M_i\left(\frac{\partial N_j}{\partial r}u_j+\frac{N_j}{r}v_j+\frac{\partial N_j}{\partial r}v_j\right)2\pi r dA^e \tag{6}$$

where n^e = total element number (73 for the present work); $i = 1, \ldots, 4$; $j = 1, 2, \ldots, 8$; A^e = area of single element.

X-momentum equation

$$\sum_{1}^{n^e}\int_{A^e}\left(N_i N_k u_k\frac{\partial N_j}{\partial x}u_j+N_i N_k v_k\frac{\partial N_j}{\partial r}u_j\right.$$
$$\left.+N_i\frac{\partial M_l}{\partial r}p_l+\frac{1}{\mathrm{Re}}\left(\frac{\partial N_i}{\partial x}\frac{\partial N_j}{\partial x}u_j+\frac{\partial N_i}{\partial r}\frac{\partial N_j}{\partial r}u_j\right)\right.$$

Nomenclature

$\tilde{A}$ = global coefficient matrix
A^e = area of single element
$\tilde{A}^e$ = coefficient matrix of single element
a_{ij} = element of global coefficient matrix
$\tilde{B}$ = natural boundary condition vector
b_j = element of natural boundary condition vector
C = specific heat
C_{ij} = element of coefficient matrix of single element
C_f = friction drag coefficient
Gr = Grashof number = $8\ g\beta(T_w - T_\infty)\ R_0^3/\nu^2$
g = gravitational acceleration
h = local heat transfer coefficient
K = thermal conductivity
N_i = shape function
Nu, $\overline{\mathrm{Nu}}$ = local and average Nusselt numbers
P = dimensionless pressure = $P^*/\rho u_\infty^2$
P^* = pressure
Pe = Peclet number = RePr
Pr = Prandtl number = $\mu c/K$
R = radial axis of cylindrical coordinates
Ra = Rayleigh number = GrPr
Re = Reynolds number = $2R_0u_\infty/\nu$
R_0 = radius of sphere
r = dimensionless radial coordinate of cylindrical coordinates = $r^*/2R_0$
r^* = radial coordinate of cylindrical coordinates
T_∞ = temperature
T_w = temperature on sphere surface with fixed value
T = free-stream temperature
u = dimensionless transverse component of velocity = u^*/u_∞
u^* = transverse component of velocity
u_∞ = free-stream velocity
V = dimensionless radial component of velocity = V^*/u_∞
V^* = radial component of velocity
X = transverse axis of cylindrical coordinates
x = dimensionless transverse coordinate of cylindrical coordinates = $x^*/2R_0$
x^* = transverse coordinate of cylindrical coordinate
β = coefficient of volumetric thermal expansion
Γ = boundary of flow domain
Γ_1 = boundary with fixed value boundary condition
Γ_2 = boundary with natural boundary condition
θ = plane angle
θ_s = separation angle
$\tilde{\lambda}$ = primitive variable vector
μ = dynamic viscosity
ν = kinematic viscosity = μ/ρ
ρ = density of fluid
τ_w = dimensionless surface shear stress = $\tau_w^*/\rho u_\infty^2$
τ_w^* = surface shear stress
ϕ = dimensionless temperature = $(T - T_\infty)/(T_w - T_\infty)$
Ω = flow domain of total elements
Ω_e = flow domain of single element

$$-\frac{\mathrm{Gr}}{\mathrm{Re}^2} N_i N_j \phi_j \Big) 2\pi r dA^e - \int_{\Gamma_1} \frac{1}{\mathrm{Re}} N_i \frac{\partial N_j}{\partial n} u_j 2\pi r d\Gamma$$

$$- \int_{\Gamma_2} \frac{1}{\mathrm{Re}} N_i \Big(\frac{\partial u}{\partial n} \Big) 2\pi r d\Gamma = 0 \tag{7}$$

R-momentum equation

$$\sum_1^{n^e} \int_{A^e} \Big(N_i N_k u_k \frac{\partial N_j}{\partial x} v_j + N_i N_k v_k \frac{\partial N_j}{\partial r} v_j + N_i \frac{\partial M_l}{\partial r} p_l + \frac{1}{\mathrm{Re}} \Big(\frac{\partial N_i}{\partial x} \frac{\partial N_j}{\partial x} v_j - N_i \frac{N_j}{r^2} v_j + \frac{\partial N_i}{\partial r} \frac{\partial N_i}{\partial r} v_j \Big) \Big) 2\pi r dA^e - \int_{\Gamma_1} \frac{1}{\mathrm{Re}} N_i \frac{\partial N_j}{\partial n} v_j 2\pi r d\Gamma - \int_{\Gamma_2} \frac{1}{\mathrm{Re}} N_i \Big(\frac{\partial v}{\partial n} \Big) 2\pi r d\Gamma = 0 \tag{8}$$

Energy equation

$$\sum_1^{n^e} \int_{A^e} \Big(N_i N_k u_k \frac{\partial N_j}{\partial x} \phi_j + N_i N_k v_k \frac{\partial N_j}{\partial r} \phi_j + \frac{1}{\mathrm{Pe}} \Big(\frac{\partial N_i}{\partial x} \frac{\partial N_j}{\partial x} \phi_j + \frac{\partial N_i}{\partial r} \frac{\partial N_j}{\partial r} \phi_j \Big) \Big) 2\pi r dA^e \tag{9}$$

$$+ \int_{\Gamma_1} \frac{1}{\mathrm{Pe}} N_i \frac{\partial N_j}{\partial n} \phi_j 2\pi r d\Gamma - \int_{\Gamma_2} \frac{1}{\mathrm{Pe}} N_i \Big(\frac{\partial \phi}{\partial n} \Big) 2\pi r d\Gamma = 0$$

where $i, j, k = 1, 2, \ldots, 8$; $l = 1, \ldots, 4$. Equations (7), (8), and (9) can be combined into the form of assembled matrix equation

$$\tilde{A}\tilde{\lambda} = \tilde{B} \tag{10}$$

where the matrix of unknowns $\tilde{\lambda}$ is

$$\lambda_j = \begin{bmatrix} u_j \\ p_j \\ v_j \\ \phi_j \end{bmatrix} \tag{11}$$

Each coefficient in the matrix $\tilde{A}$ has the form

$$a_{ij} = \sum_1^{n^e} \int_{A^e} \begin{bmatrix} C_{11} & C_{12} & C_{13} & C_{14} \\ C_{21} & C_{22} & C_{23} & C_{24} \\ C_{31} & C_{32} & C_{33} & C_{34} \\ C_{41} & C_{42} & C_{43} & C_{44} \end{bmatrix} (2\pi r) dA^e$$

$$- \int_{\Gamma_1} \begin{bmatrix} \frac{1}{\mathrm{Re}} N_i \frac{\partial N_j}{\partial n} & 0 & 0 & 0 \\ 0 & 0 & 0 & 0 \\ 0 & 0 \frac{1}{\mathrm{Re}} N_i \frac{\partial N_j}{\partial n} & & 0 \\ 0 & 0 & 0 & \frac{1}{\mathrm{Pe}} N_i \frac{\partial N_j}{\partial n} \end{bmatrix} (2\pi r) d\Gamma \tag{12}$$

where

$$C_{11} = N_i N_k u_k \frac{\partial N_j}{\partial x} + N_i N_k v_k \frac{\partial N_j}{\partial r} + \frac{1}{\mathrm{Re}} \Big(\frac{\partial N_i}{\partial x} \frac{\partial N_i}{\partial x} + \frac{\partial N_j}{\partial r} \frac{\partial N_j}{\partial r} \Big)$$

$$C_{12} = N_i \frac{\partial M_l}{\partial x}, \qquad C_{13} = 0$$

$$C_{14} = \frac{-\mathrm{Gr}}{\mathrm{Re}^2} N_j, \qquad C_{21} = M_i \frac{\partial N_j}{\partial x}$$

$$C_{22} = 0, \qquad C_{23} = M_i \frac{N_j}{r} + M_i \frac{\partial N_j}{\partial r}$$

$$C_{24} = 0, \qquad C_{31} = 0,$$

$$C_{32} = N_i \frac{\partial M_l}{\partial r}, \qquad C_{33} = -\frac{N_i}{\mathrm{Re}} \frac{N_j}{r^2} + C_{11}$$

$$C_{34} = 0, \qquad C_{41} = 0$$

$$C_{42} = 0, \qquad C_{43} = 0$$

$$C_{44} = N_i N_k u_k \frac{\partial N_j}{\partial x} + N_i N_k u_k \frac{\partial N_j}{\partial r} + \frac{1}{\mathrm{Pe}} \Big(\frac{\partial N_i}{\partial x} \frac{\partial N_j}{\partial x} + \frac{\partial N_i}{\partial r} \frac{\partial N_j}{\partial r} \Big)$$

Each coefficient in the matrix B has the form

$$b_i = \int_{\Gamma_2} \begin{bmatrix} b_1 \\ b_2 \\ b_3 \\ b_4 \end{bmatrix} 2\pi r d\Gamma \tag{13}$$

where

$$b_1 = \frac{1}{\mathrm{Re}} N_i \frac{\partial u}{\partial n}, \qquad b_2 = 0$$

$$b_3 = \frac{1}{\mathrm{Re}} N_i \Big(\frac{\partial v}{\partial n} \Big), \qquad b_4 = \frac{1}{\mathrm{Pe}} N_i \Big(\frac{\partial \phi}{\partial n} \Big)$$

Numerical Solution

There is a standard procedure for evaluating the above integrals, which is described in a number of textbooks and papers in the field of finite element analysis (such as [21–23]). This involves (*i*) the normalization of the coordinates, and (*ii*) the use of the Gauss–Legendre quadrature scheme. In the present work, 3×3 and 3×1 Gaussian integration sampling point schemes are used for the surface and line integrals, respectively. The resultant nonlinear nonsymmetric matrix equations are solved by the frontal method [23–25] and a suitable iterative process.

Calculation of Physical Parameters

(*i*) Nusselt Number. From the definition of the convective heat transfer coefficient

$$-k \nabla^* T = h(T_w - T_\infty) \qquad \text{or} \qquad -k \frac{1}{2R_0} \nabla \phi = h$$

The local Nusselt number can be written as

$$\mathrm{Nu} = \frac{2hR_0}{k} = -\nabla \phi = \frac{\partial N_j}{\partial n} \phi_j \tag{14}$$

where $j = 1, 2, \ldots, 8$.
The average Nusselt number is defined as

$$\overline{\mathrm{Nu}} = \frac{1}{\pi} \int_0^\pi \mathrm{Nu}\, d\theta \tag{15}$$

(*ii*) Shear Stress. The shear stress for a Newtonian fluid is given by

$$\tau_w^* = \mu \frac{\partial u_t^*}{\partial u^*} = \frac{\mu u_\infty}{2R_0} \frac{\partial u_t}{\partial n}$$

Table 1 Results for $\overline{Nu}$, $\overline{Nu}Re^{-1/2}$, θ_s, C_f, and $C_fRe^{1/2}$ at Pr = 0.7

Re	Gr/Re^2	Gr	$\overline{Nu}$	$\overline{Nu}Re^{-1/2}$	θ_s(deg)	C_f	$C_fRe^{1/2}$
5	0	0	2.8084	1.26	0	5.4821	8.67
10	0	0	3.2824	1.03	0	3.2270	10.20
20	0	0	3.9714	0.89	0	1.9614	8.77
40	0	0	5.0260	0.79	31.26	1.2310	7.79
40	10	16000	6.7662	1.07	0	5.4563	34.51
60	0	0	5.8892	0.76	42.05	0.9498	7.35
60	0.2	720	6.0210	0.78	26.07	1.0934	8.47
60	4	14400	7.1832	0.93	0	2.6008	20.15
60	10	36000	8.0824	1.04	0	4.0997	31.75
80	0	0	6.6428	0.74	47.38	0.7932	7.09
80	10	64000	9.2450	1.03	0	3.3041	29.55
100	0	0	7.3512	0.74	49.77	0.6934	6.93
100	0.2	2000	7.5088	0.75	37.20	0.8640	8.64
100	2	20000	8.4718	0.85	0	1.4019	14.02
100	4	40000	9.1110	0.91	0	1.8437	18.44
100	8	80000	9.9592	0.96	0	2.4999	25.00

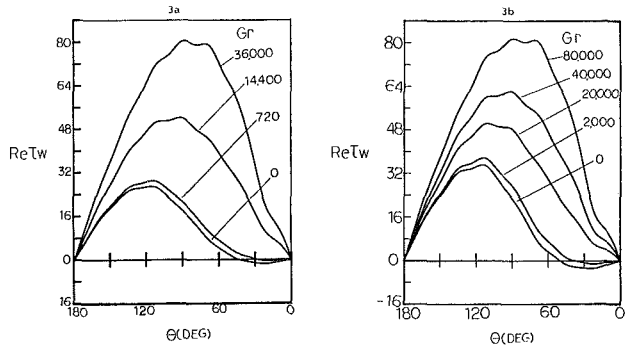

Fig. 3 Surface shear stress distributions at Pr = 0.7 for (*a*) Re = 60; (*b*) Re = 100

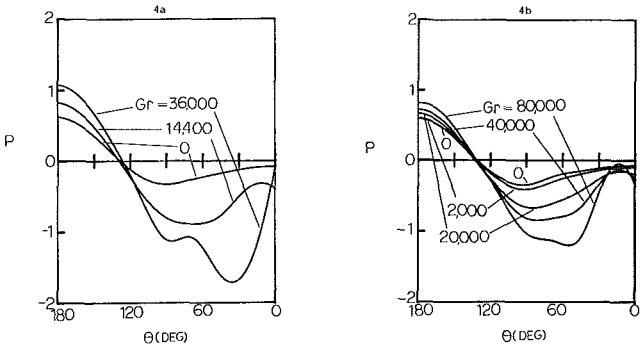

Fig. 4 Surface pressure distributions at Pr = 0.7 for (*a*) Re = 60; (*b*) Re = 100

where $\partial u_t/\partial n$ denotes the dimensionless gradient of tangential velocity in the direction normal to the sphere surface. Thus the dimensionless shear stress is

$$\tau_w = \frac{\tau_w^*}{\rho u_\infty^2} = \frac{\mu}{2\rho u_\infty R_0}\frac{\partial u_t}{\partial n} = \frac{1}{\mathrm{Re}}\frac{\partial u_t}{\partial n}$$

$$= \frac{1}{\mathrm{Re}}\frac{\partial N_j}{\partial n}(u_j \sin\theta - v_j \cos\theta) \qquad (16)$$

(*iii*) **Total Friction Drag Coefficient.** The definition is given as

$$C_f = 2\int_0^\pi \tau_w \sin\theta \, d\theta \qquad (17)$$

Results and Discussion

Computations have been made for Re = 5, 10, 20, 40, 60, 80, and 100, for Pr = 0.7, and for different values of Gr. The results of Nusselt number $\overline{Nu}$, $\overline{Nu}Re^{-1/2}$, the angle of separation θ_s, and total friction drag coefficient C_f, $C_fRe^{1/2}$ are given in Table 1.

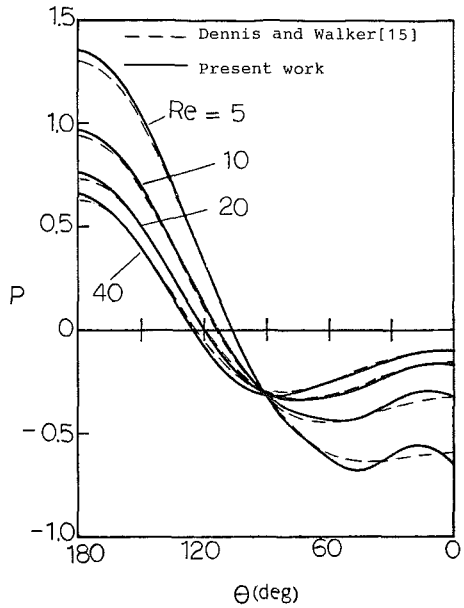

Fig. 5 Comparisons of surface pressure variation between the present results and those obtained by Dennis and Walker [15] for the forced convection case (Gr = 0)

From Table 1 it can be seen that when Re = 40 at Gr = 0, θ_s = 31.26 deg is close to that ($\theta_s \doteq 35$ deg) predicted by Dennis and Walker [15]. Donea et al. [26] presented similar results to those of [15] by a finite element method for pure forced convection situation.

It is also shown in Table 1 that the greater Re, the closer $\overline{Nu}Re^{-1/2}$ and $C_fRe^{1/2}$ are. This agrees with the results for high Re obtained by Chen and Mucoglu [16]. The angles of separation θ_s of the present work at Gr = 0 are not close to that obtained by Chen and Mucoglu [16] since Chen and Mucoglu's results are based on high Re. It is clear from Table 1 that the greater Gr/Re^2, the greater $\overline{Nu}Re^{-1/2}$ and $C_fRe^{1/2}$, but the smaller θ_s will be. There is no circulation in the wake for the Re $\leq$ 20 since θ_s = 0 deg. When $Gr/Re^2 \geq 2.0$, there exists no flow separation in the range of Re considered. For Gr = 0, the greater Re, the greater θ_s is. But for the same Re, the greater Gr, the smaller θ_s is.

Thus, increasing Gr tends to delay flow separation. Accordingly, the location of the point of separation depends on Re as well as on Gr.

The surface shear stress distributions at Re = 60 and 100 for different values of Gr are given in Figs. 3(*a*) and 3(*b*), respectively. It is clear from equation (16) that $Re\tau_w$ =

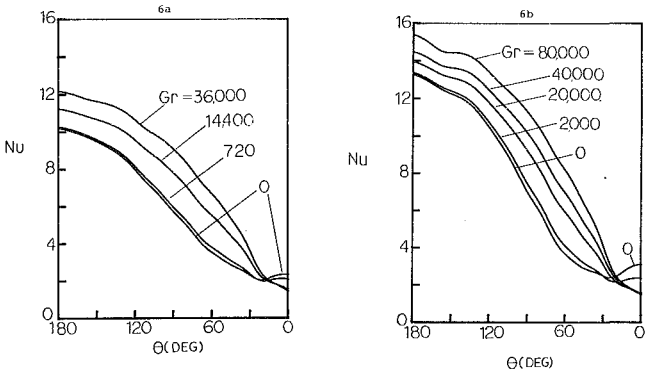

Fig. 6 Local Nusselt number variations at Pr = 0.7 for (*a*) Re = 60; (*b*) Re = 100

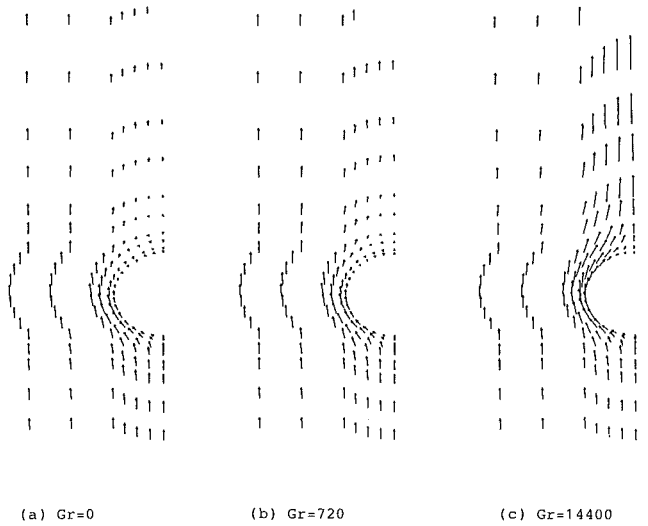

Fig. 7 Flow fields for Re = 60 when Pr = 0.7 and (*a*) Gr = 0; (*b*) Gr = 720; (*c*) Gr = 14400

$\partial u_t/\partial n$. When $\mathrm{Re}\tau_w = 0$, flow separation occurs. Thus, the angles of separation can be found at intersection points on the line $\mathrm{Re}\tau_w = 0$ in Figs. 3(*a*) and 3(*b*). It can also be seen in Figs. 3(*a*) and 3(*b*) that surface shear stress increases significantly with increasing Gr. Since the buoyancy force accelerates the flow near the surface of the sphere, it leads to a greater $\partial u_t/\partial n$ at the sphere surface.

The surface pressure distributions at Re = 60 and 100 for different values of Gr are given in Figs. 4(*a*) and 4(*b*), respectively. It can be seen in Figs. 4(*a*) and 4(*b*) that the increasing Gr leads to a significant increase in surface pressure near the front stagnation point (θ = 180 deg) and a significant decrease in surface pressure after a certain location (for example, $\theta <$ 130 deg for Re = 60 and $\theta <$ 138 deg for Re = 100) but not for the region near the rear stagnation point (θ = 0 deg). The variation of surface pressure near θ = 0 deg is complicated. Comparisons of surface pressure variation between the present results and those obtained by Dennis and Walker [15] for Re = 5, 10, 20, and 40 are given in Fig. 5. It is shown in Fig. 5 that the two numerical results are quite close.

The local Nusselt number distributions at Re = 60 and 100 for different values of Gr are given in Figs. 6(*a*) and 6(*b*). It can be seen from Figs. 6(*a*) and 6(*b*) that the increasing Gr results in a significant increase in Nu over most of the surface but a decrease near θ = 0 deg, the greater Gr, the smaller the relative decrease in Nu.

The flow field and isotherm patterns for the cases of Re = 60 and for Gr = 0, 720, and 14,400 can be seen in Figs. 7 and 8, respectively. It is found from Fig. 7, the flow field plots,

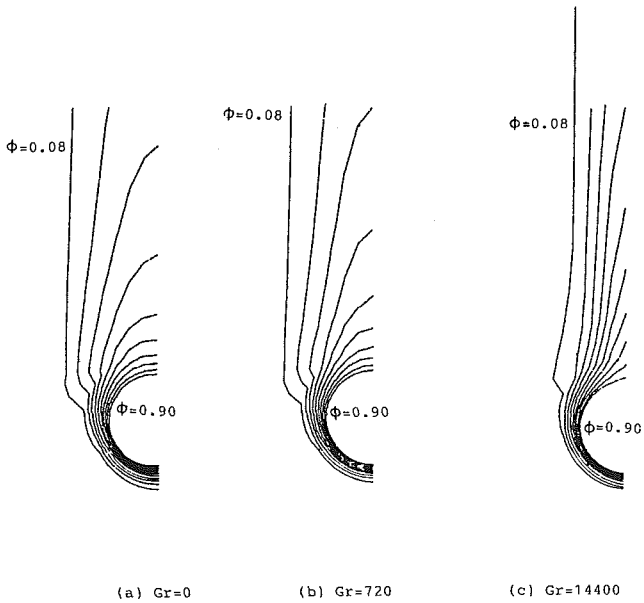

Fig. 8 Isotherms for Re = 60 when Pr = 0.7 and (*a*) Gr = 0; (*b*) Gr = 720; (*c*) Gr = 14400 (the shown isotherms are ϕ = 0.90, 0.81, 0.72, 0.63, 0.54, 0.45, 0.35, 0.26, 0.17, 0.08)

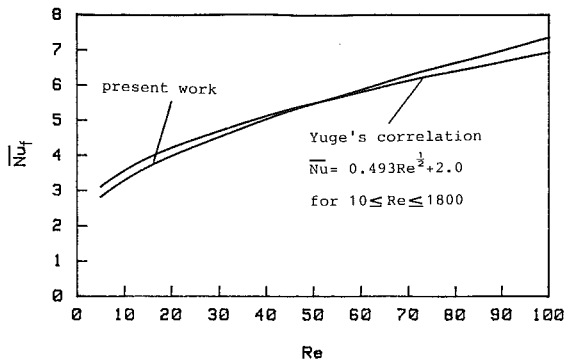

Fig. 9 A comparison of average Nusselt number between the present results and Yuge's correlations [12] for forced convection situation (Gr = 0)

Table 2 Comparison of average Nusselt number $\overline{\mathrm{Nu}}$ between the present work, and Yuge's correlation $\overline{\mathrm{Nu}}$ [12] for combined convection at Pr = 0.7

Re	Gr	$\overline{\mathrm{Nu}}$	$\overline{\mathrm{Nu}}_y$	$\overline{\mathrm{Nu}}/\overline{\mathrm{Nu}}_y$
60	720	6.0210	5.8858	1.023
100	2000	7.5088	7.3655	1.019

that increasing Gr results in decreasing the wake field until it completely disappears. It can be seen from Fig. 8 that the T = 0.90 line gets closer to the surface of sphere, which indicates higher temperature gradient and accordingly higher heat transfer rates.

A comparison of average Nusselt number between the present work and Yuge's correlation [12] for forced convection is given in Fig. 9. It is shown in Fig. 9 that the two results are close enough. The difference in $\overline{\mathrm{Nu}}$ between the two results is within 10 percent.

Comparisons of average Nusselt number between the present work and Yuge's experimental correlation [12] for combined convection are given in Table 2.

Yuge's experimental correlations of $\overline{\mathrm{Nu}}$ are as follows

$$\overline{\mathrm{Nu}} = 2 + (N_R + \Delta R), \quad \text{for } N_R > N_G \text{ and } 0 \le \mathrm{Gr} \le 1818$$

$$\overline{\mathrm{Nu}} = 2 + (N_G + \Delta G), \quad \text{for } N_R < N_G \text{ and } 0 \le \mathrm{Gr} \le 1818$$

where

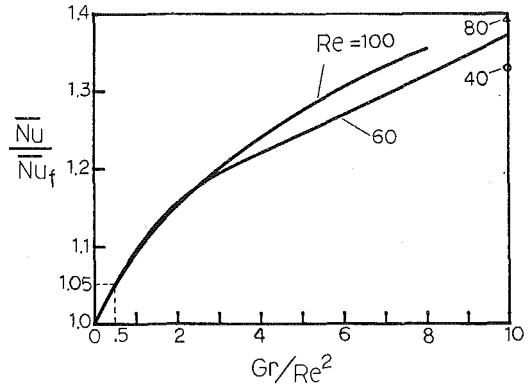

Fig. 10 The effect of Gr/Re^2 on the ratio between $\overline{Nu}$, the average Nusselt number of combined convection and $\overline{Nu}_f$, the average Nusselt number of forced convection

$$N_G = 0.392(\mathrm{Gr})^{0.25}, \qquad NR = 0.493(\mathrm{Re})^{0.5}$$

$$\Delta R = \Delta_0 \exp(-n(N_R - N_G)), \qquad \Delta G = \Delta_0 \exp(-m(N_G - N_R))$$

$$\Delta_0 = 0.0192 N_G{}^4, \quad n = 15/N_G{}^4, \quad m = 37/N_G{}^4$$

It can be seen from Table 2 that the difference in $\overline{Nu}$ between Yuge's correlations and the present results do not exceed 10 percent.

The effect of the parameter Gr/Re^2 on the ratio between $\overline{Nu}$, the average Nusselt number of combined convection, and $\overline{Nu}_f$, the average Nusselt number of forced convection, is shown in Fig. 10. If the threshold values of significant buoyancy effects are defined by 5 percent departures from pure forced convection, the buoyancy effects become significant at $Gr/Re^2 \geq 0.5$.

Accuracy and Convergence

The results seem to be useful even with the relatively coarse grid used in the present work. The fluctuations of data shown in Figs. 3 and 6 perhaps are due to the use of only eight element sides to form the surface of sphere. The position of the separation point was calculated by interpolating between two neighboring surface grid points with the reverse values of shear stress. The angular increment between two neighboring surface grid points in the present study was 11.25 deg. Obviously, the separation angle may not be very accurate with such a coarse grid.

The numerical work was done on a CDC Cyber 172 computer. The minimum CPU time was 467 s for the case of Re = 5 and Gr = 0. The maximum CPU time was 1575 s for the case of Re = 80 and Gr = 64,000.

Conclusions

The problem of laminar combined convective heat transfer from a hot sphere was studied by a finite element method and a cylindrical coordinate system. The full governing equations of motion and energy were solved in order to predict the details of the characteristics of flow and heat transfer. The results were obtained over the entire surface of the sphere including the zone beyond the point of separation. In comparisons with previous experimental and numerical results, satisfactory agreement was observed.

References

1 Chiang, T., Ossin, A., and Tien, C. L., "Laminar Free Convection From a Sphere," ASME JOURNAL OF HEAT TRANSFER, Vol. 86, 1964, pp. 537–542.

2 Lin, F. N., and Chao, B. T., "Laminar Free Convection Over Two-Dimensional and Axisymmetric Bodies of Arbitrary Contour," ASME JOURNAL OF HEAT TRANSFER, Vol. 96, 1974, pp. 435–442.

3 Cremers, C. J., and Finley, D. L., "Natural Convection About Isothermal Spheres," in: *Fourth International Heat Transfer Conference*, Paris–Versailles, Vol. 4, Elsevier, Amsterdam, 1970, Paper No. NC 1.5.

4 Kranse, A. A., and Schenk, J., "Thermal Free Convection From a Solid Spere," *Appl. Sci. Res.*, Vol. A15, 1966, pp. 397–403.

5 Chao, B. T., and Fagbenle, R. O., "On Merk's Method of Calculating Boundary Layer Transfer," *Int. J. Heat Mass Transfer*, Vol. 17, 1974, pp. 223–240.

6 Evans, H. L., *Laminar Boundary-Layer Theory*, Addison-Wesley, Reading, MA, 1968, Chap. 9.

7 Frossling, N., "Evaporation, Heat Transfer, and Velocity Distribution in Two-Dimensional and Rotationally Symmetrical Laminar Boundary-Layer Flow," National Advisory Committee for Aeronautics, TM 1432, 1958.

8 Vliet, G. C., and Lepper, G., "Forced Convection Heat Transfer From an Isothermal Sphere to Water," ASME JOURNAL OF HEAT TRANSFER, Vol. 83, 1961, pp. 163–175.

9 Cary, J. R., "The Determination of Local Forced-Convection Coefficients for Spheres," *Trans. ASME*, Vol. 75, 1953, pp. 483–487.

10 Baer, D. H. Schlinger, W. G., Berry, V. J., and Sage, B. H., "Temperature Distribution in the Wake of a Heated Sphere," ASME *J. Appl. Mech.*, Vol. 20, 1953, pp. 407–414.

11 Acrivos, A., "On the Combined Effect of Forced and Free Convection Heat Transfer in Laminar Boundary Layer Flows," *Chem. Engng. Sci.*, Vol. 21, 1966, pp. 343–352.

12 Yuge, T., "Experiment on Heat Transfer From Spheres Including Combined Natural and Forced Convection," ASME JOURNAL OF HEAT TRANSFER, Vol. 82, 1960, pp. 214–220.

13 Klyachko, L. S., "Heat Transfer Between a Gas and a Spherical Surface With the Combined Action of Free and Forced Convection," ASME JOURNAL OF HEAT TRANSFER, Vol. 85, 1963, pp. 355–357.

14 Hieber, C. A., and Gebhart, B., "Mixed Convection From a Sphere at Small Reynolds and Grashof Numbers," J. Fluid Mech., Vol. 38, 1969, pp. 137–159.

15 Dennis, S. C. R., and Walker, J. D. A., "Calculation of the Steady Flow Past a Sphere at Low and Moderate Reynolds Numbers," J. Fluid Mech., Vol. 48, Part 4, 1971, pp. 771–789.

16 Chen, T. S., and Mucoglu, A., "Analysis of Mixed Forced and Free Convection About a Sphere," *Int. J. Heat Mass Transfer*, Vol. 20, 1977, pp. 867–875.

17 Tal (Thau), R., Lee, D. N., and Sirignano, W. A., "Hydrodynamics and Heat Transfer in Sphere Assemblages – Cylindrical Cell Models," *Int. J. Heat Mass Transfer*, Vol. 26, No. 9, 1983, pp. 1265–1273.

18 Chung, T. J., *Axisymmetric Ring Element, Finite Element Analysis in Fluid Dynamics*, McGraw-Hill, New York, 1978, Section 2–5, pp. 92–93.

19 Hood, P., and Taylor C., "Navier–Stokes Equations Using Mixed Interpolation," *Proc. Ist Int. Conf. on F. E. M. in Flow Problems*, Swansea, 1974.

20 Olson, M. D., "Comparisons of Various Finite Element Solution Methods for the Navier–Stokes Equations," *Proc. Int. Conf. on Finite Elements in Water Resources*, Princeton University Press, 1976.

21 Becker, E. B., Carey, G. F., and Oden, J. T., *Finite Elements: An Introduction*, Prentice Hall, New York, 1981.

22 Baker, A. J., *Finite Element Computational Fluid Mechanics*, McGraw-Hill, New York, 1983.

23 Taylor, C., and Hood, P., "A Numerical Solution of the Navier–Stokes Equations Using the Finite Element Technique," *Int. J. Comp. Fluid*, Vol. 1, 1973.

24 Irons, B. M., "A Frontal Solution Program for Finite Element Analysis," *Int. J. Num. Meth. Engng.*, Vol. 2, 1970, pp. 5–32.

25 Hood, P., "Frontal Solution Program for Unsymmetric Matrices," *Int. J. Num. Meth. Engng.*, Vol. 10, 1976, pp. 379–399.

26 Donea, J., Giuliani, S., and Lavl, H., "Finite Element Solution of the Unsteady Navier–Stokes Equations by a Fractional Step Method," *Computer Methods in Applied Mech. Engng.*, Vol. 30, 1982, pp. 53–73.

Rafiqul M. Islam
Department of Petroleum Engineering.

K. Nandakumar
Department of Chemical Engineering.

University of Alberta,
Edmonton, Alberta, Canada

Multiple Solutions for Buoyancy-Induced Flow in Saturated Porous Media for Large Peclet Numbers

The problem of buoyancy-induced secondary flow in fluid-saturated porous media is examined using a numerical model. The natural convection is coupled either with a forced axial flow or uniform internal heat generation. In both cases the model equations are shown to exhibit dual solutions over certain ranges of flow parameter. In the two-parameter space of aspect ratio and Grashof number, the flow transition between the two-vortex and four-vortex pattern can be explained in terms of a tilted cusp.

1 Introduction

The problem of buoyancy-induced flow in fluid-saturated porous media has been studied extensively in recent years. This is because the nonisothermal flow in porous media is of interest in a number of different areas such as: (*i*) geothermal engineering, (*ii*) thermal enhanced oil recovery methods, and (*iii*) heat loss through building insulations. The problems relating to the flow in porous media for geothermal systems have been reviewed by Combarnous and Bories [1] and Cheng [2]. The problems relating to the thermal recovery methods are complicated by the simultaneous flow of more than a single phase. In both these cases the effect of forced convection on the buoyancy-induced flow could be significant. However, this problem of combined free and forced convection in confined porous media has received little attention and hence it will be the focus of study in this work. The problem of heat loss through insulation is governed mostly by pure natural convection effects in confined porous media. This problem is perhaps the most widely studied one. Some of the main characteristics of this problem are summarized next as they will be referred to later. Based on the boundary condition, this problem can be further grouped as media heated from below and those heated from the sides. Of course, the case of steady uniform heating around the boundary is trivial for natural convection, but it is nontrivial for the mixed convection problem. For the natural convection problem there are significant differences in the flow characteristics between the bottom heated and side heated cases. The stability and flow characteristics of the bottom heated case have been examined by Lapwood [3], Wooding [4], Elder [5], and a number of others. This problem is akin to the Rayleigh–Benard problem in classical fluid mechanics and is known to exhibit hysteresis and multicellular flow patterns. On the other hand, the natural convection currents set up by side heating are mostly unicellular in nature. Walker and Homsey [6] have concluded that there are no steady *two-dimensional* flows which bifurcate from the unicellular flow. Some of the recent studies on this problem have been by Shiralkar et al. [7], Bejan [8–10], and Prasad and Kulacki [11, 12]. This list is by no means exhaustive and references to earlier work can be found in the above. Prasad and Kulacki [12] report a form of multicellular flow even for the case of pure natural convection with side heating at very large aspect ratios. However it is quite distinct from the cellular flow observed for the bottom heated case. The flow transition that we wish to investigate for the mixed convection problem has more in common with the flow transitions observed for the bottom heated case.

Another aspect of flow in porous media that we wish to investigate is the existence of multiple solutions under certain flow conditions. In this context Gebhart et al. [13] have reported multiple steady-state solutions for buoyancy-induced transport in porous media saturated with fluids exhibiting density extrema. The multiplicity here is believed to be due to the nonlinearity in the density versus temperature relationship resulting in the buoyancy force reversal. We confine our study to a fluid exhibiting a linear variation in density with temperature, i.e., we invoke the Boussinesq approximation. The flow transition and multiplicity in such a case are governed by the exchange of stability [14, 16]. Similar phenomena are well known in the flow of a Newtonian fluid in ducts [17–19]. A classic example is the flow between two rotating cylinders, often called the Taylor–Couette flow. This problem can exhibit a complex pattern of multiplicities and flow transition. Benjamin and co-workers [15, 16] have investigated this problem in a systematic manner. Flow transition and bifurcation in pressure-driven flow in curved ducts have been examined by Nandakumar and Masliyah [17] and Dennis and Ng [18]. More recently Nandakumar et al. [19] have observed a similar phenomenon in the mixed convection flow of a Newtonian fluid in horizontal ducts. The major difference between these earlier studies and the current one is the replacement of the Navier–Stokes equation with the Darcy equation (or the Brinkman extension of it) to model the flow in porous media. An important consequence of this is the omission of the convective acceleration term, thus losing the quadratic nonlinearity in the equation of motion. Multiple solutions are possible in spite of the loss of this nonlinearity.

2 Problem Definition

Mixed Convection. Let us consider a horizontal porous layer (shown in Fig. 1) of width $2b$, height $2a$, and permeability K. The porous medium is saturated with a single phase fluid

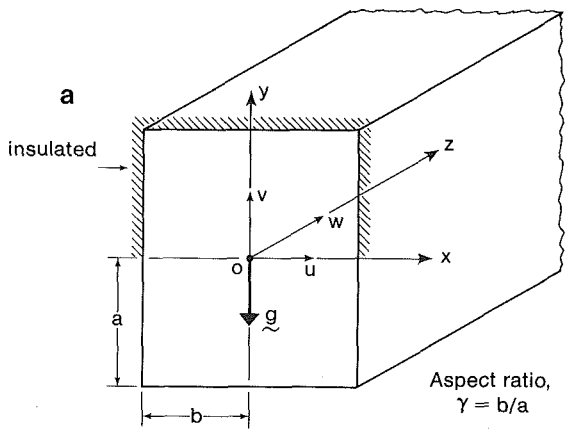

Fig. 1 Geometry and coordinate system

Contributed by the Heat Transfer Division for publication in the JOURNAL OF HEAT TRANSFER. Manuscript received by the Heat Transfer Division July 13, 1984.

of density ρ and viscosity μ. There is an axial flow maintained by a constant imposed pressure gradient (dp'/dz'). In addition, a constant rate of heat transfer per unit length Q' is maintained in the axial direction. The porous medium is isotropic and the flow is steady, fully developed, and two dimensional. In addition conduction in the axial direction is neglected. Omission of the axial conduction term in relation to the axial convection is justified if the Peclet number is large. The Boussinesq approximation is invoked to allow for a linear variation of density with temperature in the body force term, but all properties appearing elsewhere in the equations are assumed constant. Additional details can be found in [20]

$$\rho = \rho_r[1-\beta(T-T_r)] \tag{1}$$

where T_r is some reference temperature. Subject to the above conditions, the conservation equations for mass, momentum, and energy are as follows [2]

$$\nabla' \cdot \mathbf{v}' = 0 \tag{2}$$

$$\mathbf{v}' = -\frac{K}{\mu}[\nabla' p' + \rho\, \mathbf{g}] + K\, \nabla'^2 \mathbf{v}' \tag{3}$$

$$(\mathbf{v}' \cdot \nabla' T') = \alpha\, \nabla'^2 T' \tag{4}$$

Note that the Brinkman extension of the Darcy law is used for the momentum equation. The stream function and the axial vorticity are defined as follows

$$u' = \frac{\partial \psi'}{\partial y'} \qquad v' = -\frac{\partial \psi'}{\partial x'} \tag{5}$$

$$\Omega' = \frac{\partial v'}{\partial x'} - \frac{\partial u'}{\partial y'} \tag{6}$$

The equations were rendered dimensionless using the following scales

$u = u'/(\nu/a)$ $\quad v = v'/(\nu/a)$ $\quad w = w'/\left(-\frac{dp'}{dz'}\right)\left(\frac{K}{\mu}\right)$

$x = x'/a$ $\quad y = y'/a$ $\quad \psi = \psi'/\nu$

$\theta = \frac{T-T_w}{(Q'/k)}$ for Case 1, uniform wall temperature around the periphery

$= \frac{T-T_b}{(Q'/k)}$ for Case 2, top half insulated and bottom half heated at constant flux

Note that the scale for the secondary velocities is (ν/a) and that for the axial velocity is $w_0 = (-dp'/dx')(K/\mu)$ where K is the permeability of the medium. Before presenting the final nondimensional form of the equations, an order analysis of the energy equation (4) would be helpful. Since there is no natural scale (z_0) in the z (axial) direction it will be chosen to make the axial convection term of order one. The energy equation with the above scales becomes

$$\mathrm{Pr}\left(u\frac{\partial\theta}{\partial x} + v\frac{\partial\theta}{\partial y}\right) + \mathrm{Pr}\left[\frac{a^2\rho\, w_0}{\mu\, z_0}\right]\left(w\frac{\partial\theta}{\partial z}\right) = \nabla^2\theta + \frac{a^2}{z_0^2}\left(\frac{\partial^2\theta}{\partial z^2}\right) \tag{7}$$

The terms in square brackets will be of order 1 if $(z_0/a) \sim (\rho \cdot w_0\, a/\mu)$, a Reynolds number based on the axial filter velocity and duct geometry. Then the energy equation becomes

$$\left(u\frac{\partial\theta}{\partial x} + v\frac{\partial\theta}{\partial y} + w\frac{\partial\theta}{\partial z}\right) = \frac{1}{\mathrm{Pr}}\nabla^2\theta + \frac{1}{\mathrm{Pe}\cdot\mathrm{Re}}\cdot\frac{\partial^2\theta}{\partial z^2} \tag{8}$$

Thus the axial conduction term can be neglected if (Pe•Re) is large. Observe that the Peclet number can be increased by increasing either the Reynolds number or the Prandtl number. In pure natural convection problems (i.e., no axial flow) it has been pointed out[1] that the Peclet number and Prandtl number are the same. The effect of Prandtl number and in particular that of the porous medium thermal conductivity on the flow and heat transfer characteristics has been the subject of discussion in the recent works by Somerton [26] and Prasad et al. [27]. In the present work we consider the limit of large Pe and hence neglect axial conduction. In addition, a thermally developed state is also imposed in the axial direction. This implies that $\partial\theta/\partial z = [\mathrm{Pr\ A}\ \langle w\rangle]^{-1} = \text{const}$. With these restrictions on the energy equation, the nondimensional forms of the equations of motion are presented below.

Using the defining equations of stream function and vorticity (equations (5) and (6)), we get

$$\nabla^2\psi = -\Omega \tag{9}$$

The axial component of equation (3) gives the axial velocity equation as

$$\xi\, \nabla^2 w - w = -1 \tag{10}$$

where $\xi = K/a^2$.

Taking the curl of equation (3) the pressure term can be eliminated. The axial component of the resulting equation yields the axial vorticity transport equation

[1] The authors are grateful to the technical editor for bringing this to our attention.

Nomenclature

a = one half the height of rectangle
A = cross-sectional area
b = one half of the width of the channel
C_p = specific heat
De = equivalent diameter = (4 * total flow area/perimeter of duct)
g = acceleration due to gravity
Gr = Grashof number = $(Q'\, g\, \beta \cdot K\, a/k\, \nu^2)$
h = heat transfer coefficient
k = thermal conductivity of the medium
K = permeability
n = normal to a bounding wall
Nu = Nusselt number = $(h\, De/k)$
Pe = Peclet number = Re•Pr
Pr = Prandtl number of the medium = $(C_p\, \mu/k)$
p = pressure
Q' = heat transfer rate per unit length of duct
Q_G = heat generation rate per unit volume
Re = Reynolds number = $a\, p\, w_0/\mu$
T = temperature
$\mathbf{v}$ = velocity vector = (u, v, w)
w_0 = axial velocity scale = $(-dp'/dz')(K/\mu)$
x, y, z = coordinate directions
α = thermal diffusivity
β = coefficient of thermal expansion
γ = aspect ratio = (b/a)
∇^2 = two-dimensional Laplace operator
θ = dimensionless temperature
μ = viscosity
ν = kinematic viscosity
ξ = dimensionless permeability = (K/a^2)
ρ = density
ψ = stream function, equation (5)
Ω = vorticity, equation (6)

Subscripts and Symbols

b = bulk quantity
l = lower critical point
r = reference quantity
u = upper critical point
w = a quantity at the wall
$\langle\ \rangle$ = average quantity
$'$ = dimensional quantity

$$\xi\ \nabla^2\Omega-\Omega=-\mathrm{Gr}\ \frac{\partial\theta}{\partial x} \tag{11}$$

Finally, the energy equation (4), subject to the condition of axially uniform heat flux [i.e., $\partial T/\partial z' = dT_b'/dz' = Q'/(\rho\, C_p \cdot \langle w'\rangle\, A')$] becomes

$$\nabla^2\theta-\mathrm{Pr}\left(u\ \frac{\partial\theta}{\partial x}+v\ \frac{\partial\theta}{\partial y}\right)=\frac{w}{\langle w\rangle\, A} \tag{12}$$

Note that equations (9)–(11) include the second-order term of Brinkman and thus permit the imposition of the no-slip condition at the boundary. For small values of permeability (i.e., $\xi \to 0$) these equations reduce to the Darcy form (with $w = 1$ and $\Omega = \mathrm{Gr}\ \partial\theta/\partial x$) given below

$$\nabla^2\psi=-\mathrm{Gr}\ \frac{\partial\theta}{\partial x} \tag{13}$$

For Darcy's model then, one has to solve only two equations, i.e., equations (12) and (13). However, the no-slip condition cannot be satisfied. For the Brinkman model four equations (i.e., equations (9)–(12)) must be solved. The second-order terms in equations (10) and (11) become dominant only for large values of ξ, but a large value of ξ implies large permeability. Under these conditions, inertial effects may become important. This factor has been neglected in both models. In order not to violate the restriction of small inertial effects, our analysis must be restricted to small values of ξ. In this limit, as the Brinkman model approaches the Darcy model, the latter is used for the most part in this study. However, a few solutions are obtained with the full Brinkman model, in order to confirm that the solutions are not qualitatively different at low values of ξ, i.e., of the order of 10^{-3}.

An elegant discussion of other restrictions on the model equations can be found in Walker and Homsy [6]. One point that needs to be reiterated is about the physical limitations in applying Darcy's model (or inertialess flow) at high Grashof number. Since Grashof number is defined by $Q'g\,\beta\, Ka/k\,\nu^2$, high Gr implies either high permeability or a large heat transfer rate. In the former case inertia may be important while in the latter case temperature-dependent properties (particularly viscosity) may be important. Hence we shall treat the equations (9)–(12) or (12) and (13) as a model system and examine the bifurcation phenomena exhibited by this model. These models are valid approximations to the actual physical system within the limits set above.

An impermeable boundary is assumed for the Darcy model while impermeability as well as no slip at the wall are assumed for the Brinkman model. The boundary conditions are:

Darcy equation

$$\psi=0 \text{ around the boundary} \tag{14}$$

Brinkman equation

$$\psi=0 \text{ around the boundary} \tag{15a}$$

$$\Omega=-\frac{\partial^2\psi}{\partial n^2} \text{ normal to the wall} \tag{15b}$$

$$w=0 \text{ around the boundary} \tag{15c}$$

For the energy equation, two different boundary conditions are considered.

Case 1: $\theta=0$ (uniform temperature around the periphery) (16)

Case 2: $\dfrac{\partial\theta}{\partial n}=0$ (top half insulated) (17a)

$$\frac{\partial\theta}{\partial n}=\pm\frac{1}{2(1+\gamma)} \text{ (bottom half heated at constant flux)} \tag{17b}$$

Since Case 2 is given in terms of the derivative boundary conditions around the periphery, the dimensionless bulk temperature must satisfy the following equation as shown in [20, 21] in order to obtain a unique temperature profile

$$\int_{-1}^{1}\int_{0}^{1}\theta\ w\ dx\ dy=0 \tag{18}$$

Since a numerical solution procedure is used, it is beneficial to take advantage of the symmetry about $x = 0$. Thus the equations are solved in the domain $0 \le x \le 1$, $-1 \le y \le +1$, with the symmetry conditions imposed at $x = 0$. This will clearly restrict the solution set to only those with an even number of cells. There is evidence from studies on Taylor flows [16] for the existence of solutions with odd number of cells in the flow domain. Although we recognize a similar possibility with the current problem, we focus attention only on the flow transition between the two- and four-cell patterns.

The Nusselt number is calculated from the following expressions

$$\langle \mathrm{Nu}\rangle=\frac{\gamma}{(1+\gamma)^2}\ \frac{1}{\langle\theta_b\rangle} \quad \text{for Case 1} \tag{19a}$$

$$=\frac{2\gamma}{(1+\gamma)^2}\ \frac{1}{\langle\theta_w\rangle} \quad \text{for Case 2} \tag{19b}$$

Natural Convection With Heat Generation. Although the Darcy's model equations (12) and (13) simulate the mixed convection flow in porous media, they represent a valid model for another physical system: pure natural convection (i.e., $w = 0$) with heat generation. In this case the energy equation becomes

$$\rho\, C_p\left(u'\ \frac{\partial T'}{\partial x'}+v'\ \frac{\partial T'}{\partial y'}\right)=k\ \nabla'^2T'+Q_G \tag{20}$$

where Q_G is the rate of heat generation per unit volume. If the temperature around the boundary is maintained at T_w, and the dimensionless temperature is defined as $\theta = (T'-T_w')/(Q_G\, A'/k)$, then equation (20) becomes

$$\mathrm{Pr}\left(u\ \frac{\partial\theta}{\partial x}+v\ \frac{\partial\theta}{\partial y}\right)=\nabla^2\theta+\frac{1}{A} \tag{21}$$

which is identical to equation (12), except for the sign of the forcing function which is determined by the direction of heat transfer. Thus the results for the uniform temperature boundary should be applicable for both the physical situations. This analogy holds only for a Darcian model as the uniform heat generation in equation (20) is equivalent to uniform axial convection (with $w = 1$). For the Brinkman flow, the convection across the cross-sectional area is not uniform. The stability and flow behavior of natural convection with internal heat sources in a porous medium bound between infinite horizontal plates has been examined in [23]. More recently, Schulenberg and Müller [25] have studied natural convection with heat generation with some potential application in the risk assessment of nuclear power plants.

3 Method and Accuracy of Solution

The governing partial differential equations were discretized using three-point central difference approximation for all internal grid points, while forward and backward differences were used for the boundaries. The resulting algebraic equations were solved using the successive relaxation method. For the Darcy momentum equation, the discretized equations were solved first for the temperature (energy equation (12)), then these temperature values were used in the momentum equation (13) to obtain the stream function ψ. The iteration was continued until convergence. For the Brinkman model the sequence of iteration was θ–Ω–ψ. Since w is not coupled with any other equation it was solved out of sequence for a given value of ξ. The Brinkman model was used for several values of ξ. In order to gain an appreciation for the grid size requirement, we tried to compare our results with some established values in

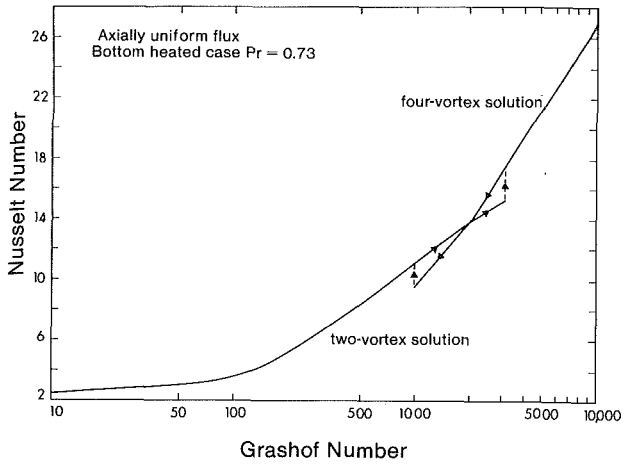

Fig. 2 Nusselt number for Case 2 in a square duct

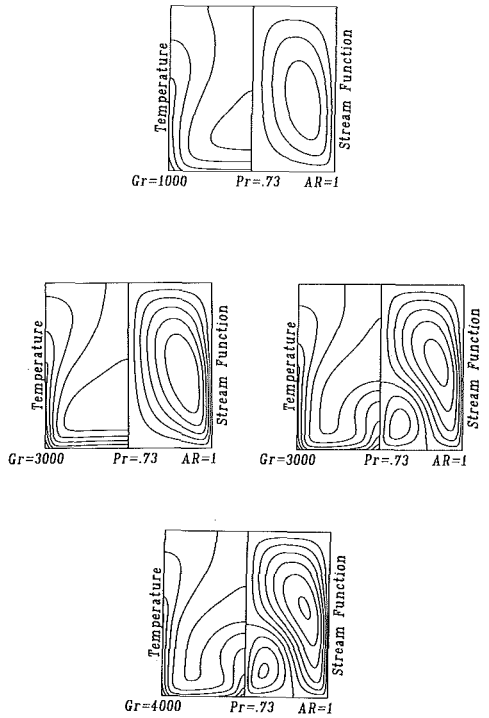

Fig. 3 Contours of stream function and temperature for Case 2

the literature. Since the mixed convection problem has not been studied before, we simulated the natural convection with side heating. This is readily accomplished by setting the forcing function in equation (12) to zero. The results are given in Table 1 for several aspect ratios and Rayleigh numbers. The results of Shiralker et al. [7] have been scaled to make them consistent with our definition of Nusselt number. The agreement with the literature values could be brought to within 5 percent only by using a 41 × 41 grid. For mixed convection, the grid sensitivity was checked by increasing the grid resolution from 21 × 21 to 41 × 41 for aspect ratio 1 and various values of Grashof numbers. For a Grashof number of 500 a 21 × 21 grid resolution gave a Nusselt number value of 8.46 whereas a 41 × 41 grid resolution gave a Nusselt number value of 8.44. For a Grashof number of 4000, where a four-cell flow pattern exists, 21 × 21 grid resolution gave a Nu number of 19.08 whereas 41 × 41 grid resolution gave 19.11. For the bottom heated case, a measure of the closure error can be obtained by examining the residual in equation (16). The computed dimensionless bulk temperature was always less than 10^{-6} for all the converged solutions. For a Grashof number of

Table 1 Grid size sensitivity for buoyancy-induced flow in porous media (natural convection with side heating)

γ	Gr	Grid size	Nu	Nu [7]
1	100	21 × 21	3.462	3.097
		31 × 31	3.337	
		41 × 41	3.258	
0.3	500	21 × 21	5.254	4.7783
		31 × 31	5.094	
		41 × 41	4.998	
0.2	100	21 × 21	1.860	1.878
		31 × 31	1.865	

1000 a change of grid size from 21 × 21 to 41 × 41 resulted in the bulk temperature change from 0.117×10^{-6} to 0.842×10^{-7}. For a grid size of 41 × 41, an increase in Grashof number from 1000 to 3000 resulted in a bulk temperature change from 0.842×10^{-7} to 0.130×10^{-6}.

The Nusselt number versus Grashof number results presented in this work were all obtained with a 41 × 41 grid. For a given aspect ratio, the critical Grashof numbers at which the flow transition from a two- to a four-vortex one occurs and vice versa were obtained using the bisection method as outlined below. Starting with a converged two-vortex solution at a low Grashof number (say 1000) as the initial guess, successive solutions are obtained at higher Gr by increasing its value in steps of, say, 1000. When a flow pattern change is observed in a step, say between 2000 and 3000, the sequence is repeated starting with the solution at the lower value (i.e., 2000) and the step size for Gr is decreased by half (i.e., 500). This procedure could be repeated until the Grashof number range over which the two to four transition occurs is narrowed to within about 5 percent. This gives the upper critical point. The lower critical point, where the transition from four to two vortex pattern occurs, is obtained in a similar way. Since this is a computationally expensive procedure and since our numerical experiments for the mixed convection case did not indicate significant grid sensitivity, the critical points were determined using a 21 × 21 grid.

4 Discussion of Results

For the bottom heated case, the Brinkman model was solved for a few select cases of Gr and compared with the Darcy model. The quantitative agreement between the two models was within 13 percent for the dimensionless permeability of $\xi = 0.001$. This difference went down to 4 percent for $\xi = 0.0001$. The secondary flow patterns for both models were quite similar with two counterrotating vortices appearing at low values of Grashof number. These cells are in a plane perpendicular to the axial flow. Thus the flow field is helicoid in nature. As the Grashof number is increased gradually the strength of the secondary flow increases, thus increasing the effectiveness of convective heat transfer. This is reflected in the increased Nusselt number seen in Fig. 2. On further increase in Grashof number, there is a gradual restructuring of the two-vortex solution close to the lower part of the duct. Soon a point is reached (labeled the upper critical Grashof number) beyond which the twin-counterrotating vortices become unstable and give rise to a stable four-vortex solution in a rather abrupt manner. This pattern is sustained with further increases in Gr. Now, starting with a four-vortex pattern, if the Grashof number is decreased, this pattern is sustained until a lower critical point is reached, below which the flow changes abruptly into a two-vortex pattern. As is evident from Fig. 2, there is a region of Grashof number between 1000 and 3250 where both the solutions are possible, exhibiting a hysteresis behavior. The contours of stream function and temperature are shown in Fig. 3. Note that due to symmetry about the $x = 0$ axis, the contours are shown in only one half of the duct. The stream function contours are shown on the

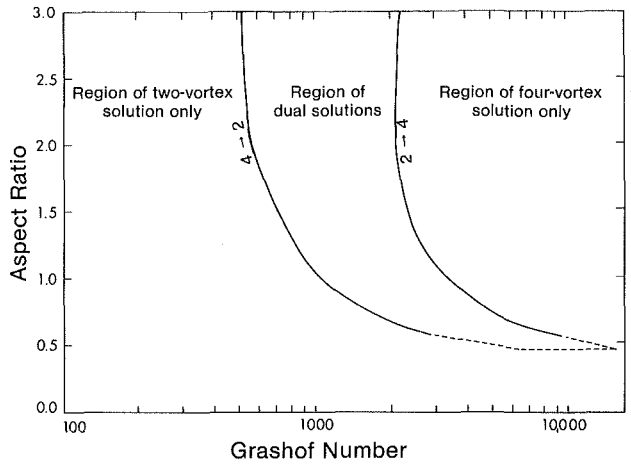

Fig. 4 Region of dual solutions in the space of aspect ratio and Grashof number for Case 2

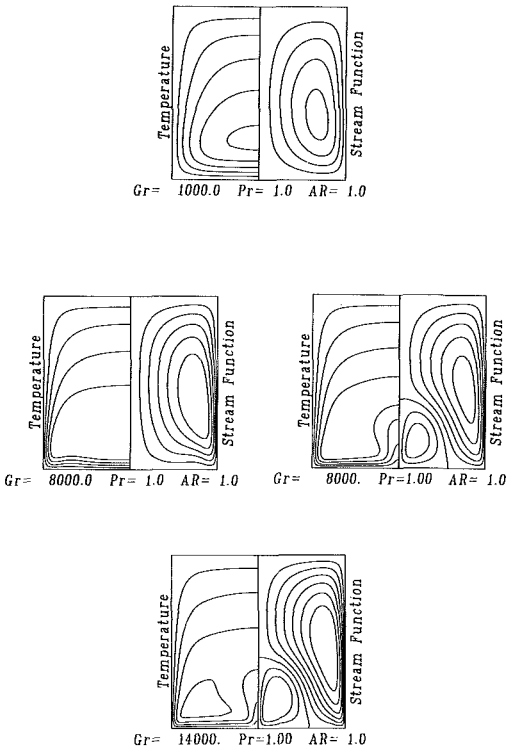

Fig. 5 Contours of stream function and temperature for Case 1

right half of the duct while the temperature profile is shown on the left side. Thus Figs. 3(*a*, *b*) correspond to the two-cell pattern and Figs. 3(*c*, *d*) correspond to the four-cell pattern. Both the two- and four-vortex pattern as well as the increase in the strength of the secondary flow are evident from this figure. A thermal boundary layer structure near the lower boundary is evident for the two-vortex solution. Such is not the case, however, for the four-vortex solution. Thus a boundary layer analysis of this problem will not allow the four-vortex pattern to unfold.

While the Brinkman model also exhibits these flow characteristics, the critical Grashof numbers, where the flow transition occurs, depend on the parameter ξ. The critical numbers were determined accurately using only the Darcian model (i.e., $\xi \to 0$ in the Brinkman model). The helicoid flow pattern observed here is in conformity with the observation by Combarnous and Bia [24]. They also observe an alternative

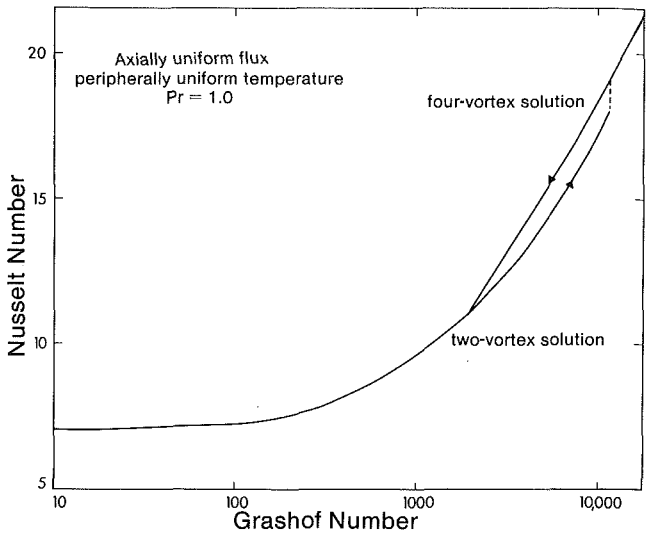

Fig. 6 Nusselt number for Case 1 in a square duct

flow pattern of moving roll cells for Peclet numbers less than 0.75. In our model equations, we have implicitly assumed a large Peclet number by neglecting axial conduction. Hence the alternative pattern observed by Combarnous and Bia [24] could not be found in this work.

The bifurcation between the two- and four-cell patterns was investigated further by changing the aspect ratio of the duct over a range of 0.6 to 3.0. Over 300 simulation runs were performed to determine the variation of the upper and lower critical Grashof numbers with aspect ratio. They are shown in Fig. 4. As the aspect ratio is decreased below one, both the upper and lower critical Gr increase very rapidly. For an aspect ratio of 0.5 the numerical method failed to converge before the critical points could be reached. On the other hand, as the aspect ratio is increased, the critical values decrease. For aspect ratios greater than 3 we once again experienced convergence difficulties. At larger aspect ratios we should expect the evolution of multicellular flow structure. But the current numerical method is not well suited for computing such flows. However, the method provides accurate results over the range of parameters (γ, Gr) where it converges. The results shown in Fig. 4 are estimated to be within 5 percent tolerance. Since there are two possible modes of behavior (the two-cell and the four-cell pattern) and two controlling parameters (γ, Gr), the changeover from one mode to the other, as the control parameters are varied, could be interpreted in terms of a cusp catastrophe. The critical curve shown in Fig. 4 is typical of a tilted cusp. Similar behavior has been observed by Nandakumar et al. [19] for the mixed convection flow of a Newtonian fluid in empty ducts. The main difference between the two problems is the lack of the convective term (with a quadratic nonlinearity) in the momentum equations for porous media. Thus the nonlinearity of the convective term in the momentum equation does not appear to be the cause of multiplicity. The common feature between the two problems is the specific manner in which the momentum and energy equations are coupled. In fact this feature is common to the Taylor [14–16] and Dean [17, 18] problems as well. All these problems in the classical fluid mechanics are known to exhibit dual solutions. The Taylor problem, in particular, has been studied extensively [15, 16] by Benjamin and co-workers and is known to exhibit profuse multiplicity and certain anomalous mode behavior. Hence there is reason to believe that the current problem can also exhibit many of these features at larger aspect ratios. However, this would require the use of more advanced numerical methods.

We did not investigate in any detail the effect of the second-

order viscous terms in the Brinkman model on the bifurcation phenomena, as they become dominant only in the region ($\xi > 1$) where the validity of the model itself is in question.

Uniform Temperature Around Periphery. Numerical solutions were also obtained for the case of axially uniform flux and peripherally uniform temperature. As one would expect, the driving force for secondary flow would be much weaker in this case. Yet this case also exhibits many of the same phenomena observed for the bottom heated case. The contours of temperature and stream function are shown in Fig. 5 and the computed Nusselt numbers are shown in Fig. 6. Since the secondary flow is weaker the bifurcation occurs at much higher Grashof numbers. The lower and upper critical Grashof numbers are 2250 and 11,500, respectively. The cusp curve was not determined in this case because of computational expense. One noticeable difference between the two boundary conditions is the crossover of the Nu versus Gr curve for the bottom heated case. One plausible explanation for this is as follows. In Fig. 2, consider a Grashof number to the left of the crossover point. In the two-vortex case, the heat delivered to the lower wall is convected effectively over the entire flow domain. However, such is not the case for a four-vortex solution at the same Grashof number. Since there is no flow across the cell boundary, heat transfer across this surface of zero stream function can be only by conduction. This sets up a local hot spot around the center of the lower wall where the new cells have formed. Thus the effectiveness for heat transfer, and hence the Nusselt number, is lower for the four-vortex case than for a two-vortex one. However, as the Grashof number is increased, the convective mechanism which delivers and removes heat across the cell boundary becomes intense, thus showing a steeper slope in this region of Grashof number. Thus the crossover is due to two competing mechanisms, one dominating on either side of the crossover point. This crossover is not observed in Fig. 6 for the uniform temperature case. Similar behavior was observed for the Newtonian fluid as well in a separate study [19]. We believe that it is due to the following two differences in the observed behavior. In the first place there is no hot spot at the lower wall near the newly formed cells as the entire wall is maintained at a uniform temperature. Secondly the lower and upper critical Grashof numbers are increased from 1000 and 3250 respectively for Case 2 to 2250 and 11,500 for Case 1. Thus convection due to secondary flow is established as the dominant mechanism by the time a stable four-vortex solution is realizable for Case 1.

Conclusion

The mixed convection flow in porous media, subjected to the condition of axially uniform flux, has been solved numerically. Dual solutions have been observed for this problem over certain ranges of flow parameter. The variation of the critical Grashof number with aspect ratio follows that of a tilted cusp. Use of the Brinkman model to account for the no-slip condition does not alter the qualitative behavior significantly in the region of low permeability.

References

1 Combarnous, M. A., and Bories, S. A., "Hydrothermal Convection in Saturated Porous Media," *Advances in Hydroscience*, Vol. 10, 1975, pp. 231-307.

2 Cheng, P., "Heat Transfer in Geothermal Systems," *Advances in Heat Transfer*, Vol. 14, 1978, pp. 1-105.

3 Lapwood, E. R., "Convection of a Fluid in a Porous Medium," *Proceedings Cambridge Phil. Soc.*, Vol. 44, 1946, pp. 508-521.

4 Wooding, R. A., "A Steady-State Free Thermal Convection of Liquid in a Saturated Permeable Medium," *J. Fluid Mech.*, Vol. 2, 1957, p. 273.

5 Elder, J. W., "Steady Free Convection in a Porous Medium Heated From Below," *J. Fluid Mech.*, Vol. 27, 1967, pp. 29-48.

6 Walker, K. L., and Homsy, G. M., "Convection in a Porous Cavity," *J. Fluid Mech.*, Vol. 87, 1978, pp. 449-474.

7 Shiralkar, G. S., Haajizadeh, M., and Tien, C. L., "Numerical Study of High Rayleigh Number Convection in a Vertical Porous Enclosure," *Numerical Heat Transfer*, Vol. 6, 1983, pp. 223-234.

8 Bejan, A., "The Boundary Layer Regime in a Porous Layer With Uniform Heat Flux From the Side," *Int. J. Heat Mass Transfer*, Vol. 26, 1983, pp. 1339-1346.

9 Bejan, A., and Tien, C. L., "Natural Convection in a Horizontal Porous Medium Subjected to an End-to-End Temperature Difference," ASME JOURAL OF HEAT TRANSFER, Vol. 100, 1978, pp. 191-198.

10 Poulikakos, D., and Bejan, A., "Natural Convection in Vertically and Horizontally Layered Porous Media Heated From the Side," *Int. J. Heat Mass Transfer*, Vol. 26, 1983, pp. 1805-1814.

11 Prasad, V., and Kulacki, F. A., "Natural Convection in a Rectangular Porous Cavity With Constant Heat Flux on One Vertical Wall," ASME JOURNAL OF HEAT TRANSFER, Vol. 106, 1984, pp. 152-157.

12 Prasad, V., and Kulacki, F. A., "Convective Heat Transfer in a Rectangular Porous Cavity—Effect of Aspect Ratio on Flow Structure and Heat Transfer," ASME JOURNAL OF HEAT TRANSFER, Vol. 106, 1984, pp. 158-165.

13 Gebhart, B., et al., "Multiple Steady-State Solutions for Buoyancy-Induced Transport in Porous Media Saturated With Cold Pure or Saline Water," *Numerical Heat Transfer*, Vol. 6, 1983, pp. 337-352.

14 Taylor, G. I., "Stability of a Viscous Liquid Contained Between Two Rotating Cylinders," *Phil. Trans. A.*, Vol. 223, 1923, pp. 289-343.

15 Benjamin, T. B., "Bifurcation Phenomena in Steady Flows of a Viscous Fluid," *Proc. Roy. Soc. London*, Vol. A359, 1978, pp. 1-43.

16 Benjamin, T. B., and Mullin, T., "Notes on the Multiplicity of Flows in the Taylor Experiment," *J. Fluid Mech.*, Vol. 121, 1982, pp. 219-230.

17 Nandakumar, K., and Masliyah, J. H., "Bifurcation in Steady Laminar Flow Through Curved Tubes," *J. Fluid Mech.*, Vol. 119, 1982, pp. 475-490.

18 Dennis, S. C. R., and Ng, M., "Dual Solutions for Steady Laminar Flow Through a Curved Tube," *Quart. J. Mech. Appl. Math.*, Vol. 35, 1982, pp. 305-324.

19 Nandakumar, K., et al., "Multiple Steady States and Hysteresis in Mixed Convection Flow in Horizontal Square Tubes," *Proc. of the 2nd International Conference on Numerical Methods for Nonlinear Problems*, Barcelona, Spain, 1984.

20 Patankar, S. V., Ramadhyani, S., and Sparrow, E. M., "Effect of Circumferentially Nonuniform Heating on Laminar Combined Convection in a Horizontal Tube," ASME JOURNAL OF HEAT TRANSFER, Vol. 100, 1978, pp. 63-70.

21 Reynolds, W. C., "Heat Transfer to Fully Developed Laminar Flow in a Circular Tube With Arbitrary Circumferential Heat Flux," ASME JOURNAL OF HEAT TRANSFER, Vol. 82, 1960, pp. 108-112.

22 Bejan, A., and Poulikakos, D., "The Non-Darcy Regime for Vertical Boundary Layer Natural Convection in a Porous Medium," *Int. J. Heat Mass Transfer*, Vol. 27, 1984, p. 717.

23 Tveitereid, M., "Thermal Convection in a Horizontal Porous Layer With Internal Heat Sources," *Int. J. Heat Mass Transfer*, Vol. 20, 1977, pp. 1045-1050.

24 Combarnous, M. A., and Bia, P., "Combined Free and Forced Convection in Porous Media," *Soc. Pet. Eng. J.*, Vol. 11, 1971, pp. 399-405.

25 Schulenberg, T., and Müller, U., "Natural Convection in Saturated Porous Layers With Internal Heat Sources," *Int. J. Heat Mass Transfer*, Vol. 27, 1984, pp. 677-685.

26 Somerton, C. W., "The Prandtl Number Effect in Porous Layer Convection," *Applied Scientific Research*, Vol. 40, 1983, pp. 333-344.

27 Prasad, V., et al., "Natural Convection in Porous Media," *J. Fluid Mech.*, Vol. 150, 1985, pp. 89-119.

The Influence of Coupled Molecular Diffusion on Double-Diffusive Convection in a Porous Medium

N. Rudraiah

M. S. Malashetty

UGC-DSA Centre in Fluid Mechanics,
Department of Mathematics,
Bangalore University,
Central College,
Bangalore 560 001 India

The effect of coupled molecular diffusion on double-diffusive convection in a horizontal porous medium is studied using linear and nonlinear stability analyses. In the case of linear theory, normal mode analysis is employed incorporating two cross diffusion terms. It is found that salt fingers can form by taking cross-diffusion terms of appropriate sign and magnitude even when both concentrations are stably stratified. The conditions for the diffusive instability are compared with those for the formation of fingers. It is shown that these two types of instability will never occur together. The finite amplitude analysis is used to derive the condition for the maintenance of fingers. The stability boundaries are drawn for three different combinations of stratification and the effect of permeability is depicted.

1 Introduction

The problem of stability of a two-component quiescent layer of fluid in a porous medium subject to gradients of temperature and concentration is important in geophysics, particularly in saline geothermal fields where hot brines remain beneath less saline, cooler ground waters. In such a two-component fluid (say heat and salt) the diffusivity of heat is usually more than the diffusivity of salt; thus, a displaced particle of fluid loses any excess heat more rapidly than any excess solute. The resulting buoyancy force may tend to increase the displacement of the particle from its original position causing instability. The same effect may cause overstability involving oscillatory motions of large amplitude.

Convection in a two-component fluid is characterized by well-mixed convecting layers which are separated by relatively sharp density steps. These steps may be of the "finger" or "diffusive" kind and both types of interface must enable a net release of potential energy preferentially transporting the destabilizing property. Salt fingers will occur when warm salty water overlies cooler fresher water and the diffusive instabilities will occur when warm salty water underlies the fresh cooler water. In other words, in a two-component system, in the absence of cross diffusion, at least one of the components should be destabilizing. However, in the presence of cross diffusion produced by simultaneous interference of two transport processes, e.g., Soret and Dufour effects (Patil and Rudraiah, 1974, 1980; and Knobloch, 1980) the situations may be quite different.

In pure viscous flow, although many investigators (Hurle and Jakeman, 1971; Giglio and Vendramini, 1975, 1977a, 1977b; Knobloch, 1980; McDougall, 1983) have studied the effect of cross diffusion (i.e., Soret and Dufour) on double-diffusive convection, the quantitative description lags behind because of the uncertainties of the values of cross-diffusion coefficients D_{12} and D_{21}.

For a saturated porous medium, the phenomenon of cross diffusion is further complicated due to the interaction between fluid and porous matrices and accurate values of cross-diffusion coefficients are not available. This makes it impossible to proceed to a quantitative discussion of the theoretical analysis of cross-diffusion effects in a porous medium. Recently, Patil and Rudraiah (1980) have studied the effect of only the Soret coefficient on the onset of convection in a porous medium. They found that the critical Rayleigh number decreases with increase in the positive values of the Soret coefficient and for negative values they found a discontinuity at -0.01. Further, they conclude that for the values of Soret coefficient less than -0.01 a separation due to Soret effect gives rise to unexpected stability. They also conclude that rigid boundaries make the flow more stable even when there is thermal diffusion.

The influence of both the molecular cross-diffusion terms on the onset of double-diffusive convection in a porous medium, which gives some interesting results, has not been investigated so far and the study of this is one of the objectives of this paper.

This study reveals the following two surprising results emerging from the linear analysis as in the pure viscous flow discussed by McDougall (1983). Under certain range of cross-diffusion coefficients a situation favorable for finger (or diffusive) instability may also give rise to diffusive (or finger) instability. Furthermore, finger and diffusive instabilities may exist even when both components have stabilizing effects.

2 Mathematical Formulation

We consider a horizontal densely packed porous layer of thickness d saturated with Boussinesq binary fluid subject to solute gradients ΔT and ΔS. Here both T and S represent solute concentrations, and positive ΔT and ΔS imply the concentrations are greater at the bottom. For simplicity we deal only with the two-dimensional instabilities from a rest state that the uniform T and S gradients across the porous layer. The basic equations (with the Darcy–Lapwood model as momentum equation) are

$$\frac{\partial \mathbf{q}}{\partial t} + (\mathbf{q}\cdot\nabla)\mathbf{q} = -\frac{1}{\rho_0}\nabla P + \frac{\rho}{\rho_0}\mathbf{g} - \frac{\nu}{k}\mathbf{q} \tag{1}$$

$$\frac{\partial T}{\partial t} + (\mathbf{q}\cdot\nabla)T = D_{11}\nabla^2 T + D_{12}\nabla^2 S \tag{2}$$

$$\frac{\partial S}{\partial t} + (\mathbf{q}\cdot\nabla)S = D_{22}\nabla^2 S + D_{21}\nabla^2 T \tag{3}$$

$$\nabla\cdot\mathbf{q} = 0 \tag{4}$$

$$\rho = \rho_0(1 + \alpha_t T + \alpha_S S). \tag{5}$$

Since the porous medium is assumed to be densely packed, the Brinkman model incorporating a diffusion term is not valid.

Contributed by the Heat Transfer Division for publication in the JOURNAL OF HEAT TRANSFER. Manuscript received by the Heat Transfer Division March 6, 1985.

Further, the resistance offered to the flow by the elements of unit volume of the medium is small enough that the nonlinear inertia term might not be negligible. Therefore, we retain the nonlinear inertia term and neglect the duffusion term in equation (1).

The property T is assumed to have diffusivity larger than that of S, i.e., $D_{11} < D_{22}$. Choosing a coordinate system (x, z) such that x is horizontal and z vertical upward, we define a stream function ψ by

$$\mathbf{q} = (u, w) = \left(\frac{\partial \psi}{\partial z}, -\frac{\partial \psi}{\partial x}\right). \tag{6}$$

By taking the curl of (1) and using (6) we obtain

$$\left(\frac{\partial}{\partial t} + \frac{\nu}{k}\right)\nabla^2\psi = \alpha_t g \frac{\partial T}{\partial x} + \alpha_s g \frac{\partial S}{\partial x} + N \tag{7}$$

where $N = \partial(\psi, \nabla^2\Psi)/\partial(x, z)$.

We now introduce nondimensional variables in the usual way so that the deviations of T and S from linear vertical gradients $-\Delta T/d$ and $-\Delta S/d$ are normalized by ΔT and ΔS, respectively, and the time scale is $d^2 D_{11}^{-1}$. Equations (2), (3), and (7) are now expressed in terms of the dimensionless variables

$$\left(\frac{\partial}{\partial t} - \nabla^2\right)T - \frac{D_{12}}{D_{11}}\frac{\Delta S}{\Delta T}\nabla^2 S = L - \frac{\partial \psi}{\partial x} \tag{8}$$

$$\left(\frac{\partial}{\partial t} - \tau\nabla^2\right)S - \frac{D_{21}}{D_{11}}\frac{\Delta T}{\Delta S}\nabla^2 T = M - \frac{\partial \psi}{\partial x} \tag{9}$$

$$\left(\frac{1}{\sigma}\frac{\partial}{\partial t} + \frac{1}{Pl}\right)\nabla^2\psi = R\frac{\partial T}{\partial x} + \mathrm{Ra}_s\frac{\partial S}{\partial x} + \frac{N}{\sigma} \tag{10}$$

where $L = \partial(\psi, T)/\partial(x, z)$; $M = \partial(\psi, S)/\partial(x, z)$.

These equations are discussed subject to the boundary conditions

$$\psi = T = S = 0 \text{ at } z = 0, 1. \tag{11}$$

We deal with the linear and nonlinear theories separately in the remaining part of this paper.

3 Linear Analysis

In the case of linear theory, we neglect the Jacobian terms N, L, and M and we look for the solutions to equations (8)–(10) of the form

$$\begin{bmatrix}\psi\\ T\\ S\end{bmatrix} = \begin{bmatrix}\psi_0 \sin a\pi x\\ T_0 \cos a\pi x\\ S_0 \cos a\pi x\end{bmatrix} e^{pt} \sin n\pi z \tag{12}$$

which satisfy equation (11).

Substituting equation (12) into equations (8)–(10), and eliminating ψ_0, T_0, and S_0, we obtain the dispersion relation

$$p^3 + [\sigma/Pl + \delta_n^2(1+\tau)]p^2 + \Big[\{\tau(1+\tau)\sigma/Pl + \tau\delta_n^2\}\delta_n^2 + \sigma\frac{(a\pi)^2}{\delta_n^2}\{\mathrm{Ra} + \mathrm{Ra}_s - A\}\Big]p + \sigma\Big[\frac{\tau\delta_n^4}{P} + (a\pi)^2\{\tau\mathrm{Ra} + \mathrm{Ra}_s - B\}\Big] = 0 \tag{13}$$

where

$$\delta_n^2 = \pi^2(a^2 + n^2)$$

$$A = \frac{\delta_n^6}{\sigma(a\pi)^2}\frac{D_{12}D_{21}}{D_{11}D_{11}}$$

$$B = \frac{\delta_n^4}{Pl(a\pi)^2}\frac{D_{12}D_{21}}{D_{11}D_{11}} + \frac{D_{12}}{D_{11}}\frac{\Delta S}{\Delta T}\mathrm{Ra} + \frac{D_{21}}{D_{11}}\frac{\Delta T}{\Delta S}\mathrm{Ra}_s.$$

If we define

$$\mathrm{Ra} + \mathrm{Ra}_s - A = \mathrm{Ra}^e + \mathrm{Ra}_s^e$$
$$\tau\mathrm{Ra} + \mathrm{Ra}_s - B = \tau\mathrm{Ra}^e + \mathrm{Ra}_s^e \tag{14}$$

then the dispersion relation (13) reduced to the one given by Rudraiah et al. (1982) for a two-component fluid in the absence of cross diffusion (i.e., when $D_{12} = D_{21} = 0$). The equivalent Rayleigh numbers are then given by

$$\mathrm{Ra}^e = \mathrm{Ra} + \frac{B - A}{1 - \tau}$$

$$\mathrm{Ra}_s^e = \mathrm{Ra}_s + \frac{\tau A - B}{1 - \tau}. \tag{15}$$

This is true for general concentration gradients. Depending on the nature of the gradients we will have a finger and diffusive instabilities. These will be discussed in the remaining part of this paper.

4 Finger Instability

The conditions for the onset of finger instability in double diffusive convection are

$$\mathrm{Ra}_s^e < 0;\ \mathrm{Ra}^e > 0;\ -\mathrm{Ra}_s^e > \tau\mathrm{Ra}^e + \frac{4\pi^2}{Pl}\tau \tag{16}$$

where the factor $4\pi^2$ is equal to $\delta_n^4/(a\pi)^2$ at the most unstable value of $n = 1$ and $a = 1$. Expressing the third inequality in (16) in terms of physical Rayleigh numbers, we obtain

$$-\mathrm{Ra}_s > \tau\mathrm{Ra} + \frac{4\pi^2}{Pl} - B. \tag{17}$$

Now for $\mathrm{Ra} > 0$, that is for the density gradient due to the fact that the faster diffusing component $\alpha_t T_z$ is negative and hence statically stabilizing, this inequality takes the form

Nomenclature

d = distance between two horizontal boundaries
D_{11} = diffusivity of T component
D_{22} = diffusivity of S component
D_{12} = cross-diffusion term caused by S component
D_{21} = cross-diffusion term caused by T component
g = acceleration due to gravity
k = permeability of the porous medium
p = growth rate
p = pressure
Pl = k/d^2 = porous parameter
$\mathbf{q}$ = mean filter velocity
Ra = $\alpha_t g \Delta T d^3/D_{11}$ = Rayleigh number with respect to T
Ra_s = $\alpha_s g \Delta S d^3/D_{11}$ = Rayleigh number with respect to S
S, T = diffusion components
t = time
(x, y, z) = space coordinates
α = expansion coefficient
ν = kinematic viscosity
ρ = fluid density
τ = S_{22}/D_{11}

Subscripts

0 = reference scale
s = S component
t = T component

$$\left(\frac{\alpha_s D_{21}}{\alpha_t D_{11}}-1\right)+\frac{1\alpha_s S_z}{\tau\alpha_t T_z}\left(\frac{\alpha_t}{\alpha_s}\frac{D_{12}}{D_{11}}-1\right)$$

$$>\frac{4\pi^2}{Pl}\frac{1}{\mathrm{Ra}}\left(1-\frac{D_{12}}{D_{11}}\frac{D_{21}}{D_{22}}\right) \tag{18}$$

where $\alpha_s S_z/\alpha_t T_z$ is equal to $\mathrm{Ra}_s/\mathrm{Ra}$. For $\mathrm{Ra} < 0$, that is $\alpha_t T_z > 0$, the above inequality is reversed. The hydrostatic stability is assumed by $\mathrm{Ra} = \mathrm{Ra}_s > 0$, $\alpha_t T_z + \alpha_s S_z < 0$. For large Ra compared to $4\pi^2/Pl$, the right-hand side of (18) is approximately zero and so the condition for the formation of fingers in the presence of cross-diffusion terms is

$$\frac{\alpha_s S_z}{\alpha_t T_z}\left(1-\frac{\alpha_t D_{12}}{\alpha_s D_{11}}\right)>\tau\left(1-\frac{\alpha_s}{\alpha_t}\frac{D_{21}}{D_{22}}\right) \tag{19}$$

with $\alpha_t T_z < 0$ and $\alpha_s S_z > 0$. In the absence of cross-diffusion terms (i.e., $D_{12} = D_{21} = 0$), equation (19) reduces to

$$\left|\frac{\alpha_S S_z}{\alpha_t T_z}\right|>\tau. \tag{20}$$

From inequality (19), it is clear that a positive D_{21} (which means that the flux of more slowly diffusing component S is augmented by the T gradient) encourages the formation of fingers, whereas a positive D_{12} discourages their appearance.

Now consider the case where the two horizontal boundaries are impervious to the S property, but a constant difference of T property is maintained. We study the stability of the system when the vertical flux of S is zero at all depths and so Ra and Ra_s are related by $\mathrm{Ra}_s/\mathrm{Ra} = -\alpha_s D_{21}/\alpha_t D_{22}$. Using this in (18) we obtain

$$\frac{\alpha_s}{\alpha_t}\frac{D_{21}}{D_{22}}>\frac{\tau}{1+\tau}\left[\left(1+\frac{D_{12}}{D_{11}}\frac{D_{21}}{D_{11}}\right)+\frac{4\pi^2}{Pl}\frac{1}{\mathrm{Ra}}\left(1-\frac{D_{12}}{D_{11}}\frac{D_{21}}{D_{22}}\right)\right]. \tag{21}$$

If both T and S are stably stratified, i.e., $\alpha_t T_z < 0$, $\alpha_s S_z < 0$, then we see from equation (18) that a neceasary condition for the formation of fingers in either $\alpha_s D_{21}/\alpha_t D_{22} > 1$ or $\alpha_t D_{22}/\alpha_s D_{11} > 1$.

Diffusive Instability

By setting the growth rate p to be purely imaginary we obtain the conditions required for the diffusive instability in the form

$$\mathrm{Ra}_s^e>0,\ \mathrm{Ra}^e<0,$$

$$-\mathrm{Ra}^e>\frac{(\sigma+\delta_n^2 Pl)}{(\sigma+\delta_n^2 Pl)}\mathrm{Ra}_s+\frac{\delta_n^4}{Pl(a\pi)^2}\frac{(1+\tau)(\sigma+\tau\delta_n^2 Pl)}{\sigma}. \tag{22}$$

In terms of physical Rayleigh numbers, the last inequality in (22) takes the form

$$-\mathrm{Ra}>\frac{(\sigma+\tau\delta_n^2 Pl)}{(\sigma+\delta_n^2 Pl)}\mathrm{Ra}_s+\frac{\delta_n^2 PlB-A[\sigma+\delta_n^2 Pl(1+\tau)]}{(\sigma+\delta_n^2 Pl)}+\frac{4\pi^2}{Pl}\frac{(1+\tau)(\sigma+\tau\delta_n^2 Pl)}{\sigma}. \tag{23}$$

In the absence of cross-diffusion terms (i.e., $D_{12} = D_{21} = 0$), equation (23) reduces to

$$-\mathrm{Ra}>\frac{(\sigma+\tau\delta_n^2 Pl)}{(\sigma+\delta_n^2 Pl)}\mathrm{Ra}_s+\frac{4\pi^2(1+\tau)(\sigma+\tau\delta_n^2 Pl)}{Pl\sigma} \tag{24}$$

which coincides with the one given by Rudraiah et al. [9]. For large Ra compared to $(4\pi^2/Pl)$ and when $\alpha_t T_z$ and $\alpha_s S_z$ are assigned independent values, we obtain the condition for the diffusive instability in the form

$$\tau\alpha_t T_z\left[\delta_n^2 Pl\frac{\alpha_s D_{21}}{\alpha_t D_{22}}+\frac{(\sigma+\delta_n^2 Pl)}{\tau}\right]$$

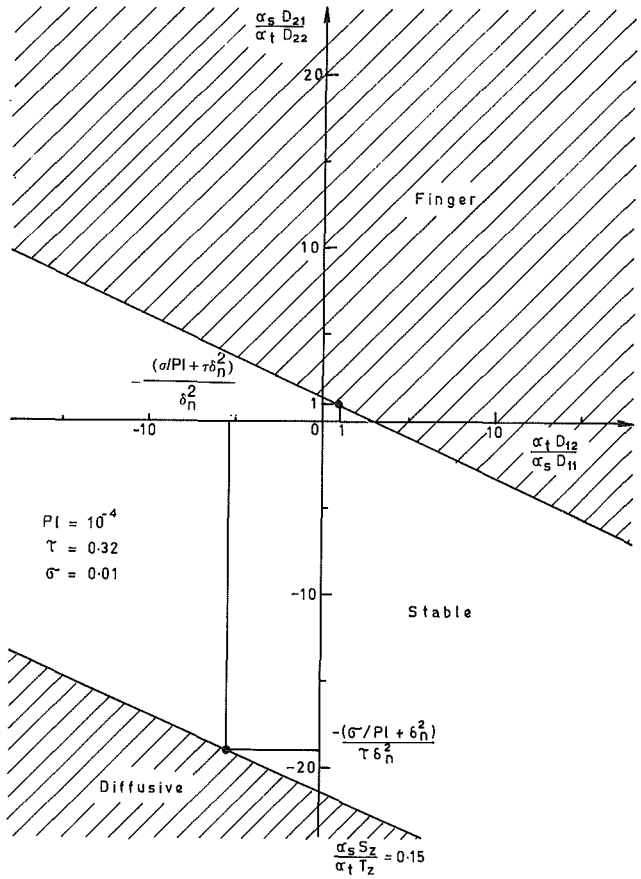

Fig. 1 Stability boundaries as a function of $\alpha_s D_{21}/\alpha_t D_{22}$ and $\alpha_t D_{12}/\alpha_s D_{11}$ for $\alpha_t T_z < 0$, $\alpha_s S_z < 0$

$$+\alpha_s S_z\left[\delta_n^2 Pl\frac{\alpha_t D_{12}}{\alpha_s D_{11}}+(\sigma+\tau\delta_n^2 Pl)\right]>0. \tag{25}$$

When both T and S are stably stratifed (i.e., $\alpha_t T_z < 0$, $\alpha_s S_z < 0$) the above inequality shows that for small porous parameter, a large negative cross-diffusion coefficient (either $\alpha_t D_{12}/\alpha_s D_{11}$ or $\alpha_s D_{21}/\alpha_t D_{22}$) is required for diffusive instability.

If the two horizontal boundaries are impervious to the S property and a constant difference of the T property is maintained, inequality (23) with $\mathrm{Ra}_s/\mathrm{Ra} = -\alpha_s D_{21}/\alpha_t D_{22}$ and $\mathrm{Ra} < 0$ takes the form

$$\frac{\alpha_s D_{21}}{\alpha_t D_{22}}<1+\left(\frac{\delta_n^2 Pl}{\sigma}\right)\left[1-\frac{D_{12}}{D_{11}}\frac{D_{21}}{D_{22}}\right]+\frac{4\pi^2}{Pl}\frac{1}{\mathrm{Ra}}\frac{(1+\tau)}{\sigma^2}\left[(\sigma+\tau\delta_n^2 Pl)(\sigma+\delta_n^2 Pl)-(\delta_n^2 Pl)^2\frac{D_{12}}{D_{11}}\frac{D_{21}}{D_{22}}\right]. \tag{26}$$

The general condition for the onset of fingers, analogous to equation (25), is

$$\alpha_t T_z\left(\frac{\alpha_s D_{21}}{\alpha_t D_{22}}-1\right)+\alpha_s S_z\left(\frac{\alpha_t D_{12}}{\alpha_s D_{11}}-1\right)<0. \tag{27}$$

We now treat $\alpha_t T_z$ and $\alpha_s S_z$ as externally imposed and plot the two inequalities (25) and (27) on the axes $\alpha_s D_{21}/\alpha_t D_{22}$ and $\alpha_t D_{12}/\alpha_s D_{11}$, subject to static stability constraint $\alpha_t T_z + \alpha_s S_z < 0$. Figures 1–3 show the regions of finger and diffusive instabilities for the three possible distributions of $\alpha_t T_z$ and $\alpha_s S_z$. The two straight lines through the points (1, 1) and $(-(\sigma/Pl + \tau\delta_n^2)/\delta_n^2,\ -(\sigma/Pl + \delta_n^2)/\delta_n^2)$ have the same slope. These stability boundaries show that the two types of double dif-

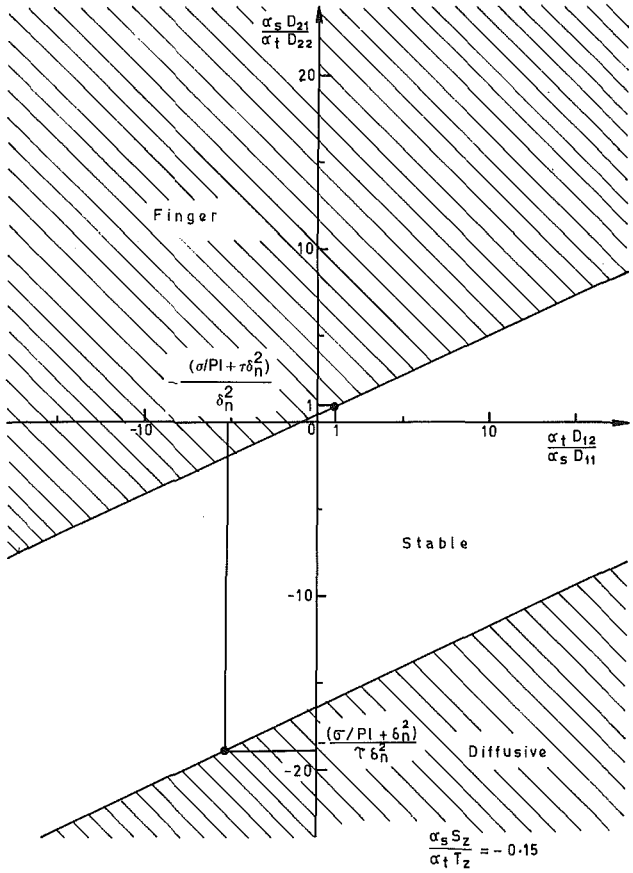

Fig. 2 Stability boundaries as a function of $\alpha_s D_{21}/\alpha_t D_{22}$ and $\alpha_t D_{12}/\alpha_s D_{11}$ for $\alpha_t T_z < 0, \alpha_s S_z > 0$

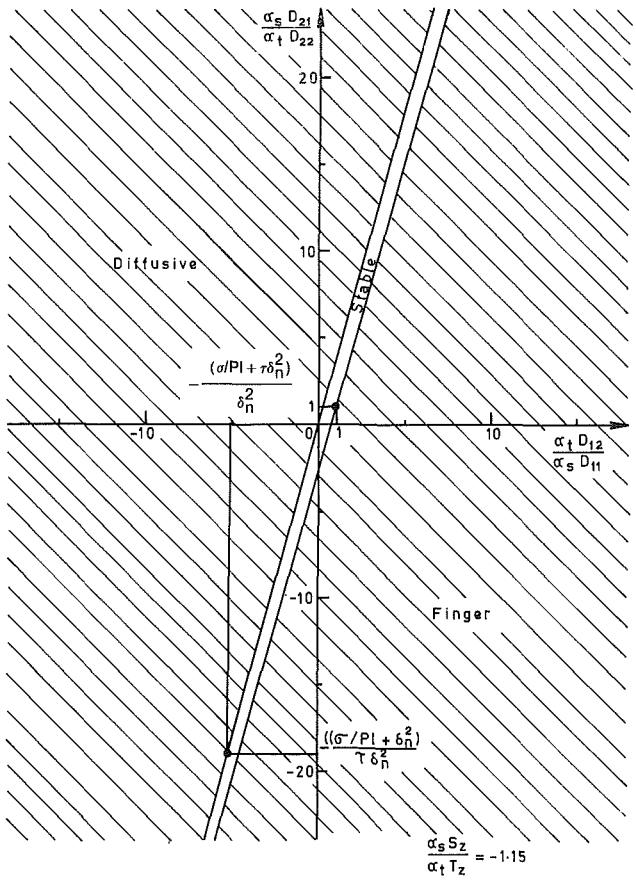

Fig. 3 Stability boundaries as a function of $\alpha_s D_{21}/\alpha_t D_{22}$ and $\alpha_t D_{12}/\alpha_s D_{11}$ for $\alpha_t T_z < 0, \alpha_s S_z < 0$

fusive instability will never occur together, even though both types of instability can occur in concentration gradients that are normally conducive to the other type of instability.

6 Finite Amplitude Finger Analysis

We assume that the motion is only in the vertical direction (i.e., $u = 0$, $v = 0$, $w \neq 0$) so that the nonlinear advective terms in the momentum equation are zero. The z component of Darcy equation is

$$0 = -\frac{1}{\rho_0}\frac{\partial P}{\partial z} - g(\alpha_t T + \alpha_s S) - \frac{\nu}{k} w. \tag{28}$$

The equations for conservation of T and S are

$$wT_z = D_{11}\nabla^2 T + D_{12}\nabla^2 S \tag{29}$$

$$wS_z = D_{22}\nabla^2 S + D_{21}\nabla^2 T. \tag{30}$$

Since horizontal velocities are zero, from the continuity equation we have $\partial w/\partial z = 0$ which implies that w is a function of only x and y, i.e., $w = w(x, y)$. Also the horizontal momentum equation shows that P is a function of only z. Hence from (5.1) we write

$$T(x, y, z) = \bar{T}(z) + T'(x, y)$$
$$S(x, y, z) = \bar{S}(z) + S'(x, y) \tag{31}$$

where the overbar means an average in the horizontal plane and T' and S' are fluctuations with zero horizontal average. Substituting equation (31) into equations (29) and (30) and taking a horizontal average we obtain either

$$D_{11}D_{22} - D_{12}D_{21} = 0$$

or

$$\frac{d^2\bar{T}}{dz^2} = 0, \quad \frac{d^2\bar{S}}{dz^2} = 0. \tag{32}$$

We assume that $D_{11}D_{22} - D_{12}D_{22} \neq 0$, so that equation (32) holds. Equation (28) and its horizontal average yield

$$0 = -g(\alpha_t T' + \alpha_s S') - \frac{\nu}{k} w. \tag{33}$$

Equations (29) and (30), using (31) and (32), become

$$w\bar{T}_z = D_{11}\nabla_1^2 T' + D_{12}\nabla_1^2 S' \tag{34}$$

$$wS_z = D_{22}\nabla_1^2 S' + D_{21}\nabla_1^2 T' \tag{35}$$

where $\nabla_1^2 = \partial^2/\partial x^2 + \partial^2/\partial y^2$.

We look for solutions of equations (33)–(35) in the form

$$(w, T', S') = (w_0, T_0, S_0)\cos mx \cos ny. \tag{36}$$

Substituting equation (36) into equations (33)–(35) and eliminating w_0, T_0, and S_0 we obtain

$$-\alpha_t \bar{T}_z\left(\frac{\alpha_s}{\alpha_t} D_{21} - D_{22}\right) - \alpha_s \bar{S}_z\left(\frac{\alpha_t}{\alpha_s} D_{12} - D_{11}\right)$$
$$= \frac{\nu\delta^2}{gk}(D_{11}D_{22} - D_{12}D_{21}) \tag{37}$$

where $\delta^2 = (m^2 + n^2)$. We assume that $(D_{11}D_{22} - D_{12}D_{21}) > 0$, so that the left-hand side of equation (37) must be positive. We consider the case where T is stably stratified, i.e., $\alpha_t \bar{T}_z < 0$; fingers will form if

$$\left(\frac{\alpha_s}{\alpha_t}\frac{D_{21}}{D_{22}} - 1\right) + \left(\frac{1}{\tau}\frac{\alpha_s}{\alpha_t}\frac{\bar{S}_z}{\bar{T}_z}\frac{D_{12}}{D_{11}} - 1\right) > 0 \tag{38}$$

If T is unstably stratified, i.e., $\alpha_t \bar{T}_z > 0$, then the inequality is reversed in (38). We see that the inequality (38) is the same as (18) except for the term proportional to $(4\pi^2/Pl)(1/\mathrm{Ra})$. The gradients $\bar{T}_z$ and $\bar{S}_z$ in (38) are the vertical gradients of horizontally averaged T and S fields whereas the gradients T_z

and S_z in (18) are uniform in the horizontal direction and are the gradients that exist before any fingering sets in.

We now consider the following two cases: (*i*) $D_{12} = 0$ and $D_{21} \neq 0$; (*ii*) $D_{12} \neq 0$ and $D_{21} = 0$; where both T and S are stably stratified (i.e., $\alpha_t T_z < 0$ and $\alpha_s S_z < 0$).

Case (*i*) $D_{12} = 0$ and $D_{21} \neq 0$. In this case where the cross diffusion affects the flux of S alone, inequality (38) takes the form

$$\frac{\alpha_s}{\alpha_t}\frac{D_{21}}{D_{22}} > 1 + \tau^{-1}\frac{\alpha_s}{\alpha_t}\frac{\bar{S}_z}{\bar{T}_z} \tag{39}$$

We observe from inequality (39) that the fingers will be formed readily for small $\alpha_s \bar{S}_z$ and large $\alpha_t \bar{T}_z$.

Case (*ii*) $D_{12} \neq 0$, and $D_{21} = 0$. In this case the cross diffusion affects only the flux of T. Inequality (38) takes the form

$$\frac{\alpha_t}{\alpha_s}\frac{D_{12}}{D_{11}} > 1 + \tau^{-1}\frac{\alpha_t \bar{T}_z}{\alpha_s \bar{S}_z} \tag{40}$$

Thus when $D_{21} = 0$, the fingers are favored by small $\alpha_t \bar{T}_z$ and large $\alpha_s \bar{S}_z$.

In the case where both D_{12} and D_{12} are nonzero, we conclude from inequality (38) that the onset of fingers will be favored by large positive values of D_{21} and D_{12} and at least one of $\alpha_s D_{21}/\alpha_t D_{22}$ and $\alpha_t D_{22}/\alpha_s D_{11}$ must exceed unity. Thus even if both T and S are stably stratified, finger convection can still occur if the cross-diffusion terms are large enough to satisfy inequality (38). This is due to the fact that the cross diffusion between the fingers allows the release of potential energy even though no separate concentration is unstably stratified.

7 Discussion

Double-diffusive convection in a porous medium with large cross-diffusion terms when the vertical gradients of the two solutes T and S are stably stratified is studied using infinitesimal and finite amplitude analysis. The stability boundaries are drawn in Figs. 1–3. It is found that the two types of double-diffusive instabilities (finger and diffusive) will never occur together even though both types of instabilities can occur in solute gradients that are favourable to the other type of instability. It is possible to have finger or diffusive instability even when both T and S are stably stratified by taking cross-diffusion coefficients of the appropriate sign and magnitude. This is due to the fact that even if both T and S are stably stratified, it is the cross diffusion that allows the release of potential energy and make the system unstable. The porous parameter Pl reduces the effect of cross diffusion. When both T and S are stably stratified, large negative cross-diffusion coefficients (either $\alpha_t D_{12}/\alpha_s D_{11}$ or $\alpha_s D_{21}/\alpha_t D_{22}$) are required to have diffusive instability.

Acknowledgements

This work was supported by the UGC under the DSA program. One of us (MSM) is grateful to the UGC for providing an FIP Teacher Fellowship and to the HKE Society for recommending him for higher studies.

The computational work in this paper was supported by the Department of Science and Technology, Government of India, under grant No. HCS/DST/11.4.81.

References

Giglio, M., Vendramini, A., 1975, "Thermal Diffusion Measurements Near a Consolate Critical Point," *Phys. Rev. Lett.*, Vol. 34, pp. 561–564.

Giglio, M., Vendramini, A., 1977a, "Soret Type Motion of Macromolecule in Solution," *Phys. Rev. Lett.*, Vol. 38, pp. 26–29.

Giglio, M., and Vendramini, A., 1977b, "Buoyancy Driven Instability in a Dilute Solution of Macromolecules," Vol. 39, pp. 1014–1017.

Hurle, D. T. J., and Jakeman, E., 1971, "Soret-Driven Thermosolutal Convection," *J. Fluid Mech.*, Vol. 47, pp. 667–670.

Knobloch, E., 1980, "Convection in Binary Fluids," *Phys. Fluids*, Vol. 23, pp. 1918–1920.

McDougall, T. J., 1983, "Double Diffusive Convection Caused by Coupled Molecular Diffusion," *J. Fluid Mech.*, Vol. 126, pp. 379–397.

Patil, O., and Rudraiah, N., 1974, "Thermal Diffusion and Convective Stability of a Two-Component Fluid in a Porous Medium," *Proc. V Int. Heat Tran. Conf.*, Tokyo, pp. 79–82.

Patil, P., and Rudraiah, N., 1980, "Linear Convective Stability and Thermal Diffusion of a Horizontal Quiescent Layer of a Two-Component Fluid in a Porous Medium," *Int. J. Engg. Sci.*, Vol. 18, pp. 1055–1059.

Rudraiah, N., Srimani, P. K., Friedrich, R., 1982, "Finite Amplitude Convection in a Two Component Fluid Saturated Porous Layer," *Int. J. Heat Mass Tranfer*, Vol. 25, pp. 715–722.

T. Tsuruda

M. Harayama

T. Hirano

Department of Reaction Chemistry,
Faculty of Engineering,
University of Tokyo,
Tokyo, Japan

Growth of Flame Front Turbulence

An experimental study was performed on the growth of flame front turbulence by stimulating a laminar propagating flame with weak pressure waves, which were generated by sudden breaking of the membrane separating a small chamber from the combustion chamber. The flame front behavior was explored by using high-speed schlieren photography. About one millisecond after the first weak pressure wave passed the flame front, a very fine disturbance appeared at the central part of the flame front, where no effect of the wall turbulence could appear. Then, the area and strength of the disturbance were observed to increase rapidly. The effects of the pressure wave intensity, fuel concentration, and fuel type on the growth of this type of flame front turbulence were examined in detail.

Introduction

The results of previous theoretical studies on flame front instability indicate that once flame front turbulence appears, it continues to grow during propagation through a gaseous flammable mixture, even if the mixture is uniform and nonturbulent [1–4]. Knowledge of the growth of the flame front turbulence in such a case seems very important to our understanding of flame behavior during accidental gas explosions [4–8] or in spark ignition engines [9].

Many studies have been carried out to study flame front instability [1–20], and various types of flame front turbulence were examined in detail. However, in very few experiments were the mechanisms of the growth of flame front turbulence clearly identified.

Studies of gas explosions in fuel gas–air mixtures showed that a sufficient distance is needed for a laminar flame, propagating through a uniform quiescent mixture, to become turbulent without wall friction effects [6, 21, 22]. However, in a laboratory-scale combustion chamber, it is not easy to generate turbulence at a propagating laminar premixed flame free from the turbulence caused by wall friction. Therefore, to observe the development of flame-induced turbulence using a laboratory-scale combustion chamber, application of some stimulation to the flame front seems indispensable [11, 12]. It is obvious that even in such a case flame front deformation caused by the overall gas flow induced by the stimulation is undesirable, because some types of flame front turbulence are very likely masked [2, 11, 12, 18]. Thus, for the observation of the initial development of flame front turbulence it is necessary to apply stimulation weak enough not to overly deform the flame front.

A shock wave was employed for this purpose by Markstein [2, 11] and Rudinger and Somers [12], and flame front turbulence was reported to have been observed. However, its behavior was found to be different from theoretical predictions under steady conditions. Concerning the discrepancy, Markstein mentioned, "In view of the impulsive acceleration of very short duration associated with passage of a shock wave, the concept of Taylor instability may have to be modified considerably" [11]. This means that if stimulation weak but sufficient to initiate flame front turbulence were employed, the experimental results should coincide well with theoretically predicted ones. However, few experimental studies have been performed which are appropriate to compare with the results of theoretical predictions under steady conditions.

In the present study, therefore, the processes of the growth of flame front turbulence have been experimentally explored when a flame, being stimulated by a weak pressure wave, propagates through a uniform flammable mixture without turbulence.

Contributed by the Heat Transfer Division and presented at the 23rd ASME/AIChE National Heat Transfer Conference, Denver, Colorado, August 4–7, 1985. Manuscript received by the Heat Transfer Division October 3, 1985.

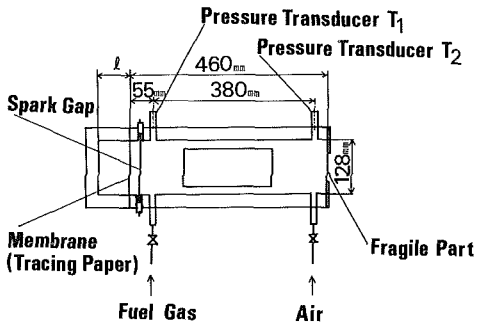

Fig. 1 Schematic of experimental setup

Experimental Apparatus and Procedure

The experimental setup is shown schematically in Fig. 1. The combustion chamber used was rectangular, the inside of which was 92 mm × 128 mm in cross section and 460 mm long. Two windows having 90 mm × 200 mm optical glass plates were installed on the side walls. A small chamber used to generate weak pressure waves was connected to the combustion chamber at one end. This structure is similar in several respects to that used by Markstein [11]. The main difference is the strength of pressure waves generated. The pressure waves generated in the present apparatus only slightly affected the overall flame front configuration so that the initial development of the fine structure of flame front turbulence could be observed. The cross section of the pressure wave generator was the same as that of the combustion chamber, and its length was varied to control the intensity of the generated pressure wave. The lengths adopted in the present experiments were 10, 20, 30, and 40 mm. Before starting each test, the small chamber was separated from the combustion chamber by using a membrane of tracing paper. On the other end of the combustion chamber, a fragile part was installed, which was designed to be broken at the final stage of each test so that the windows did not break due to pressure rise.

Fuels used in the present experiments were methane and propane. Methane or propane was injected into the air-filled combustion chamber as a strong jet and mixed with air. The mixture in the combustion chamber became uniform within one minute after injection due to strong turbulence induced by the fuel jet. The uniformity was confirmed by schlieren photography. The velocity of the gas flow induced by the fuel jet also became sufficiently small within one minute so that no effect of residual turbulence of the gas flow could be observed on flame propagation. The mixture composition was controlled by changing the amount of fuel injected into the combustion chamber. In the following sections, the mixture composition will be represented by the equivalence ratio ϕ defined as

$$\phi = ([\text{Fuel}]/[\text{Air}])/([\text{Fuel}]/[\text{Air}])_{st}$$

More than one minute after the injection of fuel, the mix-

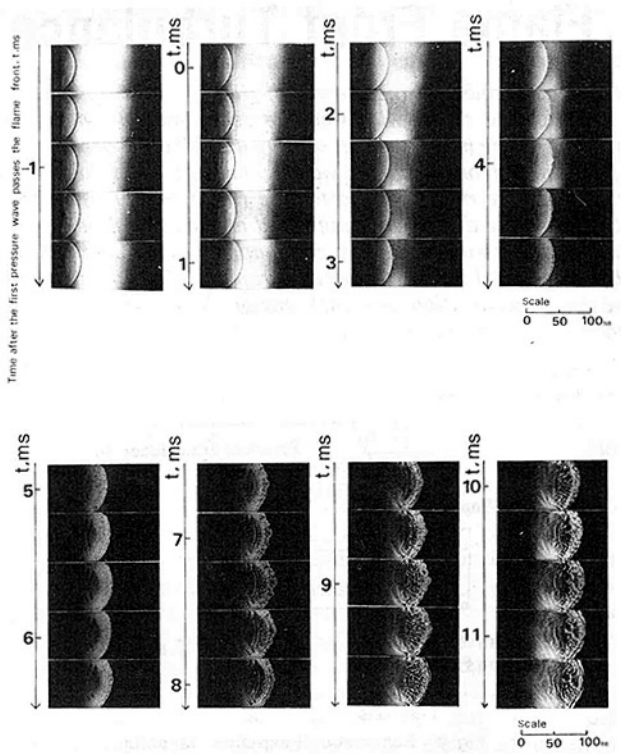

Fig. 2 Series of schlieren photographs representing the flame propagation through a methane-air mixture of $\phi = 1.1$, $l = 40$ mm

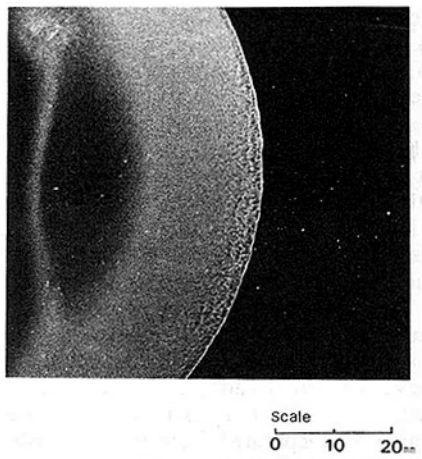

Fig. 3 Instantaneous schlieren photograph of flame front at $t \simeq 2$ ms, $\phi \simeq 1.0$, $l = 40$ mm

ture was ignited by an electric spark, beginning the propagation of a laminar premixed flame.

The pressure wave was generated by sudden breaking of the tracing paper sheet during flame propagation. In the present experiments, the tracking paper sheet broke when the pressure in the combustion chamber became 30 ~ 40 kPa higher than the initial pressure. The amplitude of pressure wave at the flame front was estimated to be less than 10 kPa.

The flame behavior was recorded by a high-speed schlieren system composed of a high-pressure 500 W mercury vapor lamp; two concave mirrors, 300 mm in diameter with a 3000 mm focal length; a knife edge; and a 16 mm high-speed cine camera.

The image recorded on film using a 16 mm high-speed cine camera was not sufficient to examine the details of the turbulent flame front. Thus, the turbulent flame front was also recorded by an instantaneous schlieren system composed of a flash lamp, an optical setup the same as the high-speed

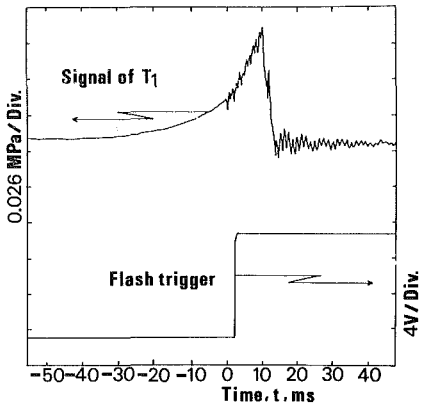

Fig. 4 Pressure record and flash timing

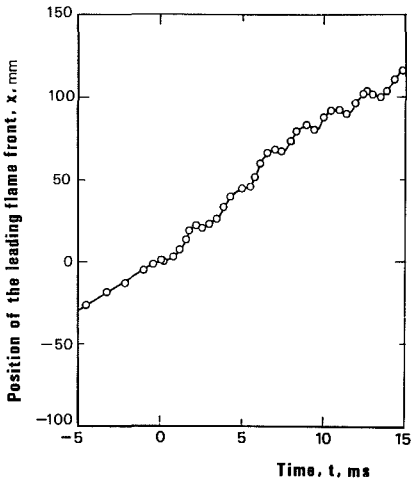

Fig. 5 x-t diagram representing flame propagation through a methane-air mixture having $\phi = 1.1$ presented in Fig. 2: $x = 0$ represents the position of the leading flame front at $t = 0$; t represents the time after the first pressure fluctuation passes the flame front

Nomenclature

[Air] = mole fraction of air in the mixture
[Fuel] = mole fraction of fuel in the mixture
l = length of the small chamber, mm
p^* = pressure which induces the overall acceleration or deceleration of gas, g/(cm·s^2)
t = time after the first pressure wave passes the flame front, ms
T_1 = pressure transducer location near the spark gap
T_2 = pressure transducer location far from the spark gap
$\mathbf{v}$ = velocity vector of gas, cm/s
x = distance from the position of the leading flame front at $t = 0$, cm
ρ = density of gas, g/cm^3
ϕ = equivalence ratio of the mixture

Subscripts

n = normal to flame front
st = stoichiometric

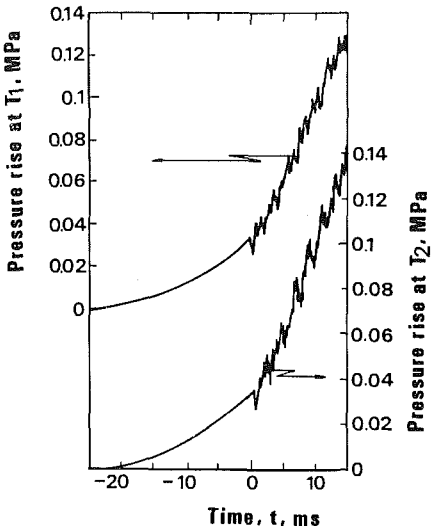

Fig. 6 Pressure fluctuations recorded during flame propagation through a methane-air mixture with $\phi = 1.1$ presented at Fig. 2

schlieren system, and a 35 mm camera. The 25 μs flash was synchronized with the time when the pressure inside the chamber attained a predetermined value.

The pressure variations during flame propagation were recorded using two pressure transducers T_1 and T_2 shown in Fig. 1. The signals obtained by them were amplified and recorded with a waveform storage system and displayed on the screen of a synchroscope as well as a pen recorder.

Results and Discussion

Behavior of Propagating Flames. A series of schlieren photographs illustrating flame propagation through a methane-air mixture with $\phi = 1.1$ is presented in Fig. 2. In the figure, t represents the time after the first pressure wave (rarefaction wave) passes the flame front.

A smooth flame front is propagating from left to right in Fig. 2 before the first pressure wave passes. Even after the first pressure wave passes the flame front, perceptible turbulence does not appear until $t \simeq 1$ ms. When t becomes larger than 1 ms, fine turbulence having very small amplitude appears at the central part of the flame front, far from the walls of the combustion chamber. The disturbance grows gradually, and at $t \simeq 3$ ms, the fine structure behind the leading flame front becomes appreciable in size. Afterward, the flame front turbulence continues to develop although the rate of development fluctuates.

A schlieren photograph representing the detailed structure of the flame front, at an early stage, is presented in Fig. 3. The recorded pressure variation and flash timing are shown in Fig. 4. The instant determined on Fig. 4 indicates that the photograph presented in Fig. 3 was taken at $t \simeq 2$ ms. Turbulence observed at the central part of flame can be clearly examined. The scale of the flame front turbulence at this moment is seen to be 3 mm ~ 6 mm.

The overall movements of the flame fronts for several cases were measured and represented in position-time, x-t, diagrams. Figure 5 shows the x-t diagram for the case presented in Fig. 2. The distance from the position of the leading flame front at $t = 0$ is represented by x. It can be seen that the flame velocity fluctuation begins just after the first pressure wave (rarefaction wave) passes the flame front. The flame velocity fluctuation must be induced by the overall gas velocity fluctuations, which are obviously coupled with the pressure wave. Figure 6 shows the pressure variation recorded in the case presented in Fig. 2. By comparing Fig. 5 with Fig. 6, the flame velocity-pressure coupling is confirmed.

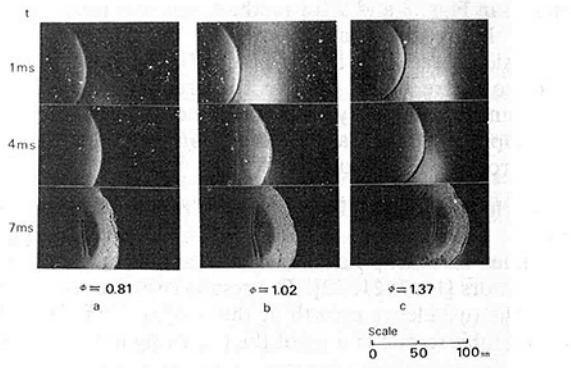

Fig. 7 Effect of the amplitude of pressure fluctuations on turbulence development at flame fronts propagating through a methane-air mixture with $\phi = 0.9$.

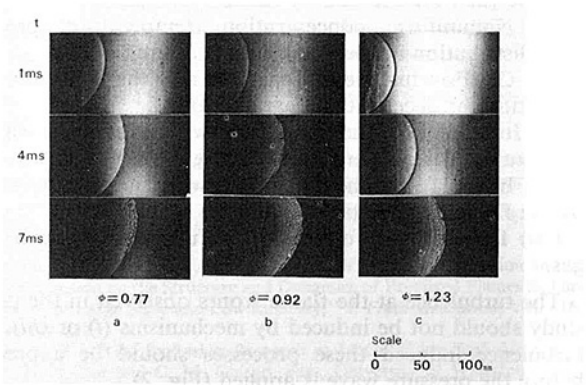

Fig. 8 Turbulence development at flame fronts propagating through methane-air mixtures having various compositions; $l = 40$ mm

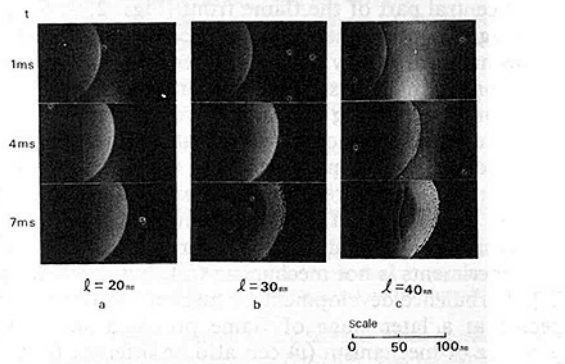

Fig. 9 Turbulence development at flame fronts propagating through propane-air mixtures having various compositions; $l = 40$ mm

Various Effects on Turbulence Development. The effect of the pressure wave intensity on turbulence growth at propagating flame fronts was examined by changing the length l of the small chamber. Typical results are shown in Fig. 7. For each length l, three schlieren photographs at $t = 1$, 4, and 7 ms are presented. For $l = 20$ mm, no perceptible turbulence can be found in the set of photographs. For $l = 30$ mm, a trace of turbulence appears at $t = 1$ ms, and appreciable turbulence is observed at the central part of the flame front when $t = 4$ ms. When $t = 7$ ms, the intensity and scale of turbulence are found to be much larger than those for $t = 4$ ms. For $l = 40$ mm, slight turbulence, similar to that at $l = 30$ mm, appears at $t = 1$ ms, and the turbulence amplitude at $t = 4$ ms and 7 ms is much larger than that for $l = 30$ mm at the same value of t.

The effect of fuel concentration on the processes of the turbulence growth was also examined. Representative results are

shown in Figs. 8 and 9 for methane–air and propane–air mixtures. It is seen that the effects of fuel type and fuel equivalence ratio on the turbulent flame fronts at the same value of t are slight. Despite the predictions by Clavin and Williams [15, 20], only a slight enhancement of the turbulence development appears at the flame front propagating through a rich propane–air mixture.

Mechanisms of Turbulence Growth in the Present Case. The mechanisms by which a propagating flame becomes turbulent have been studied by a number of investigators [1–17, 21, 22]. The results of these studies indicate that the turbulence growth at the propagating flame front is attributable to one or a set of the following mechanisms:

(*i*) Initial gas flow turbulence in the flammable mixture through which the flame propagates.

(*ii*) Gas flow turbulence in the flammable mixture generated at the shear flow region between the wall or obstacle and the gas flow induced by flame propagation.

(*iii*) Nonuniform concentration (temperature, pressure, etc.) distribution in the flammable mixture.

(*iv*) Gas flow turbulence generated near the flame due to acceleration (or deceleration) parallel to it.

(*v*) Interaction of the flame front with an acoustic wave, or acceleration (or deceleration) of the gas flow normal to it.

(*vi*) Interaction of the flame front with the gas flow induced by the flame deformation.

(*vii*) Diffusivity differences of the fuel gas from the oxidizer gas.

The turbulence at the flame fronts observed in the present study should not be induced by mechanisms (*i*) or (*iii*), since turbulence induced these processes should be appreciable before the pressure wave is applied (Fig. 2).

If turbulence at the flame front is induced by mechanism (*ii*), the turbulence development should be observed at the flame front near the walls. However, turbulence first appears at the central part of the flame front (Figs. 2, 3, 6, 7, and 9). Although the possibility of turbulence generation attributable to mechanism (*ii*) may not be rejected, the rate of turbulence development must be so small that any perceptible turbulence is not observed during the early stages of flame propagation.

At the central part of the propagating flame front, the gas flow induced by the pressure wave would be normal to the flame front. Therefore, the appearance of turbulence at the central part of the flame front implies that an effective mechanism for generating flame front turbulence in the present experiments is not mechanism (*iv*), but mechanism (*v*) [2, 23]. Turbulence development by mechanism (*iv*) would be expected at a later stage of flame propagation [7, 17]. The presence of mechanism (*v*) can also be inferred from the fact that the development of flame front turbulence depends largely on the pressure wave intensity [2, 23].

The effectiveness of the mechanism (*vi*) is not so easy to evaluate, although it must be large for the present study [1–4].

The turbulence development for a flame front propagating through a propane–air mixture with $\phi = 1.37$ seems to be faster than for any of other mixtures presented in Figs. 2, 7, 8, and 9. This phenomenon must be attributable to the differential diffusion [15, 20], i.e., the turbulence development seems to be slightly enhanced by mechanism (*vii*) in certain cases.

By closely examining the turbulence appearing on the series of high-speed schlieren photographs presented in Fig. 2, appreciable variation of the turbulence development with time can be found. At $t \simeq 1$ ms, the flame front accelerates and weak turbulence appears at the flame front. Later, at $t \simeq 2$ ms, the flame front decelerates and the turbulence at the flame front does not develop. At $t \simeq 3$ ms, the flame front accelerates again and the turbulence at the flame front starts developing again. The enhancement and suppression of flame front turbulence occur alternately. When the flame front accelerates, flame front turbulence develops rapidly and its scale seems to increase. On the contrary, when the flame front decelerates, the development of flame front turbulence is suppressed, and its scale seems to decrease.

The net rate $(D\mathbf{v}/Dt)_n$ of gas velocity change to deform the flame front configuration can be evaluated by using the following relation [4]

$$\left(\frac{D\mathbf{v}}{Dt}\right)_n = \left(\frac{D\mathbf{v}}{Dt}\right)_t + \frac{1}{\rho}\nabla p^*$$

where $(D\mathbf{v}/Dt)_t$ is the rate of gas velocity change without the effect of the overall acceleration or deceleration of gas. ρ and p^* are the gas density and the pressure which induces the overall acceleration or deceleration of gas, respectively. The rate of the flame front configuration change depends on the value and direction of $(D\mathbf{v}/Dt)_n$.

For the positive or negative value of $(D\mathbf{v}/Dt)_n$, the flame front turbulence developes or diminishes, respectively [4]. The results presented in Fig. 7 indicate that the development of flame front turbulence by a pressure wave scarcely appears when the intensity of pressure wave is less than a limiting value. This fact would imply that $(D\mathbf{v}/Dt)_n$ in the period of acceleration is almost equal to $-(D\mathbf{v}/Dt)_n$ during deceleration. This situation is possible if the deformation of the flame front is so slight that $(D\mathbf{v}/Dt)_t$ is very small compared to $(1/\rho)\ \nabla p^*$. The phenomenon that the turbulence development is enhanced or suppressed, respectively, in an accelerating or decelerating flow field can be proved by simulations based on the above concept [4].

The results of this study, therefore, seem to indicate that the early stage growth of flame front turbulence observed in the present experiments is attributable mainly to mechanism (*v*) while subsequent growth is attributable mainly to mechanisms (*v*) and (*vi*).

Comparison With the Results of Previous Studies. As discussed in the previous section, the main mechanism of the growth of flame front turbulence explored in the present study must be that proposed by Taylor [23] and Markstein [2]. The scale of flame front turbulence caused in this mechanism was predicted to depend on the burning velocity, the density ratio of unburned and burned gases, and the thermal diffusivity [2]. It should be a few mm for a flame propagating through a gaseous paraffin hydrocarbon–air mixture at atmospheric conditions.

The scale of flame front turbulence observed in previous studies, which was assumed to be attributable to the Taylor–Markstein instability, was much larger than the predicted value [2, 11, 12], while that observed in the present study was very close to predictions. This implies that the flame front turbulence observed in the present study refers to the very early stages of turbulence growth.

The behavior of flame front turbulence in an accelerating or decelerating flow field has been examined in a few previous studies [2, 12]. The main differences between the results of the present study and earlier studies are the flame front configuration and the amplitude and frequency of the velocity change. The difference between observed phenomena and conclusions should be attributed to these differences.

Rudinger and Somers [12] observed a large scale deformation of a bubble or burned gas disturbed by a shock wave. Markstein [2] examined the effect of a shock wave on a flame which is initially distorted by passage through a wire grid, and observed rapid inversion of the small-scale structure in the central portion of the flame. These phenomena are apparently very different from the development or suppression of flame front turbulence in an accelerating or decelerating flow field observed in the present study. This difference of overall behavior must be attributable to differences in the scale of turbulence, although the mechanism of the flame front deformation seems to be the same.

Summary and Conclusions

The processes of the growth of flame front turbulence have been experimentally explored when a flame propagating through a uniform nonturbulent flammable mixture is stimulated by a weak pressure wave. The weak pressure wave used to stimulate flame was generated by breaking a membrane separating a small chamber from the combustion chamber. The behavior of each propagating flame was examined using high speed schlieren photography.

During a period lasting about one millisecond after the first weak pressure wave (rarefaction wave) passed the flame front, perceptible turbulence could not be observed at the flame front. Then, flame front turbulence became detectable at the central part of the flame front and its amplitude increased rapidly, while no effect of the wall turbulence appeared.

The effects of the pressure wave intensity, fuel concentration, and fuel type on the growth of the flame front turbulence were examined. The growth of flame front turbulence was found to depend largely on the intensity of pressure wave, for a definite intensity of pressure wave, although a slight effect of the selective diffusion could be found.

The most remarkable fact revealed by this study concerns the effect of flame front velocity changes on flame front turbulence. When the flame front accelerated, flame front turbulence developed rapidly, and its scale seemed to increase. On the contrary, when the flame front decelerated, the development of flame front turbulence was suppressed, and its scale seemed to decrease.

The mechanisms of turbulence growth were discussed, and it is inferred that the early stage growth of flame front turbulence observed in the present experiments is attributable mainly to mechanism (*v*) with later growth attributable mainly to mechanisms (*v*) and (*vi*).

By comparing the scale of flame front turbulence observed in the present study with those observed in the previous studies, it becomes evident that the flame front turbulence observed in the present study refers to a very early stage of turbulence growth.

Acknowledgments

Support of this work was provided by a Grant-in-Aid for Scientific Research from the Ministry of Education, Science and Culture in Japan.

References

1 Landau, L. D., and Lifshiz, E. M., *Fluid Mechanics*, J. B. Sykes and W. H. Reid, Translators, Pergamon Press, Oxford, 1959, Chap. 16.

2 Markstein, G. H., *Nonsteady Flame Propagation*, Pergamon Press, Oxford, 1964.

3 Williams, F. A., "Laminar Flame Instability and Turbulent Flame Propagation," in: *Fuel-Air Explosions*, J. H. S. Lee and C. M. Guirao, eds., University of Waterloo Press, Waterloo, 1982, pp. 69–76.

4 Tsuruda, T., and Hirano, T., "Numerical Simulation of Turbulence Development at Propagating Flame Fronts," *10th International Colloquium on Dynamics of Explosions and Reactive Systems*, Berkeley, Aug. 1985.

5 Yao, C., "Experimental Venting of Low-Strength Equipment and Structures," *Loss Prevention*, Vol. 8, 1974, pp. 1–9.

6 Solberg, D. M., "Experimental Investigations of Flame Acceleration and Pressure Rise Phenomena in Large Scale Vented Gas Explosions," *3rd International Symposium on Loss Prevention and Safety Promotion in the Process Industries*, Basel, 1980.

7 Hirano, T., "Some Problems in the Prediction of Gas Explosions," in: *Fuel-Air Explosions*, J. H. S. Lee and C. M. Guirao, eds., University of Waterloo Press, Waterloo, 1982, pp. 823–839.

8 Hirano, T., "Gas Explosion Processes in Enclosures," *Plant/Operation Progress*, Vol. 3, No. 4, Oct. 1984, pp. 247–254.

9 Jones, W. P., and Whitelaw, J. H., "Modeling and Measurements in Turbulent Combustion," *Twentieth Symposium (International) on Combustion*, The Combustion Institute, Ann Arbor, MI, 1984, pp. 233–249.

10 Leyer, J. C., and Manson, N., "Development of Vibratory Flame Propagation in Short Closed Tubes and Vessels," *Thirteenth Symposium (International) on Combustion*, The Combustion Institute, Pittsburgh, PA, 1971, pp. 551–557.

11 Markstein, G. H., "A Shock-Tube Study of Flame Front–Pressure Wave Interaction," *Sixth Symposium (International) on Combustion*, The Combustion Institute, Pittsburgh, PA, 1957, pp. 387–398.

12 Rudinger, G., and Somers, L. M., "Behaviour of Small Regions of Different Gases Carried in Accelerated Gas Flows," *J. Fluid Mechanics*, Vol. 7, 1961, pp. 161–179.

13 Andrews, G. E., Bradley, D., and Lwakabamba, S. B., "Turbulence and Turbulent Flame Propagation – A Critical Appraisal," *Combustion and Flame*, Vol. 24, 1975, pp. 285–304.

14 Libby, P. A., and Williams, F. A., *Turbulent Reacting Flows*, Springer-Verlag, New York, 1980.

15 Clavin, P., and Williams, F. A., "Effects of Molecular Diffusion and of Thermal Expansion on the Structure and Dynamics of Premixed Flames in Turbulent Flows of Large Scale and Low Intensity," *J. Fluid Mechanics*, Vol. 116, 1981, pp. 251–282.

16 Lee, J. H., "Gas Explosion Research at McGill," in: *Fuel-Air Explosions*, J. H. S. Lee and C. M. Guirao, eds., University of Waterloo Press, Waterloo, 1982, pp. 753–770.

17 Oran, E. S., Boris, J. P., Young, T. R., Fritts, M. J., Picone, M. J., and Fyfe, D., "Numerical Simulation of Fuel-Air Explosions: Current Methods and Capabilities," in: *Fuel-Air Explosions*, J. H. S. Lee and C. M. Guirao, eds., University of Waterloo Press, Waterloo, 1982, pp. 447–473.

18 McCann, D. P. J., Thomas, G. O., and Edwards, D. H., "Gasdynamics of Vented Explosions. Part 1: Experimental Studies," *Combustion and Flame*, Vol. 59, 1985, pp. 233–250.

19 Kaneko, H., "The Effects of Extinguishing Agents on the Premixed Flame Behavior," *22nd Symposium on Combustion (Japan)*, Tokyo, Nov. 1984.

20 Clavin, P., "Dynamical Behavior of Premixed Flame Fronts in Laminar and Turbulent Flows," *Progress in Energy and Combustion Science*, Vol. 11, p. 1, 1985.

21 Zalosh, R. G., "Gas Explosion Tests in Room Size Vented Enclosures," *Loss Prevention*, Vol. 13, 1979, pp. 98–110.

22 Solberg, D. M., Pappas, J. A., and Skramstad, E., "Observations of Flame Instability in Large Scale Vented Gas Explosions," *Eighteenth Symposium (International) on Combustion*, The Combustion Institute, Pittsburgh, PA. 1981, pp. 1607–1614.

23 Taylor, G. I., "The Instability of Liquid Surfaces When Accelerated in a Direction Perpendicular to Their Planes. I." *Proc. Roy. Soc. (London) A*, Vol. 201, 1950, pp. 192–196.

Y. Hasemi
Building Research Institute,
Ministry of Construction,
Oho-machi, Tsukuba-gun,
Ibaraki-ken, 305, Japan

T. Tokunaga[1]
Faculty of Science and Technology,
Science University of Tokyo,
Noda-City, Chiba-ken, Japan

Deterministic Modeling of Unconfined Turbulent Diffusion Flames

An analytical model of the deterministic properties of turbulent diffusion flames is derived using a similarity analysis. Some parameters appearing in the model are quantified by experiments using porous round burners with propane as the fuel. The validity of the model is verified by experiments as well as by comparing the theory with previous experimental work. The model shows that the deterministic properties are insensitive to material properties.

Introduction

The turbulent diffusion flame formed above a burning object plays a significant role in the growth of a building fire during its relatively early stages. As a radiation source, it influences preheating of the surfaces of the fire compartment, or, as a pump, by driving hot smoke to the ceiling layer. The practical flame properties concerning aspects of fire safety are flame geometry, characteristic flame temperature, extinction coefficient, and mass flow rate within the flame. Among these properties, flame geometry in an unconfined quiescent environment has been studied [1–5]. Dimensional analysis of the flame geometry has established the dependence of flame height on Q^2/D^5 [1]. Steward [2] has shown that this relation can be reproduced by an integral model based on the hypothesis that the entrainment velocity at a given height is proportional to the maximum upward velocity at that height. While the flame height has been conventionally calculated using Steward's model, recent measurements [3, 6–8] seem to show that this hypothesis is not satisfied in the near field of a turbulent diffusion flame.

The purpose of this paper is to derive a mathematical model of turbulent diffusion flames to predict deterministic flame properties using assumptions consistent with measurements. Experiments using porous round propane burners were also conducted to estimate a few parameters appearing in the model. The model will be verified by comparing the theory with the current experimental results. The significance of Q^2/D^5 will be represented by $Q^* = Q/\rho_0 C_p T_0 g^{1/2} D^{5/2}$ [4].

Modeling of the Macroscopic Properties of Turbulent Diffusion Flames

Assumptions of the Model. The following assumptions are employed to formulate the basic equations describing the deterministic properties of turbulent diffusion flames:

(*a*) The shape of a turbulent diffusion flame can be approximated as a cylinder.

(*b*) The centerline temperature of the flame is constant.

(*c*) The transverse distribution of excess temperature and vertical velocity satisfies similarity conditions.

(*d*) The burning rate at every height is proportional to the air entrained in the flame at that height.

(*e*) The specific heats of air, fuel gas, and combustion products are equal and independent of temperature.

(*f*) Buoyancy is given by $\rho_0 g\beta\theta$. The Boussinesq approximation for buoyancy is to be applied in solving basic equations.

Assumptions (*a*) and (*b*) are consistent with the qualitative features of the profile of excess temperature and velocity within the continuous flaming region observed in experiments [6, 7], although there is some reduction in centerline temperature in the very low region of a diffusion flame [6, 9]. Assumption (*b*) also implies that the flame height is defined as the height where the centerline temperature starts to decline. Under these assumptions, upward velocity and excess temperature are described as $w = Az^n \cdot W(\eta)$ and $\theta = B \cdot \Theta(\eta)$ where $\eta = r^2/x^2$ and x is a characteristic flame width. Besides the usual errors introduced by the Boussinesq approximation of (*f*), in this application it has been already proved that the Boussinesq approximation will result in a wider profile than experimental results for the bottom of the intermittent flaming region [8]. The main difference between the present and Steward's models is the adoption of (*a*) and (*b*) instead of his entrainment hypothesis. A few additional assumptions will be employed in this context.

Basic Equations and Integral Equations. Under assumption (*f*), the basic equations of the flow in the continuous flaming region can be written as

$$u\frac{\partial w}{\partial r} + w\frac{\partial w}{\partial z} \simeq -\frac{1}{r}\frac{\partial}{\partial r}(r\,\overline{u'w'}) + g\beta\theta \tag{1}$$

$$u\frac{\partial \theta}{\partial r} + w\frac{\partial \theta}{\partial z} \simeq -\frac{1}{r}\frac{\partial}{\partial r}(r\,\overline{u'\theta'}) + q - q_r \tag{2}$$

$$\frac{\partial ru}{\partial r} + r\frac{\partial w}{\partial z} = 0 \tag{3}$$

In the following analysis, the turbulent transport of momentum and energy, $\overline{u'w'}$ and $\overline{u'\theta'}$ will be approximated using the Boussinesq hypothesis as $\overline{u'w'} \simeq -K_w \partial w/\partial r$ and $\overline{u'\theta'} \simeq -K_\theta \partial\theta/\partial r$. Although the turbulent vertical motion in the turbulent flame should be vigorous, the vertical turbulent transport terms were ignored in equations (1) and (2) due to the considerably smaller gradient of w or θ in the vertical direction than in the horizontal direction. Substituting $w = A \cdot z^n \cdot W(\eta)$ and $\theta = B \cdot \Theta(\eta)$ into equation (1) leads to the result $n = 1/2$. Using this result in assumption (*d*) leads to

$$2\pi C_p \int_0^\infty \rho q r dr = \frac{2\pi H_c s}{m}\frac{d}{dz}\int_0^\infty \rho w r dr$$

$$= \frac{\pi H_c s \rho_A A x^2}{2m\sqrt{z}}\int_0^\infty W(\eta)d\eta \tag{4}$$

where ρ_A is the characteristic flame density for mass flux defined as

[1] Present address: Tokunaga Real Estate Co., Saijo-City, Ehime-ken, Japan.

Contributed by the Heat Transfer Division and presented at the 21st National Heat Transfer Conference, Seattle, Washington, July 24–28, 1983. Manuscript received by the Heat Transfer Division March 28, 1984.

$$\rho_A = \frac{\int_0^\infty \rho w r dr}{\int_0^\infty w r dr} \tag{5}$$

For the assumed w and θ similarity to hold, equation (4) requires that heat release rate be proportional to $z^{-1/2}$. This result is also obtained by assuming that the convective fraction of the heat release at each height is constant in equation (2), i.e.

$$2\pi C_p \cdot \frac{d}{dz}\int_0^\infty \rho w \theta r dr = \frac{\pi \rho_B C_p A B x^2}{2\sqrt{z}} \int_0^\infty W(\eta)\Theta(\eta) d\eta$$

$$= 2\pi C_p \int_0^\infty \rho (q - q_r) r dr = 2\pi C_p k \int_0^\infty \rho q r dr \tag{6}$$

where ρ_B is the characteristic flame density for convective heat flux defined as

$$\rho_B = \frac{\int_0^\infty \rho w \theta r dr}{\int_0^\infty w \theta r dr} \tag{7}$$

Cox and Chitty [7] have shown by experiments that both the height and the width of a turbulent diffusion flame are proportional to the 2/5 power of the heat input for Q^* of order 1 or greater. In order to demonstrate that the above form of w and θ is consistent with this, we integrate equation (6) with respect to z from 0 to L_F yielding

$$kQ = \pi \rho_B C_p A B x^2 \sqrt{L_F} \int_0^\infty W(\eta)\Theta(\eta) d\eta \tag{8}$$

Since the underlined part of the above equation must be constant, we have the following relationship describing the dependence of flame geometry on heat input

$$2\lambda + \kappa/2 = 1 \tag{9}$$

where x and L_F are assumed to be related to Q by $x \propto Q^\lambda$ and $L_F \propto Q^\kappa$. For $Q^* \gtrsim 1$, equation (9) is consistent with the experiment of Cox and Chitty [7] and the analysis of Markstein [10] who assumed a fully buoyancy-controlled, turbulent symmetric flame and geometric similarity. For Q^* less than order 1, κ has been found to be 2/3 [11, 12], and therefore λ is expected to be $\lambda = 1/3$; this implies that the flame widths of small Q^* flames are slightly less sensitive to heat input than those of large Q^* flames.

The eight unknown parameters in the above formulae can be classified into two groups: A, B, L_F, and x are regarded as the "resultant properties" of the more basic properties m, k, $\int_0^\infty W(\eta)d\eta$, and $\int_0^\infty W(\eta)\cdot\Theta(\eta)d\eta$. The goal here will be to obtain functional relationships between the resultant properties and the basic properties, and finally determine parameters appearing in these relationships by experiments.

Integrating equation (4) with respect to z from 0 to L_F, we have a second relationship for the above unknowns

$$Q = \frac{\pi H_c s \rho_A A x^2 \sqrt{L_F}}{m} \int_0^\infty W(\eta) d\eta \tag{10}$$

According to Yumoto et al.'s chemical analysis on pool fires [9], most of the reaction heat (more than 85 percent) is generated in the region where the center-line temperature is constant. Therefore, we will assume for simplicity that the total heat release rate of a fire is generated in this region. We will also assume that m and the integral properties are independent of the material properties of fuels. The convective fraction of released heat k must depend on fuels, and the characteristic flame densities ρ_A and ρ_B must depend on the center-line temperature and the integral properties.

One Solution of the Basic Equations. A, B, $\int_0^\infty W(\eta)d\eta$, and $\int_0^\infty W(\eta)\Theta(\eta)d\eta$ are dependent on the flow dynamics in the flame region. Since it is thought to be impossible to solve equations (1)–(3) analytically with consideration of microscopic reaction processes, we try to derive one functional form of $W(\eta)$ and $\Theta(\eta)$ which satisfies equations (1)–(3) on the basis of qualitative impressions on the profiles of vertical velocity and excess temperature. For this purpose, it is useful to define

$$\Phi(\eta) = \int_0^\eta W(\xi) d\xi \tag{11}$$

Nomenclature

A = center-line upward velocity on each height divided by $\sqrt{z}$, $m^{1/2}/s$
B = center-line excess temperature at each height, K
C_p = specific heat of air, kJ/kgK
D = characteristic fuel size (diameter for round fuels), m
d = distance between radiometer and the center of flame, m
E = parameter characterizing the turbulence of flame = $(K\cdot\sqrt{z})$, $m^{5/2}/s$
g = acceleration of gravity, m/s^2
H_c = combustion heat per unit mass of fuel, kJ/kg
K = eddy coefficient, m^2/s
k = convective fraction ratio of heat release
L_F = flame height, m
$M(z)$ = mass flow rate, kg/s
m = air–fuel mass ratio divided by the stoichiometric air–fuel ratio
Q = heat release rate, kW
Q^* = $Q/\rho_0 T_0 C_p g^{1/2} D^{5/2}$
Q_r = radiative power output, kW
q = heat release rate per unit mass divided by specific heat, K/s
q_c = $q - q_r$, K/s
$\dot{q}_r''$ = irradiance, kW/m^2
q_r = radiation loss per unit mass divided by specific heat, K/s
r = radial coordinate, m
s = mass fuel to air ratio (stoichiometric)
T = absolute temperature, K
u = radial velocity, m/s
$W(\eta)$ = function characterizing the profile of upward velocity
w = upward velocity, m/s
x = characteristic flame width, m
z = vertical coordinate, m
β = expansion coefficient, 1/K
η = r^2/x^2
$\Theta(\eta)$ = function characterizing the profile of excess temperature
θ = excess temperature, K
κ = the power representing Q^* dependence of L_F
λ = the power representing Q^* dependence of x
ρ = density, kg/m^3
ρ_A = characteristic flame density for mass flux as defined by equation (5)
ρ_B = characteristic flame density for convective heat flux as defined by equation (7)
$\Phi(\eta)$ = function characterizing the profile of stream function
ψ = stream function, m^3/s

Subscripts

F = flame
a = center line
f = fuel
0 = ambient
max = maximum
w = upward velocity
θ = excess temperature

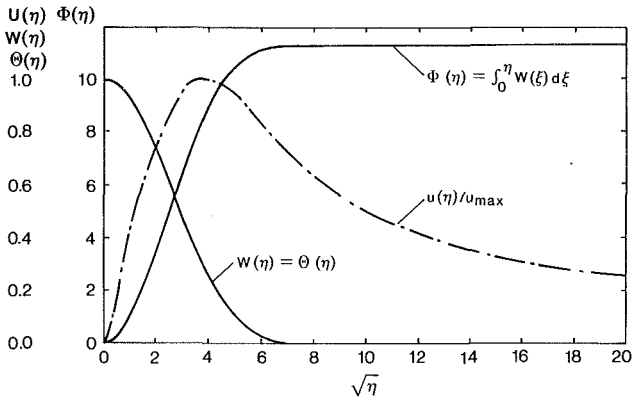

Fig. 1 Transverse distribution of $\Phi(\eta)$, $W(\eta)$, $\Theta(\eta)$, and u/u_{max}

Then equations (1) and (2) become

$$\frac{A^2}{2}\cdot\Phi\cdot\Phi'' - \frac{A^2}{2}\cdot\Phi'^2 = -\frac{4A\sqrt{z}}{x^2}\cdot(K_w\eta\cdot\Phi'')' - g\beta B\Theta \quad (12)$$

$$\frac{AB}{2\sqrt{z}}\cdot\Phi\cdot\Theta' = -\frac{4B}{x^2}\cdot(K_\theta\eta\cdot\Theta')' - q_c \quad (13)$$

where a prime denotes the differential with respect to η, and $q_c = q - q_r$.

For equations (12) and (13) to hold, the power of all terms with respect to z in equations (12) and (13) must be equal. In view of the earlier result $q_c \propto z^{-1/2}$, K_w and K_θ are taken to be proportional to $z^{-1/2}$. Defining $K_w = E_w/\sqrt{z}$ and $K_\theta = E_\theta/\sqrt{z}$, equations (12) and (13) become

$$\frac{4AE_w}{x^2}\cdot(\eta\Phi'')' + \frac{A^2}{2}\cdot\Phi\cdot\Phi'' - \frac{A^2}{2}\cdot\Phi'^2 + g\beta B\Theta = 0 \quad (14)$$

$$\frac{4BE_\theta}{x^2}\cdot(\eta\Theta')' + \frac{AB}{2}\cdot\Phi\cdot\Theta' + q_c\sqrt{z} = 0 \quad (15)$$

In dealing with equations (14) and (15), it should be noted that little is known of the dependence of q_c on η. The general forms of $W(\eta)$ and $\Theta(\eta)$ are known from experiments, i.e., they have their maximum at $\eta = 0$ and tend to decrease gradually with the increase of η [3, 6, 7]. While it has been observed that $W(\eta)$ is slightly wider than $\Theta(\eta)$ in a turbulent diffusion flame, we will assume $\Theta(\eta) = W(\eta)$ for simplicity. This assumption is equivalent to the assumption that equations (14) and (15) are essentially equal, or that $E_w = E_\theta$ $(= E)$ and $q_c(\eta) = B(2g\beta B\Theta - A^2\cdot\Phi'^2)/2A\sqrt{z}$ are taken in these equations.

From the above assumptions, and defining $x^2 = 8E/A$, equation (14) or (15) becomes

$$(\eta\Phi'')' + \Phi\cdot\Phi'' - \Phi'(\Phi' - 2g\beta B/A^2) = 0 \quad (16)$$

The problem is, then, to solve this equation under the following boundary conditions

$$\Phi(0) = 0,\ \Phi'(0) = 1,\ \Phi''(0) = 1 - 2g\beta B/A^2,\ \lim_{\eta\to\infty}\Phi'(\eta) = 0 \quad (17)$$

The value of $V \equiv A^2/2g\beta B = w_a^2/2g\beta\theta_a z$, a constant characterizing the buoyancy, must be calculated simultaneously with $\Phi(\eta)$ while solving equation (16). The uniqueness of solution of this kind of differential equation was proved by Weyl [13]. Figure 1 shows the distribution of $\Phi(\eta)$ and $W(\eta) = \Theta(\eta)$ which results from a numerical integration of equation (16). The value of V which leads to satisfaction of the boundary condition was $V = 0.932$. $W(\eta)$ or $\Theta(\eta)$ in Fig. 1 decreases with increasing $\sqrt{\eta}$ slightly faster than a Gaussian distribution, and it becomes almost zero at $\eta \simeq 7.0$. The radial velocity u is formulated from the definition of the stream function as

$$u = -\frac{1}{r}\frac{\partial\psi}{\partial z} =$$

$$-Ax^2\Phi(\eta)/4r\sqrt{z},\ \psi \equiv \int_0^\eta wrdr = Ax^2\sqrt{z}\Phi(\eta)/2 \quad (18)$$

The maximum of u on every horizontal plane u_{max} appears at $\eta \simeq 3.8$. The distribution of $u(\eta)/u_{max}$ is superimposed on Fig. 1. Since $\Phi(\eta)$ is almost constant for $\eta > 7.0$, u should be almost inversely proportional to the distance from center line in the region far from the axis of the flame.

According to the above results, the two integral properties are

$$\Phi(\infty) = \int_0^\infty W(\eta)d\eta = 11.30$$

$$\int_0^\infty W(\eta)\Theta(\eta)d\eta = 6.06 \quad (19)$$

Substituting the above values into equations (8) and (10), we have

$$B = \frac{kH_c s\Phi(\infty)}{mC_p\int_0^\infty W(\eta)\Theta(\eta)d\eta} = 1.864\,\frac{kH_c s}{mC_p} \quad (20)$$

$$x^2\sqrt{L_F} = \frac{kQ}{\pi\rho_B C_p\sqrt{2g\beta B^3 V}\cdot\int_0^\infty W(\eta)\Theta(\eta)d\eta}$$

$$= 0.121\,\frac{kQ}{\pi\rho_B C_p\sqrt{g\beta B^3}} \quad (21)$$

For $W(\eta)$ and $\Theta(\eta)$ represented as $\exp(-\sigma\eta)$ and for $\rho T =$ const, ρ_A and ρ_B are equal and obtained analytically as [6]

$$\rho_F \equiv \rho_A = \rho_B = \frac{\rho_0 T_0}{B}\cdot\ln(1 + B/T_0) \quad (22)$$

Since $W(\eta) = \Theta(\eta)$ in Fig. 1 is close to a Gaussian distribution of $\sqrt{\eta}$, the characteristic flame density in the present problem may be approximated by equation (22).

The mass flow rate at the height z is

$$M(z) = 2\pi\int_0^\infty \rho wrdr = \pi\rho_F A\Phi(\infty)x^2\sqrt{z} = \frac{1.864kQ}{C_p B}\sqrt{\frac{z}{L_F}} \quad (23)$$

Substituting equation (20) into equation (23), we have

$$\frac{M(z)}{Q} = \frac{m}{H_c s}\sqrt{\frac{z}{L_F}} \quad (24)$$

Equation (24) gives $M(L_F)/Q = m/H_c s$, which can be also derived from the definition of the excess air ratio. The dependence of mass flow rate on z is slightly weaker than the corresponding dependence proposed by McCaffrey [6].

Experimental Estimation of Parameters and Model Verification

The present model can be completed by formulating three additional relationships on the deterministic properties. The convective fraction of heat release k, the air-fuel mass ratio divided by the stoichiometric air-fuel ratio m, and the parameter characterizing turbulence E are the parameters governing the phenomena other than the physical and material properties; the purpose of this section is to estimate these parameters by experiment to complete the model and to verify its validity.

The experiments were conducted using porous burners of

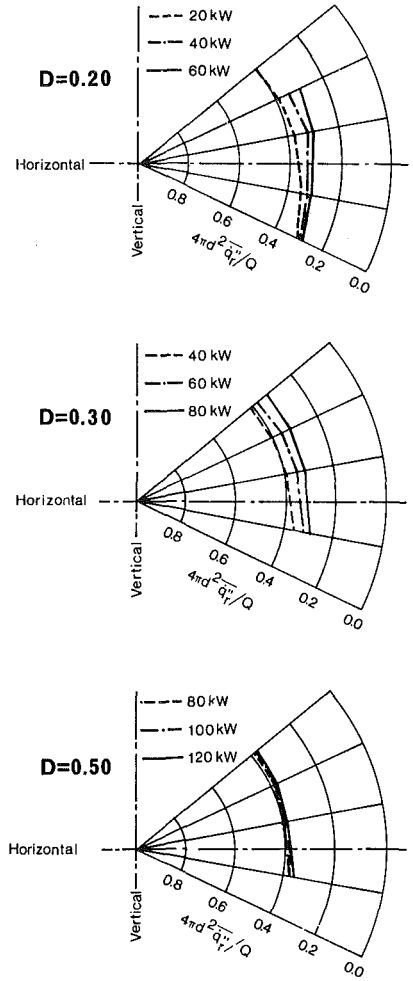

Fig. 2 Directivity of the radiation from turbulent diffusion flames using propane burners

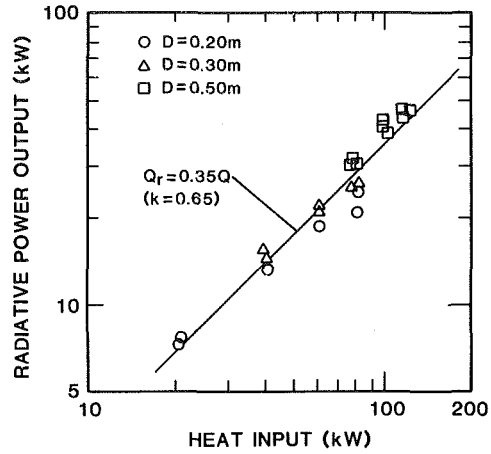

Fig. 3 Radiative power output versus heat input (for diffusion flames from propane burners)

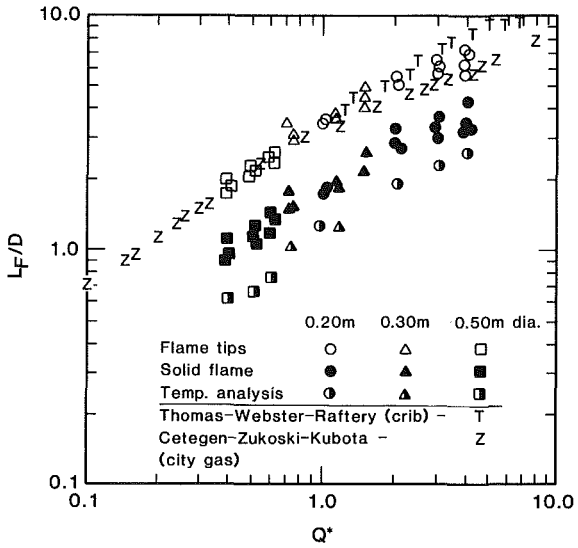

Fig. 4 Q* dependence of flame height

0.20 m, 0.30 m, and 0.50 m diameter with propane as the fuel. The burners were filled with ceramic beads of approximately 8 mm diameter. Burner conditions were chosen to simulate the early stage of compartment fires. Complete combustion was assumed in the heat input estimation. The values of Q^* cover the range of 0.4 to 4.0; this represents conditions of most natural fires without external radiation [12]. The burners were placed 0.50 m above the floor of a 27 m × 20 m × 27 m (H) confined space.

Estimation of m and E were made indirectly by measuring center-line temperature, whereas k was estimated from radiation measurements. Flame height was determined by the height where the center-line temperature starts to decline. However, visible flame height, the height of flame tips and continuous flame, was also observed for reference. The height of the flame tips is defined as the limit above which flame has never been observed by eye during each experiment. This height was consistent with the flame height in the same definition observed by a videotape. The height of continuous flame is the limit below which flame has been always observed by a videotape.

Temperature was measured with 0.1 mm diameter chromel-alumel thermocouples. The time constant of the temperature measurement system is approximately 10 s. No corrections have been made for the radiation losses from the junction of each thermocouple. Soot buildup as thick as the radius of the thermocouple junctions was observed on some thermocouples after each experiment. These errors may lead to an underestimate of gas temperature. For a 0.1–0.2 mm diameter chromel-alumel thermocouple with an emissivity of around 0.9, the error due to radiation loss will range from 2 to 20 percent over the temperature range 300–1000°C. To eliminate the influence of accidental sway of the flame, the average of the temperature output for each measurement point was obtained over more than 20 min at intervals of 10 s. The average of static pressure obtained by a bidirectional pressure probe [14] using a sampling time of more than 4 min was used to estimate the upward velocity.

Radiative fraction of heat release was estimated with a single wide-angle Schmidt–Boelter thermopile radiometer (Tokyo Seiko, RE-III[2]) viewing the flames at a considerable distance which allows the assumption of radiative isotropy. Theoretical verification of the radiative isotropy for various distances between a radiometer and a diffusion flame was given by Modak and Croce [15]. The radiation center of a flame was assumed at the center of the continuous flame, since the contribution of the intermittent flaming region to the flame radiation is believed to be fairly insignificant [16]. Errors of the radiation measurements should be within 10 percent for a gray body of the same temperature range as the flame.

Energy balance was made by comparing the estimated heat

[2]No endorsement by BRI is implied.

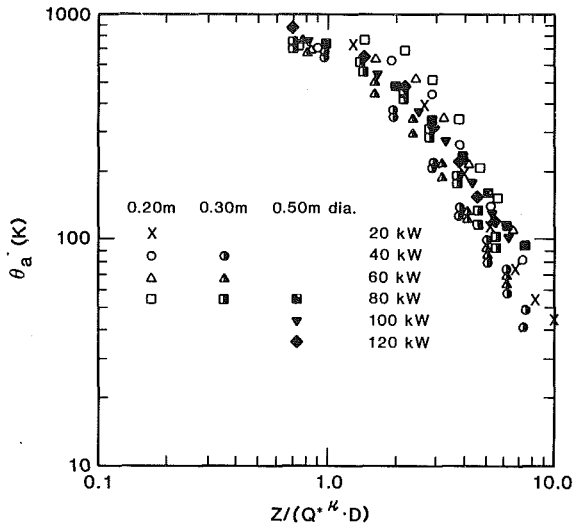

Fig. 5 Center-line excess temperature versus $z/Q^{*\kappa} \cdot D$

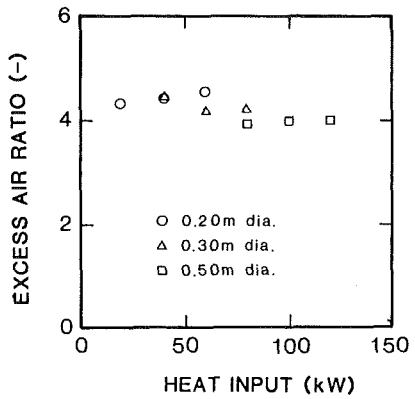

Fig. 6 Estimated excess air ratio versus heat input

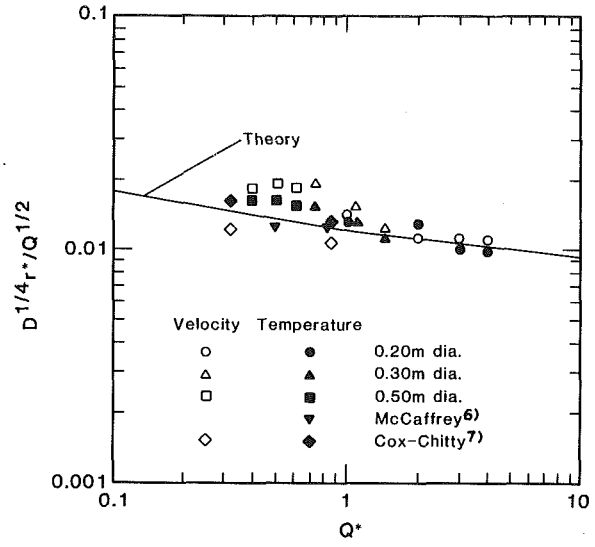

Fig. 7 Theoretical and experimental relationships between $D^{1/4} \cdot r^*/Q^{1/2}$ and Q^*

input with the sum of the radiative power output and the convective heat flow estimated from the measurements of temperature and upward velocity at 2.5 m above the burner surface. The sum of the radiative power output and convective heat flow was always 4–14 percent lower than the estimated heat input. Most of this disagreement is believed to result from incompleteness of the combustion and radiation errors in the temperature measurements. Burner exit velocity was measured for the 0.50 m diameter burner at an interval of 0.025 m between the burner center and the burner wall at 0.015 m above the burner surface. The velocity was found to be uniform within ±7 percent. Burner exit velocity for the smaller burners is believed to be more uniform.

Estimation of Parameters

Convective Fraction of Heat Release. The convective heat to heat release ratio k is estimated from $k = 1 - Q_r/Q$, since the measurement of radiative power output Q_r is believed to be more accurate than the measurement of convective heat flow in the present experiment. Q_r is estimated by the average irradiance $\dot{q}_r''$ on a spherical surface surrounding the flame.

Radiation measurements were made at four to five points on a vertical circle viewing its center at the center of the continuous flame. The distance between the radiometer and the radiation center was five times the burner diameter. Figure 2 shows the distribution of the irradiance on the circle. The distribution appears to be fairly uniform, which implies that the assumption of the radiative isotropy holds for this measurement. Figure 3 shows the correlation between heat input and radiative power output; Q_r/Q remains almost constant irrespective of fuel size and heat input. This result is consistent with the measurement of flame radiation by Markstein [10] on large Q^* flames and by Modak et al. [15] on PMMA pool fires. Thus, the convective fraction to heat release ratio k for the present experiment is estimated within a narrow range, $k = 0.6$–0.7. However, the value of k must also depend on the fuel composition, as McCaffrey [17] has shown that radiative fraction tends to increase with C/H ratio for hydrocarbons.

Parameter E. The parameter E can be estimated from equation (21) as

$$E = \frac{Ax^2}{8} = \frac{0.0151kAQ}{\pi\rho_F C_p\sqrt{g\beta B^3 L_F}} = \frac{0.0206kQ}{\pi\rho_F C_p B\sqrt{L_F}} \tag{25}$$

The unknown parameters on the right-hand side of equation (25) – ρ_F, B, and L_F – are estimated using the temperature measurements along the center line.

Figure 4 shows the Q^* dependence of the flame height based on temperature, together with the visible flame heights. The slope of the data appears to be steeper for $Q^* < 1$ than for $Q^* > 1$; the proportionality can be represented as

$$L_F = \gamma \cdot Q^{*\kappa} \cdot D \tag{26}$$

where $\kappa \simeq 2/3$ for $Q^* < 1$ and $\kappa \simeq 2/5$ for $Q^* \gtrsim 1$. The value of γ should be $\gamma \simeq 1.2$ for the present temperature analysis based on assumption (*b*), $\gamma \simeq 1.8$ for optically continuous flame and $\gamma \simeq 3.5$ for flame tips. While γ must depend on the fuel, the value of γ for the flame tips is close to γ, explaining the flame height data of Thomas et al. [1] on wood cribs by eye and those of Cetegen et al. [11] for natural gas by photographic analysis.

Figure 5 shows the center-line excess temperature as a function of the height above the fuel surface, normalized by $Q^{*\kappa} \cdot D$. The center-line excess temperature for $z < 1.2Q^{*\kappa} \cdot D$, B, was nearly constant irrespective of fuel size, and consequently, the characteristic flame density ρ_F is estimated from equation (22) as $\rho_F = 0.57$ for $B = 800$ K and $T_0 = 300$ K for the present experiment. E can be formulated with $L_F = 1.2 \cdot Q^{*\kappa} \cdot D$ as

$$E/Q \simeq 0.000041k/\pi C_p Q^{*\kappa/2} D^{1/2} \tag{27}$$

Air-Fuel Mass Ratio Divided by the Stoichiometric Air-Fuel Ratio. Air-fuel mass ratio divided by the stoichiometric air-fuel ratio m can be estimated from B and k using equation (20) as

$$m = 1.864kH_c s/C_p B \tag{28}$$

The range of m estimated by equation (28) for the present experiment, $m \simeq 4.0$–4.3 (Fig. 6), is close to the estimate of Steward [2], $m \simeq 4.0$, although the structure of the present model is considerably different. While Zukoski et al. [4] have estimated $m \simeq 15$ by mass flow measurements at the height of flame tips, the present estimate seems to be still consistent with them because the mass flow rate at the height of the flame tips is approximately three times the mass flow rate at the height of continuous flame [8].

Summary of the Model. Summarizing the above discussion to formulate A, B, L_F, and $M(z)$ as functions of the properties and conditions of fuel, we have

$$\begin{aligned} A &= 1.864(g\beta k H_c s/mC_p)^{1/2} \\ B &= 1.864 k H_c s/mC_p \\ L_F &= 7.30\times 10^4 (mC_p/\rho_F k H_c s)^2 \cdot Q^{*\kappa} D \\ M(z)/Q &= 0.00370 \rho_F k (z/Q^{*\kappa} D)^{1/2}/C_p \end{aligned} \tag{29}$$

where $\kappa = 2/5$ for $Q^* \gtrsim 1$ and $\kappa = 2/3$ for $Q^* < 1$.[3] ρ_F can be estimated from equation (22). $m = 4.0$ and $k = 0.65$ will lead to good practical estimates of the above properties. The reaction heat per unit mass of air, $H_c s$, is nearly constant for most of the natural fuels, e.g., $H_c s = 2.7\times 10^3$ kJ/kg is adequate for organic gases and liquids within the error of 6 percent. The value of $H_c s$ of synthetic polymers and typical natural fuels such as cellulose and coal is slightly higher than this value (see Huggett [19]). Consequently, the above deterministic properties are only functions of fuel size and heat release rate; therefore, the following results hold for engineering problems concerning building fires

$$\begin{aligned} &w_a \simeq 7.0\sqrt{z} \text{ [m/s]}, z \text{ [m]} \\ &\theta_a \simeq 810 \text{ [K]} \\ &L_F \simeq 0.072 Q^{2/5} \text{ [m]}, Q \text{ [kW]}, Q^* \simeq 0.0009 Q/D^{5/2} \gtrsim 1 \\ &\quad \simeq 0.011 (Q/D)^{2/3} \text{ [m]}, D \text{ [m]}, Q^* < 1 \\ &M(z)/Q \simeq 0.0056 (z/Q^{2/5})^{1/2} \text{[kg/skW]}, z \text{ [m]}, Q \text{ [kW]}, Q^* \gtrsim 1 \\ &\quad \simeq 0.0142 (zD^{2/3}/Q^{2/3})^{1/2} \text{ [kg/skW]}, D \text{ [m]}, Q^* < 1 \end{aligned} \tag{30}$$

L_F in equations (29) and (30) are based on the center-line temperature; the height of visible continuous flame is approximately 1.5 times L_F and the height of the visible flame tips is approximately three times L_F.

Model Verification. The validity of the present model can be verified by comparing the theory and the experimental values of the center-line velocity and the transverse excess temperature and velocity. Previous experimental work will be also considered for this purpose.

Center-Line Velocity. Since $V = A^2/2g\beta B = 0.932$ must hold irrespective of fuel, the comparison of V between the theory and experiments will be more meaningful than that of velocity. The value of V has been measured in some previous experiments [6, 7]; the theoretical value of V is close to McCaffrey's ($V = 0.869$, [6]) and the present experiment ($V = 0.85$), whereas the result of Cox et al. ($V = 0.69$, [7]) is approximately 25 percent lower than this theory.

Transverse Excess Temperature and Velocity. The theoretical distribution function, $W(\eta)$ or $\Theta(\eta)$, becomes $1/e$ at $\eta = r^{*2}/x^2 \simeq 12.2$ (Fig. 1). Since the characteristic flame width x is given from equations (27) and (29) by the following equation

$$x^2/Q = 8E/AQ = \frac{0.000176}{\pi}\left(\frac{km}{g\beta C_p H_c s Q^{*\kappa} D}\right)^{1/2} \tag{31}$$

r^* can be estimated for hydrocarbons and alcohols as

$$D^{1/4} \cdot r^*/Q^{1/2} \simeq 0.011 Q^{*-\kappa/4} \tag{32}$$

Figure 7 compares equation (32) with the experimental results for r^*. Although the profile of excess temperature is somewhat different from the velocity profile in each experiment, the agreement of the theory with experiments seems to be good.

Conclusions

A deterministic model of turbulent diffusion flames has been derived using similarity analysis and measurements of radiative power output and center-line temperatures in flames. This model represents the deterministic properties of turbulent diffusion flames in terms of physical constants, material properties of the fuel and parameters representing turbulence and the convective fraction of heat release.

The model derived in this paper is apparently consistent with previous measurements of the distribution of excess temperature and upward velocity. The estimated mass flow rate is approximately 25 percent lower than McCaffrey's estimate [6] based on his own theory; this discrepancy seems to result from the faster decrease of $\Phi'(\eta)$ than the Gaussian distribution which he selected for the temperature and velocity profiles. Measurement of mass flow rate is essential to discuss the validity of this model. This theory also shows that the deterministic properties are not significantly dependent on material properties of the fuel but mainly on the intensity and the size of the fuel, assuming the independence of m and E on material properties and flame temperature. This hypothesis still needs to be examined, although the above result seems to be consistent with empirical knowledge of turbulent diffusion flames.

Acknowledgments

The authors are grateful to Mr. H. Matsumoto of the Japanese Building Research Institute who designed and fabricated the fuel supply systems including the burners. The authors are also indebted to Messrs. H. Nishimura, M. Hayashi, and S. Honda of the Science University of Tokyo, for their assistance in the experiments. The analysis was partly carried out at the Center for Fire Research, NBS, during the stay of one of the authors (Y. Hasemi). He wishes to thank Drs. J. G. Quintiere, B. J. McCaffrey, and J. A. Rockett of CFR for their technical suggestions.

References

1 Thomas, P. H., Webster, C. T., and Raftery, M. M., "Some Experiments on Buoyant Diffusion Flames," *Combustion and Flame*, Vol. 5, 1961, pp. 359–367.

2 Steward, F. R., "Prediction of the Height of Turbulent Diffusion Buoyant Flames," *Combustion Science and Technology*, Vol. 2, 1970, pp. 203–212.

3 Terai, T., and Nitta, K., "On the Plumes Rising From Liquid Fires," *Meeting of Kinki Regional Branch*, Architectural Institute of Japan, 1976, pp. 65–68 [in Japanese].

4 Zukoski, E. E., Kubota, T., and Cetegen, B., "Entrainment in Fire Plumes," *Fire Safety Journal*, Vol. 3, 1980/1981, pp. 107–121.

5 Heskestad, G., "Luminous Heights of Turbulent Diffusion Flumes," *Fire Safety Journal*, Vol. 5, 1983, pp. 103–108.

6 McCaffrey, B. J., "Purely Buoyant Diffusion Flames: Some Experimental Results," NBSIR-79-1910, 1979.

7 Cox, G., and Chitty, R., "A Study of the Deterministic Properties of Unbounded Fire Plumes," *Combustion and Flame*, Vol. 39, 1980, pp. 191–209.

8 Hasemi, Y., "Deterministic Modeling of the Intermittent Flaming Region of the Upward Currents Above Diffusion Flames," *Bulletin of Japanese Association of Fire Science and Engineering*, Vol. 31, 1981, pp. 39–47 [in Japanese].

9 Yumoto, T., and Koseki, H., "Effect of Tank Diameter on Combustion

[3] Recent experiments of Cox [18] using square burners as the fuel show that the slope will become still steeper for $Q^* < 0.5$.

Characteristics of Heptane Tank Fires," *Report of Fire Research Institute*, No. 55, 1983, pp. 71–80 [in Japanese].

10 Markstein, G. H., "Radiative Energy Transfer From Turbulent Diffusion Flames," *Combustion and Flame*, Vol. 27, 1976, pp. 51–63.

11 Cetegen, B., Zukoski, E. E., and Kubota, T., "Entrainment and Flame Geometry of Fire Plumes," NBS-GCR-82-402, 1982.

12 Hasemi, Y., and Tokunaga, T., "Flame Geometry Effects on the Buoyant Plumes From Turbulent Diffusion Flames," *Fire Science and Technology*, Vol. 4, No. 1, 1984, pp. 15–26.

13 Weyl, H., "On the Differential Equations of the Simplest Boundary-Layer Problems," *Annals of Mathematics*, Vol. 49, 1942, pp. 381–407.

14 McCaffrey, B. J., and Heskestad, G., "A Robust Bidirectional Low Velocity Probe for Flame and Fire Application," *Combustion and Flame*, Vol. 26, 1976, pp. 125–128.

15 Modak, A. T., and Croce, P. A., "Plastic Pool Fires," *Combustion and Flame*, Vol. 30, 1977, pp. 251–265.

16 Orloff, L., and de Ris, J., "Froude Modeling of Pool Fires," *Nineteenth Symposium (International) on Combustion*, 1982, pp. 885–895.

17 McCaffrey, B. J., "Measurements of the Radiative Power Output of Some Buoyant Diffusion Flames," Western States Section, Combustion Institute, 81-15, Pullman, WA, 1981.

18 Cox, G., private communication, 1983.

19 Huggett, C., "Estimation of Heat Release by Means of Oxygen Consumption Measurements," *Fire and Materials*, Vol. 4, No. 2, 1980, pp. 61–65.

K. Muralidhar[1]

R. A. Baunchalk

F. A. Kulacki[2]

Department of Mechanical and Aerospace Engineering, University of Delaware, Newark, DE 19716

Natural Convection in a Horizontal Porous Annulus With a Step Distribution in Permeability

A numerical and experimental study of free convective flow and heat transfer in a horizontal annulus containing saturated porous material is reported in the present study. The special case of a step distribution in permeability, resulting in a two-layer system, has been considered. Both isothermal and constant heat flux boundary conditions have been imposed on the inner wall, while the outer wall is kept at a constant temperature. For the case of isothermal boundaries, a simple resistance law gives rise to a model of permeability which collapses the average Nusselt numbers of the variable permeability problem to that of the uniform case. Generally, agreement between experiments and calculation is satisfactory, although under certain circumstances, a systematic divergence of the data is observed. It is deduced in the present work that this is strictly related to non-Darcy effects.

Introduction

There have been only a few studies of free convection in horizontal porous annuli, as well as outside cylinders buried in a saturated porous medium. These have been both of fundamental importance and at the same time, relevant in technological applications, e.g., nuclear waste disposal technology, buried electric cables, and in analysis of heat transfer through thermal insulation. The basic problem comprises studying flow patterns arising from a nonisothermal field, leading to heat transfer rates beyond the values predicted by conduction alone. A major portion of the literature has focused on uniform porous media, where variation in permeability is limited, mostly to the region near the impermeable boundary. Naturally occurring systems do not allow this simplification and the porous media are frequently nonuniform both on local as well as global scales. Further, it remains to be seen if a deliberate variation in the characteristics of the medium favorably change the heat transfer relationships in any given situation. The present work addresses these questions by considering a two-layer, saturated porous medium in a horizontal annulus. The medium is composed of spherical balls and a step change in permeability distribution is obtained by using balls of two different diameters. Numerical work has been performed to complement measurements of overall heat transfer coefficients. Both isothermal and constant heat flux boundary conditions have been numerically studied, and the latter case has been compared to experiments.

Caltagirone (1976) has studied free convection in a horizontal annulus over a wide range of radius ratios and Rayleigh numbers, assuming the validity of Darcy's law. His calculations are for a two-dimensional flow field and its transition to three-dimensional flow. Burns and Tien (1979) have considered both annular cylinders and spheres in their analytical and numerical work, and have presented results for temperature distribution and overall Nusselt numbers. Brailovskaya et al. (1978) have also analyzed free convective flow in a porous material between horizontal concentric cylinders. Shimomura et al. (1980) have studied high-pressure insulation systems arising in piping technology using a numerical scheme, and have also partly included non-Darcy effects via inertia terms in the fluid phase. The effect of eccentricity on heat transfer has been studied by Bau (1984). The presence of a solid boundary leading to porosity variation adjacent to it has been considered by Vafai and Tien (1980) and Vafai (1984). McKibbin and Tyvand (1981, 1984) have systematically studied onset of convection in a layered porous medium, and have generalized their results to the limit of homogeneous anisotropy. Gjerde and Tyvand (1984) have analytically studied this problem when the number of layers is permitted to be large. However, these calculations are restricted to a plane geometry (for example, as observed in snow layers) and the extension of the problem to include curvature remains incomplete.

Governing Equations

Two-dimensional, steady, incompressible flow and heat transfer in a porous medium can be written in the following form, assuming the validity of Darcy's law and the Boussinesq approximation for the body force terms (Bejan, 1984).

$$a^{\phi}\left[\frac{\partial}{\partial\Theta}\left(\phi\,\frac{\partial\psi}{\partial r}\right)-\frac{\partial}{\partial r}\left(\phi\,\frac{\partial\psi}{\partial\Theta}\right)\right]-\left[\frac{\partial}{\partial\Theta}\left(\frac{b^{\phi}}{r}\,\frac{\partial\phi}{\partial\Theta}\right)+\frac{\partial}{\partial r}\left(b^{\phi}r\,\frac{\partial\phi}{\partial r}\right)\right]=d^{\phi} \tag{1}$$

Here, ϕ is a generic variable representing ψ or T, and the quantities a, b, and d are related to it as given in Table 1. For the geometry shown in Fig. (1), the following boundary conditions apply

$$\begin{aligned} &r=R_1, \quad \psi=0, \quad T=1 \quad \text{or} \quad \frac{\partial T}{\partial r}=-1\\ &r=R_2, \quad \psi=0, \quad T=0\\ &\Theta=0, \quad \psi=0, \quad \frac{\partial T}{\partial\Theta}=0\\ &\Theta=\pi, \quad \psi=0, \quad \frac{\partial T}{\partial\Theta}=0 \end{aligned} \tag{2}$$

Table 1 Coefficients appearing in equation (1)

ϕ	a^{ϕ}	b^{ϕ}	d^{ϕ}
ψ	0	$\frac{\epsilon}{k}$	$-r\ \mathrm{Ra}\left(\sin\Theta\,\frac{\partial T}{\partial r}+\frac{\cos\Theta}{r}\,\frac{\partial T}{\partial\theta}\right)$
T	ϵ	1	0

[1]Presently at Lawrence Berkeley Laboratory, CA.

[2]Presently at Colorado State University, CO.

Contributed by the Heat Transfer Division for publication in the JOURNAL OF HEAT TRANSFER. Manuscript received by the Heat Transfer Division November 22, 1985.

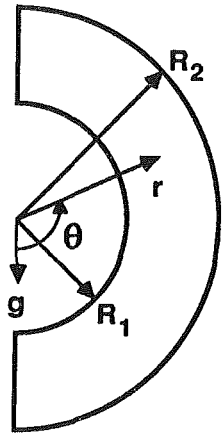

Fig. 1 Flow domain and coordinate system

For prescribed distributions of ϵ and K, equation (1) and associated boundary conditions have been solved by a numerical scheme. This involves using a control volume approach, as described by Gosman et al. (1969) and used successfully by Prasad and Kulacki (1984). A grid refinement procedure has been used in the neighborhood of the curved boundaries so as to maintain an upper limit on the excess energy balance at 2 percent. The r and Θ-directions have been discretized by a 21 × 41 mesh and a convergence criterion of 0.01 percent has been employed. The computer program has been verified by reproducing the results of Caltagirone (1976).

Experiments

In the present study, experimental results have been obtained from a test cell with 200 mm inner diameter, R_2/R_i = 1.516, and 3 and 6 mm diameter glass balls. The porosity of the system filled only with 3 mm balls is 0.375 and for the 6 mm balls, it is 0.383. The corresponding permeabilities calculated from

$$\bar{K} = \frac{\bar{\epsilon}^3 d^2}{180(1-\bar{\epsilon})^2} \tag{3}$$

are 0.675×10^{-8} m^2 and 2.95×10^{-8}m^2, respectively. The layered system is formed by filling the inner half of the annulus ($R_1 < r < (R_1 + R_2)/2$) with beads of one diameter and the outer half with the other. It is assumed that at the interface ($r = (R_2 + R_2)/2$), an arithmetic mean porosity and permeability exist, and these are used as the characteristic values for the entire annulus. The saturating liquid is water in all the experimental runs.

Details of the construction of the test cell, instrumentation, and testing procedure have been described by Baunchalk (1985). The aspect ratio of the apparatus (axial length/gap width) is 12, and hence the flow is close to being two dimensional. The inner cylinder, which is made of brass, is heated by strip heaters to provide a constant heat flux boundary condition. The outer wall is cooled by water carried in copper coils, to maintain an isothermal boundary condition. Temperature has been measured by 30 gage copper-constantan thermocouples. A multichannel data acquisition system has been used to record voltage, current, and temperature readings from the test cell. All test runs have been made under stabilized conditions of flow, and each data point is an average of ten runs taken at 5-min intervals. Typically, one such data point could be obtained every 12 h. Since the inner wall boundary condition corresponds to constant heat flux, the inner Nusselt number is proportional to the reciprocal of the temperature difference between inner and outer walls. All fluid properties have been calculated at a temperature which is the arithmetic mean of inner and outer wall values. The effective thermal conductivity is calculated by repeating experiments in the conduction regime of flow and matching this data with the numerically generated curve. Since the thermal conductivities of water and glass are close to each other, this procedure gives results which are close to the conventional rule of mixtures. Error analysis, including that in temperature measurement and fluid properties, shows that the Nusselt number has an uncertainty of 5.5 percent and the Rayleigh number is uncertain by up to 6.5 percent of the reported value.

Three cases have been identified in the present study. The test cell containing beads of uniform diameter will be referred to as case 1 (or C1); when 3 mm balls occupy the inner half of the annulus, case 2 (or C2); and when 6 mm balls occupy the same space case 3 (or C3). The characteristic temperature difference is that between the walls of the annulus when the inner

Nomenclature

a, b, d = coefficients appearing in equation (1)
c_p = specific heat, J/kg K
D = gap width between cylinders, m; (characteristic dimension)
g = acceleration due to gravity, m/s^2
k_m = stagnant thermal conductivity, W/mK
K = normalized permeability
$\bar{K}$ = permeability in equation (4), m^2
$\mathrm{Nu}_{i\Theta}$ = normalized inner Nusselt number = $-\partial T/\partial r|_{r=R_1}/R_1 \ln(R_2/R_1)$ (isothermal), or $1/T(r = R_1)$ (constant flux)
$\mathrm{Nu}_{o\Theta}$ = normalized outer Nusselt number = $-\partial T/\partial r|_{r=R_2}/R_2 \ln(R_2/R_1)$ (isothermal), or $-\partial T/\partial r|_{r=R_2}/(R_2/R_1)$ (constant flux)
$\mathrm{Nu}_i, \mathrm{Nu}_o$ = average normalized inner and outer Nusselt numbers
q_w = inner wall heat flux, W/m^2
r = dimensionless radial coordinate
R_1, R_2 = dimensionless inner and outer radii of the annulus
Ra = Rayleigh number = $g\beta \Delta T \bar{K} D/\nu\alpha$
S = source terms in equation (1)
T = dimensionless temperature
ΔT = characteristic temperature difference, K: $T_h - T_c$ (isothermal), or $q_w D/k_m$ (constant flux).
u = angular component of velocity, $-\partial\psi/\partial r$
v = radial component of velocity, $(1/r)(\partial\psi/\partial\Theta)$
α = thermal diffusivity = $k_m/(\rho c_p)_f$, m^2/s
β = volumetric expansion coefficient, K^{-1}
ϵ = porosity
$\bar{\epsilon}$ = normalized porosity
Θ = angular coordinate
ν = kinematic viscosity, m^2/s
ρ = density, kg/m^3
ϕ = generic variable = ψ or T
ψ = dimensionless stream function scaled by α

Subscripts

c = cold
f = fluid
h = hot
q = heat flux
t = isothermal

wall is treated as isothermal, and is based on heat flux when the inner wall is supplied with constant heat flux. In the numerical study, the variation in porosity at the interface is taken as linear between nodes adjacent to it.

Results and Discussion

Isothermal Boundaries. Figure 2 presents a plot of normalized inner Nusselt number as a function of Rayleigh number for all three cases. It can be seen that the curves for C2 and C3 overlap and are consistently below that of C1, which corresponds to the case of a uniform porous medium. An explanation of this result is the following. For the geometry considered here, unicellular convection prevails even when the flow domain is composed to two distinct layers of porous material. This is to be contrasted with the result of Somerton (1985) (who has observed multicellular flow) for a Rayleigh–Benard problem in a cavity. The flow along any streamline encounters two resistances, $1/K_i$ near the inner wall and $1/K_o$, and the mean permeability based on this resistance is

$$\bar{K} = \frac{2K_iK_o}{K_o + K_i} \tag{4}$$

It is noted that, if $1/\bar{K} = 1/K_i + 1/K_o$, $\bar{K} < K_i$ and $\bar{K} < K_o$. Hence, $\bar{K} < (K_i + K_o)/2$, and the effective permeability of the system with two porous layers is actually less than that of either one of them, and also their arithmetic mean. Thus, for a given Rayleigh number calculated on the basis of $(K_i + K_o)/2$, the average heat transfer coefficient of a nonuniform porous medium is lower than that of the uniform case. Figure 2 also shows data for cases 2 and 3 using equation (4) for the characteristic permeability. These data lie directly over those of the uniform case, thus validating the simple model described above.

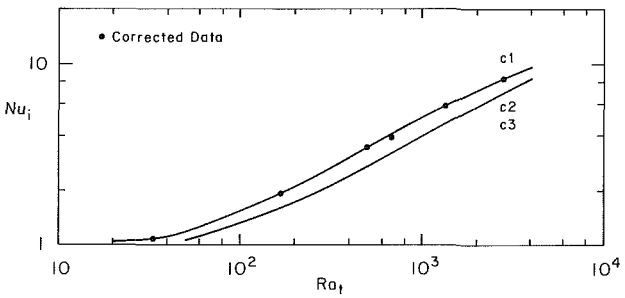

Fig. 2 Inner Nusselt number as a function of Rayleigh number for isothermal boundaries (numerical)

Figure 3 shows local Nusselt numbers on inner and outer cylinders when Ra = 500. It can be seen that the Nusselt numbers for C2 and C3 lie below that for C1 over a major portion of the annulus. The channeling phenomena leading to increased heat transfer rates and associated with increased permeability are seen only over a narrow portion of the annulus, and the increased resistance of the system is felt everywhere else. As the relative thickness of the porous layers is changed, the relative importance of channeling and resistance is likely to be reversed. However, this aspect of the problem needs further experimental and theoretical investigation.

Constant Heat Flux Boundary. Figure 4 shows the dependence of the average Nusselt number on Rayleigh number when the inner wall is supplied with a constant heat flux. This result is entirely from a numerical calculation, and the curves corresponding to cases C2 and C3 are clearly seen to lie below the one for the case of uniform porosity. However, these do not overlap, since the nature of boundary condition on the inner and outer wall are not identical. The case where a higher permeability region lies adjacent to the heated wall (i.e., C3) leads to a Nu versus Ra curve consistently above the case with the position of the layers interchanged, i.e., C2.

Figures 5(*a*) and 5(*b*) show results obtained from laboratory experiments for cases C2 and C3 and have been further compared with numerical computation. All shaded symbols in-

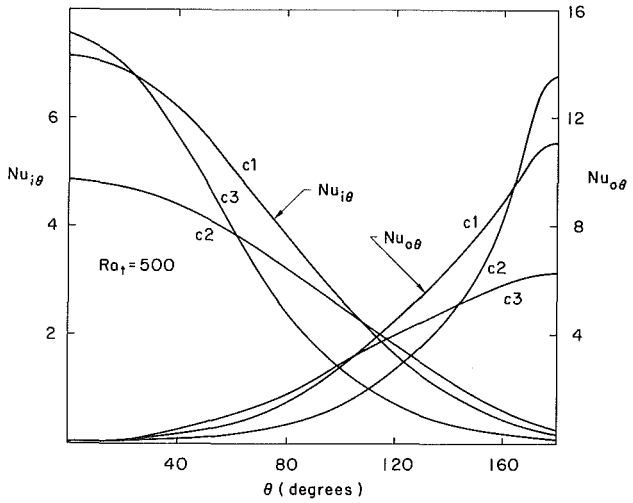

Fig. 3 Local Nusselt number, result for isothermal boundaries

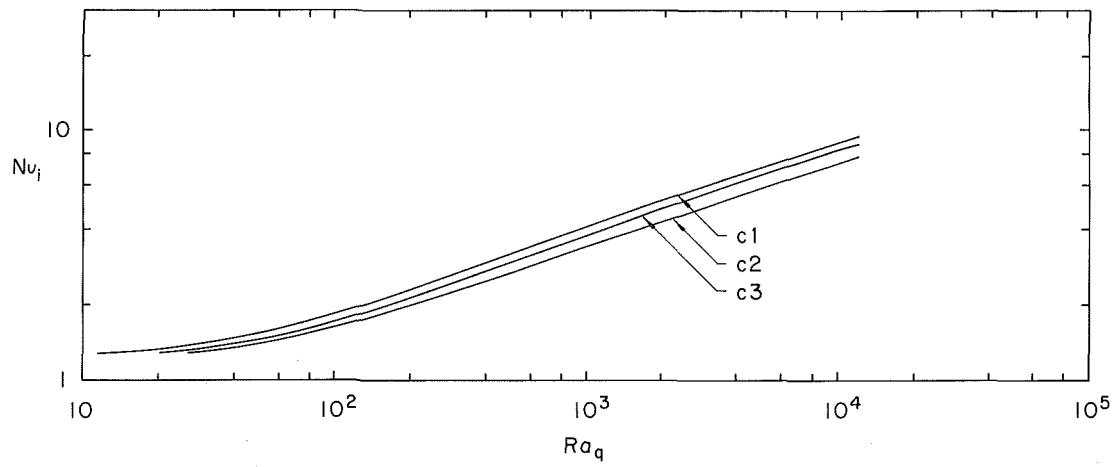

Fig. 4 Inner Nusselt number as a function of Rayleigh number, numerical results for constant heat flux inner boundary

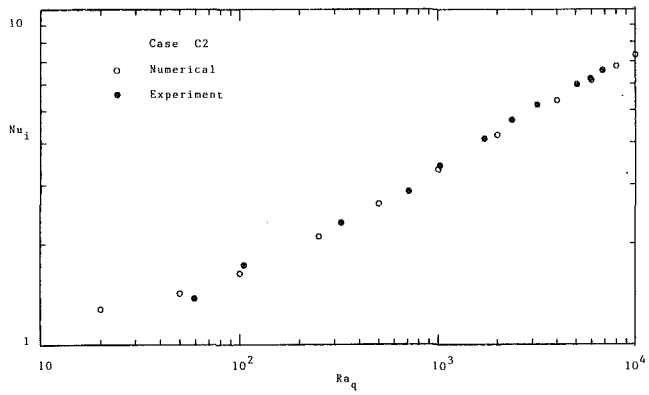

Fig. 5(*a*) Inner Nusselt number as a function of Rayleigh number for a constant heat flux inner boundary, case 2

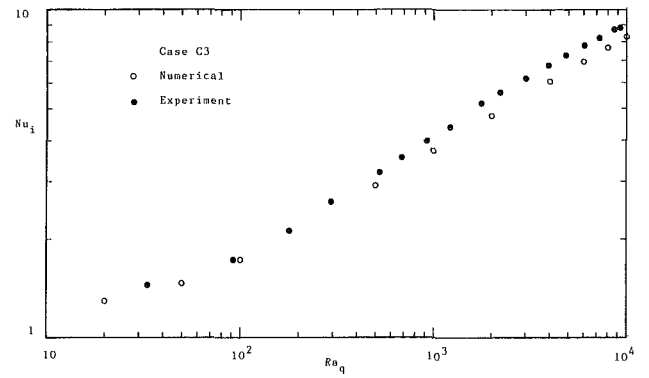

Fig. 5(*b*) Inner Nusselt number as a function of Rayleigh number for a constant heat flux inner boundary, case 3

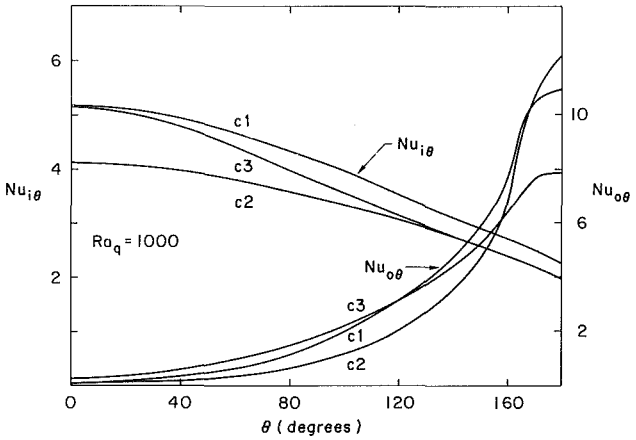

Fig. 6 Local Nusselt number, numerical results for constant heat flux inner boundary

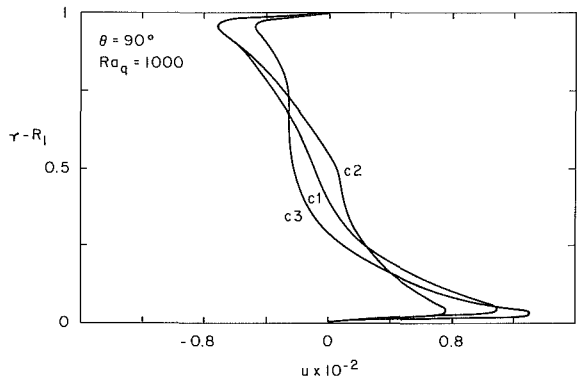

Fig. 7 Velocity profiles in the annulus for a constant heat flux inner boundary, numerical results

dicate experimentally obtained data points. It can be seen that the overall heat transfer characteristics of the two systems C2 and C3 are significantly different, and this has important implications in practical applications. For example, a lower value of Nusselt number represents a larger wall temperature, for a given heat flux, which in turn could initiate thermally induced mechanical damage.

Figures 5 also show that the comparison between analysis and experiments is satisfactory. This is particularly so for case 2, except for the single value for the lowest Rayleigh number, though it is still within the bounds of experimental accuracy. For case 3, a systematic divergence of experimental data can be seen as the Rayleigh number is increased. The origin of discrepancy seen in this work can be explained in the following manner. For case 2, a lower permeability material lies next to the hot wall, and hence the local Rayleigh number driving the flow is correspondingly lower. Figures 5 use the mean permeability of the system to define Ra, and so a given range of values of Rayleigh number corresponds to different extents of convection locally near the heated boundary. Over the reduced scale of Ra for case 2, the Darcy flow regime can be certainly expected to prevail, and this is the source of close agreement obtained here. For case 3, the local Ra scale is expanded, since the permeability next to the wall is higher than the mean value. The divergence of the experimental data with respect to the numerical result could arise from two factors, namely, convection affecting the definition of thermal conductivity of the medium, and non-Darcy effects. Prasad et al. (1985) have proposed a model to include the former, and use of this model here has produced little improvement in the results. It is thus concluded that non-Darcy factors, especially the variation of porosity near a solid boundary, are operative

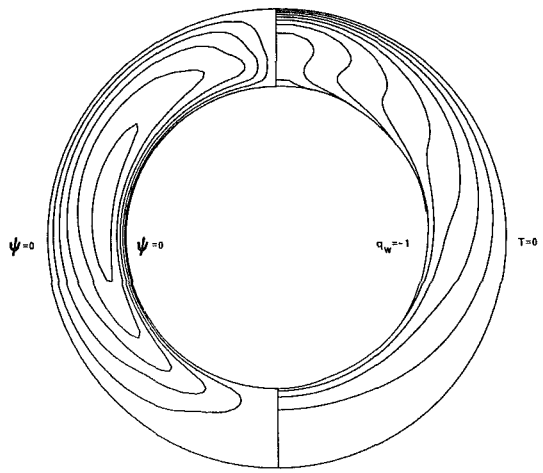

Fig. 8 Streamlines and isotherms for case 3 with constant heat flux inner boundary; Ra_q = 1000

in the present work. A detailed discussion, including non-Darcy effects in an annular geometry, will be presented by Muralidhar and Kulacki (1986) elsewhere.

Figure 6 shows local Nusselt number distribution for the three cases studied here. As for the problem with isothermal boundaries, the local Nusselt number is seen to be strongly affected by increased overall resistance in the annulus rather than locally occurring channeling affects in the high permeability regions. Figure 7 shows velocity profiles in the

annulus for $\Theta = 90$ deg and $Ra_q = 1000$. As discussed above, the effective Rayleigh numbers for the three cases are different, leading to channeling for case C3 but not for case C2. Figure 8 shows streamlines and isotherms for case 3 when $Ra_q = 1000$. As mentioned earlier, unicellular convection is seen to prevail in the annulus, despite the step change in permeability.

Conclusions

Natural convection heat transfer in a two-layer system confined in an annulus shows interesting deviation from the uniform case. Irrespective of the boundary condition as either isothermal or constant heat flux, the overall Nusselt number–Rayleigh number curve falls below that of a single layer, when the mean properties of the porous medium are employed. This has been satisfactorily explained for the isothermal case by a simple resistance law which leads to the correct model of permeability. Comparison between computation and experiments is generally found to be satisfactory when the inner wall is supplied with constant heat flux. However, when the higher permeability layer lies next to the heated surface, the variation of porosity near the boundary leads to consistently higher levels of Nusselt number above that predicted by Darcy's law. This is clearly revealed in the experiments. For the particular case of equal layer thicknesses, the competing influences of channeling on the high permeability side and the increased overall resistance lead to a situation in favor of the latter, although this balance could be upset in other cases. This aspect needs further attention.

References

Bau, H. H., 1984, "Low Rayleigh Number Thermal Convection in a Saturated Porous Medium Bounded by Two Horizontal Eccentric Cylinders," ASME JOURNAL OF HEAT TRANSFER, Vol. 106, pp. 166–176.

Baunchalk, R. A., 1985, "Experimental Study of Free Convection in a Horizontal Porous Annulus, MMAE Thesis, University of Delaware, Newark, DE.

Bejan, A., 1984, *Convection Heat Transfer*, Wiley, New York.

Brailovskaya, V. A., Petrazhitskii, G. B., and Polezhaev, V. I., 1978, "Natural Convection and Heat Transfer in Porous Interlayers Between Horizontal Coaxial Cylinder," *Zhurnal Prikladnof Mekhaniki i Tekhnicheskii Fiziki*, No. 6, pp. 90–96.

Burns, P. J., and Tien, C. L., 1979, "Natural Convection in a Porous Media Bounded by Concentric Spheres and Horizontal Spheres," *International Journal of Heat and Mass Transfer*, Vol. 22, pp. 929–939.

Caltagirone, J., 1976, "Thermoconvective Instabilities in a Porous Medium Bounded by Two Concentric Horizontal Cylinders," *Journal of Fluid Mechanics*, Vol. 76, pp. 337–362.

Gjerde, K. M., and Tyvand, P. A., 1984, "Thermal Convection in a Porous Medium With Continuous Periodic Stratification," *International Journal of Heat and Mass Transfer*, Vol. 27, pp. 2289–2295.

Gosman, A. D., Pun, W. M., Runchal, A. K., Spalding, D. B., and Wolfshtein, M., 1969, *Heat and Mass Transfer in Recirculating Flows*, Academic Press, New York.

McKibbin, R., and Tyvand, P. A., 1981, "Thermal Convection in a Porous Medium Composed of Alternating Thick and Thin Layers," *International Journal of Heat and Mass Transfer*, Vol. 26, pp. 761–780.

McKibbin, R., and Tyvand, P. A., 1984, "Thermal Convection in a Porous Medium With Horizontal Cracks," *International Journal of Heat and Mass Transfer*, Vol. 27, pp. 1007–1012.

Muralidhar, K., and Kulacki, F. A., 1986, "Non-Darcy Natural Convection in a Saturated Horizontal Porous Annulus," presented at ASME/AIAA Thermophysics Conference, Boston.

Prasad, V., and Kulacki, F. A., 1984, "Natural Convection in a Vertical Porous Annulus," *International Journal of Heat and Mass Transfer*, Vol. 27, pp. 207–219.

Prasad, V., Kulacki, F. A., and Keyhani, M., 1985, "Natural Convection in Porous Media," *Journal of Fluid Mechanics*, Vol. 150, pp. 89–119.

Shimomura, H., Okamoto, Y., and Takizuka, T., 1980, "Heat Transfer Characteristics of Horizontal Annular Insulation Layer With High Presure," *Heat Transfer Japanese Research*, pp. 1–11.

Somerton, C. W., and Goff, J. D., 1985, "Experiments on Natural Convection in Multilayer Porous Media," ASME National Heat Transfer Conference, Aug. 4–7, 1985; *HTD*, Vol. 46, Book No. G00303.

Vafai, K., and Tien, C. L., 1980, "Boundary and Inertia Effects on Flow and Heat Transfer in Porous Media," *International Journal of Heat and Mass Transfer*, Vol. 24, pp. 195–203.

Vafai, K., 1984, "Convective Flow and Heat Transfer in Variable Porosity Media," *Journal of Fluid Mechanics*, Vol. 147, pp. 233–259.

An Experimental and Analytical Study of Close-Contact Melting

M. K. Moallemi
Assoc. Mem. ASME

B. W. Webb
Assoc. Mem. ASME

R. Viskanta
Fellow ASME

School of Mechanical Engineering,
Purdue University,
West Lafayette, IN 47907

Close-contact melting was investigated by performing a series of experiments in which blocks of solid n-octadecane (with circular or rectangular cross section) were melted by a horizontal planar heat source at constant surface temperature. Close contact between the source and the solid prevailed throughout the experiments by permitting the uncontained solid to descend under its own weight while squeezing the melt out of the gap separating it from the source. The velocity of the solid was measured and is reported as a function of the instantaneous weight of the solid. Effects of the surface temperature of the source and radius of the solid on its temporal velocity are also reported. A closed-form approximate solution is developed for the motion of solid and predictions are compared with the experimental data. The results for the solid velocity are correlated in terms of the governing parameters of the problem as revealed by the approximate solution. Compared with natural convection-dominated melting from below (solid confined and contained in a rectangular cavity) close contact gives rise to approximately a sevenfold increase in the melting rate of the solid.

1 Introduction

Close-contact melting occurs if a heat source and a solid are pressed against each other while the solid is being melted. The physical situation involves motion of either the heat source or the solid which prevents accumulation of the melt between the source and the solid. This phenomenon takes place in numerous natural and technological processes such as process metallurgy and welding [1], geophysics [2], nuclear technology [3, 4] and thermal storage systems [5]. This mode of melting provides two special features which are not shared by melting problems with fixed source and solid. These features may make it attractive for other industrial applications. These characteristics which are clearly demonstrated in this work are:

1 As accumulation of the melt between the source and solid is prevented (due to motion of either of the two), the melting rate remains approximately constant and is several times higher than buoyancy-induced melting with fixed solid and source. For a constant temperature source, this results in higher extraction from the solid source. For a constant heat flux source, this mode of melting results in much lower and uniform temperature at the surface of the source.

2 The interaction of the melt and the source is in the immediate presence of the interface. Thus, the melt leaving the close-contact area is at much lower average temperature.

With regard to previous investigations, two types of studies are cited. These two groups may be classified in terms of close-contact melting arising from motion of either (1) the solid, or (2) the heat source. In the first group, motivated by application in latent heat-of-fusion thermal storage system, this phenomenon was studied by inclusion of density change during melting of unconfined solid in horizontal cylindrical [5, 6], inclined cylindrical [7], and spherical [8] cavities. In the second group, motivated by application in geophysics [2] and/or nuclear technology [4], this phenomenon was studied by permitting the heat source to respond to gravity. Emerman and Turcotte [9] formulated an approximate mathematical model for the migration velocity of a hot rigid sphere which melted its way through a solid. Moallemi and Viskanta [10, 11] reported on melting experiments with a moving horizontal cylindrical heat source.

Contributed by the Heat Transfer Division for publication in the JOURNAL OF HEAT TRANSFER. Manuscript received by the Heat Transfer Division September 17, 1985.

In this work, experiments have been performed by placing a block of solid on a horizontal planar heat source at constant surface temperature. The solid blocks were not confined or contained, and melting of the solid was accompanied by its descent (in response to gravity) and squeezing of the melt out of the small gap separating it from the source. Two types of experiments have been performed, the solid blocks being of either cylindrical or rectangular cross section. For both of the solid geometries, three different surface temperatures were employed in the course of the work. The paper also includes a mathematical model inferred from the experimental observations which is solved by an approximate integral method. The solid velocity is correlated to its instantaneous mass and surface temperature of the source. The experimental results are compared with the predictions of the approximate model, and are cast in a correlation similar to the analytical solution.

2 Experimental Setup and Procedure

The experiments were performed with horizontal planar heat sources designed to provide a constant surface temperature. In melting of rectangular solid blocks, the heat source used is made from copper with a 40×250 mm cross section and 16 mm total thickness. The heat source employed for melting of circular cylindrical blocks is also made from copper having a cross section of 65×85 mm and total thickness of 8 mm. The heat sources were maintained at constant temperature by circulating thermostated fluid through the multipass countercurrent channels machined in them. The upper surface of the heat sources were ground and polished to provide a precise planar surface.

The temperature distribution at the surface of the sources was measured by copper-constantan thermocouples inserted through small holes drilled on the bottom face of the copper plates and epoxied closed to the upper surface as shown in Fig. 1. Three 250 mm o.d. copper tubes were installed vertically 2–3 mm above the surface of the source. These prevented lateral motion of the solid blocks on the surface of the source. The vertical rods also minimized tilting of the solid blocks during their descent. The rods were polished to reduce the sliding friction force on the solid phase change material.

Research grade (99 percent pure) *n*-octadecane (T_m = 27.4°C) was used as the phase-change material in the experiments. The preparation of solid blocks always began with the degasification of the paraffin, to prevent void formation

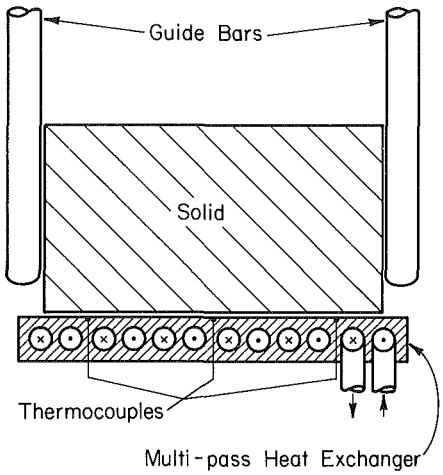

Fig. 1 Experimental setup

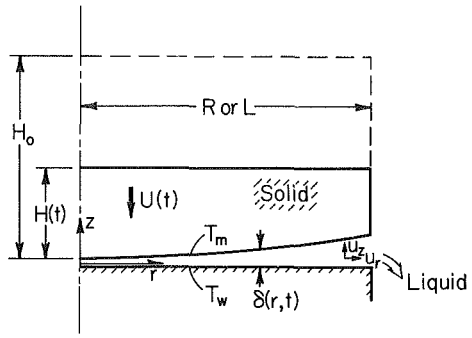

Fig. 2 Schematic of melting system with coordinate directions and pertinent parameters

during freezing. The PCM was first heated in a vacuum flask well above its fusion temperature (to about 100°C). The flask was then subjected to a solidification-melting cycle under vacuum. The degassed liquid PCM (at about 30°C) was then syphoned into molds (open-ended thin-walled copper cylinders with R = 13, 19, 25, and 30 mm or rectangular with 38×230 mm cross sections). The molds were placed in a constant temperture bath at about 0°C to solidify the PCM. During the solidification process, formation of internal voids, associated with the contraction which accompanies freezing, was avoided by irradiating the open end of the mold with a heat lamp (to prevent the formation of a frozen crust at the upper surface of the paraffin while the liquid phase still existed underneath). Degassed liquid was added at several times during the solidification process to compensate for the contraction. The solid blocks removed from the molds were cut to required heights (discarding the upper 20 mm which was suspected to contain some air bubbles or voids), and carefully planed (all sides for rectangular and end planes for circular blocks). The solid blocks were prepared several hours before each experiment and were stored at room temperature, 25°C.

An experiment was started by placing a block of solid on the carefully leveled heat source which was already in thermal equilibrium with a constant temperature bath at a preselected temperature. Initiation of melting was accompanied by a sudden drop in the surface temperature of the source, about 0.8 to 1.8°C depending on the temperature setting of the bath. This initial drop was partially recovered and the bath and heat source temperatures stabilized in about 2 to 5 min and less than 0.5°C variation at the surface was noted during a typical test. Data during this initial period were discarded and the bath was set at 0.5 to 1.5°C above the desired source temperature. In the data reduction, however, the average measured temperature of the source was used, rather than the bath temperature. In calculating the modified Stefan number the following thermophysical property data were used: c_l = 2.16 kJ/kgK, c_s = 2.15 kJ/kgK, and h_m = 240.0 kJ/kg. During a typical experiment, the temperature at the surface of the source was measured at 30 s or 60 s intervals. The instantaneous height of the solid was measured (at the same time that surface temperatures were being measured and recorded by a data logger) with a cathetometer with 0.05 mm resolution.

3 Theoretical Analysis

A schematic diagram of the physical problem considered is shown in Fig. 2. A block of solid of height H_0 and circular cross-sectional radius R (or rectangular cross section of $2L \times W$ with $L << W$) is initially at uniform temperature, $T_i < T_m$. At time $t = 0$, the solid block is placed on the horizontal planar heat source with cross section slightly larger than that of the solid and at constant surface temperature T_w, and melting begins. As melting proceeds, the solid is assumed to descend vertically under its weight with velocity $U(t)$ while

Nomenclature

A = cross-sectional melting area of solid
c = specific heat
C = constant in equation (19)
Fo = Fourier number = $\alpha t/L^2$ or $\alpha t/R^2$
g = gravitational acceleration
g^* = dimensionless gravitational acceleration = gL^3/α^2 or gR^3/α^2
h_m = latent heat
h_m^* = modified latent heat = $h_m + c_s(T_m - T_i)$
H = instantaneous height of solid = $H(t)$
H^* = dimensionless height of solid = H/L or H/R
H_0 = initial height of solid
H_0^* = dimensionless initial height of solid = H_0/L or H_0/R
H_m^* = dimensionless thickness of meniscus, equation (29)
k = thermal conductivity
K = constant in equation (24)
L = characteristic dimension of rectangular solid
M = instantaneous mass of solid
p = pressure
Pr = Prandtl number = $\mu c_l/k$
r = coordinate direction, Fig. 2
r^* = dimensionless coordinate = r/L or r/R
R = characteristic dimension of cylindrical solid
Re = Reynolds number = $\rho \bar{u}_r \delta/\mu$
Ste = Stefan number = $c_l(T_w - T_m)/h_m^*$
t = time
T = local temperature
T_i = initial temperature of solid
T_m = fusion temperature of solid
T_w = heated wall temperature
u = fluid velocity in melt channel
U = instantaneous melting velocity of solid = $U(t)$
U^* = dimensionless solid melting velocity = UL/α or UR/α
W = width of rectangular solid
z = coordinate direction, Fig. 2
α = thermal diffusivity = $k/\rho c$
δ = local thickness of melt channel
Δ = dimensionless melt channel thickness = δ/L or δ/R
μ = dynamic viscosity
ρ = density
ρ^* = solid-liquid density ratio = ρ_s/ρ_l

Subscripts

l = liquid phase
r = r-direction quantity
s = solid phase
z = z-direction quantity

squeezing the melt out of the thin channel separating it from the heat source. The thickness of the melt channel is assumed to be very small (i.e., $\delta/R << 1$ for the cylindrical solid and $\delta/L << 1$ for the solid with rectangular cross section). This assumption which is well justified by the experimental observations permits the use of the lubrication approximation [12]. That is, as long as $\delta/L << 1$ and $(\delta/L)\mathrm{Re} < 1$ (or $\delta/R << 1$ and $(\delta/R)\mathrm{Re} < 1$ for the cylindrical solid), the inertia terms are negligible compared to pressure gradient term and also, $\partial^2/\partial r^2 << \partial^2/\partial z^2$. These simplifications have also been used in other configurations involving close-contact melting [5, 9, 10].

Upon application of the above assumptions, the governing equations of the problem simplify to

Continuity:

$$\frac{1}{r^n}\frac{\partial(r^n u_r)}{\partial r}+\frac{\partial u_z}{\partial z}=0 \tag{1}$$

Momentum:

$$\mu\frac{\partial^2 u_r}{\partial z^2}=\frac{dp}{dr} \tag{2}$$

Energy:

$$u_r\frac{\partial T}{\partial r}+u_z\frac{\partial T}{\partial z}=\alpha\frac{\partial^2 T}{\partial z^2} \tag{3}$$

where $n=0$ for rectangular and $n=1$ for circular cross-sectional solids. On the surface of the source, $z=0$, the boundary conditions are

$$u_r=u_z=0 \text{ and } T=T_w \tag{4}$$

The boundary conditions at the interface, $z=\delta(r, t)$, are:

$$u_r=0,\ u_z=-U, \text{ and } T=T_m \tag{5}$$

The local energy balance at the interface yields

$$-k(1+\delta'^2)\frac{\partial T}{\partial z}=\rho U[h_m+c_s(T_m-T_i)]$$

where $\delta'=\partial\delta/\partial r$.

The solution of equation (2) with boundary conditions (4) and (5) is

$$u_r=\frac{1}{2\mu}\frac{dp}{dr}z(z-\delta) \tag{7}$$

Substituting equation (7) into the continuity equation and integrating with respect to z, with boundary condition (4), u_z is calculated. Upon enforcing $u_z=-U$ at the interface, the pressure gradient is found to be

$$\frac{dp}{dr}=\frac{-12\mu Ur}{(n+1)\delta^3} \tag{8}$$

Combining equations (7) and (8) yields

$$u_r=\frac{-6Urz(z-\delta)}{(n+1)\delta^3} \tag{9}$$

To find the spatial variation of the melt layer thickness, the energy equation is integrated over the melt layer, after first combining it with the continuity equation to yield

$$\int_0^\delta\left[\frac{\partial}{r^n\partial r}(r^n u_r T)+\frac{\partial}{\partial z}(u_z T)\right]dz=\alpha\int_0^\delta\frac{\partial^2 T}{\partial z^2}\,dz \tag{10}$$

Upon applying the boundary conditions, equations (4) and (5), this equation reduces to

$$\frac{\partial}{r^n\partial r}\int_0^\delta(r^n u_r T)dz-UT_m=\alpha\left[\frac{\partial T}{\partial z}\Big|_{z=\delta}-\frac{\partial T}{\partial z}\Big|_{z=0}\right] \tag{11}$$

To simplify the solution of equation (11), the temperature profile is approximated by a quadratic polynomial in z. The boundary condition, equations (4) and (5), and the energy balance at the interface, equation (6), are satisfied by

$$T=T_w+z\left[\frac{-2(T_w-T_m)}{\delta}+\frac{\rho h_m^* U}{k(1+\delta'^2)}\right]+z^2\left[\frac{T_w-T_m}{\delta^2}-\frac{\rho h_m^* U}{\delta k(1+\delta'^2)}\right] \tag{12}$$

Substituting equations (6), (9), and (12) into equation (11) results in

$$\frac{1}{r^{*n}}\frac{\partial}{\partial r^*}\left[\frac{\Delta r^{*n+1}}{1+\Delta'^2}\right]+\frac{3\mathrm{Ste}}{U^*}+\frac{20}{U^*(1+\Delta'^2)}-\frac{20\mathrm{Ste}}{\Delta U^{*2}}=0 \tag{13}$$

(Note that the characteristic length R in these dimensionless variables and groups is to be replaced by L for the case of a solid with rectangular cross section.) Equation (13), subject to the boundary condition

$$\Delta'=\frac{\partial\Delta}{\partial r}=0 \tag{14}$$

at $r=0$ was solved by proposing a solution of the form

$$\Delta=\sum_{i=0}^{\infty}a_i r^i.$$

Upon substitution of the proposed solution in equations (13) and (14), all coefficients a_i vanish except the constant term. This indicates that Δ is independent of r and has the form

$$\Delta=f(\mathrm{Ste})/U^* \tag{15}$$

where

$$f(\mathrm{Ste})=[\sqrt{400+(200+80n)\mathrm{Ste}+9\mathrm{Ste}^2}-3\mathrm{Ste}-20]/2(n+1) \tag{16}$$

For small Ste, $f(Ste) \approx \mathrm{Ste}$[e.g., $f(0.1)=0.0981$ for $n=0$ and $f(0.1)=0.0976$ for $n=1$].

The velocity of the solid can be determined from a balance of forces acting on it

$$M\left(g-\frac{dU}{dt}\right)=\int_A p\,dA \tag{17}$$

where A is the area of the close-contact melting surface and M is the instantaneous mass of the solid and equal to $\pi R^2 H(t)\rho_s$ for the cylindrical and $2LWH(t)\rho_s$ for the rectangular solid. To simplify equation (17), the pressure distribution in the melt-film channel is evaluated by assuming that the exit pressure $p(R)=p_{\mathrm{atm}}$. With this assumption and the fact that Δ is not a function of r [see equation (15)], integration of equation (8) results in

$$p-p_{\mathrm{atm}}=\frac{6\mu U(R^2-r^2)}{(n+1)\delta^3} \tag{18}$$

Substituting equations (15) and (18) into (17) and integrating results in

$$H^*\rho^*\left(g^*-\frac{dU^*}{d\mathrm{Fo}}\right)=C\frac{U^{*4}\mathrm{Pr}}{\mathrm{Ste}^3} \tag{19}$$

where C is a constant equal to 3/2 for a cylindrical and 4 for a rectangular solid. The dimensionless quantities introduced in equation (19) are defined in the Nomenclature. Assuming that the acceleration of the solid is negligible compared to the gravitational acceleration equation (19) can be rearranged to yield

$$U^*=\left[\frac{\rho^* g^* \mathrm{Ste}^3}{C\mathrm{Pr}}\right]^{0.25}H^{*0.25} \tag{20}$$

Validity of the above assumption will be later examined for a typical set of parameters. From Fig. 2, it can be seen that

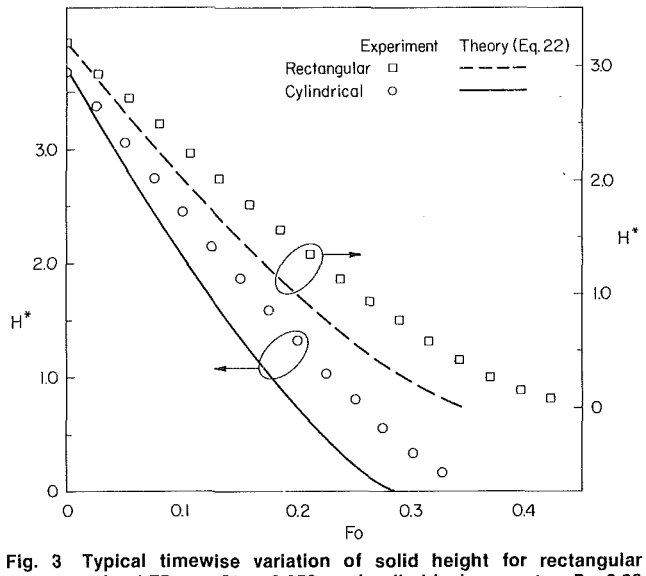

Fig. 3 Typical timewise variation of solid height for rectangular geometry, $L = 1.75$ cm, Ste = 0.059, and cylindrical geometry, $R = 2.93$ cm, Ste = 0.039

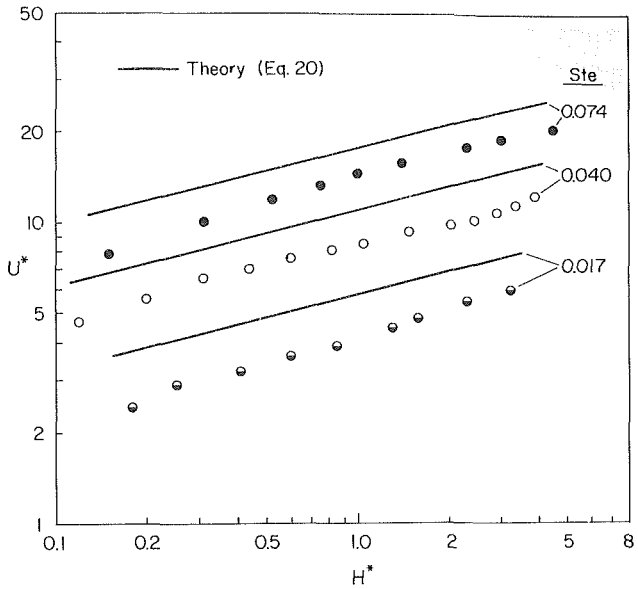

Fig. 4 Variation of melting velocity with instantaneous height of solid as a function of Ste for the cylindrical geometry, $R = 2.45$ cm

$$U^* = \dot{H}^* + \dot{\Delta} \tag{21}$$

Neglecting $\dot{\Delta}$ compared to $\dot{H}^*$, equation (21) is integrated to yield

$$H^* = \left[H_0^{*3/4} - \frac{3}{4}\,\mathrm{Fo}\left(\frac{\rho^* g^* \mathrm{Ste}^3}{C\mathrm{Pr}}\right)^{1/4} \right]^{4/3} \tag{22}$$

where H_0^* is the initial dimensionless height of the solid.

4 Results and Discussion

4.1 General Experimental Observations. Newly melted matter was squeezed out of the thin-film channel formed between the descending solid and the heat source. The melt channel height was very small and could not be measured. The surface of the solid was examined carefully by interrupting the experiments (by removing the solid and cleaning its surface off the melt quickly). The surface of the solid was found to be quite planar (with no perceptible curvature). This finding is in agreement with the prediction Δ is not a function of r, equation (15).

The melt flows out of the thin-film channel essentially in the direction of the characteristic length of the solid (i.e., R for the circular and L for rectangular solid). Outside of the film channel the melt flows with a finite thickness of about 0.8 to 1.0 mm over the uncovered portion of the heat source surface. The thickness of this free surface melt flow could not be correlated to the melting process as it was found to be controlled primarily by the surface tension force acting at the edges of the heat source while being slightly influenced by the velocity and cross-sectional area of the solid. The surface tension also caused the rise of a meniscus of about 1.5 to 2.0 mm height on the vertical surface of the solid. Neither effects of melt motion outside of the film-channel nor influence of the meniscus have been considered in the model by assuming that pressure outside of the film channel is atmospheric. This idealization results in an overestimation of the solid velocity which gradually becomes significant as the mass of the remaining solid decreases.

4.2 Results and Comparison. The height of the remaining solid was measured with a cathetometer at different times during the melting experiments. Typical results for the two geometries examined are presented in dimensionless form in Fig. 3 along with the predictions of the analytical model, equation (22), for the same initial heights of the solid H_0^*. The

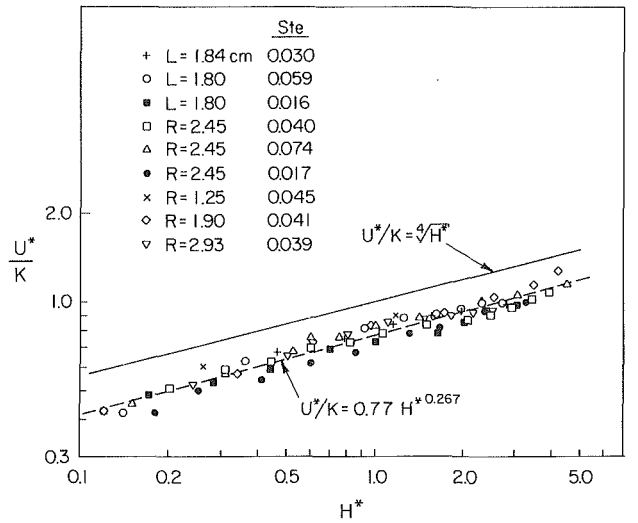

Fig. 5 Correlation of rectangular and cylindrical geometry melting rate data

analytical predictions of H^* are always below the measured values with the difference between them increasing with time. This indicates that, for both types of solid, the actual melting rates are lower than the predicted values. The difference may be attributed to the simplifications of the model (e.g., $p(R) = p_{\mathrm{atm}}$, $\dot{U}^* << g^*$, $\dot{\Delta} << \dot{H}^*$, etc.) as well as the idealizations in the experiments (e.g., uniform temperature at the surface of the source, negligible friction between the solid and the guide bars, homogeneous solid, etc.). The contribution of the model assumptions to the discrepancy between the predictions and measurements will be quantified later when the validity of the above assumptions is examined.

The velocity of the solid was determined by graphic differentiation of the instantaneous height of the solid with respect to time. Figure 4 presents the variation of the dimensionless velocity of circular blocks versus instantaneous height for different values of Stefan number. For the same value of H^*, the measured dimensionless solid velocities are between 15 and 25 percent lower than predicted by the analysis, equation (20). The form of dependence on the instantaneous height (weight) of the solid, however, is in good agreement with the

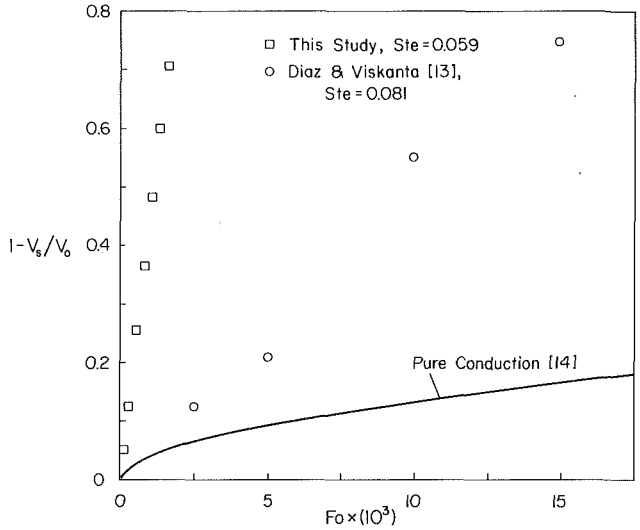

Fig. 6 Comparison of melting for close-contact melting, natural convection dominated melting from below, and pure conduction

expectation, as the lines connecting the data points are closely parallel to the theoretical (solid) lines.

In order to develop a better understanding of the origins of the discrepancy between theoretical analysis and experiments, and also to correlate the data in a more general form, equation (20) is rearranged to yield

$$U^*/K = H^{*0.25} \tag{23}$$

where

$$K = \left(\frac{\rho^* g^* \mathrm{Ste}^3}{C\mathrm{Pr}}\right)^{0.25} \tag{24}$$

The experimental results presented in Fig. 4, along with other similar data, are cast in the form of equation (23) and are compared with it in Fig. 5. The data were correlated using a least-squares regression by

$$U^*/K = 0.77H^{*0.267} \tag{25}$$

The dependence of the solid velocity on its instantaneous height (weight) is in agreement with the expectation, as the slopes of the lines in Fig. 5 [exponents of H^* in equations (23) and (25)] are quite close. The difference in the predicted and measured solid velocity is mainly in the coefficients of equations (23) and (25), indicating that thermal rather than hydrodynamic dissimilarity between the analytical and experimental model is the main reason for the discrepancy between the two. This point may be further verified by examining the major assumptions of the analytical model. In the analytical model it is assumed that

$$\Delta << 1,\ \dot{\Delta} << U^*, \text{ and } dU^*/d\mathrm{Fo} << g^* \tag{26}$$

These inequalities may be rewritten in terms of independent variable by employing equations (15) and (23) to yield

$$\frac{\mathrm{Ste}}{KH^{*0.25}} << 1,\ \frac{\mathrm{Ste}}{K^2H^{*0.5}} << 1, \text{ and } \frac{K^2}{4H^{*0.5}} << g^* \tag{27}$$

All of the above inequalities are satisfied by the experimental results of Fig. 5 for heights H^* as small as 0.1. A general condition for validity of the model for the realistic extremes $\mathrm{Ste} \leq 0.1$ and $H^* \leq 0.1$ may be derived from the first two inequalities of equation (27) as

$$K \geq \frac{1}{5} \tag{28}$$

For the cases studied K was between 3.5 and 18.0.

The effect of surface tension on the flow field leaving the melt channel may be included by postulating that the exit pressure is actually the hydrostatic pressure due to the meniscus. Equation (20) may then be modified as

$$U^* = K(H^* - H_m^*)^{0.25} \tag{29}$$

where H_m^* is the dimensionless height of the meniscus. It is obvious that only at small values of H^* will the influence of H_m^* be appreciable. For example, for $R = 25.5$ mm, H_m^* was measured to be about 0.1 and remained nearly constant in the range $0.2 < H^* < 3.0$. Exclusion of surface tension effect, for this case, results in an overestimation of 0.8 percent for $H^* \approx 3.0$ and 19 percent for $H^* = 0.2$.

From the above discussion it is concluded that the major assumptions of the analytical model, equation (26), are well justified for range of the parameters studied. The effect of neglecting the presence of the meniscus is found to be important only for small values of H^*. For larger values of H^* (e.g., $H^* \geq 0.5$), the nonuniformity in the surface temperature of the source appears to be the origin of discrepancy between the experiments and prediction. The effect of nonuniformity of T_w decreases with H^* as U^* (and consequently, the heat transfer coefficient) decreases with H^*. At the same time the effect of surface tension increases with a decrease of H^* due to melting. The combination of these two idealizations results in a consistent overestimation of the solid velocity by the model.

Figure 6 presents the temporal variation of the melted fraction of the rectangular solid block for $\mathrm{Ste} = 0.059$ along with prediction of the classical Stefan problem [14] for conduction-controlled melting. The figure also presents similar results for melting experiments in a closed rectangular cavity heated from below for $\mathrm{Ste} = 0.081$ [13] for comparison. The difference in the cross-sectional areas (36×220 mm here and 44×250 mm in [13]) is accounted for and dimensionless time is as defined in [13], $\mathrm{Fo} = \alpha t/W^2$. The comparison reveals seven to eightfold increase in the melting rate (i.e., heat transfer from the source) due to close-contact melting as compared with melting controlled by natural convection from below.

5 Conclusions

Close-contact melting experiments were performed with circular and rectangular solid blocks melting under their own weight on a horizontal heat source. The experimental results are compared with predictions based on an approximate analytical model. The measured solid velocity is cast into an empirical correlation of the form suggested by the analytical model based on the lubrication approximation. The solid-liquid interface was found to be quite planar for both geometries studied. This observation is in agreement with the analytical prediction that melt-film thickness Δ is independent of spatial coordinate r. The measured solid velocity was found to be 12 to 25 percent lower than the prediction. By examining the validity of the model assumptions, it was concluded that the discrepancy between predictions and measurements is due to the experimental idealizations (e.g., uniform surface temperature, homogeneous solid, etc.). The effect of neglecting the meniscus formed at the melt channel exit in the analysis was found to be minimal for large values of H^* while being quite appreciable when the solid height becomes of the same order of magnitude as the meniscus height.

From the analysis and also from the observation that the melt-film thickness under the solid is constant, it is concluded that heat transfer across the film is dominantly by conduction. However, as motion of solid prevents accumulation of melt between the source and solid, the melting rate remains high throughout the melting process (seven to eight times higher than melting induced by natural convection).

Acknowledgments

One of the authors (B.W.W.) wishes to acknowledge the financial support of his graduate studies by the Eastman

Kodak Company Graduate Fellowship. This work was partially supported by the National Science Foundation under Grant No. MEA-8313573.

References

1 Jackson, F., "Moving Heat Sources With Change of Phase," ASME JOURNAL OF HEAT TRANSFER, Vol. 87, 1965, pp. 329–332.

2 Marsh, B. D., and Charmichael, I. S. E., "Benioff Zone Magnetism," *Journal of Geophysical Research*, Vol. 79, 1974, pp. 1196–1206.

3 Herrmann, A. G., *Radioaktive Abfalle*, Springer-Verlag, Berlin, 1983.

4 Jansen, G., and Stepnewksi, D. D., "Fast Reactor Fuel Interactions With Floor Material After a Hypothetical Core Meltdown," *Nuclear Technology*, Vol. 17, 1973, pp. 85–96.

5 Bareiss, M., and Beer, H., "An Analytical Solution of the Heat Transfer Process During Melting of an Unfixed Solid Phase Change Material Inside a Horizontal Tube," *International Journal of Heat and Mass Transfer*, Vol. 27, 1984, pp. 739–746.

6 Nicholas, D., and Bayazitoglu, Y., "Thermal Storage of a Phase-Change Material in a Horizontal Cylinder," in: *Alternative Energy Sources I, II*, Vol. 1, T. N. Veziroglu, ed., Hemisphere Publishing Corp., Washington, 1983, pp. 351–378.

7 Sparrow, E. M., and Myrum, T. A., "Inclination-Induced Direct-Contact Melting in a Circular Tube," ASME JOURNAL OF HEAT TRANSFER, Vol. 107, 1985, pp. 533–540.

8 Moore, F. E., and Bayazitoglu, Y., "Melting Within a Spherical Enclosure," ASME JOURNAL OF HEAT TRANSFER, Vol. 104, 1982, pp. 19–23.

9 Emerman, S. H., and Turcotte, D. L., "Stokes' Problem With Melting," *International Journal of Heat and Mass Transfer*, Vol. 26, 1983, pp. 1625–1630.

10 Moallemi, M. K., and Viskanta, R., "Melting Heat Transfer Around a Migrating Heat Source," ASME JOURNAL OF HEAT TRANSFER, Vol. 107, 1985, pp. 451–458.

11 Moallemi, M. K., "Melting Around a Migrating Heat Source," Ph.D. Thesis, Purdue University, West Lafayette, IN, 1985.

12 Schlichting, H., *Boundary Layer Theory*, 7th ed., McGraw-Hill, New York, 1979, pp. 108–114.

13 Diaz, L. A., and Viskanta, R., "Visualization of the Solid–Liquid Interface Morphology Formed by Natural Convection During Melting of a Solid From Below," *International Communications in Heat and Mass Transfer*, Vol. 11, No. 1, 1984, pp. 35–43.

14 Stefan, J., "Uber die Theorie der Eisbildung, insbes ondere uber die eisbildung in Polarmeere," *Sitzungsberichie der Kaiserlichen Akademie Wiss Wien*, Mathinaturnsiss KL 98(22), 1890, pp. 965–973.

An Approximate Three-Dimensional Solution for Melting or Freezing Around a Buried Pipe Beneath a Free Surface

G.-P. Zhang

S. Weinbaum

L. M. Jiji

Department of Mechanical Engineering,
The City College of
The City University of New York,
New York, NY 10031

This paper presents a quasi-steady-state approximate solution for small Stefan number for the three-dimensional melting or freezing around a fluid-carrying pipe buried in a semi-infinite phase change medium (PCM). The two-dimensional quasi-steady approximate solution method, the virtual free surface technique [18], has been extended to three dimensions where axial thermal interaction between the moving fluid and the PCM is considered. Of particular interest in the motion of the phase change interface and the time variation of the axial temperature distribution in the fluid. Due to the singularities of the differential equations along the pipe surface, an axisymmetric analytic solution is provided for the region near the pipe wall. Solutions are presented for several representative dimensionless pipe burial depths and initial conditions. The computational time to predict the three-dimensional interface location up to 10 years is several minutes on an IBM 4341 computer.

Introduction

In recent years, melting or freezing around buried pipes at finite burial depths has attracted considerable attention because of important engineering applications in solar storage systems and pipeline transportation in permafrost regions. Numerous studies have been devoted to developing either simplified two-dimensional quasi-steady approximate analytical methods [1–8] or two-dimensional finite difference or finite element numerical solutions [9–12]. Recently studies on embedded pipe problems involving axial thermal interaction have been addressed [13–16]. All investigations involving axial interaction have focused on axisymmetric geometries where the surrounding PCM is infinite in the radial direction and initially at the phase change temperature. The simple analytic solution for a quasi-steady model without axial conduction presented by Shamsundar [16] shows excellent agreement with the numerical solutions [14] which include these effects when the Stefan number is small. This good agreement justifies the neglect of axial heat conduction and the use of the quasi-steady approximation in the present study. The steady-state solution for the three-dimensional axial interaction problem considered herein is given in [17].

For the important class of problems involving a free surface, hence finite burial depth, the three-dimensional nature of the coupled fluid/PCM domains of the problem significantly complicates the analysis. No previous transient solutions of this type exist. Although numerical techniques offer great flexibility with respect to nonhomogeneity and complicated boundary conditions, for three-dimensional problems involving axial interaction, the huge storage space and long calculation time required for the finite difference and finite element techniques rule out their practical use, at least for the present.

Weinbaum et al. [18] have recently developed a new approach for applying the quasi-steady approximation to two-dimensional problems. This approach, called the apparent free surface method, abandons the common assumption used in previous analytical studies [1–8] that the phase change interface as well as all the isotherms in both thawed and frozen zones are eccentric circles corresponding to the constant coordinate surfaces of the bicircular transformation. This isotherm representation is valid only for very large times (steady state) but is a poor description of the transient behavior because of the dramatic difference in the development of the upper and lower portions of the interface discussed in [18]. The virtual free surface method uncouples the motion of the top and bottom portions of the phase change boundary and relates the motion of the lower portion to an apparent free surface that starts at infinity and asymptotically approaches the actual free surface at large time when all isotherms are circular. This method is further improved in the present paper so that a realistic smooth noncircular interface is obtained and the approximate heat flux from the pipe surface at any instant in time can be evaluated appropriately.

Analysis and Formulation

As shown in Fig. 1, a thin-walled pipe of radius a is buried in a semi-infinite PCM at a distance $\tilde{h}_0$ beneath the surface $\tilde{y}=0$, which is maintained at a constant temperature T_0 below the melting temperature T_f of the PCM. Fluid enters the pipe at $\tilde{z}=0$ with an average velocity $\tilde{u}$ and a uniform temperature T_{a0} where $T_{a0} > T_f$. The fluid temperature at any axial position $\tilde{z}$ is assumed to be uniform across the pipe and equal to the temperature of the pipe wall. Since the initial temperature of the PCM is T_0, a melting front commences at the pipe wall at $t=0$.

Two coordinate systems, $(\tilde{x}, \tilde{y}, \tilde{z})$ and $(\tilde{r}, \phi, \tilde{z})$, are used (Fig. 1), one whose origin is in the plane of symmetry at the free surface and the other on the pipe centerline. The instan-

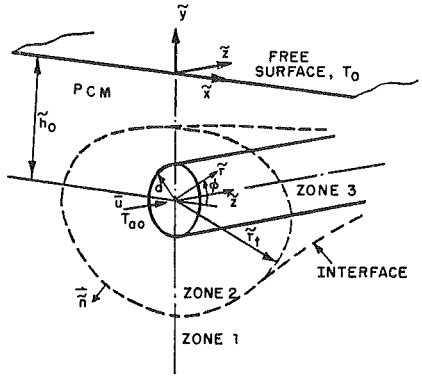

Fig. 1 Configuration and coordinate system

Contributed by the Heat Transfer Division for publication in the JOURNAL OF HEAT TRANSFER. Manuscript received by the Heat Transfer Division July 29, 1985.

taneous radius of the interface in the pipe centered coordinate system is $\tilde{r}_t(\phi, \tilde{z}, t)$. Note that the formulation and solution are the same for the freezing case wherein $T_0 > T_f > T_{a0}$.

The mathematical model is based on the following major assumptions which justify the quasi-steady and quasi-three-dimensional approximations: (1) Since the depth $(\bar{h}_0 + a)$ is small compared to the characteristic length of the pipe, the heat conduction in the PCM is dominated by temperature gradients in the cross-sectional plane. In the fluid inside the pipe, the energy transfer due to axial convection is much more significant than heat conduction because in most practical problems the Peclet number Pe is large ($\mathrm{Pe} > 10^2$). The three dimensionality of the phase change, therefore, is slowly varying in the axial direction and results from gradual bulk temperature changes in the fluid as it moves downstream and looses heat to the PCM. Consequently, the heat conduction in the axial direction $\tilde{z}$ is neglected throughout the system. (2) The slow variation with time of the fluid bulk temperature compared with the transit time for the fluid to traverse the pipe allows us to treat the axial variation of the fluid temperature in the pipe as quasi-steady. (3) The sensible heat is small in comparison with the latent heat L, i.e., the Stefan number $\mathrm{St} < 1$.

The dimensionless heat conduction equations in the two zones of the PCM (Fig. 1) are given by

$$\frac{\partial^2 \theta_1(x, y, z, \bar{t}^*)}{\partial x^2} + \frac{\partial^2 \theta_1(x, y, z, \bar{t}^*)}{\partial y^2} = 0 \tag{1}$$

and

$$\frac{\partial^2 \theta_2(x, y, z, \bar{t}^*)}{\partial x^2} + \frac{\partial^2 \theta_2(x, y, z, \bar{t}^*)}{\partial y^2} = 0 \tag{2}$$

Conservation of energy for the fluid in the pipe (zone 3 in Fig. 1) gives

$$\frac{\mathrm{Pe}^*}{\bar{\theta}_a(z, \bar{t}^*)} \frac{\partial \bar{\theta}_a(z, \bar{t}^*)}{\partial z} = \frac{2}{\pi} \int_{-\frac{\pi}{2}}^{\frac{\pi}{2}} \frac{\partial \theta_2(1, \phi, z, \bar{t}^*)}{\partial r} d\phi \tag{3}$$

where $\bar{\theta}_a$ appears in the denominator on the left-hand side due to the definition of θ_2. The transient term $\partial \bar{\theta}_a / \partial t^*$ does not appear in equation (3) because the characteristic time for convection in the fluid, $l/\bar{u}$, is assumed to be small in comparison with a^2/α_2 St, the characteristic time for thermal diffusion. The boundary conditions are

$$\theta_1(x, 0, z, \bar{t}^*) = \theta_1(x, -\infty, z, \bar{t}^*) = \theta_1(\infty, y, z, \bar{t}^*) = 1 \tag{4a}$$

$$\frac{\partial \theta_1(0, y, z, \bar{t}^*)}{\partial x} = 0 \tag{4b}$$

$$\theta_1(r_t, \phi, z, \bar{t}^*) = \theta_2(r_t, \phi, z, \bar{t}^*) = 0 \tag{4c}$$

$$\theta_2(1, \phi, z, \bar{t}^*) = 1 \tag{4d}$$

$$\theta_a(0, \bar{t}^*) = k_2(T_{a0} - T_f)/k_1(T_f - T_0) \equiv \theta_{a0} \tag{4e}$$

$$\frac{\partial \theta_2(0, y, z, \bar{t}^*)}{\partial x} = 0 \tag{4f}$$

The moving boundary condition at the interface is written as

$$\frac{\partial \theta_1(r_t, \phi, z, \bar{t}^*)}{\theta_a(z, \bar{t}^*) \partial n} + \frac{\partial \theta_2(r_t, \phi, z, \bar{t}^*)}{\partial n} = -\frac{1}{\bar{\theta}_a(z, \bar{t}^*)} \frac{\partial n}{\partial \bar{t}^*} \tag{5}$$

Since interface curvature in the axial direction is neglected (coincident with the negligible axial heat conduction), vector n is assumed to lie in the x–y plane (Fig. 1).

Two-Dimensional Solution

Because no derivatives with respect to z are involved in the conduction equations and equation (5), one can solve the two-dimensional moving boundary problem in the cross-sectional plane at any position along the pipe axis in terms of the local instantaneous surface temperature of the pipe. Equation (3) can then be integrated to determine the instantaneous quasi-steady axial temperature distribution of the pipe wall.

Consider first the simple steady-state situation when the isotherms and the interface are eccentric circles corresponding to the constant coordinate surfaces of the bicircular transformation

$$W = \frac{R_0 Z + (R_0 h_0 - 1)i}{(R_0 - h_0) - Zi}, \quad R_0 = h_0 - (h_0^2 - 1)^{1/2} \tag{6}$$

Nomenclature

a = pipe radius
$C(\bar{t}^*)$ = refer to equation (24)
C_a = specific heat of fluid
C_2 = specific heat of PCM in zone 2, Fig. 1
d_{ia} = $h_0 - (h_{ia} - r_{ia})$
d_{ib} = $(h_{ib} + r_{ib}) - h_0$
h_0 = dimensionless depth of pipe center below the free surface = $\bar{h}_0/a$, Fig. 1
h_i = dimensionless position below the free surface of center of interface circle = $\bar{h}_i/a$, Fig. 2
h_{ia} = dimensionless position below the free surface of center of interface circle passing through point $a = \bar{h}_{ia}/a$, Fig. 3
h_{ib} = dimensionless position below the free surface of center of interface circle passing through point $b = \bar{h}_{ib}/a$, Fig. 3
h'_{ib} = $(h_{ib} + r_{ib}) - r'_{ib}$
K_1, K_2 = thermal conductivities of zones 1 and 2, respectively
K_a = thermal conductivity of fluid
l = dimensional length of pipe
L = latent heat of PCM
n = normal coordinate at interface = $\tilde{n}/a$, Fig. 1
Pe* = modified Peclet number = $(K_a/K_2)\mathrm{Pe} = (K_a/K_2)(\rho_a C_a \bar{u} a/K_a)$
q_c = heat flux at topmost point of pipe, equation (17a)
q_d = heat flux at bottommost point of pipe, equation (17b)
r = dimensionless cylindrical coordinate = $\tilde{r}/a$, Fig. 1
r_i = assumed dimensionless interface radius = $\tilde{r}/a$, Fig. 2
r_{ia} = dimensionless interface radius of circle passing through point a, Fig. 3
r'_{ib} = dimensionless radius of curvature of the modified interface at point b, equation (15a)
r_t = dimensionless radial distance of the interface in pipe centered coordinates = $\tilde{r}_t/a$, equation (12), Fig. 1
R = dimensionless cylindrical coordinate, Fig. 2
R' = dimensionless cylindrical coordinate, Fig. 3
R_i = assumed dimensionless interface radius, Fig. 2
R_{ia} = dimensionless interface radius of circle passing through point a', Fig. 2
R'_{ib} = dimensionless interface

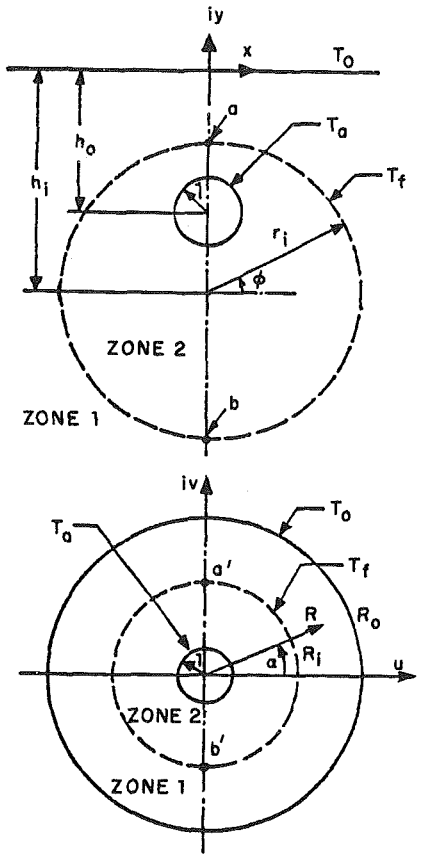

Fig. 2 Two-dimensional quasi-steady problem in the physical and transformed planes

which maps the semi-infinite region surrounding the pipe in the physical Z plane into the annular region in the complex W plane (Fig. 2). In general, a circle of radius R_i in the W plane corresponds to a circle of radius r_i with its center at $y=-h_i$ in the physical plane where

$$r_i=\frac{(R_0^2-1)R_i}{(R_0^2-R_i^2)} \tag{7a}$$

and

$$h_i=h_0-\frac{(R_i^2-1)R_0}{(R_0^2-R_i^2)} \tag{7b}$$

If this circle of radius r_i were the instantaneous interface, condition (5) when transformed into the complex W plane would become

$$R_i\frac{dR_i}{dt^*}=\frac{-1}{|Z'(W)|^2}\left[\frac{\partial\theta_1(R_i,\alpha,t^*)}{\theta_a(z,t^*)\partial R}+\frac{\partial\theta_2(R_i,\alpha,t^*)}{\partial R}\right] \tag{8}$$

where the scale factor $Z'(W)=|dZ/dW|$ is given by

$$|Z'(w)|=(R_0^2-1)/(R_0^2+R_i^2+2R_0R_i\sin\alpha) \tag{8a}$$

dR_i/dt^* in equation (8) varies from a maximum at $\alpha=\pi/2$ to a minimum at $\alpha=-\pi/2$. Since the upper and lower portions of the interface can approach steady state at vastly different rates, the motion of the upper and lower portions of the thaw boundary will be uncoupled and a separate analysis developed for each region. The reader is referred to [18] for the detailed procedure.

***(i)* The Upper Portion.** Since the thermal field in this relatively narrow region is dominated by the temperatures of the free and pipe surfaces and their geometries, the instantaneous temperature fields in this region are well represented by a family of steady state circular isotherms. A good approximation for the motion of point a in the physical plane or point a' in the complex W plane can be obtained by applying equation (8) at $\alpha=\pi/2$. Substituting the solutions for the steady-state isotherms into equation (8) and setting $\alpha=\pi/2$, one obtains

$$R_{ia}\frac{dR_{ia}}{dt^*}=\frac{(R_0+R_{ia})^4}{(R_0^2-1)^2}\left(\frac{1}{\theta_a\ln R_{ia}/R_0}+\frac{1}{\ln R_{ia}}\right) \tag{9}$$

Equations (7*a*) and (7*b*) are used to find r_{ia} and h_{ia} once R_{ia} is known.

***(ii)* The Lower Portion.** The free surface and the shapes of the isotherms in the upper region have a significant influence on the motion and curvature of the interface in the region below the pipe, except for very early times when the interface moves like concentric circles about a circular pipe in an infinite medium. For later times, the lower portion of the in-

Nomenclature (cont.)

radius of circle passing through point b', Fig. 3
R_0 = dimensionless free surface radius, Fig. 2
R'_{0b} = dimensionless apparent free surface radius, Fig. 3
S = r_f^2
St = Stefan number = $C_2(T_a-T_f)/L$
t = time
t^* = dimensionless time for the corresponding two-dimensional case = $K_2(T_a-T_f)t/\rho La^2$
$\bar{t}^*$ = dimensionless time = $K_2(T_{a0}-T_f)t/\rho La^2\equiv t^*/\bar{\theta}_a$
T_1, T_2 = temperature of zones 1 and 2, respectively
T_a = fluid bulk temperature = surface temperature of pipe
T_{a0} = fluid entrance temperature
T_f = melting temperature
T_0 = free surface temperature
$\bar{u}$ = average velocity of fluid
$\bar{v}$ = interface velocity
u, v = Cartesian coordinates in the complex W plane, Fig. 2
u', v' = Cartesian coordinates in the complex W^* plane, Fig. 3
x, y, z = dimensionless Cartesian coordinates, $x=\bar{x}/a$, etc.
W = $u+iv$, conformal transformation, equation (6)
W^* = $u'+iv'$, conformal transformation
Z = complex variable = $x+iy$
$z_{\max}$ = distance along pipe where $r_i=1$
α = cylindrical coordinate in complex plane
α_2 = thermal diffusivity of zone 2 = $k_2/\rho C_2$
δ = distance of apparent free surface from the actual free surface
θ_1 = dimensionless temperature of zone 1 = $(T_1-T_f)/(T_0-T_f)$
θ_2 = dimensionless temperature of zone 2 = $(T_2-T_f)/(T_a-T_f)$
θ_a = dimensionless bulk fluid temperature = $(K_2/K_1)(T_a-T_f)/(T_f-T_0)$
$\bar{\theta}_a$ = dimensionless bulk fluid temperature, θ_a/θ_{a0} = $(K_2/K_1)(T_{a0}-T_f)/(T_f-T_0)$
ρ = density of PCM
ρ_a = fluid density
τ = dimensionless time = $\int_0^{t^*}\bar{\theta}_a(z,\bar{t}^*)d\bar{t}^*$
ϕ = cylindrical coordinate in the physical plane, Fig. 1

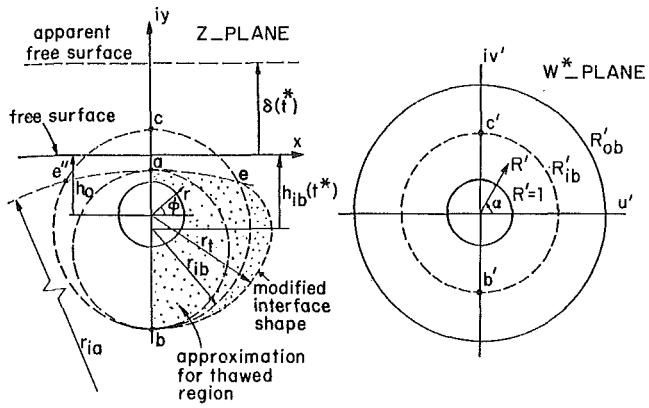

Fig. 3 Schematic diagram showing mapping of boundary value problem with apparent free surface into complex plane with apparent circles R'_{ib} and R'_{0b}

terface undergoes a continuous transition from the behavior of a pipe buried at infinity at early times to a long time behavior characterized by eccentric circles that asymptotically approach the final steady-state equilibrium position. During this transition, the isotherms in the vicinity of the $\phi = -\pi/2$ point are approximated by the bicircular coordinate transformation corresponding to the location of a virtual free surface at $y = \delta$, which varies from $\delta = \infty$ at $t^* = 0$ to $\delta = 0$ at $t^* = \infty$. Thus, as shown in Fig. 3, at each time t^*, there is a modified bicircular transformation whose free surface is at $y = \delta(t^*)$, with R_0 or h_0 appropriately redefined, which will map the pipe wall, the virtual free surface and the circle with origin at $y = -h_{ib}(t^*)$ and radius $r_{ib}(t^*)$ into concentric circles in the W^* plane. If $h_{ib}(t^*)$, $r_{ib}(t^*)$, and h_0 are known, there is only one value of δ that will permit these surfaces to be constant coordinate surfaces in transformation (6). This transformation satisfies the identity $h_0^2 - 1 = h_i^2 - r_i^2$ for $\delta = 0$, and hence for $\delta > 0$

$$(h_{ib} + \delta)^2 - r_{ib}^2 = (h_0 + \delta)^2 - 1 \tag{10}$$

Corresponding to r_{ib} and h_{ib} are the virtual circles R'_{0b} and R'_{ib} in the complex W^* plane. Applying equation (8) at $\alpha = -\pi/2$ in the W* plane one obtains

$$R'_{ib}\frac{dR'_{ib}}{dt^*} = \frac{(R'_{0b} - R'_{ib})^4}{(R'_{0b} - 1)^2}\left(\frac{1}{\theta_a \ln R'_{ib}/R'_{0b}} + \frac{1}{\ln R'_{ib}}\right) \tag{11}$$

Equation (11) thus corresponds to the instantaneous position of the fictitious free surface $y = \delta(t^*)$ and is used to approximate the motion of the lowermost point of the interface.

Up to this point, the analysis follows closely that presented in [18]. However, in the lower region a more accurate approximation for the shape of the lower portion of the interface can be obtained by using a curve whose radius of curvature varies continuously from point b to e in Fig. 3. This modified shape is described by the polynomial

$$r_t(\phi) = a_1 + a_2\left(\phi + \frac{\pi}{2}\right)^2 + a_3\left(\phi + \frac{\pi}{2}\right)^4 \tag{12}$$

where we require that r_t satisfy the following conditions on the continuity of the radius and its derivatives with respect to ϕ at both points b and e

$$r_t(-\pi/2) = r_{ib} + h_{ib} - h_0 \tag{13a}$$

$$\frac{dr_t(-\pi/2)}{d\phi} = 0 \tag{13b}$$

$$r_t(\phi_e) = r_e \tag{13c}$$

$$\frac{dr_t(\phi_e)}{d\phi} = C_e \tag{13d}$$

Here r_e, ϕ_e are the cylindrical coordinates of point e, the intersection of the upper and lower circles, and C_e is the derivative $dr_t/d\phi$ evaluated at the same point along the circle of radius r_{ia}. From the geometry, r_e can be determined as a function of r_{ia}, r_{ib}, h_{ia}, and h_{ib} which are all known. The coefficients a_1, a_2, and a_3 in equation (12) can be determined from the boundary conditions (13).

In the integration of equation (11), an independent relation to determine δ or R'_{0b} is necessary. In [18], a reasonable functional form for $\delta(t^*)$ was assumed which was then required to match with an approximate analytic solution at early times. In the present study, a more rigorous numerical method [19] has been developed to calculate the value of $\delta(\bar{t}^*, z)$ at each time step. Since equation (10) gives the relationship between δ and r_{ib} if the thaw depth $(h_{ib} + r_{ib})$ is fixed, it is reasonable to use the new radius of curvature r'_{ib} at the bottommost point of the modified curve equation (12) to calculate $\delta(t^*)$. That is

$$\delta(t^*) = \frac{h_0^2 + r_{ib}'^2 - h_{ib}^2 - 1}{2(h'_{ib} - h_0)} \tag{14}$$

where r'_{ib} is determined from equation (13) by

$$r'_{ib} = \frac{a_1^3}{|a_1^2 - 2a_1a_2|} \tag{15a}$$

and h'_{ib} is given by

$$h'_{ib} = h_{ib} + r_{ib} - r'_{ib} \tag{15b}$$

Note that the thaw depth $(h_{ib} + r_{ib})$ remains unchanged when the interface is modified.

The largest source of error in previous calculations for the growth of the thaw cylinder was that the heat flux was either calculated at a single point [1] or in some average sense using a single bicircular transformation [2–4]. Much greater accuracy can be obtained using a parabolic distribution for the wall flux

$$\frac{\partial\theta_2(1, \phi)}{\partial r} = b_1 + b_2\left(\phi + \frac{\pi}{2}\right) + b_3\left(\phi + \frac{\pi}{2}\right)^2 \tag{16}$$

which satisfies the boundary conditions

$$\frac{\partial\theta_2(1, \pi/2)}{\partial r} = q_c = -\frac{1}{\ln R_{ia}}\frac{(R_0 + 1)^2}{R_0^2 - 1} \tag{17a}$$

$$\frac{\partial\theta_2(1, -\pi/2)}{\partial r} = q_d = -\frac{1}{\ln R'_{ib}}\frac{R'_{0b} - 1}{R'_{0b} + 1} \tag{17b}$$

and

$$\frac{\partial^2\theta_2(1, \pi/2)}{\partial r\partial\phi} = 0 \tag{17c}$$

where q_c and q_d, the heat fluxes at the top and bottommost points of the pipe wall, are given by separate quasi-steady-state solutions for the upper and lower regions (equations (17*a*, *b*)).

From (16) and (17) the integrated heat flux through the pipe wall is

$$2\int_{\pi/2}^{3\pi/2}\frac{\partial\theta_2(1, \alpha)}{\partial R}d\alpha = 2\pi\left(\frac{2}{3}q_c + \frac{1}{3}q_d\right) \tag{18}$$

which shows that the average heat flux at the tube wall can be approximated by $(2q_c + q_d)/3$.

Three-Dimensional Solution

The axial thermal interaction is described by the quasi-steady energy conservation equation, equation (3), which can also be written in complex W plane as

$$\mathrm{Pe}^*\frac{\partial\bar{\theta}_a}{\bar{\theta}_a\partial z} = \frac{2}{\pi}\int_{\pi/2}^{3\pi/2}\frac{\partial\theta_2(1, \alpha, z, \bar{t}^*)}{\partial R}d\alpha \tag{19}$$

From the two-dimensional solution for the heat flow rate at the pipe wall, equation (18), the integral on the right-hand side of equation (19) can be evaluated at any position along the pipe axis. If the shape of the interface described by h_{ia}, r_{ia}, h_{ib},

and r_{ib} (or R_{ia}, R'_{ib}, and R'_{0b}) is known at each cross section along the pipe axis, one may determine $\bar{\theta}_a(z, t^*)$ by integrating equation (19) using a finite difference scheme.

Because the right-hand side of equation (19), and also equations (9) and (11), become singular as the interface intersects the pipe surface, an analytical solution has been developed for short times, and also for all times in the region near the pipe surface where the tail of the interface is in the vicinity of the pipe wall.

Solution in the Region Near the Pipe Wall. Since the shape of the interface is nearly axially symmetric when it is near the pipe wall, the energy equation in the fluid and the moving interface condition can be approximated by

$$\frac{\mathrm{Pe}^*}{\bar{\theta}_a}\frac{\partial\bar{\theta}_a}{\partial z}=2\frac{\partial\theta_2(1, z, \bar{t}^*)}{\partial r} \tag{20}$$

and

$$\frac{\partial r_t}{\bar{\theta}_a\partial\bar{t}^*}=-\frac{\partial\theta_2(r_t, z, \bar{t}^*)}{\partial r} \tag{21}$$

where the heat flux in region 1 is neglected in approximating the moving interface equation (5). This approximation is valid provided the interface is much closer to the pipe wall than the free surface and consequently the normal temperature gradient outward at the interface will be much smaller than at the pipe wall. Substituting $\theta_2=\ln(1/r_t)/\ln(1/r)$, which follows from the steady solution, into equations (20) and (21) and using $S=r_t^2$, we obtain

$$\frac{\mathrm{Pe}^*}{\bar{\theta}_a}\frac{\partial\bar{\theta}_a}{\partial z}=-\frac{4}{\ln S} \tag{20a}$$

and

$$\frac{\partial S}{\bar{\theta}_a\partial\bar{t}^*}=\frac{4}{\ln S} \tag{21a}$$

By introducing a new variable

$$\tau(z, \bar{t}^*)=\int_0^{\bar{t}^*}\bar{\theta}_a(z, \bar{t}^*)d\bar{t}^*,$$

one can show that equation (20a) has a solution of the same form as that of the Carslaw and Jaeger solution [20] for a pipe buried at infinity with initial temperature at the freezing point, and thus S is a function of τ only. Combining equations (20a) and (21a), we obtain

$$\mathrm{Pe}^*\frac{\partial\ln\bar{\theta}_a}{\partial z}=-\frac{dS}{d\tau} \tag{22}$$

Since $dS/d\tau=(\partial S/\partial z)/(\partial\tau/\partial z)$, where $\partial\tau/\partial z$ can be expressed in terms of S by using the definition of τ and equations (20a) and (21a), one can relate $\partial\ln\bar{\theta}_a/\partial z$ and $\partial S/\partial z$ using equation (22). This leads to the result

$$\frac{\partial\ln\bar{\theta}_a}{\partial z}=\frac{\partial\ln(S-1)}{\partial z} \tag{23}$$

which when integrated gives

$$\frac{\bar{\theta}_a}{S-1}=e^{c(\bar{t}^*)} \tag{24}$$

$C(\bar{t}^*)$ is obtained by applying the inlet boundary condition at $z=0$, $\bar{\theta}_a=1$, in the Carslaw and Jaeger solution. On the other hand, the combination of equations (23) and (20a) yields

$$\mathrm{Pe}^*\frac{\partial\ln(S-1)}{\partial z}=-\frac{4}{\ln S} \tag{25}$$

Integrating equation (25), we have

$$\frac{z}{\mathrm{Pe}^*}=-\frac{1}{4}\int_{r_{t0}^2}^{r_t^2}\frac{\ln S}{S-1}dS \tag{26}$$

where r_{t0} is the radius of the interface at $z=0$ obtained from the Carslaw and Jaeger solution. The integral on the right-hand side of equations (26) can be evaluated by using a Taylor expansion of $\ln S$ at $S=1$. For early times, equations (24) and (26) are used to calculate the radius of the interface $r_t(z, \bar{t}^*)$ and the temperature $\bar{\theta}_a(z, \bar{t}^*)$. A similar procedure can be employed for all times when the tail of the interface is in the vicinity of the pipe wall. The short time solution just outlined is valid for all times for an infinite axisymmetric geometry which is initially at the phase change temperature.

Numerical Solution Procedure. The original three-dimensional problem has now been reduced to a one-dimensional finite difference procedure in which equation (19) is integrated at each time step after the local two-dimensional solutions are first updated in time. The procedure is as follows:

(1) The calculation starts at $z=0$ where the Carslaw and Jaeger solution [20] is applied as if the pipe is buried at an infinite depth. At short times, one calculates the radius of the interface circle, $r_t(0, \bar{t}^*)$, and then uses the approximate analytic solution shown in the previous subsection for the axisymmetric case to obtain $r_t(z, \bar{t}^*)$ and $\bar{\theta}_a(z, \bar{t}^*)$ for $0\le z\le z_{\max}$ where $z_{\max}$ is the position at which the interface intersects the pipe wall. Note that $z_{\max}$ is a function of time.

(2) Since the z axis is divided into a finite number of segments, the two-dimensional solution can be applied to the cross section at each node. If R_{ia}, R'_{ib}, and R'_{0b} are known at time $\bar{t}^*$, the new locations of the upper and lower portions of the interface at $(\bar{t}^*+\Delta\bar{t}^*)$ can be determined using equations (9) and (11), respectively. The heat flow rate at the pipe surface at any position z is then evaluated from equation (18). Using a cubic spline to smooth the axial distribution of the heat flux, one then may readily integrate equation (19) to obtain $\bar{\theta}_a(z, \bar{t}^*+\Delta\bar{t}^*)$.

Results

Figures 4–7 show the solutions for two representative sets of input data. The first set is for a shallow burial depth $h_0=1.5$ and large $\theta_{a0}=50.49$ to illustrate the strong influence of the free surface. The second set $h_0=4$ and $\theta_{a0}=7.09$ is for a medium burial depth where the initial temperature differs significantly from the phase change temperature. The dimensionless length is 0.8 for both cases. The penetration of the top and bottom points of the interface as a function of axial distances and time is shown in Figs. 4(a, b). It can be seen from Fig. 4(b) that the thaw depth varies almost linearly with distance along the pipe axis even after three years because of the quite deep burial depth and moderate dimensionless temperature of the fluid at the inlet of the pipe. In contrast, the bottom of the thaw region is obviously curved in the z direction for the case where the influence of the free surface is important (Fig. 4a). The solution after 15 years is still very far removed from the final steady-state solution since much of the heat is removed at the free surface. The asymmetry in the heat removed from top and bottom of the pipe is shown in Figs. 5(a, b), where q_c and q_d given by equations (17a, b) represent the instantaneous heat fluxes through the topmost and bottommost points of the pipe. Since more heat leaves through the free surface in case 1 than case 2, the thaw depth decreases more rapidly in the axial direction for the shallower burial depth. This can also be observed in Figs. 6(a, b) where the dimensionless fluid temperature decreases more rapidly with axial distance. Figure 7 shows the change in cross-sectional shape of the thaw cylinder in the axial direction. As one might anticipate, the departure of the interface profile from a circular shape is most apparent at the inlet of the pipe and then gradually diminishes as one proceeds downstream.

The three-dimensional solutions presented herein differ in one very important respect from the two-dimensional solutions presented in [18] and all previous two-dimensional studies. In these studies the pipe wall temperature was assumed constant and the approach to the steady-state

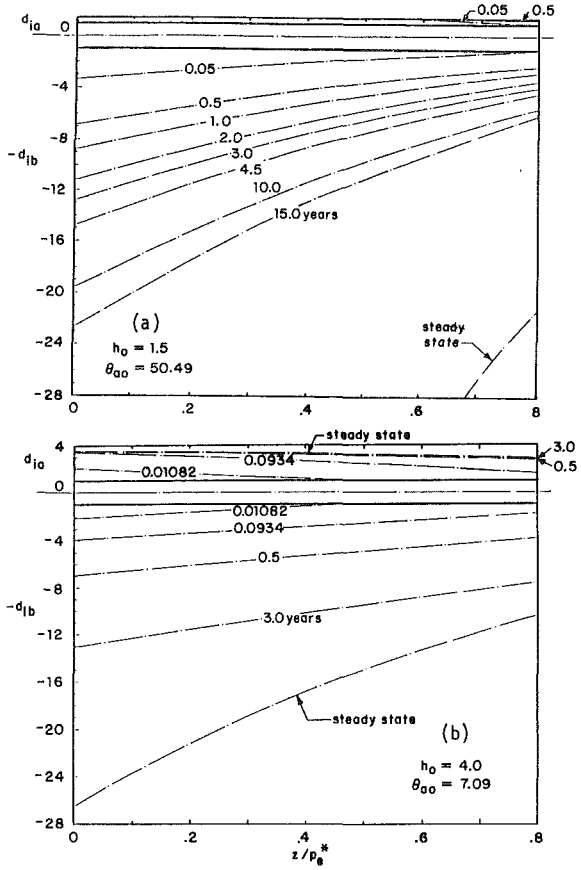

Fig. 4 Axial variation of thaw depth above and below pipe center, (*a*) $h_0 = 1.5$, $\theta_{a0} = 50.29$; (*b*) $h_0 = 4.0$, $\theta_{a0} = 7.09$

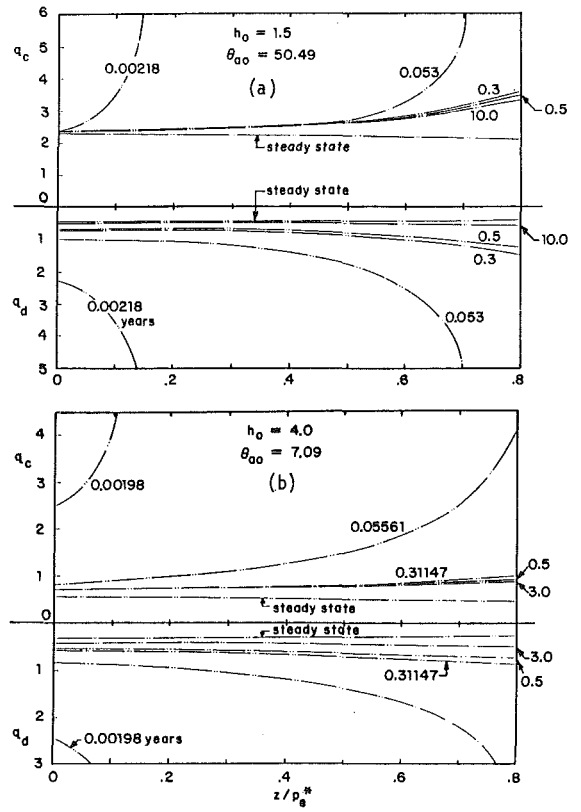

Fig. 5 Axial variation of heat flux at top and bottom points of pipe, (*a*) $h_0 = 1.5$, $\theta_{a0} = 50.49$; (*b*) $h_0 = 4.0$, $\theta_{a0} = 7.09$

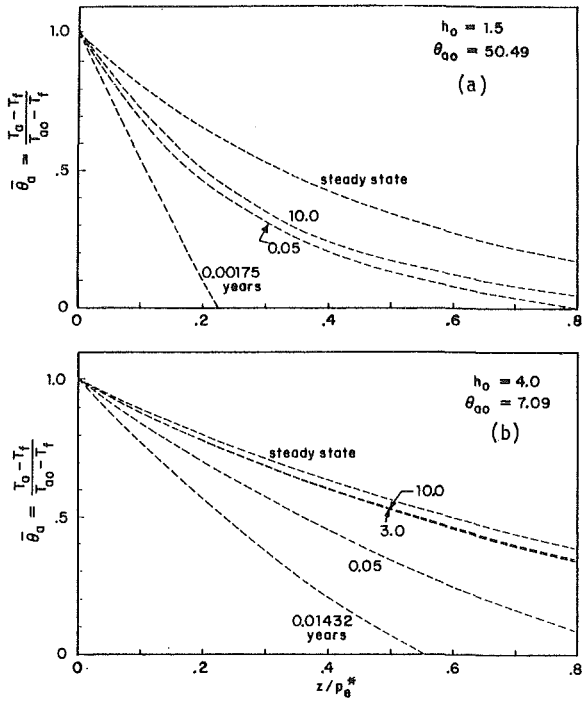

Fig. 6 Fluid axial temperature distribution, (*a*) $h_0 = 1.5$, $\theta_{a0} = 50.49$; (*b*) $h_0 = 4.0$, $\theta_{a0} = 7.09$

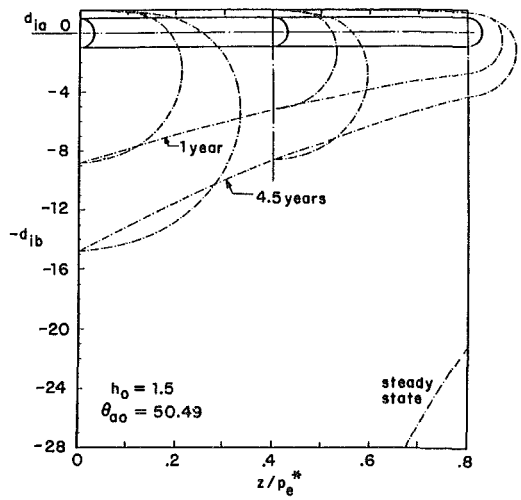

Fig. 7 Interface profile

equilibrium is uncoupled from the fluid in the pipe. It is evident from Figs. 6(*a*, *b*) that this steady-state equilibration time is actually controlled by the fluid interaction with the PCM and that the time required for the fluid in the pipe to achieve equilibrium can be much longer than the equivalent two-dimensional problem since the pipe wall temperature itself can be far from equilibrium. This behavior also has important consequences in the local heat flux and isotherms. Thus the long time required for the isotherms and thaw boundary above the pipe to achieve equilibrium is not a reflection of the conduction process in this region but of the much slower variation in pipe wall temperature. Both q_c (Fig. 5*a*) and the interface (Fig. 7) quickly approach an initial equilibrium value after approximately 0.3 years and then slowly vary on a much longer time scale which is controlled by the fluid-PCM interaction in the lower portion of the pipe. Existing two-dimensional models, which neglect the flow, can therefore lead to a very misleading estimate of the motion of the interface above the pipe surface.

Acknowledgments

This study was sponsored by the National Science Foundation under Grant No. MEA 8209034. The research was performed in partial fulfillment of the requirements for the Ph.D. degree of G. P. Zhang, School of Engineering of The City College of The City University of New York.

References

1 Porkahayev, G. V., "Temperature Fields in Foundations," *Proc. Ist Int. Conf. on Permafrost*, Lafayette, IN, 1963, pp. 285–291.

2 Thornton, D. E., "Steady State and Quasi-Static Thermal Results for Bare and Insulated Pipes in Permafrost," *Canadian Geotechnical Journal*, Vol. 13, 1976, pp. 161–170.

3 Hwang, C. T., "On Quasi-Static Solutions for Buried Pipes in Permafrost," *Canadian Geotechnical Journal*, Vol. 14, 1977, pp. 180–192.

4 Lunardini, V. J., "Thawing of Permafrost Beneath a Buried Pipe," *Journal of Canadian Petroleum Technology*, Vol. 16, 1977, pp. 34–37.

5 Hwang, C. T., Seshadri, R., and Krishnayya, A. V. G., "Thermal Design for Insulated Pipes," *Canadian Geotechnical Journal*, Vol. 17, 1980, pp. 613–622.

6 Seshadri, R., and Krishnayya, A. V. G., "Quasi-Steady Approach for Thermal Analysis of Insulated Structures," *International Journal of Heat and Mass Transfer*, Vol. 23, 1980, pp. 111–121.

7 Lunardini, V. J., "Phase Change Around Insulated Buried Pipes: Quasi-Steady Method," *J. Energy Research Tech.*, Vol. 103, No. 3, 1981, pp. 201–207.

8 Lunardini, V. J., "Approximate Phase Change Solution for Insulated Buried Cylinders," ASME JOURNAL OF HEAT TRANSFER, Vol. 105, 1983, pp. 25–32.

9 Lachenbruch, A. H., "Some Estimate of the Thermal Effects of a Heated Pipeline in Permafrost," U.S. Geological Survey, Circular 632, 1970.

10 Gold, L. W., Johnston, G. H., Slusarchuk, W. A., and Goodrich, L. E., "Thermal Effects in Permafrost," *Proc. Canadian Northern Pipeline Research Conference*, 1972, pp. 25–45.

11 Wheeler, J. A., "Simulation of Heat Transfer From a Warm Pipeline Buried in Permafrost," AIChE 74th National Meetings, New Orleans, LA, 1973.

12 Hwang, C. T., Murray, D. W., and Brooker, E. W., "A Thermal Analysis for Structures on Permafrost," *Canadian Geotechnical Journal*, Vol. 9, No. 2, 1972, pp. 33–46.

13 Asgarpour, S., and Bayazitoglu, "Heat Transfer to Laminar Flow With Phase Change Boundary," ASME JOURNAL OF HEAT TRANSFER, Vol. 104, 1982, pp. 678–682.

14 Sparrow, E. M., and Hsu, C. F., "Analysis of Two-Dimensional Freezing on the Outside of a Coolant-Carrying Tube," *International Journal of Heat and Mass Transfer*, Vol. 24, 1981, pp. 1345–1357.

15 Grossman, G., and Pesotchinski, D., "A Two-Dimensional Model for Thermal Energy Storage in a Phase Changing Material Interacting With a Heat-Carrying Fluid," ASME Winter Annual Meeting, Nov. 15–20, 1981, Paper No. 81-WA/HT-35.

16 Shamsundar, N., "Formulae for Freezing Outside a Circular Tube With Axial Variation of Coolant Temperature," *International Journal of Heat and Mass Transfer*, Vol. 25, 1982, pp. 1614–1616.

17 Zhang, G. P., Jiji, L. M., and Weinbaum, S., "Quasi-Three-Dimensional Steady State Analytic Solution for Melting Around a Buried Pipe in a Semi-infinite Medium," ASME JOURNAL OF HEAT TRANSFER, Vol. 107, 1985, pp. 245–247.

18 Weinbaum, S., Zhang, G. P., and Jiji, L. M., "An Apparent Free Surface Method for Determining the Transient Freezing Around a Buried Pipe in a Semi-infinite Region," ASME *Journal of Energy Resources Technology*, 1986 (in press).

19 Zhang, G. P., "Steady and Transient, Multi-dimensional Solutions for Melting or Freezing Around a Buried Tube in Semi-infinite Medium," Ph.D. Dissertation, The City Univ. of New York, 1985.

20 Carslaw, H. S., and Jaeger, J. C., "Conduction of Heat in Solids," 2nd ed., Clarendon Press, Oxford, 1959.

Local Heat Transfer Coefficients for Horizontal Tube Arrays in High-Temperature Large-Particle Fluidized Beds: an Experimental Study

A. Goshayeshi
Research Assistant.
Student Mem. ASME

J. R. Welty
Professor, Head.
Fellow ASME

R. L. Adams
Associate Professor.
Mem. ASME

N. Alavizadeh
Research Assistant.
Student Mem. ASME

Department of Mechanical Engineering,
Oregon State University,
Corvallis, OR 97331

An experimental study is described in which time-averaged local heat transfer coefficients were obtained for arrays of horizontal tubes immersed in a hot fluidized bed. Bed temperatures up to 1005 K were achieved. Bed particle sizes of 2.14 mm and 3.23 mm nominal diameter were employed. An array of nine tubes arranged in three horizontal rows was used. The 50.8 mm (2 in.) diameter tubes were arranged in an equilateral triangular configuration with 15.24 cm (6 in.) spacing between centers. The center tube in each of the three rows in the array was instrumented providing data for local heat flux and surface temperature at intervals of 30 deg from the bottom to the top—a total of seven sets of values for each of the center tubes. The three sets of data are representative of the heat transfer behavior of tubes at the bottom, top, and in the interior of a typical array. Data were also obtained for a single horizontal tube to compare with the results of tube bundle performance. Superficial velocities of high-temperature air ranged from the packed-bed condition through approximately twice the minimum fluidization level. Comparisons with results for a single tube in a bubbling bed indicate only slight effects on local heat transfer resulting from the presence of adjacent tubes. Tubes in the bottom, top, and interior rows also exhibited different heat transfer performance.

Introduction

Gas-fluidized beds are noted for their excellent heat transfer characteristics. It is generally acknowledged that high rates of heat transfer can be achieved between the bed and immersed surfaces or vessel walls. Fluidized bed combustion of coal in particular is receiving attention from scientists and engineers throughout the world, especially in the United States.

Fluidized-bed combustion offers great potential for the utilization of all ranks of coal to meet air standards. Crushed coal is usually burned in a bed of dolomite or limestone in which bed particles are held in suspension by upward-flowing air. The inert material reacts with the sulfur dioxide produced during combustion of high-sulfur coal to form a dry solid disposable waste. The heat produced in the bed is transferred to heat exchange tubes (which are usually horizontal) for steam generation in electric utility applications and for liquid or gas heating in process industries.

A large number of investigations reported in the literature have emphasized spatial-averaged heat transfer results. Local time-averaged heat transfer coefficients with immersed tubes provide additional information of importance to the combustor designer. A number of recent investigations (Berg and Baskakov, 1974; Gelperin and Ainshtein, 1971; Cherrington et al., 1977; Chandran et al., 1980; Golan et al., 1980; George and Welty, 1984; Baskakov et al., 1973; Vadivel and Vedamurthy, 1980; and Noak, 1970) have reported local heat transfer results for cases involving small ($d_p < 1$ mm) or large ($d_p > 1$ mm) particles and cold or hot bed conditions. Most of the previous investigations (reviewed by Saxena et al., 1978) were restricted to small particles and low bed temperatures where tubes were electrically heated and local heat fluxes were evaluated by measuring the power input along with measurements of tube wall temperatures for heat transfer coefficient calculations.

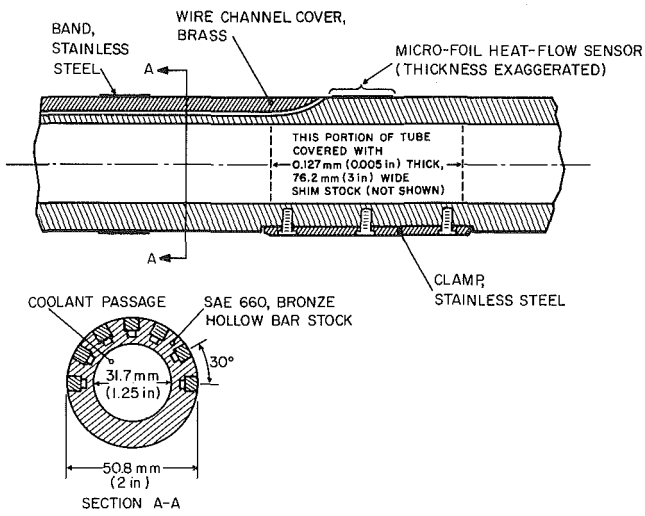

Fig. 1 Instrumented tube

In the present work, tubes were instrumented by thin thermopile-type transducers for direct measurements of local heat fluxes at hot bed conditions. A general lack of information for local heat transfer coefficients with tubes at different locations in the array was the motivation for the present study.

For the purpose of tube array design, the following considerations were made: In an array of horizontal tubes, it is known that the heat transfer to any tube, not affected by side walls [it is known that the motion of solids is different for centrally located tubes and those adjacent to a side wall (Peeler and Whitehead, 1982)], is affected only by the presence of the neighboring tubes. It is also known that the minimum spacing between tubes should not fall much below a pitch/diameter

Contributed by the Heat Transfer Division and presented at the 23rd National Heat Transfer Conference, Niagara Falls, NY, August 1984. Manuscript received by the Heat Transfer Division July 10, 1985.

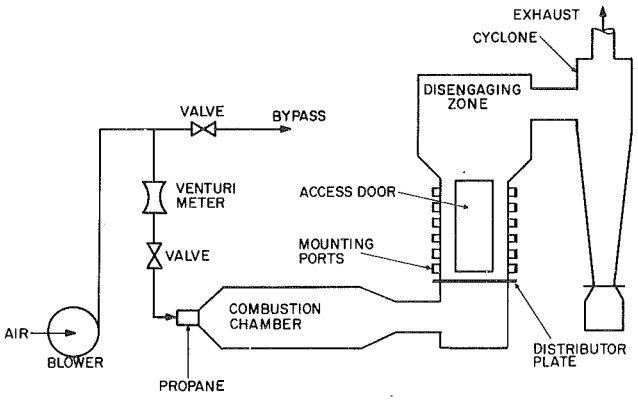

Fig. 2 Schematic illustration of the high-temperature fluidized bed facility

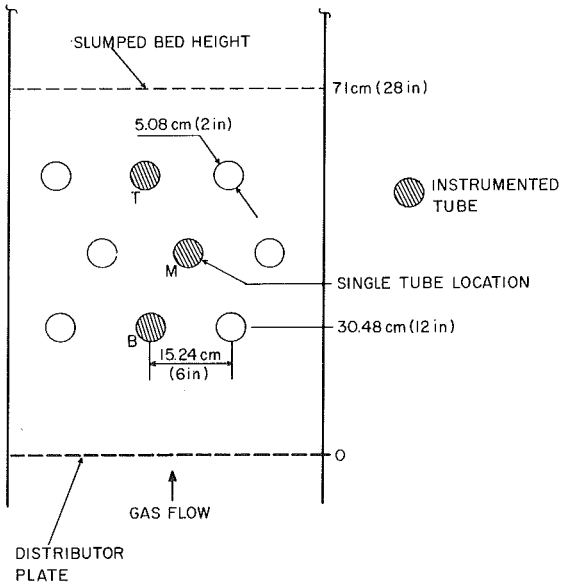

Fig. 3 Bed geometry and dimensions; T, M, and B represent top, middle, and bottom tubes in the array, respectively

ratio of 2, to prevent severe restriction of particle motion and a sharp decrease in heat transfer (Grewal and Saxena, 1983; Borodulya et al., 1980a). Typical heat exchanger designs employ tubes with diameters in the range of 50.8 mm (2 in.) arranged horizontally (Strom et al., 1977).

To fulfill all of the above design aspects, an array of nine tubes arranged in three horizontal rows was used. The 50.8-mm-dia tubes were positioned in an equilateral triangular configuration with 15.24 cm (6 in.) spacing between centers. The center tube in each of the three rows was instrumented providing data for local heat fluxes and surface temperatures at intervals of 30 deg from the bottom to the top – a total of seven sets of values for each of the center tubes. The three sets

Table 1 Summary of test conditions for Ione Grain* particles

	d_p, mm	T_B, K	U_{mf}, m/s	U_0, m/s	$\bar{T}_w$,† K
Tube array	2.14	810	1.60	1.0–2.8	404
		922	1.65	1.2–2.96	414
		1005	1.60	1.24–3.5	431
	3.23	810	2.20	1.42–2.76	392
		922	2.25	1.43–3.2	409
		1005	2.30	1.58–3.48	428
Single tube	2.14	810	1.55	1.24–2.8	391
		922	1.60	1.08–3.12	396
	3.23	810	2.20	1.58–2.76	382
		922	2.25	1.5–3.13	402

*53.5 percent silicon, 43.8 percent alumina, 2.3 percent titania, 0.4 percent other; $\rho_s = 2700$ kg/m^3; $k = 1.26$ w/mK; $c_p = 0.22$ cal/gK; $\epsilon = 0.86$ (estimated).
†Spatial-averaged tube wall temperature for tube M in the array and single tubes at bubbling bed. The spatial-averaged wall temperature for tubes T, M, and B were within a few degrees of each other at fluidized bed conditions.

of data are representative of the heat transfer behavior of tubes at the bottom, top, and the interior of a typical array. The particular equilateral triangular tube array was selected because this configuration seems to give better fluidization characteristics, and hence better heat transfer, than an in-line (square pitch) array (Gelperin et al., 1969). This tube arrangement is the most common in current industrial practice.

Data were also obtained for a single horizontal tube to compare with the results of tube bundle performance.

Experimental Apparatus

Figure 1 shows a schematic illustration of an instrumented tube. Bronze was chosen as the tube material, instead of stainless steel, to reduce the thermal resistance between the gages and the coolant so that the gage temperature limitation could be met. This has some effect, particularly regarding radiation absorption, on the data compared to the situation when stainless steel tubes were used. Knowing, however, that the maximum radiation contribution is on the order of 15 percent of the total heat transfer (Alavizadeh et al., 1985) and also considering the relatively small difference between the emissivities of bronze and stainless steel, this material substitution has a negligibly small effect on total heat transfer measurements. Additional discussion concerning the effect of different wall emissivities on radiation heat transfer is given by Alavizadeh (1985).

Three tubes were instrumented by mounting seven thermopile-type heat flux transducers side by side around half of each tube periphery (30 deg apart). The Micro-Foil Heat Flow Sensors, with copper-constantan surface temperature thermocouples, were bonded to the tubes with relatively high temperature thermal conducting epoxy and were tightly covered by 0.127 mm (0.005 in.) thick stainless-steel shim

Nomenclature

B = bottom tube in array
c_p = specific heat
d_p = surface mean particle diameter
$\bar{h}$ = spatial-averaged bed-to-tube heat transfer coefficient
h_θ = time-averaged local bed-to-tube heat transfer coefficient at angular position r
$h_{\theta_{max}}$ = maximum time-average local bed-to-tube heat transfer coefficient at angular position r
k = thermal conductivity
M = middle tube in array
T = top tube in array
T_B = temperature of fluidized bed
$\bar{T}_w$ = spatial-averaged tube wall temperature
U_0 = superficial gas velocity
U_{mf} = superficial gas velocity at minimum fluidization conditions
ϵ = emissivity
θ = angular position
ρ_s = density of solid particles

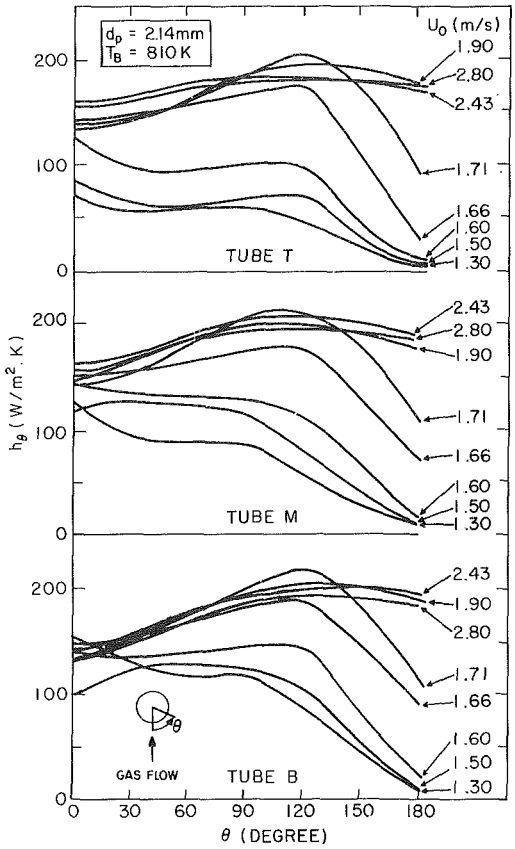

Fig. 4 Time-averaged local heat transfer coefficient versus angular position for top, middle, and bottom tubes in the array

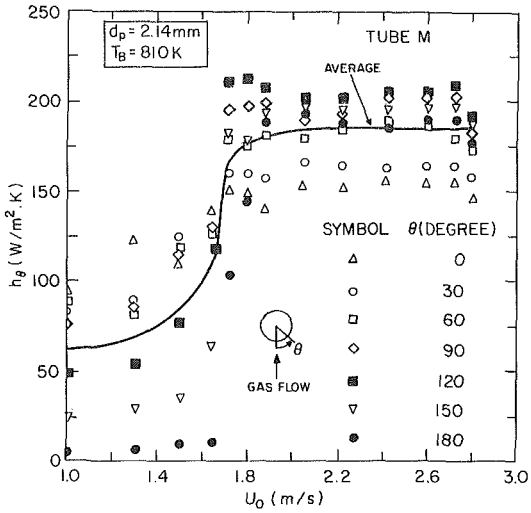

Fig. 5 Time-averaged local heat transfer coefficient versus superficial gas velocity on the middle tube in the array

stock. A schematic illustration of the high temperature fluidized bed facility is shown in Fig. 2.

Propane was burned in a refractory lined combustion chamber and the hot combustion gases directed into the 0.30 m × 0.60 m (1 ft × 2 ft) test section through a distributor plate. The tube array was positioned horizontally within the bed. A proportional-type controller was used to regulate the propane flow rate and maintain the desired gas temperature.

Two chromel-alumel thermocouples were used to measure the bed temperature. They were located centrally at 0.152 m (0.5 ft) and 0.457 m (1.5 ft) above the distributor plate and protruded into the fluidized bed 0.102 m (4 in.). The bed temperatures reported were taken from the lower-position thermocouple closer to the distributor plate, whereas the upper thermocouple was used to check the uniformity of the bed temperature during fluidization and also provided an indication of when the bed reached steady-state conditions. Galvin (1979) measured temperature distributions in the same fluidized bed for particle sizes of 1.285 mm and 3.5 mm and bed temperatures of 533 K (500°F), 810 K (1000°F), and 1144 K (1600°F). His results indicate the temperature readings from two thermocouples located at 0.152 m and 0.457 m elevations to be representative of the bed temperature. He also found that, for the larger particles, the bed temperature was better defined than in the case of the smaller ones, and measured a nearly flat temperature profile over the height of the emulsion region. Finally, he found that the temperature distribution in a hot fluidized bed is isothermal – with the stipulation that the area of concern is within the emulsion – and that boundary effects were negligible.

Bed temperatures were steady at each gas velocity; the short period of time required for data acquisition at each operating condition (about 103 s) assured constant bed conditions.

A digital data acquisition system was used to record local heat fluxes, surface temperatures and computed local heat transfer coefficients at each position on the instrumented tubes.

Experiments

Experiments were conducted at bed temperatures of 810 K (1000°F), 922 K (1200°F), and 1005 K (1350°F). A granular refractory (Ione Grain) was used as bed material. Bed particle sizes of 2.14 mm and 3.23 mm nominal diameter were employed. The size distribution of this material remained stable after many hours of bed operation.

An array of nine tubes arranged in three horizontal rows, as previously described, was used. Data were also obtained for a single horizontal tube for comparison with the results of tube bundle performance. This tube was located where tube M was positioned in the array. Figure 3 is an illustration of the array geometry.

A summary of test conditions, along with the thermal properties (measured by Gafourian, 1984) and chemical compositions of Ione Grain particles, is given in Table 1. Throughout this paper, the top, bottom, and middle tubes are designated as "T," "B," and "M," respectively.

Results and Discussion

Heat transfer results are presented both for tube arrays and single tubes as time-averaged local values. The effects of superficial gas velocity, particle size, and bed temperature are shown. Results for the top, middle, and bottom tubes are also compared with those for a single tube. Using the root sum-square (RSS) method of Thrasher and Binder (1957), the uncertainty in local heat transfer coefficient values is estimated at ±9%.

Effect of Superficial Gas Velocity. The most obvious effect is the very large change in magnitude of the local heat transfer coefficient at the upper stagnation point on each tube as the superficial gas velocity is changed. In Fig. 4, the local heat transfer coefficient h_θ on the top of tube M shows an increase from 6 to 185 W/m^2·K with a superficial gas velocity increase from 1.3 to 2.43 m/s. Similar trends are also displayed for tubes T and B. This behavior is known to be related to the formation of a relatively cool stagnant cap of particles which remain on the top of the tubes at low superficial velocities. At higher velocities, however, the stack is removed. Available information in the literature (George, 1981; Glass and Harrison, 1964; Lowe et al., 1979; Catipovic, 1979) confirms this observation.

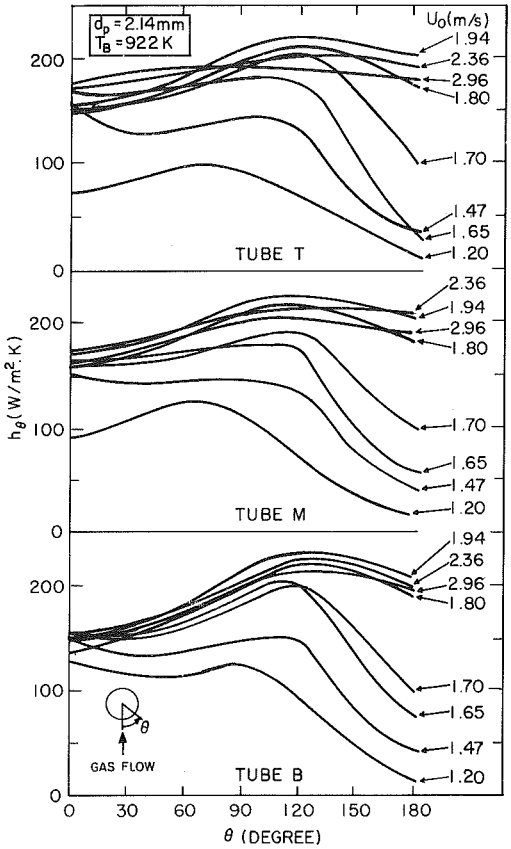

Fig. 6 Time-averaged local heat transfer coefficient versus angular position for top, middle, and bottom tubes in the array

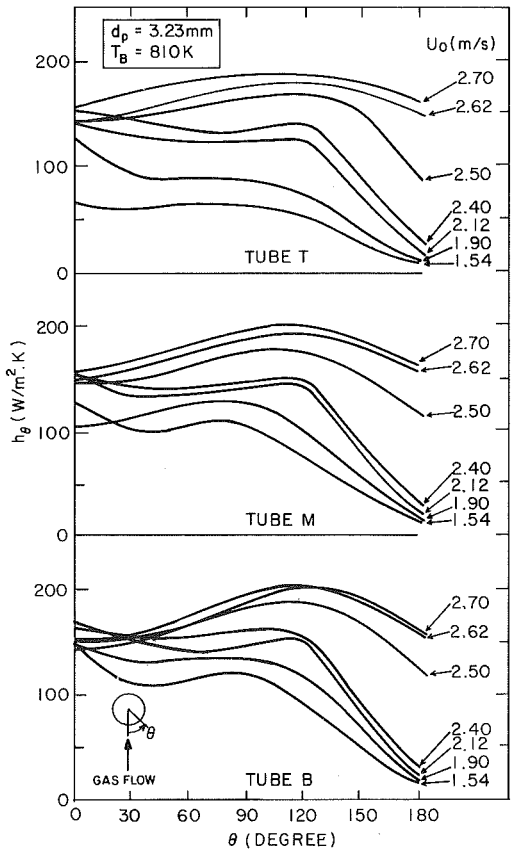

Fig. 7 Time-averaged local heat transfer coefficient versus angular position for top, middle, and bottom tubes in the array

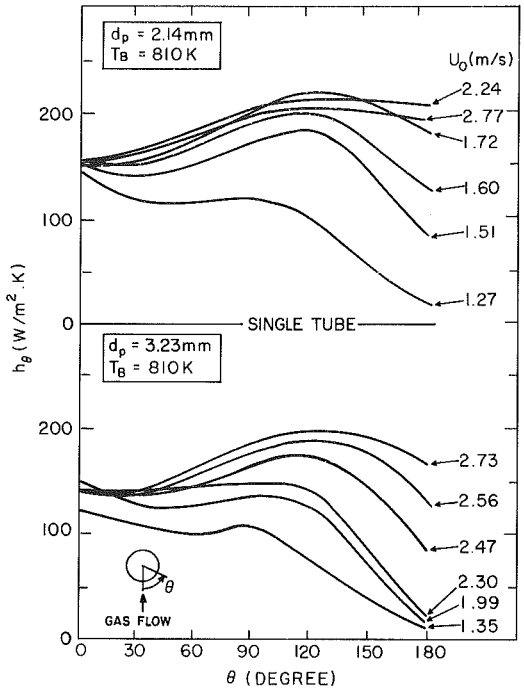

Fig. 8 Time-averaged local heat transfer coefficient versus angular position for single tubes

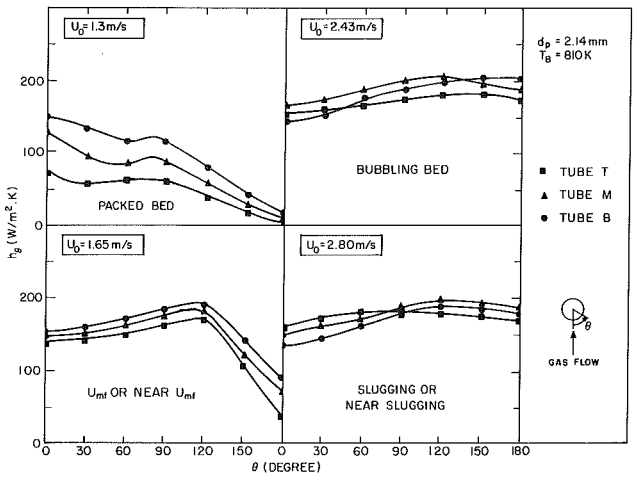

Fig. 9 Time-averaged local heat transfer coefficient versus angular position for top, middle, and bottom tubes in the array at different superficial gas velocities

The distribution of the local heat transfer coefficient around the surface of the tubes seems to approach an asymptotic limit as the gas velocity is increased. This limit was reached at a larger value of U_0/U_{mf} for the smaller particles than for the larger particles at the same bed temperature when compared with data of Alavizadeh et al. (1985) for a single tube and particle sizes of 0.52 mm and 1.0 mm. Therefore, higher velocities and larger bed particle diameters are attractive from the standpoint of thermal stresses in tubes. This behavior is also consistent with the results of George (1981) and Catipovic (1979).

At the lower stagnation points on the tubes, the heat transfer coefficient varies with U_0 in an irregular manner for packed beds. For fluidized beds, stagnation point heat transfer rates are nearly constant. The increase of h_θ at any position (except at $\theta = 180$ deg), for the range of superficial velocities considered, is higher for tube T than for tubes M and B for all bed temperatures and particle sizes considered.

As the gas velocity is increased the location of maximum local heat transfer coefficient $h_{\theta_{max}}$ varies from the bottom to the side of the tubes (around 120 to 135 deg) and in some cases tends to shift to the top.

Local heat transfer coefficients are shown as functions of U_0 for all seven locations on tube M in Fig. 5. Values of the spatial-averaged heat transfer coefficient $\bar{h}$ are also shown. Thermal stresses would, in general, be greatest at, or near, U_{mf}. Similar behavior was experienced by tubes B and T. For the smaller particles tested ($d_p = 2.14$ mm), the maximum local heat transfer coefficient $h_{\theta_{max}}$ was observed to be highest at moderate superficial gas velocities (for all tubes, Figs. 4 and 6). For the larger particle size, $h_{\theta_{max}}$ continued to increase with increasing gas velocity over the entire range (Fig. 7).

Effect of Particle Size. An observation of Figs. 4 and 7 indicates that the local coefficients at a particular angular position are significantly influenced by the particle size under certain conditions. A bed of smaller particles is more sensitive to velocity changes than one containing larger particles, except for the 180 deg position. The same behavior is true for a single tube (Fig. 8). Also, higher rates of heat transfer are obtained in a bed of smaller particles.

Effect of Bed Temperature. Local heat transfer coefficients did show a moderate increase with increasing bed temperature. For tube B, the largest local coefficient $h_{\theta_{max}}$ increased by less than 7 percent for an increase in bed temperature from 810 K to 922 K. (Smaller increases were observed for tubes M and T.) This is likely due to an increase in radiant heat transfer between the bed and the tubes, and the change in thermal properties of the gas. Alavizadeh et al. (1984) found, for $d_p = 2.14$ mm, a radiation contribution of about 8 and 13 percent for bed temperatures of 810 K and 1050 K, respectively.

Comparison of Tube Heat Transfer Performance. Figure 9 shows local heat transfer coefficients for tubes B, M, and T for different superficial gas velocities. At velocities well above U_{mf}, the difference in local values for the three tubes did not exceed 20 percent, whereas, at packed bed conditions, the differences were significantly greater. At slugging or near slugging cases (and all bed conditions), the values of local heat transfer coefficients for the side of the tubes ($\theta = 90$ deg) nearly coincide. This suggests that, at high gas velocities, similar particle motion exists near the sides of the tubes. Except at velocities near U_{mf}, tube T experienced less variation in h_θ than tubes M and B. A comparison between Figs. 4, 7, and 8 suggests that, in the case of bubbling beds, single tube studies are useful for predicting heat transfer with staggered tube bundles with a pitch-to-diameter ratio of 3 or greater. Similar conclusions have been reached in other investigations (Catipovic, 1979; Borodulya et al., 1980b) for a pitch-to-diameter ratio of 2 or greater.

Summary of Results

A summary of the findings in this study is the following:

(*a*) The tops of the tubes experienced the formation of a defluidized stack of particles at low superficial gas velocities which was removed at higher velocities. For single tubes, this behavior is less pronounced than for tube arrays for the same bed conditions.

(*b*) Local heat transfer coefficients approached an asymptotic limit as the gas velocity increased. This limit was approached at slightly larger values of U_0/U_{mf} for the smaller particles, $d_p = 2.14$ mm, than for the larger particles, $d_p = 3.23$ mm.

(*c*) At the bottom of the tubes, $\theta = 0$, h_θ varied with U_0 in an irregular manner.

(*d*) The maximum local heat transfer coefficient, occurring at $\theta = 0$ for packed-bed conditions, was observed to occur at larger values of θ as the gas velocity was increased.

(*e*) The maximum local value $h_{\theta_{max}}$ was highest at moderate superficial gas velocities with the smaller particles. For the larger particles, higher values of $h_{\theta_{max}}$ were observed to increase steadily with increasing gas velocities for both single tubes and array conditions.

(*f*) Heat transfer behavior was more sensitive to gas velocity variations for the smaller particle experiments. Also, higher rates of heat transfer were obtained in a bed of smaller particles.

(*g*) A general observation of h_θ showed a moderate increase with bed temperature.

(*h*) The difference in local values for the three tubes did not exceed 20 percent at higher gas velocities. These differences were significantly greater at packed bed conditions.

(*i*) In bubbling beds, single tube studies are representative of heat transfer behavior of tube arrays.

Acknowledgments

This work was supported by a grant from Battelle Memorial Institute, Pacific Northwest Laboratories, Richland, Washington.

References

Alavizadéh, N., 1985, "An Experimental Investigation of Radiative and Total Heat Transfer Around a Horizontal Tube Immersed in a High Temperature Gas-Solid Fluidized Bed," Ph.D. Thesis, Dept. of Mechanical Eng., Oregon State University, Corvallis, OR.

Alavizadeh, N., Fu, Z., Adams, R. L., Welty, J. R., and Goshayeshi, A., 1985, "Radiative Heat Transfer Measurements for a Horizontal Tube Immersed in Small and Large Particle Fluidized Beds," *Proceedings, International Symposium on Heat Transfer*, Beijing, China.

Alavizadeh, N., Adams, R. L., Welty, J. R., and Goshayeshi, A., 1984, "An Instrument for Local Radiative Heat Transfer Measurement in a Gas-Fluidized Bed at Elevated Temperatures," *Proceedings, 22nd ASME/AIChE National Heat Transfer Conference*, Niagara Falls, NY.

Baskakov, A. P., Berg, B. V., Vitt, O. K., Filippovsky, N. F., Goldobin, J. M., and Maskaev, V. K., 1973, "Heat Transfer to Objects Immersed in Fluidized Beds," *Powder Tech.*, Vol. 8, pp. 273–282.

Berg, B. V., and Baskakov, A. P., 1974, "Investigation of Local Heat Transfer Between a Fixed Horizontal Cylinder and a Fluidized Bed," *Int. Chem. Eng.*, Vol. 14, No. 3, pp. 440–443.

Borodulya, V. A., Ganzha, V. L., Upadhyay, S. N., and Saxena, S. C., 1980a, "Heat Transfer From In-Line and Staggered Horizontal Smooth Tube Bundles Immersed in a Fluidized Bed of Large Particles," *Int. J. of Heat & Mass Transfer*, Vol. 23, pp. 1602–1604.

Borodulya, V. A., Ganzha, V. L., Zheltov, A. I., Upadhyay, S. N., and Saxena, S. C., 1980b, "Heat Transfer Between Gas-Solid Fluidized Beds and Horizontal Tube Bundles," *Letters in Heat and Mass Transfer*, Vol. 7, pp. 83–95.

Catipovic, N. M., 1979, "Heat Transfer to Horizontal Tubes in Fluidized Beds: Experiment and Theory," Ph.D. Thesis, Dept. of Chemical Eng., Oregon State University, Corvallis, OR.

Chandran, R., Chen, J. C., and Staub, F. W., 1980, "Local Heat Transfer Coefficients Around Horizontal Tubes in Fluidized Beds," ASME JOURNAL OF HEAT TRANSFER, Vol. 102, pp. 152–157.

Cherrington, D. C., Golan, L. P., and Hammitt, F. G., 1977, "Industrial Application of Fluidized Bed Combustion – Single Tube Heat Transfer Studies," *Proceedings, Fifth International Conference on Fluidized Bed Combustion*, C. Bliss, ed., Washington, D.C., Vol. 3, pp. 184–209.

Galvin, W., 1979, "Temperature Profiles in a Hot Fluidized Bed," M.S. Project Report, Dept. of Mechanical Eng., Oregon State University, Corvallis, OR (unpublished).

Gelperin, N. I., and Ainshtein, V. G., 1971, "Heat Transfer in Fluidized Beds," *Fluidization*, J. F. Davidson and D. Harrison, eds., Academic Press, London, p. 471.

Gelperin, N. I., Ainshtein, V. G., and Korotyanskaya, L. A., 1969, "Heat Transfer Between a Fluidized Bed and Staggered Bundles of Horizontal Tubes," *Int. Che. Eng.*, Vol. 9, No. 1, pp. 137–142.

George, A. H., and Welty, J. R., 1984, "Local Heat Transfer Coefficients for a Horizontal Tube in a Large-Particle Fluidized-Bed at Elevated Temperature," *AIChE Journal*, Vol. 30.

George, A. H., 1981, "An Experimental Study of Heat Transfer to a Horizontal Tube in a Large Particle Fluidized Bed at Elevated Temperature," Ph.D. Thesis, Dept. of Mechanical Eng., Oregon State University, Corvallis, OR.

Ghafourian, M. R., 1984, "Determination of Thermal Conductivity, Specific

Heat, and Emissivity of Ione Grain," M.S. Project, Dept. of Mechanical Eng., Oregon State University, Corvallis, OR (unpublished).

Glass, D. H., and Harrison, D., 1964, "Flow Patterns Near a Solid State Obstacle in a Fluidized Bed," *Chem. Engr. Sci.*, Vol. 19, pp. 1001–1002.

Golan, L. P., Lalonde, G. V., and Weiner, S. C., 1980, "High Temperature Heat Transfer Studies in a Tube Filled Bed," Exxon Res. & Eng. Co., *6th Int. Conf. on FBC*, Atlanta, GA, Vol. 3, pp. 1173–1185.

Grewal, N. S., and Saxena, S. C., 1983, "Experimental Studies of Heat Transfer Between a Bundle of Horizontal Tubes and a Gas-Solid Fluidized Bed of Small Particles," *Ind. Eng. Chem. Process Des.*, Vol. 22, No. 3, pp. 367–376.

Loew, O., Schmutter, B., and Resnick, W., 1979, "Particle and Bubble Behavior and Velocities in a Large-Particle Fluidized Bed With Immersed Obstacles," *Powder Tech.*, Vol. 22, pp. 45–57.

Noak, R., 1970, "Lokaler Wärmeübergang an Horizontalen Rohren in Wirbelschichten," *Chem. Ing. Tech.*, Vol. 42, No. 6, pp. 371–376.

Peeler, J. P. K., and Whitehead, A. B., 1982, "Solids Motion at Horizontal Tube Surfaces in a Large Gas–Solid Fluidized Bed," *Chem. Eng. Sci.*, Vol. 17, No. 1, pp. 77–82.

Saxena, S. C., Grewal, N. S., Gabor, J. D., Zabrodsky, S. S., and Galershtein, D. M., 1978, "Heat Transfer Between a Gas Fluidized Bed and Immersed Tubes," *Advances in Heat Transfer*, Vol. 14, pp. 149–247.

Strom, S. S., Dowdy, T. E., Lapple, W. C., Kitto, J. B., Stanoch, T. P., Boll, R. H., and Sage, W. L., 1977, "Preliminary Evaluation of Atmospheric Pressure Fluidized-Bed Combustion Applied to Electric Utility Large Steam Generators," EPRI Report No. RP 412–1, Electric Power Research Institute, Palo Alto, CA.

Thrasher, L. W., and Binder, R. C., 1957, "A Practical Application of Uncertainty Calculations to Measured Data," *Trans. ASME*, Vol. 79, pp. 373–376.

Vadivel, R., and Vedamurthy, V. N., 1980, "An Investigation of the Influence of Bed Parameters on the Variation of the Local Radiative and Total Heat Transfer Around an Embedded Horizontal Tube," *Proceedings, 6th Int. Conf. on Fluidized Bed Combustion*, Atlanta, GA, Vol. 3, pp. 1159–1172.

R. S. Figliola
Mem. ASME

E. G. Suarez[1]

Thermal/Fluid Sciences Research Laboratory,
Department of Mechanical Engineering,
Clemson University,
Clemson, SC 29631

D. R. Pitts
Department of Mechanical
and Aerospace Engineering,
University of Tennessee,
Knoxville, TN
Mem. ASME

Mixed Particle Size Distribution Effects on Heat Transfer in a Fluidized Bed

Introduction

Research interest in fluidized bed heat transfer has been sustained by the increasing adaptation of this form of heat transfer device to a wide variety of applications. For both practical and economical reasons, the particle size distribution as supplied to a bed can vary widely. This initial distribution is not constant due to breakage, wear, elutriation, or combustion within the bed. Consequently a fluidized bed heat exchanger is usually operated with a broad distribution of particle sizes at any time during a process. In contrast, most of the heat transfer literature reporting analytical or experimental investigations of fluidized bed-heater surface configurations has focused on fluidized beds with nearly uniform particle sizes. Many mixed-bed experimental studies have failed to document the size distributions used. Does size distribution have an effect on heat transfer? Could it explain certain discrepancies apparent in the reported literature?

While it has been known for some time that the presence of fines in a large particle bed improves heat transfer, only isolated references to systematic studies of heat transfer in mixed-particle-size beds are available in the literature. There is some consensus that a particle size smaller than the weight mean particle size is necessary to provide agreement to established heat transfer correlations [1–3]. This paper reports on a series of systematic experiments designed to study the effects of binary mixtures on heat transfer between an isothermal horizontal cylinder and an atmospheric fluidized bed.

Experimental Apparatus

The fluidized bed vessel consisted of a rectangular column 200 cm high with a 30.5 cm × 30.5 cm cross section. The fluidizing gas was oil-free compressed air metered by an in-line laminar flow element. A 2-cm-thick porous plastic distributor plate, offering a suitable pressure drop for uniform flow, was used. Bed temperatures were measured using thermocouples located symmetrically above and below a single tube heat exchanger surface. The nominal steady-state bed temperature was 303 K.

In all tests, overall average and azimuthally dependent average heat transfer values were determined using a 5-cm-dia, 25.4-cm-long solid cylinder which was situated along a horizontal plane 15.9 cm above the distributor plate. The cylinder was heated internally, by a 25.4-cm-long resistance heater controlled by a variable d-c power supply, to 35 K above the bed temperature. Six surface and four internal thermocouples were used to monitor cylinder temperature. End effect heat losses were minimized by using teflon end plates. Conduction end losses were typically less than 3 percent of the total heat transfer. Surface radiation losses were conservatively estimated to be less than 0.5 percent of the total heat flux from the cylinder.

Table 1

Nominal composition, percent by weight*	Actual composition, percent by weight*	d_p, μm	U_{mf}, cm/s
0	2	256	4.9
15	16	276	5.5
30	35	300	6.1
50	57	340	7.0
85	84	453	11.4
90	89	497	17.4
100	100	509	19.4
100	100	568	21.2

*Percent particles larger than 297 μm.

The azimuthally dependent average heat transfer from the cylinder was determined by the heat loss from an isothermal 127-μm, 1.5-cm-wide by 25.4-cm-long stainless steel strip. The flush-mounted strip was insulated and isolated from the cylinder by a 6-mm-thick phenolic insulator. The strip was maintained at a temperature equal to that of the cylinder by surface resistance heating with current control provided by a variable power supply. Four thermocouples, located along the strip length, were used to monitor strip temperature. The cylinder could be rotated allowing repositioning of the strip. Measurements were taken at 45 deg increments from the 0 deg stagnation point.

The average convection heat transfer coefficient was estimated by

$$h = w/A_s(T_0 - T_b) \tag{1}$$

where w is the corrected power required to maintain an isothermal surface of area A_s at temperature T_0 in a bed at temperature T_b. In the course of experimentation, the integrated spatial data taken from the strip were found to agree with the overall cylinder heat transfer data to within ±3.5 percent. The cylinder and the strip were found to be isothermal along their lengths to within ±1 K and ±0.75 K, respectively, when maintained at a nominal 338 K.

For these experiments the average particle size was varied but the type and the total quantity by weight of fluidized material was kept constant. The bed was charged with 40.8 kg of spheroidal ($\phi = 0.90$) glass beads which resulted in an average stagnant bed height of 31 cm. Bed particulates were

[1]Present address: Pratt & Whitney Aircraft Co., W. Palm Beach, FL.

Contributed by the Heat Transfer Division for publication in the JOURNAL OF HEAT TRANSFER. Manuscript received by the Heat Transfer Division November 18, 1985.

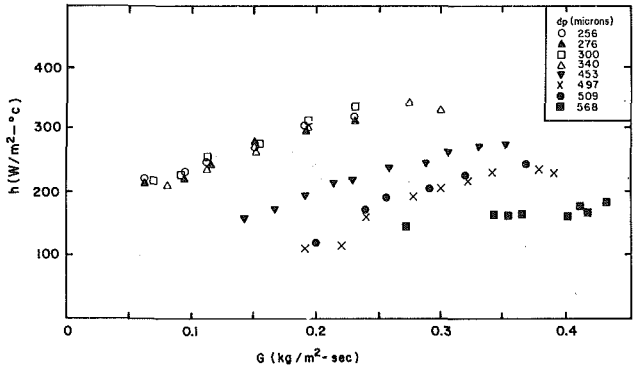

Fig. 1 Overall heat transfer coefficients versus mass fluidizing velocities for various binary mixtures

prepared from two base mixtures, each base containing a narrow particle size distribution of 509 μm (base A) and 256 μm (base B) mean particle size, respectively. Systematic tests were first conducted with the individual base sizes followed by tests conducted using various binary mixtures of the two base sizes. A third base size of 568 μm (base C) was used as a control and was not blended. A mixture mean particle size d_p was found from sieve analysis using the surface area to volume weighted diameter of

$$d_p = (\sum_i (\chi_i d_{pi}^n))^{1/n} \qquad n = -1 \tag{2}$$

where χ_i is the weight fraction of size d_{pi}. The base A batch was prepared from particles which passed through ASTM sieve size 30 but were retained by sieve size 35. Base B was prepared in a similar manner using sieve sizes 50 and 60, respectively. The reported particle sizes are based on an average of sieve analyses performed on random samples taken during the course of the tests and reflect the actual compositions. Sieve analyses were performed according to the ASTM standard and using screen sizes 20 through 100.

A complete uncertainty analysis [4] of the experimental procedure and analysis of data in the manner suggested by Abernathy et al. [5] was carried out. Results suggest that the determined values of overall and azimuthally dependent heat transfer coefficients have a typical uncertainty of ± 7.5 and ± 8 percent, respectively, at the 95 percent confidence level.

Results and Discussion

The experiments were performed in the bubbling flow regime at velocity ratios (U/U_{mf}) ranging from 0.86 to 3.6. The upper limit on U/U_{mf} was restrained in order to limit bubble size so as to minimize bubble to wall effects on the test data due to bed scale [6]. Table 1 lists the schedule of mixtures tested and the minimum fluidization velocity determined for each mixture. The values reported are in conservative agreement with available predictions [7] with an rms error of 11.5 percent.

Measured values of the overall heat transfer coefficients for each mixture versus mass fluidizing velocity G are given in Fig. 1. The measured values for the 509 μm and 256 μm base mixtures form the lower and upper bounds of the mixture results. With the addition of the fine base into the larger, a significant change in the heat transfer data is noted by 453 μm. In this case, while the bed mean particle size was reduced by about 11 percent, the average heat transfer coefficient was augmented from between 25 percent at $G = 0.23$ kg/m^{2}s to 40 percent at $G = 0.30$ kg/m^{2}s. This trend continued through the 340 μm mixture, beyond which little affect on the heat transfer coefficient was noted even though the mixture mean particle size was decreased some 33 percent further. The data for the control batch (568 μm) were taken at the onset of all testing and again at the conclusion of all testing. The data were identical to within 5 percent.

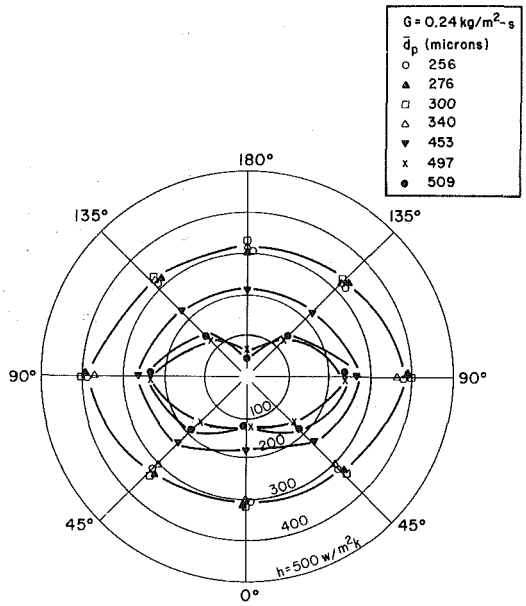

Fig. 2 Azimuthal dependency of heat transfer coefficient for various binary mixtures

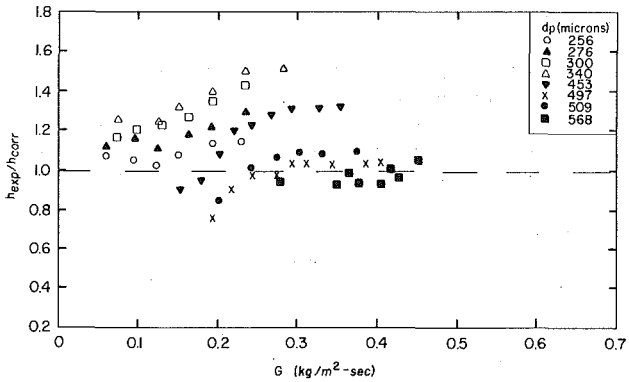

Fig. 3 Comparison of experimental data with the Grewal-Saxena correlation

As in the case of the overall heat transfer coefficient, the azimuthally dependent heat transfer was affected by mixture composition at all angular locations. For a given mass flux and angular position, the magnitude of the heat transfer coefficient was observed to remain essentially constant for mixtures containing up to 50 percent of the 509 μm particles. A representative case is shown in Fig. 2 for one nominal mass velocity. The behavior and magnitude of the azimuthal data are closely related to the hydrodynamics at a particular position on the cylinder surface. At low relative values of mass flux, the higher heat transfer coefficients were observed in the fluidized region around the cylinder. Within this region, the enhanced fluidization at the 90 deg position causes the heat transfer coefficient to attain its maximum value at lower fluidization velocities than for other angular positions. At the 90 deg position, the heat transfer coefficient remained essentially constant with mass flux for all mixtures. In the unfluidized region, the magnitude of the azimuthal coefficient was enhanced by increasing mass flux, that is by increasing the interstitial gas velocity at the tube surface. At higher values of mass flux, the entire region around the cylinder became fluidized with the heat transfer coefficient distribution becoming more symmetric. This behavior is similar to that observed in beds containing uniform distributions. For the case shown in Fig. 2, the entire region about the cylinder was fluidized for particle sizes up to 453 μm.

For practical reasons, a design engineer is interested in the prediction of the heat transfer coefficient for heat exchanger sizing requirements. For this reason, the data were compared to several pertinent correlations for fluidized beds using horizontal tubes [2, 8, 9]. All correlations were found to underpredict the heat transfer measurements in the binary beds. Best agreement was found in the comparisons between the experimental data and the Grewal–Saxena correlation [8] which are shown in Fig. 3. For this correlation, the bed void fraction [8] is based on the overall mean particle size from equation (2). The uniform distributions are within 10 percent rms error of the correlation predictions; this is good agreement for the particle materials used. However, the addition of a percentage of large particles (base A) to the small particle (base B) bed caused increasingly poor agreement between the measured data and the predictions for the binary mixtures up to 340 μm. In general, a further addition of base A particles caused a progressive reduction in this deviation down to the uniform 509 μm baseline agreement. The rms error between data and prediction is summarized as: 256 μm at 10 percent, 275 μm at 17 percent, 300 μm at 27 percent, 340 μm at 37 percent, 453 μm at 26 percent, 497 μm at 7 percent, and 509 μm at 9 percent.

Biyikli and Chen [10] reported binary bed data which also displayed a marked disparity relative to the correlations. While only mixtures with 50 percent or more large particles for a diameter ratio of 0.35 were tested, their high velocity, small bed size data displayed an rms error variation of some 27 percent between uniform and binary bed comparisons to the correlations [2, 8].

Attempts were made to redefine the mean particle size of the mixtures using different definitions arrived at by variation of the exponent in equation (2). Not unexpectedly, the mass fraction weighted values attempted ($n = 1, -0.5$) yielded larger mixture mean sizes and, hence, even poorer agreement with the established correlations.

The interaction between the heat transfer and the bed hydrodynamics suggests that the local gas velocity and the local void fraction at the cylinder surface are major parameters in the heat transfer problem. The local void fraction is strongly dependent on bed particle size distribution and interstitial velocity at the heat transfer surface. It is well documented that packed beds containing mixtures of particle sizes exhibit different void fractions from beds containing particles of uniform size and of similar weight mean size [11]. The measured packed bed void fractions were within 1.5 percent of those reported in [11]. For a binary bed with a 0.5 size ratio, a minimum voidage occurs with a 50–50 percent blend with maximum voidage occurring for either 100 percent blend. The relationship between the heat transfer data and the correlation follows this trend.

In summary, the experimental results for binary distribution beds with a size ratio of 0.5 are reported. The qualitatively known phenomenon in which the addition of smaller diameter particles to an otherwise large particle bed can significantly alter the heat transfer was documented systematically. Specifically, it was found that: (*i*) A binary bed containing mostly smaller particles provides heat transfer corresponding to particle beds of a size equivalent to that of the small particle diameter, and (*ii*) heat transfer correlations tend to underpredict systematically heat transfer in binary, bubbling regime beds. Size distribution does have an effect on heat transfer. Documentation of the bed particle size distribution is necessary if heat transfer data are to be compared.

Acknowledgments

The authors gratefully acknowledge support for this work by the National Science Foundation through Grant No. ISP-8011451, and the assistance of D. S. Eggers.

References

1 Golan, L. P., Cherrington, D. C., Deiner, R., Scarborough, C. E., and Weiner, S. C., "Particle Size Effects in Fluidized Bed Combustion," *Chemical Engineering Progress*, Vol. 75, 1969, pp. 63–66.

2 Andeen, B. R., and Glicksman, L. R., "Heat Transfer to Horizontal Tubes in Shallow Beds," *ASME-AIChE Heat Transfer Conference*, St. Louis, MO, 1976, Paper No. 76-HT-67.

3 Pitts, D. R., Figliola, R. S., and Hamlyn, K. M., "Heat Transfer Between a Horizontal Cylinder and an Air Fluidized Bed of Mixed Particle Sizes," ASME JOURNAL OF HEAT TRANSFER, Vol. 104, No. 3, 1982, pp. 563–565.

4 Suarez, E. G., "Instantaneous, Azimuthal and Average Heat Transfer Between a Horizontal Cylinder and a Gas Fluidized Bed of Mixed Particle Sizes," Ph.D. Dissertation, Clemson University, Aug. 1983.

5 Abernathy, R. B., Benedict, R. P., and Dowdell, R. B., "ASME Measurement Uncertainty," ASME *Journal of Fluids Engineering*, Vol. 107, 1985, pp. 161–164.

6 Bar-Cohen, A., Glicksman, L. R., and Hughes, R. W., "Semiempirical Prediction of Bubble Diameter in Gas Fluidized Beds," *International Journal of Multiphase Flow*, Vol. 7, 1981, pp. 101–113.

7 Cheung, L., Nienow, A. W., and Rowe, P. N., "Minimum Fluidization Velocity of a Binary Mixture of Different Sized Particles," *Chemical Engineering Science*, Vol. 29, 1974, pp. 1301–1303.

8 Grewal, N. S., and Saxena, S. C., "Heat Transfer Between a Horizontal Tube and a Gas–Solid Fluidized Bed," *International Journal of Heat and Mass Transfer*, Vol. 23, 1980, pp. 1505–1518.

9 Goel, I., and Saxena, S. C., "Dependence of Heat Transfer Coefficient for an Immersed Smooth Horizontal Tube in a Fluidized Bed on Operating and System Variables," *Proceedings 7th International Conference on Fluidized Bed Combustion*, 1982, pp. 804–818.

10 Biyikli, S., and Chen, J. C., "Effect of Mixed Particle Sizes on Local Heat Transfer Coefficients Around a Horizontal Tube in Fluidized Beds," *Proceedings 1982 International Heat Transfer Conference*, Vol. 6, 1982, pp. 39–44.

11 Ridgeway, K., and Tarbuck, K. J., "Particulate Mixture Bed Densities," *Chemical and Process Engineering*, Vol. 49, No. 2, 1968, pp. 103–104.

P. Testa
Istituto di Fisica Tecnica,
Università di Roma,
Rome, Italy

L. Nicotra
Mechanical Engineer,
Divisione Analisi Sistemi,
"Elettronica," S.p.A.,
Rome, Italy

Influence of Pressure on the Leidenfrost Temperature and on Extracted Heat Fluxes in the Transient Mode and Low Pressure

In the cooling of a hot surface by means of single water droplets impinging from above, the Leidenfrost temperature was measured as a function of pressure, below atmospheric pressure. Heat fluxes and temperature transients were recorded as functions of pressure, with relatively high time resolution, as allowed by the fast response to thermal transients of the test section and measuring equiqment especially developed for this purpose.

Introduction

The present paper reports measurements of the Leidenfrost point and transient heat flux associated with droplets of demineralized water impinging on a hot plate at pressures below atmospheric pressure.

Measurements were performed with the method and the equipment described in [1], suitably modified, as reported below, which facilitated the study of the heat and mass transfer process and the Leidenfrost phenomena, which take place when one or more liquid droplets impinge on a hot solid surface. With the relatively high time resolution of the measuring equipment and of the test section, it was possible to point out some features which were peculiar to the transient phase of the cooling process at atmospheric pressure.

It was possible to determine the Leidenfrost temperature with some accuracy by observing the cooling pulses created in a small surface area impinged upon by incident droplets. The cooling pulses, which normally have an almost rectangular shape during the evaporation phase, turn into sharp peaks when the Leidenfrost temperature is reached, because the droplets then do not adhere to the surface but rebound on the quickly generated vapor layer.

It is well known that when the surface temperature is raised beyond the Leidenfrost point, the extracted heat and, therefore, the cooling capability is considerably reduced.[1] However, it seems possible to recover good cooling efficiency even in this condition, if a pulselike mode of cooling is pursued with chopped sprays or with a properly controlled sequence of single drops, as shown in [1].

Besides the basic knowledge gained from studying the Leidenfrost temperature with single drops at low pressure, it is likely that a good base for improving comprehension of the film boiling mechanism at low pressure will be obtained. This latter type of boiling frequently occurs even at normal atmospheric pressure when, as a consequence of hydrodynamic effects, local pressure may fall below normal atmospheric pressure.[2]

A literature review [2–37] revealed that, although the dependence of the Leidenfrost temperature has been explored above atmospheric pressure [27, 28], no paper was found pulished in recent years concerning droplet cooling in the Leidenfrost temperature range, and above, at subatmospheric pressure.

Apparatus

Figure 1 shows a sketch of the whole apparatus. It consists of four sections:

1 a vacuum or low-pressure chamber VCH with cabling facilities for signal processing and power supply from outside;
2 a system for producing single drops and introducing them in a low-pressure environment with controlled timing;
3 a test section with detectors of the thermal events caused by drop cooling;
4 a signal display and measuring system.

The vacuum chamber is evacuated by a standard rotative-diffusion pump system RD.

The internal pressure is raised from its minimum by admitting atmospheric air through a needle valve NV with fine control, and is measured by a precision mercury manometer PG. The test section, enclosed within the vacuum chamber, is similar to that described in [1]; it consists essentially of a heated cavity C, which approximates a black body, and a thin molybdenum strip MS, placed over the aperture of the cavity to serve as a controlled heated surface.

The cavity is essentially a thick-walled copper cylinder heated by means of coaxially insulated high-temperature resistors. Mineral wool (Fig. 1) insulates the hot cylinder walls in every direction except that corresponding to the aperture of the cavity.

The molybdenum strip is heated primarily by radiation and convection (by the residual air) from the cavity. It is arranged

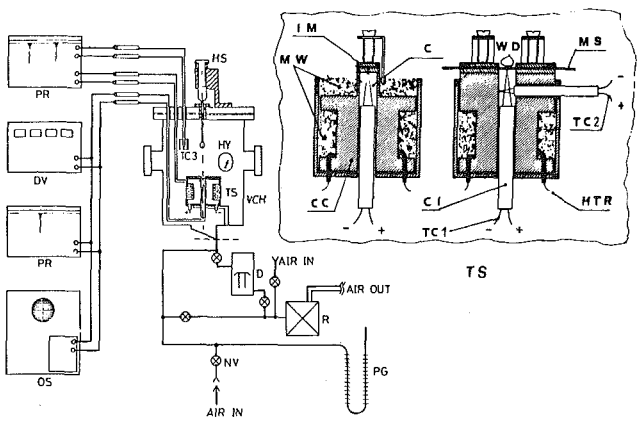

Fig. 1 The apparatus

[1] The cooling capability of the refrigerant drops due to the vapor layer which develops on the hot surface and acts as a thermal insulating layer between the surface and the refrigerant.

[2] For the abovementioned reasons of interest, it is worthwhile to study in more detail the basic phenomena involved in the transient mode of cooling.

Contributed by the Heat Transfer Division for publication in the JOURNAL OF HEAT TRANSFER. Manuscript received by the Heat Transfer Division March 6, 1984.

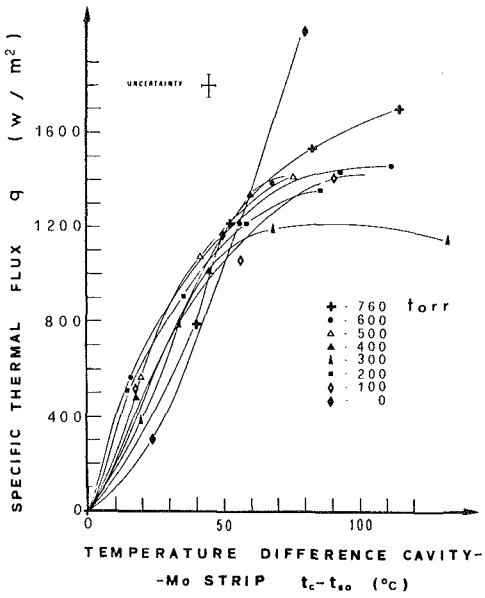

Fig. 2 Calibration curves of the specific heat flux q versus the difference of temperature $t_c - t_{so}$

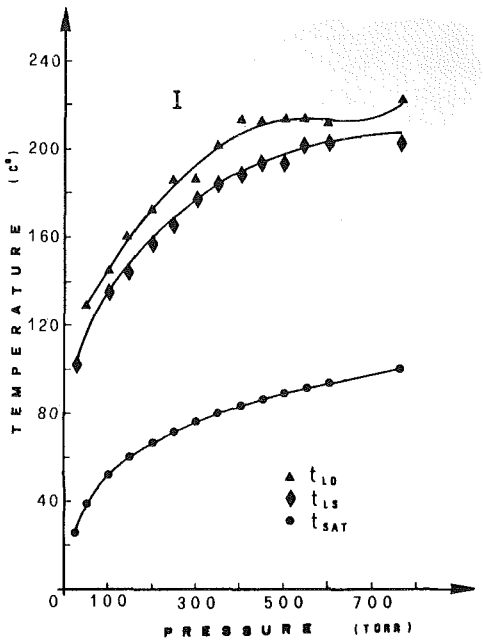

Fig. 3 The temperature of Leidenfrost versus the pressure in the two following conditions: t_{LD}—spikes begin to appear in temperature signals (dynamic case); t_{LS}—the liquid still wets the strip, but suddenly after the contact a vapor film is developed (steady case)

(Fig. 1) for the purpose of limiting transverse heat flow in favor of the vertical direction [1].

The water drops fall on a fixed small spot of this surface, to which a thermocouple TC1 is soldered on the lower side[3] corresponding with the area cooled by the drops from above. The soldering had to be performed in a high vacuum in order to avoid severe oxidation and damage to the thin strip. The thinness (0.2 mm) of the molybdenum strip combined with the excellent thermal diffusivity of molybdenum enables the thermocouple TC1 to sense, without sensible distortion, the fast temperature transients produced by the water drops impinging on the target.

The radiative heating helps to transfer considerable heat flow between the cavity and the Mo strip, with the possibility of fast variation, as required by the process involved, provided the receiver, as is the case (the Mo strip), has small thermal capacity. Having a rapidly varying heat flux is believed to be an important factor in performing experimental checks, with the purpose of assessing the true limit-cooling capability involved in the cooling process under study.

A second thermocouple TC2 senses the temperature of the radiating cavity, which is expected to be constant. The heat fluxes exchanged between the cavity and the strip are determined knowing the temperatures read by TC1 and TC2. The direct calibration of heat flux versus TC1 and TC2 was performed as described below.

The droplets are produced by means of a hypodermic syringe. A thin stainless steel wire is inserted in the duct of the syringe needle in order to increase liquid friction against needle walls and to avoid automatic suction of the liquid into the vacuum chamber, especially at the lowest pressure experienced.

A stop and a spring are fitted to the syringe piston to help produce single droplets of reproducible size. A third thermocouple TC3 (screened against the radiation emitted by the test section) measures air temperature inside the low-pressure chamber. A precision hygrometer HY was placed inside the

[3] The thermocouple was soldered on the lower side of the strip in order not to have a local nonhomogeneity on the cooled surface, which would introduce perturbations in the behavior of the cooling process.

Nomenclature

t_{so} = temperature of the strip at the steady-state condition before the arrival of the drops
t_s = running temperature of the Mo strip
t_c = temperature of the heating cavity at the steady-state condition
t_{sat} = saturation temperature
t_{sev} = minimum temperature of the Mo strip reached during the contact and evaporation of the drops
p = pressure
q_{ev} = maximum specific heat flux exchanged through the Mo strip
t_L = Leidenfrost temperature
t_{LD} = Leidenfrost temperature in the case of full rebound of the droplets of water (dynamic case)
t_{LS} = Leidenfrost temperature in the case of residual wetting of the surface by the droplet (steady case)
t_a = air temperature inside vacuum chamber
u = humidity
PR = potentiometer recorder
HS = hypodermic syringe
DV = digital voltmeter
OS = oscilloscope
VCH = vacuum chamber
TC1, TC2, TC3 = thermocouples
HY = hygrometer
TS = test section
D, R = diffusion and rotative pump system
PG = pressure gage
NV = needle valve
MS = molybdenum strip
IM = thermally insulating material
HTR = high-temperature resistors
MW = mineral wool
CC = copper cylinder
C = radiating cavity
CI = ceramic thermally insulating material
WD = water drop

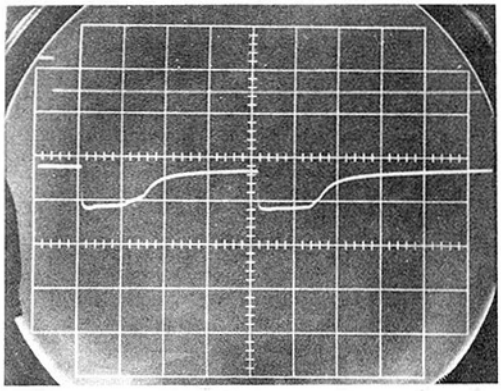

Fig. 4 Temperature pulses due to two discrete drops: upper signal—trigger signal; lower trace—thermocouple TC1; signal scales: 5 mV per main division; 5 s per main division;
$t_a = 49°C$ $t_c = 196°C$ $u = 63$ percent
$t_{so} = 193°C$ $t_{sev} = 95°C$ (first pulse)
$t_{so} = 184°C$ $t_{sev} = 95°C$ (second pulse)
$p = 600$ torr

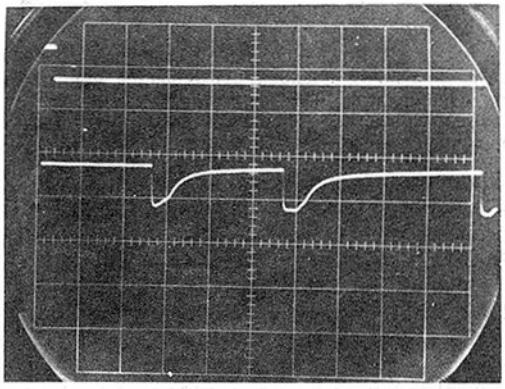

Fig. 5 Temperature pulses due to two discrete drops; signal scales as in Fig. 4
$t_a = 48°C$ $t_c = 212°C$ $u = 84$ percent
$t_{so} = 193°C$ $t_{sev} = 95°C$ (first pulse)
$t_{so} = 183°C$ $t_{sev} = 95°C$ (second pulse)
$p = 500$ torr

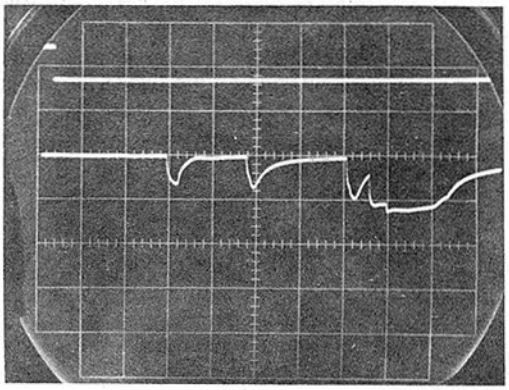

Fig. 6 Temperature pulses due to two discrete and more drops; signal scales as in Fig. 5;
$t_a = 50°C$ $t_c = 235°C$ $u = 84$ percent
$t_{so} = 214°C$ $t_{sev} = 153°C$ (first pulse)
$t_{so} = 210°C$ $t_{sev} = 145°C$ (second pulse)
$p = 500$ torr

low-pressure chamber to measure the humidity; its value was read through the window.

The temperature of the droplet was not monitored, since it was assumed to be very close to the saturation temperature. Although we have no direct evidence, a clue for this assumption was the fact that we observed inside the drop the development of microvapor bubbles, as a demonstration that the drop

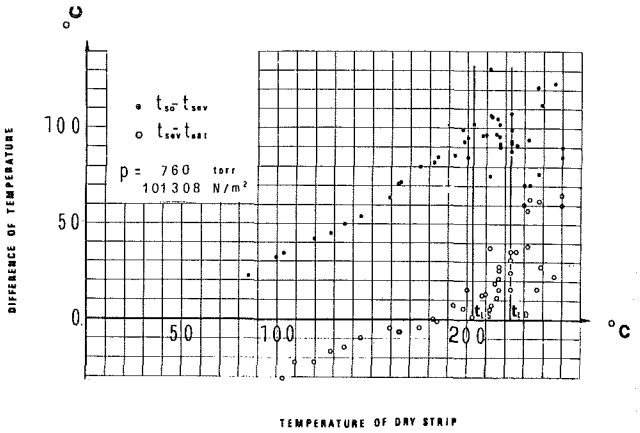

Fig. 7

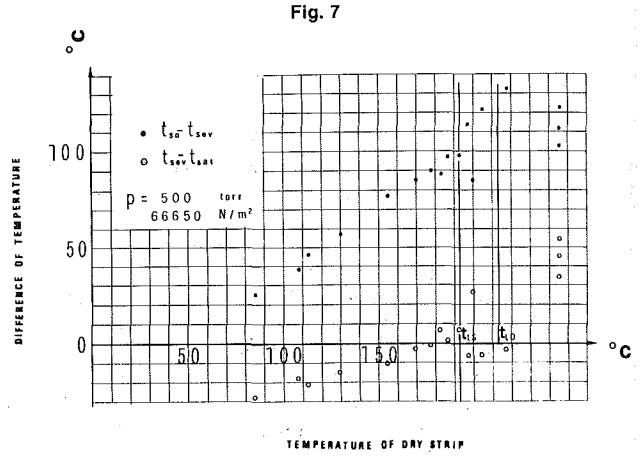

Fig. 8

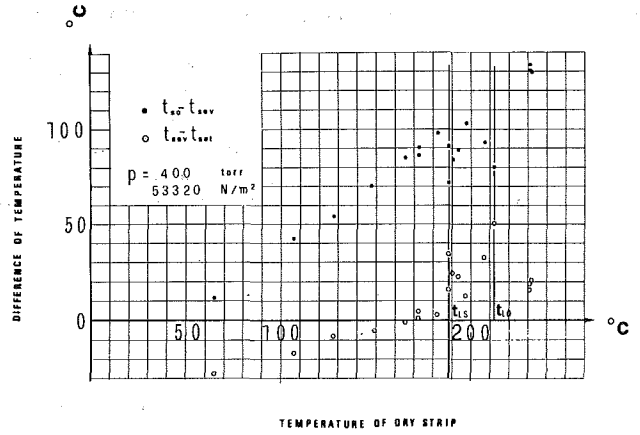

Fig. 9

was boiling. We noticed this phenomenon for the following two conditions:

- when the drop, in the steady-state condition, was at a distance (needle-test section) on the order of 1–2 cm;
- when the drop arrived at the hot surface with very low velocity by moving the needle toward the test section. The bubbles were shown even before contact.

Results

Measurements of the Leidenfrost temperature were made every 50 torr, starting from atmospheric pressure, to 25 torr; below this value, the drops disintegrate as soon as they are introduced to the low-pressure chamber.

In addition to temperature and humidity of the residual air, the following quantities were measured: the temperature t_c of

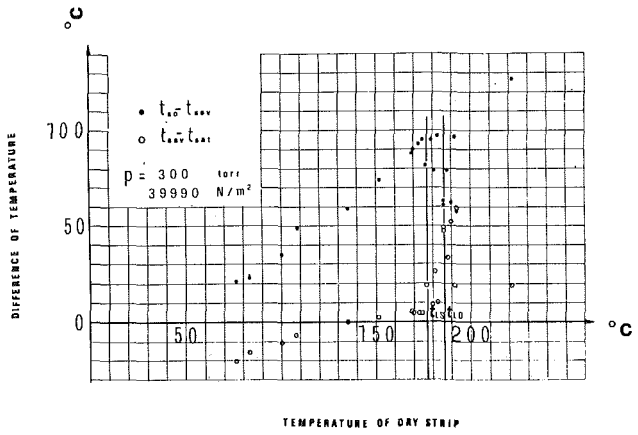

Fig. 10

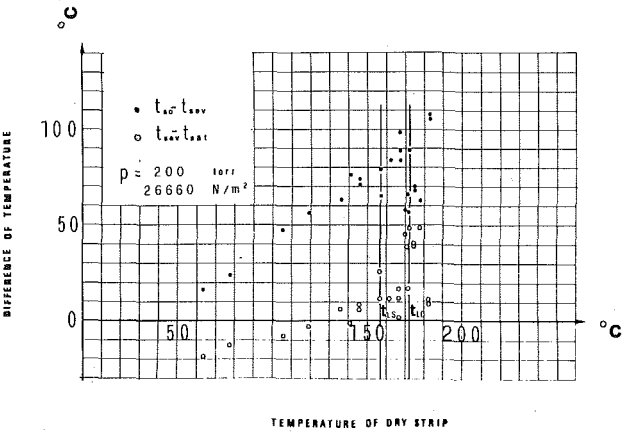

Fig. 11

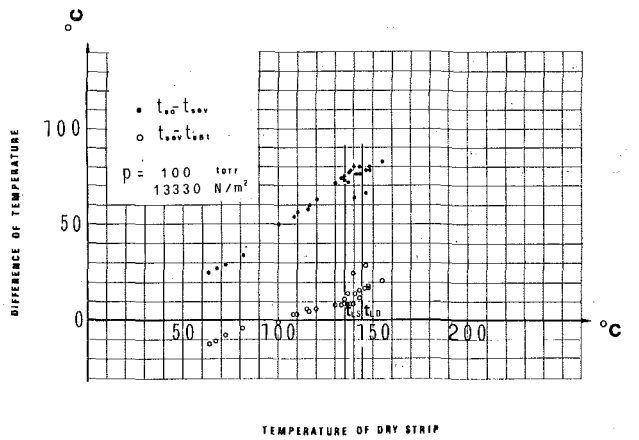

Fig. 12

Figs. 7-12 Maximum decrease in temperature $t_{so} - t_{sev}$ and overheating $t_{sev} - t_{sat}$ of the hot surface, when cooled by the droplets, as a function of the initial dry strip temperature t_{so}

the radiating cavity, the initial temperature t_{so} of the molybdenum strip, the drop size ($\phi \simeq 2$ mm), the surface mean roughness ($\sigma = 3$ μm), the emittance ($\simeq 0.34 \pm 0.02$), and the drop velocity (3 m/s).

In order to determine the specific heat fluxes exchanged through the molybdenum strip, a direct calibration of heat flux versus temperatures t_c and t_{so} was performed as follows. A constantan cylinder was soldered to the upper side of the strip. Along the axis of the cylinder, two copper wires were soldered. The distance between the wires was 2.5 cm. A differential thermocouple was thus formed which sensed the temperature difference corresponding to this distance on the cylinder axis. Thermal fluxes could be estimated through the thermal conductivity of the cylinder and the Fourier law. Transverse heat flux was made negligible, with respect to the axial flux, by means of thermal insulating material placed around the surface of the constantan cylinder.

Figure 2 shows the calibration curves, giving the specific thermal flux q as a function of the difference $(t_c - t_{so})$ and suggests that q could be expressed as $q = K(t_c - t_{so})$ with K slowly changing with pressure and $(t_c - t_{so})$, except for the largest values of $(t_c - t_{so})$. The calibration curves determined in the static case for the temperatures are assumed to be valid even in the transient case, because of the very low thermal capacitance of the Mo strip.

Table 1 presents the Leidenfrost temperature at atmospheric pressure as reported by various investigators. These values are reported here as general references. However, the surface materials for which these temperatures were recorded have an influence and therefore cannot be compared exactly with the results on a molybdenum surface of a particular roughness.

Figure 3 shows the Leidenfrost temperature at various subatmospheric pressures determined by the present investigation. The top curve of Fig. 3 shows the locus of temperatures at which the drop just begins to give rise to spikes in the temperature signals. The middle curve shows the locus of temperatures at which the Leidenfrost phenomenon is first detectable. This latter temperature corresponds to the transition condition in which the cooling pulses are no longer rectangular but not yet spikelike (Fig. 5). In this condition, it is believed that the liquid still wets the surface but, suddenly after the contact with the surface, a vapor film is developed.

Figures 4, 5, and 6, respectively, show the temperature transients as displayed on the oscilloscope for the three specific conditions examined: below the Leidenfrost point (Fig. 4), during the transition phase (Fig. 5), and when the first quite definite rebound of the drops occurs (Fig. 6). The pressure strongly influences the Leidenfrost temperature, changing it from $\simeq$ 100 °C (at 25 torr) to 220°C (at 760 torr). It can be seen from Fig. 3 that the Leidenfrost temperature curves show pressure dependence similar to that of the saturation temperature.

The curves in Fig. 3 maintain almost constant temperature difference regardless of pressure; the middle curve (steady droplets) is the most regular; the upper curve (bouncing droplets) tends toward a plateau at high pressures.

The difference between the saturation temperature and the Leidenfrost point increases slightly with pressure (within the range studied), passing from $\Delta t \simeq 90$°C to $\Delta t \simeq 125$°C (dynamic case) and from $\Delta t \simeq 85$°C to $\Delta t \simeq 105$°C (steady case) at 25 torr and 760 torr, respectively. The similarity of the pressure dependence of the Leidenfrost temperature to that of the saturation temperature has been reported for pressures above the atmospheric value [27].

Figures 7–12 show the maximum decrease in temperature of the hot surface, when cooled by the droplets, as a function of the local initial temperature t_{so} of the surface at some specific pressures. From these values, it is evident that for a given initial temperature t_{so} of the dry strip, the temperature decrease $(t_{so} - t_{sev})$ increases with decreasing pressure. It is also evident that at all pressures, the decrease in temperature of the strip increases as the initial dry strip temperature t_{so} increases, and reaches a maximum as the Leidenfrost point is approximated.

Figure 13 presents the drop evaporation time as a function of the initial dry strip temperature t_{so}, under different pressures.

Finally, Fig. 14 shows the maximum specific heat flux q_{ev} extracted from the surface by each drop as a function of the initial dry strip temperature t_{so}, under different pressures. It is evident that the maximum specific heat flux q_{ev} increases

Table 1 P = 760 torr

Drop volume, cm^3	Researcher	Year	Reference	t_L, °C
<0.05	Gottfried	1962	[6]	280
<0.25	Betta	1963	[31]	245
<0.05	Lee	1965	[32]	280
0.05–10	Patel/Bell	1965	[33]	305
0.05–1*	Schoessow	1967	[34]	180

*Revolving surface mode.

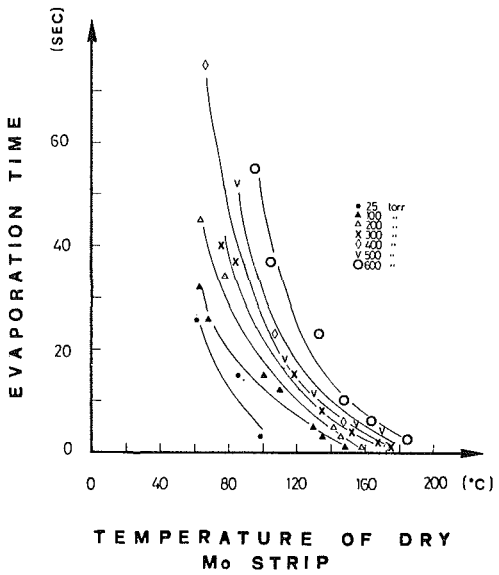

Fig. 13 Evaporation time as a function of the temperature of the dry strip under different pressures

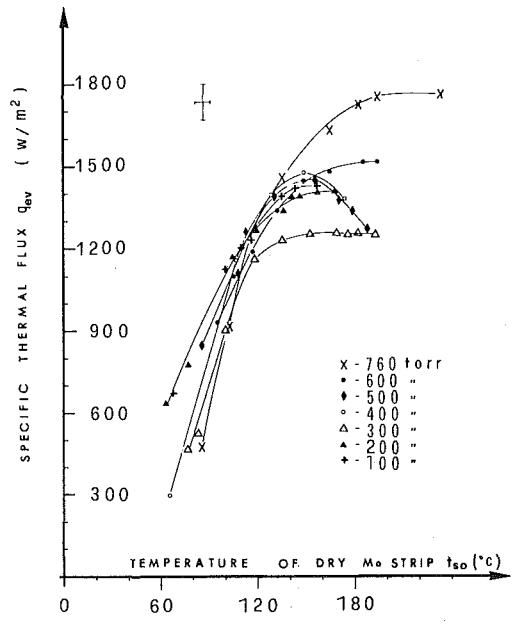

Fig. 14 The maximum specific heat flux q_{ev}, extracted from the surface by the drops, as a function of the temperature of dry strip t_{so} under different pressures

rapidly up to t_L, and then decreases or remains constant. This different behavior, however, could be significantly affected by considerable uncertainties in the evaluation of q_{ev}.

Taking into account the increasing difference of $(t_{sev} - t_{sat})$ as the Leidenfrost point is approached, a net reduction of the thermal exchange coefficient $k = q_{ev}/(t_{sev} - t_{sat})$ is evident (Fig. 15).

Actually, the heat flux was limited to 1.8×10^3 W/m^2 ac-

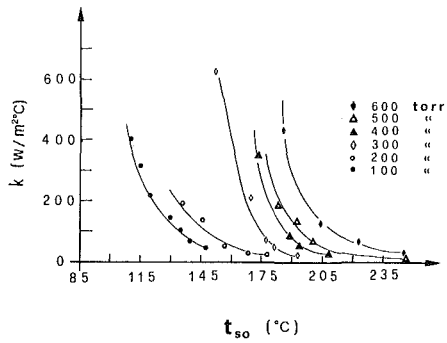

Fig. 15 The thermal exchange coefficient K as a function of the initial dry strip temperature t_{so} under different pressures

cording to the maximum difference $(t_c - t_{so})$ achievable with the apparatus.

The authors believe that the present investigation should be extended to higher heat fluxes with constant surface temperature t_s in order to assess the limiting cooling capability with drops above the Leidenfrost point and low pressure.

Acknowledgments

This research was partially supported by CNR (Consiglio Nazionale delle Ricerche), Italy.

References

1 Testa, P., "Transienti termici durante la evaporazione di gocce su substrato solido; indagine sperimentale con misure di flusso termico e di interferometria laser risolte nel tempo," *Quaderni di Fisica Tecnica*, No. 14, Università di Roma, Rome, Apr. 1976.

2 Bell, K. J., *Leidenfrost Review Chem. Eng. Prog. Symp.*, Ser. 67–63, 1967.

3 Asu, Y. Y., "A Review of Film Boiling," NASA TM 52837, 1970.

4 Finlay, I. C., "Spray Flow as Heat-Transfer Media," *Chemical Processing*, Vol. 5, 1971, pp. 25–29.

5 Wachters, L. H. J., and Westerling, N. A. J., "The Heat Transfer From a Hot Wall to Impinging Water Drops in the Spheriodal State," *Chem. Engng. Sci.*, Vol. 21, 1966, pp. 1047–1056.

6 Gottfried, B. S., and Lee, C. J., "The Leidenfrost Phenomenon: Film Boiling of Liquid Droplets on a Flat Plate," *Int. J. Heat Mass Transfer*, Vol. 9, 1966, pp. 1167–1187.

7 Harris, L. S., "For Flexibility, the Air-Evaporative Cooler," *Chem. Eng.*, Vol. 69, 1962, p. 77–82.

8 Savic, P., "The Cooling of a Hot Surface by Drops Boiling in Contact With It," Nat. Res. Lab. Canada, Report MT-i&, 1958.

9 Helenbrook, R. G., and Anthony, F. M., "Developments of Cooling Techniques for Advances Airborne Electronic Equipment," Bell Co. Report No. 2368-933001, Air Forces Flight Dynamics Lab., Wright-Patterson Air Force Base, Ohio.

10 Parker, J. D., and Grosh, R. J., "Heat Transfer to a Mistflow," USAEC report ANL-6291, 1961.

11 Tong, L. S., *Boiling Heat Transfer and Two-Phase*, Wiley, New York, 1965.

12 Cumo, M., and Pitimada, D., "Sulla determinazione della temperatura di Leidenfrost," *La Termotecnica*, No. 8, Aug. 1968.

13 Dinglinger, G., "Low Temperature Freezing of Food with Boiling Liquids," *Kaltetechnik-Klimatisierung*, Vol. 22, 1970, pp. 220–223.

14 Sills, J. T., "Recent Advances in the Liquid Nitrogen Freezing of Foods," *ASHRAE J.*, Vol. 12, No. 6, 1971, pp. 36–41.

15 Cumo, M., and Pitimada, D., "Sulla determinazione della temperatura di Leidenfrost con fluidi organici," *Rivista di Ingegneria*, No. 7–8, July-Aug. 1970.

16 Baumeister, K. J., Hendricks, R. C., and Hamil, T. D., "Metastable Leidenfrost States," NASA-RN-D-3226, 1966.

17 Betta, V., "Indagine sperimentale sulla temperatura di Leidenfrost," *Ricerche di Termotecnica*, Vol. 20, 1971.

18 Betta, V., and Naso, V., "Fenomeno di Leidenfrost: tempi di vaporizzazione é minime temperature di esistenza," *Il Calore*, No. 4, 1972.

19 Toda, S., "A Study of Mist Cooling-Thermal Behaviours of Liquid Films Formed From Mist Drops on a Heated Surface at High Temperature and High Heat Fluxes," *Technology Reports*, Tohoku University, Vol. 36, No. 2.

20 Toda, S., "A Study of Mist Cooling (1st Report: Investigation of Mist Cooling)," *Heat Transfer Japanese Research*, Vol. 1, No. 3, 1972, pp. 31–50.

21 Bonacina, C., Comini, G., and Del Giudice, S., "Evaporazione di liquidi atomizzati a contatto di superficie calde," Istituto di Fisica Tecnica—Università di Padova, Quaderno No. 58, July 1974.

22 Mikic, B. B., "On Mechanism of Dropwise Condensation," *Int. J. Heat Mass Transfer*, Vol. 12, 1969, pp. 1311–1323.
23 Baumeister, S., "Leidenfrost Temperature—Its Correlation for Liquid Metals, Cryogens, Hydrocarbons and Water," ASME JOURNAL OF HEAT TRANSFER, 1973, p. 166.
24 Cooper, L., "The Microlayer in Nucleate Pool Boiling," *Int. J. Heat Mass Transfer*, 1969, p. 895.
25 Berenson, P. J., "Film Boiling Heat Transfer From a Horizontal Surface," ASME JOURNAL OF HEAT TRANSFER, 1961, p. 351.
26 Bromley, L. A., "Heat Transfer in Stable Film Boiling," Ph.D. thesis, Dept. of Chem., Univ. of California, Berkeley, CA, 1948.
27 Galli, G., Gugliermetti, F., and Vaccaro, G., "Determinazione della temperatura di Leidenfrost per getti d'acqua nebulizzati a diverse pressioni," Edizioni Sistema, 1976.
28 Emmerson, G. S., "The Effect of Pressure and Surface Material on the Leidenfrost Point of Discrete Drops of Water," *Int. J. Heat Mass Transfer*, Vol. 18, 1975, p. 381.
29 Porteus, J., "Relation Between the Height Distribution of a Rough Surface and the Reflectance at Normal Incidence," *J.O.S.A.*, Vol. 53, No. 12, Dec. 1963, pp. 1394–1402.
30 Testa, P., "Studio sperimentale e teorico delle propietà di rinvio e di emissione di energia raggiante da parte di una superficie di alluminio indotte da asperità superficiali statistiche mediante l'impiego di un fascio laser," Quaderni di Fisica Tecnica, No. 11, Università di Roma—Maggio, 1975.
31 Betta, V., "Contributo allo studio dell'ebollizione a film," *Il Calore*, Sept. 1963.
32 Lee, C. J., "A Theoretical and Experimental Investigation of the Liedenfrost Phenomenon for Small Droplets," Ph. D. thesis, Oklahoma State University, 1965.
33 Patel, B. M., and Bell, K. J., "The Leidenfrost Phenomenon for Extended Liquid Masses," *Chem. Eng. Prog. Symp.*, Series 64, Vol. 62, 1965, pp. 62–71.
34 Schoessow, G. J., Jones, D. R., and Baumeister, K. J., "Leidenfrost Film Boiling of Drops on a Moving Surface," AIChE-ASME 9th Nat. Heat Transfer Conf., Seattle, 1967.
35 Burdukov, A. P., Kuvshinov, G. G., and Nakoryakov, V. Ye., "Investigation of Heat and Mass Transfer in Boiling on a Flat Horizontal Surface at Subatmospheric Pressures," *Heat Transfer—Soviet Research*, Vol. 12, No. 12, Mar.-Apr. 1980.
36 Peterson, C. O., "An Experimental Study of the Dynamic Behavior and Heat Transfer Characteristics of Water Droplets Impinging Upon a Heated Surface," *Int. J. Heat Mass Transfer*, Vol. 13, 1970, pp. 369–81.
37 Rizza, J. J., "A Numerical Solution to Dropwise Evaporation," ASME JOURNAL OF HEAT TRANSFER, Vol. 103, Aug. 1981.

H. Müller-Steinhagen

A. P. Watkinson

N. Epstein

Department of Chemical Engineering,
The University of British Columbia,
Vancouver, B.C.,
V6T 1W5, Canada

Subcooled-Boiling and Convective Heat Transfer to Heptane Flowing Inside an Annulus and Past a Coiled Wire: Part I—Experimental Results

Heat transfer coefficients for subcooled heptane were measured in two flow geometries for different heat fluxes, flow rates, bulk temperatures, and system pressures. Regimes of convective heat transfer and of nucleate boiling were delineated for a concentric annular test section containing an internally heated rod, and for a resistance-heated coiled wire mounted in crossflow. Second-order effects such as flow direction, hysteresis, and method of pressurization were also investigated.

1 Introduction

Flow boiling heat transfer under subcooled and saturated conditions has been the subject of numerous investigations. Although the mechanisms of boiling heat transfer are not yet fully understood, a number of semi-empirical correlations exist [1], which predict heat transfer coefficients with reasonable accuracy. Measurements with a variety of different fluids are necessary to establish the generality of these correlations and improve their reliability. The present study has its origins in fouling investigations with heptane–styrene mixtures. To establish reference conditions for these investigations, a number of nonfouling heat transfer measurements with pure heptane (99.5 percent) were performed, in which convective heat transfer and nucleate boiling regimes were mapped. Heat flux, bulk temperature, system pressure, and flow rate were varied over a wide range, given in Table 1. In addition, the nonfouling investigation included a study of parameters that are usually considered of minor importance.

In Part II of this paper, the heat transfer coefficients presented here are compared to those obtained from several correlations given in the literature.

2 Test Equipment

The equipment was described previously [2, 3]. Some changes were made, to improve the stability of the thermal circuit and to allow visual observation of the heated sections. A flow diagram is given in Fig. 1. Two test sections are mounted in parallel to measure simultaneously the heat transfer from the cylindrical rod and from the coiled wire. Some features of the flow assemblies are given in Table 2. The fluid is pumped from the pressurized supply tank via orifice flow meters to the probes. All piping was done with stainless steel degreased by running hot toluene and hot heptane for several days through the piping before the experiments.

The coiled stainless steel wire, or "hot-wire probe," which was mounted normal to the flow in a rectangular duct was heated electrically. The heat flux supplied by the wire was calculated from the current and voltage. The wire temperature could be determined by the change of electrical resistance with wire temperature. To obtain reproducible values of wire temperature, the coil was heated several days in a vacuum oven before using. The bulk temperature around the hot-wire probe was determined by two thermocouples located 19 mm upstream and downstream respectively from the coil. Due to later applications, the liquid flow velocities for the hot wire probe were chosen to be in the range of laminar flow.

The heater for the annular flow measurements was supplied by Heat Transfer Research Inc. [4]. It consisted of a stainless steel sheathed resistance heater with four thermocouples located close to the heating surface. The bulk temperature was measured with thermocouples located in mixing chambers before and after the annulus. While the usual flow direction was vertically upward, some measurements were also performed for horizontal and for vertical downward flow.

Table 1 Range of investigations

System pressure	1 bar	$<p<$	7.89 bar
Bulk temperature	30°C	$<T_b<$	95°C
Heat flux	800 W/m^2	$<\dot{q}<$	400,000 W/m^2
Mass velocity in the annulus	106 kg/m^{2}s	$<\dot{m}<$	712 kg/m^{2}s
Mass velocity around the coiled wire	5.5 kg/m^{2}s	$<\dot{m}<$	17.1 kg/m^{2}s

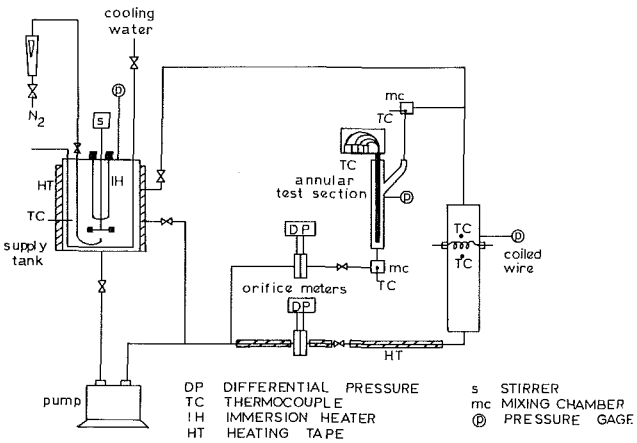

Fig. 1 Test loop

3 Procedure

All measurements were taken after the circuit had reached steady state at the chosen system pressure and mass velocity. Then, at a selected bulk temperature, the heat flux was varied systematically. In accord with common practice, most of the

Contributed by the Heat Transfer Division for publication in the JOURNAL OF HEAT TRANSFER. Manuscript received by the Heat Transfer Division January 3, 1985.

Table 2 Construction data of flow assemblies

Hot wire		Annulus	
Material	SS 410	Material	SS 316
Wire diameter	0.2 mm	Rod diameter	10.7 mm
Wire length	125 mm	Annulus outer diameter	25.4 mm
Coil diameter	1.25 mm	Heated length	102.0 mm
Coil length	40 mm	Heated length to thermocouple location	78.0 mm
Number of coils	25		
Duct cross section (width × depth)	40 mm × 13 mm	Entrance length to thermocouple location	294.0 mm

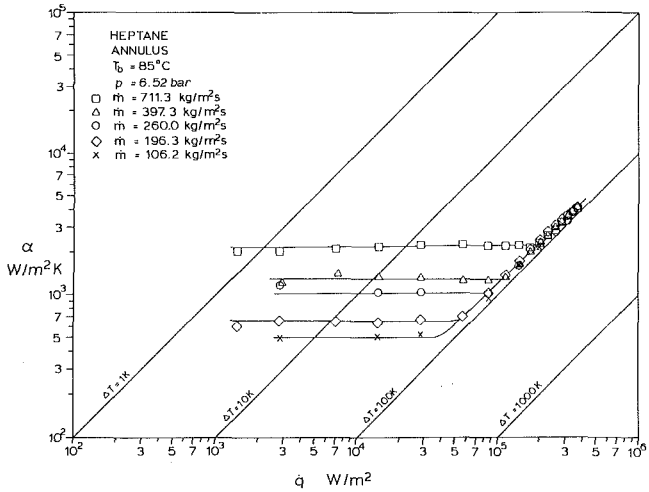

Fig. 2 Influence of heat flux and mass velocity on the heat transfer coefficient for annular flow

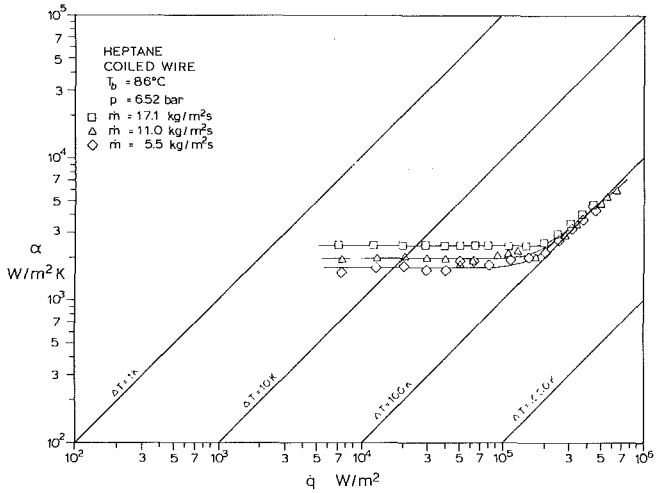

Fig. 3 Influence of heat flux and mass velocity on the heat transfer coefficient for flow around a coiled wire

measurements were taken with decreasing heat flux. However, to demonstrate possible hysteresis effects, some test series were repeated with increasing heat flux. The local heat transfer coefficient $\alpha(z)$ from a heating element is calculated from

$$\alpha(z)=\frac{\dot{Q}/A}{T_s(z)-T_b(z)}=\frac{\dot{q}}{T_s(z)-T_b(z)} \tag{1}$$

For the annular probe, the wall temperature T_w was calculated as the mean value of two thermocouple readings. From the measured value of T_w the temperature drop between thermocouple location and surface was deducted to obtain the surface temperature T_s

$$T_s=T_w-\frac{s}{\lambda}\cdot\dot{q} \tag{2}$$

The value of s/λ was specified for each thermocouple by the manufacturer. The average of the inlet and outlet temperatures was taken as the bulk temperature.

In the case of the heated coil, the heat flux was calculated from

$$\dot{Q}=I^2(V/I-R_{\text{ext}}) \tag{3}$$

where I, V, and R_{ext} are the measured current, the measured voltage, and the electrical resistance of the measuring circuit, respectively. The difference between the wire temperature under heating conditions, T_w and a chosen reference temperature T_{w0} is

$$T_w-T_{w0}=\left(\frac{R-R_0}{R_0-R_{\text{ext}}}-1\right)/\gamma \tag{4}$$

In this equation R_0 is the resistance at T_{w0} and γ is the temperature coefficient of the wire's electrical resistance,

Nomenclature

A = surface area of heater, m²
H = Henry's Law constant, bar
I = current, A
$\dot{m}$ = mass velocity, kg/m²s
p = pressure or partial pressure, bar
$\dot{Q}$ = heat flow rate, W
$\dot{q}$ = heat flux, W/m²
R = electrical resistance, Ω
r = cavity radius, m
s = distance between thermocouple location and heating surface, m
T = temperature, °C, K
V = voltage, W/A
x = mole fraction
z = length coordinate, m
α = heat transfer coefficient, W/m²K
γ = temperature coefficient of electrical resistance, 1/K
δ = degree of saturation
λ = thermal conductivity of metal in annular probe, W/mK
σ = surface tension, kg/s²

Subscripts

b = bulk
c = calculated
ext = external
H = heptane
l = laminar
meas = measured
Nb = nucleate boiling
N_2 = nitrogen
ons = onset
s = surface of heating element
sat = at saturation
sup = in the supply tank
syst = system
t = turbulent
w = wall, wire
0 = at reference conditions

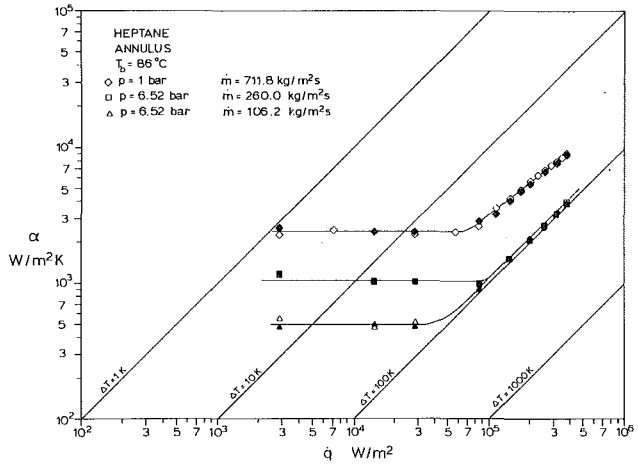

Fig. 4 Heat transfer coefficients measured with increasing (closed symbols) and decreasing (open symbols) heat flux for flow in the annulus

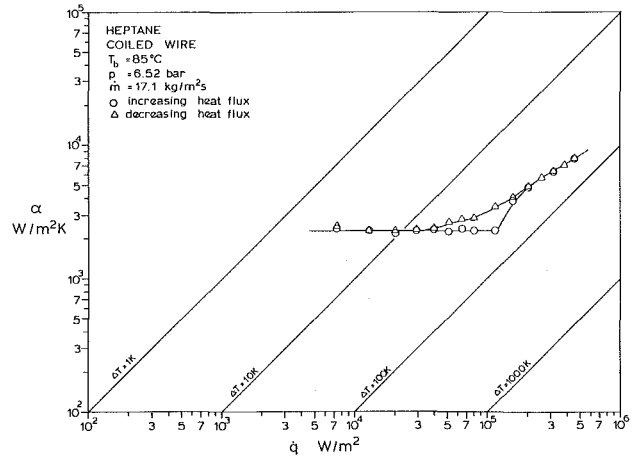

Fig. 5 Heat transfer coefficients measured with increasing and decreasing heat flux (coiled wire)

which was determined in previous measurements to be 0.00051 K^{-1}. For the wire, $T_s = T_w$.

4 Results

The influence of a number of parameters on the heat transfer coefficient for the annulus and the coiled wire will be discussed below.

4.1 Heat Flux. Figures 2 and 3 show the influence of the heat flux on the heat transfer coefficient. The parameter in both diagrams is the mass velocity $\dot{m}$.

One can clearly distinguish two different regimes: the convective heat transfer regime where the heat transfer coefficient is independent of the heat flux but dependent on the mass velocity and the nucleate boiling regime where α increases with increasing $\dot{q}$ but is independent of $\dot{m}$. For the latter condition, the observed relationship between heat transfer coefficient and heat flux may be expressed by the proportionality

$$\alpha \sim (\dot{q})^{0.8\text{-}1.0} \tag{5}$$

For both heaters, the convective heat transfer increases in value and in range, as the mass velocity is increased. The transition from one heat transfer mechanism to the other was found to be rather sharp.

Variations of the convective heat transfer coefficient, which may be found in some of the plots at low heat flux (low wall superheat), are attributed to uncertainties in the measuring system and not to physical phenomena. Especially with the hot

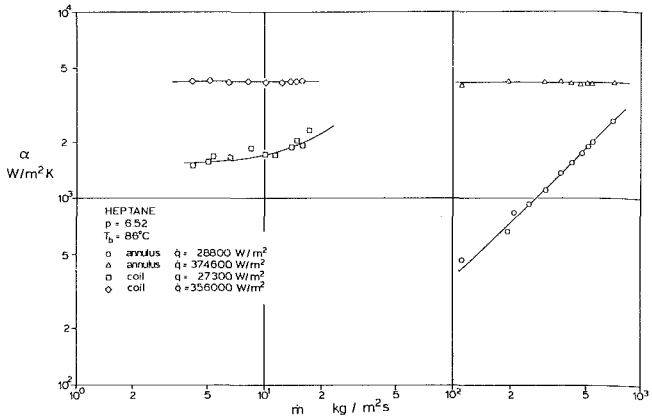

Fig. 6 Influence of the mass velocity on the heat transfer coefficient

wire it was rather difficult to determine accurately small temperature differences, due to the very small change of the electrical resistance.

A number of reports (for example [5]), which mainly deal with pool boiling heat transfer, indicate higher nucleate boiling heat transfer coefficients at medium heat fluxes if the measurements are made with decreasing heat flux rather than with increasing heat flux. This result is attributed to the activation of nucleation sites. Figures 4 and 5 show some measurements in which possible hysteresis effects for both the annulus and the coil were investigated. In the case of the annulus, no hysteresis was detected, whereas for the coil small effects of the different heating cycle are found. It seems likely that this difference may be due to the very different flow velocities in the annulus and past the coil. Comparison of flow boiling and pool boiling measurements with the same liquid [5, 6] suggest that hysteresis effects decrease as the flow velocity is increased.

4.2 Mass Velocity and Heater Geometry. The influence of the mass velocity on the heat transfer coefficient may also be seen in Figs. 2 and 3. While the heat transfer coefficient in the nucleate boiling region is independent of the mass velocity, the convective heat transfer coefficient increases with increasing liquid velocity. This result holds for both heaters. However, as can be seen in Fig. 6, the turbulent heat transfer in the annulus follows the power law

$$\alpha_t \sim \dot{m}^{0.9} \tag{6}$$

whereas the laminar heat transfer from the coil depends less strongly on the mass velocity

$$\alpha_l \sim \dot{m}^{0.25} \tag{7}$$

Since for pure forced convection in laminar flow an exponent of 0.5 was to be expected, a considerable contribution of natural convection has to be assumed. Nevertheless, the heat transfer coefficients from the coiled wire are in most cases higher than from the heating rod, presumably due to the greater thermal and hydraulic entry effects associated with the former.

As the heat transfer coefficients at fully developed nucleate boiling depend much more on the bubble mechanism than on the fluid dynamics, the heat transfer coefficients in the nucleate boiling regime were found to be identical for both heaters, as seen in Fig. 7.

4.3 Bulk Temperature. According to equation (1), the heat transfer coefficient is defined in terms of the difference between surface and bulk temperature. Assuming that the physical properties of the liquid do not change too much within the investigated range of bulk temperature, the convective heat transfer coefficient, being independent of the surface

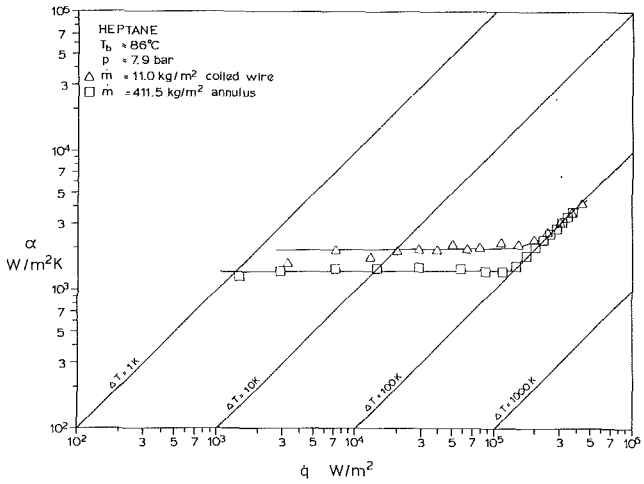

Fig. 7 Heat transfer coefficient versus heat flux for wire and annulus

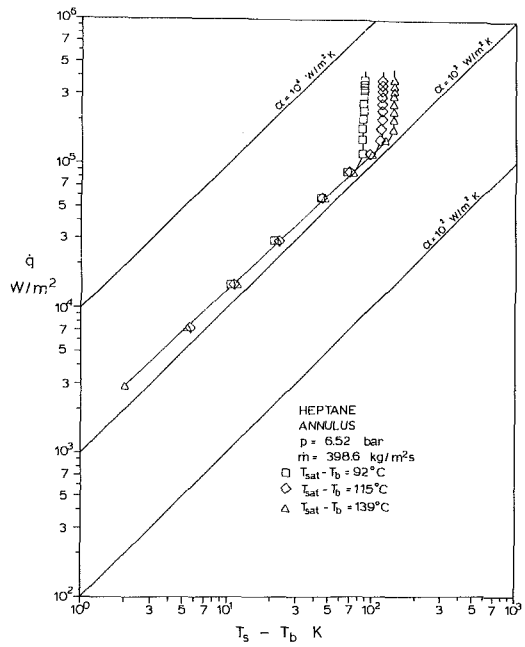

Fig. 8(*a*) Heat flux versus difference between surface and bulk temperature.

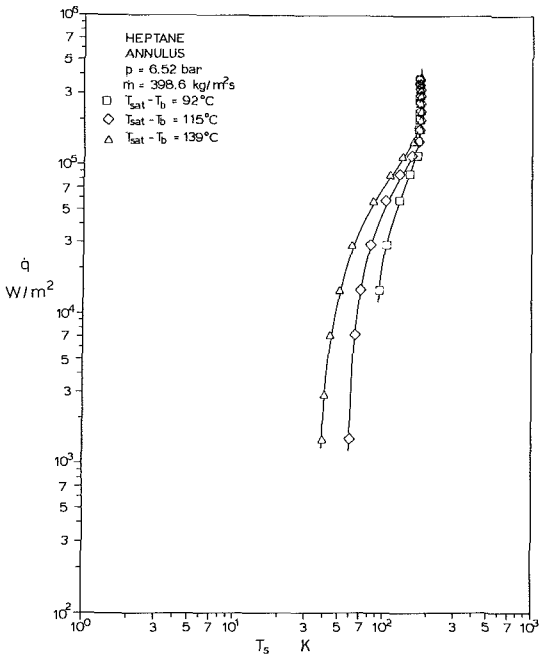

Fig. 8(*b*) Heat flux versus surface temperature for various degrees of subcooling

temperature, should be unaffected by a variation of the bulk temperature. As for the nucleate boiling heat transfer coefficient, many authors have found [1] that α_{Nb} depends on the difference between surface temperature and saturation temperature and not on the difference between surface and bulk temperature. Therefore, for a given system pressure and heat flux, the surface temperature should be independent of the degree of subcooling $(T_{sat} - T_b)$, while the heat transfer coefficient α_{Nb}, defined according to equation (1), should decrease with increasing temperature difference $(T_{sat} - T_b)$. Both assumptions are confirmed by Fig. 8, which shows the results of three runs with different degrees of subcooling. In Fig. 8(*a*), the heat flux is plotted against the difference between surface and bulk temperature, showing a decrease of the nucleate boiling heat transfer coefficient as the subcooling is increased at a given heat flux. Figure 8(*b*) demonstrates that the degree of subcooling does not affect the surface temperature at a given heat flux, if nucleate boiling predominates. The fact that the surface temperatures at nucleate boiling are only slightly higher than the saturation temperature can be attributed to some nitrogen dissolved in the heptane. This effect will be discussed in the following subsection.

4.4 System Pressure and Method of Pressurization. Figure 9 shows the influence of the system pressure on the heat transfer coefficient. For the convective heat transfer (low heat flux), there is no influence to be seen because the change of physical properties of the liquid with pressure is negligible. To discuss the influence of the pressure on the nucleate boiling, the surface temperature excess may be split into

$$T_s - T_b = (T_s - T_{sat}) + (T_{sat} - T_b) \tag{8}$$

While the saturation temperature increases with increasing pressure, the difference between surface temperature and saturation temperature decreases due to the increasing nucleation density caused by the change of the fluid properties (mainly the reduction of the surface tension) [7]. Figure 9 shows a reduction of the nucleate boiling heat transfer coefficient with rising pressure. This indicates that the increase of $(T_{sat} - T_b)$ more than compensates for the decrease in $(T_s - T_{sat})$.

With the existing equipment, the system pressure could be produced in two ways, namely

(*a*) by connecting the supply tank to a nitrogen cylinder, and
(*b*) by using the expansion of the liquid and its increasing vapor pressure with rising bulk temperature.

In Figs. 10 and 11, some results obtained with both methods of pressurization are compared. While the convective heat transfer coefficients seem to coincide, the nucleate boiling starts at lower heat fluxes and reaches higher heat transfer coefficients for the nitrogen pressurization. At very high heat fluxes, the curves approach each other. Nevertheless, the difference between heat transfer coefficients achieved at the same heat flux but with different methods of pressurization may be some hundred percent.

Similar results were also reported by McAdams et al. [8] from measurements with water and by Pike et al. [9] from measurements with water and glycerine. The increase of the heat transfer coefficient is probably caused by nitrogen, which was dissolved in the liquid at the supply tank temperature and formed bubbles at the heated surface. The nitrogen partial

Table 3 Measured and calculated temperatures at the onset of nucleate boiling ($\delta = 95$ percent)

P_{syst}, bar	T_b, °C	$\dot{m}$, kg/m^{2}s	$T_{ons,\,meas}$, °C	$T_{ons,\,calc}$, °C	T_{sat}, °C
3.76	85.0	398.0	98.8	98.5	150.4
6.52	38.5	398.0	99.2	104.3	177.6
6.52	61.0	398.0	99.3	101.9	177.6
6.52	85.0	398.0	108.7	106.4	177.6
7.89	85.0	398.0	108.3	110.5	188.3

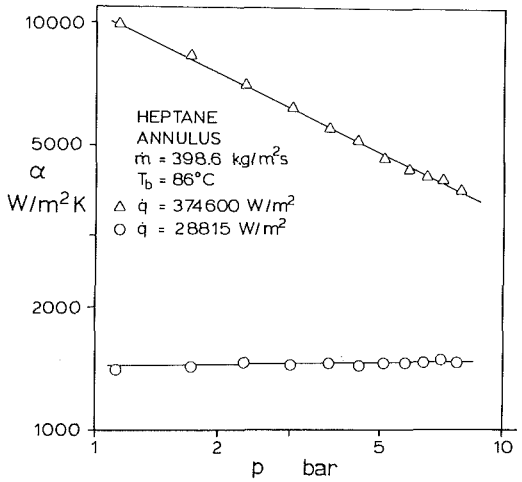

Fig. 9 Influence of the system pressure on the heat transfer coefficient for convective and nucleate boiling heat transfer

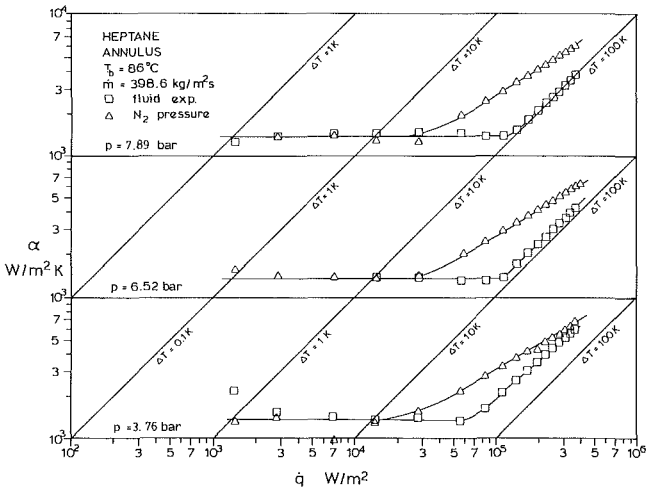

Fig. 10 Influence of pressurization method on the heat transfer from an annular core

pressure adds to that of the heptane, thus starting nucleate boiling at temperatures below the saturation temperature of the pure heptane. In what follows, an attempt is made to quantify this effect. However, as the test equipment was not designed for this kind of investigation, a number of assumptions have to be made which will have to be verified in further experiments.

Neglecting the suppression of nucleate boiling caused by the flow velocity [1], as well as the Thomson correction [10], yields

$$P_H + P_{N_2} - P_{syst} = \frac{2\sigma}{r} \tag{9}$$

where the partial pressure of the heptane is to be evaluated as a function of the liquid temperature [11]. The partial pressure of the nitrogen at the supply tank temperature is

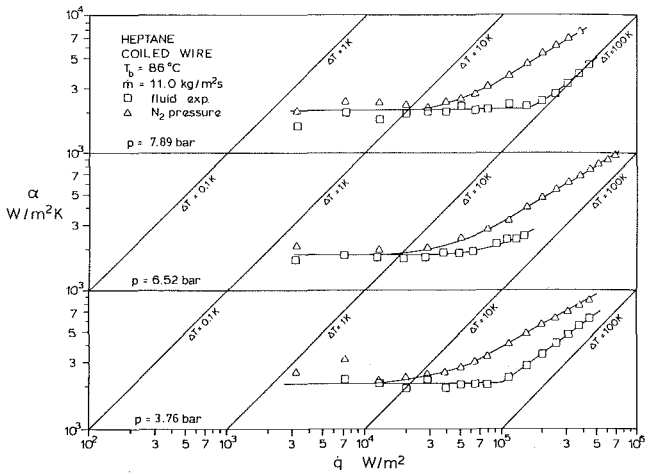

Fig. 11 Influence of pressurization method on the heat transfer from a coil

$$P_{N_2}(T_{sup}) = P_{syst} - P_H(T_{sup}) \tag{10}$$

For pressures below 10 bar, the saturation concentration of nitrogen dissolved in heptane may be calculated using Henry's Law [12]

$$P_{N_2} = xH \tag{11}$$

If the concentration remains constant, the influence of the fluid temperature on the nitrogen partial pressure is given by [12]

$$\frac{P_{N_2}}{P_{N_{2,0}}} = \left(\frac{T_0}{T}\right)^{0.6} \tag{12}$$

with T in K.

To evaluate the cavity radius r at the onset of nucleate boiling, equations (9)-(12) were applied to measured results for $p = 1.07$ bar and a low mass velocity. A cavity radius of $r = 2.15$ μm was found, which seems to be a reasonable value [1]. The degree of saturation for the nitrogen/heptane system was found by trial and error to be $\delta = 95$ percent. Then, taking r and δ as constants, the temperature at the onset of nucleate boiling could be calculated using equations (9)-(12). Table 3 shows some of the calculated results for several system pressures and bulk temperatures. The agreement between measured and calculated values is reasonably good.

Furthermore, Figs. 10 and 11 show that the influence of the heat flux on the heat transfer coefficient is smaller for the nitrogen pressurization than for the pure heptane, as long as the heat transfer is improved by the dissolved gas. This effect can be attributed to the fact that the heptane near the heated surface becomes depleted of nitrogen as the rate of evaporation is increased. A similar observation is reported by Schlünder [13] for the boiling of binary mixtures, where the decreasing concentration of the component with the lower boiling point causes an increase of the saturation temperature at the heated surface. To apply Schlünder's diffusion model [13] to the phenomena described in the present case, further measurements with various liquid-gas combinations have been completed recently.

Unless otherwise stated, the data shown in this paper have been obtained with pressurization by fluid expansion and vapor pressure.

4.5 Flow Direction. Some measurements with vertical upward, horizontal, and vertical downward flows were performed in the annulus at a heat flux of 375,000 W/m^2 and mass velocities between 96.5 kg/m^2s and 390.6 kg/m^2 s. At the higher mass velocities, no difference was found between the heat transfer coefficients for the three flow directions. In the case of the vertical downward flow, however, local dry-out occurred at mass velocities below 235 kg/m^2s, caused by the development of a large vapor bubble blocking the flow channel.

5 Conclusion

Heat transfer experiments with flowing heptane show distinguishable regimes of convective heat transfer and nucleate boiling heat transfer. In nucleate boiling, the heat transfer coefficients from a coiled wire to a fluid in cross flow and from a rod to an annular fluid in parallel flow are identical, and both are independent of the mass velocity. While no influence of the flow direction was detected, the method of pressurization strongly affected the heat transfer coefficient at intermediate heat fluxes. Boiling hysteresis was only found at low mass velocities for the coiled wire probe.

Acknowledgments

The authors are indebted to the German Research Council (D.F.G.), Bonn, Bad-Godesberg, for financing the fellowship of H.M.-St., and to the Natural Sciences and Engineering Research Council of Canada for continuing financial support.

References

1 Collier, J. G., *Convective Boiling and Condensation*, McGraw-Hill, New York, 1981.

2 Fetissoff, P. E., Watkinson, A. P., and Epstein, N., "Comparison of Two Heat Transfer Fouling Probes," *Proceedings of the 7th Int. Heat Transf. Conf.*, Munich, FRG, Vol. 6, 1982, pp. 391–396.

3 Fetissoff, P. E., "Comparison of Two Fouling Probes," M.A.Sc. Thesis, Dept. of Chem. Eng., Univ. of British Columbia, 1982.

4 Fischer, P., Suitor, J. W., and Ritter, R. B., "Fouling Measurement Techniques," *Chem. Eng. Progr.*, Vol. 71, No. 7, 1975, pp. 67–72.

5 Bland, M. E., "Bubble Nucleation in Cryogenic Fluids," Ph.D. Thesis, Oxford, 1970.

6 Klein, G., "Wärmeübertragung und Druckverlust bei der Strömung von verdampfendem Stickstoff im waagerechten Rohr," Dissertation, TH Aachen, 1975.

7 Gorenflo, D., "Wärmeübergang beim Behältersieden," *VDI-Wärmeatlas*, 4th ed., 1984.

8 McAdams, W. H., Kennel, W. E., et al., "Heat Transfer at High Rates to Water with Surface Boiling," *Ind. Eng. Chem.*, Vol. 41, No. 9, 1949, pp. 1945–1953.

9 Pike, F. P., Miller, P. D., et al., "Effect of Gas Evolution on Surface Boiling at Wire Coils," *Chem Eng. Progr. Symp. Series*, No. 17, Vol. 51, 1955, pp. 13–19.

10 Grassmann, P., *Physical Principles of Chemical Engineering*, Pergamon Press, 1971.

11 Shuzao, Ohe., *Computer Aided Data Book of Vapor Pressure*, Data Book Publ. Comp., Tokyo, Japan, 1976.

12 Landolt-Bornstein, *Zahlenwerte und Funktionen*, 6th ed., 1980, No. IV C1.

13 Schlünder, E. U., "Heat Transfer in Nucleate Boiling of Mixtures," *Int. Chem. Eng.*, No. 4, Vol. 23, 1983, pp. 589–599.

H. Müller-Steinhagen

N. Epstein

A. P. Watkinson

Department of Chemical Engineering,
The University of British Columbia,
Vancouver, B.C.,
V6T 1W5, Canada

Subcooled-Boiling and Convective Heat Transfer for Heptane Flowing Inside an Annulus and Past a Coiled Wire: Part II—Correlation of Data

In Part I of this paper, the authors reported an extensive series of heat transfer data for subcooled boiling of heptane in turbulent flow in an annulus, and in laminar flow past a coiled wire. These data plus some new measurements for laminar flow in the annulus were compared to the predictions of some 12 correlations from the literature. The applicability of these correlations to the present data is determined and a combination of correlations proposed to predict heat transfer with satisfactory accuracy.

Introduction

The calculation of convective and subcooled boiling heat transfer rates depends largely on available empirical or semi-empirical formulae [1]. The accuracy of predictions of these correlations is uncertain for conditions outside the range of the original data from which they were derived. This is especially true if the flow geometry or the fluid to be used is different from that of the original study. In Part I of this paper, the authors reported heat transfer measurements for subcooled boiling of heptane flowing in an annulus and past a coiled wire under a wide range of flow and thermal conditions. A comparison of these data to values predicted by correlations available in the literature seemed worthwhile for several reasons. The comparison would extend the range of fluids for which the correlations have been tested since subcooled boiling data for heptane were not available in the literature. A suitable correlation could be established for subcooled boiling on a cooled wire in cross flow. This configuration has been used for many heat transfer measurements or experiments [3, 4], yet a systematic investigation of heat transfer characteristics is lacking. Laminar flow data reported in this paper for the annular test section would permit a further verification of the subcooled boiling correlation of Shah [15], which is claimed to be superior to other correlations but has only been compared to few data for laminar flow. Shah himself, therefore, discourages the use of his correlation for Reynolds numbers less than 2300.

The geometry of the two test sections and the range of conditions covered in the experiments are given in Part I, Tables 1 and 2. Data correlated in this part were taken with pressurization by fluid expansion, as the nitrogen pressurization used for some runs in Part I resulted in varying and unknown degrees of nitrogen dissolution in the heptane.

Correlations Tested

The experimental data were compared with the predictions of the correlations listed in Table 1. Generally, the heat transfer coefficient for convective heat transfer is given as

$$\mathrm{Nu}_c = \frac{\alpha_c L_{ch}}{\lambda} = f(\mathrm{Re}, \mathrm{Pr}, \mathrm{Gr}, x/L) \qquad (1)$$

with the Reynolds, Prandtl, and Grashof numbers having their usual form. The (x/L) term usually holds for thermal and hydraulic entrance effects.

Only correlation (4) considers the contribution of natural convection to the heat transfer for the flow past obstacles. However, some authors, for example [18], recommend that a Reynolds number be evaluated by superposition of the forced convection Reynolds number and the Grashof number

$$\mathrm{Re} = (\mathrm{Re}_{fc}^2 + \mathrm{Gr}/2.5)^{0.5} \qquad (2)$$

This method was applied to correlations (1) and (6).

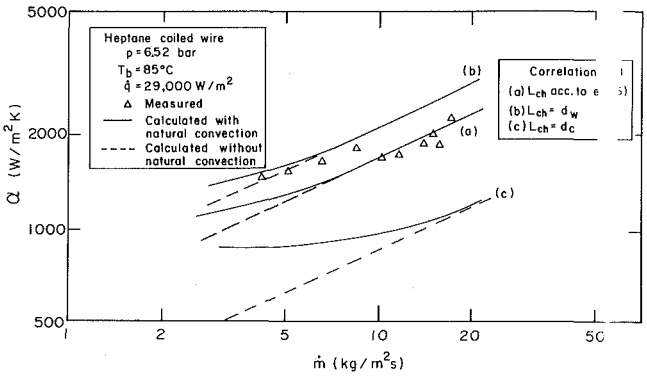

Fig. 1 Influence of the characteristic length definition and of natural convection on the calculated heat transfer coefficient past the coiled wire

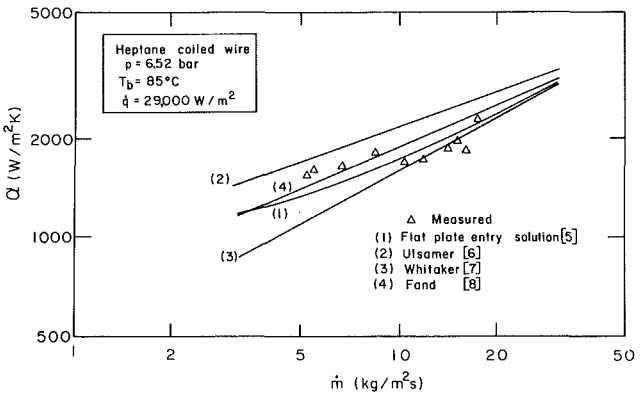

Fig. 2 Measured and calculated heat transfer coefficients as a function of the mass velocity for laminar flow past the coiled wire. For correlations (1) and (4), $L_{ch} = (\pi/2)d_w$.

Contributed by the Heat Transfer Division for publication in the JOURNAL OF HEAT TRANSFER. Manuscript received by the Heat Transfer Division March 13, 1985.

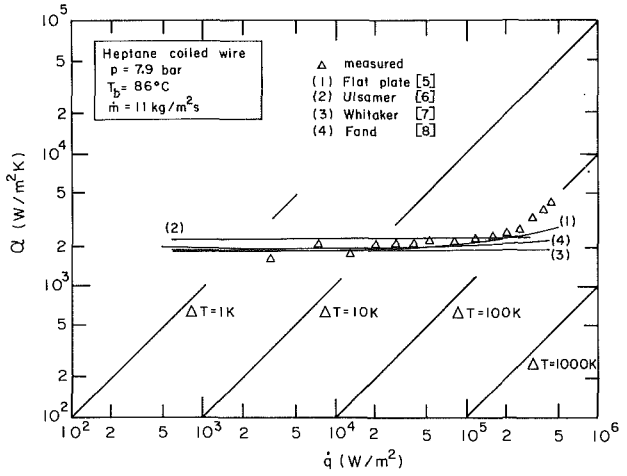

Fig. 3 Measured and calculated heat transfer coefficients as a function of the heat flux for laminar flow past the coiled wire

For flow inside ducts, the characteristic length in the Nusselt and Reynolds numbers is the equivalent diameter

$$d_{eq} = 4A_{cr}/f_w \tag{3}$$

For annular flow, Shah [15] suggests the use of equation (3) only if the annular gap, $(d_o - d_i)/2$, is larger than 4 mm. Otherwise, the heated perimeter should be used instead of the wetted perimeter in equation (3). For the annulus flow geometry given in Part I, the annular gap exceeds 4 mm and therefore

$$d_{eq} = \frac{4\pi(d_o^2 - d_i^2)}{4\pi(d_o + d_i)} = d_o - d_i \tag{4}$$

Chen [16] generally proposed the use of an equivalent diameter based on the heated perimeter. For the investigated conditions, this yields a significant decrease of the predicted heat transfer coefficients. Since the present results as well as about 1000 subsequently obtained but still unpublished data points for flow of heptane and of water indicate that equation (4) should be applied for the investigated conditions, the equivalent diameter according to equation (4) was used for all the correlations in this paper. For the flow past the coiled wire, no recommendations for the calculation of an equivalent diameter or a characteristic length could be found in the literature. However, as the coils used were not very tight, correlations for a straight wire should give satisfactory results. While correlations (2) and (3) are based on the wire diameter, Schlünder [18] suggests the use of correlation (1) with a characteristic length calculated from

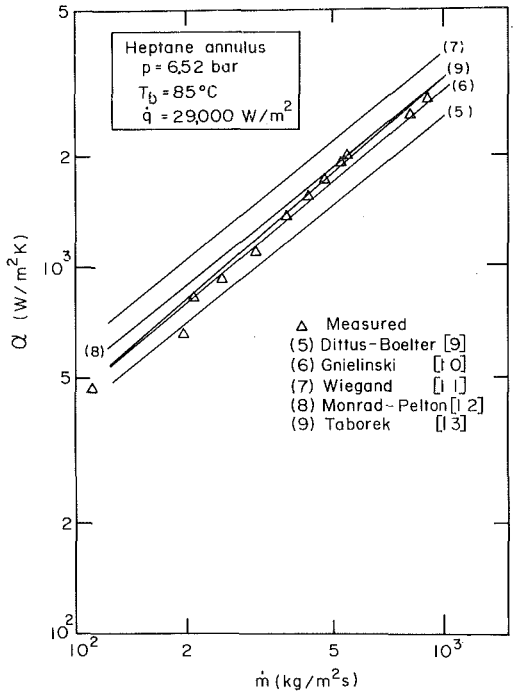

Fig. 4 Measured and calculated heat transfer coefficients as a function of the mass velocity, for turbulent flow in the annulus

$$L_{ch} = A_h/f_p \tag{5}$$

where A_h is the heated area and f_p the circumference of the projection in the direction of the flow. For a cylindrical body normal to the flow this leads to

$$L_{ch} = \frac{\pi d_w L}{2(L + d_w)} \approx \frac{\pi}{2} d_w \tag{6}$$

This definition was also applied to correlation (4). In the case of very narrow coils, L_{ch} should probably be calculated using a superposition of wire and coil diameters. The validity of this assumption will be the subject of further investigation.

Many investigations, for example [1, 2], show that the heat transfer coefficient for subcooled boiling depends on the difference between surface and saturation temperature, $(T_s - T_{sat})$, rather than on the difference between surface and bulk temperature, $(T_s - T_b)$. Therefore, correlations for saturated boiling may be applied to calculate the subcooled boiling heat transfer coefficient by evaluating $(T_s - T_{sat})$ and adding this value to the difference $(T_{sat} - T_b)$. Thus

Nomenclature

A_{cr} = cross-sectional area, m²
A_h = heated surface area, m²
c_p = heat capacity, J/(kg)(K)
d_c = coil diameter, m
d_{eq} = equivalent diameter according to equation (3), m
d_i = inside diameter of annulus, m
d_o = outside diameter of annulus, m
d_w = wire diameter, m
f_p = perimeter of projection in flow direction, m
f_w = wetted perimeter, m
g = acceleration due to gravity, m/s²
Δh_v = latent heat of evaporation, J/kg
L = length, m
L_{ch} = characteristic length, m
$\dot{m}$ = mass velocity, kg/m²s
$\bar{M}$ = molar mass, kg/kmol
p = pressure, bar
p^* = vapor pressure, bar
$\dot{q}$ = heat flux, W/m²
S = suppression factor [16]
T = temperature, °C
u = flow velocity, m/s
x = length coordinate, m
α = heat transfer coefficient, W/m²K
β = temperature coefficient of volumetric expansion, K⁻¹
ζ = friction factor
η = viscosity, kg/ms
λ = thermal conductivity, W/mK
ν = kinematic viscosity, m²/s
ρ = density, kg/m³
σ = surface tension, N/m

Subscripts

b = bulk
c = convective
crit = critical
fc = forced convection
g = gas
l = liquid
nb = nucleate boiling
s = surface
sat = saturation

Dimensionless numbers

Bo = $\dot{q}/\dot{m}\Delta h_v$ = boiling number
Gr = $g(T_s - T_b)L_{ch}^3\beta/\nu^2$ = Grashof number
Pr = $\eta c_p/\lambda$ = Prandtl number
Re = uL_{ch}/ν = Reynolds number

Table 1 Correlations used for comparison with the measured data

No.	Application and formula	Author	Reference
1	Laminar flow over flat plates $Nu_c = 0.664\ Re^{0.5}\ Pr^{0.33}$	Leveque as described by Drew	[5]
2	Laminar flow over tubes and wires $Nu_c = C Re^n Pr^{0.31}$ $C = 0.91,\ n = 0.385 \qquad 0.1 < Re < 50$ $C = 0.6,\ \ n = 0.5 \qquad 50 < Re < 10{,}000$	Ulsamer	[6]
3	Laminar flow over tubes and wires $Nu_c = (0.4\ Re^{0.5} + 0.06\ Re^{0.67}) \times Pr^{0.4}\ (\eta_w/\eta_b)^{0.25}$	Whitaker	[7]
4	Laminar forced and natural convection over cylinders $Nu_c = (0.255 + 0.699\ Re^{0.5} + 0.033 \times (Gr/Re^2)^{0.3} \cdot Gr^{0.25}) \cdot Pr^{0.29}$	Fand	[8]
5	Turbulent flow in pipes $Nu_c = 0.023\ Re^{0.8} Pr^{0.4}$	Dittus/ Boelter	[9]
6	Turbulent flow in pipes $\zeta = (1.82 \log Re - 1.64)^{-2}$ $Nu_c = \dfrac{\zeta/8(Re - 1000)Pr}{1 + 12.7(\zeta/8)^{0.5}(Pr^{2/3} - 1)} \cdot [1 + (d/L)^{0.66}]$	Gnielinski	[10]
7	Turbulent flow in annuli $Nu_c = 0.023\ Re^{0.8}\ Pr^{0.4}(d_o/d_i)^{0.45}$	Wiegand	[11]
8	Turbulent flow in annuli $Nu_c = 0.02\ Re^{0.8}\ Pr^{0.33}(d_o/d_i)^{0.53}$	Monrad/ Pelton	[12]
9	Turbulent flow in pipes $Nu_c = 0.0143\ Re^{0.85}\ Pr^{0.5}$	Taborek	[13]
10	Pool boiling heat transfer to saturated liquids $\alpha_{nb} = C_1(\dot{q})^{C_2}$ with C_1, C_2 to be taken from diagrams	Stephan	[14]
11	Flow boiling heat transfer to subcooled liquids $Bo > 3 \cdot 10^{-5} \rightarrow \phi_o = 230\ Bo^{0.5}$ $Bo < 3 \cdot 10^{-5} \rightarrow \phi_o = 1 + 46\ Bo^{0.5}$ $\dfrac{T_{sat} - T_b}{T_s - T_{sat}} > 2 \rightarrow \phi = \phi_o + \dfrac{T_{sat} - T_b}{T_s - T_{sat}}$ $\dfrac{T_{sat} - T_b}{T_s - T_{sat}} > 63000\ Bo^{1.25} \rightarrow \phi = \phi_o + \dfrac{T_{sat} - T_b}{T_s - T_{sat}}$ Otherwise $\phi = \phi_o$ α_c according to correlation No. 5 if $Re > 2300$ $\dot{q} = \alpha_c \phi (T_s - T_{sat})$	Shah	[15]
12	Flow boiling heat transfer α_c according to correlation No. 5 if $Re > 2300$ $\alpha_{nb} = 0.00122 \left(\dfrac{\lambda_l^{0.79} c_{pl}^{0.45} \rho_l^{0.49}}{\sigma^{0.5} \eta_l^{0.29} \Delta h_v^{0.24} \rho_g^{0.24}}\right) \cdot \Delta T_{sat}^{0.24} \cdot \Delta p_{sat}^{0.75}$ $\Delta T_{sat} = T_s - T_{sat},\ \Delta p_{sat} = \dfrac{(T_s - T_{sat})\Delta h_v}{T_{sat}(\rho_g^{-1} - \rho_l^{-1})}$ $\dot{q} = \alpha_c (T_s - T_b) + \alpha_{nb} (T_s - T_{sat}) \cdot S = \alpha (T_s - T_b)$ The suppression factor S is given by Chen in a diagram as a function of the Reynolds number down to $Re = 13{,}000$ at which $S = 0.85$. It was extrapolated to have a value of unity for $Re \leq 3500$.	Chen	[16]

In the above correlations the physical properties should be evaluated for the
(*a*) Grashof number at $(T_s + T_b)/2$
(*b*) forced convective heat transfer correlations at T_b
(*c*) nucleate boiling correlation at T_{sat}

$$(T_s - T_{sat}) = f(\dot{q}) \tag{7}$$

and

$$\alpha = \frac{\dot{q}}{(T_s - T_{sat}) + (T_{sat} - T_b)} \tag{8}$$

This method was used for correlations (10) and (12) (Table 1). As the nucleate boiling heat transfer coefficient was found to be independent of the mass velocity [1, 19], pool boiling correlations could also be considered.

From the numerous correlations published for boiling heat transfer, only three correlations were chosen for this study, each originally representing a different application. While the Shah correlation was suggested recently [15] for subcooled flow boiling in annuli, the correlations of Chen [16] and of Stephan [14] were developed for saturated flow boiling and for pool boiling, respectively.

Comparison Between Measured and Calculation Values

Convective Heat Transfer

(*a*) *Laminar Flow Past the Coiled Wire.* Laminar flow was investigated for the coiled wire, with Reynolds numbers between 3.5 and 14.6 based on the wire diameter and between 5.5 and 23 based on the characteristic length calculated according to equation (6). Figure 1 shows measured heat transfer coefficients as a function of the mass velocity as well as values calculated according to correlation (1), using different definitions of the characteristic length, with and without inclusion of natural convection. As can be seen, the version with L_{ch} given by equation (6), including the influence of natural convection according to equation (2), yields the best agreement with the measured data. This result also holds for correlation (4). In correlations (2) and (3) the wire diameter d_w has to be used, according to [6, 7]. A comparison of the results calculated using correlations (1–4) with the measured data is given in Fig. 2. All four correlations provide roughly comparable values; however, correlation (2) predicts coefficients that are too large. Better agreement is achieved using correlations (1) and (4). The influence of the heat flux on the convective heat transfer coefficient is shown in Fig. 3. With increasing heat flux (or excess temperature), the growing contribution of natural convection leads to a slight enhancement of the heat transfer. However, for the present investigation, the effect of natural convection was found to be small in most cases, in accordance with the criterion given in [19], which states that the contribution of natural convection may be neglected as long as $Gr/Re^2 < 1$. In the present convective heat transfer experiments, $0.0001 < Gr/Re^2 < 4.4$

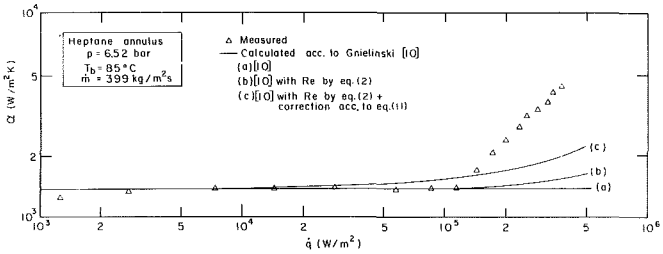

Fig. 5 Influence of the heat flux on the convective heat transfer coefficient for turbulent flow in the annulus

(*b*) *Turbulent Flow in the Annulus.* Figure 4 shows measured and calculated heat transfer coefficients for annular flow, plotted as a function of the mass velocity. For all measurements, the best results were obtained with the correlation of Gnielinski [10], which is based on all data for turbulent heat and mass transfer in pipes that Gnielinski was able to ex-

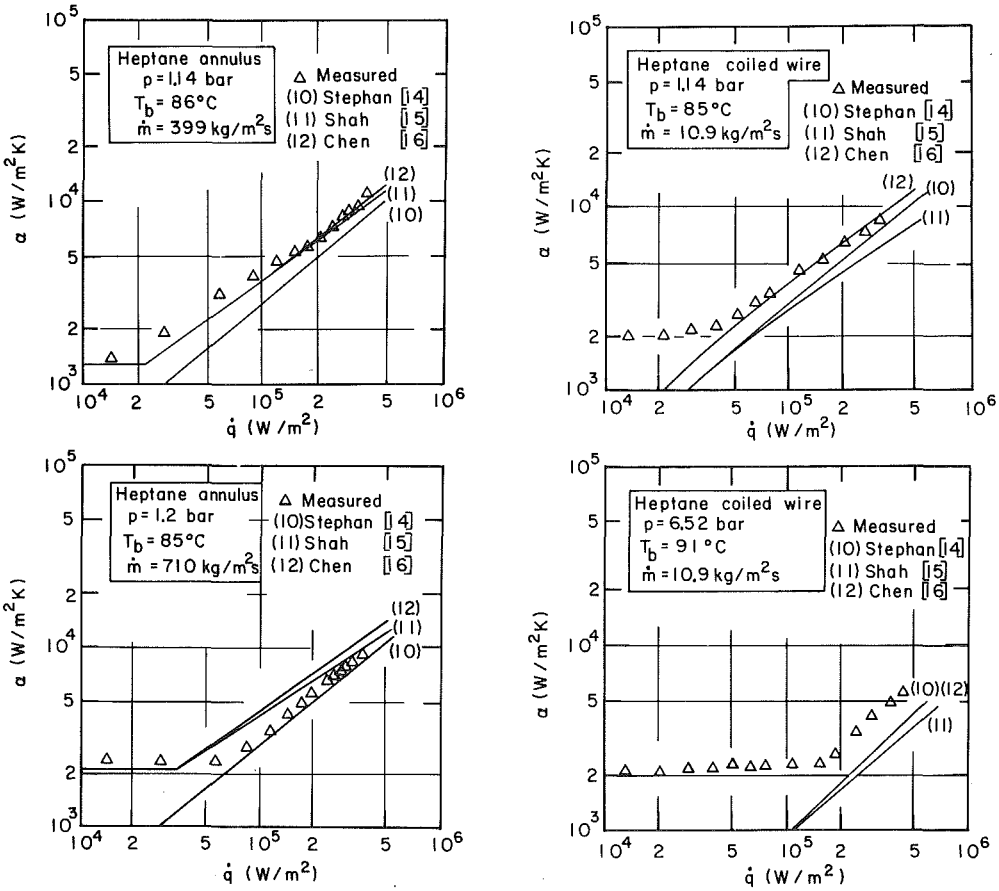

Fig. 6 Measured and calculated heat transfer coefficients for subcooled boiling as a function of the heat flux

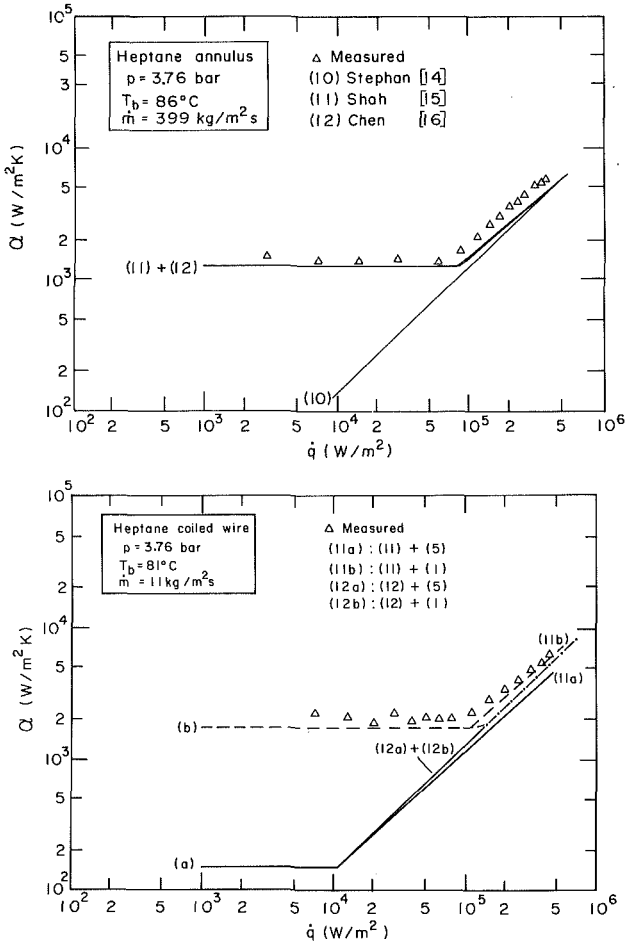

Fig. 7 Measured and calculated heat transfer coefficients for convective boiling in (a) turbulent and (b) laminar flow

tract from the literature. This equation is also recommended in [20].

The influence of the heat flux on the measured convective heat transfer coefficients for turbulent annular flow is given in Fig. 5. Again, the contribution of natural convection is negligible, as the measured heat transfer coefficients are independent of the heat flux as long as convective heat transfer predominates ($\dot{q} < 120{,}000$ W/m^2). Figure 5 also contains three curves calculated according to correlation (6), each showing a different influence of the heat flux on the calculated heat transfer coefficient. For the original correlation, curve (*a*), the heat transfer coefficient is independent of the heat flux, because the physical properties of the liquid were evaluated at the bulk temperature. Curve (*b*) shows the calculated results if the influence of natural convection is considered using equation (2). As the flow velocity is rather high, slight deviations between (*a*) and (*b*) are found only at high heat fluxes. Some authors suggest that the influence of the heat flow direction (e.g., cooling or heating) be included by multiplying the coefficient by a factor

$$F = \left(\frac{\mathrm{Pr}_b}{\mathrm{Pr}_s}\right)^n \tag{9}$$

with n being about 0.25. For the convective heat transfer measurements described in Part I, this procedure yields a small overprediction of the heat transfer coefficient at high heat fluxes as seen in Fig. 5, curve (*c*).

Subcooled Nucleate Boiling. Figure 6 shows measured and calculated subcooled boiling heat transfer coefficients plotted against the heat flux for the two different heater geometries. For the annulus, data are shown for two different mass

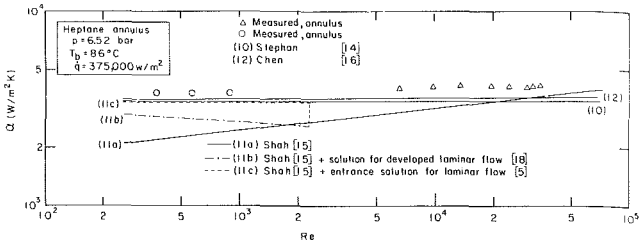

Fig. 8 Influence of the Reynolds number on the subcooled boiling heat transfer coefficient

velocities, while for the coiled wire two different pressures have been employed at the same mass velocity. All three correlations used for comparison, namely correlations (10), (11), and (12), yield results which generally agree with the measured data in the nucleate boiling region. Only at a pressure of 6.52 bar are some deviations between measured and calculated values to be noted. These deviations might be caused by minor amounts of residual nitrogen dissolved in the heptane (see Part I) and though they could also represent a more general failure of the three correlations at high pressure.

The pool boiling correlation of Stephan [14] is only applicable to the nucleate boiling region, whereas those of Shah [15] and Chen [16] are supposed to cover both the convective and the nucleate boiling regimes. According to Shah [15], there exists no experimental verification of the applicability of the Chen correlation to subcooled boiling. Figure 7 shows some measurements of the heat transfer coefficient as a function of the heat flux for both turbulent flow in the annulus (*a*) and laminar flow past the coiled wire (*b*). Both sets of measurements are compared with calculated values according to correlation (10), which only holds for fully developed nucleate boiling, and to correlations (11) and (12), which hold for both the convective and the subcooled boiling regimes. Both the latter authors use the Dittus–Boelter equation [9] for calculating the convective heat transfer; however, the increase in heat transfer as nucleate boiling occurs is accommodated by an additive expression in the correlation of Chen [16] and by a multiplication factor in the correlation of Shah [15]. Both correlations do well for the turbulent flow in the annulus (Fig. 7*a*). The flow past the coiled wire is a developing laminar flow; thus the Dittus–Boelter equation is not applicable (see Fig. 7*b*, curve (*a*)). Therefore, correlation (1) was used for the calculation of the heat transfer coefficients in the laminar convective heat transfer region. As Fig. 7(*b*) shows, this procedure gives reasonable agreement between measured and calculated values. However, while the developed boiling heat transfer coefficients according to Chen [16] are independent of the correlation used for convective heat transfer, the values calculated according to Shah [15] change if the convective heat transfer is varied.

To demonstrate the influence of the flow velocity on the heat transfer, measured and calculated heat transfer coefficients are plotted against the Reynolds number in Fig. 8. The data at low Reynolds numbers were not reported in Part I. As found by numerous authors [1, 19], the heat transfer coefficient for fully developed boiling is independent of the flow velocity. (The boiling heat transfer coefficients for the coiled wire, which were measured at characteristic length Reynolds numbers between 5 and 20, are very similar to those for the annulus.) This result is predicted only by the correlations of Stephan [14] (which was developed for pool boiling) and Chen [16], whereas Shah's correlation [15] shows a clear influence of the Reynolds number on the boiling heat transfer coefficient and considerable deviations between measured and calculated results. In Fig. 8, three possible variations of the Shah correlation were used to evaluate the heat transfer coefficients, namely, one for turbulent convective heat transfer (*a*)

and the other two for different cases of laminar convective heat transfer (*b* and *c*). For the turbulent flow region ($Re > 2300$), the agreement between predicted values and measured values decreases considerably with decreasing Reynolds number. This trend would continue if the Dittus–Boelter equation [9] were also used in the laminar flow regime ($Re < 2300$), as Shah [15] tentatively suggested for saturated flow boiling. If, for $Re < 2300$, the Shah correlation is instead combined with a correlation for laminar convective heat transfer, a clear improvement of the predicted values can be seen in Fig. 8. Although the measured heat transfer coefficients were for developed flow, the combination of the Shah correlation with the correlation for developing laminar flow gives a fortuitously good agreement with the measured data, since the Reynolds number influence is just canceled in the above combination. If the "correct" combination for developed laminar flow were used for $Re < 2300$, the agreement between predicted and measured values would be poorer, but it would tend to improve for low Reynolds numbers.

Nevertheless, the influence of mass velocity is not properly accounted for in [15] and considerable deviations between predicted and measured heat transfer coefficients cannot be avoided for Reynolds numbers between 2300 and 10,000.

As described in Part I, increasing the system pressure at constant bulk temperature or decreasing the bulk temperature at constant system pressure yields a reduction of the heat transfer coefficient defined according to equation (8). This trend is identically predicted by the three correlations for boiling heat transfer.

Conclusion

Several correlations from the literature were checked as to their applicability to subcooled boiling of heptane flowing in an annulus and past a coiled wire. The best results were obtained using the Chen correlation [16] for convective boiling. However it is suggested that the convective term in the correlation be replaced either by Gnielinski's more up-to-date correlation for turbulent heat transfer in pipes [10] or by the entrance region solution for flow along flat plates [5], for turbulent flow in the annulus and laminar flow past the coiled wire, respectively. Similar accuracy with less evaluation of physical properties is achieved by using the higher of the two values produced by using either the Stephan correlation [14] or the appropriate correlation for convective heat transfer [5, 10]. In the case of lower Reynolds numbers, the application of the Shah correlation [15] may yield considerable errors in the prediction of the subcooled boiling heat transfer coefficient.

Acknowledgments

The authors are indebted to he German Research Council (D.F.G.), Bonn, Bad-Godesberg, for financing the fellowship of H. M. -St., and to the Natural Sciences and Engineering Research Council of Canada for continuing financial support.

References

1 Collier, J. G., *Convective Boiling and Condensation*, McGraw-Hill, New York, 1972.

2 Rohsenow, W. M., and Clark, J. A., "Heat Transfer and Pressure Drop Data for High Heat Flux Densities to Water at High Subcritical Pressure," 1951 Heat Transfer and Fluid Mechanics Institute, Stanford University Press, Stanford, CA, 1951.

3 Pike, F. P., Miller, P. D., and Beatty, K. O., "Effect of Gas Evolution on Surface Boiling at Wire Coils," *Chemical Engineering Progress Symposium Series*, No. 17, Vol. 51, 1955, pp. 13–19.

4 Fetissoff, P. E., Watkinson, A. P., and Epstein, N., "Comparison of Two Heat Transfer Fouling Probes," *Proceedings of the 7th International Heat Transfer Conference*, Munich, FRG, Vol. 6, 1982, pp. 391–396.

5 Drew, T. B., "Mathematical Attacks on Forced Convection Problems," *Transactions AIChE*, Vol. 26, 1931, pp. 26–80.

6 Ulsamer, J., "Wärmeabgabe von geheizten Drähten und Rohren," *Forschungsgebiet Ingenieurwesen*, Vol. 3, No. 94, 1932 (cited in McAdams, W., *Heat Transmission*, McGraw-Hill, New York, 1954.)

7 Whitaker, S., "Forced Convection Heat Transfer Correlations for Flow in Pipes, Past Flat Plates, Single Cylinders, Single Spheres and for Flow in Packed Beds and Tube Bundles," *AIChE Journal*, Vol. 18, 1972, pp. 361–371.

8 Fand, R. M., and Keswani, K. K., "Combined Natural and Forced Convection Heat Transfer From Horizontal Cylinders to Water," *International Journal of Heat and Mass Transfer*, Vol. 16, 1973, pp. 1175–1191.

9 Dittus, F. W., and Boelter, L. M. K., "Heat Transfer in Automobile Radiators of the Tubular Type," University of California Press, Vol. 2, No. 13, 1930.

10 Gnielinski, V., "Neue Gleichungen fur den Wärme- und Stoffübergang in turbulent durchströmten Rohren und Kanälen," *Forschung im Ingenieurwesen*, Vol. 41, No. 1, 1975, pp. 8–16.

11 Wiegand, J. H., "Discussion of Annular Heat Transfer Coefficients for Turbulent Flow," *Transactions AIChE*, Vol. 41, No. 5, 1945, pp. 147–152.

12 Monrad, C. C., and Pelton, J. F., "Heat Transfer by Convection in Annular Spaces," *Transactions AIChE*, Vol. 38, 1942, pp. 593–608.

13 Taborek, J., HTRI, Alhambra, CA, private communication, 1981.

14 Stephan, K., and Abdelsalam, M., "Heat Transfer Correlations for Natural Convection Boiling," *International Journal of Heat and Mass Transfer*, Vol. 23, 1980, pp. 73–87.

15 Shah, M., "Generalized Prediction of Heat Transfer during Subcooled Boiling in Annuli," Heat Transfer Engineering, Vol. 4, No. 1, 1983, pp. 24–31.

16 Chen, J. G., "A Correlation for Boiling Heat Transfer to Saturated Fluids in Convective Flow," *Proceedings of the 6th National Heat Transfer Conference*, Boston, 1963.

17 Razjevic, K., *Handbook of Thermodynamic Tables and Charts*, Hemisphere Publishing Company, Washington, 1976.

18 Schlünder, E. U., *Einführung in die Wärme- und Stoffübertragung*, Vieweg-Verlag, 1975.

19 Grassmann, P., *Physical Principles of Chemical Engineering*, Pergamon Press, New York, 1971.

20 Gnielinski, V., "Wärmeübertragung in Rohren," *VDI-Wärmeatlas*, 3rd ed., VDI-Verlag Düsseldorf, 1975.

J. A. Orozco
Assistant Professor of Mechanical Engineering, University of Illinois at Chicago, Chicago, IL 60680

L. C. Witte
Professor of Mechanical Engineering, Heat Transfer/Phase Change Laboratory, University of Houston, University Park, Houston, TX 77004
Fellow ASME

Flow Film Boiling From a Sphere to Subcooled Freon-11

The boiling curves for flow boiling of freon-11 from a fluid-heated 3.81-cm-dia copper sphere showed dual maxima. One maximum corresponded to the nucleate peak heat flux while the other was caused by transitory behavior of the wake behind the sphere. Film boiling data were predicted well by the theory of Witte and Orozco. A semi-empirical correlation of the film boiling data accounting for both liquid velocity and subcooling predicted the heat transfer to within +/− 20 percent. The conditions at which the vapor film became unstable were also determined for various subcoolings and velocities.

Introduction

Film boiling is more mathematically tractable than nucleate or transition boiling. However, when it occurs around bodies that are submerged in a flowing, subcooled liquid, mathematical difficulties arise from phenomena that are not physically well understood – namely the formation of a wake, the influence of the liquid pressure field on the behavior of the vapor film and the effect of subcooling on the mass-energy balance that controls the vapor film thickness.

Film boiling requires relatively large temperature differences so that steady-state experiments using spheres are difficult to do. Hence, experiments using a quenching technique constitute a large percentage of the research that has been performed, e.g., [1–3]. Recent research [4–7] shows that although quenching experiments might give reasonable heat transfer results in the fully developed film boiling regime, there is a strong tendency for boiling to localize in the transition and nucleate boiling regimes. That is, spatial variations in heat flux can occur, with different boiling regimes occurring simultaneously at different points on the surface. This causes doubt about the significance of minimum and maximum heat fluxes that might be calculated from measurements of quenching in which surface temperature was assumed to be uniform.

The data of Westwater and co-workers [8, 9] and Bromley and co-workers [10] for cylinders were obtained under steady conditions and are generally accepted as the standard against which various theoretical models should be compared. Spherical data are virtually nonexistent because of the difficulty of providing enough energy to the sphere to cause film boiling. Direct electrical heating and condensation heating are easily done for cylinders but not for spheres. On the other hand, the sphere is advantageous compared to the cylinder because no end effects are present.

A flow loop was developed to study flow boiling from a sphere immersed in freon-11 (R-11). Experimental heat transfer data for all regimes of boiling – film, transition, and nucleate – were obtained over moderate ranges of liquid velocity and subcooling. High-speed motion pictures gave insight into the hydrodynamic behavior in the various boiling regimes.

Apparatus

The apparatus can be divided into three parts for convenience of description – flow loop, test section, and heating fluid loop.

Flow Loop. Figure 1 shows the flow loop used to circulate the R-11 past the heated sphere in the test section. The loop is

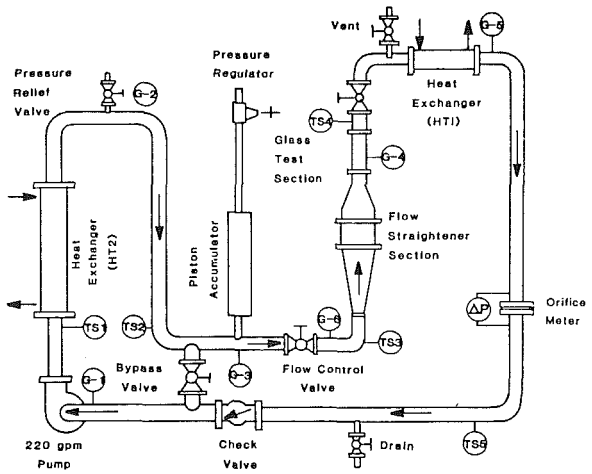

Fig. 1 Flow loop for circulating freon-11 through the test section. TS and G denote temperature and pressure measurement points.

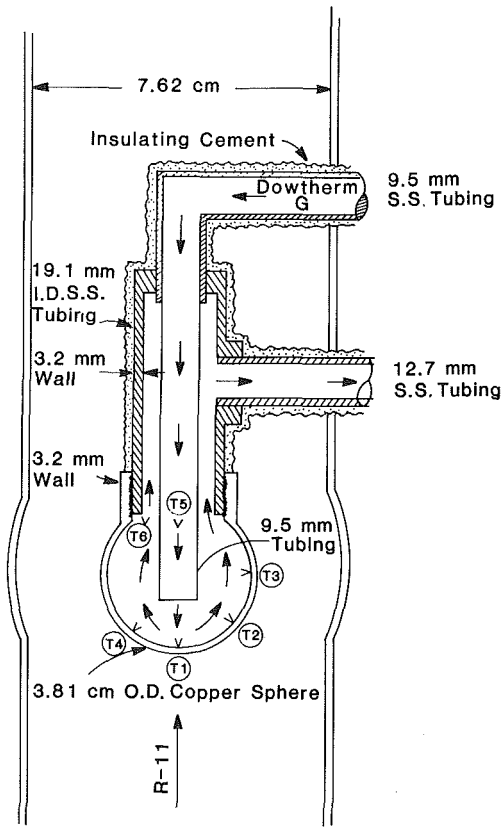

Fig. 2 Spherical heater inside the Pyrex test section, showing the Dowtherm G flow path

Contributed by the Heat Transfer Division for publication in the JOURNAL OF HEAT TRANSFER. Manuscript received by the Heat Transfer Division February 4, 1985.

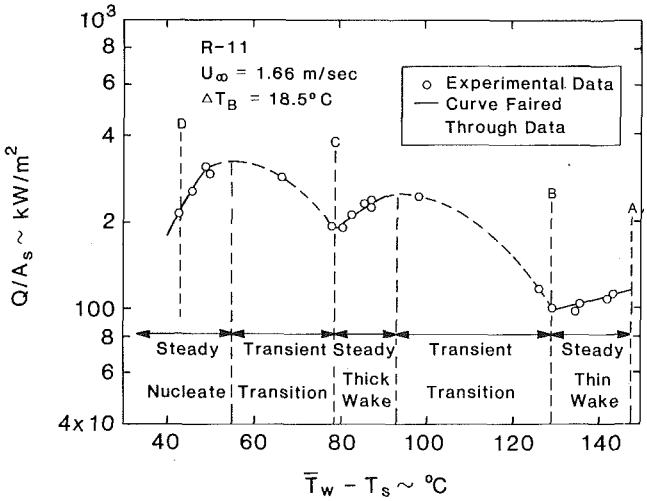

Fig. 3 Heat flux versus wall superheat for flow boiling of freon-11. Dashed lines represent transient behavior.

closed to the atmosphere; thermal expansion of the R-11 is accommodated by the piston accumulator. The accumulator also allows pressure to be exerted upon the R-11 by a piston actuated by a regulated air supply. The closed system prevents the working fluid from becoming contaminated or from absorbing air or water vapor. Fluid velocity in the test section is correlated to the mass flow rate measured by the orifice meter. The heat exchangers allow heat to be either removed from or provided to the R-11 dependent upon the desired operating conditions.

Immediately upstream of the test section is a flow straightening/turbulence reducing section designed to yield a flat, quasi-laminar velocity profile at the entrance of the test section. The Reynolds number in the test section was on the order of 300,000, which of course would have been highly turbulent if not for the turbulence-reducing screens placed below the test section. Thirty-mesh screens with a wire diameter of 0.165 mm were used, giving a solidity of 35 percent. The screens removed the large-scale eddies and did not shed fine-scale eddies since the wire Reynolds number was less than 40. A pitot tube traverse across the test section verified the flatness of the incoming profile. Complete details of the construction and operation of the flow loop can be found in [11].

Test Section. Figure 2 shows the cross section of the spherical heater inside a pyrex test section. The test section is bulged at the point where the sphere is located to account for flow blockage. This was done to simulate a sphere moving through an infinite liquid, so that the results of theoretical models could be compared to the experimental data.

The cross section of the heater shows how energy was delivered to its interior. Dowtherm G was pumped down the inner tube, flowed around the interior of the hollow sphere and then back to its heating loop. Copper-constantan thermocouples were located at various points to measure the temperature behavior of the system. Thermocouples T1, T2, T3, and T4 measured the angular dependence of the inside wall temperature at 0, 45, 90, and 35 deg, respectively, measured from the lower stagnation point. These thermocouples were embedded in a machined depression slightly larger than the bead size. The material surrounding the depression was "peened" to force the copper to fit tightly against the bead. The wires were laid along spiral lines before being brought out through the flow tubes. Thus, the wires tended to see the same fluid temperature as the bead for several wire diameters, thus minimizing conduction losses from the bead. The wires were passed through compression fittings and connected to recorders outside the system.

Thermocouples T5 and T6 differentially measured the temperature drop of the Dowtherm G as it lost heat to the R-11 boiling on the outside of the sphere. The Dowtherm flowed turbulently so the thermocouple measurements represented the mixed mean temperature adequately, especially on a differential basis.

Heating Loop. Dowtherm G was heated by bayonet electric heaters immersed in the flow, augmented by heating tapes wound around the periphery of the loop piping. Circulation was provided by a stainless steel centrifugal pump with high-temperature packing. A bypass in the loop allowed the Dowtherm to be circulated by the heaters until it reached the required temperature for boiling. It was then fed through a Fisher-Porter armored rotameter for flow rate measurement prior to passing through the spherical heater.

Boiling Experiments

The flow boiling loop was filled with R-11, approximately 25 gal, and steps were taken to purge the noncondensable gases from the system. The system working pressure was set by adjusting the pressure on the air side of the accumulator. The liquid velocity was set by flow control valves.

To commence an experiment the Dowtherm was heated to about 250°C, then the main valve and the bypass valve of the heating loop were opened and closed respectively, forcing the heating fluid to flow through the sphere. Meanwhile the R-11 velocity at the test section was lowered, allowing easier entry into the film boiling regime. Once film boiling was established the R-11 velocity was restored to its initial value. The cooling water flow rate in the heat exchangers was also increased to offset the additional heating being done on the R-11 by the sphere, as well as the pump work.

Nomenclature

A = area
A_s = spherical area up-to intersection with support cylinder
c_p = specific heat
D = body diameter
h'_{fg} = effective latent heat of vaporization
Ja_v = Jakob number, vapor $= (c_p\Delta T)_v/h'_{fg}$
Ja_l = Jakob number, liquid $= (c_p\Delta T)_l/h'_{fg}$
k = thermal conductivity
m = mass
$\dot{m}$ = mass flow rate
$\underline{Nu}$ = Nusselt number $= hD/k_v$
$\overline{Nu}$ = average Nusselt number $= \bar{h}D/k_v$
Pe = Peclet number $= DU_\infty/\alpha$
Pr = Prandtl number $= \nu/\alpha$
Q = heat transfer rate
Re = Reynolds number $= U_\infty D/\nu$
t = time
T = temperature
$\bar{T}$ = average temperature
ΔT = temperature difference
ΔT_B = temperature difference $= T_s - T_B$
ΔT_s = temperature difference $= \bar{T}_w - T_s$
U_∞ = liquid velocity
α = thermal diffusivity
θ = angle measured from stagnation point
ν = kinematic viscosity
ρ = density

Subscripts

B = bulk
Cu = copper
dow = Dowtherm
i = intersection of sphere and cylinder
l = liquid
M = minimum
s = saturation
v = vapor
w = wall

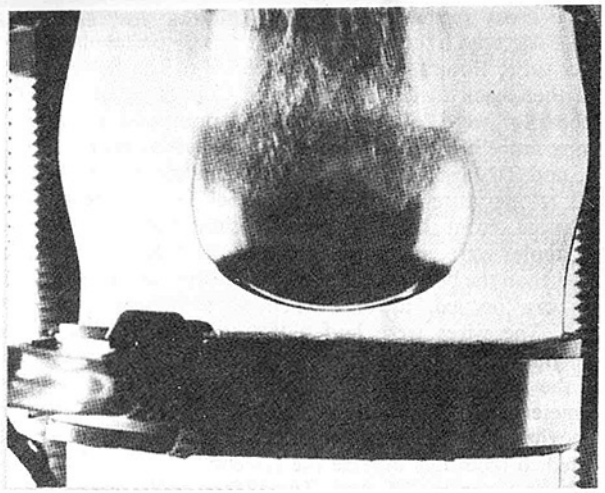

Fig. 4(a)

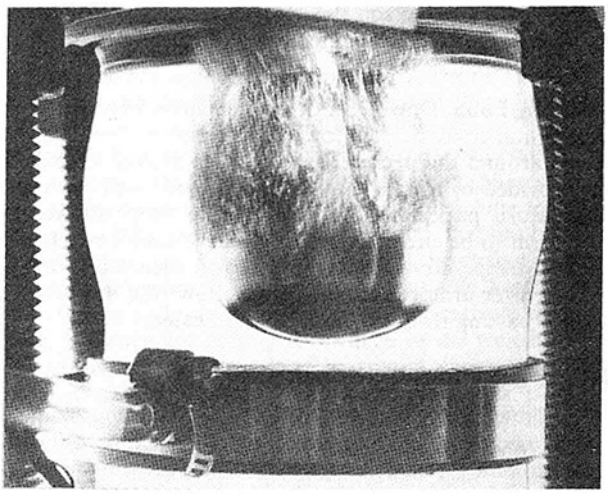

Fig. 4(b)

Fig. 4 Photographs of flow patterns during film boiling around a spherical heater: $U_\infty = 2.32$ m/s, $\Delta T_B = 12.2$°C: (*a*) thin wake pattern, $T_W = 195$°C; (*b*) thick wake pattern, $T_W = 152$°C

A boiling curve could be traced out for a given liquid velocity and subcooling by carefully lowering either the Dowtherm temperature or its flow rate. The system responded to such a change by achieving a new steady state as demonstrated by steady temperatures which were recorded on a Linear continuous strip-chart recorder. For a particular flow rate of Dowtherm, a wall temperature distribution and the corresponding Dowtherm temperature drop were measured. These data were used to compute a q versus ΔT_s curve for a particular R-11 velocity and temperature.

Data Reduction

For a given R-11 velocity, temperature, and pressure, the sphere heat flux was computed from

$$q_s = \{(\dot{m}c_p)_{\text{dow}}(T_5 - T_6) - (mc_p)_{cu}dT/dt\}/A_s$$

where

$\dot{m}$ = Dowtherm mass flow rate
$T_5 - T_6$ = Dowtherm temperature drop
mc_pdT/dt = transient experienced by the sphere mass
A_s = sphere area up to intersection with cylinder

Equation (1) allows data to be obtained during transient as well as steady operation of the system.

Such data are plotted on Fig. 3 as heat flux versus temperature difference. The temperature difference is the average wall temperature minus the saturation temperature at the existing pressure. The average wall temperature was found by fitting a modified exponential curve through the temperatures measured at various angular locations, then computing an area-weighted average using equation (2) below

$$\bar{T}_w = \frac{1}{A_s}\int_0^{\theta_i} T_w(\theta)dA \tag{2}$$

The wall temperatures were found by correcting the temperatures measured on the inside of the sphere for the heat flux across the wall.

Figure 3 will be used later to discuss the general nature of the boiling curves for the system.

Reproducibility between experiments performed at the same conditions was quite good, with deviations of only a few percent between comparable data.

An estimate of the amount of energy lost to the sphere-support cylinder indicated that it was less than 1 percent of the total energy dissipated from the Dowtherm. Hence, no correction was made for this loss.

The steady-state uncertainty in the heat transfer measurements was due to observer resolution in rotameter mass flow readings, uncertainty in the differential temperature measurements, and in temperature recording errors. A detailed uncertainty analysis [11] showed that the maximum expected uncertainty of ± 10.45 percent would occur in the nucleate boiling regime. In the film boiling regime, the uncertainty was considerably less, ranging up to only ± 6 percent.

Photographic Observations

High-speed photographs showed that two patterns of flow film boiling occurred, depending upon the sphere surface temperature.

Thin Wake Pattern. At high surface temperatures a "thin wake" pattern was observed as shown by the still photograph of Fig. 4(*a*). The wake adheres closely to the rear of the sphere and the connecting cylinder. The connecting cylinder distorted the wake that would normally occur behind an isolated sphere, but there was a region filled mostly with vapor that we call the wake region, as shown by Fig. 4. The liquid–vapor interface flowed relatively smoothly beyond the equator on the sphere. This pattern accompanied the heat transfer regime labeled as *A–B* on Fig. 3. Steady conditions were easy to maintain in this regime.

Thick Wake Pattern. The second pattern (see Fig. 4*b*) emerged as the sphere temperature was lowered toward point B on Fig. 3. A transition occurred that led to a much thicker and more chaotic-appearing wake that separated nearer the equator. Small liquid droplets in the wake moved downward counter to the main liquid flow; they behaved much like Leidenfrost drops on a hot surface. They disappeared as they approached the point where the vapor film separated to form the wake, either being caught up by the liquid overriding the film or flashed as they collapsed upon the hot surface.

The thick wake pattern persisted until the stable vapor film on the front of the sphere collapsed, at point *C* on Fig. 3. It could be maintained with the apparatus, but once the film collapsed, a transient occurred that could not be stabilized. The nucleate peak heat flux was rapidly achieved, followed by nucleate boiling on the sphere, point *D* on Fig. 3.

The collapse of the vapor film proceeded from back to front and the motion pictures showed it involved a breakdown of

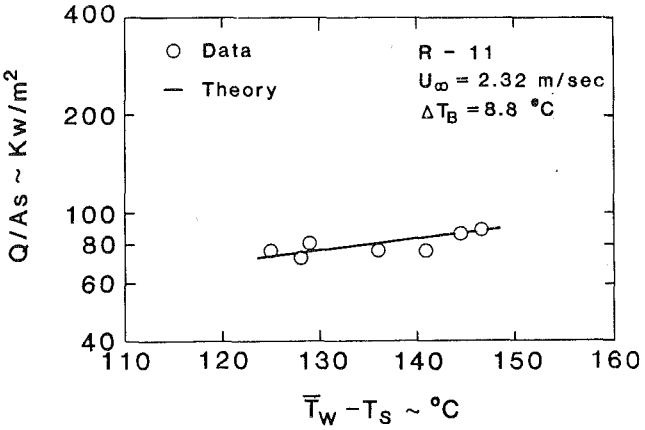

Fig. 5 Comparison of experiment to theory

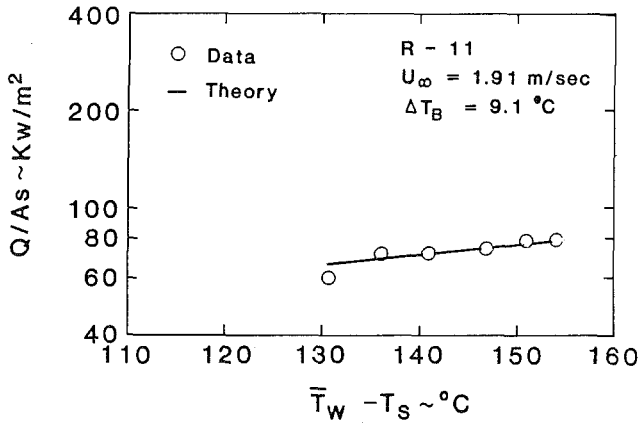

Fig. 6 Comparison of experiment to theory

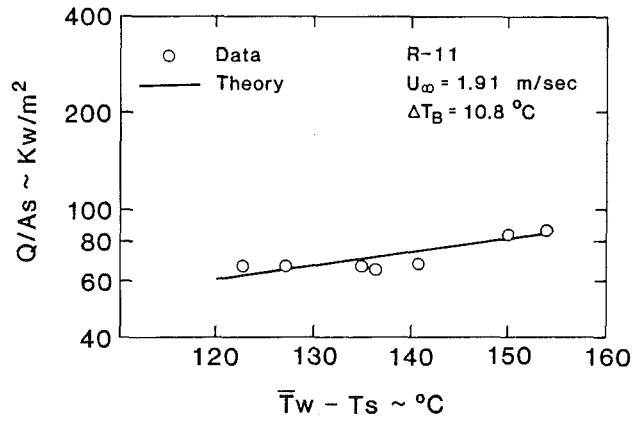

Fig. 7 Comparison of experiment to theory

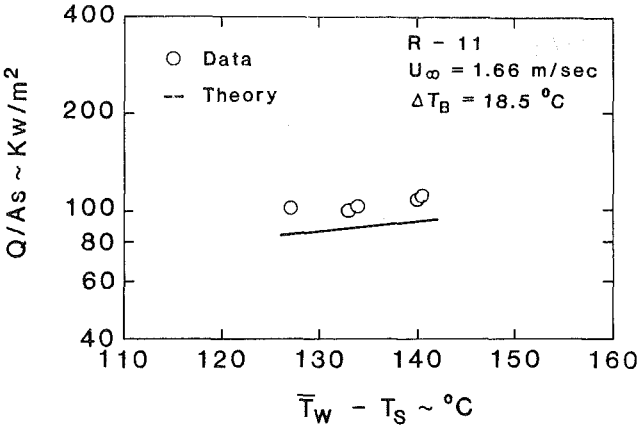

Fig. 8 Comparison of experiment to theory

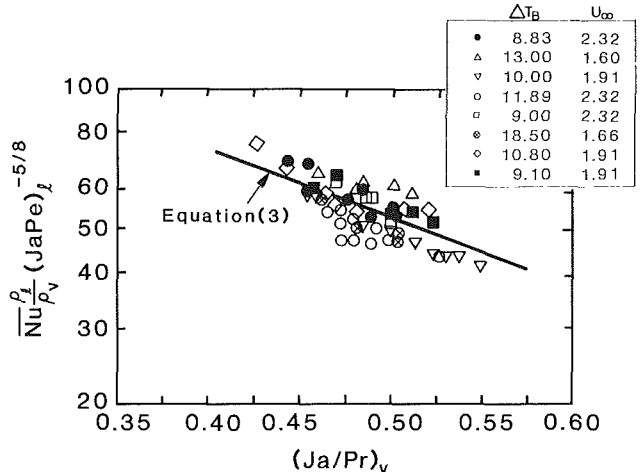

Fig. 9 Semi-empirical correlation compared to experimental data

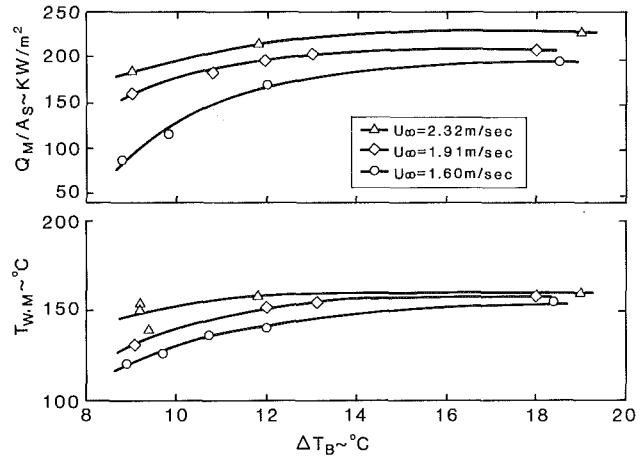

Fig. 10 Surface temperature and heat flux at the stagnation point just prior to the collapse of the vapor film

the liquid-vapor interface that propagated forward over the sphere.

We believe that the thick wake pattern consists of stable film boiling on the front and nucleate/transition boiling on the back of the sphere. The wall temperature measurements showed that there was indeed a much larger temperature drop from the front to the back for the thick wake than for the thin wake pattern.

Heat Transfer

Figure 3 shows the general nature of flow boiling of subcooled freon-11. The solid curve segments indicate stable operating regimes while the dashed lines indicate transients that the apparatus could not control. The data exhibited two maxima: one that corresponded to the transition from the thin wake to the thick wake boiling regime, and another that followed the collapse of the vapor film on the front of the sphere, at point C on Fig. 3.

Comparison of Data to Theory. The data from several typical experiments were compared to the theory of Witte and Orozco [12] in the thin wake regime. The Witte–Orozco theory is based on laminar flow, constant thermophysical properties, negligible effect of vapor drag on liquid flow, uniform surface

temperature, and other assumptions that are appropriate to film boiling. Our data in the thin wake regime displayed only small variations in surface temperature with angle, on the order of 5–10°F between the front stagnation point and the equator. We corrected our computer model based on the Witte–Orozco theory to allow the surface temperature to vary in accordance with our measurements. The data and the theory are compared on Figs. 5–8 at the appropriate average wall temperature as given by equation (2).

The data and theory are in excellent agreement, with the most deviation occurring for the more highly subcooled case of Fig. 8. Even for this case, the deviation of the theory from the data is only about 15 percent. At high subcooling there could be some liquid–solid contact that our model does not take into account. This would drive the experimental data higher than the prediction.

The theoretical flux was based on the area A_s of the sphere up to its intersection with the support cylinder. The data were based on the same area because thermocouples 5 and 6 were situated so that they measured the temperature drop caused by the heat flux crossing A_s.

Flow Film Boiling Correlation. Witte and Orozco developed a relationship for the dependence of the vapor film thickness on the dimensionless parameters Ja_v, Ja_l, Pe_l, Re_v, and ρ_l/ρ_v [12]. Since the local Nu is indirectly proportional to the dimensionless vapor film thickness, the possibility of correlating the average $\overline{Nu}$ in terms of the above-listed numbers was investigated. In light of the excellent agreement between theory and experiment shown by Figs. 5–8, the theory was used to generate curves of $(\overline{Nu}\ \rho_l/\rho_v)$ versus $(Ja/Pr)_v$. These curves showed a common slope with the intercept being controlled by the liquid subcooling and velocity. A relationship between the intercepts and the product $(Ja\ Pe)_l$, which represents the combined effects of subcooling and velocity, was developed and used to correlate all of the thin wake data gathered in this study. The resulting correlation is given by equation (3) below

$$\overline{Nu} = 18.73(\rho_v/\rho_l)(JaPe)^{5/8}(Ja/Pr)^{-3/2} \quad (3)$$

For brevity, the details of this development are omitted; they can be found in [11]. It should be pointed out, however, that the vapor properties were evaluated at the saturation conditions at the existing film temperature, as is the custom in film boiling calculations. Figure 9 shows that the data are predicted to within ± 20 percent by equation (3).

Certainly at this point, equation (3) cannot be thought of as a universal correlation since it is based on only one set of data. However, the fact that the subcooling and velocity can be accounted for in this way suggests that, in the future, data for other fluids might be correlated in the same way.

Stability

Subcooling and velocity were found to significantly influence the stagnation surface temperature (T_1) and heat flux just prior to when the vapor film collapsed, point C on Fig. 3. Figure 10 shows this dependence in terms of liquid subcooling for various velocities. An increase in either subcooling or velocity always led to an increase in both the heat flux at the time of vapor film collapse and the surface temperature at which it occurred. However, just as previously described by Bui and Dhir [13], it was observed that the heat transfer increased initially with liquid subcooling but quickly reached a near asymptotic value. Also the minimum film boiling stagnation temperature becomes virtually insensitive to velocity as the subcooling increases.

Conclusions

The theory of Witte and Orozco predicts the heat flux very well for the heat transfer regime where stable film boiling exists over the entire sphere surface. Most experimental data for film boiling over cylinders and spheres are considerably higher than predictions. However, predictive theories neglect heat transfer in the wake region. The apparatus used in these studies, in essence, removed a large part of the wake and the measured heat flux was based mostly on the part of the sphere where the vapor film remained thin. The good agreement between these data and theory indicates that most theories do not treat the wake heat transfer properly, and that wake heat transfer cannot be ignored.

This study demonstrated that care must exercised in identifying the minimum heat flux point for flow boiling over submerged bodies. The data showed two minima, neither of which corresponded to the condition where film boiling becomes unstable in a uniform fashion around the body.

High-speed photographs of the vapor film collapse showed that the instability was a hydrodynamic breakdown of the film at the point where the vapor film separates to form a wake. The collapse propagated from the back to the front of the sphere; i.e., from a colder to a hotter surface. This observation, taken along with similar observations in our laboratory [3, 7] indicates that the instability is linked to the surface temperature.

A semi-empirical correlation for the film boiling heat transfer from a sphere to flowing subcooled freon-11 was developed. It correlates the experimental data to ± 20 percent.

Acknowledgments

Both authors appreciate the support of the National Science Foundation under grant No. MEA-8008036 during this study.

References

1 Walford, F. J., "Transient Heat Transfer From a Hot Nickel Sphere Moving Through Water," *Int. J. Heat Mass Transfer*, Vol. 12, 1969, pp. 1621–1625.

2 Dhir, V. K., and Purohit, G. P., "Subcooled Film-Boiling Heat Transfer From Spheres," *Nucl. Eng. and Des.*, Vol. 47, 1978, pp. 49–66.

3 Stevens, J. W., and Witte, L. C., "Destabilization of Vapor Film Boiling Around Spheres," *Int. J. Heat Mass Transfer*, Vol. 16, 1973, pp. 669–678.

4 Mesler, R., "Peak Heat Fluxes in Boiling as Determined by Steady State and Transient Experiments," *AIChE J.*, Vol. 25, No. 3, May 1979, pp. 549–551.

5 Thibault, J., and Hoffman, T. W., "Local Boiling Heat Flux Density Around a Horizontal Cylinder Under Saturated and Subcooled Conditions," *Proc. 6th Int. Heat Transfer Conf.*, Toronto, 1978, pp. 199–204.

6 Ungar, E., and Eichhorn, R., "Local Surface Boiling Heat Transfer From a Quenched Sphere," ASME Paper No. 82-HT-27.

7 Sankaran Subramanian, "Quenching of a Hollow Sphere," MS Thesis, University of Houston, Dec. 1984.

8 Yilmaz, S., and Westwater, J. W., "Effect of Velocity on Heat Transfer to Boiling Freon-113," ASME JOURNAL OF HEAT TRANSFER, Vol. 102, No. 1, Feb. 1980, pp. 26–32.

9 Broussard, R. A., and Westwater, J. W., "Boiling Heat Tranfser of Freon-113 Flowing Normal to a Tube: Effect of Tube Diameter," AIAA Paper No. 84-1708, June 25–28, 1984, Snowmass, CO.

10 Bromley, L. A., LeRoy, N. R., and Robbers, J. A., "Heat Transfer in Forced Convection Film Boiling," *I. and E. C.*, Vol. 45, No. 12, 1953, pp. 2639–2646.

11 Orozco, J. A., "Flow Film Boiling From Submerged Bodies," PhD Dissertation, University of Houston, Dec. 1984.

12 Witte, L. C., and Orozco, J. A., "The Effect of Vapor Velocity Profile Shape on Flow Film Boiling From Submerged Bodies," ASME JOURNAL OF HEAT TRANSFER, Vol. 106, No. 1, Feb. 1984, pp. 191–197.

13 Bui, T. D., and Dhir, V. K., "Transition Boiling Heat Transfer on a Vertical Surface," ASME JOURNAL OF HEAT TRANSFER, Vol. 107, No. 4, Nov. 1985, pp. 756–763.

Water Droplet Size Measurements in an Experimental Steam Turbine Using an Optical Fiber Droplet Sizer

K. Tatsuno
Researcher,
Research and Development Center,
Toshiba Corporation,
Kawasaki, Japan

S. Nagao
Engineer,
Keihin Product Operations,
Toshiba Corporation,
Yokohama, Japan

An optical fiber droplet sizer which is applicable to droplet size measurements in a steam turbine has been developed. This sizer uses the forward scattering method. The performance of the droplet sizer was verified by 0.1–5.7 μm average diameter polystyrene particles. Using this sizer, droplet size measurements were made at the last stage moving blade outlet in a 10 MW experimental steam turbine. Average diameters between 0.2 and 1.0 μm, which depend on wetness (6–14 percent) and locations in the radial direction of the blade, were obtained.

1 Introduction

Condensation occurs and droplets grow in the low-pressure (L.P.) stages of a steam turbine. The droplets cause efficiency reduction of a turbine. Droplet size measurements are necessary in order to accurately estimate and reduce mechanical and thermodynamic losses.

Several studies of droplet size measurements have been made recently in steam turbines. In these measurements, the light extinction method [1, 2] and the side scattering method [3] were used.

In the light extinction method, the transmission of monochromatic light, measured at several wavelengths, is inverted to yield the droplet size distribution using equation (1)

$$T(\lambda) = \exp[-L\int C(\lambda, D)n(D)dD] \quad (1)$$

This method has the following disadvantages. If the droplet density is low, $T(\lambda)$ is larger than 0.9. Therefore the variation of $T(\lambda)$ with λ is very small. In that case, it is very difficult to determine the droplet size distribution using equation (1). Also, droplets larger than 2 μm diameter cannot be measured if λ is in the visible light range, because $C(\lambda, D)$ is a function of only D for $\pi D/\lambda \geq 10$.

The pulse height of light scattered by one particle is a single-valued function of D in a certain diameter range. In the side scattering method, droplet size is determined from the scattered light pulse height. In this method, the scattering zone has to be small so that it contains zero or one particle. Therefore, this method is not applicable to measurements in a steam turbine in the case of high droplet densities.

However, there is another forward scattering method besides the above-mentioned two methods. In this method, the scattered light intensity pattern by many particles is measured and inverted to droplet size distribution using

$$I(\theta) = \int i(D, \theta)n(D)dD \quad (2)$$

The forward scattering method is applicable to droplets at a high density and has a wide measurable range. However, droplets smaller than 5 μm diameter cannot be measured by the conventional droplet sizer which uses this method [4, 5] (Fig. 4), since it is based on Fraunhofer diffraction theory and the measuring range of $I(\theta)$ is less than 15 deg.

The authors have developed an optical fiber droplet sizer with which droplets larger than 0.1 μm diameter can be measured, and applied this sizer to droplet size measurements in a 10 MW experimental steam turbine. This paper describes the optical fiber droplet sizer and results of the measurements.

Contributed by the Heat Transfer Division for publication in the JOURNAL OF HEAT TRANSFER. Manuscript received by the Heat Transfer Division September 25, 1985.

2 Forward Scattering Method

A parallel monochromatic light is directed at many measured droplets. The angular pattern of the scattered light intensity, which is named the scattered light intensity pattern, is measured. The measured droplets are assumed to be spherical. This assumption is reasonable because small droplets are kept spherical by surface tension.

The light intensity scattered by a D μm diameter spherical droplet can be calculated by Mie theory [7], and is expressed by $i(D, \theta, m, \lambda)$ as a function of D, θ, m, and λ.

If the droplet is water ($m = 1.33$) and the light source is a He–Ne laser ($\lambda = 0.633$ m), $i(D, \theta, m, \lambda)$ may be expressed by $i(D, \theta)$ as a function of only D and θ. $i(D, \theta)$ is calculated under the condition that irradiation light is unpolarized and incoherent. Light emerging from a collimator lens through a multimode optical fiber satisfies this condition.

The scattered light intensity pattern of many droplets can be expressed by equation (2), as superpositions of the scattered light intensity by one droplet without considering the effect of interference. The droplet size distribution is determined by solving equation (2). The least-squares solution of equation (2) is unique if $(G^*G)^{-1}$ exists in equation (15) (see the appendix).

3 Optical Fiber Droplet Sizer

3.1 Description of the Droplet Sizer. A schematic diagram of the optical fiber droplet sizer is shown in Fig. 1, and the measuring probe of this sizer is shown in Fig. 2. The measuring probe is inserted into a turbine casing, and droplets in the scattering zone are measured.

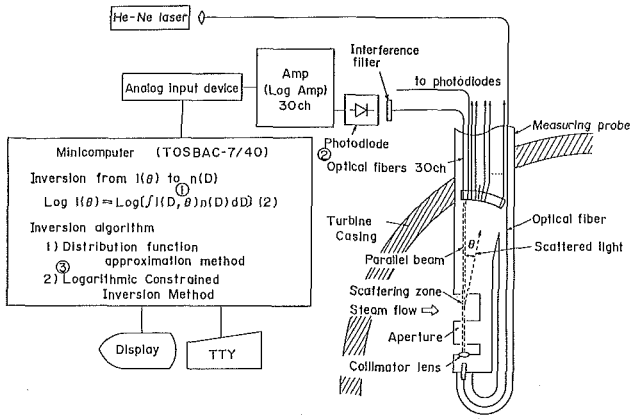

Fig. 1 Schematic diagram of an optical fiber droplet sizer

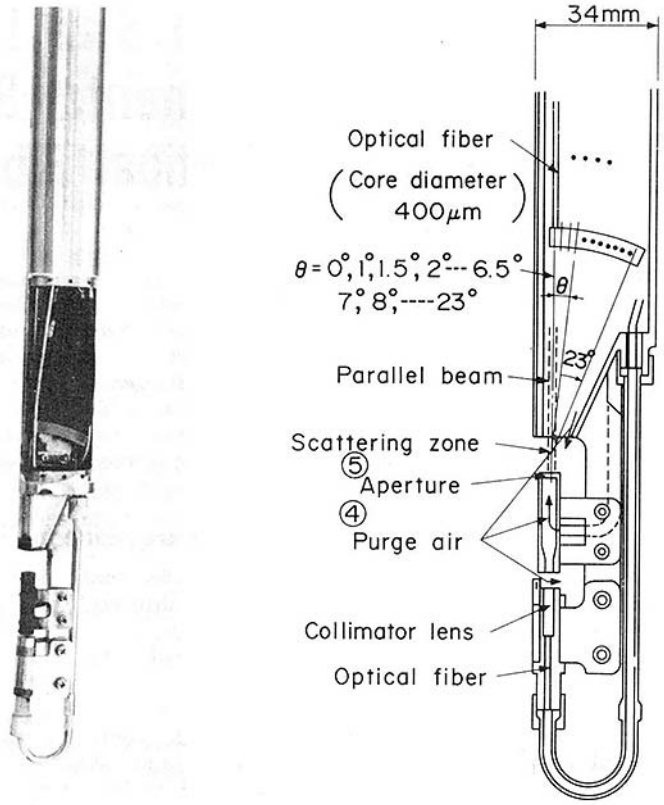

Fig. 2 Measuring probe of the optical fiber droplet sizer

The He–Ne laser beam is led to the scattering zone through an optical fiber, and a parallel beam is formed by a collimator lens. This parallel beam is directed at the measured droplets in the scattering zone, and scattered by the droplets. The scattered light is received by 30 optical fibers arranged at various scattering angles: 0, 1, 1.5, 2, 2.5, ... , 6, 6.5 deg and 7, 8, ... , 23 deg. The optical fiber arranged at θ receives the light scattered between θ_1 and θ_2, as shown in Fig. 3. θ_1 and θ_2 are expressed by

$$\tan\theta_1 = \frac{R\sin\theta}{R\cos\theta - L/2} \tag{3}$$

$$\tan\theta_2 = \frac{R\sin\theta}{R\cos\theta + L/2} \tag{4}$$

respectively, where $R = 57.5$ mm and $L = 10$ mm. In the case of $\theta = 23$ deg when $\theta_1 - \theta_2$ is larger than at another fiber position, θ_2 is 21.2 deg and θ_1 is 25.1 deg. The received light $i_r(D, \theta)$ is expressed by

$$i_r(D,\theta) = \int_V i(D,\theta)dv \tag{5}$$

where the integral is taken over the scattering zone V. $i_r(D, \theta)$ is approximated by $i(D, \theta)\cdot V$ in the sizer. The scattered light intensity pattern is defined as a set of the light intensities received by the fibers. The received light is led to photodiodes through the optical fibers. The photodiodes transform the scattered light to electric current signals. Interference filters are put in front of the photodiodes in order to exclude environmental stray light. Electric current signals are transformed to electric voltage signals and amplified by log amplifiers. The amplified signals are fed to a minicomputer (TOSBAC-7/40).

In the minicomputer, the scattered light intensity pattern is inverted to the droplet size distribution using

$$\log I(\theta) = \log\left[\int i(D,\theta)n(D)dD\right] \tag{6}$$

Equation (6) is obtained by taking the logarithm of both sides

Nomenclature

B = beam diameter, mm
$C(\lambda, D)$ = extinction cross section, m^2
D = droplet diameter, μm
$\bar{D}$ = average droplet diameter, μm
E = difference between measured $I(\theta)$ and calculated $I(\theta)$, defined by equation (5)
h = measuring location in radial direction of blade (relative value)
$I(\theta)$ = scattered light intensity pattern by measured droplets, W
$i(D, \theta)$ = scattered light intensity by D μm diameter droplet, W
$i_r(D, \theta)$ = light received by optical fiber, W
L = scattering path length, m
m = refractive index
$n(D)$ = droplet size distribution
R = distance between optical fiber and scattering zone, mm
$T(\lambda)$ = transmission ratio of monochromatic light with λ
V = scattering zone
Y = wetness of steam
$\theta, \theta_1, \theta_2$ = scattering angle, deg
λ = light wavelength, μm
π = ratio of circumference to diameter
σ = standard deviation, μm

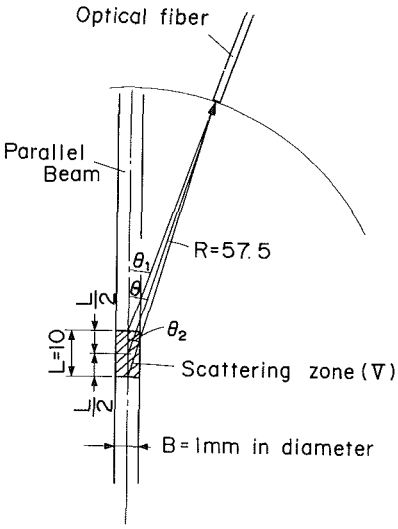

Fig. 3 Optical arrangements for measuring the scattered light intensity pattern

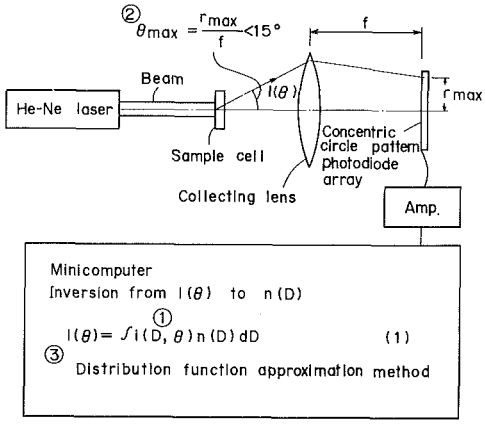

Fig. 4 Typical conventional droplet sizer

of equation (2) in order to compress the wide measuring range of the scattered light intensity pattern.

The following two inversion algorithms are used.

(*1*) *Distribution Function Approximation Method.* This method is the most popular one. A proper distribution function of the droplet size distribution $n(D)$ is assumed, and the parameters of the function are determined by the least-squares method. For example, the normal distribution function

$$n(D) = \frac{1}{\sqrt{2\pi}\sigma} \exp\left[-\frac{(D-\bar{D})^2}{2\sigma^2}\right] \tag{7}$$

is assumed as $n(D)$, and the distribution parameters D and σ are determined so as to minimize the value E represented by

$$E = \| \log I(\theta) - \log \left[\int i(D, \theta) n(D) dD\right] \|^2 \tag{8}$$

(*2*) *Logarithmic Constrained Inversion Method* [*8*]. This method was developed by Tatsuno, one of the present authors. This method can determine any form of droplet size distribution, because it doesn't require the assumption of a distribution form. This method is used in order to verify the assumption of the distribution function in the distribution function approximation method. An outline of the Logarithmic Constrained Inversion Method is described below. Equation (6) is approximated by linear equations. The linear equations are solved under the conditions: (1) $n(D)$ is smooth, and (2) $n(D)$ is nonnegative. The details of this method are described in the appendix.

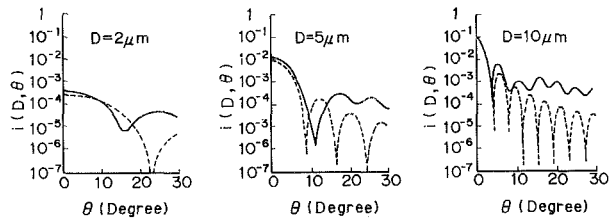

Fig. 5 Comparison between Mie theory and Fraunhofer diffraction theory: _____Mie theory; · · · · · · Fraunhofer diffraction theory, $m = 1.33$, $\lambda = 0.633$ μm

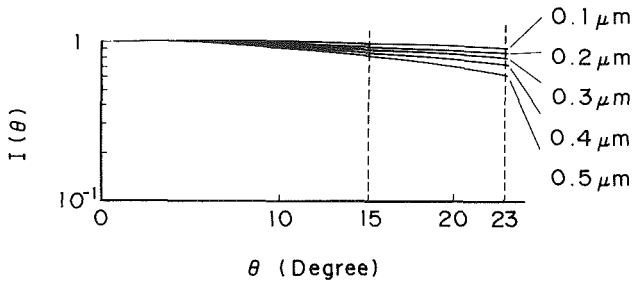

Fig. 6 Scattered light intensity patterns by small particles ($m = 1.33$, $\lambda = 0.633$ μm)

3.2 Improvements. Improvements are described below as compared with a typical conventional droplet sizer (Fig. 4).

1) The light intensity $i(D, \theta)$ scattered by a D μm diameter droplet is calculated based on Mie theory.

Mie theory strictly solves the Maxwell's equations. Therefore, Mie theory is applicable to all size droplets. In the conventional sizer, $i(D, \theta)$ is calculated based on Fraunhofer diffraction theory. Fraunhofer diffraction theory is applicable to particles which are very large compared to the wavelength of the irradiation light. A comparison of $i(D, \theta)$ based on Mie theory and Fraunhofer diffraction theory is shown in Fig. 5, where the wavelength is 0.633 μm and refractive index is 1.33. It is apparent that Fraunhofer diffraction theory cannot be applied to droplets smaller than about 5 μm diameter and to large scattering angles.

As described in Section 2, an incident light directed at droplets is not required to be coherent, since $i(D, \theta)$ is calculated by Mie theory under the condition that the incident light is incoherent and unpolarized. Therefore, interference and particle positions may be put out of consideration.

2) The measuring angle range of the scattered light intensity pattern is extended to 0–23 deg.

In the conventional droplet sizer (Fig. 4), the measuring angle range is 0–15 deg, since it is difficult to make a collecting lens with wide aperture and short focal length. The light intensity patterns scattered by 0.1–0.5 μm diameter droplets are shown in Fig. 6. It is difficult to identify the droplet diameter from the scattered light intensity pattern measured in the range of 0–15 deg, but it is easy to do so from the pattern measured in the range of 0–23 deg.

As shown in Fig. 2, the measuring angle range is expanded by arranging optical fibers in a wide scattering angle range. As $i(D, \theta)$ based on Mie theory is used, the measuring plane of the scattered light need not be far field. Therefore, a collecting lens is unnecessary, and the scattered light intensity at θ can be measured by arranging the optical fiber at θ.

Large-core (400 μm diameter) optical fibers are used in order to receive a large amount of the scattered light. The removal of the collecting lens also gave us the following advantage: In the conventional sizer, the scattered light by the collecting lens is the main source of noise. Since the above measuring arrangement does not have a collecting lens, the noise level is reduced and the light intensity scattered by low-density droplets can be measured.

3 The Logarithmic Constrained Inversion Method is used.

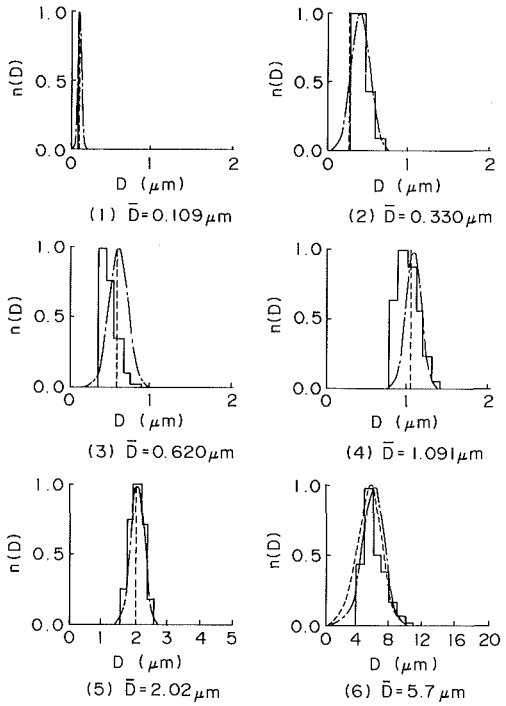

Fig. 7 Verification of droplet sizer performance using polystyrene particles: ····· actual distribution; —·— distribution function approximation method; _____ Logarithmic Constrained Inversion Method

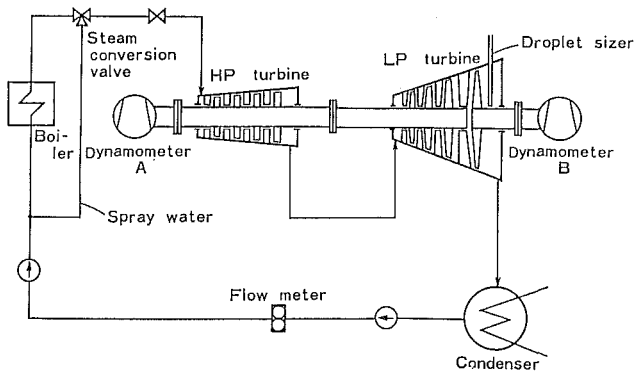

Fig. 8 Experimental steam turbine facility

As described in Section 3.1, this method doesn't require the assumption of a size distribution form. Therefore, this method can check whether the assumed function in the distribution function approximation method is proper or not.

4) The collimator lens and the optical fibers are protected from attachment of droplets by air purge.

5) The aperture is arranged, as shown in Fig. 2, to shut off the light scattered by the collimator lens.

4 Verification

In order to verify the performance of the optical fiber droplet sizer, 0.1–5.7 μm average diameter polystyrene particles (trade name: Dow Uniform Latex Particles) were measured. The polystyrene particle size distribution was measured using a scanning electron microscope by Dow Chemical Company. In our measurements, polystyrene particles were suspended in water in a glass cell.

Measured results are shown in Fig. 7. The average diameters $\bar{D}$ in Fig. 7, e.g., 0.109, are values measured by a scanning electron microscope. Measured size distributions were normalized by the maximum value of $n(D)$ in order to directly compare average diameters. In the Logarithmic Constrained Inversion Method [8], the following size ranges were used: (1) [0, 1 μm] in Figs. 7(1-4) and all of Fig. 9; (2) [0, 4 μm] in Fig. 7(5); (3) [0, 20 μm] in Fig. 7(6), where the number of partitions was 20. The size range was set initially at [0, 20 μm], and was decreased gradually. Normal distribution was assumed in the distribution function approximation method. Distributions measured by the developed sizer agree with the actual distributions measured by a scanning electron microscope.

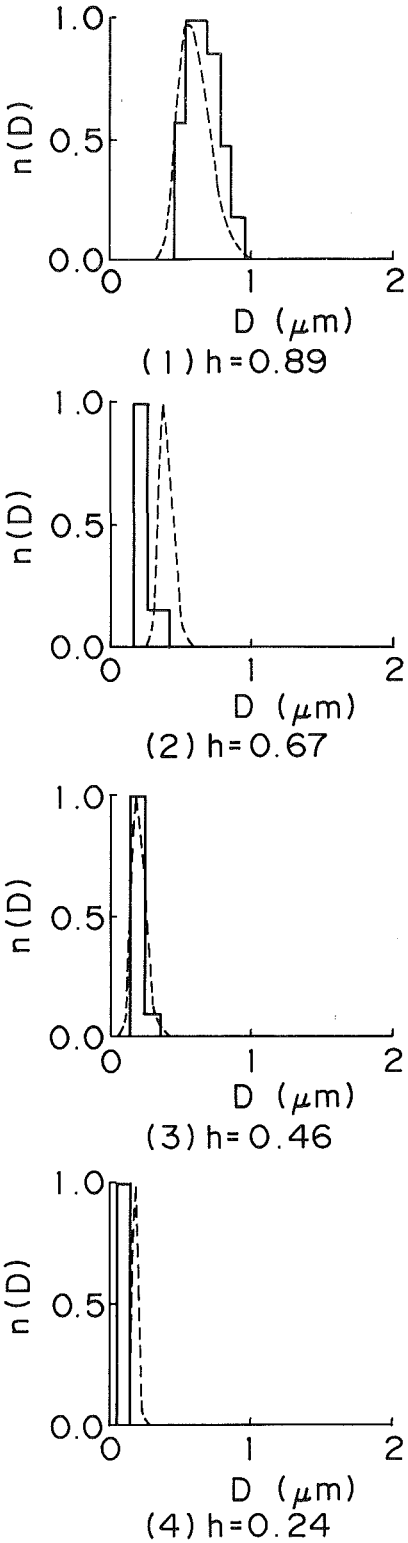

Fig. 9 Droplet size distributions in a 10 MW experimental steam turbine: ····· distribution function approximation method; _____ Logarithmic Constrained Inversion Method (Y = 6 percent)

The accuracy of measurements by the droplet sizer is listed below. The accuracy was estimated from Fig. 7.

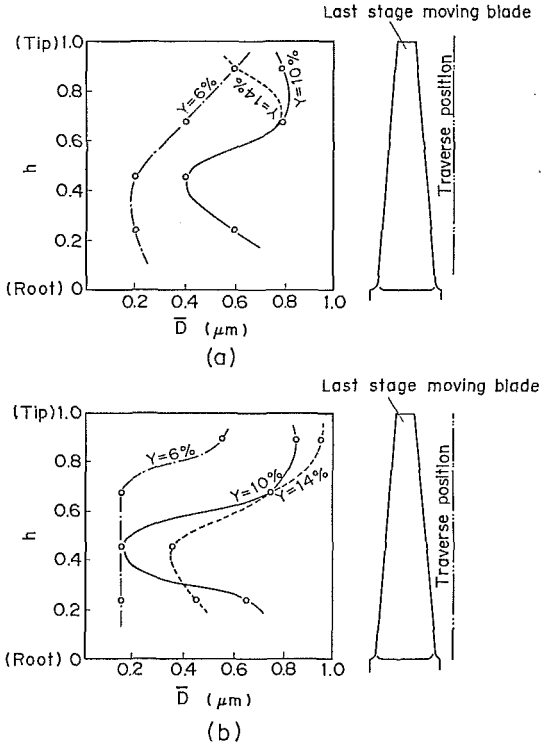

Fig. 10 Results of droplet size measurements in a 10 MW experimental steam turbine: (a) distribution function approximation method (log-normal distribution); (b) Logarithmic Constrained Inversion Method

Measuring droplet size range (for average diameter)	0.1–5 μm	
Error of average diameter	0.1 μm	($D<1$ μm)
	10 percent of average diameter	($D\geq 1$ μm)
Error of standard deviation	0.1 μm	($D<1$ μm)
	10 percent of average diameter	($D\geq 1$ μm)

5 Experiment

A schematic diagram of the 10 MW experimental steam turbine facility is shown in Fig. 8. These turbines are scale models of high power steam turbines. The boiler provides superheated steam to the high-pressure (H.P.) turbine through a conversion valve, which controls steam pressure and temperature. The superheated steam does work through the H.P. turbine and L.P. turbine, and becomes wet steam. Since the droplets are formed by expansion only, steam with various wetnesses can be naturally obtained. The measuring probe of the droplet sizer was inserted downstream of the last stage moving blades and traversed in the radial direction. Wetness was adjusted by varying the H.P. turbine inlet temperature. Steam pressure at the measuring point was maintained at about 3800 Pa.

Droplet size measurements were made at wetnesses $Y=6$, 10, and 14 percent and at several locations h in the radial direction. The measuring locations, which are represented as relative distances normalized by the blade length, were 0.24, 0.46, 0.67, and 0.89.

6 Results

Examples of the droplet size distributions measured at $Y=6$ percent are shown in Fig. 9. These droplet size distributions were normalized by the maximum value of $n(D)$ in order to directly compare the peak diameters.

Dashed lines represent droplet size distributions inverted by the distribution function approximation method. The distribution function assumed for this case was a log-normal distribution because it is said that the size distribution of growing particles is a log-normal distribution [9]. Solid lines represent droplet size distributions inverted by the Logarithmic Constrained Inversion Method [8]. The droplet size distributions inverted by these two methods agree with each other. These agreements show that the assumption of a log-normal distribution is proper.

The features of the measured droplet size distributions are as follows.

(1) Droplet size distributions are narrow as shown in Fig. 9. In other words, droplet size is nearly uniform.

(2) The distribution with a large average diameter (Fig. 9(1)) is broader than that with a small average diameter (Fig. 9(2)).

Measured average diameters at various wetnesses of steam and at several locations are shown in Figs. 10(a) and 10(b). The following facts are observed in Fig. 10:

(1) The average diameter becomes larger as wetness increases. However, it seems to be saturated in the ≥ 10 percent wetness range.

(2) The average diameter of droplets at the blade tip is larger than that at the blade root. In the case of high wetness, the average diameter of droplets at the blade root becomes larger than that at the midpoint.

In these measurements, the transmission ratio of the laser beam was more than 70 percent. Therefore, the scattered light intensity pattern was accurately measured without the effect of multiscattering.

7 Conclusion

An optical fiber droplet sizer which uses the forward scattering method has been developed. The performance of the droplet sizer was verified by 0.1–5.0 μm average diameter polystyrene particles. Using this droplet sizer, droplet size measurements were made in a 10 MW experimental L.P. turbine. Average diameters between 0.2 μm and 1.0 μm, which depend on the wetness of steam (6–14 percent) and measuring locations in the radial direction of a blade, were obtained. Measured diameters were similar to the results which Walters and Skingley obtained using the light extinction method [1].

The authors intend to improve the optical fiber droplet sizer to measure the average diameter with 0.01 μm accuracy. Then, steam wetness may be obtained with high accuracy.

Acknowledgments

The authors would like to acknowledge the assistance of Mr. H. Kawagishi, Mr. T. Imamura, and Mr. Tanuma in making measurements in the experimental turbine. It is also a pleasure to acknowledge the hospitality and encouragement of all the persons concerned in the development.

References

1 Walters, P. T., and Skingley, P. C., "An Optical Instrument for Measuring the Wetness Fraction and Droplet Size of Wet Steam Flows in LP Turbines," *Instr. Mech. Engrs.*, C141/79, 1979.

2 Kantola, R. A., "Condensation in Steam Turbines," EPRI, CS-2528, RP 735-1, Aug. 1982.

3 Ederhof, A., and Dibelius, G., "Determination of Droplet Sizes and Wetness Fraction in Two-phase-flows Using a Lightscattering Technique," Sixth Thermodynamics and Fluid Mechanics Convention, I. Mech. E., C60/76, 1976.

4 Swithenbank, J., et al., "A Laser Diagnostic Technique for the Measurement of Droplet and Particle Size Distribution," AIAA Paper No. 76-69, 1976.

5 Alger, T. W., and Giedt, W. H., "A Light Scattering Technique for Determining Droplet Size Distributions in Two-Phase Liquid-Dominated Nozzle Jets," *First International Conference on Liquid Atomization and Spray Systems*, Tokyo, Japan, Aug. 1978, pp. 301–308.

6 Van de Hulst, H. C., "Particles Very Large Compared to the Wavelengths," in: *Light Scattering by Small Particles*, Wiley, New York, 1957, pp. 103–113.

7 Van de Hulst, H. C., "Rigorous Scattering Theory for Spheres of Arbitrary Size (Mie Theory)," ibid., pp. 114–130.
8 Tatsuno, K., "The Inversion Method for Determining the Particle Size Distribution From the Scattered Light Intensity Pattern in a Laser Droplet Sizer," [in Japanese], *Transactions of the Society of Instrument and Control Engineers*, Vol. 19, No. 10, Oct. 1983, pp. 53–59.
9 Aitchison, J., and Brown, J. A. C., *The Lognormal Distribution*, Cambridge Univ. Press, 1963, p. 13.
10 Twomey, S., "Linear Inversion Methods," in: *Introduction to the Mathematics of Inversion in Remote Sensing and Indirect Measurements*, Elsevier, New York, 1977, pp. 115–149.
11 Charles, L. L., and Richard, J. H., "Linear Least Squares With Linear Inequality Constraints," in: *Solving Least Squares Problems*, Prentice-Hall, New York, 1974, pp. 158–173.

APPENDIX

Logarithmic Constrained Inversion Method [8]

The Logarithmic Constrained Inversion Method is described below in detail. In this method, equation (9) is approximated by linear equations. The linear equations are solved under the conditions: (1) $n(D)$ is smooth, and (2) $n(D)$ is nonnegative.

$$\log I(\theta) = \log \left[\int i(D, \theta) n(D) dD\right] \tag{9}$$

First, we consider equation (10)

$$I(\theta) = \int_{D_{\min}}^{D_{\max}} i(D, \theta) n(D) dD \tag{10}$$

where $[D_{\min}, D_{\max}]$ is the droplet size measuring range. When the integral domain $[D_{\min}, D_{\max}]$ is divided into N small domains $[D_{l-1}, D_l]$ $(l = 1, 2, \ldots, N)$, equation (10) is rewritten as

$$I(\theta) = \sum_{l=1}^{N} \int_{D_{l-1}}^{D_l} i(D, \theta) n(D) dD \tag{11}$$

If droplet size distribution $n(D)$ is constant in $[D_{l-1}, D_l]$ and is replaced by $n(D_j)$, equation (11) becomes

$$I(\theta) = \sum_{l=1}^{N} \left(\int_{D_{l-1}}^{D_l} i(D, \theta) dD\right) \cdot n(D_l) \tag{12}$$

If the integration in equation (12) is expressed as $i_s(D_l, \theta)$, equation (12) becomes

$$I(\theta) = \sum_{l=1}^{N} i_s(D_l, \theta) n(D_l) \tag{13}$$

Assuming the measuring angles of $I(\theta)$ are $\theta_1, \theta_2, \ldots, \theta_k$, equation (13) yields

$$I(\theta_m) = \sum_{l=1}^{N} i_s(D_l, \theta_m) n(D_l) \quad (m = 1, 2, \ldots, k) \tag{14}$$

Equation (14) is also represented as

$$\mathbf{I} = \mathbf{G} \cdot \mathbf{n} \tag{15}$$

where

$$\mathbf{I} \triangleq \begin{bmatrix} I(\theta_1) \\ I(\theta_2) \\ \cdot \\ \cdot \\ I(\theta_k) \end{bmatrix} \tag{16}$$

$$\mathbf{G} \triangleq \begin{bmatrix} i_s(D_1, \theta_1) & i_s(D_2, \theta_1) & \ldots & i_s(D_N, \theta_1) \\ i_s(D_1, \theta_2) & i_s(D_2, \theta_2) & \ldots & i_s(D_N, \theta_2) \\ \cdot & \cdot & & \cdot \\ \cdot & \cdot & & \cdot \\ i_s(D_1, \theta_k) & i_s(D_2, \theta_k) & \ldots & i_s(D_N, \theta_k) \end{bmatrix} \tag{17}$$

$$\mathbf{n} \triangleq \begin{bmatrix} n(D_1) \\ n(D_2) \\ \cdot \\ \cdot \\ n(D_N) \end{bmatrix} \triangleq \begin{bmatrix} n_1 \\ n_2 \\ \cdot \\ \cdot \\ n_N \end{bmatrix} \tag{18}$$

In order to obtain the approximate equations for equation (9), the transform matrix

$$\mathbf{T} \triangleq \begin{bmatrix} \dfrac{\log I(\theta_1)}{I(\theta_1)} & 0 \ldots\ldots & 0 \\ 0 & & \cdot \\ \cdot & & \cdot \\ \cdot & & \cdot \\ \cdot & & 0 \\ 0 \ldots\ldots\ldots & 0 & \dfrac{\log I(\theta_k)}{I(\theta_k)} \end{bmatrix} \tag{19}$$

is multiplied by both sides of equation (15) from the left-hand sides. Then

$$\mathbf{TI} = \mathbf{TGn} \tag{20}$$

is obtained. Equation (20) is rewritten as

$$\tilde{\mathbf{I}} = \tilde{\mathbf{G}}\mathbf{n} \tag{21}$$

The least-squares solution of equation (21) is obtained by equation (22)

$$\mathbf{n} = (\tilde{\mathbf{G}}^* \tilde{\mathbf{G}})^{-1} \tilde{\mathbf{G}}^* \tilde{\mathbf{I}} \tag{22}$$

where $\tilde{\mathbf{G}}^*$ represents the transpose matrix of $\tilde{\mathbf{G}}$. The solution obtained by equation (22) is very sensitive to errors in $\tilde{\mathbf{I}}$. Therefore, the least-squares solution under the following conditions $(C1)$, $(C2)$ was obtained

$$n(D) \text{ is smooth} \tag{C1}$$

$$n(D) \text{ is nonnegative} \tag{C2}$$

Condition $(C1)$ means that q is kept constant

$$q = \sum_{j=1}^{N-3} (n_j - 3n_{j+1} + 3n_{j+2} - n_{j+3})^2 \tag{23}$$

Equation (23) is rewritten as follows

$$q = (\mathbf{Kn})^*(\mathbf{Kn}) = \mathbf{n}^*\mathbf{K}^*\mathbf{Kn} = \mathbf{n}^*\mathbf{Hn} \tag{24}$$

where

$$\mathbf{K} \triangleq \begin{bmatrix} 0 & & & & & \\ 0 & 0 & 0 & & & \\ 0 & 0 & 0 & & & \\ 1 & -3 & 3 & -1 & 0 & \ldots \\ 0 & 1 & -3 & 3 & 1 & 0 \ldots \\ 0 & 0 & 1 & -3 & 3 & -1 \ldots \\ & & \cdot & & & \\ & & \cdot & & & \\ & & \cdot & & & \end{bmatrix} \tag{25}$$

$$\mathbf{H} \triangleq \mathbf{K}^*\mathbf{K} \tag{26}$$

The least-squares solution under condition $(C1)$ is obtained using Lagrange's method of indeterminate coefficients [10]. The solution $\mathbf{n}$ minimizes

$$(\tilde{\mathbf{G}}\mathbf{n} - \tilde{\mathbf{I}})^*(\tilde{\mathbf{G}}\mathbf{n} - \tilde{\mathbf{I}}) + \gamma \mathbf{n}^*\mathbf{Hn} \tag{27}$$

This solution is obtained by

$$\mathbf{n} = (\tilde{\mathbf{G}}^*\tilde{\mathbf{G}} + \gamma\mathbf{H})^{-1}\tilde{\mathbf{G}}^*\tilde{\mathbf{I}} \tag{28}$$

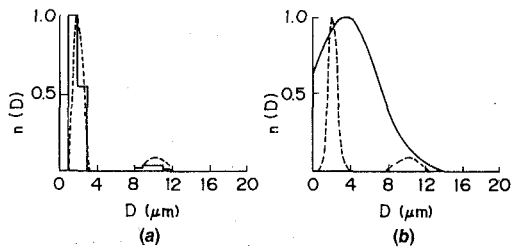

Fig. 11 Verification of Logarithmic Constrained Inversion Method: (*a*) Logarithmic Constrained Inversion Method; (*b*) distribution function approximation method

n must be nonnegative (condition (*C*2)). If **n**, obtained by equation (28), satisfies the following conditions [11], **n** is the least-squares solution under the conditions (*C*1), (*C*2).

Conditions

$$y_i \geq 0 \quad \text{for } j \text{ of } n_j = 0 \tag{29}$$

and

$$y_i = 0 \quad \text{for } j \text{ of } n_j > 0 \tag{30}$$

where y_i is an element of **y**

$$\mathbf{y} = \tilde{\mathbf{G}}^*(\tilde{\mathbf{G}}\mathbf{n} - \tilde{\mathbf{I}}) + \gamma \mathbf{H}\mathbf{n} \tag{31}$$

n is uniquely determined if $(\tilde{\mathbf{G}}^*\tilde{\mathbf{G}} + \gamma \mathbf{H})$ exists [10, 11].

In order to verify the Logarithmic Constrained Inversion Method, the bimodal distribution was inverted. $I(\theta)$ scattered by particles with a bimodal distribution was calculated. The bimodal distribution used had two normal distributions: (1) average diameter 2.0 μm, standard deviation 0.5 μm, (2) average diameter 10.0 μm, standard deviation 1.0 μm (dashed line in Fig. 11). The droplet size distribution inverted from the calculated $I(\theta)$ is shown in Fig. 11(*a*), where $[D_{min}, D_{max}] = [0, 20]$ (μm), $N = 20$, $\theta = 0.5, 1.0, 1.5, \ldots, 15$ deg. It is shown that the Logarithmic Constrained Inversion Method can determine the bimodal distribution. In Fig. 11(*b*), the distribution inverted by the distribution function approximation method is shown.

Horizontal Plain and Low-Finned Condenser Tubes—Effect of Fin Spacing and Drainage Strips on Heat Transfer and Condensate Retention

K. K. Yau
University of Cambridge, United Kingdom

J. R. Cooper

J. W. Rose

Department of Mechanical Engineering, Queen Mary College, University of London, United Kingdom

The paper reports a continuation of an experimental investigation of the effect of fin pitch on the heat transfer performance of horizontal, integral-fin tubes for condensation of steam at near-atmospheric pressure. The effects of "drainage strips" located along the lower edge of finned and plain tubes have been studied. These gave significant increases in the heat transfer coefficient for finned tubes but had only marginal effect for the plain tube. Condensate retention angles have also been measured for simulated condensation using water, ethylene glycol, and refrigerant-113 for finned tubes with and without drainage strips. In the latter case the data agreed satisfactorily with theory. Drainage strips were found to reduce the extent of holdup significantly.

Introduction

For condensation on horizontal finned tubes, enhancement of the vapor-side heat transfer coefficient may significantly exceed that to be expected simply on the basis of increase in the heat transfer surface area. This apparently arises from effects of surface tension. Surface tension also adversely affects the heat transfer coefficient owing to the phenomenon of "holdup" or condensate retention between fins on the lower part of the tube [1–6].

Analysis of the three-dimensional flow where surface tension plays an important role is very complex. Approaches to this problem have been made in recent years [7–15] but it is not surprising that established methods for predicting the vapor-side heat transfer coefficient are not yet available. In most cases the theoretical models involve simplifying assumptions for which there is, as yet, inadequate experimental backing.

Reliable data from systematic studies of the effects on heat transfer of the relevant variables (geometry and fluid properties) are vital to the development of a successful model. There is a paucity of such data and that which exists may, in some cases, be in question owing to errors arising from the presence in the vapor of noncondensing gases and the occurrence of dropwise condensation.

Apparatus

Heat Transfer Measurements. The apparatus has been described in detail in [16]. Steam flowed vertically downward in the test section where the horizontal test condenser tube was located. The steam temperature and pressure and the coolant flow rate and temperature rise were observed. Different steam velocities were obtained by varying the power input to the boiler. It is estimated that the overall heat transfer coefficient and the mean steam velocity in the test section were each determined with an accuracy better than 5 percent. Care was taken to avoid the occurrence of dropwise condensation and to ensure that the results were not vitiated by the presence in the steam of noncondensing gases.

Tests were made using 13 specially machined, integral-fin tubes and one plain tube. The internal diameter and working length of all tubes were 9.78 mm and 102 mm, respectively. The outside diameter of the plain tube and the diameter at the root of the fins was 12.7 mm. The fins were rectangular with height and width 1.59 mm and 0.5 mm, respectively, for all tubes. Results are reported here for fin spacings of 4 mm, 2 mm, 1.5 mm, 1 mm, and 0.5 mm. For the plain tubes and tubes with fin spacing 1.5 mm and 2.0 mm, tests were also made with "drainage strips" fitted to the lower edge of the tube, as indicated in Fig. 1.

Condensate Retention Measurements. The simple apparatus shown in Fig. 2 was used to simulate condensation on the finned tubes used in the heat transfer investigation. Liquid (water, ethylene glycol, and refrigerant-113) drained slowly and uniformly from a cloth onto a horizontally supported tube so that the whole of the tube was wetted. The position at

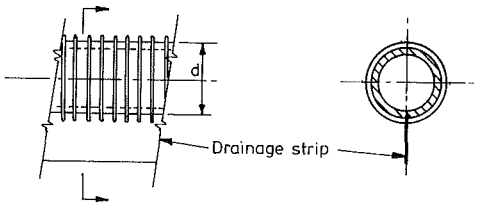

Fig. 1 Finned tube with drainage strip

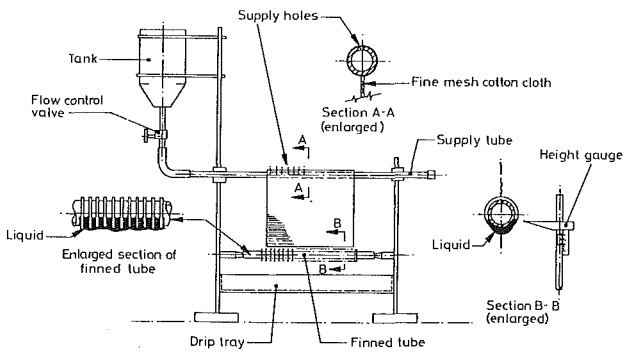

Fig. 2 Apparatus for liquid retention measurements

Contributed by the Heat Transfer Division for publication in the JOURNAL OF HEAT TRANSFER. Manuscript received by the Heat Transfer Division August 23, 1985.

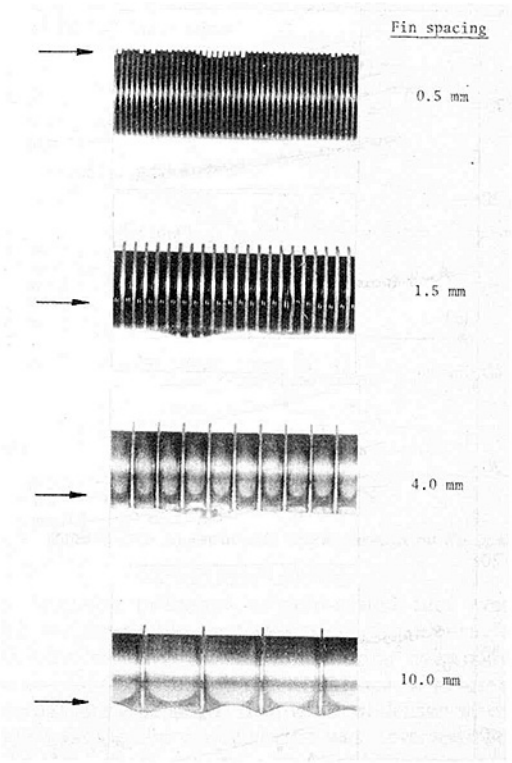

Fig. 3 Liquid retention on finned tube; fluid: ethylene glycol; arrow indicates holdup level

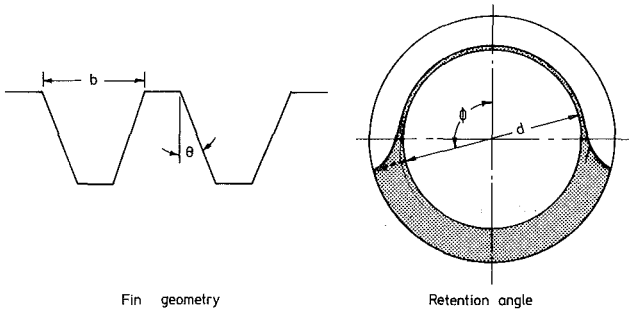

Fig. 4 Fin geometry and retention angle

which the liquid filled the interfin space ("holdup line") was measured with a height gage. The holdup position was apparently unchanged when the cloth was moved away. Measurements were generally made under this static condition when the holdup line was not disturbed by effects of drainage from the bottom of the tube. The liquid temperature was measured using a thermocouple closely wound on the tube surface away from the measuring position. This was important in the case of the refrigerant where evaporation led to temperatures significantly below ambient. The appearance of the tubes with ethylene glycol for various spacings is shown in Fig. 3.

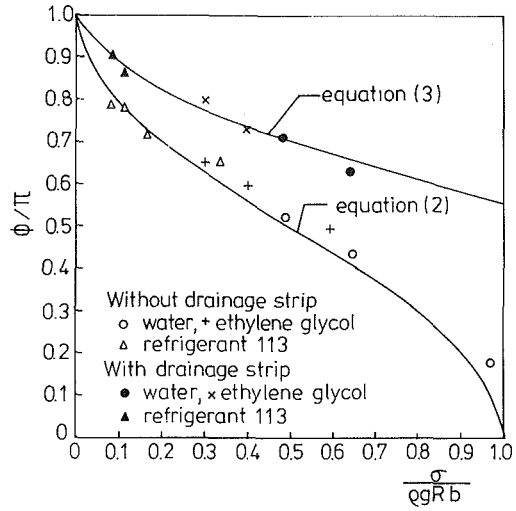

Fig. 5 Liquid retention results

Results – Liquid Retention Measurements

A detailed analysis of a static liquid film on finned surfaces has been given by Honda et al. [2]. The extent of the retained condensate in the interfin space is given by

$$\phi = \cos^{-1}\left(\frac{2\sigma\cos\theta}{\rho g b R} - 1\right) \tag{1}$$

where ϕ is the angle measured circumferentially from the upper edge of the tube to the position at which the interfin space becomes full of liquid (see Fig. 4). Equation (1) is valid provided the fin height is greater than or equal to $b(1-\sin\theta)/2\cos\theta$. For plane-sided fins $\theta = 0$ so that equation (1) becomes

$$\phi = \cos^{-1}\left(\frac{2\sigma}{\rho g b R} - 1\right) \tag{2}$$

which is valid when $b \leq 2h$.

Equation (2) has also been obtained independently by Owen et al. [5] and by Rudy and Webb [6].

In Fig. 5 the present data are compared with equation (2) for those tubes for which the fin spacing was less than twice the fin height (i.e., the tubes with pitch ≤ 2.5 mm) for which equation (2) should be valid. As may be seen the agreement is good for all three fluids.

Nomenclature

a = constant, see equations (5) and (6)
b = spacing between fins (at tip when $\theta \neq 0$)
d = outside diameter of plain tube; diameter at fin root
g = specific force of gravity
h = fin height
l = effective length of condenser tube
P = pressure
Q = heat flux $= Q_T/\pi dl$
Q_T = heat transfer rate to coolant
R = radius from tube center line to fin tip
U = overall heat transfer coefficient $= Q/\Delta T_{lm}$
T_0 = outside surface temperature of plain tube; temperature at base of fins
T_v = vapor temperature
u_v = mean vapor velocity
α = vapor-side heat transfer coefficient $= Q/\Delta T$
ΔT = vapor-side temperature difference $= T_v - T_0$
ΔT_{lm} = overall vapor-to-coolant logarithmic mean temperature difference
ϵ_Q = vapor-side coefficient for finned tube/vapor-side coefficient for plain tube for same Q and u_v
θ = half-angle at fin tip
ρ = liquid density
σ = surface tension
ϕ = retention angle, i.e., circumferential angle from upper edge of tube to position at which interfin space becomes full of liquid

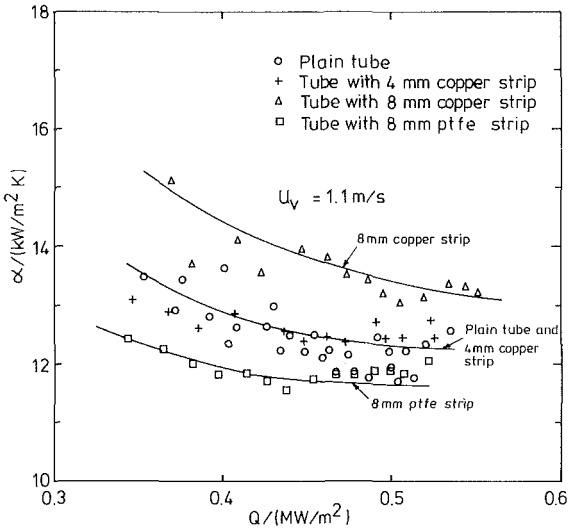

Fig. 6 Vapor-side heat transfer coefficients for plain tube and plain tubes with drainage strips

Liquid retention measurements were also made for the two tubes (fin pitches 2.0 mm and 2.5 mm) fitted with drainage strips. These data are also shown in Fig. 5. It may be seen that the holdup is significantly reduced (larger values of ϕ) by the drainage strips. This is apparently due to the pressure drop associated with the concave liquid surface resulting from the presence of the strip. The six data points appear to lie on a smooth curve and are represented quite well by the empirical equation

$$\phi = \cos^{-1}\left(\frac{0.83\sigma}{\rho g b R} - 1\right) \tag{3}$$

The form of equation (3) is based on the theoretical expression (equation (2)) for the case of finned tubes without drainage strips. The constant 0.83 was found by minimizing the sum of squares of the residuals (measured minus calculated values) of ϕ. In the absence of other information, equations (1) and (3) suggest a provisional equation for the case of fins with nonzero tip angle and a drainage strip

$$\phi = \cos^{-1}\left(\frac{0.83\sigma\cos\theta}{\rho g b R} - 1\right) \tag{4}$$

Results – Heat Transfer

The heat transfer rate was obtained from the mass flow rate and temperature rise of the cooling water, and the overall heat transfer coefficient U found using the logarithmic mean temperature difference between the steam and cooling water, and surface area as indicated below. Vapor-side heat transfer coefficients were obtained from the measured overall resistance by subtraction of wall and coolant-side resistances. The former was determined on the basis of uniform radial conduction and the latter from a pre-established correlation of data from an instrumented plain tube (see [16]). For the plain tube the outside surface area was used in the above calculations. For the finned tubes the area used was taken as that of a plain tube with outside diameter equal to the diameter at the root of the fins. The tube wall was regarded as extending to the root of the fins so that the effects of the fins and condensate are lumped together in the vapor-side coefficient.

Plain Tube. Following earlier reports [17, 18] that ptfe (polytetrafluorethylene or "teflon") strips along the lower edge of a condenser tube gave significant enhancement, tests were made with a ptfe strip (width 0.5 mm, height 8 mm) and copper strips (width 0.5 mm, height 4 mm and 8 mm) fitted in turn into a slot in the lower edge of the plain tube. In the case

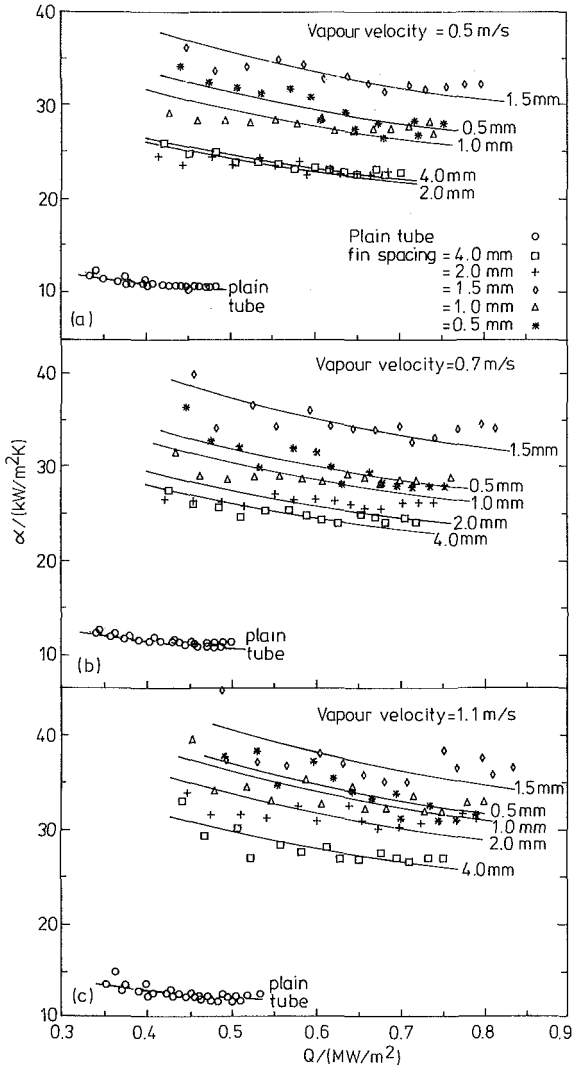

Fig. 7 Dependence of vapor-side coefficient on heat flux for finned tubes without drainage strips

of the copper strip it was felt that the pressure gradient arising from the curvature of the stabilized lower part of the condensate film could conceivably give rise to thinning of the film over a significant portion of the tube.

Vapor-side coefficients for a vapor velocity of 1.1 m/s are given in Fig. 6. It is seen that the 8-mm copper strip gave small enhancement, while the data for the 4-mm copper strip were virtually the same as for the plain tube. The results for the tube with the ptfe strip were lower than those for the plain tube. Similar results were found for vapor velocities of 0.5 m/s and 0.7 m/s.

These differences are marginal but could be explained by the changing curvature of the condensate film near the base of the tube. In the case of the larger copper strip, a stable concave surface gives rise to a surface-tension-induced pressure gradient tending to thin the film, while in the case of ptfe the nonzero contact angle (90 deg) would produce a convex surface and a thicker unstable film in the vicinity of the strip.

It may be noted that the geometries and, in particular, the heights of the "strips" used earlier (0.16 mm in [17] and 0.025 mm in [18]) were different from those used in the present work. This may warrant more detailed study.

For comparison purposes it was also planned to make measurements for dropwise condensation, since for steam, vapor-side coefficient enhancement ratios of up to about 20 may be obtained [19]. So as not to contaminate the apparatus

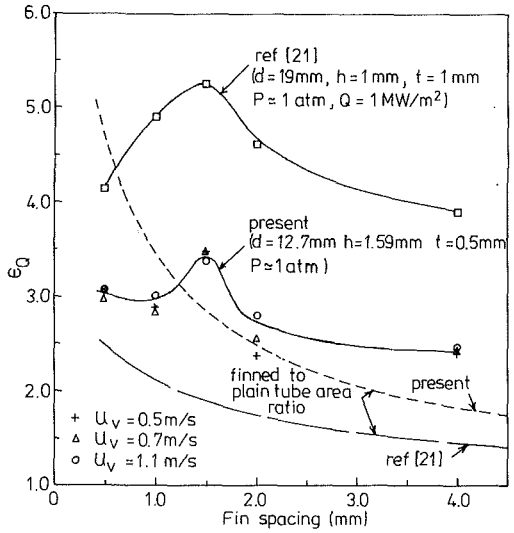

Fig. 8 Dependence of vapor-side enhancement on fin spacing

with a dropwise promoter, a gold-plated tube was used. Before being inserted in the test section, the tube surface was cleaned with hot ethyl alcohol and sodium hydroxide as indicated in [16]. Contrary to the experience of several earlier workers who have reported dropwise condensation of steam on gold surfaces, film condensation was observed. This confirms the recent finding of Woodruff and Westwater [20] that an uncontaminated gold surface does not promote dropwise condensation of steam. The heat transfer results for the gold-plated and unplated tubes were virtually identical.

Finned Tubes Without Drainage Strips. Graphs showing the dependence of vapor-side coefficient on heat flux are given in Fig. 7. The data were well fitted by equations of the form

$$Q = a\Delta T^{3/4} \tag{5}$$

or

$$\alpha = a^{4/3}Q^{-1/3} \tag{6}$$

The lines given by these curve fits are shown in Fig. 7. It may be noted that in earlier work [16] the authors also fitted data using an unfixed (disposable) index on ΔT in equation (5). The index was found to vary in the range of 0.7 to 0.8 for different tubes and different vapor velocities. The differences between the vapor-side coefficient so found, and those obtained here, where a fixed index of 0.75 was used, are insignificant.

Figure 8 shows the dependence of enhancement ratio $\epsilon_Q = (a_{\text{finned tube}}/a_{\text{plain tube}})^{4/3}$ on fin spacing. It may be seen that this is little affected by vapor velocity; i.e., in these tests, the vapor velocity affects the plain and finned tubes in approximately the same proportion. The maximum value of ϵ_Q occurs at a fin spacing of 1.5 mm. It falls to a lower value at $b = 1.0$ mm and shows evidence, for all three vapor velocities, of further increase at $b = 0.5$ mm, notwithstanding the fact that the interfin tube space was wholly flooded in this case. It seems reasonable to conclude therefore that, for the case of steam at least, significant heat transfer takes place through the flooded region when tubes are only partially flooded.

Also included in Fig. 8 are results of a recent investigation using a larger diameter tube and somewhat different fin geometry [21]. That the enhancement is larger for the larger diameter tube is expected on grounds that the extent of condensate retention is smaller (see equation (2)). It may be noted that maximum enhancement also occurs at a fin spacing of about 1.5 mm in [21] but these data do not show evidence of an upturn at smaller fin spacing.

Finned Tubes With Drainage Strips. For the tubes with fin spacing 1.5 mm and 2.0 mm, tests were also made with an 8-mm copper drainage strip fitted to the lower edge of the tube (see Fig. 1). The results obtained are shown in Fig. 9. As may be seen, the data are again satisfactorily represented by equations of the form $Q = a\Delta T^{0.75}$. It is seen that the presence of the strip leads to significant additional enhancement of the vapor-side coefficient, no doubt due to the reduction in holdup effected by the strip.

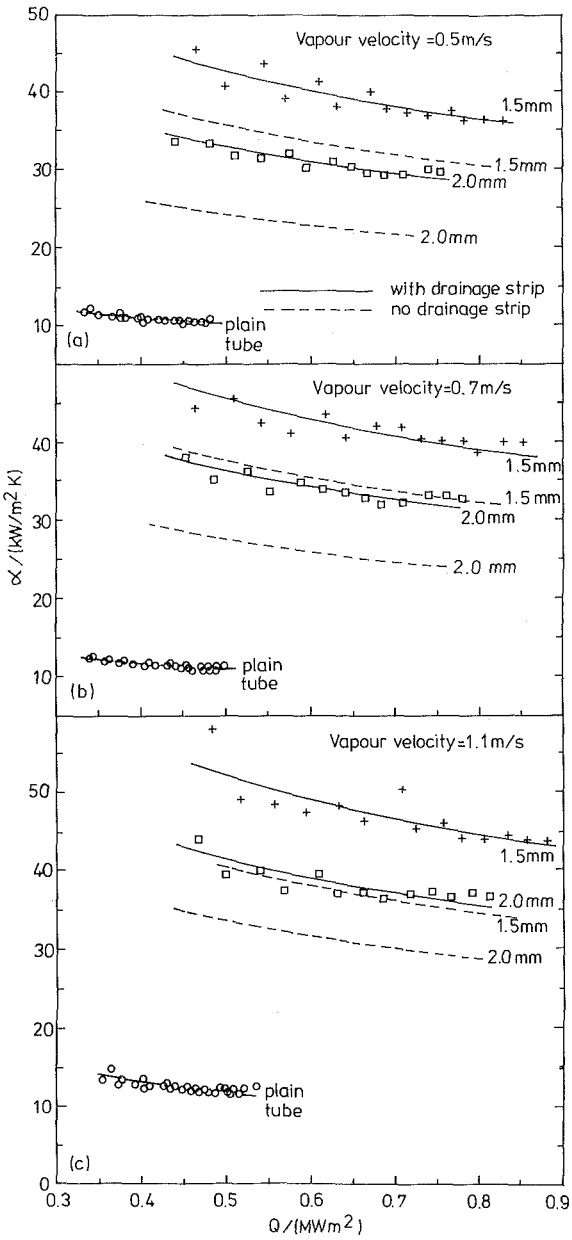

Fig. 9 Dependence of vapor-side coefficient on heat flux for finned tubes with drainage strips

Conclusions

For condensation of steam on the finned tubes, and with the present tube diameter, fin height, and width, the maximum enhancement (effective vapor-side coefficient higher than plain tube value, for the same heat flux, by a factor of 3 to 4) occurs for a fin spacing of 1.5 mm. For this tube the value of ϕ given by equation (2) is around 80 deg indicating that about 56 percent of the tube is "flooded" (i.e., the interfin space is filled with liquid around 56 percent of the perimeter). The enhancement is smaller for more densely finned tubes despite

the increase in heat transfer area. This is no doubt due to the increase in condensate retention with smaller fin spacing.

The present retention angle measurements showed that the interfin space was completely flooded for the tube with a fin spacing of 0.5 mm and almost so for the tube with a fin spacing of 1 mm. The fact that significant enhancement is found when the whole of the interfin space is filled with liquid is unexpected. This might be attributed to strong enhancement at the fin tip due to surface tension and curvature effects or perhaps to secondary flow effects in the ("flooded") interfin space.

The present liquid retention angle data are in good agreement with the theoretical results of Honda et al. [2] which have also been shown [2] to be in good agreement with other measurements [1, 2, 22].

For finned tubes, significant additional heat transfer enhancement is obtained by use of a drainage strip. Augmentation ratios (heat transfer coefficient with strip/heat transfer coefficient without strip) up to around 1.3 were found. This may be compared with values of 1.13 to 1.38 for refrigerant-113 and 1.38 to 2.08 for methanol reported in [2] when using a *porous* drainage strip of height 15 mm. The extent to which this enhancement may be affected by fluid properties and by porosity and dimensions of the drainage strip is yet to be determined.

Relatively tall drainage strips do not give significant enhancement for plain tubes.

Dropwise condensation does not occur on a clean gold surface.

References

1 Rudy, T., and Webb, R. L., "Condensate Retention on Horizontal Integral-Fin Tubing," *Advances in Heat Transfer*, ASME Symp. Vol. HTD-18, 1981, pp. 35–41.

2 Honda, H., Nozu, S., and Mitsumori, K., "Augmentation of Condensation on Horizontal Finned Tubes by Attaching a Porous Drainage Plate," *Proc. ASME-JSME Thermal Engineering Joint Conference*, Honolulu, HI, Vol. 3, 1983, pp. 289–296.

3 Rudy, T. M., and Webb, R. L., "An Analytical Model to Predict Condensate Retention on Horizontal Integral-Fin Tubes," *Proc. ASME-JSME Thermal Engineering Joint Conference*, Honolulu, HI, Vol. 1, 1983, pp. 373–378.

4 Rudy, T. M., and Webb, R. L., "Theoretical Model for Condensation on Horizontal Integral Fin Tubes," *AIChE Symp.* Serial No. 225, Vol. 79, 1983, pp. 11–18.

5 Owen, R. G., and Sardesai, R. G., Smith, R. A., and Lee, W. C., "Gravity Controlled Condensation on Horizontal Low-Fin Tube," *Condensers: Theory and Practice*, Inst. Chem. Engrs. Symp. Ser. No. 75, 1983, pp. 415–328.

6 Rudy, T. M., and Webb, R. L., "An Analytical Model to Predict Condensate Retention on Horizontal Integral-Fin Tubes," ASME JOURNAL OF HEAT TRANSFER, Vol. 107, 1985, pp. 361–368.

7 Hirasawa, S., Hijikata, K., Mori, Y., and Nakayama, W., "Effect of Surface Tension on Laminar Film Condensation (Study of Condensate Film in a Small Groove)," *Trans JSME*, Vol. 44, 1978, pp. 2041–2048.

8 Hirasawa, S., Hijikata, K., Mori, Y., and Nakayama, W., "Effect of Surface Tension on Laminar Film Condensation Along a Vertical Plate With Small Leading Radius," *Proc. 6th Int. Heat Transfer Conf.*, Vol. 2, 1978, pp. 413–418.

9 Fujii, T., and Honda, H., "Laminar Filmwise Condensation on a Vertical Single Fluted Plate," *Proc. 6th Int. Heat Transfer Conf.*, Vol. 2, 1978, pp. 419–424.

10 Mori, Y., Hijikata, K., Hirasawa, S., and Nakayama, W., "Optimised Performance of Condensers With Outside Condensing Surface," in: *Condensation Heat Transfer*, ASME, New York, 1979, pp. 55–62.

11 Panchel, C. B., and Bell, K. J., "Analysis of Nusselt-Type Condensation on a Vertical Fluted Surface," in: *Condensation Heat Transfer*, ASME New York, 1979, pp. 45–54.

12 Hirasawa, S., Hijikata, K., Mori, Y., and Nakayama, W., "Effect of Surface Tension on Condensate Motion in Laminar Film Condensation (Study of Liquid in a Small Trough," *Int. J. Heat Mass Transfer*, Vol. 23, 1980, pp. 1471–1478.

13 Adamek, T., "Besimmung der Kondensationgrossen auf feingewelten Oberflachen zur Auslegung optimaler Wandprofile," *Wärme- und Stoffübertragung*, Vol. 15, 1981, pp. 225–270.

14 Honda, H., and Nozu, S., "A Prediction Method for Heat Transfer During Film Condensation on Horizontal Integral-Fin Tubes," *Fundamentals of Phase Change: Boiling and Condensation*, HTD-Vol. 38, Proc. ASME Winter Annual Meeting, New Orleans, LA, 1984, pp. 107–114.

15 Webb, R. L., Rudy, T. M., and Kedzierski, M. A., "Prediction of the Condensation Coefficient on Horizontal Integral-Fin Tubes," ASME JOURNAL OF HEAT TRANSFER, Vol. 107, 1985, pp. 369–376.

16 Yau, K. K., Cooper, J. R., and Rose, J. W., "Effect of Fin Spacing on the Performance of Horizontal Integral-Fin Condenser Tubes," ASME JOURNAL OF HEAT TRANSFER, Vol. 107, 1985, pp. 377–383.

17 Glicksman, L. R., Mikic, B. B., and Snow, D. F., "Augmentation of Film Condensation on the Outside of Horizontal Tubes," *AIChE Journal*, 1973, pp. 636–637.

18 Desmond, R. M., and Karlekar, B. V., "Modified Condenser Tube Design to Enhance Heat Transfer in a Steam Condenser," Joint ASME/AIChE National Heat Transfer Conference, Orlando, FL, 1980, Paper No. 80-HT-53.

19 Le Fevre, E. J., and Rose, J. W., "An Experimental Study of Heat Transfer by Dropwise Condensation," *Int. J. Heat Mass Transfer*, Vol. 8, 1965, pp. 1117–1133.

20 Woodruff, D. W., and Westwater, J. W., "Steam Condensation on Various Gold Surfaces," ASME JOURNAL OF HEAT TRANSFER, Vol. 103, 1981, pp. 685–692.

21 Wanniarachchi, A. S., Marto, P. J., and Rose, J. W., "Film Condensation of Steam on Externally-Finned Horizontal Tubes," *Fundamentals of Phase Change: Boiling and Condensation*, HTD-Vol. 38, Proc. ASME Winter Annual Meeting, New Orleans, LA, 1984, pp. 133–141.

22 Katz, D. L., Hope, R. E., and Datsco, S. C., "Liquid Retention on Finned Tubes," Dept. of Eng. Res., Univ. Michigan, Project M592, 1946.

Structure of Bubbly Round Condensing Jets

T.-Y. Sun[1]

R. N. Parthasarathy

G. M. Faeth
Fellow ASME

Department of Aerospace Engineering,
The University of Michigan,
Ann Arbor, MI 48109-2140

A theoretical and experimental study of turbulent bubbly condensing jets is reported. Tests involved initially monodisperse carbon dioxide bubbles in water (~1 mm diameter bubbles with initial gas volume fractions of 2.4 and 4.8 percent) injected vertically upward in still water. Measurements were made of mean and fluctuating phase velocities, mean bubble diameters, mean bubble number intensities, and mean concentrations of dissolved carbon dioxide. Three theoretical methods were used to interpret the measurements: (1) locally homogeneous flow analysis, assuming infinitely fast interphase transport rates; (2) deterministic separated flow analysis, where finite interphase transport rates are considered but bubble/turbulence interactions are ignored; and (3) stochastic separated-flow analysis where both finite interphase transport rates and bubble/turbulence interactions are considered using random-walk methods. Both finite interphase transport rates and the turbulent dispersion of bubbles were important for present test conditions; therefore, only the stochastic separated flow analysis provided reasonable agreement with measurements.

Introduction

Turbulent bubbly condensing jets and plumes are encountered in a variety of applications, e.g., direct-contact heat exchangers, pressure-suppression devices, and gas mixing and dissolution systems. This investigation considers bubbly condensing jets, motivated by these applications. New measurements of the structure of bubbly condensing jets were completed, while analysis was undertaken to help interpret the measurements and to develop predictive methods. Experimental and theoretical uncertainties were minimized by studying dilute turbulent round bubbly condensing jets flowing upward in still liquids.

Chen and Faeth (1982) review early work on condensing jets. Most of these studies involve injection of pure vapors into subcooled liquids. This yields a complex flow with several flow regimes that eventually reaches a polydisperse bubbly flow regime when condensation nears completion. Measurements were generally limited to global parameters, e.g., the dimensions of the region containing vapor. Chen and Faeth (1982) developed a model of condensing jets based on the locally homogeneous flow (LHF) approximation, e.g., interphase transport rates are assumed to be infinitely fast so that both phases are in local kinematic and thermodynamic equilibrium. Flow structure and mixing were analyzed using a k–ϵ–g model of turbulence. The analysis was evaluated using existing data for jet Reynolds numbers greater than 15,000, where effects of buoyancy were small. Good predictions of vapor penetration lengths were obtained, using turbulence model constants established for single-phase flows.

Subsequent theoretical and experimental work by Sun and Faeth (1985) considered the structure of turbulent bubbly noncondensing jets. Dilute bubbly air/water mixtures (maximum initial gas volume fractions less than 10 percent) were injected vertically upward in still water while measuring mean and fluctuating phase velocities and bubble number intensity distributions. In addition to LHF analysis, two separated-flow analyses were considered: (1) deterministic separated-flow (DSF) analysis, where relative velocities were considered, but bubble/turbulence interactions were ignored; and (2) stochastic separated-flow (SSF) analysis, where both relative velocities and bubble/turbulence interactions were considered, using random-walk methods. LHF, DSF, and SSF analyses are typical of current treatments of dilute dispersed flows, but the particular formulations used were developed earlier in this laboratory for particle-laden jets and sprays (Shuen et al., 1983; Shuen et al., 1985a, 1985b; Solomon et al., 1985). Test conditions were limited to relatively low velocities, emphasizing effects of relative velocities between the phases and turbulent dispersion of bubbles; therefore, the LHF and DSF models did not yield very satisfactory predictions. In contrast, the SSF model, which provides for both effects, yielded encouraging agreement with measurements.

The present study extends the study of bubbly jets to conditions where the dispersed phase condenses, introducing effects of interphase mass transfer. Experimental and theoretical methods were generally similar to Sun and Faeth (1985), involving dilute bubbly flow with nearly monodisperse bubbles at the injector exit, while considering LHF, DSF, and SSF analysis of the process. The experiments involved injection of nearly monodisperse carbon dioxide bubbles and water vertically upward in a still and unsaturated (with respect to carbon dioxide) water bath. As the jet developed, the carbon dioxide bubbles dissolved in the water, providing an isothermal simulation of a condensing bubbly jet. Measurements were made of mean and fluctuating phase velocities and the following mean properties: concentration of dissolved carbon dioxide, bubble diameter, and bubble number intensity.

In the following, experimental and theoretical methods are described first of all. Results for single bubbles rising through a water bath, which were used to calibrate interphase transport analysis, are then discussed. The paper concludes with a description of the structure measurements for the bubbly condensing jets and their comparison with predictions. The discussion is brief; more details and a tabulation of data are provided by Parthasarathy (1985).

Experimental Methods

Test Arrangement. The test arrangement was modified only slightly from Sun and Faeth (1985). Low void fraction carbon dioxide/water mixtures were injected vertically upward in still water within a windowed tank (410 mm × 534 mm × 913 mm high). In order to reduce buildup of dissolved carbon dioxide in the bath, fresh liquid was supplied from a 2 m^3 auxiliary tank. The injector had a 5.08 mm exit diameter, and a 14.1:1 nozzle contraction, with carbon dioxide intro-

[1] Currently at Carnegie Mellon University, Pittsburgh, PA.

Contributed by the Heat Transfer Division and presented at the 23rd ASME/AIChE/ANS National Heat Transfer Conference, Denver, CO, August 1985. Manuscript received by the Heat Transfer Division September 13, 1985.

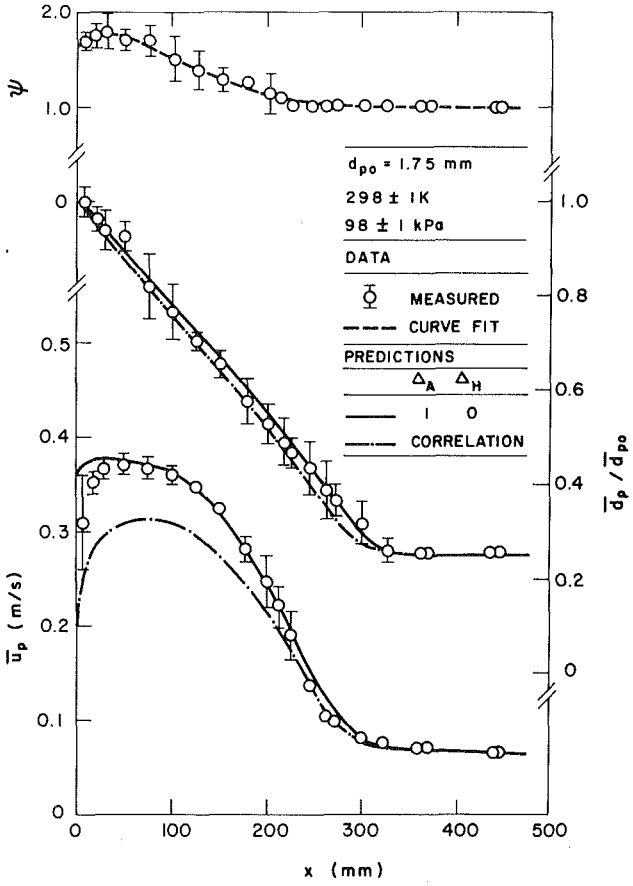

Fig. 1 Single-bubble trajectory calibration

duced at the start of contraction through five 22-gauge hypodermic needles, to yield a bubbly jet with initial bubble diameters ~1 mm. The injector could be traversed in three directions with horizontal and vertical positioning accuracies of 100 and 500 μm. Carbon dioxide (Linde, Instrument Grade, 99.99 percent purity) was supplied through a two-stage pressure regulator and filter and metered with a critical flow orifice. Injector water flow was drawn from the auxiliary tank and metered using a rotameter.

Table 1 Summary of test conditions[a]

Flow	Water jet	Bubbly jet (case I)	Bubbly jet (case II)
Water flow rate, ml/s	32.7	32.7	32.7
Carbon dioxide flow rate, ml/s	0	0.82	1.64
Gas volume flow rate fraction, percent	0	2.4	4.8
Jet momentum, nM	52.7	54.1	55.4
Jet velocity, m/s[b]	1.61	1.65	1.68
Jet Reynolds number[c]	8530	8740	8860
Jet Richardson number[d]	0	0.45×10^{-3}	0.89×10^{-3}
Bubble VMD, mm	–	0.90	1.05
Standard deviation of diameter, mm[e]	–	0.11	0.10

[a]Injector exit diameter 5.08 mm; fluid temperature 298 ± 2 K, fluid pH ~ 8.9, ambient pressure at injector exit 98 ± 3 kPa.
[b]$\tilde{u}_0 = \dot{M}_0/(m_{cd}+m_w)_0$
[c]$\mathrm{Re} = \tilde{u}_0 d/\nu_w$
[d]$\mathrm{Ri} = \Delta\rho_0 a d/(\rho\tilde{u}_0^2)$
[e]From VMD

Operation of the injector was monitored by measuring bubble sizes and injector thrust. The concentration of dissolved carbon dioxide in the bath was monitored using a pH meter (Fisher, model 640) which was calibrated using volumetrically prepared samples.

Test Conditions. Test conditions are summarized in Table 1. Three flows were considered, a pure water jet (as a baseline) and two bubbly jets having initial gas volume flow rate fractions of 2.4 and 4.8 percent. These conditions are identical to the pure water jet and the two lower initial void fraction air/water bubbly jets considered by Sun and Faeth (1985). The flows were reasonably turbulent, with initial Reynolds numbers of 8530-8860. Initial flow velocities, ~1.6 m/s, were relatively low in comparison to maximum bubble terminal velocities, ~0.1 m/s; therefore, effects of buoyancy on bubble motion were significant throughout the flow. Sampling showed that concentrations of dissolved carbon dioxide were small throughout the flow, i.e., interphase transport rates were not mixing controlled (Parthasarathy, 1985).

The standard deviation of initial bubble diameter, with respect to the VMD, was roughly 10 percent, and actual distributions showed that roughly 70 percent of the bubbles had diameters within 10 percent of the VMD; therefore, it was

Nomenclature

a = gravitational acceleration
C_D = bubble drag coefficient
c_i = concentration of species i
C_i = constants in turbulence model
d = injector diameter
d_p = bubble diameter
D_i = mass diffusivity of species i
f = mixture fraction
F_i = mass transfer correction factor
g = square of mixture fraction fluctuations
k = turbulence kinetic energy
K_i = mass diffusion coefficient of species i
$\dot{m}_{i0}$ = injector mass flow rate of species i
m_p = mass of bubble
M_A = acceleration modulus
$\dot{M}_0$ = injector thrust
r = radial distance
Re = injector Reynolds number, Table 1
Ri = injector Richardson number, Table 1
t = time
u = axial velocity
u_{ri} = relative velocity in ith direction
v = radial velocity
V_i = partial volume of species i
VMD = volume-mean diameter
x = axial distance
α = bubble number intensity
δ_{ij} = Kronecker delta function
Δ_A = correction for virtual mass force
Δ_H = correction for Basset-history force
ϵ = rate of dissipation of turbulence kinetic energy
ν = kinematic viscosity
ξ = variable of integration
ρ = density
ψ = bubble aspect ratio

Subscripts

a = air
c = centerline value
cd = carbon dioxide
p = bubble property
s = bubble surface property
sat = saturated state for pure gas
w = water property
0 = injector exit condition
∞ = ambient condition
$(\bar{\ })'$ = time-averaged fluctuating quantity
$(\bar{\ })$ = time-averaged mean quantity
$(\tilde{\ })$ = Favre-averaged mean quantity

assumed that the bubbles were monodisperse upon injection, to simplify analysis.

The bath liquid contained dissolved air and the carbon dioxide was not entirely free of noncondensible gases. Therefore, bubbles had an initial concentration of noncondensibles, and accumulated more during their motion through the bath. As a result, the bubbles never entirely disappeared, and final bubble diameters were on the order of 20 percent of the initial diameter.

Instrumentation

Liquid Velocities. Mean and fluctuating liquid-phase velocities were measured using a single-channel LDA in the dual-beam forward-scatter mode. One beam was frequency-shifted to eliminate errors due to directional bias and flow reversals. Various beam orientations were used to measure components of mean and fluctuating velocities and the Reynolds stress, following Durst and Whitelaw (1971). The measuring volume had a diameter and length of 260 and 250 μm, respectively, with a fringe spacing of 3.29 μm. Large-amplitude signals, due to bubbles, were rejected using the amplitude limiter on the burst-counter signal processor. This does not provide protection against grazing collisions of bubbles with the measuring volume, which can be misinterpreted as proper signals from seeding particles in the continuous phase. However, the approach was adequate for the present flows since bubble concentrations were dilute and bubble optical properties yielded a small grazing collision region. This was subsequently established using a phase-discriminating optical arrangement, similar to Modaress et al. (1983). Signal rates were on the order of 500-800 Hz, which was sufficient to resolve the smallest scales of the flow; therefore, the analog output of the burst counter was time-averaged using an integrating digital voltmeter. The same signal was processed with a true rms meter to yield velocity fluctuations. Experimental uncertainties were as follows: mean and fluctuating velocities, less than 5 percent; turbulence kinetic energy, less than 10 percent; Reynolds stress, less than 20 percent at its maximum, but proportionately higher elsewhere (all evaluated at 95 percent confidence).

Bubble Velocities. The LDA was modified to measure bubble velocities, similar to Sun and Faeth (1985). Beam spacing was reduced and the receiving optics were shifted 45 deg from the forward-scatter direction, yielding measuring volume dimensions having a diameter and length of 260 μm (each increased by the local bubble diameter since grazing collisions were recorded) and a fringe spacing of 19.6 μm. Frequency shifting and different beam orientations were used to obtain various velocity components, similar to the liquid velocity measurements. Signals from natural seeding in the water were eliminated by operating the detector at low gain, so that only large-amplitude signals from bubbles were recorded. This approach was effective everywhere, since the bubbles never entirely condensed due to the presence of noncondensibles. Even though bubble sizes were initially and finally nearly monodisperse, the size distribution was broader during the period of condensation, since all bubbles at a point did not follow the same trajectories. No attempt was made to quantify this by obtaining bubble size and velocity correlations; bubble averages were obtained directly from the burst-counter using a minicomputer. Predictions were averaged in the same way for comparison with measurements. Effects of gradient bias were less than 1 percent for mean velocities everywhere, and less than 1 percent for velocity fluctuations for $x/d \geq 24$. Gradient bias was largest at $x/d = 8$ for fluctuating velocities, where it reached levels of 5 percent for the case II bubbly jet. Uncertainties in $\bar{u}_p$, $\bar{u}_p'$, and $\bar{v}_p'$ from other sources were less than 5 percent; however, uncertainties in $\bar{v}_p$ were 50 percent due to its small magnitude (all 95 percent confidence).

Bubble Size. Flash photography was used to measure bubble size and number intensity distributions. The camera was operated in a darkened room with an open shutter, fixing the exposure time by the flash duration (less than 1 μs). The depth of field extended beyond the width of the flow and parallax errors were less than 7 percent; therefore, bubbles from the entire line-of-sight through the flow were recorded. Bubble VMD was averaged over the entire cross section of the flow, considering regions having streamwise lengths of 43, 46, and 72 mm, centered at $x/d = 24$, 40, and 60. Averages were obtained by counting 300-600 bubbles in each region. Effects of streamwise gradient broadening, accuracy of the size measurement, and discretization errors for finite sample sizes, yielded an uncertainty in VMD less than 10 percent.

Bubble Number Intensity. The spread of bubbles was represented by bubble number intensity, e.g., the number of bubbles per unit area of a line-of-sight observation through the flow, similar to Sun and Faeth (1985). This was found by further dividing the streamwise regions, used for VMD measurements, into seven radial regions. The number of bubbles in each region, per unit projected area, was then found. This measurement had a maximum gradient bias less than 12 percent and an uncertainty, due to effects of parallax and finite sample size, also less than 12 percent.

Theoretical Methods

Continuous Phase. The present analysis follows the approach developed by Shuen and coworkers (1983, 1985a, 1985b), Solomon et al. (1985), and Sun and Faeth (1985), aside from differences needed to treat specific aspects of the carbon dioxide condensation processes. The continuous phase is analyzed using an Eulerian calculation. This is sufficient for LHF analysis, but must be coupled to Lagrangian calculations of bubble motion and transport for separated-flow analysis. Present calculations considered interactions between the phases, resulting in source terms due to mass and momentum exchange, as well as buoyancy caused by the voidage of the bubbles, in the governing equations for the continuous phase.

The formulation for the continuous phase is identical to the approach used by Solomon et al. (1985) for evaporating sprays and this source should be consulted for details. Major assumptions of the continuous phase are: axisymmetric, steady (in the mean) flow with no swirl; boundary layer approximations apply; equal exchange coefficients of all species; buoyancy only affects the mean flow; and negligible effects of kinetic energy and viscous dissipation in the governing equations for mean quantities. The first of these is a condition of the experiments; the remainder are common assumptions for jets containing dispersed phases (Faeth, 1983). The continuous-phase analysis uses widely adopted procedures of k–ϵ–g turbulence models, which have provided good structure predictions for constant and variable density single-phase jets, particle-laden jets, and sprays, using fixed empirical constants (Shuen et al., 1983, 1985a, 1985b; Solomon et al., 1985; Sun and Faeth, 1985). The empirical constants were unchanged for present work. Favre-averaged (mass-weighted) governing equations were solved, following Bilger (1976), but for present flows differences between Favre and conventional (time) averages were negligible.

The conserved-scalar formalism was used to find scalar properties, although this was not an important part of present computations since scalar properties of the liquid within the jet were essentially identical to the ambient liquid, as noted earlier. Under present assumptions, all scalar properties are only functions of mixture fraction (the fraction of mass at a point which originated from the injector), called state relationships, and can be found once and for all by adiabatic mixing calculations. The solution is completed by solving conserva-

tion equations for mass, momentum, and mixture fraction, and modeled transport equations for k, ϵ, and g. Scalar properties are then computed from the probability density function of mixture fraction, in conjunction with the state relationships. A clipped-Gaussian probability density function was used, following past practice (Solomon et al., 1985); its two parameters were prescribed by the known local values of $\tilde{f}$ and g as described by Lockwood and Naguib (1975).

The LHF model treats the flow as a single-phase fluid with both phases in local kinematic and thermodynamic equilibrium. This involves solution of the continuous-phase equations using state relationships which account for the presence of two phases (Chen and Faeth, 1982). The present flows were very dilute; therefore, imposing equilibrium required that all the carbon dioxide should be condensed at the injector exit, leaving only the noncondensible remnant bubbles. This was clearly incorrect; however, LHF predictions will still be discussed since they provide a useful infinite transport rate bound to help interpret the measurements.

Dispersed Phase

Bubble Transport. Bubble transport is treated the same in both separated-flow models. The main difference is that the DSF model assumes that bubbles only interact with mean liquid properties, while the SSF model treats bubble/turbulence interactions so that the bubbles interact with instantaneous liquid properties. Both involve dividing the bubbles into n groups, defined by velocity and position at the initial condition, and then solving Lagrangian equations of motion and transport to find their subsequent trajectories and sizes.

Initial conditions for separated-flow analysis were specified at $x/d = 8$, which was the position nearest the injector where all needed measurements could be made with acceptable spatial resolution and accuracy. Downstream of this position, void fractions were less than 3 percent; therefore, bubble collisions were negligible, as were effects of adjacent bubbles on bubble transport properties. Bubble dimensions were less than 10 percent of the flow width; therefore, bubbles were assumed to have a locally uniform environment, based on liquid properties at their center. Similar to the earlier bubbly air jet analysis (Sun and Faeth, 1985), bubbles were assumed to be spherical and Magnus forces, Saffman-lift forces, and the inertia of the gas phase were neglected.

Under these assumptions, the motion of the dispersed phase was obtained using the formulation of Odar and Hamilton (1964) as reviewed by Clift et al. (1978)

$$((\Delta_A/2)(du_{ri}/dt)) = a(1-(\rho_p/\rho))\cdot\delta_{1i} - (3C_D/4d_p)\,|u_r|u_{ri}$$
$$+ \Delta_H(81\nu/\pi d_p^2)^{1/2}\int_{t_0}^{t}(t-\xi)^{-1/2}(du_{ri}/d\xi)d\xi \qquad (1)$$

where δ_{ji} is the Kronecker delta function and $i=1$ represents the vertically upward direction. The term on the LHS of equation (1) represents the acceleration force due to virtual mass, while the terms on the RHS represent buoyancy, drag, and Basset-history forces. The parameters Δ_A and Δ_H were empirically correlated by Odar and Hamilton (1964) as a function of an acceleration modulus M_A defined as follows

$$M_A = (du_r/dt)d_p/u_r^2 \qquad (2)$$

The values of Δ_A and Δ_H vary between 1.0–2.1 and 1.00–0.48, the former values being the correct limit for the Basset–Boussinesq–Oseen (B–B–O) formulation of equation (1). The drag coefficient was obtained from empirical expressions of Clift et al. (1978) and Moore (1965). The expression due to Moore (1965) allows for deformation of bubbles to an ellipsoid shape, which was encountered during calibration tests for single bubbles, but was not significant for the bubbly jet calculations.

In general, the bubble surface was deficient in dissolved air and the bath liquid contained low concentrations of dissolved carbon dioxide, causing a counterflow diffusion process with carbon dioxide transported to the bath and air transported to the bubbles. The process was slow and involved small energy exchange; therefore, the flow was assumed to be isothermal.

The diffusion processes of both carbon dioxide and air, at the low mass transfer rates of present conditions, are governed by (Johnson et al., 1969)

$$dV_i/dt = \pi d_p^2 K_i (c_\infty - c_s)_i \qquad (3)$$

where

$$K_i = 1.13F_i(D_i u_r/(0.0045+0.2d_p))^{1/2} \qquad (4)$$

These formulas are specific to the present bubble transport process and were used in spite of the clear limitations of a dimensional formula like equation (4). Normal values of mass diffusivities (D_a, $D_{cd} = 0.002$, 0.0018 mm^2/s from Himmelblau, 1964) are used in equation (4); the correction factors F_i are used to directly indicate departures from normal diffusivity rates required to match present calibrations. For water at 295 K, the saturated concentrations of air and carbon dioxide (volume basis) are

$$c_i = c_{i_{\text{sat}}} V_i/(V_a + V_{cd}) \qquad (5)$$

where $c_{a\text{sat}}$, $c_{cd_{\text{sat}}} = 0.0183$, 0.89 kg/m^3 from Stephen and Stephen (1979). The diameter of the bubble can be found in terms of the partial volumes, as follows

$$d_p = [6(V_a + V_{cd})/\pi]^{1/3} \qquad (6)$$

Methods used to compute bubble trajectory calculations follow past practice, e.g., Sun and Faeth (1985).

Deterministic Separated Flow Analysis. With this approach, drop transport and motion are computed using local mean properties, estimated from the continuous-phase analysis. Thus, bubble/turbulence interactions are ignored and bubbles follow deterministic paths, fixed by their initial location and velocity. Trajectories of 1200 bubbles were computed in order to obtain statistically significant results.

Stochastic Separated-Flow Analysis. This approach treats effects of turbulent fluctuations on interphase transport using a method proposed by Gosman and Ioannides (1981) and subsequently developed in this laboratory for turbulent dispersed flows (Shuen et al., 1983, 1985a, 1985b; Solomon et al., 1985; Sun and Faeth, 1985). This involves computing trajectories of a statistically significant number of bubbles (typically 2000) as they move away from the injector and encounter a succession of turbulent eddies.

Properties within each eddy are assumed to be uniform, but to change in a random fashion from eddy to eddy. Eddy properties are found by making random selections from the velocity and mixture fraction probability density functions. Isotropic turbulence is assumed, with a Gaussian PDF for each velocity component. A clipped-Gaussian PDF is used for mixture fraction, as noted earlier. All PDF's are fully defined by their mean values and variances, which are known from the k–ϵ–g analysis. A bubble is assumed to interact with an eddy as long as its relative displacement is less than a characteristic eddy size (the dissipation length scale) and its time of interaction is less than the characteristic eddy lifetime. These parameters can be found as well from the k–ϵ–g analysis of the continuous phase.

The influence of bubbles on turbulence properties, called turbulence modulation by Al Taweel and Landau (1977), can be considered using the SSF formulation (Sun and Faeth, 1985). However, since present flows were very dilute, effects of turbulence modulation were small in comparison to experimental uncertainties and uncertainties in model parameters needed for turbulence modulation computations

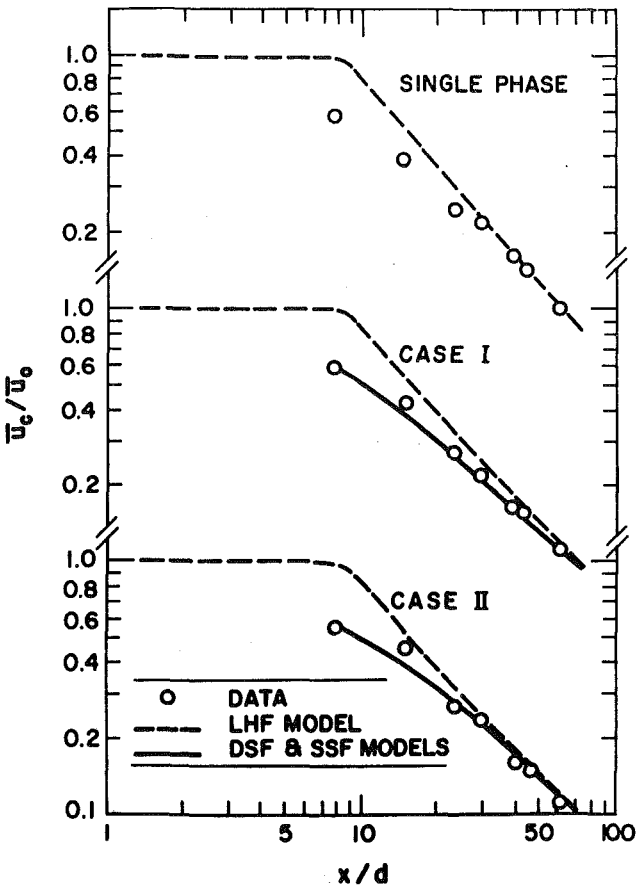

Fig. 2 Mean liquid-phase velocity along the axis

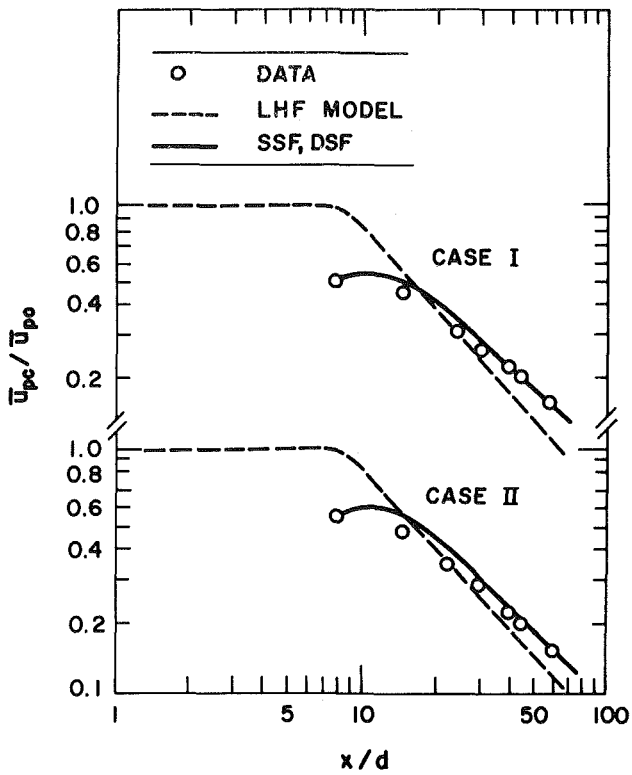

Fig. 3 Mean bubble-phase velocity along the axis

(Shuen et al., 1985a); therefore, turbulence modulation was ignored for present computations.

Bubble Trajectory Calibrations. Predictions of bubble trajectories were calibrated using data for single bubbles rising in the bath liquid. The bubbles were released in still water from a hypodermic needle. Release rates were slow, less than 0.2 Hz; therefore, wakes from preceding bubbles had negligible effect. The slow release, however, caused initial bubble diameters to be somewhat larger than the bubbly jet experiments, e.g., 1.75 mm as opposed to ~1 mm. Bubble size and velocity were measured, using multiflash photography, at various heights above the point of release.

Measurements of bubble aspect ratio, diameter and velocity are plotted as a function of height above the source in Fig. 1. The standard deviation about the mean of each measurement is shown by bars. Bubble aspect ratios are large near the injector, approaching 1.75, but are in the range 1.0–1.1 for bubble diameters less than 1.1 mm, which is the range of bubbly jet experiments. For aspect ratios near unity, the correlation of Moore (1965) yields essentially the same values as the standard drag law for solid spheres.

The final value of $d_p/d_{p0} = 0.25$ is due to the diffusion of air into the bubble. This occurs because once the air bubble is formed, by the initial presence of the carbon dioxide bubble, there is no subsequent tendency for it to dissolve, since the bath is saturated with dissolved air. After release, bubble velocities increase due to buoyancy. As the bubble size decreases due to condensation of carbon dioxide, reduced effects of buoyancy in comparison to drag cause the bubble velocity to decrease. Once all the carbon dioxide had condensed, bubble size is constant and the bubbles maintain a constant terminal velocity.

Two predictions are also shown on Fig. 1, one using the full correlation for Δ_A and Δ_H provided by Odar and Hamilton (1964), the other adopting $\Delta_A = 1$ and $\Delta_H = 0$, e.g., using the low-acceleration-rate limit for the virtual mass force and ignoring the Basset force. Best agreement between predictions and measurements is provided by the low acceleration rate limit while also ignoring the Basset force. For present transient conditions, this could be fortuitous due to circulation within the bubble, which was not considered in the drag correlation. Based on these findings, however, the bubbly jet calculations used $\Delta_A = 1$, $\Delta_H = 0$, and the standard drag law for spheres.

The correction values, $F_a = 1.37$ and $F_{cd} = 1.90$, were chosen to match predictions and measurements. Even though low levels of contaminants can influence diffusion appreciably the correction factors are reasonably close to unity. The value of F_{cd} is somewhat high; however, this is expected due to reaction of carbon dioxide when the bath liquid is basic (pH 8.9) (Weller, 1972).

Initial Conditions. Initial conditions for the separated flow models were prescribed at $x/d = 8$. Direct measurements provided $\bar{u}$, $\overline{u'v'}$, k, $\bar{f} = g \approx 0$, $\bar{u}_p$, $\bar{v}_p$, $\overline{u'_p}$, $\overline{v'_p}$, and the mean distribution of bubble number flux. The rate of dissipation of turbulence kinetic energy was estimated from the definition of turbulent viscosity in the turbulence model, e.g.,

$$\epsilon = C_\mu (\partial \bar{u}/\partial r) k^2/\overline{u'v'} \tag{7}$$

Structural Measurements and Predictions

Centerline Properties. Predicted and measured values of $\bar{u}$ along the axis of the single phase jet and the two bubbly jets are illustrated in Fig. 2. Predictions of all the models are shown; the DSF and SSF models yielded virtually identical results, however, and are represented by a single line.

Results for the single phase jet are nearly identical to earlier findings of Sun and Faeth (1985), indicating good reproducibility of both predictions and measurements. The measurements suggest a relatively short potential core, probably caused by high initial turbulence intensities due to flow

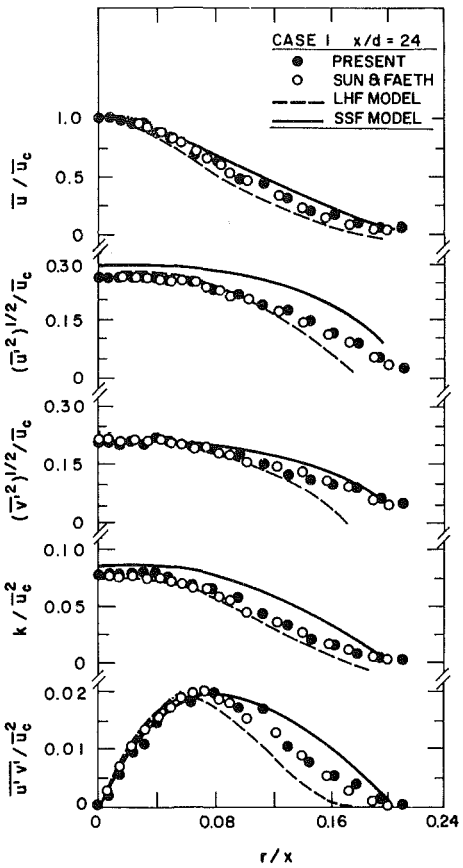

Fig. 4 Mean and turbulent liquid-phase properties for the case I jet at $x/d = 24$

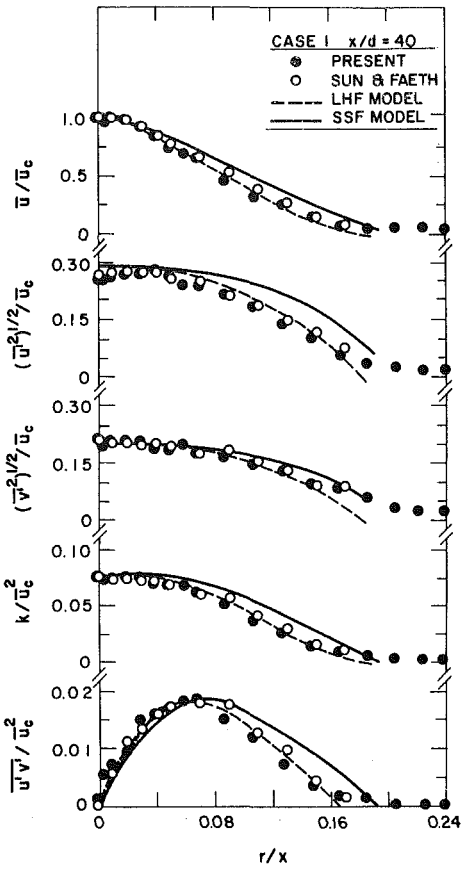

Fig. 5 Mean and turbulent liquid-phase properties for the case I jet at $x/d = 40$

disturbances from the gas injection system. The LHF predictions used standard initial conditions applied at the injector exit; therefore, the rapid development of the flow is not simulated very well, although predictions are in reasonably good agreement with measurements far from the injector.

The comparison between LHF predictions and the measurements is similar for the bubbly-jet results illustrated in Fig. 2. The DSF and SSF predictions, which use measured initial conditions, are in better agreement with measurements. However, the continuous-phase flow properties are not strongly influenced by the bubble phase; therefore, the LHF analysis would give comparable results if the same initial conditions were used. Far from the injector, all three predictions are essentially identical.

Predicted and measured mean bubble velocities along the axis are illustrated in Fig. 3. As before, the two separated-flow models give nearly the same results. Bubble velocities are lower than liquid velocities near the injector, but are higher than the liquid velocities far from the injector, due to effects of buoyancy. The separated flow models reproduce this behavior reasonably well.

Predicted and measured $\bar{d}_p/\bar{d}_{p0}$, which represent bubble diameters averaged over the flow cross section, are summarized as a function of distance above the injector in Table 2. SSF predictions are shown; however, DSF results are nearly the same. The comparison between predictions and measurements is encouraging, although there is a consistent tendency for predictions to underestimate bubble diameters. A partial explanation is provided by sensitivity studies which showed that bubble diameters were very sensitive to flow properties far from the injector – magnifying small errors (Parthasarathy, 1985). Approximating the flow as initially monodisperse may be a contributing factor, since the strong influence of bubble size on transport rates tends to bias the size distribution toward larger sizes as condensation proceeds.

Phase Velocities. Findings concerning phase velocities were similar for the two bubbly jets; therefore, only results for case I will be considered. Continuous-phase mean velocities and turbulence quantities are illustrated in Figs. 4 and 5 for $x/d = 24$ and 40. In addition to present findings for condensing jets, earlier results for noncondensing jets having the same initial conditions from Sun and Faeth (1985) are also shown. The results are plotted as a function of r/x, which is the similarity variable for fully developed turbulent jets and plumes. Predictions are shown for LHF and SSF analyses of the condensing jets; however, findings for the noncondensing jets were nearly the same. In addition, predictions of the SSF and DSF models were nearly identical for continuous-phase properties.

Predictions of velocity fluctuations were obtained by assuming $\bar{u}'^2 : \bar{v}'^2 = k : k/2$, which are the ratios usually observed in fully developed single-phase jets (Wygnanski and Fieldler, 1969). Results for condensing and noncondensing jets are nearly the same, which is expected since the flows were very dilute and are not strongly influenced by dispersed-phase properties.

Predictions of both theories agree with measurements (within experimental accuracy) when plotted in the manner of Figs. 4 and 5; however, the separated flow models provide better absolute agreement with measurements due to improved predictions of centerline velocities (Fig. 2). Levels of anisotropy of turbulent fluctuations correspond roughly to values for single-phase jets for the present dilute dispersed flows.

Predicted and measured bubble velocities for the case I bubbly jet are illustrated in Figs. 6 and 7 for $x/d = 24$ and 40. Predictions of the LHF and SSF models are illustrated, although LHF predictions essentially correspond to results for a single-phase liquid, as noted earlier. LHF predictions of fluctuating quantities are found using the same ratios

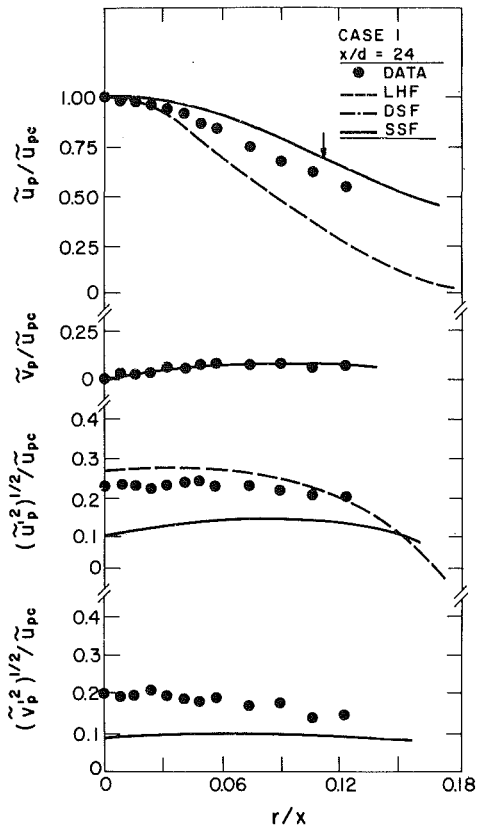

Fig. 6 Mean and turbulent bubble-phase properties for the case I jet at $x/d = 24$; arrow denotes outer edge of bubble-containing region for DSF analysis

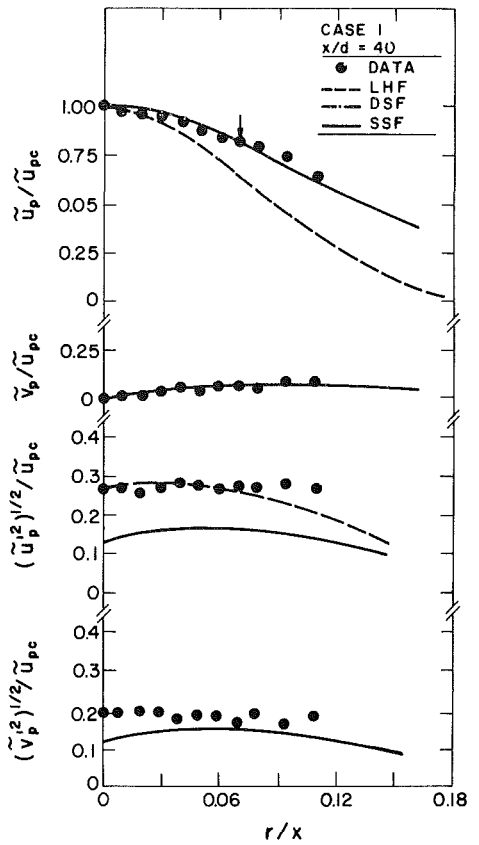

Fig. 7 Mean and turbulent bubble-phase properties for the case I jet at $x/d = 40$; arrow denotes outer edge of bubble-containing region for DSF analysis

employed earlier for continuous-phase velocities. SSF predictions were obtained directly from the calculations, averaged over all bubble sizes, similar to the measurements. DSF predictions of mean velocities were the same as SSF predictions, but this approach predicted a much narrower two-phase flow region (ending at the arrows) than observed. Naturally, the DSF model provides no predictions of fluctuating bubble velocities.

SSF predictions of mean velocities, in Figs. 6 and 7, are in reasonably good agreement with measurements. Due to the low liquid phase velocities for present test conditions, effects of slip are quite significant. This can be seen by comparing the measurements with the LHF predictions, since the latter roughly correspond to liquid-phase velocities (Figs. 4 and 5). The mean radial velocities of the bubbles increase monotonically with radial distance, unlike mean continuous-phase velocities which reach a maximum and then become negative near the edge of the jet due to entrainment of ambient fluid (Wygnanski and Fiedler, 1969). This is not seen for bubbles since no bubbles are entrained from the surroundings. SSF predictions of mean radial velocity are reasonably good.

LHF predictions of bubble velocity fluctuations in Figs. 6 and 7 are in fortuitously good agreement with measurements, i.e., in view of poor predictions of mean velocities used to normalize the data, the absolute agreement is not very satisfactory. The SSF predictions tend to underestimate velocity fluctuations, but correctly represent the trend that their levels are nearly constant over the bubble-containing region. Two major reasons can be advanced for the discrepancy in magnitudes. First of all, the assumption of a monodisperse size distribution at the initial condition is not exact; consideration of the actual initial size variation tends to increase apparent fluctuations, explaining about half the discrepancy. This occurs since slip velocities are strongly influenced by bubble size. A defect of the SSF analysis is probably also a factor. This involves the assumption that the turbulence is isotropic when randomly selecting eddy properties in SSF simulations, even though effects of anisotropy are clearly evident (Figs. 4 and 5). Including such effects would be a desirable improvement in the SSF approach.

Even though the SSF analysis assumes isotropic turbulence properties, computed particle velocity fluctuations in the streamwise direction are greater than those in the radial direction, similar to the measurements. This follows from the significant radial variation of streamwise mean bubble velocities in the present flow. As turbulent dispersion causes bubbles to move back and forth in the radial direction, they appear at a given position with different values of u_p (associated with velocities at their original location) causing higher observed values of $\tilde{u}_p'$ than $\tilde{v}_p'$.

Bubble Number Intensities. Predictions (LHF, DSF, and SSF models) and measurements of bubble number intensities are illustrated in Figs. 8 and 9 for the two bubbly jets. Near the injector, where slip velocities are relatively small in comparison to flow velocities, the LHF model only slightly overestimates the width of the bubble-containing region. Farther downstream, however, the LHF model overestimates bubble dispersion since effects of slip, which increase streamwise bubble velocities in comparison to radial fluctuations, are underestimated. The DSF approach, on the other hand, underestimates the radial spread of bubbles everywhere. This follows due to the relatively low inertia of bubbles, even when including their virtual mass, which makes them responsive to turbulent fluctuations and thus turbulent dispersion. Put another way, the DSF model only allows bubbles to move in the radial direction by virtue of drag induced by the mean radial continuous-phase velocity, which is small in comparison to the radial velocity fluctuations that are responsible for turbulent dispersion.

Table 2 Decay of d_p/d_{p0} along the axis[a]

x/d	24	40	60
Case I:			
Measured	0.83	0.66	0.46
Predicted	0.83	0.64	0.40
Case II:			
Measured	0.79	0.76	0.51
Predicted	0.83	0.64	0.39

[a]Based on VMD averaged over the flow cross section; $\bar{d}_p/\bar{d}_{p0} = 1$ at $x/d = 8$; predictions based on SSF analysis.

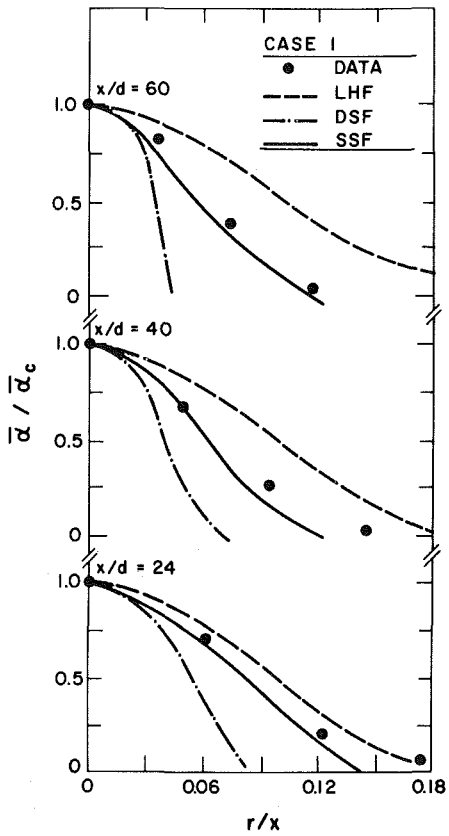

Fig. 8 Mean bubble number intensity distributions for the case I jet

In contrast to the other two methods, predictions of the SSF model, which allow for both slip and turbulent dispersion, are in reasonably good agreement with measurements in Figs. 8 and 9. This is a good test of model performance. Near the injector, slip is relatively unimportant, due to high liquid velocities, and the bubbles disperse much like the liquid. However, far from the injector, slip dominates the process and rates of bubble dispersion are reduced. This causes the bubble-containing region to progressively become narrower in terms of the r/x similarity variable, keeping in mind that the present bubbles never entirely disappear due to the presence of noncondensibles. The DSF and LHF models only provide potential bounds for this process, while the SSF model seems capable of treating the transition between the two limits, which tends to dominate the flow field for present test conditions.

Concluding Remarks

The present study considered dilute turbulent bubbly condensing (carbon dioxide) jets in still water. Maximum void fractions were less than 5 percent, centerline velocities were in the range 0.1–1.0 m/s, terminal bubble slip velocities were roughly 0.1 m/s, and the ratio of injector to initial bubble diameter was roughly 5:1. Present test conditions were similar

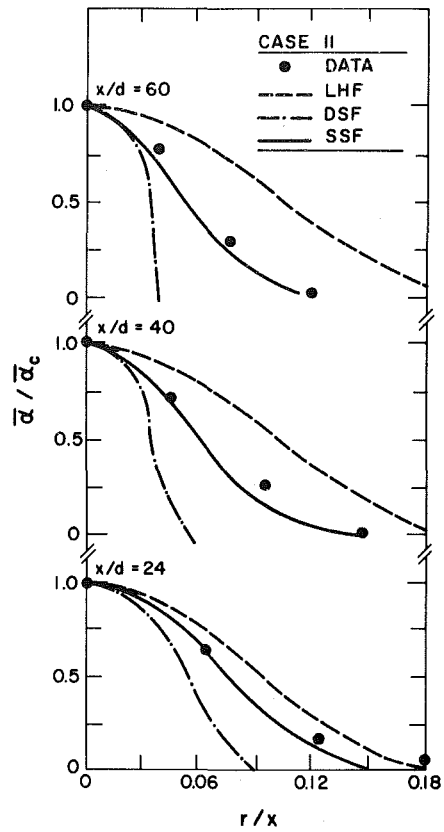

Fig. 9 Mean bubble number intensity distributions for the case II jet

to those used during a companion study of noncondensing bubbly jets (Sun and Faeth, 1985). A complete report of methods, theoretical and experimental results, and a tabulation of data is provided by Parthasarathy (1985).

Major conclusions of the study are as follows:

1 The LHF and DSF models did not provide satisfactory predictions for the present bubbly jets. The LHF model performed poorly due to omission of effects of finite interphase transport rates. The DSF model performed poorly due to omission of bubble/turbulence interactions – particularly turbulent dispersion of bubbles.

2 The SSF model yielded better predictions than the LHF and DSF models, similar to past experience with particle-laden jets (Shuen et al., 1983, 1985a), sprays (Shuen et al., 1985b; Solomon et al., 1985), and noncondensing bubbly jets (Sun and Faeth, 1985). It is encouraging that this performance was achieved for these disparate flows with all empirical aspects of the turbulence model unchanged, i.e., only essential changes to treat differences in interphase transport were made.

Acknowledgment

This research was performed while the authors were associated with the Department of Mechanical Engineering and The Applied Research Laboratory of the Pennsylvania State University. The research was supported by the Office of Naval Research, Contract No. N00014-80-C-0517, under the technical management of R. D. Ryan.

References

Al Taweel, A. M., and Landau, J., 1977, "Turbulence Modulation in Two-Phase Jets," *Int. J. Multiphase Flow*, Vol. 3, pp. 341–351.

Bilger, R. W., 1976, "The Structure of Diffusion Flames," *Comb. Sci. Tech.*, Vol. 13, pp. 155–170.

Chen, L.-D., and Faeth, G. M., 1982, "Condensation of Submerged Vapor Jets in Subcooled Liquids," ASME JOURNAL OF HEAT TRANSFER, Vol. 104, pp. 774–780.

Clift, R., Grace, J. R., and Weber, M. E., 1978, *Bubbles, Drops and Particles*, Academic Press, New York, pp. 112–133, 185–319.

Durst, F., and Whitelaw, J. H., 1971, "Measurements of Mean Velocity, Fluctuating Velocity, and Shear Stress in Air Using a Single Channel Optical Anemometer," *DISA Information*, No. 12, pp. 11–16.

Faeth, G. M., 1983, "Evaporation and Combustion in Sprays," *Prog. Energy Combust. Sci.*, Vol. 9, pp. 1–76.

Gosman, A. D., and Ioannides, E., 1981, "Aspects of Computer Simulation of Liquid-Fueled Combustors," AIAA Paper No. 81-0323.

Himmelblau, D. M., 1964, "Diffusion of Dissolved Gases in Liquids," *Chem. Rev.*, Vol. 64, pp. 527–550.

Johnson, A. J., Besik, F., and Hamielec, A. E., 1969, "Mass Transfer From a Single Rising Bubble," *Can. J. Chem. Eng.*, Vol. 47, pp. 559–564.

Lockwood, F. C., and Naguib, A. S., 1975, "The Prediction of the Fluctuations in the Properties of Free Round Jet, Turbulent Diffusion Flames," *Combustion and Flame*, Vol. 24, pp. 109–124.

Modarress, D., Tan, H., and Elghobashi, S., 1983, "Two-Component LDA Measurement in a Two-Phase Turbulent Jet," AIAA Paper No. 83-0052.

Moore, D. W., 1965, "The Velocity of Rise of Distorted Gas Bubbles in a Liquid of Small Viscosity," *J. Fluid Mech.*, Vol. 23, pp. 749–766.

Odar, F., and Hamilton, W. S., 1964, "Forces on a Sphere Accelerating in a Viscous Fluid," *J. Fluid Mech.*, Vol. 18, pp. 302–314.

Parthasarathy, R. N., 1985, "A Theoretical and Experimental Study of Turbulent Condensing Bubbly Jets," M.S. Thesis, The Pennsylvania State University, University Park, PA.

Shuen, J.-S., Chen, L.-D., and Faeth, G. M., 1983, "Evaluation of a Stochastic Model of Particle Dispersion in a Turbulent Round Jet," *AIChE J.*, Vol. 29, pp. 167–170.

Shuen, J.-S., Solomon, A.S.P., Zhang, Q.-F., and Faeth, G. M., 1985a, "Structure of Particle-Laden Jets: Measurements and Predictions," *AIAA J.*, Vol. 23, pp. 396–404.

Shuen, J.-S., Solomon, A.S.P., and Faeth, G. M., 1985b, "Drop-Turbulence Interactions in a Diffusion Flame," *AIAA J.*, Vol. 24, pp. 101–108.

Solomon, A.S.P., Shuen, J.-S., Zhang, Q.-F., and Faeth, G. M., 1985, "Measurements and Predictions of the Structure of Evaporating Sprays," ASME JOURNAL OF HEAT TRANSFER, Vol. 107, pp. 679–686.

Stephen, H., and Stephen, T., 1979, *Solubility of Inorganic and Organic Compounds*; Vol. 1, Binary Systems, Part 1, Pergamon Press, New York, pp. 88, 365.

Sun, T.-Y., and Faeth, G. M., 1985, "Structure of Turbulent Bubbly Jets – I. Methods and Centerline Properties; – II. Phase Property Profiles," *Int. J. Multiphase Flow*, Vol. 12, pp. 99–126.

Weller, K. K., 1972, "Mass Transfer from a Single Gas Bubble," *Can J. Chem. Eng.*, Vol. 50, pp. 49–58.

Wygnanski, I., and Fiedler, H. E., 1969, "Some Measurements in the Self-Preserving Jet," *J. Fluid Mech.*, Vol. 38, pp. 577–612.

Film Condensation of Steam on Horizontal Finned Tubes: Effect of Fin Spacing

A. S. Wanniarachchi
Assoc. Mem. ASME

P. J. Marto
Fellow ASME

Department of Mechanical Egineering,
Naval Postgraduate School,
Monterey, CA 93943

J. W. Rose
Department of Mechanical Engineering,
Queen Mary College,
University of London,
London, United Kingdom

The film condensation heat transfer performance of six externally finned copper tubes has been evaluated. All tubes had rectangular-shaped fins with a height and thickness of 1 mm. The spacing between fins was 0.5, 1.0, 1.5, 2.0, 4.0, and 9.0 mm. Data were also obtained for a smooth tube whose outside diameter of 19.0 mm was equal to the diameter at the base of the fins for all of the finned tubes. Tests were performed both at atmospheric pressure and under vacuum (~ 11.3 kPa). Steam flowed vertically downward with a velocity of approximately 1 and 2 m/s at atmospheric pressure and under vacuum, respectively. The smooth tube was fitted with wall thermocouples for the evaluation of the water-side heat transfer coefficient. This was used, subsequently, to determine the steam-side heat transfer coefficient for the finned tubes for which only overall measurements were made. Strenuous efforts were made to obtain high-accuracy data; in particular, the coolant temperature rise was determined by both quartz-crystal thermometers and a 10-junction thermopile. The two temperature-rise measurements always agreed to within ± 0.03 K. Care was taken to avoid errors due to the presence of noncondensing gases and to ensure that filmwise condensation conditions prevailed over the entire tube throughout all tests. The steam-side heat transfer coefficient for the smooth tube agreed closely with values found by other recent workers. Maximum steam-side enhancement was found for the tube with a fin spacing of 1.5 mm. At this fin spacing, the heat transfer enhancement ratios were around 3.6 and 5.2 for low-pressure and atmospheric pressure runs, respectively.

Introduction

Despite considerable experimental and theoretical effort in recent years, the prediction of the steam-side heat-transfer coefficient on horizontal finned tubes with a reasonable degree of accuracy is still questionable. The theoretical treatment of this problem is very difficult owing to the large number of controlling parameters such as the three-dimensional condensate-flow pattern, vapor shear, surface-tension forces, wall conduction effects, and condensate retention. At the same time, only, a few reliable data which systematically cover the relevant variables, such as fin geometry, have been reported [1].

Prior work by Staub [2] in 1961 demonstrated, at an absolute pressure of 38 mm Hg, an enhancement ratio (finned-tube steam-side coefficient to smooth-tube value) of 2.5 to 3 for a finned copper tube with 1.02 sinusoidally shaped fins/mm. Results with a coarse-pitch tube (0.67 fins/mm) for the same pressure conditions were only two times the smooth-tube results, indicating that fin spacing is an important variable. In 1963, Nabavian and Bromley [3] used a finned condenser tube with 0.3 fins/mm to make measurements of the condensation coefficient of water. They machined fins "to yield a constant and very high heat transfer coefficient along the top part of the fin." However, they did not specify the actual heat transfer enhancement obtained. In 1971, Karkhu and Borovkhov [4] obtained condensation data for steam on four horizontal tubes with different configurations of trapezoidally shaped fins. All their data were taken at a pressure of 1.1 atm, and they reported that for transverse fins with large Weber numbers (i.e., large surface-tension forces in relation to gravity forces), the average condensing heat transfer coefficient increased by 50 to 100 percent, whereas for low Weber numbers, there was little or no improvement. In 1982, Rifert [5] reported steam-condensation data on four tubes with rectangular-shaped fins, four tubes with trapezoid-shaped fins, and one tube with small wavy-type fins. He reported enhancements in the steam-side coefficient of up to twofold.

Very recently, Yau et al. [1] have shown that with an increase in fin density, up to a limit (this limit is not yet known accurately in a generalized manner), the heat transfer coefficient increases at a rate faster than the increase in the outside surface area due to the presence of fins. This additional enhancement is due to the thinning effect of the surface-tension forces on the condensate film. Unfortunately, surface-tension forces also adversely affect heat transfer by causing condensate to be retained between fins. Katz et al. [6] reported that on a finned tube, the portion of the surface occupied by condensate depends on the ratio of the condensate surface tension to density σ/ρ and the fin geometry. Their results were based on static (i.e., no condensation) liquid-retention measurements for different fin densities (0.28 to 0.98 mm^{-1}). They used acetone, aniline, carbon tetrachloride and water as test fluids with σ/ρ ranging from 15×10^{-6} to 70×10^{-6} $N \cdot m^2/kg$ and reported that in some cases as much as 100 percent of the surface was flooded by retained liquid. Rudy and Webb [7, 8] and Honda et al. [9] measured dynamic (i.e., with condensation) retention angles for fin densities of 0.75 to 2.0 mm^{-1}. They showed that the liquid retention increases with increase in σ/ρ and fin density. Rudy and Webb [8] developed a theoretical model that predicted their condensate retention angles within ± 10 percent. Honda et al. [9] and Owen et al. [10] have also made detailed theoretical studies of condensate retention and found essentially the same results.

In an attempt to predict the heat transfer results, Rudy and Webb [7] proposed a modification to the original Beatty and Katz correlation [11] by taking condensate retention into consideration. For this purpose, they simply assumed that the Beatty and Katz correlation was valid for the unflooded por-

Contributed by the Heat Transfer Division and presented at the ASME Winter Annual Meeting, New Orleans, LA, December 1984. Manuscript received by the Heat Transfer Division April 29, 1985.

tion with no heat transfer through the flooded portion. Owen et al. [10] extended the Rudy and Webb model by allowing heat transfer through the flooded portion of the tube. To account for heat transfer in this region, they assumed parallel, one-dimensional conduction paths through the fins and the condensate film. As also pointed out by Honda and Nozu [12], Owen et al. appear to have combined the unflooded and flooded portions incorrectly. The correct version of their model gives a slight improvement over the Rudy and Webb model. However, as shown by Honda and Nozu, the Owen et al. model (hence also the Rudy and Webb model) appears to be inadequate.

The heat transfer models discussed above assume gravity drainage of condensate and neglect any surface-tension-induced pressure gradients in the unflooded portion. Rudy and Webb [13] developed a heat transfer model which included surface-tension-induced pressure gradients in the unflooded portion, with, once again, no heat transfer in the flooded portion. This model resulted in from 10 percent underprediction to 60 percent overprediction of their data using R-11 as the working fluid ($\sigma/\rho = 10 \times 10^{-6}$ N•m^2/kg).

Honda and Nozu [12] present the most comprehensive analysis of the heat transfer problem, including a pressure-gradient term resulting from surface-tension forces in the momentum equation. They numerically solved their fourth-order differential equation for the film thickness subject to reasonable boundary conditions. However, owing to the complex analysis procedures involved, this model cannot be used readily as a design tool. The most recent model developed by Webb et al. [14] uses a fairly practical approach to the problem. They treat the heat transfer performance on the fins in the unflooded portion using the analysis performed by Adamek [15]. Unlike in their previous models, they allowed heat transfer through the flooded portion based on two-dimensional conduction in the fins and condensate film.

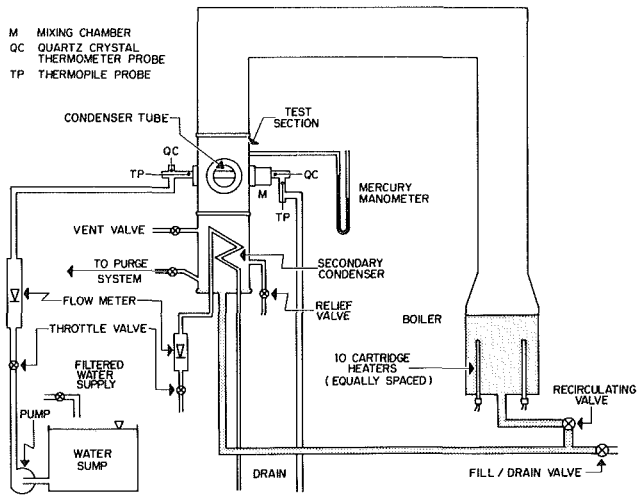

Fig. 1 Schematic of test apparatus

Reliable experimental data covering a reasonable range of relevant variables are of great importance not only in obtaining the optimum fin geometry for the fluid studied, but also in developing a satisfactory theoretical model. The authors are, therefore, engaged in a research program to obtain steam-condensation data on horizontal, finned tubes. The effects of fin spacing, fin thickness, fin height, and fin shape are being systematically examined. This paper presents data with fin spacing as the primary variable.

Nomenclature

A_f = outside area of finned tube
A_s = outside area of smooth tube
B = constant use with Sieder–Tate-type equation (1)
C = constant used with Sieder–Tate-type equation (1)
c_{pc} = constant-pressure specific heat of cooling water
D_f = diameter to outside of fins
D_i = inside diameter of condenser tube
D_o = outside diameter of smooth tube, equal to root diameter of finned tube
E_q = enhancement ratio, defined as the ratio of finned-tube steam-side coefficient to smooth-tube value at a specified heat flux and based upon the smooth tube surface area
$F = gD_o\mu_f h_{fg}/V_s^2 k_f \Delta T$
g = local gravitational acceleration = 9.8 m/s^2
h_{BK} = steam-side heat transfer coefficient predicted by Beatty and Katz correlation [11]
h_{fg} = specific enthalpy (latent heat) of vaporization
h_i = water-side heat transfer coefficient
h_o = steam-side heat transfer coefficient
h_O = steam-side heat transfer coefficient predicted by Owen et al. model [10]
h_{RW} = steam-side heat transfer coefficient predicted by Rudy and Webb model [7]
h_W = steam-side heat transfer coefficient predicted by Webb et al. model [14]
k_c = thermal conductivity of cooling water
k_f = thermal conductivity of condensate
Nu = water-side Nusselt number $= h_i D_i/k_c$
Nu_s = steam-side Nusselt number $= h_o D_o/k_f$
Pr = Prandtl number of cooling water $= \mu_c c_{pc}/k_c$
q = heat flux based on A_s
Re = coolant-side Reynolds number $= \rho_c V_c D_i/\mu_c$
$\tilde{\text{Re}}$ = steam-side, two-phase Reynolds number $= \rho_f V_s D_o/\mu_f$
s = fin spacing (i.e., distance between fins)
T_s = temperature of steam
$\bar{T}_{wo}$ = average outer wall temperature; temperature at root of fins
t = fin thickness
ΔT = local temperature drop across condensate film
$\overline{\Delta T}$ = average temperature drop across condensate film $= (T_s - \bar{T}_{wo})$
V_c = cooling water velocity
V_s = steam velocity
α = constant in Nusselt-type equation (5)
β = constant in Sieder–Tate-type equation (6)
θ = angle measured from top of tube
μ_c = viscosity of cooling water at bulk temperature
μ_f = viscosity of condensate at film temperature
μ_w = viscosity of cooling water at inner wall temperature
ρ_c = density of cooling water
ρ_f = density of condensate
σ = surface tension of condensate
ψ = condensate retention angle, i.e., angle measured from the bottom of the tube to the position at which the condensate just fills the interfin space

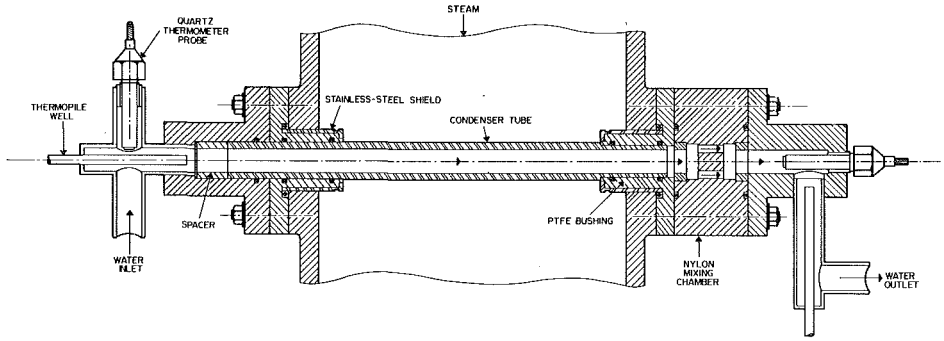

Fig. 2 Schematic details of test section (insert not shown)

Apparatus

Figure 1 shows a schematic of the test apparatus. The boiler and the steam piping were made of Pyrex glass, while the test section was made of stainless steel. The boiler was fitted with ten immersion heaters of 4 kW each. Steam was generated using distilled water. The steam flowed vertically upward through the glass piping and then downward over the test tube. Excess steam was condensed in an auxiliary condenser and all the condensate flowed by gravity to the boiler. Poole [16] provides a detailed description of the test apparatus.

Figure 2 shows a schematic of the test tube and the tube holders. The inner bushings of the tube holders were made of PTFE (polytetrafluoroethylene, or Teflon) and were shielded with stainless steel, while the outer sections were made of nylon. The exit side of the test tube was provided with a mixing chamber prior to temperature measurement. The Teflon and nylon sections provided adequate insulation, so that the coolant temperature rise would be affected negligibly by any unaccountable heat transfer.

Tests were carried out both at near atmospheric pressure and under vacuum conditions ($\sim$ 11.3 kPa or $\sim$ 85 mm Hg) for the following tubes:

(*a*) Two instrumented smooth tubes (12.7 mm i.d. and 19 mm o.d.).

(*b*) One uninstrumented smooth tube (12.7 mm i.d. and 19 mm o.d.).

(*c*) Six uninstrumented finned tubes (12.7 mm i.d., 19 mm root diameter) with both fin height and fin thickness of 1.0 mm each, but with fin spacings of 0.5, 1.0, 1.5, 2, 4, and 9 mm. All finned tubes had rectangular-shaped fins.

The condensing length of all the tubes was 0.133 m. No wall temperature measurements were made on finned tubes. The steam-side heat transfer coefficient was determined by subtracting the inside and wall resistances from the measured overall resistance. Therefore, it was first necessary to find a correlation to represent the water-side heat transfer coefficient. For this purpose, two smooth tubes were manufactured with six equispaced wall thermocouples. These instrumented tubes had an internal geometry indentical to that of the finned tubes.

The first tube was manufactured by machining six axial channels (1.0 mm wide $\times$ 1.5 mm deep) in the tube wall, equispaced 60 deg apart, and then soldering copper strips over the channels, leaving a sufficient cavity for thermocouple insertion. To obtain a clear, axial cavity, a 1.0-mm-dia aluminum wire was inserted into the cavity before soldering the strips. After the soldering process, the aluminum wire was easily pulled out from each channel and the tube wall surface was machined off to give a smooth finish. Figure 3(*a*) shows a schematic of this tube.

The second tube was made in three short lengths which were soldered together. Prior to joining these three pieces, six

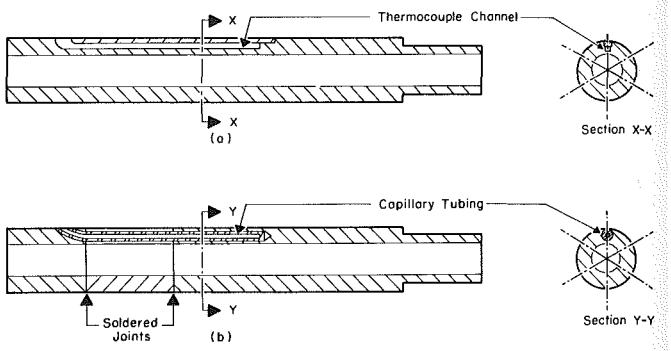

Fig. 3 Schematics of instrumented tubes: (*a*) tube with machined channels; (*b*) tube with drilled holes

2.4-mm-dia thermocouple holes were drilled axially in each section; these holes were aligned during soldering to form longer axial holes using 2.4 mm o.d. $\times$ 1.0 mm i.d., copper capillary tubing running the entire length of the holes as shown in Fig. 3(*b*). Thermocouples were later inserted into this capillary tubing.

In order to obtain more accurate steam-side coefficients and higher heat fluxes, a spiral tube insert was used on the water side with both the smooth and finned tubes. The insert was made by wrapping a 6.4-mm-dia, stainless-steel rod with a 3.2-mm-dia, copper wire at a pitch of 20 mm. After wrapping, the wire was soldered onto the rod and then the wire was machined down to give a clearance of 0.5 mm between the outer wire diameter and the tube inside wall, except for a 25-mm-long section on either end. (This clearance was considered important to avoid heat conduction, while the two ends were snug inside the tube for proper centering).

Instrumentation. Since the coolant temperature rise (which was from 0.5 to 9 K) was the most important measurement in this experiment, two independent means to measure it were used: two quartz-crystal thermometers and a ten-junction, series-connected, copper-constantan thermopile. Proper insulation and adequate immersion depths were provided for all probes. The quartz thermometers had a resolution of 0.0001 K, but calibration measurements against a platinum-resistance thermometer yielded an accuracy to within $\pm$ 0.02 K (i.e., on absolute thermodynamic temperature). The thermopile and its voltmeter had a resolution of 0.003 K. During the experiment, the coolant temperature rise measured by the quartz thermometers and the thermopile agreed to within $\pm$ 0.03 K.

Two thermocouples were located about 30 mm above the test tube to measure the steam temperature. A pressure tap was also provided about 50 mm above the test tube, and this line was connected to a mercury-in-glass manometer to measure the absolute pressure in the test condenser. The measured steam temperature, the saturation temperature cor-

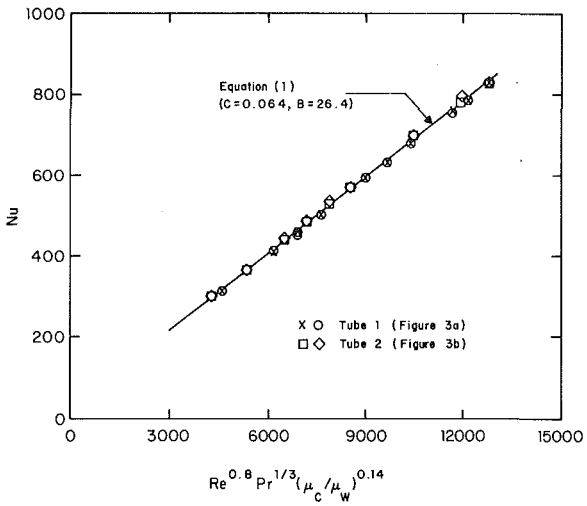

Fig. 4 Correlation of the water-side coefficient obtained from instrumented smooth tube

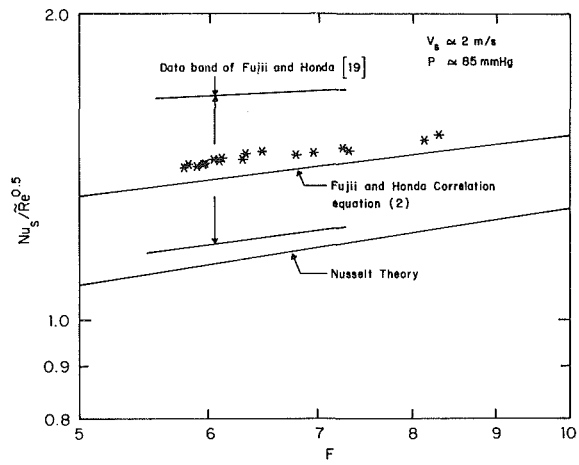

Fig. 5 Comparison of smooth-tube data with Fujii and Honda [19] correlation

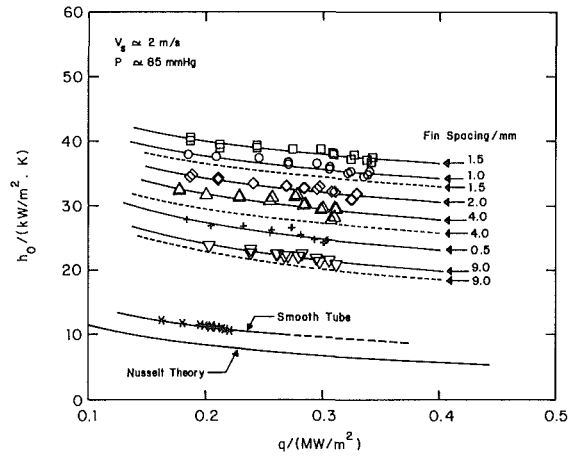

Fig. 6 Variation of steam-side heat transfer coefficient with heat flux (vacuum runs)

responding to the measured pressure, and the Gibbs–Dalton ideal-gas-mixture relations were used to compute the noncondensing gas (assumed to be air) concentration of the steam. The computed air concentration was found to be within ± 0.5 mass percent (i.e., zero to within the accuracy of the measurements).

The vapor mass flow rate and hence velocity were computed by applying an energy balance between the boiler inlet and test section. This included the estimated energy loss from the apparatus. Using a procedure similar to that of Lee at al. [17], the energy loss from the apparatus (i.e., the minimum boiler power necessary to maintain the vapor temperature) was found. This loss was found to be about 2 percent of the energy supplied to the boiler.

The cooling water flow rate was measured using a carefully calibrated rotameter, which showed an accuracy within ± 1 percent. The voltage (440 VAC max) supplied to the boiler heaters was measured precisely, using a true, root-mean-square converter. The power input was computed from the known electrical resistance.

Operational Problems. An apparatus free of noncondensing gases is imperative for taking meaningful and consistent condensation data. To achieve this end, as discussed in [18], considerable time, effort, and persistence were needed in obtaining a negligible leak rate corresponding to a pressure rise of less than 2 mm Hg in 24 hr at the minimum operating pressure (~ 85 mm Hg). In addition, continuous purging was provided using a vacuum pump–cold trap arrangement to avoid any buildup of noncondensing gases within the apparatus.

As discussed in detail in [18], extremely careful attention was needed to achieve complete filmwise condensation conditions on clean copper tubes. Systematic tests carried out with considerable attention toward ensuring a clean apparatus revealed that the procedure was inadequate in achieving complete filmwise conditions. Eventually, it was necessary to lightly oxidize the copper tubes by heating them on a steam pot while frequently applying a mixture of sodium hydroxide and ethyl alcohol (equal parts by volume). Within about an hour, the tube surface turned a dark color, resulting in very high wetting characteristics and insignificant thermal resistance. Steam-side coefficients obtained with and without oxidation agreed to within 2 percent.

Results

Water-Side Coefficient. Using the spiral insert and the two instrumented tubes described above, two sets of data runs were made for each tube under vacuum (~ 85 mm Hg), in order to measure the water-side coefficient. Two more sets of data runs were made for the first tube under atmospheric pressure. Data were correlated using a Sieder–Tate-type equation

$$\mathrm{Nu} = C\,\mathrm{Re}^{0.8}\,\mathrm{Pr}^{1/3}\,(\mu_c/\mu_w)^{0.14} + B \qquad (1)$$

The constants C and B were obtained by least-square fitting, i.e., by minimizing the sum of the squares of residuals (calculated minus measured values) of Nu.

The use of the constant B gave an improved fit of the data over the limited range of conditions (velocity, temperature, only one fluid) used in this work. The values of C and B for the above-mentioned four runs were determined to be $C = 0.064 \pm 0.001$ and $B = 26.4 \pm 5.6$, and were used subsequently to compute steam-side coefficients. Figure 4 compares the data with equation (1) using these mean values of C and B.

In calculating the inside heat flux, allowance was made for the fact that the effective inside heated length exceeded the tube length on which condensation occurred (see Fig. 2); i.e., there is an "end-fin effect." It should be noted, however, that this effect is not critical for the calculation of the steam-side coefficients for the subsequently tested tubes, since the material, wall thickness, and end lengths in the PTFE bushings were the same as for the instrumented tube.

Steam-Side Coefficient on Smooth Tube. To check the data-reduction procedures and the accuracy of the measurements, data were taken on the uninstrumented smooth tube and processed to determine the steam-side coeffi-

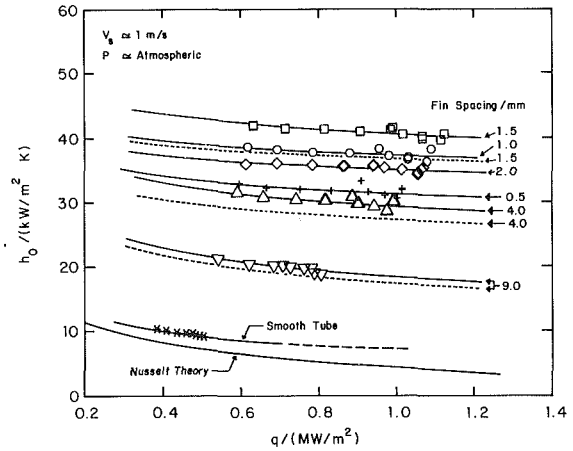

Fig. 7 Variation of heat flux with steam-side temperature drop (atmospheric runs)

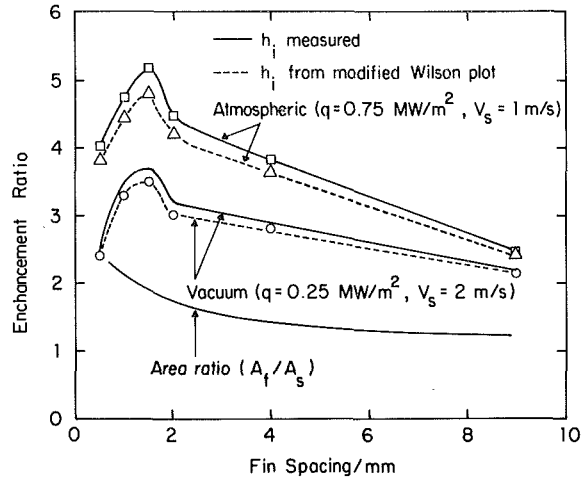

Fig. 8 Cross plots of Fig. 6 and 7 showing best fin spacing

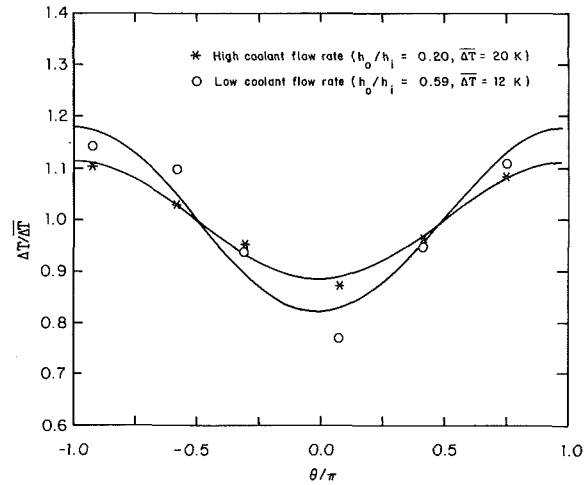

Fig. 9 Typical temperature distributions for instrumented tube (the lines are cosine fits)

cient using equation (1) for the inside coefficient. The steam-side data are compared in Fig. 5 with the correlation of Fujii and Honda [19]

$$\mathrm{Nu}_s/\tilde{\mathrm{R}}\mathrm{e}^{1/2} = 0.96\,\mathrm{F}^{1/5} \tag{2}$$

The present data are evidently in satisfactory agreement with those of Fujii and Honda. More recently, similar data (i.e., good agreement with equation (2) but less scatter than in [19]) have been obtained for condensation of steam on a horizontal plain tube [20].

Steam-Side Coefficient on Finned Tubes. Data were taken for the finned tubes both under vacuum (~ 85 mm Hg) and at atmospheric pressure with vapor velocities of 2 m/s and 1 m/s, respectively. The computed steam-side coefficient was based on the smooth-tube outside area (i.e., the area if the fins were machined off). Figure 6 shows the variation of the steam-side heat transfer coefficient h_o with heat flux (q) for the vacuum runs. The solid lines shown in this figure are least-square fits using a relation of the form (the broken lines are discussed below)

$$q = a(T_s - \tilde{T}_{wo})^b \tag{3}$$

While Nusselt theory results in an exponent $b = 0.75$, the exponents obtained for the finned tubes varied between 0.78 and 0.86 with no systematic variation with fin spacing. The coefficient a is dependent on the condensate properties and the fin geometry. The best fin spacing appears to be 1.5 mm. Figure 7 shows similar results at atmospheric pressure with a vapor velocity of 1 m/s.

Figure 8 shows cross plots of Figs. 6 and 7 to reveal the dependence of the steam-side coefficient on the fin spacing. The best tube gave an enhancement ratio E_q of around 5.2 at atmospheric pressure and around 3.6 at the lower pressure. Note that the area increase for these tubes (over the smooth tube value) due to fins is only around twofold. It is possible that the smaller enhancement found at lower pressure is associated primarily with an increase in condensate viscosity, although the change in surface tension may also play a part. (Note that μ_f (vacuum)/μ_f(atmospheric) ≈ 1.9, while σ (vacuum)/σ(atmospheric) ≈ 1.1.)

It is worth mentioning that a series of finned tubes (with a fin height of 1.6 mm, a fin thickness of 0.5 mm and a root diameter of 12.7 mm) tested by Yau et al. [21] at atmospheric conditions resulted in a best fin spacing of 1.5 mm for steam condensation. For this tube, they found an enhancement ratio of 3.5, which is considerably smaller than the value of 5.2 found in the present study. The fact that the enhancement found by Yau et al. is lower than the present value is most probably due to the difference in tube diameters, though the difference in fin thickness in the two cases may also play a part.

Honda et al. [9] recommended that, for rectangular-shaped fins, the condensate retention angle ψ be computed from the relationship

$$\psi = \cos^{-1}\left[1 - \frac{4\sigma}{\rho g s D_f}\right] \tag{4}$$

Equation (4) indicates that for the same fin spacing, a larger proportion of the surface is flooded for a smaller diameter tube. Thus, for a fin spacing of 1.5 mm and an outside fin diameter D_f equal to 21 mm, as in the present work, the retention angle is about 76 deg while for D_f equal to 14.7 mm, as in Yau et al. [1, 21], ψ is around 95 deg.

Accuracy of Steam-Side Coefficients. With the experimental techniques used in this work, the overall heat transfer coefficient was measured with an accuracy better than about 2 percent for finned tubes. It is not possible, unambiguously, to assign error estimates to the steam-side coefficient since these were obtained by subtracting water-side and wall resistances from the measured overall resistance—a procedure which is strictly valid only for uniform radial conduction. If the variation in wall temperature is provisionally ignored and an error estimate, typical of that of the local wall temperature measurement, is assigned to the mean water-side temperature difference, the estimated error in the steam-side coefficient would be around 4 percent at the highest coolant flow rate and around 20 percent at the lowest coolant flow rate.

Table 1 Comparison of heat transfer data with predictive models

Fin spacing, mm	ψ^*, deg	h_o/h_{BK}	h_o/h_{RW}	h_o/h_O	h_o/h_W
		Vacuum runs, $q = 0.25\ MW/m^2$			
0.5	180	0.323	∞	2.264	2.264
1.0	110	0.619	1.602	1.247	0.978
1.5	84	0.808	1.520	1.281	0.962
2.0	71	0.797	1.318	1.139	0.852
4.0	49	1.093	1.497	1.335	1.029
9.0	32	1.275	1.550	1.415	1.033
		Atmospheric runs, $q = 0.75\ MW/m^2$			
0.5	180	0.475	∞	3.316	3.316
1.0	103	0.741	1.744	1.402	1.103
1.5	79	0.993	1.786	1.526	1.161
2.0	67	1.014	1.627	1.419	1.076
4.0	46	1.312	1.772	1.585	1.214
9.0	31	1.368	1.653	1.509	1.073

*Predicted by equation (4)

In the above context, it is of interest to note the effects of enhancing the water-side coefficient:

1 In the absence of inside enhancement, the inside resistance is substantially greater than that on the condensing side. Thus, an error in the inside resistance results in a significantly larger error on the outside when the latter is obtained by subtracting the former (together with the wall resistance) from the measured overall resistance.

2 Internal enhancement reduces the circumferential wall temperature variation (see Fig. 9).

3 Internal enhancemnet increases the heat transfer rate for a given coolant velocity and thereby reduces the relative error in q.

4 The spiral insert greatly reduces thermal entrance effects and corresponding uncertainties for the calculation of the steam-side coefficient (note that the tube wall temperatures are measured midway along the tube).

5 Internal enhancement decreases "end-fin effects."

Data Processing by "Modified Wilson Plot" Technique. The calculation of steam-side coefficients by subtracting resistances is strictly only valid for uniform radial conduction, i.e., when the isothermal surfaces are concentric cylinders. This is not so in the case of condensation since the steam-side coefficient varies around the tube owing to the dependence of the condensate film thickness on angle (graphs showing typical variation of local steam-side temperature difference with angle are given in Fig. 9). Further, the distortion of the isotherms in the tube wall and the thermal resistance caused by the presence of the wall thermocouples introduces additional uncertainty in the water-side coefficients found using the instrumented tube. It was therefore considered that a simpler method, not requiring tube wall temperature measurements, might give equally good results. This technique, if successful, would greatly facilitate future work with tubes (e.g., commercial tubes) having inside diameters different from the standard values used to date; i.e., it would not be necessary to manufacture further instrumented tubes—a difficult, expensive, and time-consuming task.

In outline, the method, which is a modified Wilson plot technique, is to select suitable functions, involving unknown "disposable" constants, to express the water- and steam-side temperature drops in terms of the relevant parameters. The constants are determined by summing the water-side, wall, and steam-side temperature differences and "fitting" to the observed overall temperature difference. (Note that this procedure also invokes the uniform radial conduction approximation.)

Ideally, the function used to express the steam-side temperature drop should incorporate the vapor velocity (e.g., an equation based on the theoretical result of Shekriladze and Gomelauri [22]). However, in view of the relatively low vapor velocities obtained in the present work, a Nusselt-type expression was considered adequate as in [23], i.e.,

$$\mathrm{Nu}_s = \alpha\left[\frac{g\rho_f^2 h_{fg} D_o^3}{\mu_f k_f \Delta T}\right]^{1/4} \tag{5}$$

where α is a constant to be found.

For the water side, a Sieder–Tate-type expression was adopted, i.e.,

$$\mathrm{Nu} = \beta\ \mathrm{Re}^{0.8}\ \mathrm{Pr}^{1/3}(\mu_c/\mu_w)^{0.14} \tag{6}$$

where β is a constant to be found. In view of the data obtained from the instrumented tube, it might have been better to have included a constant term in equation (6) (compare B in equation (1)). However, by adopting the simpler expression (equation (6)), and with equation (5), observational equations can be arranged to incorporate α and β linearly. This greatly simplifies the minimization procedure.

Using an uninstrumented smooth tube with spiral insert, a total of four runs were made: two runs each under a vacuum and at atmospheric pressure. During these runs, the vapor velocity was held at 0.8 ± 0.1 m/s. These runs resulted in $\beta = 0.071 \pm 0.001$. The fact that these values are rather higher than the values of C which were obtained from the instrumented tube data is, in part, due to the fact that the constant term B was omitted in equation (6). The water-side coefficients obtained using this modified Wilson Plot result deviated slightly from those obtained from the previous correlation at the lowest coolant velocity and by a maximum of around 8 percent at the highest coolant velocity.

Steam-side data, obtained using the modified Wilson Plot equation for the water side, were fitted by equation (3). The broken lines (provided for three of the data runs) shown in Figs. 6 and 7 are curve fits to these data. Note that, to avoid confusion, no data points are shown. The points and fitted lines were in as close agreement as for the case where equation (1) was used for the water side.

In Fig. 8 comparisons are made of the enhancement ratio E_q. It may be seen that the steam-side enhancement based on coefficients obtained using the Wilson-Plot-derived water-side coefficients are somewhat smaller than those found with the directly measured water-side coefficients. The difference between the two curves is, however, marginal, and probably less than the uncertainty arising from the approximation of uniform radial conduction inherent in both methods of calculation. Certainly, general observations on the performance of the tubes, and in particular with regard to the best fin spacing, are the same on either basis.

Comparison of Steam-Side Measurements With Heat-Transfer Models. As shown in Table 1, four heat transfer models were selected to compare with the experimental data

(based on solid curves in Figs. 6 and 7). This table lists the computed condensate retention angle ψ and the ratios of experimental heat transfer coefficient to predicted values for the six finned tubes. As can be seen, the Beatty and Katz correlation (third column) highly overpredicts the data for the fully flooded tube ($s = 0.5$ mm). This is because their model neglects any condensate flooding. The extent of overprediction decreases with increasing fin spacing and for $s > 4.0$ mm, this model underpredicts the data. The Rudy and Webb [7] and Owen et al. [10] models (columns 4 and 5, respectively), which are extensions to the Beatty and Katz correlation, underpredict the experimental data for all six tubes. The predictions made by these three models appear to indicate the inadequacy of any heat transfer model that does not consider surface-tension-induced flow in the unflooded portion of the tube. On the other hand, the Webb et al. [14] model (column 6) appears to predict the heat transfer data quite well for the finned tubes except for the fully flooded case ($s = 0.5$ mm). In order to use the Webb et al. model, it was necessary to assume a value for the variable ζ that defines the condensate profile on the fin surface. It is not practical to compute ζ for rectangular fins. Therefore, a value of -0.95 was assumed based on similar values used by Webb et al. [14] for their trapezoidal fins. Also, in order to express the heat transfer in the flooded portion, one-dimensional conduction was assumed similar to that used by Owen et al. rather than two-dimensional conduction as proposed by Webb et al. [14]. As can be seen, except for the fully flooded tube, the Webb et al. model predicts the experimental data, both vacuum and atmospheric, within about $\pm$ 20 percent. While the Webb et al. model appears to be very encouraging, more work is needed to predict more accurately heat transfer through the flooded region. On the other hand, the Webb et al. model appears to be quite satisfactory for practical finned tubes (for example, tubes with $\psi <$ 100 deg).

Conclusions

1 For condensation of steam on finned copper tubes with root diameter of 19 mm, and for a fin height and thickness of 1 mm, maximum enhancement occurs at a fin spacing of 1.5 mm.

2 For the best fin spacing mentioned above, the steam-side coefficient is enhanced over the smooth-tube value by factors of around 5.2 and 3.6 at atmospheric and under vacuum conditions, respectively.

3 The present data and general trends are consistent with recent results of Yau et al. [1, 21], who used a smaller diameter tube and a smaller fin thickness.

4 All of the finned tubes showed heat transfer enhancements in excess of the area increase due to finning, implying that the thinning of the condensate film due to surface-tension forces plays an important role in the enhancement process.

5 The finned tube with the smallest fin spacing (0.5 mm) gave a performance increase at least equal to the area increase due to finning despite the fact that the fins were almost all flooded with condensate.

6 With appropriate functions for the inside and outside heat transfer coeffcients, and accurate smooth-tube data, the modified Wilson Plot technique appears to offer a simple, satisfactory method for obtaining an inside heat transfer coefficient correlation.

Acknowledgments

This work was supported by the National Science Foundation through Grant No. MEA 82-03567.

References

1 Yau, K. K., Cooper, J. R., and Rose, J. W., "Effect of Fin Spacing on the Performance of Horizontal Integral-Fin Condenser Tubes," ASME JOURNAL OF HEAT TRANSFER, Vol. 107, 1985, p. 337-383.

2 Staub, F. W., "Heat Transfer for Film Condensation on Vertical and Horizontal Fluted Tubes," General Electric Report No. 61GL175, Schenectady, NY, Oct. 1961.

3 Nabavian, K., and Bromley, L. A., "Condensation Coefficient of Water," *Chemical Engineering Science*, Vol. 18, 1963, pp. 651-660.

4 Karkhu, V. A., and Borovkhov, V. P., "Film Condensation of Vapor at Finely-Finned Horizontal Tubes," *Heat Transfer—Soviet Research*, Vol. 3, 1971, pp. 183-191.

5 Rifert, V. G., "Steam Condensation on Profiled Surfaces," *Heat and Mass Transfer Processes in Porous Media with Phase Change*, Academy of Science, BSSR, Minsk, 1982, pp. 149-170 [in Russian].

6 Katz, D. L., Hope, R. E., and Datsko, S. C., "Liquid Retention on Finned Tubes," Dept. of Eng. Research, Univ. of Michigan, Ann Arbor, MI, Project M592, 1946.

7 Rudy, T. M., and Webb, R. L., "Condensate Retention of Horizontal Integral-Fin Tubes," *Advances in Enhanced Heat Transfer—1981*, ASME, HTD-Vol. 18, R. L. Webb, T. C. Carnavos, E. L. Park, and K. M. Hostetler, eds., 1981, p. 35-41.

8 Rudy, T. M., and Webb, R. L., "An Analytical Model to Predict Condensate Retention on Horizontal, Integral Fin Tubes," ASME JOURNAL OF HEAT TRANSFER, Vol. 107, 1985, p. 361-368.

9 Honda, H., Nozu, S., and Mitsumori, K., "Augmentation of Condensation on Horizontal Finned Tubes by Attaching a Porous Drainage Plate," *Proc. ASME-JSME Thermal Engineering Joint Conference*, Hawaii, Vol. 3, 1983, pp. 289-296.

10 Owen, R. G., Sardesai, R. G., Smith, R. A., and Lee, W. C., "Gravity Controlled Condensation on a Horizontal Low-Fin Tube," *Condensers: Theory and Practice*, Inst. Chem. Engrs. Symp. Ser., No. 75, 1983, pp. 415-428.

11 Beatty, K. O., Jr., and Katz, D. L., 'Condensation of Vapors on Outside of Finned Tubes," *Chemical Engineering Progress*, Vol. 44, No. 1, Jan. 1948, pp. 55-70.

12 Honda, H., and Nozu, S., "A Prediction Method for Heat Transfer During Film Condensation on Horizontal Low-Intgeral-Fin Tubes," *Fundamentals of Phase Change: Boiling and Condensation*, HTD-Vol. 38, C. T. Avedisian and T. M. Rudy, eds., Dec. 1984, pp. 107-114.

13 Rudy, T. M., and Webb, R. L., "Theoretical Model for Condensation on Horizontal, Integal-Fin Tubes," AIChE Symposium Series, Vol. 79, No. 225, 1983, p. 11-18.

14 Webb, R. L., Rudy, T. M., and Kedzierski, M. A., "Prediction of the Condensation Coefficient on Horizontal Integral-Fin Tubes," ASME JOURNAL OF HEAT TRANSFER, Vol. 107, 1985, pp. 369-376.

15 Adamek, T., "Bestimmung der Kondensation-grossen auf feingewellten Oberflachen zur Auslegung aptimaler Wandprofile," *Wärme- und Stoffübertragung*, Vol. 15, 1981, pp. 255-270.

16 Poole, W. M., "Filmwise Condensation of Steam on Externally-Finned Horizontal Tubes," M. S. Thesis, Naval Postgraduate School, Monterey, CA, Dec. 1983.

17 Lee, W. C., Rahbar, S., and Rose, J. W., "Forced Convection Film Condensation of Refrigerant 113 and Ethanediol on a Horizontal Tube," *Heat Exchangers for Two-Phase Applications*, HTD-Vol. 27, J. B. Kitto, Jr. and J. M. Robertson, eds., July 1983, pp. 107-114.

18 Wanniarachchi, A. S., Marto, P. J., and Rose, J. W., "Filmwise Condensation of Steam on Externally-Finned Horizontal Tubes," *Fundamentals of Phase Change: Boiling and Condensation*, HTD-Vol. 38, C. T. Avedisian and T. M. Rudy, eds., Dec. 1984, pp. 133-1431.

19 Fujii, T., and Honda, H., "Fcrced Convection Condensation on a Horizontal Tube," *Trans. Japan Soc. of Mech. Engrs.*. Vol. 45, 1980, pp. 95-102 [in Japanese].

20 Lee, W. C., and Rose, J. W., "Forced Convection Film Condensation on a Horizontal Tube With and Without Non-condensing Gases," *Int. J. Heat Mass Transfer*. Vol. 7, 1984, p. 519-528.

21 Yau, K. K., Cooper, J. R., and Rose, J. W., "Effects of Drainage Strips and Fin Spacing on Heat Transfer and Condensate Retention for Horizontal Finned and Plain Condenser Tubes," *Fundamentals of Phase Change: Boiling and Condensation*, HTD-Vol. 38, C. T. Avedisian and T. M. Rudy, eds., Dec. 1984, pp. 151-156.

22 Shekriladze, I. G., and Gomelauri, V. I., "Theoretical Study of Laminar Film Condensation of Flowing Vapour," *Int. J. Heat Mass Transfer*, Vol. 90, 1966, pp. 581-591.

23 Nobbs, D. W., "The Effect of Downward Vapour Velocity and Inundation on the Condensation Rates on Horizontal Tubes and Tube Banks," PhD Thesis, University of Bristol, England, Apr. 1975.

Journal of Heat Transfer

Technical Notes

This section contains shorter technical papers. These shorter papers will be subjected to the same review process as that for full papers.

Analysis of Natural Convection Flow of Micropolar Fluid About a Sphere With Blowing and Suction

Fue-Sang Lien[1], Cha'o-Kuang Chen[2], and J. W. Cleaver[3]

Nomenclature

$F(x)$ = dimensionless thermal function $= (T_w - T_\infty)/(T_{w_0} - T_\infty)$(*); $= q_w/q_{w_0}$(**)
Gr, $\overline{\text{Gr}}$ = Grashof number: $\text{Gr} = \hat{g}\beta(T_{w_0} - T_\infty)R^3/\nu^2$, $\overline{\text{Gr}} = \hat{g}\beta q_{w_0}R^4/\nu^2 k$
$\hat{g}$ = gravitational acceleration
j = micro-inertia
$\hat{k}$ = vortex viscosity
Pr = Prandtl number
α = thermal diffusivity
β = coefficient of thermal expansion
γ = spin gradient viscosity
η = pseudosimilarity variable
θ = dimensionless temperature
λ, B, Δ = dimensionless material parameter
μ = dynamic viscosity
ν = kinematic viscosity
ξ = transformed axial coordinate
ρ = density of fluid
$\bar{\sigma}, \sigma$ = angular and dimensionless angular velocity
τ_w = wall shear stress
ϕ = x/R, in deg
ψ = stream function

Subscripts

0 = stagnation point condition

Introduction

The problem of natural convection boundary layer flows of incompressible Newtonian fluids past a sphere has received considerable attention from many investigators [1, 2]. The boundary layer problem of external free convective flow from a sphere with various prescribed thermal condition on the surface has been considered by Chiang et al. [3]. By a series expansion scheme, they obtained the local heat transfer results based on two major classes of surface thermal conditions: the prescribed surface-temperature distribution, and the prescribed surface-heat-flux distribution. Chen and Mucoglu have performed analyses to study the heat transfer characteristics of laminar mixed convection about isothermal and constant-heat-flux spheres [4, 5]. By employing an implicit finite difference scheme, the local Nusselt number was shown to decrease with an increasing angle from the stagnation point.

Although the above investigations have been extensively carried out for the case of classical Newtonian fluids, there exist relatively fewer works concerning non-Newtonian fluids with microstructures, such as polymeric additives, colloidal suspensions, and so on. The theory of fluids with microstructures has been the subject of a large number of investigations. For an excellent review see Ariman et al. [6]. Jena and Mathur [7] studied the problem of free convection in the laminar boundary layer flow of a thermomicropolar fluid past a vertical flat plate with suction and injection. Ramachandran et al. have also studied the heat transfer effect in boundary layer flow of a micropolar fluid past a curved surface with suction and injection [8].

The present work has been undertaken in order to study the heat transfer characteristics of the natural convection flow of micropolar fluids from a sphere with various surface thermal conditions. Since no similarity solutions exist in this case, an efficient finite difference method from Cebeci and Bradshaw [9] is employed to solve the system of transformed equations.

Analysis

The curvilinear orthogonal coordinate system for this analysis, where the wall temperature, without loss of generality, is assumed to be greater than the ambient temperature T_∞, is shown in Fig. 1. Let the coordinate $\bar{x}$ be measured along the surface of the sphere from the stagnation point, and $\bar{y}$ denote the normal distance from the surface. The surface is maintained at an arbitrary temperature $T_w(\bar{x})$ or heat flux $q_w(\bar{x})$. Surface blowing and suction are accounted for in the analysis. By employing the Boussinesq approximation, the conservation equations of the laminar boundary layer for the micropolar fluid can be written as

Mass

$$\frac{\partial(r\bar{u})}{\partial\bar{x}} + \frac{\partial(r\bar{v})}{\partial\bar{y}} = 0 \tag{1}$$

Momentum

$$\bar{u}\frac{\partial\bar{u}}{\partial\bar{x}} + \bar{v}\frac{\partial\bar{u}}{\partial\bar{y}} = \hat{g}\beta(T - T_\infty)\sin(\bar{x}/R) + \left(\nu + \frac{\hat{k}}{\rho}\right)\frac{\partial^2\bar{u}}{\partial\bar{y}^2} + \frac{\hat{k}}{\rho}\frac{\partial\bar{\sigma}}{\partial\bar{y}} \tag{2}$$

[1]Graduate Student, Department of Mechanical Engineering, National Cheng Kung University, Tainan, Taiwan, Republic of China.
[2]Professor, Department of Mechanical Engineering, National Cheng Kung University, Tainan, Taiwan, Republic of China.
[3]Senior Lecturer, Department of Mechanical Engineering, University of Liverpool, Liverpool, United Kingdom.

Contributed by the Heat Transfer Division for publication in the JOURNAL OF HEAT TRANSFER. Manuscript received by the Heat Transfer Division October 29, 1984.

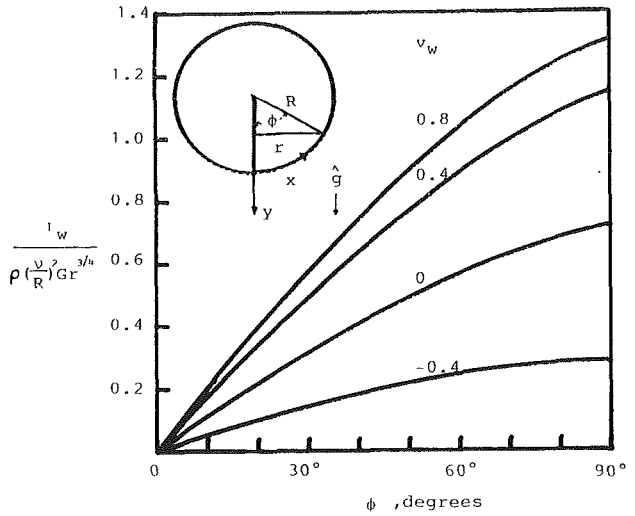

Fig. 1 Angular distributions of the local friction factor for an isothermal surface with Pr = 7, Δ = 5, λ = 5, and $B = 0.1$

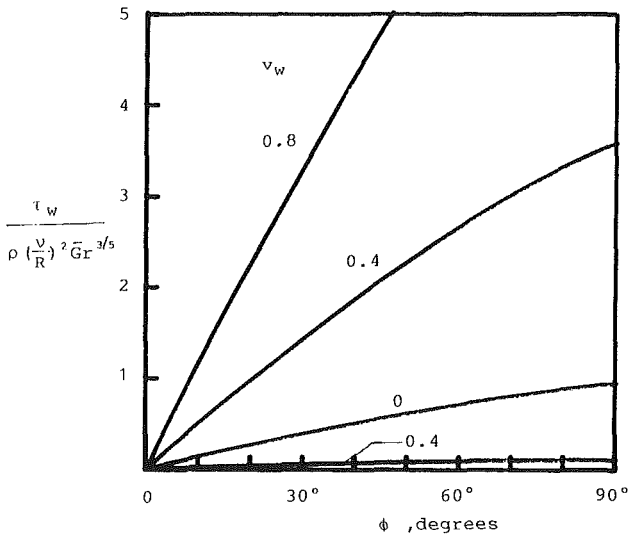

Fig. 2 Angular distributions of the local friction factor for a constant-heat-flux surface with Pr = 7, Δ = 5, λ = 5, and $B = 0.1$

Angular momentum

$$\bar{u}\frac{\partial \bar{\sigma}}{\partial \bar{x}} + \bar{v}\frac{\partial \bar{\sigma}}{\partial \bar{y}} = -\frac{\hat{k}}{\rho j}\left(2\bar{\sigma} + \frac{\partial \bar{u}}{\partial \bar{y}}\right) + \frac{\dot{\gamma}\,\partial^2 \bar{\sigma}}{\rho j \partial \bar{y}^2} \tag{3}$$

Energy

$$\bar{u}\frac{\partial T}{\partial \bar{x}} + \bar{v}\frac{\partial T}{\partial \bar{y}} = \alpha\frac{\partial^2 T}{\partial \bar{y}^2} \tag{4}$$

with boundary conditions

$$\bar{u} = 0,\ \bar{v} = \bar{v}_w(\bar{x}),\ T = T_w(\bar{x})\ (*),\ \bar{\sigma} = -1/2\frac{\partial \bar{u}}{\partial \bar{y}} \qquad \text{at } \bar{y} = 0$$

$$\text{or } -k\frac{\partial T}{\partial \bar{y}} = q_w(\bar{x})\ (**) \tag{5}$$

$$\bar{u} = 0,\ T = T_\infty,\ \bar{\sigma} = 0 \qquad \text{as } \bar{y} \to \infty$$

where the radial distance $r(\bar{x})$ is given by

$$r(\bar{x}) = R\sin(\bar{x}/R) \tag{6}$$

* = for the prescribed surface-temperature case
** = for the prescribed surface-heat-flux case

Equations (1)–(4) are first transformed into a dimensionless form by the following dimensionless variables

$$x = \bar{x}/R,\ y = \bar{y}\mathrm{Gr}^{1/4}/R,\ u = \bar{u}/\left(\frac{\nu}{R}\right)\mathrm{Gr}^{1/2},\ v = \bar{v}/\left(\frac{\nu}{R}\right)\mathrm{Gr}^{1/4},$$

$$\sigma = \bar{\sigma}/\left(\frac{\nu}{R^2}\right)\mathrm{Gr}^{3/4}(*) \tag{7}$$

$$y = \bar{y}\overline{\mathrm{Gr}}^{1/5}/R,\ u = \bar{u}/\left(\frac{\nu}{R}\right)\overline{\mathrm{Gr}}^{2/5},\ v = \bar{v}/\left(\frac{\nu}{R}\right)\overline{\mathrm{Gr}}^{1/5},$$

$$\sigma = \bar{\sigma}/\left(\frac{\nu}{R^2}\right)\overline{\mathrm{Gr}}^{3/5}(**)$$

and

$$\theta = (T - T_\infty)/(T_{w_0} - T_\infty)F(x)\ (*),$$

$$\theta = k(T - T_\infty)\overline{\mathrm{Gr}}^{1/5}/Rq_{w_0}F(x)\ (**) \tag{8}$$

Then we introduce the pseudosimilarity variables ξ and η, the dimensionless stream function $f(\xi, \eta)$, and the dimensionless microrotation $g(\xi, \eta)$ to transform the governing equations from the (x, y) coordinates to (ξ, η) coordinates.

$$\xi = \int_0^x F(x)dx,\ \eta = yF(x)^{1/2} \tag{9}$$

$$f(\xi, \eta) = F(x)^{1/2}\left[\psi(x, y) + \frac{1}{r}\int_0^x r v_w(x)dx\right]/\xi \tag{10}$$

$$g(\xi, \eta) = \sigma(x, y)/F(x)^{1/2}\xi \tag{11}$$

where the stream function $\psi(x, y)$ satisfies the continuity equation (1) with

$$u = \frac{1}{r}\frac{\partial}{\partial y}(r\psi),\ v = -\frac{1}{r}\frac{\partial}{\partial x}(r\psi) \tag{12}$$

Introducing equations (7)–(11) into equations (2)–(4) gives

$$(1+\Delta)f''' + ff''[1 + \alpha_1(x) - \alpha_2(x)] - f''\alpha_3(x) + \alpha_5(x)\theta - (f')^2 + \Delta g' = \xi\left(f'\frac{\partial f'}{\partial \xi} - f''\frac{\partial f}{\partial \xi}\right) \tag{13}$$

$$\lambda g'' + fg'[1 + \alpha_1(x) - \alpha_2(x)] - g'\alpha_3(x) - [1 + \alpha_2(x)]f'g - \alpha_4(x)[2g + f''] = \xi\left(f'\frac{\partial g}{\partial \xi} - g'\frac{\partial f}{\partial \xi}\right) \tag{14}$$

$$\mathrm{Pr}^{-1}\theta'' + f\theta'[1 + \alpha_1(x) - \alpha_2(x)] - \theta'(x)\alpha_3(x) - 2\alpha_2(x)f'\theta = \xi\left(f'\frac{\partial \theta}{\partial \xi} - \theta'\frac{\partial f}{\partial \xi}\right) \tag{15}$$

$$f = f' = 0,\ \theta = 1(*),\ g = -1/2f'' \qquad \text{at } \eta = 0$$

$$\text{or } \theta' = -F(x)^{-1/2}(**) \tag{16}$$

$$f' = 0,\ g = 0,\ \theta = 0 \qquad \text{as } \eta \to \infty$$

where

$$\alpha_1(x) = \cos(x)\xi/[\sin(x)F(x)] \tag{17a}$$

$$\alpha_2(x) = \xi\frac{dF(x)}{dx}/[2F(x)^2] \tag{17b}$$

$$\alpha_3(x) = v_w(x)F(x)^{-1/2} \tag{17c}$$

$$\alpha_4(x) = \Delta B/F(x) \tag{17d}$$

$$\alpha_5(x) = \sin(x)/\xi \tag{17e}$$

$$\Delta = \hat{k}/\mu,\ \lambda = \gamma/\rho j\nu, \qquad B = R^2/j\mathrm{Gr}^{1/2}(*)$$

$$\text{or } B = R^2/j\overline{\mathrm{Gr}}^{2/5}(**) \tag{17f}$$

In the foregoing equations, the primes stand for partial derivatives with respect to η. If $\alpha_3(x) = 0$ and $F(x) = 1$, equations (13)–(16) can be reduced to the case of uniform thermal conditions on the surface without blowing and suction.

The physical quantities of primary interest are the temperature distribution, the local friction factor C_f, and the

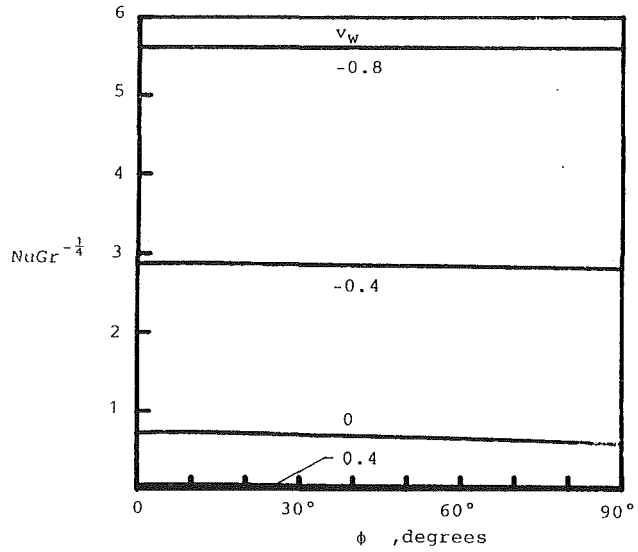

Fig. 3 Angular distributions of the local heat transfer rate for an isothermal surface with Pr = 7, $\Delta = 5$, $\lambda = 5$, and $B = 0.1$

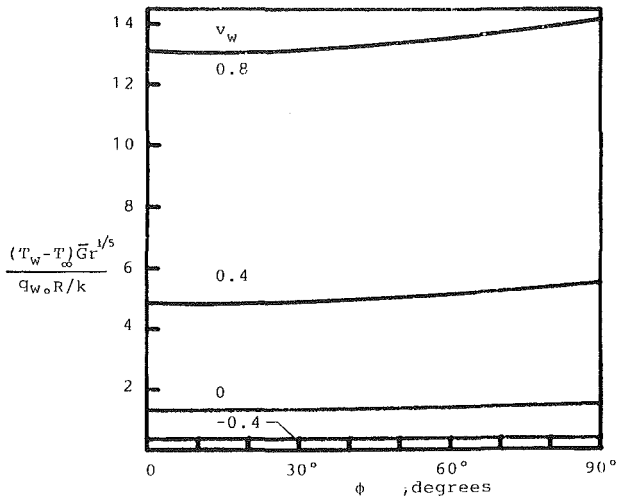

Fig. 4 Angular distributions of the local surface temperature for a constant-heat-flux surface with Pr = 7, $\Delta = 5$, $\lambda = 5$, and $B = 0.1$

Table 1 Angular distributions of the local Nusselt number $NuGr^{-1/4}$ for an isothermal surface without mass transfer; $B = 0.1$

	Pr = 0.7			Pr = 7		
ϕ	$\Delta = 5$ $\lambda = 5$	$\Delta = 5$ $\lambda = 13.5$	$\Delta = 13.5$ $\lambda = 5$	$\Delta = 5$ $\lambda = 5$	$\Delta = 5$ $\lambda = 13.5$	$\Delta = 13.5$ $\lambda = 5$
0	0.3677	0.3632	0.3106	0.7157	0.7033	0.5967
30	0.3589	0.3545	0.3031	0.6990	0.6869	0.5831
60	0.3347	0.3307	0.2805	0.6501	0.6401	0.5398
90	0.2937	0.2907	0.2435	0.5715	0.5643	0.4717

Table 2 Angular distributions of the surface temperature $(T_w - T_\infty)\overline{Gr}^{1/5}/(q_{w_0}R/k)$ for a constant-heat-flux surface without mass transfer; $B = 0.1$

	Pr = 0.7			Pr = 7		
ϕ	$\Delta = 5$ $\lambda = 5$	$\Delta = 5$ $\lambda = 13.5$	$\Delta = 13.5$ $\lambda = 5$	$\Delta = 5$ $\lambda = 5$	$\Delta = 5$ $\lambda = 13.5$	$\Delta = 13.5$ $\lambda = 5$
0	2.2203	2.2424	2.5184	1.3058	1.3234	1.5062
30	2.2507	2.2722	2.5520	1.3228	1.3409	1.5264
60	2.3437	2.3676	2.6650	1.3826	1.4008	1.5981
90	2.5158	2.5411	2.8683	1.4872	1.5046	1.7235

local Nusselt number Nu. The last two quantities are defined, respectively, by

$$C_f = \tau_w/\rho\left(\frac{\nu}{R}\right)^2, \quad \mathrm{Nu} = hR/k \tag{18}$$

From the definitions of the wall shear stress $\tau_w = [(\mu + \hat{k})\,\partial\bar{u}/\partial\bar{y} + \hat{k}\bar{\sigma}]_{\bar{y}=0}$ and the local heat transfer coefficient $h = q_w/(T_w - T_\infty)$, and Fourier's law $q_w = -k(\partial T/\partial\bar{y})_{\bar{y}=0}$, it can be readily shown that

$$C_f \mathrm{Gr}^{3/4} = \xi F(x)^{1/2} f''(\xi, 0)(1 + 0.5\Delta)(*) \tag{19}$$

$$C_f \overline{\mathrm{Gr}}^{3/5} = \xi F(x)^{1/2} f''(\xi, 0)(1 + 0.5\Delta)(**) \tag{20}$$

$$\mathrm{NuGr}^{-1/4} = -F(x)^{1/2}\theta'(\xi, 0)(*) \tag{21}$$

and

$$(T_w - T_\infty)\overline{\mathrm{Gr}}^{1/5}/(q_{w_0}R/k) = F(x)\theta(\xi, 0)(**) \tag{22}$$

Results and Discussion

Numerical results were obtained for the special cases of isothermal and constant-heat-flux surfaces with Prandtl numbers of 0.7 and 7 and various values of Δ and λ. The mass transfer parameter v_w in the computations ranged from -0.8 (suction) to 0.8 (blowing).

Figures 1 and 2 illustrate the angular distributions of the local friction factor for both isothermal and constant-heat-flux cases with $\Delta = 5$, $\lambda = 5$, $B = 0.1$, and Pr = 7 over a wide range of mass transfer parameter. An examination of Figs. 1 and 2 reveals that the local friction factor increases with increasing blowing, but decreases with increasing suction.

The angular distributions of the local Nusselt number $NuGr^{-1/4}$ for the case of isothermal surface are shown in Fig. 3 for Pr = 7. As shown in the figure, the local heat transfer rate increases as the mass transfer parameter increases for the case of suction, while the opposite trend is observed for the case of blowing.

Figure 4 shows the angular distributions of the local surface temperature $(T_w - T_\infty)\overline{\mathrm{Gr}}^{1/5}/(q_{w_0}R/k)$ for the case of a constant-heat-flux surface with Pr = 7. From the figures, it will be seen that the local surface temperature increases with increasing blowing but decreases with increasing suction.

To illustrate how the dimensionless material parameters Δ and λ affect the local heat transfer rate and local surface temperature in the boundary layer of micropolar fluid, representative local Nusselt numbers and local surface temperatures along the angular positions of the sphere are shown in Tables 1 and 2 for $v_w = 0$.

Table 1 illustrates the angular distributions of $NuGr^{-1/4}$ for isothermal surface with various values of Δ and λ. From this table we find that the local Nusselt number decreases with increasing Δ and λ, but increases with increasing Pr.

The local surface temperature distributions for the constant-heat-flux surface case in Table 2 show that an increase in Δ and λ or a decrease in Pr gives rise to a large value of the local surface temperature $(T_w - T_\infty)\overline{Gr}^{1/5}/(q_{w_0}R/k)$.

References

1 Cremers, C. J., and Finley, D. L., "Natural Convection About Isothermal Sphere," *Fourth International Heat Transfer Conference*, Paris-Versailles, Vol. 4, Paper No. NC 1.5, Elsevier, Amsterdam, 1970.

2 Kranse, A. A., and Schenk, J., "Thermal Free Convection From a Solid Sphere," *Appl. Scient. Res.*, Vol. A15, 1966, pp. 397-403.

3 Chiang, T., Ossin, A., and Tien, C. L., "Laminar Free Convection From a Sphere," ASME JOURNAL OF HEAT TRANSFER, Vol. 86, 1964, pp. 537-542.

4 Chen, T. S., and Mucoglu, A., "Analysis of Mixed Forced and Free Convection About a Sphere," *Int. J. Heat Mass Transfer*, Vol. 20, 1977, pp. 867-875.

5 Mucoglu, A., and Chen, T. S., "Mixed Convection About a Sphere With Uniform Surface Heat Flux," ASME JOURNAL OF HEAT TRANSFER, Vol. 100, 1978, pp. 542-544.

6 Ariman, T., Turk, M. A., and Sylvester, N. D., "Applications of Microcontinuum Fluid Mechanics," *Int. J. Engng. Sci.*, Vol. 12, 1974, pp. 273-293.

7 Jena, S. K., and Mathur, M. N., "Free Convection in the Laminar Boundary Layer Flow of a Thermomicropolar Fluid Past a Vertical Flat Plate With Suction and Injection," *Acta Mechanica*, Vol. 42, 1982, pp. 227-238.

8 Subhardra Ramachandran, P., Mathur, M. N., and Ojha, S. K., "Heat Transfer in Boundary Layer Flow of a Micropolar Fluid Past a Curved Surface With Suction and Injection," *Int. J. Engng. Sci.*, Vol. 17, 1979, pp. 625-639.

9 Cebeci, T., and Bradshaw, P., *Momentum Transfer in Boundary Layers*, Hemisphere, Washington, D.C., 1977.

Natural Convection in a Hemispherical Bowl With a Free Surface

O. O. Ajayi[1]

Introduction

There exists a class of physical and industrial situations where fluid motion is induced by a temperature gradient within a confined finite region having a free surface. In some of these instances, the region in which the fluid flow takes place may be approximated by a hemisphere. This is true to some extent, for example, in the cases of a welding pool and the molten pool of a burning candle. Motivated by the importance of understanding such induced fluid motion, Ajayi [1] recently discussed the time development of the thermally induced fluid flow within a hemispherical bowl. In that study, it was necessary, on account of the complexity of the governing equations, to neglect the transport of heat by fluid motion in order to obtain an analytic solution. This approximation, of course, severely limits the range of applicability of the results.

It is the aim of this paper to investigate the influence of the heat convection when a fluid contained in a hemispherical bowl is under a temperature gradient. The equations describing this problem are very involved and they must be solved by numerical techniques. In the literature, the normal practice has been to approximate the derivatives in the governing equations by a finite difference scheme, or to use finite element methods to tackle the problems. Rather than employ one of these standard procedures, a method is introduced whereby the coupled partial differential equations governing the problem are reduced to coupled ordinary differential equations for which analytic solutions are obtained. The numerical process involved in the analysis is consequently reduced to the evaluation of certain integrals.

[1] Engineering Analysis Unit, University of Lagos, Lagos, Nigeria.

Contributed by the Heat Transfer Division for publication in the JOURNAL OF HEAT TRANSFER. Manuscript received by the Heat Transfer Division December 7, 1983.

Formulation of the Problem and Its Solution

A hemispherical bowl of radius a, filled with incompressible viscous fluid, is considered such that the plane boundary of the fluid is a free horizontal surface. The spherical coordinates (r', θ, ϕ) are employed where the origin is located at the center of the hemisphere, with the $\theta = 0$ axis aligned along the axis of the bowl and directed into the fluid. Thus the free surface corresponds to $\theta = \pi/2$ and the fluid occupies the region $0 < \theta < \pi/2$, $r' < a$. The free surface is maintained at a constant temperature $T' = T_s$ while the curved surface of the hemisphere $(r' = a)$ is maintained at some prescribed azimuthally symmetric temperature $T' = T_s(1 + f(\theta))$ which varies from point to point on the surface but is otherwise independent of time.

In the following analysis, the flow due to thermal expansion is neglected and the fluid within the bowl is regarded as a Boussinesq fluid with a velocity $\mathbf{V}'$ and a density ρ such that

$$\nabla \cdot \mathbf{V}' = 0$$

$$\rho = \rho_0\{1 - \beta(T' - T_0)\}$$

where β is the coefficient of thermal expansion, T' the temperature, and ρ_0 the fluid density when $T' = T_0$.

In addition, the thermally induced fluid velocity is supposed to be small enough for the Stokes approximation to be applicable so that the governing equations are

$$\alpha \nabla^2 T' = \nabla \cdot (T'\mathbf{V}') \tag{1}$$

$$\nu \text{Curl Curl Curl} \mathbf{V}' = -\beta \nabla T' \times \mathbf{g} \tag{2}$$

where α is the thermal diffusivity, ν the kinematic viscosity, and $\mathbf{g}$ the gravitational acceleration. It is convenient to define the following dimensionless variables

$$r' = ar$$

$$\mathbf{V}' = \frac{\nu}{a}\mathbf{V}$$

$$T' - T_s = T_s T$$

in terms of which the governing equations become

$$\nabla \cdot \mathbf{V} = 0 \tag{3}$$

$$\nabla^2 T = \text{Pr} \nabla \cdot (T\mathbf{V}) \tag{4}$$

$$\text{Curl Curl Curl } \mathbf{V} = -\text{Gr} \nabla T \times \hat{z} \tag{5}$$

where $\text{Pr} = \nu/\alpha$ is the Prandtl number, $\text{Gr} = \beta g a^3 T_s/\nu^2$ the Grashof number, g the gravitational constant, and $\hat{z}$ is the unit vector along the $\theta = 0$ axis.

It is clear from the above that the governing equations are coupled partial differential equations, and the solution of such a system of equations requires some considerable effort. In the literature, a normal practice would be to replace the derivatives in the equations by a finite difference scheme and solve the resulting algebraic equations numerically. Hence a different approach is introduced. First, the system of coupled partial differential equation is reduced to a system of coupled ordinary differential equations and then solved by semi-analytic method.

Since the velocity field $\mathbf{V}$ is symmetric about the $\theta = 0$ axis, it is convenient to use a stream function ψ which automatically ensures that equation (3) is satisfied. Thus, in terms of the stream function ψ, one may write

$$\mathbf{V} = \frac{1}{r^2}\frac{\partial \psi}{\partial \mu}, \; -\frac{1}{r\sin\theta}\frac{\partial \psi}{\partial r}, \; 0 \tag{6}$$

where $\mu = \cos\theta$.

Table 1 illustrates the angular distributions of $NuGr^{-1/4}$ for isothermal surface with various values of Δ and λ. From this table we find that the local Nusselt number decreases with increasing Δ and λ, but increases with increasing Pr.

The local surface temperature distributions for the constant-heat-flux surface case in Table 2 show that an increase in Δ and λ or a decrease in Pr gives rise to a large value of the local surface temperature $(T_w - T_\infty)\overline{Gr}^{1/5}/(q_{w_0}R/k)$.

References

1 Cremers, C. J., and Finley, D. L., "Natural Convection About Isothermal Sphere," *Fourth International Heat Transfer Conference*, Paris-Versailles, Vol. 4, Paper No. NC 1.5, Elsevier, Amsterdam, 1970.

2 Kranse, A. A., and Schenk, J., "Thermal Free Convection From a Solid Sphere," *Appl. Scient. Res.*, Vol. A15, 1966, pp. 397-403.

3 Chiang, T., Ossin, A., and Tien, C. L., "Laminar Free Convection From a Sphere," ASME JOURNAL OF HEAT TRANSFER, Vol. 86, 1964, pp. 537-542.

4 Chen, T. S., and Mucoglu, A., "Analysis of Mixed Forced and Free Convection About a Sphere," *Int. J. Heat Mass Transfer*, Vol. 20, 1977, pp. 867-875.

5 Mucoglu, A., and Chen, T. S., "Mixed Convection About a Sphere With Uniform Surface Heat Flux," ASME JOURNAL OF HEAT TRANSFER, Vol. 100, 1978, pp. 542-544.

6 Ariman, T., Turk, M. A., and Sylvester, N. D., "Applications of Microcontinuum Fluid Mechanics," *Int. J. Engng. Sci.*, Vol. 12, 1974, pp. 273-293.

7 Jena, S. K., and Mathur, M. N., "Free Convection in the Laminar Boundary Layer Flow of a Thermomicropolar Fluid Past a Vertical Flat Plate With Suction and Injection," *Acta Mechanica*, Vol. 42, 1982, pp. 227-238.

8 Subhardra Ramachandran, P., Mathur, M. N., and Ojha, S. K., "Heat Transfer in Boundary Layer Flow of a Micropolar Fluid Past a Curved Surface With Suction and Injection," *Int. J. Engng. Sci.*, Vol. 17, 1979, pp. 625-639.

9 Cebeci, T., and Bradshaw, P., *Momentum Transfer in Boundary Layers*, Hemisphere, Washington, D.C., 1977.

Natural Convection in a Hemispherical Bowl With a Free Surface

O. O. Ajayi[1]

Introduction

There exists a class of physical and industrial situations where fluid motion is induced by a temperature gradient within a confined finite region having a free surface. In some of these instances, the region in which the fluid flow takes place may be approximated by a hemisphere. This is true to some extent, for example, in the cases of a welding pool and the molten pool of a burning candle. Motivated by the importance of understanding such induced fluid motion, Ajayi [1] recently discussed the time development of the thermally induced fluid flow within a hemispherical bowl. In that study, it was necessary, on account of the complexity of the governing equations, to neglect the transport of heat by fluid motion in order to obtain an analytic solution. This approximation, of course, severely limits the range of applicability of the results.

It is the aim of this paper to investigate the influence of the heat convection when a fluid contained in a hemispherical bowl is under a temperature gradient. The equations describing this problem are very involved and they must be solved by numerical techniques. In the literature, the normal practice has been to approximate the derivatives in the governing equations by a finite difference scheme, or to use finite element methods to tackle the problems. Rather than employ one of these standard procedures, a method is introduced whereby the coupled partial differential equations governing the problem are reduced to coupled ordinary differential equations for which analytic solutions are obtained. The numerical process involved in the analysis is consequently reduced to the evaluation of certain integrals.

[1] Engineering Analysis Unit, University of Lagos, Lagos, Nigeria.

Contributed by the Heat Transfer Division for publication in the JOURNAL OF HEAT TRANSFER. Manuscript received by the Heat Transfer Division December 7, 1983.

Formulation of the Problem and Its Solution

A hemispherical bowl of radius a, filled with incompressible viscous fluid, is considered such that the plane boundary of the fluid is a free horizontal surface. The spherical coordinates (r', θ, ϕ) are employed where the origin is located at the center of the hemisphere, with the $\theta = 0$ axis aligned along the axis of the bowl and directed into the fluid. Thus the free surface corresponds to $\theta = \pi/2$ and the fluid occupies the region $0 < \theta < \pi/2$, $r' < a$. The free surface is maintained at a constant temperature $T' = T_s$ while the curved surface of the hemisphere $(r' = a)$ is maintained at some prescribed azimuthally symmetric temperature $T' = T_s(1 + f(\theta))$ which varies from point to point on the surface but is otherwise independent of time.

In the following analysis, the flow due to thermal expansion is neglected and the fluid within the bowl is regarded as a Boussinesq fluid with a velocity $\mathbf{V}'$ and a density ρ such that

$$\nabla \cdot \mathbf{V}' = 0$$

$$\rho = \rho_0\{1 - \beta(T' - T_0)\}$$

where β is the coefficient of thermal expansion, T' the temperature, and ρ_0 the fluid density when $T' = T_0$.

In addition, the thermally induced fluid velocity is supposed to be small enough for the Stokes approximation to be applicable so that the governing equations are

$$\alpha \nabla^2 T' = \nabla \cdot (T'\mathbf{V}') \tag{1}$$

$$\nu \text{Curl Curl Curl} \mathbf{V}' = -\beta \nabla T' \times \mathbf{g} \tag{2}$$

where α is the thermal diffusivity, ν the kinematic viscosity, and $\mathbf{g}$ the gravitational acceleration. It is convenient to define the following dimensionless variables

$$r' = ar$$

$$\mathbf{V}' = \frac{\nu}{a}\mathbf{V}$$

$$T' - T_s = T_s T$$

in terms of which the governing equations become

$$\nabla \cdot \mathbf{V} = 0 \tag{3}$$

$$\nabla^2 T = \text{Pr} \nabla \cdot (T\mathbf{V}) \tag{4}$$

$$\text{Curl Curl Curl } \mathbf{V} = -\text{Gr} \nabla T \times \hat{z} \tag{5}$$

where $\text{Pr} = \nu/\alpha$ is the Prandtl number, $\text{Gr} = \beta g a^3 T_s/\nu^2$ the Grashof number, g the gravitational constant, and $\hat{z}$ is the unit vector along the $\theta = 0$ axis.

It is clear from the above that the governing equations are coupled partial differential equations, and the solution of such a system of equations requires some considerable effort. In the literature, a normal practice would be to replace the derivatives in the equations by a finite difference scheme and solve the resulting algebraic equations numerically. Hence a different approach is introduced. First, the system of coupled partial differential equation is reduced to a system of coupled ordinary differential equations and then solved by semi-analytic method.

Since the velocity field $\mathbf{V}$ is symmetric about the $\theta = 0$ axis, it is convenient to use a stream function ψ which automatically ensures that equation (3) is satisfied. Thus, in terms of the stream function ψ, one may write

$$\mathbf{V} = \frac{1}{r^2}\frac{\partial \psi}{\partial \mu}, \; -\frac{1}{r\sin\theta}\frac{\partial \psi}{\partial r}, \; 0 \tag{6}$$

where $\mu = \cos\theta$.

Solutions to equations (4) and (5) are then sought of the form

$$T = -\sum_{n=1} R_n(r) P_{2n-1}(\mu) \tag{7}$$

$$\psi = \sum_{n=2} \psi_n(r) I_{2n-1}(\mu) \tag{8}$$

where $I_n(\mu)$ is related to the Legendre polynomial $P_n(\mu)$ by $I_n(\mu) = \{P_{n-2}(\mu) - P_n(\mu)\}/(2n-1)$. On substituting (7) and (8) into (4) and (5), making use of (6), and after some manipulations one obtains

$$E^4(\psi_n/\mathrm{Gr}) = F_n(r) \tag{9}$$

$$\frac{d^2R_n(r)}{dr^2} + \frac{2}{r}\frac{dR_n(r)}{dr} - \frac{2n(2n-1)R_n(r)}{r^2} = S_n(r) \tag{10}$$

where

$$E^2 = \frac{\partial^2}{\partial r^2} + \frac{(1-\mu^2)}{r^2}\frac{\partial^2}{\partial \mu^2}$$

$$F_n(r) = 2(n-1)(2n-1)\left[\left\{r\frac{dR_n(\mathbf{r})}{dr} + 2nR_n(r)\right\}/(4n-1) + \left\{(2n-3)R_{n-1}(r) - r\frac{dR_{n-1}(r)}{dr}\right\}/(4n-5)\right],$$

$$\frac{S_n(r)}{\mathrm{Pr}} = \frac{(2n+1)}{r^2}\sum_{k=2}^{\infty}\sum_{m=1}^{\infty} [\psi_k(r)R_m'(r)d_1(k,m,n) - \psi_k'(r)R_m(r)d_2(k,m,n)],$$

$$d_1(k,m,n) = \int_0^1 P_{2k-2}(\mu)P_{2m-1}(\mu)P_{2n-1}(\mu)d\mu$$

and

$$d_2(k,m,n) = \int_0^1 I_{2k-1}(\mu)\frac{dP_{2m-1}(\mu)}{d\mu}P_{2n-1}(\mu)d\mu$$

The above two integrals may be evaluated analytically (see Hobson [2]).

Equations (9) and (10) are solved by an iterative process as follows: Assume, to start with, that initial approximations of the functions $R_n(r)$ are known (in practice the infinite series in (7) and (8) must be terminated at some finite value of n, say N). These guessed values of $R_n(r)$ are then used in (9) to obtain values of the functions $\psi_n(r)$. These functions are inserted in equation (10) to obtain a better approximation to the functions $R_n(r)$. This iterative process is continued until convergence is achieved. Convergence was assumed when two successive iterations produced changes of less than 1 percent in both $\psi_n(r)$ and $R_n(r)$ at all nodal points.

The boundary conditions satisfied by the velocity field are that the velocity is zero on the bowl surface, is finite at the origin; and is purely tangential on the free surface. In addition, it may be shown that since the function $I_{2n-1}(\mu)$ has a factor $(1-\mu^2)\mu$ for $n \geq 2$, the condition that the tangential stress on the free surface be zero which requires $\partial^2\psi/\partial\mu^2 = 0$ when $\mu = 0$, is automatically satisfied in view of equation (9). By employing the method of variation of parameters and on satisfying the rest of the boundary conditions one finds that

$$\frac{\psi_n(r)}{\mathrm{Gr}} = B_n r^{2n+1} + D_n r^{2n-1} + \frac{1}{2(4n+3)}\left[\frac{r^{2n-1}}{(4n-5)}\int_r^1 y^{4-2n}F_n(y)dy - \frac{r^{2n+1}}{(4n-1)}\int_r^1 y^{2-2n}F_n(y)dy + \frac{r^{4-2n}}{(4n-5)}\int_0^r y^{2n-1}F_n(y)dy - \frac{r^{2-2n}}{(4n-1)}\int_0^r y^{2n+1}F_n(y)dy\right]$$

where

$$B_n = \frac{(2n-1)\delta_n}{2} - \frac{1}{4(4n-3)}\left[\frac{(4-2n)}{(4n-5)}\int_0^1 y^{2n-1}F_n(y)dy - \frac{(2-2n)}{(4n-1)}\int_0^1 y^{2n+1}F_n(y)dy\right]$$

$$D_n = \delta_n - B_n$$

and

$$\delta_n = \frac{1}{2(4n-3)}\left[\frac{1}{(4n-5)}\int_0^1 y^{2n-1}F_n(y)dy - \frac{1}{(4n-1)}\int_0^1 y^{2n+1}F_n(y)dy\right]$$

The determination of $R_n(r)$ follows the same pattern although it differs in some details. $R_n(r)$ is determined iteratively as follows:

For given $\psi_n(r)$ one guesses initial approximations to $R_n(r)$, substitutes these in the right-hand side of (10) and solves the resulting equation for a new set of the functions $R_n(r)$. These new values are then used (in conjunction with the given $\psi_n(r)$) to obtain an improved set of $R_n(r)$. This process is carried on until convergence is achieved. If it assumed that $S_n(r)$ is known then one may show that the solution of (10) is

$$R_n(r) = \frac{1}{(4n-1)}\left[E_n r^{2n-1} - r^{2n-1}\int_r^1 x^{2-2n}S_n(x)dx - \frac{1}{r^{2n}}\int_0^r x^{2n+1}S_n(x)dx\right] \tag{12}$$

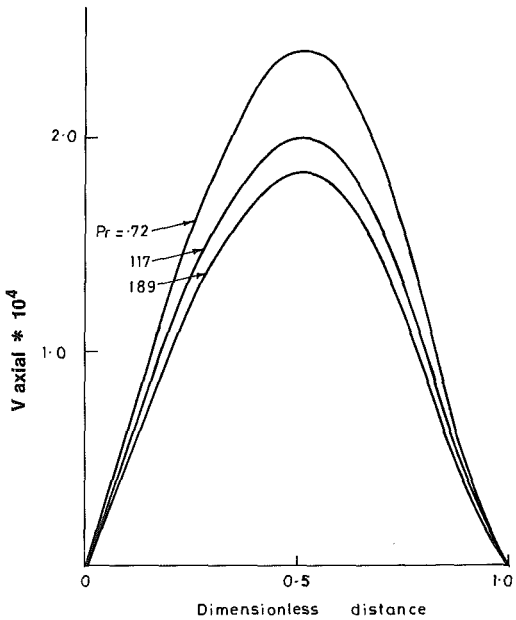

Fig. 1 Dimensionless axial velocity V_{axial} against dimensionless distance along the $\theta = 0$ axis, measured from the origin

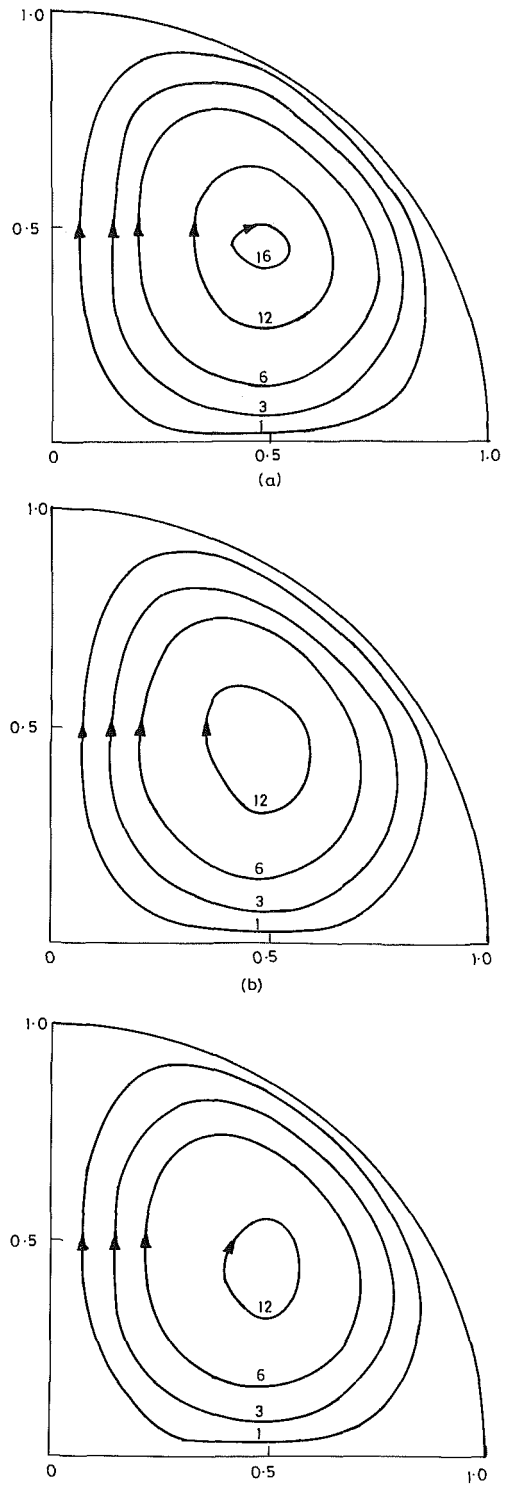

Fig. 2 Streamline patterns in half a meridian plane for the cases: (a) Pr = 0.72, (b) Pr = 117, and (c) Pr = 189; Gr = 150 in all cases and the numbers on the curves are values of $10^4\psi$

where

$$E_n = (4n-1)e_n + \int_0^1 x^{2n+1} S_n(x)dx$$

In deriving equation (12), the boundary conditions

(*i*) $T = 1, \mu = 0$

(*ii*) $$T = -\sum_{n=1}^{\infty} e_n P_{2n-1}(\mu),\ r = 1 \qquad (13)$$

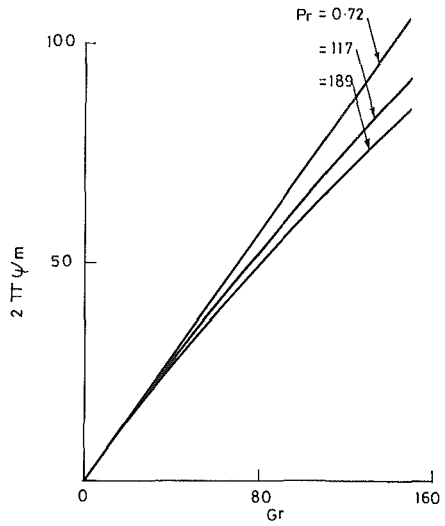

Fig. 3 Values of $2\pi\psi_m$ plotted against Gr for various values of Pr, where ψ_m is the maximum value of $10^4\psi$

where satisfied, where the expression on the right-hand side of (13 *ii*) is the Legendre expansion of $f(\theta)$.

The evaluations of the integrals involved in the above solution were carried out using the trapezoidal rule with a step length of 0.05 for all cases.

Results and Discussion

Numerical results were obtained for values of Prandtl number Pr = 0.72, 117, 189 and Grashof number Gr, ranging from 0–150.

The function $f(\theta)$ was taken as

$$f(\theta) = -\frac{w}{900}[5P_3(\mu) + 4P_5(\mu)]$$

where w is a parameter such that the temperature of the deepest end of the bowl ($r = 1$, $\theta = 0$) differs from that of the free surface by w percent. In the computations, the value of $w = 10$ was chosen.

The number of terms to be retained in the infinite series, in order to accurately evaluate the temperature and velocity fields, was resolved by considering the case Pr = 189, Gr = 150. After some trial tests, it was decided to set $N = 5$. The deviation in both $R_n(r)$ and $\psi_n(r)$ at all nodal points for this value of N differed from those obtained using $N = 4$ by less than 0.2 percent. In the iterative procedure previous values of both $R_n(r)$ and $\psi_n(r)$ were replaced by new ones without any computational instability and even for the case Pr = 189, Gr = 150 only eight iterations were needed to achieve convergence.

An examination of the present results shows that the prediction of the axial velocity (the radial velocity at $\theta = 0$) by neglecting the effect of the velocity on the temperature and vice versa leads to an overestimation of the velocity. This overprediction increases as Pr increases and is as much as 25 percent for the case Pr = 189. These trends are illustrated in Fig. 1 where we have plotted the dimensionless axial velocity against the distance along the axis measured from the origin. An "a posteriori" calculation of the Reynolds number using the maximum axial velocity shows that for the case Pr = 189, Gr = 150, the Reynolds number $\mathrm{Re} = U_m a/\nu$ was about 0.03, where U_m is the maximum axial velocity. Figure 2 shows a global view of the induced fluid motion. It is known from [1] that for the case of pure conduction the thermally induced fluid motion due to the present configuration occurs in the form of closed loops on either side of the axis of symmetry. When the effect of the fluid motion on the temperature

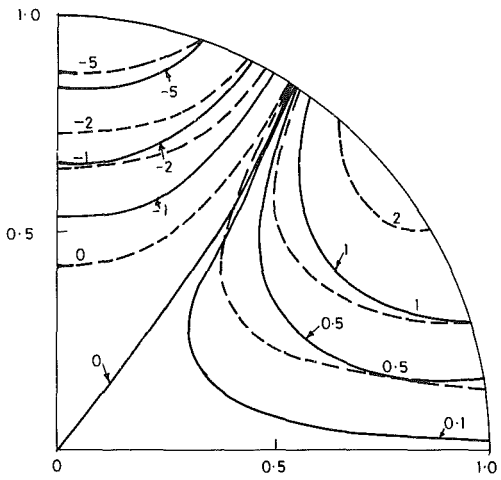

Fig. 4 Temperature distribution pattern in half a meridian plane for the case Pr = 189; the numbers on the curves are values of 100 times the dimensionless temperature, i.e., 100 $(T - T_S/T_S)$

distribution and the effect of the temperature field on the fluid motion is accounted for, the picture of the flow pattern is qualitatively preserved. However, as may be seen from Fig. 2, the intensity of the flow field is significantly altered. In this connection, the quantity $2\pi\psi_m$, which is a measure of the volume flow, where ψ_m is the maximum value of ψ, is of interest. It will be observed from Fig. 3, where the quantity $2\pi\psi_m$ is plotted against Gr for various Pr, that the pure conduction solution overpredicts the value of ψ_m when Pr is nonzero and that this overestimation increases with increasing value of Pr and is dependent also on the value of Gr.

Figure 4 shows the temperature distribution for the case Pr = 189, Gr = 150. Near the deepest end of the bowl ($r > 0.9$, $0 < \theta < 20$ deg) as well as in the region $r > 0.7$, 20 deg $< \theta <$ 40 deg there is little difference between the temperature distribution for the case of pure conduction and the situation in which the transport of heat by fluid motion is taken into consideration. This suggests that in these regions, the local heat transfer rates would be relatively independent of the Prandtl number, at least for low values of the Grashof number. In the other region, however, the temperature distribution is significantly affected by heat convection.

The present solution method may be adapted for the solution of the full Navier–Stokes equation. In that instance, $R_n(r)$ may still be determined as described in this paper and the fluid problem may be split into two parts

$$E^2\psi = \phi \tag{14}$$

$$E^2\phi = f(\phi, \psi) \tag{15}$$

Thus if ϕ is assumed known, equation (14) may be solved for ψ using the method of variation of parameters, with the unknown constants involved in this solution being determined by satisfying some of the conditions to be imposed on ϕ. The remaining boundary conditions yield conditions to be imposed on ψ, these latter conditions being in integral forms. Equation (15) may then be solved for ϕ (by an iterative process or otherwise), which may then be substituted in (14) to obtain an improved ϕ. The iteration then can continue until convergence is achieved.

References

1 Ajayi, O. O., "The Development of Induced Flow in a Hemispherical Bowl due to a Temperature Gradient," *Int. Comm. in Heat and Mass Transfer*, Vol. II, 1984, pp. 553–562.

2 Hobson, E. W., *The Theory of Spherical and Ellipsoidal Harmonics*, Chelsea, New York, 1955.

Laminar Combined Convection From a Rotating Cone to a Thermally Stratified Environment

K. Himasekhar[1] and P. K. Sarma[2]

Nomenclature

C_{fy} = friction coefficient = $\tau_y/(\rho v^2/2)$
C_m = moment coefficient = $M/(\rho v_0^2 r_0^3/2)$
C_p = specific heat of the fluid
g = gravitational acceleration
Gr = local Grashof number = $g\beta \cos \alpha (T_{w,x} - T_{\infty,x}) x^3/\nu^2$
h = local heat transfer coefficient = $q/(T_{w,x} - T_{\infty,x})$
k = thermal conductivity
L = cone slant height
M = torque for rotation
Nu = local Nusselt number = hx/k
Pr = Prandtl number = $\mu C_P/k$
q = local heat flux
r = cone radius
Re = local Reynolds number defined by equation (9*a*)
r_0 = cone radius at the base
S = stratification parameter defined by equation (9*a*)
T = temperature
$T_{\infty,x}$ = ambient temperature at any x
$T_{w,x}$ = surface temperature of the cone at any x
u, v, w = velocity components
V = local cone surface velocity
V_0 = cone surface velocity at the base
x, y, z = coordinate directions
α = cone apex half angle
β = coefficient of thermal expansion
ϵ = convergence criterion
η = dimensionless coordinate = $(\omega \sin \alpha/\nu)^{1/2} z$
θ = dimensionless temperature = $(T - T_{\infty,x})/(T_{w,x} - T_{\infty,x})$
μ = absolute viscosity
ν = kinematic viscosity
ρ = density of the fluid
τ_y = circumferential shear stress
ω = angular velocity

Subscripts

0 = zeroth order in S
1 = first order in S

Introduction

Natural convection flows in thermally stratified media have been studied both analytically and experimentally in view of the inherent practical importance arising in several heat rejection and storage processes. The class of problems solved in this area pertains to the two-dimensional flow over a vertical surface and plane and axisymmetric flows in plumes and jets [1–5]. An excellent review of the work done so far on some of these problems has been presented by Jaluria [6]. The present paper is intended to solve another problem related to a different geometry, namely a rotating cone, in a stratified medium.

Heat transfer from rotating surfaces is thoroughly reviewed

[1] Department of Mechanical Engineering and Applied Mechanics, University of Pennsylvania, Philadelphia, PA 19104; on study leave from the Department of Mechanical Engineering, Andhra University, Waltair, Andhra Pradesh, 530003 India; Student Mem. ASME.

[2] Department of Mechanical Engineering, Andhra University, Waltair-530003, India.

Contributed by the Heat Transfer Division for publication in the JOURNAL OF HEAT TRANSFER. Manuscript received by the Heat Transfer Division June 3, 1985.

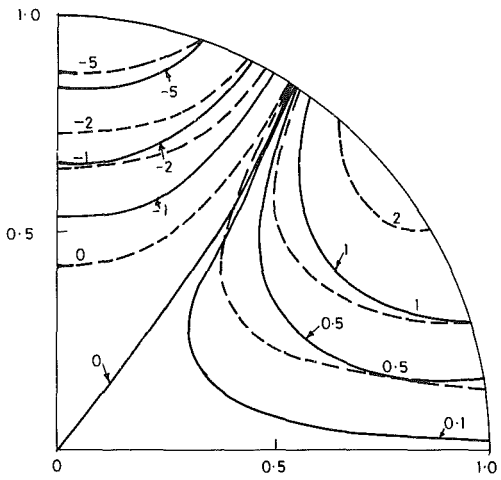

Fig. 4 Temperature distribution pattern in half a meridian plane for the case Pr = 189; the numbers on the curves are values of 100 times the dimensionless temperature, i.e., 100 $(T - T_S/T_S)$

distribution and the effect of the temperature field on the fluid motion is accounted for, the picture of the flow pattern is qualitatively preserved. However, as may be seen from Fig. 2, the intensity of the flow field is significantly altered. In this connection, the quantity $2\pi\psi_m$, which is a measure of the volume flow, where ψ_m is the maximum value of ψ, is of interest. It will be observed from Fig. 3, where the quantity $2\pi\psi_m$ is plotted against Gr for various Pr, that the pure conduction solution overpredicts the value of ψ_m when Pr is nonzero and that this overestimation increases with increasing value of Pr and is dependent also on the value of Gr.

Figure 4 shows the temperature distribution for the case Pr = 189, Gr = 150. Near the deepest end of the bowl ($r > 0.9$, $0 < \theta < 20$ deg) as well as in the region $r > 0.7$, 20 deg $< \theta <$ 40 deg there is little difference between the temperature distribution for the case of pure conduction and the situation in which the transport of heat by fluid motion is taken into consideration. This suggests that in these regions, the local heat transfer rates would be relatively independent of the Prandtl number, at least for low values of the Grashof number. In the other region, however, the temperature distribution is significantly affected by heat convection.

The present solution method may be adapted for the solution of the full Navier–Stokes equation. In that instance, $R_n(r)$ may still be determined as described in this paper and the fluid problem may be split into two parts

$$E^2\psi = \phi \tag{14}$$

$$E^2\phi = f(\phi, \psi) \tag{15}$$

Thus if ϕ is assumed known, equation (14) may be solved for ψ using the method of variation of parameters, with the unknown constants involved in this solution being determined by satisfying some of the conditions to be imposed on ϕ. The remaining boundary conditions yield conditions to be imposed on ψ, these latter conditions being in integral forms. Equation (15) may then be solved for ϕ (by an iterative process or otherwise), which may then be substituted in (14) to obtain an improved ϕ. The iteration then can continue until convergence is achieved.

References

1 Ajayi, O. O., "The Development of Induced Flow in a Hemispherical Bowl due to a Temperature Gradient," *Int. Comm. in Heat and Mass Transfer*, Vol. II, 1984, pp. 553–562.

2 Hobson, E. W., *The Theory of Spherical and Ellipsoidal Harmonics*, Chelsea, New York, 1955.

Laminar Combined Convection From a Rotating Cone to a Thermally Stratified Environment

K. Himasekhar[1] and P. K. Sarma[2]

Nomenclature

C_{fy} = friction coefficient = $\tau_y/(\rho v^2/2)$
C_m = moment coefficient = $M/(\rho v_0^2 r_0^3/2)$
C_p = specific heat of the fluid
g = gravitational acceleration
Gr = local Grashof number = $g\beta \cos\alpha(T_{w,x} - T_{\infty,x})x^3/\nu^2$
h = local heat transfer coefficient = $q/(T_{w,x} - T_{\infty,x})$
k = thermal conductivity
L = cone slant height
M = torque for rotation
Nu = local Nusselt number = hx/k
Pr = Prandtl number = $\mu C_P/k$
q = local heat flux
r = cone radius
Re = local Reynolds number defined by equation (9*a*)
r_0 = cone radius at the base
S = stratification parameter defined by equation (9*a*)
T = temperature
$T_{\infty,x}$ = ambient temperature at any x
$T_{w,x}$ = surface temperature of the cone at any x
u, v, w = velocity components
V = local cone surface velocity
V_0 = cone surface velocity at the base
x, y, z = coordinate directions
α = cone apex half angle
β = coefficient of thermal expansion
ϵ = convergence criterion
η = dimensionless coordinate = $(\omega \sin\alpha/\nu)^{1/2} z$
θ = dimensionless temperature = $(T - T_{\infty,x})/(T_{w,x} - T_{\infty,x})$
μ = absolute viscosity
ν = kinematic viscosity
ρ = density of the fluid
τ_y = circumferential shear stress
ω = angular velocity

Subscripts

0 = zeroth order in S
1 = first order in S

Introduction

Natural convection flows in thermally stratified media have been studied both analytically and experimentally in view of the inherent practical importance arising in several heat rejection and storage processes. The class of problems solved in this area pertains to the two-dimensional flow over a vertical surface and plane and axisymmetric flows in plumes and jets [1–5]. An excellent review of the work done so far on some of these problems has been presented by Jaluria [6]. The present paper is intended to solve another problem related to a different geometry, namely a rotating cone, in a stratified medium.

Heat transfer from rotating surfaces is thoroughly reviewed

[1] Department of Mechanical Engineering and Applied Mechanics, University of Pennsylvania, Philadelphia, PA 19104; on study leave from the Department of Mechanical Engineering, Andhra University, Waltair, Andhra Pradesh, 530003 India; Student Mem. ASME.

[2] Department of Mechanical Engineering, Andhra University, Waltair-530003, India.

Contributed by the Heat Transfer Division for publication in the JOURNAL OF HEAT TRANSFER. Manuscript received by the Heat Transfer Division June 3, 1985.

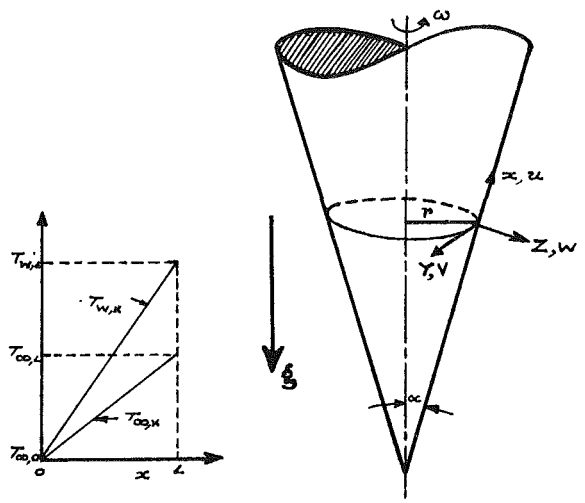

Fig. 1 Physical model

by Kreith [7]. The importance of these studies is also indicated in detail in this article. In all the previous analyses reported thus far for this geometry, the ambient medium is assumed to be isothermal [7-12]. Hering and Grosh investigated the case of combined convection from a nonisothermal rotating cone for Pr = 0.7 [8]. They made use of a similarity transformation suggested by Tien [9]. An integral analysis of this problem was performed by Himasekhar and Sarma to obtain explicit expressions for the estimation of heat transfer and moment coefficients [10]. Hartnett and Donald studied the effects of Prandtl numbers on heat transfer rates [11]. In a very recent paper, Himasekhar and Sarma considered the suction effects of friction factor and heat transfer coefficients [12].

The aim of the present paper is to obtain a similarity solution for the problem of rotating cone in a stably stratified medium. The effects of various stratification levels for Prandtl number values of 0.7 and 6.7 corresponding to air and water at normal temperature are studied.

Analysis

The configuration of the rotating cone with the coordinate system is as shown in Fig. 1. We assume that the cone is rotated under steady-state conditions in nondissipative, constant-property medium except for the density variations in the buoyancy force term. Further we consider a linear variation of the ambient medium temperature as this particular variation is the most frequently encountered case in practice [5].

The system of fundamental equations that model this flow is the same as those given in [8]. We employ the following similarity transformation proposed by Tien [9]

$$u = x\omega \sin\alpha F(\eta) \tag{1}$$

$$v = x\omega \sin\alpha G(\eta) \tag{2}$$

$$w = (\nu\omega \sin\alpha)^{1/2} H(\eta) \tag{3}$$

$$(T - T_{\infty,x}) = (T_{w,x} - T_{\infty,x})\theta(\eta) \tag{4}$$

where

$$\eta = (\omega \sin\alpha/\nu)^{1/2} z \tag{5}$$

The conservation equations given in [8] in terms of these functions can be written as

$$2F + H' = 0 \tag{6}$$

$$F'' - F^2 + G^2 - HF' + (\mathrm{Gr}/\mathrm{Re}^2)\theta = 0 \tag{7}$$

$$G'' - HG' - 2FG = 0 \tag{8}$$

$$\theta'' - \mathrm{Pr}(FS + H\theta' + F\theta) = 0 \tag{9}$$

where

$$\begin{aligned} \mathrm{Re} &= \omega \sin\alpha x^2/\nu, \\ \mathrm{Gr} &= g\cos\alpha\beta(T_{w,x} - T_{\infty,x})x^3/\nu^2 \\ S &= (T_{\infty,L} - T_{\infty,0})\cos\alpha/[(T_{w,L} - T_{\infty,0}) \\ &\quad - (T_{\infty,L} - T_{\infty,0})\cos\alpha] \end{aligned} \tag{9a}$$

The above equations are subjected to the following boundary conditions:

$$\text{At } \eta = 0,\ F = (G - 1.0) = H = (\theta - 1.0) = 0 \tag{10a}$$

$$\text{As } \eta \to \infty,\ F = G = \theta = 0 \tag{10b}$$

The local heat transfer rates are calculated from the Fourier equation:

$$q = -k\frac{\partial T}{\partial z}\bigg|_{z=0} = h(T_{w,x} - T_{\infty,x})$$

or in dimensionless form, it can be written as

$$\mathrm{Nu}/\mathrm{Re}^{1/2} = -\theta'(0) \tag{11}$$

The local friction factor

$$C_{fy} = \tau_y/\frac{1}{2}\rho\,(x\cos\alpha\,\omega)^2$$

is given by

$$C_{fy}\,\mathrm{Re}^{1/2}/2 = G'(0) \tag{12}$$

The dimensionless moment coefficient is obtained by

$$C_m = M/\frac{1}{2}\rho(L\cos\alpha\omega)^2 r_0^3 \tag{13}$$

where M is the shaft torque required to overcome the shear of the rotating cone and is given by

$$M = -\int_0^L r\tau_y 2\pi r dx \tag{14}$$

and r_0 is the cone radius at the base where $x = L$. Equation (19) in terms of the nondimensional variables becomes

$$C_m\mathrm{Re}^{1/2}(\sin\alpha)/\pi = -G'(0) \tag{15}$$

Solution Procedure

In order to obtain the solution to equations (6)-(10), we first consider the perturbation expansion valid for small values of S. We assume power series in S for the unknown functions F, G, H and θ, introduce these expansions into the governing equations and collect the terms of the same order in S to derive equations of each order in S. The equations for higher order (≥ 1) in S are subjected to the homogeneous boundary conditions.

We consider only a two-term expansion and the local heat transfer and moment coefficients can be expressed in terms of zeroth-order and first-order solutions as

$$\mathrm{Nu}/\mathrm{Re}^{1/2} = -[\theta_0'(0) + \theta_1'(0)S] \tag{16}$$

$$C_m\mathrm{Re}^{1/2}\sin\alpha/\pi = -[G_0'(0) + G_1'(0)S] \tag{17}$$

The solution to the zeroth-order equations is well documented in [8]. In our previous paper [10], using integral analysis for the same problem, we obtained the following equations for the local Nusselt numbers and moment coefficients

$$\mathrm{Nu}_0/\mathrm{Re}^{1/2} = (12/175)^{1/4}\mathrm{Pr}^{1/2}[1 + (\mathrm{Gr}/\mathrm{Re}^2) \cdot (100/27\mathrm{Pr})^{1/2}]^{1/4} \tag{18}$$

$$C_{m_0}\mathrm{Re}^{1/2}\sin\alpha/\pi = -(64/525)^{1/4}[1 + (\mathrm{Gr}/\mathrm{Re}^2) \cdot (100/27\mathrm{Pr})^{1/2}]^{1/4} \tag{19}$$

We solve numerically, using a finite-difference method, the set of equations for the first order in S. The finite-difference form of these equations leads to a system of simultaneous equations which are then solved by Gauss-Siedel technique [13]. Some of the details of the numerical scheme are given in [12].

However, the perturbation method described above is valid

Table 1 Values of $-\theta'(0)$ and $G'(0)$

Gr	Pr = 0.7		Pr = 6.7	
Re^2	$-\theta'(0)$	$G'(0)$	$-\theta'(0)$	$G'(0)$
0	0.1792	0.0	0.6250	0.0
1	0.1625	0.0550	0.4375	0.1807
10	0.2333	0.1325	0.3583	0.2086
100	0.4118	0.2004	0.4875	0.8102

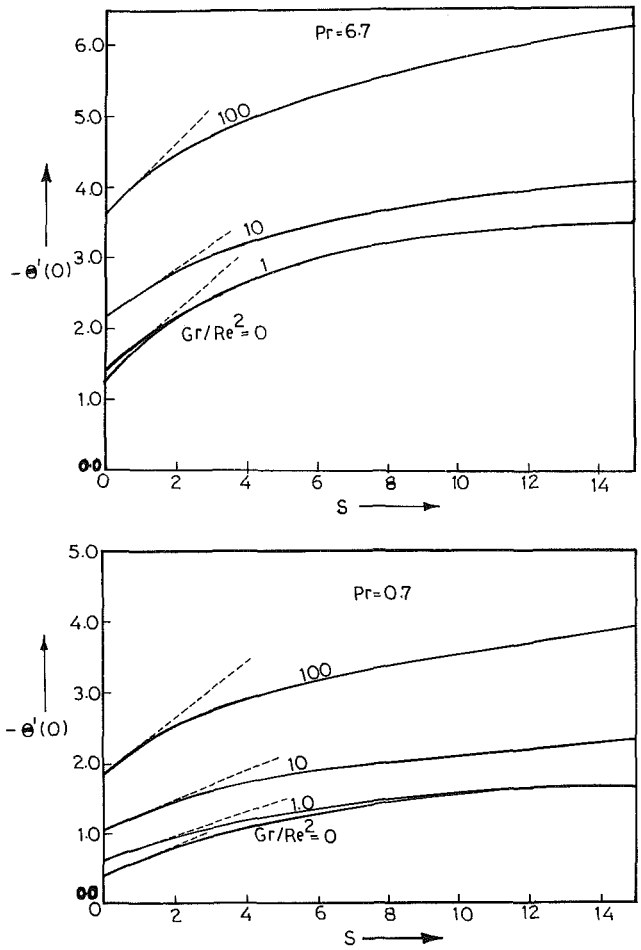

Fig. 2 Effect of stratification parameter on heat transfer rate for various values of Gr/Re^2; the solid and dashed lines represent, respectively, the solution to the full equations and the perturbation solution

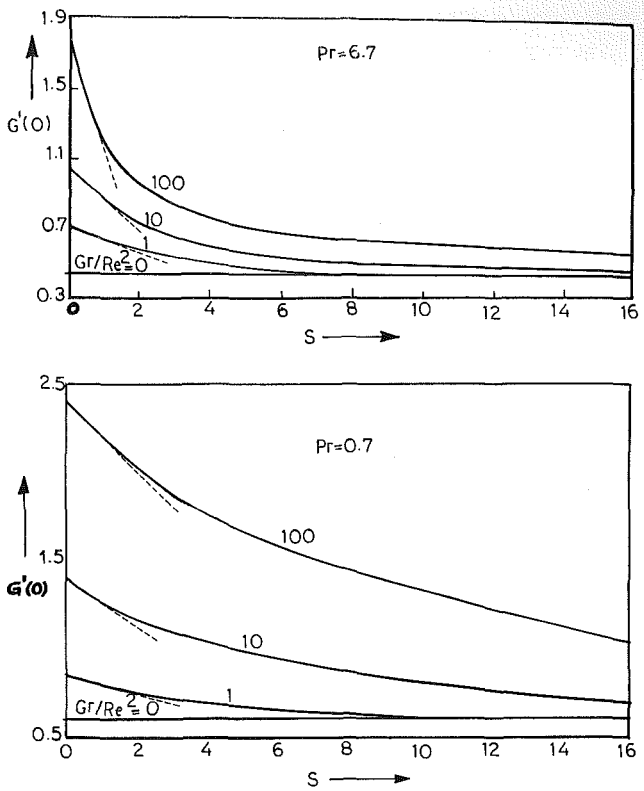

Fig. 3 Variation of moment coefficients with stratification parameter for various values of Gr/Re^2; the solid and dashed lines correspond, respectively, to the solution to the full equations and the perturbation solution

for small values of S. To verify and establish the range of utility of the two-term perturbation solution, we also solve the full equations (6)–(10). To this end, we again use the finite-difference approach described before.

Results and Discussion

Velocity and Temperature Fields. To conserve space, we briefly describe the temperature and velocity fields without depicting them in the figures.

From the present results, it is found that as S increases, the temperature profile steepens near the surface and attains increasingly negative values at large η. A negative value of temperature in the outer region indicates a temperature defect in the flow. The magnitude of temperature defect is profoundly influenced by the values of S and Pr. With increase in S, the magnitudes of the tangential and normal velocities are found to decrease due to decrease in buoyancy. Due to a substantial decrease in the mass flow of the ambient fluid into the boundary layer, the rotation is felt even by the fluid away from the surface. Consequently, the circumferential velocity decreases with an increase in S. The effect of stratification on the flow and on the temperature field is found to be relatively small for large values of Pr. Some of these trends are similar to those observed for a vertical plate [1–3].

Heat Transfer and Moment Coefficients. The results obtained by perturbation analysis are listed in Table 1.

The effect of stratification on the local heat transfer coefficients is depicted in Figs. 2(a) and 2(b) for Pr = 6.7 and 0.7, respectively. The dashed and solid lines correspond to the perturbation solution and the solution to the full equations. Clearly, there is good agreement between these two solutions for $S \leq 1$. It is evident from these figures that an increase in S would lead to enhanced values of the local heat transfer coefficients. The effect of stratification on the heat transfer coefficients for the free convective case is more pronounced than in the case of forced convection. However, the influence of stratification on the heat transfer rate at any given location is to decrease its magnitude in view of the substantial decrease in the temperature potential existing between the wall and the local ambient medium.

Figures 3(a) and 3(b) show the variation of the moment coefficients as a function of S for Pr = 6.7 and 0.7, respectively. The dashed lines indicate the perturbation solution and the solid lines represent the solution to the full equations. Again the agreement between these two solutions is good for values of $S \leq 1$. An increase in the stratification level monotonically decreases the moment coefficients and this can be attributed to a reduction in the circumferential velocity.

Conclusions

The present results can be employed in the estimation of heat transfer rates and the torque required for any specified values of rotation and stratification. For values of $S \leq 1.0$, one may use Table 1 along with equations (18) and (19), and for further values of S, Figs. 2 and 3 may be employed.

Acknowledgments

The help rendered by M. November is acknowledged.

References

1 Yang, K. T., Novotny, J. L., and Cheng, Y. S., " Laminar Convection From a Non-isothermal Plate Immersed in a Temperature Stratified Medium," *International Journal of Heat and Mass Transfer*, Vol. 15, 1972, pp. 1097–1109.

2 Eichhorn, R., "Natural Convection in a Thermally Stratified Fluid," *Progress in Heat and Mass Transfer*, Vol. 2, 1969, pp. 41–53.

3 Jaluria, Y., and Himasekhar, K., "Buoyancy-Induced Two-Dimensional Vertical Flows in a Thermally Stratified Environment," *Journal of Computers and Fluids*, Vol. 11, 1983, pp. 39–49.

4 Turner, J. S., *Buoyancy Effects in Fluids*, Cambridge University Press, England, 1973.

5 Himasekhar, K., and Jaluria, Y., "Laminar Buoyancy-Induced Axisymmetric Free Boundary Flows in a Thermally Stratified Medium," *International Journal of Heat and Mass Transfer*, Vol. 25, 1982, pp. 213–221.

6 Jaluria, Y., *Natural Convection Heat and Mass Transfer*, Pergamon Press, Oxford, 1980.

7 Kreith, F., "Convective Heat Transfer in Rotating Systems," *Advances in Heat Transfer*, Vol. 5, 1968, pp. 129–251.

8 Hering, R. G., and Grosh, R. J., "Laminar Combined Convection From a Rotating Cone," ASME JOURNAL OFF HEAT TRANSFER, Vol. 85, 1963, pp. 29–34.

9 Tien, C. L., "Heat Transfer by Laminar Flow From a Rotating Cone," ASME JOURNAL OF HEAT TRANSFER, Vol. 82, 1960, p. 252.

10 Himasekhar, K., and Sarma, P. K., "Integral Analysis of Mixed Convective Heat Transfer From a Rotating Cone," *Reg. Journal of Energy, Heat, and Mass Transfer*, Vol. 6, 1984, pp. 155–160.

11 Hartnett, J. P., and Donald, E. C., "The Influence of Prandtl Number on the Heat Transfer From Rotating Non-isothermal Disks and Cones," ASME JOURNAL OF HEAT TRANSFER, Vol. 83, 1961, pp. 95–96.

12 Himasekhar, K., and Sarma, P. K., "Effect of Suction on Heat Transfer Rates From a Rotating Cone," *International Journal of Heat and Mass Transfer*, Vol. 29, 1986, pp. 164–167.

13 Carnahan, B., Luther, H. A., and Wilkes, J. O., *Applied Numerical Methods*, Wiley, New York, 1969.

On Latent Heat Delay of Natural Convection

H. Massah,[1] D. Y. S. Lou,[1,2] and A. Haji-Sheikh[1,2]

Introduction

The natural convection in a liquid mixture bounded by a solid wall heater and a solid/liquid interface exhibits peculiar characteristics that cannot be predicted by standard natural convection analysis. A typical mixture used in this study is P-116 paraffin wax. It is shown that the natural convection in a paraffin wax layer enclosed in a cylindrical annulus begins at Rayleigh numbers higher than those expected from a single-component fluid. The cause of this peculiar behavior is attributed to two factors. First, the latent heat of fusion in a mixture is released over a rather large temperature range [1]. The second cause is that the liquid kinematic viscosity increases from $\nu = 4 \times 10^{-6}$ m^2/s at 50°C to $\nu > 15 \times 10^{-6}$ m^2/s at the solidification temperature [1]. The high viscosity at the interface delays the onset of natural convection until the buoyancy force is large enough to overcome this viscous force. Once the motion begins, the hot buoyant layer will leave the vicinity of the heater wall, proceed toward the interface, and be replaced by a colder fluid. Much of the heat transferred from the wall will be stored as latent heat in the liquid layer resulting in a considerably larger heating period than that for a single-component fluid. In addition, the warm layer that sojourned toward the interface must release the latent heat of fusion that is gained from the hot wall. As long as this heating/cooling process is slow, the buoyancy force is reduced to a level that cannot maintain the convective motion against a large frictional force. This may give rise to a pulsating motion not observed in a single-component fluid.

If the mass of the recirculating liquid during one cycle is m and the portion of the latent heat in the liquid phase is C, when conduction dominates, one can write

$$mCL + mc_p[T_{\text{hot,av}} - T_{\text{cold-av}}] = UA(T_i - T_m)\Delta t$$

where $T_{\text{hot,av}}$ and $T_{\text{cold,av}}$ are the average temperatures in the ascending and descending layers of the convecting fluid. The assumption of conduction-dominated heat transfer results in

$$T_{\text{hot,av}} - T_{\text{cold,av}} \cong (T_i - T_m)/2$$

Then

$$C/\text{Ste} + 1/2 \cong \text{Fo}$$

where $\text{Ste} = c_p(T_i - T_m)/L$, and α, c_p, L, T_i, U, A, and T_m are thermal diffusivity, specific heat, conductance, area, wall, and fusion temperatures. If liquid is between two parallel plates a distance b apart, then $\text{Fo} = \alpha\Delta t/b^2$. For other geometries, Fo can be defined accordingly. The first term on the left-hand side accounts for the latent heat and the second term for sensible heat. When Δt is longer than the time required for a simple convective layer to complete one cycle, the fluid layer will pulsate. As the temperature of the heater wall increases, there will be an increase in the Stefan number and a decrease in the value of C, hence the heating period will decrease. This latent heat effect is responsible for a lower heat tranfser rate, especially when the heater surface area is small in comparison with that of the interface. A reduced heat transfer rate from a vertical cylinder [2] has recently been reported.

The calorimetric results for P-116 paraffin wax [1] indicate that the latent heat of fusion is released upon cooling from 60°C to below 20°C. Over 60 percent of the heat of fusion is released in the liquid phase and the remaining portion is released in the solid phase. Although P-116 paraffin wax can be classified as a nearly amorphus substance, the heat released in the solid phase causes some crystal modification which, in turn, results in a significant variation of thermal conductivity with temperature. With currently available temperature-dependent thermal conductivity data [1], it is now possible to predict temperature distribution in both the liquid and solid phases with a fair degree of accuracy. This information is essential in order to have an accurate asymptotic reference value to ascertain when conduction-dominated heat transfer ceases and convection begins.

Description of Apparatus

The test apparatus consists of a concentric copper annulus, a constant-temperature bath, and a low-speed wind tunnel. The concentric annulus is 305 mm long, the inside radius r_i = 4.8 mm and the outside radius r_o = 12.7 mm. In order to release excess pressure, caused by the volumetric expansion of the medium, two risers are implemented. Both risers are necessary in order to facilitate filling of the annulus and subsequent replenishment of wax following excessive mass loss. Hot water enters the inner tube at one end and leaves from the other end. The thermal storage medium consists of P-116 paraffin wax with 0.05 percent by volume AMOCO 150 copper deactivator added to retard any catalytic effect of copper on the hot wax. This device is instrumented with seven copper-constantan thermocouples, three in the wax, one on the inner wall, one on the outer wall, one at the inlet port of the inner tube, and a differential thermocouple. The differential thermocouple detects any drop in the temperature of hot water between the inlet and outlet ports. In all the cases studied, this temperature difference is negligibly small. The thermocouples in the wax are placed on nylon supports and staggered in the vertical direction (Fig. 1) to minimize the disruption of the melting front caused by the probes. To preclude edge effects, only the middle third of this annulus is instrumented. The an-

[1]Mechanical Engineering Department, University of Texas at Arlington, Arlington, TX 76019.

[2]Mem. ASME.

Contributed by the Heat Transfer Division for publication in the JOURNAL OF HEAT TRANSFER. Manuscript received by the Heat Transfer Division June 17, 1985.

Acknowledgments

The help rendered by M. November is acknowledged.

References

1 Yang, K. T., Novotny, J. L., and Cheng, Y. S., " Laminar Convection From a Non-isothermal Plate Immersed in a Temperature Stratified Medium," *International Journal of Heat and Mass Transfer*, Vol. 15, 1972, pp. 1097–1109.

2 Eichhorn, R., "Natural Convection in a Thermally Stratified Fluid," *Progress in Heat and Mass Transfer*, Vol. 2, 1969, pp. 41–53.

3 Jaluria, Y., and Himasekhar, K., "Buoyancy-Induced Two-Dimensional Vertical Flows in a Thermally Stratified Environment," *Journal of Computers and Fluids*, Vol. 11, 1983, pp. 39–49.

4 Turner, J. S., *Buoyancy Effects in Fluids*, Cambridge University Press, England, 1973.

5 Himasekhar, K., and Jaluria, Y., "Laminar Buoyancy-Induced Axisymmetric Free Boundary Flows in a Thermally Stratified Medium," *International Journal of Heat and Mass Transfer*, Vol. 25, 1982, pp. 213–221.

6 Jaluria, Y., *Natural Convection Heat and Mass Transfer*, Pergamon Press, Oxford, 1980.

7 Kreith, F., "Convective Heat Transfer in Rotating Systems," *Advances in Heat Transfer*, Vol. 5, 1968, pp. 129–251.

8 Hering, R. G., and Grosh, R. J., "Laminar Combined Convection From a Rotating Cone," ASME JOURNAL OFF HEAT TRANSFER, Vol. 85, 1963, pp. 29–34.

9 Tien, C. L., "Heat Transfer by Laminar Flow From a Rotating Cone," ASME JOURNAL OF HEAT TRANSFER, Vol. 82, 1960, p. 252.

10 Himasekhar, K., and Sarma, P. K., "Integral Analysis of Mixed Convective Heat Transfer From a Rotating Cone," *Reg. Journal of Energy, Heat, and Mass Transfer*, Vol. 6, 1984, pp. 155–160.

11 Hartnett, J. P., and Donald, E. C., "The Influence of Prandtl Number on the Heat Transfer From Rotating Non-isothermal Disks and Cones," ASME JOURNAL OF HEAT TRANSFER, Vol. 83, 1961, pp. 95–96.

12 Himasekhar, K., and Sarma, P. K., "Effect of Suction on Heat Transfer Rates From a Rotating Cone," *International Journal of Heat and Mass Transfer*, Vol. 29, 1986, pp. 164–167.

13 Carnahan, B., Luther, H. A., and Wilkes, J. O., *Applied Numerical Methods*, Wiley, New York, 1969.

On Latent Heat Delay of Natural Convection

H. Massah,[1] D. Y. S. Lou,[1,2] and A. Haji-Sheikh[1,2]

Introduction

The natural convection in a liquid mixture bounded by a solid wall heater and a solid/liquid interface exhibits peculiar characteristics that cannot be predicted by standard natural convection analysis. A typical mixture used in this study is P-116 paraffin wax. It is shown that the natural convection in a paraffin wax layer enclosed in a cylindrical annulus begins at Rayleigh numbers higher than those expected from a single-component fluid. The cause of this peculiar behavior is attributed to two factors. First, the latent heat of fusion in a mixture is released over a rather large temperature range [1]. The second cause is that the liquid kinematic viscosity increases from $\nu = 4 \times 10^{-6}$ m^2/s at 50°C to $\nu > 15 \times 10^{-6}$ m^2/s at the solidification temperature [1]. The high viscosity at the interface delays the onset of natural convection until the buoyancy force is large enough to overcome this viscous force. Once the motion begins, the hot buoyant layer will leave the vicinity of the heater wall, proceed toward the interface, and be replaced by a colder fluid. Much of the heat transferred from the wall will be stored as latent heat in the liquid layer resulting in a considerably larger heating period than that for a single-component fluid. In addition, the warm layer that sojourned toward the interface must release the latent heat of fusion that is gained from the hot wall. As long as this heating/cooling process is slow, the buoyancy force is reduced to a level that cannot maintain the convective motion against a large frictional force. This may give rise to a pulsating motion not observed in a single-component fluid.

If the mass of the recirculating liquid during one cycle is m and the portion of the latent heat in the liquid phase is C, when conduction dominates, one can write

$$mCL + mc_p[T_{\text{hot,av}} - T_{\text{cold-av}}] = UA(T_i - T_m)\Delta t$$

where $T_{\text{hot,av}}$ and $T_{\text{cold,av}}$ are the average temperatures in the ascending and descending layers of the convecting fluid. The assumption of conduction-dominated heat transfer results in

$$T_{\text{hot,av}} - T_{\text{cold,av}} \cong (T_i - T_m)/2$$

Then

$$C/\text{Ste} + 1/2 \cong \text{Fo}$$

where $\text{Ste} = c_p(T_i - T_m)/L$, and α, c_p, L, T_i, U, A, and T_m are thermal diffusivity, specific heat, conductance, area, wall, and fusion temperatures. If liquid is between two parallel plates a distance b apart, then $\text{Fo} = \alpha\Delta t/b^2$. For other geometries, Fo can be defined accordingly. The first term on the left-hand side accounts for the latent heat and the second term for sensible heat. When Δt is longer than the time required for a simple convective layer to complete one cycle, the fluid layer will pulsate. As the temperature of the heater wall increases, there will be an increase in the Stefan number and a decrease in the value of C, hence the heating period will decrease. This latent heat effect is responsible for a lower heat tranfser rate, especially when the heater surface area is small in comparison with that of the interface. A reduced heat transfer rate from a vertical cylinder [2] has recently been reported.

The calorimetric results for P-116 paraffin wax [1] indicate that the latent heat of fusion is released upon cooling from 60°C to below 20°C. Over 60 percent of the heat of fusion is released in the liquid phase and the remaining portion is released in the solid phase. Although P-116 paraffin wax can be classified as a nearly amorphus substance, the heat released in the solid phase causes some crystal modification which, in turn, results in a significant variation of thermal conductivity with temperature. With currently available temperature-dependent thermal conductivity data [1], it is now possible to predict temperature distribution in both the liquid and solid phases with a fair degree of accuracy. This information is essential in order to have an accurate asymptotic reference value to ascertain when conduction-dominated heat transfer ceases and convection begins.

Description of Apparatus

The test apparatus consists of a concentric copper annulus, a constant-temperature bath, and a low-speed wind tunnel. The concentric annulus is 305 mm long, the inside radius r_i = 4.8 mm and the outside radius r_o = 12.7 mm. In order to release excess pressure, caused by the volumetric expansion of the medium, two risers are implemented. Both risers are necessary in order to facilitate filling of the annulus and subsequent replenishment of wax following excessive mass loss. Hot water enters the inner tube at one end and leaves from the other end. The thermal storage medium consists of P-116 paraffin wax with 0.05 percent by volume AMOCO 150 copper deactivator added to retard any catalytic effect of copper on the hot wax. This device is instrumented with seven copper-constantan thermocouples, three in the wax, one on the inner wall, one on the outer wall, one at the inlet port of the inner tube, and a differential thermocouple. The differential thermocouple detects any drop in the temperature of hot water between the inlet and outlet ports. In all the cases studied, this temperature difference is negligibly small. The thermocouples in the wax are placed on nylon supports and staggered in the vertical direction (Fig. 1) to minimize the disruption of the melting front caused by the probes. To preclude edge effects, only the middle third of this annulus is instrumented. The an-

[1]Mechanical Engineering Department, University of Texas at Arlington, Arlington, TX 76019.

[2]Mem. ASME.

Contributed by the Heat Transfer Division for publication in the JOURNAL OF HEAT TRANSFER. Manuscript received by the Heat Transfer Division June 17, 1985.

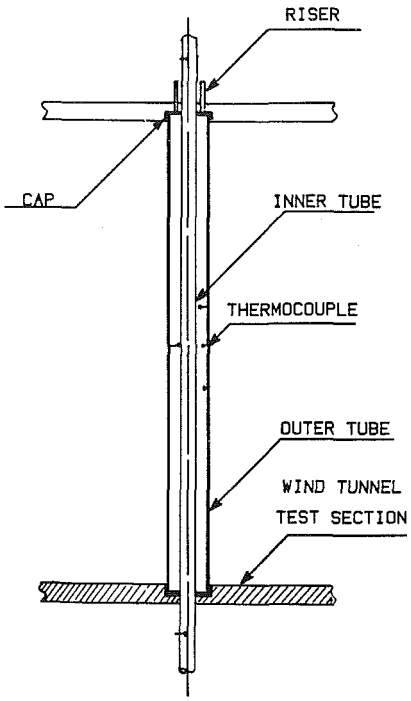

Fig. 1 Test section assembly

nulus device is then placed in a low-speed wind tunnel with a 30.5 cm by 30.5 cm cross section. Since the thermal conductivity ratio of copper to paraffin exceeds 2000, the use of a wind tunnel instead of a constant temperature bath results in a more uniform temperature distribution than if water was introduced in one port and extracted from another. The thermal energy is supplied by recirculating hot water from a constant temperature bath through the inner cylinder. All the experimental data are monitored by an HP data acquisition system. The temperature data are automatically recorded on a magnetic cassette and later used for data reduction.

Results

Four representative sets of data are presented in Fig. 2. The first set shows the temperature traces, solid lines, recorded when the melt zone is small. The second set (Fig. 2*b*) shows the response of thermocouples under the influence of the pulsating liquid. This type of pulsation appears when the Rayleigh number is larger than 20,000, signalling the start of instability. The periodic temperatures were observed in tests lasting for 3 hr. Because the viscosity variation across the liquid layer is great, the appearance of this instability is somewhat later than the onset of instability reported for high Prandtl number liquids with lesser variation in viscosity [3]. The period of oscillation of the thermocouples in Fig. 2(*b*) is nearly 20 min. A similar value can be deduced from equation (1) when $C \approx 0.6$. Figure 2(*c*) indicates the beginning of an established convective layer at a Rayleigh number of 252,000, much higher than expected. Even at such a high Rayleigh number, the output of thermocouples shows some convective pulsation effect at earlier time. The rapid temperature jump in Fig. 2(*d*) signals that a convective layer is fully established. The fusion temperature T_m and the instantaneous temperature at the inner wall T_i and the outer wall T_o constitute the necessary boundary conditions to solve the standard steady-state conduction equation in cylindrical coordinates [4]. The dashed lines in the figure are computed temperature traces in the solid phase. The thermal conductivity in the liquid phase is assumed to have a constant value at mean liquid temperature. As stated earlier, it is necessary to use temperature-dependent thermal conductivity in the solid phase.

The mean location of the interface is experimentally determined from the logarithmic interpolation of the recorded temperature data. Also, the location of the interface is computed assuming steady-state conduction. The ratio of the measured location of the interface r_m to its computed value r_{mo} is presented in Fig 3. Accordingly, the increase in the amount of liquid produced due to natural convection (Fig. 3) at Rayleigh numbers higher than 250,000 is no larger than the experimental error. The deviation of the experimental data

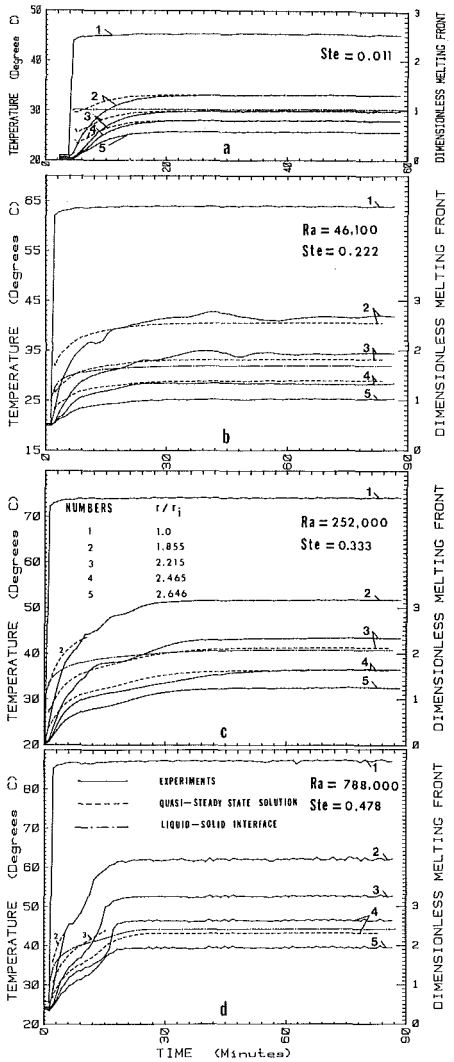

Fig. 2 Temperature traces of the probes and the computed location of interface

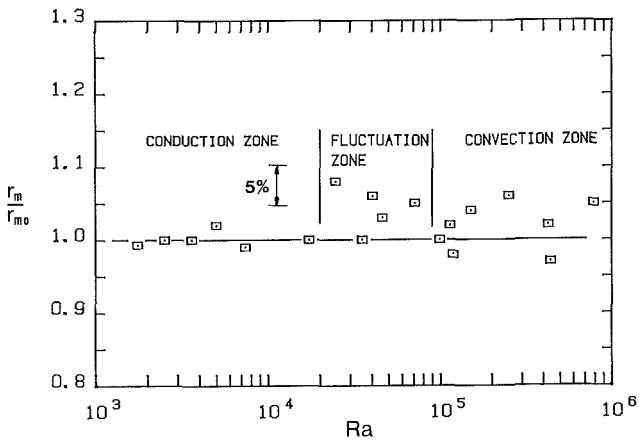

Fig. 3 Ratio of the experimental-to-analytical melt layer thickness

from unity (Fig. 3) at lower Rayleigh numbers is small. The Rayleigh number is calculated from the relation $\mathrm{Ra} = \rho g \beta (T_i - T_m)(r_m - r_i)^3/\mu\alpha$ where β, μ, ρ, and g are thermal expansion coefficient, viscosity, density, and gravitational acceleration. Other variables are defined elsewhere in this technical brief. The properties for calculation of the Rayleigh number Ra and the Stefan number Ste are based on the mean liquid temperature.

Conclusion

The latent heat of fusion in the liquid phase retards the convective motion, thereby decreasing the heat transfer rate. In this geometry, an apparent pulsating flow precedes an established convective flow. Even when the natural convection is fully established the latent heat effect has a tendency to reduce the heat flux. This problem can be remedied by increasing the surface area of the heater, e.g., via fins [2]. The next observation during this study is that the computation of steady-state conduction within the range where there is crystal modification should include temperature-dependent thermal conductivity.

In the analytical calculations, it is assumed, during the transient period, that the entire heat of fusion will be liberated at the interface. Inasmuch as the steady-state solution is the focal point of interest, the aforementioned assumption has no influence on the presented results. However, if the dashed lines in Fig. 2(*a*) are viewed as a quasi-steady solution, there is a general lack of disagreement with experimental data before the steady-state condition sets in. This is expected because the solid phase absorbs heat during crystal modification and the latent heat is not included in the steady-state calculations. This amplifies the fact that the standard transient solutions for non-heat generating liquids and solids result in erroneous information if used to predict the temperature in materials of the type used in this study.

References

1 Haji-Sheikh, A., Eftekhar, J., and Lou, D. Y. S., "Some Thermophysical Properties of Paraffin Wax as a Thermal Storage Medium," *Spacecraft Thermal Control, Design and Operation*, P. E. Bauer and H. E. Coollicott, eds., Prog. in Astronautics and Aeronautics, Vol. 86, 1983, pp. 241–253.

2 Kalhori, B., and Ramadhyani, S., "Studies on Heat Transfer From a Vertical Cylinder, With or Without Fins, Embedded in a Solid Phase Change System," ASME JOURNAL OF HEAT TRANSFER, Vol. 107, 1985, pp. 44–51.

3 MacGregor, R. K., and Emery, A. F., "Free Convection Through Vertical Plane Layers-Moderate and High Prandtl Number Fluids," ASME JOURNAL OF HEAT TRANSFER, Vol. 91, 1969, pp. 391–403.

4 Massah, H., "Melting of P116 Paraffin Wax in a Veritcal Annulus," M.S. Thesis, University of Texas at Arlington, Dec. 1985.

Three Mechanisms of Convective Enhancement in Stationary Disk Systems

S. Mochizuki[1] and Wen-Jei Yeng[2]

Nomenclature

D_H = hydraulic diameter of radial passage = $2s$, m
d = disk diameter, m; d_1, inner; d_2, outer
d_m = midpoint of test core = $(d_1 + d_2)/4$
f = Fanning friction factor = $\Delta P_f D_H/(2\rho u_m^2 L)$
h = heat transfer coefficient, W/m²•K
j = Colburn heat transfer factor = $\mathrm{Nu}/(\mathrm{RePr}^{1/3})$
k = thermal conductivity, W/(m•K)
L = length of radial passage = $(d_2 - d_1)/2$, m
Nu = Nusselt number = hD_H/k
ΔP_f = total pressure drop within test core, Pa
Pr = Prandtl number
Re = Reynolds number = $u_m D_H/\nu$; Re_c, critical value for onset of "second" laminar flow enhancement; Re_t, critical value for onset of transition-turbulent flow enhancement
Re_r = Reynolds number at inlet = $u_1 r_1/\nu$
r = radial distance from disk center, m; r_1, at inlet; r_2, at exit
s = disk spacing, m
u = radial flow velocity, m/s; u_1, at inlet; u_m, mean value at midpoint of test core $(d_1 + d_2)/4$
X = $2(r - r_1)/s$
X^* = $L\, d_m/D_H^2$
ρ = fluid density, kg/m³
ν = kinematic viscosity, m²/s

Subscripts

1 = inlet to test core
2 = outlet from test core
m = mean value

Introduction

There are various kinds of rotating mechanical devices that are associated with heat and mass transfer. Turbomachinery, rotating-disk contactors, and rotating heat exchangers are just a few examples. In order to understand the basic characteristics of the flow and transport phenomena inside these units, rotating disk systems have been used as the models. As revealed in comprehensive reviews [2–4], the literature pertinent to rotating disk systems deals mainly with the performance. Little effort has been directed toward the understanding of the mechanisms of convective transport enhancement due to the complexity introduced by the combination of surface rotation and radial diverging flow. As a first step, the mechanism of performance enhancement in parallel disk systems should be studied in the absence of surface rotation. Reference [1] has provided some clues to the answer, while the present work is to complete the whole task.

Recently, theory and flow visualization have revealed the periodic generation of vortices in the radial flow between stationary parallel circular disks with a steady influx [5]. Those vortices are formed alternately on both channel walls and migrate downstream along the walls, causing oscillations in the bulk flow. When the flow rate is reduced, the formation of vortices ceases and the flow takes a laminar pattern. The heat transfer and frictional loss performance in the stationary disk systems were theoretically and experimentally investigated in [6] and [1], respectively. In the latter study [1], a minor enhancement over the Poiseuille flow case (assumed to prevail throughout the entire radial flow field) was realized in the low laminar flow regime. When the flow rate exceeded a critical value, flow oscillations occurred, which became intensified with a further increase in the fluid flow. When the Reynolds number reached another critical value, the vortex-induced oscillating flow was grossly amplified, resulting in a flow tran-

[1]Department of Mechanical Engineering, Tokyo University of Agriculture & Technology, Koganei, Tokyo, Japan; Mem. ASME.

[2]Department of Mechanical Engineering & Applied Mechanics, University of Michigan, Ann Arbor, MI 48109; Fellow ASME.

Contributed by the Heat Transfer Division for publication in the JOURNAL OF HEAT TRANSFER. Manuscript received by the Heat Transfer Division January 31, 1985.

from unity (Fig. 3) at lower Rayleigh numbers is small. The Rayleigh number is calculated from the relation $\mathrm{Ra} = \rho g \beta (T_i - T_m)(r_m - r_i)^3/\mu\alpha$ where β, μ, ρ, and g are thermal expansion coefficient, viscosity, density, and gravitational acceleration. Other variables are defined elsewhere in this technical brief. The properties for calculation of the Rayleigh number Ra and the Stefan number Ste are based on the mean liquid temperature.

Conclusion

The latent heat of fusion in the liquid phase retards the convective motion, thereby decreasing the heat transfer rate. In this geometry, an apparent pulsating flow precedes an established convective flow. Even when the natural convection is fully established the latent heat effect has a tendency to reduce the heat flux. This problem can be remedied by increasing the surface area of the heater, e.g., via fins [2]. The next observation during this study is that the computation of steady-state conduction within the range where there is crystal modification should include temperature-dependent thermal conductivity.

In the analytical calculations, it is assumed, during the transient period, that the entire heat of fusion will be liberated at the interface. Inasmuch as the steady-state solution is the focal point of interest, the aforementioned assumption has no influence on the presented results. However, if the dashed lines in Fig. 2(*a*) are viewed as a quasi-steady solution, there is a general lack of disagreement with experimental data before the steady-state condition sets in. This is expected because the solid phase absorbs heat during crystal modification and the latent heat is not included in the steady-state calculations. This amplifies the fact that the standard transient solutions for non-heat generating liquids and solids result in erroneous information if used to predict the temperature in materials of the type used in this study.

References

1 Haji-Sheikh, A., Eftekhar, J., and Lou, D. Y. S., "Some Thermophysical Properties of Paraffin Wax as a Thermal Storage Medium," *Spacecraft Thermal Control, Design and Operation*, P. E. Bauer and H. E. Coollicott, eds., Prog. in Astronautics and Aeronautics, Vol. 86, 1983, pp. 241–253.

2 Kalhori, B., and Ramadhyani, S., "Studies on Heat Transfer From a Vertical Cylinder, With or Without Fins, Embedded in a Solid Phase Change System," ASME JOURNAL OF HEAT TRANSFER, Vol. 107, 1985, pp. 44–51.

3 MacGregor, R. K., and Emery, A. F., "Free Convection Through Vertical Plane Layers-Moderate and High Prandtl Number Fluids," ASME JOURNAL OF HEAT TRANSFER, Vol. 91, 1969, pp. 391–403.

4 Massah, H., "Melting of P116 Paraffin Wax in a Veritcal Annulus," M.S. Thesis, University of Texas at Arlington, Dec. 1985.

Three Mechanisms of Convective Enhancement in Stationary Disk Systems

S. Mochizuki[1] and Wen-Jei Yeng[2]

Nomenclature

D_H = hydraulic diameter of radial passage = $2s$, m
d = disk diameter, m; d_1, inner; d_2, outer
d_m = midpoint of test core = $(d_1 + d_2)/4$
f = Fanning friction factor = $\Delta P_f D_H/(2\rho u_m^2 L)$
h = heat transfer coefficient, W/m²•K
j = Colburn heat transfer factor = $\mathrm{Nu}/(\mathrm{RePr}^{1/3})$
k = thermal conductivity, W/(m•K)
L = length of radial passage = $(d_2 - d_1)/2$, m
Nu = Nusselt number = hD_H/k
ΔP_f = total pressure drop within test core, Pa
Pr = Prandtl number
Re = Reynolds number = $u_m D_H/\nu$; Re_c, critical value for onset of "second" laminar flow enhancement; Re_t, critical value for onset of transition-turbulent flow enhancement
Re_r = Reynolds number at inlet = $u_1 r_1/\nu$
r = radial distance from disk center, m; r_1, at inlet; r_2, at exit
s = disk spacing, m
u = radial flow velocity, m/s; u_1, at inlet; u_m, mean value at midpoint of test core $(d_1 + d_2)/4$
X = $2(r - r_1)/s$
X^* = $L\, d_m/D_H^2$
ρ = fluid density, kg/m³
ν = kinematic viscosity, m²/s

Subscripts

1 = inlet to test core
2 = outlet from test core
m = mean value

Introduction

There are various kinds of rotating mechanical devices that are associated with heat and mass transfer. Turbomachinery, rotating-disk contactors, and rotating heat exchangers are just a few examples. In order to understand the basic characteristics of the flow and transport phenomena inside these units, rotating disk systems have been used as the models. As revealed in comprehensive reviews [2–4], the literature pertinent to rotating disk systems deals mainly with the performance. Little effort has been directed toward the understanding of the mechanisms of convective transport enhancement due to the complexity introduced by the combination of surface rotation and radial diverging flow. As a first step, the mechanism of performance enhancement in parallel disk systems should be studied in the absence of surface rotation. Reference [1] has provided some clues to the answer, while the present work is to complete the whole task.

Recently, theory and flow visualization have revealed the periodic generation of vortices in the radial flow between stationary parallel circular disks with a steady influx [5]. Those vortices are formed alternately on both channel walls and migrate downstream along the walls, causing oscillations in the bulk flow. When the flow rate is reduced, the formation of vortices ceases and the flow takes a laminar pattern. The heat transfer and frictional loss performance in the stationary disk systems were theoretically and experimentally investigated in [6] and [1], respectively. In the latter study [1], a minor enhancement over the Poiseuille flow case (assumed to prevail throughout the entire radial flow field) was realized in the low laminar flow regime. When the flow rate exceeded a critical value, flow oscillations occurred, which became intensified with a further increase in the fluid flow. When the Reynolds number reached another critical value, the vortex-induced oscillating flow was grossly amplified, resulting in a flow tran-

[1]Department of Mechanical Engineering, Tokyo University of Agriculture & Technology, Koganei, Tokyo, Japan; Mem. ASME.

[2]Department of Mechanical Engineering & Applied Mechanics, University of Michigan, Ann Arbor, MI 48109; Fellow ASME.

Contributed by the Heat Transfer Division for publication in the JOURNAL OF HEAT TRANSFER. Manuscript received by the Heat Transfer Division January 31, 1985.

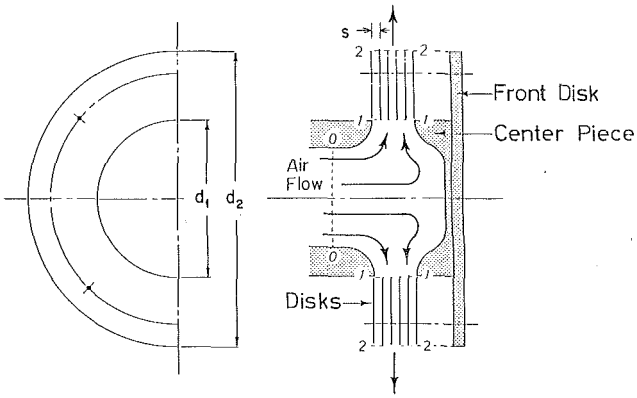

Fig. 1 Test core consisting of parallel annular disks

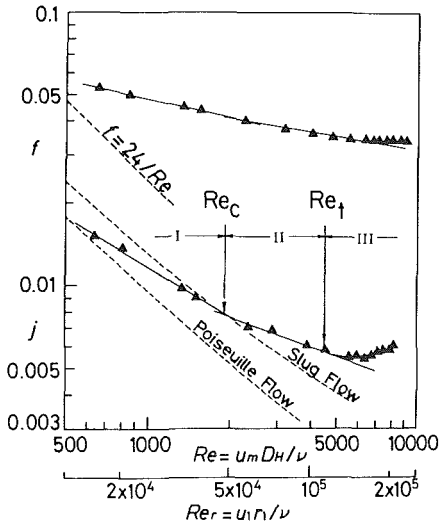

Fig. 2 Three performance enhancements in stationary disk core with $d_2/d_1 = 2.16$ and $s/d_1 = 0.0156$

sition into a turbulent manner. This observation leads to a theory that there exist three mechanisms of performance enhancement in the stationary disk system. It is desirable to verify the theory.

The present work has two major goals: (*i*) to identify the three types of performance enhancement using the results available in [1], and (*ii*) to disclose the flow mechanisms that cause such enhancement, using flow visualization techniques. The critical Reynolds numbers for the transition between the enhancements are determined.

Results and Discussion

The heat transfer system consisted of multiple disks with openings in the center, as shown in Fig. 1. Each disk was made of aluminum 0.5 mm thick with 160-mm i.d. (d_1) and a variable o.d. (d_2). The disk spacing s was varied at 1.5, 2.5, and 3.5 mm, combining with four variations in d_2, namely 240, 280, 310, and 345 mm. A total of 12 cores were tested in various flow regimes. The heat transfer and friction loss performance were obtained in terms of the Colburn factor j and the Fanning friction factor f, respectively [1]. The Reynolds number is defined on the basis of the hydraulic diameter D_H of the flow channels in the core as

$$\mathrm{Re} = u_m D_H/\nu$$

Here, u_m is the air velocity at the midpoint $(d_1 + d_2)/4$ of the test core.

The test results are correlated in terms of f and j versus Re. In the interest of brevity, only one set of representative results for the test core with $d_2/d_1 = 2.16$ and $s/d_1 = 0.0156$ is shown in Fig. 2.[3] A second abscissa for the Reynolds number Re_r used in the other literature is superimposed for convenience. The top broken line represents theoretical prediction of the friction factor for fully developed laminar flow throughout the core. The other broken lines are theoretical results for heat transfer performance for two special velocity patterns (limiting cases), uniform profile, and parabolic profile, under the thermal boundary condition of constant surface temperature. It is disclosed in [5] that the dominating flow pattern in the radial flow passage can be classified into three regimes I, II, and III, according to the magnitude of Reynolds number, as shown in Fig. 3. Laminar flow prevails in regime I, both laminar and periodic flows are evident in regime II, and laminar, periodic, and turbulent flows in sequence are all present in regime III. In a similar fashion, the test data for j and f can be fitted by three line segments representing the three flow regimes, as shown in Fig. 2. Each segment covers a range of the Reynolds numbers and thus is characterized by a distinct flow pattern to cause different performance enhancement. The intersection of two consecutive segments signifies a critical Reynolds number for the onset of a new mechanism for the performance enhancement in the subsequent flow regime. There are two critical Reynolds numbers, namely Re_c between flow regimes I and II, and Re_t between flow regimes II and III.

In regime I, for Re less than Re_c, the flow in the radial passage is laminar from the entrance to the exit. The velocity profile deviates from the limiting case of Poiseuille shape due to two special features of the radial flow [6]:

(*i*) the radius effect which is induced mainly from the increase of flow area, and
(*ii*) the viscous effect which causes pressure to decrease.

This results in an increase of f and j over the Poiseuille flow, referred to as the laminar flow enhancement. When the flow velocity reaches Re_c, separating annular bubbles (i.e., vortices) are generated periodically and alternately (between two channel walls) at a location in the radial channel [5]. These bubbles migrate downstream along the wall surfaces to form a vortex street. The flow downstream from the separation point (where the bubbles are nucleated) becomes pulsating. Since the flow is at a limit-cycle state, the oscillating flow thus induced becomes self-sustained [5]. The performance curves in Fig. 2 change their slope and exhibit an enhancement from those in regime I. This characteristic is termed the "second" laminar flow enhancement, which is credited to the self-sustained flow oscillations induced by the vortex streets.

The critical Reynolds number Re_t marks the transition from laminar to turbulent flow. When the flow reaches Re_t, the vortex-induced oscillating flow becomes over-amplified and develops into a laminar-turbulent transition. A strong mixing motion takes place in the fluid stream, resulting in a further enhancement in the transport performance. In this flow regime III, it is called the transition-turbulent flow enhancement.

Figure 3 is a flow map schematically illustrating the change of flow patterns in the radial passage as functions of the Reynolds number. A reverse transition may occur in the radial passage of parallel circular disks with large outer radius r_2. The present study is limited to the disk assemblies with moderate r_2.

The critical Reynolds numbers, Re_c and Re_t, as determined in Fig. 2 for each test core, are plotted in terms of the dimensionless geometric parameter of the test cores $X^* = L\, d_m/D_H^2$. The results are presented in Fig. 4. L denotes the length of the radial passage, i.e., $L = (d_2 - d_1)/2$. It is seen that the critical Reynolds numbers fall drastically with an increase in X^*, but gradually level off at a high value of X^*.

[3] Other results are available in [1].

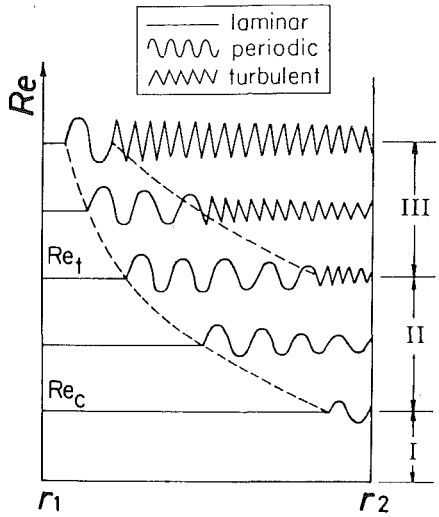

Fig. 3 Flow map for radial flow between stationary parallel disks

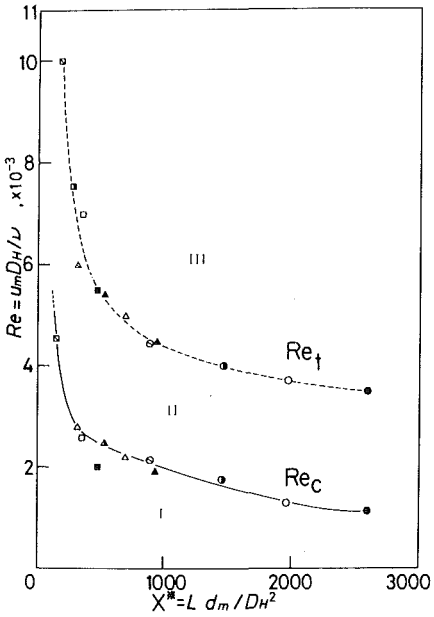

Fig. 4 Critical Reynolds numbers for onset of "second" laminar flow enhancement and transition-turbuelnt flow enhancement

Finite-difference solutions of the unsteady vorticity transport equation for the disk system [5] predict the nucleation, growth, migration, and decay of vortices alternately on both sides of the radial channel walls. Flow visualization by hydrogen bubble generation was performed on the radial flow of water between parallel circular disks with a steady influx from the disk center [5]. One representative result is shown in Fig. 5 for s/d_1 of 0.078. The dimensionless radial distance X in the figure is defined as $(r - r_1)/(s/2)$. In case (a), for the lower Re flow, the flow remains laminar throughout the radial passage. As Re is increased to or beyond a critical value Re_c in case (b), flow separation takes place alternately from both walls at the same radial location, as marked by an arrow. Downstream from the separation point, the free shear layer becomes curled up and stretched for a considerable distance. The double vortices generated periodically and alternately on both walls form a vortex street. As Re is increased to or beyond Re_t, as in case (c), the flow oscillation develop into turbulent flow. The existence of three distinct flow mechanisms is thus confirmed theoretically as well as experimentally. The velocity variations measured by hot-wire

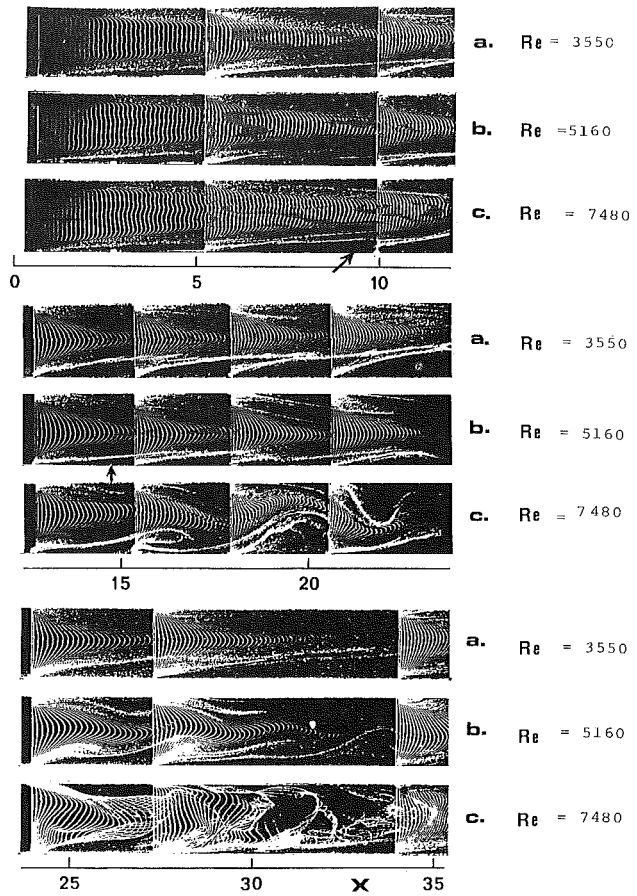

Fig. 5 Flow patterns between stationary parallel disks with s/d_1 = 0.078 and Re_r = 3550, 5160, and 7480

probes for air flow through two stationary parallel disks confirmed that the flow (i.e., vortex formation) is rotationally symmetric in nature [5].

Conclusions

Three types of augmentation in the heat transfer and friction loss performance are confirmed: the laminar flow enhancement due to inertia effects, the "second" laminar flow enhancement caused by the self-sustained vortex-induced oscillating flow, and the transition-turbulent flow enhancement due to mixing motion. Figure 5 determines the critical Reynolds numbers for the onset of flow oscillations and laminar-turbulent flow transition.

Acknowledgments

This study was partially supported by the Japanese Ministry of Education under Grant No. C 1981, and by the U.S. National Science Foundation under Grant No. ME 80-18031.

References

1 Mochizuki, S., Yang, Wen-Jei, Yati, Y., and Ueno, M., "Heat Transfer Mechanisms and Performance in Multiple Parallel Disk Assemblies," ASME JOURNAL OF HEAT TRANSFER, Vol. 105, 1983, pp. 598-604.

2 Owens, J. M., "Fluid Flow and Heat Transfer in Rotating Disk Systems," in: *Heat and Mass Transfer in Rotating Machinery*, D. E. Metzger and N. H. Afgan, eds., Hemisphere, Washington, D.C., 1984, pp. 81-103.

3 Dorfman, L. A., *Hydrodynamic Resistance and Heat Loss of Rotating Solids*, Oliver and Boyd, Edinburgh, U.K., 1963.

4 Greenspan, H. P., *The History of Rotating Fluids*, Cambridge University Press, Cambridge, U.K., 1968.

5 Mochizuki, S., and Yang, Wen-Jei, "Self-sustained Radial Oscillating Flows Between Parallel Disks," *Journal of Fluid Mechanics*, Vol. 154, 1985, pp. 377-397.

6 Sim, Y. S., "A Numerical and Experimental Study on the Flow and Heat Transfer Characteristics in Co-Rotating Disk Systems," Ph.D. Thesis, Mechanical Engineering, University of Michigan, Ann Arbor, MI, 1983.

Mass Transfer From Coaxial Cylinders With Stepwise Changes in Diameter

N. W. M. Ko[1] and P. F. Y. Wong[2]

Nomenclature

d, D = diameters of small and large cylinders, respectively
D_f = mass diffusion coefficient for naphthalene vapor in air
j_D = j factor for mass transfer = $(k_c/U)\mathrm{Sc}^{0.56}$
j_{D_1} = j factor for a two-dimensional cylinder
k_c = mass transfer coefficient based on concentration driving force
m = mass flux of diffusing species
M = molecular weight of diffusing species
p^0 = vapor pressure of diffusing species
r^2 = correlation coefficient
R = universal gas constant
Re = Reynolds number = UD/ν
Sc = Schmidt number = ν/D_f
T = absolute temperature
U = mean exit velocity
ν = kinematic viscosity of air

Introduction

The formation of vortex wakes behind cylindrical structures constitutes one of the sources of severe excitation causing wind-induced vibration, the consequence of which is damage to, or failure of, stacks, bridges, cooling towers, and buildings. Such structures, especially tall buildings, generally have spanwise variations in diameter or changes in cross section, thus resulting in three-dimensional flow situations and in different coupling characteristics between the flow and the structure in question.

The flow across and downstream of coaxial cylinders with varying or stepwise changes of diameter has thus been investigated so that a better understanding of the complicated flow field could be obtained [1–5]. Because of the change in diameter or the discontinuity, three dimensionality was found in both the flow over cylinder surfaces and the flow behind the cylinders. The vortex wakes of the two cylinders and the flow characteristics such as the drag coefficient, the pressure coefficients, and the derived pressure coefficients were also different from those of two-dimensional cylinder. Further, the flow depended on the diameter ratio d/D of the cylinders.

The performance of heat transfer effectiveness of heat exchangers depends on the flow characteristics of the fluid flowing across the cylindrical tube surfaces of the exchanger. Investigations on flow fields associated with coaxial cylinders with varying or stepwise changes in diameter have indicated that the flow might be favorable for conditions of enhanced heat transfer and hence improved heat exchanger design. With the analogy between heat and mass transfer in mind, the object of this preliminary investigation was an attempt to obtain an understanding of the gas phase mass transfer coefficients of the cylinders with stepwise changes in diameter. The coefficients on the large circular cylinder near the discontinuity were determined and are reported. Based on naphthalene sublimation, the effect of the three-dimensional flow and of varying diameter ratio of the cylinders on mass transfer will be assessed.

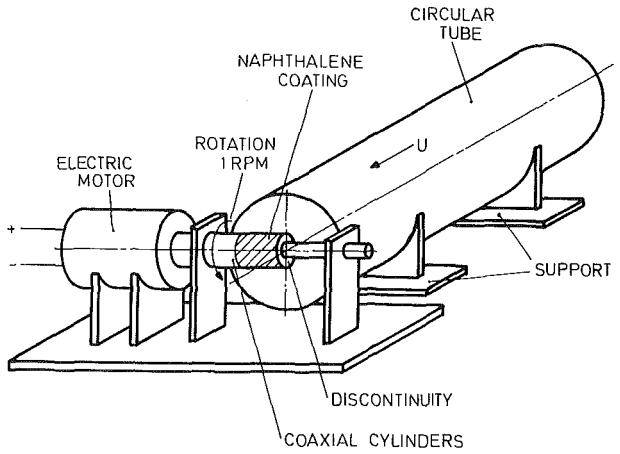

Fig. 1 Schematic diagram of apparatus

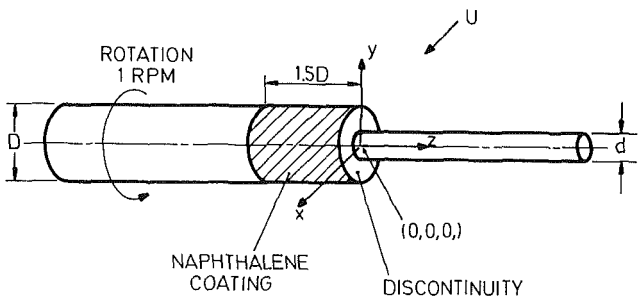

Fig. 2 Schematic diagram of coaxial cylinders

Experimental Apparatus and Measurement Technique

The experimental apparatus is shown diagrammatically in Fig. 1. The configuration of the cylinders is shown in Fig. 2. Tests on six coaxial cylinders of diameter ratio d/D from 0.25 to 0.88 were carried out. The diameter of the large cylinder D was fixed at 12.7 mm while the diameter of the small cylinder d varied. A two-dimensional cylinder and a finite cylinder of 12.7 mm diameter were also tested. Naphthalene was applied only to the large cylinder. The coating had a spanwise length of 1.5 D and extended from the plane of discontinuity. The naphthalene coating was machined to the exact diameter before it was mounted at the exit of a circular tube of 76 mm diameter. Turbulent flow with its uniform mean velocity profile was achieved at the exit. The gas flow was obtained from a central compressed air supply, and after flowing through the conduit in the laboratory and the apparatus, the gas reaching the cylinders was essentially at ambient temperature and thus the temperature of the cylinders. This was confirmed by measuring the air temperature just upstream of the cylinders. The plane of discontinuity of the coaxial cylinders coincided with the axis of the tube. The range of mean velocities U inside the tube varied from 4 to 20 m/s. The Reynolds number Re_D varied from about 3×10^3 to 1.5×10^4 and was within the subcritical regime of cylindrical flow.

During testing the coaxial cylinders were rotated by an electrical motor at 1 rpm. This ensured that geometric symmetry was retained during each run while not significantly affecting the mass transfer rate. The initial and final weight of naphthalene at the end of 30 min sublimation were measured by an electronic balance.

The mass transfer presented represents the overall value of the large cylinder over the 1.5 D spanwise length from the

[1]Reader, Department of Mechanical Engineering, University of Hong Kong, Hong Kong; Mem. ASME.
[2]Senior Lecturer, Department of Mechanical Engineering, University of Hong Kong, Hong Kong.
Contributed by the Heat Transfer for publication in the JOURNAL OF HEAT TRANSFER. Manuscript received by the Heat Transfer Division April 29, 1985.

Table 1 Values of A and B for equation (3)

d/D	A	B	r^2
1	0.352	-0.486	0.98
0.88	0.448	-0.527	0.97
0.75	0.296	-0.483	0.94
0.63	1.413	-0.580	0.97
0.5	0.752	-0.539	0.98
0.38	0.757	-0.554	0.97
0.25	0.759	-0.536	0.92
0	0.815	-0.542	0.95

discontinuity. In this preliminary study no attempt was made to measure the local mass transfer.

Results

Assuming equilibrium conditions at the interface, the partial pressure at the cylinder surface is given by the vapor pressure of the naphthalene, which was determined in mm Hg from the correlations [6] for temperatures 7°C to 20°C

$$\log p^0 = 11.597 - 3783/T \tag{1}$$

and for temperatures between 20°C and 70°C

$$\log p^0 = 11.626 - 3785/T \tag{2}$$

The temperature of the air stream was used for determining both the vapor pressure and the diffusion coefficient of naphthalene. According to Sogin [7], at the temperatures involved, the temperature difference between the air stream and the cylinders should be less than 0.1°C and no significant error is introduced by considering cylinder and air temperatures equal.

Assuming that the naphthalene vapor behaves as an ideal gas, the interfacial mass concentration is given by RT/Mp^0, where p^0 is in appropriate units.

Further assuming that the naphthalene concentration in the air stream is zero, the mass transfer coefficient based on concentration driving forces becomes

$$k_c = \frac{mRT}{Mp^0} \tag{3}$$

where the mass flux m is determined from the weight loss of the cylinders. The j_D factor for mass transfer defined by

$$j_D = \left(\frac{k_c}{U}\right)\mathrm{Sc}^{0.5} \tag{4}$$

is frequently used to correlate mass transfer experimental data and is a function of the Reynolds number [8].

The results for mass transfer in the two-dimensional cylinder are shown in Fig. 3 and are well correlated by

$$j_{D_1} = 0.352\ \mathrm{Re}_D^{-0.486} \tag{5}$$

The results for mass transfer of coaxial cylinders of different diameter ratio and of finite cylinder are also shown in Fig. 3. They are also well correlated by an equation of the form

$$j_D = A\ \mathrm{Re}_D^B \tag{6}$$

The values of A and B and the correlation coefficients for all sets of runs are given in Table 1, and good correlation of the results is shown. The results shown in Fig. 3 indicate that j_D of the coaxial cylinder is higher than that of the two-dimensional for $d/D < 0.75$ and smaller for $0.75 \le d/D \le 1$.

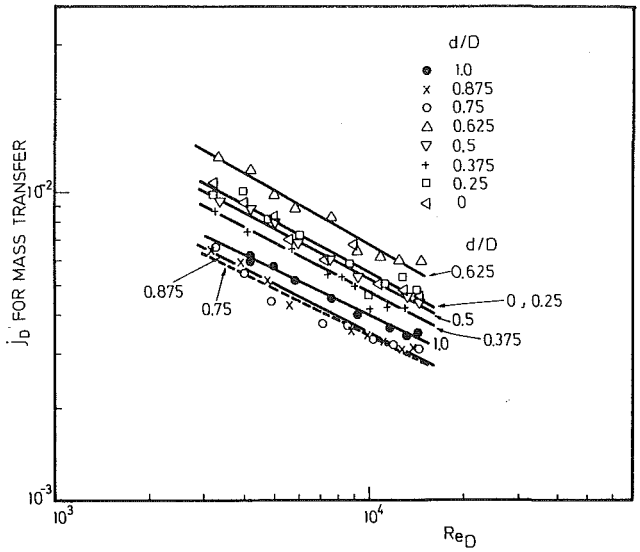

Fig. 3 Mass transfer of coaxial cylinders

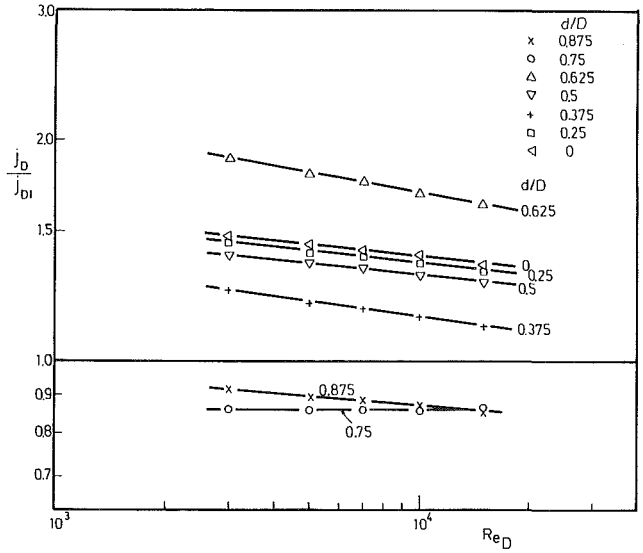

Fig. 4 Mass transfer ratios of coaxial cylinders

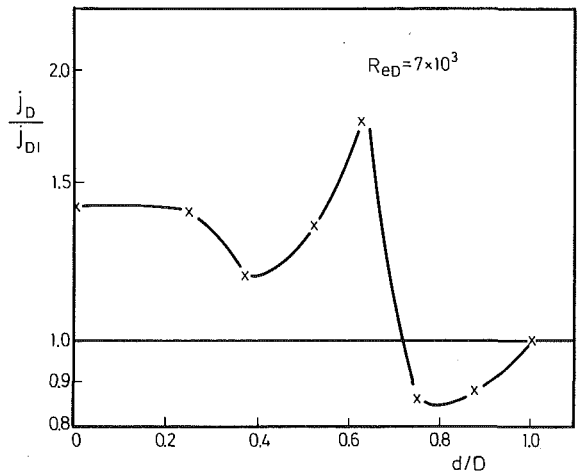

Fig. 5 Mass transfer ratios with diameter ratio; $\mathrm{Re}_D = 7 \times 10^3$

By presenting the mass transfer in the ratio j_D/j_{D_1}, the results of different coaxial cylinders and of the finite cylinder are only slightly dependent on Reynolds number Re_D (Fig. 4). Since the slopes of the ratios are nearly the same, j_D/j_{D_1} is mainly a function of the diameter ratio d/D (Fig. 5). It varies from a maximum ratio of about 1.8 at $d/D = 0.625$ to a minimum of 0.86 at $d/D = 0.8$. This means that enhancement of mass transfer of the coaxial cylinders at $d/D < 0.7$ and suppression at $0.75 \leq d/D < 1$ are found.

References

1 Niemann, H. J., "Zur stationaren Winddelastung rotationssymmetrischer Bauwerke im Bereich transkritischer Reynoldszahlen," Mitteilung Nr. 71-2, Institut fur Konstruktiven Ingenieurbau, Ruhr-Universitat Bochum, 1971.

2 Maumann, A., and Quadflieg, H., "Vortex Generation on Cylindrical Buildings and Its Simulation in Wind Tunnels," *Proceedings of International Union of Theoretical and Applied Mechanics/International Association for Hydraulic Research Symposium*, Karlsruhe, 1972, pp. 730–747.

3 Ko, N. W. M., Leung, W. L., and Au, H., "Flow Behind Two Coaxial Circular Cylinders," ASME *Journal of Fluids Engineering*, Vol. 104, 1982, pp. 223–227.

4 Ko, N. W. M., and Chan, A. S. K., "Pressure Distributions on Circular Cylinders With Stepwise Change of the Diameter," ASME Paper No. 84-WA/FE-13.

5 Yagita, M., Kojima, Y., and Matsuzaki, K., "On Vortex Shedding From Circular Cylinder With Step," *Bulletin of Japanese Society of Mechanical Engineers*, Vol. 27, 1984, pp. 426–431.

6 Preston, K., "The Properties of Naphthalene," *The Coal Tar Research Association*, Intelligence Section, 1958, Report No. 0192.

7 Sogin, H. H., "Sublimation From Disks to Air Streams Flowing Normal to Their Surfaces," *Trans. ASME*, Vol. 80, 1958, pp. 61–69.

8 Treybal, R. E., *Mass Transfer Operations*, McGraw-Hill, New York, 1955.

A General Correlation for Natural Convection in Liquid-Saturated Beds of Spheres

D. J. Close[1]

Nomenclature

A_{uv} = surface area per unit volume in packed bed, m^2/m^3
a_0–a_5 = constants in equation (10)
C_0 = Kozeney–Carman constant
C_p = specific heat of fluid, $J \cdot kg^{-1} \cdot K^{-1}$
d_p = sphere diameter, m
f = number of degrees of freedom
g = gravitational acceleration, $m \cdot s^{-2}$
H = height of packing, m
h_c = heat transfer coefficient, fluid to packing, $W \cdot m^{-2} \cdot K^{-1}$
j = Colburn number
k = $(\dot{Q}H/L\Delta T)$ = effective conductivity of convecting porous medium, $W \cdot m^{-1} \cdot K^{-1}$
k_f = conductivity of fluid, $W \cdot m^{-1} \cdot K^{-1}$
k_s = conductivity of packing material, $W \cdot m^{-1} \cdot K^{-1}$
k^* = conductivity of stagnant porous medium, $W \cdot m^{-1} \cdot K^{-1}$
k_f^* = "fluid" conductivity of porous medium, $W \cdot m^{-1} \cdot K^{-1}$
k_s^* = "solid" conductivity of porous medium, $W \cdot m^{-1} \cdot K^{-1}$
L = convection cell dimension in horizontal direction, m
Nu = $h_c d_p/k_f$ = Nusselt number
Nu* = k/k^* = Nusselt number for porous medium
Nu_i^* = Nusselt number defined in equation (11)
P_1–P_4 = dimensionless groups
Pr = $C_p\mu/k_f$ = Prandtl number
n = number of experimental points
Q_1–Q_6 = dimensionless groups
$\dot{Q}$ = heat flow rate through porous medium per unit width, $W \cdot m^{-1}$
Ra_f = $g\beta(\rho^2 C_p/\mu)(d_p^3/k_f)\Delta T$
Ra* = $g\,\beta(\rho^2 C_p/\mu)(\kappa/k^*)\Delta T\,H$
Ra_c^* = critical Rayleigh number
$Ra_{c,s}^*$ = critical Rayleigh number for convective mode s
Re_p = $\rho v d_p/\mu$ = Reynolds number
s = number of convective mode
T = temperature, K
T_f = fluid temperature, K
T_s = temperature of packing, K
T_1 = cold surface temperature, K
T_2 = hot surface temperature, K
T_f' = $(T_f - T_1)/\Delta T$
T_s' = $(T_s - T_1)/\Delta T$
u = fluid velocity in x direction, $m \cdot s^{-1}$
u' = $\rho C_p H u/k_f^*$
v = fluid velocity, $m \cdot s^{-1}$
w = fluid velocity in z direction, $m \cdot s^{-1}$
w' = $\rho C_p L w/k_f^*$
x = horizontal coordinate, m
x' = x/L
x_i = value of Nu* predicted from equation (11)
x_j = measured value of Nu*
z = vertical coordinate, m
z' = z/H
β = coefficient of volumetric expansion, K^{-1}
ΔT = $T_2 - T_1$, K
ϵ = void fraction
κ = permeability, m^2
μ = fluid viscosity, $N \cdot s \cdot m^{-2}$
ρ = fluid density, $kg \cdot m^{-3}$
σ_r = residual standard deviation
ψ = stream function: $u' = \partial\psi/\partial z'$, $w' = -\partial\psi/\partial x'$

Introduction

A well-established model for natural convection in porous media (for example in [1]) is based on the set of equations derived from conservation of energy and momentum

$$k^*\left(\frac{\partial^2 T}{\partial x^2} + \frac{\partial^2 T}{\partial z^2}\right) = \rho C_p\left(u\frac{\partial T}{\partial x} + w\frac{\partial T}{\partial z}\right) \quad (1)$$

$$-\frac{\mu}{\kappa}\frac{\partial u}{\partial z} - g\beta\rho\frac{\partial T}{\partial x} + \frac{\mu}{\kappa}\frac{\partial w}{\partial x} = 0 \quad (2)$$

Two important assumptions are (*i*) the bed material and adjacent fluid are equal in temperature, and (*ii*) an effective bed conductivity k^*, that measured under stagnant conditions, can be used. The validity of this model is well established near the critical Rayleigh number, by the data of Katto and Matsuoka [2] for a porous bed bounded by two isothermal and horizontal planes.

Recently, Somerton [3] has argued that the neglect of the inertial terms in the momentum equation is the prime deficiency in the model. It will be shown later that his results can equally well be used to support the contention that (*i*) and (*ii*) above are the critical assumptions. Prasad et al. [4] modify equations (1) and (2) by postulating an effective bed conductivity under convecting conditions. This procedure is quite successful in recorrelating their own and other data but unfortunately a fundamental mechanism for the effective conductivity is not presented.

When vigorous convection occurs the model clearly has serious flaws, as shown by the analyses of Combarnous and Bories [1], and later Chan and Banerjee [5]. The former postulated a finite and constant heat transfer coefficient be-

[1]Division of Energy Technology, Commonwealth Scientific and Industrial Research Organization, Highett, Victoria, Australia.

Contributed by the Heat Transfer Division for publication in the JOURNAL OF HEAT TRANSFER. Manuscript received by the Heat Transfer Division May 13, 1985.

By presenting the mass transfer in the ratio j_D/j_{D_1}, the results of different coaxial cylinders and of the finite cylinder are only slightly dependent on Reynolds number Re_D (Fig. 4). Since the slopes of the ratios are nearly the same, j_D/j_{D_1} is mainly a function of the diameter ratio d/D (Fig. 5). It varies from a maximum ratio of about 1.8 at $d/D = 0.625$ to a minimum of 0.86 at $d/D = 0.8$. This means that enhancement of mass transfer of the coaxial cylinders at $d/D < 0.7$ and suppression at $0.75 \leq d/D < 1$ are found.

References

1 Niemann, H. J., "Zur stationaren Winddelastung rotationssymmetrischer Bauwerke im Bereich transkritischer Reynoldszahlen," Mitteilung Nr. 71-2, Institut fur Konstruktiven Ingenieurbau, Ruhr-Universitat Bochum, 1971.

2 Maumann, A., and Quadflieg, H., "Vortex Generation on Cylindrical Buildings and Its Simulation in Wind Tunnels," *Proceedings of International Union of Theoretical and Applied Mechanics/International Association for Hydraulic Research Symposium*, Karlsruhe, 1972, pp. 730–747.

3 Ko, N. W. M., Leung, W. L., and Au, H., "Flow Behind Two Coaxial Circular Cylinders," ASME *Journal of Fluids Engineering*, Vol. 104, 1982, pp. 223–227.

4 Ko, N. W. M., and Chan, A. S. K., "Pressure Distributions on Circular Cylinders With Stepwise Change of the Diameter," ASME Paper No. 84-WA/FE-13.

5 Yagita, M., Kojima, Y., and Matsuzaki, K., "On Vortex Shedding From Circular Cylinder With Step," *Bulletin of Japanese Society of Mechanical Engineers*, Vol. 27, 1984, pp. 426–431.

6 Preston, K., "The Properties of Naphthalene," *The Coal Tar Research Association*, Intelligence Section, 1958, Report No. 0192.

7 Sogin, H. H., "Sublimation From Disks to Air Streams Flowing Normal to Their Surfaces," *Trans. ASME*, Vol. 80, 1958, pp. 61–69.

8 Treybal, R. E., *Mass Transfer Operations*, McGraw-Hill, New York, 1955.

A General Correlation for Natural Convection in Liquid-Saturated Beds of Spheres

D. J. Close[1]

Nomenclature

A_{uv} = surface area per unit volume in packed bed, m^2/m^3
a_0–a_5 = constants in equation (10)
C_0 = Kozeney–Carman constant
C_p = specific heat of fluid, $J \cdot kg^{-1} \cdot K^{-1}$
d_p = sphere diameter, m
f = number of degrees of freedom
g = gravitational acceleration, $m \cdot s^{-2}$
H = height of packing, m
h_c = heat transfer coefficient, fluid to packing, $W \cdot m^{-2} \cdot K^{-1}$
j = Colburn number
k = $(\dot{Q}H/L\Delta T)$ = effective conductivity of convecting porous medium, $W \cdot m^{-1} \cdot K^{-1}$
k_f = conductivity of fluid, $W \cdot m^{-1} \cdot K^{-1}$
k_s = conductivity of packing material, $W \cdot m^{-1} \cdot K^{-1}$
k^* = conductivity of stagnant porous medium, $W \cdot m^{-1} \cdot K^{-1}$
k_f^* = "fluid" conductivity of porous medium, $W \cdot m^{-1} \cdot K^{-1}$
k_s^* = "solid" conductivity of porous medium, $W \cdot m^{-1} \cdot K^{-1}$
L = convection cell dimension in horizontal direction, m
Nu = $h_c d_p/k_f$ = Nusselt number
Nu* = k/k^* = Nusselt number for porous medium
Nu_i^* = Nusselt number defined in equation (11)
P_1–P_4 = dimensionless groups
Pr = $C_p\mu/k_f$ = Prandtl number
n = number of experimental points
Q_1–Q_6 = dimensionless groups
$\dot{Q}$ = heat flow rate through porous medium per unit width, $W \cdot m^{-1}$
Ra_f = $g\beta(\rho^2 C_p/\mu)(d_p^3/k_f)\Delta T$
Ra* = $g\,\beta(\rho^2 C_p/\mu)(\kappa/k^*)\Delta T\,H$
Ra_c^* = critical Rayleigh number
$Ra_{c,s}^*$ = critical Rayleigh number for convective mode s
Re_p = $\rho v d_p/\mu$ = Reynolds number
s = number of convective mode
T = temperature, K
T_f = fluid temperature, K
T_s = temperature of packing, K
T_1 = cold surface temperature, K
T_2 = hot surface temperature, K
T_f' = $(T_f - T_1)/\Delta T$
T_s' = $(T_s - T_1)/\Delta T$
u = fluid velocity in x direction, $m \cdot s^{-1}$
u' = $\rho C_p H u/k_f^*$
v = fluid velocity, $m \cdot s^{-1}$
w = fluid velocity in z direction, $m \cdot s^{-1}$
w' = $\rho C_p L w/k_f^*$
x = horizontal coordinate, m
x' = x/L
x_i = value of Nu* predicted from equation (11)
x_j = measured value of Nu*
z = vertical coordinate, m
z' = z/H
β = coefficient of volumetric expansion, K^{-1}
ΔT = $T_2 - T_1$, K
ϵ = void fraction
κ = permeability, m^2
μ = fluid viscosity, $N \cdot s \cdot m^{-2}$
ρ = fluid density, $kg \cdot m^{-3}$
σ_r = residual standard deviation
ψ = stream function: $u' = \partial\psi/\partial z'$, $w' = -\partial\psi/\partial x'$

Introduction

A well-established model for natural convection in porous media (for example in [1]) is based on the set of equations derived from conservation of energy and momentum

$$k^*\left(\frac{\partial^2 T}{\partial x^2} + \frac{\partial^2 T}{\partial z^2}\right) = \rho C_p\left(u\frac{\partial T}{\partial x} + w\frac{\partial T}{\partial z}\right) \quad (1)$$

$$-\frac{\mu}{\kappa}\frac{\partial u}{\partial z} - g\beta\rho\frac{\partial T}{\partial x} + \frac{\mu}{\kappa}\frac{\partial w}{\partial x} = 0 \quad (2)$$

Two important assumptions are (*i*) the bed material and adjacent fluid are equal in temperature, and (*ii*) an effective bed conductivity k^*, that measured under stagnant conditions, can be used. The validity of this model is well established near the critical Rayleigh number, by the data of Katto and Matsuoka [2] for a porous bed bounded by two isothermal and horizontal planes.

Recently, Somerton [3] has argued that the neglect of the inertial terms in the momentum equation is the prime deficiency in the model. It will be shown later that his results can equally well be used to support the contention that (*i*) and (*ii*) above are the critical assumptions. Prasad et al. [4] modify equations (1) and (2) by postulating an effective bed conductivity under convecting conditions. This procedure is quite successful in recorrelating their own and other data but unfortunately a fundamental mechanism for the effective conductivity is not presented.

When vigorous convection occurs the model clearly has serious flaws, as shown by the analyses of Combarnous and Bories [1], and later Chan and Banerjee [5]. The former postulated a finite and constant heat transfer coefficient be-

[1]Division of Energy Technology, Commonwealth Scientific and Industrial Research Organization, Highett, Victoria, Australia.

Contributed by the Heat Transfer Division for publication in the JOURNAL OF HEAT TRANSFER. Manuscript received by the Heat Transfer Division May 13, 1985.

tween fluid and solid, and individual thermal conductivities assigned to the fluid and solid. Numerical solutions for the resulting equations showed significant effects due to both the heat transfer coefficient and to the ratio of "fluid" and "solid" thermal conductivities. Chan and Banerjee have improved the model by relating the local Colburn number, describing fluid to packing heat transfer coefficient, to the local Reynolds number via a relation of the form $j = A\ \mathrm{Re}_p^b$. They also introduce effective solid and fluid conductivities but no description of how to obtain these is given. Comparisons between calculations made by them and some Nu* versus Ra* measurements by Combarnous [6] show good agreement. In this paper, parameters derived from equations which include a fluid to solid heat transfer mechanism and a more complete description of the bed conduction are derived. A parametric equation is then fitted to data from Combarnous [6], Buretta [7], and Schneider [8].

Derivation of Parameters

From the equations in Combarnous and Bories [1], and for steady state, energy conservation yields

$$h_c A_{uv}(T_f - T_s) + k_s^*\left(\frac{\partial^2 T_s}{\partial x^2} + \frac{\partial^2 T_s}{\partial z^2}\right) = 0 \tag{3}$$

$$\rho C_p u\frac{\partial T_f}{\partial x} + \rho C_p w\frac{\partial T_f}{\partial z} = h_c A_{uv}(T_s - T_f) + k_f^*\left(\frac{\partial^2 T_f}{\partial x^2} + \frac{\partial^2 T_f}{\partial z^2}\right) \tag{4}$$

Introducing a stream function ψ into (2) and nondimensionalizing it and (3) and (4) yields dimensionless parameters

$$P_1 = \frac{H}{L} \qquad P_2 = \frac{h_c A_{uv} H^2}{k_s^*}$$

$$P_3 = \frac{h_c A_{uv} H^2}{k_f^*} \qquad P_4 = g\beta\frac{\rho^2 C_p}{\mu}\frac{\kappa}{k_f^*}\Delta T\, H$$

Conductivities k_s^* and k_f^* can be estimated using the model of Yagi and Kunii [9]. Using their relationships and also correlations in Yagi et al. [10], for liquid-filled beds

$$\frac{k^*}{k_f} = \epsilon + \frac{\alpha(1-\epsilon)}{\phi + \gamma\dfrac{k_f}{k_s}} \tag{5}$$

The factors α, ϕ, and γ are respectively a geometry factor, a description of the effective thickness of the liquid film, and an effective thickness of the solid.

From (5)

$$k^* = k_f^* + k_s^*, \text{ with } k_f^* = \epsilon k_f \text{ and } k_s^* = \frac{\alpha(1-\epsilon)}{\dfrac{\phi}{k_f} + \dfrac{\gamma}{k_s}} \tag{6}$$

The appearance of k_f in k_s^* is due to the model proposing a fluid film between particles. Yagi and Kunii argue that the resistance of this film is unaffected by fluid flow, and consequently the model described above can be used for nonstagnant conditions. Dispersion is normally assumed a function of Re_p, a parameter which will appear elsewhere. Otherwise α and γ are normally taken as constants and $\phi = \phi(k_s/k_f)$.

A well-established relation for heat transfer in packed beds is Nu = Nu(Re_p, Pr) [11]. For beds of spheres, it is also well established (see for example [12]) that when the Darcy equation applies

$$\kappa = \frac{\epsilon^3 d_p^{\,2}}{(1-\epsilon)^2 C_0} \tag{7}$$

where C_0 is the Kozeney–Carman constant. Also

$$A_{uv} = \frac{6(1-\epsilon)}{d_p} \tag{8}$$

With the local velocity, $v = \sqrt{(u^2 + w^2)}$ and using v/ϵ in Re_p, rather than v

$$\mathrm{Re}_p' = \frac{d_p}{H}\frac{k_f}{C_p\mu}\left[\mu'^2 + \left(w'\frac{H}{L}\right)^2\right]^{1/2} \tag{9}$$

Then P_1–P_4 can be modified to give a new parameter set

$$Q_1 = \frac{H}{L} \qquad Q_2 = \frac{H}{d_p} \qquad Q_3 = \frac{k_f}{k_s}$$

$$Q_4 = \frac{C_p\mu}{k_f} \equiv \mathrm{Pr} \qquad Q_5 = \frac{\epsilon}{1-\epsilon}$$

$$Q_6 = g\,\beta\,\frac{\rho^2 C_p}{\mu}\frac{d_p^3}{k_f}\Delta T \equiv \mathrm{Ra}_f$$

The redefined Rayleigh number could be defined in terms of H^3 rather than d_p^3, by combining with Q_2. The independent variable is customarily $\mathrm{Nu}^* = k/k^*$. While there may be some argument for using k_s^* or k_f^* in the definition of Nu*, using k^* ensures that Nu* is 1 for Ra_f less than critical.

Correlation of Data

A correlating equation of the form

$$\frac{\mathrm{Nu}^*}{\mathrm{Nu}_i^*} = a_0\mathrm{Ra}_f^{a_1}\left(\frac{k_f}{k_s}\right)^{a_2}\left(\frac{H}{d_p}\right)^{a_3}\left(\frac{\epsilon}{1-\epsilon}\right)^{a_4}\mathrm{Pr}^{a_5} \tag{10}$$

has been assumed. The parameter H/L has been neglected on the grounds that for the experiments used, the horizontal dimensions of the test cells were relatively large in comparison with the height.

Data from Combarnous [6], Buretta [7], and Schneider [8] were chosen since sufficient other properties were given by them. In some cases, particularly the conductivities of steel and glass, inferences had to be made from other sources, and when the bed packing was not uniform in diameter, the mean diameter was chosen. From the data of Schneider, there was some indication that for H/d_p below 8, additional effects are introduced. All experiments at these low values were excluded.

The power integral method for these boundary conditions and geometry and with $T_s = T_f$ yields (see, for example, [1])

$$\mathrm{Nu}_i^* = 1 + \sum_1^s 2\left(1 - \frac{\mathrm{Ra}_{c,s}^*}{\mathrm{Ra}^*}\right), \text{ and } \mathrm{Ra}_{c,s}^* = 4(s\pi)^2,\ s = 1, 2, \ldots \tag{11}$$

The unknowns in equation (10) above, a_0–a_5, were determined from a least-squares analysis of the experimental data. Owing to the variable number of points recorded in each experiment, four points, chosen to cover the experimental range, were used except in *C*14 and *S*7 where only three points were recorded. In all cases, values of k_f, Pr, C_p, and μ corresponding to the experimental point were used.

Results

From the least-squares fit

$$\frac{\mathrm{Nu}^*}{\mathrm{Nu}_i^*} = 1.572\times10^{-2}\times\mathrm{Ra}_f^{0.344}\left(\frac{k_f}{k_s}\right)^{0.227}\left(\frac{H}{d_p}\right)^{0.446}\left(\frac{\epsilon}{1-\epsilon}\right)^{0.996}\mathrm{Pr}^{0.279} \tag{12}$$

Graphs showing the comparison between equation (12) and the data (Fig. 1) indicate very good agreement with the exception of those cases where the Nusselt number is above 10 (particularly *B*3), and for *C*11. In the case of *C*11, Combarnous quotes the largest discrepancy of all his runs between κ/k^* determined by two separate methods. Hence some doubt exists as to the validity of the data.

The residual standard deviation defined as

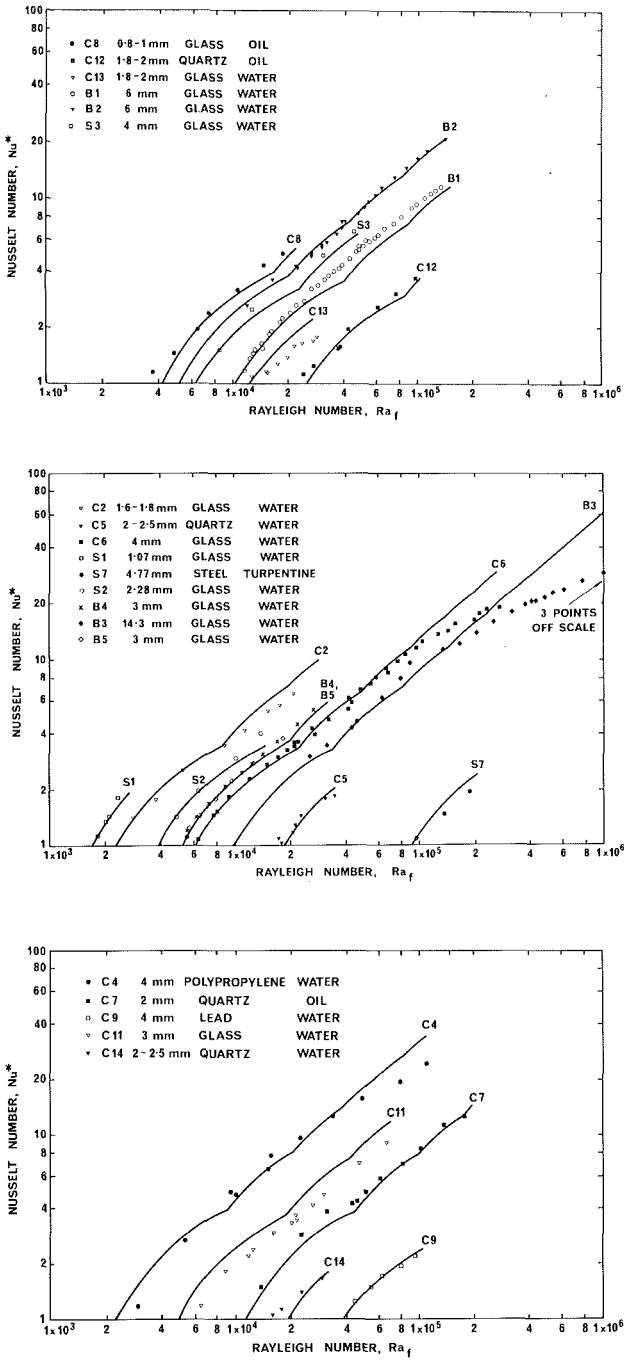

Fig. 1 Graphs showing comparison between data points and correlating equation (12): (C) Combarnous, (B) Buretta, (S) Schneider

$$\sigma_r = \left[\frac{\sum (x_i - x_j)^2}{n-f}\right]^{1/2}$$

was calculated for all measured points and found to be 6.44, mainly due to the points above Nu* of 10 and in particular by experiment *B*3. σ_r with points from *B*3 deleted is 1.11, and for all points below Nu* of 10, is 0.424. The latter value supports the very good agreement observed in the figures.

One obvious possibility for departures above Nu* of 10 alluded to by Somerton [3] and Prasad et al. [4] is that the pressure gradients within the bed are inadequately described by the Darcy equation. Reconciliation between the Darcy and the well-known Ergun equation is only possible at very low values of Re_p, and hence of Ra*. Since no new parameters are introduced if the complete form of the Ergun equation is used an alternative approach would be to perform a separate correlation for data points above what Prasad et al. refer to as the branching points. That is above values of Ra* or Ra_f where the Darcy equation appears to break down. More data are required to carry out such a correlation.

Conclusions

The satisfactory agreement between the data and the correlating function for $Nu^* < 10$ supports the mechanistic description of the processes in packed beds with natural convection, presented by Chan and Banerjee and in this paper. Inadequacies for higher values of Nu* and the corresponding values of Ra_f can be qualitatively explained by deficiencies in the Darcy equation. The introduction by Somerton of a modified Prandtl number $C_p\mu/k^*$, and its apparent success in correlating experimental data, can be explained by equation (12). The product of the terms containing k_f/k_s and Pr almost eliminates k_f as the exponents on the terms are similar. Hence to argue, as does Somerton, that the use of the modified Prandtl number supports the contention that neglect of inertial terms rather than of finite rate coefficients causes scatter in the Nu* versus Ra* experimental data is not necessarily correct. It is more likely that neglect of both causes these discrepancies.

References

1 Combarnous, M. A., and Bories, S. A., "Hydrothermal Convection in Saturated Porous Media," *Advances in Hydroscience*, Vol. 10, 1975, pp. 231-307.

2 Katto, Y., and Matsuoka, T., "Criterion for Onset of Convective Flow in a Fluid in a Porous Medium," *Int. J. Heat Mass Transfer*, Vol. 10, 1967, pp. 297-309.

3 Somerton, C. W., "The Prandtl Number Effect in Porous Layer Convection," *Applied Science Research*, Vol. 40, 1983, pp. 333-344.

4 Prasad, V., Kulacki, F. A., and Keyhani, M., "Natural Convection in Porous Media," *J. Fluid Mech.*, Vol. 150, 1985, pp. 89-119.

5 Chan, Y. T., and Banerjee, S., "Analysis of Transient Three-Dimensional Natural Convection in Porous Media," ASME JOURNAL OF HEAT TRANSFER, Vol. 103, 1981, pp. 242-248.

6 Cambarnous, M., "Convection Naturelle et Convection Mixte en Milieu Poreux," Thesis, University of Paris, 1970.

7 Buretta, R. A., "Thermal Convection in a Fluid Filled Porous Layer With Uniform Internal Heat Sources," Ph.D. Thesis, University of Minnesota, Aug. 1972.

8 Schneider, K. J., "Die Warmeleitfahigkeit korniger Stoffe und ihre Beeinflussung durch freie Konvektion," Thesis, University of Karlsruhe, 1963.

9 Yagi, S., and Kunii, D., "Studies on Effective Thermal Conductivities in Packed Beds," *J. Am. Inst. Chem. Engrs.*, Vol. 3, 1957, pp. 373-381.

10 Yagi, S., Kunii, D., and Wakao, N., "Radially Effective Thermal Conductivities in Packed Beds," *International Developments in Heat Transfer*, 1961, pp. 742-749.

11 Barker, J. J., "Heat Transfer in Packed Beds," *Ind. Eng. Chem.*, Vol. 57, 1965, pp. 43-51.

12 Wyllie, M. J. R., and Gregory, A. R., "Fluid Flow Through Unconsolidated Porous Aggregates," *Ind. and Engng. Chem.*, Vol. 47, 1955, pp. 1379-1388.

Simultaneous Radiation and Forced Convection in Thermally Developing Turbulent Flow Through a Parallel-Plate Channel

Y. Yener[1] and M. N. Özişik[2]

Introduction

Most of the work on the interaction of radiation with turbulent forced convection inside ducts is concerned either with

[1]Mechanical Engineering Department, Northeastern University, Boston, MA 02115.

[2]Mechanical and Aerospace Engineering Department, North Carolina State University, Raleigh, NC 27695, Fellow ASME.

Contributed by the Heat Transfer Division for publication in the JOURNAL OF HEAT TRANSFER. Manuscript received by the Heat Transfer Division January 14, 1985.

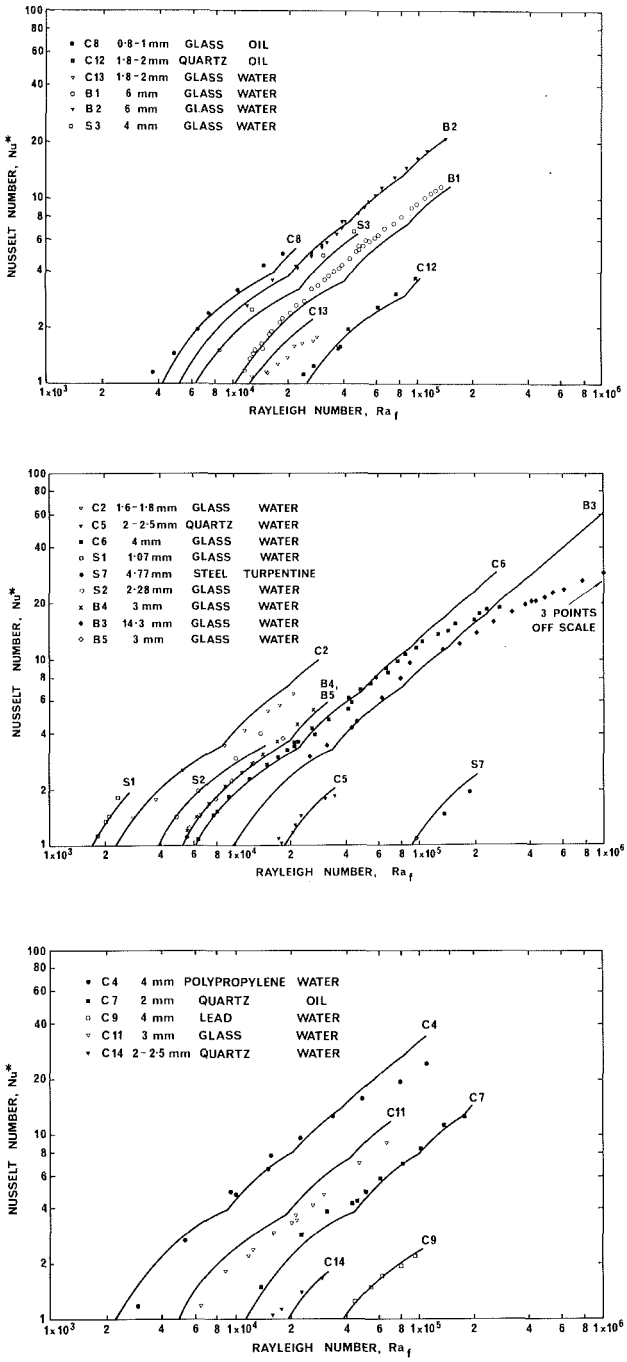

Fig. 1 Graphs showing comparison between data points and correlating equation (12): (C) Combarnous, (B) Buretta, (S) Schneider

$$\sigma_r = \left[\frac{\sum (x_i - x_j)^2}{n-f}\right]^{1/2}$$

was calculated for all measured points and found to be 6.44, mainly due to the points above Nu* of 10 and in particular by experiment *B*3. σ_r with points from *B*3 deleted is 1.11, and for all points below Nu* of 10, is 0.424. The latter value supports the very good agreement observed in the figures.

One obvious possibility for departures above Nu* of 10 alluded to by Somerton [3] and Prasad et al. [4] is that the pressure gradients within the bed are inadequately described by the Darcy equation. Reconciliation between the Darcy and the well-known Ergun equation is only possible at very low values of Re_p, and hence of Ra*. Since no new parameters are introduced if the complete form of the Ergun equation is used an alternative approach would be to perform a separate correlation for data points above what Prasad et al. refer to as the branching points. That is above values of Ra* or Ra_f where the Darcy equation appears to break down. More data are required to carry out such a correlation.

Conclusions

The satisfactory agreement between the data and the correlating function for $Nu^* < 10$ supports the mechanistic description of the processes in packed beds with natural convection, presented by Chan and Banerjee and in this paper. Inadequacies for higher values of Nu* and the corresponding values of Ra_f can be qualitatively explained by deficiencies in the Darcy equation. The introduction by Somerton of a modified Prandtl number $C_p\mu/k^*$, and its apparent success in correlating experimental data, can be explained by equation (12). The product of the terms containing k_f/k_s and Pr almost eliminates k_f as the exponents on the terms are similar. Hence to argue, as does Somerton, that the use of the modified Prandtl number supports the contention that neglect of inertial terms rather than of finite rate coefficients causes scatter in the Nu* versus Ra* experimental data is not necessarily correct. It is more likely that neglect of both causes these discrepancies.

References

1 Combarnous, M. A., and Bories, S. A., "Hydrothermal Convection in Saturated Porous Media," *Advances in Hydroscience*, Vol. 10, 1975, pp. 231-307.

2 Katto, Y., and Matsuoka, T., "Criterion for Onset of Convective Flow in a Fluid in a Porous Medium," *Int. J. Heat Mass Transfer*, Vol. 10, 1967, pp. 297-309.

3 Somerton, C. W., "The Prandtl Number Effect in Porous Layer Convection," *Applied Science Research*, Vol. 40, 1983, pp. 333-344.

4 Prasad, V., Kulacki, F. A., and Keyhani, M., "Natural Convection in Porous Media," *J. Fluid Mech.*, Vol. 150, 1985, pp. 89-119.

5 Chan, Y. T., and Banerjee, S., "Analysis of Transient Three-Dimensional Natural Convection in Porous Media," ASME JOURNAL OF HEAT TRANSFER, Vol. 103, 1981, pp. 242-248.

6 Cambarnous, M., "Convection Naturelle et Convection Mixte en Milieu Poreux," Thesis, University of Paris, 1970.

7 Buretta, R. A., "Thermal Convection in a Fluid Filled Porous Layer With Uniform Internal Heat Sources," Ph.D. Thesis, University of Minnesota, Aug. 1972.

8 Schneider, K. J., "Die Warmeleitfahigkeit korniger Stoffe und ihre Beeinflussung durch freie Konvektion," Thesis, University of Karlsruhe, 1963.

9 Yagi, S., and Kunii, D., "Studies on Effective Thermal Conductivities in Packed Beds," *J. Am. Inst. Chem. Engrs.*, Vol. 3, 1957, pp. 373-381.

10 Yagi, S., Kunii, D., and Wakao, N., "Radially Effective Thermal Conductivities in Packed Beds," *International Developments in Heat Transfer*, 1961, pp. 742-749.

11 Barker, J. J., "Heat Transfer in Packed Beds," *Ind. Eng. Chem.*, Vol. 57, 1965, pp. 43-51.

12 Wyllie, M. J. R., and Gregory, A. R., "Fluid Flow Through Unconsolidated Porous Aggregates," *Ind. and Engng. Chem.*, Vol. 47, 1955, pp. 1379-1388.

Simultaneous Radiation and Forced Convection in Thermally Developing Turbulent Flow Through a Parallel-Plate Channel

Y. Yener[1] and M. N. Özişik[2]

Introduction

Most of the work on the interaction of radiation with turbulent forced convection inside ducts is concerned either with

[1]Mechanical Engineering Department, Northeastern University, Boston, MA 02115.

[2]Mechanical and Aerospace Engineering Department, North Carolina State University, Raleigh, NC 27695, Fellow ASME.

Contributed by the Heat Transfer Division for publication in the JOURNAL OF HEAT TRANSFER. Manuscript received by the Heat Transfer Division January 14, 1985.

thermally fully developed flows or an absorbing-emitting fluid [1–8]. Simultaneous radiation and turbulent forced convection for an absorbing, emitting, isotropically scattering, thermally developing flow inside a parallel-plate channel with reflecting isothermal surfaces has been reported only very recently [9]. However, due to an error in the numerical computations the results of that work are in error. Therefore, we present here the correct results.

Analysis

Consider a thermally developing steady turbulent flow of an absorbing, emitting, isotropically scattering, gray fluid between two parallel plates separated by a distance $2L$. The channel walls are assumed to be gray, opaque, and diffuse; have an emissivity ϵ and a reflectivity ρ; and are maintained at uniform temperature T_W. The fluid enters the heated (or cooled) section of the channel at the origin of the axial coordinate $x=0$ at a uniform temperature T_i, and with a fully developed turbulent flow velocity profile $u(y)$. Assuming constant thermophysical properties for the fluid and neglecting viscous dissipation as well as axial conduction and axial radiation, the energy equation can be written, in dimensionless form, as

$$w(\eta)\frac{\partial\theta}{\partial\xi}=\frac{\partial}{\partial\eta}\left[\bar{\epsilon}(\eta)\frac{\partial\theta}{\partial\eta}\right]-\frac{\tau_0}{N_{CR}}\frac{\partial Q^r}{\partial\eta} \tag{1}$$

where various dimensionless parameters are defined as

$$\eta=\frac{y}{L},\ \xi=\frac{16}{C}\frac{x/D_e}{\mathrm{RePr}},\ D_e=4L,\ \mathrm{Re}=\frac{U_mD_e}{\nu},\ \mathrm{Pr}=\frac{\nu}{\alpha}$$

$$w(\eta)=\frac{u}{U_{\max}},\ C=\frac{U_{\max}}{U_m},\ \bar{\epsilon}(\eta)=1+\frac{\epsilon_H}{\alpha},\ \theta(\xi,\eta)=\frac{T(\xi,\eta)}{T_w}$$

$$\tau_0=(\kappa+\sigma)L,\ N_{CR}=\frac{k(\kappa+\sigma)}{4n^2\bar{\sigma}T_w^{\,3}},\ Q^r(\xi,\eta)=\frac{q^r(\xi,\eta)}{4n^2\bar{\sigma}T_w^{\,4}}$$

with k, α, ϵ_H, ν, n, κ, and σ being the thermal conductivity, thermal diffusivity, eddy diffusivity, kinematic viscosity, refractive index, absorption coefficient, and scattering coefficient of the fluid, respectively. In addition, q^r represents the y component of the radiative heat flux in the fluid; U_m and $U_{\max}$ are the mean and maximum flow velocities, respectively. Furthermore, $\bar{\sigma}$ is the Stefan–Boltzmann constant.

The inlet and boundary conditions, in dimensionless form, are

$$\theta(0,\ \eta)\ =\ \theta_i=T_i/T_w \tag{2a}$$

$$\frac{\partial\theta(\xi,\ 0)}{\partial\eta}\ =\ 0 \tag{2b}$$

$$\theta(\xi,\ 1)\ =\ 1 \tag{2c}$$

Following Azad and Modest [6] the following three-layer turbulent velocity profile for fully developed flow is used

$$u^+\ =\ y^+,\ 0<y^+<5 \tag{3a}$$

$$u^+\ =\ 5.0\ln y^+-3.05,\ 5<y^+<30 \tag{3b}$$

$$u^+\ =\ 5.5+2.5\ln\left[y^+\frac{1.5\ (1+\eta)}{1+2\eta^2}\right],\ y^+>30 \tag{3c}$$

The eddy viscosity is described by the following two-layer model

$$\frac{\epsilon_M}{\nu}=\frac{k}{E}\left[e^{ku^+}-1-ku^+-\frac{(ku^+)^2}{2!}-\frac{(ku^+)^3}{3!}\right],\ y^+<40 \tag{4a}$$

$$\frac{\epsilon_M}{\nu}=\frac{kR^+}{6}[1-\eta^2][1+2\eta^2],\ y^+\geq 40 \tag{4b}$$

where $k=0.407$ and $E=10$. In the above relations various dimensionless quantities are defined as

$$u^+=\frac{u}{U_m\sqrt{f/8}},\ y^+=(1-\eta)R^+,\ R^+=\frac{\mathrm{Re}}{4}\sqrt{\frac{f}{8}}$$

where f is the friction factor, which is calculated in such a way that

$$\frac{4}{\mathrm{Re}}\int_0^{R^+}u^+dy^+=1 \tag{5}$$

is satisfied for each Reynolds number.

Furthermore, the eddy diffusivity ϵ_H is calculated by the standard assumption that the turbulent Prandtl number is approximately equal to unity.

The solution of equation (1) is much more sensitive to $\bar{\epsilon}(\eta)$ than $w(\eta)$ [10]. In this work, therefore, a power law profile is chosen for $w(\eta)$; that is, $w(\eta)=(1-\eta)^{1/m}$ so that $C=U_{\max}/U_m=(1+m)/m$. The exponent m is determined by fitting $w(\eta)$ to the velocity profile given by equations (3) for different Re and Pr numbers. However, the $\bar{\epsilon}(\eta)$ profile is determined as described by equations (4) together with equations (3).

The dimensionless radiative heat flux is defined as

$$Q^r(\xi,\ \eta)=\frac{1}{2}\int_{-1}^{1}\psi(\xi,\ \eta,\ \mu')\mu'd\mu' \tag{6}$$

where the dimensionless radiation intensity $\psi(\xi,\ \eta,\ \mu)$ satisfies the equation of radiative transfer given in the form

$$\frac{\mu}{\tau_0}\frac{\partial\psi}{\partial\eta}+\psi(\xi,\ \eta,\ \mu)=(1-\omega)\theta^4(\xi,\ \eta)+\frac{\omega}{2}\int_{-1}^{1}\psi(\xi,\ \eta,\ \mu')d\mu' \tag{7}$$

Assuming that both plates have the same radiative properties, the boundary conditions for equation (7) are given by

$$\psi(\xi,\ 0,\ \mu)=\psi(\xi,\ 0,\ -\mu),\ \mu>0 \tag{8a}$$

$$\psi(\xi,\ 1,\ -\mu)=\epsilon+2\rho\int_0^1\psi(\xi,\ 1,\ \mu')\mu'd\mu',\ \mu>0 \tag{8b}$$

where ϵ and ρ are the emissivity and reflectivity of the boundaries, ω is the single-scattering albedo, $[\omega=\sigma/(\kappa+\sigma)]$, and μ is the direction cosine (as measured from the positive y axis) of the propagating radiation.

Method of Solution

An iterative scheme is used to solve the problem as described in [9], while the radiation problem defined by equations (7) and (8) is solved by the procedure discussed in [11]. Once the temperature distribution $\theta(\xi,\ \eta)$ and the radiation flux $Q^r(\xi,\ \eta)$ are available, the local Nusselt number is determined from its definition

$$\mathrm{Nu}(\xi)=\frac{4}{\theta_b(\xi)-1}\left[-\frac{\partial\theta(\xi,\ 1)}{\partial\eta}+\frac{\tau_0}{N_{CR}}Q^r(\xi,\ 1)\right] \tag{9}$$

where $\theta_b=T_b/T_w$ is the dimensionless local fluid bulk temperature.

Results and Discussion

We now present some representative results to illustrate the effects of the parameters ω, τ_0, ρ, and N_{CR} on the local Nusselt number for the case $\mathrm{Re}=10^5$, $\mathrm{Pr}=1$. Results for other Reynolds and Prandtl numbers follow qualitatively the same behavior. Figure 1 shows the effect of the optical thickness τ_0 on the local Nusselt number. Clearly, the Nusselt number increases with increasing optical thickness of the medium. The effects of the conduction-to-radiation parameter N_{CR} are shown in Fig. 2. With decreasing N_{CR} the radiation increases, which in turn increases the Nusselt number and the effect is more pronounced in the thermally developed region. Figure 3 shows the effect of single-scattering albedo. Increasing ω decreases the coupling between radiation and conduction,

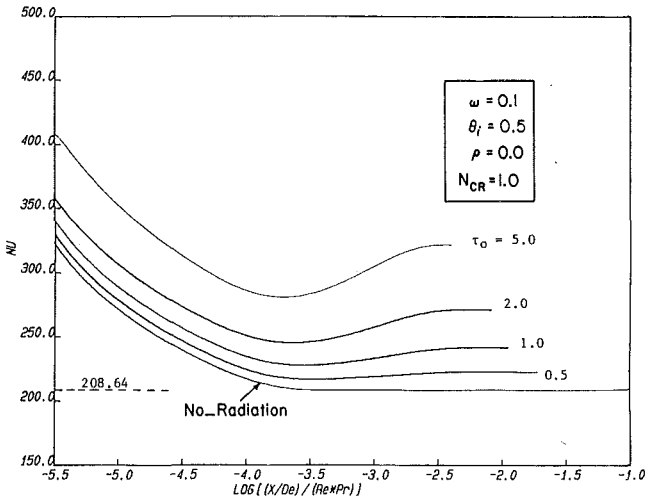

Fig. 1 Effect of optical thickness on the local Nusselt number; $Re = 10^5$, $Pr = 1$

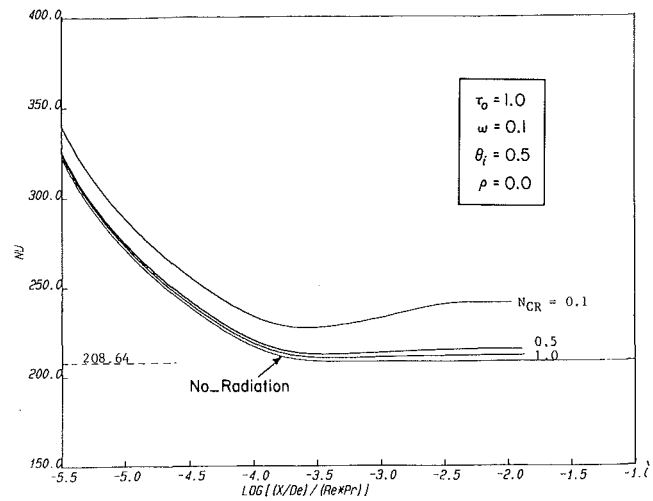

Fig. 2 Effect of conduction-radiation parameter on the local Nusselt number: $Re = 10^5$, $Pr = 1$

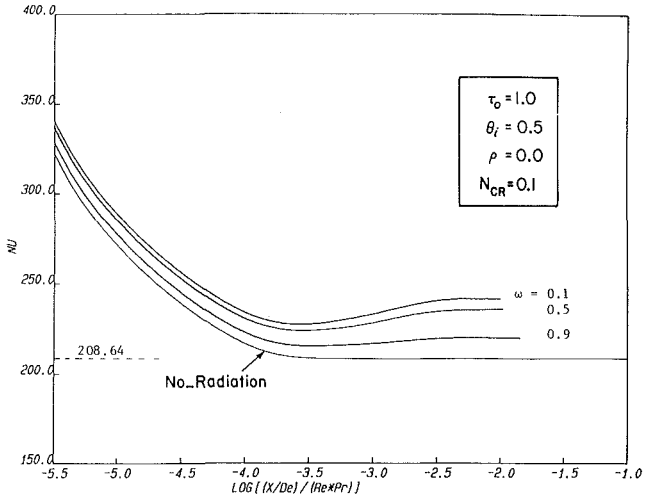

Fig. 3 Effect of single-scattering albedo on the local Nusselt number; $Re = 10^5$, $Pr = 1$

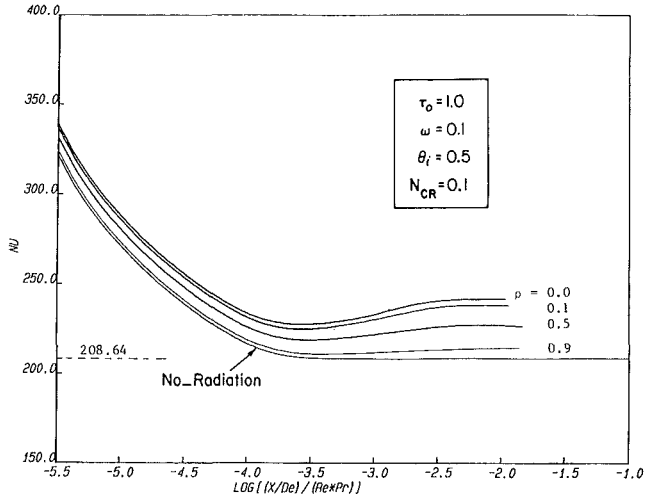

Fig. 4 Effect of reflectivity on the local Nusselt number; $Re = 10^5$, $Pr = 1$

hence the Nusselt number approaches that of nonradiating flow. Finally, Fig. 4 shows the effects of wall reflectivity on Nusselt number. As reflectivity approaches unity, the Nusselt number approaches that of nonradiating flow.

In all the results presented above, where $\theta_i = 0.5$, the local Nusselt number exhibits a minimum at certain downstream locations. As the radiation effects increase, the minimum point shifts towards the inlet section. Similar behavior has been observed for turbulent [2, 6, 8] and laminar flows [12–16]. A physical interpretation of this observation has been given in [6]. Although the results are not given here, for the case of hot fluid ($\theta_i > 1$), the local Nusselt number curves do not go through a minimum, because the effect of radiation diminishes with axial distance as the fluid temperature decreases along the channel. However, the presence of radiation still results in Nusselt numbers which are higher than the no-radiation case.

Acknowledgments

This project was supported in part by a grant from Northeastern University's Research and Scholarship Development Fund.

References

1 Edwards, D. K., and Balakrishnan, A., "Nongray Radiative Transfer in a Turbulent Gas Layer," *Int. J. Heat Mass Transfer*, Vol. 16, 1973, pp. 1003–1015.

2 Tamehiro, H., Echigo, R., and Hasegawa, S., "Radiative Heat Transfer by Flowing Multiphase Medium – Part III. An Analysis on Heat Transfer of Turbulent Flow in a Circular Tube," *Int. J. Heat Mass Transfer*, Vol. 16, 1973, pp. 1199–1213.

3 Edwards, D. K., and Balakrishnan, A., "Self-Absorption of Radiation in Turbulent Molecular Gases," *Combustion and Flame*, Vol. 20, 1973, pp. 401–417.

4 Balakrishnan, A., and Edwards, D. K., "Established Laminar and Turbulent Channel Flow of a Radiating Molecular Gas," *Heat Transfer 1974*, Vol. 1, Fifth Int. Heat Transfer Conference, Tokyo, Sept. 1974, pp. 93–97.

5 Wassel, A. T., and Edwards, D. K., "Molecular Radiation in a Laminar or Turbulent Pipe Flow," ASME JOURNAL OF HEAT TRANSFER, Vol. 98, 1976, pp. 101–107.

6 Azad, F. H., and Modest, F. F., "Combined Radiation and Convection in Absorbing, Emitting and Anisotropically Scattering Gas-Particulate Tube Flow," *Int. J. Heat Mass Transfer*, Vol. 24, 1981, pp. 1681–1697.

7 Im, K. H., and Ahluwalia, R. K., "Combined Convection and Radiation in Rectangular Ducts," ASME Paper No. 82-HT-48.

8 Smith, T. F., and Shen, Z. F., " Radiative and Convective Transfer in a Cylindrical Enclosure," ASME Paper No. 83-HT-53.

9 Yener, Y., Shahidi-Zandi, and Ozisik, M. N., "Simultaneous Radiation and Forced Convection in Thermally Developing Turbulent Flow Through a Parallel-Plate Channel," ASME Paper No. 84-WA/HT-15.

10 Notter, R. H., and Sleicher, C. A., "The Eddy Diffusivity in the Turbulent Boundary Layer Near a Wall," *Chemical Engineering Science*, Vol. 26, 1971, pp. 161–171.

11 Ozisik, M. N., and Yener, Y., "The Galerkin Method for Solving Radiation Transfer in Plane-Parallel Participating Media," ASME JOURNAL OF HEAT TRANSFER, Vol. 104, 1982, pp. 351–354.

12 Echigo, R., and Hasegawa, S., "Radiative Heat Transfer by Flowing

Multiphase Medium – Part I. An Analysis on Heat Transfer of Laminar Flow Between Parallel Flat Plates," *Int. J. Heat Mass Transfer*, Vol. 15, 1972, pp. 2519-2534.

13 Lii, C. C., and Ozisik, M. N., "Heat Transfer in an Absorbing, Emitting and Scattering Slug Flow Between Parallel Plates," ASME JOURNAL OF HEAT TRANSFER, Vol. 95, 1973, pp. 538-540.

14 Chawla, T. C., and Chan, S. H., "Spline Collocation Solution of Combined Radiation, Convection in Thermally Developing Flows With Scattering," *Numerical Heat Transfer*, Vol. 3, 1980, pp. 47-65.

15 Chawla, T. C., and Chan, S. H., "Combined Radiation and Convection in Thermally Developing Poiseuille Flow with Scattering," ASME JOURNAL OF HEAT TRANSFER, Vol. 102, 1980, pp. 297-302.

16 Menguc, M. P., Yener, Y., and Ozisik, M. N., "Interaction of Radiation and Convection in Thermally Developing Laminar Flow in a Parallel-Plate Channel," ASME Paper No. 83-HT-35.

On the Mean Period of Dryout Point Fluctuations

B. T. Beck[1] and G. L. Wedekind[2]

Introduction

The mixture-vapor transition point (liquid dryout point), encountered in horizontal tube evaporators and other types of once-through vapor generators where complete vaporization occurs, has previously been shown [1] to exhibit random fluctuations, even under what would otherwise be considered steady-state conditions. Such fluctuations can affect the dynamic behavior of downstream sensors associated with process control, and may play an important role in evaporator thermal fatigue. The fluctuations may also influence the extent of regions over which salts are deposited in certain types of once-through evaporators.

Measurements of the dryout point position probability density and distribution functions have been made for flow of Refrigerant-12 in a uniformly heated horizontal serpentine tube evaporator [1]. Furthermore, a theoretical model [2] has been developed to predict the influence of applied heat flux and inlet flow quality on these statistical characteristics. The influence of such fluctuations on other two-phase evaporating flow phenomena has also been investigated to some extent [3, 4]. However, very little information has been reported regarding the time period of these dryout point fluctuations, or the influence of important physical parameters on the fluctuation period. The purpose of this paper is to extend previous experimental and theoretical investigations of the statistical characteristics of dryout point fluctuations to include, in particular, the influence of applied heat flux and inlet flow quality on the mean period of the fluctuations.

Probability Theory

Under steady-state conditions the random process associated with the motion of the dryout point is considered to be stationary and ergodic. Consider a large number N of similar but independent evaporators functioning simultaneously under identical controlled operating conditions. Now, as suggested in Fig. 1, all such evaporators having dryout point position η within the interval $\bar{\eta} - vdt < z < \bar{\eta}$, and moving with speed $v > 0$, will cross the mean position $\bar{\eta}$ in the time interval dt. Thus, the average number of the N dryout points moving with positive speeds in the interval v to $v + dv$ that will cross the mean position in time dt is

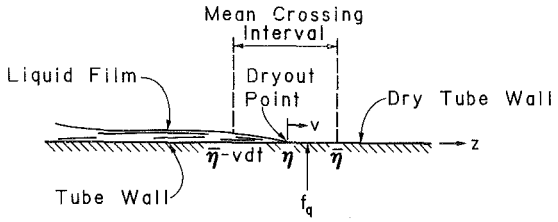

Fig. 1 Schematic of dryout point mean crossing interval

$$N\int_{\bar{\eta}-vdt}^{\bar{\eta}} f(\eta, v)d\eta dv = Nf(\bar{\eta}, v)vdvdt \tag{1}$$

where $f(\eta, v)$ is the joint probability density function for the random variables η and $v = d\eta/dt$. Integrating over all speeds $v > 0$ then yields the following expression for the average number of dryout points to cross the mean in time dt with any positive speed

$$dn = Ndt\int_{v=0}^{\infty} vf(\bar{\eta}, v)dv \tag{2}$$

Thus, the average number of mean crossings or overshoots [5, 7] per unit time per evaporator is given by

$$\bar{\nu} = \frac{1}{N}\frac{dn}{dt} = \int_{v=0}^{\infty} vf(\bar{\eta}, v)dv \tag{3}$$

where $\bar{\nu}$ is the average mean-crossing frequency of the dryout point fluctuations.

The average mean-crossing frequency is very simply related to the mean fluctuation period. First, consider a large number M of fluctuations about the mean dryout point position. Let M be sufficiently large so that a given fluctuation period T_i is negligible in comparison to the total time T_0 during which the fluctuations took place. The mean period is thus given by

$$\bar{T} \equiv \frac{1}{M}\sum_{i=1}^{M} T_i = T_0/M \tag{4}$$

However, in terms of the crossing frequency, $M = \bar{\nu}T_0$; thus

$$\bar{T} = T_0/M = T_0/\bar{\nu}T_0 = 1/\bar{\nu} \tag{5}$$

or, in other words, the mean period is just the inverse of the average mean-crossing frequency, as would also be the case if the fluctuations were deterministically periodic.

It will now be assumed that the dryout point position and speed are independent random variables[3]; then

$$f(\eta, v) = f_\eta(\eta) \cdot f_v(v) \tag{6}$$

where f_η and f_v are the marginal probability density functions for η and v, respectively. Substituting equation (6) into equation (3) yields

$$\bar{\nu} = \int_{v=0}^{\infty} vf_\eta(\bar{\eta}) \cdot f_v(v)dv = f_\eta(\bar{\eta})\int_{v=0}^{\infty} vf(v)dv \tag{7}$$

The integral appearing in equation (7) may be rearranged as follows

$$\int_{v=0}^{\infty} vf_v(v)dv = \left\{\int_{v=0}^{\infty} f_v(v)dv\right\} \cdot \left\{\int_{v=0}^{\infty} vf_v(v)dv \Big/ \int_{v=0}^{\infty} f_v(v)dv\right\} = p_+\bar{v}_+ \tag{8}$$

where p_+ is the probability of advancing and $\bar{v}_+$ is the average positive speed. Substituting equation (8) into (7) and introducing the result into equation (5) yields the following expression for the mean period of the dryout point fluctuations:

$$\bar{T} = 1/p_+\bar{v}_+ f_\eta(\bar{\eta}) \tag{9}$$

[1]Associate Professor of Mechanical Engineering, Kansas State University, Manhattan, KS; Mem. ASME.

[2]Professor of Engineering, Oakland University, Rochester, MI; Mem. ASME.

Contributed by the Heat Transfer Division for publication in the JOURNAL OF HEAT TRANSFER. Manuscript received by the Heat Transfer Division August 24, 1984.

[3]Position and speed are uncorrelated; however, independence is rigorously true only for a normal random process [5] and is assumed here for simplicity.

Multiphase Medium – Part I. An Analysis on Heat Transfer of Laminar Flow Between Parallel Flat Plates," *Int. J. Heat Mass Transfer*, Vol. 15, 1972, pp. 2519-2534.

13 Lii, C. C., and Ozisik, M. N., "Heat Transfer in an Absorbing, Emitting and Scattering Slug Flow Between Parallel Plates," ASME JOURNAL OF HEAT TRANSFER, Vol. 95, 1973, pp. 538-540.

14 Chawla, T. C., and Chan, S. H., "Spline Collocation Solution of Combined Radiation, Convection in Thermally Developing Flows With Scattering," *Numerical Heat Transfer*, Vol. 3, 1980, pp. 47-65.

15 Chawla, T. C., and Chan, S. H., "Combined Radiation and Convection in Thermally Developing Poiseuille Flow with Scattering," ASME JOURNAL OF HEAT TRANSFER, Vol. 102, 1980, pp. 297-302.

16 Menguc, M. P., Yener, Y., and Ozisik, M. N., "Interaction of Radiation and Convection in Thermally Developing Laminar Flow in a Parallel-Plate Channel," ASME Paper No. 83-HT-35.

On the Mean Period of Dryout Point Fluctuations

B. T. Beck[1] and G. L. Wedekind[2]

Introduction

The mixture-vapor transition point (liquid dryout point), encountered in horizontal tube evaporators and other types of once-through vapor generators where complete vaporization occurs, has previously been shown [1] to exhibit random fluctuations, even under what would otherwise be considered steady-state conditions. Such fluctuations can affect the dynamic behavior of downstream sensors associated with process control, and may play an important role in evaporator thermal fatigue. The fluctuations may also influence the extent of regions over which salts are deposited in certain types of once-through evaporators.

Measurements of the dryout point position probability density and distribution functions have been made for flow of Refrigerant-12 in a uniformly heated horizontal serpentine tube evaporator [1]. Furthermore, a theoretical model [2] has been developed to predict the influence of applied heat flux and inlet flow quality on these statistical characteristics. The influence of such fluctuations on other two-phase evaporating flow phenomena has also been investigated to some extent [3, 4]. However, very little information has been reported regarding the time period of these dryout point fluctuations, or the influence of important physical parameters on the fluctuation period. The purpose of this paper is to extend previous experimental and theoretical investigations of the statistical characteristics of dryout point fluctuations to include, in particular, the influence of applied heat flux and inlet flow quality on the mean period of the fluctuations.

Probability Theory

Under steady-state conditions the random process associated with the motion of the dryout point is considered to be stationary and ergodic. Consider a large number N of similar but independent evaporators functioning simultaneously under identical controlled operating conditions. Now, as suggested in Fig. 1, all such evaporators having dryout point position η within the interval $\bar{\eta} - vdt < z < \bar{\eta}$, and moving with speed $v > 0$, will cross the mean position $\bar{\eta}$ in the time interval dt. Thus, the average number of the N dryout points moving with positive speeds in the interval v to $v + dv$ that will cross the mean position in time dt is

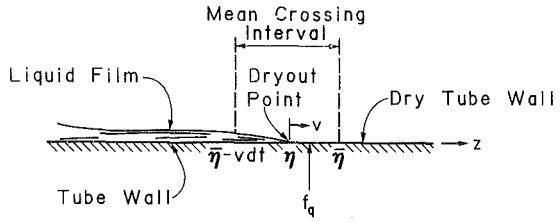

Fig. 1 Schematic of dryout point mean crossing interval

$$N\int_{\bar{\eta}-vdt}^{\bar{\eta}} f(\eta, v)d\eta dv = Nf(\bar{\eta}, v)vdvdt \tag{1}$$

where $f(\eta, v)$ is the joint probability density function for the random variables η and $v = d\eta/dt$. Integrating over all speeds $v > 0$ then yields the following expression for the average number of dryout points to cross the mean in time dt with any positive speed

$$dn = Ndt\int_{v=0}^{\infty} vf(\bar{\eta}, v)dv \tag{2}$$

Thus, the average number of mean crossings or overshoots [5, 7] per unit time per evaporator is given by

$$\bar{\nu} = \frac{1}{N}\frac{dn}{dt} = \int_{v=0}^{\infty} vf(\bar{\eta}, v)dv \tag{3}$$

where $\bar{\nu}$ is the average mean-crossing frequency of the dryout point fluctuations.

The average mean-crossing frequency is very simply related to the mean fluctuation period. First, consider a large number M of fluctuations about the mean dryout point position. Let M be sufficiently large so that a given fluctuation period T_i is negligible in comparison to the total time T_0 during which the fluctuations took place. The mean period is thus given by

$$\bar{T} \equiv \frac{1}{M}\sum_{i=1}^{M} T_i = T_0/M \tag{4}$$

However, in terms of the crossing frequency, $M = \bar{\nu}T_0$; thus

$$\bar{T} = T_0/M = T_0/\bar{\nu}T_0 = 1/\bar{\nu} \tag{5}$$

or, in other words, the mean period is just the inverse of the average mean-crossing frequency, as would also be the case if the fluctuations were deterministically periodic.

It will now be assumed that the dryout point position and speed are independent random variables[3]; then

$$f(\eta, v) = f_\eta(\eta) \cdot f_v(v) \tag{6}$$

where f_η and f_v are the marginal probability density functions for η and v, respectively. Substituting equation (6) into equation (3) yields

$$\bar{\nu} = \int_{v=0}^{\infty} vf_\eta(\bar{\eta}) \cdot f_v(v)dv = f_\eta(\bar{\eta})\int_{v=0}^{\infty} vf(v)dv \tag{7}$$

The integral appearing in equation (7) may be rearranged as follows

$$\int_{v=0}^{\infty} vf_v(v)dv = \left\{\int_{v=0}^{\infty} f_v(v)dv\right\} \cdot \left\{\int_{v=0}^{\infty} vf_v(v)dv \Big/ \int_{v=0}^{\infty} f_v(v)dv\right\} = p_+\bar{v}_+ \tag{8}$$

where p_+ is the probability of advancing and $\bar{v}_+$ is the average positive speed. Substituting equation (8) into (7) and introducing the result into equation (5) yields the following expression for the mean period of the dryout point fluctuations:

$$\bar{T} = 1/p_+\bar{v}_+ f_\eta(\bar{\eta}) \tag{9}$$

[1]Associate Professor of Mechanical Engineering, Kansas State University, Manhattan, KS; Mem. ASME.

[2]Professor of Engineering, Oakland University, Rochester, MI; Mem. ASME.

Contributed by the Heat Transfer Division for publication in the JOURNAL OF HEAT TRANSFER. Manuscript received by the Heat Transfer Division August 24, 1984.

[3]Position and speed are uncorrelated; however, independence is rigorously true only for a normal random process [5] and is assumed here for simplicity.

Now, in order to determine the influence of important evaporator parameters on the mean period it is necessary to introduce information about the known statistical characteristics of the dryout point position. Previous experimental work [1] has shown that the probability density for the dryout point position is well represented by the following transformed Rayleigh density function[4]:

$$f_\eta(\eta) = \frac{2}{\gamma}(\beta - \eta)e^{-(\beta-\eta)^2/\gamma} \tag{10}$$

where

$$\beta \equiv \frac{1}{2}(\pi\gamma)^{1/2} + \bar{\eta} \tag{11}$$

$$\gamma \equiv 4\sigma_\eta^2/(4-\pi) \tag{12}$$

and where σ_η is the standard deviation of the dryout point fluctuations. From equations (10), (11), and (12)

$$f_\eta(\bar{\eta}) = \frac{2}{\gamma}(\beta - \bar{\eta})e^{-(\beta-\bar{\eta})^2/\gamma} = e^{-\pi/4}[\pi(4-\pi)]^{1/2}/2\sigma_\eta \tag{13}$$

Substituting equation (13) into (9) gives the following

$$\bar{T} = 2\sigma_\eta/p_+\bar{v}_+ e^{-\pi/4}[\pi(4-\pi)]^{1/2} \tag{14}$$

Equation (14) suggests that the mean period is proportional to the standard deviation of the dryout point fluctuations. From previous analysis of the statistical characteristics of the dryout point fluctuations, a theoretical model [2] has been proposed for the influence of heat flux and inlet flow quality on this standard deviation. The model may be expressed in the following form

$$\sigma_\eta = \frac{(1-\alpha_i)m_{ti}h_{fg}\sigma_x}{(1-\bar{\alpha})f_q P} \tag{15}$$

where α_i is the inlet void fraction, h_{fg} is the heat of vaporation, $\bar{\alpha}$ is the time-averaged system mean void fraction, P is the tube inside perimeter and σ_x is the standard deviation of the mean flow quality perturbation. Experimental evidence [2] has shown that the parameter σ_x is approximately independent of both heat flux f_q and inlet flow quality x_i for a given total inlet mass flowrate m_{ti}, mean system pressure $\bar{p}$, fluid and evaporator geometry; very limited informatoin is currently available regarding the influence of these latter four parameters. Substituting equation (15) into (14) completes the development of the model for the mean period, yielding

$$\bar{T} = \frac{2e^{\pi/4}(1-\alpha_i)m_{ti}h_{fg}\sigma_x}{[\pi(4-\pi)]^{1/2}(1-\bar{\alpha})f_q P\, p_+ \bar{v}_+} \tag{17}$$

Experimental Results

Experimental measurements of the mean period of the dryout point fluctuations were determined from the previously obtained photographic data [1] on dryout point position versus time. These measurements represent the accumulation of 25 different tests, each of which typically yielded a sample of about 30 individual fluctuation periods; a period being determined numerically as the time between two successive positive crossings of the mean dryout point position. The mean fluctuation period was then determined simply as the arithmetic average of the individual periods. The experimental tests involved the same evaporator geometry, the same refrigerant and total mass flow rate, but were for a variety of heat fluxes and inlet flow qualities. The evaporator geometry consisted of five 1.8 m (6 ft) long, 0.742 cm (0.292 inch) i.d. horizontal borosilicate glass tubes arranged in a serpentine configuration. Refrigerant-12 was used at a flow rate of 0.82 kg/min (1.8 lbm/min). Inlet flow qualities and heat fluxes ranged from 0–29 percent and 10–29 kW/m^2 (3200–9100 Btu/hr-ft^2), respectively.

Comparison between the measured mean fluctuation period data and the predictions of the proposed model given in equation (17) requires knowledge of the three parameters σ_x, p_+, and $\bar{v}_+$. The mean flow quality perturbation σ_x has previously been shown [2] to have an approximately constant value of $\sigma_x = 0.00775$ for the entire range of test conditions indicated above. Unfortunately little data are currently available with regard to the statistical characteristics of the time derivative, or speed, of the dryout point position. Furthermore, such data would be difficult to obtain owing to the problems associated with accurately differentiating the discrete photographic dryout point data. Equation (14), however, provides a means of obtaining the required parameters, as they appear together in product form $p_+\bar{v}_+$, thorough comparison of mean period data with the corresponding standard deviation of the fluctuations. Figure 2 shows a plot of standard deviation of the dryout point fluctuations as a function of mean period for the entire set of 25 tests described above. As is apparent from the

[4] A more detailed discussion of this transformation, and its applicability to the dryout point position random variable is given in [1].

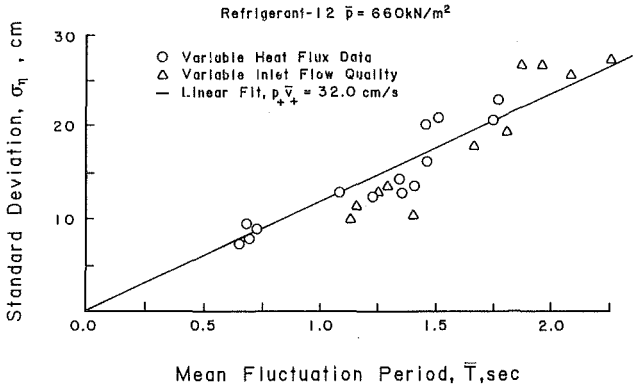

Fig. 2 Relationship between standard deviation and mean period

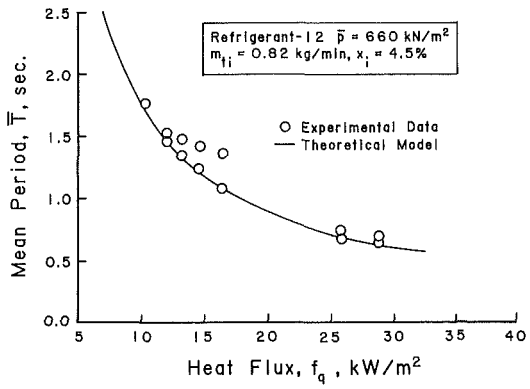

Fig. 3 Influence of heat flux on mean period

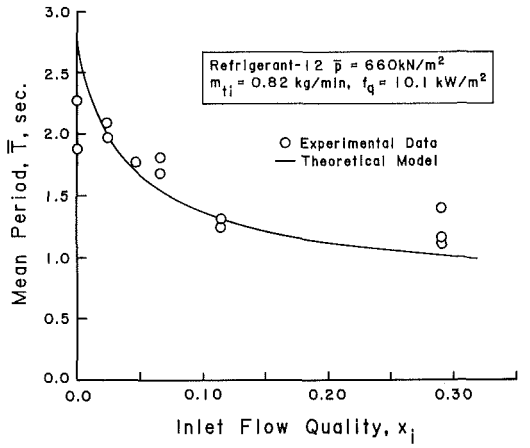

Fig. 4 Influence of inlet flow quality on mean period

figure, the data are quite well represented by a simple linear relationship corresponding to the constant value $p_+ \bar{v}_+ = 32.0$ cm/s. Thus, the parameter group $p_+ \bar{v}_+$ also appears to be approximately independent of both heat flux and inlet flow quality.

The capability of the proposed model to predict the influence of both heat flux and inlet flow quality, as expressed by equation (17), is demonstrated in Figs. 3 and 4, respectively. The void fraction relationship used in conjunction with the proposed model was that proposed by Fujie [6]. This relationship has been shown to be in reasonable agreement with measured void fraction data for Refrigerant-12 flowing in horizontal tubes, and was used in a previous theoretical analysis of the dryout point motion [2]. Both data and theory indicate that the fluctuation period decreases with increasing heat flux as well as with increasing inlet flow quality. Furthermore, the agreement between theoretical predictions and experimental data is quite good; this is particularly evident when one considers the possible uncertainties in measuring the physical parameters used in the model.

Conclusions

The proposed model for mean period provides additional insight into the important physical parameters influencing the statistical characteristics of dryout point fluctuations. A very simple relationship has been indicated between the mean fluctuation period and the standard deviation of the dryout point position, from which it is possible to predict quantitatively the influence of both heat flux and inlet flow quality. Furthermore, the expermental data suggest that, in principle, the parameters σ_x and $p_+ \bar{v}_+$ could be derived from but a single experimental test. Once these parameters have been established, the theoretical model thus provides the capability to predict the mean fluctuation period over a wide range of operating conditions. The extent to which the proposed model will be applicable to other mass flow rates, mean system pressures, fluids and evaporator geometries will require further investigation.

References

1 Wedekind, G. L., "An Experimental Investigation Into the Oscillatory Motion of the Mixture-Vapor Transition Point in Horizontal Evaporating Flow," ASME JOURNAL OF HEAT TRANSFER, Vol. 93, 1971, pp. 47–54.

2 Wedekind, G. L., and Beck, B. T., "Theoretical Model of the Mixture-Vapor Transition Point Oscillations Associated With Two-Phase Evaporating Flow Instabilities," ASME JOURNAL OF HEAT TRNSFER, Vol. 96, 1974, pp. 138–144.

3 Wedekind, G. L., and Beck, B. T., "Correlation Between Outlet Flowrate and Mixture-Vapor Transition Point Oscillations in Two-Phase Evaporating Flow," *Proceedings of the Fifth International Heat Transfer Conference*, Tokyo, Japan, Vol. IV, Sept. 1974, pp. 220–224.

4 Saito, T., Uchida, H., and Hiraoka, E., "Unsteady Characteristics of Two Phase Flow in a Horizontal Tube Evaporation," *Proceedings of the Fifth International Heat Transfer Conference*, Tokyo, Japan, Vol. IV, Sept. 1974, pp. 210–214.

5 Sveshnikov, A. A., *Applied Methods of the Theory of Random Functions*, Pergamon Press, 1966, pp. 69–80.

6 Fujie, H., "A Relation Between Steam Quality and Void Fraction in Two-Phase Flow," *AIChE Journal*, Vol. 10, No. 2, 1964, pp. 227–232.

7 Rice, S. O., "Mathematical Analysis of Random Noise," *Bell System Tech. Journal*, Vol. 25, 1945, pp. 46–156.